Decoding atrial fibrillation:
Personalized identification and quantification of electropathology

Mathijs S. van Schie

Decoding atrial fibrillation:

Personalized identifcation and quantification of electropathology

Mathijs S. van Schie

Decoding Atrial Fibrillation:
Personalized identification and quantification of electropathology

Ontcijferen van atriumfibrillatie:

Gepersonaliseerde identificatie en kwantificatie van elektropathologie

Proefschrift

ter verkrijging van de graad van doctor aan de
Erasmus Universiteit Rotterdam
op gezag van de
rector magnificus

Prof. dr. A.L. Bredenoord

en volgens besluit van het College voor Promoties.
De openbare verdediging zal plaatsvinden op

vrijdag 3 mei 2024 om 13:00 uur

door

Mathijs Sebastiaan van Schie
geboren te Almelo.

Erasmus University Rotterdam

Promotiecommissie

Promotor: Prof. dr. N.M.S. de Groot

Overige leden: Prof. dr. ir. A.F.W. van der Steen
Prof. dr. I.C. van Gelder
Prof. dr. ir. A.J. van der Veen

Copromotoren: Dr. M.C. Roos-Serote
Dr. Y.J.H.J. Taverne

List of contents

* Contributed equally

Chapter 1

General introduction

Mathijs S. van Schie

1

It remains challenging to design effective treatment strategies for persistent atrial fibrillation (AF), despite considerable technological advances in electrophysiological mapping-guided ablation strategies targeting AF over the past few years. This is mainly due to inadequate understanding of the mechanisms and electropathological substrate underlying AF. Cardiac mapping, which involves recording, processing and interpretation of atrial electrical activity, is essential to gain more insight into these mechanisms, improve (early) diagnosis and eventually develop better (ablation) therapies.[1,2] In the electrophysiology laboratory, analysis of electrograms (EGMs) plays an important role in adjunctive ablation strategies in addition to pulmonary vein isolation, particularly in patients with (long-standing) persistent AF.[3-6] However, electrical activity during AF is highly complex requiring advanced mapping systems with sophisticated processing technologies to quantify electropathology and identify suitable target sites for ablation. This chapter introduces the current challenges in AF treatment strategies, explores the technical aspects of electrophysiological mapping and discusses the current knowledge gaps in the quest to find quantified features of AF-related electropathology.

Atrial fibrillation: the cardiovascular epidemic of the 21st century

AF is the most common sustained cardiac arrhythmia worldwide, which is characterized by rapid and irregular electrical activity in the atria, resulting in an irregular and often fast heart rate.[7] On the surface electrocardiogram (ECG), regular and morphologically distinct P-waves are replaced by rapid continuous oscillations (fibrillatory waves), as illustrated in *Figure 1*.[7,8] Currently available diagnostic tools, such as surface ECGs, Holter recordings and implantable loop recorders, can detect and quantify the AF burden within a specific time frame, but none of these tools can identify or stage the substrate underlying AF. As such, only the presence of AF can be confirmed using these diagnostic tools.

Once AF is diagnosed, it is classified according to the time a patient is in AF and its response to therapy. AF is classified into paroxysmal, persistent, long-standing persistent or permanent. Paroxysmal AF episodes last for less than seven days and typically end spontaneously. Persistent AF, on the other hand, lasts longer than seven days and requires medical intervention to terminate. If persistent AF continues for more than a year, it is referred to as long-standing persistent AF. Finally, permanent AF indicates that the patient and physician have agreed to accept AF as a long-term condition.[7,8]

AF affects approximately 1–3% of the general population. In 2010, the estimated global prevalence of AF was 33.5 million people, with an annual incidence rate of 5 million people. The risk of developing AF increases significantly with age.[9] As AF can be often asymptomatic, the actual prevalence may be even higher. The incidence of AF varies considerably depending on underlying contributing factors. AF is primarily found in older individuals (>70 years) and those with lifestyle-related conditions such as hypertension, diabetes mellitus and obesity.[7] With increasing life expectancy globally, the prevalence of AF is also expected to rise sharply. AF also frequently occurs in patients with structural heart disease, which includes patients with heart failure with or without reduced ejection fraction, valvular heart disease and specific cardiomyopathies.[10,11] In these patients, atrial hypertension results in atrial dilation, extracellular matrix remodeling, autonomic imbalance and calcium handling defects, eventually resulting in initiation and perpetuation of AF.[12,13] Additionally, patients with a congenital heart disease also frequently develop AF, due to a combination of embryogenetic defects and factors related to surgical correction for their disease.[14] Post-operative AF is also common among patients undergoing cardiac surgery for structural heart disease, with reported incidences ranging from 20 to 80% depending on the type of surgery.[15] Post-operative AF is associated with an increased risk of mortality and
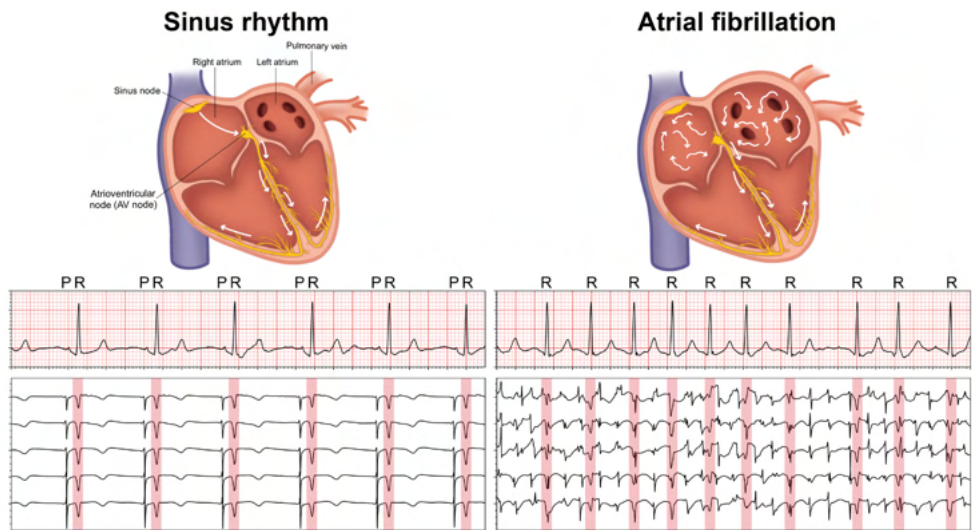
Figure 1 – Electrical conduction during sinus rhythm and atrial fibrillation. *Left panel*: during sinus rhythm an electrical pulse is generated in the sino-atrial node (SAN) and propagates through the right atrium towards the atrioventricular (AV) node and via the His-Purkinje fibers towards the ventricles (white arrows). The ECG (middle panel) shows P-waves (P) followed by a QRS-complex (R) with regular R-R intervals. Simultaneous recorded epicardial unipolar electrograms at Bachmann's bundle (lower panel) also show local atrial potentials with regular intervals followed by ventricular far-field (red). *Right panel*: during AF, activation of the atria is chaotic due to abnormal impulses within both atria. The AV node is continuously bombarded with impulses, creating a varying degree of concealed conduction. This leads to an irregular and often fast ventricular rate. The ECG (middle panel) shows irregular R-R intervals and no distinct P-waves. The epicardial unipolar electrograms recorded at the exact same location as during sinus rhythm (lower panel) now show beat-to-beat variation in intervals between consecutive fibrillation potentials and the morphology of those potentials.

morbidity, longer hospitalization and hence higher cost of post-operative care.[16-18] Taken the high prevalence and incidence rates of the arrhythmia, AF is considered the cardiovascular epidemic of the 21st century.

Improving AF therapy strategies: targeting triggers and substrates

The most optimal treatment strategy for AF remains unclear, although it is widely accepted that the initiation and perpetuation of AF requires triggers and a substrate, as illustrated in *Figure 2.* Currently, pharmacological anti-arrhythmic therapy of AF is aimed at either rate or rhythm control. Cardioversion can also be performed using a DC shock. Although AF episodes can be stopped often, the efficiency of these therapies is low and most of drugs have severe side-effects.[19] The initial nonpharmacological treatment strategy for AF involved catheter ablation of the atrioventricular junction.[20,21] Although this strategy has been very effective for rate control, it requires permanent pacemaker implantation as AF itself still persists. The main cause of failure of these therapies lies in the fact that both the triggers and substrates underlying AF are not affected. In the late 1980s, a surgical approach for AF treatment was developed by Cox et al.[22] which involved multiple incisions in the right and left atria. Although this is an often successful procedure, it is only most frequently applied as an add-on procedure during cardiovascular surgeries.[23] In 1998, human endocardial mapping studies showed that focal activity from the sleeves of the pulmonary veins may contribute to the onset and persistence of AF.[3] Cardiomyocyte fibers extending into the pulmonary veins are characterized by sudden changes in fiber orientation and a very short refractory period. This may contribute to focal activity, which may be due to triggered activity, enhanced automaticity or micro-reentry.[24,25] This observation led to the development of pulmonary vein isolation (PVI) as a strategy for catheter ablation of AF, which is still the cornerstone
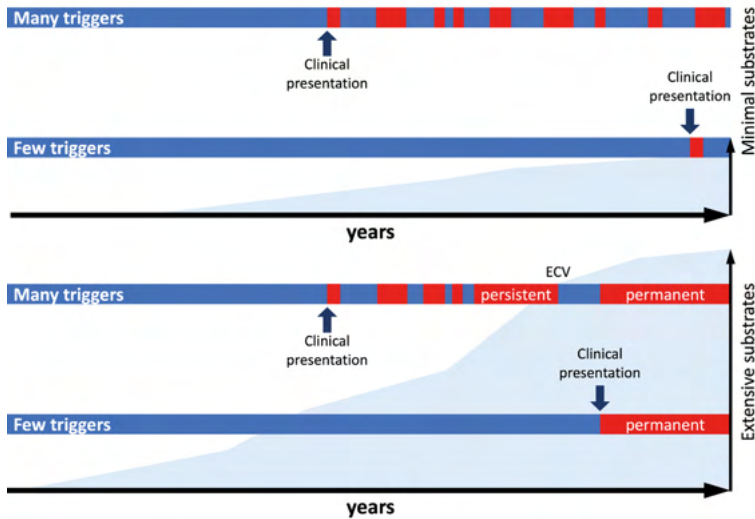
Figure 2 – Interplay of triggers and substrates in the onset of AF. Two different situations of trigger density and amount of substrates in relation to AF onset. AF episodes are shown in red. In case many triggers are present but with minimal substrates in the atria, AF will mainly present as frequent short-during episodes (paroxysmal AF). On the other hand, when there are extensive substrates present in the atria, one single trigger could already result in permanent AF. An interplay of substrate formation and presence of triggers could result in progression of AF from a paroxysmal to a permanent condition. **ECV** = electrical cardioversion.

of AF ablation.[26,27] However, reconnection of the PVI lesions is a major determinant of AF recurrence post procedure and a contributing factor to the development of post-AF-ablation atrial tachycardia. In most studies reporting on outcomes of patients undergoing repeat AF ablation, the reconnection rate for the PVI ablation lesions is as high as 80%.[28] However, with recent technological advancements, reconnection rates are decreasing but still vary between 19 and 64%.[29,30] In case of proven reconnection, repeat PVI can result in a significant improvement in long-term ablation success.[31] On the other hand, other sources of triggered activity can be found outside the pulmonary veins, including the superior caval vein, left atrial posterior free wall, left atrial appendage, terminal crest, ligament of Marshall and interatrial septum, which also play an important role in a significant part of AF patients.[32-37] Although these current treatment options are often able to stop AF, the underlying substrate persists. This means that a single trigger could be enough to re-initiate AF. Also, since different patients may have distinct mechanisms underlying their AF, a personalized approach for treatment would be more profitable. However, first a better understanding of the underlying substrate is required before this can be achieved.

Remodeling of the atria: formation of (a) substrate(s)

The architecture and anatomy of the atria is complex and plays an essential role in atrial conduction. Propagation of electrical wavefronts in the human heart is determined by membrane properties, tissue structure and wavefront geometry.[38,39] Cardiac tissue is considered to be anisotropic, meaning that conduction is faster along the longitudinal direction of myocardial fibers than in transverse direction.[38] Normal propagation through cardiac tissue can become disrupted by structural and electrical remodeling, which can promote AF persistence.[40] However, cellular and molecular bases for atrial remodeling can vary in different conditions and diseases. Remodeling can be caused by pre-existing cardiac conditions, systemic processes such as aging, or AF itself.[39,41] Also, changes in the autonomic nervous system and abnormalities in calcium handling have been shown to contribute to AF development.[42] The principal components of electrical remodeling include a decrease

in L-type calcium current, rectifier background potassium current and constitutive acetylcholine-regulated potassium current, as well as abnormal expression and distribution of gap junction connexin hemichannels that connect cardiomyocytes electrically. This creates a substrate that is prone to reentry. Structural remodeling, on the other hand, is characterized by cardiomyocyte hypertrophy, fibroblast proliferation and deposition of extracellular matrix, which can interrupt fiber bundle continuity, leading to local conduction disturbances.[43] Progressive changes in electrophysiological properties of the myocardium can lead to progression of AF. These changes result in complex electrical conduction disorders, which is defined as electropathology.[44] The degree of electropathology is thus related to severity of remodeling.

The mechanism underlying the transition from paroxysmal to persistent AF remains unclear. Mechanisms underlying AF were studied in both experimental and clinical mapping studies. In general, investigators support the presence of either a focal (repetitive ectopic discharges) or reentry mechanism (e.g., mother-waves, rotors, multiple wavelets).[3,6,45-50] Ultimately, AF is sustained by multiple independent reentrant wavelets that propagate through the atrium in an uncoordinated fashion. According to the multiple wavelet hypothesis, a critical number of wavelets must exist in the atrium at any given time to sustain and perpetuate AF.[50,51] Evidence for electropathology as a cause of AF originates from intra-operative high-resolution mapping studies of the epicardial surface of the entire left and right atrium including Bachmann's bundle. For example, it was demonstrated that Bachmann's bundle is a preferential site for conduction disorders to occur, especially in patients with history of AF.[52] Also, compared to patients with acutely induced AF in non-dilated atria, patients with longstanding persistent AF were characterized by more pronounced longitudinal dissociation in conduction, more conduction block and more focal fibrillation waves.[44,53,54] Changes in electrophysiological parameters are the result of an increased degree of electropathology. Quantification of these parameters might thus be utilized to stage the severity of AF. Quantification of the severity of electropathology present during sinus rhythm might be useful to predict late onset of AF in the individual patient.

Techniques for measuring the heart's electrical activity

Membrane potentials of cardiomyocytes produce electrical voltages in the human body. Changes in voltage occur when cardiomyocytes are depolarized or repolarized, resulting in a voltage vector. The depolarization and repolarization of cardiomyocytes produce strong patterns of voltage change which can be measured by electrodes either on the skin (electrocardiogram - ECG) or directly at the surface of the heart (electrogram - EGM). A net movement of a vector towards the positive pole will result in a positive deflection and vice versa. Thus, the recording is the sum total of electrical vectors in the direction of a lead.

Electrocardiogram (ECG)

Since the 1950s, the surface ECG has become the most important diagnostic method in cardiac medicine. However, as an ECG is measured on the body surface, far away from the heart, it has lost the geometrical information of the underlying arrhythmia. This is a major disadvantage, especially in case of AF in which atrial activity is only seen as rapid continuous oscillations, as illustrated in *Figure 1*. Only the irregular response of the ventricles can clearly be distinguished and is therefore often used to confirm the presence of AF. However, the severity of AF cannot be seen, at least by eye. Recent technologies provide more detailed analysis of the ECG during AF, often using complex machine learning algorithms.[55] On the other hand, multi-channel surface ECGs can also be combined to obtain so-called electrocardiographic imaging (ECGI) maps. Although these technologies are promising, they
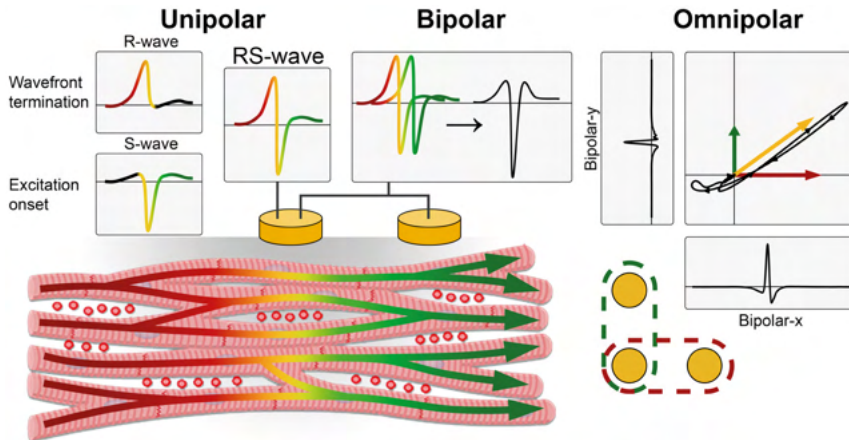
Figure 3 – Genesis of unipolar, bipolar and omnipolar electrograms. *Lower panel*: schematic representation of an activation wavefront propagating from left to right through myocardial tissue. *Left panel*: a unipolar electrogram is recorded by using one electrode located directly on the myocardial tissue. An activation wavefront propagating towards the recording electrode will result in a positive signal (red). When the activation wavefront passes the recording electrode it will be zero (yellow), after which it will be negative when the activation wavefront propagates away from the recording site (green), resulting in an RS-wave. Typical theoretical potential morphologies from two different sites along the tissue (e.g., excitation onset and wavefront termination) are illustrated in the most left panels. *Center panel*: a bipolar electrogram is constructed by subtracting two unipolar electrograms recorded from two electrodes at a close distance. Due to time delay between the two unipolar potentials, a typical bipolar electrogram is created. *Right panel*: an omnipolar electrogram is created by using two orthogonal bipolar electrograms (bipolar-x: red and bipolar-y: green). A 2-dimensional voltage loop is constructed from these bipolar electrograms. These constituent electrograms may be recovered from projecting the loop onto their corresponding directions (0° - red, and 90° - green). Virtual electrograms in any direction may be similarly created. The maximal extent of the voltage loop is calculated and corresponds to the largest possible bipolar electrogram (yellow arrow), which is defined as the omnipolar electrogram. The length of the arrows indicates the relative peak-to-peak amplitude of the corresponding electrograms. This also illustrates the significant direction-dependency of bipolar electrograms.

are still not suitable for detailed analysis of AF.[56] Therefore, to study the substrate underlying AF, more local measurements are required.

Electrograms (EGM)

An electrogram displays the electrical information at the tissue surface which occurs either by an individual electrode (unipolar) or between a set of two electrodes (bipolar signal). It only displays the electrical activity at the local myocardium.

Unipolar electrograms

In the unipolar recording mode, a different electrode is positioned at the atrial tissue surface where the extracellular potential must be determined, as illustrated in *Figure 3*. The indifferent electrode is positioned at a large distance from the heart or connected to the Wilson's Central Terminal. The local extracellular potential is changed in response to an activation wavefront propagating through the myocardial tissue. Such a wavefront can be thought of as a pair of propagating dipoles, one representing the depolarizing activation wavefront and the other representing the repolarizing wave-back.[57] Ahead of the activation wavefront, the intracellular potential is more negative than the extracellular potential resulting in a negative resting membrane potential. A cardiomyocyte becomes depolarized when a potential gradient of an adjacent cardiomyocyte drives a flow of intracellular axial current through gap junctions activating fast sodium channels, leading to a large influx of positive sodium ions. As a result, the membrane potential increases to become positive. The net effect is a biphasic membrane current which continues during the plateau phase.

The activation wavefront can therefore be represented by a positive dipole. As a result, a positive signal will be recorded by an electrode at a location where the activation wavefront propagates towards the recording site (R-wave). When the wavefront propagates away from the recording site, the recorded signal will switch to a negative signal (S-wave). The recorded signal is zero when the dipole passes exactly in line with the recording site. This process describes the morphology of unipolar electrograms recorded from the surface of the atria.

Several typical unipolar electrogram morphologies can arise due to these characteristics. At a site where the activation wavefront arises, the electrogram will only be negative as the activation wavefront only propagates away from the recording electrode (monophasic S-wave). At a site of conduction block or at the end of an activation wavefront, the electrogram will only be positive as the activation wavefront only propagates toward the recording electrode (monophasic R-wave). However, in the majority of cases the deflection will be biphasic (RS-morphology), as the activation wavefront passes the recording electrode. The morphology of atrial electrograms therefore contains information on intra-atrial conduction. Examples of unipolar electrograms during sinus rhythm and AF are illustrated in the lower panels of *Figure 1*.

Unipolar electrograms are characterized by relatively straightforward interpretation of the potential morphology, which is independent of the direction of the activation wavefront. However, unipolar electrograms are rather sensitive to remote activation caused by activity of adjacent cardiac structures or electrical disturbances.

Bipolar electrograms
As it is relatively hard to record clean unipolar electrograms without much noise interference, bipolar electrograms are more often used in daily clinical practice. These bipolar electrograms are taken as the difference between two neighboring unipolar electrograms, and can be recorded with either the use of a differential amplifier or via post-processing of unipolar electrograms, as illustrated in *Figure 3*. As noise and remote activity will be more or less similar between the two unipolar electrograms, they will be removed by the subtraction. The remaining signal reflects the temporal offset between the two unipolar potentials as the wavefront will be at a different distance between the two unipolar recording sites. The degree of offset depends on the direction of the activation wavefront and is virtually zero if the activation wavefront propagates perpendicular to the two recording electrodes. The bipolar electrogram is proportional to the first derivative of the unipolar electrograms when the time difference (dt) is small, which is the case if the distance between the recording electrodes is small ($dt = dx/cv$; dx is the distance between the electrodes, cv the conduction velocity).[55]

The greatest advantage of bipolar electrograms is that noise and remote activity are suppressed, making them less sensitive to far-field activity. A bipolar potential is also sharper than a unipolar potential, because differentiation of a signal promotes the high frequency components. However, the morphology and amplitude of bipolar potentials critically depend on the direction of the activation wavefront.

Omnipolar electrograms
Although unipolar and bipolar electrograms are the basis for electrophysiological recordings, both have some drawbacks. These can often be circumvented by using multiple adjacent electrograms for analysis, as modern mapping systems allow recording and analysis of a large number of electrograms. To overcome the directional dependency of bipolar electrograms, a so-called omnipolar mapping technique has been recently introduced which is theoretically insensitive to wavefront propagation direction.[59] This technique requires a

multielectrode grid in which different orientations of bipolar electrograms are compared. Within a square area defined by four adjacent electrodes (a clique), omnipolar electrograms are mathematically derived from an electric field (E-field) of a passing activation wavefront from which the maximal extend of two orthogonal bipolar electrograms is calculated, as illustrated in *Figure 3*. The largest bipolar electrogram can therefore be derived, removing the influence of reduced amplitude due to wavefront propagation direction. Haldar et al.[60] applied this technique in a dog model of AF and showed that omnipolar mapping is able to identify the largest possible bipolar voltages in both sinus rhythm and AF. In addition, the wavefront propagation direction can be estimated, yielding a velocity vector field.[61] However, application of this novel technique is yet limited to experimental models.

Visualization of electrical properties by electrophysiological mapping

The electrophysiological characteristics of the atria can be visualized during an electrophysiology study in which a mapping is performed. The advent of electro-anatomical mapping systems enables detailed measurement of impulse propagation inside the human atria. Detailed knowledge of atrial excitation patterns during sinus rhythm and its variations allows detection of propagation abnormalities associated with AF.

Mapping systems

Electro-anatomical three-dimensional (3D) mapping systems allow accurate measurement of impulse propagation inside the human atria in real-time. The operator would create a live reconstruction of the right and/or left atrium with a navigation catheter, as illustrated in *Figure 4*. Often a multi-polar catheter is used which adds to the speed of recreation. Each commercially available mapping system offers unique advantages. The most common systems include Carto3 (Biosense Webster, Inc., Diamond Bar, California, USA), EnSite
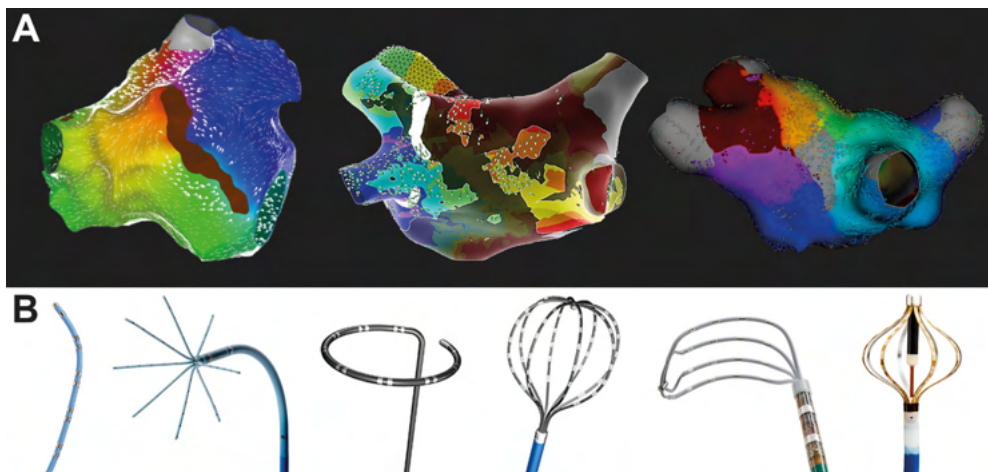
Figure 4 – Commercial mapping systems and multielectrode mapping catheters. *Panel A*: examples of atrial reconstructions created using Carto3 (left - Biosense Webster), EnSite Precision system (middle - Abbott) and Rhythmia (right - Boston Scientific). Each of the systems offer unique features. Integration of conduction velocity vectors constructed using local activation times or vectors obtained via omnipolar mapping are shown in the left and center map respectively. Mapping points are visualized as dots as in the right map. In each of the maps, activation wavefront propagation is visualized using a color scheme. *Panel B*: examples of multielectrode mapping catheters, including, from left to right, a linear catheter (Decapolar, Biosense Webster), splined catheter (Octaray, Biosense Webster), circular loop catheter, basket catheter (Constellation, Boston Scientific), grid catheter (HD Grid, Abbott) and mini-basket catheter (Orion, Boston Scientific).

Precision system (Endocardial Solutions, Abbott, Inc., St. Paul, Minnesota, USA) and Rhythmia (Boston Scientific, Cambridge, Massachusetts, USA). These systems employ magnetic based technology with additional proprietary catheter localization technology. The strength of the magnetic field measured by the location sensor triangulates the distal part of the catheter. In order to visualize the remaining electrodes a high frequency low grade current is emitted through orthogonally placed skin patches. 3D mapping is predominantly used for ablation of AF, atrial tachycardia and ventricular based ablation procedures, but can also be used during any electrophysiological procedure. Although various analytical options are available in each of the systems, the options remain rather limited. Hence, these commercially available systems are not always suitable for extensive research on electropathology.

Catheters and recording electrodes

Diagnostic catheters are positioned within the heart and record electrograms from particular locations. Each diagnostic catheter will have a certain number of electrodes. The electrode size and spacing varies between various manufacturers. Multielectrode mapping catheters speed up data acquisition and come in a variety of shapes e.g., circular, flat or balloon shaped and depend upon company specific engineering. Examples of commercially available multielectrode mapping catheters are illustrated in the lower panel of *Figure 4*. Circular catheters sitting in the pulmonary vein allow the operator to assess sleeves of myocardial tissue extending into the veins. 3D mapping catheters not only have magnet sensors embedded but can also provide tissue-contact feedback to the operator.

Higher resolution mapping can now be offered with multielectrode catheters utilizing smaller electrodes with closer inter-electrode spacing. Boston Scientific offers a mini-basket catheter (Orion) which comprises 64 mini-electrodes arranged on 8 splines. These electrodes have a surface area of 0.4 mm^2 with a 2.5 mm inter-electrode spacing. Abbott offers the HD Grid, a unique catheter which recognizes that bipolar voltage amplitude is influenced by the activation vector, and annotates only the higher voltage measured between 2 orthogonally positioned bipolar pairs within the grid (omnipolar mapping). Biosense Webster offers the Octaray, a 48-pole catheter organized along 8 branches arranged as a star to provide full and atraumatic surface coverage. These catheters allow for greater point density, and a more distinct electrogram for ease of local activation time annotation. Although the number of electrodes has been increased the past years, they are still not optimal for mapping of AF.

Other than catheters, the group of De Groot[62] introduced an electrode array containing 192 (8×24) electrodes which is suitable for surgical endo- and/or epicardial mapping procedures. These electrodes have a surface area of 0.28 mm^2 with a 2.12 mm inter-electrode spacing. This allows high-resolution and high-density mapping of a large atrial surface area. Several similar electrode arrays have been developed by various research groups worldwide. These electrode arrays are in general not commercially available and optimized for electrophysiological research purposes.

Analysis of electrograms

In the electrophysiology laboratory, analysis of electrograms recorded by catheters plays an important role in adjunctive ablation strategies performed in addition to pulmonary vein isolation, particularly in patients with (long-standing) persistent AF. However, electrical activity during AF is highly complex requiring advanced mapping systems equipped with sophisticated processing technologies for identification of suitable target sites for ablation.[1] As standard approaches for recording and processing electrical activity during AF do not exist, a lot of effort has been put in clinically evaluating a variety of mapping techniques yet

with mixed outcomes. Many of the currently available recording and processing technologies are also restricted to specific applications or have technological limitations hampering wide-spread applicability. Importantly, guidelines or recommendations in this area currently do not exist. Experimental mapping with custom-made software therefore provides the opportunity of recording electrograms after which every possible post-processing technique can be applied to study the signal characteristics. Nevertheless, several standard electrophysiological mapping techniques already exist and have been tested extensively.

Local activation time mapping

Activation time mapping is one of the most commonly used techniques and involves measurement of the relative local activation time of each potential. The activation time is defined as the time at which cardiomyocytes underneath the electrode depolarize. This coincides with the upstroke of the action potential of the cardiomyocytes. A reference signal is often used to determine the timing difference between this reference and a sampled potential. This value is then plotted on a (3D) map according to a color scale or by drawing isochrones, as illustrated in *Figure 4*. Activation time mapping requires accurate annotation of the local activation time of each acquired potential. Simultaneous recordings of action potentials and unipolar extracellular potentials have shown that the upstroke of the action potential coincides with the steepest negative deflection in the unipolar potential.[63] As large parts of unipolar potentials are in fact remote, caused by the activation wavefront propagating towards and away from the recording electrode, only the steepest negative deflection reflects local depolarization of cardiomyocytes underneath the electrode. The maximum downslope of a unipolar electrogram is currently considered the most accurate marker of local tissue activation and considered the closest representative of the upslope of the local intracellular action potential.[63] However, the presence of far-field information in unipolar electrograms makes accurate identification of local activation times in clinical electrograms challenging, leading to the routine use of bipolar electrograms. Although the minimum or maximum of a bipolar potential is most often used, the definition of local activation time for bipolar electrograms varies among literature.[64] The largest problem of using bipolar potentials for activation time mapping also lies in the fact that when an activation wavefront propagates nearly perpendicular to the two recording electrodes, the potential will be virtually zero thereby limiting assessment of local activation time. For both unipolar and bipolar electrograms, incorrect assignment of local activation times can mislead the entire activation time map, even for a small number of potentials. Also, activation time maps in commercial mapping systems often utilize an interpolation algorithm to allow a smooth display of propagation. Especially in areas where electrograms are complex, these local activation time estimates may be inaccurate.

Application of activation time mapping to unravel arrhythmogenesis
The first detailed activation time mapping was performed in dogs during sinus rhythm by Boineau et al.[65] in 1978. Later, Cox et al.[66] were the first to create an epicardial isochronal map of one sinus rhythm beat activating both the right and left atrium in a human. In addition, the first intra-operative activation time mapping of human AF was performed in 13 patients with Wolff-Parkinson-White syndrome. All patients showed non-uniform conduction, lines of bidirectional conduction block and multiple discrete wavefronts in both atria. In 1994, Konings et al.[46] showed that during acutely induced, self-terminating AF, the right atrial free wall of young patients without structural heart disease was mainly activated uniformly by broad wavefronts, with occasionally arcs of functional conduction block. Three types of AF could be distinguished; type I was characterized by single uniformly propagating waves, type II by the presence of single non-uniformly conducting waves or two wavelets, and type III by the presence of three or more wavelets associated with multiple areas of slow

conduction and arcs of functional conduction block which continuously shifted in size and location.

During sinus rhythm, electrical waves exciting the atria originate from the SAN area which is located in the high right atrium. Boineau et al.[67] performed epicardial activation time mapping in patients with Wolff-Parkinson-White syndrome to investigate the location of the SAN area and observed up to three different sites of sinus rhythm impulse origin within one patient. These pacemaker sites were mostly located along the sulcus terminalis and the junction between the right atrium and the superior caval vein, although sites of origin were also observed at the inferior caval vein or in the left atrium in case of escape beats. Prior studies also indicated that two spatially distinct dominant SAN sites are present.[68] This allows for a functional dynamic span of the SAN along the terminal crest, which has also been observed in adult patients with SAN dysfunction, in whom the SAN exit site shifts caudally.[69] AF is also commonly associated with SAN dysfunction. It has been suggested that AF-related remodeling results in structural changes within the SAN and surrounding atrial tissue that promote or accelerate SAN dysfunction. The presence of structural barriers surrounding the SAN could also result in enhanced conduction abnormalities between the endocardial and/or epicardial layer, resulting in endo-epicardial asynchrony. However, this has not yet been investigated in detail.

Bachmann's bundle serves as a specialized tract of muscle fibers and is considered the preferential route of interatrial conduction. It originates in the high right atrium and spans sub-epicardially across the inter-atrial groove to the left atrium. Furthermore, Bachmann's bundle is connected to other atrial regions through various (epicardial) bundles. Although it is generally assumed that Bachmann's bundle facilitates rapid conduction from the right to the left atrium, Teuwen et al.[52] demonstrated that the conduction velocity at Bachmann's bundle in human is only approximately 89 cm/s, which was comparable to the average conduction velocity (88 cm/s) measured during sinus rhythm at the right atrial free wall of patients with Wolff-Parkinson-White syndrome.[70] Bachmann's bundle is also a site that has been frequently associated with the onset and progression of AF. Alterations in the normal anatomy of Bachmann's bundle, such as disruptions in the parallel orientation of myocardial fibers, may lead to conduction disorders and predispose individuals to the development of AF.[52,71] These conduction disorders may cause delayed intra- and interatrial excitation. An example of epicardial activation time maps of two distinct patients is provided in *Figure 5*. Mouws et al.[71] demonstrated that patients with a history of AF were characterized by a longer total atrial excitation time compared to patients without AF (136±20 ms vs. 114±17 ms, p<0.001), which was mainly caused by longer total activation times of the right atrium and Bachmann's bundle (73±13 ms vs. 67±14 ms, p=0.018 and 106±20 ms vs. 87±16 ms, p<0.001, respectively). The presence of extensive conduction disorders at these areas resulted in alternative routes for activation of Bachmann's bundle and the left atrioventricular groove, as Bachmann's bundle could be activated via one wavefront from right to left, from the central part or via multiple wavefronts.[52] The left atrioventricular groove was then activated via either Bachmann's bundle, the pulmonary vein area or via both routes, depending on which route had the shortest interatrial excitation time. However, Mouws et al. also demonstrated that excitation of the left atrioventricular groove via only the pulmonary vein area was considerably slower than via Bachmann's bundle (90±18 ms vs. 101±20 ms, p<0.001), and increased the risk of AF.[71,72] Recently, Heida et al.[73] demonstrated that a history of AF was associated with slowing of conduction specifically at Bachmann's bundle, the left atrium and pulmonary vein area, as patients with AF had more interelectrode conduction times ≥4 ms (corresponding to ≈50 cm/s) and larger maximum interelectrode conduction times. Quantification of conduction disorders, such as local conduction delay and block, may therefore aid in determining the severity of electropathology.
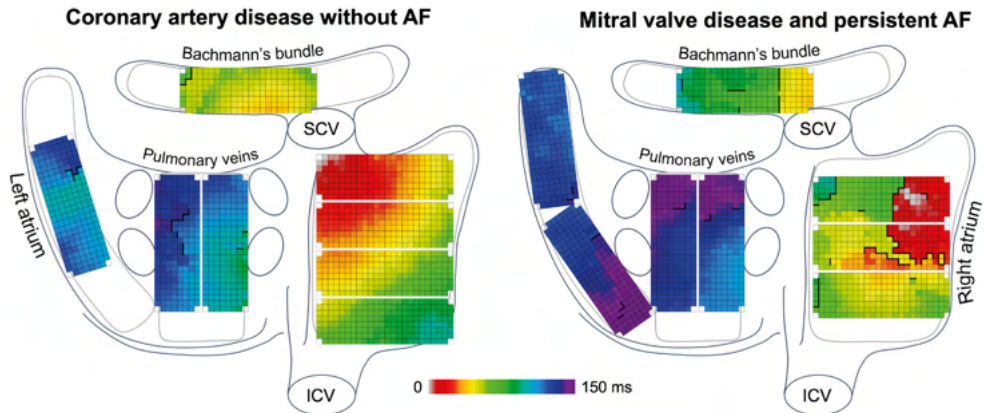
Figure 5 – Examples of atrial excitation patterns. Color-coded activation time maps of two patients during sinus rhythm obtained via intra-operative epicardial mapping using a 192-electrode array (interelectrode distance 2 mm). Thick black lines indicate lines of conduction block (interelectrode conduction times >12 ms). The patient with coronary artery disease without a history of AF (left) is characterized by a minimal amount of conduction block and a total atrial excitation time of 140 ms, while the patient with mitral valve disease and persistent AF (right) has extensive areas of conduction block at the right atrium and Bachmann's bundle, and a longer total atrial excitation time (160 ms). **ICV** = inferior caval vein; **SCV** = superior caval vein.

Quantification of conduction disorders: local conduction delay and block

The first quantitative analysis of intra-atrial conduction disturbances during human AF was performed by Allessie et al.[44] In this study, 24 patients with structural heart disease and longstanding persistent AF were compared to 25 patients with Wolff-Parkinson-White syndrome in whom AF was acutely induced. Lines of conduction block were defined as interelectrode conduction times of >12 ms, representing a lower limit of 19 cm/s which is less than 20-30% of the normal conduction velocity in atrial myocardium. The amount of intra-atrial block was quantified by measuring the percentage of conduction block around each electrode. Both AF groups exhibited continuously changing conduction block lines on a beat-to-beat basis throughout the atria. The frequency of conduction block was higher during longstanding persistent AF compared to acute AF (21.1 [16.6–27.5] vs. 6.1 [1.3–13.8] %, p<0.001). Patients with persistent AF had a higher total length of conduction block (21.1 [19.1–23.1] vs. 3.4 [0.3–8.8] mm/cm^2, p<0.001), number of fibrillation waves (4.5 [4.1–5.1] vs. 2.3 [1.7–2.9] /cm^2) and dissociation index (7.3 [5.6–9.2] vs. 1.5 [0.6–2.3], p<0.001), indicating that the frequency and severity of conduction disorders are important for AF maintenance. Long lines of conduction block result in large conduction times, and if a rotating wavefront encounters excitable tissue on the other side of the line, initiation of reentry is facilitated.

The presence of conduction disorders during sinus rhythm is related to AF development. Several mapping studies demonstrated that the presence of (transmural) conduction block at the right atrium was associated with development of post-operative AF.[74,75] Also, Teuwen et al.[52] found that the degree of conduction block and long lines of conduction block at Bachmann's bundle predisposed to early post-operative AF in patients undergoing coronary artery bypass grafting. The spatial distribution and extensiveness of conduction block in the entire atria during sinus rhythm was studied by Lanters et al.[76] in 209 patients with coronary artery disease without history of AF. Although areas with conduction delay (interelectrode conduction times ≥7 ms) and conduction block were present in all patients, the prevalence was relatively low (1.4 [0.2 to 4.0] % and 1.3 [0.1 to 4.3] % respectively). Despite the low prevalence, there was a considerable intra-atrial variation with a predilection site at the superior intercaval region and to a lesser extent at Bachmann's bundle. Patients with prior AF episodes typically had continuous lines of conduction block located at Bachmann's

bundle and the pulmonary vein area.[52,77] Heida et al.[73] have demonstrated that patients with various underlying heart diseases and a history of AF had more conduction disorders at Bachmann's bundle and the left atrium and more severe conduction disorders at the right atrium and Bachmann's bundle than patients without AF. Van der Does et al.[78] identified the lateral left atrium as a location with more conduction disorders in patients with valvular heart disease. Furthermore, by using simultaneous endo-epicardial mapping, Kharbanda et al.[74] demonstrated that conduction disorders at the right atrium were more pronounced in patients with a history of AF. These inhomogeneous patterns of conduction are reflected in electrogram morphology and cause low-amplitude, fractionated potentials.[79] However, at present, the physiological variation in electrogram morphology throughout the atria during sinus rhythm and its exact relation to conduction disorders remains unknown.

Assessment of conduction velocity

The speed and direction of atrial wavefront propagation provides important information about the underlying atrial tissue and is therefore widely used to identify potential mechanisms for arrhythmogenesis. Besides quantification of conduction disorders, local activation times can also be used to derive local conduction velocity. Areas of slowed conduction are associated with increased risk of wavefront reentry and therefore considered as diseased tissue.[80] However, there is no consensus on the best technique to compute conduction velocity.[64] Calculation of conduction velocity is often empirically determined based on relative distances and time differences derived from activation time maps. A straightforward method to estimate conduction velocity is by using isochronal maps. However, this method is time-consuming and requires manual intervention. Automatic estimation of local conduction velocity requires at least three electrodes to establish a velocity vector that also includes an estimation of the local propagation direction. Also, an adequate spatial resolution is required to minimize estimation errors, especially when working with complex and heterogeneous activation wavefronts. The spatial resolution of the conduction velocity vector field and the accuracy of the estimation should therefore be balanced. Highly localized estimations of conduction velocities will be more susceptible to errors, while estimations on larger spatial scales will only provide an average conduction velocity and therefore exhibit poor correlation with features of the underlying local substrate. The most optimal estimation technique to measure local conduction heterogeneity has not yet been determined.

Several mapping studies reported on differences in conduction velocity during sinus rhythm between patients with and without a history of AF.[81-83] Most of studies used triangulation on 3D electro-anatomical activation time maps to estimate conduction velocity. Despite
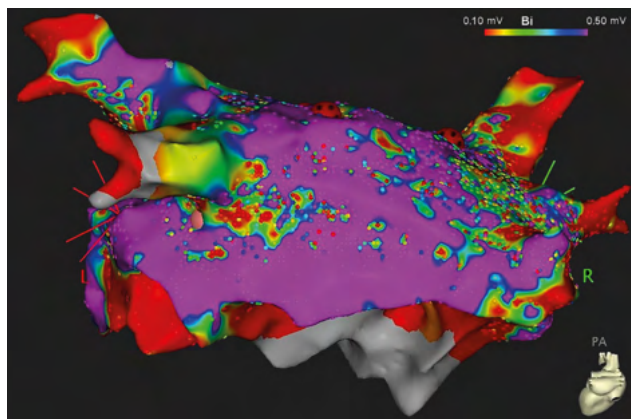
Figure 6 – Color-coded bipolar voltage map of the left atrium in the posterior projection recorded with a multielectrode catheter prior to catheter ablation. Areas of low-voltage are represented by non-purple colors (0.10–0.50 mV).

the conduction velocity estimates varied considerably among studies, lower conduction velocities were consistently found in patients with a history of AF compared to controls. Although the triangulation methodology has been automated to generate high-density conduction velocity maps of clinically acquired data (as shown in *Figure 4*), studies focusing on conduction velocity comparison in AF patients are lacking.[64] In addition, data on conduction velocity during AF is also scarce as estimation of local conduction velocity during AF is very challenging due to the unstable patterns of activation and presence of multiple wavefronts with short wavelengths, limiting sequential mapping.

Voltage mapping

The potential voltage is determined by the amount of myocardial tissue that is simultaneously activated surrounding the recording electrode. As large areas activate simultaneously in normal tissue, the amplitude will be relatively large. In diseased myocardium, activation will be more asynchronous, resulting in a decrease in potential voltages. 3D mapping systems collect voltage data simultaneous with local activation times, which can be displayed according to a color scale, as illustrated in *Figure 6*. Bipolar voltage mapping is most frequently used in clinical practice to define the substrate underlying AF, mainly focusing on areas of scarring. These areas are represented by low potential voltages. However, there are many discrepancies between studies resulting in mixed outcomes of LVA ablation.[57] The largest problem lies in the fact that the methodology for defining LVAs has not been standardized and a clear voltage threshold for tissue abnormalities has never been histologically validated.[84] It is for these reasons that unipolar electrograms are increasingly used in recent studies and newly developed mapping systems guiding (ventricular) ablation procedures.[57,85,86]

Unipolar potential morphology

In 1997, Konings et al.[87] were the first to describe various morphologies of unipolar electrograms during acutely induced AF, as well as during sinus rhythm and programmed electrical stimulation. Epicardial mapping of the right atrial free wall was performed using a 244-unipolar electrode array in 25 patients with Wolff-Parkinson-White syndrome undergoing cardiac surgery. The unipolar potentials were classified into four categories, i.e., single potentials, short-double potentials (two deflections, <10 ms apart), long-double potentials (two deflections, 10–50 ms apart) and fragmented (fractionated) potentials (>2 deflections within 50 ms). During induced AF, 77±12% of potentials were singles, 7±3% short-doubles, 10±7% long-doubles and 6±4% fragmented. Single potentials were an indicator for rapid uniform conduction (positive predictive value of 0.96). This type of conduction was present in the majority of wavefronts (79±11%); in 94±4% of potentials within these wavefronts, single potentials were observed. At sites of collision (3±2%), conduction block (15±8%), conduction slowing (2±2%) and pivoting points (2±1%), the proportions of single potentials were only 22±13%, 14±7%, 33±27% and 17±12% respectively. As illustrated in *Figure 7*, short-double potentials were primarily found at collision sites, long-double potentials at sites of conduction block, and fragmented potentials at pivoting points or areas with slow conduction. The morphology of atrial unipolar potentials thus contains information on intra-atrial conduction and hence conduction disorders giving rise to development of AF.[63,88,89] It is for these reasons that unipolar voltage mapping is increasingly used to define the substrate underlying AF.

The morphology of single potentials is represented by the relative positive (R-wave) and negative (S-wave) components (R/S ratio), as illustrated in *Figure 3*. Houben et al.[90] were the first to examine the morphology of single potentials during acutely induced AF at the right atrium. In total, 413,031 unipolar fibrillation potentials were used, as recorded from 25
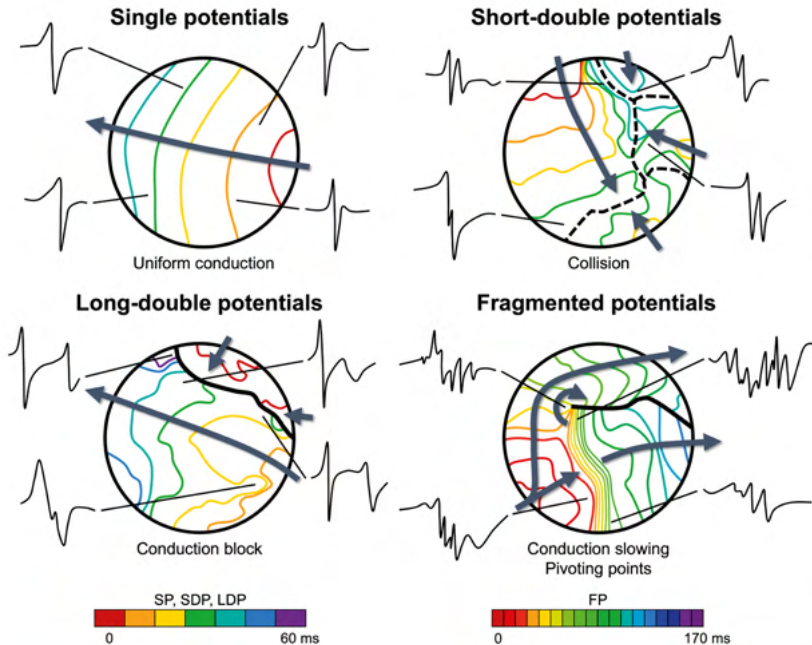
Figure 7 – Comparison of unipolar potential morphology and the underlying pattern of activation as recorded during AF by Konings et al.[84] *Upper left panel*: single potentials were mainly recorded in areas of rapid uniform conduction. *Upper right panel*: short-double potentials were mainly recorded when multiple wavefronts invaded the mapping area from different directions and collided. *Lower left panel*: long-double potentials were mainly recorded at a line of functional conduction block. *Lower right panel*: fragmented potentials were recorded both at pivot points and from areas with slow conduction (crowding of isochrones). Isochrones were drawn at 10-ms interval and color-coded. Arrows indicate the main direction of the activation wavefront. Collision is indicated by the dashed line; thick black lines represent a line of conduction block. **FP** = fragmented potentials; **LDP** = long-double potentials; **SDP** = short-double potentials; **SP** = single potentials.

patients by Konings et al.[46] A clear predominance of S-waves was found, although with a large intra- and interindividual variation. The S-wave predominance was less pronounced during more complex type of AF (type III) and could not be attributed to wavefront curvature or anisotropy. It was therefore hypothesized that a tilted transmural stance of the wavefront, resulting in an epicardial lead with constant epi-to-endocardial activation, could explain the S-wave predominance. The endocardial layer should then present with more R-wave predominance. Van der Does et al.[91] examined sinus rhythm unipolar single potential morphology during simultaneous endo-epicardial mapping of the right atrium in 26 patients. In this study, it was demonstrated that both epicardial and endocardial single potentials showed an S-predominance. Also, there were no differences in single potential morphology between both layers. Although this mapping study was performed during sinus rhythm, data clearly showed absence of an oblique transmurally propagating wave. It was therefore concluded that S-wave predominance could not be explained by epi-to-endocardial activation or vice versa.

The morphology of single potentials has also been introduced as a parameter guiding ablation therapy. Several studies demonstrated that creation of an ablation lesion was associated with loss of the S-wave and development of a monophasic R-wave close to the ablation lesion, representing transmural conduction block.[92,93] The morphology of single potentials could therefore be a valuable parameter for identification of electropathology. However, the physiological distribution of single potential morphologies across the atria among various patients with and without AF remains unknown.

Fractionation of electrograms occurs when the underlying tissue is asynchronously activated. This can be caused by e.g., heterogeneous expression of connexins, increased collagen deposition or presence of adipose or ischemic myocardium.[94] In addition, Van der Does et al.[95] showed that endo-epicardial asynchrony was the origin of fractionation in 4% of fractionated electrograms. Bipolar, complex fractionated atrial electrograms (CFAEs) are frequently used in daily clinic to detect abnormal areas in the atria of patients with AF. Although CFAEs are used to select areas for ablation, several studies have demonstrated that they are frequently passive phenomena and not critical for the perpetuation of AF.[96] Starreveld et al.[97] demonstrated that fractionation is commonly found in high proportions within all regions of both atria and without a clear preference for specific sites. Also, no differences in fractionation proportions could be found between patients with paroxysmal and persistent AF within the left and right atria. Therefore, simply targeting all fractionated electrograms would be very extensive and short-sighted. In addition, currently no clear uniform definitions or methodologies for identification of CFAE have been defined, probably explaining the lack of successful results. Van der Does et al.[98] demonstrated that in 164 studies reporting on fractionation, eleven different visual definitions for fractionation, three automated complex fractionated atrial electrogram detection algorithms, seven novel parameters for measuring fractionation and five different definitions for continuous electrical activity have been introduced. Unipolar fractionated electrograms, on the other hand, are more straightforward to interpretate, but less explored, especially during sinus rhythm.[87]

Aim of the thesis

It remains unknown which electrical signal features and spatial conduction properties are related to electropathology. In this thesis we therefore investigated the main research question "Which electrical signal features and spatial conduction properties are related to electropathology?". In addition, we investigated whether these quantified parameters are also related to post-operative AF and how these parameters could be implicated in clinical practice. Therefore, in this thesis we aim to identify features of electrophysiological properties of atrial tissue and develop novel methodologies to quantify AF-related electropathology. We hereto investigate atrial potential morphology and conduction properties during normal sinus rhythm, programmed electrical stimulation and AF in patients with various underlying heart diseases. In addition, detection of post-operative AF in surface ECGs and post-operative AF-related electropathology is identified. Potential clinical implications of high-resolution mapping and corresponding features of electrophysiological properties of atrial tissue are also explored.

Outline thesis

In **chapter 2** an overview is provided on the clinical implications of sinus rhythm mapping to identify the arrhythmogenic substrate underlying AF. **Chapter 3** describes the current knowledge on the relation between electrogram morphology and AF from an experimental point of view.

Part I of this thesis focusses on quantified features of electrical signals which are retrieved directly from the surface of the heart. As described before, these electrograms contain local information on tissue properties related to electropathology, which can be quantified using various methodologies. In **chapters 4 and 5**, unipolar voltages and single potential morphology are examined in a population of patients with mitral valve disease. In **chapter 6**, the effect of obesity on unipolar voltage and low-voltage areas in relation to post-operative AF is studied. As described before, several types of electrograms can be used to identify LVAs

as potential target sites for ablation therapy. The similarities and dissimilarities in unipolar, bipolar and omnipolar voltage distribution and the relation between these types of voltages and conduction velocity in identification of LVAs is described in **chapter 7**. As LVAs can be located exclusively at either the endocardium or epicardium, the goal of **chapter 8** was to compare simultaneously recorded endo-epicardial unipolar and omnipolar potentials and to determine whether their voltage characteristics are predictive for LVAs at the opposite layer. The relation between local conduction slowing and the occurrence of fractionated and/or low-voltage potentials is examined in **chapter 9**. In **chapter 10**, spontaneous AES were used to unravel direction- and rate-dependent unipolar electrogram characteristics. The effect of electrode size on electrogram characteristics is presented in **chapter 11**. In **chapters 12 and 13**, unipolar electrogram features of patients with coronary artery disease were used to identify conduction inhomogeneity using a signal fingerprint. The influence of age in this population was further explored in **chapter 14**. A dedicated signal fingerprint was developed to identify endo-epicardial asynchrony and transmural conduction block, which are presented in **chapters 15 and 16**.

Abnormalities in wavefront propagation due to heterogeneous conduction properties are explored in part II of this thesis. **Chapter 17** provides the first evidence of atrial conduction disorders in pediatric patients with congenital heart disease. A novel methodology to estimate local conduction velocity and identify local atrial conduction heterogeneities is presented in **chapter 18**. This methodology was then used in a case-control study to examine the influence of prior AF episodes on intra-atrial conduction velocity, which is presented in **chapter 19**. In **chapter 20**, intra-atrial conduction characteristics assessed during the supervulnerable period after electrical cardioversion were compared with long-term sinus rhythm. The first insights into endo-epicardial dynamics during SAN activation are presented in **chapter 21**. SAN activation and electrogram morphology in pediatric and adult patients with congenital heart disease were compared and presented in **chapter 22**. In **chapter 23**, intra-operative mapping of the SAN of three pediatric patients is presented who developed early post-operative sinus node dysfunction. The impact of spontaneous AES on atrial conduction in pediatric patients is examined in **chapter 24**. In **chapter 25**, a novel methodology is presented to quantify local directional heterogeneity in conduction velocity vectors. Premature AES in adult patients were used to examine differences in intra-atrial conduction between patients with and without history of AF. In **chapter 26**, a methodology is presented to estimate local conduction velocity and conduction anisotropy during AF. The degree and spatial distribution of local conduction abnormalities were quantified and compared between acutely induced and long-standing persistent AF.

Part III focusses on identification of post-operative AF and its relation with electropathology. In **chapter 27**, a pilot study is presented in which we examined the effect of programmed AES on endo-epicardial conduction disorders and asynchrony and their relation with post-operative AF. **Chapter 28** presents pre-existing differences in intra-atrial conduction parameters and electrogram morphology between patients without and with de novo early and late post-operative AF. Automated detection of AF in continuous rhythm registrations is essential in order to prevent complications and optimize treatment of AF. **Chapter 29** provides more insight into the current automated AF detection algorithms. In **chapter 30**, we provide an efficient and reliable method to train a classifier for AF detection using large datasets of real-life ECGs.

In part IV of this thesis, some clinical implications of high-resolution mapping during cardiac surgery and application of quantified electrophysiological features are discussed. **Chapter 31** presents the first-in-children epicardial mapping of the heart. In **chapter 32**, epicardial mapping in a 14-month-old patient with short QT syndrome unexpectedly revealed AF with

1

an excessively high rate of the fibrillatory process. In **chapter 33**, epicardial high-resolution mapping was used to assess atrial excitation patterns and conduction abnormalities related to advanced interatrial block. Mapping-guided placement of atrial pacing leads and the influence on conduction across Bachmann's bundle is described in **chapter 34**. **Chapter 35** focusses on the optimalisation of intra-operative electrophysiological examination of the ligament of Marshall. In **chapter 36**, we present a novel method to investigate the effect of low-level vagus nerve stimulation using epicardial mapping.

In **chapter 37**, the findings and implications of this thesis are discussed. An English and Dutch summary of this thesis are provided in **chapters 38 and 39** respectively.

References

1. de Groot NMS, Shah D, Boyle PM, Anter E, Clifford GD, Deisenhofer I, Deneke T, van Dessel P, Doessel O, Dilaveris P, et al. Critical appraisal of technologies to assess electrical activity during atrial fibrillation: a position paper from the European Heart Rhythm Association and European Society of Cardiology Working Group on eCardiology in collaboration with the Heart Rhythm Society, Asia Pacific Heart Rhythm Society, Latin American Heart Rhythm Society and Computing in Cardiology. Europace. 2021.
2. Jackson LR, 2nd, Rathakrishnan B, Campbell K, Thomas KL, Piccini JP, Bahnson T, Stiber JA, Daubert JP. Sinus Node Dysfunction and Atrial Fibrillation: A Reversible Phenomenon? Pacing Clin Electrophysiol. 2017;40:442-450.
3. Haissaguerre M, Jais P, Shah DC, Takahashi A, Hocini M, Quiniou G, Garrigue S, Le Mouroux A, Le Metayer P, Clementy J. Spontaneous initiation of atrial fibrillation by ectopic beats originating in the pulmonary veins. N Engl J Med. 1998;339:659-666.
4. Nademanee K, McKenzie J, Kosar E, Schwab M, Sunsaneewitayakul B, Vasavakul T, Khunnawat C, Ngarmukos T. A new approach for catheter ablation of atrial fibrillation: mapping of the electrophysiologic substrate. J Am Coll Cardiol. 2004;43:2044-2053.
5. Rolf S, Kircher S, Arya A, Eitel C, Sommer P, Richter S, Gaspar T, Bollmann A, Altmann D, Piedra C, et al. Tailored atrial substrate modification based on low-voltage areas in catheter ablation of atrial fibrillation. Circ Arrhythm Electrophysiol. 2014;7:825-833.
6. Narayan SM, Krummen DE, Shivkumar K, Clopton P, Rappel WJ, Miller JM. Treatment of atrial fibrillation by the ablation of localized sources: CONFIRM (Conventional Ablation for Atrial Fibrillation With or Without Focal Impulse and Rotor Modulation) trial. J Am Coll Cardiol. 2012;60:628-636.
7. Hindricks G, Potpara T, Dagres N, Arbelo E, Bax JJ, Blomstrom-Lundqvist C, Boriani G, Castella M, Dan GA, Dilaveris PE, et al. 2020 ESC Guidelines for the diagnosis and management of atrial fibrillation developed in collaboration with the European Association for Cardio-Thoracic Surgery (EACTS): The Task Force for the diagnosis and management of atrial fibrillation of the European Society of Cardiology (ESC) Developed with the special contribution of the European Heart Rhythm Association (EHRA) of the ESC. Eur Heart J. 2021;42:373-498.
8. January CT, Wann LS, Calkins H, Chen LY, Cigarroa JE, Cleveland JC, Jr., Ellinor PT, Ezekowitz MD, Field ME, Furie KL, et al. 2019 AHA/ACC/HRS Focused Update of the 2014 AHA/ACC/HRS Guideline for the Management of Patients With Atrial Fibrillation: A Report of the American College of Cardiology/American Heart Association Task Force on Clinical Practice Guidelines and the Heart Rhythm Society. J Am Coll Cardiol. 2019;74:104-132.
9. Chugh SS, Havmoeller R, Narayanan K, Singh D, Rienstra M, Benjamin EJ, Gillum RF, Kim YH, McAnulty JH, Jr., Zheng ZJ, et al. Worldwide epidemiology of atrial fibrillation: a Global Burden of Disease 2010 Study. Circulation. 2014;129:837-847.
10. Haim M, Hoshen M, Reges O, Rabi Y, Balicer R, Leibowitz M. Prospective national study of the prevalence, incidence, management and outcome of a large contemporary cohort of patients with incident non-valvular atrial fibrillation. J Am Heart Assoc. 2015;4:e001486.
11. McDonagh TA, Metra M, Adamo M, Gardner RS, Baumbach A, Bohm M, Burri H, Butler J, Celutkiene J, Chioncel O, et al. 2021 ESC Guidelines for the diagnosis and treatment of acute and chronic heart failure. Eur Heart J. 2021;42:3599-3726.
12. Spach MS, Boineau JP. Microfibrosis produces electrical load variations due to loss of side-to-side cell connections: a major mechanism of structural heart disease arrhythmias. Pacing Clin Electrophysiol. 1997;20:397-413.
13. Xu J, Cui G, Esmailian F, Plunkett M, Marelli D, Ardehali A, Odim J, Laks H, Sen L. Atrial extracellular matrix remodeling and the maintenance of atrial fibrillation. Circulation. 2004;109:363-368.
14. Waldmann V, Ladouceur M, Bougouin W, Combes N, Maltret A, Dumas F, Iserin L, Cariou A, Marijon E, Jouven X. Sudden Cardiac Arrest in Adults With Congenital Heart Disease. JACC Clin Electrophysiol. 2019;5:1355-1356.
15. D'Agostino RS, Jacobs JP, Badhwar V, Fernandez FG, Paone G, Wormuth DW, Shahian DM. The Society of Thoracic Surgeons Adult Cardiac Surgery Database: 2019 Update on Outcomes and Quality. Ann Thorac Surg. 2019;107:24-32.
16. Aranki SF, Shaw DP, Adams DH, Rizzo RJ, Couper GS, VanderVliet M, Collins JJ, Jr., Cohn LH, Burstin HR. Predictors of atrial fibrillation after coronary artery surgery. Current trends and impact on hospital resources. Circulation. 1996;94:390-397.
17. LaPar DJ, Speir AM, Crosby IK, Fonner E, Jr., Brown M, Rich JB, Quader M, Kern JA, Kron IL, Ailawadi G, et al. Postoperative atrial fibrillation significantly increases mortality, hospital readmission, and hospital costs. Ann Thorac Surg. 2014;98:527-533; discussion 533.
18. Echahidi N, Pibarot P, O'Hara G, Mathieu P. Mechanisms, prevention, and treatment of atrial fibrillation after cardiac surgery. J Am Coll Cardiol. 2008;51:793-801.
19. De Vecchis R, Di Maio M, Noutsias M, Rigopoulos AG, Ariano C, Di Biase G. High Prevalence of Proarrhythmic Events in Patients With History of Atrial Fibrillation Undergoing a Rhythm Control Strategy: A Retrospective Study. J Clin Med Res. 2019;11:345-352.
20. Scheinman MM, Morady F, Hess DS, Gonzalez R. Catheter-induced ablation of the atrioventricular junction to control refractory supraventricular arrhythmias. JAMA. 1982;248:851-855.
21. Gallagher JJ, Svenson RH, Kasell JH, German LD, Bardy GH, Broughton A, Critelli G. Catheter technique for closed-chest ablation of the atrioventricular conduction system. N Engl J Med. 1982;306:194-200.
22. Cox JL, Boineau JP, Schuessler RB, Ferguson TB, Jr., Cain ME, Lindsay BD, Corr PB, Kater KM, Lappas DG. Successful surgical treatment of atrial fibrillation. Review and clinical update. JAMA. 1991;266:1976-1980.
23. Sundt TM, 3rd, Camillo CJ, Cox JL. The maze procedure for cure of atrial fibrillation. Cardiol Clin. 1997;15:739-748.
24. Kumagai K, Ogawa M, Noguchi H, Yasuda T, Nakashima H, Saku K. Electrophysiologic properties of pulmonary

veins assessed using a multielectrode basket catheter. J Am Coll Cardiol. 2004;43:2281-2289.

25. Hamabe A, Okuyama Y, Miyauchi Y, Zhou S, Pak HN, Karagueuzian HS, Fishbein MC, Chen PS. Correlation between anatomy and electrical activation in canine pulmonary veins. Circulation. 2003;107:1550-1555.

26. Pappone C, Rosanio S, Oreto G, Tocchi M, Gugliotta F, Vicedomini G, Salvati A, Dicandia C, Mazzone P, Santinelli V, et al. Circumferential radiofrequency ablation of pulmonary vein ostia: A new anatomic approach for curing atrial fibrillation. Circulation. 2000;102:2619-2628.

27. Calkins H, Hindricks G, Cappato R, Kim YH, Saad EB, Aguinaga L, Akar JG, Badhwar V, Brugada J, Camm J, et al. 2017 HRS/EHRA/ECAS/APHRS/SOLAECE expert consensus statement on catheter and surgical ablation of atrial fibrillation. Europace. 2018;20:e1-e160.

28. Jiang RH, Po SS, Tung R, Liu Q, Sheng X, Zhang ZW, Sun YX, Yu L, Zhang P, Fu GS, et al. Incidence of pulmonary vein conduction recovery in patients without clinical recurrence after ablation of paroxysmal atrial fibrillation: mechanistic implications. Heart Rhythm. 2014;11:969-976.

29. Aryana A, Singh SM, Mugnai G, de Asmundis C, Kowalski M, Pujara DK, Cohen AI, Singh SK, Fuenzalida CE, Prager N, et al. Pulmonary vein reconnection following catheter ablation of atrial fibrillation using the second-generation cryoballoon versus open-irrigated radiofrequency: results of a multicenter analysis. J Interv Card Electrophysiol. 2016;47:341-348.

30. Wieczorek M, Sassani K, Hoeltgen R. Comparison of pulmonary vein reconnection patterns after multielectrode phased radiofrequency- and cryoballoon ablation of atrial fibrillation. BMC Cardiovasc Disord. 2020;20:197.

31. Callans DJ, Gerstenfeld EP, Dixit S, Zado E, Vanderhoff M, Ren JF, Marchlinski FE. Efficacy of repeat pulmonary vein isolation procedures in patients with recurrent atrial fibrillation. J Cardiovasc Electrophysiol. 2004;15:1050-1055.

32. Tsai CF, Tai CT, Hsieh MH, Lin WS, Yu WC, Ueng KC, Ding YA, Chang MS, Chen SA. Initiation of atrial fibrillation by ectopic beats originating from the superior vena cava: electrophysiological characteristics and results of radiofrequency ablation. Circulation. 2000;102:67-74.

33. Lin WS, Tai CT, Hsieh MH, Tsai CF, Lin YK, Tsao HM, Huang JL, Yu WC, Yang SP, Ding YA, et al. Catheter ablation of paroxysmal atrial fibrillation initiated by non-pulmonary vein ectopy. Circulation. 2003;107:3176-3183.

34. Johnson N, Danilo P, Jr., Wit AL, Rosen MR. Characteristics of initiation and termination of catecholamine-induced triggered activity in atrial fibers of the coronary sinus. Circulation. 1986;74:1168-1179.

35. Hwang C, Wu TJ, Doshi RN, Peter CT, Chen PS. Vein of marshall cannulation for the analysis of electrical activity in patients with focal atrial fibrillation. Circulation. 2000;101:1503-1505.

36. Katritsis D, Ioannidis JP, Anagnostopoulos CE, Sarris GE, Giazitzoglou E, Korovesis S, Camm AJ. Identification and catheter ablation of extracardiac and intracardiac components of ligament of Marshall tissue for treatment of paroxysmal atrial fibrillation. J Cardiovasc Electrophysiol. 2001;12:750-758.

37. Kurotobi T, Iwakura K, Inoue K, Kimura R, Okamura A, Koyama Y, Tosyoshima Y, Ito N, Fujii K. Multiple arrhythmogenic foci associated with the development of perpetuation of atrial fibrillation. Circ Arrhythm Electrophysiol. 2010;3:39-45.

38. Kleber AG, Rudy Y. Basic mechanisms of cardiac impulse propagation and associated arrhythmias. Physiol Rev. 2004;84:431-488.

39. Spach MS, Dolber PC, Heidlage JF. Influence of the passive anisotropic properties on directional differences in propagation following modification of the sodium conductance in human atrial muscle. A model of reentry based on anisotropic discontinuous propagation. Circ Res. 1988;62:811-832.

40. Nattel S, Harada M. Atrial remodeling and atrial fibrillation: recent advances and translational perspectives. J Am Coll Cardiol. 2014;63:2335-2345.

41. Wijffels MC, Kirchhof CJ, Dorland R, Allessie MA. Atrial fibrillation begets atrial fibrillation. A study in awake chronically instrumented goats. Circulation. 1995;92:1954-1968.

42. Nattel S, Dobrev D. The multidimensional role of calcium in atrial fibrillation pathophysiology: mechanistic insights and therapeutic opportunities. Eur Heart J. 2012;33:1870-1877.

43. Burstein B, Comtois P, Michael G, Nishida K, Villeneuve L, Yeh YH, Nattel S. Changes in connexin expression and the atrial fibrillation substrate in congestive heart failure. Circ Res. 2009;105:1213-1222.

44. Allessie MA, de Groot NM, Houben RP, Schotten U, Boersma E, Smeets JL, Crijns HJ. Electropathological substrate of long-standing persistent atrial fibrillation in patients with structural heart disease: longitudinal dissociation. Circ Arrhythm Electrophysiol. 2010;3:606-615.

45. Allessie MA, Bonke FI, Schopman FJ. Circus movement in rabbit atrial muscle as a mechanism of tachycardia. III. The "leading circle" concept: a new model of circus movement in cardiac tissue without the involvement of an anatomical obstacle. Circ Res. 1977;41:9-18.

46. Konings KT, Kirchhof CJ, Smeets JR, Wellens HJ, Penn OC, Allessie MA. High-density mapping of electrically induced atrial fibrillation in humans. Circulation. 1994;89:1665-1680.

47. Mandapati R, Skanes A, Chen J, Berenfeld O, Jalife J. Stable microreentrant sources as a mechanism of atrial fibrillation in the isolated sheep heart. Circulation. 2000;101:194-199.

48. Jalife J, Berenfeld O, Mansour M. Mother rotors and fibrillatory conduction: a mechanism of atrial fibrillation. Cardiovasc Res. 2002;54:204-216.

49. Waldo AL. Mechanisms of atrial fibrillation. J Cardiovasc Electrophysiol. 2003;14:S267-274.

50. Moe GK, Rheinboldt WC, Abildskov JA. A Computer Model of Atrial Fibrillation. Am Heart J. 1964;67:200-220.

51. Moe GK, Abildskov JA. Atrial fibrillation as a self-sustaining arrhythmia independent of focal discharge. Am Heart J. 1959;58:59-70.

52. Teuwen CP, Yaksh A, Lanters EA, Kik C, van der Does LJ, Knops P, Taverne YJ, van de Woestijne PC, Oei FB, Bekkers JA, et al. Relevance of Conduction Disorders in Bachmann's Bundle During Sinus Rhythm in Humans. Circ

Arrhythm Electrophysiol. 2016;9:e003972.

53. de Groot N, van der Does L, Yaksh A, Lanters E, Teuwen C, Knops P, van de Woestijne P, Bekkers J, Kik C, Bogers A, et al. Direct Proof of Endo-Epicardial Asynchrony of the Atrial Wall During Atrial Fibrillation in Humans. Circ Arrhythm Electrophysiol. 2016;9.

54. de Groot NM, Houben RP, Smeets JL, Boersma E, Schotten U, Schalij MJ, Crijns H, Allessie MA. Electropathological substrate of longstanding persistent atrial fibrillation in patients with structural heart disease: epicardial breakthrough. Circulation. 2010;122:1674-1682.

55. Moghaddasi H, Hendriks RC, van der Veen AJ, de Groot NMS, Hunyadi B. Classification of De novo post-operative and persistent atrial fibrillation using multi-channel ECG recordings. Comput Biol Med. 2022;143:105270.

56. Salinet J, Molero R, Schlindwein FS, Karel J, Rodrigo M, Rojo-Alvarez JL, Berenfeld O, Climent AM, Zenger B, Vanheusden F, et al. Electrocardiographic Imaging for Atrial Fibrillation: A Perspective From Computer Models and Animal Experiments to Clinical Value. Front Physiol. 2021;12:653013.

57. Sim I, Bishop M, O'Neill M, Williams SE. Left atrial voltage mapping: defining and targeting the atrial fibrillation substrate. J Interv Card Electrophysiol. 2019.

58. de Bakker JM. Electrogram recording and analyzing techniques to optimize selection of target sites for ablation of cardiac arrhythmias. Pacing Clin Electrophysiol. 2019;42:1503-1516.

59. Deno DC, Balachandran R, Morgan D, Ahmad F, Masse S, Nanthakumar K. Orientation-Independent Catheter-Based Characterization of Myocardial Activation. IEEE Trans Biomed Eng. 2017;64:1067-1077.

60. Haldar SK, Magtibay K, Porta-Sanchez A, Masse S, Mitsakakis N, Lai PFH, Azam MA, Asta J, Kusha M, Dorian P, et al. Resolving Bipolar Electrogram Voltages During Atrial Fibrillation Using Omnipolar Mapping. Circ Arrhythm Electrophysiol. 2017;10.

61. Masse S, Magtibay K, Jackson N, Asta J, Kusha M, Zhang B, Balachandran R, Radisic M, Deno DC, Nanthakumar K. Resolving Myocardial Activation With Novel Omnipolar Electrograms. Circ Arrhythm Electrophysiol. 2016;9:e004107.

62. Yaksh A, Kik C, Knops P, Roos-Hesselink JW, Bogers AJ, Zijlstra F, Allessie M, de Groot NM. Atrial fibrillation: to map or not to map? Neth Heart J. 2014;22:259-266.

63. Spach MS, Miller WT, 3rd, Miller-Jones E, Warren RB, Barr RC. Extracellular potentials related to intracellular action potentials during impulse conduction in anisotropic canine cardiac muscle. Circ Res. 1979;45:188-204.

64. Cantwell CD, Roney CH, Ng FS, Siggers JH, Sherwin SJ, Peters NS. Techniques for automated local activation time annotation and conduction velocity estimation in cardiac mapping. Comput Biol Med. 2015;65:229-242.

65. Boineau JP, Schuessler RB, Mooney CR, Wylds AC, Miller CB, Hudson RD, Borremans JM, Brockus CW. Multicentric origin of the atrial depolarization wave: the pacemaker complex. Relation to dynamics of atrial conduction, P-wave changes and heart rate control. Circulation. 1978;58:1036-1048.

66. Cox JL, Canavan TE, Schuessler RB, Cain ME, Lindsay BD, Stone C, Smith PK, Corr PB, Boineau JP. The surgical treatment of atrial fibrillation. II. Intraoperative electrophysiologic mapping and description of the electrophysiologic basis of atrial flutter and atrial fibrillation. J Thorac Cardiovasc Surg. 1991;101:406-426.

67. Boineau JP, Canavan TE, Schuessler RB, Cain ME, Corr PB, Cox JL. Demonstration of a widely distributed atrial pacemaker complex in the human heart. Circulation. 1988;77:1221-1237.

68. Brennan JA, Chen Q, Gams A, Dyavanapalli J, Mendelowitz D, Peng W, Efimov IR. Evidence of Superior and Inferior Sinoatrial Nodes in the Mammalian Heart. JACC Clin Electrophysiol. 2020;6:1827-1840.

69. Sanders P, Morton JB, Kistler PM, Spence SJ, Davidson NC, Hussin A, Vohra JK, Sparks PB, Kalman JM. Electrophysiological and electroanatomic characterization of the atria in sinus node disease: evidence of diffuse atrial remodeling. Circulation. 2004;109:1514-1522.

70. Hansson A, Holm M, Blomstrom P, Johansson R, Luhrs C, Brandt J, Olsson SB. Right atrial free wall conduction velocity and degree of anisotropy in patients with stable sinus rhythm studied during open heart surgery. Eur Heart J. 1998;19:293-300.

71. Mouws E, Lanters EAH, Teuwen CP, van der Does L, Kik C, Knops P, Yaksh A, Bekkers JA, Bogers A, de Groot NMS. Impact of Ischemic and Valvular Heart Disease on Atrial Excitation:A High-Resolution Epicardial Mapping Study. J Am Heart Assoc. 2018;7.

72. Mouws E, Kik C, van der Does L, Lanters EAH, Teuwen CP, Knops P, Bogers A, de Groot NMS. Novel Insights in the Activation Patterns at the Pulmonary Vein Area. Circ Arrhythm Electrophysiol. 2018;11:e006720.

73. Heida A, van der Does WFB, van Staveren LN, Taverne Y, Roos-Serote MC, Bogers A, de Groot NMS. Conduction Heterogeneity: Impact of Underlying Heart Disease and Atrial Fibrillation. JACC Clin Electrophysiol. 2020;6:1844-1854.

74. Kharbanda RK, Knops P, van der Does L, Kik C, Taverne Y, Roos-Serote MC, Heida A, Oei FBS, Bogers A, de Groot NMS. Simultaneous Endo-Epicardial Mapping of the Human Right Atrium: Unraveling Atrial Excitation. J Am Heart Assoc. 2020;9:e017069.

75. Sakamoto S, Yamauchi S, Yamashita H, Imura H, Maruyama Y, Ogasawara H, Hatori N, Shimizu K. Intraoperative mapping of the right atrial free wall during sinus rhythm: variety of activation patterns and incidence of postoperative atrial fibrillation. Eur J Cardiothorac Surg. 2006;30:132-139.

76. Lanters EAH, Yaksh A, Teuwen CP, van der Does L, Kik C, Knops P, van Marion DMS, Brundel B, Bogers A, Allessie MA, et al. Spatial distribution of conduction disorders during sinus rhythm. Int J Cardiol. 2017;249:220-225.

77. Mouws E, van der Does L, Kik C, Lanters EAH, Teuwen CP, Knops P, Bogers A, de Groot NMS. Impact of the arrhythmogenic potential of long lines of conduction slowing at the pulmonary vein area. Heart Rhythm. 2019;16:511-519.

78. van der Does L, Lanters EAH, Teuwen CP, Mouws E, Yaksh A, Knops P, Kik C, Bogers A, de Groot NMS. The Effects of Valvular Heart Disease on Atrial Conduction During Sinus Rhythm. J Cardiovasc Transl Res. 2020;13:632-639.

79. de Groot NM, Schalij MJ, Zeppenfeld K, Blom NA, Van der Velde ET, Van der Wall EE. Voltage and activation mapping: how the recording technique affects the outcome of catheter ablation procedures in patients with congenital heart disease. Circulation. 2003;108:2099-2106.

80. King JH, Huang CL, Fraser JA. Determinants of myocardial conduction velocity: implications for arrhythmogenesis. Front Physiol. 2013;4:154.

81. Stiles MK, John B, Wong CX, Kuklik P, Brooks AG, Lau DH, Dimitri H, Roberts-Thomson KC, Wilson L, De Sciscio P, et al. Paroxysmal lone atrial fibrillation is associated with an abnormal atrial substrate: characterizing the "second factor". J Am Coll Cardiol. 2009;53:1182-1191.

82. Prabhu S, Voskoboinik A, McLellan AJA, Peck KY, Pathik B, Nalliah CJ, Wong GR, Azzopardi SM, Lee G, Mariani J, et al. A comparison of the electrophysiologic and electroanatomic characteristics between the right and left atrium in persistent atrial fibrillation: Is the right atrium a window into the left? J Cardiovasc Electrophysiol. 2017;28:1109-1116.

83. Zheng Y, Xia Y, Carlson J, Kongstad O, Yuan S. Atrial average conduction velocity in patients with and without paroxysmal atrial fibrillation. Clin Physiol Funct Imaging. 2017;37:596-601.

84. Josephson ME, Anter E. Substrate Mapping for Ventricular Tachycardia: Assumptions and Misconceptions. JACC Clin Electrophysiol. 2015;1:341-352.

85. Venlet J, Piers SRD, Kapel GFL, de Riva M, Pauli PFG, van der Geest RJ, Zeppenfeld K. Unipolar Endocardial Voltage Mapping in the Right Ventricle: Optimal Cutoff Values Correcting for Computed Tomography-Derived Epicardial Fat Thickness and Their Clinical Value for Substrate Delineation. Circ Arrhythm Electrophysiol. 2017;10.

86. Bazan V, Frankel DS, Santangeli P, Garcia FC, Tschabrunn CM, Marchlinski FE. Three-dimensional myocardial scar characterization from the endocardium: Usefulness of endocardial unipolar electroanatomic mapping. J Cardiovasc Electrophysiol. 2019;30:427-437.

87. Konings KT, Smeets JL, Penn OC, Wellens HJ, Allessie MA. Configuration of unipolar atrial electrograms during electrically induced atrial fibrillation in humans. Circulation. 1997;95:1231-1241.

88. Spach MS, Dolber PC. Relating extracellular potentials and their derivatives to anisotropic propagation at a microscopic level in human cardiac muscle. Evidence for electrical uncoupling of side-to-side fiber connections with increasing age. Circ Res. 1986;58:356-371.

89. Spach MS, King TD, Barr RC, Boaz DE, Morrow MN, Herman-Giddens S. Electrical potential distribution surrounding the atria during depolarization and repolarization in the dog. Circ Res. 1969;24:857-873.

90. Houben RP, de Groot NM, Smeets JL, Becker AE, Lindemans FW, Allessie MA. S-wave predominance of epicardial electrograms during atrial fibrillation in humans: indirect evidence for a role of the thin subepicardial layer. Heart Rhythm. 2004;1:639-647.

91. van der Does L, Knops P, Teuwen CP, Serban C, Starreveld R, Lanters EAH, Mouws E, Kik C, Bogers A, de Groot NMS. Unipolar atrial electrogram morphology from an epicardial and endocardial perspective. Heart Rhythm. 2018;15:879-887.

92. Villacastin J, Almendral J, Arenal A, Castellano NP, Gonzalez S, Ortiz M, Garcia J, Vallbona B, Moreno J, Portales JF, et al. Usefulness of unipolar electrograms to detect isthmus block after radiofrequency ablation of typical atrial flutter. Circulation. 2000;102:3080-3085.

93. Bortone A, Appetiti A, Bouzeman A, Maupas E, Ciobotaru V, Boulenc JM, Pujadas-Berthault P, Rioux P. Unipolar signal modification as a guide for lesion creation during radiofrequency application in the left atrium: prospective study in humans in the setting of paroxysmal atrial fibrillation catheter ablation. Circ Arrhythm Electrophysiol. 2013;6:1095-1102.

94. Prudat Y, Kucera JP. Nonlinear behaviour of conduction and block in cardiac tissue with heterogeneous expression of connexin 43. J Mol Cell Cardiol. 2014;76:46-54.

95. van der Does L, Starreveld R, Kharbanda RK, Knops P, Kik C, Bogers A, de Groot NMS. Detection of Endo-epicardial Asynchrony in the Atrial Wall Using One-Sided Unipolar and Bipolar Electrograms. J Cardiovasc Transl Res. 2021;14:902-911.

96. Rostock T, Rotter M, Sanders P, Takahashi Y, Jais P, Hocini M, Hsu LF, Sacher F, Clementy J, Haissaguerre M. High-density activation mapping of fractionated electrograms in the atria of patients with paroxysmal atrial fibrillation. Heart Rhythm. 2006;3:27-34.

97. Starreveld R, van der Does L, de Groot NMS. Anatomical hotspots of fractionated electrograms in the left and right atrium: do they exist? Europace. 2019;21:60-72.

98. van der Does LJ, de Groot NM. Inhomogeneity and complexity in defining fractionated electrograms. Heart Rhythm. 2017;14:616-624.
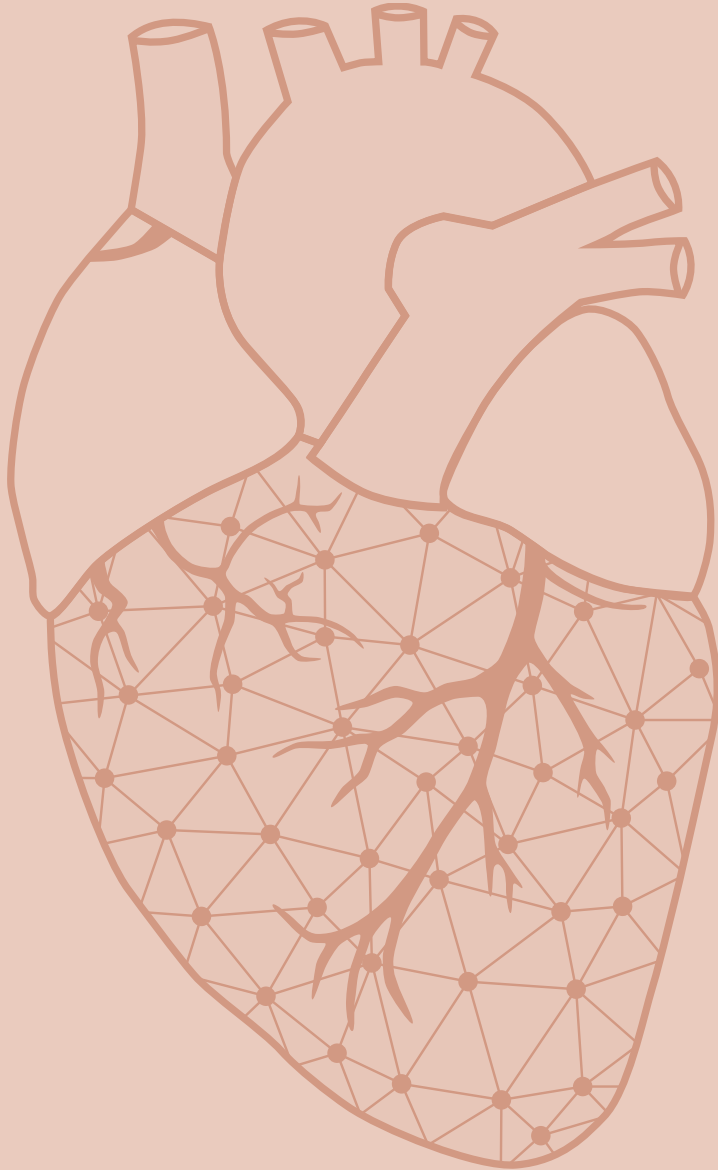
Chapter 2

Clinical relevance of sinus rhythm mapping to quantify electropathology related to atrial fibrillation

Mathijs S. van Schie

Natasja M.S. de Groot

Abstract

Progression of atrial fibrillation (AF) is accompanied by structural and electrical remodeling, resulting in complex electrical conduction disorders. This is defined as electropathology and increases with progression of AF. The severity of electropathology thus defines the stage of AF and is a major determinant of effectiveness of AF therapy. As specific features of AF related electropathology are still unknown, it is essential to first quantify electrophysiological properties of atrial tissue and then to examine the inter- and intra-individual variation during normal sinus rhythm. Next, comparison of these parameters between patients with and without a history of AF unravels quantified electrophysiological features specific for AF patients. This can then aid in identifying patients at risk for early onset or progression of AF. This review summarizes current knowledge on quantified features of atrial electrophysiological properties during sinus rhythm and discusses its relevance in identifying AF related electropathology.

Journal site

Introduction

Electrophysiological mapping strategies targeting atrial tachyarrhythmia, such as atrial fibrillation (AF), have been improved considerably over the past few years. However, designing effective ablation strategies for persistent AF remains a major challenge.[1] Since the development of the pulmonary vein isolation procedure in the late 1990s[2], several additional ablation strategies have been proposed, including linear lesions, complex fractionated electrogram (EGM) ablation[3], low-voltage area (LVA) ablation[4], and identification and ablation of rotational activity and presumed trigger sites.[5] Although these techniques showed promising results in single-center studies, they did not lead to widespread improvement in procedural outcome in multicenter studies.[6] This can only partly be due to the fact that there is still an inadequate understanding of the mechanisms and electropathological substrate underlying AF.

Arrhythmogenesis depends on the presence of a substrate and a trigger. AF initially starts in a paroxysmal form, which is mainly based on the presence of triggers.[2] Progression of AF is accompanied by structural and electrical remodeling, which can typically be described as a progressive change in electrophysiological properties of the myocardium caused by cardiovascular comorbidities and AF itself.[7] This results in complex electrical conduction disorders, which is defined as electropathology.[8] With the progression of AF, there is an increase in electropathology. The severity of electropathology thus defines the stage of AF and is a major determinant of effectiveness of AF therapy.

In an attempt to find the substrate underlying AF, the vast majority of studies directly focus on electrophysiological properties measured during AF or during atrial pacing. However, what the specific features of AF related electropathology are, is at present unknown. These features may include conduction delay and block, signal morphology (e.g., potential voltages and fractionation) and electrical asynchrony between the endo- and epicardium, as illustrated in *Figure 1*. It is essential to first quantify electrophysiological properties of atrial tissue and then to examine the inter- and intra-individual variation in these quantified parameters during normal sinus rhythm (SR). Next, comparison of these parameters between patients with and without a history of AF unravels quantified electrophysiological features specific for AF patients. The most suitable objective parameter can then aid in identifying patients at risk for early onset or progression of AF. This review summarizes current knowledge on quantified features of atrial electrophysiological properties during SR and discusses its relevance in identifying AF related electropathology.

Excitation of the atria

It is nowadays common knowledge that during SR, electrical activity originates from the sino-atrial node (SAN) area, from where the activation first spreads over the right atrium (RA) and towards the left atrium (LA) via Bachmann's bundle (BB), coronary sinus (CS) musculature or interatrial septum. BB is considered to be the preferential route of interatrial conduction, as it is a highly organized bundle of muscular fibers arranged in parallel fashion and by far the largest of the anatomic interatrial connections.[9] Detailed analysis of SR activation was first performed by Boineau et al.[10], who performed epicardial mapping in dogs. Later, Cox et al.[11] were the first to create an epicardial isochronal map of one SR beat activating both the right and left atrium in a human. Since the 1990s, the advent of electro-anatomical mapping systems skyrocketed detailed measurement of impulse propagation inside the human atria. Knowledge on atrial excitation patterns during SR and its variations enabled detection of propagation abnormalities associated with arrhythmia such as AF.
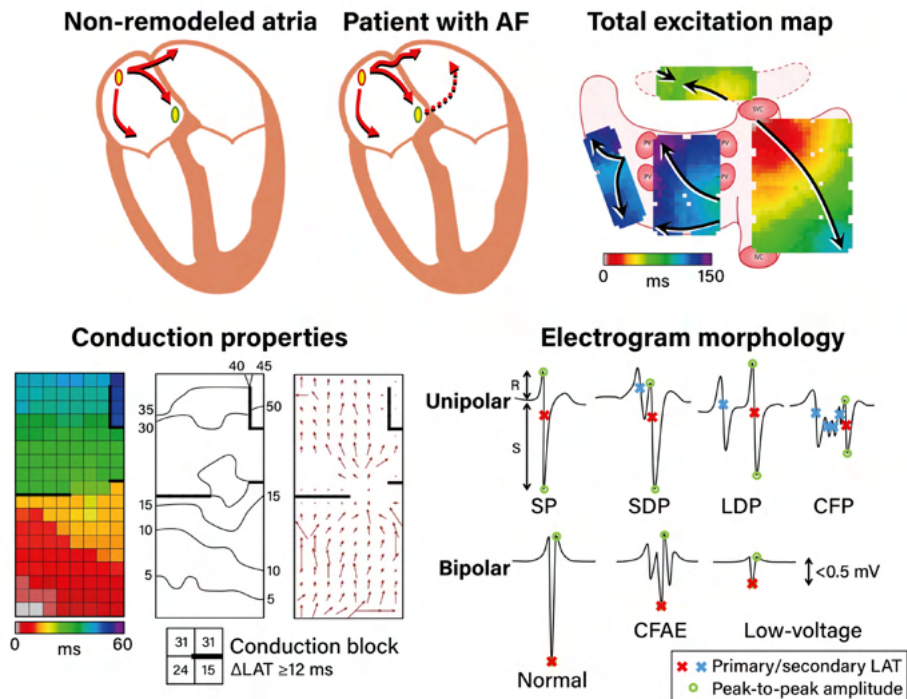
Figure 1 – Excitation and electrophysiological properties of the atria. *Upper left panel*: smooth excitation of the right and left atrium via Bachmann's bundle. *Upper middle panel*: impaired conduction across Bachmann's bundle in a patient with AF results in alternative interatrial routes. *Upper right panel*: color-coded total excitation maps of the right and left atrium on a schematic posterior view of the atria derived from epicardial mapping. Arrows indicate main trajectories of sinus rhythm wavefront at different atrial regions. *Lower left panel*: quantification of conduction disorders. Left: color-coded activation map based on local activation times. Thick black lines represent conduction block according to a time difference between adjacent electrodes of ≥12 ms. Middle: local activation pattern with isochronal map. Isochrones are drawn at 5 ms. Right: conduction velocity map of the corresponding local activation maps. *Lower right panel*: typical examples of different types of unipolar (upper) and bipolar (lower) electrograms. Morphology of unipolar single potentials is classified according to the relative R to S wave amplitude. **CFAE** = complex fractionated atrial electrograms; **CFP** = complex fractionated potential; **IVC** = inferior vena cava; **LAT** = local activation time; **LDP** = long double potential; **PV** = pulmonary vein; **SDP** = short double potential; **SP** = single potential; **SVC** = superior vena cava.

Spread of the SR wavefront is influenced by membrane properties, tissue structure and wavefront geometry.[12,13] Conduction disorders are caused by structural atrial remodeling due to e.g. (long-standing) pressure and/or volume overload, inflammation, atherosclerosis, myocardial ischemia/infarction, interstitial fibrosis or an abnormal anatomy.[14-18] Structural remodeling may lead to non-uniform tissue anisotropy and local disorders in conduction, such as slowing of conduction or conduction block (CB). Areas of CB (frequently defined as large activation time differences between two adjacent electrodes or the presence of double potentials) are thought to play a crucial role in both genesis and perpetuation of AF.[12,19] The presence of lines of CB makes it more likely for reentrant circuits to develop, which may increase the likelihood of AF.[20] Lines of CB affect propagation of the expanding SR wavefront and could be either structural or functional in nature. Spach et al.[21] demonstrated that ageing leads to greater changes in conduction when wavefront directions are differed, leading to low-voltage, fractionated potentials. Wong et al.[22] used CS pacing to assess electrophysiological features during wavefronts propagating in different directions. They observed that there was direction dependent slowing of conduction, prolongation of total atrial excitation times and increase in number and length of CB lines. These differences were more pronounced in patients with chronic atrial stretch and associated with a greater

2

susceptibility to develop AF. On the other hand, conduction abnormalities could also be rate-dependent. Huang et al.[23] used CS pacing with cycle lengths varying between 1000 and 250 ms and demonstrated that rate-dependent CB was present in 94% of patients with AF induction. However, by examining 339 atrial extrasystoles during epicardial mapping, Teuwen et al.[24] showed that incidence of conduction disorders was mainly associated with the degree of aberrancy, but not with prematurity. Conduction abnormalities could therefore be hidden during normal SR, resulting in possible underestimation of conduction disorders in studies performed only during SR.

Conduction abnormalities in electrically non-remodeled atria

In patients with Wolff-Parkinson White syndrome with nondilated atria, Konings et al.[25] were the first to demonstrate that the RA free wall of these near healthy hearts was activated uniformly by a single broad activation wave without any conduction disorders. Hansson et al.[26], however, demonstrated in 3 out of 12 patients undergoing coronary artery bypass grafting (CABG, 63±7.6 years) or surgical transection of an accessory pathway (55±9.9 years) that epicardial mapping of the RA free wall during SR revealed small areas of conduction disorders, covering 2 to 12% of the total recording area. Moreover, the presence of areas of CB was also described at the junction of the right superior pulmonary vein (PV) and the LA in 18 patients (67±11 years) without AF.[27] In contrast, Lanters et al.[28] demonstrated in 209 CABG patients (66±9.6 years) with electrically non-remodeled atria that some degree of CB (median 1.3%, range 0.1–4.3%) was present in all patients. There was a considerable intra-atrial, but also inter-individual variation in prevalence of CB. However, a predilection site was present at the superior intercaval RA although it did not reflect CB elsewhere in the atria and had no correlation with development of post-operative AF.

Conduction abnormalities predisposing to post-operative AF

Various studies report on an association between CB during SR and development of AF. Sakamoto et al.[29] performed intra-operative mapping during SR of the RA free wall in 52 patients with a variety of structural heart diseases. The presence of non-uniform activation patterns (defined as areas of CB or fusion of multiple wavefronts) was observed in 15 patients (29%) and was associated with development of post-operative AF. Kharbanda et al.[30] examined the RA by simultaneous endo-epicardial mapping in 80 patients and found a relationship between transmural CB at the inferior RA and post-operative AF. Other atrial sites were also related to development of post-operative AF. By performing epicardial mapping at BB, Teuwen et al.[9] found that a high amount (defined as >4% CB) and long lines of CB (defined as ≥12 mm) predisposed for early post-operative AF in CABG patients (*Table 1*).

Two studies described the association between areas of CB during SR for intra-operative AF inducibility in patients without a history of AF. Roberts-Thomson et al.[36] compared atrial septal defect patients with control subjects and demonstrated the presence of conduction disorders in the LA and increased inducibility of AF in atrial septal defect patients. In 54 patients with structural heart disease without a history of AF, Van Staveren et al.[37] recently described that longer lines of CB at BB were related to AF inducibility. These observations further support a relation between the presence of conduction abnormalities and development AF.

Conduction abnormalities associated with AF episodes

During SR, electrical activity originates from the SAN area and conducts to the atrial myocardium via several exit pathways.[38] The presence of areas of CB around the SAN

Table 1 – Atrial excitation in patients with AF.

Authors	Study population	Site of interest	Mapping sites	Recording site	Patients (n)	AF patients (n)	AF type	Outcomes
Kharbanda et al. 2021[31]	CAD MVD AVD	SAN exit pathways	RA	Endo-epi	20	8	PAF	AF patients: caudal sinus node activity caused by changes in preferential SAN exit pathways
Lemery et al. 2004[32]	AF	Interatrial conduction	RA, LA	Endo	20	15 5	PAF PsAF	LA activation mainly via BB
Tapanainen et al. 2009[33]	AF	Interatrial conduction	RA, LA	Endo	50	50	PAF	Although BB is the most common route between the atria, the LA was activated primarily via: • Rim of the oval fossa • CS ostial connections
Teuwen et al. 2016[9]	CAD	Interatrial conduction	BB	Epi	185	13 56	PAF DN PoAF	Conduction disorders delay right-to-left excitation, thereby favouring conduction via other interatrial routes
Mouws et al. 2018[34]	CAD MVD AVD	Interatrial conduction	RA, BB, PVA, LA	Epi	253	33 9 1	PAF PsAF LPsAF	AF patients: • Alternative routes for BB and LAVG activation • Prolongation of TAT
Mouws et al. 2018[35]	CAD MVD AVD	LA	PVA	Epi	327	47 14 1	PAF PsAF LPsAF	AF patients: • Complex patterns with multiple entry sites

(L)PsAF = (long-standing) persistent atrial fibrillation; **AF** = atrial fibrillation; **AVD** = aortic valve disease; **BB** = Bachmann's bundle; **CAD** = coronary artery disease; **(DN) PoAF** = (de-novo) post-operative atrial fibrillation; **endo** = endocardial; **epi** = epicardial; **LA** = left atrium; **LAVG** = left atrioventricular groove; **MVD** = mitral valve disease; **PAF** = paroxysmal atrial fibrillation; **PVA** = pulmonary vein area; **RA** = right atrium; **SAN** = sino-atrial node; **TAT** = total activation time.

causes blockage of these exit pathways, leading to shifts of SAN exit sites. In patients with AF, Kharbanda et al.[31] indeed demonstrated that the SAN exit pathway was located more caudally compared to patients without AF. By using simultaneous endo-epicardial mapping, Kharbanda et al.[30] also demonstrated that conduction disorders at the RA were more pronounced in patients with a history of AF. In contrast, in an epicardial mapping study using 253 patients with various underlying heart diseases, Mouws et al.[34] demonstrated that although RA excitation during SR was prolonged in patients with history of AF, there was no relation between the SAN exit site and total atrial excitation time.

Previous studies have also demonstrated that patients with a history of AF have more conduction disorders in the RA and LA compared to patients without AF. In 268 patients with and without a history of AF, Mouws et al.[39] showed that patients with AF more often present with continuous lines of CB located at the PV area. Recently, Heida et al.[40] demonstrated that patients with various underlying heart diseases and history of AF had more conduction disorders than patients without AF throughout both atria. Van der Does et al.[41] identified the lateral LA as a location with more conduction disorders in patients with valvular heart disease. Interestingly, in all aforementioned studies, disturbed conduction at BB during SR was most strongly correlated with the presence of atrial remodeling related to AF episodes (*Table 2*).

Bachmann's bundle: a key player in arrhythmogenesis?

BB is the preferential route of interatrial conduction. Lemery et al.[32] performed endocardial mapping in 20 patients with either paroxysmal or persistent AF and demonstrated that LA activation occurred via BB in all patients. However, Tapanainen et al.[33] demonstrated that although BB is the most common interatrial route, the LA was activated primarily via the rim of the oval fossa region at the interatrial septum or via the CS ostial connections in 15 out of 50 patients with paroxysmal AF. A limitation of these studies was that mapping was performed with a low spatial resolution in a small number of patients. Most importantly, BB was not included in these studies as mapping was performed only at the endocardial side.

In several studies it was demonstrated that BB is a predilection site for conduction disorders to occur.[34,40,42] In an intra-operative epicardial mapping study of Mouws et al.[34], it was demonstrated that total atrial excitation times were longer in patients with a history of AF compared to those without AF (136 ± 20 ms vs 114 ± 17 ms, p<0.001). This was mainly caused by longer total activation time of the RA and BB (RA: 73 ± 13 ms vs 67 ± 14 ms, p=0.018; BB: 106 ± 20 ms vs 87 ± 16 ms, p<0.001). This resulted in alternative routes for BB and left atrioventricular groove (LAVG) activation, as BB was activated either via one wavefront from right-to-left, from the central part or via multiple wavefronts. The LAVG was then activated via either BB, the PV area or via both routes, depending on which route had the shortest interatrial excitation time. An increased total activation time of BB was caused by the presence of extensive conduction disorders. Teuwen et al.[9] indeed demonstrated in patients with AF episodes undergoing CABG that particularly long lines of longitudinal CB are more pronounced. The resulting delayed right-to-left excitation favored conduction via other interatrial routes, such as the limbus of the oval fossa, the CS and interatrial bundles both superior and inferior along BB. As demonstrated by Mouws et al.[35], a combination of conduction disorders and distinct parts of the SR wavefront entering asynchronously the posterior LA can lead to an increased risk of AF. Conduction disorders giving rise to alternative propagation routes may be the result of damage to the thick and thin septa surrounding BB myocytes, considerably affecting interatrial conduction.[50] This was further supported by the observation of Mouws et al.[34] that LAVG excitation via only PV area was considerably slower than via BB (90 ± 18 ms vs 101 ± 20 ms, p<0.001). Particularly patients with either AF, LA dilation or mitral valve

Table 2 – Comparison between patients with AF and controls.

Authors	Study population	Mapping sites	Recording site	Patients (n)	AF patients (n)	AF type	Outcome parameter	Control	AF group	p-value
Teuwen et al. 2016[9]	CAD	BB	Epi	185	13	PAF	CB	0.9 [0–12.8] %	3.2 [0–11.6] %	0.03
							Longitudinal CB	4.0 [90–11.7] %	1.1 [0–12.8] %	0.03
							Transverse CB	1.0 [0–12.8] %	1.9 [0–12.3] %	0.03
							Longitudinal CB	2 mm	8 mm	0.03
					56	DN PoAF	>4% CB	OR 3.1 [1.2–8.1]		0.02
							≥12 mm longitudinal CB	OR 2.9 [1.1–8.2]		0.04
Mouws et al. 2018[35]	CAD MVD AVD	PVA	Epi	327	47 14 1	PAF PsAF LPsAF	CD ≥6 mm	OR 2.29 [1.18–4.44]		0.014
							CB ≥6 mm	OR 2.04 [1.09–3.83]		0.027
							CDCB ≥16 mm	OR 2.06 [1.08–3.93]		0.029
Sakamoto et al. 2006[29]	CAD MVD AVD ASD	RA	Epi	52	21	PoAF	CD/CB/mosaic activation	N=3 [9%]	N=13 [61%]	<0.001
Kharbanda et al. 2020[30]	CAD MVD AVD	RA	Endo-epi	80	25 4 2 30	PAF PsAF LPsAF PoAF	Endo - epicardial CB	0.8 [0.2–2.0] %	3.9 [1.9–5.9] %	0.007
							Continuous CDCB	1.0 [0.2–3.5] %	6.5 [3.7–11.5] %	0.001
							Median length CDCB	8 [0–12] mm	16 [12–20] mm	0.005
							Max length CDCB	12 [6–22] mm	28 [21–55] mm	0.004
Van Staveren et al. 2021[37]	CAD VHD CHD	BB	Epi	54	0	-	Max length CB	2 [2–28] mm	18 [2–164] mm	0.031
Mouws et al. 2019[39]	CAD MVD AVD	PVA	Epi	268	38 11	PAF PsAF	Continuous CDCB	N=132 [60%]	N=37 [76%]	0.046
							CD	4 [0–22]	7 [0–30]	<0.001
							CB	1 [0–12]	3 [0–11]	0.003
							CDCB	1 [0–8]	2 [0–6]	0.004
							CD ≥6 mm	N=108 [49%]	N=23 [69%]	0.011
							CB ≥6 mm	N=91 [42%]	N=29 [59%]	0.025
							CDCB ≥16 mm	N=50 [25%]	N=20 [41%]	0.027
Van der Does et al. 2020[41]	MVD AVD	RA, BB, PVA, LA	Epi	139	38	P(s)AF	Total CDCB	2.3±2.0 %	2.7±2.3 %	0.044
							BB CDCB	2.3±4.4 %	5.9±6.4 %	<0.001
							LA CDCB	1.0±1.9 %	1.8±2.5 %	0.009
Houck et al. 2020[42]	CHD	RA, BB, PVA, LA	Epi	31	5	PAF	BB CB	2.0 [0–10.9] %	6.3 [1.3–8.5] %	0.047
							BB max length of CB	12 [12–54] mm	34 [12–40] mm	0.041

2

Authors	Study population	Mapping sites	Recording site	Patients (n)	AF patients (n)	AF type	Outcome parameter	Control	AF group	p-value
Heida et al. 2020[40]	CAD MVD AVD CHD	RA, BB, PVA, LA	Epi	447	52 21 2	PAF PsAF LPsAF	Max CT CT ≥4 ms BB CT ≥4 ms LA CT ≥4 ms PVA CT ≥4 ms CT ≥50 ms BB CT ≥30 ms	45 [33–54] ms 12.8 [10.9–14.6] % 15.2 [11.8–19.5] % 9.0 [6.5–11.9] % 10.9 [8.4–14.1] % N=34.4% N=36.0%	54 [40–66] ms 14.9 [11.8–17.0] % 20.5 [14.0–26.2] % 10.0 [7.0–13.3] % 13.4 [9.0–17.6] % N=54.7% N=56.2%	0.006 <0.001 <0.001 0.045 0.001 <0.004 <0.004
Lin et al. 2014[43]	AF, left-sided accessory pathway	LA	Endo	102	30 22 30	PAF PsAF LPsAF	TAT	75.3±5.4 ms	89.7±12.3 ms & 104.9±6.1 ms & 115.6±12.1 ms	<0.001
Zheng et al. 2017[44]	AF, AVNRT	RA	Endo	20	8	PAF	Total CV Posterior CV Septal CV Tricuspid annulus CV	83±13 cm/s 82±25 cm/s 93±32 cm/s 61±21 cm/s	60±12 cm/s 54±19 cm/s 64±20 cm/s 36±22 cm/s	<0.05 <0.05 <0.05 <0.05
Van Schie et al. 2021[45]	CAD MVD AVD	RA, BB, PVA, LA	Epi	412	58	PAF	BB CV BB CV <28 cm/s PVA CV <28 cm/s	88 [79–97] cm/s 6.6 [3.9–11.1] % 0.9 [0.3–1.9] %	79 [72–91] cm/s 8.3 [5.8–13.6] % 1.4 [0.5–3.3] %	<0.001 0.004 0.014
Heida et al. 2021[46]	CAD MVD AVD	RA, BB, PVA, LA	Epi	34	6 9 2	PAF PsAF LPsAF	BB CV Total TAT BB TAT	88±11 cm/s 120±22 ms 58±22 ms	79±12 cm/s 156±21 ms 76±31 ms	0.02 <0.001 0.03
Van Schie et al. 2020[47]	MVD	RA, BB, PVA, LA	Epi	67	23	PAF	BB CV	97 [70–121] cm/s	89 [62–116] cm/s	<0.001
Teh et al. 2012[48]	AF, left-sided accessory pathway	LA	Endo	46	17 14	PAF PsAF	Total AI Isthmus AI Posterior AI Anterior AI LAA AI Roof AI Floor AI	131±24 cm²/s 46±28 cm²/s 49±19 cm²/s 79±67 cm²/s 42±24 cm²/s 41±19 cm²/s 56±11 cm²/s	86±17 cm²/s & 79±15 cm²/s 23±9 cm²/s & 26±12 cm²/s 51±27 cm²/s & 29±11 cm²/s 35±7 cm²/s & 40±14 cm²/s 26±12 cm²/s & 18±12 cm²/s 24±13 cm²/s & 19±9 cm²/s 46±22 cm²/s & 37±9 cm²/s	<0.001 0.01 0.02* 0.03 0.003* 0.001 0.02*

Authors	Study population	Mapping sites	Recording site	Patients (n)	AF patients (n)	AF type	Outcome parameter	Control	AF group	p-value
Stiles et al. 2009[49]	AF, left-sided accessory pathway	RA, LA	Endo	50	25	PAF	CT	47±10 ms	57±18ms	0.01
							Total TAT	89±10 ms	128±17 ms	<0.001
							RA CV	210±50 cm/s	130±30 cm/s	<0.001
							LA CV	220±40 cm/s	120±20 cm/s	<0.001

* p<0.05 for comparison between both groups. **(L)PsAF** = (long-standing) persistent atrial fibrillation; **AF** = atrial fibrillation; **AI** = activation index; **AVD** = aortic valve disease; **BB** = Bachmann's bundle; **CAD** = coronary artery disease; **CD(/)CB** = conduction delay and/or block; **CHD** = congenital heart disease; **CT** = conduction times; **CV** = conduction velocity; **(DN) PoAF** = (de-novo) post-operative atrial fibrillation; **endo** = endocardial; **epi** = epicardial; **LA** = left atrium; **LAA** = left atrial appendage; **MVD** = mitral valve disease; **OR** = odds ratio; **PAF** = paroxysmal atrial fibrillation; **PVA** = pulmonary vein area; **RA** = right atrium; **TAT** = total activation time.

disease (MVD) had longer total excitation times of the atria, which was mainly determined by impaired conduction along BB. Based on these observations it was suggested that total atrial excitation times are particularly affected by conduction disorders at BB and RA, which are likely related to the presence of AF. This was also demonstrated by Heida et al.[40], who recently showed in a large cohort of 447 patients that a history of AF was associated with slowing of conduction; patients with AF had more conduction times (CT) ≥4 ms (≈50 cm/s), especially at BB, LA and PV area. In addition, maximum CT for AF patients was larger than in non-AF patients. In the majority of studies, it was consistently demonstrated that an increased amount of conduction disorders at BB is present in AF patients. The highly organized architecture of BB could make this structure more vulnerable to structural remodeling and consequently disturbances in conduction that can even be identified during SR.

Pro-arrhythmic features of ablation created conduction block

There appears to be a clear link between the presence of conduction disorders and development of AF. However, CB can also be introduced during extensive catheter ablation procedures targeting complex fractionated EGMs or LVAs, for example. From a theoretical point of view, the resulting ablation lesions causing local CB may be involved in initiation and perpetuation of AF. This is also the case if linear lesions were incomplete. Post-operative arrhythmias are not uncommon after AF surgery and are typically reentrant and related to the surgically created lesions.[51] A combination of pre-existing conduction disorders and manually created lesions can therefore also provide additional substrate underlying AF recurrence.

Assessment of the cardiac conduction velocity

Cardiac conduction velocity (CV) provides important information on the properties of the underlying myocardium and is therefore widely used in electrophysiological studies. Changes in intercellular electrical coupling and tissue structure contribute to conduction heterogeneity and CV reduction, which in turn play a major role in the initiation and perpetuation of AF.[21] However, there is no agreement which is the best technique to compute CV.[52] Calculation of CV is frequently based on a certain distance travelled by a propagating wavefront in a unit of time. This results in an accurate CV estimate if the propagation is uniform and the direction is known. A straightforward method to estimate CV is by using isochronal maps in which isopotential lines are drawn over a fixed time interval. The CV is then estimated by examining the distance travelled over a fixed time window. In order to also automatically include an estimation of the local propagation direction, a minimum of three electrodes is typically required to establish a velocity vector. Also, an adequate spatial resolution is required to minimize CV estimation errors, especially when working with complex and heterogeneous activation wavefronts. During standard electrophysiology studies, multi-electrode catheters enable CV estimation by techniques such as triangulation.[52] Using regularly spaced high-density electrode arrays, simultaneous recordings on a high spatial resolution scale enable analysis of complex and heterogeneous patterns of activation by using techniques such as finite differences, polynomial surface fitting, discrete velocity vectors or omnipolar EGMs (O-EGMs).[45,53] A disadvantage of the finite differences, polynomial surface fitting and O-EGM techniques is that it requires data interpolation and smoothening, thereby masking local conduction heterogeneity.

Local CV can be estimated by triangulation using 3D electro-anatomical activation maps. Using this methodology, Stiles et al.[49] demonstrated in patients with paroxysmal AF that CV was especially lower at the RA and LA septal parts compared to controls with a left-sided accessory pathway (RA: 210±50 cm/s vs 130±30 cm/s, p<0.001; LA: 220±40 cm/s vs 120±20

cm/s, p<0.001). During CS pacing in patients with (long-standing) persistent AF, Prabhu et al.[54] demonstrated that CV in the RA was lower compared to the LA (93±15 cm/s vs 101±19 cm/s, p=0.02), also particularly at the septal parts of the atria. Another study of Zheng et al.[44] reported that during SR, the average CVs of the RA were lower in paroxysmal AF patients compared to controls with atrioventricular nodal reentrant tachycardia (60±12 cm/s vs 83±13 cm/s, p<0.05). Remarkably, CV estimates in this control group were much lower than CVs assessed in other studies.[9,26,55] In addition, no differences were found between the septum and other parts of the atria. Although the triangulation methodology has been automated to generate high-density CV maps of clinically acquired data, studies focusing on CV comparison in AF patients are lacking.[56]

Teuwen et al.[9] reported that CV (measured by using isochronal maps) across BB is around 90 cm/s in patients undergoing CABG, which was comparable with an average CV of 88 cm/s at the RA free wall in patients with Wolff-Parkinson-White syndrome and patients with ischemic and/or valvular heart disease.[26,45,46] However, in the case of local conduction heterogeneities, a more sophisticated method is required. Recently, Van Schie et al.[45] developed a discrete velocity vectors methodology to estimate local CVs. It was demonstrated that patients with paroxysmal AF have slower conduction across BB (±10 cm/s) during SR compared to patients without AF. In addition, more areas of slow CV (<30 cm/s) were found at both BB and PV area. Heida et al.[46] recently reported similar observations in a case-control study of 34 patients without and with a history of AF. In a specific population of MVD patients, a history of AF was characterized by decreased CV and unipolar single potential amplitudes at BB due to loss of S-wave amplitudes.[47] Areas of slowed conduction have frequently been linked to low-voltage potentials, which formed the basis for current ablation strategies targeting LVAs for AF.[12,57-59]

Voltage mapping techniques

Structurally remodeled tissue gives rise to slowing of conduction or conduction disorders. These areas are frequently identified using the spatial distribution of EGM amplitudes, commonly known as voltage mapping. There is, however, still lack of consensus on how to accurately use voltage mapping to target the AF substrate and how to define abnormal voltage.[60] Also, there are several voltage modalities which can be used such as unipolar, bipolar and multipolar (omnipolar/Laplacian) voltage mapping.[61] In the basis, a unipolar EGM (U-EGM) is recorded as an extracellular potential difference between one single electrode on the tissue relative to an indifferent electrode, while a bipolar EGM (Bi-EGM) is simply the subtraction of two U-EGMs. Therefore, a U-EGM can be regarded as the sum of instantaneous current dipoles of a wavefront, reflecting cardiac electrical activity of the tissue surrounding the recording electrode. As the amplitude depends on the volume of simultaneously activated cardiac tissue, synchronous activation of myocardium results in relative large amplitude U-EGMs, whereas areas of asynchronously activated myocardium cause a decrease in U-EGM amplitudes.[19] Although U-EGMs are more sensitive to far-field and remote activations, U-EGM potential morphology contains additional information on the progression of the wavefront.[47] Nevertheless, Bi-EGMs are still predominantly used in clinical practice as Bi-EGMs are less sensitive to noise and represent more local information from the tissue between two electrodes. However, Bi-EGMs are very directional sensitive, which is particularly important when targeting voltage abnormalities during stable SR.[62] To overcome this directional sensitivity, a so-called omnipolar mapping technique has recently been proposed. Using multiple neighboring electrodes, O-EGMs are mathematically constructed that represent maximal bipolar voltage along the direction of a propagating wavefront.[53] However, a major disadvantage of all voltage mapping techniques is their dependency on the electrode size, as larger electrodes result in lower voltages and consequently more LVAs

2

in the tissue.[63] It therefore remains difficult to directly compare various study outcomes.

Bipolar voltage mapping

Several studies have shown local variation in bipolar voltages during SR, in which the majority of the studies focused on the LA only (*Table 3*). In addition, all studies described regional voltage analyses as part of ablation therapy targeting LVAs. These areas are commonly defined as bipolar voltages ≤0.5 mV.[64] Marcus et al.[65] were the first to characterize regional differences in bipolar voltage during SR in 22 patients with paroxysmal AF. They demonstrated that AF patients exhibited significantly more LVAs in the septum and posterior LA walls compared to patients with focal atrial tachycardia. However, a major disadvantage of this study was that the AF patients were mapped with an 8-mm catheter, whereas all control patients were mapped with a 4-mm catheter. During pacing from the CS, Teh et al.[48] demonstrated that patients with AF have circumscriptive areas of lower voltages, more LVAs, slowing of conduction and fractionated EGMs compared to age-matched control patients with a left-sided accessory pathway. These changes were more pronounced in persistent AF patients, who were first cardioverted when they did not present in SR.

Two years later, Rolf et al.[4] were then the first to describe the use of SR voltage mapping guiding AF substrate modification after circumferential PV isolation and demonstrated that LVAs occur more frequently in patients with persistent AF compared to patients with paroxysmal AF. Lin et al.[43] also demonstrated a decrease in mean LA voltage and a higher incidence of LVAs during SR with progression of AF. Regional LA differences were studied in more detail by Kapa et al.[69], who demonstrated that there was a heterogeneity in voltage distribution in all patients regardless of prior LA ablation. The highest voltage was found in the LA floor and lowest in posterior LA wall adjoining the PVs, while Rodríguez-Mañero et al.[70] found the highest values in the LA appendage. Kogawa et al.[66] compared these regional differences between patients with paroxysmal or persistent AF during SR. They demonstrated that bipolar voltages were specifically lower at the LA septum, roof and posterior wall, right superior PV and its antrum, right superior PV carina and right inferior PV antrum in patients with persistent AF.

As AF therapy commonly targets only in the LA, data on regional differences in bipolar bi-atrial voltage during SR is lacking. However, Stiles et al.[49] showed that mean RA and LA bipolar voltage was reduced in 25 patients with paroxysmal AF compared with 25 patients with left-sided accessory pathways. More specifically, areas at the high-lateral RA, posterior LA and LA roof in AF patients were more likely to be LVAs. Although during CS pacing, Prabhu et al.[54] demonstrated that global bipolar voltage did not differ between the RA and LA, but voltages were larger at the posterior LA compared to posterior RA in patients with (long-standing) persistent AF. Although specific regional differences in bipolar voltages are more recognized, cutoff values to identify LVAs are currently not customized to the different atrial voltage distributions. Despite ablation therapy based on bipolar LVAs may be beneficial in certain patient populations, the efficacy and long-term outcome remains controversial.[58] It is for these reasons that U-EGMs are regaining popularity in the last years.

Unipolar voltage mapping

Unlike Bi-EGMs, U-EGMs are directional independent and provide additional information on wavefront progression. Remarkably, studies focusing on unipolar voltage distribution during SR are still lacking, although the use of U-EGMs regains interest in clinical practice. Using biatrial electro-anatomical mapping, Prabhu et al.[54] demonstrated that unipolar voltages were higher in the LA compared to the RA in patients with (long-standing) persistent AF

Table 3 – Comparison of EGM characteristics between patients with AF and controls.

Authors	Study population	Mapping sites	Recording site	Patients (n)	AF patients (n)	AF type	Outcome parameter	Control	AF group	p-value
Heida et al. 2021[46]	CAD MVD AVD	RA, BB, PVA, LA	Epi	34	6 9 2	PAF PsAF LPsAF	BB U-voltage P_S	1.5±0.9 mV	0.9±0.6 mV	0.02
Van Schie et al. 2020[47]	MVD	RA, BB, PVA, LA	Epi	67	23	PAF	SP U-voltage RA U S-wave predominance	5.1 [2.5–7.6] mV 88.8%	4.8 [2.1–7.2] mV 85.7%	<0.001 0.021
							BB U S-wave predominance	92.3%	85.2%	0.003
							LA U S-wave predominance	41.1%	48.0%	0.013
							BB U S-wave voltage	4.1 [2.5–6.1] mV	2.9 [1.4–4.8] mV	<0.001
Teh et al. 2012[48]	AF, left-sided LA accessory pathway		Endo	46	17 14	PAF PsAF	B-voltage	2.8±0.4 mV	2.2±0.4 mV & 1.8±0.3 mV	<0.001*
							CFAE	1.8%	4.9% & 7.3%	<0.001*
Lin et al. 2014[43]	AF, left-sided LA accessory pathway		Endo	102	30 22 30	PAF PsAF LPsAF	B-voltage B-LVA index B-LVA	3.67±0.68 mV	2.16±0.63 mV & 1.81±0.36 mV & 1.48±0.34 mV	<0.001
							CFAE	0.78±0.10	0.95±0.20 & 0.98±0.16 & 1.11±0.19	<0.05
								N=0 [0%]	N=14 [46.7%] & N=12 [54.5%] & N=23 [82.1%]	<0.05
								2.3±1.1%	5.6±3.1% & 7.7±2.5% & 13.6±9.6%	<0.05

2

Authors	Study population	Mapping sites	Recording site	Patients (n)	AF patients (n)	AF type	Outcome parameter	Control	AF group	p-value
Kogawa et al. 2017[66]	AF	LA	Endo	36	23 13	PAF PsAF	Total B-voltage		2.50±1.66 mV & 1.58±1.35 mV	<0.001*
							Septal B-voltage		2.06±1.48 mV & 1.03±1.07 mV	0.023*
							Roof B-voltage		2.50±1.59 mV & 1.61±0.92 mV	0.046*
							Posterior B-voltage		3.44±1.50 mV & 2.10±1.66 mV	0.007*
							RSPV antrum B-voltage		1.81±1.46 mV & 1.00±0.64 mV	0.008*
							RSPV B-voltage		1.19±0.72 mV & 0.64±0.43 mV	0.017*
							RPV carina B-voltage		1.98±1.07 mV & 1.00±0.64 mV	0.004*
							RIPV antrum		1.91±1.36 mV & 1.23±1.09 mV	0.033*
Stiles et al. 2009[49]	AF, left-sided accessory pathway	RA, LA	Endo	50	25	PAF	Fractionation	8±5%	27±8%	<0.001
							RA B-voltage	2.9±0.4 mV	1.7±0.4 mV	<0.001
							LA B-voltage	3.3±0.7 mV	1.7±0.7 mV	<0.001
							High-lateral RA LVA	OR 2.9 [1.4–6.3]		
							Posterior LA LVA	OR 1.7 [1.1–2.6]		
							LA roof LVA	OR 3.3 [1.8–6.3]		
Lin et al. 2005[67]	AF, AVNRT, AT, AFL	RA	Endo	40	10	PAF	U-peak negative voltage >-0.28 mV	5.0% & 15.8% & 16.9%	19.0%	<0.001
							U-peak negative voltage	-1.34±0.22 mV & -0.90±0.40 mV & -1.00±0.36 mV	-0.85±0.35 mV	0.04
Van Schie et al. 2021[68]	MVD	RA, BB, PVA, LA	Epi	67	23	PAF	BB U-voltage	4.9 [3.5–6.1] mV	3.0 [2.2–4.6] mV	0.007
							BB U-LVA	1.8 [0.4–8.0] %	12.0 [3.0–21.5] %	0.001
							PVA fractionation	11.9 [9.1–17.0] %	21.7 [13.5–28.6] %	<0.001

* p<0.05 for comparison between both groups. (L)PsAF = (long-standing) persistent atrial fibrillation; AF = atrial fibrillation; AFL = atrial flutter; AT = atrial tachycardia; AVD = aortic valve disease; AVNRT = atrioventricular nodal reentrant tachycardia; BB = Bachmann's bundle; B- = bipolar; CAD = coronary artery disease; CFAE = complex fractionated atrial electrograms; endo = endocardial; epi = epicardial; LA = left atrium; LVA = low-voltage area; MVD = mitral valve disease; OR = odds ratio; PAF = paroxysmal atrial fibrillation; PVA = pulmonary vein area; RA = right atrium; R(I/S)PV = right (inferior/superior) pulmonary vein; U- = unipolar.

(2.95±1.14 vs 2.28±0.65 mV, p=0.002) during CS pacing. More specifically, unipolar voltages were particularly higher in the posterior, lateral and septal parts of the LA. Another U-EGM voltage parameter was introduced by Lin et al.[67], who used peak negative voltages to study the voltage distribution in patients with paroxysmal AF compared to other supraventricular tachycardia. These peak negative voltages are defined as the negative portions of U-EGMs. They demonstrated that global RA peak negative voltages were reduced and more heterogeneously distributed in AF patients compared to patients with either atrioventricular nodal reentrant tachycardia, focal atrial tachycardia or atrial flutter. Recently, Van Schie et al.[68] demonstrated that unipolar voltage is lower in areas of slowed conduction or CB, or areas containing fractionated potentials, which might indicate areas of arrhythmogenic tissue. In this study, unipolar LVAs were found in all 67 patients with MVD with and without history of paroxysmal AF, although lower voltages and more LVAs were found at BB in paroxysmal AF patients. There were no predilection sites for low voltages to occur. Patients with paroxysmal AF were also characterized by decreased single potential amplitudes at BB due to loss of S-wave amplitudes together with a decreased CV.[47] Remarkably, no further studies are available focusing on unipolar voltages during SR. Recently, Van Schie et al.[62] demonstrated that bipolar LVAs still can contain large unipolar voltages and high CVs. Future studies could therefore focus on the combination of unipolar and bipolar voltages to improve voltage guided ablation therapy.

Usage of electrogram morphology and fractionation

Another parameter of potential morphology includes potential fractionation. However, it remains unclear how fractionated potentials need to be defined as many different definitions and recording methodologies have been introduced.[71] Although fractionated EGMs are frequently linked to LVAs and slowed conduction, Viles-Gonzalez et al.[72] demonstrated that fractionation during SR is also found in areas characterized by normal voltages and CV. Nevertheless, fractionation is still commonly used to identify arrhythmogenic substrate with either U-EGMs or Bi-EGMs. However, fractionation can also occur during SR in patients without electrically remodeled atria, although more frequently in patients with AF.[73]

While potential annotation in U-EGMs is quite straightforward, Bi-EGM annotation is more complex, particularly in identification of complex fractionated potentials. It is therefore not surprising that no predilection sites for fractionation or differences in the degree and spatial distribution of fractionation between patients with paroxysmal or persistent AF could be found in a large review of 84 studies targeting, mostly Bi-EGM, complex fractionated EGMs.[74]

Fractionation of U-EGMs, on the other hand, has been studied less extensively. Already in the late 1990s, Konings et al.[75] described a classification of U-EGMs based on the number of negative deflections, which is, especially during SR, easy to measure. Recently, Van Schie et al.[68] demonstrated that MVD patients with paroxysmal AF had more unipolar fractionated potentials at the PV area compared to those without history of AF. However, fractionation can also be a consequence of variation in the anatomy of the atrial wall and therefore functional anisotropy. U-EGM and Bi-EGM fractionation has also recently been linked to asynchronous activation of the endo- and epicardium, which may be a significant mechanism for persistence of AF.[76-78] Van der Does et al.[77] demonstrated for both U-EGM and Bi-EGM fractionation a moderate high sensitivity (65-78%) for areas of electrical asynchrony between endo- and epicardial layer. However, fractionation could not only be explained by local endo-epicardial differences in fractionation, but also by inhomogeneous conduction patterns in solely the endo- or epicardial plane. Whether EGM fractionation therefore represents a proper target for ablative therapy remains, however, questionable.
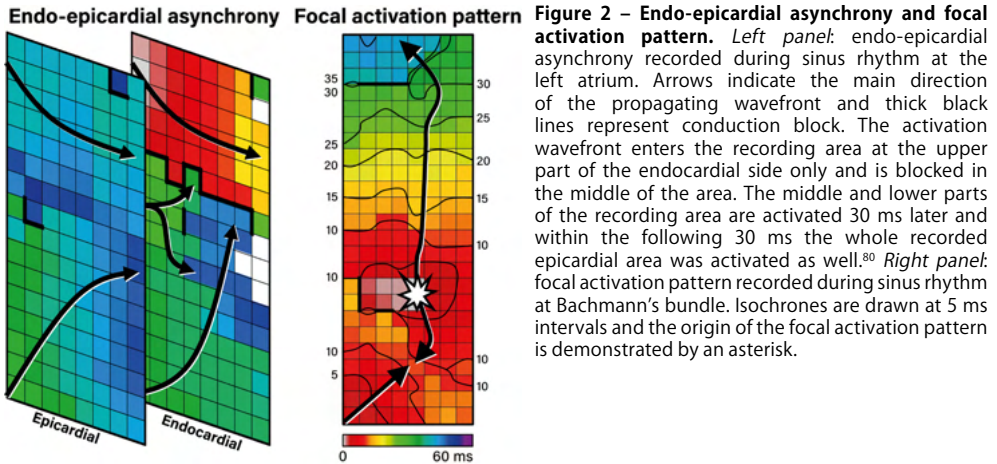
Figure 2 – **Endo-epicardial asynchrony and focal activation pattern.** *Left panel*: endo-epicardial asynchrony recorded during sinus rhythm at the left atrium. Arrows indicate the main direction of the propagating wavefront and thick black lines represent conduction block. The activation wavefront enters the recording area at the upper part of the endocardial side only and is blocked in the middle of the area. The middle and lower parts of the recording area are activated 30 ms later and within the following 30 ms the whole recorded epicardial area was activated as well.[80] *Right panel*: focal activation pattern recorded during sinus rhythm at Bachmann's bundle. Isochrones are drawn at 5 ms intervals and the origin of the focal activation pattern is demonstrated by an asterisk.

2

Endo-epicardial asynchrony and breakthrough waves

Endo-epicardial asynchrony (EEA) and breakthrough waves do not only exist during AF, but also during SR, particularly in areas with a thicker atrial wall.[79] The presence of intramural conduction disorders may enhance EEA (*Figure 2*). Kharbanda et al.[30] were the first to demonstrate that patients with (long-standing) persistent AF have already more EEA during SR in the inferior RA compared to those without AF. This was also linked to a higher amount of conduction disorders in that area. Kharbanda et al.[80] also demonstrated in a case report that extensive EEA is present in the LA in three patients with paroxysmal AF. Although this study included only three patients, the highest degree of EEA was found in the patient with the longest history of AF. This indicates that even during SR the degree of EEA could indeed be related to AF duration and that early intervention may prevent progression of AF.

Enhanced EEA may result in transmural propagation of waves which breakthrough in the opposite layer. These sites can be identified as focal patterns of activation (FAP). These FAPs occur frequently during AF and they are the key elements of AF related electropathology.[81,82] FAPs are not only present during AF, but also during SR. Mouws et al.[83] demonstrated that epicardial FAPs are present in over a third of patients at various sites in the RA, LA and BB, particularly in thicker parts of the atrial wall. There was also a clear difference in R/S ratio between unipolar potentials recorded at SAN-FAP sites and other epicardial FAPs; SAN-FAPs were more often characterized by a full S-wave morphology while other FAPs consisted more often of a RS- or rS-wave morphology. This could indicate that muscular connections between the endo- and epicardium underlie FAPs and that a slight degree of EEA is already enough for FAPs to occur in some areas during SR. As the incidences and spatial distribution of these FAPs during SR were similar between patients with and without history of AF, most of these FAPs could be based on anatomical substrate and therefore be physiological. It is likely that further aggravation of structural remodeling enhances local conduction disorders and EEA, facilitating transmural propagation of wavefronts and hence development of AF. In addition, AF-induced remodeling may further facilitate EEA and enhance the occurrence of FAPs during AF, thereby promoting AF persistence. When a more extensive arrhythmogenic substrate is present in the atria, ablative therapy is more likely to fail.

Clinical implications and future directions

During SR, several electrophysiological parameters have been identified as indicators of AF related electropathology. These indicators were not only found at the LA, but also at

the RA and even more frequently at BB. This clearly indicates the presence of AF related electropathology outside the LA, confirming the hypothesis that AF is not just a solely left-sided disease. Even during SR, electropathology may be missed when mapping is performed at only the endo- or epicardium. Hence, even during SR, conduction is 3D and complex. Remarkably, patients with AF already have more electropathology detectable during SR compared to patients without AF, particularly at BB. However, which (set of) parameter(s) are most suitable as indicators for this purpose remains unknown. It also remains unclear whether electropathology is a cause or consequence of AF. For sure, AF itself can also contribute to a certain amount of electropathology. On the other hand, electropathology can be manually introduced during catheter ablation therapy. To investigate whether electropathology during SR is associated with AF, the next step in mapping is to correlate quantified electrophysiological parameters during SR with parameters measured during AF at same site. Once AF related electropathology is identified, it can be used as an electrical marker to guide ablative therapy of AF.

References

1. Roten L, Derval N, Jais P. Catheter ablation for persistent atrial fibrillation: elimination of triggers is not sufficient. Circ Arrhythm Electrophysiol. 2012;5:1224-1232; discussion 1232.

2. Haissaguerre M, Jais P, Shah DC, Takahashi A, Hocini M, Quiniou G, Garrigue S, Le Mouroux A, Le Metayer P, Clementy J. Spontaneous initiation of atrial fibrillation by ectopic beats originating in the pulmonary veins. N Engl J Med. 1998;339:659-666.

3. Nademanee K, McKenzie J, Kosar E, Schwab M, Sunsaneewitayakul B, Vasavakul T, Khunnawat C, Ngarmukos T. A new approach for catheter ablation of atrial fibrillation: mapping of the electrophysiologic substrate. J Am Coll Cardiol. 2004;43:2044-2053.

4. Rolf S, Kircher S, Arya A, Eitel C, Sommer P, Richter S, Gaspar T, Bollmann A, Altmann D, Piedra C, et al. Tailored atrial substrate modification based on low-voltage areas in catheter ablation of atrial fibrillation. Circ Arrhythm Electrophysiol. 2014;7:825-833.

5. Narayan SM, Krummen DE, Shivkumar K, Clopton P, Rappel WJ, Miller JM. Treatment of atrial fibrillation by the ablation of localized sources: CONFIRM (Conventional Ablation for Atrial Fibrillation With or Without Focal Impulse and Rotor Modulation) trial. J Am Coll Cardiol. 2012;60:628-636.

6. Schmidt B, Brugada J, Arbelo E, Laroche C, Bayramova S, Bertini M, Letsas KP, Pison L, Romanov A, Scherr D, et al. Ablation strategies for different types of atrial fibrillation in Europe: results of the ESC-EORP EHRA Atrial Fibrillation Ablation Long-Term registry. Europace. 2020;22:558-566.

7. Wijffels MC, Kirchhof CJ, Dorland R, Allessie MA. Atrial fibrillation begets atrial fibrillation. A study in awake chronically instrumented goats. Circulation. 1995;92:1954-1968.

8. Allessie MA, de Groot NM, Houben RP, Schotten U, Boersma E, Smeets JL, Crijns HJ. Electropathological substrate of long-standing persistent atrial fibrillation in patients with structural heart disease: longitudinal dissociation. Circ Arrhythm Electrophysiol. 2010;3:606-615.

9. Teuwen CP, Yaksh A, Lanters EA, Kik C, van der Does LJ, Knops P, Taverne YJ, van de Woestijne PC, Oei FB, Bekkers JA, et al. Relevance of Conduction Disorders in Bachmann's Bundle During Sinus Rhythm in Humans. Circ Arrhythm Electrophysiol. 2016;9:e003972.

10. Boineau JP, Schuessler RB, Mooney CR, Wylds AC, Miller CB, Hudson RD, Borremans JM, Brockus CW. Multicentric origin of the atrial depolarization wave: the pacemaker complex. Relation to dynamics of atrial conduction, P-wave changes and heart rate control. Circulation. 1978;58:1036-1048.

11. Cox JL, Canavan TE, Schuessler RB, Cain ME, Lindsay BD, Stone C, Smith PK, Corr PB, Boineau JP. The surgical treatment of atrial fibrillation. II. Intraoperative electrophysiologic mapping and description of the electrophysiologic basis of atrial flutter and atrial fibrillation. J Thorac Cardiovasc Surg. 1991;101:406-426.

12. Kleber AG, Rudy Y. Basic mechanisms of cardiac impulse propagation and associated arrhythmias. Physiol Rev. 2004;84:431-488.

13. Spach MS, Dolber PC, Heidlage JF. Influence of the passive anisotropic properties on directional differences in propagation following modification of the sodium conductance in human atrial muscle. A model of reentry based on anisotropic discontinuous propagation. Circ Res. 1988;62:811-832.

14. Darby AE, Dimarco JP. Management of atrial fibrillation in patients with structural heart disease. Circulation. 2012;125:945-957.

15. Alasady M, Abhayaratna WP, Leong DP, Lim HS, Abed HS, Brooks AG, Mattchoss S, Roberts-Thomson KC, Worthley MI, Chew DP, et al. Coronary artery disease affecting the atrial branches is an independent determinant of atrial fibrillation after myocardial infarction. Heart Rhythm. 2011;8:955-960.

16. Harada M, Van Wagoner DR, Nattel S. Role of inflammation in atrial fibrillation pathophysiology and management. Circ J. 2015;79:495-502.

17. Heeringa J, van der Kuip DA, Hofman A, Kors JA, van Rooij FJ, Lip GY, Witteman JC. Subclinical atherosclerosis and risk of atrial fibrillation: the rotterdam study. Arch Intern Med. 2007;167:382-387.

18. Hernandez-Madrid A, Paul T, Abrams D, Aziz PF, Blom NA, Chen J, Chessa M, Combes N, Dagres N, Diller G, et al. Arrhythmias in congenital heart disease: a position paper of the European Heart Rhythm Association (EHRA), Association for European Paediatric and Congenital Cardiology (AEPC), and the European Society of Cardiology (ESC) Working Group on Grown-up Congenital heart disease, endorsed by HRS, PACES, APHRS, and SOLAECE. Europace. 2018;20:1719-1753.

19. Spach MS, Boineau JP. Microfibrosis produces electrical load variations due to loss of side-to-side cell connections: a major mechanism of structural heart disease arrhythmias. Pacing Clin Electrophysiol. 1997;20:397-413.

20. Ortiz J, Niwano S, Abe H, Rudy Y, Johnson NJ, Waldo AL. Mapping the conversion of atrial flutter to atrial fibrillation and atrial fibrillation to atrial flutter. Insights into mechanisms. Circ Res. 1994;74:882-894.

21. Spach MS, Dolber PC. Relating extracellular potentials and their derivatives to anisotropic propagation at a microscopic level in human cardiac muscle. Evidence for electrical uncoupling of side-to-side fiber connections with increasing age. Circ Res. 1986;58:356-371.

22. Wong CX, John B, Brooks AG, Chandy ST, Kuklik P, Lau DH, Sullivan T, Roberts-Thomson KC, Sanders P. Direction-dependent conduction abnormalities in the chronically stretched atria. Europace. 2012;14:954-961.

23. Huang D, Marine JE, Li JB, Zghaib T, Ipek EG, Sinha S, Spragg DD, Ashikaga H, Berger RD, Calkins H, et al. Association of Rate-Dependent Conduction Block Between Eccentric Coronary Sinus to Left Atrial Connections With Inducible Atrial Fibrillation and Flutter. Circ Arrhythm Electrophysiol. 2017;10.

24. Teuwen CP, Kik C, van der Does L, Lanters EAH, Knops P, Mouws E, Bogers A, de Groot NMS. Quantification of the Arrhythmogenic Effects of Spontaneous Atrial Extrasystole Using High-Resolution Epicardial Mapping. Circ Arrhythm Electrophysiol. 2018;11.

25. Konings KT, Kirchhof CJ, Smeets JR, Wellens HJ, Penn OC, Allessie MA. High-density mapping of electrically

induced atrial fibrillation in humans. Circulation. 1994;89:1665-1680.

26. Hansson A, Holm M, Blomstrom P, Johansson R, Luhrs C, Brandt J, Olsson SB. Right atrial free wall conduction velocity and degree of anisotropy in patients with stable sinus rhythm studied during open heart surgery. Eur Heart J. 1998;19:293-300.

27. Lee G, Spence S, Teh A, Goldblatt J, Larobina M, Atkinson V, Brown R, Morton JB, Sanders P, Kistler PM, et al. High-density epicardial mapping of the pulmonary vein-left atrial junction in humans: insights into mechanisms of pulmonary vein arrhythmogenesis. Heart Rhythm. 2012;9:258-264.

28. Lanters EAH, Yaksh A, Teuwen CP, van der Does L, Kik C, Knops P, van Marion DMS, Brundel B, Bogers A, Allessie MA, et al. Spatial distribution of conduction disorders during sinus rhythm. Int J Cardiol. 2017;249:220-225.

29. Sakamoto S, Yamauchi S, Yamashita H, Imura H, Maruyama Y, Ogasawara H, Hatori N, Shimizu K. Intraoperative mapping of the right atrial free wall during sinus rhythm: variety of activation patterns and incidence of postoperative atrial fibrillation. Eur J Cardiothorac Surg. 2006;30:132-139.

30. Kharbanda RK, Knops P, van der Does L, Kik C, Taverne Y, Roos-Serote MC, Heida A, Oei FBS, Bogers A, de Groot NMS. Simultaneous Endo-Epicardial Mapping of the Human Right Atrium: Unraveling Atrial Excitation. J Am Heart Assoc. 2020;9:e017069.

31. Kharbanda RK, Wesselius FJ, van Schie MS, Taverne Y, Bogers A, de Groot NMS. Endo-Epicardial Mapping of In Vivo Human Sinoatrial Node Activity. JACC Clin Electrophysiol. 2021;7:693-702.

32. Lemery R, Soucie L, Martin B, Tang AS, Green M, Healey J. Human study of biatrial electrical coupling: determinants of endocardial septal activation and conduction over interatrial connections. Circulation. 2004;110:2083-2089.

33. Tapanainen JM, Jurkko R, Holmqvist F, Husser D, Kongstad O, Makijarvi M, Toivonen L, Platonov PG. Interatrial right-to-left conduction in patients with paroxysmal atrial fibrillation. J Interv Card Electrophysiol. 2009;25:117-122.

34. Mouws E, Lanters EAH, Teuwen CP, van der Does L, Kik C, Knops P, Yaksh A, Bekkers JA, Bogers A, de Groot NMS. Impact of Ischemic and Valvular Heart Disease on Atrial Excitation:A High-Resolution Epicardial Mapping Study. J Am Heart Assoc. 2018;7.

35. Mouws E, Kik C, van der Does L, Lanters EAH, Teuwen CP, Knops P, Bogers A, de Groot NMS. Novel Insights in the Activation Patterns at the Pulmonary Vein Area. Circ Arrhythm Electrophysiol. 2018;11:e006720.

36. Roberts-Thomson KC, John B, Worthley SG, Brooks AG, Stiles MK, Lau DH, Kuklik P, Shipp NJ, Kalman JM, Sanders P. Left atrial remodeling in patients with atrial septal defects. Heart Rhythm. 2009;6:1000-1006.

37. van Staveren LN, van der Does WFB, Heida A, Taverne Y, Bogers A, de Groot NMS. AF Inducibility Is Related to Conduction Abnormalities at Bachmann's Bundle. J Clin Med. 2021;10.

38. Stiles MK, Brooks AG, Roberts-Thomson KC, Kuklik P, John B, Young GD, Kalman JM, Sanders P. High-density mapping of the sinus node in humans: role of preferential pathways and the effect of remodeling. J Cardiovasc Electrophysiol. 2010;21:532-539.

39. Mouws E, van der Does L, Kik C, Lanters EAH, Teuwen CP, Knops P, Bogers A, de Groot NMS. Impact of the arrhythmogenic potential of long lines of conduction slowing at the pulmonary vein area. Heart Rhythm. 2019;16:511-519.

40. Heida A, van der Does WFB, van Staveren LN, Taverne Y, Roos-Serote MC, Bogers A, de Groot NMS. Conduction Heterogeneity: Impact of Underlying Heart Disease and Atrial Fibrillation. JACC Clin Electrophysiol. 2020;6:1844-1854.

41. van der Does L, Lanters EAH, Teuwen CP, Mouws E, Yaksh A, Knops P, Kik C, Bogers A, de Groot NMS. The Effects of Valvular Heart Disease on Atrial Conduction During Sinus Rhythm. J Cardiovasc Transl Res. 2020;13:632-639.

42. Houck CA, Lanters EAH, Heida A, Taverne Y, van de Woestijne PC, Knops P, Roos-Serote MC, Roos-Hesselink JW, Bogers A, de Groot NMS. Distribution of Conduction Disorders in Patients With Congenital Heart Disease and Right Atrial Volume Overload. JACC Clin Electrophysiol. 2020;6:537-548.

43. Lin Y, Yang B, Garcia FC, Ju W, Zhang F, Chen H, Yu J, Li M, Gu K, Cao K, et al. Comparison of left atrial electrophysiologic abnormalities during sinus rhythm in patients with different type of atrial fibrillation. J Interv Card Electrophysiol. 2014;39:57-67.

44. Zheng Y, Xia Y, Carlson J, Kongstad O, Yuan S. Atrial average conduction velocity in patients with and without paroxysmal atrial fibrillation. Clin Physiol Funct Imaging. 2017;37:596-601.

45. van Schie MS, Heida A, Taverne Y, Bogers A, de Groot NMS. Identification of local atrial conduction heterogeneities using high-density conduction velocity estimation. Europace. 2021;23:1815-1825.

46. Heida A, van Schie MS, van der Does WFB, Taverne Y, Bogers A, de Groot NMS. Reduction of Conduction Velocity in Patients with Atrial Fibrillation. J Clin Med. 2021;10.

47. van Schie MS, Starreveld R, Roos-Serote MC, Taverne Y, van Schaagen FRN, Bogers A, de Groot NMS. Classification of sinus rhythm single potential morphology in patients with mitral valve disease. Europace. 2020;22:1509-1519.

48. Teh AW, Kistler PM, Lee G, Medi C, Heck PM, Spence SJ, Sparks PB, Morton JB, Kalman JM. Electroanatomic remodeling of the left atrium in paroxysmal and persistent atrial fibrillation patients without structural heart disease. J Cardiovasc Electrophysiol. 2012;23:232-238.

49. Stiles MK, John B, Wong CX, Kuklik P, Brooks AG, Lau DH, Dimitri H, Roberts-Thomson KC, Wilson L, De Sciscio P, et al. Paroxysmal lone atrial fibrillation is associated with an abnormal atrial substrate: characterizing the "second factor". J Am Coll Cardiol. 2009;53:1182-1191.

50. van Campenhout MJ, Yaksh A, Kik C, de Jaegere PP, Ho SY, Allessie MA, de Groot NM. Bachmann's bundle: a key player in the development of atrial fibrillation? Circ Arrhythm Electrophysiol. 2013;6:1041-1046.

51. McElderry HT, McGiffin DC, Plumb VJ, Nanthakumar K, Epstein AE, Yamada T, Kay GN. Proarrhythmic aspects of atrial fibrillation surgery: mechanisms of postoperative macroreentrant tachycardias. Circulation. 2008;117:155-162.

2

52. Cantwell CD, Roney CH, Ng FS, Siggers JH, Sherwin SJ, Peters NS. Techniques for automated local activation time annotation and conduction velocity estimation in cardiac mapping. Comput Biol Med. 2015;65:229-242.
53. Deno DC, Balachandran R, Morgan D, Ahmad F, Masse S, Nanthakumar K. Orientation-Independent Catheter-Based Characterization of Myocardial Activation. IEEE Trans Biomed Eng. 2017;64:1067-1077.
54. Prabhu S, Voskoboinik A, McLellan AJA, Peck KY, Pathik B, Nalliah CJ, Wong GR, Azzopardi SM, Lee G, Mariani J, et al. A comparison of the electrophysiologic and electroanatomic characteristics between the right and left atrium in persistent atrial fibrillation: Is the right atrium a window into the left? J Cardiovasc Electrophysiol. 2017;28:1109-1116.
55. Kojodjojo P, Kanagaratnam P, Markides V, Davies DW, Peters N. Age-related changes in human left and right atrial conduction. J Cardiovasc Electrophysiol. 2006;17:120-127.
56. Cantwell CD, Roney CH, Ali RL, Qureshi NA, Lim PB, Peters NS. A software platform for the comparative analysis of electroanatomic and imaging data including conduction velocity mapping. Annu Int Conf IEEE Eng Med Biol Soc. 2014;2014:1591-1594.
57. Miyamoto K, Tsuchiya T, Narita S, Yamaguchi T, Nagamoto Y, Ando S, Hayashida K, Tanioka Y, Takahashi N. Bipolar electrogram amplitudes in the left atrium are related to local conduction velocity in patients with atrial fibrillation. Europace. 2009;11:1597-1605.
58. Yagishita A, Gimbel JR, S DEO, Manyam H, Sparano D, Cakulev I, Mackall J, Arruda M. Long-Term Outcome of Left Atrial Voltage-Guided Substrate Ablation During Atrial Fibrillation: A Novel Adjunctive Ablation Strategy. J Cardiovasc Electrophysiol. 2017;28:147-155.
59. Roberts-Thomson KC, Kistler PM, Sanders P, Morton JB, Haqqani HM, Stevenson I, Vohra JK, Sparks PB, Kalman JM. Fractionated atrial electrograms during sinus rhythm: relationship to age, voltage, and conduction velocity. Heart Rhythm. 2009;6:587-591.
60. Sim I, Bishop M, O'Neill M, Williams SE. Left atrial voltage mapping: defining and targeting the atrial fibrillation substrate. J Interv Card Electrophysiol. 2019.
61. de Groot NMS, Shah D, Boyle PM, Anter E, Clifford GD, Deisenhofer I, Deneke T, van Dessel P, Doessel O, Dilaveris P, et al. Critical appraisal of technologies to assess electrical activity during atrial fibrillation: a position paper from the European Heart Rhythm Association and European Society of Cardiology Working Group on eCardiology in collaboration with the Heart Rhythm Society, Asia Pacific Heart Rhythm Society, Latin American Heart Rhythm Society and Computing in Cardiology. Europace. 2021.
62. van Schie MS, Kharbanda RK, Houck CA, Lanters EAH, Taverne Y, Bogers A, de Groot NMS. Identification of Low-Voltage Areas: A Unipolar, Bipolar, and Omnipolar Perspective. Circ Arrhythm Electrophysiol. 2021;14:e009912.
63. Abdi B, van Schie MS, Groot NMS, Hendriks RC. Analyzing the effect of electrode size on electrogram and activation map properties. Comput Biol Med. 2021;134:104467.
64. Kottkamp H, Berg J, Bender R, Rieger A, Schreiber D. Box Isolation of Fibrotic Areas (BIFA): A Patient-Tailored Substrate Modification Approach for Ablation of Atrial Fibrillation. J Cardiovasc Electrophysiol. 2016;27:22-30.
65. Marcus GM, Yang Y, Varosy PD, Ordovas K, Tseng ZH, Badhwar N, Lee BK, Lee RJ, Scheinman MM, Olgin JE. Regional left atrial voltage in patients with atrial fibrillation. Heart Rhythm. 2007;4:138-144.
66. Kogawa R, Okumura Y, Watanabe I, Nagashima K, Takahashi K, Iso K, Watanabe R, Arai M, Kurokawa S, Ohkubo K, et al. Left atrial remodeling: Regional differences between paroxysmal and persistent atrial fibrillation. J Arrhythm. 2017;33:483-487.
67. Lin YJ, Tai CT, Huang JL, Lee KT, Lee PC, Hsieh MH, Lee SH, Higa S, Yuniadi Y, Liu TY, et al. Characterization of right atrial substrate in patients with supraventricular tachyarrhythmias. J Cardiovasc Electrophysiol. 2005;16:173-180.
68. van Schie MS, Starreveld R, Bogers A, de Groot NMS. Sinus rhythm voltage fingerprinting in patients with mitral valve disease using a high-density epicardial mapping approach. Europace. 2021;23:469-478.
69. Kapa S, Desjardins B, Callans DJ, Marchlinski FE, Dixit S. Contact electroanatomic mapping derived voltage criteria for characterizing left atrial scar in patients undergoing ablation for atrial fibrillation. J Cardiovasc Electrophysiol. 2014;25:1044-1052.
70. Rodriguez-Manero M, Valderrabano M, Baluja A, Kreidieh O, Martinez-Sande JL, Garcia-Seara J, Saenen J, Iglesias-Alvarez D, Bories W, Villamayor-Blanco LM, et al. Validating Left Atrial Low Voltage Areas During Atrial Fibrillation and Atrial Flutter Using Multielectrode Automated Electroanatomic Mapping. JACC Clin Electrophysiol. 2018;4:1541-1552.
71. van der Does LJ, de Groot NM. Inhomogeneity and complexity in defining fractionated electrograms. Heart Rhythm. 2017;14:616-624.
72. Viles-Gonzalez JF, Gomes JA, Miller MA, Dukkipati SR, Koruth JS, Eggert C, Coffey J, Reddy VY, d'Avila A. Areas with complex fractionated atrial electrograms recorded after pulmonary vein isolation represent normal voltage and conduction velocity in sinus rhythm. Europace. 2013;15:339-346.
73. Tanigawa M, Fukatani M, Konoe A, Isomoto S, Kadena M, Hashiba K. Prolonged and fractionated right atrial electrograms during sinus rhythm in patients with paroxysmal atrial fibrillation and sick sinus node syndrome. J Am Coll Cardiol. 1991;17:403-408.
74. Starreveld R, van der Does L, de Groot NMS. Anatomical hotspots of fractionated electrograms in the left and right atrium: do they exist? Europace. 2019;21:60-72.
75. Konings KT, Smeets JL, Penn OC, Wellens HJ, Allessie MA. Configuration of unipolar atrial electrograms during electrically induced atrial fibrillation in humans. Circulation. 1997;95:1231-1241.
76. de Groot N, van der Does L, Yaksh A, Lanters E, Teuwen C, Knops P, van de Woestijne P, Bekkers J, Kik C, Bogers A, et al. Direct Proof of Endo-Epicardial Asynchrony of the Atrial Wall During Atrial Fibrillation in Humans. Circ Arrhythm Electrophysiol. 2016;9.
77. van der Does L, Starreveld R, Kharbanda RK, Knops P, Kik C, Bogers A, de Groot NMS. Detection of Endo-

epicardial Asynchrony in the Atrial Wall Using One-Sided Unipolar and Bipolar Electrograms. J Cardiovasc Transl Res. 2021;14:902-911.

78. van der Does L, Knops P, Teuwen CP, Serban C, Starreveld R, Lanters EAH, Mouws E, Kik C, Bogers A, de Groot NMS. Unipolar atrial electrogram morphology from an epicardial and endocardial perspective. Heart Rhythm. 2018;15:879-887.

79. Schuessler RB, Kawamoto T, Hand DE, Mitsuno M, Bromberg BI, Cox JL, Boineau JP. Simultaneous epicardial and endocardial activation sequence mapping in the isolated canine right atrium. Circulation. 1993;88:250-263.

80. Kharbanda RK, Kik C, Knops P, Bogers A, de Groot NMS. First Evidence of Endo-Epicardial Asynchrony of the Left Atrial Wall in Humans. JACC Case Rep. 2020;2:745-749.

81. de Groot NM, Houben RP, Smeets JL, Boersma E, Schotten U, Schalij MJ, Crijns H, Allessie MA. Electropathological substrate of longstanding persistent atrial fibrillation in patients with structural heart disease: epicardial breakthrough. Circulation. 2010;122:1674-1682.

82. Eckstein J, Zeemering S, Linz D, Maesen B, Verheule S, van Hunnik A, Crijns H, Allessie MA, Schotten U. Transmural conduction is the predominant mechanism of breakthrough during atrial fibrillation: evidence from simultaneous endo-epicardial high-density activation mapping. Circ Arrhythm Electrophysiol. 2013;6:334-341.

83. Mouws E, Lanters EAH, Teuwen CP, van der Does L, Kik C, Knops P, Bekkers JA, Bogers A, de Groot NMS. Epicardial Breakthrough Waves During Sinus Rhythm: Depiction of the Arrhythmogenic Substrate? Circ Arrhythm Electrophysiol. 2017;10.

2
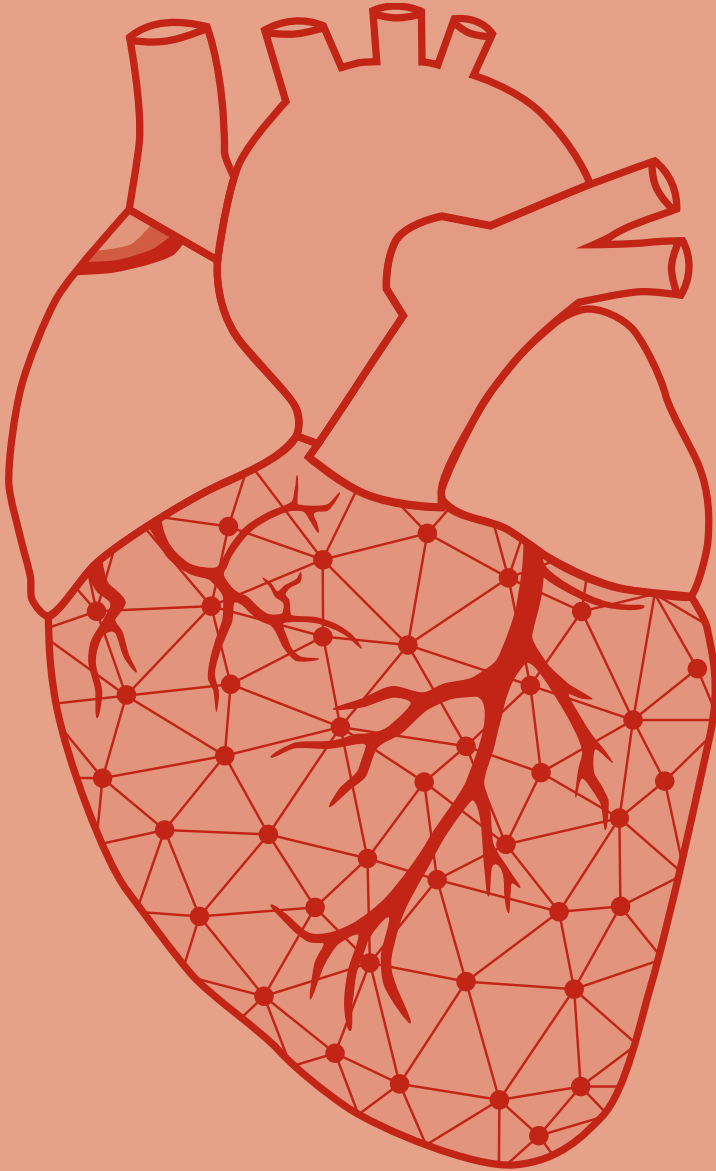
Chapter 3

Electrogram morphology and atrial fibrillation: experimental point of view

Natasja M.S. de Groot

Mathijs S. van Schie

'The first step towards recognizing abnormal fibrillation electrograms is understanding variations in electrogram morphology during sinus rhythm'

Introduction

The hallmark of the most common cardiac arrhythmia atrial fibrillation (AF) is continuous beat-to-beat variation in propagation of fibrillation waves activating atrial tissue. As a consequence, an electrogram (EGM) recorded at any random recording site in the atria is characterized by beat-to-beat variation in intervals between consecutive fibrillation potentials and fibrillation potential morphology (*Figure 1*). The morphology of a fibrillation potential provides not only information on the moment of local excitation of cardiac tissue beneath the recording electrodes but also on the presence of atrial electropathology. Electropathology is defined as intra-atrial conduction abnormalities caused by structural damage of atrial tissue.[1,2] From a theoretically point of view, targeting fibrillation potentials indicative of electropathology may be an alternative selective substrate-based AF ablation approach. However, substrate-based ablation approaches so far applied failed to demonstrate long-term freedom of AF. In this chapter, we critically review methodologies and outcomes of EGM guided AF ablation approaches and discuss current knowledge of sinus rhythm and fibrillation EGM morphology from an experimental point of view.

Complex fractionated EGM as target sites for ablation

The 2017 HRS/EHRA/ECAS/APHRS/SOLAECE expert consensus statement of catheter and surgical ablation of atrial fibrillation reports that '*ablation approaches targeting complex,*
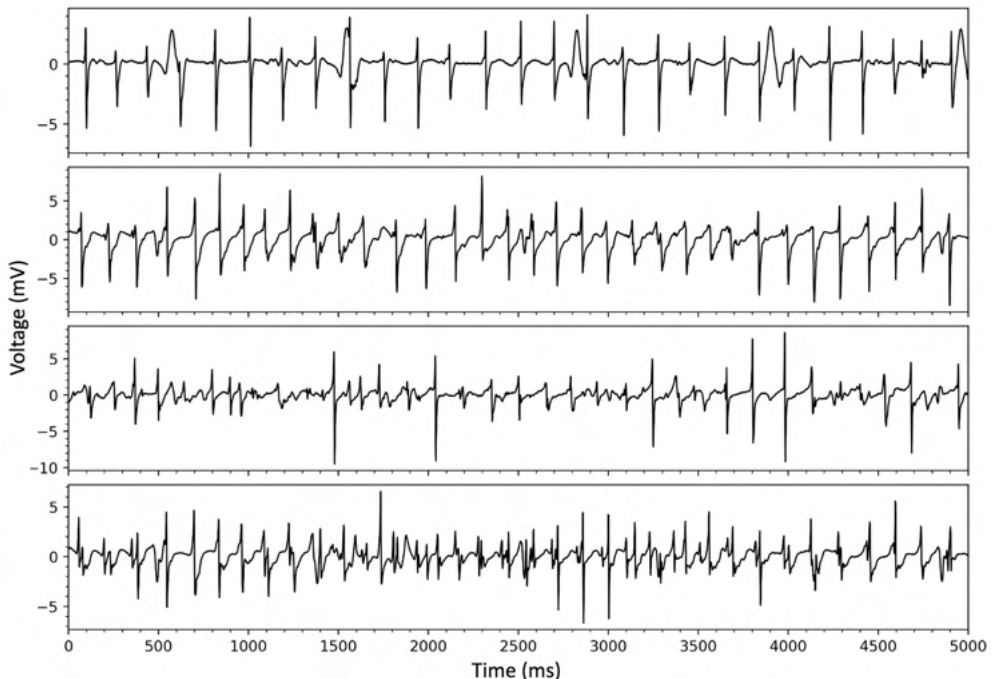
Figure 1 – Examples of fibrillation EGMs. Fibrillation EGMs recorded from the left atrial free wall obtained from 4 different patients with variable complexity, demonstrating clearly beat-to-beat differences in fibrillation intervals and potential morphology.

fractionated EGMs have clearly lost momentum', as multicenter, randomized trials failed to demonstrate that catheter ablation targeting complex, fractionated EGMs reduce AF recurrences on the longterm.[3] Mapping of the atria during these ablation procedures revealed numerous sites throughout the atria from which complex, fractionated EGMs were recorded. This observation raises the question whether fractionated EGMs truly represented the arrhythmogenic substrate underlying AF or whether they are merely the result of the more or less simultaneously presence of multiple fibrillation waves.

A first step towards answering this question is to investigate whether there are anatomical hotspots for fractionated potentials in the right and/or left atrium and whether there are differences with respect to the prevalence of fractionated potentials between patients with paroxysmal and persistent AF.

For this purpose, Starreveld et al.[4] reviewed 565 studies describing fractionation during human electrophysiological measurements. Based on these studies, nine separate regions for the left atria (pulmonary veins, atrial appendage, septum, posterior wall, lateral wall, anterior wall, atrial floor, atrial roof, and the mitral annulus) and right atria (caval veins, atrial appendage, atrial septum, posterior wall, lateral wall, anterior wall, atrial roof, tricuspid annulus, crista terminalis and coronary sinus) were defined. In all these regions of both the right and left atrium, there was a high prevalence of (mainly) bipolar fractionated potentials without a clear preferential site for fractionation to occur. Remarkably, the degree of fractionation did not differ between patients with paroxysmal and persistent AF.

There are two major problems with respect to ablation approaches targeting complex fractionated EGMs.

The first problem is that there is *lack of a uniform definition of fractionation*. Van der Does et al.[5] reviewed 164 studies reporting on fractionation during electrophysiology studies in humans and screened for definitions of fractionation. These studies included eleven different visual definitions for fractionation, three automated complex fractionated atrial EGMs detection algorithms and seven novel parameters for measuring fractionation. In addition, five different definitions for continuous electrical activity were introduced. The definitions of fractionation varied with respect the number of deflections, EGM duration, interval between deflections, number of short durations between deflections, amplitude of deflections, slope of deflections and number of polarity changes of deflections.

The second problem is that there is also *no uniform approach for recording and processing of fibrillation potentials*. Van der Does et al.[5] also found that in studies reporting on catheter ablation of complex fractionated potentials electrode properties were often not described, (e.g. using either endocardial or epicardial recordings) mainly bipolar and rarely unipolar recordings were used, electrode diameters of the recording catheters' tip ranged from 1 to 8 mm with inter-electrode distance varying between 2 to 5 mm, and also variable filter settings were used.

Starreveld et al.[6] demonstrated that the impact of filter settings on fibrillation potential morphology was considerable. Fibrillation potentials (N=2,557,045) obtained from 10 patients with AF were subjected to 32 different filters setting to study the effects on slopes, peak-to-peak amplitudes and fractionation. High-pass filtering decreased the number of detected potentials, peak-to-peak amplitudes, percentage of fractionated potentials and fractionation duration. The proportion of single potentials was increased. Low-pass filtering decreased the number of detected potentials, percentage of fractionated potentials, whereas the peak-to-peak amplitudes, percentage of single potentials, and fraction duration

Variable morphology of single potentials
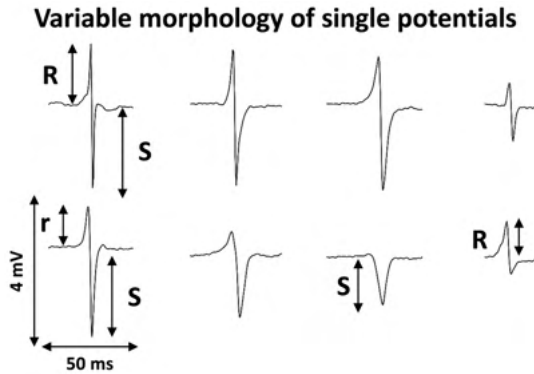
Figure 2 – Examples of single potentials. Typical examples of single, fibrillation potentials demonstrating variation in peak-to-peak amplitudes, slopes and potential durations. A single potential consisting of solely an R-wave occurs when a fibrillation wave encounters a conduction barrier while a single potential consisting of solely an S-wave occurs at a focal site.

3

increased. Notch filtering (50 Hz) decreased the number of potentials and the peak-to-peak amplitudes, whereas the percentage of complex fractionated potentials increased. Hence, filtering significantly impacted morphology of unipolar fibrillation potentials, becoming a potential source of error in identification of ablative targets.

Also, the electrode size (or diameter) has a considerable impact on the recorded EGMs. Abdi et al.[7] used both simulated and clinical AF data to analyze the effect of electrode size on overall error in local activation time estimation, length of slow conduction or conduction block lines, areas of low-voltage and potential fractionation. By increasing the electrode size, the error in local activation time estimation increased. Moreover, by increasing the electrode size, local activation time maps became more homogeneous with a reduction in the number of fibrillation waves. As a consequence, potential fractionation disappeared, the number of low-voltage areas (LVAs) increased and potentials became less steep. This effect was even more pronounced in areas with large heterogeneity in conduction. The electrode size thus considerably affects EGM morphology. These effects need to be considered when performing any analysis on EGMs or when comparing results obtained via electrodes with different sizes.

Given these limitations of ablation strategies targeting complex, fractionated potentials tested so far, we believe that the potential of this approach has not yet been fully explored and that it is still reasonable to further investigate EGM morphology as indicator of AF-related electropathology. However, features of *unipolar, and not bipolar* potentials should be examined, as the interpretation of unipolar potential morphology is more straightforward.

Classification of unipolar potentials

Unipolar single potentials

When a fibrillation wave propagates smoothly through cardiac tissue with a constant conduction velocity, a unipolar electrode will record a potential consisting of a single negative deflection preceded and followed by respectively a R- and S-wave. These 'single potentials' may vary in peak-to-peak amplitude, slope, ratio between the R- and S-wave (R/S ratio) and thus also potential duration (upper panel of *Figure 2*).

Konings et al.[8] were the first to investigate the correlation between fibrillation potential morphology and patterns of activation by performing epicardial, high-resolution and high-density mapping of the right atrial free wall. Most fibrillation potentials recorded from the right atrial wall during induced AF in
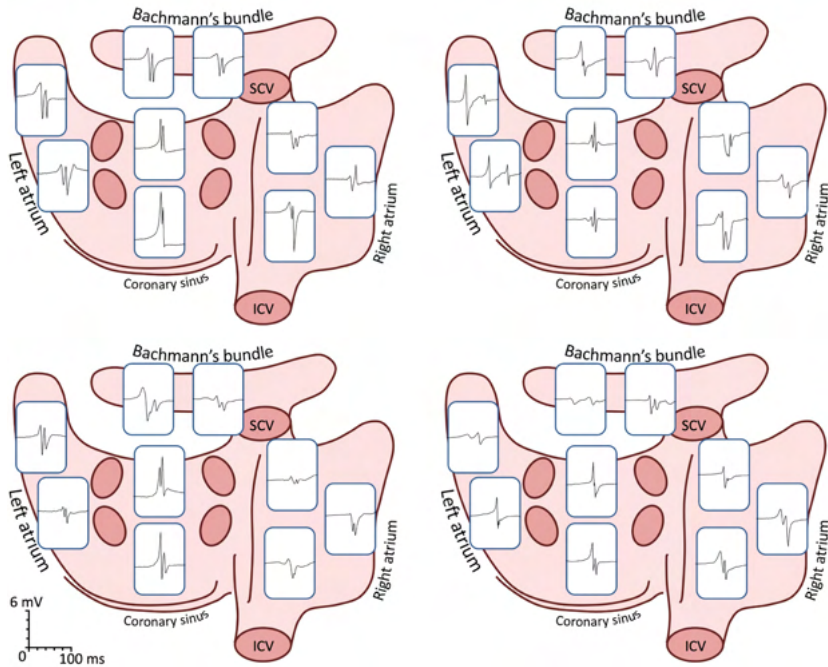
Figure 3 – Examples of short- and long double potentials. Typical examples of short and long double, unipolar fibrillation potentials recorded from the right atrium, Bachmann's bundle, left atrium and the area between the pulmonary veins obtained from 4 different patients.

patients with Wolf-Parkinson-White syndrome, consisted of single potentials (77 12%) and they occurred when broad fibrillation waves activated atrial tissue. During collision, conduction block, slowing of conduction or pivoting, the percentage of single potentials was respectively 22±13%, 14±7%, 33±27% and 17±12%.

As demonstrated in the lower panel of *Figure 2*, a single potential may also consist of a pure R- or S-wave. An R-wave occurs when the fibrillation wave encounters a conduction barrier (panel A) or when two fibrillation waves collide (panel B). In the latter case, the R-wave contains a notch, each peak representing the arrival time at the fusion site of the two colliding wavefronts.

Using mapping data from the patients with Wolf-Parkinson-White syndrome, Houben et al.[9] measured the R- and S-waves of single potentials and found that the single fibrillation potentials had a clear S-wave predominance. This S-wave dominance was not caused by conduction anisotropy, and could only partly be explained by increased fibrillation wavefront curvature. The authors attributed the S-wave predominance to a predominant epi- to endocardial activation. When the patterns of activation during AF became more complex, the S-wave predominance diminished. This observation was explained by loss of the leading role of the epicardial layer in activation of atrial myocardium due to damage caused by e.g., AF-related structural remodeling.

Unipolar double potentials

In the high-density mapping study of Konings et al.[8], double potentials were further subdivided into short and long double potentials (*Figure 3*). When a fibrillation potential
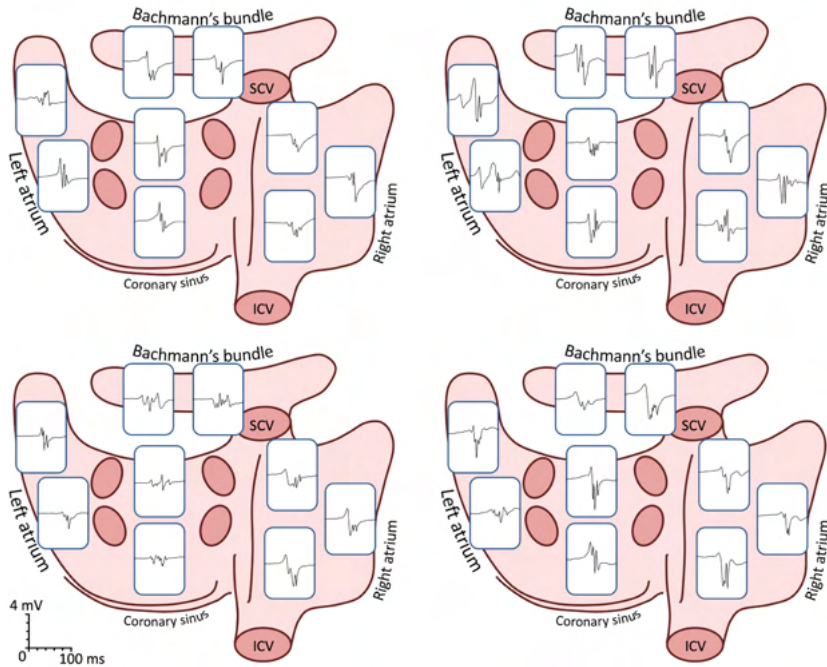
Figure 4 – Examples of fractionated potentials. Typical examples of fractionated, unipolar fibrillation potentials recorded from the right atrium, Bachmann's bundle, left atrium and the area between the pulmonary veins obtained from 4 different patients.

contains two consecutive negative deflections it is classified as either a short double potential (time interval between the two components less or equal to 10 ms) or a long double potential in which the two components are separated by more than 10 ms. Short double potentials were recorded during uniform conduction of broad fibrillation waves and at collision sites of fibrillation waves whereas long double potentials occurred mainly along long arcs of conduction block.

Unipolar fractionated potentials

When a unipolar fibrillation potential contains more than three negative deflections, it is classified as a fractionated potential (*Figure 4*). The degree of fractionation is classified by simply counting the components of each fibrillation potential. Fractionated potentials are observed at areas of conduction slowing or at pivot points.

Additional deflections in double and fractionated potentials are only taken into account when the peak-to-peak amplitude of the additional deflection was at least 25% of the amplitude of the largest deflection. This cut-off value was chosen to ascertain that only fibrillation wavefronts within a distance of approximately one space constant were included.

As demonstrated in *Figures 3 and 4*, double and fractionated potentials can vary in peak-to-peak amplitudes, slopes, duration of all distinct negative deflections, but also in the number of deflections ('*degree of fractionation*', e.g., triple, quad, penta, etc.) and time between the first and last deflection ('*fractionation duration*'). When different components can no longer be discriminated, the EGM is labelled as continuous electrical activity, as demonstrated in *Figure 5*.
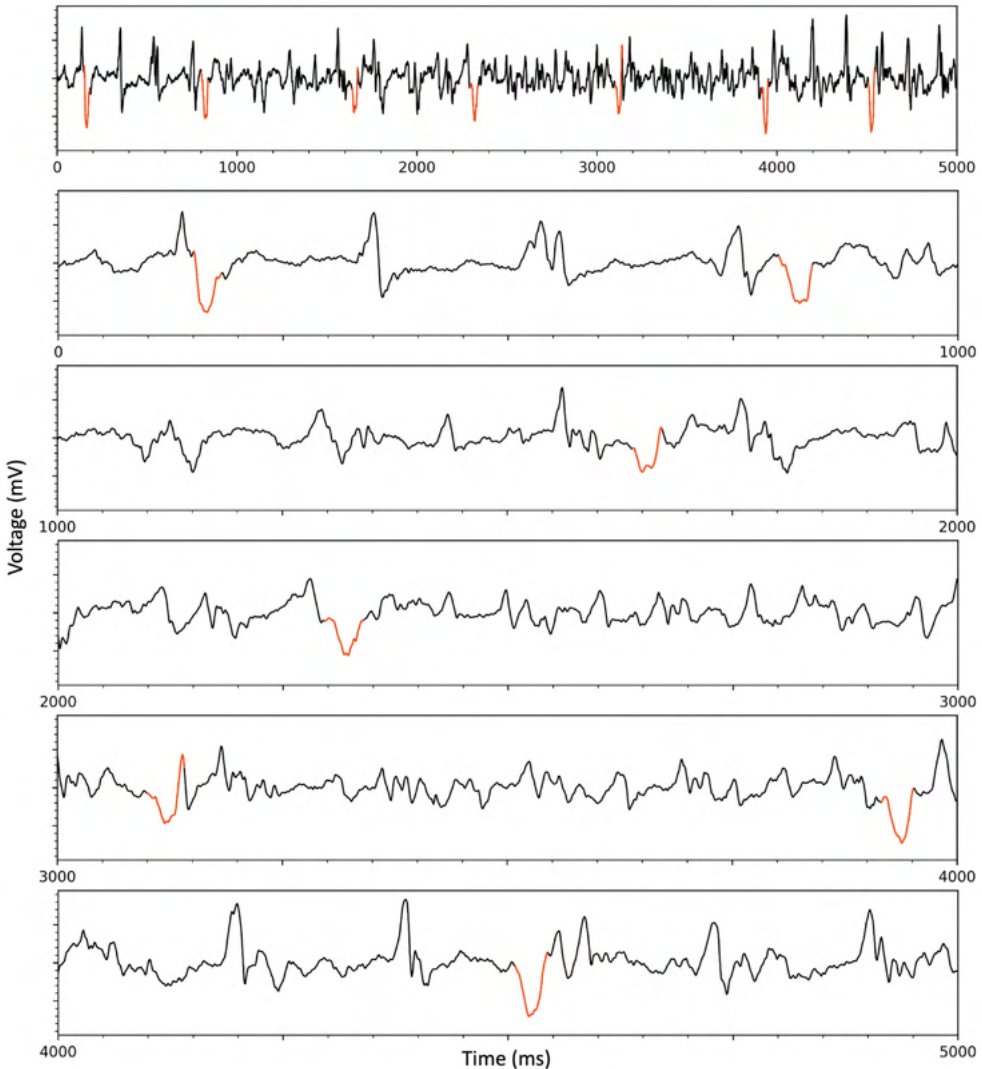
Figure 5 – Continuous electrical activity recorded from the middle of Bachmann's bundle. The top panel shows a 5-second recording. The lower panels show segments of this recording of 1-second duration each. Ventricular far-field is highlighted in orange. Continuous electrical activity can be seen from around 1000 ms.

Causes underlying potential fractionation

There are four main causes that can explain fractionation of unipolar potentials. These include: 1) artifacts due to filtering or activity of other muscles, 2) remote electrical activation such as ventricular excitation, 3) local asynchronous activation of myocardium surrounding the recording electrode caused by spatial dispersion in refractoriness or non-uniform anisotropic conduction and 4) electrical asynchrony between the endo-and epicardial layer due to transmural inhomogeneous conduction. In addition, potential fractionation may also be influenced by hyperactivity of the intrinsic cardiac autonomic nervous system. As a result, fractionated potentials can be either functional or structural in nature, and at present we cannot accurately discriminate between these two different main underlying causes of fractionation.
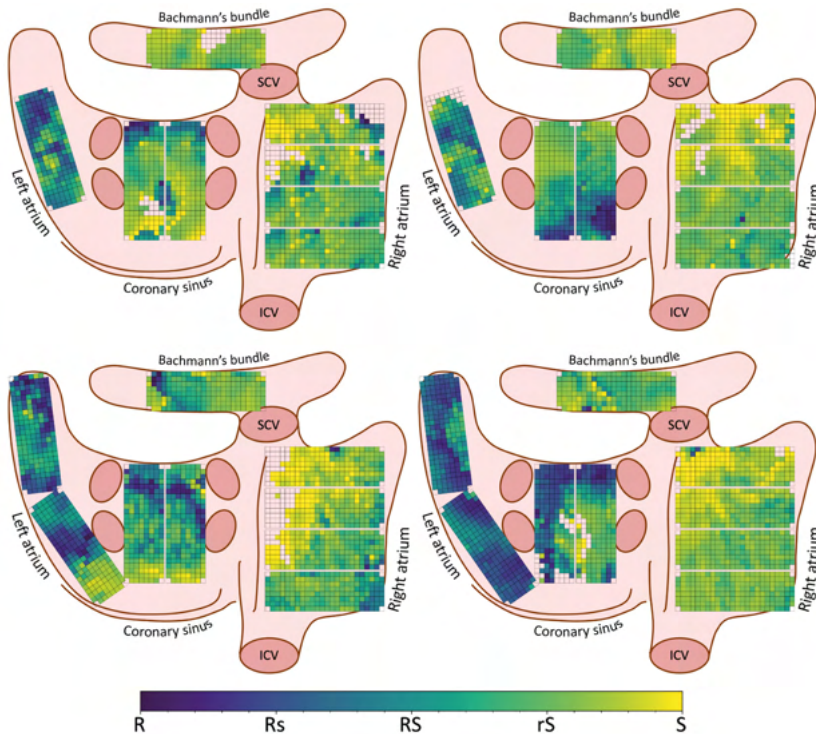
Figure 6 – Example of R/S ratio maps. Color-coded maps of the R/S ratios constructed during a single sinus rhythm beat obtained from 4 different patients. Despite comparable clinical profiles, there is a considerable interindividual variation in R/S ratios.

The gold standard mapping approach

An important step towards understanding the morphology of potentials recorded during AF is to gain insight into variation of potential morphologies recorded during sinus rhythm. For this purpose, we choose epicardial mapping as we consider this the gold standard approach.[10] This technique has several advantages, including 1) stable contact as the operator slightly presses the electrode on the atrial tissue, 2) exact positioning of the electrode array on the atrial anatomy as the operator actually sees the position of the device on the surface of the heart, 3) the possibility of recording contact potentials from a very large number of recording sites simultaneously (high-density and high-resolution), 4) access to epicardial structures such as Bachmann's bundle and 5) possibility of simultaneous high-resolution and high-density mapping of the endo- and epicardial layers.

Simplicity of sinus rhythm

R/S ratios of unipolar single potentials

During sinus rhythm, variations in the positive R-wave and negative S-wave of single potentials were used to classify sinus rhythm potentials recorded during cardiac surgery for structural heart disease. *Figure 6* shows color-coded maps of the R/S ratios during a single sinus rhythm beat obtained from four different patients with comparable clinical profiles (all male, age: 65 years, underlying heart disease: coronary artery disease). The color scale of the R/S ratios ranges from S-waves (yellow), biphasic RS-waves (green) to R-waves (blue). These four examples clearly show large inter-individual differences in R/S ratios despite

similar clinical profiles. Interestingly, despite intra-atrial variations in the R/S ratios of single potentials, there were clearly specific regional differences.

Most single potentials obtained from the superior part of the right atrium consisted of monophasic S-waves, compared to rS-waves and biphasic RS-waves obtained from the middle and inferior part of the right atrium. Hence, similar to right atrial single potentials recorded during *AF*, right atrial single potentials recorded during *sinus rhythm* were also characterized by dominant S-waves. In addition, predominant S-wave potentials with large amplitudes were also recorded at Bachmann's bundle. In contrast, R/S ratios of sinus rhythm single potentials recorded from the left atrial free wall and in between the pulmonary veins were more variable. At both areas, there was a clear R-wave predominance of single potentials.

In the study of Van Schie et al.[11], also R/S ratios of single potentials obtained from patients without a history of AF and patients with paroxysmal AF were compared. In patients with paroxysmal AF, single potentials – especially at Bachmann's bundle – were characterized by lower peak-to-peak amplitudes due to loss of the S-wave amplitudes. This resulted in single potentials with more an R-wave predominance at the right atrium, Bachmann's bundle and pulmonary vein area.

Peak-to-peak amplitudes of unipolar single potentials

In the same study population as described above, peak-to-peak amplitudes (voltages) of 523,019 different types of unipolar potentials recorded during sinus rhythm were measured.[12] As expected, lower unipolar voltages were related to areas of conduction slowing and conduction block. Also, there was a clear inversely proportional relationship between unipolar voltages and the number of deflections. Although there were no differences in median voltage between the right- and left atrium and Bachmann's bundle, potentials obtained from Bachmann's bundle of patients with paroxysmal AF had lower unipolar voltages.

Areas containing low-voltage potentials – defined as potentials with peak-to-peak amplitudes <1.0 mV – were present in all patients. However, there were no predilection sites for low voltages in this study population found.

Discrepancies between various types of voltages during sinus rhythm

Peak-to-peak amplitudes of potentials are frequently used as a feature of EGM morphology using both unipolar and bipolar EGMs. Especially LVAs are commonly used to identify arrhythmogenic tissue as target for ablative therapy. It is generally thought that areas of low bipolar voltage represent areas of slow conduction, which might underlie intra-atrial reentrant tachycardias or focal atrial tachycardias. However, voltage mapping critically depends on the use of either unipolar or bipolar EGMs, each having its own advantages and disadvantages as discussed before. To overcome the directional sensitivity of bipolar EGMs, omnipolar EGMs have been recently introduced. These omnipolar EGMs are constructed from two perpendicularly recorded bipolar EGMs by mathematically obtaining the highest possible bipolar voltage without physically rotating the recording electrodes. Even using omnipolar EGMs, Van Schie et al.[13] recently demonstrated that bi-/omnipolar LVAs still contain a large variety of unipolar voltages, and although conduction velocity was generally decreased, high conduction velocities and large unipolar voltages could still be found within these areas. Also, there were considerable directional differences in bipolar voltages, as 20% of the largest bipolar voltage differed even more than 50% from the corresponding

perpendicular bipolar voltages. This had a major impact on identification of LVAs. The use of omnipolar voltages reduced the number of LVAs by 15%, indicating a considerable number of false-positive areas which could be wrongfully targeted during catheter ablation. As there was no clear relation between bi-/omnipolar voltage and conduction velocity, it could be questioned whether ablation targeting solely bipolar LVAs is warranted. A combination of multiple techniques could provide additional information on the underlying tissue and hence arrhythmogenic substrates.

Another factor influencing the mixed results of voltage-guided ablation strategies is the fact that LVAs could be located exclusively at either the endocardium or epicardium. One of the characteristics of bipolar EGMs is that it represents more local activity. Unipolar EGMs, on the other hand, comprise a larger region of myocardial electrical activity, and are therefore preferred to identify intramural or epicardial substrates during endocardial ventricular ablation therapy. Recently, Van Schie et al.[14] examined endo- and epicardial characteristics of unipolar and omnipolar voltages at the atria, and explored the relation with identification of LVAs at either the endo- or epicardium. They demonstrated that there were considerable differences between endo- and epicardial voltages. In the majority of potentials, both unipolar and omnipolar voltages were larger at the epicardium than endocardium. However, especially larger voltages revealed to be larger at the endocardial side. The majority of both unipolar and omnipolar LVAs were located at the endocardium, and only partly corresponded to LVAs located at the epicardium. LVAs located at the epicardium more frequently corresponded to endocardial LVAs. Therefore, epicardial voltages were more accurate in identifying dual-layer LVAs. A combination of unipolar and omnipolar voltages resulted in the highest predictive value of dual-layer LVAs. A combination of multiple mapping techniques could therefore more accurately identify the arrhythmogenic substrate underlying arrhythmias.

Signal fingerprinting as a novel diagnostic tool to identify conduction inhomogeneity

Based on the observation that the profiles of R/S ratios of single potentials and peak-to-peak amplitude of unipolar potentials varied considerably between patients, we hypothesized that individualized electrical signal profiles reflect inhomogeneity in conduction.

For this purpose, we constructed a signal profile containing quantified features of all types of atrial potentials reflecting the severity and extensiveness of inhomogeneity in conduction.[15] These features included R/S ratios of single potentials, the relative frequency distribution of peak-to-peak amplitudes of the different types of potentials, the proportion of LVAs, the proportion of the different types of potentials (single-short double, long-double and fractionated potentials) and durations of long double and fractionated potentials.

Consequently, such a 'signal fingerprint' provides an individualized arrhythmogenic substrate profile which can in future studies also be tailored to possible gender and age-specific features of potentials. Finally, invasively determined signal fingerprints will become the gold standard for development of less and in the near-future even non-invasive fingerprints.

References

1. Allessie MA, de Groot NM, Houben RP, Schotten U, Boersma E, Smeets JL, Crijns HJ. Electropathological substrate of long-standing persistent atrial fibrillation in patients with structural heart disease: longitudinal dissociation. Circ Arrhythm Electrophysiol. 2010;3:606-615.
2. Brundel B, Ai X, Hills MT, Kuipers MF, Lip GYH, de Groot NMS. Atrial fibrillation. Nat Rev Dis Primers. 2022;8:21.
3. Calkins H, Hindricks G, Cappato R, Kim YH, Saad EB, Aguinaga L, Akar JG, Badhwar V, Brugada J, Camm J, et al. 2017 HRS/EHRA/ECAS/APHRS/SOLAECE expert consensus statement on catheter and surgical ablation of atrial fibrillation. Heart Rhythm. 2017;14:e275-e444.
4. Starreveld R, van der Does L, de Groot NMS. Anatomical hotspots of fractionated electrograms in the left and right atrium: do they exist? Europace. 2019;21:60-72.
5. van der Does LJ, de Groot NM. Inhomogeneity and complexity in defining fractionated electrograms. Heart Rhythm. 2017;14:616-624.
6. Starreveld R, Knops P, Roos-Serote M, Kik C, Bogers A, Brundel B, de Groot NMS. The Impact of Filter Settings on Morphology of Unipolar Fibrillation Potentials. J Cardiovasc Transl Res. 2020;13:953-964.
7. Abdi B, van Schie MS, Groot NMS, Hendriks RC. Analyzing the effect of electrode size on electrogram and activation map properties. Comput Biol Med. 2021;134:104467.
8. Konings KT, Smeets JL, Penn OC, Wellens HJ, Allessie MA. Configuration of unipolar atrial electrograms during electrically induced atrial fibrillation in humans. Circulation. 1997;95:1231-1241.
9. Houben RP, de Groot NM, Smeets JL, Becker AE, Lindemans FW, Allessie MA. S-wave predominance of epicardial electrograms during atrial fibrillation in humans: indirect evidence for a role of the thin subepicardial layer. Heart Rhythm. 2004;1:639-647.
10. de Groot NMS, Shah D, Boyle PM, Anter E, Clifford GD, Deisenhofer I, Deneke T, van Dessel P, Doessel O, Dilaveris P, et al. Critical appraisal of technologies to assess electrical activity during atrial fibrillation: a position paper from the European Heart Rhythm Association and European Society of Cardiology Working Group on eCardiology in collaboration with the Heart Rhythm Society, Asia Pacific Heart Rhythm Society, Latin American Heart Rhythm Society and Computing in Cardiology. Europace. 2021.
11. van Schie MS, Starreveld R, Roos-Serote MC, Taverne Y, van Schaagen FRN, Bogers A, de Groot NMS. Classification of sinus rhythm single potential morphology in patients with mitral valve disease. Europace. 2020;22:1509-1519.
12. van Schie MS, Starreveld R, Bogers A, de Groot NMS. Sinus rhythm voltage fingerprinting in patients with mitral valve disease using a high-density epicardial mapping approach. Europace. 2021;23:469-478.
13. van Schie MS, Kharbanda RK, Houck CA, Lanters EAH, Taverne Y, Bogers A, de Groot NMS. Identification of Low-Voltage Areas: A Unipolar, Bipolar, and Omnipolar Perspective. Circ Arrhythm Electrophysiol. 2021;14:e009912.
14. Van Schie MS, Knops P, Zhang L, Van Schaagen FRN, Taverne Y, De Groot NMS. Detection of endo-epicardial atrial low-voltage areas using unipolar and omnipolar voltage mapping. Front Physiol. 2022;13:1030025.
15. Ye Z, van Schie MS, de Groot NMS. Signal Fingerprinting as a Novel Diagnostic Tool to Identify Conduction Inhomogeneity. Front Physiol. 2021;12:652128.

3

PART I

POTENTIAL MORPHOLOGY: ELECTRICAL SIGNAL MARKERS RELATED TO ELECTROPATHOLOGY
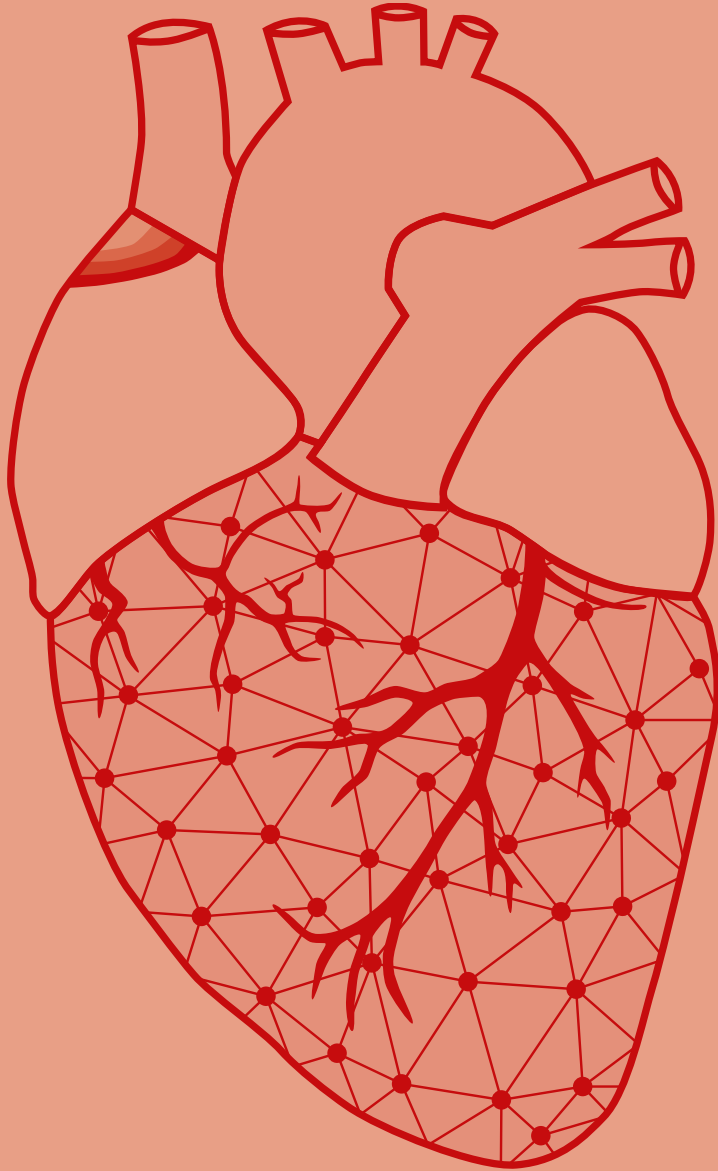
Chapter 4

Sinus rhythm voltage fingerprinting in patients with mitral valve disease using a high-density epicardial mapping approach

Mathijs S. van Schie

Roeliene Starreveld

Ad J.J.C. Bogers

Natasja M.S. de Groot

Abstract

Aims: Unipolar voltage (UV) mapping is increasingly used for guiding ablative therapy of atrial fibrillation (AF) as unipolar electrograms (U-EGMs) are independent of electrode orientation and atrial wavefront direction. This study was aimed at constructing individual, high-resolution sinus rhythm (SR) UV fingerprints in order to identify low-voltage areas and study the effect of AF episodes in patients with mitral valve disease (MVD).

Methods: Intra-operative epicardial mapping (interelectrode distance 2 mm) of the right and left atrium (RA, LA), Bachmann's bundle (BB) and pulmonary vein area (PVA) was performed in 67 patients (27 male, 67±11 years) with or without a history of paroxysmal AF (PAF).

Results: In all patients, there were considerable regional variations in voltages. UVs at BB were lower in patients with PAF compared to those without (no AF: 4.94 [3.56–5.98] mV, PAF: 3.30 [2.25–4.57] mV, p=0.006). A larger number of low-voltage potentials were recorded at BB in the PAF group (no AF: 2.13 [0.52–7.68] %, PAF: 12.86 [3.18–23.59] %, p=0.001). In addition, areas with low-voltage potentials were present in all patients, yet we did not find any predilection sites for low-voltage potentials to occur.

Conclusion: Even in SR, advanced atrial remodeling in MVD patients shows marked inter-individual and regional variation. Low UVs are even present during SR in patients without a history of AF indicating that low UVs should carefully be used as target sites for ablative therapy.

Journal site

4

Introduction

Unipolar voltage (UV) mapping is increasingly used to define the substrate of cardiac arrhythmias like atrial fibrillation (AF).[1] In recent studies, low bipolar voltage areas are regarded sites of structurally remodeled tissue and have therefore become targets for AF ablation.[2-4] However, there are many discrepancies between studies in for example mapping and ablation strategies, rhythm during mapping and patient selection, resulting in mixed outcomes.[5] In daily clinical practice, electro-anatomical mapping is performed via endovascular catheters at the endocardial side, using bipolar electrograms (EGMs). However, non-substrate related factors such as activation direction also influences voltages of bipolar EGMs.[5] Unipolar electrograms (U-EGMs), on the other hand, are independent of the electrode orientation and atrial wavefront direction, and have the benefit over bipolar EGMs that their morphology contains additional information on the progression of the wavefront and remote activations. It is for these reasons that U-EGMs are increasingly used in recent electrophysiological studies and newly developed mapping systems guiding (ventricular) ablation procedures.[1,5,6] However, the use of unipolar voltage mapping remains less established in mapping of the atrial substrate.

Nevertheless, multiple methods and thresholds have been defined to identify low-voltage areas and abnormal tissue in both bipolar- as U-EGMs. In addition, several studies have shown local variation in endocardial bipolar EGM voltages during sinus rhythm (SR) between atrial regions and that specific regional differences exist between patients with and without AF, especially within the left atrium (LA).[7,8]

As no significant differences were found between endocardial and epicardial U-EGM voltages by Van der Does et al.[9], high-resolution epicardial mapping data of the entire atria can be used to create a representative UV profile, reflecting characteristics of unipolar potentials. These voltage fingerprints can be used to identify low-voltage areas and to examine the effect of AF episodes on SR potential voltages. Therefore, this study was aimed at constructing individual, high-resolution unipolar SR voltage profiles in order to identify low UV areas and study the effect of AF episodes on UV potentials in patients with mitral valve disease (MVD).

Methods

Study population

The study population consisted of 67 successive adult patients undergoing mitral valve surgery or a combination of mitral valve and coronary bypass surgery in the Erasmus Medical Center Rotterdam. This study was approved by the institutional medical ethical committee (MEC2010-054/MEC2014-393).[10,11] Written informed consent was obtained from all patients and patient characteristics (e.g., age, medical history, cardiovascular risk factors, time in AF) were obtained from the patient's medical record. The study population was classified into two groups: those without a history of AF (no AF group) and those with a history of paroxysmal AF (PAF group).

Mapping procedure

Epicardial high-resolution mapping was performed prior to commencement of extra-corporal circulation, as previously described in detail.[10,11] A temporal bipolar epicardial pacemaker wire attached to the RA free wall served as a reference electrode and a steel wire fixed to subcutaneous tissue of the thoracic cavity was used as an indifferent
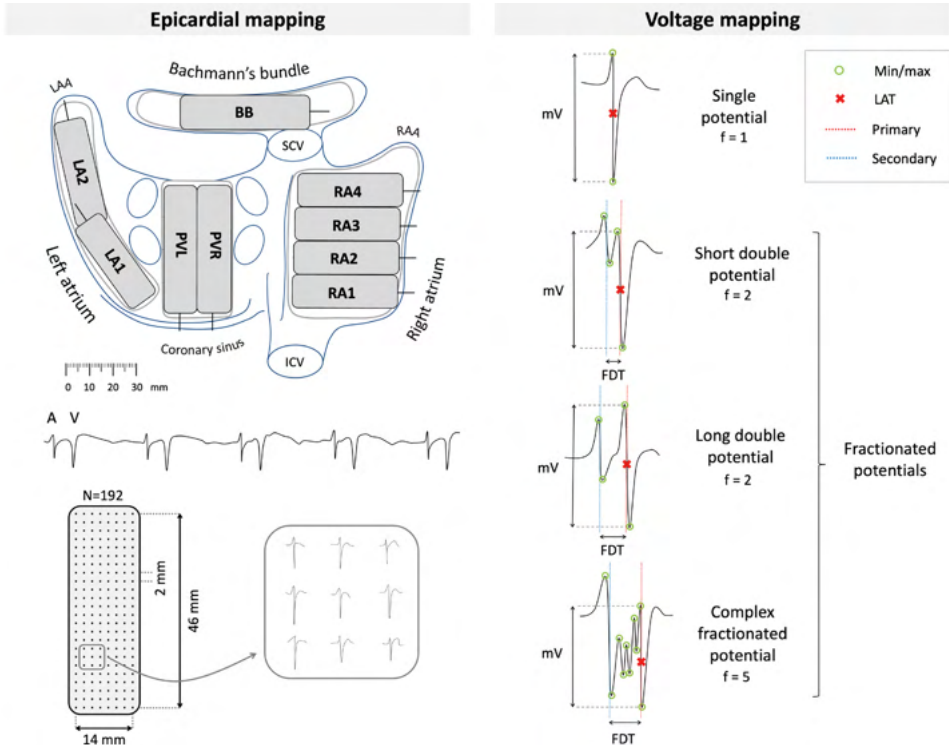
Figure 1 – Epicardial high-resolution mapping. *Upper left panel*: projection of the 192-unipolar electrode array on a schematic posterior view of the atria. *Lower left panel*: epicardial, unipolar potentials recorded during 5 seconds of SR containing atrial deflections (A) and far-field ventricular signals (V). Typical examples of 9 unipolar potentials obtained from the RA are shown outside the mapping. *Right panel*: classification of potential type according to the number of deflections (f). EGM voltage is determined as the peak-to-peak amplitude of the steepest (primary) deflection. **FDT** = fractionation delay time; **ICV** = inferior caval vein; **SCV** = superior caval vein; **LAA** = left atrial appendage; **RAA** = right atrial appendage; **RA** = right atrium; **BB** = Bachmann's bundle; **PV** = pulmonary veins; **LA** = left atrium.

electrode. Epicardial mapping was performed with a 128-electrode array or 192-electrode array (electrode diameter respectively 0.65 mm or 0.45 mm, interelectrode distances 2.0 mm). Mapping was conducted by shifting the electrode array along imaginary lines with a fixed anatomic orientation, covering the entire epicardial surface of the right atrium (RA), Bachmann's bundle (BB), pulmonary vein area (PVA) and left atrium (LA), following a predefined mapping scheme as illustrated in the upper left panel of *Figure 1*. Omission of areas was avoided at the expense of possible small overlap between adjacent mapping sites. The RA was mapped from the cavo-tricuspid isthmus, shifting perpendicular to the caval veins towards the RA appendage. The PVA was mapped from the sinus transversus fold along the borders of the right and left pulmonary veins (PVR and PVL) down towards the atrioventricular groove. The left atrio-ventricular groove (LAVG) was mapped from the lower border of the left inferior pulmonary vein towards the LA appendage. BB was mapped from the tip of the LA appendage across the roof of the LA, behind the aorta towards the superior cavo-atrial junction.

Five seconds of SR were recorded from every mapping site, including a surface ECG lead, a calibration signal of 2 mV and 1000 ms, a bipolar reference electrogram and all unipolar epicardial EGMs. In patients who presented in AF, SR mapping was performed after electrical cardioversion. Patients who could not be converted to SR were excluded from analysis. Data

Table 1 – Patient characteristics (N=67).

	No AF	PAF	*p*-value
Patients	44 (66)	23 (34)	-
Male	17 (39)	10 (43)	0.903
Age (y)	65±12	73±6	0.003
Cardiovascular risk factors			
• BMI (kg/m^2)	24.5 [22.1–26.8]	25.3 [22.2–31.9]	0.281
- Underweight (<18.5)	2 (5)	0 (0)	0.778
- Normal weight (18.5-25)	22 (50)	11 (48)	0.866
- Overweight (25-30)	15 (34)	5 (22)	0.443
- Obese (≥30)	5 (11)	7 (30)	0.110
• Hypertension	15 (34)	12 (52)	0.242
• Dyslipidemia	14 (32)	2 (9)	0.071
• Diabetes mellitus	7 (16)	3 (13)	0.755
Left atrial dilatation >45 mm	28 (64)	16 (70)	0.830
Left ventricular dysfunction	15 (34)	6 (26)	0.694
Mitral stenosis			
• No	41 (93)	22 (96)	0.685
• Severe	3 (7)	1 (4)	0.685
Mitral insufficiency severity			
• Mild	1 (2)	0 (0)	0.466
• Moderate	8 (18)	3 (13)	0.848
• Moderate-to-severe	4 (9)	4 (17)	0.550
• Severe	31 (70)	16 (70)	0.940
Coronary artery disease	20 (45)	6 (26)	0.200
Antiarrhythmic agents			
• Class I	1 (2)	0 (0)	0.466
• Class II	23 (52)	11 (48)	0.930
• Class III	0 (0)	7 (30)	<0.001
• Class IV	1 (2)	2 (9)	0.559

Values are presented as mean ± standard deviation, median [interquartile ranges] or as N (%). **(P)AF** = (paroxysmal) atrial fibrillation; **BMI** = body mass index.

was stored on a hard disk after amplification (gain 1000), filtering (bandwidth 0.5–400 Hz), sampling (1 kHz) and analogue-to-digital conversion (16 bits).

Data analysis

U-EGM morphology was semi-automatically analyzed using custom-made software. EGMs with injury potentials, recording sites with ≥25% excluded or missing EGMs and atrial extrasystoles were excluded from analysis. The steepest negative slope of an atrial deflection was marked as the local activation time (LAT), provided that the amplitude of the deflection was at least two times the signal-to-noise ratio of the EGM. The minimal time between two successive deflections ('latency') was set to 2 ms. All signal markings were manually checked and corrected in case of markings on electrical artifacts evaluated by a consensus of two investigators.

The potential amplitude is defined as the peak-to-peak voltage of the steepest deflection. Low voltage is defined as the fraction of potentials with an amplitude below the 5th percentile of all potentials obtained from all MVD patients without AF. Fractionated potentials are defined as potentials with ≥2 deflections. Conduction velocity (CV) is computed using discrete velocity vectors as previously described. Slowing of conduction was defined as a local CV of <28 cm/s and conduction block as a local conduction delay of <18 cm/s. Simultaneous activated areas without CV were excluded to avoid inclusion of far-field potentials.

Table 2 – Analysis of electrophysiological parameters per patient (N = 67).

	MVD without AF (N=44)	MVD with AF (N=23)	*p*-value
Right atrium			
Number of potentials	4,067 [3,346–5,797]	4,229 [2,881–4,936]	0.086
Amplitude (mV)	4.86 [3.97–5.71]	4.75 [3.84–6.15]	0.492
Fractionated potentials (%)	14.79 [9.76–19.60]	16.55 [8.70–23.83]	0.197
Low voltage (%)	6.49 [2.34–9.15]	8.37 [2.94–14.06]	0.150
Fractionated low voltage (%)	50.0 [37.5–64.4]	54.4 [37.2–65.0]	0.433
Bachmann's bundle			
Number of potentials	984 [783–1,206]	940 [779–1,126]	0.295
Amplitude (mV)	4.92 [3.45–6.09]	2.95 [2.24–4.57]	0.007
Fractionated potentials (%)	19.58 [12.40–31.72]	28.68 [17.70–39.55]	0.064
Low voltage (%)	1.79 [0.37–8.02]	11.98 [2.95–21.50]	0.001
Fractionated low voltage (%)	85.0 [77.5–98.3]	74.6 [50.2–96.2]	0.080
Pulmonary vein area			
Number of potentials	1,979 [1,441–2,608]	2,136 [1,592–2,596]	0.497
Amplitude (mV)	3.84 [2.45–7.15]	3.95 [2.62–5.02]	0.268
Fractionated potentials (%)	11.89 [9.08–17.01]	21.70 [13.48–28.63]	<0.001
Low voltage (%)	6.49 [0.20–13.31]	10.19 [3.89–14.28]	0.061
Fractionated low voltage (%)	36.7 [18.5–61.7]	51.3 [23.6–65.4]	0.342
Left atrium			
Number of potentials	1,626 [1,132–2,302]	1,777 [1,062–2,077]	0.439
Amplitude (mV)	4.42 [2.99–5.87]	4.64 [3.65–5.72]	0.363
Fractionated potentials (%)	10.92 [6.43–17.74]	17.47 [11.30–20.54]	0.062
Low voltage (%)	3.63 [1.57–11.35]	4.04 [0.72–8.98]	0.358
Fractionated low voltage (%)	25.9 [10.7–48.8]	29.6 [17.5–73.4]	0.144

Values are presented as median [interquartile ranges] or as N (%). **MVD** = mitral valve disease; **(P)AF** = (paroxysmal) atrial fibrillation.

Statistical analysis

All data were tested for normality. Normally distributed data are expressed as mean ± standard deviation and analyzed with a paired *t*-test or one-way ANOVA. Skewed data are expressed as median [25th–75th percentile] and analyzed with a Kruskal-Wallis test, Mann-Whitney U test or Wilcoxon signed-rank test, whichever appropriate. Categorical data are expressed as numbers and percentages and analyzed with a χ^2 or Fisher exact test. Correlation was determined by an ordinary least squares regression model. Distribution data was analyzed with a two-sample Kolmogorov-Smirnov test. A *p*-value <0.05 was considered statistically significant. Bonferroni correction was applied for comparison of the four atrial regions; a *p*-value of <0.0083 (0.05/6) was considered statistically significant.

Results

Study population

Clinical characteristics of the study population, including 44 patients without ('no AF group') and 23 patients with PAF, are described in detail in *Table 1*. These groups differed in age (no AF: 65±12 vs. PAF: 73±6 years, p=0.003) and the use of class III antiarrhythmic drugs (no AF: 0 vs. PAF: 7 (30%), p<0.001). Patients had either ischemic and mitral valve disease (no AF: 20 [45%], PAF: 6 [26%]) or only solely mitral valve disease. The gradient of both mitral insufficiency and stenosis did not differ between both groups; the majority of the patients had severe mitral insufficiency (no AF: 31 (70%), PAF: 13 (70%), p=0.940). LA dilation was present in 28 patients without AF (64%) and in 16 patients with PAF (70%). Most patients in both groups had normal left ventricular function (no AF: 29 [66%], PAF: 17 [74%]).
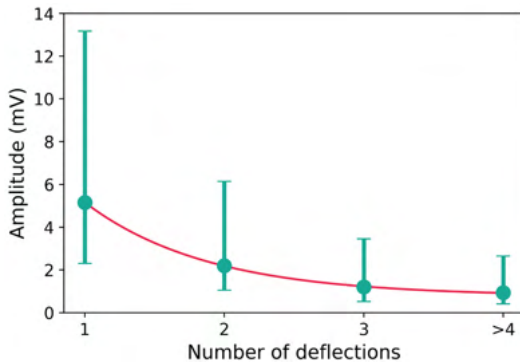
Figure 2 – Relation between potential amplitude and number of deflections. Potential amplitude is given as median with interquartile ranges.

4

Data characteristics

As demonstrated in *Table 2*, a total of 600,722 potentials were analyzed out of 829 SR recordings of 5-seconds duration. There was no difference between the median number of potentials between the no AF and PAF group and the median amplitude of all potentials recorded from the entire epicardial surface did also not differ between these two groups (no AF: 4.70 [4.05–5.43] mV vs. PAF: 4.52 [3.73–5.25] mV, p=0.138).

Correlation between unipolar voltage and interatrial conduction

There was no clear correlation between UV and CV, though smaller voltages were recorded in areas of conduction slowing (1.74 [0.88–3.53] mV vs. 4.72 [2.46–7.61] mV, p<0.001) and conduction block (1.22 [0.69–2.26] mV vs. 4.79 [2.55–7.65] mV, p<0.001). There was a clear difference in UV between fractionated potentials and single potentials in which the former type results in smaller voltages compared to the latter (2.05 [1.04–3.75] mV vs. 5.16 [2.85–8.01] mV, p<0.001). In addition, as demonstrated in *Figure 2*, there was a clear inversely proportional relationship between UV and the number of additional deflections (1: 5.16 [2.85–8.01] mV; 2: 2.20 [1.14–3.95] mV; 3: 1.21 [0.68–2.26] mV; ≥4: 0.94 [0.52–1.71] mV, p<0.001 for all). Furthermore, UV was inversely correlated with age and BMI (R^2=0.21; age: -0.04 mV/year, p=0.005; BMI: -0.07 mV/kg/m^2, p=0.043). There was no difference in UV between patients with different gradients of mitral insufficiency or stenosis.

Unipolar voltage mapping

In *Figure 3*, 12 representative examples of color-coded spatial distributions of potential voltages during SR in 6 patients without and 6 with PAF are shown. In all patients, there is a wide variation in potential voltages throughout the entire atrial surface without a clear predilection site for low voltages.

Regional differences in unipolar voltages

In the following step, U-EGMs were subdivided according to the corresponding atrial recording regions (RA, BB, PVA and LA); their characteristics are listed in *Table 2*. In the no AF group, there were no significant differences in median potential voltages between the various atrial regions (p=0.750). However, in the PAF group, UVs of potentials recorded at BB (2.95 [2.24–4.57] mV) were significantly lower compared to RA potentials (4.75 [3.84–6.15] mV, p=0.004) and LA potentials (4.64 [3.65–5.72] mV, p=0.003). Comparing the no AF and PAF group, UVs at BB were significantly lower in the latter group (no AF: 4.92 [3.45–6.09] mV, PAF: 2.95 [2.24–4.57] mV, p=0.007).
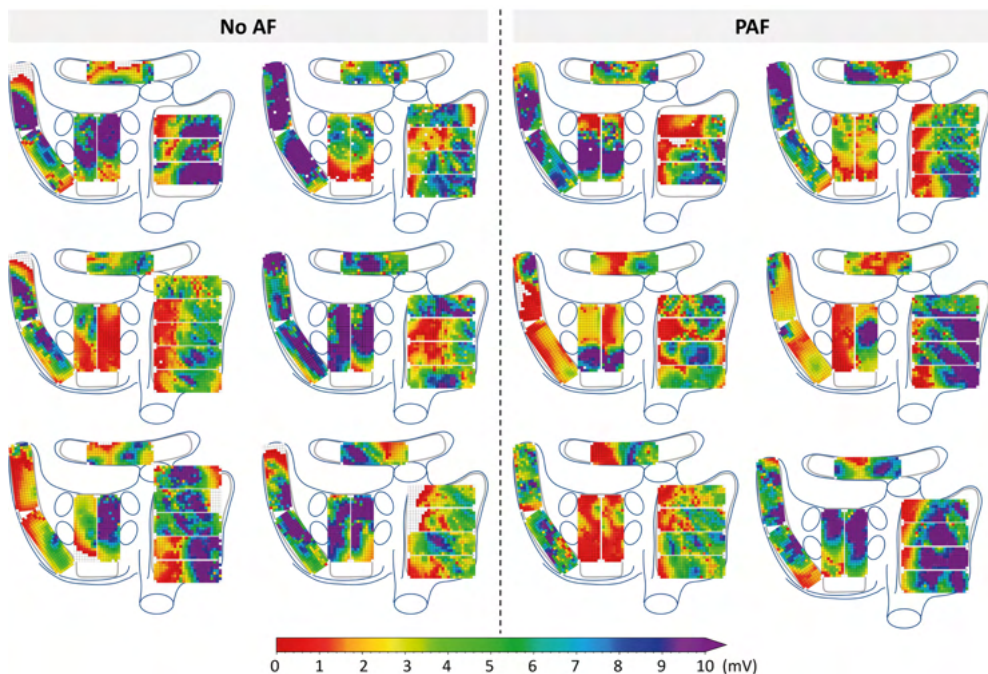
Figure 3 – Representative examples of unipolar epicardial voltage maps. Maps during one sinus beat in 6 patients without history of AF (left) and 6 patients with PAF (right). **(P)AF** = (paroxysmal) atrial fibrillation.

In the no AF group, there was a significantly higher number of fractionated potentials at BB (19.58 [12.40–31.72] %) compared to the RA (14.79 [9.76–19.60] %, p<0.001), PVA (11.89 [9.08–17.01] %, p<0.001) and LA (10.92 [6.43–17.74] %, p<0.001). In the PAF group, a significantly higher number of fractionated potentials was observed in BB (28.68 [17.70–39.55] %) compared to the RA (16.55 [8.70–23.83] %, p<0.001) and LA (17.47 [11.30–20.54] %, p=0.001), but not at the PVA (21.70 [13.48–28.63] %, p=0.114). Compared to the no AF group, more fractionated potentials at the PVA were found in the PAF group (no AF: 11.89 [9.08–17.01] %; PAF: 21.70 [13.48–28.63] %; p<0.001).

Determination of low-voltage areas

The P_5 of all potentials obtained from all MVD patients without AF was 1.0 mV, which was therefore used as cut-off value in identification of low-voltage areas. As demonstrated in *Table 2*, a larger number of low-voltage potentials were recorded at BB in the PAF group compared to the no AF group (no AF: 1.79 [0.37–8.02] %, PAF: 11.98 [2.95–21.50] %, p=0.001).

Regional differences in low-voltage areas

Within the areas of low voltage, 46.2 [31.0–59.8] % of the potentials were fractionated in the no AF group and 47.1 [38.9–56.4] % in the PAF group (p=0.450). Specifically, in the no AF group, most fractionated low-voltage potentials were found at BB (BB: 85.0 [77.5–98.3] % vs. RA: 50.0 [37.5–64.4] %, p<0.001; PVA: 36.7 [18.5–61.7] %, p<0.001; LA: 25.9 [10.7–48.8] %, p<0.001). In addition, the amount of fractionated low-voltage potentials was higher at the RA compared to the LA (p<0.001). In the PAF group, however, BB was only higher compared to the PVA and LA (BB: 74.6 [50.2–96.2] % vs. PVA: 51.3 [23.6–65.4] % and LA: 29.6 [17.5–73.4] %, p=0.003 & p=0.006 respectively).

No AF
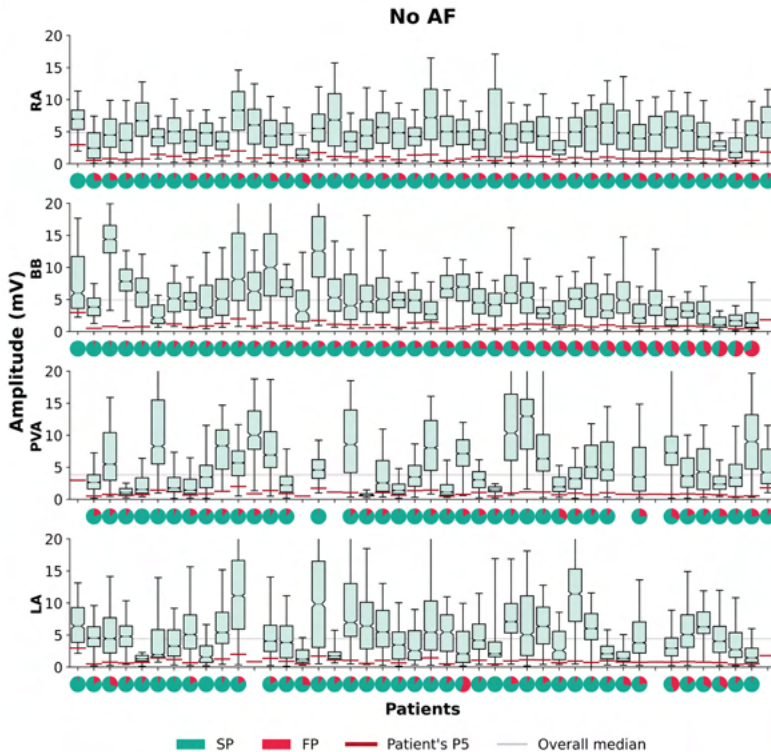
Figure 4 – Boxplots of the voltage distributions during SR depicted for each patient without AF separately recorded at the right atrium, Bachmann's bundle, pulmonary vein area and left atrium. For each patient a pie plot of the potential type distribution is given, indicating the number of single potentials (turquoise) and fractionated potentials (red). For each patient, a dark red line indicates a patient's voltage P_5 and the grey line represents the overall voltage median per atrial region. Patients are ranked in descending order according to the amount of single potentials at Bachmann's bundle. **AF** = atrial fibrillation; **BB** = Bachmann's bundle; **FP** = fractionated potentials; **LA** = left atrium; **PVA** = pulmonary vein area; **RA** = right atrium; **SP** = single potentials.

Individual Voltage Fingerprints

The voltage distribution is depicted for each individual patient in a so-called voltage fingerprint, as demonstrated in *Figures 4 and 5*. In all patients, there was a considerable variation in voltage distribution between all atrial regions and clear inter-individual differences were found. In the no AF group, considerable inter-individual variations in the dispersion of median voltages were found between the atrial regions ranging from 0.78 to 9.90 mV (median: 4.11 mV), while in the PAF group the variations ranged from 0.51 to 7.23 mV (median: 3.45 mV) (p=0.070). The P_5 of the voltages differed between the individual patients, and between the patients without AF and with PAF (no AF: 0.84 [0.71–1.12] mV; PAF: 0.65 [0.57–1.01] mV; p=0.041). In all patients, fractionation was found in one or more atrial regions, ranging in the no AF group from 0.54 % to 31.89 % (median: 15.60 %) and from 8.86 % to 29.77 % (median: 18.61 %) in the PAF group (p=0.037).

Predilection sites for low-voltage areas

For each individual patient, the location with the highest amount of low voltage was determined, as demonstrated in *Figure 6*. In the no AF group, there was no clear predilection site for low-voltage areas. However, the amount of low-voltage areas at the RA (7.8 [3.1–11.4]
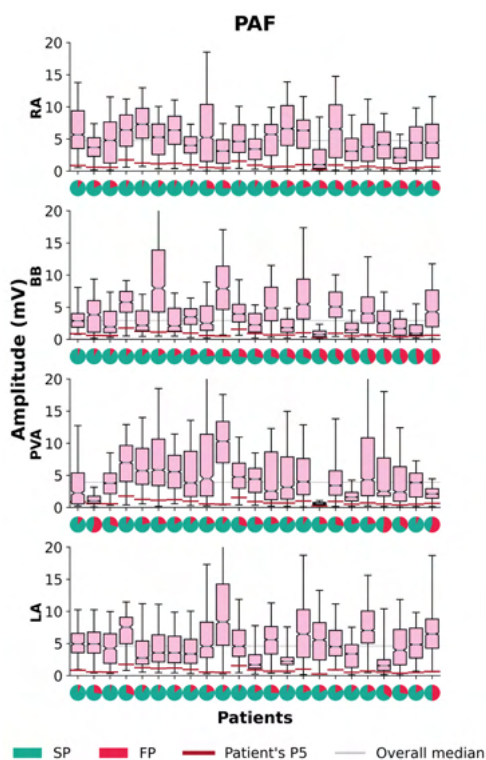
Figure 5 – Boxplots of the voltage distributions during SR depicted for each patient with PAF separately recorded at the right atrium, Bachmann's bundle, pulmonary vein area and left atrium. For each patient a pie plot of the potential type distribution is given, indicating the number of single potentials (turquoise) and fractionated potentials (red). For each patient, a dark red line indicates a patient's voltage P_5 and the grey line represents the overall voltage median per atrial region. Patients are ranked in descending order according to the amount of single potentials at Bachmann's bundle. **BB** = Bachmann's bundle; **FP** = fractionated potentials; **LA** = left atrium; **PAF** = paroxysmal atrial fibrillation; **PVA** = pulmonary vein area; **RA** = right atrium; **SP** = single potentials.

%) was lower compared to BB and PVA (22.3 [11.6–26.2] % and 19.8 [12.5–32.5] %; p=0.007 & p<0.001 respectively). In the PAF group, low-voltage areas occurred more frequently at BB (48%), yet, comparable to the no AF group, there were no significant regional differences in the amount of low-voltage areas. Comparing the no AF and PAF group, low-voltage areas occurred more frequently at BB (21% vs. 48%; p=0.020) in the PAF group. However, the amount of low-voltage sites did not differ at any region between both groups.

Discussion

In this study, we measured UVs at a high-resolution scale in MVD patients with and without history of PAF and demonstrated extensive inter-individual and regional differences in voltage distribution in both patients without and with a history of AF. Even in SR, patients with PAF have lower UVs at BB and a higher number of low-voltage potentials. In addition, areas with low-voltage potentials were present in all patients, yet we did not find any predilection sites for low-voltage potentials to occur.

Unipolar Voltage Mapping

Structural properties of atrial tissue can be estimated from the spatial distribution of EGM amplitudes, commonly known as voltage mapping. These EGMs are recorded in either the unipolar or bipolar configuration. In daily clinical practice, the bipolar EGM is more commonly used as it contains more local information from the area of myocardium between two electrodes. However, in bipolar recordings, several non-substrate related factors can theoretically influence the EGM voltage, like activation orientation, electrode spacing, electrode size, tissue contact and filtering, and may therefore provide less accurate
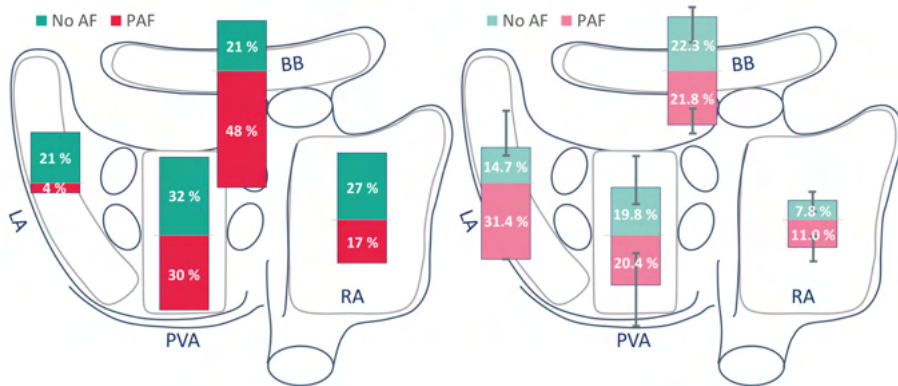
Figure 6 – Areas of low voltage and amount of low voltage. Bars plotted on a schematic posterior view of the atria demonstrating the most prominent site of low-voltage areas (left panel) and amount of low voltage (right panel) depicted for patients without AF (turquoise) and with PAF (red) in the right atrium, Bachmann's bundle, pulmonary vein area and left atrium. **BB** = Bachmann's bundle; **LA** = left atrium; **(P)AF** = (paroxysmal) atrial fibrillation; **PVA** = pulmonary vein area; **RA** = right atrium.

information on the arrhythmogenicity of the underlying myocardial tissue.[5,12,13] U-EGMs, on the other hand, can be regarded as the sum of instantaneous current dipoles of a wavefront, reflecting cardiac electrical activity of the tissue surrounding the recording electrode. As the amplitude depends on the volume of simultaneously activated cardiac tissue, synchronous activation of myocardium results in relative large amplitude U-EGMs, whereas areas of asynchronously activated myocardium cause a decrease in U-EGM amplitudes.[14] It is for these reasons that U-EGMs are more and more used in newly developed mapping systems.[6,15]

Determination of low-voltage areas

Low-UV EGMs are commonly associated with areas of fibrosis, which produce reduced electric fields and consequently lower potential differences.[16] The relationship between clinical outcomes, AF substrate factors, AF triggers and low-voltage areas depend critically on the voltage threshold chosen to define low voltage. A value of 0.5 mV is commonly used to define low voltage in atrial bipolar EGMs which is not based on the presence of defined underlying abnormalities in atrial structure or function.[17] In our study, we used a value of 1.0 mV, which was based on the 5th percentile of all measured potential amplitudes in the MVD patients without AF. Other studies define abnormal voltage as the voltage at the 5th percentile of all mapping points within one patient, resulting in a wide range of threshold values and various thresholds for different atrial segments depending on the locations of the mapping points. In both groups, there was a large inter-individual variability in the 5th percentile. We only used data of the patients without AF to determine a 'threshold' for identification of low-voltage areas, although structural remodeling is most likely also present in this population. The extent of remodeling is more pronounced in patients with AF, which is reflected by the lower 5th percentiles observed in the PAF group. However, the absolute voltage threshold for structural remodeling remains arbitrary, as we have no true healthy population undergoing cardiac surgery available.

Determinants of atrial voltage

UV is primarily determined by cardiac electrical activity of the tissue surrounding the recording electrode which decreases with distance. Areas of synchronous activation in the longitudinal axis of myocardial fibers result in fast wavefront propagation and large UV

potentials.[14] In addition, thicker cardiac muscle bundles will result in larger UV potentials as compared to small bundles. In case of areas with non-uniform anisotropy, activation becomes asynchronous. This will result in smaller UV potentials as smaller volumes of cardiac tissue are simultaneously activated. In particular, low-voltage fractionated potentials with multiple additional deflections are regarded as part of the arrhythmogenic substrate underlying AF.[16] We demonstrated that UV decreases when the number of additional deflections increases. It is generally assumed that low amplitude, fractionated potentials reflect critical regions of slow conduction or conduction block.[18] Moreover, we demonstrated that UV is lower in areas of slowed conduction or conduction block, which might indicate areas of fibrotic tissue. However, even in the areas of conduction block, not all recorded potentials were fractionated, low amplitude potentials and there was therefore no generally clear relation between UV and CV. In a previous study, we demonstrated that UV of single potentials are mainly determined by their relative R- and S-wave morphology, which could provide additional information on CV and wavefront propagation.[19] Consequently, low-voltage potentials could also be explained by asymmetry of the relative R- and S-wave amplitudes. It is for these reasons that (low) UV alone does not automatically indicate 'diseased' atrial tissue and therefore an absolute voltage threshold for structural remodeling remains arbitrary.

Regional differences in epicardial voltage

Several studies have described differences in voltages between various atrial regions as well as regional differences between paroxysmal and persistent AF patients.[7,8,20] We did not find regional differences in median voltages in patients without AF. However, as demonstrated by our Voltage Fingerprints, there were considerable differences in voltage distributions throughout the atria in all patients.

Given that voltage is affected by atrial wall thickness and that wall thickness varies throughout the atria, it is likely that some of these differences are explained by variations in wall thickness. Nevertheless, other factors such as external pressing with the electrode array and atrial walls stress may also influence the recorded voltages.

Structural remodeling

MVD patients undergoing cardiac surgery, -even without a history of AF- usually have advanced structurally remodeled atria due to altered hemodynamics and therefore MVD is a well-known risk factor for developing AF.[21-23] Extensive areas of low-voltage potentials are therefore also present in MVD patients without history of AF. In addition, AF itself also causes electrical remodeling, thereby increasing the arrhythmogenic substrate. While these changes may be a consequence of AF, it could also be a result of primary structural abnormalities caused by MVD. In addition, in patients with MVD it has been demonstrated that there are electrophysiological differences between and within both the LA and RA. Based on these observations, it was suggested that the structural changes responsible for initiating and maintaining AF could be diffusely located and different to patients with lone AF.[23]

A prior study in MVD patients with AF suggested that the posterior wall may be especially rich in fibrotic tissue compared to the LA appendage.[24] In addition, patients with MVD with enlarged LA dimensions – resulting in elevated atrial wall stress – have an increased risk of developing AF.[25] Interestingly, in our population, there were no differences in voltages obtained from the LA and PVA between the no AF and PAF group. However, more fractionated potentials were found in these areas in patients with PAF. As fractionation represents asynchronous activation caused by e.g. fibrotic tissue, this could also be indicative of an

increased deposition of fibrotic tissue in these areas.[16] This is supported by a study of Boldt et al. who found an increased expression of fibrosis in the left atrial tissue of patients with MVD.[26]

Multiple earlier mapping studies found clear correlations between the presence of low-voltage areas and the development of AF.[2-4] In our study, low-voltage areas were found in all patients, although lower UVs and more low-voltage areas were found in the PAF group at BB. In addition, we could not find any predilection site for low-voltage areas in both of our groups, although significant inter-individual differences were found in UV and low-voltage areas. Besides, earlier studies found more conduction disorders at BB in patients with valvular heart disease, possibly relating to the increased amount of low-voltage areas and lower epicardial voltage at this region.[27,28] These observations further support the concept that structural remodeling associated with AF development is diffusely located in the atria in this patient population.

Clinical implications

MVD patients frequently undergo cardiac surgery and concomitant arrhythmia surgery is performed when AF is present. In these patients, next to PV isolation, epicardial mapping during surgery could provide additional information on the arrhythmogenic substrate as potential target sites for ablation. However, although the extend of remodeling is more pronounced in patients with AF, the absolute voltage threshold applied in this study for structurally remodeled atria does not permit to clearly separate patients for whom those areas may be suitable target sites for ablation. Therefore, low-voltage areas during SR should carefully be used as target sites for (surgical) ablative therapy in this patient population.

In addition, large intra- and inter-individual variation in potential voltages found in our study population highlights the requirement of an individualized, patient tailored diagnosis and therapy of the arrhythmogenic substrate in patients with MVD and AF. It is likely, that due to increased non-uniform anisotropic properties of atrial myocardium in MVD patients, UVs alter when the direction of the activation wavefront, during e.g. atrial extrasystolic beats and tachyarrhythmias, changes. Therefore, the next step is to examine voltage maps during tachyarrhythmias such as AF and to compare them with SR voltage maps in order to decode electrical conduction properties and possible additional frequency- and direction dependent conduction disorders.

Study limitations

Most patients with AF in our study had PAF instead of (long-standing) persistent AF. Electrical and structural remodeling in these patients is considered to be less extensive, therefore more differences in SP morphology are expected with increasing AF persistence. In addition, as MVD patients undergoing cardiac surgery, – even without a history of AF – usually have advanced structurally remodeled atria, this population is not representative of all patients undergoing AF ablation.

The recorded UV might also be influenced by variable contact of the electrode array with the cardiac tissue, which could have introduced a bias in the data. However, this bias is considered to be minimal as confirmation of good contact of the electrode array with cardiac tissue was an important step in the mapping procedure. Besides, loss of contact could be easily recognized during post processing of the data. In addition, the presence of epicardial fat could have influenced our results as earlier studies showed that the presence of thick fat is associated with attenuated EGM voltages.[29] Although these observations are based on

bipolar EGMs and we did not experience any large effects of visually present epicardial fat, we cannot ascertain that the presence of epicardial fat has influenced our results.

Whether general anesthesia and intra-operative drugs influence conduction is yet to be investigated; however, a standard anesthetic protocol was used for all patients and SR was confirmed during all mapping procedures. Possible effects of anesthesia would therefore be equally dispersed among the patient population. In addition, high-resolution mapping of the interatrial septum could not be performed with our closed beating heart approach.

Conclusion

Unipolar voltage mapping at high resolution scale in patients with MVD, demonstrated marked inter-individual and regional variation with advanced atrial remodeling. Despite highly individualized patterns, even in SR, potential voltages at BB were lower in MVD patients with PAF compared to those without AF. Although there were no predilection sites for low voltages to occur, low-voltage areas were even present in MVD patients without a history of AF. In addition, an increased number of low-voltage potentials was found at BB in MVD patients with PAF. Both considerable intra- and inter-individual variation in potential voltages were found in our study population, which underlines the importance of an individualized electrical signal profile which can be used to characterize complex conduction disorders and to develop patient-tailored diagnoses and therapy.

References

1. Bazan V, Frankel DS, Santangeli P, Garcia FC, Tschabrunn CM, Marchlinski FE. Three-dimensional myocardial scar characterization from the endocardium: Usefulness of endocardial unipolar electroanatomic mapping. J Cardiovasc Electrophysiol. 2019;30:427-437.
2. Yagishita A, Gimbel JR, S DEO, Manyam H, Sparano D, Cakulev I, Mackall J, Arruda M. Long-Term Outcome of Left Atrial Voltage-Guided Substrate Ablation During Atrial Fibrillation: A Novel Adjunctive Ablation Strategy. J Cardiovasc Electrophysiol. 2017;28:147-155.
3. Rolf S, Kircher S, Arya A, Eitel C, Sommer P, Richter S, Gaspar T, Bollmann A, Altmann D, Piedra C, et al. Tailored atrial substrate modification based on low-voltage areas in catheter ablation of atrial fibrillation. Circ Arrhythm Electrophysiol. 2014;7:825-833.
4. Kottkamp H, Bender R, Berg J. Catheter ablation of atrial fibrillation: how to modify the substrate? J Am Coll Cardiol. 2015;65:196-206.
5. Sim I, Bishop M, O'Neill M, Williams SE. Left atrial voltage mapping: defining and targeting the atrial fibrillation substrate. J Interv Card Electrophysiol. 2019.
6. Venlet J, Piers SRD, Kapel GFL, de Riva M, Pauli PFG, van der Geest RJ, Zeppenfeld K. Unipolar Endocardial Voltage Mapping in the Right Ventricle: Optimal Cutoff Values Correcting for Computed Tomography-Derived Epicardial Fat Thickness and Their Clinical Value for Substrate Delineation. Circ Arrhythm Electrophysiol. 2017;10.
7. Kogawa R, Okumura Y, Watanabe I, Nagashima K, Takahashi K, Iso K, Watanabe R, Arai M, Kurokawa S, Ohkubo K, et al. Left atrial remodeling: Regional differences between paroxysmal and persistent atrial fibrillation. J Arrhythm. 2017;33:483-487.
8. Marcus GM, Yang Y, Varosy PD, Ordovas K, Tseng ZH, Badhwar N, Lee BK, Lee RJ, Scheinman MM, Olgin JE. Regional left atrial voltage in patients with atrial fibrillation. Heart Rhythm. 2007;4:138-144.
9. van der Does L, Knops P, Teuwen CP, Serban C, Starreveld R, Lanters EAH, Mouws E, Kik C, Bogers A, de Groot NMS. Unipolar atrial electrogram morphology from an epicardial and endocardial perspective. Heart Rhythm. 2018;15:879-887.
10. Lanters EA, van Marion DM, Kik C, Steen H, Bogers AJ, Allessie MA, Brundel BJ, de Groot NM. HALT & REVERSE: Hsf1 activators lower cardiomyocyt damage; towards a novel approach to REVERSE atrial fibrillation. J Transl Med. 2015;13:347.
11. van der Does LJ, Yaksh A, Kik C, Knops P, Lanters EA, Teuwen CP, Oei FB, van de Woestijne PC, Bekkers JA, Bogers AJ, et al. QUest for the Arrhythmogenic Substrate of Atrial fibRillation in Patients Undergoing Cardiac Surgery (QUASAR Study): Rationale and Design. J Cardiovasc Transl Res. 2016;9:194-201.
12. Blauer JJ, Swenson D, Higuchi K, Plank G, Ranjan R, Marrouche N, Macleod RS. Sensitivity and specificity of substrate mapping: an in silico framework for the evaluation of electroanatomical substrate mapping strategies. J Cardiovasc Electrophysiol. 2014;25:774-780.
13. Kovoor P, Daly M, Pouliopoulos J, Dewsnap MB, Eipper V, Ross DL. Effect of inter-electrode distance on bipolar intramural radiofrequency ablation. Pacing Clin Electrophysiol. 2005;28:514-520.
14. Spach MS, Miller WT, 3rd, Miller-Jones E, Warren RB, Barr RC. Extracellular potentials related to intracellular action potentials during impulse conduction in anisotropic canine cardiac muscle. Circ Res. 1979;45:188-204.
15. Chinyere IR, Hutchinson M, Moukabary T, Lancaster J, Goldman S, Juneman E. Monophasic action potential amplitude for substrate mapping. Am J Physiol Heart Circ Physiol. 2019;317:H667-H673.
16. Nademanee K, McKenzie J, Kosar E, Schwab M, Sunsaneewitayakul B, Vasavakul T, Khunnawat C, Ngarmukos T. A new approach for catheter ablation of atrial fibrillation: mapping of the electrophysiologic substrate. J Am Coll Cardiol. 2004;43:2044-2053.
17. Josephson ME, Anter E. Substrate Mapping for Ventricular Tachycardia: Assumptions and Misconceptions. JACC Clin Electrophysiol. 2015;1:341-352.
18. Konings KT, Smeets JL, Penn OC, Wellens HJ, Allessie MA. Configuration of unipolar atrial electrograms during electrically induced atrial fibrillation in humans. Circulation. 1997;95:1231-1241.
19. van Schie MS, Starreveld R, Roos-Serote MC, Taverne Y, van Schaagen FRN, Bogers A, de Groot NMS. Classification of sinus rhythm single potential morphology in patients with mitral valve disease. Europace. 2020;22:1509-1519.
20. Prabhu S, Voskoboinik A, McLellan AJA, Peck KY, Pathik B, Nalliah CJ, Wong GR, Azzopardi SM, Lee G, Mariani J, et al. A comparison of the electrophysiologic and electroanatomic characteristics between the right and left atrium in persistent atrial fibrillation: Is the right atrium a window into the left? J Cardiovasc Electrophysiol. 2017;28:1109-1116.
21. Anne W, Willems R, Roskams T, Sergeant P, Herijgers P, Holemans P, Ector H, Heidbuchel H. Matrix metalloproteinases and atrial remodeling in patients with mitral valve disease and atrial fibrillation. Cardiovasc Res. 2005;67:655-666.
22. Castonguay MC, Wang Y, Gerhart JL, Miller DV, Stulak JM, Edwards WD, Maleszewski JJ. Surgical pathology of atrial appendages removed during the cox-maze procedure: a review of 86 cases (2004 to 2005) with implications for prognosis. Am J Surg Pathol. 2013;37:890-897.
23. John B, Stiles MK, Kuklik P, Chandy ST, Young GD, Mackenzie L, Szumowski L, Joseph G, Jose J, Worthley SG, et al. Electrical remodelling of the left and right atria due to rheumatic mitral stenosis. Eur Heart J. 2008;29:2234-2243.
24. Corradi D, Callegari S, Benussi S, Maestri R, Pastori P, Nascimbene S, Bosio S, Dorigo E, Grassani C, Rusconi R, et al. Myocyte changes and their left atrial distribution in patients with chronic atrial fibrillation related to mitral valve disease. Hum Pathol. 2005;36:1080-1089.
25. Kim HJ, Cho GY, Kim YJ, Kim HK, Lee SP, Kim HL, Park JJ, Yoon YE, Zo JH, Sohn DW. Development of atrial fibrillation in patients with rheumatic mitral valve disease in sinus rhythm. Int J Cardiovasc Imaging. 2015;31:735-742.
26. Boldt A, Wetzel U, Lauschke J, Weigl J, Gummert J, Hindricks G, Kottkamp H, Dhein S. Fibrosis in left atrial tissue

4

of patients with atrial fibrillation with and without underlying mitral valve disease. Heart. 2004;90:400-405.

27. van der Does L, Lanters EAH, Teuwen CP, Mouws E, Yaksh A, Knops P, Kik C, Bogers A, de Groot NMS. The Effects of Valvular Heart Disease on Atrial Conduction During Sinus Rhythm. J Cardiovasc Transl Res. 2020;13:632-639.

28. Mouws E, Lanters EAH, Teuwen CP, van der Does L, Kik C, Knops P, Yaksh A, Bekkers JA, Bogers A, de Groot NMS. Impact of Ischemic and Valvular Heart Disease on Atrial Excitation:A High-Resolution Epicardial Mapping Study. J Am Heart Assoc. 2018;7.

29. Saba MM, Akella J, Gammie J, Poston R, Johnson A, Hood RE, Dickfeld TM, Shorofsky SR. The influence of fat thickness on the human epicardial bipolar electrogram characteristics: measurements on patients undergoing open-heart surgery. Europace. 2009;11:949-953.

4
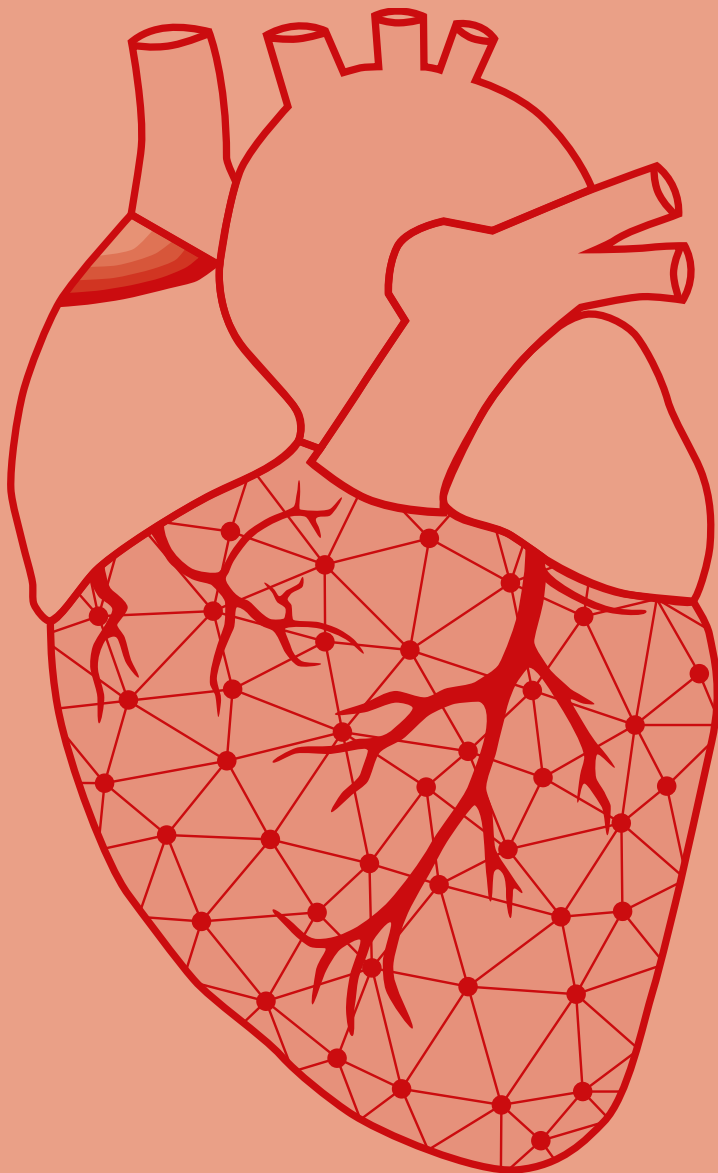
Chapter 5

Classification of sinus rhythm single potential morphology in patients with mitral valve disease

Mathijs S. van Schie

Roeliene Starreveld

Maarten C. Roos-Serote

Yannick J.H.J. Taverne

Frank R.N. van Schaagen

Ad J.J.C. Bogers

Natasja M.S. de Groot

Abstract

Aims: The morphology of unipolar single potentials (SPs) contains information on intra-atrial conduction disorders and possibly the substrate underlying atrial fibrillation (AF). This study examined the impact of AF episodes on features of SP morphology during sinus rhythm (SR) in patients with mitral valve disease.

Methods: Intra-operative epicardial mapping (interelectrode distance 2 mm) of the right and left atrium (RA, LA), Bachmann's bundle (BB) and pulmonary vein area (PVA) was performed in 67 patients (27 male, 67±11 years) with or without a history of paroxysmal AF (PAF). Unipolar SPs were classified according to their differences in relative R- and S-wave amplitude ratios.

Results: A clear predominance of S-waves was observed at BB and the RA in both the no AF and PAF groups (BB 88.8% vs. 85.9%, RA: 92.1% vs. 85.1%, respectively). Potential voltages at the RA, BB and PVA were significantly lower in the PAF group (p<0.001 for each) and were mainly determined by the size of the S-waves amplitudes. The largest difference in S-wave amplitudes was found at BB; the S-wave amplitude was lower in the PAF group (4.08 [2.45–6.13] mV vs. 2.94 [1.40–4.75] mV; p<0.001). In addition, conduction velocity (CV) at BB was lower as well (0.97 [0.70–1.21] m/s vs. 0.89 [0.62–1.16] m/s, p<0.001).

Conclusions: Although excitation of the atria during SR is heterogeneously disrupted, a history of AF is characterized by decreased SP amplitudes at BB due to loss of S-wave amplitudes and decreased CV. This suggests that SP morphology could provide additional information on wavefront propagation.

Journal site

Introduction

Analysis of atrial electrical activity plays an important role in revealing the underlying electrophysiological mechanisms responsible for the initiation and perpetuation of atrial fibrillation (AF). In daily clinical practice, electro-anatomical mapping is performed via endovascular catheters at the endocardial side, presenting a bipolar electrogram (EGM).[1,2] The bipolar EGM is commonly used as it contains local information from the area of myocardium at the catheter tip between two electrodes. However, unipolar EGMs have the benefit over bipolar EGMs that their morphology carries additional information about the progression of the wavefront and remote activations, which are independent of the electrode orientation and wavefront direction.[2] Cardiac electrophysiologists often rely on low-voltage areas which are suggestive of the presence of atrial substrate.[3] However, low-voltage potentials are highly determined by their morphology, but these are currently not fully classified in clinical practice. Therefore, unipolar EGMs can provide additional helpful information in electrophysiological studies and ablation procedures, and are therefore increasingly used in newly developed mapping systems.

The morphology of atrial EGMs, represented by the relative positive (R-wave) and negative (S-wave) components of a unipolar EGM, contains information on intra-atrial conduction and hence conduction disorders giving rise to development of AF.[2,4,5] Prior studies have indeed demonstrated that areas of abnormal EGM morphologies of single potentials (SPs) are indicators of conduction abnormalities underlying AF.[6-8] Therefore, creation of an electrical signal profile obtained from high-resolution mapping data of the entire atria during AF -a so-called AF Fingerprint- may be used to determine the severity and extensiveness of local conduction disorders. The first step towards development of such an 'AF Fingerprint', is understanding variation in EGM morphologies of SPs during sinus rhythm (SR). The goal of this study is therefore to examine the impact of AF episodes on features of SP morphology at a high-resolution scale during SR in patients with mitral valve disease (MVD).

Methods

Study population

The study population consisted of 67 adult patients undergoing mitral valve surgery or a combination of mitral valve and coronary bypass surgery in the Erasmus Medical Center Rotterdam. This study was approved by the institutional medical ethical committee (MEC2010-054/MEC2014-393).[9,10] Written informed consent was obtained from all patients. Patient characteristics (e.g., age, medical history, cardiovascular risk factors, time in AF) were obtained from the patient's medical record. The study population was classified into patients without a history of AF (no AF group) and with a history of paroxysmal AF (PAF group).

Mapping procedure

Epicardial high-resolution mapping was performed prior to commencement of extra-corporal circulation, as previously described in detail.[11-13] A temporal bipolar epicardial pacemaker wire attached to the RA free wall served as a reference electrode. A steel wire fixed to subcutaneous tissue of the thoracic cavity was used as an indifferent electrode. Epicardial mapping was performed with a 128-electrode array or 192-electrode array (electrode diameter respectively 0.65 mm or 0.45 mm, interelectrode distances 2.0 mm). Mapping was conducted by shifting the electrode array along imaginary lines with a fixed anatomic orientation, following a predefined mapping scheme. The procedure covers the entire epicardial surface of the right atrium (RA), Bachmann's bundle (BB), pulmonary vein
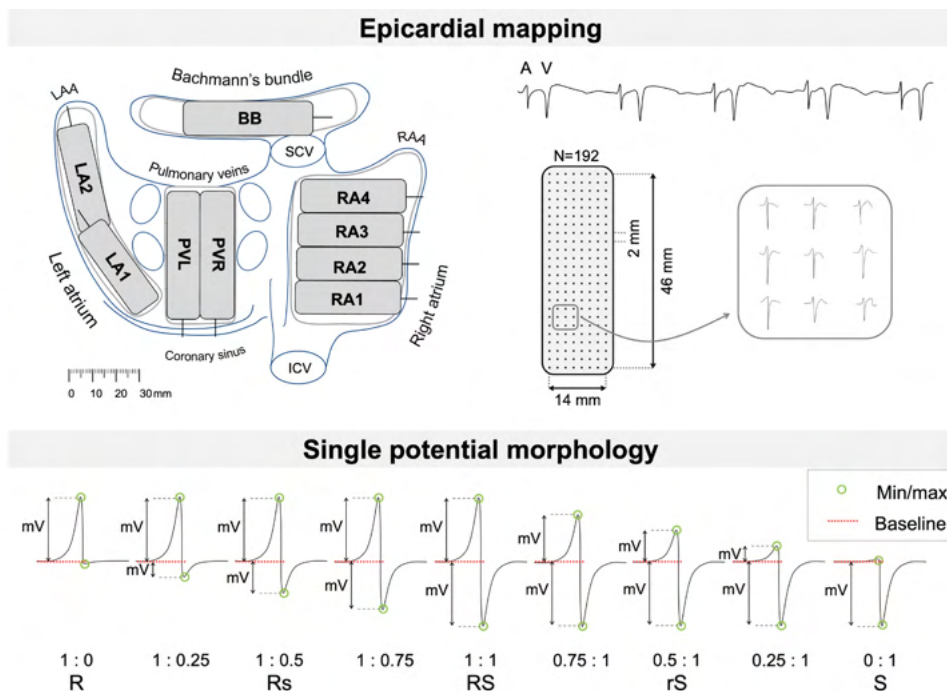
Figure 1 – Epicardial high-resolution mapping. *Upper left panel*: projection of the 192-unipolar electrode array on a schematic posterior view of the atria. *Upper right panel*: epicardial, unipolar potentials recorded during 5 seconds of SR containing atrial deflections (A) and far-field ventricular signals (V). Typical examples of 9 EGMs obtained from the RA are shown outside the mapping. *Lower panel*: EGMs with variable R/S ratios calculated by dividing the R-wave amplitude by the S-wave amplitude. **ICV** = inferior caval vein; **SCV** = superior caval vein; **LAA** = left atrial appendage; **RAA** = right atrial appendage; **RA** = right atrium; **BB** = Bachmann's bundle; **PV** = pulmonary veins; **LA** = left atrium.

area (PVA) and left atrium (LA), as illustrated in the upper panel of left panel of *Figure 1*. Omission of areas was avoided at the expense of possible small overlap between adjacent mapping sites. The RA was mapped from the cavotricuspid isthmus, shifting perpendicular to the caval veins towards the RA appendage. The PVA was mapped from the sinus transversus fold along the borders of the right and left pulmonary veins (PVR and PVL) down towards the atrioventricular groove. The left atrioventricular groove (LAVG) was mapped from the lower border of the left inferior pulmonary vein towards the LA appendage. BB was mapped from the tip of the LA appendage across the roof of the LA, behind the aorta towards the superior cavo-atrial junction.

Five seconds of SR were recorded from every mapping site, including a surface ECG lead, a calibration signal of 2 mV and 1000 ms, a bipolar reference EGM and all unipolar epicardial EGMs. In patients who presented in AF, SR mapping was performed after electrical cardioversion. Data was stored on a hard disk after amplification (gain 1000), filtering (bandwidth 0.5–400 Hz), sampling (1 kHz) and analogue-to-digital conversion (16 bits).

Data analysis

Unipolar EGM morphology was semi-automatically analyzed in custom-made software using Python 3. EGMs with injury potentials, recording sites with ≥25% excluded or missing EGMs and premature atrial complexes or aberrant beats were excluded from analysis. Atrial deflections were marked when the negative slope of a deflection was ≥10% of the steepest slope in the EGM and the amplitude of the deflection was at least two times the signal-to-

Table 1 – Patient characteristics (N=67).

	No AF	PAF	*p*-value
Patients	44 (66)	23 (34)	-
Male	17 (39)	10 (43)	0.903
Age (y)	65±12	73±6	0.003
Cardiovascular risk factors			
• BMI (kg/m²)	24.5 [22.1–26.8]	25.3 [22.2–31.9]	0.281
- Underweight (<18.5)	2 (5)	0 (0)	0.778
- Normal weight (18.5-25)	22 (50)	11 (48)	0.866
- Overweight (25-30)	15 (34)	5 (22)	0.443
- Obese (≥30)	5 (11)	7 (30)	0.110
• Hypertension	15 (34)	12 (52)	0.242
• Dyslipidemia	14 (32)	2 (9)	0.071
• Diabetes mellitus	7 (16)	3 (13)	0.755
Left atrial dilatation >45 mm	28 (64)	16 (70)	0.830
Left ventricular dysfunction	15 (34)	6 (26)	0.694
Mitral stenosis	3 (7)	1 (4)	0.685
Severe mitral insufficiency	31 (70)	16 (70)	0.940
Coronary artery disease	20 (45)	6 (26)	0.200
Antiarrhythmic agents			
• Class I	1 (2)	0 (0)	0.466
• Class II	23 (52)	11 (48)	0.930
• Class III	0 (0)	7 (30)	<0.001
• Class IV	1 (2)	2 (9)	0.559

Values are presented as mean ± standard deviation, median [interquartile ranges] or as N (%). **(P)AF** = (paroxysmal) atrial fibrillation; **BMI** = body mass index.

noise ratio of the EGM. The steepest negative deflection of a potential was marked as the local activation time (LAT). The minimal time between two successive deflections ('latency') was set to 2 ms. All EGM markings were manually checked and corrected in case of markings on electrical artefacts evaluated by a consensus of two investigators. Potentials were classified as single potential (SP, one deflection) or fractionated potential (FP, ≥2 deflections). SPs are characterized by a rapid negative deflection preceded by a positive R-wave and returning to the baseline (S-wave). As demonstrated in the lower panel of *Figure 1*, SPs were classified according to their differences in relative R- and S-wave amplitude and scaled from -1 (R-wave) to 1 (S-wave).

$$RS = \begin{cases} 1 - RS(n) & for\ RS(n) \leq 1 \\ \dfrac{1}{RS(n)} - 1 & for\ RS(n) > 1 \end{cases}$$

Furthermore, SPs were analyzed for peak-to-peak voltage (amplitude), relative R- and S-wave amplitudes and local wavefront conduction velocity (CV). Local CV was computed as an average of velocity estimations between neighboring electrodes (longitudinal, transversal and diagonal) based on a techniques derived from a finite differences method developed and described by Salama et al.[14]

Statistical analysis

All data were tested for normality. Normally distributed data are expressed as mean ± standard deviation and analyzed with a paired *t*-test or one-way ANOVA. Skewed data are expressed as median [25th–75th percentile] and analyzed with a Kruskal-Wallis test or Mann-Whitney U test. Categorical data are expressed as numbers and percentages and analyzed with a χ^2 or Fisher exact test when appropriate. Distribution data was analyzed with a two-

5

Table 2 – Mapping data characteristics (N=523,019).

	No AF	PAF	*p*-value
Right atrium			
Single potentials	179,700 (85)	77,060 (85)	
Amplitude (mV)	5.21 [3.03–7.67]	5.10 [2.89–7.55]	<0.001
R-wave (mV)	1.65 [0.74–2.79]	1.69 [0.79–2.81]	<0.001
S-wave (mV)	3.48 [2.07–5.08]	3.30 [1.86–4.97]	<0.001
R/S ratio	0.52 [0.28–0.71]	0.46 [0.22–0.67]	<0.001
Conduction velocity (m/s)	0.93 [0.71–1.15]	0.94 [0.72–1.17]	<0.001
Bachmann's bundle			
Single potentials	34,069 (76)	16,260 (73)	
Amplitude (mV)	5.71 [3.40–8.87]	4.09 [2.18–6.70]	<0.001
R-wave (mV)	1.57 [0.74–3.00]	1.11 [0.49–2.21]	<0.001
S-wave (mV)	4.08 [2.45–6.13]	2.94 [1.40–4.75]	<0.001
R/S ratio	0.57 [0.35–0.76]	0.58 [0.29–0.77]	<0.001
Conduction velocity (m/s)	0.97 [0.70–1.21]	0.89 [0.62–1.16]	<0.001
Pulmonary vein area			
Single potentials	64,254 (84)	35,305 (83)	
Amplitude (mV)	4.72 [2.19–8.24]	4.74 [2.47–7.63]	0.067
R-wave (mV)	2.44 [1.13–4.39]	2.24 [1.21–3.94]	<0.001
S-wave (mV)	1.91 [0.83–3.89]	2.12 [0.93–3.86]	<0.001
R/S ratio	-0.16 [-0.52–0.30]	-0.03 [-0.46–0.38]	<0.001
Conduction velocity (m/s)	0.91 [0.54–1.23]	0.94 [0.60–1.23]	<0.001
Left atrium			
Single potentials	77,651 (87)	38,720 (77)	
Amplitude (mV)	4.48 [2.03–8.19]	4.36 [1.95–8.38]	<0.001
R-wave (mV)	1.94 [0.94–3.72]	1.98 [0.84–4.10]	0.177
S-wave (mV)	2.28 [0.92–4.12]	2.13 [0.94–4.22]	<0.001
R/S ratio	0.14 [-0.33–0.45]	0.12 [-0.29–0.44]	0.156
Conduction velocity (m/s)	0.98 [0.66–1.25]	1.00 [0.70–1.25]	<0.001

Values are presented as median [interquartile ranges] or as N (%). **(P)AF** = (paroxysmal) atrial fibrillation.

sample Kolmogorov-Smirnov test. A *p*-value <0.05 was considered statistically significant. A Bonferroni correction was applied for comparison of the four atrial regions; a *p*-value of <0.0083 (0.05/6) was considered statistically significant.

Results

Study population

Clinical characteristics of the study population, including 44 patients in the 'no AF' group and 23 patients in the 'PAF' group are described in *Table 1*. These groups differed in age (no AF: 65±13 years, PAF: 73±6 years, p=0.003). Patients had either ischemic and MVD (no AF: 20 [45%], PAF: 6 [26%]) or only MVD. LA dilation was present in 28 patients without AF (64%) and in 16 patients with PAF (70%). Most patients in both groups had normal left ventricular function (no AF: 29 [66%], PAF: 17 [74%]). 30% of the patients with PAF used class III antiarrhythmic drugs (no AF: 0 vs. PAF: 7 (30%), p<0.001).

Mapping data

As demonstrated in *Table 2*, a total of 523,019 SPs were analyzed out of 852 SR recordings of 5-seconds duration (no AF: RA: 179,700; BB: 34,069; PVA: 77,651; LA: 64,254; PAF: RA: 77,060; BB: 16,260; PVA: 38,720; LA: 35,305). Median unipolar SP amplitude in the PAF group was lower than in the no AF group (4.78 [2.14–7.21] mV vs. 5.05 [2.48–7.64] mV respectively (p<0.001)).

In both the no AF and PAF group, SP amplitudes differed between the atrial regions (no AF:
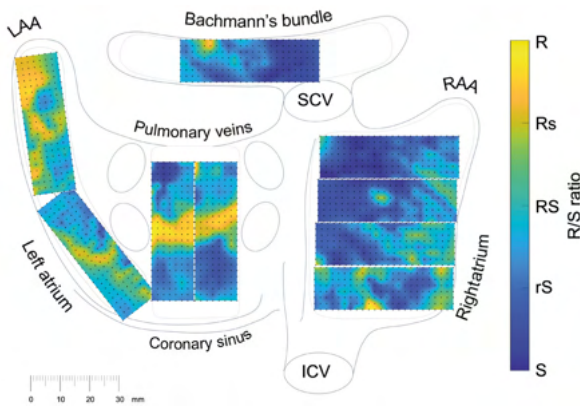
Figure 2 – Typical example of the color-coded spatial distribution of the R/S ratios during one sinus beat in a patient without AF. The color scale of the R/S ratios ranges from S-waves (blue), via biphasic RS-waves (green) to R-waves (yellow). **ICV** = inferior caval vein; **SCV** = superior caval vein; **LAA** = left atrial appendage; **RAA** = right atrial appendage.

5

RA: 5.21 [3.03–7.67] mV, BB: 5.71 [3.40–8.87] mV, PVA: 4.48 [2.03–8.19] mV, LA: 4.72 [2.19–8.24] mV (p<0.001 for all comparisons); PAF group: RA: 5.10 [2.89–7.55] mV, BB: 4.09 [2.18–6.70] mV, PVA: 4.36 [1.95–8.38] mV, LA: 4.74 [2.47–7.63] mV (p<0.001 for all comparisons)). Furthermore, SP amplitudes of the RA, BB and PVA were lower in the PAF group compared to the no AF group (RA: 5.21 [3.03–7.67] mV vs. 5.10 [2.89–7.55] mV (p<0.001), BB: 5.71 [3.40–8.87] mV vs. 4.09 [2.18–6.70] mV (p<0.001), PVA: 4.48 [2.03–8.19] mV vs. 4.36 [1.95–8.38] mV (p<0.001)).

Focusing only on the magnitude of the R- and S-wave, the largest R-wave amplitude was found in the LA in both the no AF group (2.44 [1.13–4.39] mV) and PAF group (2.24 [1.21–3.94] mV), whereas the largest S-wave amplitude was found in BB in the no AF group (4.08 [2.45–6.13] mV) and in the RA in the PAF group (3.30 [1.86–4.97] mV). In general, the amplitude of the atrial potential was mainly determined by the S-wave amplitude.

The largest difference in S-wave amplitudes between both groups was found at BB; the S-wave median amplitude was higher in the no AF group (4.08 [2.45–6.13] mV) than in the PAF group (2.94 [1.40–4.75] mV; p<0.001).

The CV differed between atrial regions in both the no AF and PAF group (no AF: RA: 0.93 [0.71–1.15] m/s, BB: 0.97 [0.70–1.21] m/s, PVA: 0.98 [0.66–1.25] m/s, LA: 0.91 [0.54–1.23] m/s (p<0.001 for all comparisons); PAF group: RA: 0.94 [0.72–1.17] m/s, BB: 0.89 [0.62–1.16] m/s, PVA: 1.00 [0.70–1.25] m/s, LA: 0.94 [0.60–1.24] m/s (p<0.001 for all comparisons)). In the PAF group, CVs at BB were lower compared to the no AF group (0.97 [0.70–1.21] m/s vs. 0.89 [0.62–1.16] m/s, p<0.001).

Regional differences in R/S ratio

Figure 2 shows a typical example of the color-coded spatial distribution of the R/S ratios during one SR beat in a patient without AF. This map shows a wide variation of R/S ratios throughout the atria. The majority of the SPs recorded in the superior part of RA consisted of monophasic S-waves, compared to rS-waves and biphasic RS-waves in the mid and inferior part of the RA. A clear R-wave predominance was found in between the pulmonary veins, whereas biphasic RS-waves and rS-waves were recorded from the superior and inferior sites of the PVA. The LA appendage revealed a R-wave predominance as well, whereas S-wave predominance was mainly found in the RA and BB.

Figure 3 shows the regional differences in the distribution of the R/S ratios in the RA, BB, PVA and LA in the no AF group (upper panels) and PAF group (lower panels). The relative
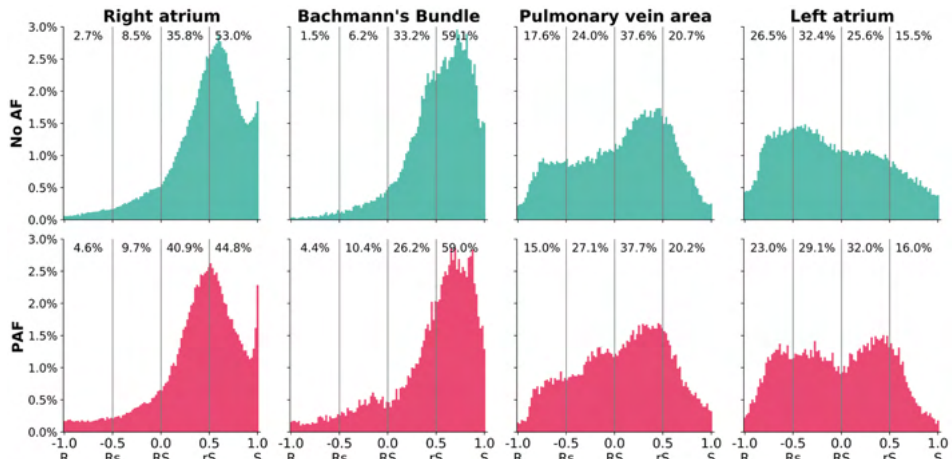
Figure 3 – Relative frequency histograms of all R/S ratios. The R/S ratios of unipolar SPs during SR in patients without AF (turquoise) and patients with PAF (red), recorded from BB (n = 34,069 vs. n = 16,260), LA (n = 64,254 vs. n = 35,305), PVA (n = 77,651 vs. n = 38,720) and RA (n = 179,700 vs. n = 77,060). The histograms are divided into four equal quartiles; for each quartile the relative number of potentials is given on top of the plots. **(P)AF** = (paroxysmal) atrial fibrillation.
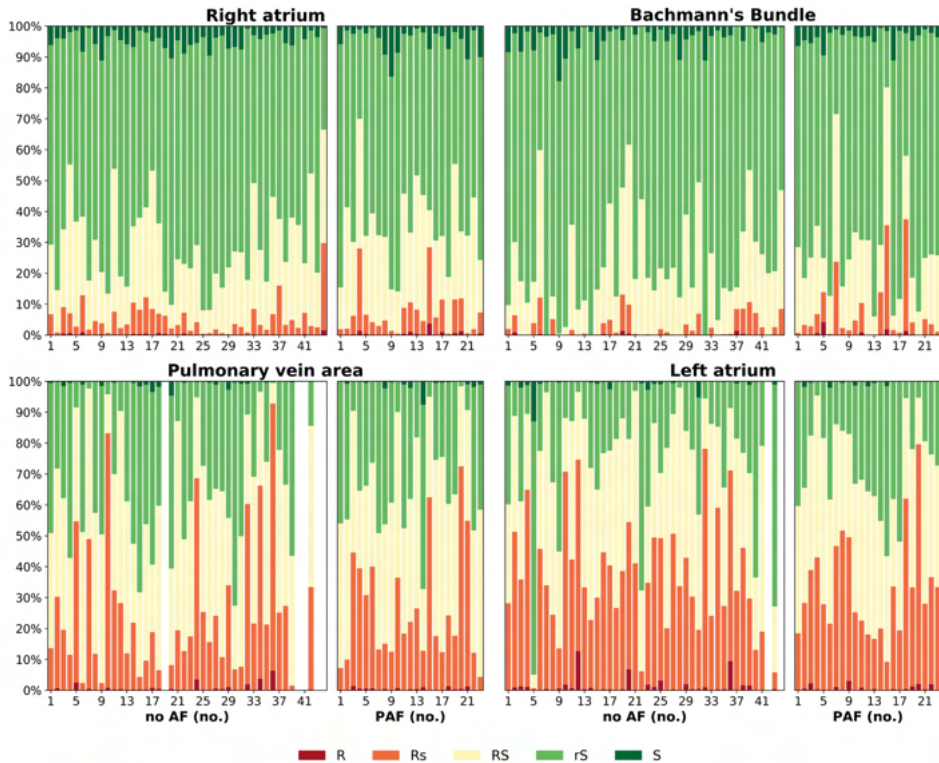
Figure 4 – R/S ratio distribution per patient. Stacked bar plots of the R/S distributions depicted for each patient separately in the RA, BB, PVA and LA. **(P)AF** = (paroxysmal) atrial fibrillation.

5
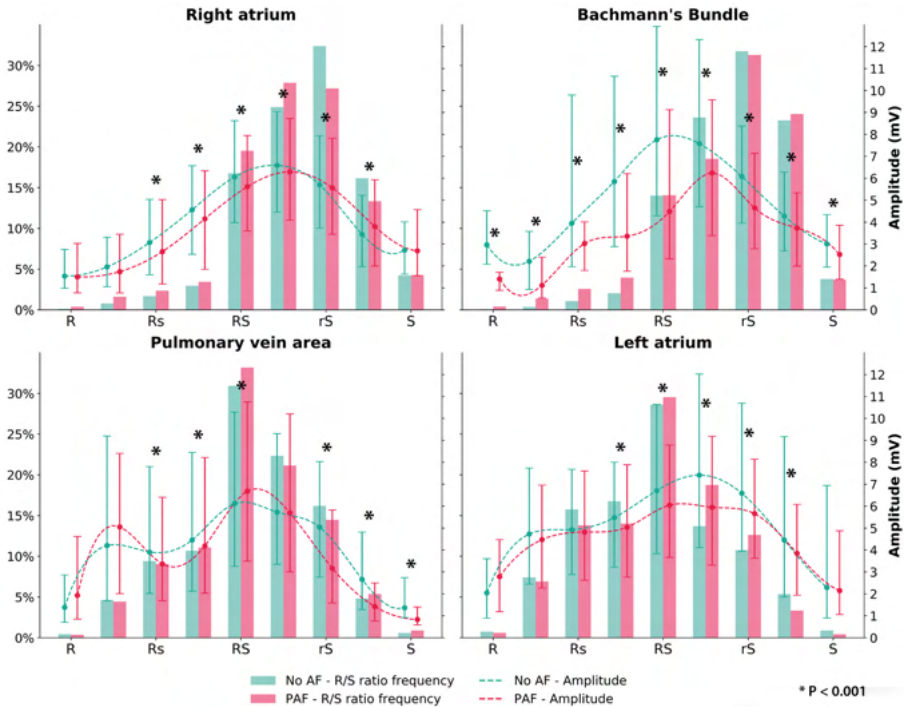
Figure 5 – Relative frequency histograms of the R/S ratios and amplitudes of unipolar SPs during SR in patients without AF (turquoise) and with PAF (red). The bars represent the relative frequency of the R/S ratios and the dotted line the median amplitudes with interquartile ranges. The asterisk indicates a significant difference in median amplitudes between the patients without AF and patients with PAF (p<0.001). **(P)AF** = (paroxysmal) atrial fibrillation.

frequency of the R/S ratios are ranked from -1 (R-waves) to 1 (S-waves) and divided into four equal quartiles. For each quartile the relative number of potentials is given on top of the plots. The SPs revealed a wide variation of R- and S-wave amplitude ratios. However, a clear predominance of S-waves was observed in the BB and RA in both the no AF group (88.8% and 92.1% respectively) as PAF group (85.9% and 85.1% respectively). Differences between the no AF and PAF groups were found at the RA, BB and LA (p=0.021, p=0.003 and p=0.013). In the PAF group, there was a larger number of dominant R-waves in both the RA and BB and a higher number of rS-waves in the LA.

Individual differences in R/S ratios

Figure 4 demonstrates interindividual differences in R/S ratios. In all patients there was a clear S-wave predominance in the RA and BB. In contrast, in the PVA and LA there was less S-wave predominance and a wider variation in SP morphology.

Figure 5 demonstrates all R/S ratios (subdivided into nine categories) with their corresponding amplitudes. In both the no AF and PAF group, the largest SP amplitudes were observed in the range of biphasic RS- to rS-waves (no AF: RA: 6.39 [4.25–8.89] mV, BB: 7.61 [4.51–12.55] mV, PVA: 5.96 [3.30–9.86] mV, LA: 6.77 [3.78–10.95] mV; PAF: RA: 5.96 [3.83–8.34] mV, BB: 5.45 [2.78–9.28] mV, PVA: 6.10 [3.21–10.44] mV, LA: 6.02 [3.53–8.90] mV). In the PAF group, SP amplitudes of all different R/S ratios were smaller in BB compared to the no AF group (p<0.001). At the other atrial regions, there were no consistent significant differences in amplitudes of the various R/S ratios. The majority of the monophasic S-wave potentials were found in the RA
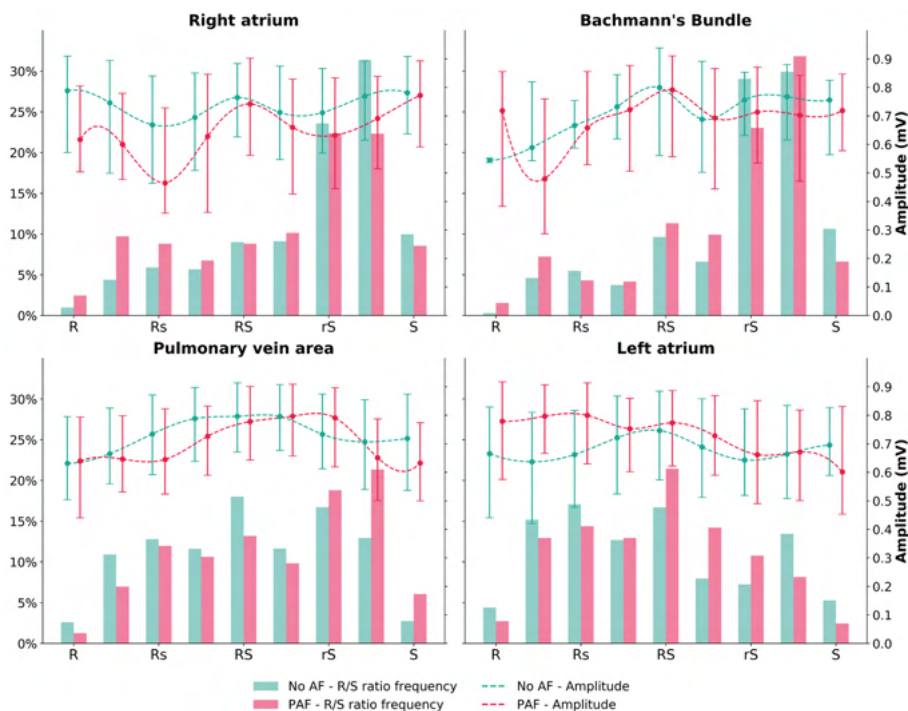
Figure 6 – Relative frequency histograms of the R/S ratios and amplitudes of unipolar SPs in low-voltage areas during SR in patients without AF (turquoise) and with PAF (red). The bars represent the relative frequency of the R/S ratios and the dotted line the median amplitudes with interquartile ranges. **(P)AF** = (paroxysmal) atrial fibrillation.

in both groups (4.2% and 4.3% respectively). A high number of S-wave potentials (3.7% for both groups) were found in BB as well, whereas these potentials were rarely present in the PVA and LA.

R/S ratio in low-voltage areas

The P_5 of all measured SPs was 1.0 mV, which was used as a cut-off value for low voltages. *Figure 6* illustrates the regional distribution of the R/S ratios of low-voltage potentials. Although a wide variation of R/S ratios was observed, an S-wave predominance was found in the RA and BB in both groups. Compared to the no AF group, the relative number of dominant R-waves in low-voltage areas in the PAF group was larger in the RA and BB, whereas a larger number of dominant S-waves was observed in the PVA.

Discussion

High-resolution mapping of the atria in patients with MVD demonstrated a wide variation of unipolar SP morphology throughout the atria, resulting in specific regional differences in SP amplitude and R/S ratios. Amplitudes were mainly determined by the S-wave amplitude, which resulted in a high number of predominant S-wave potentials with large amplitudes in the RA and BB, whereas a larger range of SP amplitudes was found in the LA and PVA together with a high variation in R/S ratios. Compared to the no AF group, lower SP amplitudes and S-wave amplitudes were found in patients with PAF, along with more R-wave predominance in the RA, BB and PVA.

5

Genesis of unipolar potential morphologies

EGM morphology is often used for the identification of structural or electrical remodeled areas with arrhythmogenic properties. In most settings, electro-anatomical mapping is performed via endovascular catheters at the endocardial side, recording EGMs which are the product of a voltage difference between recording electrodes (bipolar recordings).[1,15] In case of unipolar EGMs, the signal reflects the cardiac electrical activity of the tissue surrounding the recording electrode which decreases with distance. It is obtained by an exploring electrode positioned in the heart and an indifferent electrode located at an infinite distance.[2,16] It is for these reasons that there is an increase in mapping systems using unipolar EGMs.

The morphology of unipolar potentials can be regarded as the sum of instantaneous current dipoles of a wavefront, generating a positive deflection when the activation wavefront propagates towards the electrode and a steeply negative deflection as the wavefront reaches the electrode and propagates away, thereby generating a biphasic RS-wave.[2,5,17] When the electrode is located at a site of initial activation, depolarization produces a wavefront that propagates radially away from the electrode, thus generating a monophasic S-wave. In contrast, positive R-waves are characteristic of termination of the activation wavefront. Areas of fast conduction with conduction along the longitudinal axis of the fibers are characterized by large amplitude RS-waves, whereas in slow areas the potentials are of lower amplitude.[5] Abnormal myocardial substrate can be defined by substrate mapping by identifying areas of low voltage, as amplitude also depends on the volume of simultaneously activated cardiac tissue.[5,6] In addition, asymmetry of unipolar potentials has been proposed as a morphology parameter, determined by wavefront curvature, wavefront collisions, anisotropy and conduction heterogeneity.[18,19]

Regional differences in single potential morphology

In our study population, there were clear regional differences in potential morphology. During SR, the initial excitation site is located in the RA in which wavefronts are generated by cells in the sinoatrial (SA) node area. From there, a wavefront is propagated by the prominent muscle bundles contiguous with the SA node; i.e. the crista terminalis, Bachmann's bundle and the septo-pulmonary bundle, which contributes to fast electrical propagation and enables efficient electromechanical coupling of both atria during each normal sinus beat.[4,20] At sites of wavefront activation, monophasic S-waves were expected and were - indeed - mainly recorded in the RA in our study population. In addition, fast propagating wavefronts are characterized by EGMs with large amplitude, predominant S-waves, which evolve towards biphasic RS-waves when the wavefront propagates away from the excitation site. These types of potentials were indeed mainly found in the RA and BB.

Using diffusion tensor imaging of human hearts, Pashakhanloo et al.[21] have demonstrated that in some areas of the atrial wall, e.g., the crista terminalis and the antrum of the PVs, the uniform distribution of myocardial fibers is disrupted by multiple complex crossings of multiple fibers, which underlies non-uniform anisotropic propagation. Previous studies have demonstrated that there are changes in patients with MVD in the myocardial structure of the atria due to altered hemodynamic effects.[22-24] Structural remodeling affects intra-atrial conduction and thereby predisposes to development of atrial tachyarrhythmias. The higher incidence of AF in patients with MVD suggests the presence of a higher degree of atrial remodeling in these patients, characterized by LA enlargement, loss of myocardium and scarring.[25-27] The resulting anisotropic propagation causes local wavefront termination or collision, resulting in more R-wave predominance and monophasic R-waves, which were - indeed - mainly found in the LA and PVA.

In our study, we demonstrated inter-individual differences in R/S ratios in – especially – the LA and PVA areas. Anatomic studies of the fiber orientation using dissection, visual tracing or MR techniques demonstrated variations in the location and orientation of bundles between human hearts, in which mixed and oblique patterns of fibers were present in the roof of the atria encircling the pulmonary veins.[21,28] In addition, intra-operative epicardial mapping also demonstrated that atrial excitation during SR is affected by the underlying heart disease and AF, resulting in alternative routes for BB and PVA with high inter-individual variability.[29,30] Together with the patient specific impact of the presence of MVD, these differences might have resulted in the more prominent inter-individual R/S differences in these areas.

Several computer models of electrical propagation in the atria have been developed and showed mostly single biphasic potentials in the uniform atria, whereas dominant S-waves were more common in anisotropic tissue and dominant R-waves were found due to the multiple collisions.[19] Using such computer models it has been demonstrated that anisotropy has a greater impact on amplitude variation and asymmetry than the shape and curvature of the conducting wavefront. However, the models differ in the level of electrophysiological and anatomical details, such as fiber orientation, presence of the main muscle bundles, structural modifications and anisotropy, and mainly focus on arrhythmia simulations.[19,31-34] S-wave predominance has also been reported in the RA in patients during AF, but could not be strongly correlated to wavefront curvature or anisotropy.[35] A tilted transmural stance of the wavefront resulting in an epicardial lead with constant epicardial to endocardial activation was proposed as a theoretical explanation for S-wave predominance during AF, which would present with more R-wave predominance at the endocardium.[35] However, Van der Does et al.[36] reported that both epicardial and endocardial EGMs showed an S-wave predominance, and endocardial EGMs did not have higher R/S ratios than epicardial EGMs. Although these mapping studies were performed during SR, data clearly showed absence of an oblique transmurally propagating wave. In our study, we indeed demonstrated an S-wave predominance in the RA but not in the LA and PVA.

Influence of paroxysmal atrial fibrillation

In our study, SP morphology differences between patients without AF and with PAF were most prominent in the BB. Patients with PAF had lower amplitudes, more R-wave predominance and slower wavefront propagation. The lower amplitude was mainly determined by a decrease in S-wave amplitude, which is observed with reversible tissue injury and is associated with conduction block during ablative therapy.[18,37] Recent studies indeed found more conduction abnormalities in the BB during SR in patients with AF or patients who developed post-operative AF.[11,38] BB is by far the largest of the anatomic interatrial connections and probably accounts for the largest part of interatrial conduction. It is a highly organized bundle of muscular fibers arranged in parallel fashion, but due to its anisotropic features BB is more vulnerable to structural remodeling that can even be identified during SR. In addition, the muscular fibers of the BB are not enclosed by fibrous tissue and may therefore also be vulnerable to disruption by stretch due to the hemodynamic changes in the atria caused by MVD.[20,22,39] This could lead to slower wavefront propagation and slower CVs which were – indeed – found in patients with PAF. Structural changes of the atrial myocardium are more extensive in patients with PAF than in patients without AF, especially involving the BB.[40]

Clinical implications

Despite most of atrial mapping procedures are performed endocardially using bipolar EGMs, there is an increase in mapping systems using unipolar EGMs. Therefore, detailed knowledge

of unipolar EGM morphology becomes more important. In a prior study of Van der Does et al.[36], no differences were found between unipolar endo- and epicardial EGMs. This indicates that the observed change in R/S ratios and decrease of S-wave amplitudes will also be found at the endocardium.

In clinical practice, low-voltage areas are regarded as part of the arrhythmogenic substrate underlying AF. However, our data shows that the EGM voltage is mainly determined by the R/S ratio which differs per region. In addition, low peak-to-peak voltages do not automatically indicate 'diseased' tissue, but can also be explained by the potential morphology as R- and S-waves have a smaller amplitude compared to RS-waves. Therefore, using voltage mapping alone to guide ablative therapy might be misleading.

5

Study limitations

Whether general anesthesia and intra-operative drugs influence conduction is unknown; however, a standard anesthetic protocol was used for all patients and SR was confirmed during all mapping procedures. Therefore, possible effects of anesthesia would be equally dispersed among the patient population. High-resolution mapping of the interatrial septum could not be performed with our closed beating heart approach.

Several patients with history of AF used antiarrhythmic drugs class III. Amiodarone has class I antiarrhythmic properties via inhibition of sodium channels during phase 0 of the cardiac action potential which can slow intra-atrial conduction. Therefore, the use of amiodarone could have affected our results.

There was a difference in age between the no AF and PAF group. Therefore, the differences between both groups could be related to the impact of age. However, no correlation was found between any of signal profiles and age. Still, the possible effect could not be completely excluded, just as the effects of hypertension or obesity, although not significantly different between the groups.

Conclusion

A specific regional distribution of EGM morphology, involving R/S ratios, EGM voltage and R- and S-wave amplitudes exist during SR in patients with MVD. Although excitation of the atria during SR is heterogeneously disrupted in patients with MVD, the occurrence of AF in this patient group is characterized by decreased SP amplitudes at BB due to loss of S-wave amplitudes together with a decreased CV. Therefore, BB is an area that could especially be interesting for AF Fingerprinting. Our findings that variation in EGM morphologies in our population is considerable –particularly at the LA and PVA- and specific EGM morphologies at regions such as BB are related to AF suggest that the potential morphology could provide additional information on CV and wavefront propagation, and emphasizes the need for a diagnostic tool enabling identification of arrhythmogenic substrate in the individual patient.

References

1.   Koutalas E, Rolf S, Dinov B, Richter S, Arya A, Bollmann A, Hindricks G, Sommer P. Contemporary Mapping Techniques of Complex Cardiac Arrhythmias - Identifying and Modifying the Arrhythmogenic Substrate. Arrhythm Electrophysiol Rev. 2015;4:19-27.

2.   Stevenson WG, Soejima K. Recording techniques for clinical electrophysiology. J Cardiovasc Electrophysiol. 2005;16:1017-1022.

3.   Wong GR, Nalliah CJ, Lee G, Voskoboinik A, Prabhu S, Parameswaran R, Sugumar H, Anderson RD, McLellan A, Ling LH, et al. Dynamic Atrial Substrate During High-Density Mapping of Paroxysmal and Persistent AF: Implications for Substrate Ablation. JACC Clin Electrophysiol. 2019;5:1265-1277.

4.   Spach MS, King TD, Barr RC, Boaz DE, Morrow MN, Herman-Giddens S. Electrical potential distribution surrounding the atria during depolarization and repolarization in the dog. Circ Res. 1969;24:857-873.

5.   Spach MS, Miller WT, 3rd, Miller-Jones E, Warren RB, Barr RC. Extracellular potentials related to intracellular action potentials during impulse conduction in anisotropic canine cardiac muscle. Circ Res. 1979;45:188-204.

6.   de Groot NM, Schalij MJ, Zeppenfeld K, Blom NA, Van der Velde ET, Van der Wall EE. Voltage and activation mapping: how the recording technique affects the outcome of catheter ablation procedures in patients with congenital heart disease. Circulation. 2003;108:2099-2106.

7.   Otomo K, Uno K, Fujiwara H, Isobe M, Iesaka Y. Local unipolar and bipolar electrogram criteria for evaluating the transmurality of atrial ablation lesions at different catheter orientations relative to the endocardial surface. Heart Rhythm. 2010;7:1291-1300.

8.   Bortone A, Appetiti A, Bouzeman A, Maupas E, Ciobotaru V, Boulenc JM, Pujadas-Berthault P, Rioux P. Unipolar signal modification as a guide for lesion creation during radiofrequency application in the left atrium: prospective study in humans in the setting of paroxysmal atrial fibrillation catheter ablation. Circ Arrhythm Electrophysiol. 2013;6:1095-1102.

9.   Lanters EA, van Marion DM, Kik C, Steen H, Bogers AJ, Allessie MA, Brundel BJ, de Groot NM. HALT & REVERSE: Hsf1 activators lower cardiomyocyt damage; towards a novel approach to REVERSE atrial fibrillation. J Transl Med. 2015;13:347.

10. van der Does LJ, Yaksh A, Kik C, Knops P, Lanters EA, Teuwen CP, Oei FB, van de Woestijne PC, Bekkers JA, Bogers AJ, et al. QUest for the Arrhythmogenic Substrate of Atrial fibRillation in Patients Undergoing Cardiac Surgery (QUASAR Study): Rationale and Design. J Cardiovasc Transl Res. 2016;9:194-201.

11. Teuwen CP, Yaksh A, Lanters EA, Kik C, van der Does LJ, Knops P, Taverne YJ, van de Woestijne PC, Oei FB, Bekkers JA, et al. Relevance of Conduction Disorders in Bachmann's Bundle During Sinus Rhythm in Humans. Circ Arrhythm Electrophysiol. 2016;9:e003972.

12. Mouws E, Lanters EAH, Teuwen CP, van der Does L, Kik C, Knops P, Bekkers JA, Bogers A, de Groot NMS. Epicardial Breakthrough Waves During Sinus Rhythm: Depiction of the Arrhythmogenic Substrate? Circ Arrhythm Electrophysiol. 2017;10.

13. Kik C, Mouws E, Bogers A, de Groot NMS. Intra-operative mapping of the atria: the first step towards individualization of atrial fibrillation therapy? Expert Rev Cardiovasc Ther. 2017;15:537-545.

14. Salama G, Kanai A, Efimov IR. Subthreshold stimulation of Purkinje fibers interrupts ventricular tachycardia in intact hearts. Experimental study with voltage-sensitive dyes and imaging techniques. Circ Res. 1994;74:604-619.

15. Friedman PA. Novel mapping techniques for cardiac electrophysiology. Heart. 2002;87:575-582.

16. Blanchard SM, Damiano RJ, Jr., Asano T, Smith WM, Ideker RE, Lowe JE. The effects of distant cardiac electrical events on local activation in unipolar epicardial electrograms. IEEE Trans Biomed Eng. 1987;34:539-546.

17. Cantwell CD, Roney CH, Ng FS, Siggers JH, Sherwin SJ, Peters NS. Techniques for automated local activation time annotation and conduction velocity estimation in cardiac mapping. Comput Biol Med. 2015;65:229-242.

18. Villacastin J, Almendral J, Arenal A, Castellano NP, Gonzalez S, Ortiz M, Garcia J, Vallbona B, Moreno J, Portales JF, et al. Usefulness of unipolar electrograms to detect isthmus block after radiofrequency ablation of typical atrial flutter. Circulation. 2000;102:3080-3085.

19. Jacquemet V, Virag N, Ihara Z, Dang L, Blanc O, Zozor S, Vesin JM, Kappenberger L, Henriquez C. Study of unipolar electrogram morphology in a computer model of atrial fibrillation. J Cardiovasc Electrophysiol. 2003;14:S172-179.

20. Ho SY, Anderson RH, Sanchez-Quintana D. Atrial structure and fibres: morphologic bases of atrial conduction. Cardiovasc Res. 2002;54:325-336.

21. Pashakhanloo F, Herzka DA, Ashikaga H, Mori S, Gai N, Bluemke DA, Trayanova NA, McVeigh ER. Myofiber Architecture of the Human Atria as Revealed by Submillimeter Diffusion Tensor Imaging. Circ Arrhythm Electrophysiol. 2016;9:e004133.

22. Anne W, Willems R, Roskams T, Sergeant P, Herijgers P, Holemans P, Ector H, Heidbuchel H. Matrix metalloproteinases and atrial remodeling in patients with mitral valve disease and atrial fibrillation. Cardiovasc Res. 2005;67:655-666.

23. Castonguay MC, Wang Y, Gerhart JL, Miller DV, Stulak JM, Edwards WD, Maleszewski JJ. Surgical pathology of atrial appendages removed during the cox-maze procedure: a review of 86 cases (2004 to 2005) with implications for prognosis. Am J Surg Pathol. 2013;37:890-897.

24. Kim SJ, Choisy SC, Barman P, Zhang H, Hancox JC, Jones SA, James AF. Atrial remodeling and the substrate for atrial fibrillation in rat hearts with elevated afterload. Circ Arrhythm Electrophysiol. 2011;4:761-769.

25. Nowicki ER, Birkmeyer NJ, Weintraub RW, Leavitt BJ, Sanders JH, Dacey LJ, Clough RA, Quinn RD, Charlesworth DC, Sisto DA, et al. Multivariable prediction of in-hospital mortality associated with aortic and mitral valve surgery in Northern New England. Ann Thorac Surg. 2004;77:1966-1977.

5

26. Messika-Zeitoun D, Bellamy M, Avierinos JF, Breen J, Eusemann C, Rossi A, Behrenbeck T, Scott C, Tajik JA, Enriquez-Sarano M. Left atrial remodelling in mitral regurgitation--methodologic approach, physiological determinants, and outcome implications: a prospective quantitative Doppler-echocardiographic and electron beam-computed tomographic study. Eur Heart J. 2007;28:1773-1781.

27. John B, Stiles MK, Kuklik P, Chandy ST, Young GD, Mackenzie L, Szumowski L, Joseph G, Jose J, Worthley SG, et al. Electrical remodelling of the left and right atria due to rheumatic mitral stenosis. Eur Heart J. 2008;29:2234-2243.

28. Nathan H, Eliakim M. The junction between the left atrium and the pulmonary veins. An anatomic study of human hearts. Circulation. 1966;34:412-422.

29. Mouws E, Lanters EAH, Teuwen CP, van der Does L, Kik C, Knops P, Yaksh A, Bekkers JA, Bogers A, de Groot NMS. Impact of Ischemic and Valvular Heart Disease on Atrial Excitation:A High-Resolution Epicardial Mapping Study. J Am Heart Assoc. 2018;7.

30. Mouws E, Kik C, van der Does L, Lanters EAH, Teuwen CP, Knops P, Bogers A, de Groot NMS. Novel Insights in the Activation Patterns at the Pulmonary Vein Area. Circ Arrhythm Electrophysiol. 2018;11:e006720.

31. Seemann G, Hoper C, Sachse FB, Dossel O, Holden AV, Zhang H. Heterogeneous three-dimensional anatomical and electrophysiological model of human atria. Philos Trans A Math Phys Eng Sci. 2006;364:1465-1481.

32. Aslanidi OV, Colman MA, Stott J, Dobrzynski H, Boyett MR, Holden AV, Zhang H. 3D virtual human atria: A computational platform for studying clinical atrial fibrillation. Prog Biophys Mol Biol. 2011;107:156-168.

33. Krogh-Madsen T, Abbott GW, Christini DJ. Effects of electrical and structural remodeling on atrial fibrillation maintenance: a simulation study. PLoS Comput Biol. 2012;8:e1002390.

34. Tobon C, Ruiz-Villa CA, Heidenreich E, Romero L, Hornero F, Saiz J. A three-dimensional human atrial model with fiber orientation. Electrograms and arrhythmic activation patterns relationship. PLoS One. 2013;8:e50883.

35. Houben RP, de Groot NM, Smeets JL, Becker AE, Lindemans FW, Allessie MA. S-wave predominance of epicardial electrograms during atrial fibrillation in humans: indirect evidence for a role of the thin subepicardial layer. Heart Rhythm. 2004;1:639-647.

36. van der Does L, Knops P, Teuwen CP, Serban C, Starreveld R, Lanters EAH, Mouws E, Kik C, Bogers A, de Groot NMS. Unipolar atrial electrogram morphology from an epicardial and endocardial perspective. Heart Rhythm. 2018;15:879-887.

37. Kumar S, Michaud GF. Unipolar electrogram morphology to assess lesion formation during catheter ablation of atrial fibrillation: successful translation into clinical practice. Circ Arrhythm Electrophysiol. 2013;6:1050-1052.

38. Roberts-Thomson KC, Stevenson I, Kistler PM, Haqqani HM, Spence SJ, Goldblatt JC, Sanders P, Kalman JM. The role of chronic atrial stretch and atrial fibrillation on posterior left atrial wall conduction. Heart Rhythm. 2009;6:1109-1117.

39. Ho SY, Anderson RH, Sanchez-Quintana D. Gross structure of the atriums: more than an anatomic curiosity? Pacing Clin Electrophysiol. 2002;25:342-350.

40. Becker AE. How structurally normal are human atria in patients with atrial fibrillation? Heart Rhythm. 2004;1:627-631.
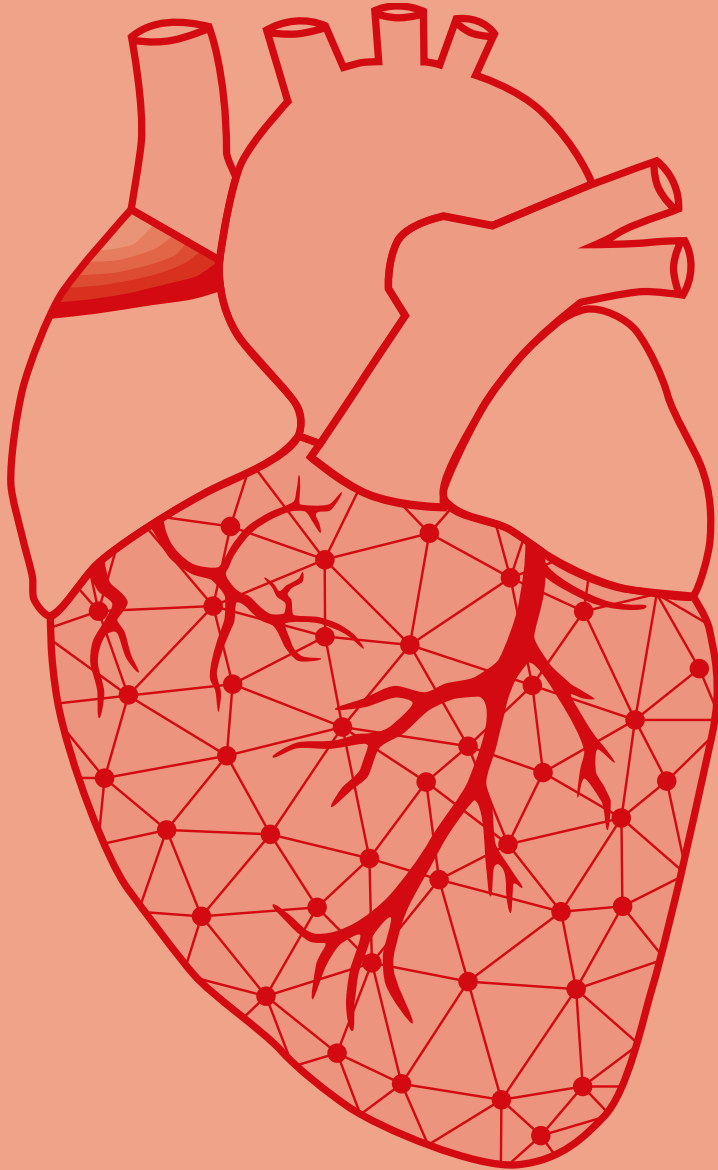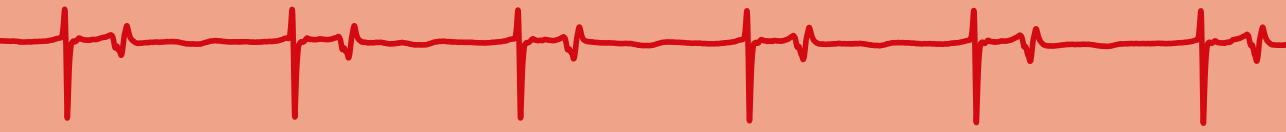
Chapter 6

Low-voltage potentials contribute to post-operative atrial fibrillation development in obese patients

Corina Schram-Serban

Mathijs S. van Schie

Paul Knops

Charles Kik

Ad J.J.C. Bogers

Natasja M.S. de Groot

Abstract

Background: Obesity predisposes to the development of atrial fibrillation (AF). However, the pathophysiology underlying this relation is only partly understood. As low-voltage areas are considered indicators of the arrhythmogenic substrates promoting AF, our study aimed to compare the extensiveness of atrial low-voltage areas between obese and non-obese patients by using high-resolution epicardial mapping in order to identify predilection sites of low-voltage areas.

Methods: A total of 430 patients (131 (30%) obese and 299 (70%) non-obese) were matched resulting in 212 patients (body mass index [BMI] ≥30 kg/m^2: n=106; BMI <30 kg/m^2: n=106) undergoing cardiac surgery (mean age 63±11 years; 161 male). All patients underwent epicardial mapping of the right atrium, Bachmann bundle (BB) and left atrium during sinus rhythm. Low-voltage potentials were defined as potentials with peak-to-peak amplitudes below the 5th percentile of all potential amplitudes obtained from non-obese patients.

Results: Compared with non-obese patients, obese patients have potentials with lower voltages (4.5 [0.4–16.2] mV vs. 5.5 mV [0.8–18.0] mV, p<0.001), especially at BB (4.1 [0.4–12.3] mV vs. 6.2 [1.0–14.3] mV, p<0.001) and left atrium (5.1 [0.5–10.1] mV vs. 6.2 [0.8–15.9] mV, p=0.003). The percentage of low-voltage potentials was higher in obese than in non-obese patients (3.6 [0–77.1] % vs. 2.3 [0–57.9] %, p<0.001), again at BB (obese: 2.9 [0–77.1] % vs. non-obese: 0.9 [0–42.0] %, p<0.001). Percentages of low-voltage potentials correlated with incidences of conduction block (p<0.001), while BMI (p=0.044) and low-voltage potentials (p=0.001) were independent predictors for the incidence of early post-operative AF.

Conclusion: Obesity may predispose to an overall decrease in atrial voltage and a higher percentage in low-voltage potentials. BB was a predilection area for low voltage within the atria of obese patients.

Journal site &
supplementary material

Introduction

Obesity is a well-established, independent risk factor for the most common type of arrhythmia, atrial fibrillation (AF).[1-3] In obese patients, risk factors (e.g. hypertension (HT), diabetes (DM), hyperlipidemia (HL) and coronary artery disease (CAD)) and atrial substrate alterations[4] (epicardial fat infiltrations, atrial fibrosis and enhanced local inflammation due to increased adipocytokines and pro-inflammatory cytokines) are related to AF development.

Previous experimental and human studies have reported on the association between the presence of epicardial adipose tissue (EAT) and atrial electropathology.[2,5]

6

In a previous study, we showed that obese patients undergoing cardiac surgery have higher incidences of conduction disorders compared to non-obese patients making them more vulnerable to developing early post-operative AF (EPoAF).[6] In 16 obese patients, Mahajan et al.[2] observed lower regional mean voltages of bipolar electrograms recorded during sinus rhythm (SR) in the posterior and inferior left atrial (LA) walls compared to 10 non-obese patients.

In the ovine experimental model of chronic obesity,[5] there was an increased voltage heterogeneity with reduction of voltages in the posterior LA wall in addition to increased incidence of complex fractionated electrograms and heterogeneous conduction.

As low-voltage areas are considered to be indicators of the arrhythmogenic substrates promoting AF in patients with a history of AF,[7] low-voltage areas in the LA are targeted in addition to pulmonary vein isolation to prevent AF recurrences.[7-9] It is unknown whether this approach is also suitable for obese patients, as they may have a more extensive arrhythmogenic substrate. So far, it is unknown whether and to what extent voltage distributions differ between non-obese and obese patients and whether there is larger amount of low-voltages areas in the latter group.

The aim of our study is therefore to compare the extensiveness and severity of atrial low-voltage areas identified during SR between obese and matched non-obese patients measured at high-resolution scale.

Methods

Study population

The study population consisted of adult patients scheduled for elective cardiac surgery for CAD, either isolated or in combination with aortic (CAD+AVD) or mitral (CAD+MVD) valve disease, isolated aortic (AVD) or mitral (MVD) valve disease or correction of congenital heart defects (CHD). Exclusion criteria were history of AF, prior ablation of atrial tachyarrhythmias, severe renal failure, atrial pacing and patients requiring mechanical or inotropic support. Patients with sleep apnea were not included in the study. The population was divided into two categories: 1) the study group, obese patients (BMI ≥30) and 2) the control group, non-obese patients (BMI <30).

This study was conducted as part of two prospective observational projects including Quest for Arrhythmogenic Substrate of Atrial fibRillation (QUASAR, MEC 2010-054) and Hsf1 Activators Lower cardiomyocyte damage Towards a novel approach to REVERSE atrial fibrillation (HALT & REVERSE, MEC 2014-393). Both projects were approved by the local ethics committee of the Erasmus Medical Center and adhere to the Declaration of Helsinki
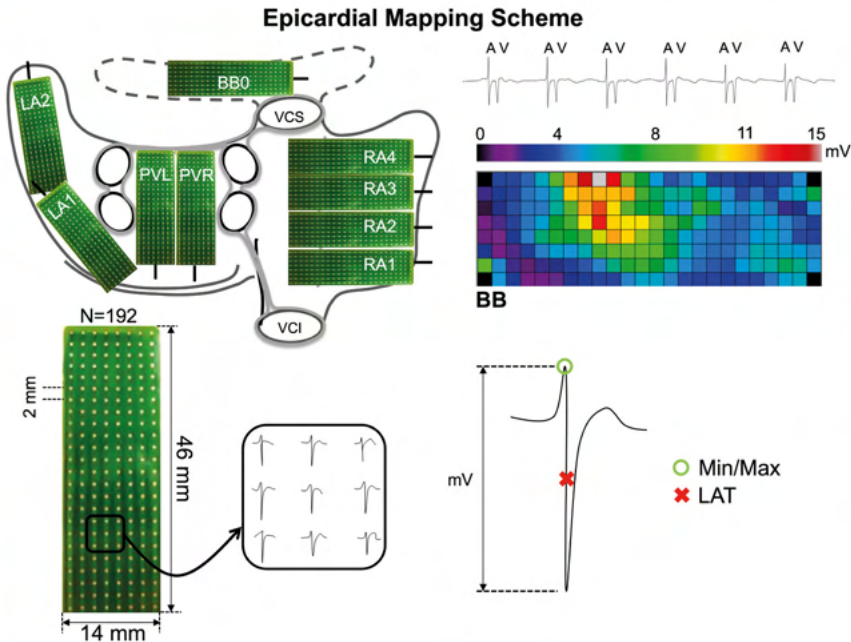
Figure 1 – Epicardial mapping during SR. *Upper left panel*: projection of the 192-unipolar electrode array on a schematic posterior view of the atria. *Upper right panel*: epicardial unipolar potentials recorded during 5 seconds of SR (A = atrial potential, V = ventricular potential) at BB and corresponding color-coded voltage map. *Lower left panel*: typical examples of 9 unipolar potentials. *Lower right panel*: potential voltage is defined as the peak-to-peak amplitude of the steepest deflection. **RA** = right atrium; **BB** = Bachmann's bundle; **PV** = pulmonary veins; **LA** = left atrium; **LAT** = local activation time.

principles. Accordingly, written consent was obtained from the participating patients before surgical intervention.

Epicardial High-Resolution Mapping

Epicardial high-resolution mapping was performed during open chest cardiac surgery after sternotomy, before connecting the patient to the cardiopulmonary bypass circulation.[10,11] A bipolar pacemaker wire was placed at the right atrial free wall to serve as a temporal reference electrode. The indifferent electrode was a steel wire attached to thoracic subcutaneous tissue.[10] The mapping procedure was performed using 16 mm width electrode arrays containing either 128 or 192 unipolar electrodes (2.0 mm inter-electrode distance) with diameters of 0.65 and 0.45 mm respectively.[11]

Epicardial mapping during SR was conducted following a predefined mapping scheme as shown in *Figure 1* (left upper panel), approaching the entire epicardial surface of the right atrium (RA), Bachmann's bundle (BB) and LA.[10] As previously described,[10-12] the electrode array was shifted along imaginary lines with a fixed orientation at each position. Mapping of the RA started at the cavo-tricuspid isthmus and continued perpendicular to the caval veins towards the RA appendage (RAA). BB was mapped starting at the tip of the LA appendage (LAA) across the roof of the LA, behind the aorta towards the superior cavo-atrial junction.[11] Mapping of the LA was performed from the lower margin of the left inferior pulmonary vein (PV) along the left atrioventricular groove (LAVG) towards the LAA.[10] The PV area (PVA) was mapped from the sinus transversus fold, in between the right and left PV towards the left atrioventricular groove.[11]

Table 1 – Patient characteristics.

	Obese patients (BMI ≥30 kg/m²) (n = 106)	Non-obese patients (BMI <30 kg/m²) (n = 106)	*p*-value
Age (y)	63.5±9.6	62.3±11.8	0.742
Male	78 (74)	83 (78)	0.521
BMI (kg/m²)	32.9±2.9	25.4±2.4	<0.001
Cardiovascular risk factors			
• Hypertension	65 (61.3)	60 (56.6)	0.577
• Diabetes mellitus	37 (35)	25 (23.5)	0.096
• Dyslipidemia	44 (41.5)	42 (39.6)	0.889
Left ventricular function			0.357
• Normal (EF >55%)	84 (79.2)	83 (78.3)	
• Mild impairment (EF 46-55%	21 (19.8)	18 (17)	
• Moderate impairment (EF 36-45%)	1 (0.9)	3 (2.8)	
• Severe impairment (EF <35%)	0 (0)	2 (1.9)	
Left atrial dilatation	15 (14.1)	16 (15)	0.863
Preoperative medication			
• Anti-arrhythmic drugs			
- Class II	46 (68.6)	59 (66.2)	0.863
- Class IV	2 (3)	4 (4.4)	0.467
• ACE inhibitors	42 (62.6)	49 (55)	0.412
Surgical procedure			0.277
• CABG	70 (66)	64 (60.3)	
• AVD	10 (9.4)	12 (11.3)	
• MVD	2 (1.8)	7 (6.6)	
• CABG + AVD	15 (14.1)	11 (10.3)	
• CABG + MVD	3 (2.8)	1 (0.9)	
• CHD	6 (5.6)	11 (10.3)	

Values are presented as mean ± standard deviation or n (%). Statistically significant values: *p*<0.05. **ACE** = angiotensin-converting enzyme; **AVD** = aortic valve disease; **BMI** = body mass index; **CABG** = coronary artery bypass grafting; **CHD** = congenital heart disease; **EF** = ejection fraction; **MVD** = mitral valve disease.

6

From every atrial mapping site, five seconds of SR were recorded, including surface ECG (lead l), a bipolar reference electrogram, a calibration signal with an amplitude of 2 mV and 1000 ms and unipolar epicardial electrograms. Recordings were sampled with a rate of 1 kHz, amplified (gain: 1000), filtered (bandwidth: 0.5–400 Hz), converted from analogue-to-digital (16 bits) and stored on a hard disk.

Analysis of mapping data

Semi-automatic analysis of unipolar electrogram morphology was performed using Python 3.6 software. Recording sites with ≥25% excluded or missing electrograms, injury potentials electrograms and premature atrial complexes or aberrant beats were excluded from analysis. Local activation time (LAT) was established by marking the steepest negative slope of an atrial deflection, with a minimum slope threshold of 0.05 V/s. The amplitude threshold was set at two times the signal noise level. All signal markings were manually checked and corrected by a consensus of two investigators.

Unipolar electrogram voltage was defined as peak-to-peak amplitude of the steepest deflection. Unipolar electrograms with peak-to-peak amplitudes below the 5th percentile (P_5) of all deflection amplitudes obtained from non-obese patients were defined as low-voltage potentials.

Evaluation of EPoAF

The heart rhythm was continuously monitored in all patients during the first five post-operative days.

EPoAF was defined as the incidence of at least one AF episode with a duration of minimally 30 seconds. EPoAF was also confirmed by documentation in patient discharge letters and clinical notes.

Statistical analysis

Statistical analysis was performed using the IBM SPSS Statistics 24 software (Corp., Armonk, NY software). Propensity score matching analysis on age and gender was performed using logistic regression, cases being randomly assigned to controls based on the nearest neighboring propensity score (match tolerance 0.05). Data were tested using Shapiro Wilk test of normality. Continuous, normally distributed data is expressed as mean ± standard deviation and skewed data as median and range (minimum-maximum). One sample *t*-test was used to compare normally distributed continuous variables. Comparisons between related skewed variables were performed using one sample Wilcoxon rank-sum test. Categorical variables were compared using Fisher's exact test and are presented as percentages. Bonferroni correction was used to control for family-wise error when comparing voltage characteristics for the four atrial locations. Pearson correlation test was used to evaluate the linear relationship between variables. Possible predictors for EPoAF in univariate conditional binary logistic regression ($p \leq 0.15$) were manually entered in a multivariate conditional binary logistic regression. A two-sided *p*-value of <0.05 was considered statistically significant.

Results

Study population

Baseline characteristics of both the obese (N=106, 64±10 years; 78 (74%) male) and non-obese group (N=106, 62±12; 83 (78%) male) are presented in *Table 1*. Clinical characteristics between these groups only differed in BMI (32.9±2.9 vs. 25.4±2.4; p<0.001). Coronary artery bypass grafting (CABG) was the main surgical procedure performed in both groups (obese patients: 70 (66%) and non-obese patients: 64 (60%)).
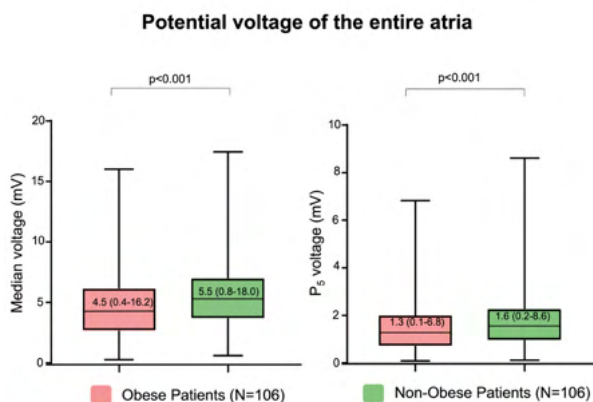
Figure 2 – Graphs demonstrating differences in median and 5th percentile voltages between obese and nonobese patients. *Left panel*: obese patients had a significantly lower median voltage (4.5 [0.4–16.2] mV) than non-obese patients (5.5 [0.8–18.0] mV, p<0.001). *Right panel*: for potentials within the 5th percentile, the amplitude was significantly lower in obese (median 1.3 [0.1–6.8] mV) than in non-obese (median 1.6 [0.2–8.6] mV, p<0.001) patients.
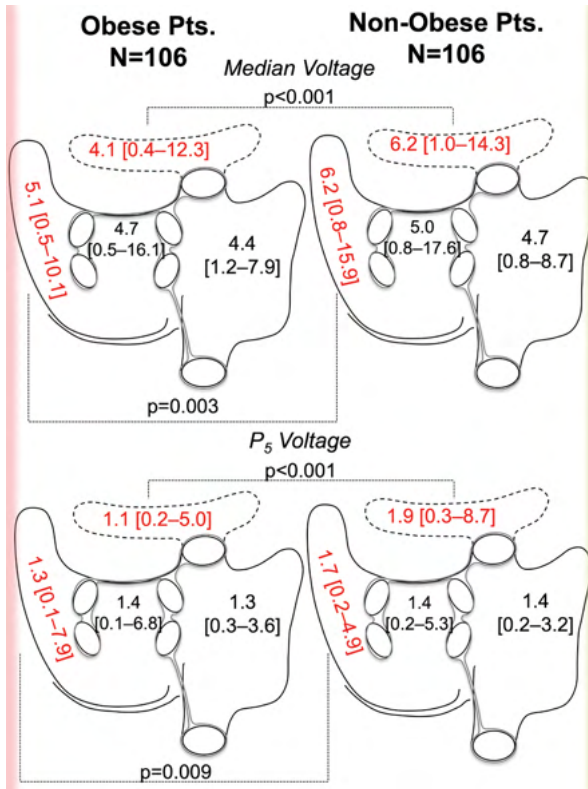
Figure 3 – Graphic representation of differences in median and P_5 voltage between obese and non-obese patients. The areas that are significantly different between obese and non-obese patients are highlighted in red. The upper panel shows a significantly lower median voltage in obese than in non-obese patients, particularly at BB (p<0.001) and LA (p=0.003). The lower panel shows that obese patients also have a significantly lower P_5 voltage mainly at BB (p<0.001) and LA (p=0.009). Statistical significance: p<0.0125. **BB** = Bachmann bundle; **P_5** = 5th percentile; **Pt.** = patient.

6

Mapping data

The total number of recording sites in the obese group was 202,304 (1,909±321 electrograms/patient) and 200,192 in the non-obese group (1,889±311 electrograms/patient, p=0.411). After exclusion of 0.65% of the mapping sites due to electrograms with poor signal-to-noise ratios, respectively 1,333 (12.5±4.2 per patient) and 1,321 (12.4±4.1 per patient, p=0.617) mapping locations were available for analysis.

Differences in Unipolar voltages Distribution

Figure 2 shows the median voltage of the entire atria for the obese and non-obese patients. The left panel shows that voltages were lower in obese compared to non-obese patients (4.5 [0.4–16.2] mV vs. 5.5 [0.8–18.0] mV, p<0.001).

The right panel of *Figure 2* demonstrates that the 5th percentile of the voltage for each patient was significantly lower in obese (median 1.3 [0.1–6.8] mV) compared to non-obese patients (median 1.6 [0.2–8.6] mV, p<0.001).

Regional heterogeneity in unipolar voltages

Regional differences in unipolar voltages between obese and non-obese patients are depicted in *Figure 3* and summarized in *Supplementary Table 1*. As demonstrated in the upper panel, obese patients have significantly lower unipolar voltages, specifically at BB (4.1 [0.4–12.3] mV vs. 6.2 [1.0–14.3] mV, p<0.001) and LA (5.1 [0.5–10.1] mV vs. 6.2 [0.8–15.9] mV,
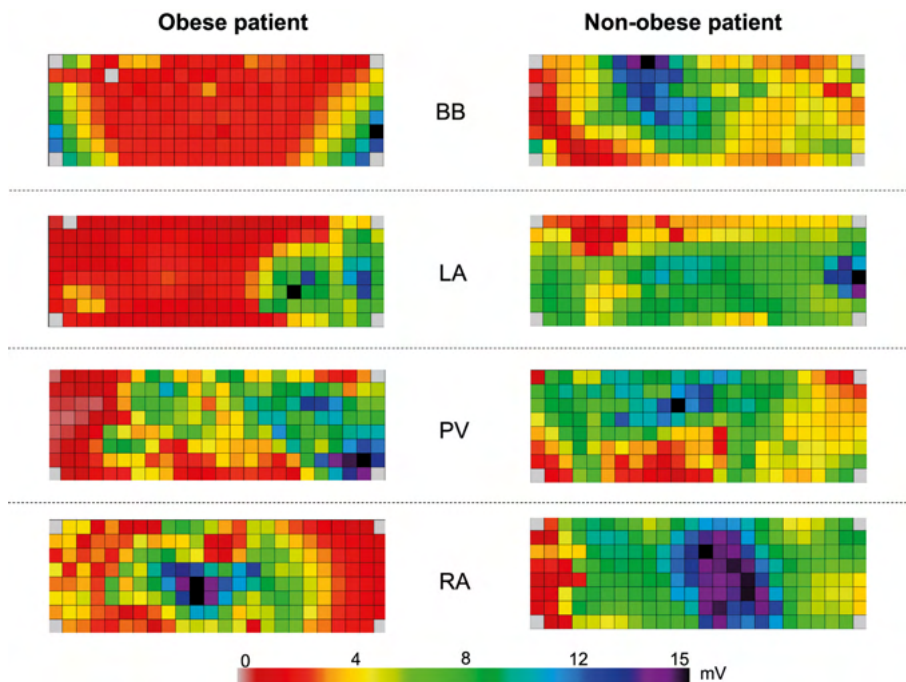
Figure 4 – Examples of color-coded voltage maps. Maps show the distribution of potentials within the predefined atrial areas from an obese patient (left panel) and a non-obese-matched control patient (right panel). These maps show that there is an increase in lower-voltage areas in the obese patient. **BB** = Bachmann bundle; **LA** = left atrium; **PV** = pulmonary vein; **RA** = right atrium.

p=0.003).

Similarly, as shown in the lower panel of *Figure 3*, the 5th percentile of unipolar voltages was also significantly lower in obese compared to non-obese patients at BB (1.1 [0.1–5.0] mV vs. 1.9 [0.3–8.7] mV, p<0.001) and LA (1.3 [0.2–7.9] mV vs. 1.7 [0.2–4.9] mV, p=0.009).

Spatial distribution of unipolar low-voltage potentials

Low-voltage areas were observed in all non-obese and obese patients. *Figure 4* depicts examples of color-coded unipolar voltage maps obtained from a typical obese and non-obese patient constructed from respectively the RA, BB, LA and PV. Though these maps demonstrate that there is a wide variation in unipolar voltages throughout the entire atrial surface in both the obese and non-obese patient, the extent of low-voltage areas is higher in the obese patient. The cut-off value for low-voltage areas, defined as the 5th percentile of all unipolar voltages in non-obese patients was 0.833 mV. *Figure 5* shows incidences of low-voltage potentials within the entire atria for obese and non-obese patients separately. There was a significantly higher incidence of low-voltage potentials in obese (3.6 [0–77.1] %) compared to non-obese patients (2.3 [0–57.9] %), p<0.001.

Predilection sites for low-voltage potentials

Figure 6 depicts the spatial distribution of low-voltage potentials for every atrial location separately; corresponding values are summarized in *Supplementary Table 1*. Although percentages of low-voltage potentials were similar between obese and non-obese patients
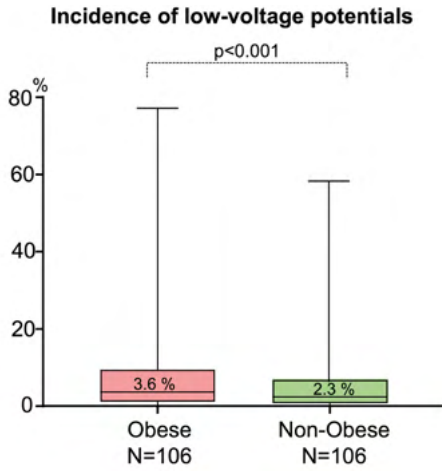
Figure 5 – Graphic representation of the difference in the percentage of low-voltage potentials between obese and nonobese patients. There was a significant increase in the percentage of low-voltage potentials in obese compared with non-obese patients (p<0.001).

6
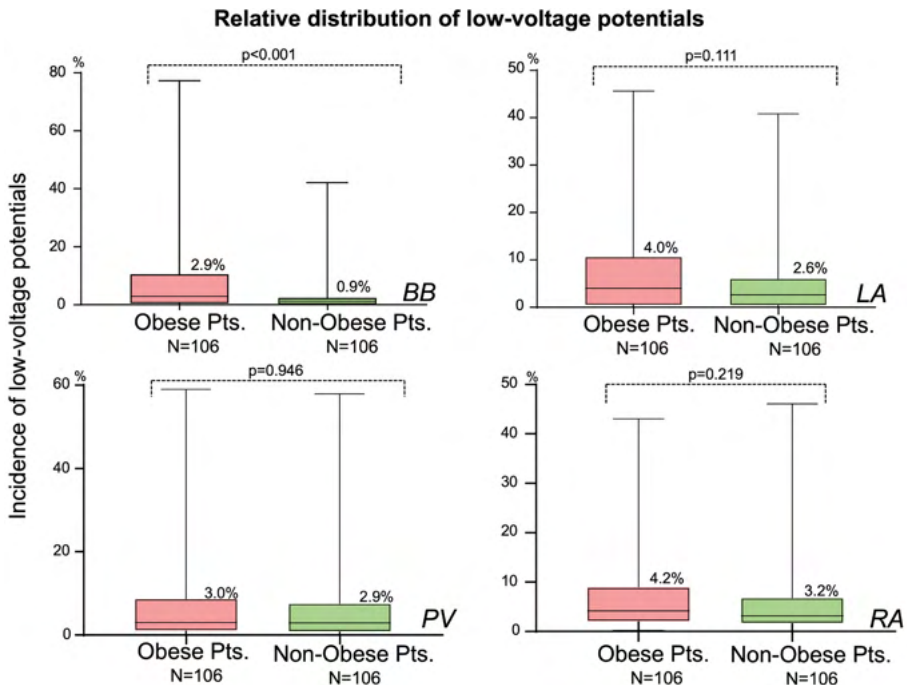
Figure 6 – Graphic representation of the relative distribution of low-voltage potentials within different atrial areas. Although there were a higher percentage of low-voltage potentials within all atrial areas, BB was the only region where the differences between obese and nonobese patients were significant (p<0.001). Statistical significance: p<0.0125. **BB** = Bachmann bundle; **LA** = left atrium; **Pt.** = patient; **PV** = pulmonary vein; **RA** = right atrium.

Table 2 – Clinical risk factors for EPoAF.

	OR	95% CI for OR	*p*-value
Univariable analysis			
• HT	1.559	1.149–2.115	0.004
• HL	1.332	0.991–1.792	0.058
• DM	1.126	0.816–1.554	0.471
• LAE	1.908	1.186–3.072	0.008
• BMI	1.084	1.050–1.120	<0.001
• AVD	1.321	0.487–2.061	0.219
• AVD+CABG	1.486	0.958–2.304	0.177
• CABG	1.114	0.662–1.217	0.486
• MVD	3.013	1.058–8.581	0.039
• MVD+CABG	9.159	2.925–28.679	<0.001
• Median voltage	1.279	0.822–2.938	0.552
• Low-voltage (%)	1.023	1.008–1.038	0.002
Surgical procedure			
• HT	2.496	1.519–4.102	<0.001
• LAE	1.890	1.107–3.227	0.020
• BMI	1.058	1.006–1.112	0.028
• MVD+CABG	4.953	1.344–18.256	0.016
• Low-voltage (%)	1.041	1.017–1.064	0.001

BMI was used as a continuous variable in the conditional univariable and multivariable binary logistic regression analysis. **AVD** = atrial valve disease; **BMI** = body mass index; **CABG** = coronary artery bypass grafting; **CI** = confidence interval; **DM** = diabetes mellitus; **EPoAF** = early post-operative atrial fibrillation; **HL** = hyperlipidemia; **HT** = hypertension; **LAE** = left atrial enlargement; **MVD** = mitral valve disease; **OR** = odds ratio.

within the majority of atrial locations, there was a significantly higher percentage of low-voltage potentials at BB in obese (2.9 [0–77.1] %) compared to non-obese patients (0.9 [0–42.0] %, p<0.001).

Correlations between heterogeneity in conduction and potential voltages

In our previous paper, we have shown that heterogeneity in conduction was higher in obese patients thus increasing their vulnerability towards AF.[6] Therefore, we wanted to assess the relationship between potential voltages including the extent of low-voltage areas and conduction abnormalities. Correlations between potential voltages and various conduction parameters for all patients, obese and non-obese separately are summarized in *Supplementary Table 2*. Most correlations were weak to moderate, although significant. The highest correlation coefficient was observed between the percentage of low-voltage potentials and percentage of CB (entire population: ρ=0.442, p<0.001; obese group: ρ=0.473, p<0.001 and non-obese patients: ρ=0.381, p<0.001).

Risk factors of EPoAF

As shown in our previous paper,[6] the incidence of EPoAF in our population was higher in obese (36% [n=38]) compared to non-obese patients (17% [n=18]), p=0.003. Univariable and multivariable predictors of EPoAF with their respective OR (95% CI) are summarized in *Table 2*. Significant univariable predictive factors for incidence of EPoAF include HT (OR 1.559, p=0.004), left atrial enlargement (LAE) (OR 1.908, p=0.008), BMI (OR 1.084, p<0.001), MVD (OR 3.013, p=0.039), MVD and CABG (OR 9.159, p<0.001) and percentage of low-voltage potentials (OR 1.023, p=0.002). In the multivariable analysis, percentage of low-voltage potentials was the only significant electrophysiological parameter for development of EPoAF (OR 1.041, p=0.001). Other significant associations between clinical parameters and incidence of EPoAF include HT (OR 2.496, p<0.001), LAE (OR 1.890, p=0.020) and BMI (OR 1.058, p=0.028).

Discussion

This study compared the magnitude and spatial distribution of unipolar voltages between obese and non-obese patients. Obesity is associated with lower unipolar voltages, particularly at BB and LA. Low-voltage areas were predominantly found at BB. Moderate correlations were observed between voltage characteristics and conduction abnormalities in both obese and non-obese patients. In addition, both BMI and percentage of low-voltage areas were independent predictors for development of EPoAF.

Obesity and voltage characteristics

Previous studies have shown the link between obesity and development of AF, however the underlying electrophysiological mechanism are still incompletely understood.[3,13,14] BMI has been associated with an increased amount of pericardial and epicardial fat.[15,16] EAT, through its paracrine effect contributes to development of atrial interstitial fibrosis.[17]

In a study conducted by Mahajan et al.[2] low atrial voltages were observed in the posterior and inferior LA. These areas were adjacent to the posteriorly located fat pad in obese patients undergoing electro-anatomical mapping during SR before AF ablation.[2] In our study population, consisting of patients without a history of AF, we observed that obesity was associated with a higher incidence of low-voltage potentials particularly at BB. BB is the preferential inter-atrial connection insuring bi-atrial synchronous contraction.[18] This observation suggests that deposition of EAT may be more pronounced at BB. Indeed, Saremi et al.[19] demonstrated that in some patients BB is replaced by fat.

Our previous study showed relationships between conduction abnormalities and obesity.[6] In this study we demonstrated correlations between conduction abnormalities and low-voltage areas. This finding further supports the associations between obesity and electrophysiological abnormalities.

Obesity, voltage characteristics and EPoAF

Previous studies have shown that BMI, as a measure of adiposity is a strong independent factor for both AF and PoAF.[14,20,21] Phan et al.[22] demonstrated in a meta-analysis focusing on patients without a history of AF, that obesity was associated with an increased risk of developing PoAF. In our study, the multivariate analysis showed that a 1.058 unit increase in BMI resulted in a higher incidence of EPoAF (p=0.028). Csige et al.[23] demonstrated that 1-unit increase in BMI can increase the incidence of newly developed AF by 4%. Clinical factors including HT, HL and LAE were also independently associated with the development of EPoAF. These findings being reported by prior studies.

Atrial fibrosis is a feature in obesity related structural remodeling. Prior studies demonstrated relations between histological evidence of increased atrial fibrosis, indirect evidence of reduced endocardial atrial voltages.[24] Development of obesity is associated with hypoxia of the expanded adipose tissue resulting in adipose tissue fibrosis and production of various adipo-cytokines including TGFβ family.[25] The combination between increased epicardial adiposity, atrial fibrosis and altered three-dimensional atrial architecture could be pro-fibrillatory with increased likelihood of conduction heterogeneity that may sustain reentry.[24] Our previous study has shown that the incidence of CB was an independent predictor for EPoAF occurrence.[6] In this study, we found that the percentage of low-voltage potentials is also independently associated with development of EPoAF in obese patients. The correlation between the two electrophysiological parameters could therefore potentially explain the

6

higher risk of EPoAF development in obese patients.

Study limitations

Recordings of the interatrial septum could not be obtained during the closed beating heart epicardial mapping approach. Due to the invasive mapping approach, healthy patients could not be included. EAT, whenever present on the atria was not dissected prior to myocardial sampling. Distribution of EAT could not be examined through imaging due to logistic reasons. Lipotoxicity of the underlying myocardial tissue was not assessed.

Conclusion

Obesity may predispose to an overall decrease in atrial voltage and a higher percentage in low-voltage potentials. BB was a predilection area for low voltage within the atria of the obese patients. However, whether obesity alone is responsible for the low-voltage areas remains to be further investigated. In order to determine the impact of obesity induced low-voltage areas during long-term clinical outcome, further prospective studies are mandatory.

References

1. Dublin S, French B, Glazer NL, Wiggins KL, Lumley T, Psaty BM, Smith NL, Heckbert SR. Risk of new-onset atrial fibrillation in relation to body mass index. Arch Intern Med. 2006;166:2322-2328.
2. Mahajan R, Nelson A, Pathak RK, Middeldorp ME, Wong CX, Twomey DJ, Carbone A, Teo K, Agbaedeng T, Linz D, et al. Electroanatomical Remodeling of the Atria in Obesity: Impact of Adjacent Epicardial Fat. JACC Clin Electrophysiol. 2018;4:1529-1540.
3. Tedrow UB, Conen D, Ridker PM, Cook NR, Koplan BA, Manson JE, Buring JE, Albert CM. The long- and short-term impact of elevated body mass index on the risk of new atrial fibrillation the WHS (women's health study). J Am Coll Cardiol. 2010;55:2319-2327.
4. Lin YK, Chen YJ, Chen SA. Potential atrial arrhythmogenicity of adipocytes: implications for the genesis of atrial fibrillation. Med Hypotheses. 2010;74:1026-1029.
5. Mahajan R, Lau DH, Brooks AG, Shipp NJ, Manavis J, Wood JP, Finnie JW, Samuel CS, Royce SG, Twomey DJ, et al. Electrophysiological, Electroanatomical, and Structural Remodeling of the Atria as Consequences of Sustained Obesity. J Am Coll Cardiol. 2015;66:1-11.
6. Schram-Serban C, Heida A, Roos-Serote MC, Knops P, Kik C, Brundel B, Bogers A, de Groot NMS. Heterogeneity in Conduction Underlies Obesity-Related Atrial Fibrillation Vulnerability. Circ Arrhythm Electrophysiol. 2020;13:e008161.
7. Masuda M, Fujita M, Iida O, Okamoto S, Ishihara T, Nanto K, Kanda T, Tsujimura T, Matsuda Y, Okuno S, et al. Left atrial low-voltage areas predict atrial fibrillation recurrence after catheter ablation in patients with paroxysmal atrial fibrillation. Int J Cardiol. 2018;257:97-101.
8. Ahmed-Jushuf F, Murgatroyd F, Dhillon P, Scott PA. The impact of the presence of left atrial low voltage areas on outcomes from pulmonary vein isolation. J Arrhythm. 2019;35:205-214.
9. Katritsis D, Sougiannis D, Giazitzoglou E, Kourlaba G, Ellenbogen KA. Regional endocardial left atrial voltage and electrogram fractionation in patients with atrial fibrillation. J Cardiovasc Electrophysiol. 2008;19:1254-1258.
10. Lanters EAH, Yaksh A, Teuwen CP, van der Does L, Kik C, Knops P, van Marion DMS, Brundel B, Bogers A, Allessie MA, et al. Spatial distribution of conduction disorders during sinus rhythm. Int J Cardiol. 2017;249:220-225.
11. Teuwen CP, Yaksh A, Lanters EA, Kik C, van der Does LJ, Knops P, Taverne YJ, van de Woestijne PC, Oei FB, Bekkers JA, et al. Relevance of Conduction Disorders in Bachmann's Bundle During Sinus Rhythm in Humans. Circ Arrhythm Electrophysiol. 2016;9:e003972.
12. Teuwen CP, Ramdjan TT, Gotte M, Brundel BJ, Evertz R, Vriend JW, Molhoek SG, Dorman HG, van Opstal JM, Konings TC, et al. Time Course of Atrial Fibrillation in Patients With Congenital Heart Defects. Circ Arrhythm Electrophysiol. 2015;8:1065-1072.
13. Gami AS, Hodge DO, Herges RM, Olson EJ, Nykodym J, Kara T, Somers VK. Obstructive sleep apnea, obesity, and the risk of incident atrial fibrillation. J Am Coll Cardiol. 2007;49:565-571.
14. Wang TJ, Parise H, Levy D, D'Agostino RB, Sr., Wolf PA, Vasan RS, Benjamin EJ. Obesity and the risk of new-onset atrial fibrillation. JAMA. 2004;292:2471-2477.
15. Sons HU, Hoffmann V. Epicardial fat cell size, fat distribution and fat infiltration of the right and left ventricle of the heart. Anat Anz. 1986;161:355-373.
16. Iacobellis G, Ribaudo MC, Zappaterreno A, Iannucci CV, Leonetti F. Relation between epicardial adipose tissue and left ventricular mass. Am J Cardiol. 2004;94:1084-1087.
17. Csige I, Ujvarosy D, Szabo Z, Lorincz I, Paragh G, Harangi M, Somodi S. The Impact of Obesity on the Cardiovascular System. J Diabetes Res. 2018;2018:3407306.
18. van Campenhout MJ, Yaksh A, Kik C, de Jaegere PP, Ho SY, Allessie MA, de Groot NM. Bachmann's bundle: a key player in the development of atrial fibrillation? Circ Arrhythm Electrophysiol. 2013;6:1041-1046.
19. Saremi F, Torrone M, Yashar N. Cardiac conduction system: delineation of anatomic landmarks with multidetector CT. Indian Pacing Electrophysiol J. 2009;9:318-333.
20. Serban C, Arinze JT, Starreveld R, Lanters EAH, Yaksh A, Kik C, Acardag Y, Knops P, Bogers A, de Groot NMS. The impact of obesity on early postoperative atrial fibrillation burden. J Thorac Cardiovasc Surg. 2020;159:930-938 e932.
21. Munger TM, Dong YX, Masaki M, Oh JK, Mankad SV, Borlaug BA, Asirvatham SJ, Shen WK, Lee HC, Bielinski SJ, et al. Electrophysiological and hemodynamic characteristics associated with obesity in patients with atrial fibrillation. J Am Coll Cardiol. 2012;60:851-860.
22. Phan K, Khuong JN, Xu J, Kanagaratnam A, Yan TD. Obesity and postoperative atrial fibrillation in patients undergoing cardiac surgery: Systematic review and meta-analysis. Int J Cardiol. 2016;217:49-57.
23. Camm AJ, Kirchhof P, Lip GY, Schotten U, Savelieva I, Ernst S, Van Gelder IC, Al-Attar N, Hindricks G, Prendergast B, et al. Guidelines for the management of atrial fibrillation: the Task Force for the Management of Atrial Fibrillation of the European Society of Cardiology (ESC). Europace. 2010;12:1360-1420.
24. Lau DH, Schotten U, Mahajan R, Antic NA, Hatem SN, Pathak RK, Hendriks JM, Kalman JM, Sanders P. Novel mechanisms in the pathogenesis of atrial fibrillation: practical applications. Eur Heart J. 2016;37:1573-1581.
25. Sun K, Halberg N, Khan M, Magalang UJ, Scherer PE. Selective inhibition of hypoxia-inducible factor 1alpha ameliorates adipose tissue dysfunction. Mol Cell Biol. 2013;33:904-917.

6
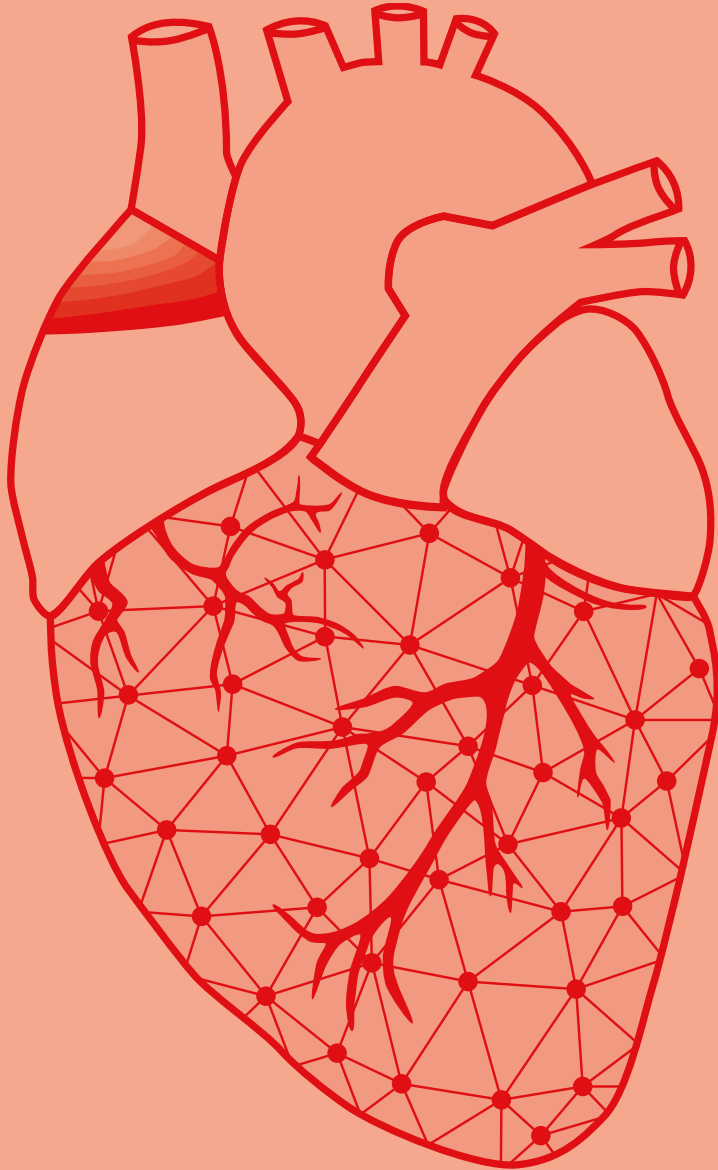
Chapter 7

Identification of low-voltage areas: a unipolar, bipolar and omnipolar perspective

Mathijs S. van Schie

Rohit K. Kharbanda

Charlotte A. Houck

Eva A.H. Lanters

Yannick J.H.J. Taverne

Ad J.J.C. Bogers

Natasja M.S. de Groot

Abstract

Background: Low-voltage areas (LVAs) are commonly considered surrogate markers for an arrhythmogenic substrate underlying tachyarrhythmias. It remains challenging to define a proper threshold to classify LVA, and it is unknown whether unipolar, bipolar, and the recently introduced omnipolar voltage mapping techniques are complementary or contradictory in classifying LVAs. Therefore, this study examined similarities and dissimilarities in unipolar, bipolar, and omnipolar voltage mapping and explored the relation between various types of voltages and conduction velocity (CV).

Methods: Intra-operative epicardial mapping (interelectrode distance 2 mm, ±1900 sites) was performed during sinus rhythm in 21 patients (48±13 years, 9 male) with atrial volume overload. Cliques of 4 electrodes (2×2 mm) were used to calculate the maximal unipolar, bipolar, and omnipolar voltages and mean CV. Areas with maximal bipolar or omnipolar clique voltage ≤0.5 mV were defined as LVA.

Results: The maximal unipolar clique voltage was not only larger than maximal bipolar clique voltage but also larger than maximal omnipolar clique voltage (7.08 [4.22–10.59] mV vs. 5.27 [2.39–9.56] mV and 5.77 [2.58–10.52] mV, respectively, p<0.001). In addition, the largest bipolar clique voltage was on average 1.66 (range: 1.0–59.0) times larger to the corresponding perpendicular bipolar voltage pair. LVAs identified by a bipolar or omnipolar threshold corresponded to a broad spectrum of unipolar voltages and, although CV was generally decreased, still high CVs and large unipolar voltages were found in these LVAs.

Conclusions: In patients with atrial volume overload, there were considerable discrepancies in the different types of LVAs. Additionally, the identification of LVAs was hampered by considerable directional differences in bipolar voltages. Even using directional independent omnipolar voltage to identify LVAs, high CVs and large unipolar voltages are present within these areas. Therefore, a combination of low unipolar and low omnipolar voltage may be more indicative of true LVAs.

Journal site

Introduction

Low-voltage areas (LVA) are commonly considered surrogate markers for arrhythmogenic atrial tissue containing areas of slow conduction, thereby serving as potential target sites for ablation therapy of atrial tachyarrhythmias including intra-atrial reentrant tachycardias and focal atrial tachycardias.[1-3] However, whether LVAs also play a role in the pathogenesis of atrial fibrillation (AF) in patients with congenital heart disease remains unknown. Voltage mapping considerably depends on the use of either unipolar or bipolar electrograms (EGMs), each having its own advantages and disadvantages.[1,4]

7

As unipolar EGMs comprise a larger region of myocardial electrical activity, bipolar recordings are mainly used to detect scar tissue areas as it represents more local information. Although ablation of bipolar LVAs has shown a possible benefit in certain patient populations, the efficacy of such bipolar voltage-guided ablation strategies remains controversial.[5-8] This can only partly be explained by the complexity of bipolar EGMs and the directional sensitivity on the potential voltage, which decreases when wavefront propagation is perpendicular to the recording electrodes. To overcome the directional sensitivity, a so-called omnipolar mapping technique has been recently developed which mathematically extracts maximal bipolar voltage from a collection of EGMs, independently of wavefront propagation direction.[9-11] On the other hand, it has been suggested that unipolar voltage mapping is preferred to identify intramural arrhythmogenic substrate.[1] It is for these reasons that unipolar and bipolar voltage mapping are increasingly combined to provide additional information on the underlying tissue.[12-17] Still, it remains very challenging to define a proper threshold to identify LVAs and it also remains unknown whether unipolar, bipolar and omnipolar voltages are complementary or contradictory on identifying LVAs at a high-resolution scale. Therefore, we performed high-density epicardial mapping in patients with atrial volume overload to 1) examine similarities and dissimilarities in unipolar, bipolar and omnipolar voltage distribution and 2) explore the relation between various types of voltages and conduction velocity (CV) in identification of LVA.

Methods

The data that support the findings of this study are available from the corresponding author upon reasonable request.

Study population

The study population consisted of 21 adult patients with atrial volume overload due to an interatrial left-to-right shunt undergoing surgical correction in the Erasmus Medical Center Rotterdam. This study was approved by the institutional medical ethical committee (MEC2010-054/MEC2014-393).[18,19] Written informed consent was obtained from all patients. Patient characteristics were obtained from the patient's medical record.

Epicardial mapping procedure

Epicardial high-resolution mapping was performed before commencement to extra-corporal circulation, as previously described in detail.[20-22] A temporal bipolar epicardial pacemaker wire attached to the RA free wall served as a reference electrode. A steel wire fixed to subcutaneous tissue of the thoracic cavity was used as an indifferent electrode. Epicardial mapping was performed with a 128-electrode array or 192-electrode array (GS Swiss PCB AG, Küssnacht, Switzerland; interelectrode distance 2.0 mm, both vertically and horizontally; electrode diameter 0.45 mm; array surface 14×30 mm and 14×46 mm).[22]
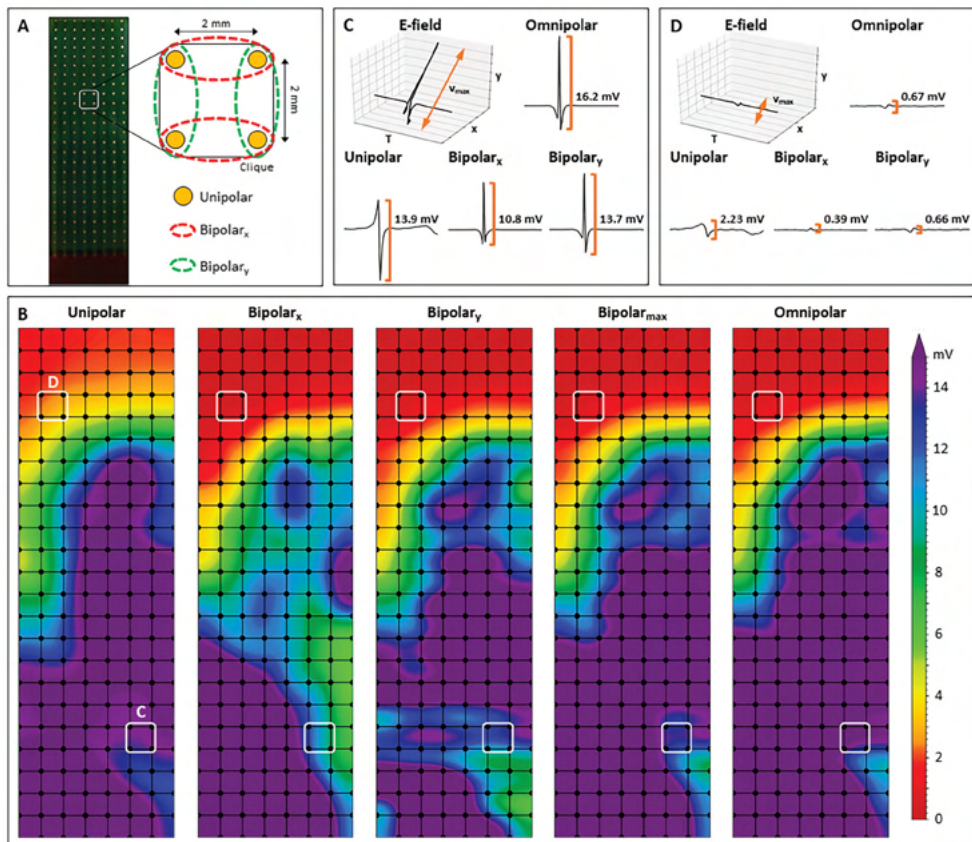
Figure 1 – Construction of unipolar, bipolar, and omnipolar voltages in 2x2 mm cliques. *Panel A*: a high-density electrode array consisting of 192 unipolar electrodes (2 mm interelectrode distance) was used to map the epicardial surface of the atria during open-chest surgery. For each square area, enclosed by 4 electrodes, 4 unipolar electrograms (EGMs), and matched bipolar and omnipolar EGMs were derived from 2 electrode orientations (along the vertical y axis [green] and horizontal x axis [red]) as indicated by the dotted lines. *Panel B*: peak-to-peak voltages of corresponding EGMs are used to create different voltage maps. The electrode orientation dependence of bipolar mapping is clearly visualized by the considerable differences in voltages between the bipolar-x and bipolar-y voltage maps. Bipolar-max voltage map illustrates the maximal bipolar voltage in both horizontal and vertical orientations within one clique. *Panels C and D*: examples of a unipolar, horizontal bipolar-x, vertical bipolar-y and omnipolar EGM. The 2 bipolar EGMs differed considerably, illustrating the electrode orientation dependence of bipolar mapping. Omnipolar mapping provides electrode orientation-independent voltages that are larger (C) and similar (D) to the bipolar with the largest measurable peak-to-peak voltage, in both cases the vertical bipolar-y EGMs.

Mapping was conducted by shifting the electrode array along imaginary lines with a fixed anatomic orientation, following a predefined mapping scheme, covering the entire epicardial surface of the right atrium (RA), Bachmann's bundle (BB), pulmonary vein area (PVA) and left atrium (LA).[18] Omission of areas was avoided at the expense of possible small overlap between adjacent mapping sites. The RA was mapped from the cavo-tricuspid isthmus, shifting perpendicular to the caval veins towards the RA appendage. The PVA was mapped from the sinus transversus fold along the borders of the right and left pulmonary veins down towards the atrioventricular groove. The left atrioventricular groove was mapped from the lower border of the left inferior pulmonary vein towards the LA appendage. BB was mapped from the tip of the LA appendage across the roof of the LA, behind the aorta towards the superior cavo-atrial junction.

Five seconds of stable SR were recorded from every mapping site, including a surface ECG lead, a calibration signal of 2 mV and 1000 ms, a bipolar reference EGM and all unipolar epicardial EGMs. Data was stored on a hard disk after amplification (gain 1000), filtering (bandwidth 0.5–400 Hz), sampling (1 kHz) and analogue-to-digital conversion (16 bits). Bipolar EGMs were created by subtracting two neighboring unipolar EGMs in horizontal (bipolar-x) and vertical direction (bipolar-y) and subsequently filtered (bandwidth 30–400 Hz) as demonstrated in *Figure 1A*.

Omnipolar voltage mapping

7

Omnipolar EGMs were created from the bipolar EGMs using a technique described by Deno et al.[10] Within a square area defined by 4 adjacent electrodes (a clique), omnipolar EGMs were used to mathematically obtain bipolar EGMs in any direction without physically rotating the sensing electrodes of the bipolar pair. As demonstrated in *Figure 1B*, within a clique, a 2-dimensional voltage vector $\vec{v}(t)$ is derived from an electric field of a passing activation wavefront from which the maximal extend of two orthogonal bipolar EGMs is calculated over the interval (T)[9]:

$$V_{max} = \max_{t_i, t_j \in T}\left\{\left|\vec{v}(t_i) - \vec{v}(t_j)\right|\right\}$$

V_{max} corresponds to the peak-to-peak amplitude of a bipolar voltage signal obtained along the unit vector direction $\hat{m}$ where t_i and t_j are now the times associated with V_{max} in which $t_i > t_j$:

$$\hat{m} = \frac{\vec{v}(t_i) - \vec{v}(t_j)}{V_{max}}$$

V_{max} provides an objective measure of the largest possible bipolar EGM within a clique without the ambiguity of electrode orientation and is used to describe omnipolar EGM voltages.

Data analysis

Unipolar, bipolar and omnipolar EGMs were semi-automatically analyzed using custom-made software. The steepest negative slope of a unipolar atrial potential was marked as the local activation time (LAT), providing that the amplitude of the deflection was at least two times the signal-to-noise ratio of the unipolar EGM. Double and fractionated potentials were defined as potentials with respectively 2 and ≥3 deflections. All annotations were manually checked with a consensus of two investigators. CV was computed from LATs using discrete velocity vectors as previously described.[23] Signal voltage was defined as the peak-to-peak amplitude of the steepest deflection (unipolar) or highest peak (bipolar and omnipolar) as demonstrated in *Figure 1B*. As omnipolar EGMs can only be derived in square areas, unipolar and bipolar potentials were correlated to each other in areas of 2×2 mm -a clique- which contain 4 unipolar EGMs, the corresponding bipolar-x/y EGMs and the omnipolar EGM (*Figure 1A*). Subsequently, the maximal potential voltage of the unipolar EGMs, maximal potential voltage of the bipolar-x/y EGMs and omnipolar EGM pertaining to that area were computed, resulting in 3 values ($V_{uni,max}$, $V_{bi,max}$ and $V_{omni,max}$). In addition, the mean of the 4 CV estimates derived from the 4 unipolar LATs was used as indication of the CV through the 2×2 mm area. As a bipolar voltage cut-off of ≤0.5 mV is most frequently used in daily clinical practice to identify LVAs, we also used this value as the "gold standard" to identify low-voltage cliques.[24] Areas corresponding to a mean CV of 0 cm/s were excluded to avoid inclusion of far-field potentials.

Table 1 – Baseline characteristics.

Patients	21
Male	9 (43)
Age (y)	48±13 (18–70)
Type of congenital heart defect	
• ASD type I	1 (5)
• ASD type II	12 (57)
• SVD with PAPVR	7 (33)
• PAPVR	1 (5)
BMI (kg/m²)	28.7±4.7
RA volume (ml/m²)	53±16
RA dilatation	19 (90)
LA dimension (cm/m²)	2.0 [1.9–2.2]
LA dilatation	5 (24)
Left ventricular function	
• Normal	19 (90)
• Mild dysfunction	1 (5)
• Moderate dysfunction	1 (5)
Right ventricular function*	
• Normal	17 (81)
• Mild dysfunction	1 (5)
• Moderate dysfunction	1 (5)
Antiarrhythmic agents	
• Class II	6 (29)

Values are presented as N (%), mean ± standard deviation (min–max) or median [interquartile ranges]. *Not available in 2 patients. **ASD** = atrial septal defect; **BMI** = body mass index; **LA** = left atrium; **PAPVR** = partial abnormal pulmonary venous return; **SVD** = sinus venosus defect; **RA** = right atrium.

Statistical analysis

Normally distributed data are expressed as mean ± standard deviation, whereas skewed data are expressed as median [25th–75th percentile]. Clinical characteristics were compared using Student's *t*-test or Mann-Whitney U test when appropriate. Categorical data are expressed as numbers (percentages) and analyzed with a χ^2 or Fisher exact test. Paired voltage data was analyzed between patients using a Wilcoxon signed-rank test. A *p*-value <0.05 was considered statistically significant. A Bonferroni correction was applied when appropriate.

Results

Study population

Clinical characteristics of the study population (N=21, age 48±13 years, 9 male (43%)) are summarized in *Table 1*. Most patients had an atrial septal defect (ASD) type II (N=12, 57%). The other patients had a sinus venosus defect (SVD) with partial abnormal pulmonary venous return (PAPVR, N=7), and ASD type I (N=1) and isolated PAPVR (N=1). Right and left atrial dilatation was respectively present in 19 (90%) and 5 (24%) patients. Patients had no history of atrial arrhythmias.

Unipolar, bipolar and omnipolar voltage maps

In the entire study population, a total of 193 mapping locations resulted in 175,667 unipolar and 306,685 bipolar recordings from which 146,015 cliques were created. Within the 2×2 mm areas, there were considerable directional differences in bipolar voltages. The largest bipolar voltage was on average 1.66 (ranging from 1.0 to 59.0) times larger than the corresponding perpendicular bipolar voltages.
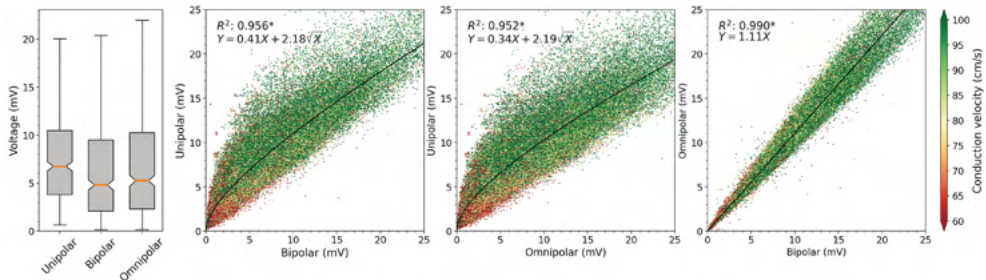
Figure 2 – Relation between unipolar, bipolar and omnipolar voltages and CV. Quantitative analysis of unipolar clique voltage ($V_{uni,max}$), bipolar clique voltage ($V_{bi,max}$), and omnipolar clique voltage ($V_{omni,max}$) distributions (left) and the similarity of $V_{uni,max}$, $V_{bi,max}$, and $V_{omni,max}$ voltages (other). The conduction velocity (CV) is color-coded, ranging from 60 to 100 cm/s, visualized in which green represents high CV and red low CV. A black line indicates the ordinary least squares prediction. Statistical significance is indicated by an asterisk (p<0.001).

7

Differences in voltage maps constructed by using unipolar and corresponding bipolar-x, bipolar-y or omnipolar EGMs are illustrated in *Figure 1B*. *Figure 1C* shows the EGMs derived from the highlighted area at the bottom of the mapping array. The largest unipolar EGM had an amplitude of 13.9 mV, while its corresponding bipolar-x and bipolar-y EGMs had an amplitude of respectively 10.8 mV and 13.7 mV. The amplitude of the corresponding omnipolar EGM was larger compared to the largest bipolar-x/y EGM (16.2 mV). *Figure 1D* shows the EGMs derived from the highlighted area at the top of the mapping array containing smaller voltages. Likewise, the largest unipolar EGM (2.23 mV) was much larger than the corresponding bipolar-x (0.39 mV) and bipolar-y EGMs (0.66 mV). However, it now critically depends on the bipolar electrode orientation whether this clique was identified as LVA as only the bipolar-y EGM was >0.5 mV. Furthermore, the corresponding omnipolar EGMs only resulted in an amplitude slightly larger than the largest bipolar-x/y EGM (0.67 mV). As a result, there are differences between corresponding unipolar, bipolar and omnipolar voltage maps as demonstrated in *Figure 1B*.

The left panel of *Figure 2* demonstrates the distribution of $V_{uni,max}$, $V_{bi,max}$ and $V_{omni,max}$ from all cliques obtained from all patients. $V_{uni,max}$ was larger than both $V_{bi,max}$ and $V_{omni,max}$ (7.08 [4.22–10.59] mV vs. 5.27 [2.39–9.56] mV and 5.77 [2.58–10.52] mV respectively, p<0.001 for each). In addition, $V_{omni,max}$ was larger than $V_{bi,max}$ (5.77 [2.58–10.52] mV vs. 5.27 [2.39–9.56] mV, p<0.001).

Relationship between unipolar, bipolar and omnipolar voltages and conduction velocity

The right panel of *Figure 2* demonstrates the relationship between $V_{uni,max}$, $V_{bi,max}$ and $V_{omni,max}$. The mean CV of each clique was 92.0 [73.2–109.1] cm/s and is indicated by color-coded scatters; larger voltages (both $V_{uni,max}$ and $V_{bi,max}$) are associated with higher CVs. Double and fractionated potentials were present in 36.9% of the cliques. In only 24.7% of the cliques, bipolar voltages were larger than unipolar voltages. As a consequence, there was a strong inversely quadratic relation with linear component (R^2=0.956; $Y \sim 0.41X + 2.18\sqrt{X}$) between $V_{uni,max}$ and $V_{bi,max}$. Similar results were obtained by comparing $V_{uni,max}$ and $V_{omni,max}$ (R^2=0.952; $Y \sim 0.34X + 2.19\sqrt{X}$). Furthermore, there was a strong, positive linear correlation (R^2=0.990; $Y \sim 1.11X$) between $V_{bi,max}$ and $V_{omni,max}$. When all $V_{bi,max}$ are subdivided into three groups (<0.5 mV, 0.5–1.0 mV and >1.5 mV) and compared with the corresponding $V_{omni,max}$, there was an increasing influence of $V_{omni,max}$ on the different $V_{bi,max}$ groups (<0.5 mV: 4.4%; 0.5–1.0 mV: 5.0%; >1.5 mV: 8.8%; all p<0.001). However, in terms of absolute values, the added effect of $V_{omni,max}$ on lower voltages was only minimal (±0.02 mV).

Table 2 – Characteristics of low-voltage areas (N=146,015).

		Bipolar LVA	Omnipolar LVA
% LVA		4.30	3.77
$V_{uni,max}$	LVA (mV)	1.36 [0.99–1.86]	1.31 [0.97–1.80]
	normal (mV)	7.33 [4.60–10.80]	7.30 [4.55–10.77]
CV	LVA (cm/s)	60.2 [37.2–85.2]	58.7 [35.2–83.7]
	normal (cm/s)	92.9 [74.7–109.6]	92.8 [74.6–109.5]
Fractionation	LVA (%)	48.1	49,3
	normal (%)	36.4	36.4

CV = conduction velocity; **LVA** = low-voltage area; **$V_{uni,max}$** = unipolar clique voltage.

Characteristics of low-voltage areas

In our data, the 5th percentile of the relative frequency $V_{bi,max}$ histogram was 0.55 mV, which is comparable to the voltage cut-off value of ≤0.5 mV which is most frequently used in daily clinical practice to identify LVAs. We therefore also used this value to identify low-voltage cliques.

Application of this threshold on $V_{bi,max}$ and $V_{omni,max}$ is demonstrated in *Figure 3*. As shown in the left panel, respectively 4.30% of $V_{bi,max}$ and 3.77% of $V_{omni,max}$ were classified as LVA; the corresponding $V_{uni,max}$ and CV of these cliques are listed in *Table 2*. For both recording techniques, $V_{uni,max}$ and CV was lower in LVAs, and double and fractionated potentials were more often recorded from these areas compared to 'normal' areas (p<0.001 for all). Using only either the bipolar-x or -y values of all cliques, respectively 37% and 21% additional cliques were classified as LVA.

When the threshold of 0.5 mV was applied to $V_{omni,max}$ clique values, 14.6% of the bipolar LVA cliques were now identified as 'normal' area. Although the majority of $V_{bi,max}$ in these areas were in a relatively small range, a great variety of $V_{uni,max}$ and CV was found ($V_{bi,max}$ of 0.46 [0.41–0.48] mV ranging from 0.17 to 0.499 mV, corresponding $V_{uni,max}$ of 1.77 [1.31–2.27] mV and CV of 69.1 [47.0–92.6] cm/s). On the other hand, 2.6% of the omnipolar LVA cliques (0.1% of all cliques) had 'normal' $V_{bi,max}$ values and were so falsely identified as LVA. However, this only accounted for cliques which were already very close to 0.5 mV; $V_{omni,max}$ in these LVAs was 0.49 [0.47–0.49] mV against the corresponding $V_{bi,max}$ of 0.52 [0.51–0.53] mV.
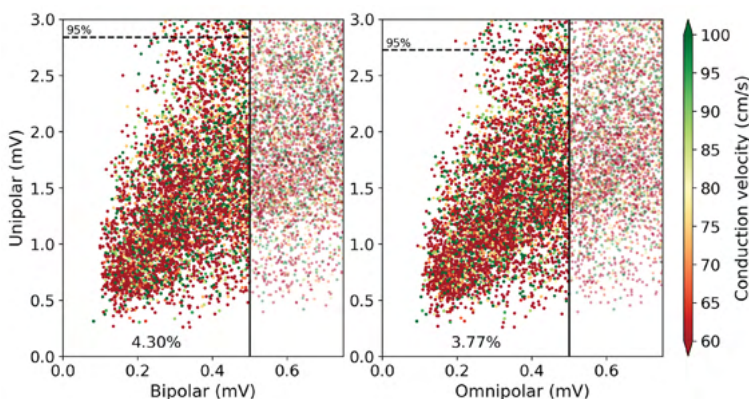
Figure 3 – Characteristics of LVAs. Visualization of $V_{uni,max}$ in LVAs (left of black solid line) identified using the gold standard threshold of 0.5 mV applied on $V_{bi,max}$ (left panel) and $V_{omni,max}$ (right panel). Conduction velocity (CV) is color-coded visualized in which green represents high CV and red low CV. The dashed line indicates the 95th percentile of $V_{uni,max}$ within the corresponding LVA. 4.30% of $V_{bi,max}$ was classified as LVA and 3.77% of $V_{omni,max}$. **CV** = conduction velocity; **LVA** = low-voltage area; **$V_{bi,max}$** = bipolar clique voltage; **$V_{omni,max}$** = omnipolar clique voltage; **$V_{uni,max}$** = unipolar clique voltage.
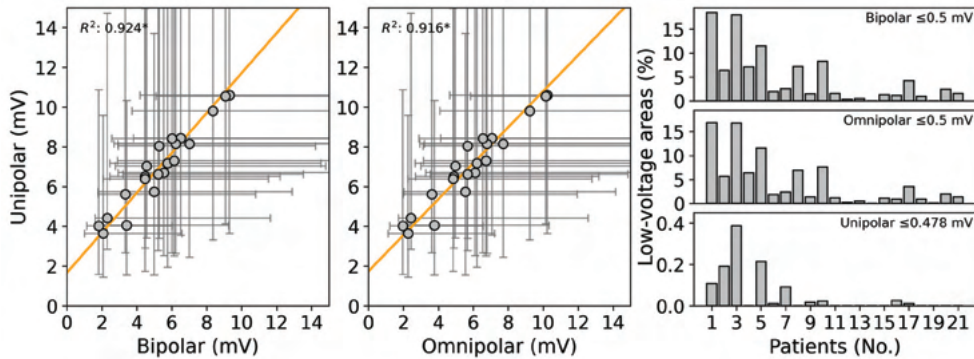
Figure 4 – Patient voltage fingerprints. Relation of the patient voltage distributions (left and center). Each dot represents the median value of the corresponding individual unipolar and bipolar voltage distribution (*left*) or unipolar and omnipolar voltage distributions (*center*). The error bars represent the 25th and 75th quartile of each distribution. The relationship is illustrated by the orange line. Statistical significance of the relationship is indicated by an asterisk (p<0.01). The right panels show the amount of LVAs (top: bipolar ≤0.5 mV; middle: omnipolar ≤0.5 mV; and bottom: unipolar ≤0.478 mV) in each patient separately ranked by the median bipolar voltage.

7

Does a unipolar low-voltage threshold exist?

As demonstrated in *Figure 2*, low $V_{bi,max}$ and $V_{omni,max}$ are related to $V_{uni,max}$ by, in particular, the inversely quadratic component of the relationships. Therefore, a small increase in either $V_{bi,max}$ or $V_{omni,max}$ will result in a relatively large increase in $V_{uni,max}$. This relation can be used to determine a unipolar threshold to identify the LVAs using only $V_{uni,max}$. In order to detect the "gold standard" bipolar LVAs of ≤0.5 mV with a precision of at least 90%, a unipolar threshold of 0.53 mV should be used. Vice versa, by using this unipolar threshold only 1.8% of the bipolar LVAs was classified as true positive. On the other hand, applying the "gold standard" threshold of ≤0.5 mV for $V_{omni,max}$, a unipolar threshold of 0.48 mV should be used. Using this unipolar threshold only 1.1% of the omnipolar LVAs could be identified as true positive. Hence, using solely $V_{uni,max}$, only a limited number of these "gold standard" LVAs could be correctly identified and therefore usage of $V_{uni,max}$ alone is not suitable in identifying these LVAs.

Patient voltage Fingerprints

Next, all types of clique voltages were collected for each individual patient. As illustrated in *Figure 4*, there was a strong linear relationship between median $V_{uni,max}$ and corresponding median $V_{bi,max}$ and $V_{omni,max}$ for every patient separately (R^2=0.924, p<0.01 and R^2=0.916, p<0.01 respectively). Voltage distribution of $V_{uni,max}$, $V_{bi,max}$ and $V_{omni,max}$ varied considerably between various patients, as listed in *Table 2*. The largest median voltages were found in $V_{uni,max}$ (7.03 [5.74–8.15] mV), followed by $V_{omni,max}$ (5.68 [4.85–6.80] mV) and $V_{bi,max}$ (5.27 [4.47–6.22] mV, p<0.001 for each).

Table 3 – Regional voltage mapping results (N=21).

Parameter	RA	BB	PVA	LA	*p*-value
Unipolar (mV)	6.21 [5.30–7.67]	6.81 [5.31–9.15]	6.86 [3.64–8.32]	9.65 [7.16–10.73]	0.016
Bipolar (mV)	4.91 [3.93–6.57]	4.30 [2.54–6.11]	4.49 [1.67–6.84]	6.88 [5.03–9.87]	0.022
Omnipolar (mV)	5.55 [4.23–7.28]	4.73 [2.69–6.37]	4.80 [1.72–7.40]	7.55 [5.43–11.11]	0.019
CV (cm/s)	90.7 [86.7–94.4]	93.9 [83.7–99.0]	96.0 [88.6–104.7]	93.3 [87.5–96.0]	0.299
LVA bipolar (%)	1.9 [0.5–2.7]	1.2 [0.0–10.6]	1.9 [0.0–17.8]	0.2 [0.0–2.4]	0.441
LVA omnipolar (%)	1.2 [0.2–2.2]	0.2 [0.0–8.8]	1.6 [0.0–10.5]	0.1 [0.0–2.1]	0.356

CV = conduction velocity; **LVA** = low-voltage area; **RA** = right atrium; **BB** = Bachmann's bundle, **PVA** = pulmonary vein area; **LA** = left atrium.

Applying the gold standard threshold of 0.5 mV on $V_{bi,max}$, LVAs were present in all patients (1.9 [1.1–7.1] %, ranging from 0.01% to 18.5%), while applying this threshold on $V_{omni,max}$, LVAs were present in only 19 out of 21 patients (1.8 [0.9–4.9] %, ranging from 0.2% to 16.8%). The amount of LVAs was smaller when using $V_{omni,max}$ compared to $V_{bi,max}$ (p<0.001). As demonstrated in the left panel of *Figure 4*, patients with higher median $V_{bi,max}$ had smaller amounts of LVAs compared to patients with lower median $V_{bi,max}$. When applying the unipolar threshold of ≤0.48 mV on $V_{uni,max}$, LVAs were only present in patients who also have a large amount of bipolar and omnipolar LVAs.

Next, all parameters were subdivided according to the corresponding atrial recording regions (RA, BB, PVA and LA) and are demonstrated in *Table 3*. $V_{uni,max}$ was larger at LA compared to all other atrial regions (9.65 [7.16–10.73] mV vs. RA: 6.21 [5.30–7.67] mV, BB: 6.81 [5.31–9.15] mV and PVA: 6.86 [3.64–8.32] mV, all P<0.0083), and $V_{bi,max}$ and $V_{omni,max}$ were larger at LA compared to RA and BB ($V_{bi,max}$ LA: 6.88 [5.03–9.87] mV vs. RA: 4.91 [3.93–6.57] mV and BB: 4.30 [2.54–6.11] mV; $V_{omni,max}$ LA: 7.55 [5.43–11.11] mV vs. RA: 5.55 [4.23–7.28] mV and BB: 4.73 [2.69–6.37] mV, all P<0.0083). There were no regional differences in CV, amount of bipolar LVAs and omnipolar LVAs.

Discussion

High resolution voltage mapping in patients with congenital heart disease demonstrated that within an area of 2×2 mm, omnipolar voltages were larger than maximal bipolar voltages but smaller than maximal unipolar voltages. There were considerable directional differences in bipolar voltages; more than 20% of the largest bipolar voltage differed even more than 50% from the corresponding perpendicular bipolar voltages. These differences have a major impact on identification of LVAs. Using omnipolar voltages, 15% of the bipolar LVAs were not identified, although it also resulted in 2.6% additional LVAs which had 'normal' bipolar voltages. All LVAs contained a large variety of unipolar voltages and even though CV was generally decreased, high CVs and large unipolar voltages could still be found within these areas. Due to high inter-individual unipolar voltage variations within LVAs, no clear unipolar threshold corresponded with "correct" identification of LVAs in patients with interatrial left-to-right shunts. Although all different types of voltage maps demonstrated interregional differences, no predilection sites for LVAs were found.

Voltage mapping

In current clinical practice, atrial arrhythmogenic areas are identified using bipolar voltage mapping or by visualization of fibrotic areas using imaging techniques such as MRI. Although there is still limited theoretical understanding of the determinants of bipolar EGMs, their amplitude has become the backbone of clinical substrate mapping approaches.[25] Areas with low bipolar voltages are regarded as indicators of arrhythmogenic tissue and used as target sites for ablation therapy.[2] However, bipolar voltage is not only affected by the underlying myocardial tissue, but also by tissue proximity, cycle length, CV, fiber orientation and curvature. Additionally, characteristics of the recording electrode such as the angle of the electrodes on tissue, interelectrode distance and electrode size may influence bipolar EGM voltages as well.[1,25-28]

Although frequently debated, a recent study has shown that in simulated and clinical data, the amplitude of bipolar EGMs changes from a maximum value parallel to the propagation direction to 0 mV perpendicular to the propagation direction. This direction dependency may account for up to a 49% difference in bipolar voltage particularly during SR.[4,9,26] In our study, more than 20% of the largest bipolar voltage differed even more than 50% than the

corresponding perpendicular bipolar voltages. Therefore, bipolar EGMs at one orientation could erroneously indicate that certain areas are 'diseased' but not if examined at another orientation. In our study, 3.7% of the investigated areas could be identified as LVA if only one electrode orientation was taken into account. This would have resulted in a LVA overestimation of 17.6%. Therefore, by using solely bipolar EGMs, (non-)arrhythmogenic areas can possibly be misclassified.

To overcome the directional dependency of bipolar voltage mapping, omnipolar EGMs have been introduced to improve substrate mapping by providing wavefront orientation-independent measurements revealing the highest possible bipolar voltage.[9,11] However, the advantage of omnipolar mapping on low-amplitude voltages is relatively low due to its linear relationship with the corresponding bipolar voltages. The same implies for unipolar voltages that are also unaffected by the electrode orientation and electrode distances, although unipolar EGMs are more susceptible to noise and (ventricular) far-field. Moreover, it is assumed that unipolar EGMs have a deeper field of view in the myocardium, which improves detection of intramural and endo- or epicardial arrhythmogenic tissue.[1] This can also explain the large range of unipolar voltages compared to the bipolar voltages within the cliques.

Interrelationship between voltage and conduction velocity

It is generally assumed that bipolar voltage is affected by several factors, including CV.[1] Multiple studies showed clear associations between bipolar voltage and CV, in which it was predominantly stated that areas of low bipolar voltage are associated with low CV.[26,29] Due to the slowed conduction in these areas, neighboring unipolar EGMs may overlap resulting in a low amplitude bipolar EGM. This is similar to constructing a bipolar EGM perpendicular to the propagation direction. In a study of Itoh et al.[30] a logarithmic relationship was found between right atrial CV and local bipolar voltage during atypical atrial flutter. Although in our study larger voltages were associated with higher CVs, we could not find a clear relationship between CV and bipolar voltage as there was too much variation in CV across all recorded bipolar voltages.

Unipolar voltage has also previously been linked to CV. Fast conduction along the longitudinal axis of the atrial fibers is characterized by large unipolar voltages, whereas in areas of slowed conduction unipolar potentials have low amplitude.[31] In addition, loss of S-wave amplitude in patients with paroxysmal AF and decrease of peak negative voltage during atrial flutter have been previously correlated to a decrease of CV.[32,33] This is in accordance with our study, in which lower CVs were predominantly found in areas with lower unipolar voltages.

Ablation targeting low-voltage areas

Multiple ablation strategies of atrial and ventricular tachyarrhythmias target diseased myocardium identified by bipolar voltage, which are associated with structurally remodeled areas with local slowing of conduction. 'Abnormal' LVAs in the atria are usually identified with voltage cut-off values in SR of ≤0.5 mV and scar ≤0.05 mV as it is then indistinguishable from noise.[25,34] However, there is still much debate on which thresholds to use and when classifying tissue as diseased, healthy or as an 'intermediate' zone that does not contain substantial remodeled areas but also not only healthy tissue.[34] In addition, Soejima et al.[35] have shown that there are still be surviving excitable fibers within LVAs which are important pathways within reentry circuits underlying ventricular tachycardias. From our data, it is clear that there is no single straightforward method to identify arrhythmogenic areas, but different grades can be observed.[34]

It becomes even more difficult as directional sensitivity of bipolar EGMs limit the accuracy of these approaches by causing underestimation of bipolar voltage, especially when using narrowly spaced electrodes and in regions with normal CV.[26] Although unipolar EGMs are not affected by directional sensitivity, substrate assessment by solely unipolar voltage is also limited.[36] We found that even in omnipolar LVAs there are still high unipolar voltages and a large variety of CVs. The logarithmic relationship between right atrial CV and bipolar voltage found by Itoh et al.[30] also shows that for a relatively narrow interval of bipolar voltages a broad spectrum of CVs can be found. In this study it was reported that all bipolar voltages ≤0.5 mV covered more than half of the CVs. This is comparable to our results, in which we also found a wide range of CVs within the LVAs. Furthermore, we also demonstrated that unipolar- and bipolar voltages could vary considerably in LVAs. Hence, bipolar voltages do not necessarily represent an arrhythmogenic substrate. For these reasons, fixed voltage thresholds are questionable.

Several studies also reported on the combination of unipolar- and bipolar voltage mapping to characterize the atrial substrate.[15,37,38] Although results were mixed, Chopra et al.[37] proposed that the mismatch between bipolar and unipolar LVAs represents zones of scar that extend deep to and beyond the endocardial abnormal voltage area. This is in line with the deeper field of view of unipolar EGMs. Furthermore, it has been suggested that the bipolar voltage threshold of 0.5 mV overestimates the size of dense scar and still harbors islets and channels of viable tissue, while a unipolar threshold of <1.0 mV showed no discernible or excitable tissue and represents electrically dense scar. LVAs containing both low omnipolar and low unipolar voltage could therefore be more indicative of 'true' arrhythmogenic tissue.

Low-voltage areas and congenital heart disease

Especially in patients with an interatrial shunt, significant inter-individual variation in the spatial distribution of atrial conduction disorders exist even during SR.[38-41] In addition, lower voltages, both unipolar and bipolar, were found in this patient population as compared to patients without structural heart disease, although 'normal' and scar tissue could not clearly be delineated.[17] Larger LVAs in patients with congenital heart disease and complex atrial tachyarrhythmias are associated with worse acute and midterm clinical outcomes.[42] As demonstrated by Houck et al.[39], conduction disorders in patients with an interatrial shunt are most pronounced in the RA and BB. Furthermore, other studies showed the presence of functional conduction delay in the region of the crista terminalis in patients with (chronic) atrial overload, which are related to development of atrial tachyarrhythmias.[24,40,43] In our study, we found a large interindividual and interregional variety of unipolar, bipolar and omnipolar voltages.

Although conduction disorders are frequently present in this patient population, LVAs were not identified in all patients. Specifically, LVAs were most often found at the RA, although the amount of LVAs did not differ between all atrial regions. The patients with LVAs, however, showed not only a large variety in the amount of LVAs, but also corresponding unipolar voltages varied considerably. Also, even though CV was generally decreased, still high CVs were found in these areas while LVAs are commonly considered surrogate markers for diseased atrial tissue with slowed conduction. Therefore, accurate identification of target sites for ablation therapy can be very challenging in this patient population.

Study limitations

This study focused on the comparison of the different voltage mapping methodologies and identification of LVAs without interventions. The next step will be to incorporate the results

of this study with ablation targeting LVAs in order to determine whether the combination of low unipolar and low omnipolar voltage can improve ablation outcomes.

Conclusion

In patients with congenital heart disease, there were considerable discrepancies in the different types of LVAs, which are particularly important as LVAs are considered surrogate markers for arrhythmogenic tissue. There were considerable directional differences in bipolar voltages hampering identification of LVAs. Even using directional independent omnipolar voltage to identify LVAs, high CVs and large unipolar voltages could still be found within these areas. In addition, the added value of omnipolar voltage in identifying LVAs is questionable as the amount of LVAs was only minimally decreased using this technique compared to maximal bipolar clique voltage. Given the various (often non-substrate related) factors affecting bipolar voltage, a combination of low omnipolar and low unipolar voltage may be more indicative of 'true' LVAs rather than only one approach. Future studies are required to determine whether incorporation of unipolar voltage in these techniques to guide ablative therapy increases the ability to identify 'true' LVAs and thus diseased atrial tissue.

7

References

1.   Sim I, Bishop M, O'Neill M, Williams SE. Left atrial voltage mapping: defining and targeting the atrial fibrillation substrate. J Interv Card Electrophysiol. 2019.
2.   Kottkamp H, Bender R, Berg J. Catheter ablation of atrial fibrillation: how to modify the substrate? J Am Coll Cardiol. 2015;65:196-206.
3.   Murphy JG, Gersh BJ, McGoon MD, Mair DD, Porter CJ, Ilstrup DM, McGoon DC, Puga FJ, Kirklin JW, Danielson GK. Long-term outcome after surgical repair of isolated atrial septal defect. Follow-up at 27 to 32 years. N Engl J Med. 1990;323:1645-1650.
4.   Takigawa M, Relan J, Martin R, Kim S, Kitamura T, Frontera A, Cheniti G, Vlachos K, Massoullie G, Martin CA, et al. Effect of bipolar electrode orientation on local electrogram properties. Heart Rhythm. 2018;15:1853-1861.
5.   Yagishita A, Gimbel JR, S DEO, Manyam H, Sparano D, Cakulev I, Mackall J, Arruda M. Long-Term Outcome of Left Atrial Voltage-Guided Substrate Ablation During Atrial Fibrillation: A Novel Adjunctive Ablation Strategy. J Cardiovasc Electrophysiol. 2017;28:147-155.
6.   Rolf S, Kircher S, Arya A, Eitel C, Sommer P, Richter S, Gaspar T, Bollmann A, Altmann D, Piedra C, et al. Tailored atrial substrate modification based on low-voltage areas in catheter ablation of atrial fibrillation. Circ Arrhythm Electrophysiol. 2014;7:825-833.
7.   Cutler MJ, Johnson J, Abozguia K, Rowan S, Lewis W, Costantini O, Natale A, Ziv O. Impact of Voltage Mapping to Guide Whether to Perform Ablation of the Posterior Wall in Patients With Persistent Atrial Fibrillation. J Cardiovasc Electrophysiol. 2016;27:13-21.
8.   Yamaguchi T, Tsuchiya T, Nakahara S, Fukui A, Nagamoto Y, Murotani K, Eshima K, Takahashi N. Efficacy of Left Atrial Voltage-Based Catheter Ablation of Persistent Atrial Fibrillation. J Cardiovasc Electrophysiol. 2016;27:1055-1063.
9.   Haldar SK, Magtibay K, Porta-Sanchez A, Masse S, Mitsakakis N, Lai PFH, Azam MA, Asta J, Kusha M, Dorian P, et al. Resolving Bipolar Electrogram Voltages During Atrial Fibrillation Using Omnipolar Mapping. Circ Arrhythm Electrophysiol. 2017;10.
10. Deno DC, Balachandran R, Morgan D, Ahmad F, Masse S, Nanthakumar K. Orientation-Independent Catheter-Based Characterization of Myocardial Activation. IEEE Trans Biomed Eng. 2017;64:1067-1077.
11. Masse S, Magtibay K, Jackson N, Asta J, Kusha M, Zhang B, Balachandran R, Radisic M, Deno DC, Nanthakumar K. Resolving Myocardial Activation With Novel Omnipolar Electrograms. Circ Arrhythm Electrophysiol. 2016;9:e004107.
12. Hutchinson MD, Gerstenfeld EP, Desjardins B, Bala R, Riley MP, Garcia FC, Dixit S, Lin D, Tzou WS, Cooper JM, et al. Endocardial unipolar voltage mapping to detect epicardial ventricular tachycardia substrate in patients with nonischemic left ventricular cardiomyopathy. Circ Arrhythm Electrophysiol. 2011;4:49-55.
13. Polin GM, Haqqani H, Tzou W, Hutchinson MD, Garcia FC, Callans DJ, Zado ES, Marchlinski FE. Endocardial unipolar voltage mapping to identify epicardial substrate in arrhythmogenic right ventricular cardiomyopathy/dysplasia. Heart Rhythm. 2011;8:76-83.
14. Enriquez A, Ali FS, Boles U, Michael K, Simpson C, Abdollah H, Baranchuk A, Redfearn D. Unipolar voltage threshold of 5.0 mV is optimal to localize critical isthmuses in post-infarction patients presenting with ventricular tachycardia. Int J Cardiol. 2015;187:438-442.
15. Spears DA, Suszko AM, Dalvi R, Crean AM, Ivanov J, Nanthakumar K, Downar E, Chauhan VS. Relationship of bipolar and unipolar electrogram voltage to scar transmurality and composition derived by magnetic resonance imaging in patients with nonischemic cardiomyopathy undergoing VT ablation. Heart Rhythm. 2012;9:1837-1846.
16. Yalin K, Golcuk E, Bilge AK, Aksu T, Buyukbayrak H, Tiryakioglu SK, Emet S, Adalet K. Combined analysis of unipolar and bipolar voltage mapping identifies recurrences after unmappable scar-related ventricular tachycardia ablation. Europace. 2015;17:1580-1586.
17. de Groot NM, Schalij MJ, Zeppenfeld K, Blom NA, Van der Velde ET, Van der Wall EE. Voltage and activation mapping: how the recording technique affects the outcome of catheter ablation procedures in patients with congenital heart disease. Circulation. 2003;108:2099-2106.
18. Lanters EA, van Marion DM, Kik C, Steen H, Bogers AJ, Allessie MA, Brundel BJ, de Groot NM. HALT & REVERSE: Hsf1 activators lower cardiomyocyt damage; towards a novel approach to REVERSE atrial fibrillation. J Transl Med. 2015;13:347.
19. van der Does LJ, Yaksh A, Kik C, Knops P, Lanters EA, Teuwen CP, Oei FB, van de Woestijne PC, Bekkers JA, Bogers AJ, et al. QUest for the Arrhythmogenic Substrate of Atrial fibRillation in Patients Undergoing Cardiac Surgery (QUASAR Study): Rationale and Design. J Cardiovasc Transl Res. 2016;9:194-201.
20. Teuwen CP, Yaksh A, Lanters EA, Kik C, van der Does LJ, Knops P, Taverne YJ, van de Woestijne PC, Oei FB, Bekkers JA, et al. Relevance of Conduction Disorders in Bachmann's Bundle During Sinus Rhythm in Humans. Circ Arrhythm Electrophysiol. 2016;9:e003972.
21. Mouws E, Lanters EAH, Teuwen CP, van der Does L, Kik C, Knops P, Bekkers JA, Bogers A, de Groot NMS. Epicardial Breakthrough Waves During Sinus Rhythm: Depiction of the Arrhythmogenic Substrate? Circ Arrhythm Electrophysiol. 2017;10.
22. Kik C, Mouws E, Bogers A, de Groot NMS. Intra-operative mapping of the atria: the first step towards individualization of atrial fibrillation therapy? Expert Rev Cardiovasc Ther. 2017;15:537-545.
23. van Schie MS, Heida A, Taverne Y, Bogers A, de Groot NMS. Identification of local atrial conduction heterogeneities using high-density conduction velocity estimation. Europace. 2021;23:1815-1825.
24. Sanders P, Morton JB, Davidson NC, Spence SJ, Vohra JK, Sparks PB, Kalman JM. Electrical remodeling of the atria in congestive heart failure: electrophysiological and electroanatomic mapping in humans. Circulation.

2003;108:1461-1468.

25. Josephson ME, Anter E. Substrate Mapping for Ventricular Tachycardia: Assumptions and Misconceptions. JACC Clin Electrophysiol. 2015;1:341-352.

26. Gaeta S, Bahnson TD, Henriquez C. Mechanism and magnitude of bipolar electrogram directional sensitivity: Characterizing underlying determinants of bipolar amplitude. Heart Rhythm. 2020;17:777-785.

27. Blauer JJ, Swenson D, Higuchi K, Plank G, Ranjan R, Marrouche N, Macleod RS. Sensitivity and specificity of substrate mapping: an in silico framework for the evaluation of electroanatomical substrate mapping strategies. J Cardiovasc Electrophysiol. 2014;25:774-780.

28. Kovoor P, Daly M, Pouliopoulos J, Dewsnap MB, Eipper V, Ross DL. Effect of inter-electrode distance on bipolar intramural radiofrequency ablation. Pacing Clin Electrophysiol. 2005;28:514-520.

29. Miyamoto K, Tsuchiya T, Narita S, Yamaguchi T, Nagamoto Y, Ando S, Hayashida K, Tanioka Y, Takahashi N. Bipolar electrogram amplitudes in the left atrium are related to local conduction velocity in patients with atrial fibrillation. Europace. 2009;11:1597-1605.

30. Itoh T, Kimura M, Sasaki S, Owada S, Horiuchi D, Sasaki K, Ishida Y, Takahiko K, Okumura K. High correlation of estimated local conduction velocity with natural logarithm of bipolar electrogram amplitude in the reentry circuit of atrial flutter. J Cardiovasc Electrophysiol. 2014;25:387-394.

31. Spach MS, Miller WT, 3rd, Miller-Jones E, Warren RB, Barr RC. Extracellular potentials related to intracellular action potentials during impulse conduction in anisotropic canine cardiac muscle. Circ Res. 1979;45:188-204.

32. van Schie MS, Starreveld R, Roos-Serote MC, Taverne Y, van Schaagen FRN, Bogers A, de Groot NMS. Classification of sinus rhythm single potential morphology in patients with mitral valve disease. Europace. 2020;22:1509-1519.

33. Huang JL, Tai CT, Lin YJ, Huang BH, Lee KT, Higa S, Yuniadi Y, Chen YJ, Chang SL, Lo LW, et al. Substrate mapping to detect abnormal atrial endocardium with slow conduction in patients with atypical right atrial flutter. J Am Coll Cardiol. 2006;48:492-498.

34. Kottkamp H, Berg J, Bender R, Rieger A, Schreiber D. Box Isolation of Fibrotic Areas (BIFA): A Patient-Tailored Substrate Modification Approach for Ablation of Atrial Fibrillation. J Cardiovasc Electrophysiol. 2016;27:22-30.

35. Soejima K, Stevenson WG, Maisel WH, Sapp JL, Epstein LM. Electrically unexcitable scar mapping based on pacing threshold for identification of the reentry circuit isthmus: feasibility for guiding ventricular tachycardia ablation. Circulation. 2002;106:1678-1683.

36. van Schie MS, Starreveld R, Bogers A, de Groot NMS. Sinus rhythm voltage fingerprinting in patients with mitral valve disease using a high-density epicardial mapping approach. Europace. 2021;23:469-478.

37. Chopra N, Tokuda M, Ng J, Reichlin T, Nof E, John RM, Tedrow UB, Stevenson WG. Relation of the unipolar low-voltage penumbra surrounding the endocardial low-voltage scar to ventricular tachycardia circuit sites and ablation outcomes in ischemic cardiomyopathy. J Cardiovasc Electrophysiol. 2014;25:602-608.

38. De Groot NM, Kuijper AF, Blom NA, Bootsma M, Schalij MJ. Three-dimensional distribution of bipolar atrial electrogram voltages in patients with congenital heart disease. Pacing Clin Electrophysiol. 2001;24:1334-1342.

39. Houck CA, Lanters EAH, Heida A, Taverne Y, van de Woestijne PC, Knops P, Roos-Serote MC, Roos-Hesselink JW, Bogers A, de Groot NMS. Distribution of Conduction Disorders in Patients With Congenital Heart Disease and Right Atrial Volume Overload. JACC Clin Electrophysiol. 2020;6:537-548.

40. Morton JB, Sanders P, Vohra JK, Sparks PB, Morgan JG, Spence SJ, Grigg LE, Kalman JM. Effect of chronic right atrial stretch on atrial electrical remodeling in patients with an atrial septal defect. Circulation. 2003;107:1775-1782.

41. Roberts-Thomson KC, John B, Worthley SG, Brooks AG, Stiles MK, Lau DH, Kuklik P, Shipp NJ, Kalman JM, Sanders P. Left atrial remodeling in patients with atrial septal defects. Heart Rhythm. 2009;6:1000-1006.

42. Mantziari L, Butcher C, Shi R, Kontogeorgis A, Opel A, Chen Z, Haldar S, Panikker S, Hussain W, Jones DG, et al. Characterization of the Mechanism and Substrate of Atrial Tachycardia Using Ultra-High-Density Mapping in Adults With Congenital Heart Disease: Impact on Clinical Outcomes. J Am Heart Assoc. 2019;8:e010535.

43. Olgin JE, Kalman JM, Fitzpatrick AP, Lesh MD. Role of right atrial endocardial structures as barriers to conduction during human type I atrial flutter. Activation and entrainment mapping guided by intracardiac echocardiography. Circulation. 1995;92:1839-1848.
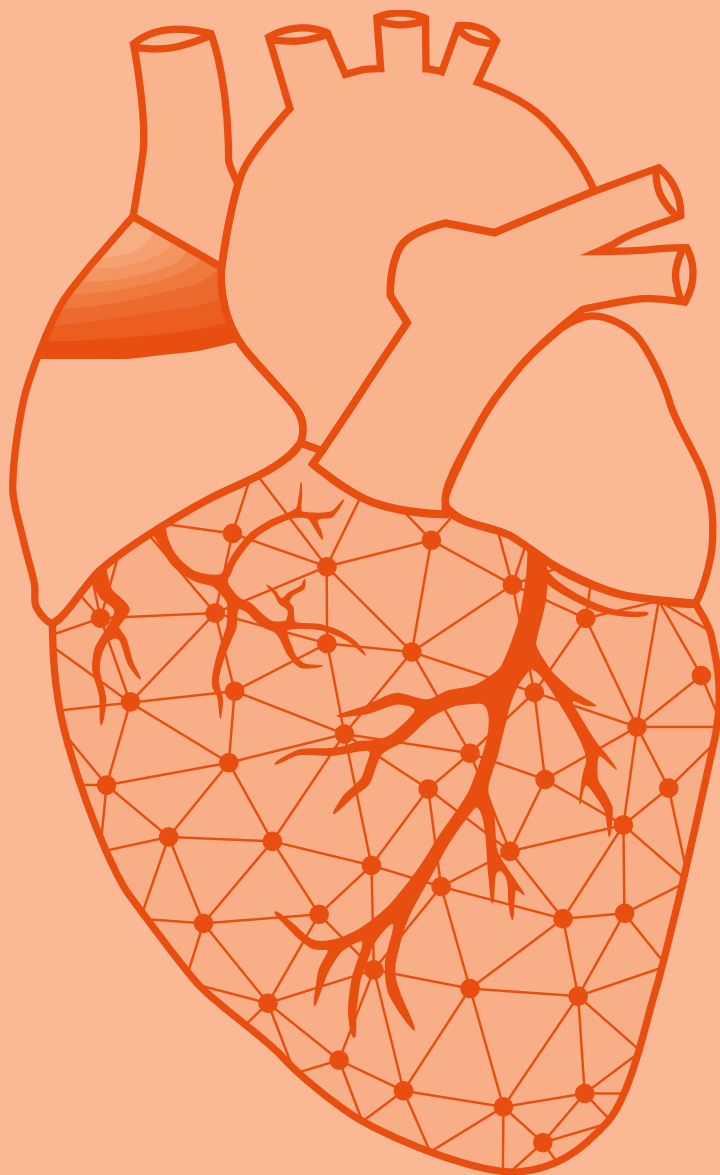
Chapter 8

Detection of endo-epicardial atrial low-voltage areas using unipolar and omnipolar voltage mapping

Mathijs S. van Schie

Paul Knops

Lu Zhang

Frank R.N. van Schaagen

Yannick J.H.J. Taverne

Natasja M.S. de Groot

Abstract

Background: Low-voltage areas (LVA) can be located exclusively at either the endocardium or epicardium. This has only been demonstrated for bipolar voltages, but the value of unipolar and omnipolar voltages recorded from either the endocardium and epicardium in predicting LVAs at the opposite layer remains unknown. The goal of this study was therefore to compare simultaneously recorded endo-epicardial unipolar and omnipolar potentials and to determine whether their voltage characteristics are predictive for opposite LVAs.

Methods: Intra-operative simultaneous endo-epicardial mapping (256 electrodes, interelectrode distances 2 mm) was performed during sinus rhythm at the right atrium in 93 patients (67 ± 9 years, 73 male). Cliques of four electrodes (2×2 mm) were used to define maximal omnipolar ($V_{omni,max}$) and unipolar ($V_{uni,max}$) voltages. LVAs were defined as $V_{omni,max}$ ≤0.5 mV or $V_{uni,max}$ ≤1.0 mV.

Results: The majority of both unipolar and omnipolar LVAs were located at only the endocardium (74.2% and 82.0% respectively) or epicardium (52.7% and 47.6% respectively). Of the endocardial unipolar LVAs, 25.8% were also located at the opposite layer and 47.3% vice-versa. In omnipolar LVAs, 18.0% of the endocardial LVAs were also located at the epicardium and 52.4% vice-versa. The combination of epicardial $V_{uni,max}$ and $V_{omni,max}$ was most accurate in identifying dual-layer LVAs (50.4%).

Conclusion: Unipolar and omnipolar LVAs are frequently located exclusively at either the endocardium or epicardium. Endo-epicardial LVAs are most accurately identified using combined epicardial unipolar and omnipolar voltages. Therefore, a combined endo-epicardial unipolar and omnipolar mapping approach is favored as it may be more indicative of possible arrhythmogenic substrates.

Journal site

Introduction

Endocardial bipolar voltage mapping has emerged as an invasive tool for defining potential target sites for ablation therapy of atrial tachyarrhythmia such as atrial fibrillation (AF). Low-voltage areas (LVA) are commonly considered surrogate markers for areas of conduction disorders, which play a key role in perpetuation of AF.[1,2] However, the efficacy of such bipolar voltage-guided ablation strategies remains controversial. Especially in patients with persistent AF, the presence of intramural or epicardial substrate limits the efficacy of endocardial ablation strategies.[3] Recently, Piorkowski et al.[4] showed that bipolar LVAs can also be located exclusively at either the endocardium or epicardium, therefore favoring an endo-epicardial ablation approach.

8

We demonstrated that identification of LVAs was considerably directional dependent when using bipolar voltages.[5] Bipolar LVAs could also contain large unipolar voltages. In addition, there were not solely conduction disorders within LVAs, but also high conduction velocities (CV). It could therefore be that the bipolar low-voltage threshold overestimates the size of dense scar and still harbors islets and channels of viable tissue.[6]

Endocardial bipolar recordings are still mainly used to detect scar tissue areas as it represents more local activity. In the ventricles it has been demonstrated that unipolar voltage mapping is preferred to identify intramural or epicardial substrates as unipolar electrograms (EGM) comprise a larger region of myocardial electrical activity.[1] On the other hand, omnipolar voltage mapping can be used to extract maximal bipolar voltage from a collection of EGMs in order to minimize directional differences of bipolar voltages. A combination of unipolar and omnipolar voltage may therefore provide additional information on the underlying tissue and it may also be more indicative of transmural substrates.[5,6]

It, however, remains unknown whether simultaneously recorded atrial endo- and epicardial unipolar and omnipolar voltages are complementary or contradictory on identifying LVAs at the opposite layer. We therefore performed simultaneously endo-epicardial high-density mapping to 1) examine endo- and epicardial characteristics of unipolar and omnipolar voltages, 2) explore the relation between various types of voltages in identification of LVAs from an endocardial and epicardial point of view and 3) examine whether characteristics of LVAs can be predictive for LVAs at the opposite layer.

Materials and Methods

Study population

The study population consisted of 93 successive adult patients undergoing elective open heart coronary artery bypass grafting, aortic or mitral valve surgery or a combination of valvular surgery and bypass grafting in the Erasmus Medical Center Rotterdam. This study was approved by the institutional medical ethical committee (MEC2015-373). Written informed consent was obtained from all patients and patient characteristics (e.g., age, medical history and cardiovascular risk factors) were obtained from the patient's medical record.

Simultaneous endo-epicardial mapping procedure

An overview of the methodology is provided in *Figure 1A* and previously described in detail.[7] Two electrode arrays, each containing 128 (8×16) unipolar electrodes with a diameter of 0.45 mm and 2 mm interelectrode spacing, were secured on 2 bendable spatulas and were located on the exact opposite side of each other. A temporally bipolar epicardial pacemaker
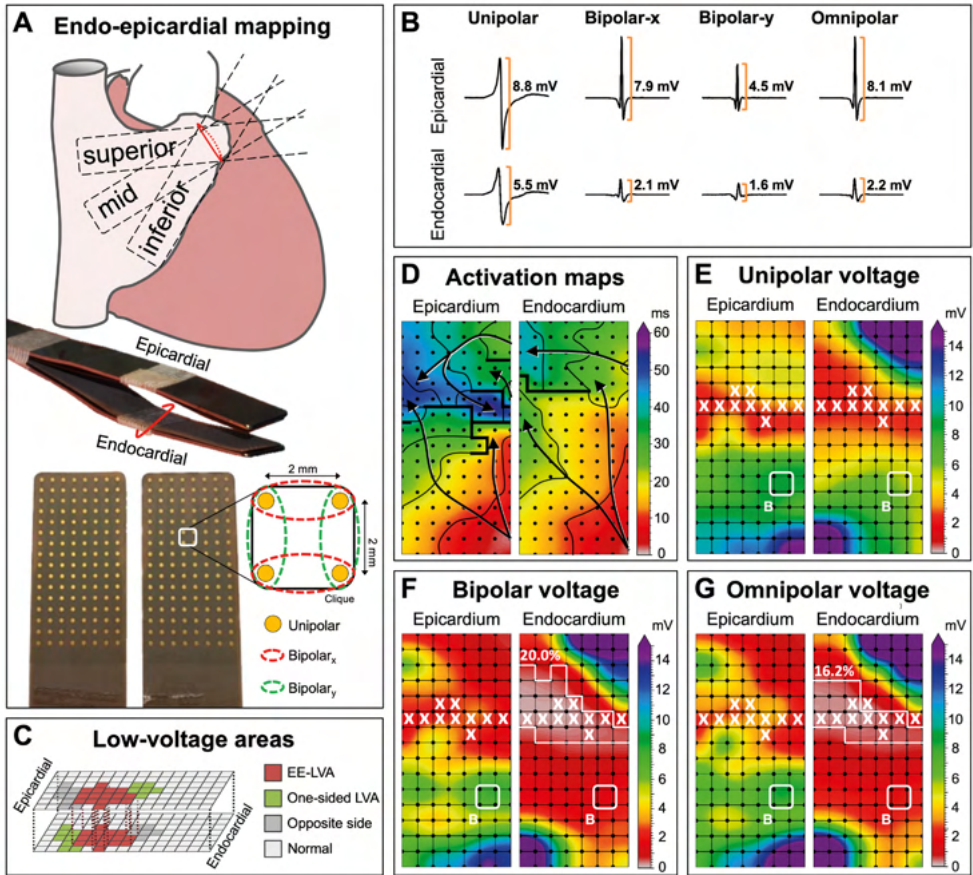
Figure 1 – Construction of unipolar, bipolar and omnipolar voltages in 2×2 mm cliques. *Panel A*: Two high-density electrode arrays consisting of 128 unipolar electrodes are fixed together. One array was placed on the epicardium and one array is introduced into the RA using the incision for venous cannulation to map the endocardium and epicardium simultaneously. The RA was mapped with the tip of the electrode arrays toward the inferior vena cava (inferior), the superior vena cava (superior) and in between, toward the terminal crest (mid). For each square area, enclosed by 4 electrodes, 4 unipolar EGMs and matched bipolar and omnipolar EGMs were derived from 2 electrode orientations (along the vertical y-axis [green] and horizontal x-axis [red]) as indicated by the dotted lines. *Panel B*: Examples of a unipolar, horizontal bipolar-x, vertical bipolar-y and omnipolar EGM recorded from both the epicardium (upper) and endocardium (lower). The two bipolar EGMs differed considerably, illustrating the electrode orientation dependence of bipolar mapping. Omnipolar mapping provides electrode orientation-independent voltages that are larger than the bipolar with the largest measurable peak-to-peak voltage, in both cases the vertical bipolar-y EGMs. *Panel C*: LVAs can be either located at solely the endocardium or epicardium (green) or at both sides (red). The corresponding clique at the exact opposite side is highlighted (grey). The other cliques are then indicated as normal voltage (light grey). *Panel D*: Example of endo-epicardial activation time maps with isochrones drawn at every 10 ms. Arrows indicate the main direction of the propagation wavefront and thick black lines indicate areas of conduction block (time difference between adjacent electrodes ≥12 ms). *Panels E-G*: Peak-to-peak voltages of corresponding EGMs are used to create different voltage maps. Bipolar voltage map illustrates the maximal bipolar voltage in both horizontal and vertical orientations within one clique. LVAs are highlighted by a white line and areas of EEA are indicated by a white X. In this example, endocardial bipolar and omnipolar LVA are present in respectively 20.0% and 16.2% of the cliques. EEA was present in 9.5% of the cliques at both the endocardium and epicardium. **EEA** = endo-epicardial asynchrony; **EGM** = electrogram; **(EE-)LVA** = (endo-epicardial-)low-voltage area.

wire attached to the right atrial (RA) free wall served as a reference electrode and the indifferent electrode consisted of a steel wire fixed to subcutaneous tissue of the thoracic cavity. Simultaneous endo- and epicardial mapping was performed after heparinization and arterial cannulation but before commencement of extracorporeal circulation. One spatula

(marked as the endocardial electrode array) was introduced in the RA after incising the RA appendage and closed with the purse-string suture. To prevent overlap of recording areas near the right atrial incision, the endocardial electrode array was introduced into the RA for at least 1.5 cm extra after introducing the last row of electrodes. Unipolar electrograms (EGMs) were recorded for 5 seconds during stable sinus rhythm at the superior, middle and inferior RA free wall (*Figure 1A*), including a surface ECG lead, a calibration signal of 2 mV and 1000 ms and a bipolar reference EGM. Data were stored on a hard disk after amplification (gain 1000), filtering (bandwidth 0.5–400 Hz), sampling (1 kHz) and analogue-to-digital conversion (16 bits).

Omnipolar voltage mapping

In order to create omnipolar EGMs, bipolar EGMs were first created by subtracting two neighboring unipolar EGMs in horizontal (bipolar-x) and vertical direction (bipolar-y) and subsequently filtered (bandwidth 30-400 Hz) as demonstrated in *Figure 1A*. Omnipolar EGMs were then created from these bipolar EGMs as previously described.[5,8] Within a square area defined by 4 adjacent electrodes (a *clique*), omnipolar EGMs were used to mathematically obtain bipolar EGMs in any direction without physically rotating the sensing electrodes of the bipolar pair. Within a clique, a 2-dimensional voltage vector $\vec{v}(t)$ is derived from an electric field of a passing activation wavefront from which the maximal extent of two orthogonal bipolar EGMs is calculated over the interval (T) containing one SR beat[9]:

$$V_{max} = \max_{t_i, t_j \in T}\{|\vec{v}(t_i) - \vec{v}(t_j)|\}$$

V_{max} corresponds to the peak-to-peak amplitude of a bipolar voltage signal obtained along the unit vector direction $\hat{m}$ where t_i and t_j are now the times associated with V_{max} in which $t_i > t_j$:

$$\hat{m} = \frac{\vec{v}(t_i) - \vec{v}(t_j)}{V_{max}}$$

V_{max} provides an objective measure of the largest possible bipolar EGM within a clique without the ambiguity of electrode orientation and is used to describe omnipolar EGM voltages.

Data analysis

Unipolar and omnipolar EGMs were semi-automatically analyzed using custom-made software. The steepest negative slope of a unipolar atrial potential was marked as the local activation time (LAT), providing that the amplitude of the deflection was at least two times the estimated noise level of the unipolar EGM.[10] In case of fractionated potentials, the deflection with the steepest slope was taken as LAT. All annotations were manually checked with a consensus of two investigators. CV was computed at each electrode from LATs using discrete velocity vectors (DVV) as previously described.[11] The DVV method uses all eight neighboring electrodes to compute an average local propagation velocity for the center electrode. Endo-epicardial LAT differences were determined by selecting the median of the LAT differences within the exact opposite electrode and its 8 surrounding electrodes.[12] Potential voltage was defined as the peak-to-peak amplitude of the steepest deflection (unipolar) or highest peak (omnipolar) as demonstrated in *Figure 1B*.

As omnipolar EGMs can only be derived in square areas, unipolar potentials were correlated to each other in areas of 2×2 mm – a *clique* – which contain 4 unipolar EGMs and the corresponding omnipolar EGMs (*Figure 1A*). Subsequently, the maximal potential voltage

Table 1 – Baseline characteristics.

Patients	N=93
Male	73 (78.5%)
Age (y)	67 [61–72]
BMI (kg/m²)	28.0 [24.6–31.1]
Underlying heart disease	
• iHD	47 (50.5%)
• vHD	24 (25.8%)
• cHD	21 (22.6%)
History of AF	37 (39.8%)
• Paroxysmal	31 (33.3%)
• Persistent	4 (4.3%)
• Long-standing persistent	2 (2.2%)
Cardiovascular risk factors	
• Hypertension	56 (60.2%)
• Diabetes mellitus	32 (34.4%)
• Hypercholesterolemia	50 (53.8%)
• Left ventricular ejection fraction <40%	12 (12.9%)
Antiarrhythmic agents	
• Class I	1 (1.1%)
• Class II	64 (68.8%)
• Class III	6 (6.5%)
• Class IV	7 (7.5%)

Values are presented as N (%) or median [interquartile ranges]. **BMI** = body mass index; **iHD** = ischemic heart disease; **vHD** = valvular heart disease; **cHD** = combined heart disease; **AF** = atrial fibrillation; **LVEF** = left ventricular ejection fraction.

of the unipolar and omnipolar EGMs pertaining to that area were computed, resulting in 2 values ($V_{uni,max}$ and $V_{omni,max}$). In addition, the mean of the magnitudes of the 4 CV estimates derived from the 4 unipolar LATs was used as indication of the CV within the 2×2 mm area. Areas corresponding to a mean CV of 0 cm/s were excluded to avoid inclusion of far-field potentials. To calculate endo-epicardial asynchrony (EEA), the minimum of endo-epicardial LAT differences within a clique was taken. EEA was then defined as a transmural difference in electrical activation of ≥15 ms.[10] As a unipolar voltage cut-off of ≤1.0 mV and bipolar voltage cut-off of ≤0.5 mV are most frequently used in daily clinical practice to identify LVAs, we also used these values as the "gold standard" to identify low-voltage cliques.[13,14] Endo-epicardial LVAs (EE-LVA) are defined as LVA cliques located at both the endocardium and epicardium at the exact same site (*Figure 1C*).

Statistical analysis

Normally distributed data are expressed as mean ± standard deviation, whereas skewed data are expressed as median [25th–75th percentile]. Clinical characteristics were compared using Student's *t*-test or Mann-Whitney U test when appropriate. Categorical data are expressed as numbers (percentages) and analyzed with a χ^2 or Fisher exact test. Paired voltage and velocity data were analyzed between the endo- and epicardium using a paired *t*-test or Wilcoxon signed-rank test. Correlation was determined by ordinary least squares regression. A *p*-value <0.05 was considered statistically significant.

Results

Study population

Clinical characteristics of the study population (N=93, age 67 [61–72] years, 73 male (78.5%)) are summarized in *Table 1*. A history of AF was present in 37 (39.8%) patients. Ischemic- or
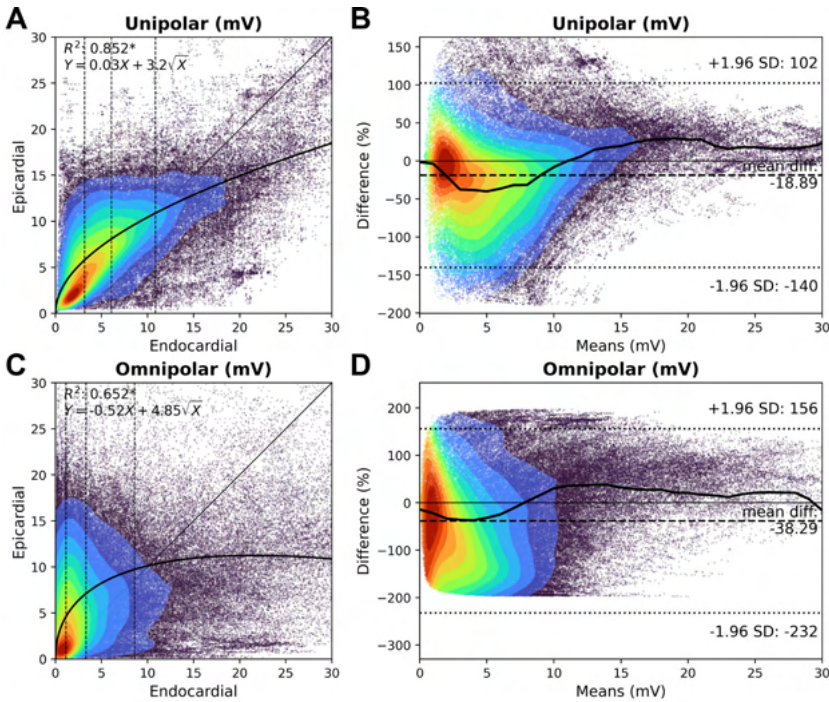
Figure 2 – Relation between endocardial and epicardial unipolar and omnipolar voltage. *Panels A and C*: Kernel density plots of $V_{uni,max}$ (A) and $V_{omni,max}$ (C) voltages between the endocardium and epicardium. The colors indicate the data density. A black line indicates the ordinary least squares prediction. Statistical significance is indicated by an asterisk (p<0.001). $V_{uni,max}$ and $V_{omni,max}$ are subdivided according to the 25th, 50th and 75th percentiles of the endocardial voltages, and are indicated by dashed vertical lines. *Panels B and D*: Bland-Altman plots of endocardial versus epicardial $V_{uni,max}$ (B) and $V_{omni,max}$ (D) voltages. The colors indicate the data density. A black line indicates the median per 1 means mV. The mean difference and 95% confidence intervals are indicated by the dashed lines. **$V_{omni,max}$** = omnipolar clique voltage; **$V_{uni,max}$** = unipolar clique voltage.

valvular heart disease or combined heart diseases were present in 47 (50.5%), 24 (25.8%) and 21 (22.6%) patients respectively. Most patients used class ll antiarrhythmic drugs (N=64, 68.8%).

Clique characteristics

In the entire study population, a total of 281 mapping locations resulted in 406,571 unipolar and 723,695 bipolar potentials from which 164,704 cliques were created for both the endocardium and epicardium (329,408 cliques in total; 3,542±1,610 per patient). The mean CV of each clique was 83.6 [62.3–103.4] cm/s at the endocardium and 84.4 [67.0–100.5] cm/s at the epicardium (p<0.001, R^2=0.853, $CV_{epi} = 0.91 \cdot CV_{endo}$). EEA was present in 2.9% of all cliques. An example of differences in activation and voltage maps constructed by using unipolar and corresponding bipolar and omnipolar EGMs are illustrated in *Figures 1D–G.*

Relation between endo- and epicardial voltages

The upper panel of *Figure 2* demonstrates the relationship between endocardial and the corresponding epicardial $V_{uni,max}$. In 61% of the cliques, $V_{uni,max}$ at the epicardium was larger than the corresponding $V_{uni,max}$ at the endocardium (8.2 [4.9–11.6] mV vs. 6.1 [3.2–10.9] mV, p<0.001). When $V_{uni,max}$ was subdivided into 4 quartiles, $V_{uni,max}$ at the epicardium was especially

Table 2 – Characteristics of low-voltage areas.

Parameter	Unipolar		Omnipolar	
	Normal	LVA (≤.0 mV)	Normal	LVA (≤.5 mV)
Endocardial	96.9%	3.1%	88.3%	11.7%
• Unipolar (mV)	6.3 [3.4–11.1]	0.8 [0.6–0.9]	6.9 [4.1–11.8]	1.5 [1.1–2.0]
• Omnipolar (mV)	3.5 [1.3–8.9]	0.2 [0.2–0.4]	4.2 [1.7–9.7]	0.3 [0.2–0.4]
• CV (cm/s)	84.3 [63.3–103.8]	52.0 [28.6–79.2]	86.3 [66.4–105.2]	55.7 [34.2–80.6]
• EEA (%)	2.4%	18.3%	2.1%	8.8%
Epicardial	98.3%	1.7%	96.0%	4.0%
• Unipolar (mV)	8.3 [5.1–11.7]	0.8 [0.7–0.9]	8.5 [5.3–11.8]	1.3 [0.9–1.8]
• Omnipolar (mV)	6.8 [3.4–11.0]	0.3 [0.2–0.5]	7.0 [3.6–11.1]	0.3 [0.2–0.4]
• CV (cm/s)	84.7 [67.6–100.7]	53.5 [31.9–79.2]	85.0 [68.3–100.9]	57.2 [35.0–82.8]
• EEA (%)	2.7%	14.2%	2.6%	10.5%

Values are presented as median [interquartile ranges] or incidence (distribution of parameter). Sum of the normal and LVA values correspond to the total number of cliques (N=164,704) per parameter. **CV** = conduction velocity; **EEA** = endo-epicardial asynchrony; **LVA** = low-voltage area.

larger at the lower $V_{uni,max}$ values at the endocardium (P_0-P_{25}: 83.7%; P_{25}-P_{50}: 79.8%; P_{50}-P_{75}: 61.7%; P_{75}-P_{100}: 18.6%). As a consequence, there was a strong inversely quadratic relation with linear component (R^2=0.852, $Y = 0.03X + 3.2\sqrt{X}$) between $V_{uni,max}$ at the endocardium and epicardium. As illustrated in *Figure 2B*, $V_{uni,max}$ up to 12 mV were particularly larger at the epicardium than the endocardium, although there was a large variation in the differences. Epicardial $V_{uni,max}$ were on average 19% larger than endocardial $V_{uni,max}$.

The lower panel of *Figure 2* demonstrates the relationship between endocardial and the corresponding epicardial $V_{omni,max}$. In 64% of the cliques, $V_{omni,max}$ at the epicardium was larger compared to the corresponding endocardial cliques (6.7 [3.2–10.9] mV vs. 3.3 [1.1–8.6] mV, p<0.001, respectively). When $V_{omni,max}$ was subdivided into 4 quartiles, $V_{omni,max}$ at the epicardium was especially larger at the lower $V_{omni,max}$ values at the endocardium (P_0-P_{25}: 91.3%; P_{25}-P_{50}: 86.5%; P_{50}-P_{75}: 62.2%; P_{75}-P_{100}: 15.5%). However, there was no clear relationship between the endocardial and epicardial $V_{omni,max}$, although lower endocardial voltages were associated with a larger range of epicardial voltages. As illustrated in *Figure 2D*, $V_{omni,max}$ up to 8 mV were particularly larger at the epicardium than the endocardium. Epicardial $V_{omni,max}$ were on average 38% larger than endocardial $V_{omni,max}$.

Endo-epicardial differences in low-voltage areas

Characteristics of unipolar and omnipolar LVAs at the endo- and epicardium are listed in *Table 2*. Endocardial and epicardial unipolar LVAs were present at respectively 3.1% and 1.7% of the mapping areas. At the endo- and epicardium, unipolar LVAs corresponded to respectively 86.8% and 73.3% of the omnipolar LVA.

Omnipolar LVAs were present at 11.7% of the endocardium and 4.0% of the epicardium. However, only 22.7% and 30.6% of omnipolar LVAs corresponded to unipolar LVAs at respectively the endo- and epicardial side.

As demonstrated in *Table 2*, CV was lower and EEA was more pronounced in both unipolar and omnipolar LVAs compared to the non-LVAs. The difference in CV and EEA between LVAs and non-LVAs was smaller in omnipolar LVAs than in unipolar LVAs (p<0.001).

Prediction of unipolar opposite LVAs

To determine the predictive value of endocardial or epicardial LVAs for the opposite layer,

Table 3 – Characteristics of low-voltage areas at the opposite side (N = 164,704 per parameter).

Parameter	Unipolar			Omnipolar		
Endocardial	**Normal**	*Epi*-LVA	EE-LVA	**Normal**	*Epi*-LVA	EE-LVA
N (%)	96.0%	0.9%	0.8%	86.3%	1.9%	2.1%
Unipolar (mV)	6.3 [3.4–11.1]	2.2 [1.4–5.0]	0.8 [0.6–0.9]	7.0 [4.2–11.9]	3.2 [1.8–6.2]	1.2 [0.8–1.6]
Omnipolar (mV)	3.5 [1.3–8.9]	1.6 [0.6–4.8]	0.2 [0.2–0.3]	4.2 [1.7–9.8]	2.1 [0.9–6.2]	0.3 [0.2–0.4]
CV (cm/s)	84.4 [63.5–104.0]	68.4 [48.6–89.0]	53.9 [29.2–81.6]	86.7 [66.8–105.4]	70.0 [50.0–91.4]	54.6 [32.7–82.0]
EEA (%)	2.2%	18.3%	9.3%	1.8%	14.0%	7.2%
Epicardial	**Normal**	*Endo*-LVA	EE-LVA	**Normal**	*Endo*-LVA	EE-LVA
N (%)	96.0%	2.3%	0.8%	86.3%	9.6%	2.1%
Unipolar (mV)	8.4 [5.2–11.8]	3.8 [2.0–6.5]	8.8 [5.7–12.1]	8.8 [5.7–12.1]	5.6 [3.2–8.8]	1.2 [0.9–1.6]
Omnipolar (mV)	6.9 [3.4–11.0]	3.5 [1.3–7.0]	0.2 [0.2–0.4]	7.1 [3.8–11.3]	5.2 [2.1–9.2]	0.3 [0.2–0.4]
CV (cm/s)	84.8 [67.8–100.8]	78.8 [59.1–98.4]	57.5 [32.7–84.2]	85.7 [69.1–101.4]	78.9 [62.0–95.5]	55.9 [34.2–81.3]
EEA (%)	2.2%	21.3%	9.5%	1.8%	9.2%	7.3%

Values are presented as median [interquartile ranges] or incidence (distribution of parameter). **CV** = conduction velocity; **EEA** = endo-epicardial asynchrony; **EE-LVA** = endo-epicardial low-voltage area; ***Endo*-LVA** = endocardial low-voltage area; ***Epi*-LVA** = epicardial low-voltage area.

8

149

Table 4 – Characteristics of low-voltage areas at the opposite side using combined unipolar and omnipolar voltage mapping (N=164,704 per parameter).

Endocardial	Normal	*Epi*-LVA	EE-LVA
N (%)	96.9%	3.1%	88.3%
Unipolar (mV)	6.3 [3.4–11.1]	0.8 [0.6–0.9]	6.9 [4.1–11.8]
Omnipolar (mV)	3.5 [1.3–8.9]	0.2 [0.2–0.4]	4.2 [1.7–9.7]
CV (cm/s)	84.3 [63.3–103.8]	52.0 [28.6–79.2]	86.3 [66.4–105.2]
EEA (%)	2.4%	18.3%	2.1%
Epicardial	Normal	*Endo*-LVA	EE-LVA
N (%)	98.3%	1.7%	96.0%
Unipolar (mV)	8.3 [5.1–11.7]	0.8 [0.7–0.9]	8.5 [5.3–11.8]
Omnipolar (mV)	6.8 [3.4–11.0]	0.3 [0.2–0.5]	7.0 [3.6–11.1]
CV (cm/s)	84.7 [67.6–100.7]	53.5 [31.9–79.2]	85.0 [68.3–100.9]
EEA (%)	2.7%	14.2%	2.6%

Values are presented as median [interquartile ranges] or incidence (distribution of parameter). **CV** = conduction velocity; **EEA** = endo-epicardial asynchrony; **EE-LVA** = endo-epicardial low-voltage area; ***Endo*-LVA** = endocardial low-voltage area; ***Epi*-LVA** = epicardial low-voltage area.

all cliques were subdivided into cliques with either LVA in only one layer (*endo/epi*-LVA) or cliques with LVAs present at both layers (EE-LVA). Characteristics of these clique categories are listed in *Table 3*. Of all endocardial LVA cliques, 25.8% corresponded to an epicardial LVA and 47.3% of the epicardial LVA cliques corresponded to an endocardial LVA. Therefore, 0.8% of all cliques were identified as EE-LVA, 0.9% as *epi*-LVA and 2.3% as *endo*-LVA. At the opposite site of unipolar *endo*- and *epi*-LVAs, 'normal' cliques were characterized by lower $V_{uni,max}$, $V_{omni,max}$, lower CV and enhanced EEA compared to the other non-LVA cliques (p<0.001). Most EEA was found at endo-LVA cliques.

Prediction of omnipolar opposite LVAs

Of all endocardial omnipolar LVA cliques, 18.0% corresponded to an epicardial LVA and 52.4% of the epicardial LVA cliques corresponded to an endocardial LVA. Therefore, 2.1% of all cliques were identified as EE-LVA, 1.9% as *epi*-LVA and 9.6% as *endo*-LVA. At the opposite site of omnipolar *endo*- and *epi*-LVAs, 'normal' cliques were characterized by lower $V_{uni,max}$, $V_{omni,max}$, lower CV and enhanced EEA compared to the other non-LVA cliques (p<0.001). Only 7.6% of these cliques corresponded to unipolar LVAs.

Identification of LVAs by combined unipolar and omnipolar voltage mapping

Cliques containing both unipolar and omnipolar LVAs were identified. Characteristics of these overlapping LVAs are listed in *Table 4*. At the endocardium, overlapping LVAs consisted of 86.8% of $V_{uni,max}$ and 22.7% of $V_{omni,max}$ compared to 73.7% of $V_{uni,max}$ and 30.6% of $V_{omni,max}$ at the epicardium.

In total, 2.6% overlapping endocardial LVAs were identified, compared to 1.2% at the epicardium; 0.6% were identified as EE-LVAs. These EE-LVAs consisted of 23.3% of all endocardial overlapping LVAs and 50.4% at the epicardium. At the opposite site of overlapping endo- and epi-LVAs, 'normal' cliques were characterized by lower $V_{uni,max}$, $V_{omni,max}$, lower CV and enhanced EEA compared to the other non-LVA cliques (p<0.001).

Figure 3 demonstrates ROC-curves of the accuracy of identifying overlapping endocardial and epicardial LVAs based on all parameters recorded at the opposite layer. Combined unipolar and omnipolar voltages were most accurate in identifying overlapping LVAs at the opposite layer (endocardial LVAs: AUC=0.83; epicardial LVAs: AUC=0.89).
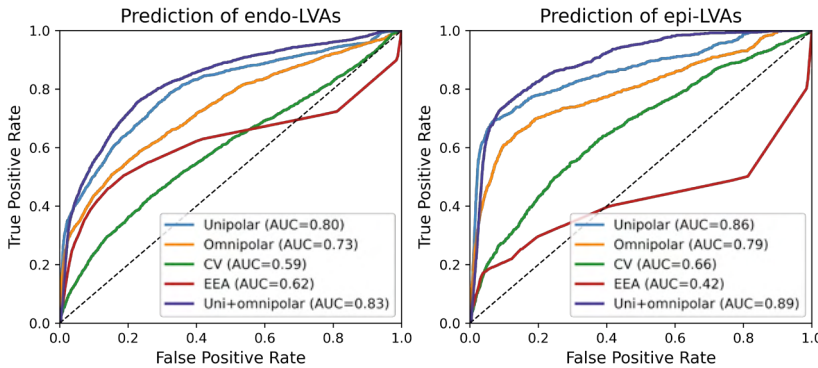
Figure 3 – ROC-curves of the prediction of overlapping LVAs. ROC-curves of the prediction of overlapping endocardial (left) and epicardial (right) LVAs based on all parameters recorded from the opposite layer. **AUC** = area under the curve; **CV** = conduction velocity; **EEA** = endo-epicardial asynchrony.

Discussion

In most clinical settings, endocardial bipolar voltage mapping is mainly used to identify LVAs, which are considered surrogate markers for areas of diseased tissue. However, in recent perspective, it has become clear that bipolar LVAs can also be located exclusively at the epicardium.[4] Our study demonstrated that also by using unipolar and omnipolar EGMs, the majority of unipolar and omnipolar LVAs are also located exclusively at either the endocardium or epicardium. More importantly, we have shown that the most accurate methodology to identify EE-LVAs is to combine epicardial unipolar and omnipolar voltages. When using either unipolar or omnipolar voltages separately, epicardial LVAs still corresponded well with endocardial LVAs, but not vice-versa. Within the same layer, only unipolar LVAs corresponded well with omnipolar LVAs. Furthermore, there was a clear relationship between endo-epicardial unipolar voltages, but not between endo-epicardial omnipolar voltages.

Endo-epicardial voltage mapping

Data on the relationship between atrial endocardial and epicardial voltages is lacking, although it has been studied in the ventricles.[15,16] In the atria, Van der Does et al.[17] demonstrated a linear relationship between unipolar endocardial and epicardial voltage in which epicardial voltages were larger than endocardial voltages. Other studies also reported higher mean voltage values in the epicardium compared to mean endocardial voltage, in both atria and ventricles.[15,16,18,19] Using our clique voltages, we demonstrated a clear inverse quadratic relation with linear component between endocardial and epicardial unipolar clique voltages. Therefore, unipolar voltages recorded at the endocardium are predictive for epicardial unipolar voltages. In contrast, we found no relationship between endocardial and epicardial omnipolar voltages. This could likely be caused by the limited field-of-view of omnipolar voltages. Consequently, omnipolar voltages recorded at the endocardium are a poor predictor for voltages at the other layer.

Anatomy of the right atrium

Variations between endocardial and epicardial voltages can also be explained by the anatomical structure of the RA. The surface of the endocardium is very irregular due to the presence of the pectinate muscles and terminal crest, in contrast to the smooth epicardium.

Diameters and therefore cardiac mass of the pectinate muscles may vary considerably.[20] In addition, the arrangement of pectinate muscles causes variation in the level of contact with the electrodes. Furthermore, due to atrial remodeling and varying wall stress, the atria and therefore the pectinate muscles may elongate resulting in alternation of the bundle density.[21] This results in a non-uniform spread of activation and can consequently also considerably affect omnipolar voltages. Moreover, Kharbanda et al.[12] demonstrated that conduction disorders occur more frequently at the endocardium. These features could explain the large discrepancies in unipolar and omnipolar voltages at endocardial LVAs. As the epicardial surface is more smooth, proper tissue contact with the entire electrode array can be achieved more easily. Therefore, epicardial LVAs could be more likely indicative of structural abnormalities and hence EE-LVAs.

Identification of endo-epicardial substrate

The arrhythmogenic substrate can be located either subendocardially, subepicardially, intramurally or transmurally.[15,22,23] Piorkowski et al.[4] recently demonstrated by bipolar endo-epicardial mapping in the left and RA that LVAs were present in 44 patients with history of AF in either both layers (N=33, 75%) or in solely the endocardium (N=6, 14%) or epicardium (N=6, 14%). However, all patients already had (multiple) ablation procedures. Our study population consisted of patients without previous ablation therapy and we demonstrated that the majority of the LVAs at the RA were exclusively located at either the endocardium or epicardium. These findings demonstrate that the arrhythmogenic substrates may not necessarily be transmural present. Verheule et al.[24] also demonstrated in a goat model of AF that formation of endomysial fibrosis located within the outer millimeter of the epicardial layer accompanied the transition from persistent to permanent AF, while endocardial bundles remained unaffected. Hence, as structural remodeling can occur locally within one layer, the presence of a LVA can also be confined to either the endocardial or epicardial layer. This could in turn lead to increased EEA due to progressive uncoupling between the epicardial layer and the endocardial bundles, which also has been proposed as an important mechanism for AF.[10]

On the other hand, as omnipolar voltages represent more local activity, this recording modality is more likely to only detect LVAs representing substrate located either (sub) endocardially or (sub)epicardially depending on the recording location. Several studies have shown an added value of combining unipolar and bipolar voltages to detect intramural or transmural substrates.[25-27] Hutchinson et al.[16] demonstrated that epicardial bipolar LVAs can be identified in most patients with left ventricular cardiomyopathy using endocardial unipolar voltage mapping. However, Tokuda et al.[15] observed discrepancies in the accuracy of epicardial bipolar LVA identification using endocardial unipolar voltages between patients with nonischemic and ischemic cardiomyopathy. In our present study, we demonstrated that endocardial LVAs at the atria frequently did not correspond to LVAs at the epicardium, independently of the recording technique used. Even by combining unipolar and omnipolar voltages, only 23.3% of the endocardial LVAs corresponded to epicardial LVAs, favoring a combined endocardial *and* epicardial mapping approach.

Endo-epicardial ablation therapy

Especially in patients with persistent AF, the presence of complex 3-dimensional arrhythmogenic substrates limits the efficacy of endocardial ablation strategies. Minimally invasive surgical ablation of AF is therefore increasingly combined with the endocardial transcatheter procedures in so-called hybrid procedures, showing promising results.[3,4,28,29] In the study of Piorkowski et al.[4], 73% of complex AF patients remained free from AF during

2 years of follow-up, although other studies encountered higher recurrence rates.[28,30,31] However, LVAs frequently occur at either the endocardium or epicardium alone and the opposite areas could contain normal voltages. These areas are therefore 'invisible' when recording from only one side. Diseased tissue could then consequently be missed using a one-sided approach. In addition, epicardial mapping provides more often accurate identification of EE-LVAs and the role of epicardial structures, such as Bachmann's bundle, become more recognized in the pathogenesis of AF.[3,32] This suggests that a strategy of combined endo-epicardial access for mapping and ablation may provide superior efficacy to an endocardial-only approach.

Study limitations

Intra-operative simultaneous endo-epicardial mapping in humans can only be safely performed during cardiac surgical procedures. Therefore, as endo-epicardial mapping was only performed on a limited area of the RA free wall, we could not evaluate the relation of endocardial and epicardial voltages in the complete atria, specifically not in the left atrium. The recorded potentials might be influenced by the presence of epicardial fat as previous studies demonstrated that the presence of thick epicardial fat is associated with attenuated bipolar voltage.[33,34] Although we did not experience any large effects of visually present epicardial fat at the RA, we cannot ascertain that the presence of epicardial fat has influenced our results. In addition, the underlying anatomy such as variability in atrial wall thickness and the degree of trabeculation cannot be retrieved, and exact tissue histology could not be performed. Therefore, we were unable to correlate the exact underlying anatomy and histology with the mapping data. This study focused on the comparison of the different voltage mapping methodologies and identification of LVAs without interventions. The next step will be to incorporate the results of this study with ablation targeting EE-LVAs in order to determine whether the combination of low unipolar and low omnipolar voltage can improve ablation outcomes.

Conclusion

When using unipolar and omnipolar EGMs, LVAs are frequently located exclusively at either the endocardium or epicardium and could be undetectable when measuring from the opposite layer only. An endo-epicardial mapping approach is therefore favored to accurately identify LVAs. EE-LVAs are most accurately identified using combined epicardial unipolar and omnipolar voltages. Therefore, a combination of simultaneously recorded endo-epicardial low unipolar and low omnipolar voltage may be more indicative of dual-layer LVAs and probably arrhythmogenic substrates.

8

References

1. Sim I, Bishop M, O'Neill M, Williams SE. Left atrial voltage mapping: defining and targeting the atrial fibrillation substrate. J Interv Card Electrophysiol. 2019.
2. Kottkamp H, Bender R, Berg J. Catheter ablation of atrial fibrillation: how to modify the substrate? J Am Coll Cardiol. 2015;65:196-206.
3. De Martino G, Compagnucci P, Mancusi C, Vassallo E, Calvanese C, Della Ratta G, Librera M, Franciulli M, Marino L, Russo AD, et al. Stepwise endo-/epicardial catheter ablation for atrial fibrillation: The Mediterranea approach. J Cardiovasc Electrophysiol. 2021;32:2107-2115.
4. Piorkowski C, Kronborg M, Hourdain J, Piorkowski J, Kirstein B, Neudeck S, Wechselberger S, Passler E, Lowen A, El-Armouche A, et al. Endo-/Epicardial Catheter Ablation of Atrial Fibrillation: Feasibility, Outcome, and Insights Into Arrhythmia Mechanisms. Circ Arrhythm Electrophysiol. 2018;11:e005748.
5. van Schie MS, Kharbanda RK, Houck CA, Lanters EAH, Taverne Y, Bogers A, de Groot NMS. Identification of Low-Voltage Areas: A Unipolar, Bipolar, and Omnipolar Perspective. Circ Arrhythm Electrophysiol. 2021;14:e009912.
6. Chopra N, Tokuda M, Ng J, Reichlin T, Nof E, John RM, Tedrow UB, Stevenson WG. Relation of the unipolar low-voltage penumbra surrounding the endocardial low-voltage scar to ventricular tachycardia circuit sites and ablation outcomes in ischemic cardiomyopathy. J Cardiovasc Electrophysiol. 2014;25:602-608.
7. Knops P, Kik C, Bogers AJ, de Groot NM. Simultaneous endocardial and epicardial high-resolution mapping of the human right atrial wall. J Thorac Cardiovasc Surg. 2016;152:929-931.
8. Deno DC, Balachandran R, Morgan D, Ahmad F, Masse S, Nanthakumar K. Orientation-Independent Catheter-Based Characterization of Myocardial Activation. IEEE Trans Biomed Eng. 2017;64:1067-1077.
9. Haldar SK, Magtibay K, Porta-Sanchez A, Masse S, Mitsakakis N, Lai PFH, Azam MA, Asta J, Kusha M, Dorian P, et al. Resolving Bipolar Electrogram Voltages During Atrial Fibrillation Using Omnipolar Mapping. Circ Arrhythm Electrophysiol. 2017;10.
10. de Groot N, van der Does L, Yaksh A, Lanters E, Teuwen C, Knops P, van de Woestijne P, Bekkers J, Kik C, Bogers A, et al. Direct Proof of Endo-Epicardial Asynchrony of the Atrial Wall During Atrial Fibrillation in Humans. Circ Arrhythm Electrophysiol. 2016;9.
11. van Schie MS, Heida A, Taverne Y, Bogers A, de Groot NMS. Identification of local atrial conduction heterogeneities using high-density conduction velocity estimation. Europace. 2021;23:1815-1825.
12. Kharbanda RK, Knops P, van der Does L, Kik C, Taverne Y, Roos-Serote MC, Heida A, Oei FBS, Bogers A, de Groot NMS. Simultaneous Endo-Epicardial Mapping of the Human Right Atrium: Unraveling Atrial Excitation. J Am Heart Assoc. 2020;9:e017069.
13. Sanders P, Morton JB, Davidson NC, Spence SJ, Vohra JK, Sparks PB, Kalman JM. Electrical remodeling of the atria in congestive heart failure: electrophysiological and electroanatomic mapping in humans. Circulation. 2003;108:1461-1468.
14. van Schie MS, Starreveld R, Bogers A, de Groot NMS. Sinus rhythm voltage fingerprinting in patients with mitral valve disease using a high-density epicardial mapping approach. Europace. 2021;23:469-478.
15. Tokuda M, Tedrow UB, Inada K, Reichlin T, Michaud GF, John RM, Epstein LM, Stevenson WG. Direct comparison of adjacent endocardial and epicardial electrograms: implications for substrate mapping. J Am Heart Assoc. 2013;2:e000215.
16. Hutchinson MD, Gerstenfeld EP, Desjardins B, Bala R, Riley MP, Garcia FC, Dixit S, Lin D, Tzou WS, Cooper JM, et al. Endocardial unipolar voltage mapping to detect epicardial ventricular tachycardia substrate in patients with nonischemic left ventricular cardiomyopathy. Circ Arrhythm Electrophysiol. 2011;4:49-55.
17. van der Does L, Knops P, Teuwen CP, Serban C, Starreveld R, Lanters EAH, Mouws E, Kik C, Bogers A, de Groot NMS. Unipolar atrial electrogram morphology from an epicardial and endocardial perspective. Heart Rhythm. 2018;15:879-887.
18. van der Does L, Starreveld R, Kharbanda RK, Knops P, Kik C, Bogers A, de Groot NMS. Detection of Endo-epicardial Asynchrony in the Atrial Wall Using One-Sided Unipolar and Bipolar Electrograms. J Cardiovasc Transl Res. 2021;14:902-911.
19. Lemery R, Birnie D, Tang AS, Green M, Gollob M, Hendry M, Lau E. Normal atrial activation and voltage during sinus rhythm in the human heart: an endocardial and epicardial mapping study in patients with a history of atrial fibrillation. J Cardiovasc Electrophysiol. 2007;18:402-408.
20. Sanchez-Quintana D, Anderson RH, Cabrera JA, Climent V, Martin R, Farre J, Ho SY. The terminal crest: morphological features relevant to electrophysiology. Heart. 2002;88:406-411.
21. Schuessler RB, Kawamoto T, Hand DE, Mitsuno M, Bromberg BI, Cox JL, Boineau JP. Simultaneous epicardial and endocardial activation sequence mapping in the isolated canine right atrium. Circulation. 1993;88:250-263.
22. Gharaviri A, Bidar E, Potse M, Zeemering S, Verheule S, Pezzuto S, Krause R, Maessen JG, Auricchio A, Schotten U. Epicardial Fibrosis Increases Endo-Epicardial Dissociation and Epicardial Breakthroughs in Human Atrial Fibrillation. Front Physiol. 2020;11:68.
23. Chen R, Wen C, Fu R, Li J, Wu J. The effect of complex intramural microstructure caused by structural remodeling on the stability of atrial fibrillation: Insights from a three-dimensional multi-layer modeling study. PLoS One. 2018;13:e0208029.
24. Verheule S, Tuyls E, Gharaviri A, Hulsmans S, van Hunnik A, Kuiper M, Serroyen J, Zeemering S, Kuijpers NH, Schotten U. Loss of continuity in the thin epicardial layer because of endomysial fibrosis increases the complexity of atrial fibrillatory conduction. Circ Arrhythm Electrophysiol. 2013;6:202-211.
25. Yalin K, Golcuk E, Bilge AK, Aksu T, Buyukbayrak H, Tiryakioglu SK, Emet S, Adalet K. Combined analysis of unipolar and bipolar voltage mapping identifies recurrences after unmappable scar-related ventricular tachycardia ablation. Europace. 2015;17:1580-1586.

26. Casella M, Pizzamiglio F, Dello Russo A, Carbucicchio C, Al-Mohani G, Russo E, Notarstefano P, Pieroni M, D'Amati G, Sommariva E, et al. Feasibility of combined unipolar and bipolar voltage maps to improve sensitivity of endomyocardial biopsy. Circ Arrhythm Electrophysiol. 2015;8:625-632.
27. Spears DA, Suszko AM, Dalvi R, Crean AM, Ivanov J, Nanthakumar K, Downar E, Chauhan VS. Relationship of bipolar and unipolar electrogram voltage to scar transmurality and composition derived by magnetic resonance imaging in patients with nonischemic cardiomyopathy undergoing VT ablation. Heart Rhythm. 2012;9:1837-1846.
28. Edgerton Z, Perini AP, Horton R, Trivedi C, Santangeli P, Bai R, Gianni C, Mohanty S, Burkhardt JD, Gallinghouse GJ, et al. Hybrid Procedure (Endo/Epicardial) versus Standard Manual Ablation in Patients Undergoing Ablation of Longstanding Persistent Atrial Fibrillation: Results from a Single Center. J Cardiovasc Electrophysiol. 2016;27:524-530.
29. Zheng Z, Yao Y, Li H, Zheng L, Liu S, Lin H, Duan F. Simultaneous hybrid maze procedure for long-standing persistent atrial fibrillation with dilated atrium. JTCVS Techniques. 2021;5:34-42.
30. Jiang R, Buch E, Gima J, Upadhyay GA, Nayak HM, Beaser AD, Aziz Z, Shivkumar K, Tung R. Feasibility of percutaneous epicardial mapping and ablation for refractory atrial fibrillation: Insights into substrate and lesion transmurality. Heart Rhythm. 2019;16:1151-1159.
31. Gehi AK, Mounsey JP, Pursell I, Landers M, Boyce K, Chung EH, Schwartz J, Walker TJ, Guise K, Kiser AC. Hybrid epicardial-endocardial ablation using a pericardioscopic technique for the treatment of atrial fibrillation. Heart Rhythm. 2013;10:22-28.
32. Teuwen CP, Yaksh A, Lanters EA, Kik C, van der Does LJ, Knops P, Taverne YJ, van de Woestijne PC, Oei FB, Bekkers JA, et al. Relevance of Conduction Disorders in Bachmann's Bundle During Sinus Rhythm in Humans. Circ Arrhythm Electrophysiol. 2016;9:e003972.
33. Saba MM, Akella J, Gammie J, Poston R, Johnson A, Hood RE, Dickfeld TM, Shorofsky SR. The influence of fat thickness on the human epicardial bipolar electrogram characteristics: measurements on patients undergoing open-heart surgery. Europace. 2009;11:949-953.
34. Desjardins B, Morady F, Bogun F. Effect of epicardial fat on electroanatomical mapping and epicardial catheter ablation. J Am Coll Cardiol. 2010;56:1320-1327.

8
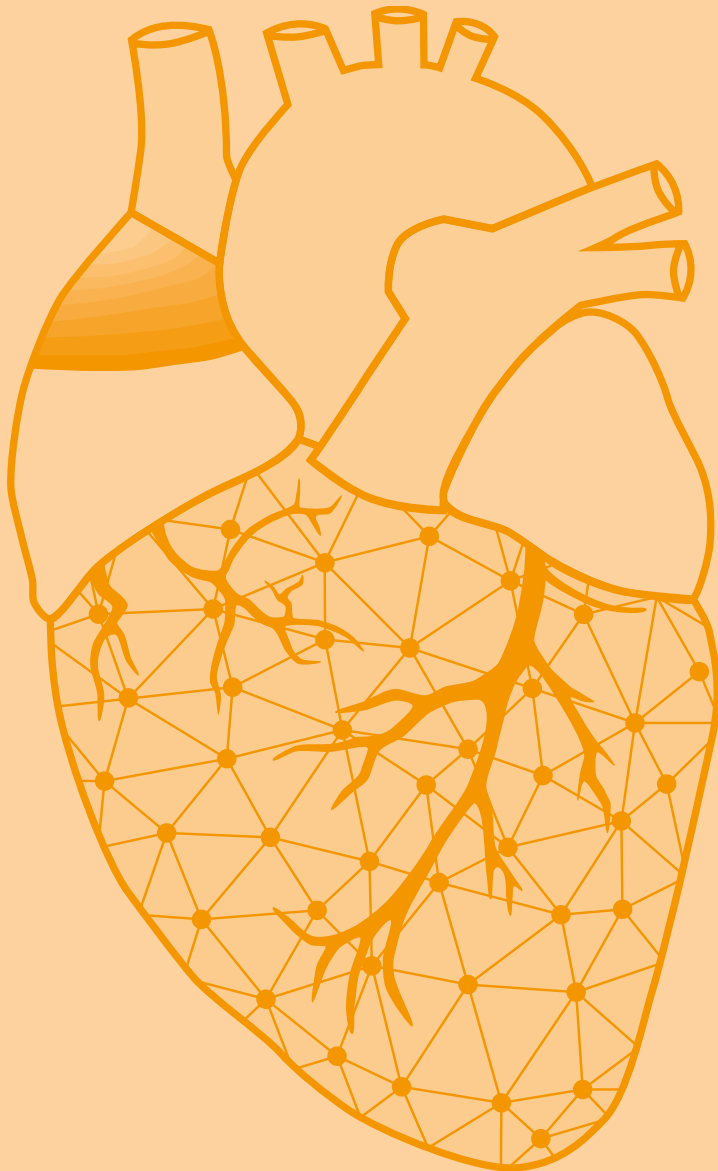
Chapter 9

Identification of critical slowing of conduction using unipolar atrial voltage and fractionation mapping

Ziliang Ye*

Nawin L. Ramdat Misier*

Mathijs S. van Schie

Hongxian Xiang

Paul Knops

Jolanda Kluin

Yannick J.H.J. Taverne

Natasja M.S. de Groot

* Contributed equally

Abstract

Background: Catheter ablation strategies targeting fractionated or low-voltage potentials have been widely used in patients with persistent types of atrial fibrillation (AF). However, recent negative results in clinical trials have questioned their role in effectively representing sites of slowing of conduction, and thus a critical arrhythmogenic substrate. We therefore studied the relationship between local conduction velocity (CV) and the occurrence of fractionated, and/or low-voltage potentials in order to identify areas with critically slowing of conduction.

Methods: Intra-operative bi-atrial high-density epicardial mapping was performed during sinus rhythm. Unipolar potentials with an amplitude <1.0 mV were classified as low-voltage and potentials with ≥3 deflections as fractionation. Local CV was computed as average of velocity estimations between neighboring electrodes using discrete velocity vectors.

Results: A total of 319 patient were included. Fractionated, low-voltage potentials were rare, accounting for only 0.36 [0.15–0.78] % of all atrial sites. Local CV at sites with fractionated, low-voltage potentials (46.0 [22.6–72.7] cm/s) was considerably lower compared to sites with either low-voltage, non-fractionated potentials (64.5 [34.8–99.4] cm/s) and fractionated, high-voltage potentials (65.9 [41.7–92.8] cm/s; p<0.001 for each). Slow conduction areas (CV <50 cm/s) could be most accurately identified by using a low voltage threshold (<1 mV) and a minimum of 3 deflections (positive predictive value: 54.2–70.7%), although the overall sensitivity remained low (0.1–1.9%).

Conclusions: Sites with fractionated, low-voltage potentials have substantially slower local CV compared to sites with either low-voltage, non-fractionated potentials or fractionated, high-voltage potentials. However, the strong inverse relationship between the positive predictive value and sensitivity of combined voltage and fractionation threshold for slowed CV is likely to complicate the use of these signal-based ablation approaches in AF patients.

Introduction

In the search to improve ablation outcomes in patients with (persistent) atrial fibrillation (AF), various substrate-based ablation approaches have been introduced over the years. Among these strategies, ablation targeting fractionated potentials or low-voltage potentials are the most common.[1] The application of these strategies in AF treatment initially showed positive outcomes in mostly single center studies, but are now increasingly followed by negative outcomes in (large) randomized controlled trials.[2-4]

The reason for the lack of benefit associated with additional ablation of fractionated and/or low-voltage potentials is not well understood. Limited knowledge on the exact arrhythmogenic properties of both fractionated and low-voltage potentials underlies in part the inability to discern the additional value of modification of both parameters. While fractionation and low-voltage are considered to occur at sites of conduction slowing, and therefore critical in initiation and perpetuation of AF, they can also occur due to non-pathologic reasons (e.g., wavefront collisions and diffuse fiber orientation). Several studies have attempted to characterize the relationship between conduction velocity (CV) and either fractionated or low-voltage potentials.[5-12] However, these studies not only yielded in contradicting results, they also lacked the interrelationship between the three parameters. Small sample size, lack of high-density mapping (across both atria) and variation in recording techniques could explain the inconsistent findings among these studies.

In order to better understand the arrhythmogenic properties of fractionated and low-voltage potentials, a comprehensive assessment of both potential characteristics and the relationship with local CV is needed. Therefore, the aim of our study was to study the relationship between local CV and the occurrence of fractionated and/or low-voltage potentials in order to identify areas with critically slowing of conduction as indicator of potential arrhythmogenic substrate.

Methods

Study population

Participants (≥18 years) who underwent elective cardiac surgery, including coronary artery bypass surgery and/or mitral valve surgery, in the Erasmus Medical Center Rotterdam were included. Exclusion criteria were the presence of prior ablative therapy or cardiac surgery, radiation therapy of the chest, atrial pacemaker leads, an estimated glomerular filtration rate <30 ml/min, and the need for inotropic or mechanical support at the time of surgery. This study has been approved by the Institutional Medical Ethics Committee (MEC2010-054/MEC2014-393). Written informed consent was required from all patients prior to recruitment, and patient's baseline characteristics (e.g., age, medical history, and underlying heart diseases) were extracted from the patient's medical record.

Mapping procedure

As described previously, epicardial high-resolution mapping was performed before cardiopulmonary bypass.[13] A temporal bipolar epicardial pacemaker wire connected to the free wall of right atrium (RA) was used as a reference electrode, and a steel wire attached to the subcutaneous tissue of thoracic cavity served as an indifferent electrode. Epicardial mapping was performed using a 128-electrode or 192-electrode array (electrode diameter 0.65 mm or 0.45 mm, distance 2.0 mm, respectively).
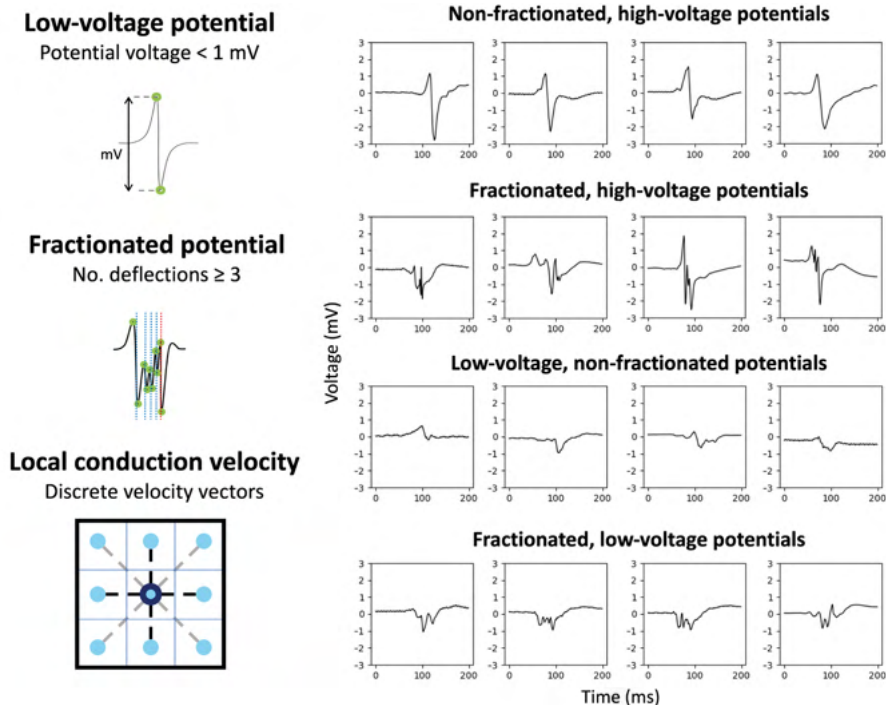
Figure 1 – Electrogram processing approach and potential types. The left panels illustrate the definitions for low-voltage and fractionated potentials and conduction velocity. The right panels display typical examples of different unipolar potentials, including 1) non-fractionated, high-voltage potentials, 2) fractionated, high-voltage potentials, 3) low-voltage, non-fractionated potentials, and 4) fractionated, low-voltage potentials.

Mapping of the RA was performed from the inferior to superior caval vein perpendicular to the terminal crest. The pulmonary vein area (PVA) was mapped from the transverse sinus fold down along the margins of the left and right pulmonary veins towards the atrioventricular groove and the left atrioventricular groove (LAVG) from the lower margin of the left inferior pulmonary vein to the left atrial appendage. Bachmann's bundle (BB) was mapped from the border of the left atrial appendage, across the roof of the left atrium (LA), behind the aorta toward the superior cavo-atrial junction. At each mapping location, 5-second unipolar electrograms (EGM) were recorded during SR including an individual surface electrocardiogram lead, 2 mV and 1000 ms calibration signal and bipolar reference EGM. Data was amplified (gain 1000), filtered (bandwidth 0.5–400 Hz), sampled (1kHz), and analog-to-digital converted (16-bit) and stored on a hard disk.

Data analysis

Customized software was used for semi-automatic analysis of EGM morphology. EGMs with ≥25% loss of recording site and atrial extrasystoles were excluded. Mapping areas with simultaneous activation were excluded from the analysis to avoid inclusion of far-field potentials. Local activation time (LAT) was defined as the steepest negative slope of a unipolar potential. All annotations were manually inspected by two researchers.

Peak-to-peak amplitudes of all unipolar potentials were evaluated, as illustrated in *Figure 1*. In line with previous studies, low-voltage was defined as a potential voltage <1.0 mV.[9] A unipolar potential was classified as fractionated when it contained ≥3 deflections.[14] As

previously described, discrete velocity vectors were used to estimate local CV by using all adjacent electrodes (longitudinal, transverse and diagonal directions).[15] Areas with slowed localized conduction were defined as a CV <50 cm/s.[16]

Statistical Analysis

The Shapiro-Wilk test was used to inspect normality before data analysis. Normally distributed data are presented as mean ± standard deviation and compared using independent samples *t*-test or analysis of variance appropriately. Skewed data are presented as median [25th–75th percentile] and difference between groups was compared using the Kruskal-Wallis test, the Mann-Whitney U test, or the Wilcoxon signed-rank test appropriately. Categorical data are presented as numbers and percentages and were compared using χ^2 or Fisher's exact test. A two-sided *p*-value less than 0.05 was considered statistically significant. Data analysis was performed using IBM SPSS Statistics (version 28), R Studio (version 4.1.3) and Python (version 3.8).

9

Table 1 – Patient characteristics (N=319).

	Without AF	With AF	*p*-value
Patients	256 (81)	63 (20)	-
Male	208 (81)	38 (60)	0.001
Age (y)	65±10	71±8	0.003
Underlying heart disease			<0.001
• CAD	213 (83)	23 (37)	
• MVD	27 (11)	29 (46)	
• MVD with CAD	16 (6)	11 (17)	
Type of AF			<0.001
• No AF	256 (100	0 (0)	
• Paroxysmal AF	0 (0)	43 (68)	
• Persistent AF	0 (0)	16 (26)	
• Long-standing persistent AF	0 (0)	4 (6)	
Cardiovascular risk factors			
• BMI (kg/m^2)	27.8±4.3	27.1±4.0	0.188
• Hypertension	144 (56)	35 (56)	1.000
• Dyslipidemia	103 (40)	15 (24)	0.023
• Diabetes mellitus	80 (31)	12 (19)	0.078
• Myocardial infarction	112 (44)	17 (27)	0.022
Left ventricular function			0.035
• Normal (EF >55%)	190 (74)	41 (66)	
• Mild impairment (EF 46–55%)	52 (20)	14 (23)	
• Moderate impairment (EF 36–45%)	13 (5)	4 (6)	
• Severe impairment (EF <35%)	1 (1)	3 (5)	
Left atrial dilatation >45 mm	46 (18)	39 (62)	<0.001
ACEI/ARB/AT2 antagonist	167 (65)	38 (60)	0.534
Statin	208 (81)	31 (50)	<0.001
Antiarrhythmic agents			
• Class I	1 (1)	1 (2)	0.852
• Class II	192 (75)	36 (57)	0.008
• Class III	3 (1)	15 (24)	<0.001
• Class IV	12 (5)	2 (3)	0.856
• Digoxin	3 (1)	12 (19)	<0.001

Values are presented as mean ± standard deviation or as N (%). **ACEI** = angiotensin-converting enzyme inhibitors; **ARB** = angiotensin receptor blockers; **AT2** = angiotensin type 2 receptor; **CAD** = coronary artery disease; **EF** = ejection fraction; **MVD** = mitral valve disease; **PAF** = atrial fibrillation; **BMI** = body mass index.
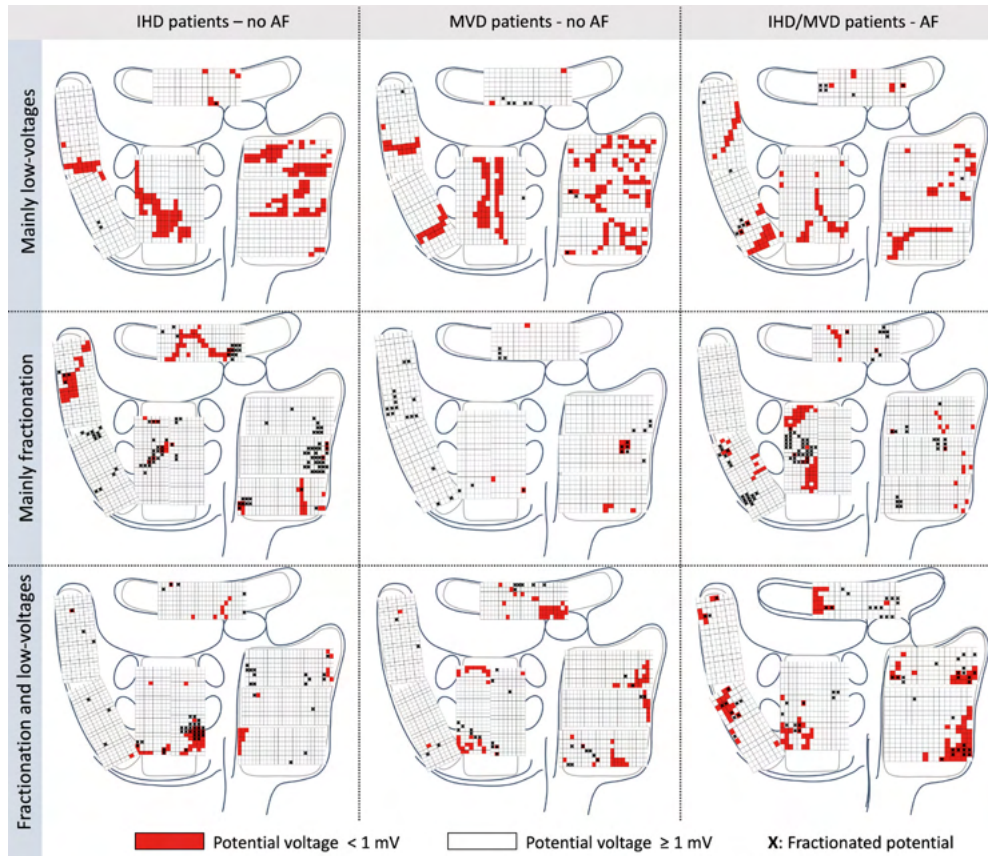
Figure 2 – Spatial distribution of fractionation and low-voltage potentials. Bi-atrial maps, including Bachmann's bundle, indicate variations in spatial distributions of fractionation and low-voltage potentials in different patient groups, including patients with ischemic heart disease and mitral valve disease with and without a history of AF. The upper panels show patients with mainly low-voltage potentials, while the middle panels show patients from whom mainly fractionated potentials were recorded. The lower panels show patients with a large number of fractionated, low-voltage potentials. **AF** = atrial fibrillation; **IHD** = ischemic heart disease; **MVD** = mitral valve disease.

Results

Study population

A total of 319 adult patients (mean age: 66±10 years, 246 (77.1%) males) were included. Sixty-three patients (19.8%) had a history of AF. The majority of patients (72.6%) had normal left ventricular function and 86 patients (26.7%) had left atrial dilation. Clinical characteristics of the study population are summarized in *Table 1*.

Mapping data

Average SR cycle length was 874±166 ms and did not differ between patients with (871±162 ms) and without AF (875±167 ms, p=0.889). A total of 2,943,017 atrial potentials (9,225±3,051 per patient) were included for analysis. Most potentials were recorded from the RA (N=1,390,027; 47.2%), followed by the PVA (N=649,852; 22.1%) and LA (N=572,269; 19.4%) and BB (N=330,869; 11.3%).

Table 2 – Prevalence and regional distribution of fractionation and low-voltage potentials.

	Fractionated potentials (%)	Low-voltage potentials (%)	Fractionated, low-voltage potentials (%)
Total population			
Entire atria	1.72 [0.87–2.75]	6.22 [3.73–10.18]	0.36 [0.15–0.78]
RA	1.31 [0.41–2.92]	6.06 [2.83–10.72]	0.41 [0.10–0.98]
BB	1.74 [0.54–4.20]	2.41 [0.62–8.40]	0.25 [0.00–0.84]
PVA	0.74 [0.23–2.22]	4.79 [1.63–12.35]	0.08 [0.00–0.34]
LA	1.07 [0.35–2.57]	3.84 [1.25–8.92]	0.05 [0.00–0.25]
Without AF			
Entire atria	1.62 [0.84–2.56]	6.04 [3.70–9.49]	0.36 [0.14–0.75]
RA	1.39 [0.41–2.91]	5.95 [2.81–10.39]	0.46 [0.10–0.99]
BB	1.43 [0.43–3.63]	1.67 [0.47–6.19]	0.16 [0.00–0.73]
PVA	0.71 [0.20–2.04]	4.44 [1.21–11.45]	0.07 [0.00–0.25]
LA	1.07 [0.37–2.41]	3.84 [1.00–9.11]	0.04 [0.00–0.22]
With AF			
Entire atria	1.87 [1.20–3.23]*	9.01 [4.43–11.52]*	0.37 [0.21–0.93]
RA	1.04 [0.42–3.10]	6.84 [3.15–12.83]	0.29 [0.11–0.71]
BB	3.10 [1.18–5.88]*	7.25 [2.80–18.88]*	0.61 [0.10–1.83]*
PVA	1.07 [0.56–4.05]*	8.12 [3.82–14.72]*	0.31 [0.00–0.57]*
LA	1.05 [0.31–3.25]	3.82 [1.96–8.11]	0.08 [0.00–0.32]

*$p<0.05$ between patients with and without history of AF at corresponding location. **AF** = atrial fibrillation; **RA** = right atrium; **BB** = Bachmann's bundle; **LA** = left atrium; **PVA** = pulmonary vein area.

9

Spatial distribution of fractionation and low-voltage potentials

Figure 2 shows the spatial distribution of fractionated and low-voltage potentials across the atria in nine different patients. In the upper panels, patients were characterized by a high amount of low-voltage potentials without fractionation. In the middle panels, patients were characterized by mainly fractionated, high-voltage potentials. The lower panels contain examples from patients who were characterized by the presence of both low-voltage potentials with or without fractionation, and fractionated, high-voltage potentials. In all examples, only a minority of the potentials contained fractionated and low-voltage components. The maps reveal a substantial regional and inter-individual variation in the occurrence of fractionation and low-voltage potentials.

Compared to patients without AF, fractionated potentials and low-voltage potentials were more common among patients with history of AF (1.62 [0.84–2.56] vs. 1.87 [1.20–3.23], p=0.017 and 6.04 [3.70–9.49] vs. 9.01 [4.43–11.52], p=0.022, respectively). Fractionated, low-voltage potentials were rare and equally common in patients with AF and patients without AF (0.37 [0.21–0.93] vs. 0.36 [0.14–0.75], p=0.195).

Regional differences in prevalence of fractionation and low-voltage potentials

Table 2 summarizes the regional prevalence of both fractionation and low-voltage potentials across all patients. The prevalence of fractionated potentials in the RA, BB, PVA and LA was respectively 1.31 [0.41–2.92] %, 1.74 [0.54–4.20] %, 0.74 [0.23–2.22] % and 1.07 [0.35–2.57] % whereas the prevalence of low-voltage potentials was 6.06 [2.83–10.72] %, 2.41 [0.62–8.40] %, 4.79 [1.63–12.35] % and 3.84 [1.25–8.92] %, respectively. Fractionated, low-voltage potentials were most common at the RA (0.41 [0.10–0.98] %), followed by BB (0.25 [0.00–0.84] %), PVA (0.08 [0.00–0.34] %) and LA (0.05 [0.00–0.25] %). Patients with AF were characterized by a higher amount of fractionated potentials, low-voltage potentials and fractionated, low-voltage potentials only at BB and PVA (p<0.005).

Table 3 – Distribution of potentials per potential type.

	Non-fractionated, high-voltage	Fractionated, high-voltage	Low-voltage, non-fractionated	Fractionated, low-voltage
Entire atria	2,691,366 (91.5)	45,114 (1.5)	190,758 (6.5)	15,779 (0.5)
RA	1,266,118 (91.1)	19,305 (1.4)	94,280 (6.8)	10,324 (0.7)
BB	303,261 (91.7)	7,476 (2.2)	17,900 (5.4)	2,232 (0.7)
PVA	593,312 (91.3)	8,359 (1.3)	46,347 (7.1)	1,834 (0.3)
LA	528,675 (92.4)	9,974 (1.7)	32,231 (5.6)	1,389 (0.3)

Values are presented as N (%). **RA** = right atrium; **BB** = Bachmann's bundle; **LA** = left atrium; **PVA** = pulmonary vein area.

Interrelationship between fractionation, low-voltage and local CV

All potentials were subdivided into four different groups: 1) fractionated, low-voltage potentials, 2) low-voltage, non-fractionated potentials, 3) fractionated, high-voltage potentials and 4) non-fractionated, high-voltage potentials. The distribution of each category across the four atrial regions is listed in *Table 3*. *Figure 3* illustrates the differences in local CV between the four categories. Local CV at sites with fractionated, low-voltage potentials (46.0 [22.6–72.7] cm/s) was considerably lower compared to sites with either low-voltage, non-fractionated potentials (64.5 [34.8–99.4] cm/s) and fractionated, high-voltage potentials (65.9 [41.7–92.8] cm/s) or sites with non-fractionated, high-voltage potentials (92.3 [66.7–117.9] cm/s, p<0.001 for each comparison). A similar trend in local CV differences was also found for each atrial region separately, indicating that sites with fractionated, low-voltage potentials differ considerably from the other 3 categories, regardless of the anatomical location (*Supplementary Figure 1*).

As demonstrated in *Figure 3*, slowed conduction (CV <50 cm/s) was most common at areas containing fractionated, low-voltage potentials (54.7%), followed by low-voltage, non-fractionated potentials (38.0%), fractionated, high-voltage potentials (33.5%) and non-fractionated, high-voltage potentials (14.4%).

Identification of slow conduction areas

The left panel of *Figure 4* demonstrates the positive predictive values to identify slow conduction areas by using various voltage thresholds and a minimal number of deflections. The highest predictive values can be achieved by using a small voltage threshold (<1 mV) and a minimum of 3 deflections, which resulted in positive predictive values ranging from
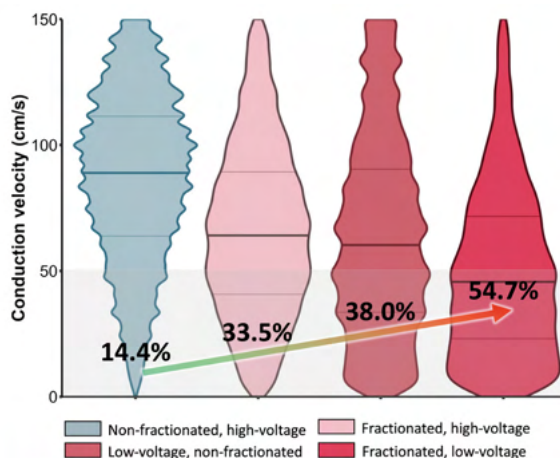
Figure 3 – Local conduction velocity distribution for each potential type. Violin plots of local conduction velocities at sites with 1) non-fractionated, high-voltage potentials, 2) fractionated, high-voltage potentials, 3) low-voltage, non-fractionated potentials and 4) fractionated, low-voltage potentials. The numbers within the shaded area indicate the percentage of slow conduction velocities (<50 cm/s).

Positive predictive value (%)

Potential voltage (mV)	1	2	3	4	5
<0.35	49.2	61.3	70.7	68.0	60.0
	47.4	59.6	68.2	69.6	69.0
	45.5	57.8	65.4	66.2	65.5
	44.3	56.2	63.8	65.0	61.9
	43.5	55.1	63.0	64.1	61.0
<0.60	42.8	54.2	61.9	62.5	56.9
	42.2	53.2	60.6	61.6	57.3
	41.7	52.3	59.4	61.3	58.0
	41.3	51.5	58.5	61.0	57.7
	40.8	50.8	57.6	59.9	58.0
<0.85	40.3	50.1	56.8	59.2	59.5
	39.9	49.5	56.1	58.8	59.2
	39.6	48.9	55.4	58.4	59.0
	39.2	48.3	54.7	57.4	58.9
	38.9	47.8	54.2	57.1	59.1
<1.10	38.6	47.3	53.6	56.9	58.3
	38.3	46.8	53.0	56.1	56.8
	38.1	46.4	52.5	56.1	57.4
	37.9	45.9	52.0	56.0	57.0
	37.6	45.5	51.7	56.0	57.6
<1.35	37.4	45.2	51.2	56.0	57.7
	37.2	44.8	50.8	56.0	56.9
	37.0	44.4	50.6	56.0	58.3
	36.8	44.1	50.2	55.7	58.0
<1.60	36.5	43.8	49.8	55.6	57.9
	36.3	43.5	49.5	55.3	57.4
	36.1	43.2	49.1	54.6	57.1
	35.9	42.8	48.8	54.3	56.6
	35.7	42.5	48.6	54.2	57.0
<1.85	35.5	42.2	48.2	53.9	57.1
	35.2	41.9	48.0	53.6	57.1
	35.0	41.7	47.7	53.4	57.0
	34.8	41.4	47.4	53.0	57.0
<2.00	34.6	41.1	47.1	52.7	56.6

Number of deflections · <40% · 40-50% · 50-60% · >70%

Sensitivity (%)

Potential voltage (mV)	1	2	3	4	5
<0.35	0.93	0.62	0.16	0.02	0.00
	1.82	1.19	0.29	0.05	0.01
	2.86	1.81	0.43	0.07	0.01
	3.89	2.41	0.56	0.09	0.01
	5.06	3.08	0.70	0.10	0.02
<0.60	6.25	3.72	0.82	0.12	0.02
	7.54	4.41	0.95	0.14	0.02
	8.84	5.07	1.08	0.15	0.03
	10.16	5.72	1.21	0.17	0.03
	11.44	6.34	1.33	0.19	0.03
<0.85	12.74	6.97	1.45	0.21	0.03
	14.05	7.58	1.56	0.22	0.04
	15.38	8.18	1.67	0.23	0.04
	16.73	8.76	1.78	0.24	0.04
	18.06	9.33	1.89	0.26	0.04
<1.10	19.41	9.90	1.99	0.27	0.04
	20.73	10.45	2.08	0.29	0.05
	22.05	10.99	2.18	0.30	0.05
	23.37	11.50	2.26	0.31	0.05
	24.65	12.01	2.35	0.33	0.05
<1.35	25.91	12.50	2.44	0.34	0.05
	27.15	12.97	2.52	0.35	0.06
	28.37	13.42	2.60	0.36	0.06
	29.59	13.89	2.68	0.37	0.06
<1.60	30.78	14.35	2.76	0.39	0.06
	31.94	14.78	2.83	0.39	0.06
	33.11	15.20	2.89	0.40	0.06
	34.25	15.61	2.96	0.41	0.06
	35.34	16.00	3.03	0.41	0.07
<1.85	36.43	16.38	3.09	0.42	0.07
	37.53	16.76	3.16	0.43	0.07
	38.58	17.13	3.22	0.43	0.07
	39.62	17.48	3.28	0.44	0.07
<2.00	40.61	17.82	3.33	0.44	0.07

Number of deflections · <5% · 5-20% · 20-30% · 30-40% · >40%

Figure 4 – Positive predictive values and sensitivity for identifying slow conduction areas. The left and right panel illustrates respectively the positive predictive values and sensitivity for identifying slow conduction areas according to different voltage thresholds and a minimal number of deflections. The color gradients of the heat maps illustrate the performance of each metric, ranging from weak (light orange) to strong (dark red).

54.2 to 70.7%. However, as demonstrated in the right panel of *Figure 4*, the sensitivity of these thresholds was relatively low (0.003-1.89%). Therefore, many slow conduction areas are still missed when using these potential morphology parameters only. However, in the case when fractionated, low-voltage potentials are present, they are very likely to correspond to slow conduction.

Discussion

In this bi-atrial epicardial mapping study, we report an in-depth analysis of the relationship between fractionation, low-voltage potentials and local CV during SR. Particularly fractionated, low-voltage potentials were related to a reduced CV and were linked to the largest degree of slowed conduction. These specific potentials were more common in patients with prior AF episodes, particularly at the PVA and BB. However, many areas of slowed conduction could still be missed when using solely potential voltage and fractionation as these areas also frequently occur in the presence of non-fractionated, high-voltage potentials. The strong inverse relationship between the positive predictive value and sensitivity will therefore likely complicate the use of these signal-based ablation approaches in AF patients for identifying slow conduction zones.

Prevalence and regional distribution of fractionation and low-voltage

Despite the usage of fractionation- and low-voltage-guided ablation approaches, detailed understanding of substrates have been hampered by the use of non-uniform definitions, lack of high-density mapping and various electrogram processing technologies.[1] In the present study, we systematically examined the prevalence of fractionation and low-voltage potentials across both atria, including BB. Where previous studies lacked exact quantification of the amount of fractionated and/or low-voltage potentials during SR[5-12], we now demonstrate

that sites with fractionated, low-voltage potentials are rare across all atrial regions, but were particularly present at BB and PVA in patients with a history of AF. Moreover, fractionated, low-voltage potentials only accounted for a modest portion of either all fractionated or all low-voltage potentials, which is in contrast with the general assumption that fractionation relates to low potential voltage and vice versa.[17,18]

There are numerous factors that influence atrial potential morphology, including underlying electrophysiological properties, tissue structure and recording technology.[1] A considerable amount of fractionation, particularly those with a high potential voltage, may be caused by colliding wavefronts and diffuse fiber orientation.[19] Even in the PVA, only a minority of fractionated potentials had low voltage components, while this area is assumed to be the preferential site for fractionation-based ablation therapy in daily practice. Pashakhanloo et al.[20] examined the left atrial wall at a submillimeter resolution and showed a local, disorganized transmural fiber distribution. A heterogeneous transmural fiber orientation was especially observed at the poster-inferior region of the LA, which correspond to the PVA in our study. The architecture of the left atrial wall may therefore explain the presence of fractionated, high-voltage potentials at these sites.

On the other hand, a large proportion of low-voltage potentials had no fractionated components. Unipolar potential voltage reflects the summation of action potentials within the recording area of 1 electrode, and its shape and amplitude are influenced by electrophysiological and structural characteristics of the myocardial tissue.[1] The myocardial architecture can attenuate unipolar voltage by atrial wall thickness and the presence of epicardial fat[21,22], which does not necessarily result in inhomogeneous conduction. In a previous study, we also demonstrated that unipolar voltage of single potentials are mainly determined by their relative R- and S-wave morphology, which is influenced by the wavefront propagation.[23] Consequently, a large amount of low-voltage, non-fractionated potentials could also be explained by asymmetry of the relative R- and S-wave amplitudes. It is for these reasons that low-voltage potentials do not equal fractionation and absolute low-voltage thresholds for inhomogeneous conduction remain arbitrary.

Relation between conduction velocity, fractionation and low-voltage

Sites containing fractionation and low-voltage potentials are considered targets for substrate modification therapy as they are indicative of slowing of conduction. The relationship between either CV, fractionation and low-voltages have been described in various studies.[5-12] However, the methodology to define either of three parameters differed considerably. First, clinical studies mostly use bipolar electrograms during the measurements which have a considerable direction-dependent effect on potential voltages and lack a standardized definition for fractionation.[10,18] In contrast, characterization of fractionation by using unipolar electrograms is more straightforward and is therefore preferred. Second, there are many different techniques to compute CV.[15,24-27] In most studies, global CV instead of local CV is used to correlate to fractionation and low-voltage.[6,7] In addition, our method of discrete velocity vectors showed important superiority to previously used local CV techniques, such as finite differences and polynomial surface fitting.[15] These other CV estimation techniques masked local areas of conduction slowing more often due to smoothing of wavefront propagation.

To date, no study has investigated local CV while discriminating between sites with both fractionation and low-voltage, or the presence of solely fractionated or low-voltage potentials. In a recent study, Van Schie et al.[9] demonstrated that there was no clear correlation between unipolar potential voltage and local CV, although smaller voltages were observed in areas of slowed conduction. Also, they demonstrated that unipolar potential

voltages were decreased in fractionated potentials compared to potentials with one single deflection, showing a clear inversely proportional relationship between unipolar potential voltage and the number of deflections. In a following study, Van Schie et al.[10] showed that bipolar low-voltage areas were characterized by a decreased CV and more fractionation. However, it was also demonstrated that high unipolar potential voltages and CVs could still be recorded in these bipolar low-voltage areas, even by using direction-independent omnipolar electrograms. In the current study, we demonstrated the importance of differentiating between 1) fractionated, low-voltage potentials, 2) low-voltage, non-fractionated potentials, and 3) fractionated, high-voltage potentials. Local CV at sites with fractionated, low-voltage potentials was considerably lower compared to sites with either low-voltage, non-fractionated potentials and fractionated, high-voltage potentials.

Recently, Frontera et al.[16] demonstrated the importance of slowing of conduction by analyzing CV during SR. Their data revealed that the number and density of slow conduction corridors, defined as discrete areas of CV <50 cm/s, increased in parallel with the progression of AF. The observed slow conduction corridors were often associated with pivot points, defined as sites characterized by a high wavefront curvature. We further expanded on identification of these slow conduction zones by showing that fractionated, low-voltage potentials most often coincide with slowed CV (<50 cm/s). However, 14.4% of all non-fractionated, high-voltage potentials had slowed CV. These findings highlight therefore the complexity of the conventional signal-based thresholds for slowed CV.

If a signal-based approach would be attempted to target slowed CV, the voltage thresholds and number of deflections will have significant impact on the positive predictive value. While high positive predictive values would result in avoidance of needless scarring, it will be accompanied by a low sensitivity (<50%). Hence, this first-time granular approach targeting slow conduction areas shows the limitations of fractionated and/or voltage based ablations. Also, this may provide in part the rational why either approach currently appears to be ineffective in improving ablation outcomes in persistent types of AF.[2-4] Future studies should therefore explore additional (non-signal based) parameters or approaches if slowed conduction is to be targeted.

Limitations

In daily clinical practice, electrophysiological studies are performed from the endocardium. Although properties of endocardial potentials are unknown in the current study, simultaneous epicardial and endocardial mapping studies during SR demonstrated only limited differences in fractionation.[28] In addition, epicardial mapping assures better close-contact recordings than conventional endocardial mapping thereby decreasing the chance that low voltage potentials are the result of poor contact. In the current study, we did not perform structural analysis to further provide insight in the relation between fractionation, low-voltage and CV. Histological examination and/or integration with other imaging modalities, such as late gadolinium enhancement magnetic resonance images, will aid in further characterizing the underlying (arrhythmogenic) substrate.

Conclusion

Sites with fractionated, low-voltage potentials have substantially lower local CV compared to sites with either low-voltage, non-fractionated potentials or fractionated, high-voltage potentials. However, the strong inverse relationship between the positive predictive value and sensitivity of combined voltage and fractionation threshold for slowed CV is likely to complicate the use of these signal-based ablation approaches in AF patients.

References

1. de Groot NMS, Shah D, Boyle PM, Anter E, Clifford GD, Deisenhofer I, Deneke T, van Dessel P, Doessel O, Dilaveris P, et al. Critical appraisal of technologies to assess electrical activity during atrial fibrillation: a position paper from the European Heart Rhythm Association and European Society of Cardiology Working Group on eCardiology in collaboration with the Heart Rhythm Society, Asia Pacific Heart Rhythm Society, Latin American Heart Rhythm Society and Computing in Cardiology. Europace. 2022;24:313-330.

2. Verma A, Jiang CY, Betts TR, Chen J, Deisenhofer I, Mantovan R, Macle L, Morillo CA, Haverkamp W, Weerasooriya R, et al. Approaches to catheter ablation for persistent atrial fibrillation. N Engl J Med. 2015;372:1812-1822.

3. Marrouche NF, Wazni O, McGann C, Greene T, Dean JM, Dagher L, Kholmovski E, Mansour M, Marchlinski F, Wilber D, et al. Effect of MRI-Guided Fibrosis Ablation vs Conventional Catheter Ablation on Atrial Arrhythmia Recurrence in Patients With Persistent Atrial Fibrillation: The DECAAF II Randomized Clinical Trial. JAMA. 2022;327:2296-2305.

4. Masuda M, Asai M, Iida O, Okamoto S, Ishihara T, Nanto K, Kanda T, Tsujimura T, Matsuda Y, Okuno S, et al. Additional Low-Voltage-Area Ablation in Patients With Paroxysmal Atrial Fibrillation: Results of the Randomized Controlled VOLCANO Trial. J Am Heart Assoc. 2020;9:e015927.

5. Park JH, Pak HN, Kim SK, Jang JK, Choi JI, Lim HE, Hwang C, Kim YH. Electrophysiologic characteristics of complex fractionated atrial electrograms in patients with atrial fibrillation. J Cardiovasc Electrophysiol. 2009;20:266-272.

6. Roberts-Thomson KC, Kistler PM, Sanders P, Morton JB, Haqqani HM, Stevenson I, Vohra JK, Sparks PB, Kalman JM. Fractionated atrial electrograms during sinus rhythm: relationship to age, voltage, and conduction velocity. Heart Rhythm. 2009;6:587-591.

7. Viles-Gonzalez JF, Gomes JA, Miller MA, Dukkipati SR, Koruth JS, Eggert C, Coffey J, Reddy VY, d'Avila A. Areas with complex fractionated atrial electrograms recorded after pulmonary vein isolation represent normal voltage and conduction velocity in sinus rhythm. Europace. 2013;15:339-346.

8. Teh AW, Kistler PM, Lee G, Medi C, Heck PM, Spence SJ, Sparks PB, Morton JB, Sanders P, Kalman JM. The relationship between complex fractionated electrograms and atrial low-voltage zones during atrial fibrillation and paced rhythm. Europace. 2011;13:1709-1716.

9. van Schie MS, Starreveld R, Bogers A, de Groot NMS. Sinus rhythm voltage fingerprinting in patients with mitral valve disease using a high-density epicardial mapping approach. Europace. 2021;23:469-478.

10. van Schie MS, Kharbanda RK, Houck CA, Lanters EAH, Taverne Y, Bogers A, de Groot NMS. Identification of Low-Voltage Areas: A Unipolar, Bipolar, and Omnipolar Perspective. Circ Arrhythm Electrophysiol. 2021;14:e009912.

11. Kuo MJ, Ton AN, Lo LW, Lin YJ, Chang SL, Hu YF, Chung FP, Tuan TC, Chao TF, Liao JN, et al. Abnormal Conduction Zone Detected by Isochronal Late Activation Mapping Accurately Identifies the Potential Atrial Substrate and Predicts the Atrial Fibrillation Ablation Outcome After Pulmonary Vein Isolation. Circ Arrhythm Electrophysiol. 2023;16:e011149.

12. Ramirez FD, Meo M, Dallet C, Krisai P, Vlachos K, Frontera A, Takigawa M, Nakatani Y, Nakashima T, Andre C, et al. High-resolution mapping of reentrant atrial tachycardias: Relevance of low bipolar voltage. Heart Rhythm. 2023;20:430-437.

13. Kik C, Mouws E, Bogers A, de Groot NMS. Intra-operative mapping of the atria: the first step towards individualization of atrial fibrillation therapy? Expert Rev Cardiovasc Ther. 2017;15:537-545.

14. Konings KT, Smeets JL, Penn OC, Wellens HJ, Allessie MA. Configuration of unipolar atrial electrograms during electrically induced atrial fibrillation in humans. Circulation. 1997;95:1231-1241.

15. van Schie MS, Heida A, Taverne Y, Bogers A, de Groot NMS. Identification of local atrial conduction heterogeneities using high-density conduction velocity estimation. Europace. 2021;23:1815-1825.

16. Frontera A, Pagani S, Limite LR, Peirone A, Fioravanti F, Enache B, Cuellar Silva J, Vlachos K, Meyer C, Montesano G, et al. Slow Conduction Corridors and Pivot Sites Characterize the Electrical Remodeling in Atrial Fibrillation. JACC Clin Electrophysiol. 2022;8:561-577.

17. Kalarus Z, Mairesse GH, Sokal A, Boriani G, Sredniawa B, Casado-Arroyo R, Wachter R, Frommeyer G, Traykov V, Dagres N, et al. Searching for atrial fibrillation: looking harder, looking longer, and in increasingly sophisticated ways. An EHRA position paper. Europace. 2023;25:185-198.

18. van der Does LJ, de Groot NM. Inhomogeneity and complexity in defining fractionated electrograms. Heart Rhythm. 2017;14:616-624.

19. Jadidi AS, Duncan E, Miyazaki S, Lellouche N, Shah AJ, Forclaz A, Nault I, Wright M, Rivard L, Liu X, et al. Functional nature of electrogram fractionation demonstrated by left atrial high-density mapping. Circ Arrhythm Electrophysiol. 2012;5:32-42.

20. Pashakhanloo F, Herzka DA, Ashikaga H, Mori S, Gai N, Bluemke DA, Trayanova NA, McVeigh ER. Myofiber Architecture of the Human Atria as Revealed by Submillimeter Diffusion Tensor Imaging. Circ Arrhythm Electrophysiol. 2016;9:e004133.

21. Saba MM, Akella J, Gammie J, Poston R, Johnson A, Hood RE, Dickfeld TM, Shorofsky SR. The influence of fat thickness on the human epicardial bipolar electrogram characteristics: measurements on patients undergoing open-heart surgery. Europace. 2009;11:949-953.

22. Desjardins B, Morady F, Bogun F. Effect of epicardial fat on electroanatomical mapping and epicardial catheter ablation. J Am Coll Cardiol. 2010;56:1320-1327.

23. van Schie MS, Starreveld R, Roos-Serote MC, Taverne Y, van Schaagen FRN, Bogers A, de Groot NMS. Classification of sinus rhythm single potential morphology in patients with mitral valve disease. Europace. 2020;22:1509-1519.

24. Bayly PV, KenKnight BH, Rogers JM, Hillsley RE, Ideker RE, Smith WM. Estimation of conduction velocity vector fields from epicardial mapping data. IEEE Trans Biomed Eng. 1998;45:563-571.

25. Weber FM, Schilling C, Seemann G, Luik A, Schmitt C, Lorenz C, Dossel O. Wave-direction and conduction-

velocity analysis from intracardiac electrograms--a single-shot technique. IEEE Trans Biomed Eng. 2010;57:2394-2401.

26. Konings KT, Kirchhof CJ, Smeets JR, Wellens HJ, Penn OC, Allessie MA. High-density mapping of electrically induced atrial fibrillation in humans. Circulation. 1994;89:1665-1680.

27. Cantwell CD, Roney CH, Ng FS, Siggers JH, Sherwin SJ, Peters NS. Techniques for automated local activation time annotation and conduction velocity estimation in cardiac mapping. Comput Biol Med. 2015;65:229-242.

28. van der Does L, Knops P, Teuwen CP, Serban C, Starreveld R, Lanters EAH, Mouws E, Kik C, Bogers A, de Groot NMS. Unipolar atrial electrogram morphology from an epicardial and endocardial perspective. Heart Rhythm. 2018;15:879-887.

9
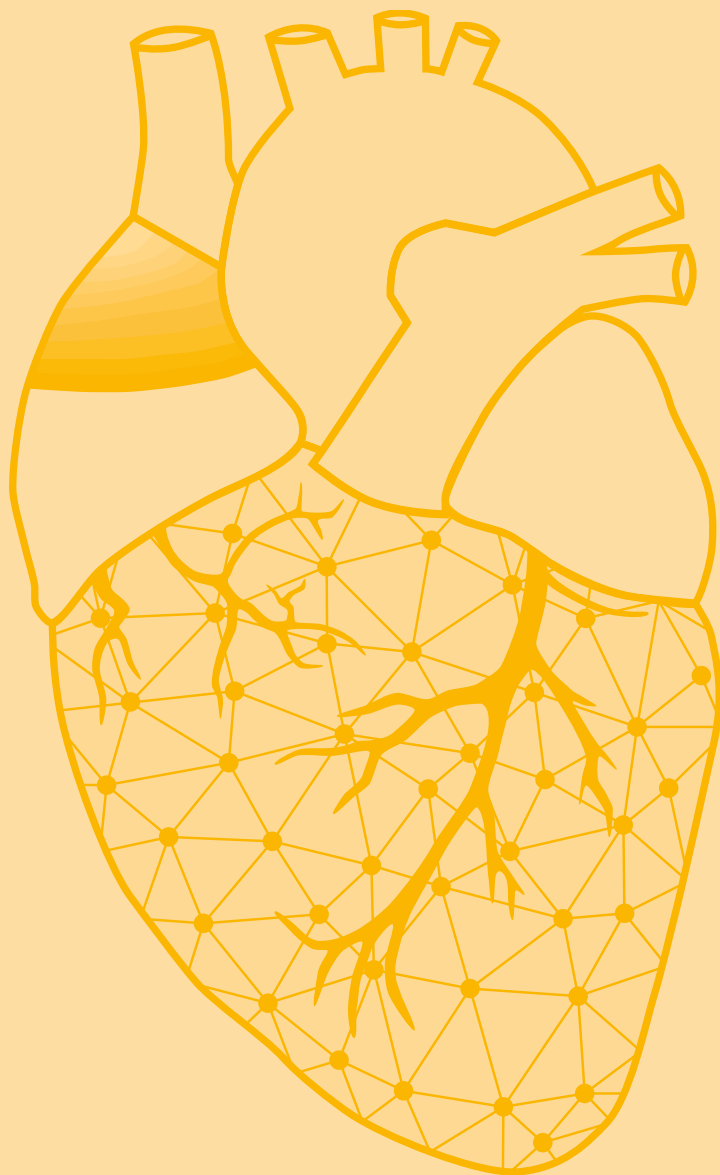
Chapter 10

Atrial extrasystoles enhance low-voltage fractionation electrograms in patients with atrial fibrillation

Mathijs S. van Schie

Rongheng Liao

Nawin L. Ramdat Misier

Paul Knops

Annejet Heida

Yannick J.H.J. Taverne

Natasja M.S. de Groot

Abstract

Background: Atrial extrasystoles (AES) provoke conduction disorders and may trigger episodes of atrial fibrillation (AF). However, the direction- and rate-dependency of electrophysiological tissue properties on epicardial unipolar electrogram (EGM) morphology is unknown. Therefore, this study examined the impact of spontaneous AES on potential amplitude, -fractionation, -duration and low-voltage areas (LVA), and correlated these differences with various degrees of prematurity and aberrancy.

Methods: Intra-operative high-resolution epicardial mapping of the right and left atrium (RA, LA), Bachmann's bundle (BB) and pulmonary vein area (PVA) was performed during SR in 287 patients (60 with AF). AES were categorized according to their prematurity index (>25% shortening) and degree of aberrancy (none, mild/opposite, moderate and severe).

Results: In total, 837 unique AES (457 premature; 58 mild/opposite-, 355 moderate- and 154 severe aberrant) were included. The average prematurity index was 28% [12–45]. Comparing SR and AES, average voltage decreased (-1.1 [-1.2, -0.9] mV, p<0.001) at all atrial regions, whereas the amount of LVA and fractionation increased (respectively +3.4 [2.7, 4.1] % and +3.2 [2.6, 3.7] %, p<0.001). Only weak or moderate correlations were found between EGM morphology parameters and prematurity indices (R^2<0.299, p<0.001). All parameters were, however, most severely affected by either mild/opposite or severely aberrant AES, in which the effect was more pronounced in AF patients. Also, there were considerable regional differences in effects provoked by AES.

Conclusions: Unipolar EGM characteristics during spontaneous AES are mainly directional-dependent and not rate-dependent. AF patients have more direction-dependent conduction disorders, indicating enhanced non-uniform anisotropy that is uncovered by spontaneous AES.

Journal site &
supplementary material

Introduction

Non-remodeled atrial tissue is considered to be anisotropic, resulting in a much faster electrical conduction along the longitudinal direction of myocardial fibers than in transverse direction.[1] Altered cell-to-cell communication and tissue damage results in a discontinuous distribution of conduction properties, which is known as non-uniform anisotropy. The presence of non-uniform anisotropy results in local conduction disorders and heterogeneous conduction, leading to increased susceptibility to tachyarrhythmias such as atrial fibrillation (AF).[2]

Atrial extrasystoles (AES) are common interruptions of sinus rhythm (SR), which may trigger episodes of AF. AES triggering AF most often originate from within the pulmonary veins (PV), especially in patients with paroxysmal AF.[3] However, non-PV triggers, emerging from e.g. the superior vena cava, left atrial (LA) posterior free wall, LA appendage, terminal crest and interatrial septum, also play an important role in a significant part of AF patients.[4] Especially in non-uniform anisotropic tissue, conduction disorders are direction and frequency dependent. Extracellular potentials recorded in these areas may be fractionated. This could be caused by asynchronous activation of two or more groups of cardiomyocytes that are separated by areas in which there is diminished or no cell-to-cell coupling.[5] The morphology of extracellular unipolar potentials can therefore be used to detect non-uniform anisotropic tissue.[6] High-resolution mapping during AES provides the opportunity to detect areas of direction and frequency dependent non-uniform anisotropy. The goal of this study was therefore to examine the impact of spontaneous AES on unipolar potential morphology and to correlate these differences with various degrees of prematurity and aberrancy in patients with and without history of AF.

Methods

Study population

The study population consisted of 287 successive adult patients with or without a history of AF undergoing open heart coronary artery bypass grafting (CABG), aortic or mitral valve surgery or a combination of valvular surgery and CABG in the Erasmus Medical Center Rotterdam. This study was approved by the institutional medical ethical committee (MEC2010-054/MEC2014-393).[7,8] Written informed consent was obtained from all patients. Patient characteristics (e.g., age, medical history, cardiovascular risk factors, time in AF) were obtained from the patient's medical record.

Mapping procedure

Epicardial high-resolution mapping was performed prior to commencement to extra-corporal circulation, as previously described in detail.[9] Epicardial mapping was performed with a 128-electrode array or 192-electrode array (electrode diameter respectively 0.65 mm or 0.45 mm, interelectrode distances 2.0 mm). Mapping was conducted by shifting the electrode array along imaginary lines with a fixed anatomic orientation, following a predefined mapping scheme, covering the entire epicardial surface of the right atrium (RA), Bachmann's bundle (BB), pulmonary vein area (PVA) and left atrium (LA), as illustrated in *Figure 1*.

Five seconds of SR were recorded from every mapping site, including a surface ECG lead, a calibration signal of 2 mV and 1000 ms, a bipolar atrial reference electrogram (EGM) and all unipolar epicardial EGMs. In patients who presented in AF, SR mapping was performed

10
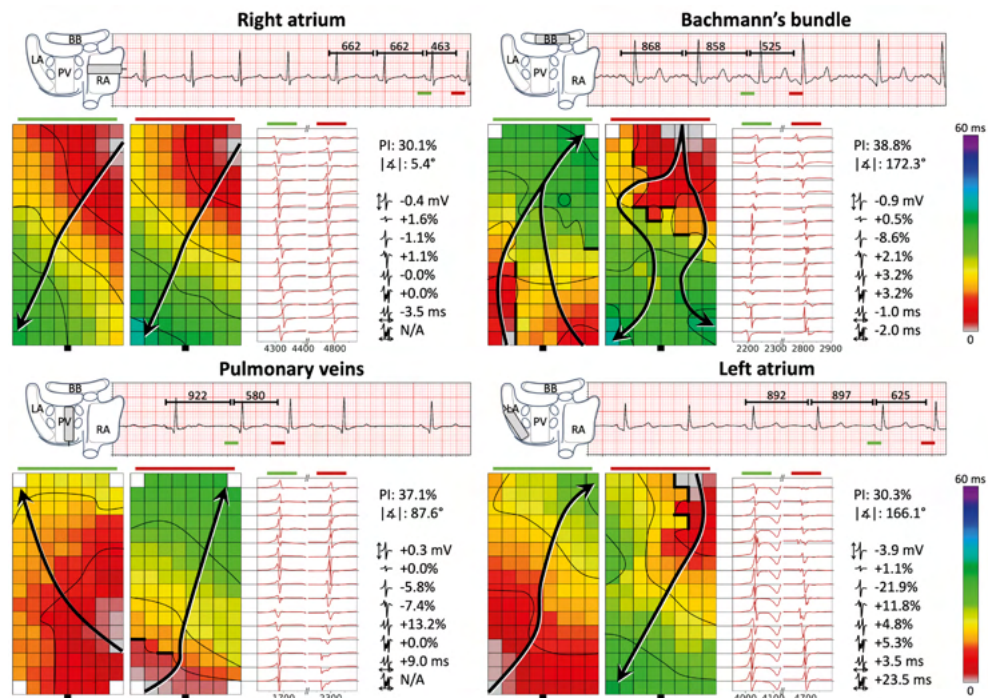
Figure 1 – Examples of SR beats and AES recorded at various atrial sites. Four examples of 5 second SR recordings including AES and corresponding color-coded activation maps and EGMs. Thick black lines in the activation maps correspond with conduction block according to a time difference between adjacent electrodes of ≥12 ms. For each patient, the PI, and average difference in wavefront direction, potential voltage, LVAs, amount of SP, SDP, LDP and FP and their corresponding FD is given. *Upper left panel*: one SR beat and a mild-premature, non-aberrant AES (origin right-sided) recorded at the RA. Although average potential voltages decreased, several electrodes demonstrate a local increase in potential voltages. Potential morphology was comparable between SR and AES. *Upper right panel*: one SR beat and a moderate premature AES with mild/opposite aberrancy (origin left-sided) recorded at BB. Compared with SR, the AES resulted in a decrease of potential voltages and an increase in the number of SDPs, LDPs and FPs. *Lower left panel*: one SR beat and a moderate premature AES with severe aberrancy (origin left-sided) recorded at the PVA. There was a large spatial variability in potential voltage differences between SR and the AES. Compared to SR, there was a specific increase in the number of LDPs and fractionation duration. *Lower right panel*: one SR beat and a mild premature AES with mild/opposite aberrancy (origin left-sided) recorded at the LA. Compared with SR, there was a large decrease in potential voltages and number of SPs. There was a large increase in the number of SDPs, LDPs and FPs, with severe prolongation of FPs. **AES** = atrial extrasystole; **AF** = atrial fibrillation; **BB** = Bachmann's bundle; **FD** = fractionation duration; **FP** = fractionated potentials; **LA** = left atrium; **LDP** = long-double potentials; **LVA** = low-voltage area; **PI** = prematurity index; **PVA** = pulmonary vein area; **RA** = right atrium; **SDP** = short-double potentials; **SP** = single potentials; **SR** = sinus rhythm.

after electrical cardioversion. Data were stored on a hard disk after amplification (gain 1000), filtering (bandwidth 0.5–400 Hz), sampling (1 kHz) and analogue-to-digital conversion (16 bits).

Data analysis

Unipolar EGMs were semi-automatically analyzed using custom-made software. The steepest negative slope of an atrial potential was marked as the local activation time (LAT). All annotations were manually checked with a consensus of two investigators. Several electrophysiological parameters were computed, including potential voltages and fractionation. The potential voltage was defined as the peak-to-peak amplitude of the steepest deflection; potentials with an amplitude below 1.0 mV were defined as low

voltage.[10] The proportion of low-voltage potentials was used as quantification of the amount of low-voltage areas (LVAs).

Potentials were classified as single- (SP, single negative deflection), short-double- (SDP, interval between deflections <15 ms), long-double- (LDP, deflection interval ≥15 ms), or fractionated potentials (FP, ≥3 deflections), as illustrated in *Supplementary Figure 1*. The time difference (ms) between the first and last deflection of double potentials (DP; SDP+LDP) and FPs is defined as fractionation duration (FD). Areas of simultaneous activation were excluded from analysis in order to avoid inclusion of far-field potentials. For all electrophysiological parameters the median of the preceding sinus beats was taken and compared to the median of the AES. The difference was considered as the effect provoked by AES.

Classification of atrial extrasystoles

AES were defined as beats with either a shortening in cycle length of ≥25% compared to the previous sinus beat measured at the same mapping site and/or an aberrant activation pattern compared to the SR beats.[6] The degree of prematurity (prematurity index) was determined for beats preceded by at least two sinus beats, as:

$$PI = \frac{CL_{SR} - CL_{AES}}{CL_{SR}} \cdot 100\%$$

with CL_{AES} equals the cycle length of the spontaneous AES and CL_{SR} the cycle length of the preceding two sinus beats. Premature AES were categorized into three groups based on their prematurity as mild (25<PI<35%), moderate (35<PI<50%) and severe (PI>50%). The degree of aberrancy was determined by estimating the local propagation angle relying on fitting polynomial surfaces, as described before.[11] Aberrancy was categorized according to the shift in direction of the local wavefront trajectory (∡) as: none (|∡|<22.5°), mild/opposite (|∡|>157.5°), moderate (22.5≤|∡|<67.5° or 112.5<|∡|≤157.5°) and severe/perpendicular (67.5≤|∡|≤112.5°). As AES emerging as an epicardial breakthrough spread in multiple directions, the degree of aberrancy could not be determined and therefore these AES were excluded from analyses.

Statistical analysis

Normally distributed data are expressed as mean ± standard deviation, whereas skewed data are expressed as median [25th–75th percentile]. Clinical characteristics were compared using Student's *t*-test or Mann-Whitney U test when appropriate. Categorical data are expressed as number (percentage) and analyzed with a χ^2 or Fisher exact test.

To analyze the difference between SR and AES, a paired *t*-test or Wilcoxon signed-rank test was used. The differences were presented as mean [95% CI]. Correlation was determined by ordinary least squares regression. A *p*-value <0.05 was considered statistically significant. A Bonferroni correction was applied when appropriate.

Results

Study population

Clinical characteristics of the study population (N=287, 198 male (69%), age 68±10 years) are summarized in *Supplementary Table 1*. Patients underwent either CABG (IHD: N=133; 46%), aortic valve surgery with or without CABG ((i)AVD: N=80; 28%) or mitral valve surgery with or without CABG ((i)MVD: N=74; 26%). Sixty patients (21%) had a history of AF including paroxysmal (N=40; 67%), persistent (N=18; 30%) and long-standing persistent AF (N=2; 3%).

10
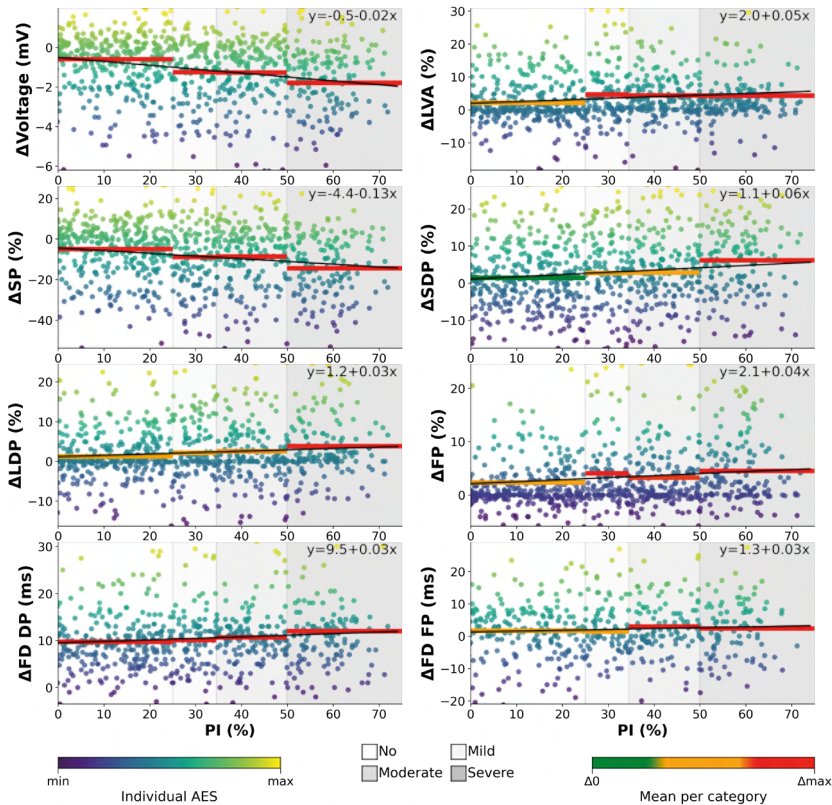
Figure 2 – Relation between prematurity index and potential characteristics. In each panel, prematurity indices are plotted against each of the EGM parameters. Each individual AES is indicated by a dot of which color indicates the average provoked effect. The color scale ranges from the smallest to the largest effect of all AES. The black line indicates the linear correlation between prematurity index and the effect provoked by all AES. Four (none, mild, moderate, severe) prematurity classes are separately highlighted by a grayscale, ranging from light grey to dark grey respectively. The average for each class is colored according to the mean effect, ranging from 0 to the maximum difference of all classes. **AES** = atrial extrasystole; **DP** = short+long-double potentials; **FD** = fraction duration; **FP** = fractionated potentials; **LDP** = long-double potentials; **LVA** = low-voltage area; **SDP** = short-double potentials; **SP** = single potentials.

Characteristics of AES

In total, 837 unique AES were included for analysis (2 [1–4] AES per patient). Most AES were recorded at the RA (N=355, 42%) followed by LA (N=186, 22%), PVA (N=149, 18%) and BB (N=147, 18%). Average CL_{SR} was 842±191 ms, while average CL_{AES} was 592±202 ms resulting in an average prematurity index of 28% [12–45]. A total of 457 (55%) AES were classified as premature. Of all AES, 581 (69%) were recorded in patients without AF. On average, 2 [1–4] AES per patient were included in both the no AF and AF group (p=0.393).

Figure 1 illustrates 4 typical examples of local activation time maps and unipolar potentials during SR and corresponding AES during different degrees of prematurity and aberrancy. In all recordings, spontaneous AES resulted in clear changes in either potential voltages or potential type morphologies. Remarkably, within the recording area, there was a large spatial variation in effect provoked by the AES; e.g., 1) potential voltages either increased or decreased; 2) fractionation either arose or disappeared and 3) FD of fractionated potentials either increased or decreased.

Effect of prematurity on potential morphology

Only weak or moderate correlations were found between EGM morphology parameters and prematurity indices of all AES ($R^2 < 0.299$, $p < 0.001$). All premature AES were further subdivided into four classes according to their prematurity as non- (N=380), mild (N=117), moderate (N=184) and severe (N=156) premature AES. Electrophysiological characteristics of potentials within each of these classes are listed in *Supplementary Table 2* and visualized in *Figure 2*. Although there were only weak correlations between EGM morphology parameters and prematurity indices, there was a larger decrease in average potential voltage and number of SPs, as well as a larger increase in the number of LVAs, SDPs, LDPs and FPs ($p < 0.015$) during
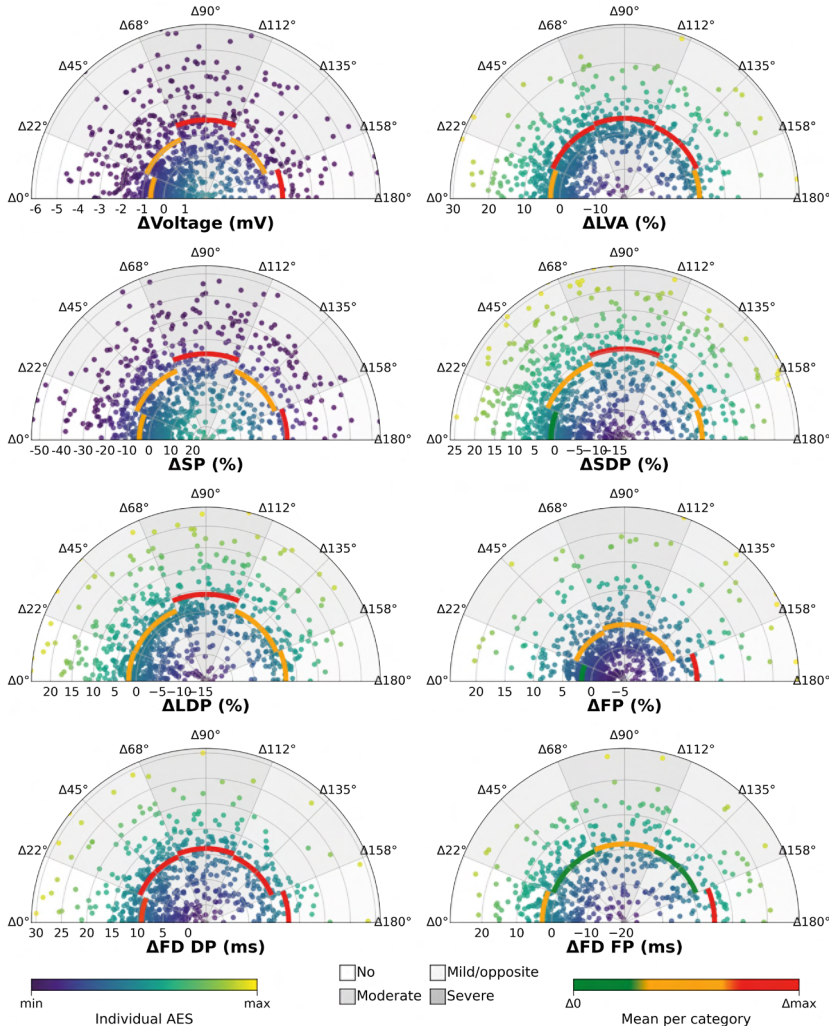
Figure 3 – Relation between aberrancy and potential characteristics. In each panel, the absolute difference in propagation direction for each AES is plotted against the various EGM parameters in polar plots. Each individual AES is indicated by a dot of which color indicates the average provoked effect. The color scale ranges from the smallest to the largest effect of all AES. Four (none, mild/opposite, moderate, severe) aberrancy classes are separately highlighted by a grayscale, ranging from light grey to dark grey respectively. The average for each class is colored according to the mean effect ranging from 0 to the maximum difference of all classes. **AES** = atrial extrasystole; **DP** = short+long-double potentials; **FD** = fractionation duration; **FP** = fractionated potentials; **LDP** = long double potentials; **LVA** = low-voltage area; **SDP** = short double potentials; **SP** = single potentials.
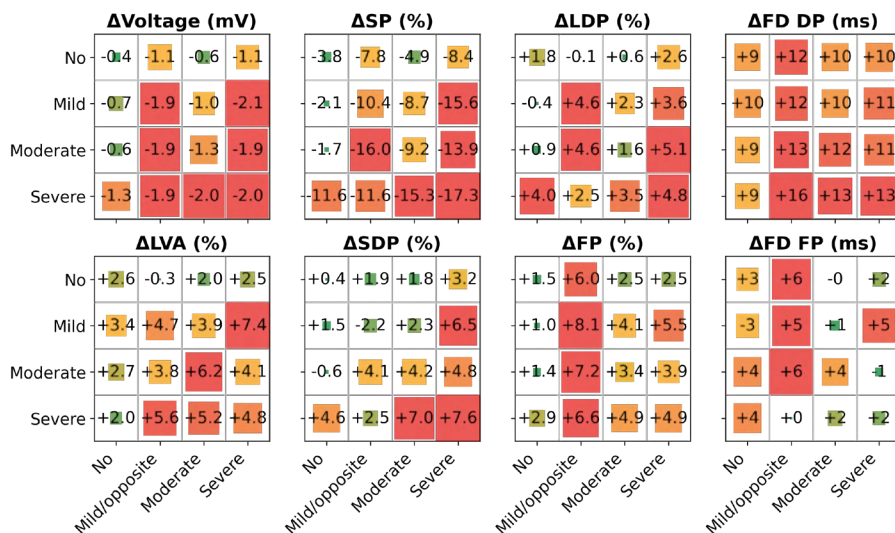
Figure 4 – Interrelationship between aberrancy and prematurity. The mean effect of each parameter is visualized for all AES with varying degrees of aberrancy (x-axis) and prematurity (y-axis). The size and color (from green to red) of the squares represent the mean effect provoked by the AES in each class. **DP** = short+long-double potentials; **FD** = fractionation duration; **FP** = fractionated potentials; **LDP** = long double potentials; **LVA** = low-voltage area; **SDP** = short double potentials; **SP** = single potentials.

severe premature AES compared to non-premature AES. There was no effect of prematurity on FD of both DP and FP.

There were considerable regional differences in the effect of prematurity on potential voltages and fractionation. At the RA, potential voltages and the number of SPs decreased and the number of SDPs increased with increasing severity of prematurity (p<0.001), while at BB only potential voltages decreased considerably during severe premature AES. At all other sites, no clear relations were found between various EGM morphology parameters and prematurity.

Effect of aberrancy on potential morphology

All 837 AES were categorized according to the mean shift in direction of the propagating wavefront as non- (N=270), mild/opposite (N=58), moderate (N=355) and severe (N=154) aberrant. Directional effects of AES on potential morphology characteristics are listed in *Supplementary Table 3* and illustrated in *Figure 3*. Although potential voltages decreased during all aberrant AES, the largest decrease was found in mild/opposite and severe aberrant AES (-1.6 [-2.2, -1.1] mV and -1.7 [-2.0, -1.4] mV respectively, p<0.001). In all aberrancy categories, the number of SPs decreased compared to non-aberrant AES (p<0.001).

There were significant interregional differences in the impact of aberrant AES on potential morphology characteristics. At the RA, the most prominent effect of aberrancy was caused by severe aberrant AES, consisting of a decrease in potential voltages and number of SPs, and an increase in the number of SDPs (p<0.001 for each). Moderate aberrant AES resulted only in an increase in the number of SDP (p<0.001). At BB, only mild/opposite AES resulted in a decrease in potential voltages (p=0.009), whereas at the LA, both mild/opposite and severe aberrant AES provoked the largest differences in potential morphology characteristics. This consisted of a decrease in potential voltages and number of SPs, as well as an increase in the amount of LDPs and FPs (p≤0.001 for each). At the PVA, only severe aberrant AES resulted

Table 1 – Influence of AF episodes in mild/opposite and severe aberrant AES.

Parameter	Δ (AES-SR) without AF	Δ (AES-SR) with AF	*p*-value
Voltage (mV) - All beats	-1.6 [-1.9, -1.3]	-1.9 [-2.3, -1.4]	0.179
• RA	-1.2 [-1.7, -0.7]	-2.8 [-3.5, -2.1]	<0.001
• BB	-1.5 [-1.8, -1.1]	-1.3 [-1.7, -0.9]	0.301
• PVA	-1.5 [-2.3, -0.7]	-1.0 [-1.9, -0.0]	0.193
• LA	-2.8 [-3.7, -1.9]	-2.3 [-3.5, -1.0]	0.181
LVA (%) - All beats	+3.8 [2.3, 5.4]	+4.3 [1.6, 6.9]	0.114
• RA	+3.1 [1.0, 5.1]	+5.8 [2.6, 9.0]	0.103
• BB	+5.3 [2.0, 8.7]	+8.6 [0.8, 16.5]	0.493
• PVA	+3.6 [-0.7, 7.9]	-0.1 [-6.5, 6.3]	0.466
• LA	+4.7 [0.6, 8.9]	+4.5 [2.2, 6.8]	0.123
SP (%) - All beats	-10.6 [-13.7, -7.6]	-17.6 [-22.8, -12.4]	0.014
• RA	-8.9 [-13.5, -4.4]	-25.6 [-34.7, -16.5]	0.002
• BB	-9.2 [-14.5, -4.0]	-15.1 [-23.9, -6.4]	0.121
• PVA	-11.3 [-20.7, -1.8]	-9.2 [-20.9, 2.6]	0.308
• LA	-15.4 [-21.1, -9.7]	-20.6 [-29.9, -11.2]	0.200
SDP (%) - All beats	+3.5 [1.8, 5.3]	+6.2 [3.3, 9.2]	0.153
• RA	+4.6 [2.1, 7.1]	+13.5 [8.4, 18.5]	0.003
• BB	+3.0 [-1.0, 7.1]	+4.7 [-1.0, 10.4]	0.353
• PVA	-0.2 [-5.8, 5.5]	+2.2 [-2.4, 6.9]	0.325
• LA	+4.3 [1.4, 7.2]	+4.1 [-2.5, 10.7]	0.250
LDP (%) - All beats	+3.7 [2.1, 5.2]	+3.4 [1.0, 5.9]	0.398
• RA	+2.2 [0.1, 4.3]	+5.5 [1.7, 9.2]	0.110
• BB	+4.0 [1.3, 6.8]	+1.2 [-2.0, 4.4]	0.063
• PVA	+7.0 [1.0, 13.0]	+0.8 [-5.5, 7.2]	0.087
• LA	+4.4 [2.0, 6.8]	+5.9 [2.1, 9.8]	0.425
FP (%) - All beats	+3.4 [2.2, 4.6]	+7.9 [5.2, 10.7]	0.002
• RA	+2.1 [0.5, 3.7]	+6.6 [2.8, 10.4]	0.030
• BB	+2.1 [-0.7, 5.0]	+9.3 [1.8, 16.8]	0.058
• PVA	+4.4 [1.6, 7.3]	+6.1 [0.3, 11.9]	0.343
• LA	+6.8 [3.8, 9.7]	+10.5 [5.2, 15.9]	0.168
FD DP (ms) - All beats	+11.4 [10.4, 12.5]	+12.0 [9.9, 14.0]	0.079
• RA	+11.5 [9.8, 13.2]	+10.4 [8.3, 12.6]	0.295
• BB	+10.5 [7.3, 13.7]	+8.4 [6.4, 10.3]	0.091
• PVA	+12.5 [11.4, 13.6]	+10.7 [8.1, 13.4]	0.010
• LA	+11.4 [9.8, 13.1]	+18.6 [12.0, 25.3]	0.047
FD FP (ms) - All beats	+1.6 [-1.0, 4.2]	+4.6 [2.1, 7.1]	0.276
• RA	-0.7 [-5.2, 3.7]	+3.1 [-0.2, 6.5]	0.179
• BB	-0.0 [-3.7, 3.6]	+0.2 [-3.4, 3.9]	0.478
• PVA	+0.8 [-4.4, 6.0]	+4.5 [-0.5, 9.5]	0.279
• LA	+7.8 [1.4, 14.1]	+11.0 [4.7, 17.2]	0.326

Values are presented as mean [95% CI]. **AES** = atrial extrasystole; **AF** = atrial fibrillation; **BB** = Bachmann's bundle; **DP** = short+long-double potentials; **FD** = fractionation duration; **FP** = fractionated potentials; **LA** = left atrium; **LDP** = long double potentials; **LVA** = low-voltage area; **PVA** = pulmonary vein area; **RA** = right atrium; **SDP** = short double potentials; **SP** = single potentials; **SR** = sinus rhythm.

in a significant increase in the number of FPs (p=0.004). There were no regional differences between the degree of aberrancy and FD of both DPs and FPs.

Interplay of prematurity and aberrancy

Figure 4 shows the mean effect of AES with various degrees of prematurity and aberrancy combined on the various EGM morphology characteristics. As can be seen, all EGM morphology parameters are most severely affected by either mild/opposite or severe aberrant AES, independently of the degree of prematurity. The smallest effect had, not surprisingly, non-premature AES with a comparable direction of activation as during SR.

Influence of atrial fibrillation episodes

As the effect of mild/opposite and severe aberrant AES was most prominent, these types of AES were further compared between patients with and without AF. In total, 147 AES were recorded in patients without AF and 65 in patients with AF. As listed in *Table 1*, there was a more prominent effect of AES on EGM morphology parameters in patients with AF; SPs changed more often to FPs during AES as compared with patients without AF (74% vs 83% of the AES; 4.7 [1.8–9.6] % vs 7.2 [4.1–12.0] %, p=0.007). Comparing the effects of AES for each atrial region separately, clear differences between patients with and without AF were only found at the RA. At this site, potential voltages were lower in patients with AF (no AF: -1.2 [-1.7, -0.7] mV vs AF: -2.8 [-3.5, -2.1] mV, p<0.001). In addition, the number of SPs was lower (no AF: -8.9 [-13.5, -4.4] % vs AF: -25.6 [-34.7, -16.5] %, p=0.002) as there were more SDPs (no AF: +4.6 [2.1, 7.1] % vs AF: +13.5 [8.4, 18.5] %, p=0.003) and FPs (no AF: +2.1 [0.5, 3.7] % vs AF: +6.6 [2.8, 10.4] %, p=0.030). There was a trend towards a higher number of FPs in patients with AF at BB (no AF: +2.1 [-0.7, 5.0] % vs AF: +9.3 [1.8, 16.8] %, p=0.058), while no clear differences were found at the PVA and LA between patients with and without AF.

Discussion

This is the first study reporting on the impact of spontaneous AES and SR on EGM morphology. The degree of aberrancy and not the degree of prematurity had the most prominent effect on EGM morphology, including potential voltage and fractionation. Mild/opposite and severe aberrant AES caused the largest decrease in potential voltages and increase in fractionation. In patients with AF there was a considerable decrease in potential voltages and increase in fractionation caused by spontaneous AES compared to patients without AF particularly at the RA. These observations indicate enhanced direction-dependency of intra-atrial conduction in patients with AF.

Arrhythmogenic effect of AES

Spontaneous AES are often referred as benign interruptions of SR, although AES are known to trigger episodes of AF, as in more than 90% of the AF cases episodes are preceded by an AES.[12,13] While the majority of AES triggering AF originate from within the PVs, AES emerging from e.g. the superior vena cava, LA posterior free wall, LA appendage, terminal crest and interatrial septum also play an important role.[4] It is therefore not surprising that isolation of the PVs alone is not always successful to prevent initiation of AF episodes. In clinical practice, mapping of AES is often limited to identification of its origin by identifying the earliest activation site relative to the fixed timing reference rather than studying its mechanistic (electrical) effects on the atrial tissue. This is mainly due to technical challenges as the number of simultaneous recording electrodes is limited during endovascular mapping procedures. Consequently, little is known about the ultimate determinant factors of AF initiation by spontaneous AES. However, novel approaches, such as the dual-reference approach, might enable more extensive research on electrophysiological characteristics of frequent spontaneous AES in the near future.[14] Mechanistic insights of spontaneous AES are therefore mainly limited to intra-operative (endo-)epicardial mapping procedures in patients with structural heart disease.

(Non-uniform) Anisotropic conduction

Atrial tissue is considered to be anisotropic, implying that electrical conduction is much faster along the longitudinal direction of myocardial fibers than in transverse direction.[1] Within the atria, there are specific regions of preferential conduction, e.g. terminal crest

and Bachmann's bundle, which appear to be optimized for fast excitation of atrial tissue.[15] However, altered cell-to-cell communication and tissue damage can result in a discontinuous distribution of conduction properties. This is known as non-uniform anisotropy. These changes in anisotropic properties of cardiomyocytes can be pro-arrhythmogenic as they may cause unidirectional block and reentry. It is likely that the magnitude of changes in tissue anisotropy depends on the location within the atria, caused by i.e., tissue thickness, fiber orientation, local tissue damage and underlying heart disease. In addition, as conduction disorders are direction and frequency dependent, electrophysiological properties indicating non-uniform anisotropy can be 'hidden' during normal SR. In these areas, potential fractionation can occur, caused by asynchronous activation of groups of cardiomyocytes that are separated by areas in which there is diminished or no cell-to-cell coupling.[5] Starreveld[16] presented the first human case illustrating EGM morphological manifestations of direction- and rate-dependent anisotropic conduction in a 76-year old patient with long-standing persistent AF, resulting in low-amplitude, fractionated unipolar potentials. In this study, we now demonstrated in a large population of patients with and without a history of AF that spontaneous AES are characterized by a clear increase of potential fractionation and a decrease of potential voltages, which depended particularly on the degree of aberrancy. This indicates the presence of irregular discontinuous propagation by anisotropic structural discontinuities that could be proarrhythmic, even in patients without prior AF episodes. These areas, however, were more pronounced in AF patients, indicating a higher degree of tissue remodeling compared to patients without AF. This finding could explain the higher vulnerability to AES in triggering AF in patients with spontaneous AF episodes.

Rate- and direction dependency

Anisotropy is not only determined by structural determinants such as cell size and shape, myocardial fibrosis and gap junction distribution, but it can also be influenced by functional contributors.[15] Spach et al. demonstrated anisotropy to be rate- and direction dependent, as higher pacing rates resulted in lower transverse conduction velocity in relation to longitudinal conduction velocity, and premature electrical stimulation in non-uniform but not in uniform anisotropic tissue resulted in unidirectional longitudinal conduction block or a dissociated type of zigzag longitudinal conduction.[17,18] Consistent with these studies, we also observed more low-voltage fractionated potentials during spontaneous AES. Also, we demonstrated that in a significant part of the AES, smooth and biphasic extracellular potentials transformed into fractionated potentials, particularly in AF patients. These observed fractionated potentials reveal the enhanced non-uniformity of anisotropic tissue in AF patients. Although in our study there was no clear relation between the change in electrophysiological parameters and prematurity, lower potential voltages and more fractionation were found in the most severe premature AES. Several studies also showed that more severe premature AES provoke more conduction block, slower conduction and more local directional heterogeneity in conduction velocity vectors compared to non/mild-premature AES.[6,19] However, as AES near the refractory period are more likely to initiate AF episodes, it is expected that AES near the refractory period will result in even more severe alterations in unipolar potential morphology.[20,21]

As demonstrated in our current study, AES with severe aberrancy result in the most severe changes in unipolar voltage and potential morphology. However, we also demonstrated that AES with a wavefront direction opposite to the wavefront direction during SR frequently presented with similar alterations as compared with the severe aberrant AES. While Teuwen et al.[6] and Van der Does et al.[22] only demonstrated a severe increase in conduction block and endo-epicardial asynchrony during severe aberrant AES, they did not find similar results during mild/opposite aberrant AES. We also demonstrated significant regional differences

10

in effect of aberrancy. It is therefore likely that the condition of the underlying tissue predominantly determines the effect of either prematurity or aberrancy. Since the largest effect provoked by AES is achieved by any change in wavefront direction, in theory, any premature aberrant AES originating not from the sino-atrial node area may result in severe conduction disorders in non-uniform anisotropic tissue, thereby facilitating initiation of AF.

Clinical implications

In the current study, we demonstrated that spontaneous AES are particularly directional-dependent, with a more prominent effect of these AES in patients with history of AF. Hence, a significant part of conduction disorders would be missed when performing electrophysiological examination during sinus rhythm alone. As these direction-dependent conduction disorders were particularly found at the RA in patients with AF, one could consider more extensive substrate identification by using multisite pacing and focusing on unipolar EGM characteristics. However, whether additional ablation strategies targeting these regions truly helps improving ablation outcomes needs to be examined in future studies.

Limitations

Atrial tachyarrhythmias were not initiated by the AES in this study. Although the prematurity index was relatively high in some AES, the CL_{AES} was frequently still above the expected refractory period.[20,21] Therefore, AES with more shortening of the cycle length are expected to result in a more pronounced effect. The arrhythmogenic effect of AES could only be studied at one single mapping site and not at multiple atrial regions simultaneously. Consequently, the origin of each AES and the effect on multiple atrial sites simultaneously remain unknown.

Conclusion

Spontaneous AES with an opposite or perpendicular wavefront direction to SR provoked the largest changes in unipolar potential morphology, independently of the degree of prematurity. Therefore, unipolar EGM characteristics during spontaneous AES are mainly directional-dependent and not rate-dependent. As AF patients have more severe direction-dependent conduction disorders, enhanced non-uniform anisotropy probably explains the higher vulnerability to trigger episodes of AF.

References

1. Kleber AG, Rudy Y. Basic mechanisms of cardiac impulse propagation and associated arrhythmias. Physiol Rev. 2004;84:431-488.
2. Spach MS, Dolber PC. Relating extracellular potentials and their derivatives to anisotropic propagation at a microscopic level in human cardiac muscle. Evidence for electrical uncoupling of side-to-side fiber connections with increasing age. Circ Res. 1986;58:356-371.
3. Haissaguerre M, Jais P, Shah DC, Takahashi A, Hocini M, Quiniou G, Garrigue S, Le Mouroux A, Le Metayer P, Clementy J. Spontaneous initiation of atrial fibrillation by ectopic beats originating in the pulmonary veins. N Engl J Med. 1998;339:659-666.
4. Kawai S, Mukai Y, Inoue S, Yakabe D, Nagaoka K, Sakamoto K, Takase S, Chishaki A, Tsutsui H. Non-Pulmonary Vein Triggers of Atrial Fibrillation Are Likely to Arise from Low-Voltage Areas in the Left Atrium. Sci Rep. 2019;9:12271.
5. Spach MS. Anisotropy of cardiac tissue: a major determinant of conduction? J Cardiovasc Electrophysiol. 1999;10:887-890.
6. Teuwen CP, Kik C, van der Does L, Lanters EAH, Knops P, Mouws E, Bogers A, de Groot NMS. Quantification of the Arrhythmogenic Effects of Spontaneous Atrial Extrasystole Using High-Resolution Epicardial Mapping. Circ Arrhythm Electrophysiol. 2018;11.
7. Lanters EA, van Marion DM, Kik C, Steen H, Bogers AJ, Allessie MA, Brundel BJ, de Groot NM. HALT & REVERSE: Hsf1 activators lower cardiomyocyt damage; towards a novel approach to REVERSE atrial fibrillation. J Transl Med. 2015;13:347.
8. van der Does LJ, Yaksh A, Kik C, Knops P, Lanters EA, Teuwen CP, Oei FB, van de Woestijne PC, Bekkers JA, Bogers AJ, et al. QUest for the Arrhythmogenic Substrate of Atrial fibRillation in Patients Undergoing Cardiac Surgery (QUASAR Study): Rationale and Design. J Cardiovasc Transl Res. 2016;9:194-201.
9. Kik C, Mouws E, Bogers A, de Groot NMS. Intra-operative mapping of the atria: the first step towards individualization of atrial fibrillation therapy? Expert Rev Cardiovasc Ther. 2017;15:537-545.
10. van Schie MS, Starreveld R, Bogers A, de Groot NMS. Sinus rhythm voltage fingerprinting in patients with mitral valve disease using a high-density epicardial mapping approach. Europace. 2021;23:469-478.
11. van Schie MS, Heida A, Taverne Y, Bogers A, de Groot NMS. Identification of local atrial conduction heterogeneities using high-density conduction velocity estimation. Europace. 2021;23:1815-1825.
12. Johnson LS, Juhlin T, Juul-Moller S, Hedblad B, Nilsson PM, Engstrom G. A prospective study of supraventricular activity and incidence of atrial fibrillation. Heart Rhythm. 2015;12:1898-1904.
13. Vincenti A, Brambilla R, Fumagalli MG, Merola R, Pedretti S. Onset mechanism of paroxysmal atrial fibrillation detected by ambulatory Holter monitoring. Europace. 2006;8:204-210.
14. Chen M, Yang M, Li W, Zhang PP, Zhang R, Mo BF, Gong CQ, Han YQ, Sun XH, Wang QS, et al. Novel dual-reference approach facilitates the activation mapping and catheter ablation of premature atrial complexes with non-pulmonary vein and non-superior vena cava origins. Europace. 2022.
15. Kotadia I, Whitaker J, Roney C, Niederer S, O'Neill M, Bishop M, Wright M. Anisotropic Cardiac Conduction. Arrhythm Electrophysiol Rev. 2020;9:202-210.
16. Starreveld R, de Groot NMS. Direction- and rate-dependent fractionation during atrial fibrillation persistence: Unmasking cardiac anisotropy? J Cardiovasc Electrophysiol. 2020;31:2206-2209.
17. Spach MS, Kootsey JM, Sloan JD. Active modulation of electrical coupling between cardiac cells of the dog. A mechanism for transient and steady state variations in conduction velocity. Circ Res. 1982;51:347-362.
18. Spach MS, Dolber PC, Heidlage JF. Influence of the passive anisotropic properties on directional differences in propagation following modification of the sodium conductance in human atrial muscle. A model of reentry based on anisotropic discontinuous propagation. Circ Res. 1988;62:811-832.
19. van Schie MS, Misier NLR, Razavi Ebrahimi P, Heida A, Kharbanda RK, Taverne Y, de Groot NMS. Premature atrial contractions promote local directional heterogeneities in conduction velocity vectors. Europace. 2023.
20. Schmitt C, Ndrepepa G, Weber S, Schmieder S, Weyerbrock S, Schneider M, Karch MR, Deisenhofer I, Schreieck J, Zrenner B, et al. Biatrial multisite mapping of atrial premature complexes triggering onset of atrial fibrillation. Am J Cardiol. 2002;89:1381-1387.
21. Kawai S, Mukai Y, Inoue S, Yakabe D, Nagaoka K, Sakamoto K, Takase S, Chishaki A, Tsutsui H. Location and coupling interval of an ectopic excitation determine the initiation of atrial fibrillation from the pulmonary veins. J Cardiovasc Electrophysiol. 2022;33:629-637.
22. van der Does L, Kharbanda RK, Teuwen CP, Knops P, Kik C, Bogers A, de Groot NMS. Atrial Ectopy Increases Asynchronous Activation of the Endo- and Epicardium at the Right Atrium. J Clin Med. 2020;9.
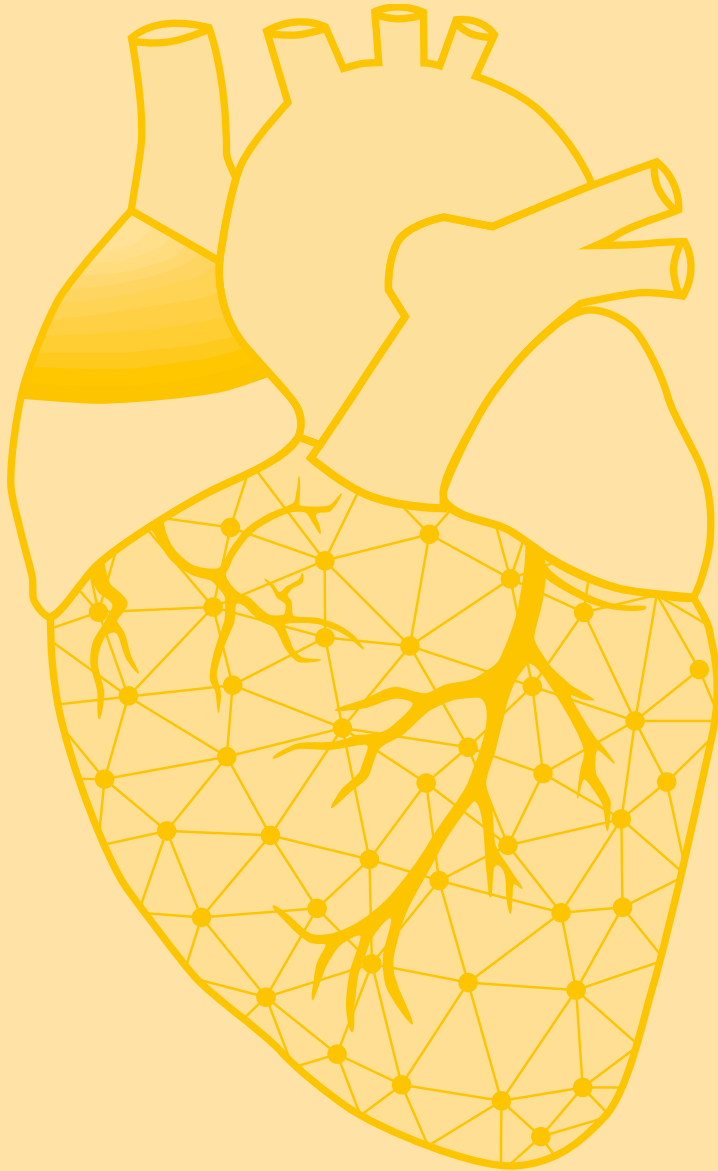
Chapter 11

Analyzing the effect of electrode size on electrogram and activation map properties

Bahareh Abdi

Mathijs S. van Schie

Natasja M.S. de Groot

Richard C. Hendriks

Abstract

Background: Atrial electrograms recorded from the epicardium provide an important tool for studying the initiation, perpetuation and treatment of AF. However, the properties of these electrograms depend largely on the properties of the electrode arrays that are used for recording these signals.

Method: In this study, we use the electrode's transfer function to model and analyze the effect of electrode size on the properties of measured electrograms. To do so, we use both simulated as well as clinical data. To simulate electrogram arrays we use a two-dimensional (2D) electrogram model as well as an action propagation model. For clinical data, however, we first estimate the transmembrane current for a higher resolution 2D modeled cell grid and later use these values to interpolate and model electrograms with different electrode sizes.

Results: We simulate electrogram arrays for 2D tissues with 3 different levels of heterogeneity in the conduction and stimulation pattern to model the inhomogeneous wave propagation observed during atrial fibrillation. Four measures are used to characterize the properties of the simulated electrogram arrays of different electrode sizes. The results show that increasing the electrode size increases the error in LAT estimation and decreases the length of conduction block lines. Moreover, visual inspection also shows that the activation maps generated by larger electrodes are more homogeneous with a lower number of observed wavelets. The increase in electrode size also increases low-voltage areas in the tissue while decreasing the slopes and the number of detected deflections. The effect is more pronounced for a tissue with a higher level of heterogeneity in the conduction pattern. Similar conclusions hold for the measurements performed on clinical data.

Conclusion: The electrode size affects the properties of recorded electrogram arrays which can respectively complicate our understanding of atrial fibrillation. This needs to be considered while performing any analysis on the electrograms or comparing the results of different electrogram arrays.

Journal site

Introduction

Recording and processing of electrograms (EGMs) is the cornerstone of mapping procedures guiding ablative therapies of cardiac arrhythmias. Thorough understanding of the impact of recording technology on EGM morphology is of paramount importance, particularly in case of complex tachyarrhythmias such as atrial fibrillation (AF).[1,2] However, the properties of these EGMs depend to a large extent on the physical dimensions of the electrode arrays that are used for recording these signals.

As shown in several studies, the electrode's size (or diameter) is an important parameter that can affect the characteristics of the recorded EGMs. Most studies focus on bipolar EGMs and measurements that are performed only on clinical recordings.[3-7] There are only a few studies investigating the effect of the electrode size on the properties of the unipolar EGMs using both electrophysiological models and clinical recordings. These properties include signal-to-noise ratio (SNR), fractionation level, voltage level and the error in local activation time (LAT) estimation.[8-10] In general, these studies show that increasing the electrode size increases the SNR and consequently the atrial activity is less affected by noise and artifacts.[11,12] However, this is mainly the case for homogeneous tissue. It has also been shown that the number of deflections and the level of fractionation also increases by increasing the electrode size.[7-9] Moreover, low-voltage areas in the tissue also increase when using bigger electrode sizes.[6,8] It has also been shown that using larger electrodes, which increases the error in LAT estimation,[10] will result in activation maps with less detail and less conduction blocks.[3,5] These effects are more pronounced in zones of conduction block or slow conduction in the tissue (i.e., scarred tissue).[3,4]

Some of these studies use clinical recorded EGMs using different EGM arrays with different electrode sizes that are successively positioned on similar locations on the atria. However, it should be noted that not all observed changes in the EGM properties are due to changes in electrode size, but also due to the spatio-temporal varying nature of electrical wave propagation (especially during AF) and the changes in the inter-electrode distances. Moreover, bipolar EGMs are also affected by varying propagation directions. In this study, we exclusively investigate the effect of the electrode size on the properties of high resolution unipolar EGM arrays by keeping the other parameters like inter-electrode distances and electrical wave propagation patterns fixed. We use both clinical observation and electrophysiological models that govern the wave propagation and EGM generation to analyze and investigate these effects. This is done by investigating the electrode's transfer function and its properties, making the comparisons and conclusions more robust. Moreover, we investigate these results for tissues with different levels of inhomogeneity in the conductivity map. We also focus on the overall properties of the EGM array and not only on the per-electrode features. These include the overall error in local activation time estimation, length of slow conduction or block lines, low-voltage areas in the tissue, as well as the number of deflections.

We first present the EGM model, our approach for generating simulated EGMs, and our proposed framework for generating high resolution EGM arrays with different electrode sizes from clinical EGMs. We also provide a description of our clinical recording setup and employed measures for characterizing the EGM array properties. Furthermore, we perform our approach on simulated and clinical EGMs, respectively, and present the final results. We also discuss the optimal electrode diameter and appropriate inter-electrode distances for electrode arrays with different electrode sizes, the maximum electrode size for capturing scarred tissue of different sizes, and a proper scaling of the EGM amplitude for a better comparison of EGMs recorded with different arrays.

11

Methods

Atrial tissue computer model

In our model we consider the atrial tissue as a two-dimensional mono-layer grid of cells where the electrode array is positioned at a constant height z_0 above the atrial tissue. We model the EGM as a weighted summation of transmembrane currents produced by the cells in the tissue in the vicinity of the electrode, where the weights depend on the inverse of the cell-to-electrode distances. An EGM at location (x, y) and at time sample t can then be modeled as:[13]

$$\phi(X - m, y_m, t) = \frac{1}{4\pi\sigma_e} \int_{\mathcal{A}} \frac{I_{tr}(x, y, t)}{\sqrt{(x - x_m)^2 + (y - Y_m)^2 + z_0^2}} dA(x, y) \quad (1)$$

where $m = 1, 2, \dots, M$ is the electrode index with M the total number of electrodes, $I_{tr}(x, y, t)$ the transmembrane current, $\mathcal{A}$ is the area in which the modeled cells are located, $A(x, y)$ is the area variable, and σ_e is the constant extra-cellular conductivity. Note that for now we assume that we are recording the EGMs with point electrodes whose diameters can be neglected.

The transmembrane current produced by each cell can be computed using the following equation:[14]

$$I_{tr}(x, y, t) = S_v^{-1} \nabla \cdot \Sigma(\text{xy}) \nabla V(\text{x}, \text{y}, \text{t}) \quad (2)$$

where $V(x, y, t)$ is the per cell potential, $\Sigma(x, y)$ is the intracellular conductivity tensor, and $S_v = 0.24 \, \mu m^{-1}$ is the cellular surface-to-volume ratio. The potential and transmembrane current can simultaneously be calculated using the reaction-diffusion equation that governs the action potential propagation in the tissue:[14]

$$C \frac{\delta V(x, y, t)}{\delta t} = i_{tr}(x, y, t) + I_{st}(x, y, t) - I_{ion}(x, y, t, V) \quad (3)$$

where $C = 1 \mu F cm^{-2}$ is the total membrane capacitance, I_{st} is the stimulus current, and I_{ion} is the total ionic current computed according to the Courtemanche model.[15]

Electrode's transfer function model

For a uniform grid of cells with Δx denoting the cell-to-cell distance, we can rewrite *Equation 1* as a 2D spatial convolution of transmembrane currents with an appropriate electrode transfer function $R_0(x, y)$ as

$$\varphi(x, y, t) = c \, S_o(x, y) \left(R_0(x, y) ** I_{tr}(x, y, t) \right) \quad (4)$$

where $**$ denotes the 2D spatial convolution, and $c = \Delta x^2 / 4\pi\sigma_e$ contains all constants and will be omitted for simplification. We introduced in *Equation 4* the sampling operator $S_o(x, y) = \sum_m \delta(x - x_m, y - y_m)$ with Dirac delta functions to select the M spatial locations on the grid on which we have measurements and replace the other locations with zero. This can also be used to deselect faulty electrodes. The electrode transfer function is

$$R_0(r) = \frac{1}{\sqrt{r^2 + z_0^2}} \quad (5)$$

where $r = \sqrt{x^2 + y^2}$ is the horizontal distance between the electrode (at origin) and a cell at location (x, y). However, an electrode whose diameter is bigger than the modeled cell size (i.e., $d_0 > \Delta x$) can no longer be considered as a point electrode. The transfer function should

therefore take the diameter of the electrode into account:[8]

$$R_{d_0}(r) = 2 \arcsin \frac{d_0}{\sqrt{(r - d_0/2)^2 + z_0^2} + \sqrt{(r + d_0/2)^2 + z_0^2}} \quad (6)$$

The first row of *Figure 1* shows the 2D representation of the electrode normalized transfer function of a point electrode from *Equation 5* as a function of x and y, as well as the normalized transfer function based on r, both computed by setting z_0=0.5 mm. As can be seen, the value of the transfer function, or the weight of the transmembrane current in *Equation 4*, for the cell that is exactly under the electrode's center equals to 1. A large weight indicates more influence on the final recorded EGM. As we move further from the center, the weights decrease but the values are still noticeable. One important parameter commonly used to characterize the transfer function is the full width at half maximum (FWHM), denoted on the plot. It shows the diameter at which the weight of the cells is greater than half of the maximum value, indicating their significant influence on the final recorded EGM. A small FWHM (a narrower transfer function) denotes that the electrode records data from a smaller area thus providing more local EGMs. However, a large FWHM denotes that the recorded EGM will be the summation of activities in a larger area. This can severely affect the morphology of the local activities if the propagation is not homogeneous in the electrode's neighborhood. In general, summing up activities in a larger area will smooth out the important local details.

The bottom left plot in *Figure 1* shows the transfer functions for different electrode diameters $d_0 \in$ 0.5,2,4,8 mm with z_0=0.5 mm. The bottom right plot in *Figure 1*, also shows the transfer functions when z_0=1 mm, assuming a thicker tissue. As can be seen in both plots, as the electrode diameter increases, the transfer function gets wider (larger FWHM) indicating that the recorded EGM will be more influenced by the neighboring activities. The difference in FWHM is more evident in thinner tissues and for smaller diameters.

Modeling abnormal tissue

To generate simulated fractionated EGMs that are representative for clinical data, various approaches have been suggested in literature. Jacquemet et al.[8] incorporate the heterogeneities in the conductivity as a set of randomly positioned lines of conduction block that disconnect the coupling between the cells on the grid. However, Vigmond et
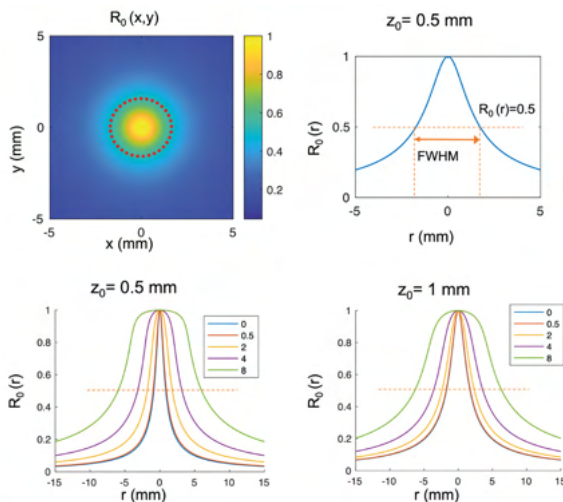
Figure 1 – Transfer function of a point electrode. *Top left*: the 2D representation of the electrode normalized transfer function $R_0(x, y)$ of a point electrode. The red dashed circle represents the FWHM. *Top right*: the electrode transfer function based on $R_0(r)$. *Bottom*: $R_{d_0}(r)$ for different electrode diameters $d_0 \in$ 0,0.5,2,4,8 mm with z_0=0.5 mm (left) and z_0=1 mm (right).
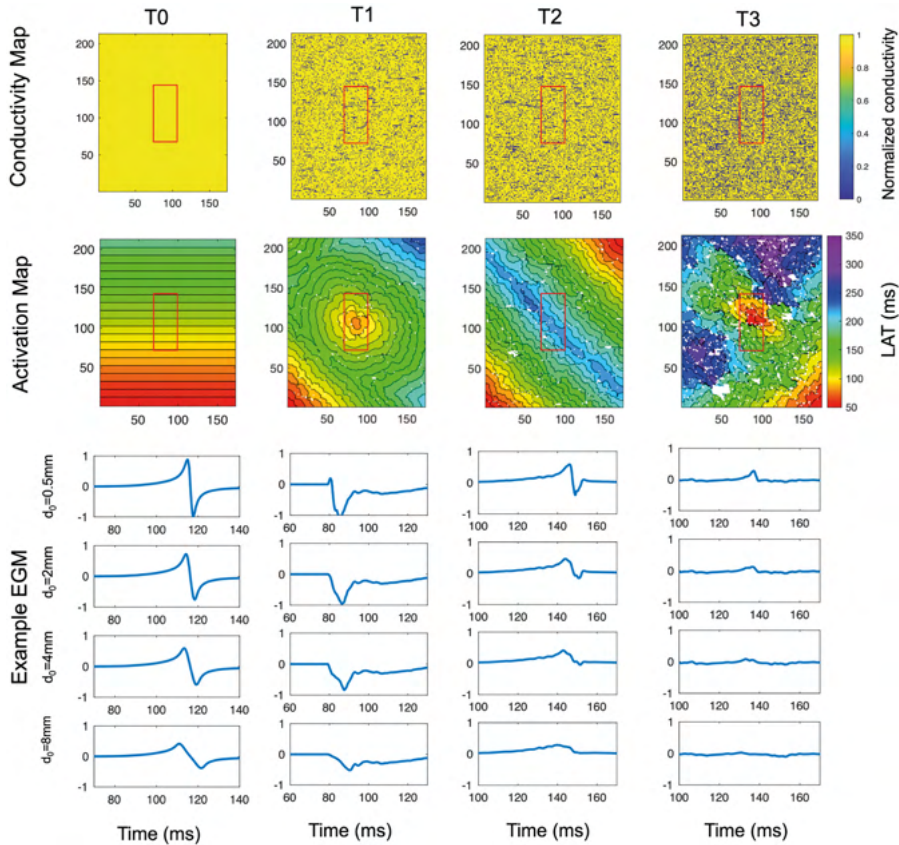
Figure 2 – Conductivity map, activation map and an example EGM simulated for different electrode sizes of four simulated tissues. T_0 is modeled as a homogeneous tissue while T_1, T_2 and T_3 have a low, medium and high density of conduction block in their conductivity map, respectively. The red rectangle represents the electrode array position. We assume there is one electrode on top of each modeled cell.

al.[16] model the conduction disturbance by randomly disconnecting the coupling between some modeled cells and their neighbors through randomly positioned dots of conduction block. In this study we use both patterns simultaneously for simulated conductivity maps of modeled tissue. This provides simulated EGMs and activation maps that are more similar to clinical recordings (by visual inspection).

To simulate EGMs with different levels of fractionation, we use conductivity maps with varied levels of conduction block density. These are shown in the first row of *Figure 2* denoted as T_1, T_2 and T_3 having a low, medium and high density of conduction block, respectively. For comparison, we have also shown the results for a homogeneous tissue with planar wave propagation, denoted by T_0, which serves as a standard reference for other tissue types. The size of each tissue is 213×173 cells, with a cell-to-cell distance of $\Delta x = 0.5$ mm. We also activate the tissues using one or two activation waves entering the tissue from different locations to simulate the activation maps during AF.

To model action potential propagation in the simulated tissues, *Equation 3* is discretized and solved using a finite difference method with no flux boundary condition. The activities are simulated for 1000 ms to include one complete atrial beat, but only a selected time window of 150 ms in length is used for evaluation of EGMs as it includes all the atrial activities. A

more detailed description of the simulation steps and parameters is described previously.[17] The resulting activation maps are shown in the second row of *Figure 2*. Each pixel in the activation map represents the true activation time of its corresponding cell which is annotated as the time when the cell's potential V reaches a threshold value of -40 mV in the depolarization phase of its action potential. The white pixels belong to the cells that were positioned on a conduction block and did not get activated. Finally, *Equation 1* is used to compute the simulated EGMs recorded by an assumed electrode array of size 77×33 cells positioned on the center of the tissue at a constant height of z_0=0.5 mm, which is denoted by a red rectangle on the maps. The last panels in *Figure 2* show example EGMs from each tissue computed for four different electrode diameters $d_0 \in$0.5,2,4,8 mm.

Clinical studies

The study population consisted of 10 adult patients undergoing surgery in the Erasmus Medical Center Rotterdam. This study was approved by the institutional medical ethical committee (MEC2010-054/MEC2014-393).[18,19] Written informed consent was obtained from all patients. Patient characteristics (e.g., age, medical history, cardiovascular risk factors) were obtained from the patient's medical record. Epicardial high-resolution mapping was performed prior to commencement to extra-corporal circulation, as previously described in detail.[20] A temporal bipolar epicardial pacemaker wire attached to the RA free wall served as a reference electrode. A steel wire fixed to subcutaneous tissue of the thoracic cavity was used as an indifferent electrode. Epicardial mapping was performed with a 192-electrode array (electrode diameter 0.45 mm, inter-electrode distances 2.0 mm). The electrode array is subsequently positioned visually by the surgeon on 9 mapping atrial sites using the anatomical borders. We only use the data recorded from Bachmann's bundle. Ten seconds of induced AF were recorded from every mapping site, including a surface ECG lead, a calibration signal of 2 mV and 1000 ms, a bipolar reference EGM and all unipolar epicardial EGMs. Data was stored on a hard disk after amplification (gain 1000), filtering (bandwidth 0.5–400 Hz), sampling (1 kHz) and analogue-to-digital conversion (16 bits).

Interpolating (clinical) EGMs and estimating EGMs for different electrode sizes

Due to the unstable and unpredictable nature of electrical wave propagation during AF, it is not possible to repeat similar recordings with different electrode arrays (having different electrode diameters and therefore different inter-electrode distances) during AF. To overcome this issue and to interpolate and estimate the EGMs recorded with different arrays, we first estimate high resolution transmembrane currents and subsequently model the effect of larger electrode dimensions. We discretize the 3D tissue activity in space. We use source clamping and replace each block of cells in the real three-dimensional tissue with a modeled "cell" on a uniform 2D grid of cells similar to the simulated data. Next, we estimate the high-resolution transmembrane currents using *Equation 4* and the recorded EGMs. This can be done by solving the following regularized optimization problem:[21]

$$\min_I \|\phi - S_0(R_0 ** I)\|_2^2 + \lambda \|I'\|_1 \quad (7)$$

where

$$\|I\|_2^2 := \sum_x \sum_y \sum_t |I[x,y,t]|^2, \qquad \|I'\|_1 := \sum_x \sum_y \sum_t |I'[x,y,t]|$$

and where λ is the regularization parameter. Employing the ℓ_1-norm regularization function (i.e., $\|.\|_1$ helps to preserve the main features of the transmembrane currents among which sparse fast temporal changes (deflections). These are of high importance for correct LAT

estimation. More details on an efficient approach to solve *Equation 7* are given by Abdi et al.[22] After estimating the high resolution transmembrane current, we can estimate different EGMs for varying electrode sizes and inter-electrode distances using *Equation 4* with an appropriate transfer function from *Equation 6*.

EGM analysis

Here, we introduce four measures that are used to characterize the properties of the EGM arrays. Notice that both simulated and clinical EGMs' amplitudes are scaled with a constant value so that the amplitude of the EGMs of a homogeneous wave propagating through the tissue (as in tissue type T_0) recorded by the smallest electrode (d_0=0.5 mm) equals 1 V. The scaling value is different for clinical and simulated recordings but similar for different electrode sizes. We characterize the properties of the simulated and clinical high resolution EGM arrays recorded during one atrial beat using the following four measures:

1. **LATE**: percentage of large absolute errors in LAT estimation denoted by LATE. These are the error values that are larger than 10 ms. This measure is only evaluated for simulated tissue where we have access to true activation times. The true activation time is annotated as the time when the potential of the cell that is exactly under the electrode reaches the value of -40 mV, ensuring that the action potential is triggered. The estimated activation time of the simulated EGM is annotated as the point with the steepest descent. The threshold value of 10 ms was selected heuristically. However, different threshold values yield a similar pattern of changes.

2. **LSC/B**: length of lines of slow conduction or block in the tissue denoted by LSC/B. To compute this value, we first find the delay between each cell and its four direct neighbors on the grid of cells. If the delay is bigger that 0.7 ms it will be considered as a slow conduction or block with the length of Δx. This threshold value is selected with respect to the standard delay between neighboring cells estimated from the standard tissue T_0. Note that this is not a small threshold considering the cell-to-cell distances of Δx=0.5 mm in the simulation. Moreover, since we model inhomogeneity in the tissue using dots and small lines of block, their effects on the LAT also ranges from very small to large values. *Figure 3b* shows an example activation map with its lines of slow conduction or block denoted by thick black lines.

3. **LVA**: percentage of EGMs with lower peak-to-peak voltage than 0.2 V denoted by LVA. The peak-to-peak voltage is defined as the difference between the maximum and the
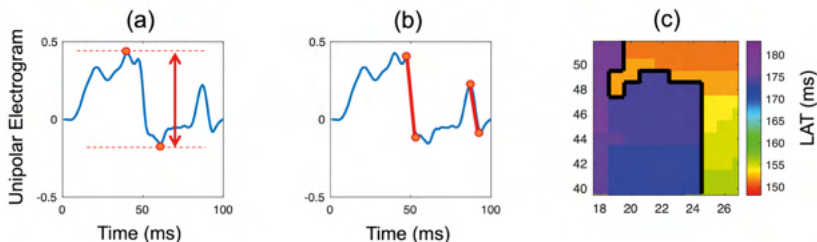
Figure 3 – Example of an activation map with lines of conduction block. *Panel a*: unipolar EGM with the peak-to-peak voltage denoted by the red two-sided arrow. If the peak-to-peak voltage is smaller than 0.2 V, the EGM will be counted as a low-voltage EGM. *Panel b*: unipolar EGM from (a) with two of its deflections (downward slopes) denoted by red lines. As can be seen there are more deflections in the signal but we only count those with an average slope that is smaller than -0.02 V/ms. *Panel c*: example activation map (a segment of T_7 in *Figure 10*) with the lines of block denoted by black lines. These are the areas between two neighboring cells with delays in LAT that are larger than 0.7 ms.
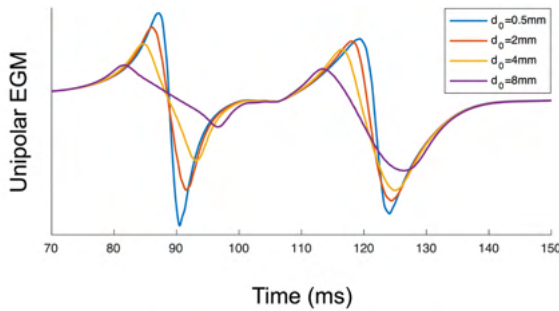
Figure 4 – An example of a simulated atrial activity recorded by different electrode sizes.

minimum EGM amplitude and is shown in an example EGM in *Figure 3a*. The threshold value was selected heuristically, making sure it is small enough to indicate the changes in between different tissue types and electrode diameters.

4. **ND, SD and MD**: percentage of EGMs having no deflection (ND), a single deflection (SD), or multiple deflections (MD). We only count the deflections having a smaller average slope than -0.02 V/ms. The threshold value was selected heuristically to avoid small negligible deflections caused by noise and artifacts. *Figure 3b* shows an example EGM with 2 deflections.

It is important to note that all the measures are evaluated for high resolution EGM arrays assuming that there is one electrode on top of each cell. This is not possible in practice because the inter-electrode distance should be larger than the electrode diameter. However, the results will confirm that the changes in the measures are due to the changes in the electrode's size and not due to the different inter-electrode distances. The above-mentioned measures are computed using custom written MATLAB codes.
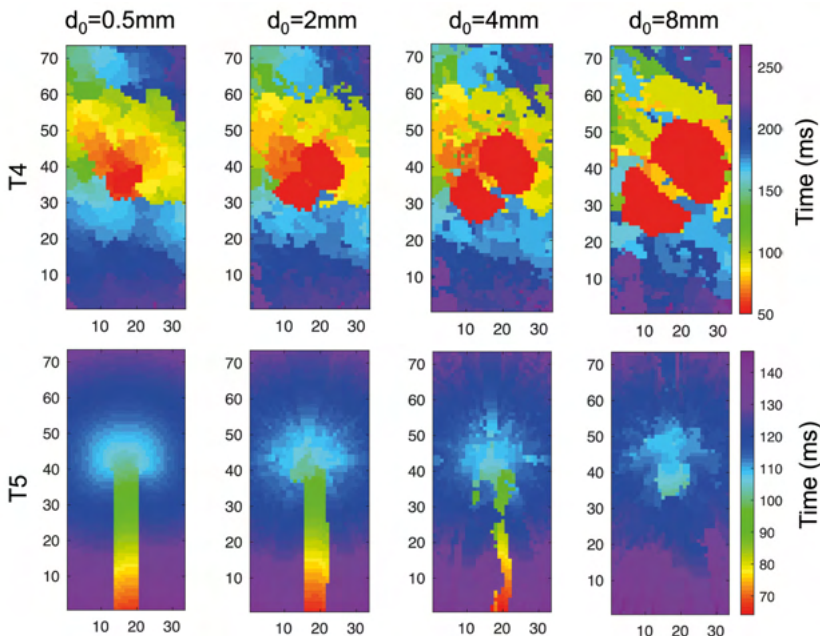
Figure 5 – Activation map estimated from high resolution EGM arrays with different electrode sizes. T_4 has the same tissue conductivity pattern as T_2 and in T_5 two lines of block are positioned along the center of the tissue.

Simulation results

Effect of electrode size on EGM properties

Five randomly generated conductivity maps were modeled for each tissue type T_1 to T_3, which were previously shown in *Figure 2*. The tissues were stimulated with one or two activation waves entering the tissue from different locations and the resulting EGMs were computed for four different electrode diameters $d_0 \in 0.5, 2, 4, 8$ mm. The last row of *Figure 2* shows an example EGM from each tissue computed for the four different electrode diameters. For a better comparison, *Figure 4* also shows simulated EGMs for different electrode sizes in one plot. These EGMs belong to T_5 in *Figure 5* with two distinct deflections as a result of a long line of block.

The measures introduced in the previous section were evaluated for all $2541 \times 5 = 12{,}705$ simulated EGMs for each tissue type ($77 \times 33 = 2{,}541$ EGMs per map) and are presented in *Table 1*, *Table 2*, *Table 3* and *Table 4*. As can be seen in the resulting tables, increasing the electrode size increases the error in LAT estimation while the length of detected slow conduction or block lines in the tissue decreases. Except for the homogeneous tissue T_0, where using bigger electrode diameters results in an increase in LSC/B which is almost similar for all electrode diameters. As a result, the final activation maps seem smoother.

The percentage of low-voltage areas in the tissue also increases by increasing the electrode size, indicating that using bigger electrodes decreases the amplitudes of recorded EGMs. However, by comparing the results of lower voltage areas in *Table 1*, *Table 2*, *Table 3*, *Table 4*, it seems that a larger diameter is more useful at indicating the differences in low-voltage areas of different tissue types and respectively the mean conductivity of the underlying substrate, even if the discrete block lines in the simulation are missed.

The percentage of single and multiple deflections in the EGMs decreases by increasing the diameter. This is because the slope of some of the deflections gets very small and it will not be annotated as a deflection anymore.

However, as can be seen in the tables, the variations in EGM properties caused by using different electrode diameters are more evident in tissues with higher level of heterogeneity or more scarred tissues. This also indicates that EGMs generated in homogeneous tissues will not be much affected by the electrode diameter.

Effect of electrode size on the activation map

We use some examples to visualize the effect of electrode size on the resulting activation maps. As discussed earlier, using bigger electrode sizes increases the error in LAT estimation and decreases the length of detected conduction block lines. This happens because the EGMs recorded by bigger electrodes are affected more by neighboring activities. Therefore, the deflection generated by larger and stronger inhomogeneous waves in the neighborhood may over-impose the small, but main, local deflections. As a result, the final activation maps seem smoother and more homogeneous.

Figure 4 shows an example of a simulated atrial activity recorded by different electrode sizes. As can be seen, two deflections are visible in each activity. The first deflection (at 90 ms) belongs to the local main activity and the second deflection (at 123 ms) belongs to a strong neighboring activity. As the electrode size increases, the second deflection gets steeper compared to the first deflection. Annotating the steepest descent as the LAT will then result in annotating the second deflection for electrode of diameters $d_0 = 4$ mm and 8 mm. That is

Table 1 – Measures evaluated for m=77×33×5 EGMs of tissue type T_0.

d_0 (mm)	Late %	LSC/B (cm)	LVA %	No. deflections %		
				ND	SD	MD
0.5	0	0	0	0	100	0
2	0	46.2	0	0	100	0
4	0	41.25	0	100	0	0
8	0	44.55	0	100	0	0

Table 2 – Measures evaluated for m=77×33×5 EGMs of tissue type T_1.

d_0 (mm)	Late %	LSC/B (cm)	LVA %	No. deflections %		
				ND	SD	MD
0.5	0.97	86.15	0	0.97	70.70	28.32
2	2.36	80.18	0.07	98.09	1.90	0
4	5.23	79.37	0.90	99.26	0.73	0
8	18.79	66.10	25.42	100	0	0

Table 3 – Measures evaluated for m=77×33×5 EGMs of tissue type T_2.

d_0 (mm)	Late %	LSC/B (cm)	LVA %	No. deflections %		
				ND	SD	MD
0.5	2.35	98.24	0	2.30	65.54	32.14
2	6.07	85.11	0.72	98.64	1.35	0
4	12.61	82.63	7.41	99.39	0.60	0
8	38.57	68.35	71.54	100	0	0

Table 4 – Measures evaluated for m=77×33×5 EGMs of tissue type T_3.

d_0 (mm)	Late %	LSC/B (cm)	LVA %	No. deflections %		
				ND	SD	MD
0.5	11.19	115.03	0.32	10.01	62.19	27.79
2	32.61	94.06	17.35	97.99	2.00	0
4	49.34	84.16	65.09	98.58	1.41	0
8	72.19	65.44	99.28	99.89	0.10	0

an absolute error of about 33 ms in LAT estimation.

Figure 5 shows estimated activation maps of two simulated tissues recorded by electrode arrays having different electrode sizes. These examples imitate the two patterns of common changes that we observed in clinical cases. T_4 has the same tissue conductivity pattern as T_2 (medium density of conduction blocks) with a different stimulation pattern resulting in generation of complex fractionated atrial EGMs. As can be seen, small waves in the tissue are over-imposed by larger and stronger activities in their surrounding and the smooth variations from one color to another are replaced by sharp variations. In T_5 (second row of *Figure 5*) two lines of block are positioned along the center of the tissue. The activation map starts from the area in-between these lines and then propagates through the whole tissue. As can be seen, this abnormal area is completely lost when we use bigger electrode sizes. As mentioned before, this happens because the activities generated in this abnormal area have lower amplitude compared to the stronger activities outside the block lines and a bigger sized electrode records more activities from its neighborhood.

Optimal electrode diameter and inter-electrode distance

The electrode transfer function in *Equation 6* and shown in *Figure 1* can be used for calculating the optimal electrode diameter and inter-electrode distance. This can be done by investigating the FWHM of different electrode diameters. *Figure 6* shows the calculated FWHM as a function of the electrode's diameter (with $z_0=0.5$ mm). This plot has two important features. First, even for a point electrode, FWHM=1.73 mm is nonzero. Secondly,

11

FWHM is almost constant for small diameters and the curve bends around d_0=0.5 mm. These observations can lead to two important conclusions:

1. Optimal electrode diameter: an optimal electrode diameter is around d_0=0.5 mm. This is the largest value with a similar FWHM to a point electrode. Note that smaller electrodes are affected more by noise so there is a tradeoff between high SNR and small FWHM. Therefore, it is also not preferred to use the smallest electrode possible.

2. Optimal inter-electrode distance (in order to capture all the spatial information of the electrical activities in the tissue): to find this parameter, we first need to estimate the maximum spatial frequency that is presented in electrical activities. This can be a quite complicated task due to the three-dimensional inhomogeneous structure of the atrial tissue and the complex unstable wave propagation patterns. On the other hand, no matter how high these spatial frequencies are, they will eventually be recorded by surface electrodes which inherently perform as a spatial low-pass filter. As shown previously[22], the FWHM can be also used as a short-hand measure of the appropriate inter-electrode distance. As an example, for an electrode with d_0=0.5 mm, we suggest an optimal inter-electrode distance of around 1.9 mm, which is equal to its FWHM at z_0=0.5 mm.

Figure 7 shows the FWHM as a function of both d_0 and z_0. As can be seen in this figure, as the electrode diameter or the electrode height (or equivalently tissue thickness) increases, the required inter-electrode distance also increases. This means that FWHM and the low-pass filtering effect of the electrode increases. This will result in losing spatial information by electrodes. Even putting them closer to each other in an array will not compensate that loss. Therefore, we can effectively use larger inter-electrode distances. Conversely, electrodes with smaller diameters have smaller FWHM and can potentially capture spatial information with higher frequencies and by putting these electrodes closer to each other on an array, we can record this information.

Maximum electrode size for recording scarred tissue

In this section, we perform an experiment to investigate the maximum electrode size for the detection of abnormal areas and conduction block lines using simulated tissue. We use the same pattern as in T_5 in *Figure 5* for the scarred tissue where two lines of conduction block are positioned along the center of the tissue with a distance of L_{block}. The activation wave starts from the area in between these lines and then propagates through the whole tissue. As can be seen in T_5, this abnormal area is completely lost when we use bigger electrode sizes. As
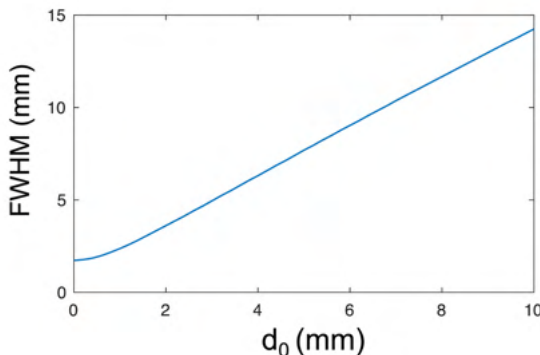
Figure 6 – FWHM calculated for different electrode diameters with z_0=0.5 mm.
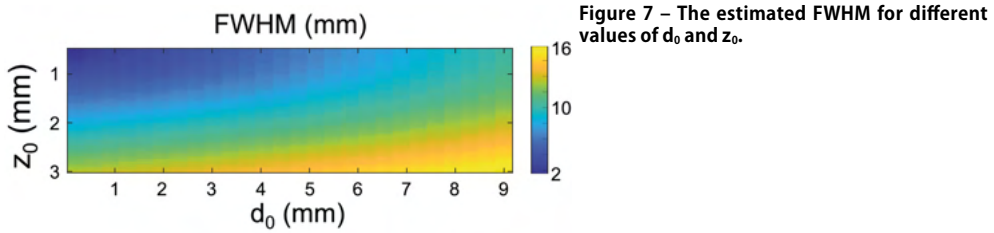
Figure 7 – The estimated FWHM for different values of d_0 and z_0.

mentioned before, this happens because the activities generated in this abnormal area have lower amplitude compared to the stronger activities outside the block lines and a bigger sized electrode records more activities from its neighborhood. We increased the distance between the two parallel lines of blocks and visually inspect the activation map estimated from different electrode arrays to determine the maximum electrode diameter $d_{(0,max)}$ that can still provide some evidence of the abnormality in the tissue. The results can be seen in *Figure 8*. As an example, the two block lines in T_5 are distanced at L_{block}=3.5 mm, and, as can be seen in *Figure 8*, the maximum electrode diameter that can still provide evidence of this abnormality is around 4.2 mm. Notice that this is a simple example compared to complex clinical cases where the results are affected by many underlying parameters of the tissue.

11

Clinical results

Due to the unstable and unpredictable nature of electrical wave propagation during AF, it is not possible to repeat similar clinical recordings with different electrode arrays. Therefore, to model these recordings, we to first estimated high resolution transmembrane currents and then used them to interpolate and calculate EGMs with bigger electrode sizes. The methodology used for estimation of transmembrane current is discussed and evaluated previously.[22] Here, to evaluate its performance in reproducing the EGMs, we find the mean correlation coefficient between the real clinical EGMs and their simulated EGMs after finding the transmembrane currents and recalculating the EGMs. The mean correlation coefficient is equal to 0.97±0.004 (mean ± standard deviation) which indicates a good simulation. Note that we can only calculate this measure for the low resolution 24×8 clinical EGMs and for d_0=0.5 mm, as we do not have the ground-truth EGMs for bigger electrode sizes or higher resolutions. *Figure 9* shows four neighboring clinical (real) EGMs and the interpolated EGMs in between them.
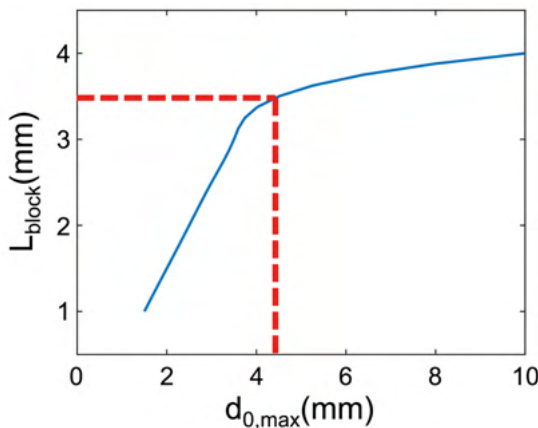
Figure 8 – Maximum electrode diameter $d_{(0,max)}$ for recording a visible scarred tissue, as a function of L_{block} which denotes the distance between two lines of block.
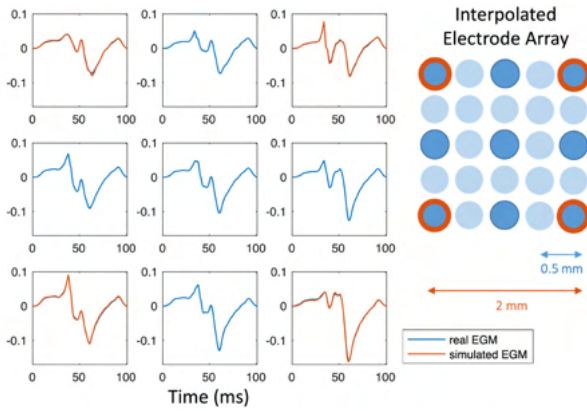
Figure 9 – Real (in orange) and interpolated EGMs (In blue) for clinical recordings with d_0=0.5 mm. Note that for an easier inspection, only EGMs from dark blue electrodes have been shown.

Statistical analysis

An analysis was performed on 10 clinical EGM arrays of size 24×8 recorded from Bachmann's bundle for 10 different patients. The signals were recorded for 10 seconds during induced AF resulting in fractionated EGMs with various levels of fractionation. Note that the EGMs were initially interpolated and modeled for different electrode sizes. This resulted in 24×8×4 EGMs in total. The measures were evaluated for one atrial beat of length 150 ms (visually selected to make sure each EGM contained atrial activity) and are presented in *Table 5*. We did not present the result for the error in LAT estimation because we do not have access to the true values in clinical data. As can be seen in the table, the changes in the properties of EGMs recorded by different electrodes follows the same pattern as for the simulated data.

Changes in activation maps

Similar patterns as in the simulation data are also seen in the clinical data. *Figure 10* shows two examples of how the high-resolution activation maps change by using different electrode sizes. As expected, the small deflections and small wavelets in T_6 are over-imposed by larger and stronger activities in their surrounding area as the electrode size increases. This leads to a decrease at the total number of wavelets in the area. T_7 also shows an example where the abnormal area with long delays in the activation map is partly or completely missed due to the increase in the electrode size.

Scaling EGMs' amplitude

A proper scaling of the EGMs' amplitudes recorded with different electrode sizes can to some extent compensate for differences in the measures that characterize the EGMs. We propose to use the ratio between the norm of the transfer functions of the electrodes for scaling their amplitudes for a better comparison of their recorded EGMs. This can be formulated as:

$$\hat{\varphi}_{d_0}(x_m, y_m, t) = \frac{\|R_0(r)\|_2}{\|R_{d_0}(r)\|_2} \varphi_{d_0}(x_m, y_m, t) \quad (8)$$

Table 5 – Measures evaluated for 24×8×4×10 interpolated clinical EGMs recorded from Bachmann's bundle.

d_0 (mm)	LSC/B (cm)	LVA %	No. deflections %		
			ND	SD	MD
0.5	80.34	47.38	77.31	25.56	3.12
2	68.47	53.13	77.72	20.99	1.27
4	59.95	60.28	84.25	15.62	0.12
8	56.09	78.40	93.46	6.52	0
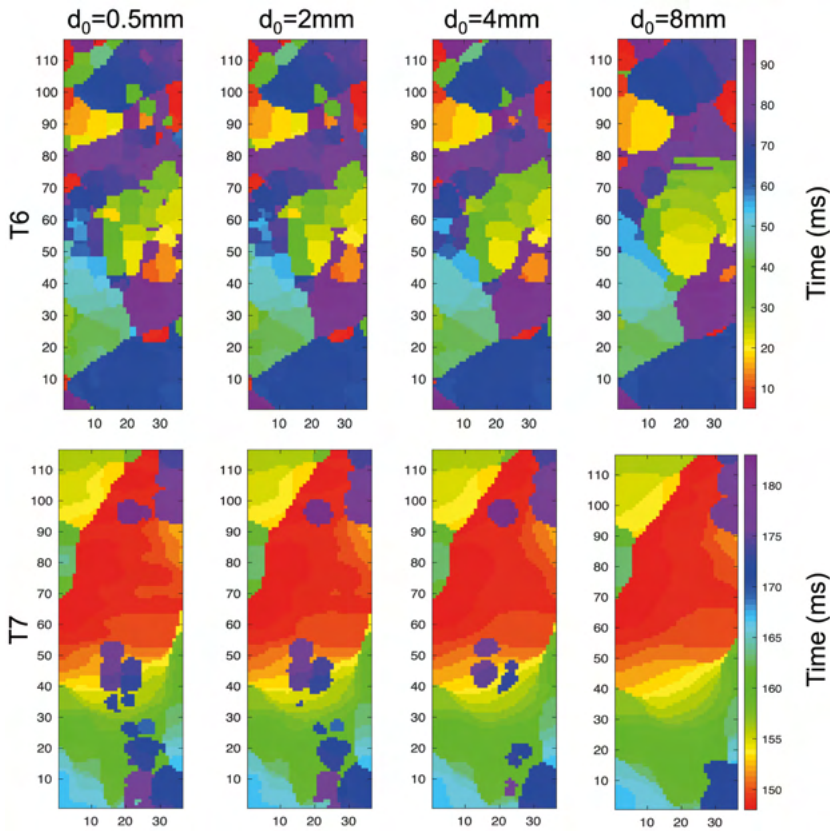
Figure 10 – Example activation maps estimated from high resolution EGM arrays with different electrode sizes, estimated from clinically recorded EGM arrays.

where $R_0(r)$ and $R_{d_0}(r)$ are calculated from *Equations 5 and 6*, $\hat{\varphi}$ is the scaled EGM, and $\|.\|_2$ is the Euclidean norm or l2-norm. This will make the measures like LVA and the number of deflections more invariant to the electrode's diameter. However, it will not affect the estimation of LATs or any parameter that is extracted from it like LSC/B.

Table 6 shows the new measures (cf. the non-scaled version in *Table 5*) after using the norm of the distance kernel for scaling the data. Notice that approaches like the maximum amplitude or steepness of the recorded EGMs for scaling or normalizing them are realization based and thus less stable. Such parameters will depend on the propagation patterns and are prone to spatial and temporal variations, making the results incomparable and not generalizable.

Table 6 – Measures evaluated for 24×8×4²×10 interpolated clinical EGMs recorded from Bachmann's bundle after scaling the EGMs.

d₀ (mm)	LSC/B (cm)	LVA %	No. deflections %		
			ND	SD	MD
0.5	80.34	47.38	71.31	25.56	3.12
2	68.47	46.62	74.11	24.13	1.75
4	59.95	47.67	77.20	22.19	0.69
8	56.09	52.40	82.41	17.47	0.10

Discussion and conclusion

In this paper, we studied the effect of electrode size on the properties of the recorded EGMs. We started by simulated EGMs of 2D atrial tissues and present the effect of different electrode sizes on EGM properties including the error in LAT estimation, the length of slow conduction or blocks (LSC/B) observed on the resulting activation map, percentage of observed low-voltage areas (LVA), and the number of deflections in the recorded EGMs. The results were then tested on clinical EGMs of 10 patients recorded from Bachmann's bundle. Since we had no access to the recorded EGMs recorded with different electrode diameters, we first estimated the high resolution transmembrane current maps[22] and then used the currents and the electrode transfer function to generate such recordings. The results were comparable to those of simulated data.

The results show that using bigger electrodes produces larger error in LAT estimation, which is in accordance with previous results shown in a previous study.[10] These errors in LAT estimation will result in the estimation of a smoother activation map than the true map. These results were also observed in previous experiments on clinical bipolar EGMs.[3,5]

The EGMs recorded with a bigger electrode size are in general smoother with smaller slopes and smaller peak-to-peak voltages. Some of the deflections in these signals are so smooth that they are not annotated as a deflection in the recording. This will result in an increase in low-voltage areas in the tissue, which agrees with the result of previous studies.[6,8] However, if there is no recording with a smaller electrode available for setting the proper thresholds, one might use smaller threshold values for detecting such deflections. This can result in detecting more deflections. This can explain why some studies suggest that increasing the electrode size increases the fractionation level in the tissue.[7-9]

However, by comparing the results of lower voltage areas in *Table 1*, *Table 2*, *Table 3* and *Table 4*, it seems that a larger diameter is more useful at indicating the difference in low-voltage areas in between different tissue types with different inhomogeneity levels. Considering that in the inhomogeneous cardiac tissue, lower conductivity also means lower voltage in that area, we can conclude that bigger electrodes are more useful at indicating the mean conductivity of the underlying substrate, even if the discrete slow conduction or block lines in the activation map are missed.

Although these conclusions have been partly discussed or hinted in previous studies, in the current study, we focused on a more systematic approach towards them. By employing the electrophysiological models and the electrode's transfer function, we could analyze and discuss these effects in more depth. Moreover, the introduced approach for interpolating and modeling clinical EGMs with different electrode sizes allowed us to investigate these effects for recordings of similar wave propagation patterns. It also enabled us to only focus on the electrode's diameter and not the inter-electrode distances.

Moreover, we discussed the effect of the optimal electrode diameter and the required inter-electrode distances (or the array resolution) for capturing all the possible spatial information. We performed an experiment to investigate the required minimum electrode size for capturing an inhomogeneous activity in between two parallel block lines in the tissue. We also introduced a proper way for scaling EGMs with different electrode's diameter for a better comparison.

These results show the importance of the recording electrode array on the properties of the EGMs, and this needs to be considered in any further evaluation and analysis of the data;

especially if considered for treatment such as EGM-based ablations.

Study limitations

In this study, we modeled the 3D tissue of the atria as a 2D grid of cells assuming a constant electrode height of z_0 for the whole tissue that is under the electrode array. Although 3D forward tissue models of the atria with varying values z_0 have already been developed in literature, employing them in an inverse problem for estimation of transmembrane current is not practical due to the complexity of these models. Moreover, that would require a proper estimation of z_0 for each recording site beforehand.

We did not have access to EGMs recorded from similar locations and different electrode sizes for a more complete evaluation of our results, as this is not possible in practice due to the temporal and spatial variations of the underlying wave propagation patterns during AF and especially for areas with complex fractionated EGMs.

The clinical EGMs used in this study were recorded from Bachmann's bundle with a predominant route of conduction from right to left and with a potential role in AF which may differ from the rest of atria.[23] However, there are already regional differences in potentials in the atria even during sinus rhythm.[24] Although our method does not depend on these specific properties, the exact results in *Table 1*, *Table 2*, *Table 3*, *Table 4*, *Table 5* and *Table 6* may not be generalizable to other regions in atria.

We used similar threshold values for evaluation of the measures for simulated and real EGMs. Although both types of EGMs were scaled such that a homogeneous planar wave has a maximum absolute amplitude of 1 V, exact selection of these parameters is more prone to error in real EGMs as we do not have access to such exact recordings.

Moreover, we ignored the effect of noise in our simulations. Although smaller electrodes provide sharper and more localized recordings, they are affected more by noise and artifacts. Therefore, using a smaller electrode may not always improve the recordings.

11

References

1. de Bakker JM. Electrogram recording and analyzing techniques to optimize selection of target sites for ablation of cardiac arrhythmias. Pacing Clin Electrophysiol. 2019;42:1503-1516.

2. Takahashi Y, O'Neill MD, Hocini M, Dubois R, Matsuo S, Knecht S, Mahapatra S, Lim KT, Jais P, Jonsson A, et al. Characterization of electrograms associated with termination of chronic atrial fibrillation by catheter ablation. J Am Coll Cardiol. 2008;51:1003-1010.

3. Anter E, Tschabrunn CM, Josephson ME. High-resolution mapping of scar-related atrial arrhythmias using smaller electrodes with closer interelectrode spacing. Circ Arrhythm Electrophysiol. 2015;8:537-545.

4. Hwang M, Kim J, Lim B, Song JS, Joung B, Shim EB, Pak HN. Multiple factors influence the morphology of the bipolar electrogram: An in silico modeling study. PLoS Comput Biol. 2019;15:e1006765.

5. Lin CY, Te ALD, Lin YJ, Chang SL, Lo LW, Hu YF, Chung FP, Tuan TC, Chao TF, Liao JN, et al. High-resolution mapping of pulmonary vein potentials improved the successful pulmonary vein isolation using small electrodes and inter-electrode spacing catheter. Int J Cardiol. 2018;272:90-96.

6. Huemer M, Qaiyumi D, Attanasio P, Parwani A, Pieske B, Blaschke F, Boldt LH, Haverkamp W, Wutzler A. Does the extent of left atrial arrhythmogenic substrate depend on the electroanatomical mapping technique: impact of pulmonary vein mapping catheter vs. ablation catheter. Europace. 2017;19:1293-1301.

7. Andronache M, Drca N, Viola G. High-resolution Mapping in Patients with Persistent AF. Arrhythm Electrophysiol Rev. 2019;8:111-115.

8. Jacquemet V, Henriquez CS. Genesis of complex fractionated atrial electrograms in zones of slow conduction: a computer model of microfibrosis. Heart Rhythm. 2009;6:803-810.

9. Correa de Sa DD, Thompson N, Stinnett-Donnelly J, Znojkiewicz P, Habel N, Muller JG, Bates JH, Buzas JS, Spector PS. Electrogram fractionation: the relationship between spatiotemporal variation of tissue excitation and electrode spatial resolution. Circ Arrhythm Electrophysiol. 2011;4:909-916.

10. Stinnett-Donnelly JM, Thompson N, Habel N, Petrov-Kondratov V, Correa de Sa DD, Bates JH, Spector PS. Effects of electrode size and spacing on the resolution of intracardiac electrograms. Coron Artery Dis. 2012;23:126-132.

11. Rocha PR, Schlett P, Kintzel U, Mailander V, Vandamme LK, Zeck G, Gomes HL, Biscarini F, de Leeuw DM. Electrochemical noise and impedance of Au electrode/electrolyte interfaces enabling extracellular detection of glioma cell populations. Sci Rep. 2016;6:34843.

12. Wiley JJ, Ideker RE, Smith WM, Pollard AE. Measuring surface potential components necessary for transmembrane current computation using microfabricated arrays. Am J Physiol Heart Circ Physiol. 2005;289:H2468-2477.

13. Plonsey R, Barr RC. Bioelectricity: a Quantitative Approach. Springer Science & Business Media; 2007.

14. Virag N, Jacquemet V, Henriquez CS, Zozor S, Blanc O, Vesin JM, Pruvot E, Kappenberger L. Study of atrial arrhythmias in a computer model based on magnetic resonance images of human atria. Chaos. 2002;12:754-763.

15. Courtemanche M, Ramirez RJ, Nattel S. Ionic mechanisms underlying human atrial action potential properties: insights from a mathematical model. Am J Physiol. 1998;275:H301-321.

16. Vigmond E, Pashaei A, Amraoui S, Cochet H, Hassaguerre M. Percolation as a mechanism to explain atrial fractionated electrograms and reentry in a fibrosis model based on imaging data. Heart Rhythm. 2016;13:1536-1543.

17. Abdi B, Hendriks RC, van der Veen AJ, de Groot NMS. A compact matrix model for atrial electrograms for tissue conductivity estimation. Comput Biol Med. 2019;107:284-291.

18. Lanters EA, van Marion DM, Kik C, Steen H, Bogers AJ, Allessie MA, Brundel BJ, de Groot NM. HALT & REVERSE: Hsf1 activators lower cardiomyocyt damage; towards a novel approach to REVERSE atrial fibrillation. J Transl Med. 2015;13:347.

19. van der Does LJ, Yaksh A, Kik C, Knops P, Lanters EA, Teuwen CP, Oei FB, van de Woestijne PC, Bekkers JA, Bogers AJ, et al. QUest for the Arrhythmogenic Substrate of Atrial fibRillation in Patients Undergoing Cardiac Surgery (QUASAR Study): Rationale and Design. J Cardiovasc Transl Res. 2016;9:194-201.

20. Mouws E, Lanters EAH, Teuwen CP, van der Does L, Kik C, Knops P, Bekkers JA, Bogers A, de Groot NMS. Epicardial Breakthrough Waves During Sinus Rhythm: Depiction of the Arrhythmogenic Substrate? Circ Arrhythm Electrophysiol. 2017;10.

21. Abdi B, Hendriks RC, van der Veen AJ, de Groot NMS. Improved local activation time annotation of fractionated atrial electrograms for atrial mapping. Comput Biol Med. 2020;117:103590.

22. Abdi B, van der Veen AJ, de Groot NMS, Hendriks RC. Local Activation Time Estimation in Fractionated Electrograms of Cardiac Mappings. Annu Int Conf IEEE Eng Med Biol Soc. 2019;2019:285-288.

23. Teuwen CP, Yaksh A, Lanters EA, Kik C, van der Does LJ, Knops P, Taverne YJ, van de Woestijne PC, Oei FB, Bekkers JA, et al. Relevance of Conduction Disorders in Bachmann's Bundle During Sinus Rhythm in Humans. Circ Arrhythm Electrophysiol. 2016;9:e003972.

24. van Schie MS, Starreveld R, Bogers A, de Groot NMS. Sinus rhythm voltage fingerprinting in patients with mitral valve disease using a high-density epicardial mapping approach. Europace. 2021;23:469-478.

11
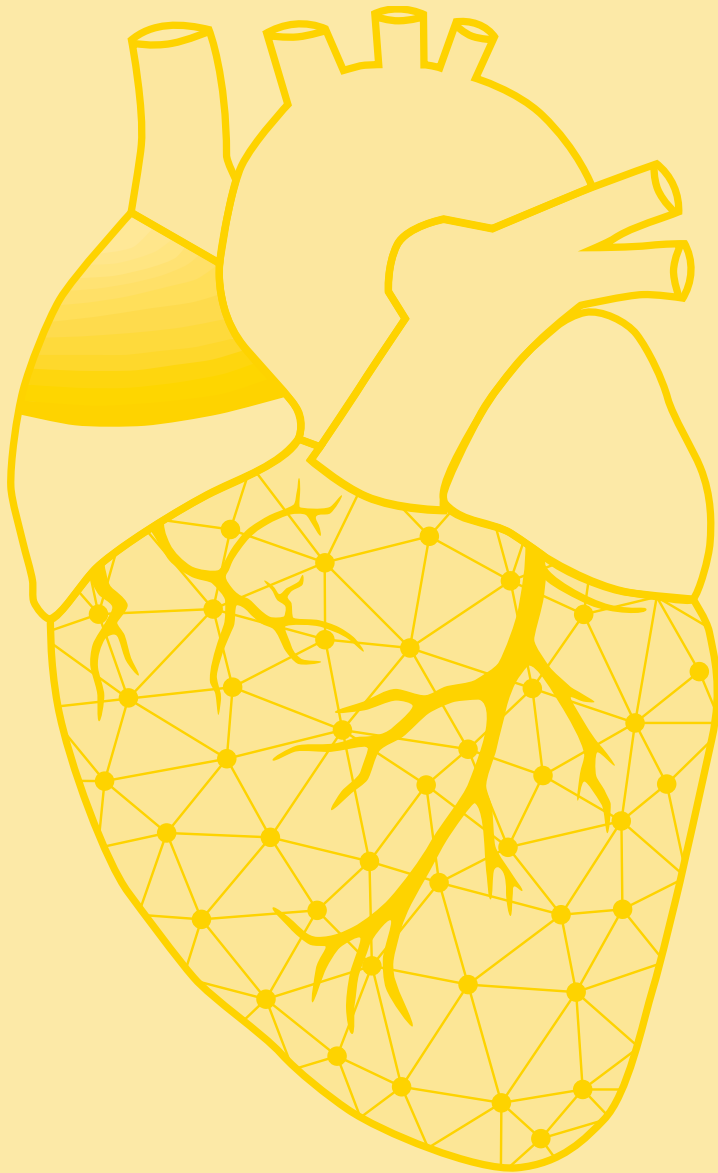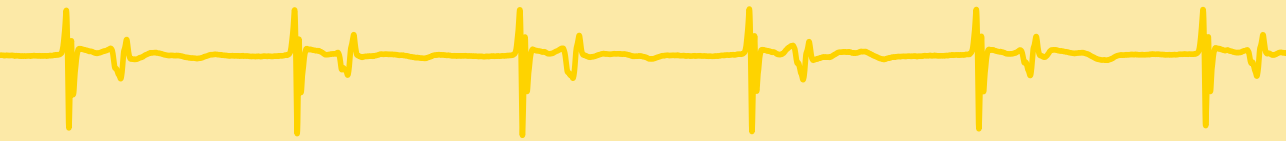
Chapter 12

Signal fingerprinting as a novel diagnostic tool to identify conduction inhomogeneity

Ziliang Ye*

Mathijs S. van Schie*

Natasja M.S. de Groot

* Contributed equally

Abstract

Background: Inhomogeneous intra-atrial conduction facilitates both initiation and perpetuation of atrial fibrillation (AF) and is reflected in electrogram (EGM) morphology. The primary objective of this study was to investigate regional differences in features of different EGM types during sinus rhythm (SR) and to design a patient-specific signal fingerprint, which quantifies the severity and extensiveness of inhomogeneity in conduction.

Methods: Patients (N=189, 86% male; mean age 65±9 years) undergoing coronary artery bypass grafting underwent high-resolution mapping of the right atrium (RA), left atrium (LA), pulmonary vein area (PVA) and Bachmann's bundle (BB). EGMs during 5 seconds of sinus rhythm (SR) were classified as single potentials (SP), short double potentials (SDP, interval between deflections <15 ms), long double potentials (LDP, deflection interval ≥15 ms) or fractionated potentials (FP, ≥3 deflections). Of all SPs, differences in relative R- and S-wave amplitude were calculated (R/S ratios). Time differences between the first and last deflection were determined (fractionation duration, FD) and potentials with amplitudes <1.0 mV were labeled as low voltage. Conduction block (CB) was defined as a difference in local activation time between adjacent electrodes of ≥12 ms.

Results: A total of 1,9645,637 EGMs (9,331±3,336 per patient) were classified.

Table 1 – Overview of all signal features for each atrial region separately.

Variables	RA	BB	PVA	LA
Median voltage (mV)	4.68 [3.43–5.72]	5.07 [3.16–6.99]	4.73 [2.52–6.44]	5.54 [3.28–7.30]
Low-voltage (%)	5.75 [2.31–10.64]	2.20 [0.55–8.43]	4.34 [1.23–15.87]	4.47 [1.26–9.53]
R/S ratio	0.54 [0.47–0.60]	0.63 [0.55–0.71]	0.25 [0.02–0.40]	-0.02 [-0.21–0.20]
SP (%)	83.7 [75.7–89.3]	77.4 [67.3–87.3]	81.9 [69.5–88.1]	80.6 [72.0–86.5]
SDP (%)	9.8 [5.9–13.4]	11.5 [7.2–16.3]	10.3 [6.9–16.0]	11.6 [8.7–16.2]
LDP (%)	4.0 [1.9–6.8]	3.8 [0.9–9.1]	1.6 [0.3–5.5]	1.7 [0.6–4.1]
FP (%)	1.3 [0.4–3.2]	1.4 [0.2–3.6]	0.7 [0.2–2.5]	1.3 [0.4–2.5]
FD (ms)	10.0 [8.0–14.0]	11.0 [9.0–14.0]	9.0 [8.0–12.0]	9.0 [7.0–12.0]
CB (%)	2.4 [1.2–3.8]	2.3 [1.0–5.1]	1.1 [0.2–2.8]	0.7 [0.2–1.7]

BB = Bachmann's bundle; **CB** = conduction block; **FD** = fractionation duration; **FP** = fractionated potentials; **LA** = left atrium; **LDP** = long double potentials; **PVA** = pulmonary vein area; **RA** = right atrium; **SDP** = short double potentials; **SP** = single potentials.

Conclusion: The signal fingerprint, consisting of quantified EGM features, including the R/S ratio of SPs, the relative frequency distribution of unipolar voltages, the proportion of low-voltage areas, the proportion of the different types of EGMs and durations of LDP and FDP, may serve as a diagnostic tool to determine the severity and extensiveness of conduction inhomogeneity. Further studies are required to determine whether the signal fingerprint can be used to identify patients at risk for AF onset or progression.

Journal site &
supplementary material

Introduction

Inhomogeneous intra-atrial conduction facilitates both initiation and perpetuation of atrial fibrillation (AF). An inhomogeneous pattern of conduction is reflected in electrogram (EGM) morphology and causes low amplitude, fractionated potentials.[1] Substrate-based ablation approaches in patients with AF therefore target low-voltages areas or fractionated EGMs.[2-4] These additional ablation approaches in patients with AF have not yet resulted in beneficial long-term outcomes.[4,5] This is, however, not surprising. Inhomogeneous conduction and hence EGM fractionation can also be physiological in nature, due to for example tissue discontinuities caused by anatomical structures such as capillaries. In addition, different use of filter settings can create or either mask fractionation.

At present, data on physiological variation in EGM morphology throughout the atria is scarce. Recently, Van Schie et al.[6] investigated the impact of AF episodes on the relative R- and S-wave ratio of unipolar, non-fractionated potentials during sinus rhythm (SR) and demonstrated that there was a loss of S-wave amplitude in patients with AF. This reduction of S-wave amplitude was associated with a decrease in conduction velocity. We hypothesize that construction of a signal profile containing quantified features of all types of EGMs may reflect the severity and extensiveness of inhomogeneity in conduction. Such a diagnostic tool would provide an individualized arrhythmogenic substrate profile which can also be tailored to possible gender and age specific features of EGMs.

The goal of this study, as a first step towards construction of a diagnostic signal fingerprint, is to investigate regional differences in features of different EGM types in relation to inhomogeneous intra-atrial conduction during SR at a high resolution in a large cohort of patients without atrial tachyarrhythmias.

12

Methods

Study population

The study population consisted of 189 adult patients undergoing coronary artery bypass grafting (CABG) in the Erasmus Medical Center Rotterdam. This study was approved by the institutional medical ethical committee (MEC2010-054/MEC2014-393).[7,8] Written informed consent was obtained from all patients. Patient characteristics (e.g., age, medical history, cardiovascular risk factors) were obtained from the patient's medical record. Only patients without a history of arrhythmias were included in the present study.

Mapping procedure

As previously described, high-resolution epicardial mapping is performed before the start of extracorporeal circulation.[7,8] Briefly, a temporary bipolar pacemaker wire was stitched to the right atrial free wall and served as a reference electrode, while a steel wire fixed to the subcutaneous tissue of the thoracic cavity was used as an indifferent electrode. Atrial epicardial mapping was performed using a 128 or 192 electrode array (electrode diameter respectively 0.65 or 0.45 mm, interelectrode distances 2.0 mm). Mapping was conducted by shifting the electrode array along imaginary lines with a fixed anatomic orientation, following a predefined mapping scheme, covering the entire epicardial surface of the right atrium (RA), Bachmann's bundle (BB), pulmonary vein area (PVA) and left atrium (LA), as demonstrated in *Figure 1*. The RA was mapped from the cavo-tricuspid isthmus, shifting perpendicular to the caval veins towards the RA appendage. The PVA was mapped from the sinus transversus fold along the borders of the right and left pulmonary veins (PVA) down
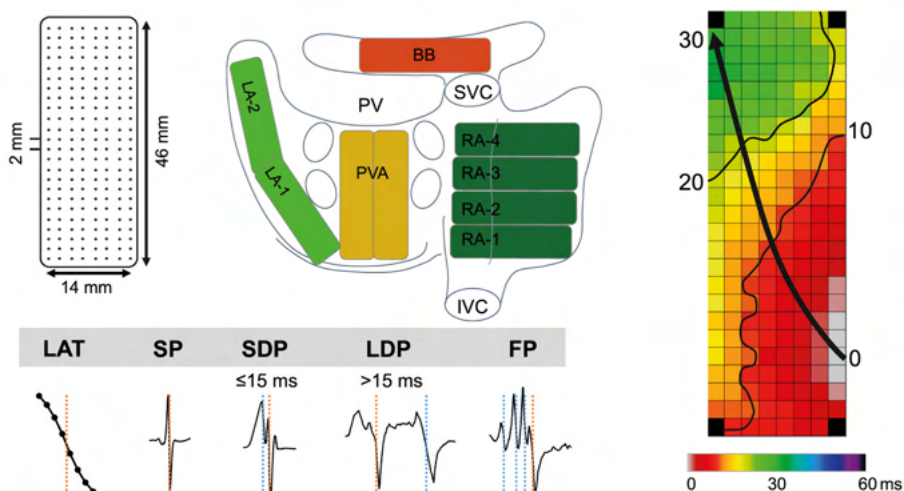
Figure 1 – Epicardial mapping of the atria. The upper left panel demonstrates a schematic presentation of the 192-unipolar electrode array and the projection of this array on a schematic posterior view of the atria. The lower left panel demonstrates typical examples of the different types of EGM classified in this study. The right panel shows a color-coded activation map; isochrones (thin black lines) are drawn at 10 ms intervals and the black arrow indicates wavefront propagation. **IVC** = inferior vena cava; **SVC** = superior vena cava; **RA** = right atrium; **BB** = Bachmann's bundle; **LA** = left atrium; **PV(A)** = pulmonary vein (area); **EGM** = electrogram; **SP** = single potential; **SDP** = short double potential; **LDP** = long double potential; **FP** = fractionated potential.

towards the atrioventricular groove. The left atrioventricular groove was mapped from the lower border of the left inferior pulmonary vein towards the LA appendage. BB was mapped from the tip of the LA appendage across the roof of the LA, behind the aorta towards the superior cavo-atrial junction.

Five seconds of SR were recorded at each mapping site, including a surface ECG lead, a bipolar reference EGM and all unipolar epicardial EGMs. Data was stored on a hard disk after amplification (gain 1000), filtering (bandwidth 0.5–400 Hz), sampling (1 kHz) and analogue-to-digital conversion (16 bits).

Data analysis

Custom-made software was used to automatically measure EGM features. Missing or poor-quality EGMs and premature atrial complexes or aberrant beats were excluded from analysis. The steepest negative slope of a unipolar EGM was annotated as the local activation time (LAT), providing that the amplitude of the deflection was at least two times the signal-to-noise. All annotations were manually checked with a consensus of two investigators. LATs of EGMs at each electrode were used to reconstruct color-coded activation maps (right panel of *Figure 1*).

As shown in the lower panel of *Figure 1*, EGMs were classified as single potentials (SP, single negative deflection), short double potentials (SDP, interval between deflections <15 ms), long double potentials (LDP, deflection interval ≥15 ms) or fractionated potentials (FP, ≥3 deflections). The time difference (ms) between the first and last deflection of fractionated potentials is defined as fractionation duration. As described in our previous study, single potentials were classified according their differences in relative R- and S-wave amplitudes and scaled from -1 (R-wave) to 1 (S-wave):[6]

Table 2 – Baseline characteristics of the study population (N=189).

Variables	Mean + SD / N(%)
Age (year)	65.44±9.26
Age	
• <60 years	51 (26.98%)
• ≥60 years	138 (73.02%)
Male (N, %)	163 (86.24%)
BMI (kg/m²)	28.29±3.87
BMI	
• Normal weight (18.5–25 kg/m²)	38 (20.11%)
• Overweight (25–30 kg/m²)	91 (48.15%)
• Obese (≥30 kg/m²)	60 (31.75%)
Cardiovascular risk factors	
• Hypertension (N, %)	113 (59.79%)
• Dyslipidemia (N, %)	77 (40.74%)
• Diabetes mellitus (N, %)	62 (32.80%)
• Left ventricular dysfunction (N, %)	42 (22.22%)
• Left atrial dilatation >45 mm (N, %)	21 (11.11%)
ACEI / ARB / AT2 antagonist (N, %)	131 (69.31%)
Statin (N, %)	170 (89.95%)
Antiarrhythmic drugs	
• Class I (N, %)	1 (0.53%)
• Class II (N, %)	150 (79.37%)
• Class III (N, %)	3 (1.59%)
• Class IV (N, %)	11 (5.82%)
• Digoxin (N, %)	2 (1.07%)

Values are presented as N (%), mean ± standard deviation. **ACEI** = angiotensin-converting enzyme inhibitors; **ARB** = angiotensin receptor blockers; **AT2** = angiotensin type 2 receptor; **BMI** = body mass index.

$$RS = \begin{cases} 1 - RS(n) & for\ RS(n) \leq 1 \\ \dfrac{1}{RS(n)} - 1 & for\ RS(n) > 1 \end{cases}$$

Furthermore, peak-to-peak amplitudes of all potentials were measured. Low-voltage potentials were, in line with prior mapping studies, defined as potentials with an amplitude <1.0 mV.[9]

Conduction block (CB) was defined as a difference in LAT between adjacent electrodes of ≥12 ms.[10] Areas of simultaneous activation were excluded from analysis in order to avoid inclusion of far-field potentials.

Statistical analysis

Before statistical analysis, the Shapiro-Wilk test was used to determine whether the continuous variables are normally distributed. Continuous variables that are normally distributed are represented by the mean and standard deviation (SD), and differences between groups are compared by an independent sample *t*-test or least significant difference (LSD) analysis of variance. Continuous variables that are not normally distributed are represented by the median [25th–75th percentile] or minimum to maximum. Differences between groups are compared using Wilcoxon rank sum test or Kruskal-Wallis test. Categorical variables are expressed as the number and percentages, and differences between groups are compared using χ^2 test or Rank sum test if appropriate. Spearman correlations were calculated to determine whether CB was associated with the EGM features. Spearman's correlation coefficients were categorized as weak (<0.4), moderate (0.4-0.6) or strong (>0.6) correlation.
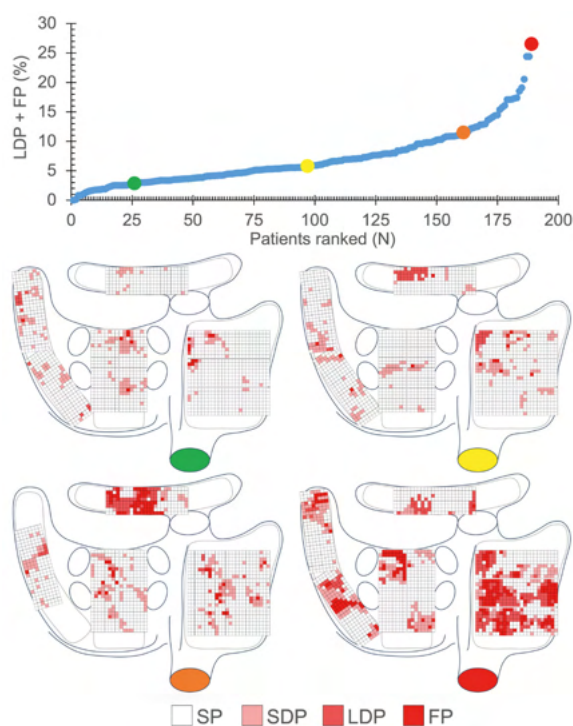
Figure 2 – The amount of fractionation per patient. The upper panel shows the proportion of long double and fractionated potentials for each individual patient, patients are ranked according to an increase in fractionation. The lower panel demonstrates typical examples of color-coded signal maps from four different patients, showing the proportion of the different EGM types at the various recording sites. These maps correspond to the patients marked in the graph by colored dots (green, yellow, orange and red). **FP** = fractionated potential; **EGM** = electrogram; **LDP** = long double potential; **SDP** = short double potential; **SP** = single potential.

In this study, SPSS software version 20.0 and R software were used for data analysis, and p<0.05 indicated significant difference. Bonferroni correction was applied to compare each of the four atrial regions with each other; a *p*-value of <0.0083 (0.05/6) was considered statistically significant (*Supplementary Figure 1*).

Results

Study population

Baseline characteristics of the study population (N=189; 86% male; mean age 65±9 years) are described in *Table 2*. The majority of the patients had normal left ventricular function; left atrial dilatation was present in 11% of the patients.

Classification of EGM

A total of 1,9645,637 EGMs (9,331±3,336 per patient) were analyzed; these EGMs were recorded from the RA (N=841,215), BB (N=196,709), LA (N=343,447) and PVA (N=382,222). Per region respectively 1.1%, 4.2%, 4.0% and 3.7% of the EGMs were excluded from analysis due to a poor signal-to-noise ratio. In each patient, the majority of all SR EGMs consisted of SP (81.4 (48.88 to 100) %). The remainder of the EGMs were mainly either SDP (10.9 (0 to 24.1) % or LDP (4.0 (0 to 20.7) %). The upper panel of *Figure 2* shows the proportion of LDP+FP (5.6 (0 to 26.5) %) plotted for each patient individually; patients are ranked according to an increase in fractionation. The lower panel of *Figure 2* demonstrates typical examples of color-coded signal maps obtained from 4 different patients; these signal maps show the proportion of LDP and FP at every recording site. As can be seen, LDP and FP predominantly occur at the RA and BB.
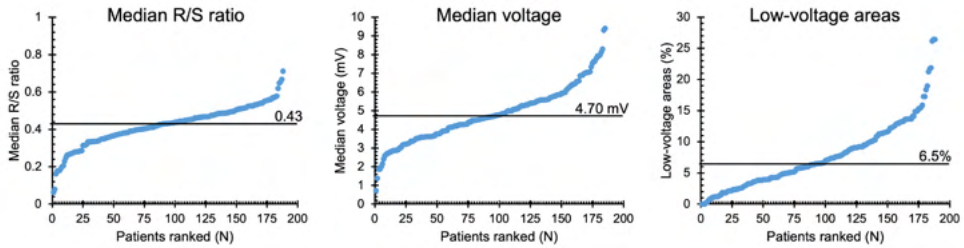
Figure 3 – Median R/S ratios, voltage and proportion of low-voltage areas plotted for each individual patient. Patients are ranked according to increasing values of these parameters. The median value of each parameter is indicated by the horizontal line.

Features of EGM

The left panel of *Figure 3* shows the median R/S ratio of all SP per patient (N=7,452±2,565); the median R/S ratio was 0.43 and ranged from 0.06 to 0.71. Most EGMs (97%) had a R-wave preceding the negative deflection; only 49,896 SPs consisted of solely R- or S-waves. (R-wave: 0.26%, S-wave: 3.29%). The middle and right panel of *Figure 3* show respectively median voltage of all atrial EGMs and the prevalence of low-voltage EGMs (<1 mV) for each patient individually. Median atrial voltage was 4.7 mV and ranged from 0.7 to 9.4 mV. Low-voltage EGMs were found in the majority of the patients (98%) and accounted for 6.5 (0 to 26.4) % of the EGMs.

Regional differences in EGM Features

At all atrial regions, most EGMs consisted of SPs; the proportion of SPs was significantly lower at BB and LA compared to the RA (RA: 83.7 (48.2 to 100) % vs. BB: 77.4 (35.2 to 100) % and LA: 80.6 (33.9 to 99.3) %, p<0.001 and p=0.004). The proportion of SDPs at both BB and LA was higher compared to the RA (RA: 9.8 (0 to 26.8) % vs. BB: 11.5 (0 to 36.2) % and LA: 11.6 (0.7 to 44.3) %, p=0.039 and p=0.001) whereas the proportion of LDP at RA and BB (4.0 (0 to 35.5) % and 3.8 (0 to 28.3) % were considerably higher than at the PVA (1.6 (0 to 78.1) %, p<0.001 and p=0.001) and LA (1.7 (0 to 35.8) %, p<0.001 for both). The proportion of FP was also highest at BB compared to all other atrial regions (BB: 1.4 (0 to 14.8) % vs. RA: 1.3 (0 to 14.8) %, LA: 1.3 (0 to 16.2) %, PVA: 0.7 (0 to 11.8) %, p<0.008 for all).

Figure 4 demonstrates the relative incidence of FPs at BB in a subset of patients (N=123 (65%) who were mapped with the 192-electrode array which covered the whole BB region. Although FPs could be found over the entire mapping area, most FPs were recorded near the center of BB and its entrance to the LA.
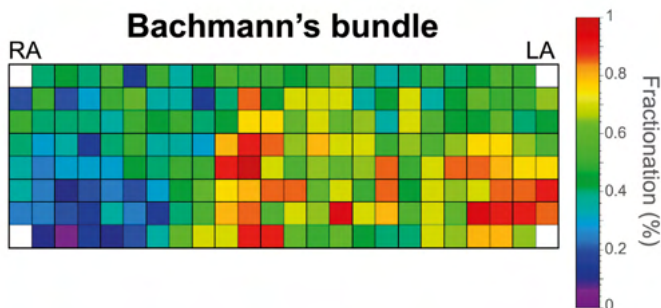
Figure 4 – Relative incidence of fractionated potentials at Bachmann's bundle of a subset of 123 patients who were mapped with the 192-electrode array. LA = left atrium; **RA** = right atrium.
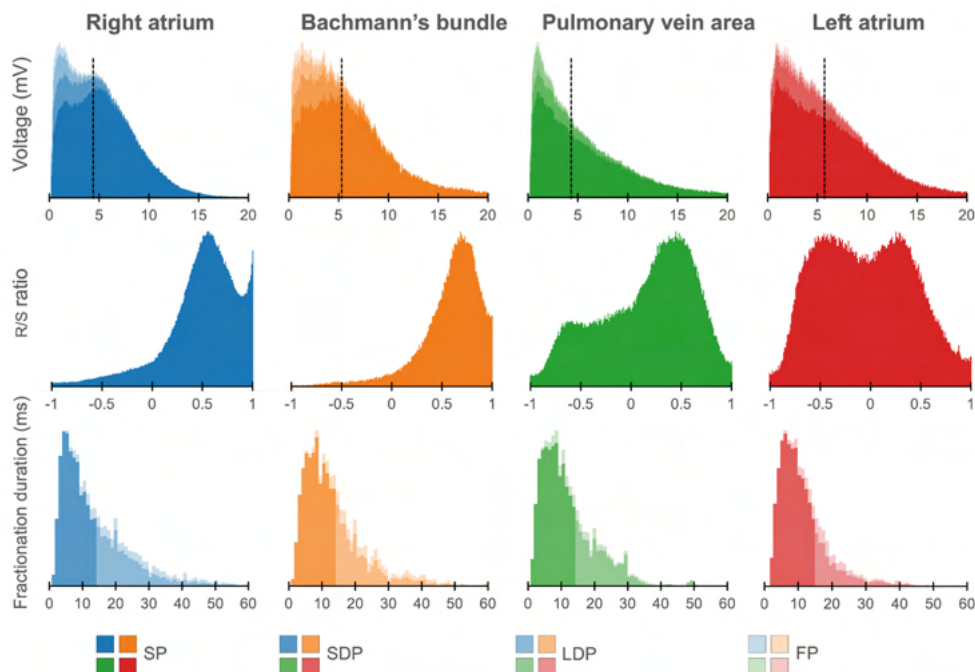
Figure 5 – Histograms of the relative frequency distribution of all voltages (upper), R/S ratios (middle) and fractionation durations (lower) recorded at the right atrium (blue), Bachmann's bundle (orange), pulmonary vein area (green) and left atrium (red). Median voltage values are indicated by the black dotted lines. All histograms are subdivided and stacked according to the potential type classification (SP, SDP, LDP or FP). **SP** = single potential; **SDP** = short double potential; **LDP** = long double potential; **FP** = fractionated potential.

Figure 5 shows regional differences in the features of the various EGM types. Histograms in the upper panel show the relative frequency distribution of voltages of SP, SDP, LDP and FP separately obtained from the RA, BB, PVA and LA. The lowest median voltages were recorded at the PVA (RA: 4.68 [2.39–7.33] mV; BB: 5.29 [2.75–8.65] mV; LA: 5.38 [2.68–9.18] mV; PVA 4.55 [2.14–8.72] mV).

The RA region has the highest proportion of low-voltage EGMs (RA: 5.75 [2.31–10.64] %, LA: 4.47 [1.26–9.53] %, PVA: 4.34 [1.23–15.87] % and BB: 2.20 [0.55–8.43] %).

The middle panel of *Figure 5* shows histograms of the relative frequency distribution of R/S ratios of SP for the 4 different atrial regions separately. These R/S ratios differed significantly between the four atrial regions (BB: 0.63 [0.55–0.71], RA: 0.54 [0.47–0.60], PVA: 0.25 [0.02–0.40] and LA -0.02 [-0.21–0.20], p<0.001 for each). SPs at the RA and BB had a clear predominant S-wave morphology (ratio R- and S-wave: RA 1:2 and BB 1:2.5). In addition, there was also a large number of SP consisting mainly of solely a S-wave at the RA. In contrast to the RA and BB, SPs recorded from the LA and PVA had a more widespread distribution of R/S ratios. The histogram of the LA had a bimodal distribution with a preference for both predominant R-wave (2:1) and predominant S-wave morphology (1:1.7), whereas the histogram derived from the PVA contained a clear second peak at predominant S-waves (1:2).

Histograms in the lower panel show the relative frequency distribution of FD of the SP, SDP, LDP and FP separately. FP with the longest FD were recorded at BB (FD BB: 11.0 [9.0–14.0] ms; RA: 10.0 [8.0–14.0] ms, PVA: 9.0 [8.0–12.0] ms, LA: 9.0 [7.0–12.0] ms, p<0.001 for each).
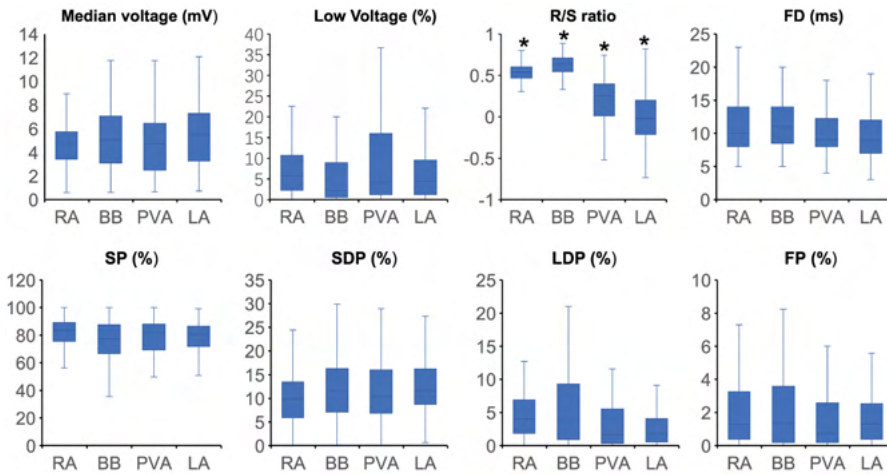
Figure 6 – Boxplots depicting the median value of the EGM features for each region separately. Statistical significance for comparison between all other atrial regions is indicated by an asterisk. **SP** = single potential; **SDP** = short double potential; **LDP** = long double potential; **FP** = fractionated potential; **FD** = fractionation duration.

Correlations between clinical characteristics and EGM features

Supplementary Table 1 shows the correlations between clinical characteristics and EGM features for all regions combined and for each region separately. As can be seen in this table, correlations are either not significant or weak.

Correlations between conduction block and EGM features

Figure 6 shows that for every atrial region there is considerable interindividual variation of each EGM feature. These EGM features were correlated with the amount of CB. As expected, there was a strong positive correlation between the prevalence of CB and the proportion of LDP (r=0.70) and FP (r=0.53). *Table 3* summarizes Spearman's rank correlation coefficients

Table 3 – Regional correlations between conduction block and EGM features.

	RA	Rho (CB)	BB	Rho (CB)	PVA	Rho (CB)	LA	Rho (CB)
CB (%)	2.4 [1.2–3.8]							
Voltage (mV)	4.68 [3.43–5.72]	-0.47*	5.07 [3.16–6.99]	-0.64*	4.73 [2.52–6.44]	-0.54*	5.54 [3.28–7.30]	-0.05
Low-voltage (%)	5.75 [2.31–10.64]	0.69*	2.20 [0.55–8.43]	0.73*	4.34 [1.23–15.87]	0.57*	4.47 [1.26–9.53]	0.14
R/S ratio	0.54 [0.47–0.60]	0.20*	0.63 [0.55–0.71]	0.16*	0.25 [0.02–0.40]	0.08	-0.02 [-0.21–0.20]	0.22*
SP (%)	83.7 [75.7–89.3]	-0.65*	77.4 [67.3–87.3]	-0.59*	81.9 [69.5–88.1]	-0.51*	80.6 [72.0–86.5]	-0.41*
SDP (%)	9.8 [5.9–13.4]	0.28*	11.5 [7.2–16.3]	0.33*	10.3 [6.9–16.0]	0.12	11.6 [8.7–16.2]	0.18*
LDP (%)	4.0 [1.9–6.8]	0.83*	3.8 [0.9–9.1]	0.80*	1.6 [0.3–5.5]	0.82*	1.7 [0.6–4.1]	0.61*
FP (%)	1.3 [0.4–3.2]	0.64*	1.4 [0.2–3.6]	0.69*	0.7 [0.2–2.5]	0.64*	1.3 [0.4–2.5]	0.46*
FD (%)	10.0 [8.0–14.0]	0.73*	11.0 [9.0–14.0]	0.68*	9.0 [8.0–12.0]	0.77*	9.0 [7.0–12.0]	0.59*

Values are presented as median [min–max]. Rho values with asterisk are statistically significant. **RA** = right atrium; **BB** = Bachmann's bundle; **PVA** = pulmonary vein area; **LA** = left atrium; **CB** = conduction block; **SP** = single potential; **SDP** = short double potential; **LDP** = long double potential; **FP** = fractionated potential; **FD** = fractionation duration.
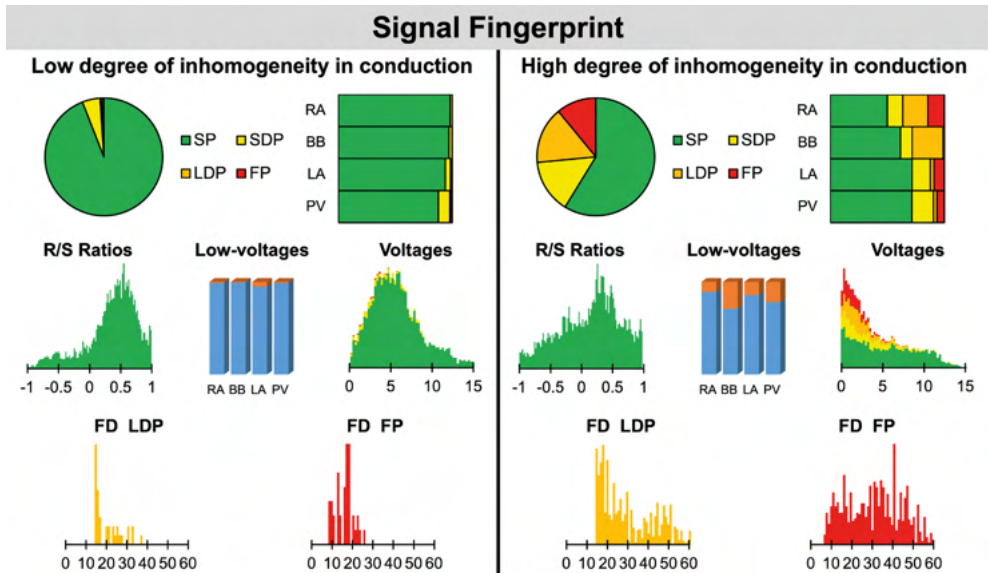
Figure 7 – Two examples of a signal fingerprint obtained from one patient with a low and one with a high degree of inhomogeneity in conduction. The upper panels show the distribution of potential types of the entire (left, pie plot) and for each region separately (right, stacked bars). The middle left plot shows the R/S ratio distribution of all SPs of the entire atrium. The middle center bar plot displays the number of low-voltage potentials plotted for each region separately. The middle right plot shows the distribution of voltages (mV) of SPs (green), SDPs (yellow), LDPs (orange) and FPs (red) from all atrial regions. The lower panel displays the distribution of fractionation duration (ms) for LDPs (left) and FPs (right). **SP** = single potential; **SDP** = short double potential; **LDP** = long double potential; **FP** = fractionated potential; **FD** = fractionation duration.

between CB and EGM features for the 4 atrial regions separately. CB was strongly correlated with the proportion of LDP at all atrial regions and with the proportion of FP at RA, BB and PVA. Likewise, FD was correlated with CB at the RA, BB and PVA. The presence of low-voltage areas was strongly related with the occurrence of CB at RA and BB. The strongest correlation was found between CB and the proportion of LDP at the RA (r=0.83).

In order to test whether various degrees of inhomogeneity in conduction indeed translates into EGM morphology on the individual level, we compared EGM features between two patients with a high and low degree of inhomogeneous conduction. These examples of the resulting electrical signal fingerprints consisting of all quantified EGM features as described above are shown in *Figure 7*.

Discussion

This is the first report on quantification of EGM properties measured during SR at a high-resolution scale throughout the right and left atrium including Bachmann's bundle. Data was obtained from a large cohort of patients without a history of atrial tachyarrhythmias. In all atrial regions, the majority of the EGMs consisted of SP; the highest proportion of LDP and FP were mainly recorded at the RA and BB; fractionation at BB also had the longest durations. The largest prevalence of low-voltage areas was found at the RA. CB was correlated with the proportion of LDP and FP, fractionation duration of FP, and the prevalence of low-voltage areas. Thus, conduction inhomogeneity can be identified by a signal fingerprint containing specific quantified EGM features.

Relation between R/S ratio and conduction inhomogeneity

EGM morphology of SPs, mainly determined by the magnitude of the R- and S-wave, contains information on conduction inhomogeneity. The unipolar EGM morphology represents the sum of instantaneous current dipoles of a propagating wavefront, generating a positive deflection (R-wave) and negative deflection (S-wave) as the activation wavefront propagates respectively towards and away from the recording electrode.[11,12] This results in the typical R-S morphology of the majority of the SPs. Certain EGM morphologies are found at specific atrial regions. For example, wavefront propagation during normal SR is initiated at the sino-atrial node from where it spreads in contiguous, prominent muscle bundles. When recording EGMs near this area, the activation wavefront only propagates away from the recording electrodes resulting in SPs consisting of solely S-wave morphologies. As intra-atrial conduction during SR is generally characterized by smooth and fast propagation, the majority of the SPs, however, have a typical large amplitude R-S morphology.

Van der Does et al.[13] performed high resolution mapping of the RA wall and evaluated differences in EGM morphology of >2000 pairs of simultaneously acquired endo- and epicardial EGMs. There was no difference in R/S ratios of opposite endo- and epicardial EGMs and both sites showed a predominant S-wave morphology. The cause of S-wave predominance was further investigated by Van Schie et al.[6] They investigated the impact of AF episodes on SP morphology. In patients with AF, there was a loss of S-wave amplitude resulting in SPs with lower amplitudes and shifted R/S ratios. This reduction of S-wave amplitude was also associated with a decrease in conduction velocity. Hence, these observations indicate that the R/S ratio of SPs is a suitable marker of conduction inhomogeneity and it should therefore be incorporated in the diagnostic electrical signal fingerprint.

12

Relation between fractionation, fractionation duration and conduction inhomogeneity

Fractionation of EGMs is caused by asynchronous activation of adjacent cardiomyocytes, due to the presence of structural barriers such as fibrotic strands. This in turn gives rise to inhomogeneous intra-atrial conduction. In addition, increased slowing of intra-atrial conduction is related to prolonged duration of fractionated potentials.[14,15]

Konings et al.[16] were the first to demonstrate the relation between EGM morphology and specific patterns of activation. During induced AF in patients with the Wolf-Parkinson White syndrome, SDP were mainly caused by collision of fibrillation waves, LDP were recorded along long lines of CB and FP in areas of slow conduction or at pivot points. Collision of wavefronts may also occur during SR, for example when the SR wavefront divides to turn around small barriers such as tissue discontinuities caused by fibrotic strands and merges again at the opposite sites.

The relation between LDP and FP and patterns of activation has also been investigated during SR. Simultaneous endo-epicardial high-resolution mapping studies demonstrated that fractionation of unipolar EGMs during SR is not only the result of slowing of conduction or pivoting of the wavefront around a line of conduction block, but that it can also be attributed to asynchronous activation of the endo- and epicardial wall. Even during SR, asynchronous activation up to 84 ms has been described.[17]

Inhomogeneous conduction and hence EGM fractionation may also be caused by normal properties of the myocardial tissue. For example, the trabeculated parts of the atria contain muscle bundles of variable thickness. As a consequence, small myocardial strands excite

larger myocardial areas leading to source-to-sink mismatches which also causes slowing of conduction. This explains recordings of LDP and FP during SR in all patients. In a series of prior mapping studies of the atria during SR, it was demonstrated that lines of CB most frequently occur at the superior part of the RA (sino-atrial node area) and BB, which is consistent with the high proportion of LDP and FP observed in the present study.[17,18]

Relation between unipolar voltages and conduction inhomogeneity

Peak-to-peak amplitudes of unipolar EGM are affected by numerous variables including not only tissue related factors, but also to EGM recording and processing technologies. In general, areas of low voltages are considered as surrogate markers of fibrotic tissue and have therefore become targets for ablative therapy in patients with AF.[2-4] This even includes low-voltage areas identified during SR. Regional differences in unipolar voltages has recently been investigated in a cohort of 67 patients with mitral valve disease undergoing cardiac surgery by Van Schie et al.[9] Not only marked inter-individual differences in unipolar voltages, but also regional differences in unipolar voltages were observed. Patients with AF had lower EGM voltages during SR, particularly at BB. There were also regional differences in the proportion of low-voltage EGMs; the lowest and highest number of low-voltage EGM were found at respectively BB (2.20%) and RA (5.75%). Comparable to the patients with mitral valve disease, we also observed in our patients with coronary artery disease the highest proportion of low-voltage EGMs at the RA and BB. The wide distribution of low-voltage areas particularly at RA, BB, LA and PVA may explain why ablation approaches in patients with AF targeting low-voltages areas during SR solely in the LA may not be beneficial.

Mapping of right atrium

Current ablation procedures mostly consist of a pulmonary vein isolation and focus on the LA. However, other procedures like the Cox-Maze include the RA as well. Prior studies have demonstrated that the RA is driving AF in ≈20% of persistent AF.[19] Thus, the signal fingerprints of the RA should not be ignored. We performed mapping of the cavo-tricuspid isthmus area. Thus far, we have no additional evidence that the cavo-tricuspid isthmus is a major player in the pathophysiology of AF or that it is a predilection site for electropathology in these patients. As described above, the highest proportion of LDP and FP were mainly recorded at the RA and BB, and the largest prevalence of low-voltage areas was found at the RA, which might partly explain why catheter ablation based on low-voltage areas or FP at RA region cannot achieve ideal benefits. Since low-voltage potentials and fractionation have been recorded during SR, it is still challenging to identify whether this phenomenon is caused by physiology or pathology. This should be a new direction for subsequent studies.

Limitations

The high-resolution epicardial mapping is an invasive approach and cannot easily be translated to non-invasive data. The impact of endo-epicardial asynchrony, on differences between the endo- and epicardial fingerprint is at present unknown and needs to be further investigated. Additionally, we performed mapping of the cavo-tricuspid isthmus area. Thus far, we have no additional evidence that the cavo-tricuspid isthmus is a major player in the pathophysiology of AF or that it is a predilection site for electropathology in these patients.

Conclusion

At present, we have no diagnostic tool to determine the severity and extensiveness of conduction inhomogeneity, which plays a major role in initiation and perpetuation of atrial

tachyarrhythmias, including AF. The signal fingerprint, consisting of quantified EGM features, including the R/S ratio of SPs, the relative frequency distribution of unipolar voltages, the proportion of low-voltage areas, the proportion of the different types of EGMs and durations of LDP and FDP, serves as a marker of the severity and extensiveness of conduction inhomogeneity. Additional studies are required to further develop the signal fingerprint in order to identify patients at risk for AF onset or progression. The invasively determined signal fingerprint will serve as a gold standard in less- or even non-invasive fingerprints.

12

References

1. de Groot NM, Schalij MJ, Zeppenfeld K, Blom NA, Van der Velde ET, Van der Wall EE. Voltage and activation mapping: how the recording technique affects the outcome of catheter ablation procedures in patients with congenital heart disease. Circulation. 2003;108:2099-2106.
2. Rolf S, Kircher S, Arya A, Eitel C, Sommer P, Richter S, Gaspar T, Bollmann A, Altmann D, Piedra C, et al. Tailored atrial substrate modification based on low-voltage areas in catheter ablation of atrial fibrillation. Circ Arrhythm Electrophysiol. 2014;7:825-833.
3. Kottkamp H, Bender R, Berg J. Catheter ablation of atrial fibrillation: how to modify the substrate? J Am Coll Cardiol. 2015;65:196-206.
4. Yagishita A, Gimbel JR, S DEO, Manyam H, Sparano D, Cakulev I, Mackall J, Arruda M. Long-Term Outcome of Left Atrial Voltage-Guided Substrate Ablation During Atrial Fibrillation: A Novel Adjunctive Ablation Strategy. J Cardiovasc Electrophysiol. 2017;28:147-155.
5. Yamaguchi T, Tsuchiya T, Nakahara S, Fukui A, Nagamoto Y, Murotani K, Eshima K, Takahashi N. Efficacy of Left Atrial Voltage-Based Catheter Ablation of Persistent Atrial Fibrillation. J Cardiovasc Electrophysiol. 2016;27:1055-1063.
6. van Schie MS, Starreveld R, Roos-Serote MC, Taverne Y, van Schaagen FRN, Bogers A, de Groot NMS. Classification of sinus rhythm single potential morphology in patients with mitral valve disease. Europace. 2020;22:1509-1519.
7. Lanters EA, van Marion DM, Kik C, Steen H, Bogers AJ, Allessie MA, Brundel BJ, de Groot NM. HALT & REVERSE: Hsf1 activators lower cardiomyocyt damage; towards a novel approach to REVERSE atrial fibrillation. J Transl Med. 2015;13:347.
8. van der Does LJ, Yaksh A, Kik C, Knops P, Lanters EA, Teuwen CP, Oei FB, van de Woestijne PC, Bekkers JA, Bogers AJ, et al. QUest for the Arrhythmogenic Substrate of Atrial fibRillation in Patients Undergoing Cardiac Surgery (QUASAR Study): Rationale and Design. J Cardiovasc Transl Res. 2016;9:194-201.
9. van Schie MS, Starreveld R, Bogers A, de Groot NMS. Sinus rhythm voltage fingerprinting in patients with mitral valve disease using a high-density epicardial mapping approach. Europace. 2021;23:469-478.
10. Allessie MA, de Groot NM, Houben RP, Schotten U, Boersma E, Smeets JL, Crijns HJ. Electropathological substrate of long-standing persistent atrial fibrillation in patients with structural heart disease: longitudinal dissociation. Circ Arrhythm Electrophysiol. 2010;3:606-615.
11. Stevenson WG, Soejima K. Recording techniques for clinical electrophysiology. J Cardiovasc Electrophysiol. 2005;16:1017-1022.
12. Spach MS, Miller WT, 3rd, Miller-Jones E, Warren RB, Barr RC. Extracellular potentials related to intracellular action potentials during impulse conduction in anisotropic canine cardiac muscle. Circ Res. 1979;45:188-204.
13. van der Does L, Knops P, Teuwen CP, Serban C, Starreveld R, Lanters EAH, Mouws E, Kik C, Bogers A, de Groot NMS. Unipolar atrial electrogram morphology from an epicardial and endocardial perspective. Heart Rhythm. 2018;15:879-887.
14. van der Does LJ, de Groot NM. Inhomogeneity and complexity in defining fractionated electrograms. Heart Rhythm. 2017;14:616-624.
15. de Bakker JM, Wittkampf FH. The pathophysiologic basis of fractionated and complex electrograms and the impact of recording techniques on their detection and interpretation. Circ Arrhythm Electrophysiol. 2010;3:204-213.
16. Konings KT, Smeets JL, Penn OC, Wellens HJ, Allessie MA. Configuration of unipolar atrial electrograms during electrically induced atrial fibrillation in humans. Circulation. 1997;95:1231-1241.
17. Kharbanda RK, Knops P, van der Does L, Kik C, Taverne Y, Roos-Serote MC, Heida A, Oei FBS, Bogers A, de Groot NMS. Simultaneous Endo-Epicardial Mapping of the Human Right Atrium: Unraveling Atrial Excitation. J Am Heart Assoc. 2020;9:e017069.
18. Teuwen CP, Yaksh A, Lanters EA, Kik C, van der Does LJ, Knops P, Taverne YJ, van de Woestijne PC, Oei FB, Bekkers JA, et al. Relevance of Conduction Disorders in Bachmann's Bundle During Sinus Rhythm in Humans. Circ Arrhythm Electrophysiol. 2016;9:e003972.
19. Hocini M, Nault I, Wright M, Veenhuyzen G, Narayan SM, Jaïs P, Lim K-T, Knecht S, Matsuo S, Forclaz A. Disparate evolution of right and left atrial rate during ablation of long-lasting persistent atrial fibrillation. Journal of the American College of Cardiology. 2010;55:1007-1016.

12
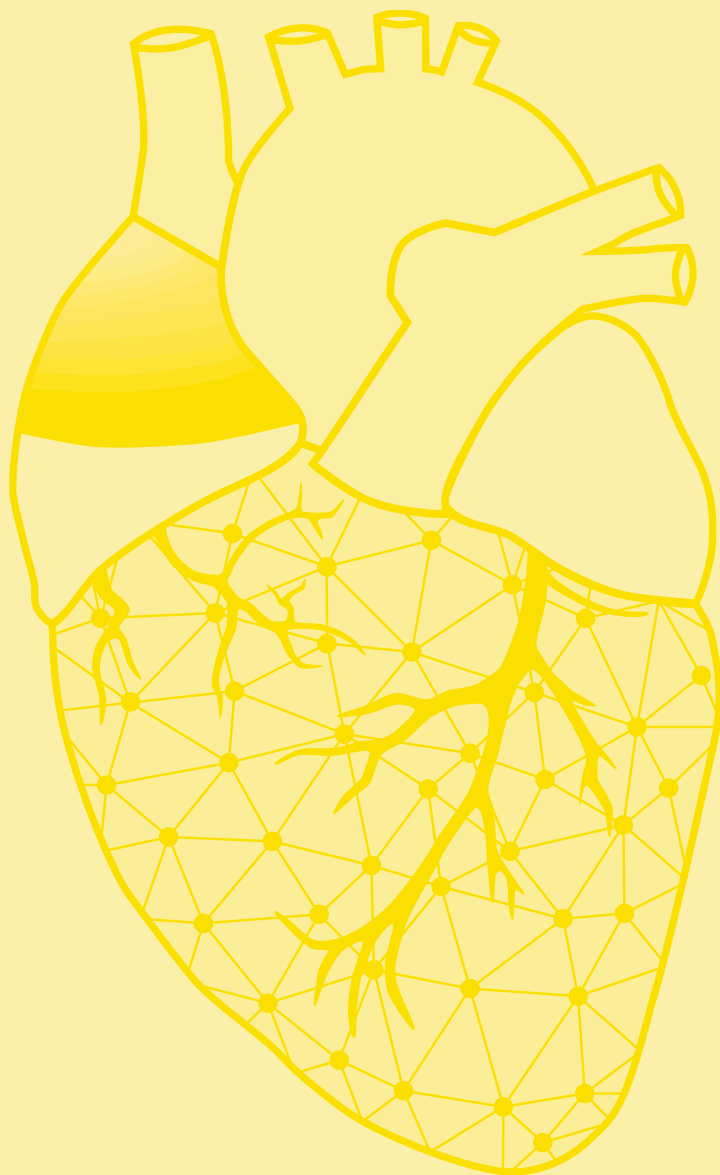
Chapter 13

Characterization of unipolar electrogram morphology: a novel tool for quantifying conduction inhomogeneity

Ziliang Ye

Mathijs S. van Schie

Lisa Pool

Annejet Heida

Paul Knops

Yannick J.H.J. Taverne

Bianca J.J.M. Brundel

Natasja M.S. de Groot

Abstract

Aims: Areas of conduction inhomogeneity (CI) during sinus rhythm (SR) may facilitate initiation and perpetuation of atrial fibrillation (AF). Currently, no tool is available to quantify the severity of conduction inhomogeneity. Our purpose is to develop and validate a novel tool using unipolar electrograms (EGMs) only to quantify the severity of conduction inhomogeneity in the atria.

Methods and results: Epicardial mapping of the right (RA) and left atrium, including Bachmann's bundle was performed in 235 patients undergoing coronary artery bypass grafting surgery. CI was defined as the amount of conduction block. EGMs were classified as single, short and long double (LDP) and fractionated potentials (FP), and the fractionation duration (FD) of non-single potentials was measured. The proportion of low-voltage areas (LVA, <1 mV) was calculated. Increased CI was associated with decreased potential voltages and increased LVAs, LDPs and FPs. The Electrical Fingerprint Score consisting of RA EGMs features, including LVAs and LDPs, was most accurate in predicting CI severity. The RA Electrical Fingerprint Score demonstrated the highest correlation with the amount of CI in both atria (r=0.70, p<0.001).

Conclusion: The Electrical Fingerprint Score is a novel tool to quantify severity of CI using only unipolar EGM characteristics. This tool can be used to stage the degree of conduction abnormalities without construction of spatial activation patterns, potentially enabling early identification of patients at high risk of post-operative AF or selection of the appropriate ablation approach in addition to pulmonary vein isolation at the EP lab.

Journal site &
supplementary material

Introduction

Conduction disorders, such as slowing of conduction and conduction block, play a role in both initiation and perpetuation of cardiac arrhythmias.[1] Conduction inhomogeneity during sinus rhythm (SR) is more pronounced in patients with atrial fibrillation (AF) episodes compared to patients without atrial tachyarrhythmias.[2,3] Prior experimental and clinical studies demonstrated that conduction inhomogeneity affects electrogram (EGM) morphology and causes low-amplitude, fractionated potentials (FPs).[4-7] Recently, it has been suggested that the so-called *Electrical Signal Fingerprint* may serve as a potential diagnostic tool to determine the severity and extensiveness of conduction inhomogeneity.[8] This signal fingerprint contained a large number of quantified unipolar EGM features recorded during SR such as peak-to-peak amplitudes, fractionation and EGM duration. However, it is still unknown which EGM features are predictive of conduction inhomogeneity or whether EGM features of one atrial region are predictive of other atrial regions. The purpose of this study was therefore to further develop the *Electrical Signal Fingerprint* as a novel, patient-tailored tool to quantify the severity of conduction inhomogeneity without construction of spatial patterns of activation, involving various unipolar EGM characteristics.

Methods

Study population

The study population included 235 consecutive adult patients who underwent elective coronary artery bypass grafting (CABG) at the Erasmus Medical Center in Rotterdam, The Netherlands. This study was approved by the Institutional Medical Ethics Committee (MEC2010-054/MEC2014-393).[9,10] Written informed consent was acquired for all patients before enrollment, and patient characteristics (such as age, gender, body mass index, echocardiogram features, medical histories and comorbidities) were extracted from the patient's medical record system.

Mapping procedure

As previously described, epicardial high-resolution mapping was conducted before the beginning of extracorporeal circulation.[9,10] A temporal bipolar epicardial pacemaker wire connected to the right atrial free wall was used as a reference electrode, and the indifferent electrode made of a steel wire was fixated to the subcutaneous tissue of the thorax.

Epicardial mapping was performed using a 128 or 192-electrode array (electrode diameter 0.65 or 0.45 mm, respectively; interelectrode distances 2 mm). During the mapping procedure, the electrode array was shifted across predefined areas at the right atrium (RA), Bachmann's bundle (BB), posterior wall of the left atrium (LA) between the pulmonary veins area (PVA) and LA appendage, as shown in the middle panel of *Figure 1*. The RA was mapped from the cavo-tricuspid isthmus, shifting perpendicular to the caval veins towards the RA appendage. The PVA was mapped from the transverse sinus fold along the margins of the left and right pulmonary veins towards the atrioventricular groove, and the left atrioventricular groove region from the lower margin of the left inferior pulmonary vein towards the LA appendage. BB was mapped from the roof of the LA appendage across the roof of the LA, behind the aorta towards the superior cavo-atrial junction.

If AF was present at the start of the mapping procedure, electrical cardioversion was conducted to restore SR. A 5-second SR episode was recorded from each mapping site, including a surface electrocardiogram lead, bipolar reference EGM and all unipolar epicardial
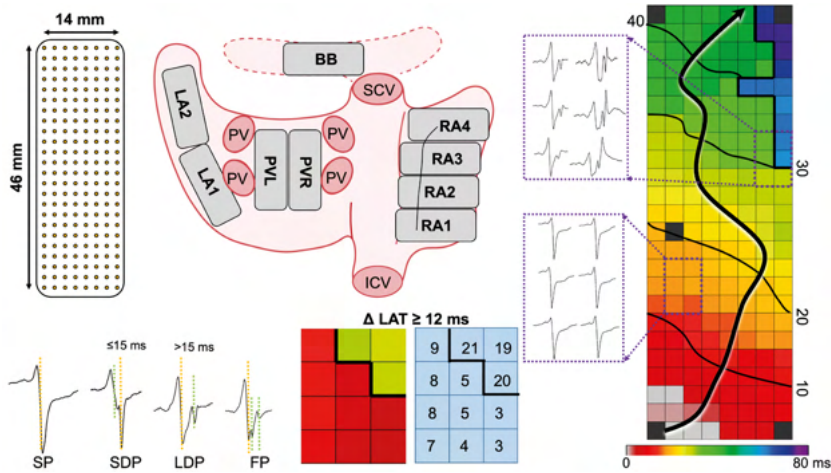
Figure 1 – Epicardial mapping procedure. *Upper left panel*: a 192-unipolar electrode array (left panel) is used for atrial mapping. *Upper center panel*: projection of the electrode array on a schematic posterior view of the entire atria. *Right panel*: a color-coded activation time map demonstrating both areas of uniform fast conduction and conduction block. From both areas, unipolar potentials are shown outside the activation time map. *Lower left panel:* examples of different potentials. *Lower center panel*: example of a line of conduction block. Differences in local activation time (LAT) between two adjacent electrodes ≥12 ms was defined as conduction block. Isochronal lines (thin black lines) are drawn at 10 ms intervals, black arrow indicate direction of wavefront propagation. **BB** = Bachmann's bundle; **IVC** = inferior vena cava; **LA** = left atrium; **PV(A)** = pulmonary vein (area); **RA** = right atrium; **SVC** = superior vena cava.

EGMs. Recordings were amplified (gain 1000), filtered (bandwidth 0.5–400 Hz), sampled (1 kHz) and analog-to-digital converted (16 bits) and then stored on a hard disk.

Data analysis

Customized software was used for semi-automatic analysis of unipolar EGMs. The steepest part of a negative deflection was automatically annotated to construct color-coded local activation time maps.[11] Recordings were excluded when less than 30% of the mapping area was annotated. All annotations were manually verified by two investigators. Potential voltage was measured as the peak-to-peak amplitude of the steepest negative deflection. Low-voltage potentials were defined as potentials with an amplitude <1.0 mV.[12] Conduction block (CB) was defined as a difference in LAT between two adjacent electrodes ≥12 ms.[1] The total proportion of CB measured from the entire atrium was used as an indication for the degree of conduction inhomogeneity.

Consistent with prior mapping studies[8], EGMs were categorized into single- (SP), short double- (SDP), long double- (LDP) and fractionated potentials (FP). Fractionation duration (FD) was defined as the time difference between the first and last deflection of non-SP. As described previously[13], for SPs, the ratio between the R- and S-wave amplitude (R/S ratio) was calculated, with a scale ranging from -1 (R-wave) to 1 (S-wave), estimated by the following formula:

$$RS = \begin{cases} 1 - RS(n) & for\ RS(n) \leq 1 \\ \dfrac{1}{RS(n)} - 1 & for\ RS(n) > 1 \end{cases}$$

Detection of post-operative atrial fibrillation

Cardiac rhythms of all patients were continuously recorded from the moment of arrival on the surgical ward to the end of the 5th post-operative day using bedside monitors (Draeger

Infinity™). Automatic algorithms were used to detect early post-operative AF (E-PoAF) episodes lasting >30 seconds. All episodes detected by the software were cross-checked by two blinded operators in order to eliminate potential false positive registrations induced by artefacts.

After the hospitalization period, patients were periodically seen at the outpatient clinic at 3 and 6 months, 1 year and yearly afterwards for a period of five years. Presence of late post-operative AF (L-PoAF) was confirmed by a surface ECG or Holter.

Statistical Analysis

A Shapiro–Wilk test was used to verify normal distribution of continuous variables. Continuous variables that were normally distributed are expressed as mean ± standard deviation, while non-normal distributed continuous variables are expressed as median [25th–75th percentile]. Continuous variables between groups were compared using either independent sample *t*-test or one-way ANOVA in case of normal distributed variables and Mann–Whitney U-test or Kruskal-Wallis test in case of not normally distributed variables.

13

Categorical variables were described as number and percentage, and a χ^2 test was used for comparison. Pearson or Spearman correlation analysis was used to explore the correlation between variables where appropriate. In addition, univariable and multivariable logistic regression analysis was performed to investigate variables associated with a higher degree of conduction inhomogeneity, and results were presented as odds ratio (OR) with 95% confidence interval (CI). Least absolute shrinkage and selection operator (LASSO) regression analysis was also conducted to further select EGM features associated with a higher degree of conduction inhomogeneity. Receiver operating characteristic (ROC) curves were constructed to investigate the diagnostic value of EGM features for a high degree of conduction inhomogeneity. The *Electrical Fingerprint Score* was constructed using a nomogram approach, using the 'rms' and 'nomogramFormula' packages in R software. This score was calculated based on variables identified as significant in multivariable logistic regression analysis. A concordance index (C-index) was calculated to examine the predictive value of the *Electrical Fingerprint Score*.
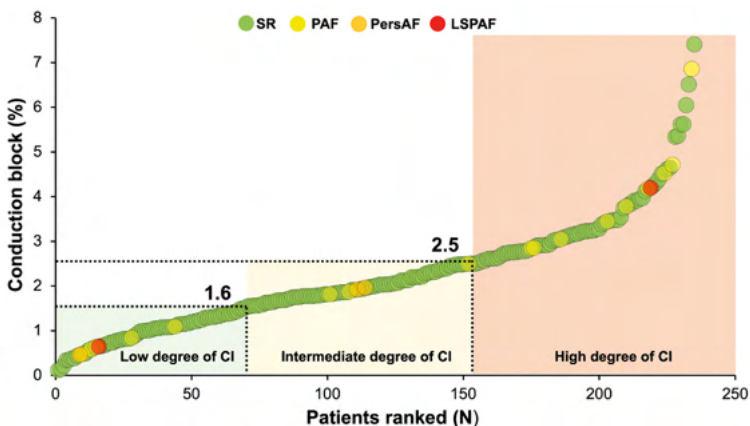
Figure 2 – Graph depicting the percentage of conduction block (CB) for each patient individually. Green dots represent patients with sinus rhythm (SR), whereas the yellow, orange and red dots represent patients with respectively paroxysmal, persistent and long-standing persistent atrial fibrillation (AF). The number of 1.6 and 2.5 on the ranking plot correspond to 33% and 66% of CB, respectively. **CI** = conduction inhomogeneity; **LSPAF** = long-standing persistent atrial fibrillation; **PAF** = paroxysmal atrial fibrillation; **PersAF** = persistent atrial fibrillation; **SR** = sinus rhythm.

Table 1 – Baseline characteristics.

Variables	Overall	Low CI group	Intermediate CI group	High CI group	p-value
N	235	78	77	80	
Range of CB		CB<1.6	1.6≤CB<2.5	CB≥2.5	
Age (y)	67 [60–73]	64 [57–69]	69 [64–75]	68 [60–74]	0.002
Male	198 (84.3)	70 (89.7)	65 (84.4)	63 (78.8)	0.165
BMI (kg/m²)	27.6 [25.5–31.1]	27.4 [25.1–31.2]	27.7 [25.7–30.8]	27.9 [25.8–31.3]	0.719
Type of AF					0.396
• No AF	213 (90.6)	71 (91.0)	72 (93.5)	70 (87.5)	
• Paroxysmal AF	17 (7.2)	5 (6.4)	3 (3.9)	9 (11.2)	
• Persistent AF	3 (1.3)	1 (1.3)	2 (2.6)	0 (0.0)	
• Long-standing persistent AF	2 (0.9)	1 (1.3)	0 (0.0)	1 (1.2)	
Cardiovascular risk factors					
• Hypertension	148 (63.0)	43 (55.1)	54 (70.1)	51 (63.7)	0.152
• Dyslipidemia	103 (43.8)	28 (35.9)	32 (41.6)	43 (53.8)	0.069
• Diabetes mellitus	81 (34.5)	17 (21.8)	29 (37.7)	35 (43.8)	0.011
• Myocardial infarction	116 (49.4)	44 (56.4)	38 (49.4)	34 (42.5)	0.217
Left ventricular function					0.739
• Normal (EF >55%)	174 (74.0)	56 (71.8)	59 (76.6)	59 (73.8)	
• Mild impairment (EF 46–55%)	50 (21.3)	18 (23.1)	13 (16.9)	19 (23.8)	
• Moderate impairment (EF 36–45%)	8 (3.4)	3 (3.8)	3 (3.9)	2 (2.5)	
• Severe impairment (EF <35%)	3 (1.3)	1 (1.3)	2 (2.6)	0 (0.0)	
Left atrial dilation >45 mm	32 (13.6)	8 (10.3)	8 (10.4)	16 (20.0)	0.304
ACEI / ARB / AT2 antagonist	159 (67.9)	61 (78.2)	47 (61.8)	51 (63.7)	0.057
Statin	207 (88.1)	69 (88.5)	69 (89.6)	69 (86.2)	0.803
Antiarrhythmic agents					
• Class I	0 (0.0)	0 (0.0)	0 (0.0)	0 (0.0)	NA
• Class II	183 (77.9)	60 (76.9)	60 (77.9)	63 (78.8)	0.962
• Class III	9 (3.8)	4 (5.1)	2 (2.6)	3 (3.8)	0.713
• Class IV	11 (4.7)	3 (3.8)	4 (5.2)	4 (5.0)	0.911
• Digoxin	3 (1.3)	0 (0.0)	1 (1.3)	2 (2.5)	0.803
Cycle length (ms)	885±166	870±165	864±161	918±166	0.122

Values are presented as N (%), mean ± standard deviation or median [interquartile ranges]. **ACEI** = angiotensin-converting enzyme inhibitors; **AF** = atrial fibrillation; **ARB** = angiotensin receptor blockers; **AT2** = angiotensin type 2 receptor; **BMI** = body mass index; **CI** = conduction inhomogeneity; **CB** = conduction block; **EF** = ejection fraction.

All statistical analysis was completed using IBM SPSS Statistics 28, RStudio (version 4.2.1) and Python (version 3.7). A two-sided p-value was considered statistically significant if its value <0.05.

Results

Study population

As demonstrated in *Figure 2*, the proportion of CB in the entire study population ranged from 0.11 to 7.41% (median: 2.00%). The largest proportion of CB was found at the RA (2.38 [1.18–3.86] %), followed by BB (2.28 [0.86–4.76] %), PVA (1.12 [0.31–2.41] %) and LA (0.76 [0.13–4.76] %). Based on the 33rd and 66th percentiles of the total proportion of CB, the study population was categorized into 3 different groups with a low (CB: <1.6%), intermediate (CB: 1.6–2.5%) and high degree of conduction inhomogeneity (CB ≥2.5%). Baseline characteristics of the three different patient groups are demonstrated in *Table 1*. There were no significant differences in baseline characteristics between the three groups except for age (p=0.002)
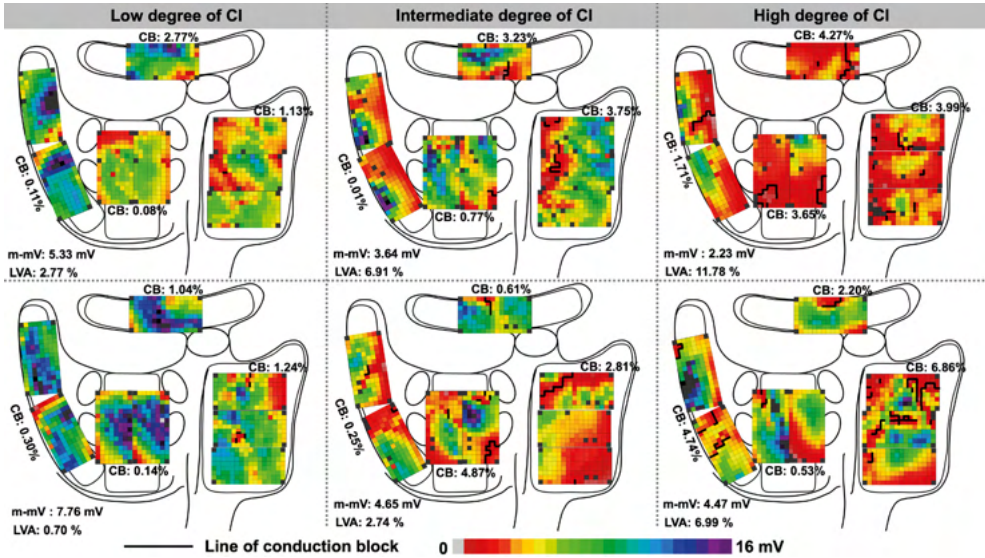
Figure 3 – Graph illustrating representative examples of unipolar voltage maps obtained from two patients from each of the three groups. *Left panel*: maps obtained from two patients of the low conduction inhomogeneity group; the total amount of conduction block (CB) was 0.79% and 0.73%, respectively. *Center panel*: maps obtained from two patients of intermediate conduction inhomogeneity group; the amount of CB was 2.35% and 2.29%, respectively. *Right panel*: maps obtained from two patients of the high conduction inhomogeneity group; the amount of CB was 3.44% and 4.39%, respectively. In general, unipolar voltages decrease when CB increases. **CI** = conduction inhomogeneity; **LVA** = low-voltage area; **m-mV** = median unipolar potential voltage.

13
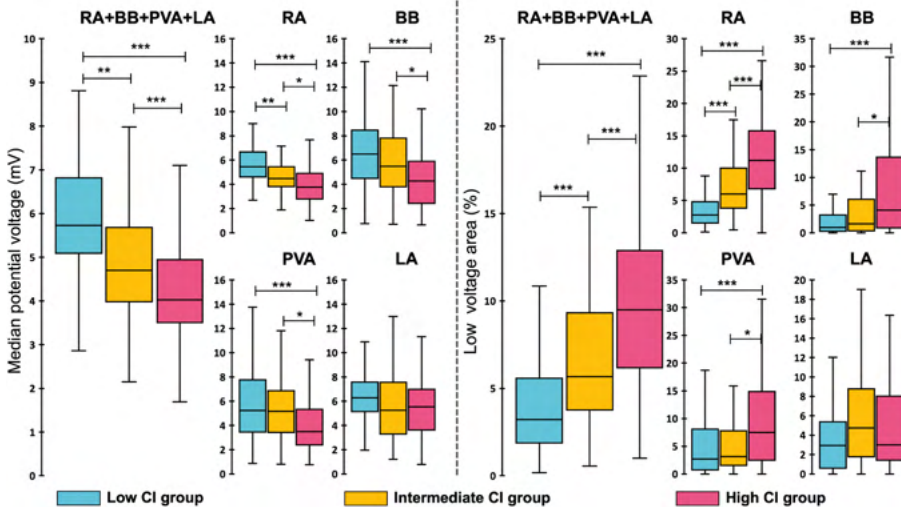
Figure 4 – Boxplots comparing the differences in median potential voltage and low-voltage areas between the three groups in each atrial region. * p<0.05; ** p<0.01; *** p<0.001. **BB** = Bachmann's bundle; **CI** = conduction inhomogeneity; **LA** = left atrium; **PVA** = pulmonary vein area; **RA** = right atrium.
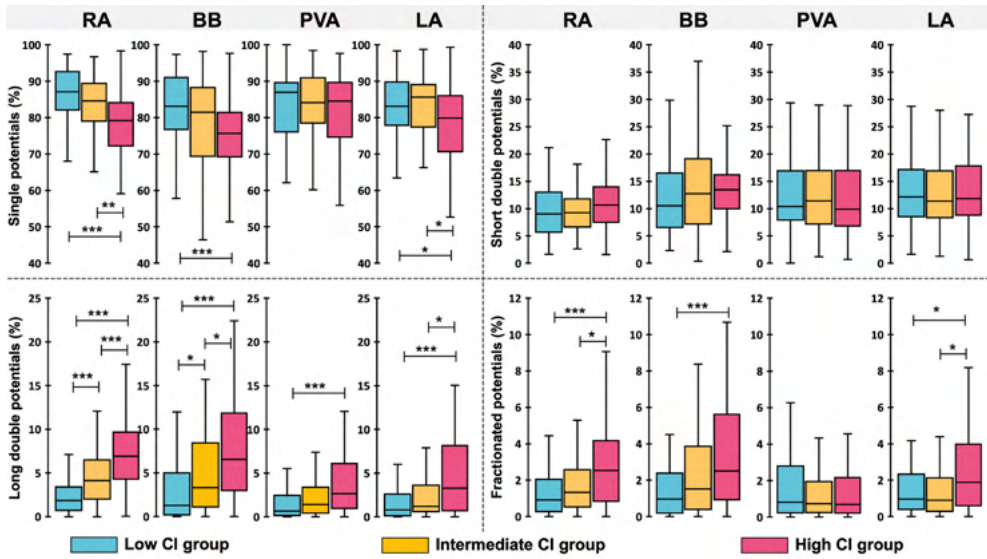
Figure 5 – Boxplots evaluating the differences in different atrial morphologies between the three groups in each atrial region. * p<0.05; ** p<0.01; *** p<0.001. **BB** = Bachmann's bundle; **CI** = conduction inhomogeneity; **LA** = left atrium; **PVA** = pulmonary vein area; **RA** = right atrium.

and diabetes mellitus (p=0.011).

Mapping database

A total of 17,189 heartbeats were recorded, including 2,188,835 potentials (9,314±2,893 per patient). The average SR cycle length was 885±166 ms. The total number of potentials in the low, intermediate and high conduction inhomogeneity group was respectively 696,351, 759,570 and 732,914. Average cycle length did not differ between the three groups (*Table 1*, p=0.122).

Conduction inhomogeneity and median potential voltages

Figure 3 illustrates representative examples of unipolar potential voltage maps obtained from two patients from each of the three groups. These voltage maps show lower unipolar potential voltages and more LVAs in patients with a higher degree of conduction inhomogeneity, although there was no predilection site for LVAs to occur.

The left panel of *Figure 4* shows differences in median potential voltages between the three groups for the entire atria and each atrial region separately. For the entire atria, median potential voltages were lower in the high conduction inhomogeneity group (low: 5.73 [5.05–6.87] mV; intermediate: 4.70 [3.98–5.69] mV; high: 4.03 [3.49–4.96] mV, p<0.05 for each comparison),while the amount of LVAs was highest in the high conduction inhomogeneity group [high: 9.49 [6.12–12.99] %, intermediate: 5.67 [3.76–9.32] % and low: 3.21 [1.81–5.64], p<0.05 for each comparison, right panel of *Figure 4*).

Supplementary Table 1 summarizes the magnitudes of median potential voltages and proportions of LVAs for each region separately, demonstrating that the highest median potential voltages were observed in the patients of the low conduction inhomogeneity group and the largest proportion of LVAs in the high conduction inhomogeneity group; this trend was, however, not found at the LA.

Conduction inhomogeneity and potential morphology

For the entire atria, patients with a high degree of conduction inhomogeneity had the lowest proportion of SPs (high: 78.88 [74.11, 82.57] %; low: 85.77 [81.98, 89.84] %, p<0.001). A higher degree of conduction inhomogeneity was also associated with a significantly increase in the proportion of LDPs (high: 6.24 [4.59, 8.07] %; low: 1.82 [1.13, 3.20] %, p<0.001) and FPs (high: 2.47 [1.47, 3.92] %; low: 1.25 [0.59, 2.02] %, p<0.001). However, there was no relation between the degree of conduction inhomogeneity and the proportion of SDPs (p>0.05).

Figure 5 illustrates the proportion of the different types of potentials in the three groups for each atrial region separately. As expected, the lowest proportions of SPs were found in the high conduction inhomogeneity group, although there was no difference in the

Table 2 – Regional interdependency of electrogram features.

Variables	RA	BB	PVA	LA
Median potential voltage				
RA	1	0.344**	0.194**	0.251**
BB	0.344**	1	0.121	0.137
PVA	0.194**	0.121	1	0.235**
LA	0.251**	0.137	0.235**	1
Low-voltage area				
RA	1	0.327**	0.216**	0.209**
BB	0.327**	1	0.01	0.156*
PVA	0.216**	0.01	1	0.145*
LA	0.209**	0.156*	0.145*	1
R/S ratio				
RA	1	0.058	-0.088	-0.143*
BB	0.058	1	-0.128	-0.041
PVA	-0.088	-0.128	1	0.112
LA	-0.143*	-0.041	0.112	1
Single potentials				
RA	1	0.208**	0.081	0.172*
BB	0.208**	1	0.02	0.114
PVA	0.081	0.02	1	0.192**
LA	0.172*	0.114	0.192**	1
Short double potentials				
RA	1	0.180*	0.102	0.228**
BB	0.180*	1	0.116	0.038
PVA	0.102	0.116	1	0.218**
LA	0.228**	0.038	0.218**	1
Long double potentials				
RA	1	0.177*	0.016	-0.034
BB	0.177*	1	-0.008	0.153*
PVA	0.016	-0.008	1	0.059
LA	-0.034	0.153*	0.059	1
Fractionated potentials				
RA	1	0.234**	0.131	0.179*
BB	0.234**	1	0.118	0.177*
PVA	0.131	0.118	1	0.261**
LA	0.179*	0.177*	0.261**	1
Fractionation delay				
RA	1	0.068	0.088	-0.095
BB	0.068	1	0.01	0.169*
PVA	0.088	0.01	1	0.079
LA	-0.095	0.169*	0.079	1

*Correlation is significant at the 0.05 level (2-tailed); **Correlation is significant at the 0.01 level (2-tailed). **BB** = Bachmann's bundle; **FD** = fractionation duration; **FP** = fractionated potential; **LA** = left atrium; **LDP** = long double potential; **PVA** = pulmonary vein area; **RA** = right atrium; **SDP** = short double potential; **SP** = single potential.

13

Table 3 – Electrogram features independently associated with a high degree of conduction inhomogeneity.

Variables	OR	95% CI	*p*-value
Entire atria			
• Low-voltage area	1.26	1.13–1.41	<0.001
• Long double potentials	1.79	1.23–2.66	0.003
• Fractionation delay	1.45	1.08–2.00	0.017
RA			
• Low-voltage area	1.13	1.07–1.20	<0.001
• Long double potentials	1.32	1.20–1.48	<0.001
BB			
• Long double potentials	1.09	1.03–1.16	0.005
PVA			
• Median potential voltage	0.89	0.79–0.99	0.041
• Long double potentials	1.07	1.01–1.15	0.023
LA			
• Long double potentials	1.10	1.03–1.20	0.012
• Fractionated potentials	1.18	1.02–1.37	0.025

BB = Bachmann's bundle; **CI** = confidence interval; **PVA** = pulmonary vein area; **LA** = left atrium; **OR** = odds ratio.

proportion of SPs recorded from the PVA between the three groups (*Supplementary Table 2*). A high proportion of LDPs in each region was related with a high degree of conduction inhomogeneity. An increase in conduction inhomogeneity was associated with a higher proportion of FPs at the RA, BB and LA. However, there was no relation between the degree of conduction inhomogeneity and the proportion of FPs at the PVA (p=0.887). The amount of SDPs did not differ at any region between the three groups (p>0.05 for each comparison).

Conduction inhomogeneity and R/S ratio

Comparisons of R/S ratios between the three groups for the entire atria and each region separately are summarized in *Supplementary Table 3*. The R/S ratio only differed between the three groups at the RA region (p=0.017).
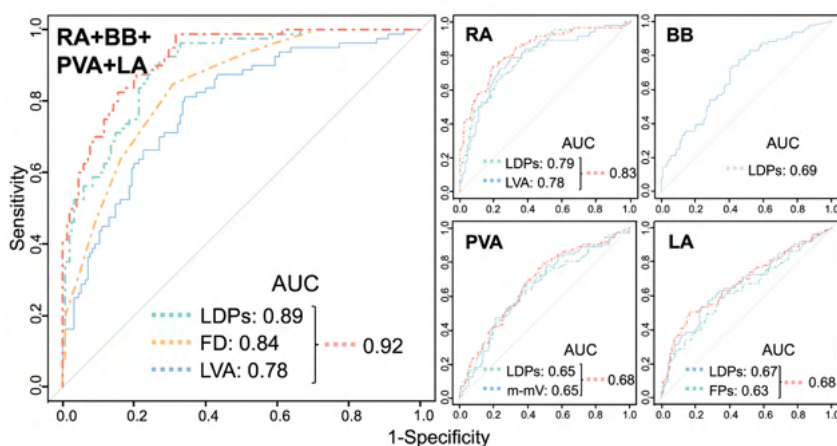
Figure 6 – Receiver operating characteristic (ROC) curves of the prediction of conduction inhomogeneity. ROC curves were calculated for the EGM features recorded from the entire atria and each atrial region separately. **AUC** = area under the curve; **BB** = Bachmann's bundle; **FD** = fractionation duration; **FP** = fractionated potential; **LA** = left atrium; **LDP** = long double potential; **LVA** = low-voltage area; **m-mV** = median unipolar potential voltage; **PVA** = pulmonary vein area; **RA** = right atrium.
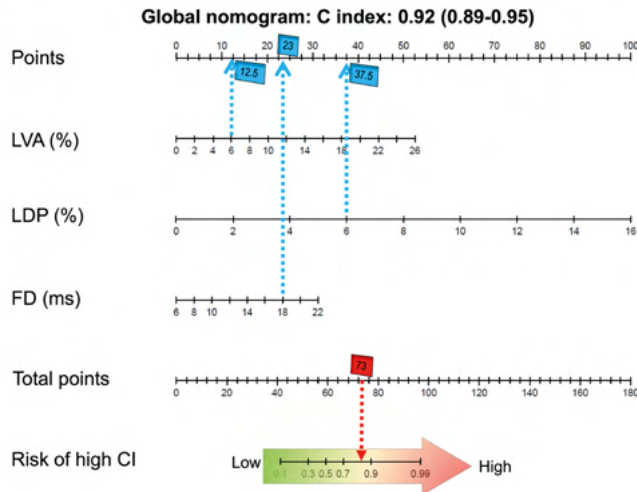
Figure 7 – Nomogram for quantifying the severity of CI in the entire atria. The influence of each parameter on nomogram predicting the risk of high CI is exhibited on the horizontal axes of variable lengths. The usage of this nomogram is described below: chose a specific value of one parameter, draw a vertical line up to "Points" to determine the score of this parameter earned. The sum of those scores corresponding to the "Total Points" axis on the bottom, and another vertical line is drawn up to the axis of "Risk of high conduction inhomogeneity" to determine the risk of high conduction inhomogeneity. **CI** = conduction inhomogeneity; **FD** = fractionation duration; **LDP** = long double potential; **LVA** = low-voltage area.

Conduction inhomogeneity and FD

FD were longer in the high conduction inhomogeneity group compared to the low conduction inhomogeneity group. This was observed for the entire atria (p<0.001) and also for each region separately (RA: p<0.001; BB: p<0.001; PVA: p=0.004, and LA: p=0.004), as summarized in *Supplementary Table 3*.

Regional interdependency of EGM features

Table 2 demonstrates correlations of all EGM features between the various atrial regions; all correlation coefficients are either too weak and/or not significant, indicating that, unfortunately, EGM features assessed at one specific region are not predictive for features of EGMs recorded at other regions.

Selection of EGM features for Electrical Signal Fingerprint

In order to construct an *Electrical Signal Fingerprint Score* for prediction of the degree of conduction inhomogeneity in each individual patient, patients in the low and intermediate conduction inhomogeneity group were combined and compared with the high conduction inhomogeneity group. Results of the univariable logistic regression for potential determinants of a high degree of conduction inhomogeneity are displayed in *Supplementary Table 4*. To identify parameters related to a high degree of conduction inhomogeneity, EGM features associated with a high degree of conduction inhomogeneity in univariable regression were further included in a LASSO regression analysis. Based on the LASSO analysis, the following EGM features were identified LVA, SP, LDP and FD (entire atria, *Supplementary Figure 1*), LVA and LDP (RA, *Supplementary Figure 2*), median potential voltage, LDP and FP (BB, *Supplementary Figure 3*); median potential voltage and LDP (PVA, *Supplementary Figure 4*); LDP and FP (LA, *Supplementary Figure 5*). These EGM features were entered into
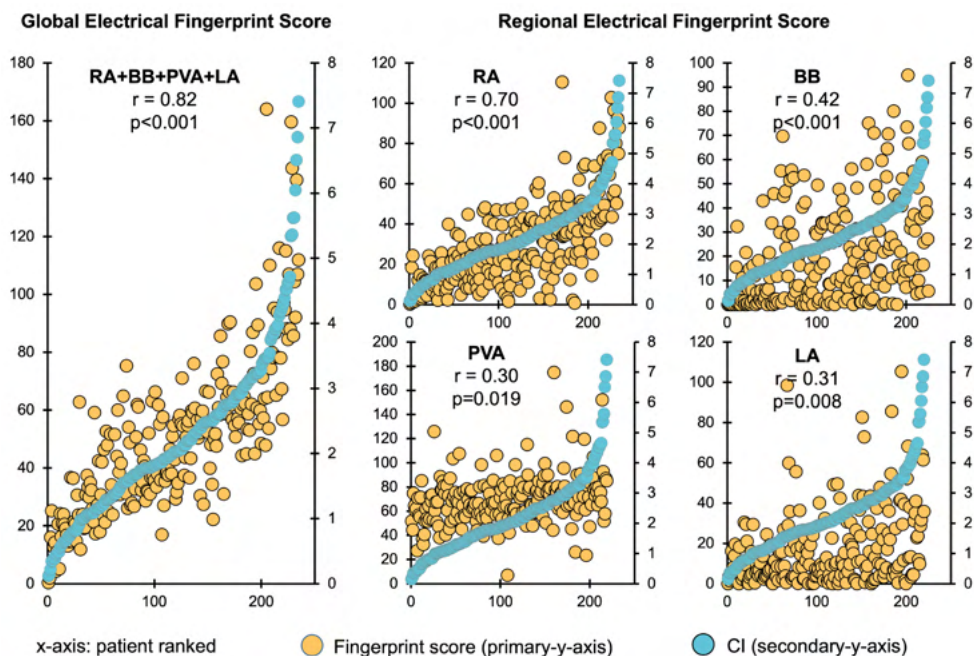
Figure 8 – Correlation of the *Global Electrical Fingerprint Score* and *Regional Electrical Fingerprint Scores* and CB in the individual patient. CB = conduction block; **CI** = conduction inhomogeneity; **BB** = Bachmann's bundle; **LA** = left atrium; **PVA** = pulmonary vein area; **RA** = right atrium.

multivariable regression models, and their results are listed in *Table 3*. For the entire atria, the amount of LVAs (OR=1.26, p<0.001), the proportion of LDPs (OR=1.79, p=0.003) and FD (OR=1.45, p=0.017) were associated with a higher degree of conduction inhomogeneity. For RA EGM features, the amount of LVAs (OR=1.13, p<0.001) and the proportion of LDPs (OR=1.32, p<0.001) were associated with a higher degree of conduction inhomogeneity. For BB, PVA and LA, an increased proportion of LDPs (BB: OR=1.09; PVA: OR=1.07, LA: OR=1.10) was associated with a higher degree of conduction inhomogeneity. In addition, median potential voltage (OR=0.89, p=0.041) at the PVA and the proportion of FPs (OR=1.18, p=0.025) at the LA were also associated with a higher degree of conduction inhomogeneity.

As demonstrated by the ROC-curves for the entire atria in *Figure 6*, the combination of LDPs, FD and LVAs have an excellent predictive value for a high degree of conduction inhomogeneity (AUC=0.92). In addition, EGM features recorded at the RA also have a high predictive value for a high degree of conduction inhomogeneity (AUC=0.83), while EGM features recorded at the other regions did not have adequate predictive values.

The Electrical Signal Fingerprint Score

Figure 7 demonstrates the *Global Electrical Signal Fingerprint Score* based on the EGM features obtained from the entire atria (C-index: 0.92 [0.89, 0.95]). The *Regional Electrical Signal Fingerprint Scores* for prediction of the total degree of conduction inhomogeneity in the entire atria are shown in *Supplementary Figure 6*. As demonstrated in this figure, EGM features obtained from the RA had the highest predictive value for the total amount of conduction inhomogeneity (C-index: 0.83 [0.78, 0.89]), followed by BB (C-index: 0.69 [0.61, 0.76]), PVA (C-index: 0.68 [0.60, 0.75]) and LA (C-index: 0.68 [0.60, 0.76]).

Individual Electrical Signal Fingerprint Score

The next step was to validate the *Electrical Signal Fingerprint Scores* by calculating the scores for each patient individually. As illustrated in *Figure 8*, the *Global Electrical Signal Fingerprint Score* was strongly related to the total degree of conduction inhomogeneity (r=0.82, p<0.001). Using the *Regional Electrical Signal Fingerprint Scores*, only EGM features recorded at the RA were strongly related to the total degree of conduction inhomogeneity (r=0.70, p<0.001). Moderate or weak correlations were found between the total degree of conduction inhomogeneity and *Electrical Signal Fingerprint Scores* computed from BB, PVA and LA (r=0.42, r=0.30 and r=0.31 respectively, p<0.001 for each).

Relation with post-operative AF

Data on post-operative AF (PoAF) was available in 203 patients of whom 89 developed early PoAF (43.8%) and 10 late PoAF (4.9%). The *Global Electrical Signal Fingerprint Score* was increased in patients who developed early PoAF (without PoAF: 42.9 [27.7–64.6] vs. early PoAF: 50.3 [31.0–63.7], p<0.001) and even more in patients who developed late PoAF (63.1 [39.3–70.3], p<0.001). The *Regional Electrical Signal Fingerprint Score* of the RA was only increased in patients who developed late PoAF (without PoAF: 22.8 [12.5–43.5] vs. early PoAF: 25.1 [14.0–43.1], p=0.500 and late PoAF: 39.8 [23.1–43.3], p<0.001).

Discussion

The severity of conduction inhomogeneity can be accurately predicted by a *Global Electrical Fingerprint Score*, containing quantified features of EGM morphology obtained from the entire atria, including the amount of LVAs, LDPs and FD. Conduction inhomogeneity in the entire atria can also be predicted with the *Regional Electrical Signal Fingerprint Score* of the RA, containing the amount of LVAs and LDPs.

Conduction inhomogeneity and potential voltages

Although unipolar potential voltages are affected by numerous factors, Spach et al.[7] demonstrated in a dog model that fast conduction is characterized by high-voltage biphasic deflections, while low-voltage, triphasic deflections were recorded during slow conduction.[14,15] In patients with mitral valve disease, it was demonstrated that smaller voltages were indeed recorded in areas of conduction slowing but also around lines of CB.[12,13] In our previous study, we demonstrated that the presence of LVAs was strongly related with the occurrence of CB at the RA and BB.[8] The presence of extensive areas of CB could therefore result in a decrease in median unipolar potential voltage and increase in LVAs. We now demonstrated that a higher total degree of conduction inhomogeneity was indeed related to lower unipolar potential voltages and a larger amount of LVAs, and were important parameters integrated in the *Electrical Signal Fingerprint Scores*.

Conduction inhomogeneity and potential morphology

As described by Konings et al.[16], unipolar potentials are classically categorized into SPs, SDPs, LDPs and FPs. The morphology of SPs can be further described by the ratio between a positive R-wave and negative S-wave respectively preceding and following the negative deflection (R/S ratio).[13] We did not find a correlation between R/S ratio and conduction inhomogeneity. Prior mapping studies demonstrated that during SR, R/S ratios of unipolar SPs were considerably variable and that high-voltage SPs were mainly recorded during fast, uniform wavefront propagation.[13,16] In patients with AF, there was a loss of S-wave amplitude

13

233

resulting in SPs with lower amplitudes and shifted R/S ratios, which was also associated with reduced conduction velocity. In case of extensive conduction inhomogeneity, more LDPs instead of SPs are recorded. R/S ratios of the remaining SPs could therefore only be changed minimally, as they are recorded further away from the lines of CB. Indeed, the amount of LDPs was predictive for the total degree of conduction inhomogeneity.

Although a substantial proportion of SDPs and even LDPs reflect the physiological heterogeneity of atrial tissue, LDPs and particularly FPs have been associated with conduction inhomogeneity. During AF at the RA, Konings et al.[16] demonstrated that LDPs and FPs were predominantly found near areas of CB. It is therefore not surprising that the proportions of LDPs and FPs were correlated to conduction inhomogeneity. The duration of FPs was also associated with conduction inhomogeneity. As demonstrated by previous studies, potentials with a prolonged FD are associated with local areas of impaired conduction.[17,18] A prolonged FD also indicates that a wavefront takes longer to propagate around a line of CB and activate the other side. With more and longer lines of CB, the delay of the wavefront is also more likely to increase. Our results indeed showed that prolongation of FPs was related with a higher degree of conduction inhomogeneity.

The role of the RA in signal fingerprinting

Remarkably, our study demonstrated that the severity and extensiveness of conduction inhomogeneity in the *entire* atria can be estimated using EGM features recorded only from the RA. In a previous mapping study of Lanters et al.[19], the superior inter-caval region was found to be a predilection site for CB in patients with coronary artery disease without AF. Heida et al.[20] showed that patients with history of AF have more severe conduction disorders at the RA and BB. In the current study, a certain degree of CB at the RA was present in each patient. When structural remodeling occurs in the (right) atria, the degree of conduction inhomogeneity increases thereby increasing the amount of LDPs and FPs and decreasing unipolar potential voltages. It is believed that atrial structural remodeling plays an important role in initiation and perpetuation of AF, although most studies mainly focus on the LA. In patients undergoing ablation therapy for persistent AF, Prabhu et al.[21] demonstrated that AF is associated with remodeling processes affecting both atria and that electrical and structural remodeling within the RA correlated with the LA. Recently, Heida et al.[22] were the first to investigate conduction disorders due to AF-related electrical remodeling immediately after electrical cardioversion and demonstrated that there was no significant impairment in intra-atrial conduction when compared to conduction patterns observed during long periods of SR. Also, Takagi et al.[23] recently demonstrated that only structural remodeling in the RA was a useful predictor of clinical outcome after pulmonary vein isolation. It could be that structural remodeling in the RA more easily results in changes in EGM morphology, as the RA is not uniform in thickness due to the trabeculated wall. This might explain why the RA is a good predictor for the general degree of conduction inhomogeneity across both atria using unipolar EGM morphology characteristics.

Future clinical implications

Areas of conduction inhomogeneity identified during SR may play a pivotal role in initiation and maintenance of atrial tachyarrhythmias such as AF.[24,25] Heida et al.[20] indeed showed that patients with AF have more severe conduction inhomogeneity than patients without prior AF episodes. The individualized *Electrical Signal Fingerprint Score* as proposed in this study can be used as a novel tool for determination of the severity of conduction inhomogeneity during SR using electrograms only, without construction of spatial patterns of activation. We also demonstrated that an increased *Electrical Signal Fingerprint Score* is

related to development of PoAF. The next step will be to test whether this SR *Electrical Signal Fingerprint Score* can actually predict AF development during short and long-term follow up or whether they can predict AF recurrences of arrhythmia surgery outcome.

The high-resolution, invasive gold standard *Electrical Signal Fingerprint* is also the foundation for development of less- or even non-invasive fingerprints. In patients undergoing cardiac surgery, application of this tool may help to early identify patients at high risk of post-operative AF. For instance, if the *Electrical Signal Fingerprint Score* indicates high conduction inhomogeneity in SR patients, patients should be long-term monitored during the post-operative period. Also, preventive strategies may be taken to prevent development of post-operative AF. With the ongoing development of high-density electrode arrays for endovascular mapping, less invasive fingerprints could be constructed in the near future at the EP lab. They can aid in selecting the appropriate ablation approach. For example, when the fingerprint score is too high, the degree of conduction inhomogeneity is severe and pulmonary vein isolation alone may not be successful in eliminating AF.

Study limitations

Whether *Electrical Signal Fingerprints* are truly indicative of the AF-related substrate needs to be further investigated. Follow-up of many patients is still ongoing and therefore the number of patients is limited for prediction of especially late PoAF. However, the preliminary results on PoAF prediction presented in this study show a potential clinical application of the *Electrical Signal Fingerprint Score*. The numbers of patients with AF in our study population was too small to compare *Electrical Signal Fingerprint Scores* between different subtypes of AF. Also, although the study population is not a reflection of the general AF population, 27–33% of the patients who undergo CABG experience AF, indicating that the participants of this study at least represent a group in which AF occurs frequently.[26,27] In addition, this is a single-center study, and further validation is still needed through subsequent multicenter studies.

Conclusion

The severity of conduction inhomogeneity can be accurately quantified by the *Electrical Signal Fingerprint Score*, using solely electrophysiological characteristics of unipolar EGMs. EGM characteristics recorded from the easily accessible RA alone have the best predictive value for the severity of conduction inhomogeneity of both atria including BB. The next step in developing the *Electrical Signal Fingerprint Score* as a novel tool is to determine whether the *Electrical Signal Fingerprint Scores* can be used to identify patients at high risk of onset and/or progression of AF.

13

References

1. Allessie MA, de Groot NM, Houben RP, Schotten U, Boersma E, Smeets JL, Crijns HJ. Electropathological substrate of long-standing persistent atrial fibrillation in patients with structural heart disease: longitudinal dissociation. Circ Arrhythm Electrophysiol. 2010;3:606-615.
2. Williams SE, Linton NWF, Harrison J, Chubb H, Whitaker J, Gill J, Rinaldi CA, Razavi R, Niederer S, Wright M, et al. Intra-Atrial Conduction Delay Revealed by Multisite Incremental Atrial Pacing is an Independent Marker of Remodeling in Human Atrial Fibrillation. JACC Clin Electrophysiol. 2017;3:1006-1017.
3. Pytkowski M, Jankowska A, Maciag A, Kowalik I, Sterlinski M, Szwed H, Saumarez RC. Paroxysmal atrial fibrillation is associated with increased intra-atrial conduction delay. Europace. 2008;10:1415-1420.
4. de Groot NM, Schalij MJ, Zeppenfeld K, Blom NA, Van der Velde ET, Van der Wall EE. Voltage and activation mapping: how the recording technique affects the outcome of catheter ablation procedures in patients with congenital heart disease. Circulation. 2003;108:2099-2106.
5. Miyamoto K, Tsuchiya T, Narita S, Yamaguchi T, Nagamoto Y, Ando S, Hayashida K, Tanioka Y, Takahashi N. Bipolar electrogram amplitudes in the left atrium are related to local conduction velocity in patients with atrial fibrillation. Europace. 2009;11:1597-1605.
6. Zhang J, Sacher F, Hoffmayer K, O'Hara T, Strom M, Cuculich P, Silva J, Cooper D, Faddis M, Hocini M, et al. Cardiac electrophysiological substrate underlying the ECG phenotype and electrogram abnormalities in Brugada syndrome patients. Circulation. 2015;131:1950-1959.
7. Spach MS, Miller WT, 3rd, Miller-Jones E, Warren RB, Barr RC. Extracellular potentials related to intracellular action potentials during impulse conduction in anisotropic canine cardiac muscle. Circ Res. 1979;45:188-204.
8. Ye Z, van Schie MS, de Groot NMS. Signal Fingerprinting as a Novel Diagnostic Tool to Identify Conduction Inhomogeneity. Front Physiol. 2021;12:652128.
9. Lanters EA, van Marion DM, Kik C, Steen H, Bogers AJ, Allessie MA, Brundel BJ, de Groot NM. HALT & REVERSE: Hsf1 activators lower cardiomyocyt damage; towards a novel approach to REVERSE atrial fibrillation. J Transl Med. 2015;13:347.
10. van der Does LJ, Yaksh A, Kik C, Knops P, Lanters EA, Teuwen CP, Oei FB, van de Woestijne PC, Bekkers JA, Bogers AJ, et al. QUest for the Arrhythmogenic Substrate of Atrial fibRillation in Patients Undergoing Cardiac Surgery (QUASAR Study): Rationale and Design. J Cardiovasc Transl Res. 2016;9:194-201.
11. de Groot NMS, Shah D, Boyle PM, Anter E, Clifford GD, Deisenhofer I, Deneke T, van Dessel P, Doessel O, Dilaveris P, et al. Critical appraisal of technologies to assess electrical activity during atrial fibrillation: a position paper from the European Heart Rhythm Association and European Society of Cardiology Working Group on eCardiology in collaboration with the Heart Rhythm Society, Asia Pacific Heart Rhythm Society, Latin American Heart Rhythm Society and Computing in Cardiology. Europace. 2022;24:313-330.
12. van Schie MS, Starreveld R, Bogers A, de Groot NMS. Sinus rhythm voltage fingerprinting in patients with mitral valve disease using a high-density epicardial mapping approach. Europace. 2021;23:469-478.
13. van Schie MS, Starreveld R, Roos-Serote MC, Taverne Y, van Schaagen FRN, Bogers A, de Groot NMS. Classification of sinus rhythm single potential morphology in patients with mitral valve disease. Europace. 2020;22:1509-1519.
14. Roberts-Thomson KC, Kistler PM, Sanders P, Morton JB, Haqqani HM, Stevenson I, Vohra JK, Sparks PB, Kalman JM. Fractionated atrial electrograms during sinus rhythm: relationship to age, voltage, and conduction velocity. Heart Rhythm. 2009;6:587-591.
15. Teh AW, Kistler PM, Lee G, Medi C, Heck PM, Spence SJ, Sparks PB, Morton JB, Kalman JM. Electroanatomic remodeling of the left atrium in paroxysmal and persistent atrial fibrillation patients without structural heart disease. J Cardiovasc Electrophysiol. 2012;23:232-238.
16. Konings KT, Smeets JL, Penn OC, Wellens HJ, Allessie MA. Configuration of unipolar atrial electrograms during electrically induced atrial fibrillation in humans. Circulation. 1997;95:1231-1241.
17. Frontera A, Mahajan R, Dallet C, Vlachos K, Kitamura T, Takigawa M, Cheniti G, Martin C, Duchateau J, Lam A, et al. Characterizing localized reentry with high-resolution mapping: Evidence for multiple slow conducting isthmuses within the circuit. Heart Rhythm. 2019;16:679-685.
18. Hocini M, Shah AJ, Nault I, Sanders P, Wright M, Narayan SM, Takahashi Y, Jais P, Matsuo S, Knecht S, et al. Localized reentry within the left atrial appendage: arrhythmogenic role in patients undergoing ablation of persistent atrial fibrillation. Heart Rhythm. 2011;8:1853-1861.
19. Lanters EAH, Yaksh A, Teuwen CP, van der Does L, Kik C, Knops P, van Marion DMS, Brundel B, Bogers A, Allessie MA, et al. Spatial distribution of conduction disorders during sinus rhythm. Int J Cardiol. 2017;249:220-225.
20. Heida A, van der Does WFB, van Staveren LN, Taverne Y, Roos-Serote MC, Bogers A, de Groot NMS. Conduction Heterogeneity: Impact of Underlying Heart Disease and Atrial Fibrillation. JACC Clin Electrophysiol. 2020;6:1844-1854.
21. Prabhu S, Voskoboinik A, McLellan AJA, Peck KY, Pathik B, Nalliah CJ, Wong GR, Azzopardi SM, Lee G, Mariani J, et al. A comparison of the electrophysiologic and electroanatomic characteristics between the right and left atrium in persistent atrial fibrillation: Is the right atrium a window into the left? J Cardiovasc Electrophysiol. 2017;28:1109-1116.
22. Heida A, van der Does WFB, van Schie MS, van Staveren LN, Taverne Y, Bogers A, de Groot NMS. Does conduction heterogeneity determine the supervulnerable period after atrial fibrillation? Med Biol Eng Comput. 2023;61:897-908.
23. Takagi T, Nakamura K, Asami M, Toyoda Y, Enomoto Y, Moroi M, Noro M, Sugi K, Nakamura M. Impact of right atrial structural remodeling on recurrence after ablation for atrial fibrillation. J Arrhythm. 2021;37:597-606.
24. van der Does WFB, Heida A, van der Does L, Bogers A, de Groot NMS. Conduction Disorders during Sinus Rhythm in Relation to Atrial Fibrillation Persistence. J Clin Med. 2021;10.

25. Teuwen CP, Yaksh A, Lanters EA, Kik C, van der Does LJ, Knops P, Taverne YJ, van de Woestijne PC, Oei FB, Bekkers JA, et al. Relevance of Conduction Disorders in Bachmann's Bundle During Sinus Rhythm in Humans. Circ Arrhythm Electrophysiol. 2016;9:e003972.
26. Mathew JP, Parks R, Savino JS, Friedman AS, Koch C, Mangano DT, Browner WS. Atrial fibrillation following coronary artery bypass graft surgery: predictors, outcomes, and resource utilization. MultiCenter Study of Perioperative Ischemia Research Group. JAMA. 1996;276:300-306.
27. Amar D, Shi W, Hogue CW, Jr., Zhang H, Passman RS, Thomas B, Bach PB, Damiano R, Thaler HT. Clinical prediction rule for atrial fibrillation after coronary artery bypass grafting. J Am Coll Cardiol. 2004;44:1248-1253.

13
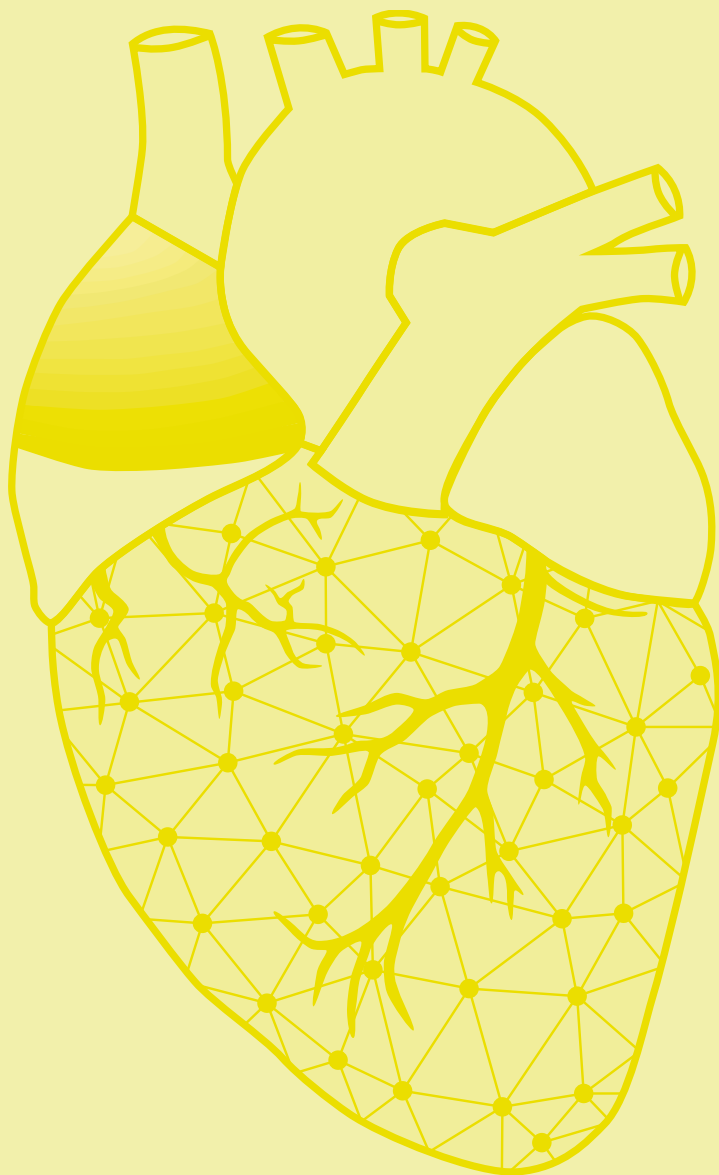
Chapter 14

Unipolar atrial electrogram morphology is affected by age: evidence from high-resolution epicardial mapping

Ziliang Ye

Mathijs S. van Schie

Annejet Heida

Lianne N. van Staveren

Frank R.N. van Schaagen

Yannick J.H.J. Taverne

Natasja M.S. de Groot

Abstract

Background: It is unknown which features of unipolar atrial electrogram (U-AEGM) morphology are affected by ageing and whether age-related changes in U-AEGM morphology are equally distributed throughout the right and left atria.

Methods: Epicardial high-resolution mapping was performed in patients undergoing coronary artery bypass grafting surgery during sinus rhythm (SR). Mapping areas include the right atrium (RA), left atrium (LA), pulmonary vein area (PVA) and Bachmann's bundle (BB). Patients were categorized into a young (age<60) and aged (age≥60) group. U-AEGM were classified as single potentials (SPs, one deflection), short double potentials (SDPs, deflection interval <15 ms), long double potentials (LDPs, deflection interval ≥15 ms) and fractionated potentials (FPs, ≥3 deflections).

Results: A total of 213 patients (age: 67 [59–73] years; young group N=58, aged group N=155) were included. Only at BB, the proportion of SPs (p=0.007) was significantly higher in the young group, while the proportion of SDPs (p=0.051), LDPs (p=0.004) and FPs (p=0.006) was higher in the aged group. After adjusting for potential confounders, older age was associated with a reduction in SPs [regression coefficient (β): -6.33, 95% confident interval (CI): -10.37 to -2.30] at the expense of an increased proportion of SDPs (β: 2.49, 95% CI: 0.09 to 4.89), LDPs (β: 1.94, 95% CI: 0.21 to 3.68) and FPs (β: 1.90, 95% CI: 0.62 to 3.18).

Conclusions: Age-related remodeling particularly affects BB as indicated by the decreased amount of non-SP at this location in the elderly.

Journal site &
supplementary material

Introduction

Ageing is one of the principal risk factors for development of atrial fibrillation (AF).[1-3] The reported prevalence of AF ranges between 0.12 and 0.16% in subjects younger than 49 years and increases up to 17% above 80 years or older.[4] Although ageing is currently one of the most important factors resulting in worldwide health issues such as AF,[5] data on age-related changes in atrial electrophysiology is scarce.

In canine models, Anyukhovsky et al.[1] demonstrated that the average action potential duration was significantly longer in the right and left atria of elderly dogs compared to adult dogs. Also, action potential duration heterogeneity was more pronounced in atrial tissues of old dogs. In humans, endocardial mapping studies revealed that ageing is associated with slowing of conduction at the right atrium (RA) and the presence of diffusely spread low-voltage areas.[6] Recently, Van der Does et al.[7] revealed that ageing was associated with more conduction disorders, especially at Bachmann's bundle (BB) and the RA.

However, current data on age-related changes in electrogram (EGM) morphology is limited to the RA. Kistler et al.[6] demonstrated in 41 patients that ageing was related to a larger number of double and fractionated potentials along the crista terminalis. However, it is unknown which features of EGM morphology are affected by ageing and whether the age-related changes in EGM morphology are equally distributed throughout the right and left atria (LA). The purpose of this study is therefore to investigate the influence of age on unipolar atrial EGM (U-AEGM) morphology recorded from the RA and LA including BB in a large cohort of patients undergoing cardiac surgery.

14

Methods

Study population

The study population included adult participants, who underwent coronary artery bypass grafting (CABG) surgery at Erasmus Medical Center in Rotterdam between March 2012 to August 2020.[8,9] This project has been approved by the institutional medical ethics committee (MEC2010-054/MEC2014-393)[8,9], and written informed consent was obtained from all participants before enrolling. Baseline demographic and clinical profiles (e.g., age, gender, body mass index and underlying heart diseases) were attained from the hospital's electronic medical system. None of the patients included in this study had a history of AF. All included participants were grouped into a young (age<60) and aged (age≥60) group, which was based on previous studies.[10,11]

Mapping Procedure

As described in our previous studies, epicardial high-resolution mapping was carried out before extracorporeal circulation.[8,9] In short, a temporary bipolar pacemaker lead was sutured on the free wall of the RA and served as a reference electrode, and a steel wire was fixed on subcutaneous tissue of the thoracic cavity as a neutral electrode. A 128- or 192- electrode array (electrode diameter: 0.65 or 0.45 mm, interelectrode distances: 2.0 mm) was used for epicardial mapping of the atria (upper left panel of *Figure 1*). According to a predefined mapping scheme (upper left panel of *Figure 1*), the electrode array was moved along an imaginary line with a fixed anatomical orientation for mapping, covering the entire epicardial atrial surface (including RA, BB, pulmonary vein area (PVA) and LA). Mapping of the RA was performed from the inferior to superior caval vein perpendicular to the terminal crest. The PVA was accessed through the oblique sinus along the boundary of the left and
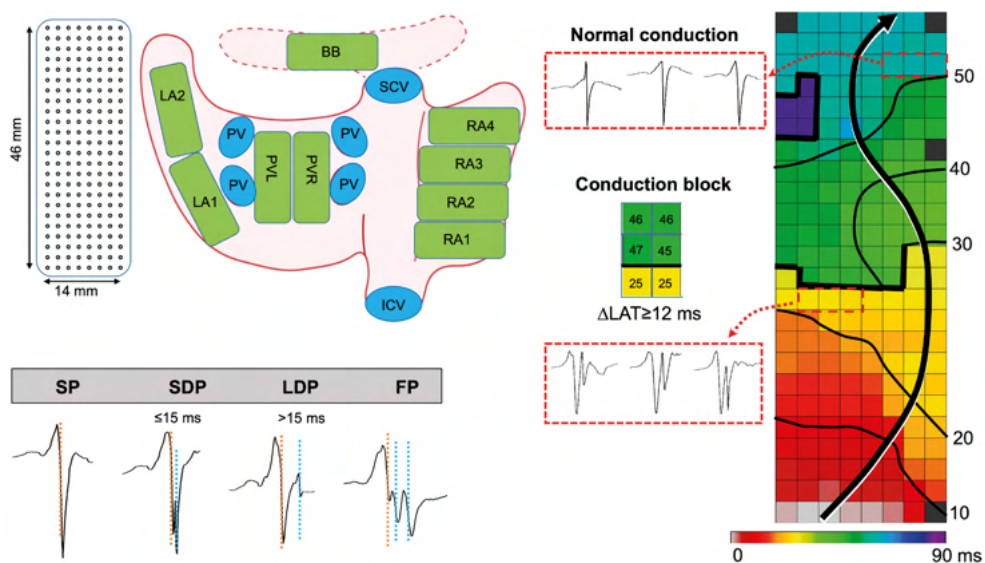
Figure 1 – Epicardial mapping of the atria. The upper left panel shows a schematic presentation of the 192-unipolar electrode array on the RA, LA and BB. The upper right panel demonstrates a typical color-coded activation map demonstrating lines of conduction block, defined as local activation time differences between adjacent electrodes of ≥12ms; corresponding long double potentials are shown outside the activation map. Isochronal lines (thin black lines) are drawn at 10-millisecond intervals, and the black arrow indicates the propagation direction of the SR wavefront. **IVC** = inferior vena cava; **SVC** = superior vena cava; **RA** = right atrium; **BB** = Bachmann's bundle; **LA** = left atrium; **PV(A)** = pulmonary vein (area); **SP** = single potential; **SDP** = short double potential; **LDP** = long double potential; **FP** = fractionated potential.

right PV. Mapping of the LA was performed from the lower border of the left inferior PV towards the LA appendage. Additionally, BB was mapped from the tip of the LA appendage across the top of the LA and RA, behind the aorta towards the superior cavo-atrial junction. Five seconds of sinus rhythm (SR) was recorded at each mapping location, with a surface electrocardiogram (ECG) lead, a bipolar reference EGM and all unipolar epicardial EGMs. Data were processed by amplification (gain 1,000), filtering (bandwidth 0.5–400 Hz), sampling (1 kHz) and analog-to-digital conversion (16 bits) and then saved on a hard disk.

Data Analysis

Customized software was used to semi-automatically analyze U-AEGM morphology. U-AEGMs with injury potentials or recording sites with ≥25% missing U-AEGMs were excluded. In addition, U-AEGMs recorded during premature atrial beats or aberrant beats were eliminated. Under the premise that the deflection amplitude was at least twice the signal-to-noise ratio, the steepest negative slope of U-AEGMs was marked as the local activation time (LAT). All U-AEGM annotations were manually inspected by two researchers with consensus, and color-coded activation maps were reconstructed using the LATs on each electrode (upper right panel of *Figure 1*).

Consistent with Konings et al.[12], U-AEGMs were categorized as single potentials (SPs), short double potentials (SDPs), long double potentials (LDPs) and fractionated potentials (FPs). In brief, SPs only consist of a single negative deflection; SDPs and LDPs contain two negative deflections with time interval between deflections of respectively <15 ms and ≥15 ms; FPs were defined as ≥3 deflections. Examples of the different U-AEGM morphologies are shown in the lower left panel of *Figure 1*.

Table 1 – Baseline characteristics of the study population.

Variables	Overall	Young group (age<60 years)	Aged group (age≥60 years)	p-value
N	213	58	155	
Age (years)	67 [59–73]	54 [50–57]	70 [66–75]	<0.001
Male (N, %)	182 (85.45)	48 (82.76)	134 (86.45)	0.644
BMI (kg/m²)	27.7 [25.5–31.2]	29.5 [26.3–33.3]	27.4 [25.2–30.3]	0.004
Cardiovascular risk factors				
• Hypertension (N, %)	132 (61.97)	35 (60.34)	97 (62.58)	0.888
• Dyslipidemia (N, %)	93 (43.66)	26 (44.83)	67 (43.23)	0.956
• Diabetes mellitus (N, %)	74 (34.74)	17 (29.31)	57 (36.77)	0.392
• Myocardial infarction	105 (49.30)	30 (51.72)	75 (48.39)	0.780
• Left atrial dilatation >45 mm (N, %)	24 (11.27)	5 (8.62)	19 (12.26)	0.673
Left ventricular function				0.914
• Normal (EF >55%)	160 (75.12)	44 (75.86)	116 (74.84)	
• Mild impairment (EF 46-55%)	46 (21.60)	12 (20.69)	34 (21.94)	
• Moderate impairment (EF 36-45%)	6 (2.82)	2 (3.45)	4 (2.58)	
• Severe impairment (EF <35%)	1 (0.47)	0 (0.00)	1 (0.65)	
ACEI / ARB / AT2 antagonist (N, %)	147 (69.34)	40 (68.97)	107 (69.48)	1
Statin (N, %)	188 (88.26)	49 (84.48)	139 (89.68)	0.418
Antiarrhythmic drugs				
• Class I (N, %)	0 (0.00)	0 (0.00)	0 (0.00)	NA
• Class II (N, %)	170 (79.81)	51 (87.93)	119 (76.77)	0.107
• Class III (N, %)	3 (1.41)	2 (3.45)	1 (0.65)	0.372
• Class IV (N, %)	11 (5.16)	2 (3.45)	9 (5.81)	0.730
• Digoxin (N, %)	2 (0.94)	0 (0.00)	2 (1.29)	0.943

Values are presented as N (%) or median (IQR). **BMI** = body mass index; **EF** = ejection fraction; **ACEI** = angiotensin-converting enzyme inhibitors; **ARB** = angiotensin receptor blockers; **AT2** = angiotensin type 2 receptor.

14

Statistical Analysis

A Shapiro–Wilk test was applied to inspect the distribution of continuous variables. Continuous variables conforming to a normal distribution were described as mean ± standard deviation, and the differences were compared using an independent t-test. Skewed distributed variables were described as median [25th–75th percentile], and a Mann–Whitney U test was performed to compare differences between groups. Categorical variables were described as the number and percentage, and the differences were assessed by χ^2 test. A p-value (two-sided) less than 0.05 indicates significant difference.

Univariable linear regression analysis was performed to investigate which variables were associated with different U-AEGM morphologies (including SP, SDP, LDP and FP). We further explored the independent relationship between age (independent variable) and different U-AEGMs morphologies (dependent variables) using a multivariable linear regression model. In this process of multivariable linear regression analysis, two models were performed: model I, covariates related to different U-AEGM morphologies in univariable linear regression analysis were adjusted; model II, all covariates, including body mass index, gender, hypertension, dyslipidemia, diabetes mellitus, myocardial infarction, left ventricular function, left atrial dilatation and medication, were adjusted. Results were described as regression coefficient (β) and 95% confidence interval (CI).

Furthermore, a generalized linear model (GLM) was performed to visualize the independent relationship between age (considering as continuous variable) and different U-AEGM morphologies (considering as continuous variables), with the same adjustment for covariates in model I and model II. R software (version 4.1.3) and IBM SPSS Statistics (version 28) were used to analyze the data.
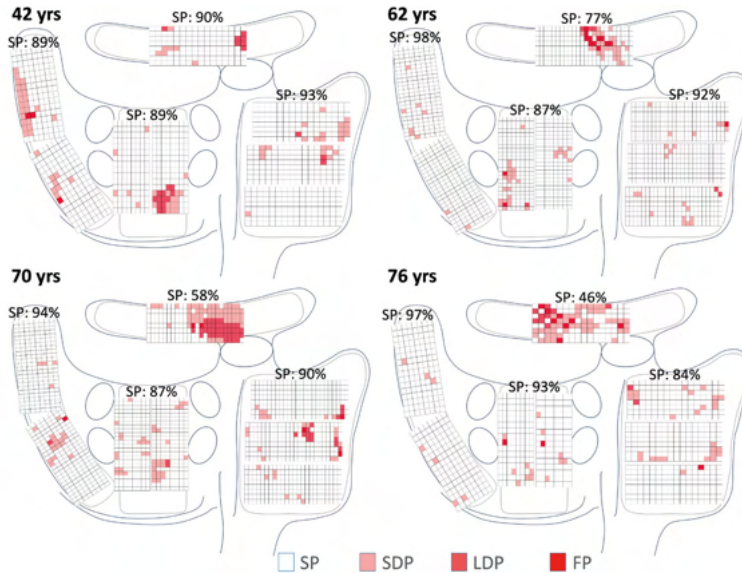
Figure 2 – U-AEGM type maps demonstrating the proportions of the different U-AEGM morphologies, obtained from four representative patients of different ages ranging from 42 to 76 years. These maps clearly show that the proportion of SDPs, LDPs and FPs at BB is higher in the oldest patient. **U-AEGM** = unipolar atrial electrogram; **SP** = single potential; **SDP** = short double potential; **LDP** = long double potential; **FP** = fractionated potential; **BB** = Bachmann's bundle.

Results

Study Population

A total of 213 patients with an age ranging from 37 to 84 years (median age: 67 [59–73], 85.45% male) were enrolled. This study population was categorized into a young (age<60 years, N=58, 82.76% male) and aged (age≥60 years, N=155, 86.45% male) group. Except

Table 2 – Comparison of U-AEGMs characteristics between young and aged group.

	Young group (age <60 years)	Aged group (age ≥60 years)	*p*-value
Right atrium			
SPs (%)	83.3 [77.4–88.4]	84.0 [77.9–89.9]	0.511
SDPs (%)	10.2 [6.6–12.1]	9.6 [5.8–13.1]	0.379
LDPs (%)	4.1 [2.0–6.6]	4.2 [1.7–6.9]	0.727
FPs (%)	1.8 [0.6–3.4]	1.4 [0.4–2.9]	0.290
Bachmann's bundle			
SPs (%)	84.1 [76.6–91.3]	79.0 [71.2–87.2]	0.007
SDPs (%)	9.9 [6.4–15.8]	12.8 [8.5–17.5]	0.051
LDPs (%)	1.6 [0.2–5.3]	4.3 [1.3–9.4]	0.004
FPs (%)	0.8 [0.3–2.1]	1.6 [0.7–3.9]	0.006
Pulmonary vein area			
SPs (%)	84.4 [74.6–89.0]	86.0 [77.9–90.6]	0.180
SDPs (%)	11.3 [8.4–17.3]	10.3 [6.8–16.7]	0.231
LDPs (%)	1.3 [0.3–5.2]	1.4 [0.3–4.0]	0.978
FPs (%)	0.7 [0.2–2.7]	0.8 [0.2–1.9]	0.961
Left atrium			
SPs (%)	82.1 [76.9–89.4]	82.8 [75.9–88.6]	0.617
SDPs (%)	12.0 [9.1–17.3]	11.3 [8.3–16.4]	0.512
LDPs (%)	0.8 [0.1–3.6]	1.5 [0.6–4.9]	0.150
FPs (%)	1.0 [0.3–2.5]	1.2 [0.4–2.5]	0.767

SPs = single potentials; **SDPs** = short double potentials; **LDPs** = long double potentials; **FPs** = fractionated potentials.

for age (young: 54 [50–57] years vs. aged: 70 [66–75] years, p<0.001] and BMI [young: 29.5 [26.3–33.3] kg/m^2 vs. aged: 27.4 [25.2–30.3] kg/m^2, p=0.004], baseline characteristics of these 2 groups did not differ (*Table 1*).

U-AEGM Database

A total of 2,007,403 U-AEGMs (9,424±2,818 per patient) with a mean SR cycle length of 886±166 ms were recorded. The number of U-AEGMs obtained from the RA, BB, PVA and LA area was respectively 938,093 (46.73%), 227,465 (11.33%), 445,334 (22.19%) and 396,511 (19.75%). Characteristics of U-AEGMs recorded from all patients for every atrial region separately are shown in *Supplementary table 1*. At each atrial region, the proportion of SPs was the largest (RA: 82.49%, BB: 79.76%, PVA: 83.58% and LA: 81.79%), whereas the proportion of FPs was the smallest (RA: 2.33%, BB: 2.60%, PVA: 1.52% and LA: 1.97%).

Table 3 – Variables related to BB U-AEGM morphologies in univariable linear regression analysis.

Variables	β	95% CI	*p*-value
Single potentials			
Aged (age ≥60 years)	**-5.43**	**-9.27 to -1.58**	**0.006**
Male	2.47	-2.42 to 7.36	0.321
BMI	-0.14	-0.57 to 0.30	0.542
Hypertension	-1.17	-4.77 to 2.43	0.522
Dyslipidemia	-0.42	-3.95 to 3.12	0.817
Diabetes mellitus	-2.25	-5.91 to 1.41	0.228
Myocardial infarction	0.12	-3.38 to 3.63	0.945
Left ventricular function			
Normal (EF >55%)	Ref	Ref	Ref
Mild impairment (EF 46%–55%)	0.07	-4.24 to 4.38	0.975
Moderate impairment (EF 36%–45%)	-4.10	-14.59 to 6.40	0.442
Severe impairment (EF <35%)	4.44	-20.87 to 29.74	0.730
Left atrial dilatation > 45 mm	-2.11	-8.15 to 3.93	0.492
ACEI/ARB/AT2 antagonist	**4.14**	**0.37 to 7.91**	**0.032**
Statin	2.22	-3.33 to 7.78	0.431
Digoxin	-13.25	-31.02 to 4.53	0.143
Class I	-	-	-
Class II	2.49	-1.97 to 6.95	0.273
Class III	-8.77	-23.35 to 5.80	0.237
Class IV	-4.90	-13.02 to 3.22	0.236
Short double potentials			
Aged (age ≥60 years)	1.82	-0.55 to 4.19	0.132
Male	**-3.46**	**-6.40 to -0.51**	**0.022**
BMI	0.14	-0.12 to 0.41	0.284
Hypertension	1.62	-0.56 to 3.81	0.144
Dyslipidemia	-0.08	-2.23 to 2.07	0.944
Diabetes mellitus	2.19	-0.02 to 4.41	0.053
Myocardial infarction	-0.24	-2.38 to 1.89	0.822
Left ventricular function			
Normal (EF >55%)	Ref	Ref	Ref
Mild impairment (EF 46%–55%)	-0.21	-2.82 to 2.41	0.875
Moderate impairment (EF 36%–45%)	4.26	-2.11 to 10.64	0.189
Severe impairment (EF <35%)	2.90	-12.47 to 18.28	0.710
Left atrial dilatation > 45 mm	**4.18**	**0.56 to 7.80**	**0.024**
ACEI/ARB/AT2 antagonist	-1.81	-4.11 to 0.49	0.123
Statin	-1.04	-4.43 to 2.35	0.546
Digoxin	3.33	-7.55 to 14.21	0.547
Class I	-	-	-
Class II	0.71	-3.44 to 2.01	0.605
Class III	8.36	-0.47 to 17.20	0.063
Class IV	4.09	-0.84 to 9.03	0.104

14

245

Variables	β	95% CI	*p*-value
Long double potentials			
Aged (age ≥60 years)	**1.90**	**0.25 to 3.54**	**0.024**
Male	0.74	-1.34 to 2.82	0.486
BMI	-0.04	-0.23 to 0.14	0.660
Hypertension	-0.36	-1.89 to 1.17	0.640
Dyslipidemia	0.44	-1.06 to 1.94	0.565
Diabetes mellitus	-0.05	-1.61 to 1.51	0.951
Myocardial infarction	-0.23	-1.72 to 1.26	0.762
Left ventricular function			
Normal (EF >55%)	Ref	Ref	Ref
Mild impairment (EF 46%–55%)	-0.11	-1.94 to 1.72	0.907
Moderate impairment (EF 36%–45%)	-0.08	-4.54 to 4.38	0.973
Severe impairment (EF <35%)	-4.94	-15.69 to 5.81	0.366
Left atrial dilatation > 45 mm	-2.17	-4.73 to 0.39	0.096
ACEI/ARB/AT2 antagonist	**-1.88**	**-3.47 to -0.29**	**0.020**
Statin	-0.53	-2.89 to 1.83	0.659
Digoxin	**7.89**	**0.38 to 15.41**	**0.040**
Class I	-	-	-
Class II	-1.47	-3.36 to 0.42	0.127
Class III	0.57	-5.65 to 6.78	0.857
Class IV	0.57	-2.90 to 4.03	0.748
Fractionated potentials			
Aged (age ≥60 years)	**1.71**	**0.52 to 2.89**	**0.005**
Male	0.25	-1.26 to 1.76	0.742
BMI	0.03	-0.10 to 0.17	0.639
Hypertension	-0.09	-1.20 to 1.02	0.874
Dyslipidemia	0.05	-1.03 to 1.14	0.922
Diabetes mellitus	0.10	-1.03 to 1.23	0.861
Myocardial infarction	0.35	-0.73 to 1.43	0.524
Left ventricular function			
Normal (EF >55%)	Ref	Ref	Ref
Mild impairment (EF 46%–55%)	0.25	-1.08 to 1.58	0.711
Moderate impairment (EF 36%–45%)	-0.08	-3.32 to 3.15	0.959
Severe impairment (EF <35%)	-2.40	-10.20 to 5.40	0.545
Left atrial dilatation > 45 mm	0.10	-1.76 to 1.96	0.914
ACEI/ARB/AT2 antagonist	-0.44	-1.61 to 0.73	0.458
Statin	-0.65	-2.36 to 1.06	0.452
Digoxin	2.03	-3.47 to 7.52	0.468
Class I	-	-	-
Class II	-0.30	-1.68 to 1.07	0.665
Class III	-0.15	-4.66 to 4.35	0.946
Class IV	0.24	-2.27 to 2.75	0.849

β = regression coefficient; **Ref** = reference; **CI** = confident interval; **BMI** = body mass index; **ACEI** = angiotensin-converting enzyme inhibitors; **ARB** = angiotensin receptor blockers; **AT2** = angiotensin type 2 receptor.

Impact of ageing on U-AEGM morphology

Figure 2 shows a color-coded distribution of SPs, SDPs, LDPs and FPs measured at all mapping areas in four typical patients of various ages (42-, 62-, 70- and 76-year-old). These maps show that at all areas, but particularly at BB, there are age-related changes in U-AEGM morphology consisting of an increase in non-SP.

The impact of ageing on U-AEGM morphology in the different areas in the entire study population is summarized in *Table 2*. In the aged group, only at BB the proportion of SPs was significantly lower compared to the young group (p=0.007) whereas the proportions of SDPs (border significant, p=0.051), LDPs (p=0.004) and FPs (p=0.006) were higher. However, an increased age did not have significant impact on U-AEGM morphology recorded from the RA, PVA and LA.

Age-related changes in BB U-AEGM morphology

Univariable predictors of age-related changes in U-AEGMs at BB with their respective β (95% CI) are summarized in *Table 3*. In univariable analyses, ageing was associated with a decrease in the proportion of SPs (β=-5.43, p=0.006), and an increase in the proportions of LDPs (β=1.90, p=0.024) and FPs (β=1.71, p=0.005). Furthermore, the use of ACEI/ARB/AT2 antagonists was associated with an increase in the proportion of SPs (β=4.14, p=0.032) and a reduction in the proportion of LDPs (β=-1.88, p=0.020); male (β=-3.46, p=0.022) was associated with a decrease in the proportion of SDPs, while LA dilatation (β=4.18, p=0.024) was correlated with an increased SDP proportion. Additionally, we also found that digoxin usage was associated with a higher proportion of LDPs (β=7.89, p=0.040).

Variables introduced in the multivariable linear regression model of age-related changes U-AEGM morphology at BB are shown in *Table 4*. In model I, variables associated with different U-AEGMs morphologies (p<0.05) in univariable linear regression were adjusted. Age was associated with a reduction in the proportion of SPs (β=-5.50, p=0.005), and an increase in the proportions of LDPs (β=1.78, p=0.031) and FPs (β=1.71, p=0.005). No significant correlation between age and SDPs was found in model I (p=0.128). The relation between age and U-AEGM morphology at BB is illustrated in the upper panel of *Figure 3*. After adjusting for all potential covariates in model II, age was associated with a decrease in the proportion of SPs (β=-6.33, p=0.002), an increase in proportion of SDPs (β=2.49, p=0.042), LDPs (β=1.94, p=0.028) and FPs (β=1.90, p=0.004). The independent relationship between age and BB U-AEGM morphology is shown in the lower panel of *Figure 3*.

14

Discussion

This is the first study exploring the relation between age and morphology of U-AEGMs obtained from both atria including BB. For this purpose, we used a large sample of 2,007,403 U-AEGMs. Ageing resulted in a substantial alteration in U-AEGM morphology at BB, manifested by a reduction in the proportion of SPs and an increase in proportion of SDPs, LDPs and FPs. However, ageing had no significant effect on U-AEGM morphology recorded from the RA, PVA and LA.

Table 4 – Independent relationship between aged (independent variable and BB U-AEGMs morphologies (dependent variables).

Independent variable	Dependent variables	β	95% CI	*p*-value
Model I				
Aged	Single potentials	-5.50	-9.32 to -1.68	0.005
	Short double potentials	1.79	-0.52 to 4.11	0.128
	Long double potentials	1.78	0.16 to 3.39	0.031
	Fractionated potentials	1.71	0.52 to 2.89	0.005
Model II				
Aged	Single potentials	-6.33	-10.37 to -2.30	0.002
	Short double potentials	2.49	0.09 to 4.89	0.042
	Long double potentials	1.94	0.21 to 3.68	0.028
	Fractionated potentials	1.90	0.62 to 3.18	0.004

Variable(s) associated with different U-AEGMs morphologies in univariable linear regression was (were) adjusted in model I. BMI, gender, hypertension, dyslipidemia, diabetes mellitus, myocardial infarction, left ventricular function, left atrial dilatation, ACEI/ARB/AT2 antagonist, Statin, Digoxin, Class II, Class III and Class IV were all adjusted in model II. **β** = regression coefficient; **CI** = confident interval; **BMI** = body mass index; **ACEI** = angiotensin-converting enzyme inhibitors; **ARB** = angiotensin receptor blockers; **AT2** = angiotensin type 2 receptor.
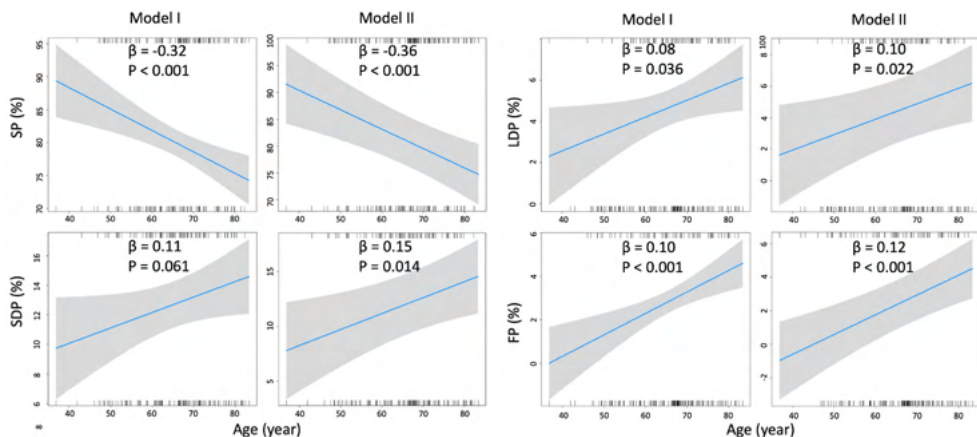
Figure 3 – Relationship between age and U-AEGMs at Bachmann's bundle. Age is negatively correlated with SPs, and positively correlated with LDPs and FPs in model I. After adjusting for all confounding factors in model II, age is negatively correlated with SPs and positively correlated with SDPs, LDPs and FPs. Variables related to U-AEGM morphology in univariable linear regression analysis were adjusted in model I; body mass index, gender, hypertension, dyslipidemia, diabetes mellitus, myocardial infarction, left ventricular function, left atrial dilatation, and medications were adjusted in model II. **SP** = single potential; **SDP** = short double potential; **LDP** = long double potential; **FP** = fractionated potential.

Regional differences in age-related EGM morphology

Double potentials (including SDPs and LDPs) and FPs are frequently associated with areas of conduction delay and/or block which play a fundamental role in the pathophysiology of atrial tachyarrhythmias such as AF.[12-14] Significant alterations in EGM morphology with increasing age have been demonstrated in previous studies, although these only focused on the RA. Roberts-Thomson et al.[15] categorized 21 patients without a history of AF into three groups (age<30 years [N=7]; 31<age<59 years [N=6]; age>60 years [N=8]), and compared the proportion of bipolar complex fractionated atrial EGMs (CFAE) during SR in the RA. Their results demonstrated that the proportion of CFAE in the oldest patients was significantly higher compared to the youngest patients (14.6±7.7% vs. 2.7±2.1%, p=0.001), but no difference was observed compared to the middle group (8.5±3.5%, p=0.14).

Unlike the study of Roberts-Thomson et al.[15], our study did not show an influence of ageing on the U-AEGM morphology at the RA. However, as the youngest group in the study of Roberts-Thomson et al.[15] was much younger than our young group, only the middle and oldest groups can be compared to our results. Then, indeed, no difference could be found in the proportion of CFAE with age, which is consistent with the results of our present study. It should still be noted that Roberts-Thomson et al.[15] used bipolar endocardial EGMs compared to our unipolar epicardial EGMs. As Van der Does et al.[16] demonstrated that there are no differences between endo- and epicardial U-AEGM morphology recorded at the RA, our findings can still be extrapolated to endocardial U-AEGMs.

In another study of 106 patients without a history of AF, Centurion et al.[17] indicated that the number of abnormal atrial EGMs (defined as fractionation duration ≥100 ms and/or ≥8 negative deflections) in the RA during SR was considerably higher in patients over 60 years compared to younger (13 to 60 years) patients (0.61±1.43 vs. 0.14±0.44, p<0.02). The age of the patients in the young group in the study of Centurion et al.[17] was also considerably younger compared to our young group (age range from 37 to 60 years). It could therefore be that the largest differences in EGM morphology at the RA can only be found at an earlier age than included in our present study. This implies that the largest part of age-related remodeling

occurs at a younger age (before approximately 50 years) after which it gradually continues, which may explain why in the present study there were no significant alterations in U-AEGM morphologies at RA (and also LA and PVA).

However, we investigated for the first time BB and found that ageing was associated with considerable changes in U-AEGM morphology at this site. This observation suggests that BB is extra vulnerable for age related remodeling. As prior studies already suggested that BB plays an important role in the pathophysiology of AF[18,19], our observations may partly explain why elderly are more prone to develop atrial tachyarrhythmia such as AF.

Age related structural remodeling

Spach et al.[20] demonstrated that extensive collagenous septa caused by ageing resulted in electrical uncoupling of the side-to-side connections at RA, which in turn promotes variability in wave propagation direction and the complexity of EGMs. As a consequence, age-related electrophysiological alterations resulted in significant reduction in conduction velocity of transverse propagation, which makes reentry more likely to occur. Xu et al.[21] investigated the influence of ageing on atrial cellular properties in an in-vivo rat model, and demonstrated that the ratio of interstitial fibrotic areas to atrial surface area (2.1±0.6% vs. 1.0±0.3%, p<0.05) and cellular diameter (5.3±1.1 μm vs. 4.1±0.8 μm, p<0.05) at the LA were significantly higher in middle-aged rats (9 months) compared with those measured from young rats (3 months), but not at the RA. In a canine model, Anyukhovsky et al.[22] found that dogs older than 8 years had more connective tissue (8.4±1.0% vs. 4.8±1.1%, p<0.05) in the RA compared with dogs of 1–5 years. In addition, they found that large strands of connective tissue separated muscle bundles of elderly atrial tissue into smaller components. In our study, abnormal atrial EGMs related to ageing occurred especially at BB, indicating that age-related remodeling particularly affects BB. This observation could indicate that the parallel oriented muscle bundles contained within BB are more easily disrupted by structural remodeling. However, this hypothesis still needs further verification by subsequent histopathological studies.

Study limitations

Morphology of U-AEGMs was not repeatedly measured at different ages of each individual patient. Therefore, the influence of individual heterogeneity cannot be excluded. Due to the invasive characteristics of intra-operative mapping, it was not possible to include patients of all ages. In addition, it cannot be completely excluded that various occlusion sites affect the atria differently. However, it is expected that the influence of coronary stenosis is comparable between the young and aged group.

Conclusions

Ageing affects particularly BB as indicated by the increased amount of abnormal U-AEGM (SDPs, LDPs and FPs) recorded from this location in the elderly. This observation further supports the concept that BB may play an important role in development of age-related arrhythmias such as AF.

14

References

1.   Anyukhovsky EP, Sosunov EA, Chandra P, Rosen TS, Boyden PA, Danilo P, Jr., Rosen MR. Age-associated changes in electrophysiologic remodeling: a potential contributor to initiation of atrial fibrillation. Cardiovasc Res. 2005;66:353-363.

2.   Dun W, Boyden PA. Aged atria: electrical remodeling conducive to atrial fibrillation. J Interv Card Electrophysiol. 2009;25:9-18.

3.   Ohlmeier C, Mikolajczyk R, Haverkamp W, Garbe E. Incidence, prevalence, and antithrombotic management of atrial fibrillation in elderly Germans. Europace. 2013;15:1436-1444.

4.   Zoni-Berisso M, Lercari F, Carazza T, Domenicucci S. Epidemiology of atrial fibrillation: European perspective. Clin Epidemiol. 2014;6:213-220.

5.   Beard JR, Officer A, de Carvalho IA, Sadana R, Pot AM, Michel JP, Lloyd-Sherlock P, Epping-Jordan JE, Peeters G, Mahanani WR, et al. The World report on ageing and health: a policy framework for healthy ageing. Lancet. 2016;387:2145-2154.

6.   Kistler PM, Sanders P, Fynn SP, Stevenson IH, Spence SJ, Vohra JK, Sparks PB, Kalman JM. Electrophysiologic and electroanatomic changes in the human atrium associated with age. J Am Coll Cardiol. 2004;44:109-116.

7.   van der Does WFB, Houck CA, Heida A, van Schie MS, van Schaagen FRN, Taverne Y, Bogers A, de Groot NMS. Atrial electrophysiological characteristics of aging. J Cardiovasc Electrophysiol. 2021;32:903-912.

8.   Lanters EA, van Marion DM, Kik C, Steen H, Bogers AJ, Allessie MA, Brundel BJ, de Groot NM. HALT & REVERSE: Hsf1 activators lower cardiomyocyt damage; towards a novel approach to REVERSE atrial fibrillation. J Transl Med. 2015;13:347.

9.   van der Does LJ, Yaksh A, Kik C, Knops P, Lanters EA, Teuwen CP, Oei FB, van de Woestijne PC, Bekkers JA, Bogers AJ, et al. QUest for the Arrhythmogenic Substrate of Atrial fibRillation in Patients Undergoing Cardiac Surgery (QUASAR Study): Rationale and Design. J Cardiovasc Transl Res. 2016;9:194-201.

10.   Han KH, O'Neill WC. Increased Peripheral Arterial Calcification in Patients Receiving Warfarin. J Am Heart Assoc. 2016;5.

11.   Pedersen MGB, Olsen MS, Schmidt M, Johnsen SP, Learn C, Laursen HB, Madsen NL. Ischemic Stroke in Adults With Congenital Heart Disease: A Population-Based Cohort Study. J Am Heart Assoc. 2019;8:e011870.

12.   Konings KT, Smeets JL, Penn OC, Wellens HJ, Allessie MA. Configuration of unipolar atrial electrograms during electrically induced atrial fibrillation in humans. Circulation. 1997;95:1231-1241.

13.   Frontera A, Takigawa M, Martin R, Thompson N, Cheniti G, Massoullie G, Duchateau J, Wielandts JY, Teijeira E, Kitamura T, et al. Electrogram signature of specific activation patterns: Analysis of atrial tachycardias at high-density endocardial mapping. Heart Rhythm. 2018;15:28-37.

14.   Jacquemet V, Virag N, Ihara Z, Dang L, Blanc O, Zozor S, Vesin JM, Kappenberger L, Henriquez C. Study of unipolar electrogram morphology in a computer model of atrial fibrillation. J Cardiovasc Electrophysiol. 2003;14:S172-179.

15.   Roberts-Thomson KC, Kistler PM, Sanders P, Morton JB, Haqqani HM, Stevenson I, Vohra JK, Sparks PB, Kalman JM. Fractionated atrial electrograms during sinus rhythm: relationship to age, voltage, and conduction velocity. Heart Rhythm. 2009;6:587-591.

16.   van der Does L, Knops P, Teuwen CP, Serban C, Starreveld R, Lanters EAH, Mouws E, Kik C, Bogers A, de Groot NMS. Unipolar atrial electrogram morphology from an epicardial and endocardial perspective. Heart Rhythm. 2018;15:879-887.

17.   Centurion OA, Shimizu A, Isomoto S, Konoe A, Kaibara M, Hayano M, Yano K. Influence of advancing age on fractionated right atrial endocardial electrograms. Am J Cardiol. 2005;96:239-242.

18.   van Campenhout MJ, Yaksh A, Kik C, de Jaegere PP, Ho SY, Allessie MA, de Groot NM. Bachmann's bundle: a key player in the development of atrial fibrillation? Circ Arrhythm Electrophysiol. 2013;6:1041-1046.

19.   Enriquez A, Conde D, Hopman W, Mondragon I, Chiale PA, de Luna AB, Baranchuk A. Advanced interatrial block is associated with recurrence of atrial fibrillation post pharmacological cardioversion. Cardiovasc Ther. 2014;32:52-56.

20.   Spach MS, Dolber PC. Relating extracellular potentials and their derivatives to anisotropic propagation at a microscopic level in human cardiac muscle. Evidence for electrical uncoupling of side-to-side fiber connections with increasing age. Circ Res. 1986;58:356-371.

21.   Xu D, Murakoshi N, Tada H, Igarashi M, Sekiguchi Y, Aonuma K. Age-related increase in atrial fibrillation induced by transvenous catheter-based atrial burst pacing: an in vivo rat model of inducible atrial fibrillation. J Cardiovasc Electrophysiol. 2010;21:88-93.

22.   Anyukhovsky EP, Sosunov EA, Plotnikov A, Gainullin RZ, Jhang JS, Marboe CC, Rosen MR. Cellular electrophysiologic properties of old canine atria provide a substrate for arrhythmogenesis. Cardiovasc Res. 2002;54:462-469.

14
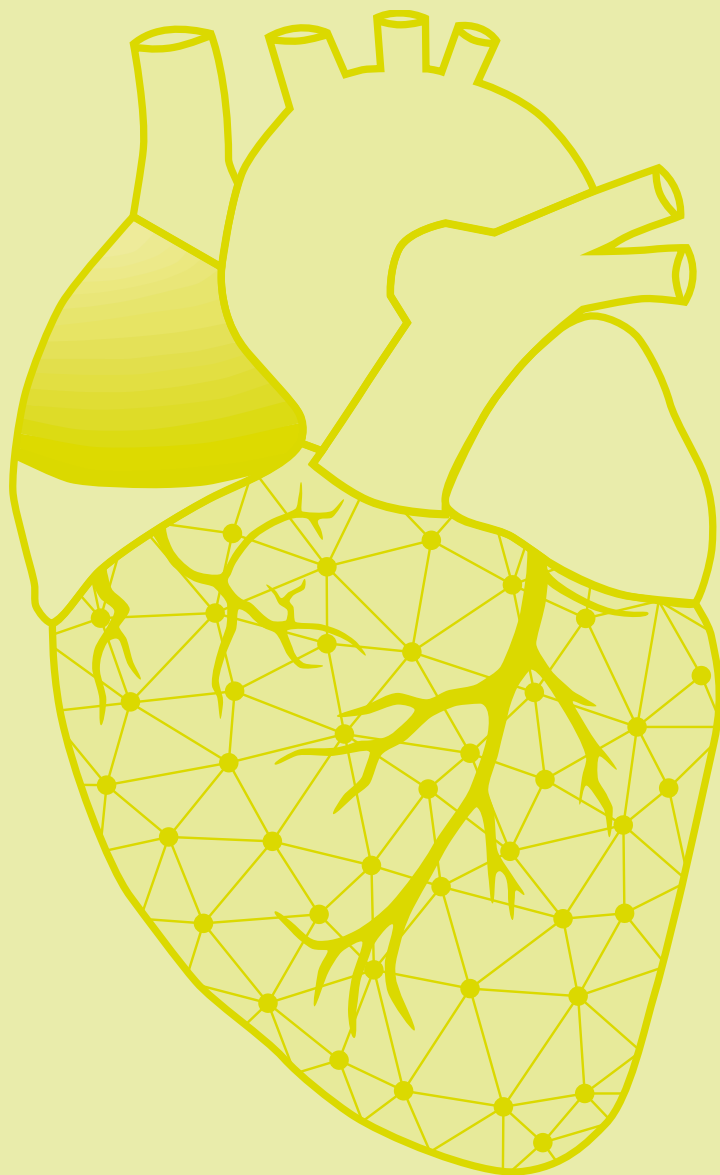
Chapter 15

A novel diagnostic tool to identify atrial endo-epicardial asynchrony using signal fingerprinting

Lu Zhang

Mathijs S. van Schie

Paul Knops

Yannick J.H.J. Taverne

Natasja M.S. de Groot

Abstract

Background: Patients with persistent atrial fibrillation (AF) have more electrical endo-epicardial asynchrony (EEA) during sinus rhythm (SR) than patients without AF. Prior mapping studies indicated that particularly unipolar, endo- and/or epicardial electrogram (EGM) morphology may be indicators of EEA. This study aims to develop a novel method for estimating the degree of EEA by using unipolar EGM characteristics recorded from either the endo- and/or epicardium.

Methods: Simultaneous endo-epicardial mapping during SR was performed in 86 patients. EGM characteristics, including unipolar voltages, low-voltage areas (LVAs), potential types (single, short/long double and fractionated potentials: SP, SDP, LDP and FP) and fractionation duration (FD) of double potentials (DP) and FP were compared between EEA and non-EEA areas. Asynchrony Fingerprinting Scores (AFS) containing quantified EGM characteristics were constructed to estimate the degree of EEA.

Results: Endo- and epicardial sites of EEA areas are characterized by lower unipolar voltages, a higher number of LDPs and FPs, and longer DP and FP durations. Patients with AF have lower potential voltages in EEA areas, along with alterations in the potential types. The EE-AFS, containing the proportion of endocardial LVAs and FD of epicardial DPs, had the highest predictive value for determining the degree of EEA (AUC: 0.913). Endo- and epi-AFS separately also showed good predictive values (AUC: 0.901 and 0.830 respectively).

Conclusions: EGM characteristics can be used to identify EEA areas. AFS can be utilized as a novel diagnostic tool for accurately estimating the degree of EEA. These characteristics potentially indicate AF related arrhythmogenic substrates.

Journal site &
supplementary material

Introduction

Electrical asynchrony between the endo- and epicardium contribute to the perpetuation of atrial fibrillation (AF).[1,2] Several mapping studies have demonstrated that endo-epicardial asynchrony (EEA) occurs during AF and is associated with AF severity.[3-7] Even during sinus rhythm (SR), it has been demonstrated that EEA was more apparent in individuals with persistent AF compared to those without AF.[8] Recently, van der Does et al.[9] found that, although local endo-epicardial discrepancies in electrogram (EGM) fractionation occurred infrequently, fractionated EGMs could originate from areas of EEA. It was also shown that unipolar EGMs are more suitable for identifying EEA than bipolar EGMs.[10] These observations indicate that unipolar, endo- and/or epicardial EGM characteristics during SR may contain information on the presence of EEA. However, the EGM characteristics that can be used to accurately identify EEA remain uknown.

In this study, the hypothesis that specific atrial unipolar endo- and/or epicardial EGM characteristics reflect areas of EEA and estimate the degree of EEA was tested. For this purpose, simultaneous endo-epicardial mapping was conducted and EGM characteristics between EEA and non-EEA areas were compared. In addition, a novel diagnostic tool, the Asynchrony Fingerprinting Score (AFS), using quantified EGM characteristics for estimation of the degree of EEA was introduced.

Methods

Study population

The study population consisted of 86 patients undergoing elective open-heart surgery (coronary artery bypass surgery, valvular heart surgery or a combination of both) in the Erasmus Medical Center Rotterdam. Patient characteristics (e.g., age, medical history and cardiovascular risk factors) were obtained from the patient's medical record. This study was approved by the institutional medical ethical committee (MEC2015-373) and written informed consent was obtained from all patients.

Simultaneous endo-epicardial mapping of the right atrium

Simultaneous endo-epicardial high-resolution mapping was performed prior to extra-corporal circulation. A summary of the methodology is provided in *Supplementary Figure 1A* and described in detail previously.[8] Two electrode arrays were used for simultaneously mapping of the endocardium and epicardium, each containing 128 (8×16) unipolar electrodes with a diameter of 0.45 mm and 2 mm interelectrode distance (IED). They were fixed on 2 bendable spatulas and were located on the exact opposite position of right atrial (RA) wall. After heparinization and arterial cannulation, the endocardial electrode array of spatula was introduced into the right atriotomy in which the venous canula will be inserted. The last row of electrodes of the endocardial spatula was introduced at least 1.5 cm into the RA to avoid overlap of the mapping area near the incision. To allow hemostatic measurements, the pursestring suture was secured. A temporal bipolar epicardial pacemaker wire was attached to the free wall as a reference electrode. An indifferent electrode was fixed to the subcutaneous tissue of the thoracic cavity. Simultaneous endo-epicardial mapping was performed at 3 different locations on the RA superior, mid and inferior free wall, as depicted in *Supplementary Figure 1A*. EGMs were recorded for 5 seconds during stable SR, including a surface electrocardiogram (ECG) lead, a calibration signal of 2 mV and 1000 ms and a bipolar reference EGM. Data were stored on a hard disk after sampling (1 kHz), amplification (gain 1000), filtering (bandwidth 0.5–400 Hz) and analog-to-digital conversion (16 bits).

Mapping Data analysis

Mapping data were analyzed using semi-automatized in custom-made Python 3.8 software. Premature and aberrant beats were excluded. Areas of simultaneous activation were also excluded from analysis in order to avoid inclusion of far-field potentials. All annotations were manually checked with a consensus of two investigators.

The steepest negative slope of a unipolar potential was annotated as local activation time (LAT) and used to compose color-coded activation maps.[11] As shown in the lower right panel of *Supplementary Figure 1*, potentials were classified into 4 types according to their morphology: 1. single potentials (SP), consisting of one single negative deflection; 2. double potentials (DP): a. short double potentials (SDP) containing two deflections separated by <15 ms; b. long double potentials (LDP), containing two deflection separated by ≥15 ms and 3. fractionated potentials (FP) composed of more than three deflections. Fractionation duration (FD) was defined as the time difference (ms) between the first and last deflection of double-(DP: SDP+LDP) and FP. Potential voltage was defined as the peak-to-peak amplitude of the steepest deflection and low-voltage areas (LVAs) as recordings sites from which potentials with voltages <1.0 mV were recorded.[12]

As shown in upper right panel of *Supplementary Figure 1*, endo-epicardial dissociation (EED) was determined by selecting the median of the LAT differences within the endo- and epicardial electrodes and its 8 surrounding electrodes from the opposite side.[8] When EED exceeded 15 ms between every endo-epicardial electrode pair, as previously described,

Table 1 – Baseline characteristics.

Patients	N=86
Male	68 (79.1%)
Age (y)	67 [61–72]
BMI (kg/m²)	27.9 [24.8–31.0]
Underlying heart disease	
• iHD	43 (50.0%)
• vHD	22 (25.6%)
• cHD	20 (23.2%)
• Arrhythmia	1 (1.2%)
History of AF	37 (43.0%)
• Paroxysmal	31 (36.0%)
• Persistent	4 (4.7%)
• Long-standing persistent	2 (2.3%)
Cardiovascular risk factors	
• Hypertension	54 (62.8%)
• Hypercholesterolemia	46 (53.5%)
• Diabetes mellitus	28 (32.6%)
Left ventricular function	
• Mild impairment (>50% LVEF ≥40%)	12 (14.0%)
• Moderate impairment (LVEF 30-39%)	10 (11.6%)
• Severe impairment (LVEF <30%)	1 (1.2%)
Antiarrhythmic agents	
• Class I	1 (1.2%)
• Class II	59 (68.6%)
• Class III	6 (7.0%)
• Class IV	6 (7.0%)

Values are presented as N (%) or median [IQR]. **BMI** = body mass index; **iHD** = ischemic heart disease; **vHD** = valvular heart disease; **cHD** = combined heart disease; **AF** = atrial fibrillation; **LVEF** = left ventricular ejection fraction.

Table 2 – EGM characteristics and endo-epicardial differences.

EGM features	Endocardium	Epicardium	*p*-value
Median voltage (mV)	4.65 [3.15–6.52]	7.01 [5.34–8.35]	<0.001
LVA (%)	4.22 [1.71–8.10]	2.86 [1.15–5.93]	0.024
SP (%)	81.62 [73.14–88.74]	83.31 [76.5–88.73]	0.295
SDP (%)	8.87 [6.67–12.42]	9.47 [6.96–13.09]	0.523
LDP (%)	5.12 [3.15–10.96]	3.98 [1.68–7.53]	0.019
FP (%)	1.66 [0.63–3.28]	1.33 [0.54–2.98]	0.351
FD (ms)			
FD-SDP	9 [8–10]	8 [6–9]	<0.001
FD-LDP	20 [18–24]	20 [18–25]	0.808
FD-DP	12 [10–16]	10 [7–12]	<0.001
FD-FP	22 [16–26]	20 [16–27]	0.968

Values are presented as median [IQR]. **EGM** = electrogram; **LVA** = low-voltage area; **SP** = single potential; **SDP** = short double potential; **LDP** = long double potential; **FP** = fractionated potential; **DP** = double potential; **FD** = fractionation duration.

it was defined as endo-epicardial asynchrony (EEA).[8] The total amount of EEA for each patient was calculated as the proportion (EEA%) of the total mapping area during the entire recording period. Patients who have more than the 50th percentile of EEA% measured in the entire study population were defined as a high-degree of EEA.

15

Statistical analysis

Normally distributed continuous variables were presented as mean ± standard deviation and skewed data were presented as median [25th–75th percentile]. A Mann–Whitney U test or Kruskal-Wallis test was used to compare differences between groups of non-normally distributed data. Categorical data were presented as numbers and percentages and compared with a χ^2 test. Spearman correlations were performed to determine correlations between endo- and epicardial EGM characteristics. Spearman's correlation coefficients were categorized as weak (<0.4), moderate (0.4-0.6) or strong (>0.6). A *p*-value of <0.05 was considered statistically significant. Statistically significant variables were included in the multivariate logistic regression analysis for predicting high-amount EEA. Statistical analyses were performed using Python (SciPy) and IBM SPSS Statistics version 26 (IBM Corp, Armonk, NY). *R* (4.2.1) software (rms, pROC and nomogramFormula package) was used to construct and visualize a nomogram as a tool for an Asynchrony Fingerprinting Score (AFS), as well as the receiver operator characteristic curve (ROC).
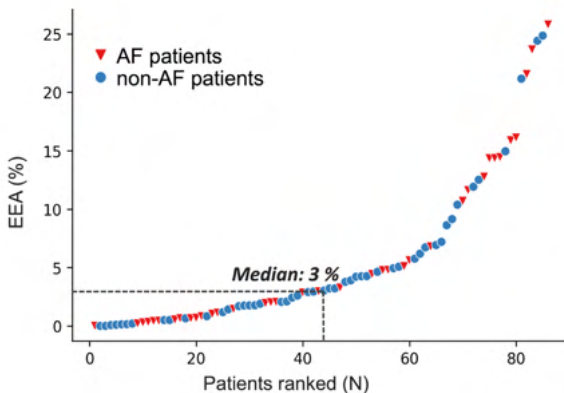
Figure 1 – The amount of EEA for each individual patient. Patients are ranked according to the increasing EEA (%). The median value of EEA (%) is marked by the median dot (3%). **EEA** = endo-epicardial asynchrony.
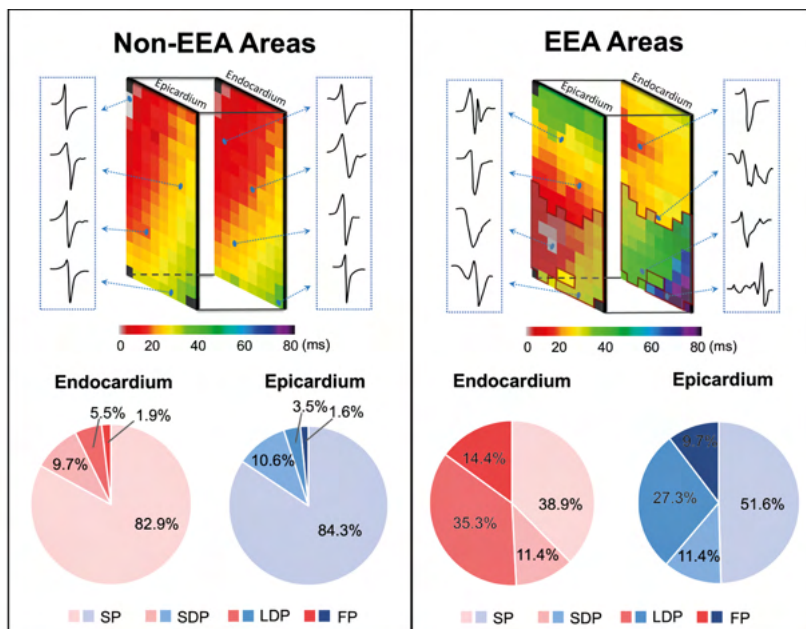
Figure 2 – Representative examples of potential types and their proportion in the non-EEA and EEA areas. *Upper panel*: two examples of activation maps depict non- and EEA areas; EEA areas were marked with scarlet red frame. *Lower panel*: the composition of potential types in non- and EEA areas at the endo- (red pies) and epicardium (blue pies). **SP** = single potential; **SDP** = short double potential; **LDP** = long double potential; **FP** = fractionated potential; **EEA** = endo-epicardial asynchrony.

Results

Study population

Clinical characteristics of the study population (N=86, age 67 [61–72] years, 68 male (79.1%)) are summarized in *Table 1*. Thirty-seven (43.0%) patients had a history of AF. Ischemic-, valvular heart disease or combined ischemic and valvular heart disease were present in respectively 43 (50.0%), 22 (25.6%) and 20 (23.3%) patients. Most patients used class II antiarrhythmic drugs (N=59, 68.6%).

Mapping Data

In the entire study population, a total of 1,641 (19±7.5 per patient) heart beats were recorded during sinus rhythm (876±190 ms). The resulting mapping locations consisted of 162,443 endocardial and 162,443 epicardial potentials.

As listed in *Table 2*, in every patient, endocardial voltages were lower than epicardial voltages (4.65 [3.15– 6.52] mV vs. 7.01 [5.34–8.35] mV, p<0.001). Correspondingly, LVAs were more frequently found at the endocardium (2.86 [1.15–5.93] % vs. 4.22 [1.71–8.10] %, p=0.024). The proportions of SP, SDP and FP at the endo- and epicardium did not differ; only LDP were more often recorded at the endocardium (5.1 [3.2–11.0] % vs. 4.0 [1.7–7.5] %, p=0.019). The FD of SDP was longer at the endocardium (9 [8–10] ms vs. 8 [6–9] ms, p<0.001) whereas FD of LDP and FP was comparable between both layers (LDP: 20 [18–24] ms vs. 20 [18–25] ms, p=0.808; FP: 22 [16–26] ms vs. 20 [16–27] ms, p=0.968).

In total, 9,474 (5.8%) areas of EEA were found in 83 (96.5%) patients. *Figure 1* illustrates the amount of EEA for each individual patient, which ranged from 0 to 25.8% (median: 3.0%).
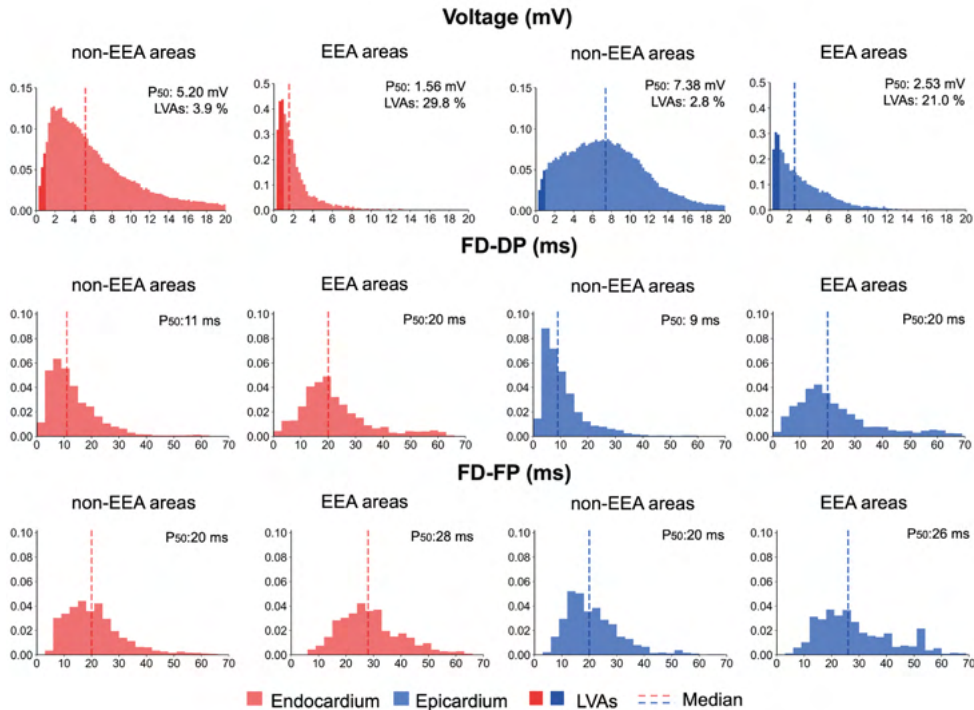
Figure 3 – Histograms of the relative frequency distribution of voltages and FD in the non- and EEA areas at the endo- and epicardium. Red and blue colors represent endocardial and epicardial mapping data, respectively. In the upper panel, LVAs are highlighted by darker colors. Dashed lines indicate median values. **FD** = fractionation duration; **DP** = double potential; **FP** = fractionated potential; **EEA** = endo-epicardial asynchrony; **LVAs** = low-voltage areas.

Potential fractionation in relation to EEA

The upper panel of *Figure 2* shows typical examples of non-EEA and EEA areas; potentials recorded from various electrodes scattered across the mapping array are depicted outside the activation maps. In non-EEA areas, mainly SP were found in contrast to EEA areas from which mainly non-SP were recorded.

The lower panel of *Figure 2* illustrates the proportion of various types of potentials in all mapping areas with and without EEA at both the endo- and epicardium. At areas of EEA, particularly the proportions of LDP (endocardium: 5.5% vs. 35.3%, epicardium: 3.5% vs. 27.3%) and FP (endocardium: 1.9% vs. 14.4%, epicardium: 1.6% vs. 9.7%) increased, at the expense of the proportion of SP (endocardium: 82.9% vs. 38.9%, epicardium: 84.3% vs. 51.6%). Hence, the composition of all potential types in EEA and non-EEA regions differed significantly (p<0.001).

Table 3 – The correlation of EGM characteristics between endo- and epicardium.

	Voltage (mV)	LVA (%)	SP (%)	SDP (%)	LDP (%)	FP (%)	FD-SDP (ms)	FD-LDP (ms)	FD-DP (ms)	FD-FP (ms)
Rho	0.681	0.753	0.749	0.589	0.702	0.603	0.245	0.444	0.475	0.289
***p*-value**	<0.001	<0.001	<0.001	<0.001	<0.001	<0.001	0.023	<0.001	<0.001	0.007

EGM = electrogram; **LVA** = low-voltage area; **SP** = single potential; **SDP** = short double potential; **LDP** = long double potential; **FP** = fractionated potential; **DP** = double potential; **FD** = fractionation duration.

Unipolar voltages in relation to EEA

Unipolar voltage distribution histograms in both non-EEA and EEA areas at the endo- and epicardium are depicted in the upper panel of *Figure 3*. At both layers, potential voltages in EEA areas were lower than non-EEA areas (endocardium: 5.20 [2.81–9.22] mV vs. 1.56 [0.89–2.70] mV, p<0.001; epicardium: 7.38 [4.36–10.61] mV vs. 2.53 [1.15–4.74] mV, p<0.001) and the proportion of LVAs was higher (endocardium: 3.9% vs. 29.8%, p<0.001; epicardium: 2.8% vs. 21.0%, p<0.001).

Fractionation duration (FD) in relation to EEA

The middle and lower panel of *Figure 3* shows the relative frequency distribution histograms of the FD of DP and FP measured in EEA and non-EEA areas at the endo- and epicardium separately. At both layers, FD of DP and FP in EEA areas were increased compared to non-EEA areas (FD-DP: endocardium: 11 [7–18] vs. 20 [15–28] ms, p<0.001; epicardium: 9 [6–14] vs. 20 [13–30] ms, FD-FP: endocardium: 20 [14–27] vs. 28 [21–36] ms, p<0.001; epicardium: 20 [15–27] vs. 26 [19–39] ms).

Correlation between endo-epicardial unipolar potential characteristics

The relationships between endo- and epicardial potential characteristics are listed in *Table 3*. There was a strong correlation between the endo-epicardial proportion of LVAs (r=0.753, p<0.001), while there was a moderate correlation between endo-epicardial potential voltages (r=0.681, p<0.001). With respect to the different potential types, only the amount of SP and LDP were strongly correlated (r=0.749, r=0.702, respectively, p<0.001) between both layers. There were moderate correlations between endo-epicardial SDP and FP (r=0.589, r=0.603, respectively, p<0.001). In addition, FD of LDP was moderately correlated (r=0.444, p<0.001), while the FDs of SDP and FP were weakly correlated (r=0.289, p=0.007; r=0.245, p=0.023, respectively).

Influence of AF episodes on unipolar potential characteristics in EEA areas

Of the 9,474 EEA areas, 4,373 (11.4%) were found in patients with history of AF, while 5,101 (8.9%) sites were found in patients without AF (p<0.001). As illustrated in *Table 4*, patients with AF had lower potential voltages in EEA areas at both the endo- and epicardium (endocardium: 1.66 [0.89–2.94] vs. 1.48 [0.88–2.45], p<0.001; epicardium: 3.01 [1.34–5.5] vs. 2.15 [1.03–3.82], p<0.001) compared to patients without AF, while the proportion of LVAs in

Table 4 – Subgroup analysis of EGM characteristics in EEA areas.

	Endocardium			Epicardium		
	non-AF	AF	*p*-value	non-AF	AF	*p*-value
Voltage (mV)	1.66 [0.89–2.94]	1.48 [0.88–2.45]	<0.001	3.01 [1.34–5.5]	2.15 [1.03–3.82]	<0.001
LVA (%)	29.2	30.6	0.289	18.4	24	<0.001
FD (ms)						
FD-SDP	20.0 [14.0–26.0]	20.0 [15.0–31.0]	<0.001	18.0 [13.0–26.0]	21.0 [15.0–33.0]	<0.001
FD-LDP	28.0 [21.0–37.0]	28.0 [21.0–37.0]	0.972	21.0 [15.0–28.0]	30.5 [22.0–42.0]	<0.001
Potential type (%)			<0.001			<0.001
SP	39.4	35.5		51.1	47.7	
SDP	11.5	11.8		13.8	9.2	
LDP	32.8	39.5		27.3	29.6	
FP	16.4	13.3		7.7	13.4	

Values are presented as median [IQR]. **EGM** = electrogram; **LVA** = low-voltage area; **SP** = single potential; **SDP** = short double potential; **LDP** = long double potential; **FP** = fractionated potential; **DP** = double potential; **FD** = fractionation duration.

Table 5 – Univariate and multivariate logistic regression analysis of EGM characteristics.

Univariate logistic regression	OR	95% CI for OR	*p*-value
Endocardium			
• Median voltage	0.673	0.542-0.836	<0.001
• LVA	1.623	1.314-2.004	<0.001
• SP%	0.927	0.885-0.971	0.001
• SDP%	1.01	0.928-1.100	0.81
• LDP%	1.196	1.083-1.322	<0.001
• FP%	1.348	1.086-1.674	0.007
• FD			
- FD-SDP	1.351	1.073-1.701	0.01
- FD-LDP	1.115	1.021-1.217	0.016
- FD-DP	1.314	1.151-1.501	<0.001
- FD-FP	1.071	1.015-1.129	0.011
Epicardium			
• Median voltage	0.597	0.457-0.780	<0.001
• LVA	1.497	1.213-1.847	<0.001
• SP%	0.916	0.868-0.966	0.001
• SDP%	1.047	0.968-1.133	0.249
• LDP%	1.28	1.113-1.472	0.001
• FP%	1.458	1.127-1.887	0.004
• FD			
- FD-SDP	1.38	1.071-1.780	0.013
- FD-LDP	1.121	1.036-1.214	0.005
- FD-DP	1.251	1.095-1.429	<0.001
- FD-FP	1.049	1.003-1.097	0.036
Multivariate logistic regression	**OR**	**95% CI for OR**	***p*-value**
Endocardium			
• LVA	1.644	1.307-2.068	<0.001
• SP%	0.916	0.861-0.975	0.006
Epicardium			
• Median voltage	0.647	0.489-0.856	0.002
• LDP%	1.185	1.037-1.354	0.012
EE			
• Endo LVA	1.728	1.334-2.238	<0.001
• Epi FD-DP	1.305	1.108-1.538	0.001

EGM = electrogram; **LVA** = low-voltage area; **SP** = single potential; **SDP** = short double potential; **LDP** = long double potential; **FP** = fractionated potential; **DP** = double potential; **FD** = fractionation duration; **Endo** = endocardial; **Epi** = epicardial; **EE** = endo- and epicardium.

15

AF patients was higher at the epicardium only (no AF: 18.4% vs. AF: 24.0%, p<0.001). Also, longer FD were found in patients with AF, with exception of FD of endocardial FP (28.0 [21.0–37.0] vs. 28.0 [21.0–37.0], p=0.972). A larger proportion of LDP was present at both layers in AF patients (endocardium: 32.8% vs. 39.5%; epicardium: 27.3 vs. 29.6%), while these patients had a lower proportion of FP at the endocardium, and a higher proportion at the epicardium (endocardium: 16.4% vs. 13.3%; epicardium: 7.7% vs. 13.4%).

Identification of potential characteristics predictive for EEA

Outcomes of uni- and multivariable logistic regression analyses to determine appropriate EGM characteristics for predicting the degree of EEA are depicted in *Table 5*. Univariable logistic analysis was performed between the degree of EEA and all endo- and epicardial potential characteristics. For both layers, all characteristics – except the proportion of SDP – were significantly associated with a higher degree of EEA.

Potential characteristics that were significantly related to EEA in univariable logistic regression were incorporated into multivariable regression models to establish the AFS. This
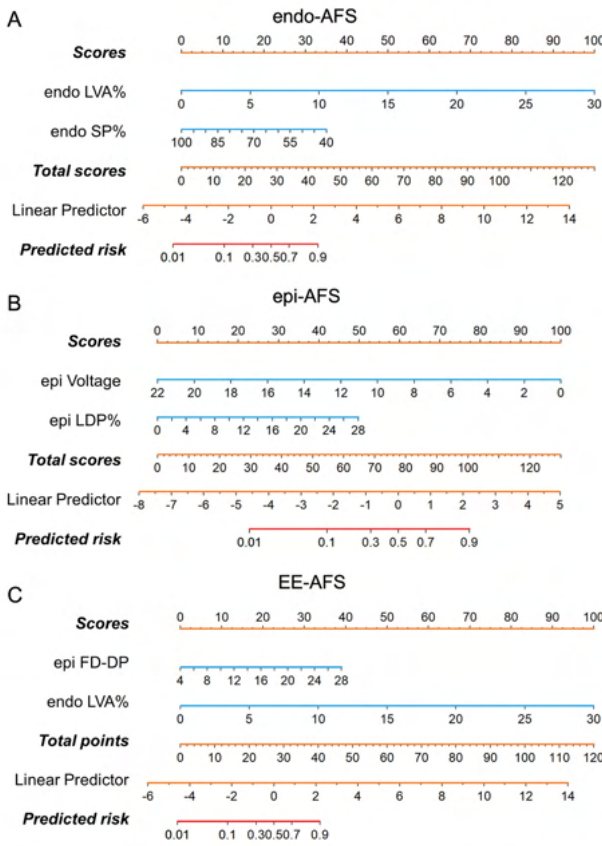
Figure 4 – Three types of AFS for quantifying the severity of EEA in the RA obtained from the endo- and/or epicardium. *Panel* A: endo-AFS. A nomogram was established using the endocardial amount of LVAs and SPs. *Panel B*: epi-AFS. A nomogram was established using unipolar potential voltages and amount of LDPs. *Panel C*: EE-AFS. A nomogram was established using epicardial FD-DP and endocardial amount of LVAs. The first row ('scores') is used as a scale to calculate the corresponding scores for each variable, resulting in total scores for each patient which can be used to determine the predicted risk based on the row of the total scores. **AFS** = Asynchrony Fingerprinting Score; **EEA** = endo-epicardial asynchrony; **LDP** = long double potential; **SP** = single potential; **FD** = fractionation duration; **LVAs** = low-voltage areas.
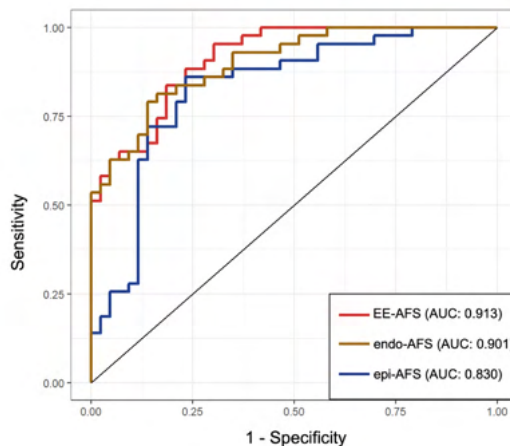
Figure 5 – ROC of the three types of AFS. The red, yellow and blue lines represent EE-AFS, endo-AFS and epi-AFS respectively. AUCs are depicted in the lower right box. **AFS** = Asynchrony Fingerprinting Score; **endo-AFS** = endocardial Asynchrony Fingerprinting Score; **epi-AFS** = epicardial Asynchrony Fingerprinting Score; **EE-AFS** = endo- and epicardial Asynchrony Fingerprinting Score.
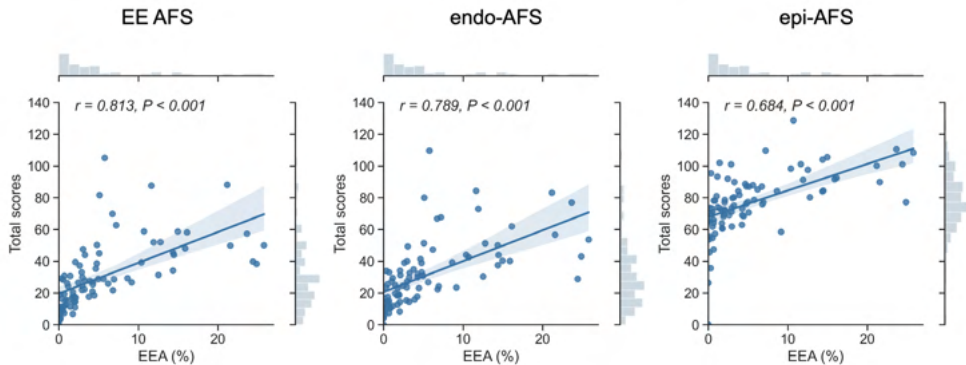
Figure 6 – Correlation plot of the total scores calculated by the three different types of AFS (EE-, endo- and epi-AFS) and the amount of EEA (%). AFS = Asynchrony Fingerprinting Score; **EEA** = endo-epicardial asynchrony; **endo-AFS** = endocardial Asynchrony Fingerprinting Score; **epi-AFS** = epicardial Asynchrony Fingerprinting Score; **EE-AFS** = endo- and epicardial Asynchrony Fingerprinting Score.

resulted in an endocardial AFS (endo-AFS) containing the proportion of LVAs (OR: 1.644, 95% CI: 1.307–2.068, p<0.001) and SPs (OR: 0.916, 95% CI: 0.861–0.975, p=0.006) and an epicardial AFS (epi-AFS) containing median voltages (OR: 0.647, 95% CI: 0.489–0.856, p=0.002) and the proportion of LDP (OR: 1.185, 95% CI: 1.037–1.354, p=0.012). For the AFS containing both endo- and epicardial EGM characteristics (EE-AFS), the proportion of endocardial LVAs (OR: 1.728, 95% CI: 1.334–2.238, p<0.001) and the FD of epicardial DP (OR: 1.305, 95% CI: 1.108–1.538, p=0.001) were included. The endo-/epi-AFS and EE-AFS are illustrated in *Figure 4*.

15

Assessment of the Asynchrony Fingerprint Scores (AFS)

Figure 5 demonstrates ROC-curves of the accuracy of the endo-/epi-AFS and EE-AFS in estimating the degree of EEA. Although the EE-AFS shows the best predictive value (AUC: 0.913, 95% CI: 0.860–0.967), both the endo-AFS and epi-AFS both also showed good discrimination with AUCs of 0.901 (95% CI: 0.840–0.962) and 0.830 (95% CI: 0.740–0.920) respectively.

Subsequently, the endo-AFS, epi-AFS and EE-AFS were computed for each individual patient and illustrated in *Figure 6*. EE-AFS has the best correlation with the amount of EEA per patient (r=0.813, p<0.001), although both the endo-AFS and epi-AFS also have a good correlation (r=0.789 and r=0.684, respectively, p<0.001 for both).

Discussion

Simultaneous endo-epicardial SR mapping of the human RA demonstrated that both endo- and epicardial areas of EEA are characterized by decreased potential voltages, an increase in the number of LDP and FP and prolongation of DP and FP durations. EE-AFS has the highest predictive value for identification of EEA and determining the amount of EEA. In addition, the AFS derived from solely the endo- or epicardium also has a good predictive value.

Endo-epicardial asynchrony

Discordant activation between the endo- and epicardium was initially described in isolated canine atria by Schuessler et al.[3] in 1993, by performing simultaneous endo-epicardial mapping. They observed that EEA increased during atrial tachyarrhythmias compared to SR and also demonstrated that EEA was correlated with heterogeneity of the anatomical

architecture of the RA, especially regions composed of pectinate muscles and cardiac fibers with different alignments. Several studies revealed that the severity of EEA is associated with AF progression in animal models.[4-6] Our research group performed simultaneous endo-epicardial high-resolution in-vivo mapping and provided evidence of EEA occurring during AF in human LA and RA.[7,13] A recent endo-epicardial mapping study in the RA showed that during SR, EEA was more frequently present in patients with persistent AF than patients without AF.[8] These observations indicate that the presence of EEA may not only be determined by the underlying anatomy, but also by pathological alterations of the tissue structure. This hypothesis is further supported by the results of the present study demonstrating clear differences in EGM characteristics derived from non-EEA and EEA areas. By comparing the EGM characteristics of EEA areas in patients with and without AF, we found that EEA areas in patients with AF were characterized by lower potential voltages, longer FD-DP, and a higher proportion of LDPs at both the endo- and epicardium. However, the proportion of low-voltage potentials and FD-FP in the endocardial EEA areas of AF patients was similar to patients without AF. This may because in the remodeled atrial areas, the loss of endo-epicardial coupling caused by structural remodeling, particularly at the epicardium, may facilitate the development of an arrhythmogenic substrate which resulted in EEA.[14] In addition, a growing amount of evidence indicates that inflammation plays a role in promoting both structural and electrical remodeling of the atria. These remodeling processes involve atrial fibrosis, modulation of gap junctions and abnormalities in intracellular calcium handling.[15-18] Ryu et al.[19] demonstrated a transmural gradient in Cx40 and Cx43 expression and a loss of epicardial myocytes in response to epicardial inflammation may provide the substrate for the abnormal atrial conduction including EEA. Further studies are needed to reveal the direct effect of inflammation on EEA.

EEA and unipolar voltages

In this study, endocardial unipolar potential voltages are considerably lower than epicardial potential voltages and correspondingly higher amounts of LVAs. This finding is in line with previous mapping studies performed in atria.[9,10,15] This may be attributed to the complex atrial structure which, particularly at the endocardium, contains a complex network of myocardial fibers. Irregular endocardial surfaces due to varying diameters of pectinate muscles, the presence of a thick and anisotropic terminal crest and branching of myocardial fibers may cause source-sink mismatches. Hence, conduction disorders and low-voltage, fractionated potentials develop. In addition, lack of good contact between the electrodes and atrial tissue, which occurs mainly at the endocardium, could potentially explain the observed endo-epicardial potential voltage differences. In addition, lower unipolar potential voltages were found in EEA areas at both the endo- and epicardium. LVAs were also more pronounced in EEA areas; even up to 29.8% at the endocardium. As potential voltage depends on e.g., catheter design, myocardial fiber orientation and cycle length, any chosen LVA-threshold remains questionable. In literature, different cut-off values have been used, depending on e.g., mapping system and patient features.[11] However, as endo- and epicardial potential voltages and the amount of LVAs were included in either the endo-/epi- and EE-AFS, potential voltage characteristics from both layers are good indicators of the presence of areas of EEA. A previous high-resolution epicardial mapping study performed in a cohort of 67 patients showed that during SR patients with a history of AF are characterized by lower potential voltages compared to patients without AF.[12] Recently, Van Schie et al.[20] studied the relationship between endo-epicardial voltages and their predictive potential for LVAs. They showed that unipolar and omnipolar LVAs are frequently located exclusively at either the endo- or epicardium. Therefore, a combined endo-epicardial mapping approach was proposed to accurately identify dual-layer LVAs. Numerous other studies suggested that LVAs, whether unipolar or bipolar, are considered surrogate markers for the presence of

local fibrotic tissue.[21,22] Also, the existence and extensiveness of LVAs have been shown to be a powerful predictor of arrhythmia recurrence.[23,24] We now demonstrated that decreased unipolar potential voltages are indicative of EEA areas and could also be used to estimate the amount of EEA during SR.

EEA and fractionated EGMs

Fractionated EGMs are mainly regarded as a combination of multiple electrical signals caused by asynchronous activation of adjacent cardiomyocytes.[25] Several studies have shown that the clinical beneficial effect of ablation targeting complex fractionated atrial electrograms (CFAEs) is still controversial as CFAEs may have multiple causes of both pathologic and non-pathologic origin.[26-28] Fractionated of EGMs can be either physiological or pathological in nature caused by structural or cellular barriers. Pathological factors include e.g., collagen deposition which separates adjacent myocardial cells giving rise to intra-atrial inhomogeneous conduction, including conduction block and/or EEA.[29-32] The resulting asynchronous activation of atrial tissue causes fractionation of potentials. Previous simultaneous endo-epicardial mapping studies demonstrated that fractionation of unipolar EGMs during SR can be attributed to asynchronous activation of the endo- and epicardial wall[9], whereas bipolar EGMs demonstrated to be less ideal for detection of EEA.[10] By further investigating the relationship between fractionated EGMs and EEA using unipolar EGMs, we demonstrated for the first time that LDPs are most often linked to EEA in comparison to SDP and FP. Also, particularly fractionated EGMs with lower potential voltages and prolonged FD are recorded from EEA areas. Our results showed that LDP and FD of DP were the most sensitive potential characteristics to detect EEA within the atrial wall during SR, indicating the presence of extensive intramural conduction block resulting in EEA.

Clinical implications

In previous experimental and clinical mapping studies, it has been demonstrated that EEA may contribute to the perpetuation of AF. In the current study, we performed simultaneous endo-epicardial high-resolution mapping of the human right atrium and demonstrated that EEA areas characterized by lower potential voltages and a higher number of fractionated potentials. These features may aid in identifying EEA areas that may be potential targets for AF therapy. Moreover, three different types of AFS were created (endo-/epi-AFS and EE-AFS) for identifying and determining the degree of EEA. Not surprisingly, EE-AFS has the most accurate predictive value compared to the single-layer AFS as it contains more information from both atrial layers. Nevertheless, the three different AFS all showed good performance for predicting EEA. This indicates that AFS might be a potential diagnostic tool to classify patients according to the severity of EEA and enables a more personalized AF ablation strategy. As both single-layer AFS could also be used, the degree of EEA can be estimated by performing either endo- or epicardial mapping alone.

Limitations

Only limited areas of the right atrial free wall and the left atrium was not studied due to the risk of air embolisms. Given the association between EEA and AF, future studies should validate the proposed AFS in the left atrium.

Conclusions

In human RA, areas of EEA are mainly characterized by decreased potential voltages, an increase in the number of LDP and FP, and prolongation of DP and FP durations. The amount

15

of EEA areas can be most accurately determined by the EE-AFS, incorporating epicardial FD-DP and amount of endocardial LVAs, or the AFS derived from solely the endo- or epicardium. Therefore, AFS, as a novel approach utilizing integrated data from the endo- and/or epicardium, may enable precise determination of the amount of EEA, including potentially AF related arrhythmogenic substrates.

References

1.   de Groot NM, Houben RP, Smeets JL, Boersma E, Schotten U, Schalij MJ, Crijns H, Allessie MA. Electropathological substrate of longstanding persistent atrial fibrillation in patients with structural heart disease: epicardial breakthrough. Circulation. 2010;122:1674-1682.

2.   Hansen BJ, Zhao J, Csepe TA, Moore BT, Li N, Jayne LA, Kalyanasundaram A, Lim P, Bratasz A, Powell KA, et al. Atrial fibrillation driven by micro-anatomic intramural re-entry revealed by simultaneous sub-epicardial and sub-endocardial optical mapping in explanted human hearts. Eur Heart J. 2015;36:2390-2401.

3.   Schuessler RB, Kawamoto T, Hand DE, Mitsuno M, Bromberg BI, Cox JL, Boineau JP. Simultaneous epicardial and endocardial activation sequence mapping in the isolated canine right atrium. Circulation. 1993;88:250-263.

4.   Everett THt, Wilson EE, Hulley GS, Olgin JE. Transmural characteristics of atrial fibrillation in canine models of structural and electrical atrial remodeling assessed by simultaneous epicardial and endocardial mapping. Heart Rhythm. 2010;7:506-517.

5.   Eckstein J, Maesen B, Linz D, Zeemering S, van Hunnik A, Verheule S, Allessie M, Schotten U. Time course and mechanisms of endo-epicardial electrical dissociation during atrial fibrillation in the goat. Cardiovasc Res. 2011;89:816-824.

6.   Eckstein J, Zeemering S, Linz D, Maesen B, Verheule S, van Hunnik A, Crijns H, Allessie MA, Schotten U. Transmural conduction is the predominant mechanism of breakthrough during atrial fibrillation: evidence from simultaneous endo-epicardial high-density activation mapping. Circ Arrhythm Electrophysiol. 2013;6:334-341.

7.   de Groot N, van der Does L, Yaksh A, Lanters E, Teuwen C, Knops P, van de Woestijne P, Bekkers J, Kik C, Bogers A, et al. Direct Proof of Endo-Epicardial Asynchrony of the Atrial Wall During Atrial Fibrillation in Humans. Circ Arrhythm Electrophysiol. 2016;9.

8.   Kharbanda RK, Knops P, van der Does L, Kik C, Taverne Y, Roos-Serote MC, Heida A, Oei FBS, Bogers A, de Groot NMS. Simultaneous Endo-Epicardial Mapping of the Human Right Atrium: Unraveling Atrial Excitation. J Am Heart Assoc. 2020;9:e017069.

9.   van der Does L, Knops P, Teuwen CP, Serban C, Starreveld R, Lanters EAH, Mouws E, Kik C, Bogers A, de Groot NMS. Unipolar atrial electrogram morphology from an epicardial and endocardial perspective. Heart Rhythm. 2018;15:879-887.

10.   van der Does L, Starreveld R, Kharbanda RK, Knops P, Kik C, Bogers A, de Groot NMS. Detection of Endo-epicardial Asynchrony in the Atrial Wall Using One-Sided Unipolar and Bipolar Electrograms. J Cardiovasc Transl Res. 2021;14:902-911.

11.   de Groot NMS, Shah D, Boyle PM, Anter E, Clifford GD, Deisenhofer I, Deneke T, van Dessel P, Doessel O, Dilaveris P, et al. Critical appraisal of technologies to assess electrical activity during atrial fibrillation: a position paper from the European Heart Rhythm Association and European Society of Cardiology Working Group on eCardiology in collaboration with the Heart Rhythm Society, Asia Pacific Heart Rhythm Society, Latin American Heart Rhythm Society and Computing in Cardiology. Europace. 2021.

12.   van Schie MS, Starreveld R, Bogers A, de Groot NMS. Sinus rhythm voltage fingerprinting in patients with mitral valve disease using a high-density epicardial mapping approach. Europace. 2021;23:469-478.

13.   Kharbanda RK, Kik C, Knops P, Bogers A, de Groot NMS. First Evidence of Endo-Epicardial Asynchrony of the Left Atrial Wall in Humans. JACC Case Rep. 2020;2:745-749.

14.   Maesen B, Zeemering S, Afonso C, Eckstein J, Burton RA, van Hunnik A, Stuckey DJ, Tyler D, Maessen J, Grau V, et al. Rearrangement of atrial bundle architecture and consequent changes in anisotropy of conduction constitute the 3-dimensional substrate for atrial fibrillation. Circ Arrhythm Electrophysiol. 2013;6:967-975.

15.   Saba S, Janczewski AM, Baker LC, Shusterman V, Gursoy EC, Feldman AM, Salama G, McTiernan CF, London B. Atrial contractile dysfunction, fibrosis, and arrhythmias in a mouse model of cardiomyopathy secondary to cardiac-specific overexpression of tumor necrosis factor-alpha. Am J Physiol Heart Circ Physiol. 2005;289:H1456-1467.

16.   Liew R, Khairunnisa K, Gu Y, Tee N, Yin NO, Naylynn TM, Moe KT. Role of tumor necrosis factor-alpha in the pathogenesis of atrial fibrosis and development of an arrhythmogenic substrate. Circ J. 2013;77:1171-1179.

17.   Baum JR, Long B, Cabo C, Duffy HS. Myofibroblasts cause heterogeneous Cx43 reduction and are unlikely to be coupled to myocytes in the healing canine infarct. Am J Physiol Heart Circ Physiol. 2012;302:H790-800.

18.   Nattel S, Burstein B, Dobrev D. Atrial remodeling and atrial fibrillation: mechanisms and implications. Circ Arrhythm Electrophysiol. 2008;1:62-73.

19.   Ryu K, Li L, Khrestian CM, Matsumoto N, Sahadevan J, Ruehr ML, Van Wagoner DR, Efimov IR, Waldo AL. Effects of sterile pericarditis on connexins 40 and 43 in the atria: correlation with abnormal conduction and atrial arrhythmias. Am J Physiol Heart Circ Physiol. 2007;293:H1231-1241.

20.   Van Schie MS, Knops P, Zhang L, Van Schaagen FRN, Taverne Y, De Groot NMS. Detection of endo-epicardial atrial low-voltage areas using unipolar and omnipolar voltage mapping. Front Physiol. 2022;13:1030025.

21.   Huo Y, Gaspar T, Pohl M, Sitzy J, Richter U, Neudeck S, Mayer J, Kronborg MB, Piorkowski C. Prevalence and predictors of low voltage zones in the left atrium in patients with atrial fibrillation. Europace. 2018;20:956-962.

22.   Blandino A, Bianchi F, Grossi S, Biondi-Zoccai G, Conte MR, Gaido L, Gaita F, Scaglione M, Rametta F. Left Atrial Substrate Modification Targeting Low-Voltage Areas for Catheter Ablation of Atrial Fibrillation: A Systematic Review and Meta-Analysis. Pacing Clin Electrophysiol. 2017;40:199-212.

23.   Rolf S, Kircher S, Arya A, Eitel C, Sommer P, Richter S, Gaspar T, Bollmann A, Altmann D, Piedra C, et al. Tailored atrial substrate modification based on low-voltage areas in catheter ablation of atrial fibrillation. Circ Arrhythm Electrophysiol. 2014;7:825-833.

24.   Yang G, Yang B, Wei Y, Zhang F, Ju W, Chen H, Li M, Gu K, Lin Y, Wang B, et al. Catheter Ablation of Nonparoxysmal Atrial Fibrillation Using Electrophysiologically Guided Substrate Modification During Sinus Rhythm After

15

Pulmonary Vein Isolation. Circ Arrhythm Electrophysiol. 2016;9:e003382.

25. Narayan SM, Wright M, Derval N, Jadidi A, Forclaz A, Nault I, Miyazaki S, Sacher F, Bordachar P, Clementy J, et al. Classifying fractionated electrograms in human atrial fibrillation using monophasic action potentials and activation mapping: evidence for localized drivers, rate acceleration, and nonlocal signal etiologies. Heart Rhythm. 2011;8:244-253.

26. Providencia R, Lambiase PD, Srinivasan N, Ganesh Babu G, Bronis K, Ahsan S, Khan FZ, Chow AW, Rowland E, Lowe M, et al. Is There Still a Role for Complex Fractionated Atrial Electrogram Ablation in Addition to Pulmonary Vein Isolation in Patients With Paroxysmal and Persistent Atrial Fibrillation? Meta-Analysis of 1415 Patients. Circ Arrhythm Electrophysiol. 2015;8:1017-1029.

27. Verma A, Jiang CY, Betts TR, Chen J, Deisenhofer I, Mantovan R, Macle L, Morillo CA, Haverkamp W, Weerasooriya R, et al. Approaches to catheter ablation for persistent atrial fibrillation. N Engl J Med. 2015;372:1812-1822.

28. Calvert P, Lip GYH, Gupta D. Radiofrequency catheter ablation of atrial fibrillation: A review of techniques. Trends Cardiovasc Med. 2022.

29. Kostin S, Klein G, Szalay Z, Hein S, Bauer EP, Schaper J. Structural correlate of atrial fibrillation in human patients. Cardiovasc Res. 2002;54:361-379.

30. Gaudesius G, Miragoli M, Thomas SP, Rohr S. Coupling of cardiac electrical activity over extended distances by fibroblasts of cardiac origin. Circ Res. 2003;93:421-428.

31. de Bakker JM, Wittkampf FH. The pathophysiologic basis of fractionated and complex electrograms and the impact of recording techniques on their detection and interpretation. Circ Arrhythm Electrophysiol. 2010;3:204-213.

32. Gardner PI, Ursell PC, Fenoglio JJ, Jr., Wit AL. Electrophysiologic and anatomic basis for fractionated electrograms recorded from healed myocardial infarcts. Circulation. 1985;72:596-611.

15
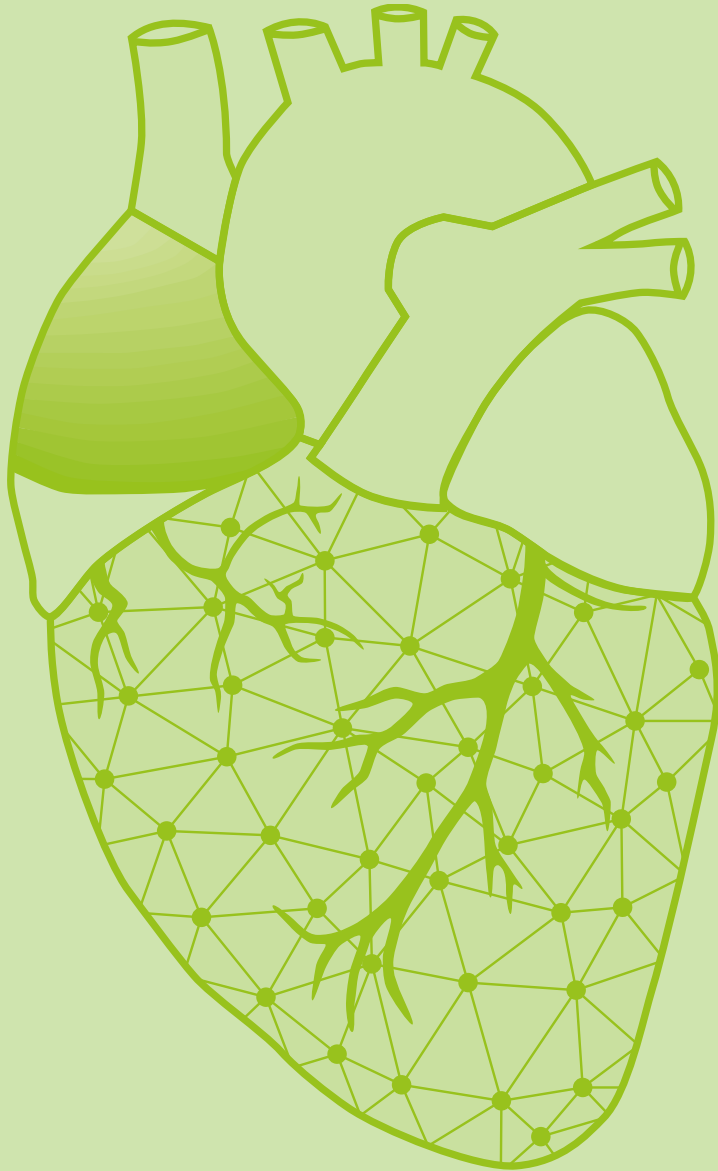
Chapter 16

Identification of atrial transmural conduction inhomogeneity using unipolar electrogram morphology

Lu Zhang

Mathijs S. van Schie

Hongxian Xiang

Rongheng Liao

Jiahao Zheng

Paul Knops

Yannick J.H.J. Taverne

Natasja M.S. de Groot

Abstract

Background: Structural remodeling plays an important role in the pathophysiology of atrial fibrillation (AF). It is likely that structural remodeling occurs transmurally, giving rise to electrical endo-epicardial asynchrony (EEA). Recent studies have suggested that areas of EEA may be suitable targets for ablation therapy of AF. We hypothesized that the degree of EEA is more pronounced in areas of transmural conduction block (T-CB) than single-sided CB (SS-CB). This study examined to which degree SS-CB and T-CB enhance EEA and which specific unipolar potential morphology parameters are predictive for SS-CB or T-CB.

Methods: Simultaneous endo-epicardial mapping in the human right atrium (RA) was performed in 86 patients. Potential morphology parameters included unipolar potential voltages, low-voltage areas, potential complexity (long double and fractionated potentials: LDPs and FPs), and the duration of fractionation.

Results: EEA was mostly affected by the presence of T-CB areas. Lower potential voltages and more LDPs and FPs were observed in T-CB areas compared to SS-CB areas. Areas of T-CB could be most accurately predicted by combining epicardial potential morphology parameters, including potential voltages, fractionation and fractionation duration (AUC=0.91).

Conclusion: Electrical conduction delay between the endo- and epicardium is mostly affected by the presence of transmural areas of CB, which can be most accurately predicted by combining epicardial potential morphology parameters. If these areas play a pivotal role in the pathophysiology of AF, they could theoretically be used as target sites for ablation.

Journal site &
supplementary material

Introduction

Structural remodeling plays an important role in the pathophysiology of atrial fibrillation (AF).[1,2] Although there is still ongoing debate on the mechanism underlying AF, several main theories have been described over the past few years, as recently discussed in the 2023 ACC/AHA/ACCP/HRS Guideline for the Diagnosis and Management of Atrial Fibrillation.[3] Key elements in the pathophysiology of persistent AF are areas of conduction block (CB) and electrical asynchrony between the endo- and epicardial layers.[2,4-8] Prior mapping studies demonstrated that even during sinus rhythm, CB is more prevalent in patients with AF compared to patients without AF.[9] The increase in conduction disorders can be explained by a higher degree of structural remodeling consisting of e.g., interstitial fibrosis and proteostasis derailment, which occurs not only at the endo- or epicardium but also transmurally.[10-12]

Previous simultaneous endo-epicardial mapping studies demonstrated that lines of CB can be located at either the endo- or epicardium only (single-sided (SS-CB)) or at both layers (transmural CB (T-CB)).[13] Areas of CB give rise to abnormalities in potential morphology, including a reduction in voltage and fractionation.[14-16] It is likely that CB enhances endo-epicardial delay (EED), although this relationship has so far not been confirmed. Recently, it has been suggested that AF can be treated by ablation therapy of areas of endo-epicardial asynchrony.[17] We hypothesize that the degree of EED is more pronounced in areas of T-CB than SS-CB at either the endo- or epicardium. Hence, we investigated the degree to which SS-CB and T-CB enhance EED and whether unipolar potential morphology associated with the different types of CB is predictive for T-CB.

16

Methods

Study population

Eighty-six patients (68 (79%) male, age: 67 [61–72] years) undergoing cardiac surgery for coronary artery disease (N=43), heart valve disease (N=42), or arrhythmia surgery (N=1) in the Erasmus Medical Center Rotterdam were included. The study was conducted according to the guidelines of the Declaration of Helsinki, and approved by the Institutional Medical Ethics Committee of Erasmus MC (MEC2015-373, 29 October 2015). Written informed consent was obtained from all patients. Patient characteristics (e.g., age, medical history and cardiovascular risk factors) were obtained from each patient's medical record. Patients with hemodynamic instability, atrial paced rhythm, previous open cardiac surgery, severe liver, or renal failure, or severely impaired left ventricular function were excluded from the study.

Simultaneous endo-epicardial mapping of the RA

The methodology of simultaneous endo-epicardial high-resolution mapping has been described in detail previously.[12] The mapping procedure was performed with two electrode arrays, each of which had 128 (8×16) unipolar electrodes with a 0.45 mm diameter and 2 mm interelectrode spacing. The arrays were secured on two flexible spatulas and positioned directly across from the right atrial (RA) wall. A temporal bipolar epicardial pacemaker wire was connected to the free wall as a reference electrode following heparinization and arterial cannulation. The indifferent electrode was anchored to the subcutaneous tissue of the thoracic cavity. After an incision into the RA appendage was made, the spatula designated as the endocardial electrode array was inserted, and the RA was subsequently closed with a purse-string suture.

Three separate areas on the superior, mid and inferior free walls of the RA underwent

simultaneous endo-epicardial mapping, as shown in *Supplementary Figure 1.* After the insertion of the final row of electrodes in the array, the endocardial spatula was inserted at least 1.5 cm deeper into the RA to prevent overlap of the mapping area close to the incision site. During stable sinus rhythm, electrograms (EGMs) were collected for 5 seconds. Surface ECG leads, a calibration signal of 2 mV and 1000 ms, and a bipolar reference EGM were all recorded. After sampling (1 kHz), amplification (gain 1000), filtering (bandwidth 0.5–400 Hz), and analog-to-digital conversion, data were saved on a hard drive (16 bits).

Mapping data analysis

Mapping data were evaluated using dedicated custom-made Python 3.8 software. Color-coded activation maps were created by annotating the steepest negative slope of a unipolar potential as local activation time (LAT). All annotations were manually reviewed by two investigators. As illustrated in *Supplementary Figure 1*, unipolar potentials were divided into four distinct groups according to their morphology, including 1) single potentials (SPs) consisting of a single negative deflection; 2) double potentials (DPs) subdivided into short double potentials (SDPs) and long double potentials (LDPs) containing two deflections separated by <15 ms and ≥15 ms, respectively; and 3) fractionated potentials (FPs) consisting of ≥3 deflections. Fractionation duration (FD) was defined as the time difference between the first and last deflection of non-single potentials.[19]

The peak-to-peak amplitude of the steepest deflection was defined as potential voltage, and low-voltage areas (LVAs) were defined as sites from which potentials with voltages <1.0 mV were recorded. Endo-epicardial dissociation (EED) was defined as LAT differences between the endo- and epicardial layers as previously described and EEA as an EED >15 ms.[7] The

Table 1 – Baseline characteristics.

Patients	N=86
Male	68 (79.1%)
Age (y)	67 [61–72]
BMI (kg/m²)	27.9 [24.8–31.0]
Underlying heart disease	
• iHD	43 (50.0%)
• vHD	22 (25.6%)
• cHD	20 (23.2%)
History of AF	37 (43.0%)
• Paroxysmal	31 (36.0%)
• Persistent	4 (4.7%)
• Long-standing persistent	2 (2.3%)
Cardiovascular risk factors	
• Hypertension	54 (62.8%)
• Hypercholesterolemia	46 (53.5%)
• Diabetes mellitus	28 (32.6%)
Left ventricular function	
• Mild impairment (>50% LVEF ≥40%)	12 (14.0%)
• Moderate impairment (LVEF 30-39%)	10 (11.6%)
• Severe impairment (LVEF <30%)	1 (1.2%)
Antiarrhythmic agents	
• Class I	1 (1.2%)
• Class II	59 (68.6%)
• Class III	6 (7.0%)
• Class IV	6 (7.0%)

Values are presented as N (%) or median [IQR]. **BMI** = body mass index; **iHD** = ischemic heart disease; **vHD** = valvular heart disease; **cHD** = combined heart disease; **AF** = atrial fibrillation; **LVEF** = left ventricular ejection fraction.

Figure 1 – Examples of color-coded activation maps demonstrating SS-CB$_{endo}$, SS-CB$_{epi}$ and T-CB areas constructed by simultaneous endo-epicardial mapping. Thick black lines indicate lines of CB and black arrows show the main activation wavefront trajectories. The numbers on the electrodes indicate the local activation time. Opposite endo-(blue) and epicardial (red) potentials are depicted below the activation maps. **A** = atrial potential; **CB** = conduction block; **endo** = endocardial; **epi** = epicardial; **SS-CB$_{endo}$** = endocardial single-sided conduction block; **SS-CB$_{epi}$** = epicardial single-sided conduction block; **T-CB** = transmural conduction block; **V** = ventricular far-field.

total amount of EEA for each patient was calculated as the proportion (EEA%) of the total mapping area.

Local CB was defined as an LAT difference of ≥12 ms between adjacent electrodes (*Supplementary Figure 1*), which corresponds to an effective conduction velocity of <19 cm/s as previously described.[8] SS-CB was defined as CB confined to only the endo- or epicardium and was referred to as SS-CB$_{endo}$ or SS-CB$_{epi}$, respectively. T-CB was defined as the presence of CB lines in opposite endocardial and epicardial mapping sites. In addition, all electrophysiological parameters were separately measured at electrodes adjacent to each line of CB.

Statistical analysis

Continuous variables with normally distributed distributions were displayed as mean ± standard deviation, whereas skewed data were given as median [25th–75th percentile]. The Mann–Whitney U test or the Kruskal-Wallis test was employed to compare differences across groups. The χ^2 test was used to compare categorical data provided as numbers and

Figure 2 – Amount of conduction block. *Left panel*: the amount of total CB at the endo- and epicardium for each individual patient; patients are ranked according to an increasing number of total CB (%). *Right panel*: the amount of SS-CB_endo, SS-CB_epi and T-CB for each patient. * *p*-value <0.05; ** *p*-value <0.01; *** *p*-value <0.001. **CB_endo** = endocardial conduction block; **CB_epi** = epicardial conduction block; **SS-CB_endo** = endocardial single-sided conduction block; **SS-CB_epi** = epicardial single-sided conduction block; **T-CB** = transmural conduction block.

percentages. A statistically significant *p*-value of 0.05 was used. IBM SPSS Statistics version 26 (IBM Corp, Armonk, NY) and Python 3.8 were used for statistical analysis.

Results

Study population

The characteristics of the population (n=86, age 67 [61–72] years, 68 (79.1%) male) are listed in *Table 1*. A history of AF was present in 37 (43.0%) patients.

Mapping data

A total of 1,641 (19±7.5 per patient) sinus rhythm beats were recorded (cycle length: 876±190 ms). A total of 162,443 potentials were recorded from both the endo- and epicardium (total: 324,886). Unipolar potential voltages at the endo- and epicardium were 4.65 [3.15–6.52] mV and 7.01 [5.34–8.35] mV, respectively (r=0.681, p<0.001). EEA was present in 5.8% of all mapping areas.

Table 2 – EGM characteristics in endo- and epicardial SS-CB and T-CB areas.

	SS-CB_endo/epi	T-CB	*p*-value
Endocardium			
Potential voltage (mV)	1.93 [1.03–3.47]	1.62 [0.95–2.86]	<0.001
EED (ms)	9 [4–15]	13 [6–21]	<0.001
FD (ms)			
FD-DP	16 [12–22]	20 [15–30]	<0.001
FD-FP	25 [19–33]	28 [20–36]	<0.001
Epicardium			
Potential voltage (mV)	2.11 [1.1–3.75]	1.67 [0.9–3.0]	<0.001
EED (ms)	8 [4–15]	13 [6–21]	<0.001
FD (ms)			
FD-DP	17 [12–25]	21 [14–31]	<0.001
FD-FP	23 [15–29]	23 [16–31]	0.392

EED = endo-epicardial delay; **DP** = double potential; **FD** = fractionation delay; **FP** = fractionated potential; **SS-CB_endo/epi** = endo- or epicardial single-sided conduction block; **T-CB** = transmural conduction block.
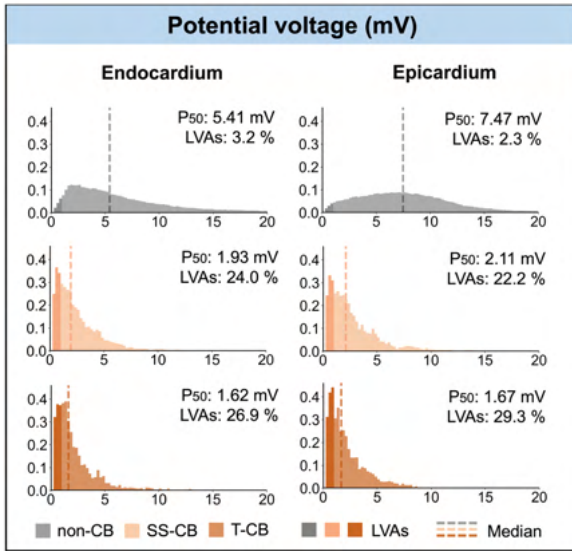
Figure 3 – Histograms of the relative frequency distribution of potential voltages in non-CB, SS-CB$_{endo/epi}$ and T-CB areas at the endocardium (left panel) and epicardium (right panel). Grey, peach puff and brown colors represent potential voltages in the non-CB, total CB, SS-CB and T-CB areas, respectively. Darker colors highlight LVAs. Dashed lines indicate median values. **CB** = conduction block; **SS-CB** = single-sided conduction block; **T-CB** = transmural conduction block; **LVA** = low-voltage area.

16

Prevalence of transmural conduction block

Figure 1 illustrates three opposite endo- and epicardial activation maps. These maps show SS-CB$_{endo}$, SS-CB$_{epi}$ and T-CB, as indicated by the thick black lines. T-CB was present at 4,301 recording sites which was 26.4% of the total amount of CB at the endocardium (N=16,307) and 37.1% of that at the epicardium (N= 11,594).
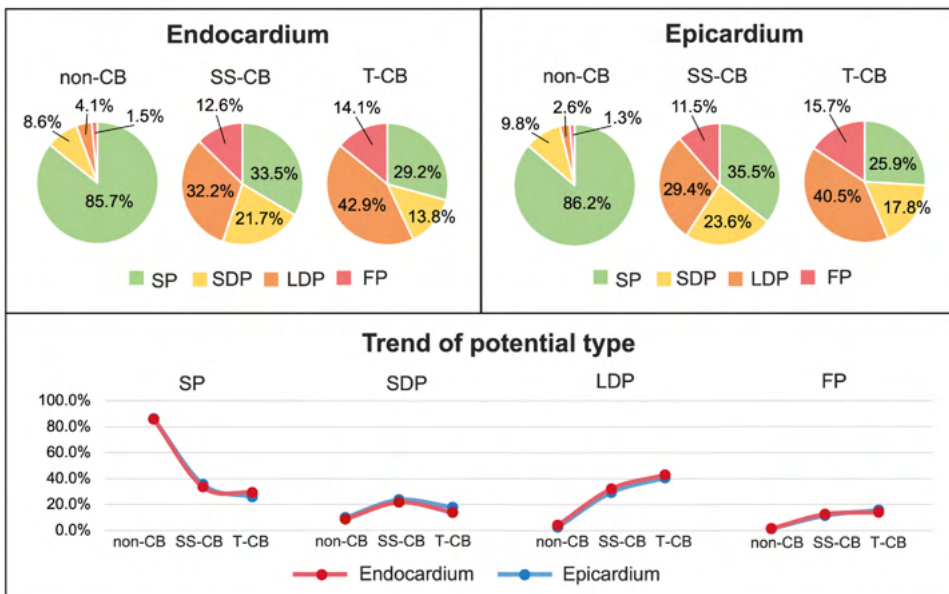
Figure 4 – Relationship between CB and potential types. *Upper panel*: composition of various potential types in non-CB, SS-CB and T-CB areas at endocardium (left) and epicardium (right), respectively. *Upper panel*: trends from non-CB to SS-CB$_{endo/epi}$ to T-CB areas for each potential type at the endocardium (red dots) and epicardium (blue dots), respectively. **CB** = conduction block; **SS-CB** = single-sided conduction block; **T-CB** = transmural conduction block; **SP** = single potential; **SDP** = short double potential; **LDP** = long double potential; **FP** = fractionated potential.
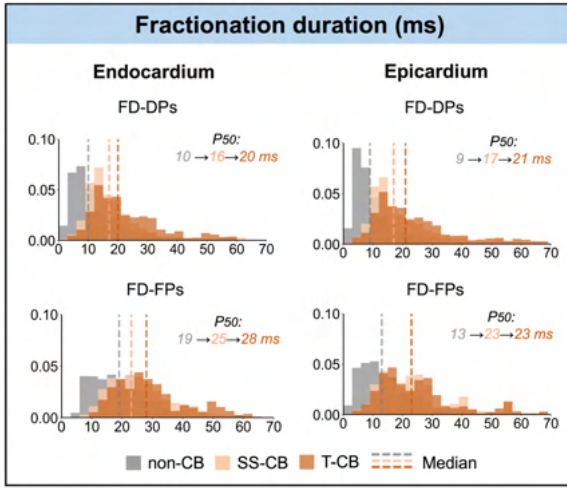
Figure 5 – Relative frequency distribution of FD in non-CB, SS-CB$_{endo/epi}$, and T-CB areas of the endocardium (left) and epicardium (right). Grey, peach puff and brown colors represent FD in the non-CB, total CB, SS-CB and T-CB areas, respectively. Dashed lines indicate median values. **CB** = conduction block; **SS-CB** = single-sided conduction block; **T-CB** = transmural conduction block; **FD** = fractionation duration; **DP** = double potential; **FP** = fractionated potential.

The left panel of *Figure 2* demonstrates the amount of total CB at the endo- and epicardium for each individual patient. Areas of CB were found in 85 (98.8%) and 82 (95.3%) patients at the endo- and epicardium, respectively; the corresponding proportions of CB areas ranged from 0 to 38.6% and 0 to 31.0%. CB areas were found more frequently at the endocardium than at the epicardium (9.9 [4.9–14.2] % vs 5.9 [3.1–11.1] %, p<0.001).

The right panel of *Figure 2* illustrates the amount of SS-CB$_{endo}$, SS-CB$_{epi}$ and T-CB for each patient separately. SS-CB was more frequently found at the endocardium than epicardium (7.25 [3.8–10.97] % vs 4.11 [1.81–6.49] %, p<0.001) and areas of SS-CB at either the endo- or epicardium occurred more frequently than T-CB (1.51 [0.35–4.2] %, p<0.001).
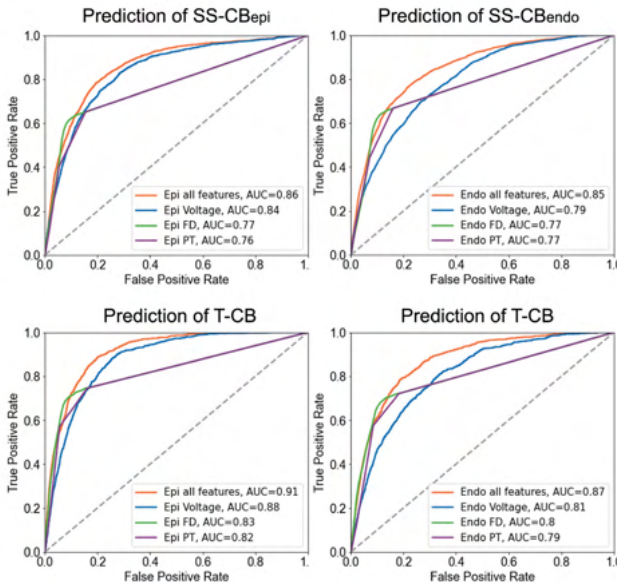
Figure 6 – ROC curves of the prediction of SS-CB$_{endo/epi}$ (upper panel) and T-CB areas (lower panel) based on EGMs features recorded from the endo- or epicardium. AUC = area under the curve; **SS-CB$_{endo}$** = endocardial single-sided conduction block; **SS-CB$_{epi}$** = epicardial single-sided conduction block; **T-CB** = transmural conduction block; **FD** = fractionation duration; **PT** = potential types.

Relation between different types of CB and EED

As listed in *Table 2*, EED was more pronounced in CB areas than non-CB areas (10 [5–17] ms vs. 3 [2–5] ms, p<0.001) and the largest degree of EED was found in T-CB areas (T-CB: 13 [6–21] ms vs. SS-CB$_{endo}$: 9 [4–15] ms and SS-CB$_{epi}$: 8 [4–15] ms, p<0.001).

T-CB and unipolar potential voltages

Figure 3 shows unipolar potential voltages in areas without CB and areas with SS-CB$_{endo}$, CB$_{epi}$ or T-CB. In areas of T-CB measured from either the endo- or epicardium, unipolar potential voltages were lower compared to those in areas of SS-CB at both the endocardium (1.62 [0.95–2.86] mV vs. 1.93 [1.03–3.47] mV, p<0.001) and epicardium (1.67 [0.9–3.0] mV vs. 2.11 [1.1–3.75] mV, p<0.001).

LVAs were rare at both the endo- and epicardial layer but were most prevalent in T-CB areas (endocardium: T-CB: 26.9% vs. SS-CB$_{endo}$: 24.0% vs. non-CB areas: 3.2%, p<0.001; epicardium: T-CB: 29.3% vs. SS-CB$_{endo}$: 22.2% vs. non-CB areas: 2.3%, p<0.001).

T-CB and unipolar potential morphology

Figure 4 shows the proportion of different potential types (SP, SDP, LDP and FP) in mapping areas with SS-CB or T-CB at the endo- and epicardium separately. At the endocardium, T-CB areas contained more LDP and FP, and less SP and SDP compared to SS-CB$_{endo}$ areas (SP: 29.2% vs. 33.5%, SDP: 13.8% vs. 21.7%, LDP: 42.9% vs. 32.2%, FP: 14.1% vs. 12.6%). Likewise, at the epicardium, T-CB areas also contained more LDP and FP, and less SP and SDP compared to SS-CB$_{epi}$ areas (SP: 25.9% vs. 35.6%, SDP: 17.8% vs. 23.6%, LDP: 40.5% vs. 29.4%, FP: 15.7% vs. 11.5%).

Figure 5 demonstrates the FD of DP and FP for the different categories of CB at the endo- and epicardium separately. FD of DP was most prolonged in areas of T-CB at both the endo- and epicardium (LDP: endocardium: T-CB: 20 [15–30] ms vs. SS-CB$_{endo}$: 16 [12–22] ms, p<0.001; epicardium: T-CB: 21 [14–31] ms vs. SS-CB$_{epi}$: 17 [12–25] ms, p<0.001). FD of FP was only prolonged in T-CB areas at the endocardium (T-CB: 28 [20–36] ms vs. SS-CB$_{endo}$: 25[19–33] ms, p<0.001).

Prediction of T-CB areas

Figure 6 demonstrates the receiver operating characteristic (ROC) curves of the accuracy of identifying SS-CB or T-CB areas using the potential morphology parameters. When using a single potential variable, unipolar potential voltages were the optimal parameter for predicting both SS-CB and T-CB. However, prediction of the different types of CB areas was most accurate when combining all three parameters (endocardium: SS-CB: AUC$_{endo}$=0.85, T-CB: AUC$_{endo}$=0.87, epicardium: SS-CB: AUC$_{epi}$=0.86, T-CB: AUC$_{epi}$=0.91). All epicardial potential morphology parameters were most accurate for prediction of T-CB and the epicardial potential voltage had the highest predictive value for T-CB areas (AUC=0.88).

Discussion

Electrical conduction delay between the endo-and epicardium is mostly affected by the presence of transmural areas of CB. These areas of T-CB can be most accurately predicted by combining epicardial potential morphology parameters, including voltages, fractionation and FD.

Endo-epicardial asynchrony related to transmural conduction block

Prior mapping studies demonstrated that focal waves and long lines of CB are key elements in AF persistence.[8,20] However, focal waves can only arise in the presence of EEA. Indeed, electrical asynchrony between the epi- and endocardial layers occurs more frequently in patients with persistent types of AF.[4] A previous simultaneous endo-epicardial mapping study showed that even during SR, a certain degree of EEA is present and may be more pronounced in patients with AF compared to patients without atrial tachyarrhythmias.[13] However, the relation between (different types of) CB and asynchrony between the endo- and epicardial layer has so far never been examined. In areas of SS-CB, a certain degree of endo-epicardial conduction delay was observed which further increased in T-CB areas. This may be explained by more severe structural remodeling such as deposition of fibrotic tissue or loss of cell-to-cell communications, which enhance discontinuities between the endo- and epicardium. This in turn results in an increase in the length of the activation pathway and hence prolonged differences in activation time between both layers.[4]

Potential morphology as indicator of transmural conduction block

The structure of the atrial wall has a considerable impact on elements of unipolar potential morphology such as potential voltages and fractionation.[16,21,22] It is assumed that LVAs may be surrogate indicators of arrhythmogenic substrates.[23-25] Indeed, in the present study, we showed that unipolar potential voltages were particularly lower in areas of T-CB compared to SS-CB, which confirmed the observations of Van Schie et al.[26], who demonstrated that unipolar potential voltages were lower near lines of CB. By correlating mapping data with the histology of atrial biopsies, the relation between low-voltage potentials and structural changes such as fibrotic depositions, increases in intercellular space, and myofibrillar loss has been confirmed.[27] In particular, voltages of epicardial potentials are related to T-CB, which may be explained by the considerably larger epicardial than endocardial potentials. Consequently, a moderate degree of remodeling may particularly affect the endocardial potential voltages as they are smaller than epicardial potential voltages, whereas a severe degree of remodeling will also affect the larger epicardial potential voltages.

As low-voltage areas commonly contain prolonged FPs and LDPs around lines of CB, they are also abundant in areas of T-CB. Hence, the combination of all three potential morphology parameters (potential voltages, fractionation and FD) is most accurate in identifying areas of T-CB.

Clinical implications

In the present study, we demonstrated that epicardial potential morphology parameters are particularly valuable in predicting areas of T-CB. In a previous mapping study, Van Schie et al.[28] also demonstrated that, in particular for voltage mapping, an epicardial approach is favored for identifying low-voltage areas. However, low-voltage areas frequently occurred only at either the endo- or epicardium alone and were not visible when recording from one side only. Although endocardial mapping is more standardly used in clinical practice, there is an increasing use of a so-called hybrid procedure for more persistent types of AF.[29-31] Using this hybrid approach, epicardial access would be possible and can more easily be performed. Using the suggested potential morphology parameters, areas of T-CB can thus be targeted with these procedures, which may eventually improve ablation outcomes. Recently, Tung et al.[17] described four cases in which endo-epicardial mapping of the left atrium during AF showed a significant degree of EEA and areas of T-CB. It was suggested that ablation therapies that achieve complete transmurality may be necessary to specifically direct treatment at the

epicardium. However, future studies should first reveal whether areas of T-CB play a pivotal role in the pathophysiology of AF.

Limitations

As we performed mapping in humans during cardiac surgery, we could not correlate mapping data with histological analysis of the right atrial free wall. We assumed that opposite endo-epicardial CB lines are representative of T-CB lines, but slow intramural zones of conduction could still be present. We only regarded exact opposite lines of CB as T-CB, but we cannot exclude that more oblique-orientated CB lines are also T-CB lines. Due to concerns regarding the possible presence of air embolisms in the left atrium, only the RA free wall was routinely investigated.

Conclusion

Electrical conduction delay between the endo- and epicardium is mostly affected by the presence of transmural areas of CB. Areas of T-CB can be most accurately predicted by combining epicardial potential voltages, fractionation and FD. Hence, we have identified potential features that can be used to locate T-CB areas which in turn are indicative of areas of endo-epicardial conduction delay. If these areas play a pivotal role in the pathophysiology of AF, they could theoretically be used as target sites for ablation.

16

References

1. Pytkowski M, Jankowska A, Maciag A, Kowalik I, Sterlinski M, Szwed H, Saumarez RC. Paroxysmal atrial fibrillation is associated with increased intra-atrial conduction delay. Europace. 2008;10:1415-1420.

2. Zaman JA, Harling L, Ashrafian H, Darzi A, Gooderham N, Athanasiou T, Peters NS. Post-operative atrial fibrillation is associated with a pre-existing structural and electrical substrate in human right atrial myocardium. Int J Cardiol. 2016;220:580-588.

3. Joglar JA, Chung MK, Armbruster AL, Benjamin EJ, Chyou JY, Cronin EM, Deswal A, Eckhardt LL, Goldberger ZD, Gopinathannair R, et al. 2023 ACC/AHA/ACCP/HRS Guideline for the Diagnosis and Management of Atrial Fibrillation: A Report of the American College of Cardiology/American Heart Association Joint Committee on Clinical Practice Guidelines. Circulation. 2024;149:e1-e156.

4. de Groot N, van der Does L, Yaksh A, Lanters E, Teuwen C, Knops P, van de Woestijne P, Bekkers J, Kik C, Bogers A, et al. Direct Proof of Endo-Epicardial Asynchrony of the Atrial Wall During Atrial Fibrillation in Humans. Circ Arrhythm Electrophysiol. 2016;9.

5. Schuessler RB, Kawamoto T, Hand DE, Mitsuno M, Bromberg BI, Cox JL, Boineau JP. Simultaneous epicardial and endocardial activation sequence mapping in the isolated canine right atrium. Circulation. 1993;88:250-263.

6. Eckstein J, Maesen B, Linz D, Zeemering S, van Hunnik A, Verheule S, Allessie M, Schotten U. Time course and mechanisms of endo-epicardial electrical dissociation during atrial fibrillation in the goat. Cardiovasc Res. 2011;89:816-824.

7. Ortiz J, Niwano S, Abe H, Rudy Y, Johnson NJ, Waldo AL. Mapping the conversion of atrial flutter to atrial fibrillation and atrial fibrillation to atrial flutter. Insights into mechanisms. Circ Res. 1994;74:882-894.

8. Allessie MA, de Groot NM, Houben RP, Schotten U, Boersma E, Smeets JL, Crijns HJ. Electropathological substrate of long-standing persistent atrial fibrillation in patients with structural heart disease: longitudinal dissociation. Circ Arrhythm Electrophysiol. 2010;3:606-615.

9. Heida A, van der Does WFB, van Staveren LN, Taverne Y, Roos-Serote MC, Bogers A, de Groot NMS. Conduction Heterogeneity: Impact of Underlying Heart Disease and Atrial Fibrillation. JACC Clin Electrophysiol. 2020;6:1844-1854.

10. Verheule S, Tuyls E, Gharaviri A, Hulsmans S, van Hunnik A, Kuiper M, Serroyen J, Zeemering S, Kuijpers NH, Schotten U. Loss of continuity in the thin epicardial layer because of endomysial fibrosis increases the complexity of atrial fibrillatory conduction. Circ Arrhythm Electrophysiol. 2013;6:202-211.

11. Gharaviri A, Bidar E, Potse M, Zeemering S, Verheule S, Pezzuto S, Krause R, Maessen JG, Auricchio A, Schotten U. Epicardial Fibrosis Explains Increased Endo-Epicardial Dissociation and Epicardial Breakthroughs in Human Atrial Fibrillation. Front Physiol. 2020;11:68.

12. Ramos KS, Li J, Wijdeveld LFJ, van Schie MS, Taverne Y, Boon RA, de Groot NMS, Brundel B. Long Noncoding RNA UCA1 Correlates With Electropathology in Patients With Atrial Fibrillation. JACC Clin Electrophysiol. 2023;9:1097-1107.

13. Kharbanda RK, Knops P, van der Does L, Kik C, Taverne Y, Roos-Serote MC, Heida A, Oei FBS, Bogers A, de Groot NMS. Simultaneous Endo-Epicardial Mapping of the Human Right Atrium: Unraveling Atrial Excitation. J Am Heart Assoc. 2020;9:e017069.

14. Jadidi AS, Duncan E, Miyazaki S, Lellouche N, Shah AJ, Forclaz A, Nault I, Wright M, Rivard L, Liu X, et al. Functional nature of electrogram fractionation demonstrated by left atrial high-density mapping. Circ Arrhythm Electrophysiol. 2012;5:32-42.

15. Ghoraani B, Dalvi R, Gizurarson S, Das M, Ha A, Suszko A, Krishnan S, Chauhan VS. Localized rotational activation in the left atrium during human atrial fibrillation: relationship to complex fractionated atrial electrograms and low-voltage zones. Heart Rhythm. 2013;10:1830-1838.

16. Ye Z, van Schie MS, de Groot NMS. Signal Fingerprinting as a Novel Diagnostic Tool to Identify Conduction Inhomogeneity. Front Physiol. 2021;12:652128.

17. Tung R, Burris R, Salazar P, Aziz Z. Human Recordings of Left Atrial Epicardial-Endocardial Asynchrony During Persistent Atrial Fibrillation. Circ Arrhythm Electrophysiol. 2022;15:e010605.

18. Knops P, Kik C, Bogers AJ, de Groot NM. Simultaneous endocardial and epicardial high-resolution mapping of the human right atrial wall. J Thorac Cardiovasc Surg. 2016;152:929-931.

19. de Groot NMS, Shah D, Boyle PM, Anter E, Clifford GD, Deisenhofer I, Deneke T, van Dessel P, Doessel O, Dilaveris P, et al. Critical appraisal of technologies to assess electrical activity during atrial fibrillation: a position paper from the European Heart Rhythm Association and European Society of Cardiology Working Group on eCardiology in collaboration with the Heart Rhythm Society, Asia Pacific Heart Rhythm Society, Latin American Heart Rhythm Society and Computing in Cardiology. Europace. 2022;24:313-330.

20. de Groot NM, Houben RP, Smeets JL, Boersma E, Schotten U, Schalij MJ, Crijns H, Allessie MA. Electropathological substrate of longstanding persistent atrial fibrillation in patients with structural heart disease: epicardial breakthrough. Circulation. 2010;122:1674-1682.

21. van der Does L, Knops P, Teuwen CP, Serban C, Starreveld R, Lanters EAH, Mouws E, Kik C, Bogers A, de Groot NMS. Unipolar atrial electrogram morphology from an epicardial and endocardial perspective. Heart Rhythm. 2018;15:879-887.

22. van der Does LJ, de Groot NM. Inhomogeneity and complexity in defining fractionated electrograms. Heart Rhythm. 2017;14:616-624.

23. Yamaguchi T, Otsubo T, Takahashi Y, Nakashima K, Fukui A, Hirota K, Ishii Y, Shinzato K, Osako R, Tahara M, et al. Atrial Structural Remodeling in Patients With Atrial Fibrillation Is a Diffuse Fibrotic Process: Evidence From High-Density Voltage Mapping and Atrial Biopsy. J Am Heart Assoc. 2022;11:e024521.

24. Hohendanner F, Romero I, Blaschke F, Heinzel FR, Pieske B, Boldt LH, Parwani AS. Extent and magnitude of low-

voltage areas assessed by ultra-high-density electroanatomical mapping correlate with left atrial function. Int J Cardiol. 2018;272:108-112.

25. Kurata N, Masuda M, Kanda T, Asai M, Iida O, Okamoto S, Ishihara T, Nanto K, Tsujimura T, Matsuda Y, et al. Left Atrial Localized Low-Voltage Areas Indicate Whole Left Atrial Electrophysiological Degeneration in Atrial Fibrillation Patients. Circ J. 2022;86:192-199.

26. van Schie MS, Starreveld R, Bogers A, de Groot NMS. Sinus rhythm voltage fingerprinting in patients with mitral valve disease using a high-density epicardial mapping approach. Europace. 2021;23:469-478.

27. Takahashi Y, Yamaguchi T, Otsubo T, Nakashima K, Shinzato K, Osako R, Shichida S, Kawano Y, Fukui A, Kawaguchi A, et al. Histological validation of atrial structural remodelling in patients with atrial fibrillation. Eur Heart J. 2023;44:3339-3353.

28. Van Schie MS, Knops P, Zhang L, Van Schaagen FRN, Taverne Y, De Groot NMS. Detection of endo-epicardial atrial low-voltage areas using unipolar and omnipolar voltage mapping. Front Physiol. 2022;13:1030025.

29. Zheng Z, Yao Y, Li H, Zheng L, Liu S, Lin H, Duan F. Simultaneous hybrid maze procedure for long-standing persistent atrial fibrillation with dilated atrium. JTCVS Techniques. 2021;5:34-42.

30. De Martino G, Compagnucci P, Mancusi C, Vassallo E, Calvanese C, Della Ratta G, Librera M, Franciulli M, Marino L, Russo AD, et al. Stepwise endo-/epicardial catheter ablation for atrial fibrillation: The Mediterranea approach. J Cardiovasc Electrophysiol. 2021;32:2107-2115.

31. Piorkowski C, Kronborg M, Hourdain J, Piorkowski J, Kirstein B, Neudeck S, Wechselberger S, Passler E, Lowen A, El-Armouche A, et al. Endo-/Epicardial Catheter Ablation of Atrial Fibrillation: Feasibility, Outcome, and Insights Into Arrhythmia Mechanisms. Circ Arrhythm Electrophysiol. 2018;11:e005748.

16
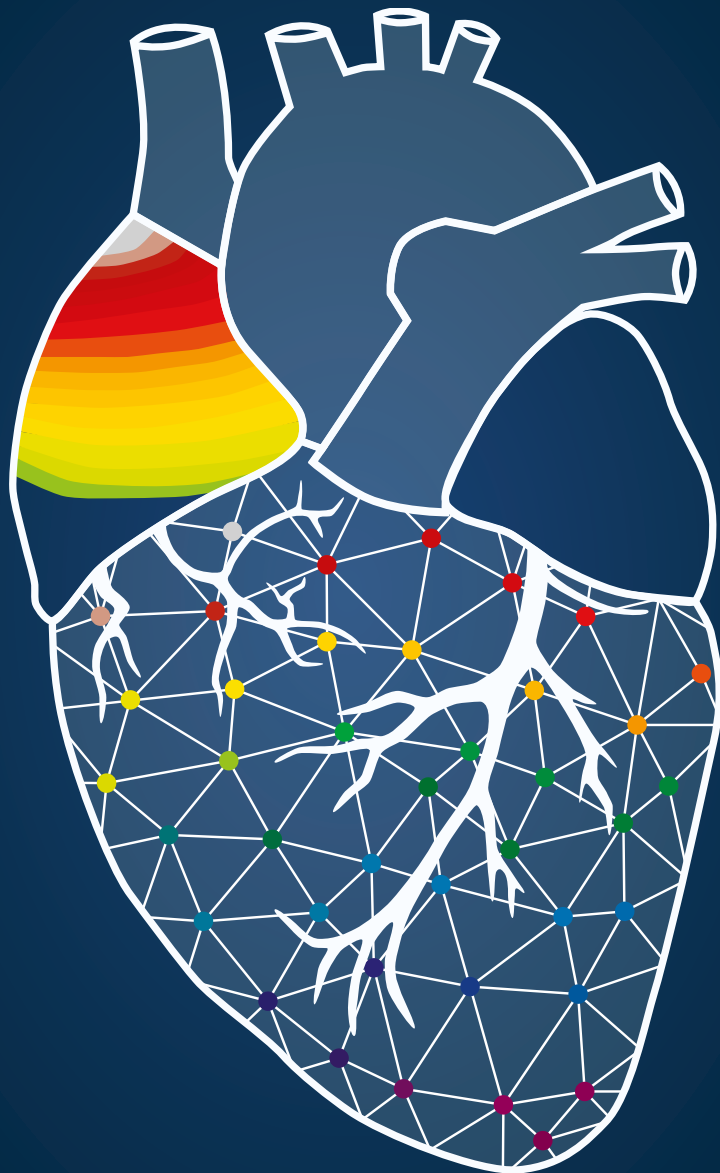
PART III

CONDUCTION HETEROGENEITY: ABNORMALITIES IN WAVEFRONT PROPAGATION
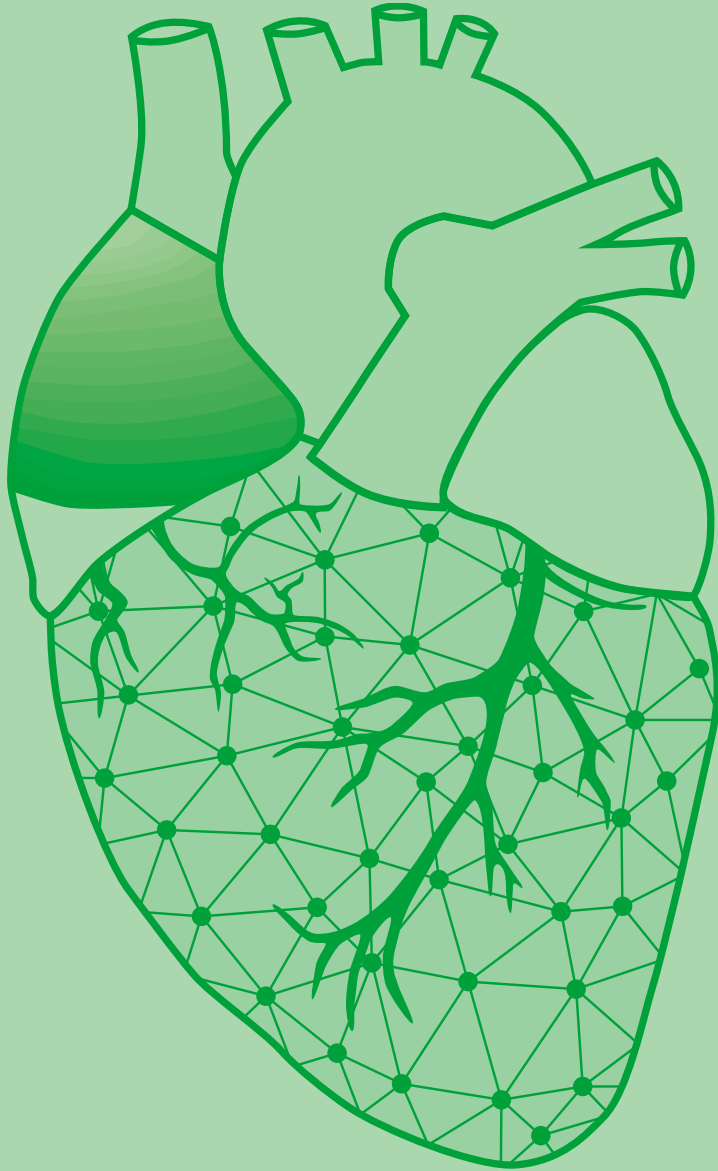
Chapter 17

First evidence of atrial conduction disorders in pediatric patients with congenital heart disease

Rohit K. Kharbanda

Mathijs S. van Schie

Nawin L. Ramdat Misier

Wouter J. van Leeuwen

Yannick J.H.J. Taverne

Pieter C. van de Woestijne

Janneke A.E. Kammeraad

Beatrijs Bartelds

Ad J.J.C. Bogers

Natasja M.S. de Groot

Abstract

This study sought to investigate whether pediatric patients with congenital heart disease (CHD) already have atrial conduction disorders early in life. The authors conducted first-in-children epicardial mapping in 10 pediatric patients with CHD undergoing primary open heart surgery. Areas of conduction delay (CD) and block (CB) were present in all patients and were particularly observed at Bachmann's bundle (CD: 4.9%; CB: 2.3%), followed by the right atrium (CD: 3.7%; CB: 1.6%) and, to a lesser degree, the left atrium (CD: 1.8%; CB: 1.0%). Conduction abnormalities may by aggravated over time (e.g., aging, residual lesions or valvular dysfunction), predisposing these patients to atrial arrhythmias early in life.

Journal site

Introduction

Abnormalities in myocardial conduction play a crucial role in both genesis and perpetuation of tachyarrhythmias. In patients with congenital heart disease (CHD), chronic volume and/or pressure overload is an important contributor to structural remodeling giving rise to atrial conduction abnormalities.[1] An inevitable consequence of this ageing population is the rising number of CHD patients presenting with complex atrial tachyarrhythmias such as atrial fibrillation (AF). Prior studies have demonstrated that acute atrial stretch causes atrial conduction abnormalities.[2,3] It is therefore likely that even relatively short-lasting volume/pressure overload early after birth causes atrial conduction abnormalities that might persist beyond CHD repair predisposing these patients to arrhythmias later in life.

At present, it is unknown whether, and to what extent, pediatric patients with CHD already have atrial conduction disorders early in life. To investigate the early effects of short-lasting volume/pressure overload on atrial conduction properties, we conducted epicardial high-density mapping in pediatric patients with CHD undergoing primary open-heart surgery.

Epicardial high density mapping approach

Parents gave informed consent to participate in the study protocol approved by the local ethics committee (MEC-2019-0543) of the Erasmus Medical Center Rotterdam. Epicardial mapping of the right atrial (RA) appendage, intercaval region, Bachmann's bundle (BB), left atrial (LA) appendage, and pulmonary vein region was performed before commencement of extracorporeal circulation (upper panel of *Figure 1*).[4] A custom-made electrode array (192 electrodes, electrode diameter 0.6 mm, interelectrode distance 2.1 mm) was used to record unipolar electrograms during sinus rhythm (SR). Local activation maps were constructed by annotating the steepest negative deflection. Because of a lack of any reference values and to be consistent with previous epicardial mapping studies, conduction delay (CD) and block

17
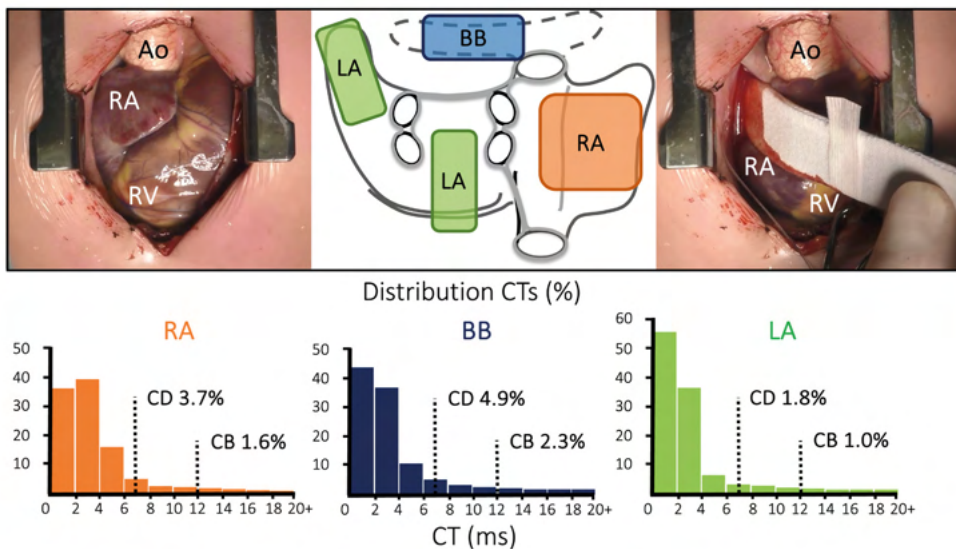
Figure 1 – First evidence of atrial conduction disorders in pediatric patients with congenital heart disease. *Upper panel*: intra-operative images of the mapping procedure and a schematic overview of the mapping sites from a posterior view of the atria. *Lower panel*: spatial distribution of conduction times specified for each atrial region separately. Percentages of CD and CB are depicted by dashed lines. **Ao** = aorta; **BB** = Bachmann's bundle; **CB** = conduction block; **CD** = conduction delay; **CT** = conduction time; **LA** = left atrium; **RA** = right atrium; **RV** = right ventricle.
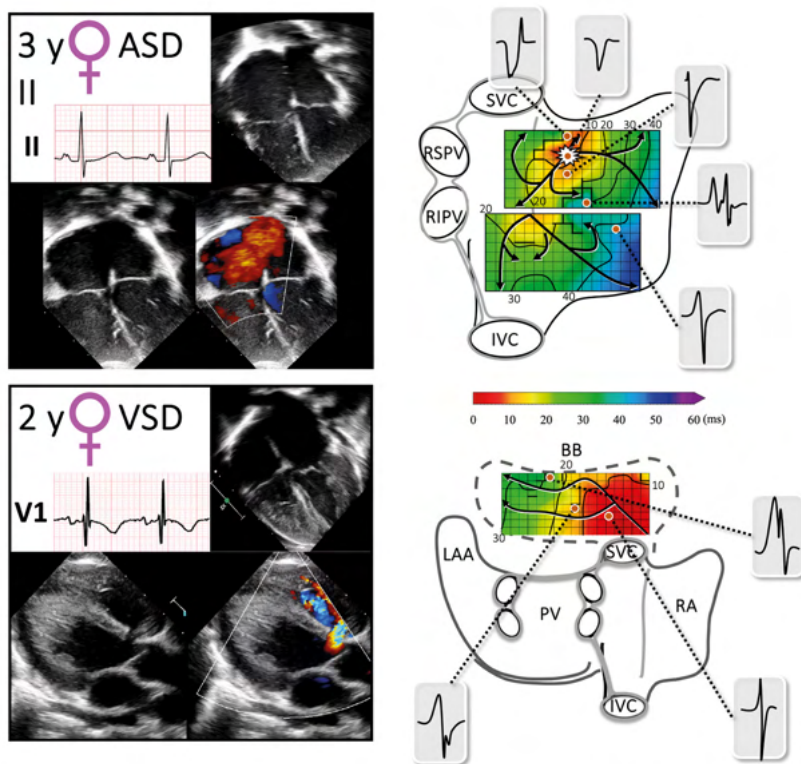
Figure 2 – Linking electro- and echocardiographic data with characteristics of epicardial atrial conduction. *Left panel*: signs of right and left atrial dilatation on different echocardiographic views and leads II and V1 from the surface ECG. *Right panel*: color-coded activation maps of the RA and BB. The arrows display the main trajectories of the electrical wavefront. Thick black lines indicate areas of CD and CB (CT>7ms). **BB** = Bachmann's bundle; **CB** = conduction block; **CD** = conduction delay; **CT** = conduction time; **IVC** = inferior vena cava; **LAA** = left atrial appendage; **PV** = pulmonary vein region; **RA** = right atrium; **SVC** = superior vena cava.

(CB) were defined as local conduction time (CT) differences of, respectively, 7 to 11 ms and ≥12 ms between adjacent electrodes, corresponding with effective conduction velocities of 17 to 29 cm/s for CD and <17 cm/s for CB.[4] The amount of CD and CB was calculated as a percentage of the total mapping area.

Study population

Our study population consists of 10 pediatric patients with CHD (median age: 6 months; range 3 to 43 months; female: n=5) scheduled for repair of an atrial septal defect type II (n=1), ventricular septal defect (n=7; 3 of them also have an atrial septal defect type II, and 2 have a patent foramen ovale), complete atrioventricular septal defect (n=1), and sinus venosus defect (n=1). Perimembranous and malalignment outlet ventricular septal defect were present in 6 patients and 1 patient, respectively. None of the patients had a history of atrial tachyarrhythmias.

Results

The upper left panel of *Figure 2* demonstrates signs of RA dilatation on apical 4-chamber echocardiographic view and lead II from the surface ECG from a patient with an atrial septal

defect type II. Color-coded activation maps of the RA are shown in the upper right panel. The SR wavefront originates from the superior part of the RA from where it spreads to the surrounding area in a radial fashion. Areas of CD and CB were found at both the superior and inferior RA, indicated by respectively crowding of the isochrones and thick black lines (CT >7 ms). The lower left panel of *Figure 2* shows signs of LA dilatation on apical 4-chamber echocardiographic view and lead V1 from the surface ECG in a 2-year-old patient with a perimembranous ventricular septal defect. As shown in the right lower panel of *Figure 2*, areas of conduction abnormalities are present in different parts of BB. The lower panel of *Figure 1* demonstrates the relative frequency distribution of CTs for all patients specified per atrial region. Areas of CD and CB were present in all patients and were particularly observed at BB (CD: 4.9% and CB: 2.3%), followed by the RA (CD: 3.7% and CB: 1.6%) and to a lesser degree in the LA (CD: 1.9% and CB: 1.0%). The amount of CD and CB in the entire atria ranged from 1.8–4.9% and 1.0–2.3%, respectively. The highest CTs measured at the RA, BB and LA were respectively 44, 25 and 23 ms. Conduction abnormalities in patients with an isolated ASD II (n=2) or VSD (n=2) were more pronounced at the RA (1.9%, maximal CT 34 ms) and BB (2.1%, maximal CT 17 ms), respectively. Post-operative atrial arrhythmias were not observed in the study population.

Discussion

In this first-in-children epicardial mapping study, we demonstrated, for the first time, that conduction abnormalities are already present early after birth in pediatric CHD patients without history of atrial tachyarrhythmias. In general, slowing of conduction was more pronounced at the RA (maximal CT 44 ms) and BB (maximal CT 25 ms).

Recently, Rouatbi et al.[5] investigated structural myocardial changes in the RA tissue of pediatric patients with an atrial septal defect and demonstrated that myocardial damage and fibrotic tissue are already present early in life. In line with these findings, we now provide the first evidence of conduction abnormalities in this population.

Epicardial mapping in 31 adult patients with congenital heart disease (age 49±14 years; 16% with a history of AF) also showed conduction abnormalities, particularly at the RA and BB rather than the LA.[4] Comparison of mapping data derived from pediatric and adult CHD patients with respectively short- and long-term volume overload shows that areas of conduction abnormalities are less extensive and severe in pediatric CHD patients. At present, our data suggests that the duration of volume overload and increase in the amount and extent of conduction disorders go hand in hand. Over time, our CHD epicardial mapping dataset will enable us to investigate the characteristics of atrial conduction disorders from childhood to adulthood and to correlate these findings with clinical characteristics such as age and type of CHD.

Conduction abnormalities at Bachmann's bundle

Based on several epicardial mapping studies, conduction abnormalities at BB are considered to play an important role in atrial arrhythmogenesis.[6] For the first time, we demonstrate that conduction abnormalities are already present at BB in pediatric CHD patients with right and left atrial volume overload.[7] The right side of BB is connected to the septum spurium and the left side is attached to the left atrioventricular ring bundle, which continues into the posterior LA wall including the pulmonary veins. Hence, from an anatomical point of view, BB is more attached to the LA than to the RA. Therefore, it is more likely that LA volume overload induces more stretch at BB than RA volume overload, eventually resulting in conduction abnormalities at BB.

17

Atrial conduction abnormalities: result of congenital heart disease or a physiological phenomenon?

The observed atrial conduction abnormalities in our study might be a result of: 1) structural remodeling induced by short-lasting volume/pressure overload; 2) genetically determined (e.g., abnormalities in cell structures relevant for electrical conduction); or 3) a physiological phenomenon. Because of the invasive nature of our pediatric epicedial mapping technique, it is not possible to study atrial conduction properties or histology at different right- and left atrial regions in healthy controls. However, other histological[5] and epicardial mapping[8] studies substantiate that presence of atrial conduction abnormalities in pediatric CHD patients is presumably a result of CHD rather than a physiological phenomenon.

Structural remodeling underlies development of conduction disorders. As Rouatbi et al.[5] demonstrated that myocardial damage and structural remodeling are present in a similar non-operated pediatric CHD group with RA volume overload, it is most likely that atrial structural remodeling is also present in our cohort giving rise to conduction abnormalities. Previous epicardial mapping studies in 25 patients with Wolff-Parkinson-White syndrome showed smooth right atrial conduction without any areas of conduction disorders.[8] None of these patients had a history of AF or atrial dilatation. Conduction times larger than 14 ms were not observed in these patients without structural heart disease. At present, there are no validated CT cut-off values for pediatric patients. In order not to overestimate areas of conduction abnormalities, we used the same cut-off values as used in adult patients during SR. In our pediatric cohort, we observed CTs up to 44 ms, which are presumably a result of CHD rather than a physiological phenomenon.

Limitations

Due to the invasive nature of our mapping technique, we did not perform epicardial mapping in pediatric patients without structural heart disease for comparison. In addition, endocardial mapping is not possible with the present epicardial mapping approach.

Conclusion

Epicardial mapping in pediatric patients with CHD revealed that atrial conduction abnormalities are already present before surgical correction in their first year of life, primarily at the RA and BB. Over time, surgical scar tissue, aging and volume/pressure overload from residual lesions or valvular dysfunction may aggravate these atrial conduction abnormalities, predisposing these patients to atrial arrhythmias early in life.

References

1. Stout KK, Daniels CJ, Aboulhosn JA, Bozkurt B, Broberg CS, Colman JM, Crumb SR, Dearani JA, Fuller S, Gurvitz M, et al. 2018 AHA/ACC Guideline for the Management of Adults With Congenital Heart Disease: A Report of the American College of Cardiology/American Heart Association Task Force on Clinical Practice Guidelines. J Am Coll Cardiol. 2019;73:e81-e192.
2. Ravelli F, Allessie M. Effects of atrial dilatation on refractory period and vulnerability to atrial fibrillation in the isolated Langendorff-perfused rabbit heart. Circulation. 1997;96:1686-1695.
3. Ravelli F, Mase M, del Greco M, Marini M, Disertori M. Acute atrial dilatation slows conduction and increases AF vulnerability in the human atrium. J Cardiovasc Electrophysiol. 2011;22:394-401.
4. Houck CA, Lanters EAH, Heida A, Taverne Y, van de Woestijne PC, Knops P, Roos-Serote MC, Roos-Hesselink JW, Bogers A, de Groot NMS. Distribution of Conduction Disorders in Patients With Congenital Heart Disease and Right Atrial Volume Overload. JACC Clin Electrophysiol. 2020;6:537-548.
5. Rouatbi H, Farhat N, Heying R, Gerard A, Vazquez-Jimenez JF, Seghaye MC. Right Atrial Myocardial Remodeling in Children With Atrial Septal Defect Involves Inflammation, Growth, Fibrosis, and Apoptosis. Front Pediatr. 2020;8:40.

17
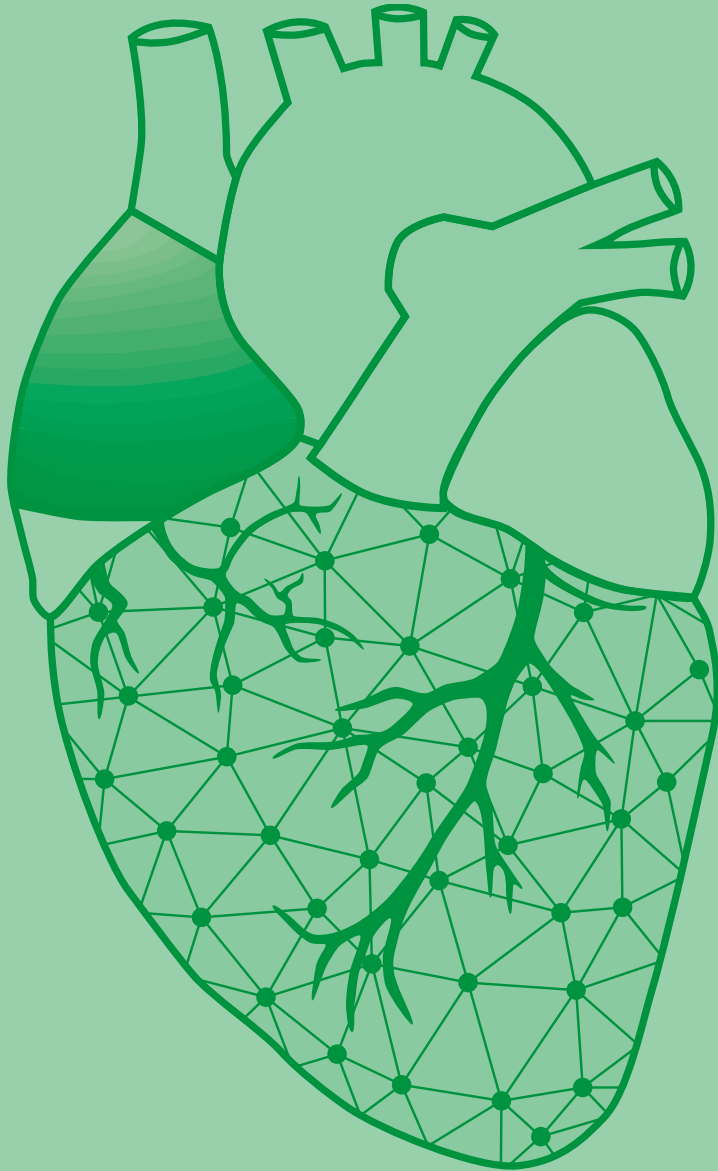
Chapter 18

Identification of local atrial conduction heterogeneities using high-density conduction velocity estimation

Mathijs S. van Schie

Annejet Heida

Yannick J.H.J. Taverne

Ad J.J.C. Bogers

Natasja M.S. de Groot

Abstract

Aims: Accurate determination of intra-atrial conduction velocity (CV) is essential to identify arrhythmogenic areas. The most optimal, commonly used, estimation methodology to measure conduction heterogeneity, including finite differences (FiD), polynomial surface fitting (PSF) and a novel technique using discrete velocity vectors (DVV), has not been determined. We aim to identify 1) the most suitable methodology to unravel local areas of conduction heterogeneities using high density CV estimation techniques, 2) to quantify intra-atrial differences in CV and 3) localize areas of CV slowing associated with paroxysmal atrial fibrillation (PAF).

Methods: Intra-operative epicardial mapping (>5,000 sites, interelectrode distances 2 mm) of the right and left atrium and Bachmann's bundle (BB) was performed during sinus rhythm (SR) in 412 patients with or without PAF.

Results: The median atrial CV estimated using the DVV, PSF and FiD techniques was 90.0 [62.4–116.8] cm/s, 92.0 [70.6–123.2] cm/s and 89.4 [62.5–126.5] cm/s respectively. The largest difference in CV estimates was found between PSF and DVV which was caused by smaller CV magnitudes detected only by the DVV technique. Using DVV, a lower CV at BB was found in PAF patients compared to those without AF (79.1 [72.2–91.2] cm/s vs. 88.3 [79.3–97.2] cm/s, p<0.001).

Conclusions: Areas of local conduction heterogeneities were most accurately identified using the DVV technique whereas PSF and FiD techniques smoothen wavefront propagation thereby masking local areas of conduction slowing. Comparing patients with and without AF, slower wavefront propagation during SR was found at BB in PAF patients, indicating structural remodeling.

Journal site &
supplementary material

Introduction

Speed and direction of atrial wavefront propagation through myocardium is described by the cardiac conduction velocity (CV). It provides important information about the underlying myocardium and is therefore widely used in electrophysiological studies to identify potential mechanisms for arrhythmogenesis. Areas with slower CV are considered as 'diseased tissue' and are associated with increased risk of wavefront reentry which may initiate arrhythmias.[1] Calculation of wavefront CV is frequently empirically determined based on relative distances and time differences of local tissue activation derived from activation maps, which requires that the direction of activation is known. However, the complexity of activity during arrhythmias such as atrial fibrillation (AF), low signal-to-noise ratio and interference of far-field signals hampers accurate estimation of CV. Prior studies have introduced several techniques to estimate CV based on single- or multi-electrode catheters, such as finite differences (FiD) and polynomial surface fitting (PSF).[2-5] However, spatial and temporal resolution is typically coarse and local conduction heterogeneities could be easily missed. Therefore, we developed a novel technique using discrete velocity vectors (DVV) to estimate CV and identify these areas of conduction heterogeneities. Intra-operative mapping during cardiac surgery provides the opportunity to collect high-density recordings of the epicardial surface of both atria. These recordings can be used to compute effective CV, and test and compare the different methodologies on large-scale high-density mapping data. The goal of this study is therefore to identify 1) the most suitable methodology to unravel local areas of conduction heterogeneities using high density CV estimation techniques, 2) to quantify intra-atrial differences in CV and 3) localize areas of CV slowing associated with paroxysmal atrial fibrillation (PAF).

18

Methods

Study population

The study population consisted of 412 successive adult patients undergoing elective open heart coronary artery bypass grafting, aortic or mitral valve surgery or a combination of valvular and bypass grafting surgery in the Erasmus Medical Center Rotterdam. This study was approved by the institutional medical ethical committee (MEC2010-054/MEC2014-393).[6,7] Written informed consent was obtained from all patients and patient characteristics (e.g., age, medical history, cardiovascular risk factors and time in AF) were obtained from the patient's medical record. The study population was classified into two groups: those without a history of AF (no AF group) and those with a history of paroxysmal AF (PAF group).

Mapping procedure

Epicardial high-resolution mapping was performed prior to commencement of extra-corporal circulation, as previously described in detail.[6,7] A temporal bipolar epicardial pacemaker wire attached to the RA free wall served as a reference electrode and the indifferent electrode consisted of a steel wire fixed to subcutaneous tissue of the thoracic cavity.

Epicardial mapping was performed with a 128-electrode array or 192-electrode array (electrode diameter respectively 0.65 or 0.45 mm, interelectrode distances 2.0 mm). Mapping was conducted by shifting the electrode array along predefined areas of the right atrium (RA), Bachmann's bundle (BB), posterior wall between the pulmonary veins (PVA) and left atrial free wall (LA) between anatomical borders in a systematic order, covering the entire atrial epicardial surface as illustrated in the left panel of *Figure 1*. Omission of areas was avoided at the expense of possible small overlap between adjacent mapping sites. The
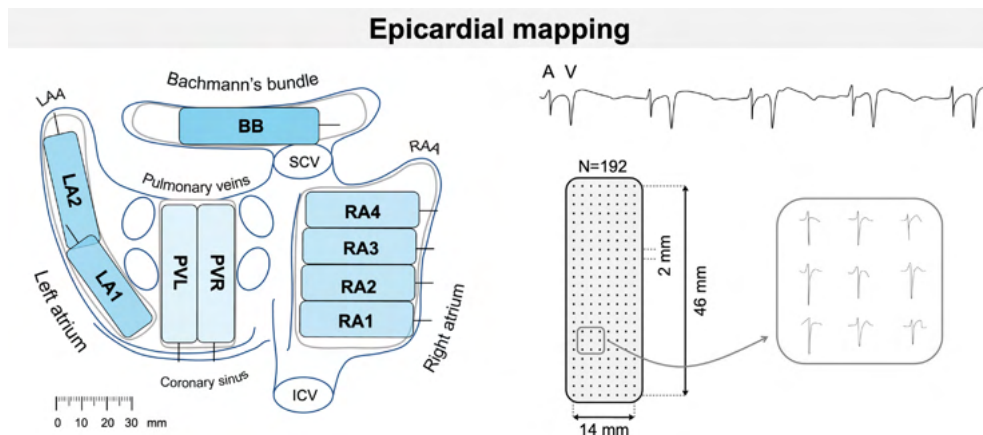
Figure 1 – Epicardial mapping of the atria. Projection of the 192-unipolar electrode array on a schematic posterior view of the atria (left) and epicardial, unipolar potentials recorded during 5 seconds of sinus rhythm containing atrial deflections (A) and far-field ventricular signals (V). Typical examples of 9 unipolar potentials obtained from the RA are shown outside the mapping (right). **ICV** = inferior caval vein; **SCV** = superior caval vein; **LAA** = left atrial appendage; **RAA** = right atrial appendage; **RA** = right atrium; **BB** = Bachmann's bundle; **PV** = pulmonary veins; **LA** = left atrium.

RA was mapped from the cavo-tricuspid isthmus, shifting perpendicular to the caval veins towards the RA appendage; the PVA from the transverse sinus fold along the borders of the right and left pulmonary veins (PVR and PVL) down towards the atrioventricular groove and the left atrioventricular groove (LAVG) from the lower border of the left inferior pulmonary vein towards the LA appendage. BB was mapped from the tip of the LA appendage across the roof of the LA, behind the aorta towards the superior cavo-atrial junction.

Five seconds of SR were recorded from every mapping site, including a surface ECG lead, a calibration signal of 2 mV and 1000 ms, a bipolar reference electrogram (EGM) and all unipolar epicardial EGMs. In patients who presented in AF, SR mapping was performed after electrical cardioversion. Data was stored on a hard disk after amplification (gain 1000), filtering (bandwidth 0.5–400 Hz), sampling (1 kHz) and analogue-to-digital conversion (16 bits).

Data analysis

Unipolar EGMs were semi-automatically analyzed using custom-made software. EGMs with injury potentials, recording sites with ≥25% excluded or missing EGMs and premature atrial complexes or aberrant beats were excluded from analysis.

The steepest negative slope of an atrial potential was marked as the local activation time (LAT), provided that the amplitude of the deflection was at least two times the signal-to-noise ratio of the EGM. In case of fractionated potentials, the activation time of the deflection with the steepest negative slope within a potential was taken as LAT. All annotations were manually checked with a consensus of two investigators. CV was computed from LATs using three different methodologies including a finite differences (FiD), polynomial surface fitting (PSF) and discrete velocity vectors (DVV) technique. Slowing of conduction was defined as a local CV of <28 cm/s and conduction block as a difference in local activation time between adjacent electrodes of ≥12 ms.[8]
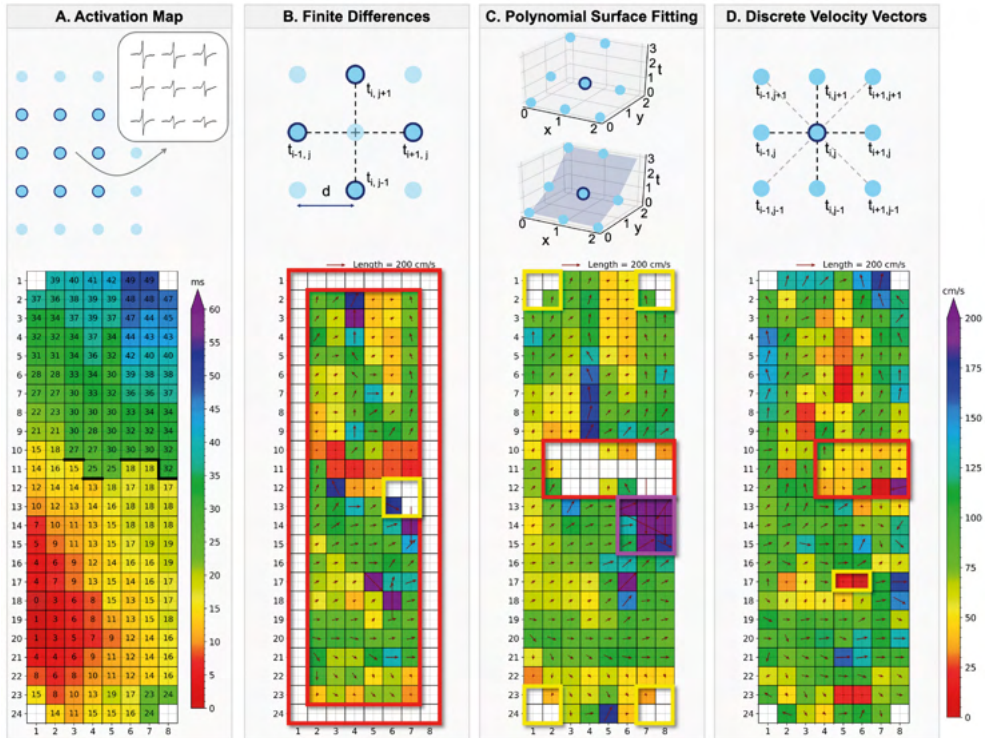
Figure 2 – Example of a color-coded activation map (A) with corresponding CV maps estimated using the FiD (B), PSF (C) and DVV (D) techniques recorded at Bachmann's bundle. Thick black lines in the activation map correspond with conduction block according to a time difference between adjacent electrodes of ≥12ms. The colored boxes indicate areas interest, e.g., border electrodes, areas of conduction block, simultaneous activated electrodes and conduction heterogeneities. *Panel A*: selection of a 3×3 area containing LATs obtained from an activation map. *Panel B*: the FiD technique uses LATs on a grid with interelectrode distance ***d***. Gradients are computed along the dotted lines in the horizontal and vertical directions, using the LATs of the four highlighted electrodes to calculate the CV for the active point in the centre. *Panel C*: the PSF technique fits the surface ***T(x, y)*** (blue area) to a set of LATs adjacent to an active point (circled). The gradients of the fitted surface are used to calculate the CV for the active point. *Panel D*: the DVV technique uses LATs on a grid with interelectrode distance ***d***. Velocities are computed along the dotted lines in the horizontal, vertical and diagonal directions, using the LATs of the adjacent electrodes of an active point (circled). CV of this active point is computed as the average of the velocity components in the horizontal and vertical directions. **CV** = conduction velocity; **DVV** = discrete velocity vectors; **FiD** = finite differences; **LAT** = local activation time; **PSF** = polynomial surface fitting.

Estimation of local conduction velocity

The CV vector of a point on a wavefront is given by

$$v = \begin{bmatrix} dx/dt \\ dy/dt \end{bmatrix} \quad (1)$$

To estimate this vector, derivatives approximated at a given active grid-point are used to compute local CV estimates through time differences between neighboring grid-points, as illustrated in panel B of *Figure 2*.[2,9] Using this FiD technique, CV vectors are computed at each point (i, j) in the grid. Gradients of activation were computed horizontally and vertically using the LATs of the neighboring electrodes:

$$\boldsymbol{G_x} = \frac{1}{2}\left[\frac{t_{i+1,j} - t_{i,j}}{d} + \frac{t_{i,j} - t_{i-1,j}}{d}\right] = \frac{t_{i+1,j} - t_{i-1,j}}{2d} \quad (2)$$

and

$$G_y = \frac{t_{i,j+1} - t_{i,j-1}}{2d} \quad (3)$$

The CV vector is then defined as

$$\boldsymbol{v_{fid}} = \begin{bmatrix} \dfrac{\boldsymbol{G_x}}{\boldsymbol{G_x^2 + G_y^2}} \\ \dfrac{\boldsymbol{G_y}}{\boldsymbol{G_x^2 + G_y^2}} \end{bmatrix} \quad (4)$$

To reduce the impact of outliers and noise, local CV can also be estimated relying on fitting polynomial surfaces $T(x,y)$ to space-time (x, y, t) coordinates of activity, as demonstrated in panel C of *Figure 2*.[3] Both CV and direction of propagation are then computed from the gradient of the local polynomial surface. To estimate this vector, each active electrode and its neighbors were fitted using a standard least-squares algorithm to a smooth local quadratic polynomial surface covered by at least six electrodes

$$T(x,y) = a_0 + a_1 x + a_2 y + a_3 xy + a_4 x^2 + a_5 y^2 \quad (5)$$

The fitted surface describes activation time T as a function of continuous position (x, y), and a_0 to a_5 as coefficients of the fitted quadratic surface. If there are more than six electrodes available, the fit is minimized to smooth the data and reduce the impact of outliers. The gradient vector of the fitted surface defines the direction of propagation and can be found analytically,

$$\nabla T = \begin{bmatrix} \partial T / \partial y \\ \partial T / \partial x \end{bmatrix} \quad (6)$$

The CV vector is then expressed as

$$\boldsymbol{v_{psf}} = \begin{bmatrix} \dfrac{dx}{dT} \\ \dfrac{dy}{dT} \end{bmatrix} = \begin{bmatrix} \dfrac{T_x}{T_x^2 + T_y^2} \\ \dfrac{T_y}{T_x^2 + T_y^2} \end{bmatrix} \quad (7)$$

where $T_x = T(x, 0)$ and $T_y = T(0, y)$. A measure for the reliability of the fit is the residual error estimated from the standard deviation over the N electrode site involved in the calculation of the polynomial surface:

$$\varepsilon = \sqrt{\frac{1}{N} \sum_{i=1}^{N} \left(t_{act_i} - t_{calc_i} \right)^2} \quad (8)$$

where t_{act_i} are the measured and t_{calc_i} the calculated LATs at N electrode sites. To avoid inclusion of inadequately represented CV vectors of areas containing spatial LAT heterogeneities, only surfaces with a residual error of <1.5 and quadratic coefficients (a_3, a_4 and a_5) <1.5 were included in the analysis.[10]

A third method to estimate a CV vector uses neighboring electrodes to the center electrode at coordinates (i, j) to compute an average local propagation velocity by DVV, as illustrated in panel D of *Figure 2*. There is a maximum of eight pairs of electrodes, the four diagonal pairs have components in both the horizontal and vertical directions, the horizontal pairs components in only the horizontal direction and the two vertical pairs in only the vertical direction. All the pairs with valid LATs are used to compute the mean velocity in both directions:

$$\boldsymbol{v}_x = \frac{1}{N}\left(d\left(\frac{1}{t_{i,j} - t_{i-1,j}} + \frac{1}{t_{i+1,j} - t_{i,j}} \right) + \boldsymbol{v}_{x_d} \right) \quad (9)$$

where

$$\boldsymbol{v}_{x_d} = \cos(\pi/4)\sqrt{2d^2}\left(\frac{1}{t_{i,j} - t_{i-1,j+1}} + \frac{1}{t_{i+1,j+1} - t_{i,j}} + \frac{1}{t_{i,j} - t_{i-1,j-1}} + \frac{1}{t_{i+1j,j-1} - t_{i,j}} \right)$$

$$= d\left(\frac{1}{t_{i,j} - t_{i-1,j+1}} + \frac{1}{t_{i+1,j+1} - t_{i,j}} + \frac{1}{t_{i,j} - t_{i-1,j-1}} + \frac{1}{t_{i+1,j-1} - t_{i,j}} \right)$$

and

$$\boldsymbol{v}_y = \frac{1}{M}\left(d\left(\frac{1}{t_{i,j} - t_{i,j+1}} + \frac{1}{t_{i,j-1} - t_{i,j}} \right) + \boldsymbol{v}_{y_d} \right) \quad (10)$$

where

$$\boldsymbol{v}_{y_d} = d\left(\frac{1}{t_{i,j} - t_{i-1,j+1}} + \frac{1}{t_{i,j} - t_{i+1,j+1}} + \frac{1}{t_{i-1,j-1} - t_{i,j}} + \frac{1}{t_{i+1,j-1} - t_{i,j}} \right)$$

The number of valid electrode pairs in the horizontal and vertical direction are represented by N and M respectively, which can be six at most. If adjacent electrodes have the same LAT, the velocity element of that electrode pair becomes zero. In order to increase the reliability of the CV estimate, only CVs with at least three CV vector estimates in both the horizontal and vertical direction are included. The average CV vector is then expressed as

$$\boldsymbol{v}_{dvv} = \begin{bmatrix} \boldsymbol{v}_x \\ \boldsymbol{v}_y \end{bmatrix} \quad (11)$$

From all CV vector estimates, the magnitude is calculated to compare all estimates independently of the propagation direction angle. The difference in CVs computed using two different methods is quantified by the normalized difference velocity index (NDVI) and is expressed as

$$NDVI = \frac{CV_{m1} - CV_{m2}}{CV_{m1} + CV_{m2}} \quad (12)$$

The NDVI always ranges from -1 to +1, in which a negative value accounts for a larger CV of method 2, whereas a positive value accounts for a larger CV of method 1.

Statistical analysis

All data were tested for normality. Normally distributed data are expressed as mean ± standard deviation and analyzed with a (paired) *t*-test or one-way ANOVA. Skewed data are expressed as median [25th–75th percentile] and analyzed with a Kruskal-Wallis test, Mann-Whitney U test or Wilcoxon signed-rank test. Categorical data are expressed as numbers and percentages, and analyzed with a χ^2 or Fisher exact test when appropriate. Correlation was determined by an ordinary least squares regression model. Distribution data was analyzed with a two-sample Kolmogorov-Smirnov test. A *p*-value <0.05 was considered statistically significant. A Bonferroni correction was applied for comparison of the four atrial regions; a *p*-value of <0.0083 (0.05/6) was considered statistically significant.

Results

Study population

Clinical characteristics of the study population (N=412, 305 male (74%), age 67±10 years) are summarized in *Supplementary Table 1*. Patients had either ischemic heart disease (IHD)

18

(N=238, 58%), valvular heart disease (VHD) (N=97, 24%) or a combination of ischemic and valvular heart disease (iVHD) (N=77, 19%). (i)VHD (N=174, 42%) was categorized by the predominant valvular lesion and consisted of aortic valve disease (AVD) (N=107, 61%) or mitral valve disease (MVD) (N=67, 39%). A minority of patients (N=58, 14%) had a history of PAF.

PAF was most prevalent in patients with MVD (N=22, 33%) compared to patients with AVD (N=18, 17%) or only IHD (N=18, 8%) (both p<0.001). In addition, PAF was also more prevalent in patients with LA dilation (N=24, 27% vs. N=25, 14%, p=0.011). Most patients had a normal left ventricular function (LVF) (N=314, 76%) and the majority used class II (N=271, 66%) antiarrhythmic drugs.

Mapping data characteristics

A total of 4,019,926 potentials were analyzed out of 5,261 SR recordings of 5-seconds duration (±6 beats per recording). For all atrial regions, there was no difference between the median number of potentials per patient between the no AF and PAF group (RA: 4,293 [3,516–5,554] vs. 4,293 [3,287–5,412], p=0.213; BB: 1,110 [752–1,316] vs. 954 [739–1,217], p=0.048; PVA: 2,172 [1,692–2,719] vs. 2,112 [1,681–2,602], p=0.253; LA: 1,861 [1,303–2,531] vs. 1,669 [1,292–2,279], p=0.201).

Figure 2 shows a reference activation map during one SR beat (panel A) and the corresponding CV maps estimated using FiD, PSF and DVV techniques (panels B, C and D). The CV estimates ranged from 78.4 [55.5–97.0] cm/s (FiD) to 80.7 [60.0–101.9] cm/s (PSF) and 88.2 [61.1–106.1] cm/s (DVV). Slowed CV was present in 10 mm^2 [3.88%] (FiD), 0 mm^2 (PSF) and 18 mm^2 [4.79%] (DVV) of the estimated CV sites.

As demonstrated in panel B of *Figure 2*, using the FiD technique, it was not possible to compute CVs of the electrodes located on the outer edge of the array (red box) or when LATs of all neighboring electrodes contained the same LAT (yellow box). The FiD technique even estimated CVs up to maximal 400 cm/s, corresponding to twice the inter-electrode distance divided by the time resolution (1 kHz).

Table 1 – Conduction velocity (CV) and propagation direction estimation.

Method	Location	N	CV (cm/s)	θ (deg)
Finite differences	Total	2,517,183 (63)	89.4 [62.5–126.5]	45.0 [-90.0–135.0]
	RA	1,208,426 (64)	80.0 [57.1–100.0]	108.4 [-18.4–146.3]
	BB	275,007 (64)	89.4 [55.5–126.5]	-53.1 [-90.0–0.0]
	PVA	561,418 (61)	97.0 [66.7–133.3]	-71.6 [-135.0–143.1]
	LA	472,332 (60)	110.9 [78.4–178.9]	0.0 [-76.0–63.4]
Polynomial surface fitting	Total	3,127,549 (78)	92.0 [70.6–123.2]	18.4 [-105.4–126.9]
	RA	1,507,290 (80)	83.2 [66.6–102.9]	108.4 [-58.4–144.0]
	BB	324,667 (76)	92.0 [68.2–121.8]	-56.3 [-90.0–-15.9]
	PVA	708,280 (77)	99.7 [77.3–130.2]	-102.5 [-145.0–123.7]
	LA	587,312 (74)	120.0 [85.7–187.4]	-21.8 [-82.4–51.1]
Discrete velocity vectors	Total	3,904,928 (97)	90.0 [62.4–116.8]	12.5 [-102.5–125.0]
	RA	1,847,152 (98)	89.4 [64.9–111.8]	91.7 [-85.9–143.1]
	BB	423,033 (98)	88.6 [58.3–117.3]	-56.1 [-90.7–0.0]
	PVA	881,090 (96)	94.3 [62.9–121.8]	-78.2 [-135.0–126.5]
	LA	753,653 (96)	89.6 [56.6–121.7]	-15.0 [-83.9–66.8]

Values are presented as median [interquartile ranges] or as N (%). **BB** = Bachmann's bundle; **CV** = conduction velocity; **LA** = left atrium; **PVA** = pulmonary vein area; **RA** = right atrium; **θ** = propagation direction angle.
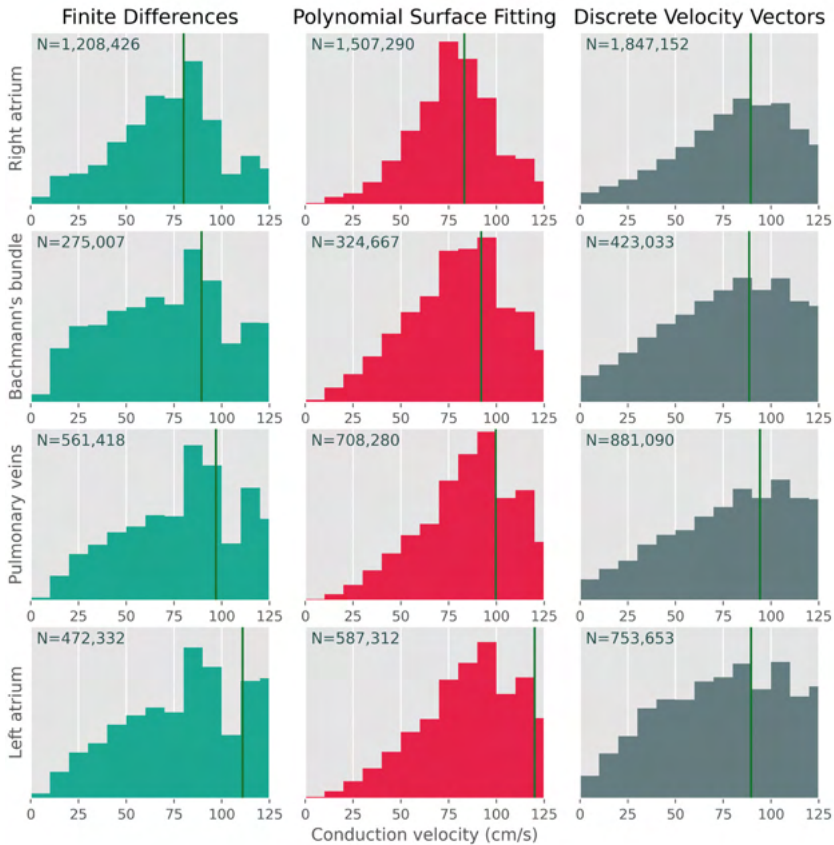
Figure 3 – Distribution histograms of all CV estimates computed using the FiD (turquoise/left, N=2,517,549), PSF (red/middle, N=3,127,549) and DVV (grey/right, N=3,904,928) techniques visualized between 0-100 cm/s. Each row represents CV estimate distribution recorded at the right atrium, Bachmann's bundle, pulmonary vein area and left atrium respectively. The green vertical line represents the median of the corresponding distribution. **CV** = conduction velocity; **DVV** = discrete velocity vectors; **FiD** = finite differences; **PSF** = polynomial surface fitting.

The PSF technique resulted in smoothened CV maps (panel C of *Figure 2*), but therefore failed near areas of large local differences between LATs (caused by e.g., conduction block) as the residual error and quadratic error was too large (red box). The PSF technique also failed to estimate CV vectors at electrodes adjacent to missing LATs near the outer edge of the electrode as less than 6 electrodes remained available at those areas (yellow boxes). In addition, this technique estimated very large CVs up to 600 cm/s or even larger at areas with multiple simultaneously activated electrodes (purple box).

In contrast, as demonstrated in panel D of *Figure 2*, complete CV maps using all available LATs were constructed by applying the DVV technique. In addition, the DVV technique enables visualization of local conduction heterogeneities (yellow box), which were, in contrast, masked by the FiD and PSF techniques (panels B and C). In areas of conduction block and delay, the technique resulted in fasting of CV, while the PSF technique was not able to visualize CV (red boxes in panels C and D). The maximal CV estimated was 200 cm/s (corresponding to the inter-electrode distance divided by the time resolution), whereas areas of simultaneously activated electrodes resulted in a CV of 0 cm/s.
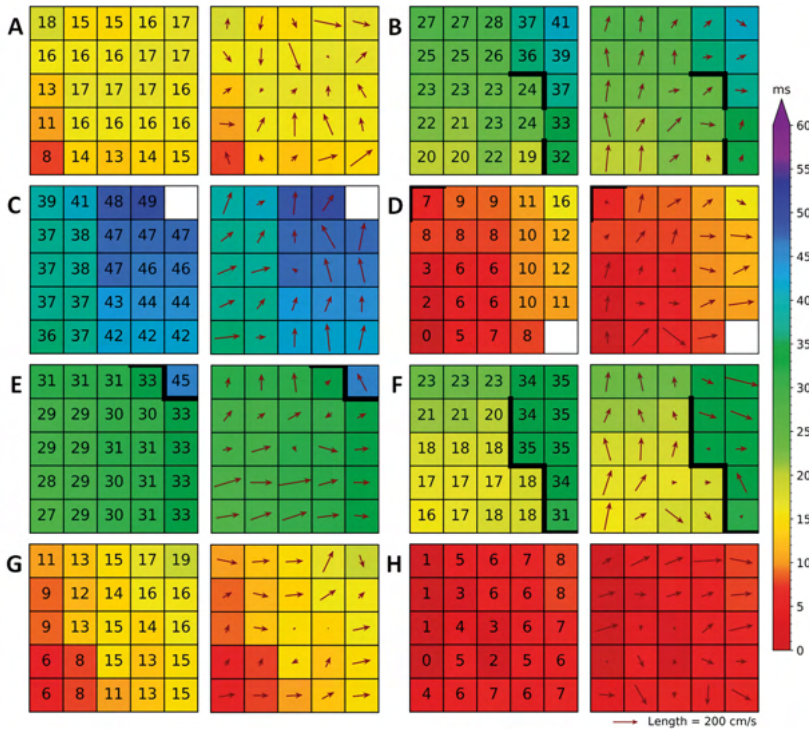
Figure 4 – Examples of local conduction heterogeneities. Various examples (A-H) of local heterogeneities visualized by the discrete velocity vectors (DVV) technique (right with vectors) accompanied by the color-coded local activation maps (left with local activation times). Thick black lines in the activation map correspond with conduction block according to a time difference between adjacent electrodes of ≥12ms.

Efficiency of CV estimation techniques

Comparisons of the CV magnitudes and propagation directions estimated by the three investigated methodologies are demonstrated in *Table 1*. The highest number of CVs were estimated using the DVV technique (N=3,904,928 (97%)), followed by the PSF technique (N=3,127,549 (78%), p<0.001), whereas the FiD technique accounted for the least amount of CV estimates (N=2,517,183 (63%), p<0.001). The distributions of CV estimates are demonstrated in *Figure 3*; ranges between 0 and 100 cm/s are depicted as especially areas of slow conduction are of particular interest in determining local conduction heterogeneities. Although the median CVs of the distributions for every region were relatively comparable between the three techniques, the PSF technique detected only a few very low CV estimates, while the FiD and specifically the DVV technique identified a larger number of low CV estimates.

Comparison of the conduction velocity estimates

As demonstrated in *Supplementary Table 2*, CV magnitudes of the FiD technique strongly correlated with estimates of the PSF technique (R^2=0.864), while the largest difference in CV magnitudes and propagation direction angles was found between the PSF and DVV technique. These differences were mainly provoked by a larger amount of low CV magnitudes estimated by the DVV technique.

Focusing on the atrial regions, differences in the three techniques were most pronounced at the LA. While the differences between the FiD and PSF were again relatively small, between

Table 2 – Conduction velocities per patient subdivided in those with or without AF.

	Total	Without AF	PAF	*p*-value
Right atrium				
Number of potentials	4,293 [3,485–5,511]	4,293 [3,516–5,554]	4,293 [3,287–5,412]	0.213
FiD: CV (cm/s)	78.4 [74.3–80.0]	78.4 [74.3–80.0]	78.4 [74.3–80.0]	0.284
Slow CV (%)	5.5 [2.6–9.2]	5.5 [2.6–9.1]	5.3 [2.5–9.9]	0.462
PSF: CV (cm/s)	82.4 [77.3–88.2]	83.2 [77.3–88.2]	80.4 [77.6–89.2]	0.284
Slow CV (%)	1.6 [0.7–2.7]	1.6 [0.7–2.6]	1.8 [0.8–3.0]	0.250
DVV: CV (cm/s)	89.1 [83.3–94.3]	89.3 [83.3–94.3]	88.0 [82.3–93.4]	0.309
Slow CV (%)	4.9 [3.6–6.8]	4.9 [3.6–6.7]	5.2 [3.6–6.9]	0.422
Bachmann's bundle				
Number of potentials	1,104 [748–1,314]	1,110 [752–1,316]	954 [739–1,217]	0.048
FiD: CV (cm/s)	80.0 [74.3–97.0]	89.4 [78.4–97.0]	78.4 [65.1–89.4]	<0.001
Slow CV (%)	6.5 [2.4–14.2]	5.8 [2.2–13.3]	10.1 [5.5–18.2]	<0.001
PSF: CV (cm/s)	92.3 [84.4–99.7]	94.3 [85.5–99.7]	85.9 [79.2–94.9]	<0.001
Slow CV (%)	2.4 [0.8–4.6]	2.1 [0.8–4.3]	3.9 [2.3–7.8]	<0.001
DVV: CV (cm/s)	86.9 [77.3–96.4]	88.3 [79.3–97.2]	79.1 [72.2–91.2]	<0.001
Slow CV (%)	6.7 [4.1–11.5]	6.6 [3.9–11.1]	8.3 [5.8–13.6]	0.004
Pulmonary vein area				
Number of potentials	2,146 [1,692–2,717]	2,172 [1,692–2,719]	2,112 [1,681–2,602]	0.254
FiD: CV (cm/s)	97.0 [89.4–100.0]	97.0 [89.4–100.0]	94.3 [80.0–97.0]	0.012
Slow CV (%)	2.5 [0.5–6.4]	2.4 [0.4–6.0]	3.8 [0.8–8.5]	0.077
PSF: CV (cm/s)	99.7 [92.3–110.9]	99.7 [93.7–111.0]	98.6 [89.4–104.0]	0.009
Slow CV (%)	1.0 [0.3–2.1]	0.9 [0.3–1.9]	1.4 [0.5–3.3]	0.014
DVV: CV (cm/s)	94.3 [83.4–101.0]	94.3 [83.3–101.0]	91.7 [85.8–100.5]	0.371
Slow CV (%)	5.6 [3.5–9.4]	5.6 [3.5–9.4]	5.8 [3.5–9.6]	0.486
Left atrium				
Number of potentials	1,853 [1,303–2,515]	1,861 [1,303–2,531]	1,669 [1,292–2,279]	0.201
FiD: CV (cm/s)	110.9 [100.0–133.3]	110.9 [100.0–133.3]	110.9 [97.0–126.5]	0.003
Slow CV (%)	1.5 [0.2–4.6]	1.5 [0.2–4.5]	2.6 [0.6–6.6]	0.060
PSF: CV (cm/s)	120.0 [107.3–134.2]	121.8 [108.6–139.5]	115.0 [105.2–123.0]	0.002
Slow CV (%)	0.7 [0.2–1.8]	0.7 [0.2–1.7]	0.7 [0.2–2.0]	0.280
DVV: CV (cm/s)	90.2 [82.2–97.0]	90.4 [82.2–97.2]	89.6 [83.1–95.0]	0.450
Slow CV (%)	6.8 [5.1–9.7]	6.8 [5.1–9.8]	7.0 [5.0–9.2]	0.354

Values are presented as median [interquartile ranges]. The *p*-values indicate significance between the without AF and PAF group. **DVV** = discrete velocity vectors; **FiD** = finite differences; **(P)AF** = (paroxysmal) atrial fibrillation; **PSF** = polynomial surface fitting.

18

the FiD and DVV, and PSF and DVV techniques the differences were more pronounced. In both comparisons, the majority of these CV magnitudes estimated by DVV were lower.

Examples of heterogeneous conduction using discrete velocity vectors

Figure 4 shows eight examples of local heterogeneous conduction at various locations of the atria. As demonstrated by the corresponding colored activation maps, activation is locally disrupted. This is in turn visualized by a deviant CV vector as compared to the surrounding electrodes. At some sites local heterogeneous conduction is accompanied by a line of conduction block (time difference between adjacent electrodes of ≥12ms), near areas of conduction delay (time difference between adjacent electrodes of ≥7ms), a colliding wavefront or small local changes in activation direction and velocity.

Regional differences in conduction velocity

Characteristics of CV estimates were subdivided according to the corresponding atrial recording regions (RA, BB, PVA and LA) and are demonstrated in *Table 2*. All atrial regions differed significantly (p<0.001 for each), except between the RA and LA using the DVV technique (p=0.021). In general, higher CV estimates were found on the left side of the atria.
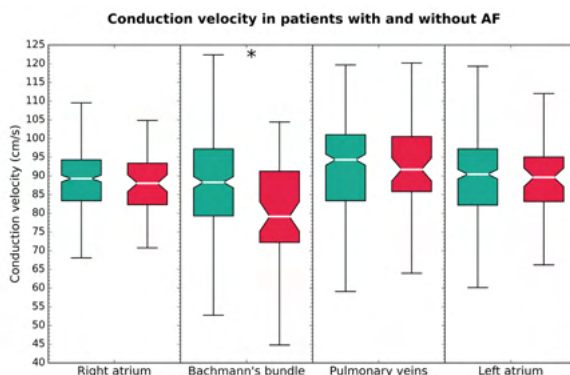
Figure 5 – Impact of AF episodes on conduction velocity. Boxplots of the conduction velocities at various atrial regions in patients without (turquoise) and with (red) history of paroxysmal atrial fibrillation. Statistical significance is indicated by an asterisk.

Interestingly, CVs estimated at BB were higher compared to the RA, but lower compared to the left side.

All atrial regions differed significantly in the amount of slow CV areas (p<0.006 for each). The most amount of slow CV areas were found at BB, followed by the RA. Using the DVV technique, a high amount of slow CV areas was found at the LA while the other techniques did not identify large areas of slow CV.

Impact of AF episodes

Regional median CV distributions using the DVV technique in patients with and without history of AF are illustrated in *Figure 5*. All CV techniques demonstrated that the median CV at BB was lower in PAF patients compared to those without AF (p<0.001 for all comparisons). In addition, using the FiD and PSF techniques, a lower median CV was found at the PVA and LA in PAF patients as well (FiD, PVA: 94.3 [80.0–97.0] cm/s vs. 97.0 [89.4–100.0] cm/s; p=0.012 & LA: 110.9 [97.0–126.5] cm/s vs. 110.9 [100.0–133.3] cm/s; p=0.003. PSF, PVA: 98.6 [89.4–104.0] cm/s vs. 99.7 [93.7–111.0] cm/s; p=0.009 & LA: 115.0 [105.2–123.0] cm/s vs. 121.8 [108.6–139.5] cm/s; p=0.002), although the difference was less prominent compared to BB.

Using all CV techniques, more slow CV areas were identified at BB in patients with history of PAF compared to those without AF (FiD: 10.1 [5.5–18.2] % & 5.8 [2.2–13.3] %; p<0.001 & PSF: 3.9 [2.3–7.8] % vs. 2.1 [0.8–4.3] %; p<0.001 & DVV: 8.3 [5.8–13.6] % vs. 6.6 [3.9–11.1] %; p=0.004). In addition, using the PSF technique, more slow CV areas were found at the PVA in patients with PAF (0.9 [0.3–1.9] % vs. 1.4 [0.5–3.3] %, p=0.014).

Discussion

By estimating high density CVs, this study demonstrated that local conduction heterogeneities could be most accurately identified by the DVV technique. All techniques revealed that the slowest conduction was observed at the RA and BB yet both the FiD and PSF techniques were unable to identify local conduction heterogeneities as these were masked by the smoothing properties of both techniques. All CV estimation techniques showed that there was a considerable variation in CV between all atrial regions. A lower CV was found at BB in patients with PAF compared to those without AF.

Conduction velocity estimate techniques

Calculation of CV is frequently based on a distance travelled by a wavefront in a unit of time, resulting in an accurate estimate if there is a one-dimensional propagation and the direction of propagation is known. However, in the case of local conduction heterogeneities, a more sophisticated method is required enabling estimation of local CV ('effective' CV estimate) indicative of the underlying local substrate.

During a standard electrophysiology study, multi-electrode catheters enable CV estimation by triangulation. However, this methodology is limited by the number and size of electrodes and it is assumed that the wavefront is locally planar.[9] In a number of mapping studies, this method has been used to construct global CV maps which were sequentially acquired during stable rhythms. Data interpolation was then additionally used to generate high-density CV maps. However, this technique may be sensitive to errors as exact positions of the catheter electrodes with relatively larger electrode diameters and interelectrode distances are required in order to estimate CV and reconstruct global CV maps. Using regularly spaced high-density electrode arrays, simultaneous recordings on a high spatial resolution scale enable analysis of complex and heterogeneous patterns of activation. Hence, insufficient spatial and temporal resolution is therefore essential. A low temporal resolution can result in areas of simultaneous activation, although simultaneous activated electrodes on a larger area (e.g., the full 3×3 area) were a very rare event in our data. Furthermore, the handling of simultaneous activation by the three different techniques varies as well, although this is mostly in the methods' nature. Inappropriate application may result in high conduction velocities which are physiologically impossible. These areas can, however, easily be recognized and removed from the data. Despite a widely use of the FiD and PSF techniques in literature, these methodologies have disadvantages as demonstrated in the present study and these techniques are mainly applied on optical mapping recordings.

18

Although the FiD technique is straightforward to implement, it is very sensitive to missing data and generally amplifies noise artefacts. These effects could be prevented by data interpolation or modification of the algorithm, but the accuracy of such interpolation can be questioned. In addition, as this technique uses only 4 LATs with twice the interelectrode distance, the FiD technique has a lower resolution compared to the other techniques. This lower resolution leads to less detailed velocity estimates which result in more smoothened velocity vectors, thereby masking areas of local conduction heterogeneity. The PSF technique, on the other hand, is robust to missing or noisy data, but needs at least six electrodes to estimate a local polynomial surface from which the CV can be determined, which is a problem at electrodes near the outer edge of a multi-electrode array. A solution might be to include a larger area of electrodes in the algorithm. However, this is disadvantageous as a larger atrial area is then fitted to a polynomial surface, thereby generalizing local conduction heterogeneities which, consequently, may disappear. Moreover, as this technique is based on surface fitting, in which a fit is minimized to smooth the data and reduce the impact of outliers, it also smoothens true local conduction heterogeneities. This approach masks these conduction heterogeneities which is of specific interest in defining areas of structural remodeled tissue. The DVV technique, however, is always able to perform a CV estimation using the surrounding electrodes, but its reliability drops when there are less electrodes available. Therefore, at least two electrodes in both the horizontal and vertical direction have to be available to perform an estimation. In addition, by using all surrounding electrodes, but without any smoothing properties, the DVV technique is able to identify local conduction heterogeneity whereas these areas are missed by both other techniques.

Regional differences in conduction velocity

Atrial wavefront propagation occurs preferentially and faster along the longitudinal direction to the fiber orientation.[11] It is therefore generally assumed that the longitudinal parallel orientation of prominent muscle bundles, e.g. the crista terminalis and BB, results in a higher CV, making it preferential routes of interatrial conduction. On the other hand, differently aligned overlapping fibers will result in more complex activation patterns. All techniques tested use the same LATs. The major difference between the techniques is that the FiD and PSF techniques resulted in more smoothened velocity maps which may mask areas with varying fiber orientations. Hence, chaotic fiber arrangement causing conduction heterogeneity might be missed with the FiD and PSF methodologies.

In early animal studies, CV in these bundles was indeed increased.[12-14] However, Teuwen et al.[15] demonstrated that CV at BB is only approximately 90 cm/s in patients without AF, comparable with a CV of 88 cm/s recorded at the RA free wall in a study of Hansson et al.[16] As in the early animal studies CV was measured between only a few points, CV at BB could have easily been overestimated because wavefronts from the RA could have been fused with wavefronts entering the central part of BB from the septum. Our study showed that CV computed locally from high-density electrode arrays at the RA and BB is indeed comparable with the CV estimates at RA and BB of both studies.

In our study, CV estimates from the PVA were even higher compared to the RA and BB in all used techniques. Arora et al.[17] found slowed epicardial conduction of 31.3 cm/s at the superior pulmonary veins, while an epicardial CV of 90.2 cm/s was recorded at the remainder of the PVA. These results are in accordance with our results computed using the DVV technique and the LA recordings. However, even larger CV estimates were computed using the FiD and PSF techniques at these areas. This could be the result of the smoothing properties of the aforementioned techniques, as the absolute differences and NDVI between these techniques were very small at the PVA.

However, at the LA these differences were much larger, probably caused by the limited time resolution (1 kHz), which results in simultaneously activated electrodes. A high CV at the LA and PVA could be caused by their tissue structure and wavefront geometry. As the excitation front in the RA is mostly convex (curving outward), CV is consequently slower compared to a planar or concave (curving inward) wavefronts resulting into current-to-load mismatches.[18] In addition, the LA is composed of several overlapping layers of differently aligned myocardial fibers, resulting a smooth and uniform thick wall, although small regional variations in thickness have been found.[19] In contrast, muscular bundles in the RA are larger, e.g. the terminal crest, and due to the presence of pectinate muscles, the RA wall is not of uniform thickness. As CV is also affected by muscle thickness and wall curvature, these smaller differences in the LA could result in higher CVs.[20] In addition, as morphology of the LA and RA is completely different (smooth vs. trabeculated wall), regional differences between the LA and RA could be expected.

Influence of atrial fibrillation episodes

Changes in CV can be caused by various mechanisms, e.g., remodeling of gap junctions, mechanical stress or non-uniform anisotropy. In our study, the most prominent differences in CV between patients with and without AF were found at BB. At this site, recent studies indeed found more conduction disorders and decreased unipolar single potential amplitudes due to loss of S-wave amplitudes during SR in patients with AF or developed post-operative AF.[15] In addition, more fibro-fatty tissue and fibrotic patches were found at BB in patients with

PAF, which may result in a decreased CV caused by impaired cell-to-cell connections.[21] This could also explain the increased amount of slow CV areas at BB in patients with PAF.

Study limitations

Whether general anesthesia and intra-operative drugs influence conduction is yet to be investigated; however, a standard anesthetic protocol was used for all patients and SR was confirmed during all mapping procedures. Therefore, possible effects of anesthesia would be equally dispersed among the patient population. In addition, high-resolution mapping of the interatrial septum could not be performed with our closed beating heart approach.

Conclusion

Areas of local conduction heterogeneities were most accurately identified using the DVV technique whereas PSF and FiD techniques smoothen wavefront propagation thereby masking local areas of conduction slowing. In addition, DVV is able to estimate substantially more CVs as compared to the other techniques. Using all techniques, various regional differences in CV were found in all patients. Comparing patients with and without AF, slower wavefront propagation during SR and an increased amount of slow CV areas were found at BB in PAF patients, indicating areas of structural remodeled tissue.

18

References

1. King JH, Huang CL, Fraser JA. Determinants of myocardial conduction velocity: implications for arrhythmogenesis. Front Physiol. 2013;4:154.

2. Salama G, Kanai A, Efimov IR. Subthreshold stimulation of Purkinje fibers interrupts ventricular tachycardia in intact hearts. Experimental study with voltage-sensitive dyes and imaging techniques. Circ Res. 1994;74:604-619.

3. Bayly PV, KenKnight BH, Rogers JM, Hillsley RE, Ideker RE, Smith WM. Estimation of conduction velocity vector fields from epicardial mapping data. IEEE Trans Biomed Eng. 1998;45:563-571.

4. Weber FM, Schilling C, Seemann G, Luik A, Schmitt C, Lorenz C, Dossel O. Wave-direction and conduction-velocity analysis from intracardiac electrograms--a single-shot technique. IEEE Trans Biomed Eng. 2010;57:2394-2401.

5. Konings KT, Kirchhof CJ, Smeets JR, Wellens HJ, Penn OC, Allessie MA. High-density mapping of electrically induced atrial fibrillation in humans. Circulation. 1994;89:1665-1680.

6. Lanters EA, van Marion DM, Kik C, Steen H, Bogers AJ, Allessie MA, Brundel BJ, de Groot NM. HALT & REVERSE: Hsf1 activators lower cardiomyocyt damage; towards a novel approach to REVERSE atrial fibrillation. J Transl Med. 2015;13:347.

7. van der Does LJ, Yaksh A, Kik C, Knops P, Lanters EA, Teuwen CP, Oei FB, van de Woestijne PC, Bekkers JA, Bogers AJ, et al. QUest for the Arrhythmogenic Substrate of Atrial fibRillation in Patients Undergoing Cardiac Surgery (QUASAR Study): Rationale and Design. J Cardiovasc Transl Res. 2016;9:194-201.

8. Allessie MA, de Groot NM, Houben RP, Schotten U, Boersma E, Smeets JL, Crijns HJ. Electropathological substrate of long-standing persistent atrial fibrillation in patients with structural heart disease: longitudinal dissociation. Circ Arrhythm Electrophysiol. 2010;3:606-615.

9. Cantwell CD, Roney CH, Ng FS, Siggers JH, Sherwin SJ, Peters NS. Techniques for automated local activation time annotation and conduction velocity estimation in cardiac mapping. Comput Biol Med. 2015;65:229-242.

10. Houben RP, Allessie MA. Processing of intracardiac electrograms in atrial fibrillation. Diagnosis of electropathological substrate of AF. IEEE Eng Med Biol Mag. 2006;25:40-51.

11. Spach MS, Miller WT, 3rd, Geselowitz DB, Barr RC, Kootsey JM, Johnson EA. The discontinuous nature of propagation in normal canine cardiac muscle. Evidence for recurrent discontinuities of intracellular resistance that affect the membrane currents. Circ Res. 1981;48:39-54.

12. Dolber PC, Spach MS. Structure of canine Bachmann's bundle related to propagation of excitation. Am J Physiol. 1989;257:H1446-1457.

13. Goodman D, van der Steen AB, van Dam RT. Endocardial and epicardial activation pathways of the canine right atrium. Am J Physiol. 1971;220:1-11.

14. Wagner ML, Lazzara R, Weiss RM, Hoffman BF. Specialized conducting fibers in the interatrial band. Circ Res. 1966;18:502-518.

15. Teuwen CP, Yaksh A, Lanters EA, Kik C, van der Does LJ, Knops P, Taverne YJ, van de Woestijne PC, Oei FB, Bekkers JA, et al. Relevance of Conduction Disorders in Bachmann's Bundle During Sinus Rhythm in Humans. Circ Arrhythm Electrophysiol. 2016;9:e003972.

16. Hansson A, Holm M, Blomstrom P, Johansson R, Luhrs C, Brandt J, Olsson SB. Right atrial free wall conduction velocity and degree of anisotropy in patients with stable sinus rhythm studied during open heart surgery. Eur Heart J. 1998;19:293-300.

17. Arora R, Verheule S, Scott L, Navarrete A, Katari V, Wilson E, Vaz D, Olgin JE. Arrhythmogenic substrate of the pulmonary veins assessed by high-resolution optical mapping. Circulation. 2003;107:1816-1821.

18. Kleber AG, Rudy Y. Basic mechanisms of cardiac impulse propagation and associated arrhythmias. Physiol Rev. 2004;84:431-488.

19. Ho SY, Anderson RH, Sanchez-Quintana D. Atrial structure and fibres: morphologic bases of atrial conduction. Cardiovasc Res. 2002;54:325-336.

20. Rossi S, Gaeta S, Griffith BE, Henriquez CS. Muscle Thickness and Curvature Influence Atrial Conduction Velocities. Front Physiol. 2018;9:1344.

21. Becker AE. How structurally normal are human atria in patients with atrial fibrillation? Heart Rhythm. 2004;1:627-631.

18
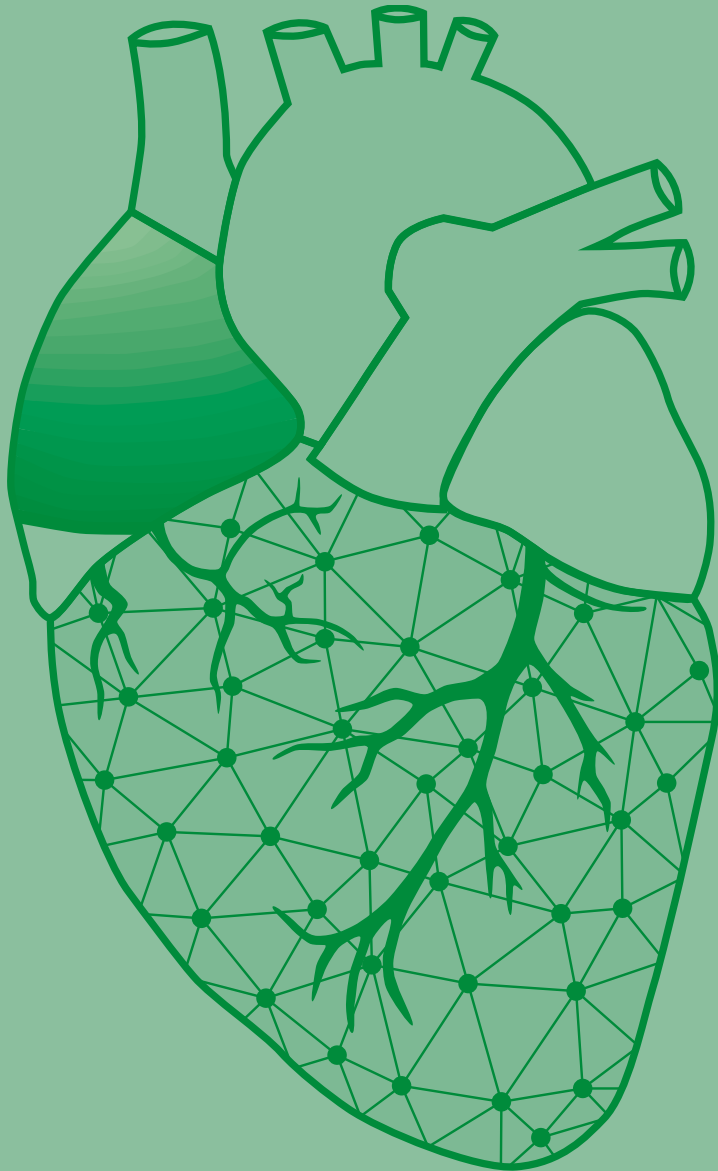
Chapter 19

Reduction of conduction velocity in patients with atrial fibrillation

Annejet Heida

Mathijs S. van Schie

Willemijn F.B. van der Does

Yannick J.H.J. Taverne

Ad J.J.C. Bogers

Natasja M.S. de Groot

Abstract

Background: It is unknown to what extent atrial fibrillation (AF) episodes affect intra-atrial conduction velocity (CV) and whether regional differences in local CV heterogeneities exist during sinus rhythm. This case-control study aims to compare CV assessed throughout both atria between patients with and without AF.

Methods: Patients (N=34) underwent intra-operative epicardial mapping of the right atrium (RA), Bachmann's bundle (BB), left atrium (LA) and pulmonary vein area (PVA). CV vectors were constructed to calculate median CV in addition to total activation times (TAT) and unipolar voltages.

Results: Biatrial median CV did not differ between patients with and without AF (90±8 cm/s vs. 92±6 cm/s, p=0.56); only BB showed a CV reduction in the AF group (79±12 cm/s vs. 88±11 cm/s, p=0.02). In patients without AF, there was no predilection site for the lowest CV (P_5, RA: 12%; BB: 29%; LA: 29%; PVA: 29%). In patients with AF, lowest CV was most often measured at BB (53%) and ranged between 15 to 22 cm/s (median: 20 cm/s). Lowest CVs were also measured at the LA (18%) and PVA (29%), but not at the RA. AF was associated with a prolonged TAT (p=0.03) and decreased voltages (P_5) at BB (p=0.02).

Conclusions: BB was a predilection site for slowing of conduction in patients with AF. Prolonged TAT and decreased voltages were also found at this site. The next step will be to determine the relevance of a reduced CV at BB in relation to AF development and maintenance.

Journal site

Introduction

Intra-atrial conduction velocity (CV) is determined by ion channel properties, cell-to-cell coupling, wavefront geometry and muscle thickness.[1,2] Areas of reduced CV are associated with initiation and perpetuation of atrial fibrillation (AF).[3] In 12 patients with ischemic heart disease or Wolff-Parkinson-White syndrome who underwent cardiac surgery, the average CV measured during sinus rhythm (SR) at the right atrial free wall in an area of 3×4 cm was 88 cm/s.[4] A comparable average CV of 89±13 cm/s was found at Bachmann's bundle (BB) in 185 patients undergoing coronary artery bypass surgery.[5]

There is only one report on comparison of CV during SR between patients with and without AF.[6] In this endocardial mapping study, paroxysmal AF was associated with a reduction of CV to 60±12 cm/s at the right atrium (RA) and to 51±11 cm/s at the left atrium (LA) compared to patients with atrioventricular nodal reentrant tachycardia and Wolff-Parkinson-White syndrome, respectively (RA: 83±13 cm/s and LA: 70±10 cm/s).[6] Additionally, the basal, septal and annular regions of the RA showed a reduction in CV in patients with paroxysmal AF (basal region: 54±19 cm/s vs. 82±25 cm/s; septal region: 64±20 cm/s vs. 93±32 cm/s; annular region: 60±12 cm/s vs. 83±13 cm/s, all p<0.05).[6] However, mapping was performed at only a limited number of sites at the RA and LA. Remarkably, the CV in this control group was much lower than CVs assessed in the studies described above.

To date, it is unknown to what extent AF episodes affect intra-atrial CV and whether there are regional differences in local CV during SR at the RA, BB and the LA including the pulmonary vein area (PVA). The aim of our case-control study is therefore to compare CV assessed at a high-resolution scale throughout both atria in patients with AF and without atrial tachyarrhythmias and to investigate which region is most affected by AF episodes.

19

Methods

Study population and setting

The study population consisted of participants undergoing elective open-heart surgery in the Erasmus Medical Center. Indications for elective cardiac surgery were either coronary artery disease, aortic valve- or mitral valve disease, or a combination of these. The case group consisted of patients with a history of documented AF. SR recordings were made after electrical cardioversion. The control group consisted of patients without atrial tachyarrhythmias such as AF. Participants were matched based on known confounders of intra-atrial conduction disorders, i.e. age[7], BMI[8] and left atrial enlargement[9]. Echocardiographic images were used to identify atrial dilatation. Participants were enrolled between March 2012 and April 2018. This study is approved by the institutional Medical Ethical Committee (MEC 2010-05410 and MEC 2014-39311). Written informed consent was obtained from all patients prior to the surgical procedure. The study complied with the Declaration of Helsinki. Clinical data was extracted from electronic patient files.

Mapping procedure

As previously described, high-resolution epicardial mapping was performed during open heart surgery.[12] A bipolar pacemaker wire was temporarily attached to the right atrial free wall to function as a reference electrode. A steel wire was fixed in the thoracic subcutaneous tissue serving as an indifferent electrode. Epicardial mapping was performed using a unipolar 128- or a 192-electrode array (electrode diameter respectively 0.65 and 0.45 mm, interelectrode distances of 2 mm) and following a predefined scheme (upper panel *Figure*
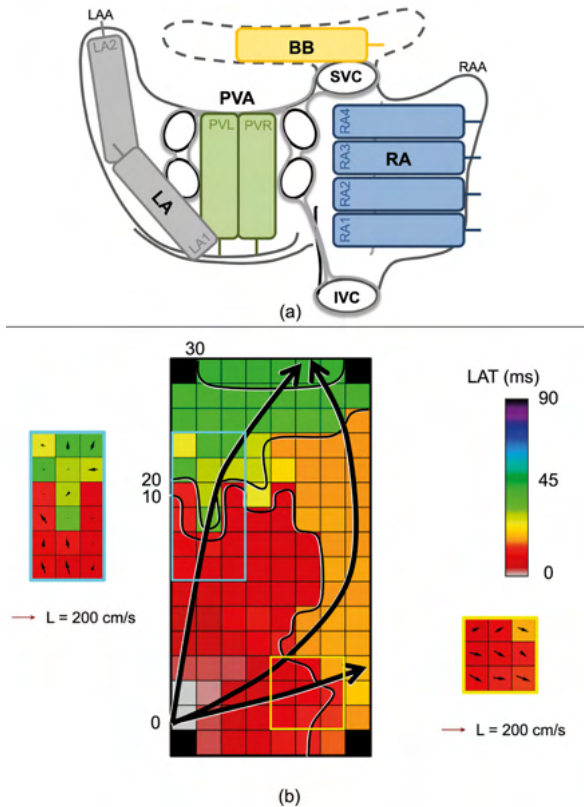
Figure 1 – Epicardial mapping of the atria. *Upper panel*: mapping scheme on a schematic posterior view of the RA, BB, LA and PVA. *Lower panel*: an example of a color-coded activation map with isochrones (black lines) drawn at 10 ms. The black arrow indicates the main wave direction. Examples of the corresponding CV map using discrete velocity vectors are shown next to the activation map. CV vectors are depicted per electrode. **BB** = Bachmann's bundle; **CT** = conduction time; **IVC** = inferior vena cava; **LA** = left atrium; **LAA** = left atrial appendage; **LAT** = local activation time; **PVA** = pulmonary vein area; **PVL** = left pulmonary vein; **PVR** = right pulmonary vein; **RA** = right atrium; **RAA** = right atrial appendage; **SVC** = superior vena cava.

1), covering the epicardial surface of the RA (from the inferior caval vein up to the right atrial appendage, perpendicular to the caval veins), PVA (from the sinus transversus, alongside the borders of the pulmonary veins towards the atrioventricular groove), LA (from the lower border of the left pulmonary vein along the left atrioventricular groove towards the left atrial appendage), and BB (from the tip of left atrial appendage behind the aorta towards the superior cavo-atrial junction).

At each site, five seconds of SR mapping were recorded, including unipolar epicardial electrograms, a surface electrocardiogram, a bipolar reference electrogram and a calibration signal (amplitude: 2 mV, duration: 1000 ms). Recordings were sampled with a rate of 1 kHz, amplified (gain: 1000), filtered (bandwidth: 0.5-400 Hz), analogue-to-digital-converted (16-bits) and stored on a hard disk.

Mapping data processing

The steepest negative slopes of all atrial potentials were automatically annotated using custom-made mapping software when the amplitude exceeded twice the signal-to-noise ratio.[5,13] For each electrode, the local activation time was determined, and color-coded activation maps were reconstructed as illustrated in the lower panel of *Figure 1*. All annotations were visually verified. Premature extrasystoles and aberrant beats were excluded from analysis, along with mapping sites in which less than 50% was annotated. Areas of simultaneous activation were excluded from analysis in order to avoid inclusion of far-field potentials.

Table 1 – Characteristics of participants.

	AF group (N=17)	No AF group (N=17)	*p*-value
Patients	73±7	74±7	0.60
Male	11 (64.7)	9 (52.9)	0.69
BMI (kg/m²)	24.9 [23.0–29.2]	25.3 [22.9–29.1]	0.16
Underlying heart disease			1.00
• IHD	2 (11.8)	2 (11.8)	
• (i)VHD	15 (88.2)	15 (88.2)	
- AVD	2 (11.8)	3 (17.6)	
- AVD and CAD	2 (11.8)	2 (11.8)	
- MVD	9 (52.9)	7 (41.2)	
- MVD and CAD	2 (11.8)	3 (17.6)	
Echocardiography			
• LVF			1.00
- Normal	11 (64.7)	12 (70.6)	
- Mild dysfunction	3 (17.6)	2 (11.8)	
- Moderate dysfunction	3 (17.6)	3 (17.6)	
- Severe dysfunction	0 (0.0)	0 (0.0)	
• Dilated LA >45 mm	11/13 (84.6)	9/15 (60.0)	0.41
Medication			
• Antiarrhythmic drugs			0.45
- Class I	0 (0.0)	0 (0.0)	
- Class II	11 (64.7)	7 (41.2)	
- Class III	4 (23.5)	0 (0.0)	
- Class IV	1 (5.9)	1 (5.9)	
• Digoxin	5 (29.4)	0 (0.0)	0.06

Values are presented as mean ± standard deviation, median [interquartile ranges] or as N (%). **AF** = atrial fibrillation; **AVD** = aortic valve disease; **BMI** = body mass index; **CAD** = coronary artery disease; **IHD** = ischemic heart disease; **LA** = left atrium; **LVF** = left ventricular function; **MVD** = mitral valve disease; **(i)VHD** = (ischemic and) valvular heart disease.

19

Calculation of local conduction velocities

Local CV was computed as an average of velocity estimations between neighboring electrodes (longitudinal, transversal and diagonal) using discrete velocity vectors as previously described by Van Schie et al.[14] Relative frequency distribution histograms of CVs were constructed to calculate median CV and variance of CV (ΔP_5-P_{95}). For identification of areas of 'slow conduction', the 5th percentiles of the relative frequency distribution of CVs were determined. Additionally, the total activation times (TAT) of both atria and for each mapping site separately was determined by relating the first and last local activation time to the reference electrode. To compare voltage characteristics between patients with and without AF, we measured the peak-to-peak amplitude of the steepest deflection of each unipolar potential to construct relative frequency histograms. For determination of 'low voltage', we calculated the 5th percentile of the relative frequency distribution histograms of the voltages of all unipolar potentials.

Statistical analysis

Statistical analysis was performed with SPSS version 25 (IBM Corporation, Armonk, New York). All data were tested for normality using Shapiro-Wilk test. Continuous normally distributed data were expressed as mean ± standard deviation and skewed data as median [25th–75th percentile]. To compare continuous parameters between the AF and no AF group, a paired samples *t*-test or Wilcoxon signed rank test was used. Categorical data is expressed as absolute numbers (percentages) and analyzed with (McNemar's symmetry) χ^2 or McNemar's exact test, if applicable. A two-sided *p*-value of <0.05 was considered statistically significant.
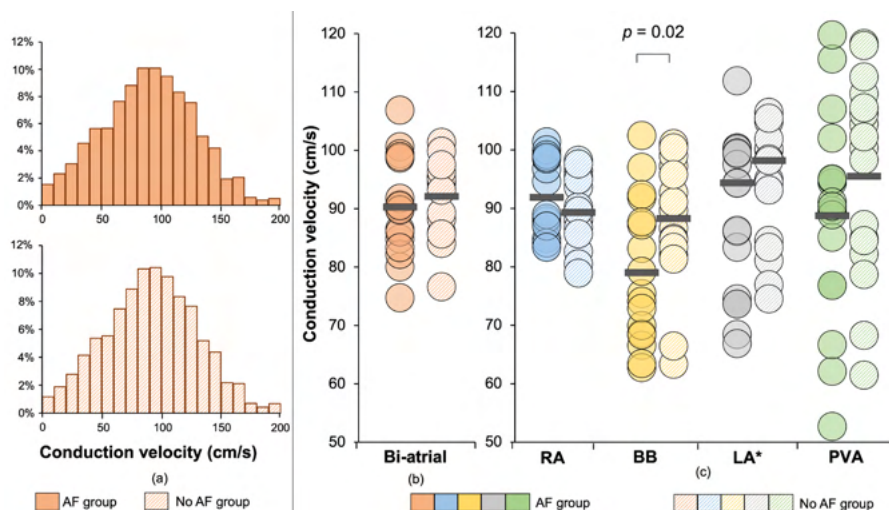
Figure 2 – Relative frequency distribution of conduction velocity. *Left panel*: biatrial CV histograms of patients with and without an history of AF. *Center panel*: biatrial median CV displayed for each patient. *Right panel*: median CV displayed for each patient per region separately. *Non-normally distributed. **CV** = conduction velocity; **AF** = atrial fibrillation; **BB** = Bachmann's bundle; **LA** = left atrium; **PVA** = pulmonary vein area; **RA** = right atrium.

Results

Study population

As presented in *Table 1*, baseline characteristics between the AF group (N=17, 73±7 years; 11 (64.7%) male) and no AF group (N=17, 74±7 years; 9 (52.9%) male) did not differ (all p≥0.05). Participants in the AF group either had paroxysmal AF (N=6, 27.3%), persistent AF (N=9, 40.9%) or long-standing persistent AF (N=2, 9.1%). Patients in the AF group had 1 [0.5–4.0] month AF before electrical cardioversion.

Mapping data characteristics

In total, 164,099 potentials (9,192 [7,421–11,250] potentials/patient) in the AF group and 150,015 potentials (8,533 [7,392–10,699] potentials/patient) in the no AF group were analyzed (p=0.23). Due to simultaneous activation, 2.4% of the potentials in the AF group and 2.5% of the potentials in the no AF group were excluded from analysis. SR cycle length during epicardial mapping was 808±117 ms in the AF group and 881±213 ms in the no AF group (p=0.17).

Conduction velocity throughout both atria

The left panel of *Figure 2* shows histograms of the relative frequency distribution of CVs throughout both atria for the AF group and no AF group separately. As can be seen, the CV histograms of both groups are comparable. Furthermore, *Figure 2* demonstrates the median CV in the AF and no AF group for both atria (middle panel) and for each location separately (right panel).

Biatrial median CV in the no AF group ranged from 77 to 107 cm/s and in the AF group from 75 to 101 cm/s. There was no difference in biatrial median CV between both groups (AF: 90±8 cm/s vs. no AF: 92±6 cm/s, p=0.56, middle panel *Figure 2*). Additionally, variation of CV
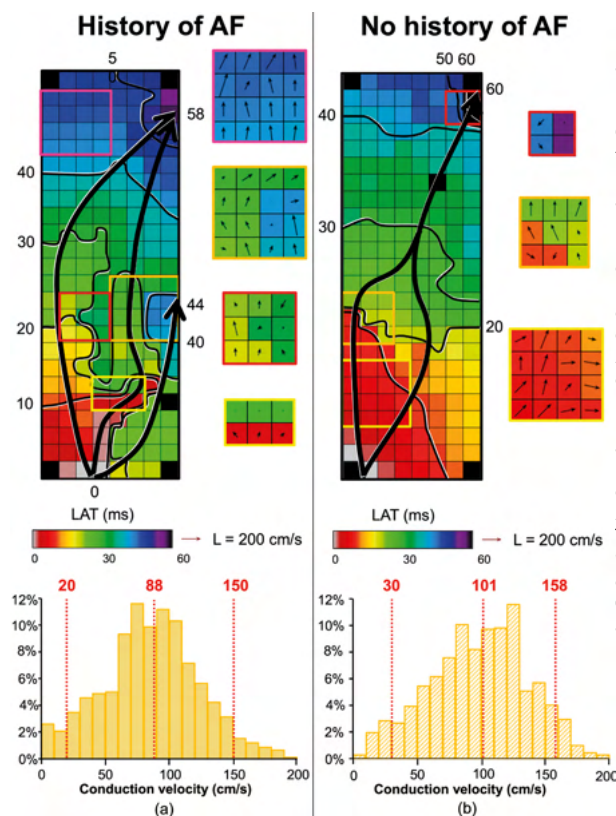
Figure 3 – Examples of Bachmann's bundle. *Upper panel*: two examples of a color-coded activation maps at BB obtained from a patient with a history of AF (left panel) and a patient without a history of AF (right panel). Corresponding CV maps are depicted next to the activation map. CV vectors are depicted per electrode. In the patient with AF, a large area of slowing of conduction is present in the lower part of the activation map, represented by crowding of isochrones. The colored boxes indicate smooth wavefront propagation (pink rectangle) and local conduction heterogeneities (yellow, red and orange rectangles). In the patient without AF, the sinus rhythm wavefront encounters only some small areas of conduction delay (orange and red rectangles). Isochrones (black lines) drawn at 10 ms. The black arrows indicate the main wave direction. *Lower panel*: corresponding CV histograms of the patient with AF (left) and without AF (right) recorded at Bachmann's bundle. The dashed lines represent the 5th, 50th and 95th percentiles of the relative frequency distribution of CVs. **BB** = Bachmann's bundle; **CV** = conduction velocity; **LAT** = local activation time.

19

was also comparable between the AF and no AF group (ΔP_5-P_{95}: 129±8 ms vs. 129±10 ms, p=0.88).

AF-related reduction of conduction velocity

The upper panel of *Figure 3* illustrates two examples of color-coded activation maps at BB obtained from a patient with an history of AF (left panel) and a patient without an history of AF (right panel). Corresponding CV maps are depicted next to the activation map. In the control patient, the SR wavefront encounters only some small areas of conduction delay, represented by crowding of isochrones in the left middle part of the array and right upper corner, resulting in a median CV of 101 cm/s. However, in the patient with a history of AF, a large area of slowing of conduction is present in the lower part of the activation map, resulting in a lower median CV of 88 cm/s. The lower panel of *Figure 3* illustrates the corresponding relative frequency distribution of CVs at BB of the same patients.

Table 2 – Variance of conduction velocity (ΔP_5-P_{95}).

	AF group (N=17)	No AF group (N=17)	*p*-value
Right atrium (cm/s)	118±9	114±8	0.14
Bachmann's bundle (cm/s)	121 [114–133]	129 [119–137]	0.31
Pulmonary vein area (cm/s)	129±12	130±21	0.87
Left atrium (cm/s)	139±11	143±13	0.42

Values are presented as mean ± standard deviation or median [interquartile ranges]. **AF** = atrial fibrillation.
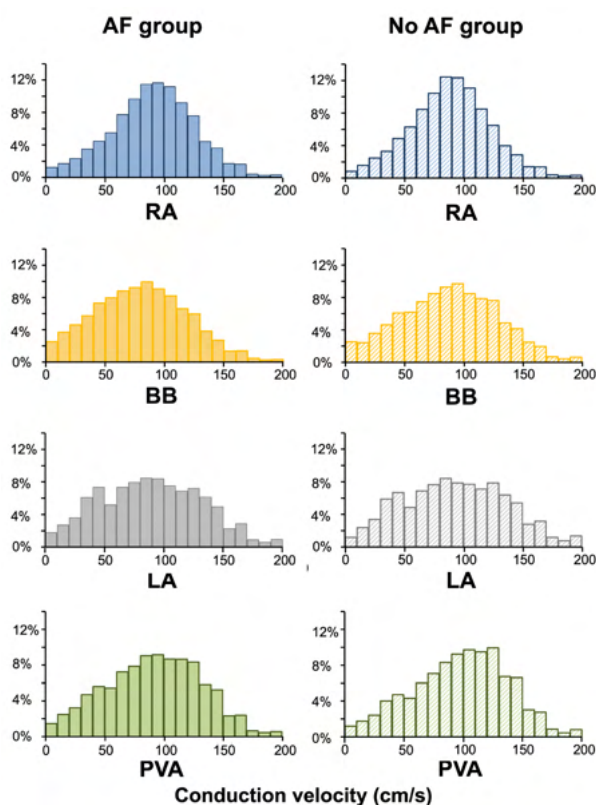
Figure 4 – Relative frequency distributions of CVs histograms in the AF (left panel) and no AF group (right panel) shown for each location separately. AF = atrial fibrillation; **BB** = Bachmann's bundle; **LA** = left atrium; **PVA** = pulmonary vein area; **RA** = right atrium.

Figure 4 shows relative frequency distributions of CVs in the entire AF and no AF group for each location separately. Compared to patients without AF, slowing of conduction was solely found at BB in patients with AF (BB: 79±12 cm/s vs. 88±11 cm/s, p=0.02; RA: 92±7 cm/s vs. 89±6 cm/s, p=0.35; PVA: 89±18 cm/s vs. 96±17 cm/s, p=0.32, LA: 94 [84–101] cm/s vs. 98 [84–101], p=0.21, right panel of *Figure 2*). However, as shown in *Table 2*, the variance of CV per location, including BB, was comparable between patients in the AF and no AF group (all p≥0.05).

The upper panel of *Figure 5* shows for the AF and no AF group at which region the lowest CV (5th percentile of the CV histogram) within each patient occurred. In patients without AF, there was no predilection site for the lowest CVs (P_5) (RA: 12%, N=2; BB: 29%, N=5; LA: 29%, N=5; PVA: 29%, N=5). In patients with AF, lowest CV was most often measured at BB (53%, N=9) and were also measured at the LA (18%, N=3) and PVA (29%, N=5), but not at the RA (RA: 0%, N=0). The lower panel of *Figure 5* shows the distribution of the lowest CV for each location separately. At BB, the lowest CV (interquartile range) ranged between 15 and 22 cm/s (median 20 cm/s), while in the no AF group it ranged between 23 and 31 cm/s

Table 3 – 5th percentiles of unipolar voltages.

	AF group (N=17)	No AF group (N=17)	*p*-value
Bi-atrial (mV)	0.6 [0.6–1.0]	0.8 [0.6–1.1]	0.44
Right atrium (mV)	1.1±0.6	0.9±0.3	0.20
Bachmann's bundle (mV)	0.9±0.6	1.5±0.9	0.02
Pulmonary vein area (mV)	0.6 [0.5–1.4]	1.4 [0.6–2.7]	0.08
Left atrium (mV)	1.2±0.7	1.2±0.7	0.83

Values are presented as mean ± standard deviation or median [interquartile ranges]. **AF** = atrial fibrillation.
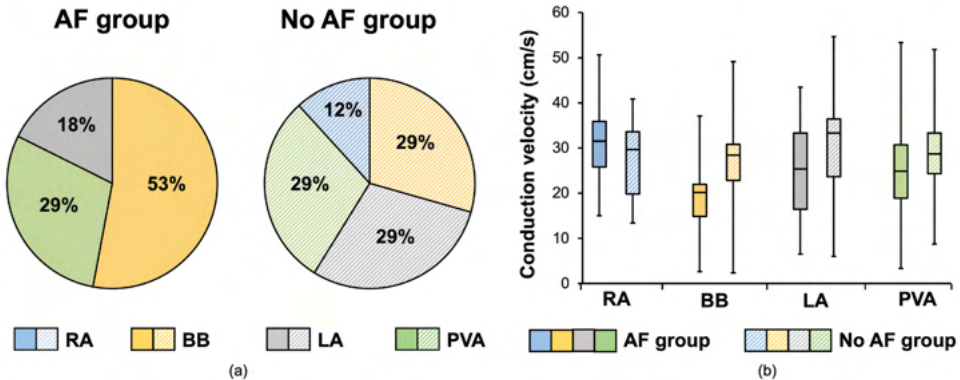
Figure 5 – Lowest conduction velocities. *Upper panel*: location of the lowest CV (defined as the 5th percentile of the relative frequency distribution of CV), within each AF patient (left) and no AF patient (right). *Lower panel*: distribution of the lowest CVs shown for each location separately. **AF** = atrial fibrillation; **BB** = Bachmann's bundle; **LA** = left atrium; **PVA** = pulmonary vein area; **RA** = right atrium.

(median: 28 cm/s). At the RA, LA and PVA, lowest CVs are comparable between the AF and no AF group.

Relation between conduction heterogeneity and total activation time

Figure 6 illustrates for each patient the TAT (left panel), and the TAT per region separately (right panel). AF was associated with a prolonged TAT (156±21 ms vs. 120±22 ms, p<0.001) and TAT was particularly prolonged at BB (76±31 ms vs. 58±23 ms, p=0.03).

Atrial fibrillation episodes and unipolar voltages

The lowest voltages (5th percentiles of the voltage histogram) differed between the AF and no AF group only at BB (*Table 3*). Patients in the AF group had a low voltage of 0.9±0.6 mV at this location, whereas in the control group it was 1.5±0.9 mV (p=0.02). The lowest voltages did not differ between both groups at RA, PVA and LA (all p≥0.05).

19
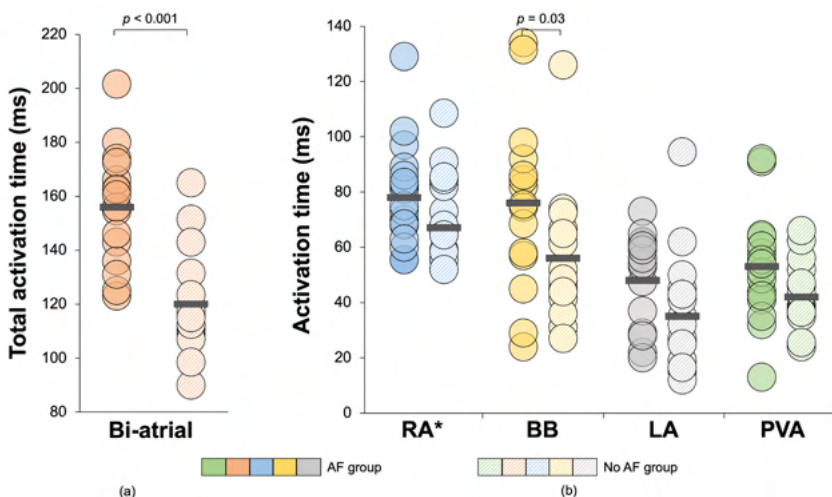
Figure 6 – Relation between conduction heterogeneity and total activation time. *Left panel*: biatrial TAT displayed for each individual patient. *Right panel*: TAT displayed for each patient per region separately. **BB** = Bachmann's bundle; **LA** = left atrium; **PVA** = pulmonary vein area; **TAT** = total activation time; **RA** = right atrium.

Discussion

This high-resolution intra-operative mapping study is the first to explore the association between CV and a history of AF in both atria. CV was reduced in the AF group only at BB. However, the variance of CV was comparable between both groups at this site. BB was also a predilection site for slowing of conduction in the AF group, as the lowest CVs were mostly located at this site. In patients without AF, the lowest CVs were found at all locations. Moreover, TAT was prolonged and voltages were decreased at BB in patients with AF. AF was not associated with a reduced CV, a prolonged TAT or lower voltages at the RA, PVA and LA.

Reduced conduction velocity as a prerequisite for AF onset

AF is the most common arrhythmia and induces both electrical and structural remodeling.[15,16] Longer duration of AF increases the degree of structural and electrical remodeling.[17,18] Electrical remodeling consists of alterations in ion channel expression and is reversible within one week of SR.[16,19-24] Structural remodeling consists of atrial fibrosis and side-to-side cell uncoupling and is still or partially present after 4 months of SR.[24-27] Both remodeling processes affect intra-atrial CV and may explain the increased vulnerability to AF. In the present study, we measure immediately after ECV, which means that both electrical and structural remodeling are present. After AF termination, it is generally assumed that the combination of increased dispersion of the refractory period and a reduced CV in combination with the presence of triggers such as premature beats may increase the susceptibility to AF recurrence.

As previously mentioned, the average CV measured during SR at the right atrial free wall in patients without atrial remodeling is 88±9 cm/s.[4] A similar CV of 89±13 cm/s was found at BB in 185 patients undergoing coronary artery bypass surgery, of whom only 13 had paroxysmal AF.[5] Comparing these CVs to the CV in our no AF group, our results are comparable at RA and BB with a median CV of 89±6 cm/s and 88±11 cm/s, respectively.

In our AF group, CV was reduced and TAT was prolonged only at BB compared to patients without AF. Previously, we determined the most accurate methodology to measure local conduction heterogeneity and, as a sub-analysis, we determined the median CV at all locations in patients with paroxysmal AF and no AF.[14] Subsequently, we also found a reduced CV at BB in patients without AF.[14] However, in that study we did not include patients with persistent or long-standing persistent AF who have varying degrees of atrial remodeling. Also, confounders of intra-atrial conduction, such as age, body mass index and left atrial enlargement, were not considered.[7-9] Patients were significantly older in the paroxysmal AF group (71±9 years vs. 66±10 years, p<0.001) and more patients had left atrial enlargement (41% vs. 19%, p<0.001).[14] Another study, performed by Zheng et al.[6], compared the average CV at the RA and LA between patients with paroxysmal AF and control patients with respectively atrioventricular nodal reentry tachycardia and Wolff-Parkinson-White syndrome using three-dimensional endocardial mapping. In that study, a history of AF was associated with a reduced CV at both locations which was more pronounced at the LA than the RA.[6] Remarkably, CV was much lower than our findings in the AF group (LA: 50 cm/s vs. 94 cm/s; RA: 60 cm/s vs. 92 cm/s). To estimate CV, they only compared a triplet of sites, when we computed, for each atrial potential, an average of velocity estimations between all eight adjacent electrodes.[6,14] Furthermore, those triplet numbers of locations were not measured simultaneously during the same beat, as we did in our study with the 128- or 192 electrode array.[6] It is likely that the CV measured in our study population is more accurate and therefore did not show a difference in CV at the RA and LA between patients with and without AF. In addition, no measurements were made of the PVA and BB, and the study population was underpowered with only six paroxysmal AF patients for comparison.[6]

We only evaluated regional differences in CV between patients with and without AF, and not specific areas within each region. As previously mentioned, CV is determined, among other things, by wavefront geometry and muscle thickness.[1,2] The smooth, apparently uniform walls of the LA are composed of multiple layers of differently aligned myocardial fibers, with marked regional variations in thickness.[28,29] In the RA, muscular bundles are larger, e.g. the terminal crest, and as a result of the presence of pectinate muscles, the RA wall is not uniform in thickness.[30] In normal hearts, inhomogeneities are already present in both gross structure and myoarchitecture.[30] Future studies should investigate whether there is a relation between the magnitude of CV and specific anatomic features in patients with AF.

Bachmann's bundle as a predilection site for atrial fibrillation

The propagation of wavefronts occurs preferably and more rapidly along longitudinal cardiac fibers instead of perpendicular to them.[31,32] BB has parallel aligned muscle bundles, making it the preferred route for interatrial conduction.[33] BB is also believed to play an important role in the pathophysiology of AF.[34,35] Clinical studies have found an association between interatrial block and development of AF.[34,36] In our study, patients with AF had a reduced CV with TAT prolongation at this site. A histological examination of 10 hearts from patients with paroxysmal AF and 10 hearts from patients without AF showed that fibro-fatty tissue was much more extensive in patients with AF.[37] This can lead to a disruption of cell-to-cell connections, disturbed wavefront geometry and thus a reduced CV and prolonged TAT.

Low voltages and atrial fibrillation

Low-voltage areas are a commonly used surrogate marker for the presence of atrial fibrosis, which plays a key role in the maintenance of AF.[38] Atrial fibrosis, in turn, affects local CV by forming 'zig-zag' like conduction paths, leading to anisotropy, and thus a reduced CV.[1] In the present study, we did not correlate low-voltage areas with CV, as it remains very challenging to identify a correct threshold to define low-voltage areas. Additionally, prior high-resolution epicardial mapping studies demonstrated no clear relationship between CV and low-voltage areas.[14,39] In our study population, in general we have found lower voltages at BB in patients with AF compared to patients without AF.

Study limitations

Patients in the AF group may have had varying degrees of atrial remodeling as some patients had persistent or long-standing persistent AF, while other patients had paroxysmal AF. In addition, in the AF group, SR recordings were made immediately after ECV, resulting in a different degree of electrical remodeling. Moreover, at different sinus rates, different exit pathways occur that can affect the CV. Direction-dependent CV heterogeneities could be missed as we only analyzed SR.

Conclusion

This high-resolution intra-operative mapping study is the first to examine the association between CV and a history of AF in both atria. At BB only, CV was reduced in the AF group. However, the variance of CV was comparable between both groups at this site. Additionally, BB was also a predilection site for slowing of conduction in the AF group, as the lowest CV was mostly located at this site. Moreover, the TAT was prolonged and voltages were decreased at BB in patients with AF. The next step will be to determine the relevance of a reduced CV at BB in relation to AF development and maintenance.

19

References

1. Kleber AG, Rudy Y. Basic mechanisms of cardiac impulse propagation and associated arrhythmias. Physiol Rev. 2004;84:431-488.
2. Rossi S, Gaeta S, Griffith BE, Henriquez CS. Muscle Thickness and Curvature Influence Atrial Conduction Velocities. Front Physiol. 2018;9:1344.
3. King JH, Huang CL, Fraser JA. Determinants of myocardial conduction velocity: implications for arrhythmogenesis. Front Physiol. 2013;4:154.
4. Hansson A, Holm M, Blomstrom P, Johansson R, Luhrs C, Brandt J, Olsson SB. Right atrial free wall conduction velocity and degree of anisotropy in patients with stable sinus rhythm studied during open heart surgery. Eur Heart J. 1998;19:293-300.
5. Teuwen CP, Yaksh A, Lanters EA, Kik C, van der Does LJ, Knops P, Taverne YJ, van de Woestijne PC, Oei FB, Bekkers JA, et al. Relevance of Conduction Disorders in Bachmann's Bundle During Sinus Rhythm in Humans. Circ Arrhythm Electrophysiol. 2016;9:e003972.
6. Zheng Y, Xia Y, Carlson J, Kongstad O, Yuan S. Atrial average conduction velocity in patients with and without paroxysmal atrial fibrillation. Clin Physiol Funct Imaging. 2017;37:596-601.
7. van der Does WFB, Houck CA, Heida A, van Schie MS, van Schaagen FRN, Taverne Y, Bogers A, de Groot NMS. Atrial electrophysiological characteristics of aging. J Cardiovasc Electrophysiol. 2021;32:903-912.
8. Schram-Serban C, Heida A, Roos-Serote MC, Knops P, Kik C, Brundel B, Bogers A, de Groot NMS. Heterogeneity in Conduction Underlies Obesity-Related Atrial Fibrillation Vulnerability. Circ Arrhythm Electrophysiol. 2020;13:e008161.
9. Schotten U, Verheule S, Kirchhof P, Goette A. Pathophysiological mechanisms of atrial fibrillation: a translational appraisal. Physiol Rev. 2011;91:265-325.
10. van der Does LJ, Yaksh A, Kik C, Knops P, Lanters EA, Teuwen CP, Oei FB, van de Woestijne PC, Bekkers JA, Bogers AJ, et al. QUest for the Arrhythmogenic Substrate of Atrial fibRillation in Patients Undergoing Cardiac Surgery (QUASAR Study): Rationale and Design. J Cardiovasc Transl Res. 2016;9:194-201.
11. Lanters EA, van Marion DM, Kik C, Steen H, Bogers AJ, Allessie MA, Brundel BJ, de Groot NM. HALT & REVERSE: Hsf1 activators lower cardiomyocyt damage; towards a novel approach to REVERSE atrial fibrillation. J Transl Med. 2015;13:347.
12. Yaksh A, Kik C, Knops P, Roos-Hesselink JW, Bogers AJ, Zijlstra F, Allessie M, de Groot NM. Atrial fibrillation: to map or not to map? Neth Heart J. 2014;22:259-266.
13. Mouws E, van der Does L, Kik C, Lanters EAH, Teuwen CP, Knops P, Bogers A, de Groot NMS. Impact of the arrhythmogenic potential of long lines of conduction slowing at the pulmonary vein area. Heart Rhythm. 2019;16:511-519.
14. van Schie MS, Heida A, Taverne Y, Bogers A, de Groot NMS. Identification of local atrial conduction heterogeneities using high-density conduction velocity estimation. Europace. 2021;23:1815-1825.
15. Allessie M, Ausma J, Schotten U. Electrical, contractile and structural remodeling during atrial fibrillation. Cardiovasc Res. 2002;54:230-246.
16. Wijffels MC, Kirchhof CJ, Dorland R, Allessie MA. Atrial fibrillation begets atrial fibrillation. A study in awake chronically instrumented goats. Circulation. 1995;92:1954-1968.
17. Ausma J, Litjens N, Lenders MH, Duimel H, Mast F, Wouters L, Ramaekers F, Allessie M, Borgers M. Time course of atrial fibrillation-induced cellular structural remodeling in atria of the goat. J Mol Cell Cardiol. 2001;33:2083-2094.
18. Schotten U, Duytschaever M, Ausma J, Eijsbouts S, Neuberger HR, Allessie M. Electrical and contractile remodeling during the first days of atrial fibrillation go hand in hand. Circulation. 2003;107:1433-1439.
19. Gaspo R, Bosch RF, Bou-Abboud E, Nattel S. Tachycardia-induced changes in Na+ current in a chronic dog model of atrial fibrillation. Circ Res. 1997;81:1045-1052.
20. Yue L, Feng J, Gaspo R, Li GR, Wang Z, Nattel S. Ionic remodeling underlying action potential changes in a canine model of atrial fibrillation. Circ Res. 1997;81:512-525.
21. Bosch RF, Zeng X, Grammer JB, Popovic K, Mewis C, Kuhlkamp V. Ionic mechanisms of electrical remodeling in human atrial fibrillation. Cardiovasc Res. 1999;44:121-131.
22. Van Wagoner DR, Pond AL, Lamorgese M, Rossie SS, McCarthy PM, Nerbonne JM. Atrial L-type Ca2+ currents and human atrial fibrillation. Circ Res. 1999;85:428-436.
23. Van Wagoner DR, Pond AL, McCarthy PM, Trimmer JS, Nerbonne JM. Outward K+ current densities and Kv1.5 expression are reduced in chronic human atrial fibrillation. Circ Res. 1997;80:772-781.
24. Everett THt, Li H, Mangrum JM, McRury ID, Mitchell MA, Redick JA, Haines DE. Electrical, morphological, and ultrastructural remodeling and reverse remodeling in a canine model of chronic atrial fibrillation. Circulation. 2000;102:1454-1460.
25. Spach MS, Boineau JP. Microfibrosis produces electrical load variations due to loss of side-to-side cell connections: a major mechanism of structural heart disease arrhythmias. Pacing Clin Electrophysiol. 1997;20:397-413.
26. Darby AE, Dimarco JP. Management of atrial fibrillation in patients with structural heart disease. Circulation. 2012;125:945-957.
27. Psaty BM, Manolio TA, Kuller LH, Kronmal RA, Cushman M, Fried LP, White R, Furberg CD, Rautaharju PM. Incidence of and risk factors for atrial fibrillation in older adults. Circulation. 1997;96:2455-2461.
28. Wang K, Ho SY, Gibson DG, Anderson RH. Architecture of atrial musculature in humans. Br Heart J. 1995;73:559-565.
29. Ho SY, Sanchez-Quintana D, Cabrera JA, Anderson RH. Anatomy of the left atrium: implications for radiofrequency ablation of atrial fibrillation. J Cardiovasc Electrophysiol. 1999;10:1525-1533.

30. Ho SY, Anderson RH, Sanchez-Quintana D. Atrial structure and fibres: morphologic bases of atrial conduction. Cardiovasc Res. 2002;54:325-336.
31. Roberts DE, Hersh LT, Scher AM. Influence of cardiac fiber orientation on wavefront voltage, conduction velocity, and tissue resistivity in the dog. Circ Res. 1979;44:701-712.
32. Spach MS, Miller WT, 3rd, Geselowitz DB, Barr RC, Kootsey JM, Johnson EA. The discontinuous nature of propagation in normal canine cardiac muscle. Evidence for recurrent discontinuities of intracellular resistance that affect the membrane currents. Circ Res. 1981;48:39-54.
33. Bachmann G. The inter-auricular time interval. Am J Physiol. 1916;41:309-320.
34. Agarwal YK, Aronow WS, Levy JA, Spodick DH. Association of interatrial block with development of atrial fibrillation. Am J Cardiol. 2003;91:882.
35. Duytschaever M, Danse P, Eysbouts S, Allessie M. Is there an optimal pacing site to prevent atrial fibrillation?: an experimental study in the chronically instrumented goat. J Cardiovasc Electrophysiol. 2002;13:1264-1271.
36. Ariyarajah V, Fernandes J, Kranis M, Apiyasawat S, Mercado K, Spodick DH. Prospective evaluation of atrial tachyarrhythmias in patients with interatrial block. Int J Cardiol. 2007;118:332-337.
37. Becker AE. How structurally normal are human atria in patients with atrial fibrillation? Heart Rhythm. 2004;1:627-631.
38. Sim I, Bishop M, O'Neill M, Williams SE. Left atrial voltage mapping: defining and targeting the atrial fibrillation substrate. J Interv Card Electrophysiol. 2019.
39. van Schie MS, Starreveld R, Bogers A, de Groot NMS. Sinus rhythm voltage fingerprinting in patients with mitral valve disease using a high-density epicardial mapping approach. Europace. 2021;23:469-478.

19
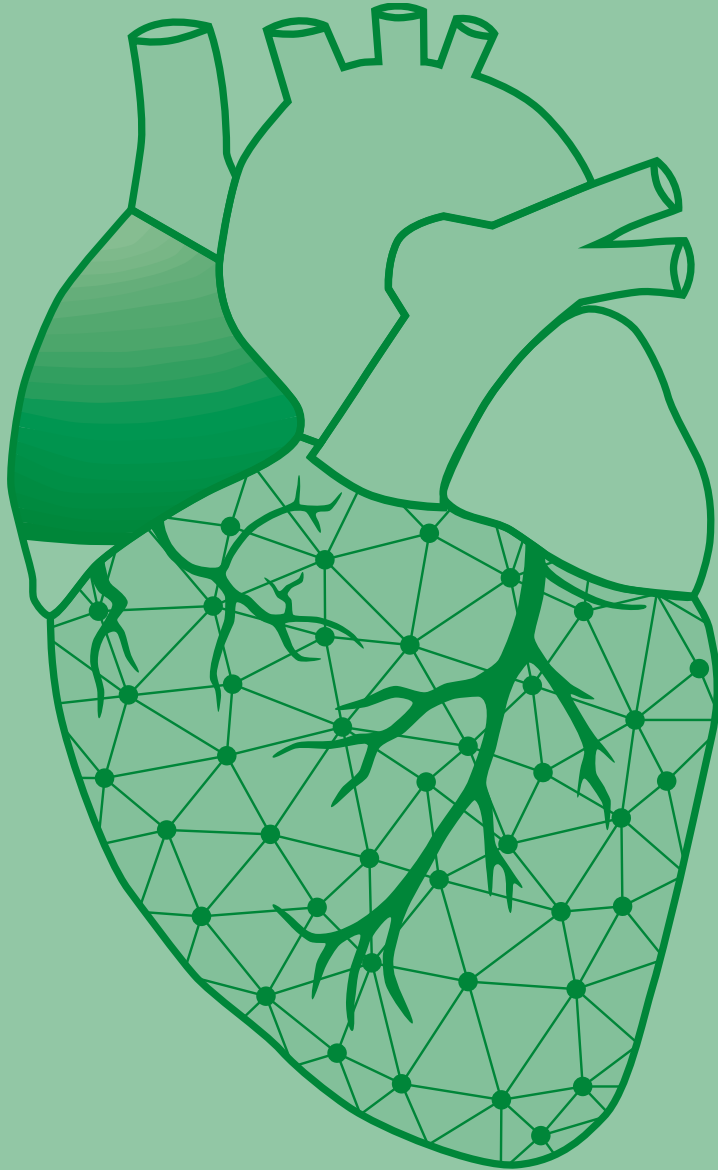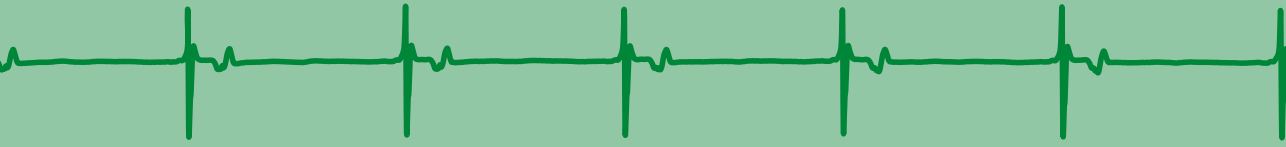
Chapter 20

Does conduction heterogeneity determine the supervulnerable period after atrial fibrillation?

Annejet Heida

Willemijn F.B. van der Does

Mathijs S. van Schie

Lianne N. van Staveren

Yannick J.H.J. Taverne

Ad J.J.C. Bogers

Natasja M.S. de Groot

Abstract

Atrial fibrillation (AF) resumes within 90 seconds in 27% of patients after sinus rhythm (SR) restoration. The aim of this study is to compare conduction heterogeneity during the supervulnerable period immediately after electrical cardioversion (ECV) with long-term SR in patients with AF. Epicardial mapping of both atria was performed during SR and premature atrial extrasystoles in patients in the ECV (N=17, age: 73±7 years) and control group (N=17, age: 71±6 years). Inter-electrode conduction times were used to identify areas of conduction delay (CD, conduction times 7–11 ms) and conduction block (CB, conduction times ≥12 ms). For all atrial regions, prevalence and length of longest CB and continuous CDCB lines, magnitude of conduction disorders, conduction velocity, biatrial activation time, and voltages did not differ between the ECV and control group during both SR and premature atrial extrasystoles (p≥0.05). Hence, our data suggest that there may be no difference in biatrial conduction characteristics between the supervulnerable period after ECV and long-term SR in AF patients.

Journal site &
supplementary material

Introduction

The recurrence rate of atrial fibrillation (AF) after electrical cardioversion (ECV) is as high as 57% during the first month after cardioversion, with a peak incidence during the first five days.[1] In fact, AF even resumes within 1 or 2 minutes in up to 27% of patients after restoration of sinus rhythm (SR).[2-5] This immediate recurrence of AF (IRAF) can be explained by either a high frequency of ectopic beats or the presence of a supervulnerable period immediately after ECV. Duytschaever et al.[2] studied electrophysiological properties in a goat model after spontaneous termination of at least 5 minutes of AF-induced electrical remodeling and found during SR a transient shortening of the atrial effective refractory period, reduction of intra-atrial conduction velocity (CV) and shortening of the atrial wavelength compared to baseline. During this so-called supervulnerable period, the atria are more susceptible to re-initiation of AF triggered by premature beats.[2] However, heterogeneity in conduction as a result of AF-induced electrical remodeling during this period during SR and premature atrial complexes has never been examined in humans. It is unknown to what extent intra-atrial conduction is impaired during this phase and whether different right and left atrial regions are equally affected. The aim of this case-control study is therefore to compare conduction heterogeneity assessed during the supervulnerable period with long-term SR at a high-resolution scale. To our knowledge, this is the first study investigating differences in prevalence and severity of conduction disorders at the epicardial surface of the right atrium, Bachmann's bundle and left atrium including the pulmonary vein area immediately after ECV.

Methods

Study population and setting

The study population consisted of participants undergoing elective open-heart surgery in the Erasmus Medical Center. Indications for elective cardiac surgery were either coronary artery disease, aortic valve disease or mitral valve disease, or the combination of these. The case group consisted of AF patients who presented with AF at the onset of the surgical procedure and were electrically cardioverted to SR (structural and electrically remodeled atria). The control group consisted of AF patients who presented with SR (solely structurally remodeled atria as they were in SR for a longer period of time).[6-10] Thus, only AF-induced electrical remodeling is studied. Participants were matched based on age[11], body mass index[12] and left atrial enlargement[13], known confounders of intra-atrial conduction disorders. In a previous paper of our group[14], we studied the impact of underlying heart disease on conduction heterogeneity during sinus rhythm and did not find any differences between patients with valvular heart disease and ischemic heart disease. Echocardiographic images were used to assess atrial dilatation. This study is approved by the institutional Medical Ethical Committee (MEC 2010-05415 and MEC 2014-39316). Prior to the surgical procedure written informed consent was obtained from all patients. The study complied with the Declaration of Helsinki. Clinical data was extracted from electronic patient files.

Mapping procedure

High-resolution epicardial mapping was performed during open heart surgery, prior to extracorporeal circulation.[17] A pacemaker wire temporarily attached to the right atrial free wall functioned as a bipolar reference electrode. A steel wire fixed to the subcutaneous tissue of the thoracic wall was used as an indifferent electrode. Epicardial mapping was performed by shifting a unipolar 128- or a 192-electrode array (electrode diameter respectively 0.65 and 0.45 mm, interelectrode distances of 2 mm) in a systematic order along predefined

20
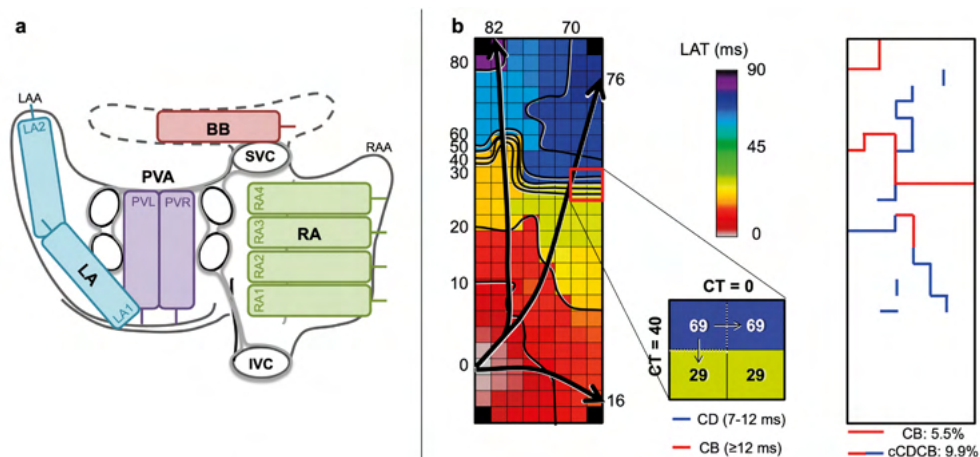
Figure 1 – Epicardial mapping method. *Panel a*: mapping scheme of RA (RA1-RA4), BB, LA (LA1-LA2) and PVA (PVR and PVL). *Panel b*: example of a color-coded activation map with isochrones (black lines) drawn at 10 ms. The black arrows indicate the main wavefront directions. An example of calculation of CTs by subtracting the LAT of adjacent electrodes is shown next to the activation map. The right panel shows an example of the corresponding CB and cCDCB map. **BB** = Bachmann's bundle; **cCDCB**; continuous lines of conduction delay- and block lines; **CB** = conduction block; **CD** = conduction delay; **CT** = conduction time; **IVC** = inferior vena cava; **LA** = left atrium; **LAA** = left atrial appendage; **LAT** = local activation time; **PVA** = pulmonary vein area; **PVL** = left pulmonary vein; **PVR** = right pulmonary vein; **RA** = right atrium; **RAA** = right atrial appendage; **SVC** = superior vena cava.

sites covering the epicardial surface of both atria (*Figure 1a*), including right atrium (from the inferior caval vein up to the right atrial appendage, perpendicular to the caval veins), pulmonary vein area (from the sinus transversus, alongside the borders of the pulmonary veins towards the atrioventricular groove), left atrium (from the lower border of the left pulmonary vein along the left atrioventricular groove towards the left atrial appendage), and Bachmann's bundle (from the tip of left atrial appendage behind the aorta towards the superior cavo-atrial junction).

At each site, five seconds of SR mapping were recorded, including unipolar epicardial electrograms, a surface electrocardiogram, a bipolar reference electrogram and a calibration signal (amplitude: 2 mV, duration: 1000 ms). Recordings were sampled with a rate of 1 kHz, amplified (gain: 1000), filtered (bandwidth: 0.5–400 Hz), analogue-to-digital-converted (16-bits) and stored on hard disk.

Mapping data processing

The steepest negative slopes of all atrial potentials were automatically annotated with custom-made software. For each electrode the local activation time was determined, and color-coded activation maps were reconstructed as illustrated in *Figure 1b*.[18,19] All annotations were visually verified. Mapping sites with less than 50% annotation were excluded from analysis.

Analysis of intra-atrial conduction disorders

As previously described in a number of mapping studies, inter-electrode conduction times (CTs) were calculated by subtracting the local activation times of each electrode from the adjacent right and lower electrode (*Figure 1b*).[18,19] Conduction delay (CD) and conduction
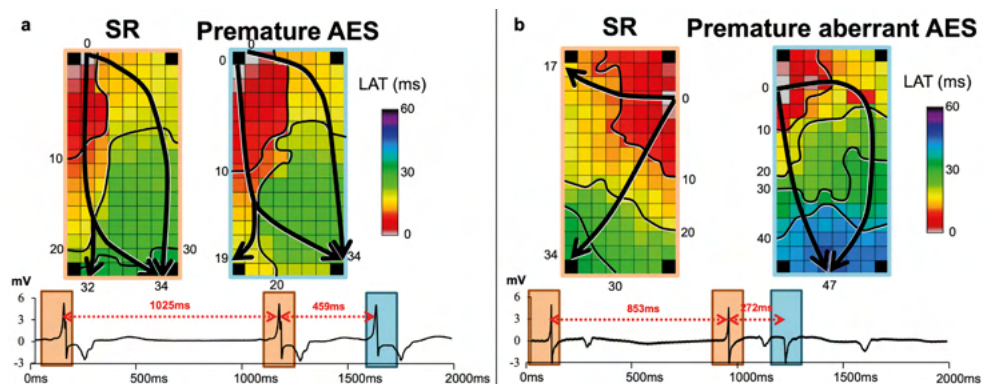
Figure 2 – Premature atrial extrasystoles. *Panel a*: examples of color-coded activation maps during SR (left) and during a premature atrial extrasystole (right) with a shortening in cycle length ≥25% compared to the previous SR beat. *Panel b*: examples of color-coded activation maps during SR (left) and during a prematurely aberrant atrial extrasystole (right) with a shortening in cycle length ≥25% and a different direction of propagation compared to the previous SR beat. Isochrones (black lines) drawn at 10 ms increments. The black arrows indicate the main trajectories of activation. **AES** = atrial extrasystoles; **LAT** = local activation time; **SR** = sinus rhythm.

block (CB) were defined as conduction times of respectively 7–11 ms and ≥12 ms, which corresponds to effective conduction velocities of respectively 17 to 29 cm/s and <17 cm/s.[20,21] Lines of CB and continuous CDCB (cCDCB) were defined as uninterrupted series of respectively inter-electrode CB or a combination of CD and CB (*Figure 1b*). Prevalence of lines of CB and cCDCB lines are expressed as a percentage of the total available number of interelectrode connections. In all patients, lengths of the longest CB or cCDCB line were assessed at every atrial region. The magnitude of conduction times was defined as the size of inter-electrode time differences in milliseconds and the percentage of patients with conduction times above different magnitudes were calculated. The magnitude of conduction times was analyzed in 10 ms increments. Local CV was computed as an average of velocity estimations between neighboring electrodes (longitudinal, transversal and diagonal) using discrete velocity vectors as previously described by Van Schie et al.[22] From these local CVs, median CV and variation in CV (ΔP_5-P_{95}) were calculated for every mapping site. Total activation time and the activation time for each mapping site separately were determined by relating the first and last activation to the reference electrode. Voltage was defined as the peak-to-peak amplitude of the steepest deflection of the unipolar potential. We determined the 5th percentile of the relative frequency histograms of the voltages of all unipolar potentials and compared them between the ECV and control group. Areas of simultaneous activation were excluded from analysis in order to avoid inclusion of far-field potentials.

Intra-atrial conduction disorders during premature beats

To study whether conduction disorders are more pronounced at shorter coupling intervals during the supervulnerable period, conduction heterogeneity during spontaneously occurring premature atrial complexes (PACs) were also investigated. PACs included premature and premature aberrant atrial extrasystoles (*Figure 2*). PACs are defined as beats with a shortening in cycle length of ≥25% compared to the previous SR beat (*Figure 2*). Additionally, the premature aberrant beat has a different direction of propagation compared to the previous SR beat (*Figure 2b*).[23] Prematurity index of PACs was expressed as the ratio between the coupling interval of the PAC and the preceding SR cycle length:

Table 1 – Characteristics of participants.

	ECV group (N=17)	Control group (N=17)	*p*-value
Patients	73±7	71±6	0.32
Male	11 (64.7)	12 (70.6)	1.00
BMI (kg/m²)	27±5	26±5	0.42
History of AF	17 (100.0)	17 (100.0)	1.00
• Paroxysmal	6 (35.3)	11 (64.7)	≥0.017*
• Persistent	9 (52.9)	6 (35.3)	≥0.017*
• Long-standing persistent	2 (11.8)	0 (0.0)	≥0.017*
Underlying heart disease			1.00
• IHD	2 (11.8)	2 (11.8)	
• (i)VHD	15 (88.2)	15 (88.2)	
- AVD	2 (11.8)	4 (23.5)	
- AVD and CAD	2 (11.8)	1 (5.9)	
- MVD	9 (52.9)	8 (47.1)	
- MVD and CAD	2 (11.8)	2 (11.8)	
Echocardiography			
• LVF			1.00
- Normal	11 (64.7)	16 (94.1)	
- Mild dysfunction	3 (17.6)	0 (0.0)	
- Moderate dysfunction	3 (17.6)	0 (0.0)	
- Severe dysfunction	0 (0.0)	1 (5.9)	
• LAVI (ml/m²)	47 [43–63]†	46 [38–66]‡	0.72
Medication			
• Antiarrhythmic drugs			0.45
- Class I	0 (0.0)	0 (0.0)	
- Class II	11 (64.7)	7 (41.2)	
- Class III	4 (23.5)	0 (0.0)	
- Class IV	1 (5.9)	1 (5.9)	
• Digoxin	5 (29.4)	0 (0.0)	0.06

Values are presented as mean ± standard deviation, median [interquartile ranges] or as N (%). **AF** = atrial fibrillation; **AVD** = aortic valve disease; **BMI** = body mass index; **CAD** = coronary artery disease; **ECV** = electrical cardioversion; **IHD** = ischemic heart disease; **LA** = left atrium; **LAVI** = left atrial volume index; **LVF** = left ventricular function; **MVD** = mitral valve disease; **(i)VHD** = (ischemic and) valvular heart disease. † N=15; ‡ N=12; * Bonferroni correction was applied.

$$I_{prematurity} = -\frac{CL_{PAC}}{CL_{SR}} \cdot 100\%$$

CL_{PAC} equals the cycle length of the spontaneous PAC and CL_{SR} the cycle length of the preceding two sinus beats. The difference (Δ) of conduction parameters between the previous SR beat and the PACs were compared between the ECV and the control group.

Statistical analysis

Statistical analysis was performed with SPSS version 25 (IBM Corporation, Armonk, New York). All data were tested for normality using Shapiro-Wilk test. Normally distributed continuous data were expressed as mean ± standard deviation and skewed data as median [25th–75th percentile]. A paired samples *t*-test or Wilcoxon signed rank test was used to compare continuous parameters for the comparison of SR between the ECV and the control group. For the comparison of continuous data during PACs, an independent samples *t*-test or Mann-Whitney U test was performed. Categorical data are expressed as absolute numbers (percentages) and analyzed with (McNemar's symmetry) χ² or McNemar's exact test if appropriate. For the comparison of magnitude of conduction times between the ECV and control group, correction for multiple testing was applied. Corrected *p*-values will be reported. A two-sided *p*-value of <0.05 was considered statistically significant.
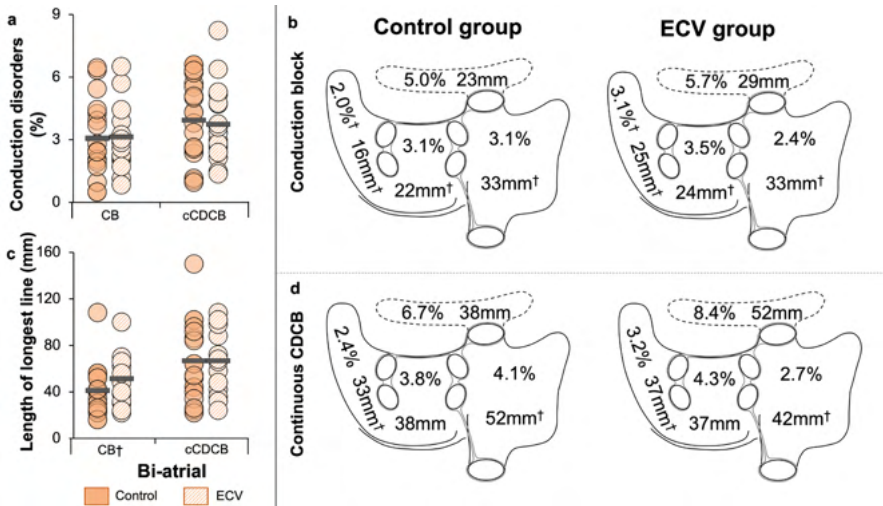
Figure 3 – Prevalence and length of longest CB and cCDCB lines. *Panel a*: prevalence of CB and cCDCB in both atria. *Panel b*: spatial distribution of prevalence of CB and length of longest CB lines. *Panel c*: length of longest lines of CB and cCDCB in both atria. *Panel d*: spatial distribution of prevalence of cCDCB and length of longest cCDCB lines. †Non-normally distributed. **cCDCB** = continuous lines of conduction delay- and block; **CB** = conduction block; **ECV** = electrical cardioversion.

Results

Study population

As presented in *Table 1*, baseline characteristics between the ECV (N=17, 73±7 years; 11 (64.7%) male) and control group (N=17, 71±6 years; 12 (70.6%) male) did not differ (all p≥0.05). Participants in the ECV group had either paroxysmal AF (N=6, 35.3%), persistent AF (N=9, 52.9%) or long-standing persistent AF (N=2, 11.8%), while in the control group participants had paroxysmal AF (N=11, 64.7%) or persistent AF (N=6, 35.3%, p=1.00). Patients in the ECV group had an AF episode duration of 1 month [0.5–4.0] before AF was terminated. Patients in the control group were 54 [13–234] days in SR before surgery.

Mapping data characteristics

In the ECV and control group, a total of respectively 164,099 unipolar potentials (9,192 [7,421–11,250] potentials/patient) and 149,521 unipolar potentials (8,418 [7112–10,831] potentials/patient) were available for further analysis (p=0.52). Due to simultaneous activation, 2.3% of the potentials in the ECV group and 1.1% of the potentials in the control group were excluded from analysis. SR cycle length during epicardial mapping was 788 [736–894] ms in the ECV group and 855 [764–962] ms in the control group (p=0.10).

Biatrial conduction

In the entire study population, each patient in the ECV group, as well as in the control group, had areas of CD and CB. Differences in prevalence and length of longest lines of CB and cCDCB in both atria between the ECV and control group are shown in *Figure 3*. As illustrated in *Figure 3a*, the prevalence of CB and cCDCB in both atria did not differ between the control and ECV group (CB: 3.1±1.7 % vs. 3.1±1.9 %, p=0.93; cCDCB: 3.7±1.8 % vs. 3.9±1.9 %, p=0.78). Additionally, the length of the longest lines of both CB and cCDCB were the same in patients immediately after ECV and during long-term SR (CB: 48 [31–66] mm vs. 40 [25–53] mm, p=0.0.23; cCDCB: 67±26 mm vs. 67±35 mm, p=1.00).

20
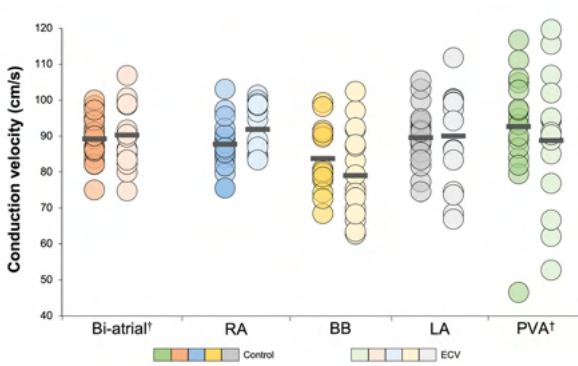
Figure 4 – Biatrial and regional conduction velocity. *Left panel:* biatrial median conduction velocity displayed for each patient. *Right panel:* median conduction velocity displayed for each patient per region separately. [†]Non-normally distributed. **BB** = Bachmann's bundle; **ECV** = electrical cardioversion. **LA** = left atrium; **PVA** = pulmonary vein area; **RA** = right atrium.

Regional differences in prevalence and the length of longest lines of CB and cCDCB between the control and the ECV group are shown in the *Figure 3* and *Supplementary Table 1*. Conduction disorders are observed in both groups at all locations, but mainly at Bachmann's bundle. *Figure 3* and *Supplementary Table 1* show that both the prevalence of CB and cCDCB as well as the length of the longest CB lines and cCDCB lines at every location did not differ between the ECV and control group (all p≥0.05).

Figure 4 shows the median CV for each patient in both atria and for each location separately. Biatrial median CV was not reduced in the ECV group (90 [84–99] cm/s vs. 89 [85–95] cm/s, p=0.69). Biatrial variation in CV also did not differ between both groups (ΔP_5–$P9_5$: 127 [123–132] cm/s vs. 125 [121–136] cm/s, p=0.87). Comparing CV for each location separately, again no differences in median CV were found between the ECV and the control group (right atrium: 92±7 cm/s vs. 88±7 cm/s, p=0.11; Bachmann's bundle: 80±12 cm/s vs. 84±9 cm/s, p=0.22; pulmonary vein area: 90 [77–98]] cm/s vs. 93 [85–104], p=0.34; left atrium: 90±13 cm/s vs. 90±8 cm/s, p=0.90). As shown in *Supplementary Table 1*, the variation in CV per location also was comparable between patients in the ECV and control group (all p≥0.05).

Severity of conduction disorders

Figure 5 shows the magnitude of conduction times in both atria for the ECV and control group separately. Each patient in both groups had at least one CT ≥32 ms. The magnitude of conduction times was comparable in the ECV and control group (Bonferroni corrected p≥0.006). By comparing the different atrial regions separately between both groups, again
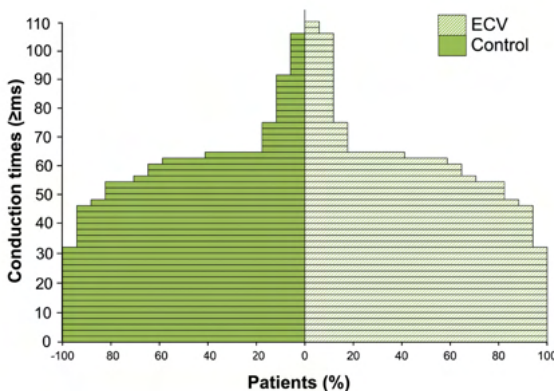
Figure 5 – Severity of conduction disorders. Magnitude of CTs measured after ECV and during long-term SR for the entire study population in increments of 10 ms. **CTs** = conduction times; **ECV** = electrical cardioversion; **SR** = sinus rhythm.
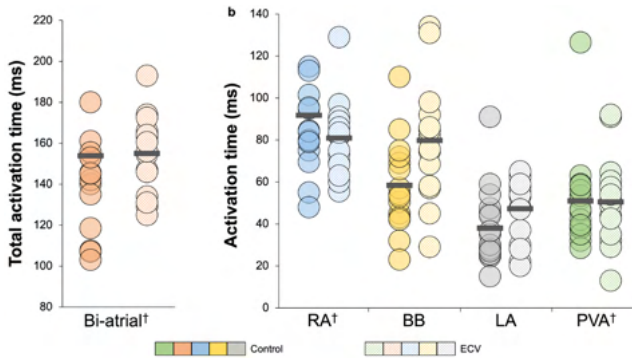
Figure 6 – Total activation time. *Panel a:* biatrial total activation time displayed for each individual patient. *Panel b*: activation time displayed for each patient per region separately. [†]Non-normally distributed **BB** = Bachmann's bundle; **ECV** = electrical cardioversion; **LA** = left atrium; **PVA** = pulmonary vein area; **RA** = right atrium.

there were no differences in the magnitude of conduction times (right atrium: Bonferroni corrected p≥0.008; Bachmann's bundle: Bonferroni corrected p≥0.005; pulmonary vein area: Bonferroni corrected p≥0.01; left atrium: Bonferroni corrected p≥0.01).

Relation between conduction heterogeneity and biatrial activation time

Figure 6 illustrates for each patient the total activation times and the activation time per region separately. The supervulnerable period was not associated with a prolonged biatrial total activation times (158 [137–166] ms vs. 145 [122–160] ms, p=0.41) or a prolonged activation time for each location separately (all p≥0.05). Activation time was longest at the right atrium (ECV: 82 [69–90] ms vs. control: 84 [76–110] ms, p=0.57).

Unipolar voltages

Comparison of the 5th percentile of all biatrial voltages between the control and ECV group did not reveal lower unipolar voltages during the supervulnerable period (*Table 2*; ECV: 0.8±0.4 mV vs. control: 0.9±0.5 mV; p=0.31). When comparing the 5th percentile of voltages for each location separately there were also no differences between both groups (all p≥0.05).

Conduction disorders during premature beats

Seven patients (41%) in the control group had a total of 11 PACs (4 premature atrial extrasystoles (36%); 7 premature aberrant atrial extrasystoles (64%)) whereas in the ECV group, seven patients (41%) had a total of 22 PACs (6 premature atrial extrasystoles (27%); 16 premature aberrant atrial extrasystoles (73%)). The prematurity index of the PACs did not differ between the control and ECV group (61.2±10.3 % vs. 55.6±12.6 %, p=0.22).

Table 3 shows for both groups the difference (Δ) in conduction disorders during the PAC compared to the corresponding SR beat. The increase in conduction disorders was not more pronounced during the supervulnerable period, as the Δ prevalence and Δ length of longest

Table 2 – Unipolar voltages in the ECV and control group.

	ECV (N=17)	Control (N=17)	*p*-value
Bi-atrial (mV)	0.7±0.3	0.9±0.5	0.31
Right atrium (mV)	1.0 [0.7–1.3]	0.9 [0.5–1.3]	0.83
Bachmann's bundle (mV)	1.0±0.6	1.1±0.8	0.49
Pulmonary vein area (mV)	0.6 [0.5–1.4]	0.9 [0.6–1.2]	0.94
Left atrium (mV)	1.2±0.7	1.6±0.7	0.22

Values are presented as mean ± standard deviation or median [interquartile ranges]. **ECV** = electrical cardioversion.

20

Table 3 – Differences (Δ) in conduction during PACs compared SR.

	ECV (N=22)	Control (N=11)	*p*-value
Δ CB			
Prevalence (%)	1.0 [-0.7–3.6]	2.6 [0–5.6]	0.30
Length of longest CB line (mm)	6.0 [2.0–10]	12.5 [3.0–27.0]	0.27
Δ cCDCB			
Prevalence (%)	3.6±6.2	1.1±5.3	0.23
Length of longest CB line (mm)	0 [-2–8]	18 [-12.0–28]	0.13
Δ CV (cm/s)	-6±19	-11±13	0.48
Δ P$_5$ of unipolar voltages (mV)	-0.3 [-1.0–0.4]	-0.2 [-2.2–0.6]	0.87

Values are presented as mean ± standard deviation or median [interquartile ranges]. **CB** = conduction block; **cCDCB** = continuous lines of conduction delay and -block; **CV** = conduction velocity; **PAC** = premature atrial complexes.

CB and cCDCB lines did not differ between both groups (all p≥0.05). Additionally, ΔCV was similar between the control and the ECV group as the CV decreased with respectively 11±13 cm/s and 6±19 cm/s between SR and PACs (p=0.48). The supervulnerable period was also not associated with a more pronounced decrease of the 5th percentile of the voltages histograms in patients after ECV (-0.3 [-1.0–0.4] mV vs. -0.2 [-2.2–0.6] mV, p=0.87).

Discussion

This high-resolution intra-operative mapping study is the first to investigate biatrial heterogeneity in conduction during the so-called supervulnerable period immediately after ECV. Compared to long-term SR, no increased conduction heterogeneity was found immediately after ECV, since the frequency and severity of conduction disorders, as well as CV and TAT, did not differ during SR between the control and ECV group. Additionally, conduction disorders during PACs were not more pronounced immediately after ECV. Hence, our data suggest that the supervulnerable period may not be characterized by impaired intra-atrial conduction.

Conduction disorders as a predictor for early atrial fibrillation recurrences

Rosenbaum introduced the term 'domestication of AF', meaning that the longer the duration of AF episodes, the more difficult it becomes to achieve SR. After termination of AF, 27% of patients have an IRAF within 1 minute after successful ECV.[3-5] At a higher heart rate, e.g. during AF, atrial CV will decrease while the wavelength of the atrial impulse and the atrial effective refractory period shortens.[24,25] These changes during AF promote reentry as they reduce the likelihood that a wavefront circling around a line of CB collides with its refractory tail.[26] After AF termination, it is generally assumed that the combination of increased dispersion of the atrial effective refractory period and a reduced CV in combination with the presence of triggers such as PAC may increase the susceptibility to AF recurrence.

Duytschaever et al.[2] examined the supervulnerable phase immediately after AF termination in goats with non-remodeled and electrically remodeled atria (48 hours of electrically maintained AF). Baseline atrial effective refractory period, intra-atrial CV and atrial wavelength were determined.[2] After the baseline study, AF was induced lasting at least 5 minutes and all measures were repeated immediately after spontaneous restoration of SR. They found transient shortening of the atrial effective period, reduction of intra-atrial CV during SR, and shortening of the atrial wavelength compared to baseline. These observations implied the existence of a vulnerable substrate for initiation of reentry after AF termination in goats. One possible explanation for slowing of conduction after AF termination is a decrease in sodium and increase in potassium currents due to high atrial rates during AF.[27-30] The resting membrane potential, and as a result the driving force for sodium ions exchange, will decrease resulting in a lower action potential velocity upstroke and thus a lower CV.[2]

However, we did not observe a reduction of CV in humans immediately after AF termination. We found that intra-atrial conduction during the supervulnerable period and long-term SR were comparable. Also, during PACs, there was no reduction of CV. In other words, our findings suggests that an increased susceptibility to AF re-initiation during the so-called supervulnerable period may be not determined by a reduction in CV.

A possible explanation may be that the normalization of intracellular sodium concentrations is restored within only a few SR beats and is not present for 1 to 2 minutes as previously suggested. Another explanation may be the duration of AF and its impact on electrical remodeling.[31,32] In our ECV group, patients had 1 month AF before termination of AF ranging (IQR) between 2 weeks and 4 months. Only 2 patients had long-standing persistent AF (AF duration of 1 year and 1.5 year) before termination, while longer AF episodes are correlated with more electrical remodeling and thus a reduced CV.[31,32]

In humans, atrial conduction during the supervulnerable period has not been previously investigated. However, a few studies reported on the reversal of electrical remodeling over time after termination of AF. Yu et al.[33] performed endocardial mapping of the left atrium and right atrium 30 minutes (t=30) after restoration of SR in humans and studied conduction times during four consecutive days using two ten-polar electrode catheters positioned at the right atrial appendage and distal coronary sinus. Conduction times were measured from the second to the fifth pairs of electrodes (5 mm inter-pair distance), while the first pair was used for pacing at a basic cycle length of 700 ms. After termination of AF, inter atrial conduction did not change during these four days. We studied conduction times during SR as a measure of inter-electrode differences in local activation time ≥12 ms (CB) and as the activation time of the right atrium and left atrium. Moreover, we investigated these conduction properties during the supervulnerable period rather than the reversal of electrical remodeling over time starting at t=30 minutes. However, our findings that there are no differences in frequency of CB and activation time of the right atrium and left atrium during the supervulnerable period are consistent with these findings. Additionally, Yu et al.[33] examined surface electrocardiograms over the same time course after AF termination using the duration of the P-wave as a measure of total activation times in patients with persistent AF. They found no change in P-wave duration over time. In contrast, in another study, P-wave duration was prolonged within 5 to 20 minutes after AF termination compared to 24 hours and one month post-conversion.[34] However, in both studies, there were no measurements during the supervulnerable period. The control group in our study was in SR for approximately 1.5 months and still no differences in intra-atrial conduction were found between control and ECV group.

Premature beats as a trigger for early atrial fibrillation recurrences

Triggers, e.g., PACs, play an important role in AF onset in patients with an IRAF.[2,35] In our study population, a higher incidence of PACs was present during the supervulnerable period compared to long-term SR. In both groups seven patients had PACs, but 22 PACs were found in the ECV group, while only 11 PACs were found in the control group. A possible mechanism that enhances PAC-initiated IRAF is the occurrence of intracellular calcium overload due to the previous high-rate AF episode promoting late phase 3 early afterdepolarization-induced PACs.[36] The high AF rates result in an increase in intracellular sodium leading to cellular calcium load mediated by sodium-calcium exchange.[36] After AF termination, strong calcium release in the sarcoplasmic reticulum stimulates extrusion of calcium through sodium-calcium exchanger.[36] As a result, a transient period of hypercontractility occurs.[37] Additionally, the inward current of calcium mediated by the exchanger is most likely responsible for the transient action potential duration prolongation and early afterdepolarizations.[36]

20

Additionally, to the occurrence of atrial triggers, IRAF requires a vulnerable substrate for reentry. In our study population, even conduction disorders caused by PACs were not more pronounced during the supervulnerable period. A limitation is that we did not study PACs that did indeed trigger an IRAF, yet the prematurity of PACs is comparable to previously reported PACs inducing AF. In the goat model of AF, all IRAFs episodes were triggered by PACs with coupling intervals ranging between 310 and 580 ms; ectopic beats with a coupling interval >600 ms never resulted in IRAF.[2] In humans, the coupling intervals of PACs initiating IRAF were shorter (418 ms) than PACs which did not initiate IRAF (661 ms, p<0.05).[3] PACs in our study population had a mean coupling interval of 482 ms (prematurity index: 61.2%) and 470 ms (prematurity index: 55.6%) in respectively the control and ECV group. Although no IRAF was initiated, these coupling intervals were short enough to initiate AF.

Potential other mechanisms leading to early atrial fibrillation recurrences

Since intra-atrial conduction is not impaired after AF termination during both SR and PACs, other mechanisms may be responsible for the occurrence of IRAF. As previously mentioned, an increased dispersion of atrial effective refractory period, a reduced CV and the frequency of triggers may enhance the susceptibility to AF recurrences. In the present study, we did not investigate atrial effective refractory period, as our study was designed to study conduction during SR and PACs. However, several other human studies found a shortening of atrial effective refractory period during the supervulnerable period.[34,38-40] Additionally, a significant dispersion of atrial refractoriness between different right atrial sites was present.[38] This, in combination with a higher frequency of PACs, may be a possible explanation for the occurrence of IRAF, as it facilitates the likelihood of encountering unidirectional conduction block, which is a prerequisite for development of reentrant circuits.

In the present study, biatrial CV was not reduced in the ECV group (p=0.69). However, we have not studied the rate-dependent slowing of CV (CV restitution) which may precede AF initiation.[41] Narayan et al. showed that patients with paroxysmal AF had steep CV restitution interacting with steep action potential restitution, which may cause rapid tachycardias to initiate AF.[41,42] On the other hand, patients with persistent AF, with more advanced remodeling of the atria, and broad CV restitution developed AF at lower heartrates.[41-44] However, the precise mechanism underlying the relationship between CV restitution and AF initiation is still unclear.

Low-voltage areas during the supervulnerable period

In our present study, we found no relationship between low-voltage areas and the supervulnerable period. Little is known about the impact of electrical remodeling on unipolar voltages. As previously mentioned, it is likely that due to electrical remodeling during AF, sodium current is reduced resulting in a decrease of voltages displayed in the unipolar electrogram which may still be present after AF termination.[27-30] However, we did not find low-voltage areas during the supervulnerable period.

Study limitations

Patients with a history of AF may have had variable degrees of atrial remodeling as some patients had persistent or long-standing persistent AF, while other patients had paroxysmal AF. Even if we perform a subanalysis in patients with paroxysmal AF between the ECV and control group, there were no differences found in any of the conduction parameters. In patients with persistent and long-standing persistent AF comparable results were found. Additionally, PACs triggering AF were not investigated.

Clinical relevance

This study is the first to investigate conduction disorders due to AF-related electrical remodeling immediately after ECV in high-resolution of the entire atrial surface. Since intra-atrial conduction is not impaired after AF termination during both SR and PACs compared to long-term SR, it is suggested that IRAF is not enhanced by conduction disorders. To further investigate conduction impairment during the shortest coupling intervals, programmed electrical stimulation reaching atrial refractoriness should be performed to examine CV restitution in relation to AF initiation. Other mechanisms, such as an increased dispersion of atrial effective refractory period and the frequency of triggers, may also be possible explanations for the occurrence of IRAF. These findings help to better understand the mechanism behind the IRAF and improve treatment strategies aimed at eliminating IRAF.

Conclusion

This high-resolution intra-operative mapping study is the first to investigate characteristics of biatrial conduction immediately after ECV during the so-called supervulnerable period. Compared to long-term SR, there was no impaired intra-atrial conduction immediately after ECV. These observations suggest that the supervulnerable period is not characterized by increased conduction heterogeneity during SR or PACs. However, to further investigate conduction impairment during the shortest coupling intervals, programmed electrical stimulation reaching atrial refractoriness should be performed to examine CV restitution.

20

References

1. Tieleman RG, Van Gelder IC, Crijns HJ, De Kam PJ, Van Den Berg MP, Haaksma J, Van Der Woude HJ, Allessie MA. Early recurrences of atrial fibrillation after electrical cardioversion: a result of fibrillation-induced electrical remodeling of the atria? J Am Coll Cardiol. 1998;31:167-173.
2. Duytschaever M, Danse P, Allessie M. Supervulnerable phase immediately after termination of atrial fibrillation. J Cardiovasc Electrophysiol. 2002;13:267-275.
3. Timmermans C, Rodriguez LM, Smeets JL, Wellens HJ. Immediate reinitiation of atrial fibrillation following internal atrial defibrillation. J Cardiovasc Electrophysiol. 1998;9:122-128.
4. Sra J, Biehl M, Blanck Z, Dhala A, Jazayeri MR, Deshpande S, Akhtar M. Spontaneous reinitiation of atrial fibrillation following transvenous atrial defibrillation. Pacing Clin Electrophysiol. 1998;21:1105-1110.
5. Wellens HJ, Lau CP, Luderitz B, Akhtar M, Waldo AL, Camm AJ, Timmermans C, Tse HF, Jung W, Jordaens L, et al. Atrioverter: an implantable device for the treatment of atrial fibrillation. Circulation. 1998;98:1651-1656.
6. Spach MS, Boineau JP. Microfibrosis produces electrical load variations due to loss of side-to-side cell connections: a major mechanism of structural heart disease arrhythmias. Pacing Clin Electrophysiol. 1997;20:397-413.
7. Darby AE, Dimarco JP. Management of atrial fibrillation in patients with structural heart disease. Circulation. 2012;125:945-957.
8. Wijffels MC, Kirchhof CJ, Dorland R, Allessie MA. Atrial fibrillation begets atrial fibrillation. A study in awake chronically instrumented goats. Circulation. 1995;92:1954-1968.
9. Everett THt, Li H, Mangrum JM, McRury ID, Mitchell MA, Redick JA, Haines DE. Electrical, morphological, and ultrastructural remodeling and reverse remodeling in a canine model of chronic atrial fibrillation. Circulation. 2000;102:1454-1460.
10. Psaty BM, Manolio TA, Kuller LH, Kronmal RA, Cushman M, Fried LP, White R, Furberg CD, Rautaharju PM. Incidence of and risk factors for atrial fibrillation in older adults. Circulation. 1997;96:2455-2461.
11. van der Does WFB, Houck CA, Heida A, van Schie MS, van Schaagen FRN, Taverne Y, Bogers A, de Groot NMS. Atrial electrophysiological characteristics of aging. J Cardiovasc Electrophysiol. 2021;32:903-912.
12. Schram-Serban C, Heida A, Roos-Serote MC, Knops P, Kik C, Brundel B, Bogers A, de Groot NMS. Heterogeneity in Conduction Underlies Obesity-Related Atrial Fibrillation Vulnerability. Circ Arrhythm Electrophysiol. 2020;13:e008161.
13. Schotten U, Verheule S, Kirchhof P, Goette A. Pathophysiological mechanisms of atrial fibrillation: a translational appraisal. Physiol Rev. 2011;91:265-325.
14. Heida A, van der Does WFB, van Staveren LN, Taverne Y, Roos-Serote MC, Bogers A, de Groot NMS. Conduction Heterogeneity: Impact of Underlying Heart Disease and Atrial Fibrillation. JACC Clin Electrophysiol. 2020;6:1844-1854.
15. van der Does LJ, Yaksh A, Kik C, Knops P, Lanters EA, Teuwen CP, Oei FB, van de Woestijne PC, Bekkers JA, Bogers AJ, et al. QUest for the Arrhythmogenic Substrate of Atrial fibRillation in Patients Undergoing Cardiac Surgery (QUASAR Study): Rationale and Design. J Cardiovasc Transl Res. 2016;9:194-201.
16. Lanters EA, van Marion DM, Kik C, Steen H, Bogers AJ, Allessie MA, Brundel BJ, de Groot NM. HALT & REVERSE: Hsf1 activators lower cardiomyocyt damage; towards a novel approach to REVERSE atrial fibrillation. J Transl Med. 2015;13:347.
17. Yaksh A, Kik C, Knops P, Roos-Hesselink JW, Bogers AJ, Zijlstra F, Allessie M, de Groot NM. Atrial fibrillation: to map or not to map? Neth Heart J. 2014;22:259-266.
18. Teuwen CP, Yaksh A, Lanters EA, Kik C, van der Does LJ, Knops P, Taverne YJ, van de Woestijne PC, Oei FB, Bekkers JA, et al. Relevance of Conduction Disorders in Bachmann's Bundle During Sinus Rhythm in Humans. Circ Arrhythm Electrophysiol. 2016;9:e003972.
19. Mouws E, van der Does L, Kik C, Lanters EAH, Teuwen CP, Knops P, Bogers A, de Groot NMS. Impact of the arrhythmogenic potential of long lines of conduction slowing at the pulmonary vein area. Heart Rhythm. 2019;16:511-519.
20. Allessie M, Ausma J, Schotten U. Electrical, contractile and structural remodeling during atrial fibrillation. Cardiovasc Res. 2002;54:230-246.
21. de Groot NM, Houben RP, Smeets JL, Boersma E, Schotten U, Schalij MJ, Crijns H, Allessie MA. Electropathological substrate of longstanding persistent atrial fibrillation in patients with structural heart disease: epicardial breakthrough. Circulation. 2010;122:1674-1682.
22. van Schie MS, Heida A, Taverne Y, Bogers A, de Groot NMS. Identification of local atrial conduction heterogeneities using high-density conduction velocity estimation. Europace. 2021;23:1815-1825.
23. Teuwen CP, Kik C, van der Does L, Lanters EAH, Knops P, Mouws E, Bogers A, de Groot NMS. Quantification of the Arrhythmogenic Effects of Spontaneous Atrial Extrasystole Using High-Resolution Epicardial Mapping. Circ Arrhythm Electrophysiol. 2018;11.
24. Smeets JL, Allessie MA, Lammers WJ, Bonke FI, Hollen J. The wavelength of the cardiac impulse and reentrant arrhythmias in isolated rabbit atrium. The role of heart rate, autonomic transmitters, temperature, and potassium. Circ Res. 1986;58:96-108.
25. Rensma PL, Allessie MA, Lammers WJ, Bonke FI, Schalij MJ. Length of excitation wave and susceptibility to reentrant atrial arrhythmias in normal conscious dogs. Circ Res. 1988;62:395-410.
26. Mines GR. On dynamic equilibrium in the heart. J Physiol. 1913;46:349-383.
27. Gaspo R, Bosch RF, Bou-Abboud E, Nattel S. Tachycardia-induced changes in Na+ current in a chronic dog model of atrial fibrillation. Circ Res. 1997;81:1045-1052.
28. Bosch RF, Zeng X, Grammer JB, Popovic K, Mewis C, Kuhlkamp V. Ionic mechanisms of electrical remodeling in human atrial fibrillation. Cardiovasc Res. 1999;44:121-131.

29. Van Wagoner DR, Pond AL, McCarthy PM, Trimmer JS, Nerbonne JM. Outward K+ current densities and Kv1.5 expression are reduced in chronic human atrial fibrillation. Circ Res. 1997;80:772-781.
30. Nattel S, Maguy A, Le Bouter S, Yeh YH. Arrhythmogenic ion-channel remodeling in the heart: heart failure, myocardial infarction, and atrial fibrillation. Physiol Rev. 2007;87:425-456.
31. Ausma J, Litjens N, Lenders MH, Duimel H, Mast F, Wouters L, Ramaekers F, Allessie M, Borgers M. Time course of atrial fibrillation-induced cellular structural remodeling in atria of the goat. J Mol Cell Cardiol. 2001;33:2083-2094.
32. Schotten U, Duytschaever M, Ausma J, Eijsbouts S, Neuberger HR, Allessie M. Electrical and contractile remodeling during the first days of atrial fibrillation go hand in hand. Circulation. 2003;107:1433-1439.
33. Yu WC, Lee SH, Tai CT, Tsai CF, Hsieh MH, Chen CC, Ding YA, Chang MS, Chen SA. Reversal of atrial electrical remodeling following cardioversion of long-standing atrial fibrillation in man. Cardiovasc Res. 1999;42:470-476.
34. Manios EG, Kanoupakis EM, Chlouverakis GI, Kaleboubas MD, Mavrakis HE, Vardas PE. Changes in atrial electrical properties following cardioversion of chronic atrial fibrillation: relation with recurrence. Cardiovasc Res. 2000;47:244-253.
35. Inoue K, Kurotobi T, Kimura R, Toyoshima Y, Itoh N, Masuda M, Higuchi Y, Date M, Koyama Y, Okamura A, et al. Trigger-based mechanism of the persistence of atrial fibrillation and its impact on the efficacy of catheter ablation. Circ Arrhythm Electrophysiol. 2012;5:295-301.
36. Burashnikov A, Antzelevitch C. Reinduction of atrial fibrillation immediately after termination of the arrhythmia is mediated by late phase 3 early afterdepolarization-induced triggered activity. Circulation. 2003;107:2355-2360.
37. Denham NC, Pearman CM, Caldwell JL, Madders GWP, Eisner DA, Trafford AW, Dibb KM. Calcium in the Pathophysiology of Atrial Fibrillation and Heart Failure. Front Physiol. 2018;9:1380.
38. Pandozi C, Bianconi L, Villani M, Gentilucci G, Castro A, Altamura G, Jesi AP, Lamberti F, Ammirati F, Santini M. Electrophysiological characteristics of the human atria after cardioversion of persistent atrial fibrillation. Circulation. 1998;98:2860-2865.
39. Kamalvand K, Tan K, Lloyd G, Gill J, Bucknall C, Sulke N. Alterations in atrial electrophysiology associated with chronic atrial fibrillation in man. Eur Heart J. 1999;20:888-895.
40. Lubinski A, Kempa M, Lewicka-Nowak E, Krolak T, Raczak G, Swiatecka G. Electrical atrial remodeling assessed by monophasic action potential and atrial refractoriness in patients with structural heart disease. Pacing Clin Electrophysiol. 1998;21:2440-2444.
41. Lalani GG, Schricker A, Gibson M, Rostamian A, Krummen DE, Narayan SM. Atrial conduction slows immediately before the onset of human atrial fibrillation: a bi-atrial contact mapping study of transitions to atrial fibrillation. J Am Coll Cardiol. 2012;59:595-606.
42. Narayan SM, Kazi D, Krummen DE, Rappel WJ. Repolarization and activation restitution near human pulmonary veins and atrial fibrillation initiation: a mechanism for the initiation of atrial fibrillation by premature beats. J Am Coll Cardiol. 2008;52:1222-1230.
43. Rohr S, Kucera JP, Kleber AG. Slow conduction in cardiac tissue, I: effects of a reduction of excitability versus a reduction of electrical coupling on microconduction. Circ Res. 1998;83:781-794.
44. Shaw RM, Rudy Y. Ionic mechanisms of propagation in cardiac tissue. Roles of the sodium and L-type calcium currents during reduced excitability and decreased gap junction coupling. Circ Res. 1997;81:727-741.

20
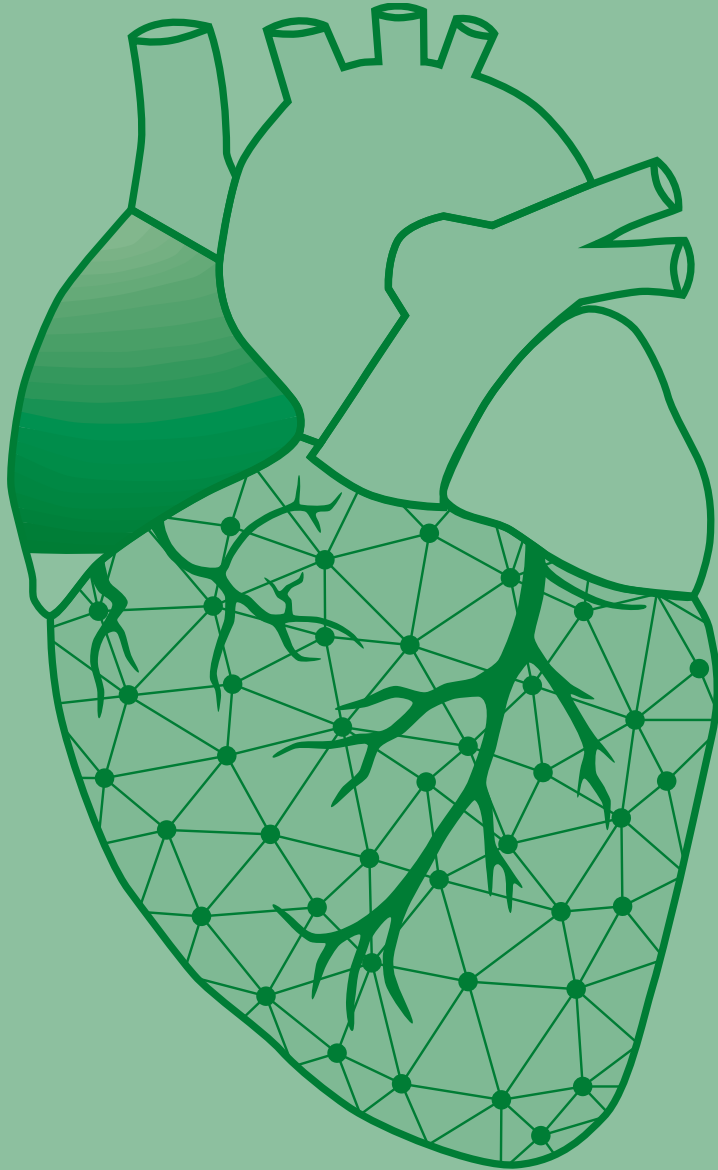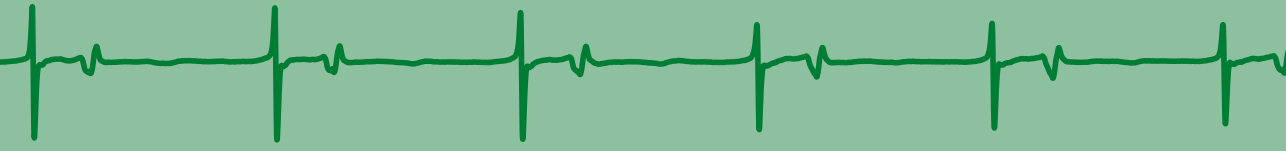
Chapter 21

Endo-epicardial mapping of in-vivo human sino-atrial node activity

Rohit K. Kharbanda*

Fons J. Wesselius*

Mathijs S. van Schie

Yannick J.H.J. Taverne

Ad J.J.C. Bogers

Natasja M.S. de Groot

* Contributed equally

Abstract

Background: Electrophysiological properties of the in-vivo human sino-atrial node (SAN) and its exit pathways remain poorly understood. The aim of the present study was therefore to examine electrophysiological characteristics of SAN activity from an endo-epicardial perspective.

Methods: Twenty patients (75% male, 66±7 years) with structural heart disease underwent simultaneous endo-epicardial mapping (256 unipolar electrodes, interelectrode distance 2 mm). Conduction times (CTs), endo-epicardial delays (EED) and R/S-ratio were examined in the surrounding 10 mm of SAN activation. Areas of conduction block (CB) were defined as conduction delays of ≥12 ms and endo-epicardial asynchrony (EEA) as EED ≥15m.

Results: Three distinct activation patterns were observed in a total of 28 SAN – focal activation patterns (SAN-FAPs) (4 patients showed >1 different exit site), including SAN activation patterns with 1) solely an endocardial exit site (n=10 (36%)), 2) solely an epicardial exit site (n=13 (46%)) and 3) simultaneously activated endo-epicardial exit sites, (n=5 (18%)). EED at the origin of the SAN-FAP was 10 [6-14] ms and the prevalence of EEA in the surroundings of the SAN-FAP was 5 [2–18] %. Electrograms at the origin of SAN-FAPs showed significantly larger R-peaks in mid RA compared to superior RA (mid R/S-ratio: 0.15 [0.067–0.34] vs. superior R/S-ratio: 0.045 [0.026–0.062], p=0.004). Conduction velocity within a distance of 10 mm from the SAN-FAP was 125 [80–250] cm/s. All six SAN-FAPs at mid RA were observed in patients with a history of AF.

Conclusions: Variations in activation patterns of the SAN observed in our study highlight the complex 3-dimensional SAN geometry and indicate presence of inter-individual differences in SAN exit pathways. Solely in patients with a history of atrial fibrillation, SAN activity occurred more caudally, which indicates changes in preferential SAN exit pathways.

Journal site

Introduction

Propagation of the electrical wavefront from the sino-atrial node (SAN) into the surrounding atrial tissue is a complex 3-dimensional process. Boineau and Schuessler postulated that the SAN is isolated from the right atrial myocardium by the SAN artery and fibro-fatty tissue except for several exit pathways. These exit pathways enable atrial excitation at multiple sites simultaneously and are influenced by neurohormonal factors.[1,2] Subsequently, Fedorov et al.[3] used optical mapping of the isolated coronary-perfused human SAN in combination with histological examination to demonstrate that SAN arteries, fibrotic and fatty tissue surrounding the SAN indeed form significant conduction barriers. By demonstrating that propagation from the SAN occurred via multiple sino-atrial exit pathways bypassing these structural barriers, the Boineau and Schuessler hypothesis was further substantiated. A recent study by Bychkov et al.[4] in ex-vivo mice, provided novel insights into the role of subcellular Ca^{2+} signaling pathways within and among cells comprising the SAN. Microscopic assessment of the SAN revealed synchronized action potentials emerging from heterogeneous subcellular subthreshold Ca^{2+} currents, which highlight the functional complexity of the SAN. Although the SAN was described more than a century ago, electrophysiological properties of the SAN and its sino-atrial exit pathways remain poorly understood.

Sánchez-Quintana et al.[5] studied the architecture of the SAN in 47 post-mortem hearts, and demonstrated that the SAN is a highly complex irregular structure packed within a dense matrix of connective tissue with multiple radiations interdigitating with the surrounding myocardium. The authors postulated that the anatomy of the SAN may facilitate slowing of conduction thereby providing a substrate for reentry. Recent data suggests that SAN activity provokes endo-epicardial asynchrony (EEA).[6] Whether structural barriers surrounding the SAN also result in enhanced conduction abnormalities between the endo- and/or epicardial layer is unknown.

So far, few studies have described the simultaneously occurring patterns of activation in the endo- and epicardial layer surrounding the SAN area in the intact human heart. We therefore investigated SAN activation in patients undergoing open-heart surgery by performing simultaneous endo-epicardial mapping at a high density scale.

Methods

Study population

Patients with structural heart disease undergoing elective open-heart surgery were included in the present study. Exclusion criteria were hemodynamic instability, implanted pacemaker with atrial pacing, previous cardiac surgery, end stage renal failure or severely impaired left ventricular function. The study was approved by the institutional medical ethical committee (MEC2015-373) and written informed consent was obtained from all patients. The study was carried out according to the principles of the Declaration of Helsinki. Patient characteristics were obtained from electronic medical files.

Simultaneous endo-epicardial mapping procedure

An overview of the methodology is provided in *Figure 1*. After heparinization and arterial cannulation, simultaneously endo- and epicardial mapping was performed prior to commencing of extra-corporal circulation. Two electrode arrays, each containing 128 unipolar electrodes with a diameter of 0.45 mm and 2 mm inter-electrode spacing, were secured on two bendable spatulas. As demonstrated in panel B of *Figure 1*, the electrode arrays

21
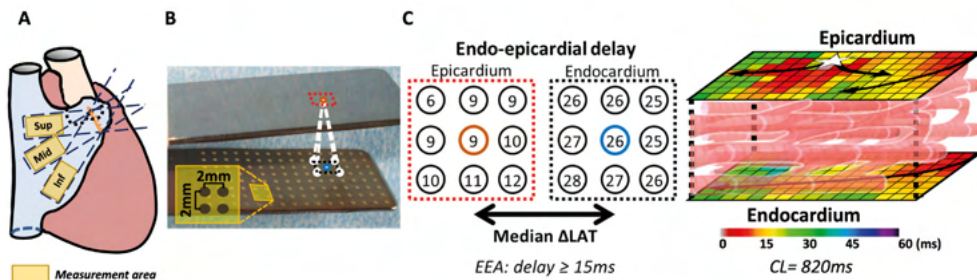
Figure 1 – Overview of the methodology. *Panel A*: two 128-electrode arrays were secured exactly opposite of each other on two spatulas (Ø electrode=0.45 mm, interelectrode distance=2 mm). One spatula was placed in the right atrium on the endocardial surface through the incision for venous cannulation. The other spatula was placed on the opposite epicardial surface. Recordings were performed at three locations, towards the 1) superior caval vein (superior), 2) terminal crest (mid), and 3) inferior caval vein (inferior). *Panel B*: in order to calculate EED, the local activation times of the direct opposite electrode and its 8 surrounding electrodes were used. *Panel C*: color-coded activation map of the endo- and epicardium covering the SAN region demonstrating an epicardial SAN exit site. EED was calculated by determining local endo-epicardial activation time differences. For each electrode, the median of the time delays within the exact opposite electrode and its eight surrounding electrodes was selected. LAT indicates local activation time. EEA was defined as EED ≥15 ms. **CL** = cycle length; **EEA** = endo-epicardial asynchrony; **EED** = endo-epicardial delay; **Inf** = inferior; **LAT** = local activation time; **Mid** = middle; **Sup** = superior.

were located on the exact opposite side of each other.[7] A temporary epicardial pacemaker wire was stitched to the RA free wall and served as the reference electrode. The indifferent electrode was connected to a steel wire, which was stitched to the subcutaneous tissue of the thoracic wall. Prior to venous cannulation, one spatula (marked as the endocardial electrode array) was introduced in the RA after incising the RA appendage and the incision site was closed with the purse string suture. In order to prevent overlap of measurement area near the right atrial incision, the endocardial electrode array was introduced into the right atrium for at least 1.5 cm extra after introducing the last row of electrodes. Simultaneous endo-epicardial mapping was performed following a predefined mapping scheme with 3 different mapping locations on the right atrial (RA) free wall as illustrated in panel A of *Figure 1*. Mapping of the superior RA started at the junction of the superior caval vein and RA also covering the sulcus terminalis. Due to the large dynamic range of SAN activity, the mapping clamp was subsequently moved to the middle and inferior part of the right atrium.

Simultaneous endo-epicardial mapping was performed for 5 seconds during SR, and included a calibration signal of 2 mV and 1000 ms, a bipolar reference electrogram and all endo- and epicardial unipolar electrograms. Recordings were analogue-to-digital converted (16-bits), sampled with a rate of 1 kHz, amplified (gain 1000) and filtered (bandwidth 0.5–400 Hz).

Mapping Data Analysis

Mapping data was analyzed using custom made software previously described in detail.[8] For both the endo- and epicardial layer, color-coded activation maps were reconstructed by annotating the steepest negative slope of atrial potentials recorded at every electrode.[9] Consistent with prior intra-operative mapping studies, areas of CB were defined as interelectrode differences in local activation times (LATs) of ≥12 ms corresponding with effective conduction velocities of <17 cm/s.[9]

SAN activation

All recordings were independently screened by two researchers based on the selection

criteria for focal activation patterns (FAPs), as described in previous studies.[9-11] These criteria include: 1) the electrode from which the SAN-FAP originates (SAN-FAP origin) is not activated more than 1 ms after activation of the first electrode of the entire electrode array, 2) in case of a neighboring electrode being activated at the same time, this electrode should be activated at least 2 ms earlier than its surrounding electrodes and 3) the distance between the border of the mapping area and the SAN-FAP origin should be at least 2 electrodes.

In case of repetitive SAN activation patterns which were nearly distinguishable from one another, only one SAN-FAP arising at the same location during the entire recording was included for analyses. If the SAN-FAP origin covered more electrodes with similar LATs, the electrode closest to the center of this earliest activated area was chosen as the SAN-FAP origin. In order to investigate conduction properties at different distances relative to the SAN-FAP origin, the Euclidean distances between the SAN-FAP origin and surrounding electrodes within a range of 10 mm were calculated. This yielded fourteen predefined distances from the SAN-FAP origin: 0 mm (origin), 2 mm, 2.8 mm, 4.0 mm, 4.5 mm, 5.6 mm, 6.0 mm, 6.3 mm, 7.2 mm, 8.0 mm, 8.2 mm, 8.5 mm, 8.9 mm, and 10.0 mm. SAN-FAPs with their origin within a range of 6 mm from a line of CB were labeled as FAPs near lines of CB.

Propagation of SAN-FAPs in either the endo- or epicardium

Conduction velocity (CV) in an area with a radius of 10 mm around the SAN-FAP was analyzed by calculating the conduction time (CT) between the SAN-FAP origin and the neighboring electrodes in the same plane. As there are multiple electrodes with the same distance to the SAN-FAP origin in the different directions, the shortest CT from the origin of SAN-FAP towards the predefined distances within this area was calculated reflecting the fastest conduction of the SR wavefront away from the SAN-FAP origin.

Endo-epicardial delay at the sino-atrial node area

Endo-epicardial delay (EED) was calculated by determining differences in local endo-epicardial activation times, as illustrated in panel B and C of *Figure 1*. In accordance with previous mapping studies, for each electrode, the median of the time delays within the

21

Table 1 – Patient characteristics.

Patients	21
Age (y)	66 [59–73]
Male	15 (75%)
BMI (kg/m²)	27 [23–31]
Underlying heart disease	
• iHD	9 (45%)
• vHD	4 (20%)
• cHD	7 (35%)
History of AF	
• Paroxysmal	8 (40%)
Cardiovascular risk factors	
• Hypertension	10 (50%)
• Diabetes mellitus	7 (35%)
• Hypercholesterolemia	10 (50%)
Left ventricular function	
• Good or mild impairment (LVEF ≥40%)	17 (85%)
• Moderate impairment (LVEF 30–39%)	3 (15%)

Values are presented as N (%) or median [interquartile ranges]. **SAN-FAP** = sino-atrial node – focal activation pattern; **BMI** = body mass index; **iHD** = ischemic heart disease; **vHD** = valvular heart disease; **cHD** = combined heart disease; **AF** = atrial fibrillation; **LVEF** = left ventricular ejection fraction.

Table 2 – Characteristics of SAN-FAPs.

Characteristic	
Number of SAN-FAPs	28
• Repetitive	25 (89%)
• Near lines of CB	16 (57%)
RA location	
• Superior	22 (79%)
• Middle	6 (21%)
• Inferior	- (0%)
Layer of exit site	
• Epicardial exit site	13 (46%)
• Endocardial exit site	10 (36%)
• Endo- and epicardial exit site	5 (18%)
Median CL (ms)	793 [672–964]
• Superior	829 [705–938]
• Mid	545 [417–1009]

Values are presented as N (%) or median [interquartile ranges]. **SAN-FAP** = sino-atrial node – focal activation pattern; **CB** = conduction block; **RA** = right atrium; **CL** = cycle length.

exact opposite electrode and its eight surrounding electrodes was selected.[8] For each set of electrodes at the same distance in each direction from the SAN-FAP origin, the median EED was selected. In line with previous studies, EEA was defined as EED ≥15 ms.[9] Percentage of EEA was calculated within a radius of 10 mm from the SAN-FAP origin.
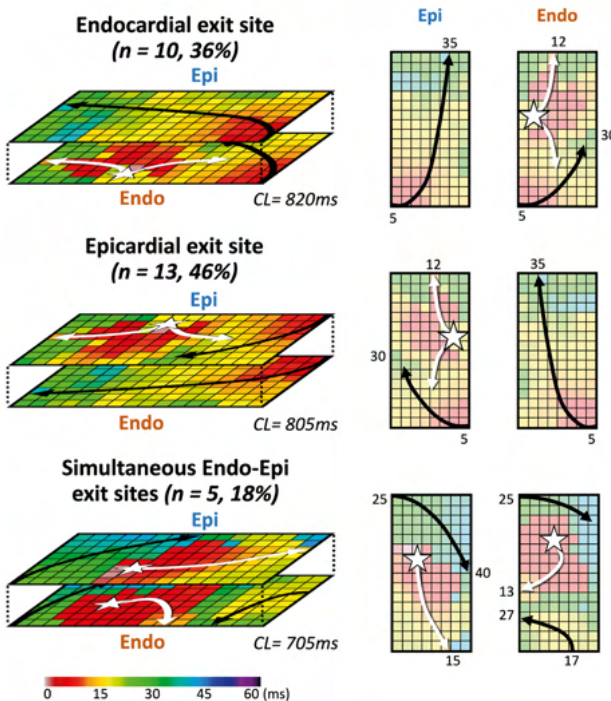
Figure 2 – Three types of SAN-FAPs were observed. 1) solely an endocardial exit site (n=10 (36%), upper panel), 2) solely an epicardial exit site (N=13 (46%), middle panel), 3) simultaneously activated endo-epicardial exit sites, (N=5 (18%), lower panel). Stars indicate origins of SAN-FAPs and arrows main trajectories of the SAN-FAP. Local activation times are depicted near the head and tail of arrows. **CL** = cycle length; **Epi** = epicardium; **Endo** = endocardium; **SAN-FAP** = sino-atrial node – focal activation pattern.

R/S-ratio

R/S-ratios of unipolar potentials were calculated for all electrodes at the origin of the SAN-FAP. Firstly, correction for the baseline amplitude was calculated per deflection between 70 and 30 ms before the deflection. Subsequently, the amplitudes of the R- and S-peak were extracted, and the baseline correction was applied. The R/S-ratio was calculated by dividing the corrected amplitude of the R-peak by the corrected amplitude of the S-peak.[12]

Statistical analysis

Normally distributed continuous variables were expressed as mean ± standard deviation and skewed variables as median [25th–75th percentile]. Continuous data was analyzed using the Mann-Whitney U test or the Kruskal-Wallis H test. A *p*-value of <0.05 was considered statistically significant. Statistical testing was performed using IBM SPSS Statistics version 25 (IBM Corp, Armonk, NY) and plots were created using R (version 3.6.1).

Results

Study population

A total of 20 patients were included (15 (75%) male, median age 66 years [59–73]; median BMI 27 [23–31]); 8 patients (40%) had a history of paroxysmal atrial fibrillation (AF)), as listed in *Table 1*. Ischemic heart disease, valvular heart disease or combined heart diseases were present in 9 (45%), 4 (20%) and 7 (35%) patients, respectively. Most patients had a good left ventricular function (LVF) or mild impairment (left ventricular ejection fraction 50–70% and 40–49%, respectively); only three patients showed moderate impairment of LVF (left ventricular ejection fraction 30–39%). None of the patients had heart failure or sinus node dysfunction.

21
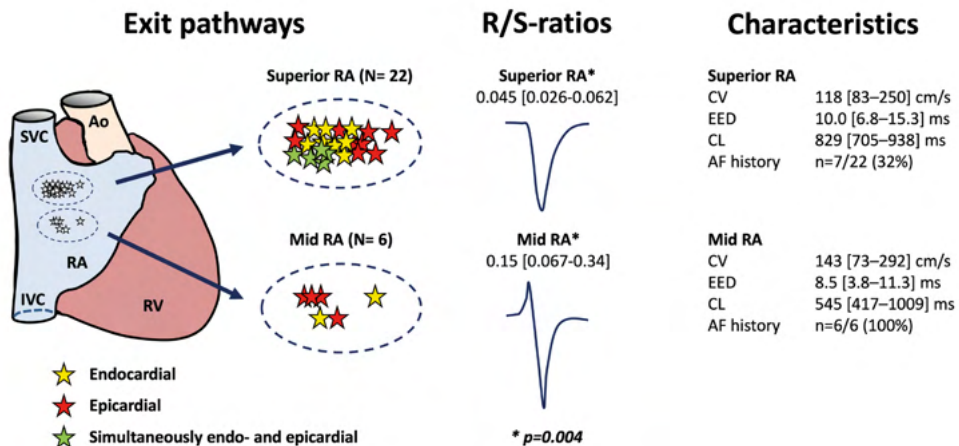
Figure 3 – Distribution of SAN-FAP exit pathways. *Left panel*: distribution of SAN-FAP exit pathways are illustrated per location and per layer separately. Yellow, red and green stars indicate SAN-FAPs with endocardial-, epicardial- and simultaneous endo-epicardial exit sites, respectively. *Center panel*: R/S-ratio at the origin of SAN-FAPs specified per location. A significant difference in R/S-ratio was observed between superior RA and mid RA (p=0.004). *Right panel*: characteristics of SAN-FAPs in superior RA and mid RA. **AF** = atrial fibrillation; **Ao** = aorta; **CL** = cycle length; **CV** = conduction velocity; **EED** = endo-epicardial delay; **IVC** = inferior vena cava; **RA** = right atrium; **RV** = right ventricle; **SAN-FAP** = sino-atrial node – focal activation pattern; **SVC** = superior vena cava.
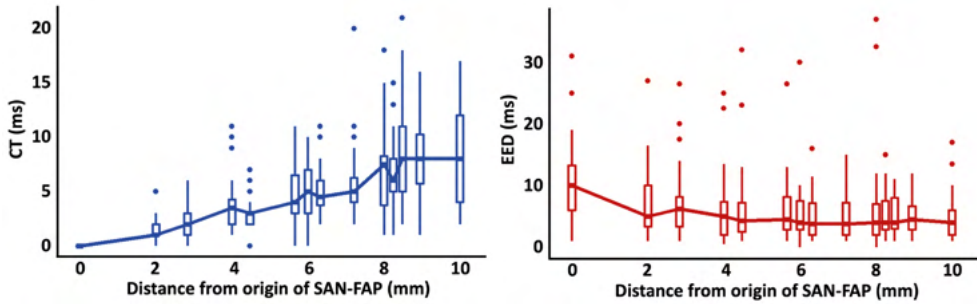
Figure 4 – Conduction times (left panel) and EED (right panel) of SAN-FAPs for each measured electrode distance up to 10 mm. Median conduction velocity was 125 [80–250] cm/s. Highest EED was found at the SAN-FAP origin. **EED** = endo-epicardial delay; **Endo** = endocardium; **Epi** = epicardium; **SAN-FAP** = sino-atrial node – focal activation pattern.

Characteristics of sino-atrial node activation

In 15 patients, repetitive SAN activity at the same exit site was observed and five patients showed more than 1 different exit site (2 patients showed 2 different exit sites; 3 patients showed 3 different exit sites). Characteristics of all 28 included SAN-FAPs are specified in *Table 2*. As demonstrated in *Figure 2*, three distinct activation patterns were observed after analyses of 28 SAN-FAPs, including SAN activation patterns with 1) solely an endocardial exit site (n=10 (36%), upper panel), 2) solely an epicardial exit site (N=13 (46%), middle panel), 3) simultaneously activated endo-epicardial exit sites, (N=5 (18%), lower panel). Although SAN activity was expected to be repetitive, 3 SAN-FAPs (11%) had non-repetitive activation patterns, suggesting beat-to-beat variations in the origin of the SAN-FAP.

The left panel of *Figure 3* demonstrates the distribution of SAN-FAP exit pathways in the RA for both layers separately. As expected, SAN-FAPs were solely observed in the superior (n=22, 79%) and mid RA (n=6, 21%) but not in the inferior RA. All three patients with moderate
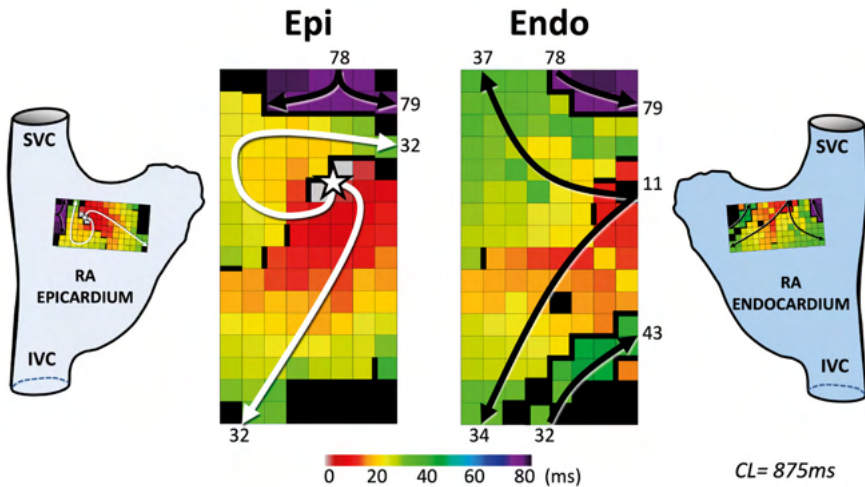
Figure 5 – Example of endo- and epicardial color coded activation maps of the superior right atrium. The arrows display the main trajectories of the electrical wavefronts and local activation times are depicted at the head and tail. The star indicates the origin of SAN activation which is observed in the epicardial layer. Thick black lines indicate lines of conduction block. The distal part of both activation maps show a typical area of CB in both atrial layers, which corresponds to the area lateral to the SAN. **CB** = conduction block; **CL** = cycle length; **Endo** = endocardium; **Epi** = epicardium; **IVC** = inferior caval vein; **RA** = right atrium; **SAN** = sino-atrial node; **SVC** = superior caval vein.

LVF impairment showed exit pathways in the superior RA. No significant difference in cycle length was observed between superior and mid RA (superior: 828 [705–938] ms vs. mid: 545 [417–1009] ms; p=0.194). As demonstrated in the middle panel of *Figure 3*, the morphology of unipolar potentials recorded from the SAN-FAP origins in the superior RA differed significantly from the electrogram morphology observed at the mid RA; (middle panel: superior RA: S-wave morphologies (R/S-ratio 0.045 [0.026–0.062]) versus mid RA: rS-wave morphology (R/S-ratio 0.15 [0.067–0.34]), p=0.004).

Characteristics of all SAN-FAPs are depicted in the right panel of *Figure 3*; there were no significant differences in CV and degree of EED between superior and mid RA SAN-FAPs. Interestingly, all six SAN-FAPs on mid RA occurred in patients with a history of AF.

The left panel of *Figure 4* shows the relation between CTs at every predefined distance from the SAN-FAP origin. The CTs increase linearly from 1 to 8 [4–12] ms over a distance of 10 mm, which corresponds with a CV of 125 [80–250] cm/s. The right panel of *Figure 4* shows the degree of EED at every predefined distance within 10 mm from the SAN-FAP origin. The highest degree of EED (10 [6–14] ms) was found at the SAN-FAP origin and decreased with increasing distance from the SAN-FAP. The percentage of EEA within this area ranged from 2 to 18% (median: 5%).

Within a radius of 6 mm from the origin, 16 SAN-FAPs (57%) showed lines of CB in the same endo- or epicardial plane as the SAN-FAP of whom 10 (63%) also showed CB lines in the opposite plane. Within a range of 10 mm from the origin of a SAN-FAP, lines of CB were found in 22 (79%) activation maps, either on both endo- and epicardial layer (N=17 (77%), solely on the same side of the SAN-FAP (N=4 (18%)) and only once on the opposite side of the SAN-FAP (5%).

Figure 5 illustrates a SAN-FAP with a typical area of CB in both layers distal to its origin, which corresponds to the area lateral to the SAN. The area behind the line of CB is activated by a wavefront approximately 78 ms later than start of SAN activation. These typical areas of CB present in both the endo- and epicardium, were observed in 9 patients (45%). This area lateral to the SAN was activated with a delay ranging between 18 ms and 78 ms (median 34 ms) after the onset of SAN activation.

Discussion

Simultaneous endo-epicardial mapping of the SAN area revealed 3 different patterns of SAN activation: SAN activation with 1) an epicardial exit site, 2) an endocardial exit site, or 3) simultaneous endo- and epicardial exit sites. SAN activity was mainly found in the epicardium of either the superior or mid RA, suggesting that SAN activation predominantly starts at the epicardium. However, in 36% of the SAN-FAPs the earliest activated site was observed at the endocardium. Solely in patients with a history of AF, a caudal shift in SAN exit site was observed, which indicate changes in preferential sino-atrial exit pathways due to structural remodeling. Moreover, CB and EEA were commonly observed at the surrounding of the SAN area.

Dynamic range of SAN activation

The SAN is a complex three-dimensional structure located at the superior region of the sulcus terminalis isolated from the surrounding atria by blood vessels, fibrotic tissue and fat.[3,5] As expected, SAN activity was mainly observed in the superior RA (79%) and to a lesser degree in the mid RA (21%). While the intrinsic length of the human SAN is only ≈1–2 cm,

21

the dynamic range of SAN activation may cover a larger area reaching up to the inferior caval vein.[3,5,13-15] The large dynamic range of SAN activity was recently highlighted by ex-vivo experiments in mice. Bychkov et al.[4] demonstrated synchronized action potential emerging from heterogeneous subcellular subthreshold Ca^{2+} currents with a functional dynamic range extending from the superior to inferior vena cava. In accordance, we also observed a large dynamic range of SAN activation reaching from the junction of the superior caval vein towards mid RA, which is approximately 3 cm in length. Fedorov et al.[3] have also shown that sino-atrial exit pathways can be at distances of 2.61±0.79 cm from each other, which is in line with our findings of the in-vivo human heart.

Conduction velocity at the RA free wall and near the origin of SAN activity

Conduction velocity is dependent on fiber-direction enabling higher velocities in longitudinal rather than transverse cardiac muscle fiber direction. Right atrial CV has been measured at different anatomical locations and heterogeneity and variety of the RA architecture should therefore be taken into account when comparing study outcomes. Konings et al.[16] reported average epicardial CV of 72±5 cm/s during SR at the RA free wall in patients with Wolff-Parkinson-White syndrome (244 unipolar electrodes, interelectrode distance 2.25 mm). Hansson et al.[17] found slightly higher epicardial CV in 12 patients undergoing open-heart surgery due to ischemic heart disease (N=8) or Wolf-Parkinson-White syndrome (N=3). Prior commencement of extracorporeal circulation, a mean CV of 88±9 (68 to 103) cm/s was observed during SR at the RA free wall (3×4 cm mapping array, 56 bipolar electrodes). We calculated local CV at the SAN area (<10 mm of SAN exit site) and observed a median atrial CV of 125 cm/s. This higher CV near the surrounding of the SAN compared to CV measured at the RA free wall may be explained by longitudinal alignment of muscle fibers in the terminal crest that favors preferential conduction.

Sino-atrial node: anatomical substrate for arrhythmogenesis?

Fedorov et al.[18] examined 3-dimensional arrhythmogenic features of the SAN during optical mapping of coronary perfused canine hearts. They demonstrated that the SAN created a substrate for an atrial flutter (AFL) reentry circuit, which anchored around the SAN structure. Moreover, the SAN exit pathways conducted bidirectionally, allowing SAN overdrive suppression during atrial pacing, AFL and AF. However, they also demonstrated that SAN exit pathways can block entering of wavefronts, thereby preventing electrically induced remodeling of the SAN. After administration of acetylcholine, hence increasing SAN entrance block, SAN activity was observed independently from the macro-reentry circuit of AFL in the RA. Based on the presence of bi-directional slow conducting SAN exit pathways the authors postulated that this area may furnish an anatomical pathway for reentrant arrhythmias.[18]

In the present study, we measured EED, at the exit site of SAN activity and the surrounding atrial tissue within a radius of 10 mm. The percentage of EEA (EED≥15 ms) observed at the surrounding of the SAN area ranged from 2 to 18% (median: 5%). Previous research has shown that EEA in the atrial wall plays an important role in the development of atrial tachyarrhythmias and may initiate reentry.[9,19,20] A recent study by Parameswaran et al.[6] also identified EEA at SAN exit sites (4×4 electrodes, 3 mm interelectrode distance). Endo-epicardial asynchrony was determined by 1) comparing regional differences in distribution of SAN exit sites; 2) assessing endo-epicardial wavefront propagation sequence; and 3) determining the difference in phase value ≥20 ms between opposing endo-epicardial electrodes. Interestingly, after post-overdrive suppression at 600 and 400 ms, the amount of EEA in percentage increased, but paradoxically the degree of endo-epicardial delay decreased. This raises the question of whether overdrive suppression of the SAN results in

an increased degree of EEA, or solely an increased amount of EEA. Our study demonstrates that not only slowing of atrial conduction but also EEA is present at and surrounding the SAN which may contribute to atrial arrhythmogenesis.

Sino-atrial node exit pathways in patients with a history of atrial fibrillation

Several studies have demonstrated a caudal shift of SAN activity in patients with heart failure and sinus node dysfunction. Sanders et al. performed endocardial mapping of SAN activation in 18 patients with symptomatic heart failure, 16 patients with sinus node dysfunction and age-matched control subjects. Patients with heart failure or sinus node dysfunction, both conditions which are associated with development of AF, showed more caudal SAN exit sites.[21-23] A caudal shift of SAN activity has also been observed after SAN overdrive pacing and episodes of AFL.[3,15] Interestingly, we also observed a caudal shift in SAN activity in patients with a history of AF. None of the patients included in the present study had heart failure or were diagnosed with sinus node dysfunction or AFL. The underlying mechanism of caudal shifting of SAN activity in patients with heart failure or persistent arrhythmias remains poorly understood.[15,22] Stiles et al.[15] hypothesized that the superior relatively shorter SAN exit pathway is more susceptible to undergo structural remodeling resulting in conduction abnormalities. It is most likely that atrial structural remodeling in patients with a history of atrial fibrillation may result in conduction block in superior SAN exit pathways that may ensue caudal shift of SAN exit sites, as observed in the present study.

Limitations

Although strict selection criteria were used to select SAN-FAPs, due to lack of histology it still might be possible that some SAN-FAPs were not caused by SAN activity, but by ectopic focal discharges in the RA wall. Furthermore, due to the limited size of the electrode arrays, it might be possible that the actual earliest activation site was outside the measurement area. However, because during stable SR all SAN-FAPs were found in the superior and mid RA and mostly repetitive, this is very unlikely. An inevitable effect of in-vivo mapping is lack of histology and intramural SAN analyses. In addition, we could not perform simultaneous endo-epicardial mapping of the entire RA simultaneously to investigate the effect of beat-to-beat variation on SAN exit sites. Another limitation of our study is that we measured fastest apparent CV in the 2-dimensional plane, whereas SAN activation occurs in the 3-dimensional plane. Therefore, our method over-estimates real CV surrounding the SAN. Lastly, this study described conduction in the SAN region. Recordings with an even higher spatial resolution are required to analyze wave propagation within the SAN itself.

Conclusion

Our study is one of the first to analyze in-vivo patterns of activation surrounding the SAN from an endo-and epicardial perspective by performing simultaneous endo-epicardial mapping of the human RA in patients undergoing cardiac surgery. The observed variations in patterns of activation highlight the complex 3-dimensional spread of SR wavefronts emerging from the SAN and the presence of inter-individual differences in SAN exit pathways. Solely in patients with a history of AF, SAN activity occurred more caudally, which may reflect changes in preferential sino-atrial exit pathways as a result of structural remodeling.

21

References

1. Boineau JP, Canavan TE, Schuessler RB, Cain ME, Corr PB, Cox JL. Demonstration of a widely distributed atrial pacemaker complex in the human heart. Circulation. 1988;77:1221-1237.
2. Schuessler RB. Abnormal sinus node function in clinical arrhythmias. J Cardiovasc Electrophysiol. 2003;14:215-217.
3. Fedorov VV, Glukhov AV, Chang R, Kostecki G, Aferol H, Hucker WJ, Wuskell JP, Loew LM, Schuessler RB, Moazami N, et al. Optical mapping of the isolated coronary-perfused human sinus node. J Am Coll Cardiol. 2010;56:1386-1394.
4. Bychkov R, Juhaszova M, Tsutsui K, Coletta C, Stern MD, Maltsev VA, Lakatta EG. Synchronized Cardiac Impulses Emerge From Heterogeneous Local Calcium Signals Within and Among Cells of Pacemaker Tissue. JACC Clin Electrophysiol. 2020;6:907-931.
5. Sanchez-Quintana D, Cabrera JA, Farre J, Climent V, Anderson RH, Ho SY. Sinus node revisited in the era of electroanatomical mapping and catheter ablation. Heart. 2005;91:189-194.
6. Parameswaran R, Lee G, Morris GM, Royse A, Goldblatt J, Larobina M, Watts T, Nalliah CJ, Wong G, Al-Kaisey AM, et al. Simultaneous epicardial-endocardial mapping of the sinus node in humans with structural heart disease: Impact of overdrive suppression on sinoatrial exits. Heart Rhythm. 2020;17:2154-2163.
7. Knops P, Kik C, Bogers AJ, de Groot NM. Simultaneous endocardial and epicardial high-resolution mapping of the human right atrial wall. J Thorac Cardiovasc Surg. 2016;152:929-931.
8. Kharbanda RK, Knops P, van der Does L, Kik C, Taverne Y, Roos-Serote MC, Heida A, Oei FBS, Bogers A, de Groot NMS. Simultaneous Endo-Epicardial Mapping of the Human Right Atrium: Unraveling Atrial Excitation. J Am Heart Assoc. 2020;9:e017069.
9. de Groot N, van der Does L, Yaksh A, Lanters E, Teuwen C, Knops P, van de Woestijne P, Bekkers J, Kik C, Bogers A, et al. Direct Proof of Endo-Epicardial Asynchrony of the Atrial Wall During Atrial Fibrillation in Humans. Circ Arrhythm Electrophysiol. 2016;9.
10. Allessie MA, de Groot NM, Houben RP, Schotten U, Boersma E, Smeets JL, Crijns HJ. Electropathological substrate of long-standing persistent atrial fibrillation in patients with structural heart disease: longitudinal dissociation. Circ Arrhythm Electrophysiol. 2010;3:606-615.
11. Mouws E, Lanters EAH, Teuwen CP, van der Does L, Kik C, Knops P, Bekkers JA, Bogers A, de Groot NMS. Epicardial Breakthrough Waves During Sinus Rhythm: Depiction of the Arrhythmogenic Substrate? Circ Arrhythm Electrophysiol. 2017;10.
12. van Schie MS, Starreveld R, Roos-Serote MC, Taverne Y, van Schaagen FRN, Bogers A, de Groot NMS. Classification of sinus rhythm single potential morphology in patients with mitral valve disease. Europace. 2020;22:1509-1519.
13. Boineau JP, Schuessler RB, Hackel DB, Miller CB, Brockus CW, Wylds AC. Widespread distribution and rate differentiation of the atrial pacemaker complex. Am J Physiol. 1980;239:H406-415.
14. Cosio FG, Martin-Penato A, Pastor A, Nunez A, Montero MA, Cantale CP, Schames S. Atrial activation mapping in sinus rhythm in the clinical electrophysiology laboratory: observations during Bachmann's bundle block. J Cardiovasc Electrophysiol. 2004;15:524-531.
15. Stiles MK, Brooks AG, Roberts-Thomson KC, Kuklik P, John B, Young GD, Kalman JM, Sanders P. High-density mapping of the sinus node in humans: role of preferential pathways and the effect of remodeling. J Cardiovasc Electrophysiol. 2010;21:532-539.
16. Konings KT, Kirchhof CJ, Smeets JR, Wellens HJ, Penn OC, Allessie MA. High-density mapping of electrically induced atrial fibrillation in humans. Circulation. 1994;89:1665-1680.
17. Hansson A, Holm M, Blomstrom P, Johansson R, Luhrs C, Brandt J, Olsson SB. Right atrial free wall conduction velocity and degree of anisotropy in patients with stable sinus rhythm studied during open heart surgery. Eur Heart J. 1998;19:293-300.
18. Fedorov VV, Chang R, Glukhov AV, Kostecki G, Janks D, Schuessler RB, Efimov IR. Complex interactions between the sinoatrial node and atrium during reentrant arrhythmias in the canine heart. Circulation. 2010;122:782-789.
19. Schuessler RB, Kawamoto T, Hand DE, Mitsuno M, Bromberg BI, Cox JL, Boineau JP. Simultaneous epicardial and endocardial activation sequence mapping in the isolated canine right atrium. Circulation. 1993;88:250-263.
20. Hansen BJ, Zhao J, Csepe TA, Moore BT, Li N, Jayne LA, Kalyanasundaram A, Lim P, Bratasz A, Powell KA, et al. Atrial fibrillation driven by micro-anatomic intramural re-entry revealed by simultaneous sub-epicardial and sub-endocardial optical mapping in explanted human hearts. Eur Heart J. 2015;36:2390-2401.
21. Sanders P, Morton JB, Kistler PM, Spence SJ, Davidson NC, Hussin A, Vohra JK, Sparks PB, Kalman JM. Electrophysiological and electroanatomic characterization of the atria in sinus node disease: evidence of diffuse atrial remodeling. Circulation. 2004;109:1514-1522.
22. Sanders P, Kistler PM, Morton JB, Spence SJ, Kalman JM. Remodeling of sinus node function in patients with congestive heart failure: reduction in sinus node reserve. Circulation. 2004;110:897-903.
23. John RM, Kumar S. Sinus Node and Atrial Arrhythmias. Circulation. 2016;133:1892-1900.

21
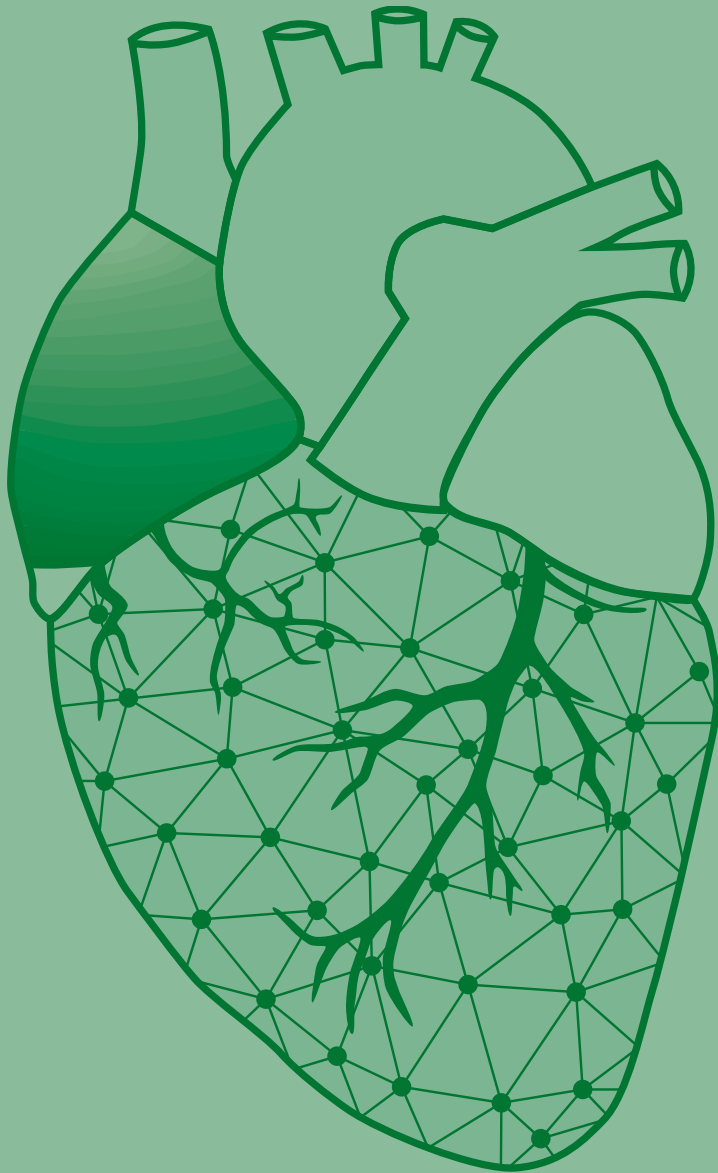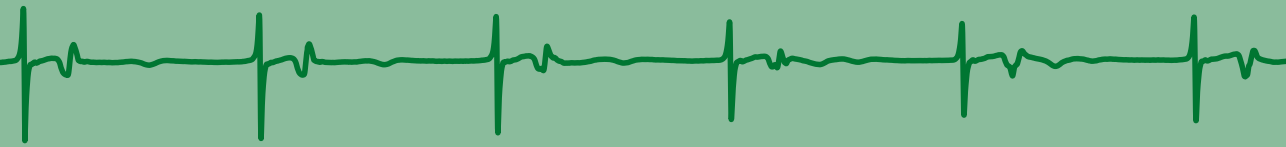
Chapter 22

In-vivo sino-atrial node mapping in children and adults with congenital heart disease

Rohit K. Kharbanda*

Mathijs S. van Schie*

Nawin L. Ramdat Misier

Fons J. Wesselius

Roxanne D. Zwijnenburg

Wouter J. van Leeuwen

Pieter C. van de Woestijne

Peter L. de Jong

Ad J.J.C. Bogers

Yannick J.H.J. Taverne

Natasja M.S. de Groot

* Contributed equally

Abstract

Background: Sinus node dysfunction (SND) and atrial tachyarrhythmias frequently co-exist in the ageing patient with congenital heart disease (CHD), even after surgical correction early in life. We examined differences in electrophysiological properties of the sino-atrial node (SAN) area between pediatric and adult patients with CHD.

Methods: Epicardial mapping of the SAN was performed during sinus rhythm in 12 pediatric (0.6 [0.4–2.4] years) and 15 adult (47 [40–55] years) patients. Unipolar potentials were classified as single-, short or long double- and fractionated potentials. Unipolar voltage, relative R-to-S-amplitude ratio and duration of all potentials was calculated. Conduction velocity (CV) and the amount of conduction block (CB) was calculated.

Results: SAN activity in pediatric patients was solely observed near the junction of the superior caval vein and the right atrium, while in adults SAN activity was observed even up to the middle part of the right atrium. Compared to pediatric patients, the SAN region of adults was characterized by lower CV, lower voltages, more CB and a higher degree of fractionation. At the earliest site of activation, single potentials from pediatrics consisted of broad monophasic S-waves with high amplitudes, while adults had smaller rS-potentials with longer duration which were more often fractionated.

Conclusions: Compared to pediatric patients, adults with uncorrected CHD have more inhomogeneous conduction and variations in preferential SAN exit site, which are presumable caused by ageing related remodeling. Long-term follow-up of these patients is essential to demonstrate whether these changes are related to development of SND and also atrial tachyarrhythmias early in life.

Journal site &
supplementary material

Introduction

The population of patients with congenital heart disease (CHD) is increasing, as the survival of CHD patients has improved considerably due to advances in medical care early in life. However, with ageing also the risk of developing atrial tachyarrhythmias such as atrial fibrillation (AF) increases.[1] Furthermore, AF tends to develop in CHD patients at a younger age, resulting in greater mortality rates in this patient group.[2] Sinus node dysfunction (SND) is also a common sequel in CHD patients and is in turn associated with heart failure and AF.[3] SND encompasses disturbances in sino-atrial node (SAN) impulse generation and/or its propagation from SAN exit sites towards the atrial myocardium.

There is increasing evidence that genetic mutations which cause CHD are also associated with SND.[4] Prior studies have indicated that abnormalities in anatomy and function of the SAN in patients with CHD are already present at birth predisposing them to development of SND relatively early in life.[5] During ageing, additional progressive structural remodeling of the right atrium (RA) of children with CHD may explain enhanced susceptibility to SND. In addition, progressive structural remodeling in the atria promotes inhomogeneous conduction which is associated with alterations in electrogram (EGM) morphology, such as fractionation and decreased peak-to-peak amplitudes.

Based on these observations, we therefore hypothesize that adult patients with CHD have more inhomogeneous conduction at the SAN area compared to pediatric patients. To confirm this hypothesis, we performed intra-operative high-resolution epicardial mapping of SAN activity in pediatric and adult patients with CHD undergoing primary surgical correction.

Materials and Methods

Study population

Patients with CHD undergoing elective open-heart surgery were included in the present study. Exclusion criteria were hemodynamic instability, atrial pacing and previous cardiac surgery. The study was approved by the institutional medical ethical committee (MEC2015-373, MEC2019-0543) and written informed consent was obtained from all patients older than 16 years and from parents of children below the age of 16 years. The study was conducted according to the principles of the Declaration of Helsinki.

Epicardial mapping procedure

An overview of our data recording and processing approach is provided in *Figure 1*. Before institution of cardiopulmonary bypass, high-density (192 unipolar electrodes) and high-resolution (interelectrode distance 2 mm) epicardial mapping of SAN activity was performed.[6] The indifferent electrode was connected to the subcutaneous tissue of the thoracic wall in the surgical field. Subsequently, a pacemaker wire, serving as a temporal reference electrode, was stitched to the superior lateral wall of the RA. Mapping of the superior RA started at the junction of the superior caval vein and RA, also covering the sulcus terminalis. Due to the large functional dynamic range of the SAN, the mapping array was subsequently moved to the middle and inferior part of the RA. Epicardial mapping at each location was performed for 5 seconds and included a calibration signal of 2 mV and 1000 ms, a unipolar or bipolar reference EGM and all epicardial unipolar EGMs. Data were stored on a hard disk after amplification (gain 1000), filtering (bandwidth 0.5–400 Hz), sampling (1 kHz) and analogue-to-digital conversion (16 bits).

22
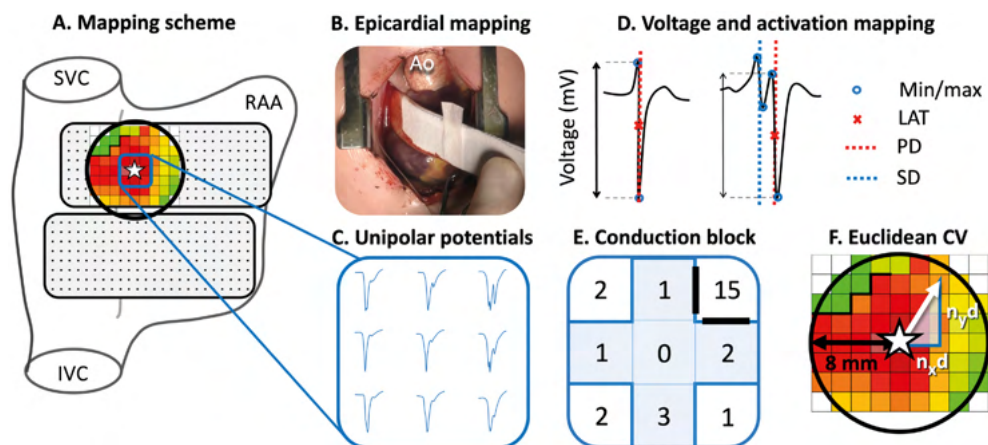
Figure 1 – Epicardial mapping of the SAN. Projection of the 192-unipolar electrode array on a schematic posterior view of the right atrium (A) and intra-operative image of the mapping procedure (B). An area with a radius of 8 mm around the SAN-FAP origin (star) is selected (black circle). Typical examples of nine unipolar potentials obtained at the center of the SAN-FAP are shown outside the mapping scheme (C). These potentials are classified according to the number of deflections and potential voltage is determined as the peak-to-peak amplitude of the steepest (primary) deflection (D). Five potentials directly surrounding the SAN-FAP origin (blue highlighted plus) are used to characterize potentials at the origin of SAN activation (E). Conduction block is defined as a difference in local activation times (conduction time) between adjacent electrodes ≥12 ms. The Euclidean CV is analyzed by calculating the conduction times between the SAN-FAP origin and the neighboring electrodes in superior, caudal, lateral and medial direction divided by the distance $n_x d$ and $n_y d$ (F). **SVC** = superior vena cava; **IVC** = inferior vena cava; **RAA** = right atrial appendage; **Ao** = aorta; **LAT** = local activation time; **PD** = primary deflection; **SD** = secondary deflection; **CV** = conduction velocity.

Mapping Data Analysis

Mapping data were analyzed using custom-made software. Color-coded activation maps were constructed by annotating the steepest negative slope of atrial potentials recorded at every electrode, provided that the amplitude of an atrial deflection was at least two times the signal-to-noise ratio. In order to investigate conduction properties at different distances relative to the SAN focal activation pattern (SAN-FAP) origin, the Euclidean distances between the SAN-FAP origin and surrounding electrodes within a range of 8 mm were calculated (*Figure 1*). Consistent with prior intra-operative mapping studies, areas of CB were defined as interelectrode differences in local activation times (LATs) of ≥12 ms corresponding with an effective conduction velocity (CV) of <17 cm/s (right panel of *Figure 1*).[6] Because of the lack of any reference values, the same cut-off values were used for pediatric patients.[5] The amount of CB is expressed as the number of interelectrode conduction times (CTs) ≥12 ms as a percentage of the total number of interelectrode CTs measured within 8 mm of the SAN-FAP.

SAN activation

All recordings were independently screened by two researchers based on the selection criteria for SAN-FAPs, as described previously.[7] These criteria include: 1) the electrode from which the SAN-FAP originates (SAN-FAP origin) is the earliest site of activation in the atria, 2) in case of a neighboring electrode being simultaneously activated at the same time, this electrode should in turn be activated at least 2 ms earlier than its surrounding electrodes and 3) the distance between the border of the mapping area and the SAN-FAP origin should be at least one electrode.

Table 1 – Patient characteristics.

	Pediatric patients (N=12)	Adult patients (N=15)
Age (y)	0.6 [0.4–2.4]	46±14
Female	4 (33.3%)	4 (27%)
BMI (kg/m²)	14.8 [13.9–16.4]	25.1 [22.8–35.1]
Underlying heart disease		
• ASD II	2	5
• VSD	2	1
• ASD II + VSD	4	-
• Supravalvular AoS	1	-
• Malalignment VSD + ASD II	1	-
• ToF + ASD II	1	-
• DSAS	1	-
• PAVSD	-	1
• PAPVR	-	1
• SVD + PAPVR	-	5
• Ebstein	-	1
• DORV + VSD	-	1
History of AF		
• Paroxysmal	-	4
• Persistent	-	1
Cardiovascular risk factors		
• Hypertension	-	2
• Hypercholesterolemia	-	4
Left ventricular function		
• Good	12	12
• Mild impairment	-	3
Right atrial dilatation	2	9

Values are presented as N (%) or median [interquartile ranges]. **AF** = atrial fibrillation; **AoS** = aortic stenosis, **ASD** = atrial septal defect; **BMI** = body mass index, **DSAS** = discrete subaortic stenosis; **PAPVR** = partial anomalous venous return; **PAVSD** = partial atrioventricular septal defect; **SVD** = sinus venosus defect; **ToF** = Tetralogy of Fallot; **VSD** = ventricular septal defect.

22

In case of stable, repetitive SAN activation patterns throughout the entire recording, the middle beat was included for analysis. Otherwise, one beat per unique SAN-FAP was included. If the SAN-FAP origin covered multiple electrodes with the same LATs, the electrode closest to the center of this earliest activated area was chosen as the SAN-FAP origin.

Propagation velocity of SAN-FAPs

CV within a radius of 8 mm around the origin of the SAN-FAP was analyzed by calculating the CTs between the SAN-FAP origin and the neighboring electrodes in superior, caudal, lateral and medial direction (Left panel *Figure 1*).

$$CV = \frac{\sqrt{(n_x d)^2 + (n_y d)^2}}{t_2 - t_1} \cdot 100 \ [cm/s]$$

With n_x and n_y the number of electrodes from the SAN-FAP origin in respectively the x and y direction, d the interelectrode distance (mm) and t the local activation time.

As there are multiple electrodes with the same distance to the SAN-FAP origin in the different directions, the median CVs from the origin of SAN-FAP towards the predefined distances within this area were calculated reflecting the overall SAN CV.

Analysis of EGM morphology

EGM morphology was automatically analyzed using custom-made software. As shown in the right lower panel of *Figure 1*, unipolar potentials were classified as single potentials (SP, one deflection), short double potentials (SDP, interval between deflections <15 ms), long double potentials (LDP, deflection interval ≥15 ms) or fractionated potentials (FP, ≥3 deflections). Fractionation delay is defined as the time difference between the first and last deflection of SDP, LDP and FP. From every potential, the peak-to-peak voltage and slope of the steepest deflection was measured. R/S-ratios of all SP were calculated by dividing the relative R- and S-wave amplitudes.[8] Furthermore, duration of each SP within a radius of 8 mm around the origin of the SAN-FAP was calculated from the start to the end of the potential.

Statistical analysis

Normally distributed continuous variables were expressed as mean ± standard deviation and skewed variables as median [25th–75th percentile]. Continuous data was analyzed using the Mann-Whitney U test or the Kruskal-Wallis H test. A *p*-value of <0.05 was considered statistically significant. Statistical testing was performed using Python.

Results

Pediatric study population

Twelve pediatric patients (median age 0.6 years [0.4–2.4], 4 females (33.3%)) scheduled for repair of ventricular septal defect (VSD) (n=7, VSD in combination with atrial septal defect (ASD) type II (n=5) or patent foramen ovale (n=1)), ASD type II (n=2), Tetralogy of Fallot
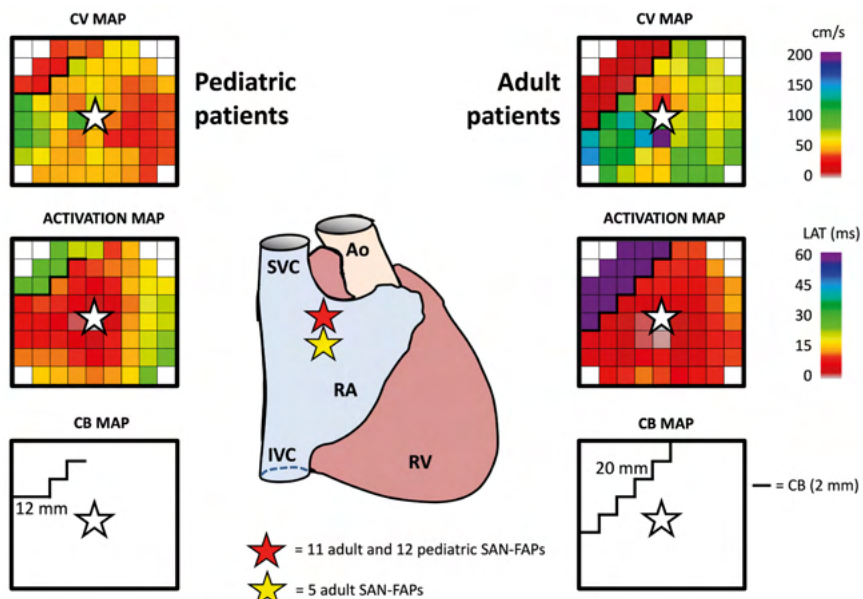
Figure 2 – Typical example of SAN activation. The center panel demonstrates the location of the SAN-FAPs in both an adult and pediatric patient. Characteristics of SAN activation in a pediatric (left) and adult (right) patient include CV (top), activation map (middle) and CB (bottom). The SAN-FAP origin is indicated by a white star. **SVC** = superior vena cava; **IVC** = inferior vena cava; **RA** = right atrium; **RAA** = right atrial appendage; **RV** = right ventricle; **Ao** = aorta; **CV** = conduction velocity; **CB** = conduction block; **SAN-FAP** = sino-atrial node – focal activation pattern.

Table 2 – Characteristics of SAN-FAPs.

	Pediatric patients	Adult patients	*p*-value
Number of SAN-FAPs	12	16	-
Median CL (ms)	465 [421–491]	835 [754–873]	<0.001
RA location			
Superior	12	11	-
Middle	0	5	-
Electrogram characteristics at the SAN-FAP region			
Fractionation (%)	22.8 [18.8–29.8]	40.2 [25.0–45.3]	0.019
- SP	77.2 [70.2–81.2]	59.8 [54.7–75.0]	0.019
- SDP	10.5 [7.5–14.7]	14.1 [7.2–21.2]	0.289
- LDP	6.3 [3.8–10.4]	10.7 [5.3–20.3]	0.201
- FP	3.4 [1.3–5.3]	5.3 [0.0–14.1]	0.191
Voltage (mV)	5.2 [4.1–6.4]	2.6 [1.8–4.5]	0.004
- SP	6.4 [4.8–7.2]	3.4 [2.7–5.2]	0.010
- SDP	3.4 [2.3–4.0]	2.8 [1.6–3.8]	0.281
- LDP	2.1 [1.7–2.6]	1.2 [0.9–1.5]	0.041
- FP	1.2 [1.0–2.2]	0.9 [0.7–1.3]	0.435
Slope (V/s)	-2.04 [-2.31–-1.62]	-0.96 [-1.50–-0.53]	0.005
- SP	-1.14 [-1.36–-0.91]	-0.36 [-0.76–-0.24]	0.007
- SDP	-0.88 [-0.98–-0.77]	-0.61 [-0.93–-0.37]	0.055
- LDP	-0.56 [-0.69–-0.35]	-0.19 [-0.23–-0.14]	<0.001
- FP	-0.38 [-0.54–-0.37]	-0.24 [-0.40–-0.20]	0.118
Potential duration (ms)	40 [30–41]	61 [59–64]	<0.001
Fractionation delay (ms)	15 [12–18]	21 [12–27]	0.132
- SDP	8 [6–8]	6 [5–7]	0.265
- LDP	18 [17–24]	26 [20–31]	0.007
- FP	19 [15–26]	22 [18–31]	0.189
R/S ratio	0.91 [0.90–0.93]	0.90 [0.87–0.93]	0.381
CV (cm/s)	67.3 [62.1–74.5]	70.7 [63.9–75.0]	0.258
CB (%)	6.0 [4.9–7.6]	10.6 [7.7–13.1]	0.011
CB (mm)	12 [9–13]	20 [12–26]	0.030

Values are presented as median [interquartile ranges] or incidence. **SAN-FAPs** = sino-atrial node – focal activation patterns; **CL** = cycle length; **RA** = right atrium; **SP** = single potential; **SDP** = short double potential; **LDP** = long double potential; **FP** = fractionated potential; **CV** = conduction velocity; **CB** = conduction block.

22

with ASD type II (n=1), subaortic stenosis (n=1) and supravalvular aortic stenosis (n=1) were included. RA dilatation was present in 2 patients. None of these patients had a history of atrial tachyarrhythmia, SND or heart failure.

Adult study population

As shown in *Table 1*, a total of 15 adults were included (median age 47 years [40–55], 4 females (27%)) of whom 5 had a history of AF. Patients were scheduled for repair of partial anomalous venous return (n=6, including repair of sinus venosus defect (n=5)), ASD type II (n=5), partial atrioventricular septal defect (n=1), VSD (n=2) and Ebstein anomaly (n=1). RA dilatation was present in 9 patients and no patients had heart failure or SND. Characteristics of both pediatric and adult patients are summarized in Table 1.

Functional dynamic range of the SAN

In one patient, who underwent cardiac surgery for a sinus venosus defect and partial anomalous pulmonary venous return, two different SAN exit sites were observed. All other patients had one SAN exit site giving rise to 28 SAN-FAPs. Repetitive SAN activity at the exact same site, as shown in *Video 1*, was observed in the whole population. As illustrated in *Figure 2*, SAN activity in pediatric patients was solely observed near the junction of the superior

Table 3 – Characteristics of SAN-FAPs origin.

	Pediatric patients	Adult patients	*p*-value
Voltage (mV)	4.9 [3.4–6.0]	2.6 [1.9–4.2]	0.014
R/S ratio	0.98 [0.96–1.00]	0.92 [0.87–0.96]	<0.001
R-wave (mV)	0.10 [0.00–0.13]	0.17 [0.06–0.45]	0.036
S-wave (mV)	5.06 [3.35–5.96]	2.49 [1.85–3.90]	0.007
Slope (V/s)	-0.65 [-0.84--0.35]	-0.30 [-0.55--0.15]	0.030
Potential duration (ms)	45 [37–50]	66 [60–70]	<0.001
R-wave duration (ms)	1 [0–3]	6 [5–12]	0.003
S-wave duration (ms)	41 [36–45]	56 [53–58]	<0.001

Values are presented as median [interquartile ranges]. **SAN-FAPs** = sino-atrial node – focal activation patterns.

caval vein and RA. In contrast, in adults the functional dynamic range of the SAN was larger; SAN activity was observed from the superior caval vein-RA junction up to the middle part of the RA. Characteristics of all SAN-FAPs are specified in *Table 2*.

Propagation velocity of SAN-FAPs

Median CV within 4 electrodes (corresponding with a radius of 8 mm) from the origin of the SAN-FAPs did not significantly differ between adult and pediatric patients (70.7 [63.9–75.0] cm/s vs. 67.3 [62.1–74.5] cm/s, p=0.258). However, CV within 2 mm of the origin was significantly lower in adult patients (46.5 [29.9–56.4] cm/s vs. 25.4 [8.9–50.0] cm/s, p=0.011).

Figure 2 demonstrates typical differences in characteristics of SAN activation in a pediatric (left panel) and adult patient (right panel). Within an area of 201 mm² (corresponding with a radius of 8 mm) around the origin of the SAN-FAP, significant more CB was observed in adults compared to pediatric patients (10.6 [7.7–13.1] % vs. 6.0 [4.9–7.6] %, p=0.011). In addition, lines of CB were also longer in adult patients (12 [9–13] mm vs. 20 [12–26] mm, p=0.030).

Characteristics of unipolar potentials at the SAN-FAP region

Compared to pediatric patients, there were less SPs in adult patients (59.8 [54.7–75.0] % vs. 77.2 [70.2–81.2] %, p=0.019); although there were no significant differences in the prevalence of SDPs (10.5 [7.5–14.7] % vs. 14.1 [7.2–21.2] %, p=0.289), LDPs (6.3 [3.8–10.4] % vs. 10.7 [5.3–20.3] %, p=0.201) and FPs (3.4 [1.3–5.3] % vs. 5.3 [0.0–14.1] %, p=0.191).

SPs in the adult population had lower voltages (3.4 [2.7–5.2] mV vs. 6.4 [4.8–7.2] mV, p=0.010) and were less steep (-0.36 [-0.76– -0.24] V/s vs. -1.14 [-1.36– -0.91] V/s, p=0.007), while the R/S ratio was comparable (0.90 [0.87–0.93] vs. 0.91 [0.90–0.93], p=0.381). Also, the potential duration of SPs was longer in adult patients compared to pediatric patients (61 [59–64] ms vs. 40 [30–41] ms, p<0.001).

SDPs, LDPs and FPs were present in respectively 75%, 92% and 92% of the pediatric and in 63%, 88% and 81% of the adult population. SDPs and FPs in pediatric patients did not differ from adult patients in voltage, slope or duration (all p>0.055). Compared to adult patients, LDPs obtained from pediatric patients had lower voltages (1.2 [0.9–1.5] mV vs. 2.1 [1.7–2.6] mV, p=0.041) and less steep potential slopes (-0.19 [-0.23– -0.14] V/s vs. -0.56 [-0.69– -0.35] V/s, p<0.001). The delay of only LDPs was longer in adult patients (26 [20–31] ms vs. 18 [15–24] ms, p=0.007).

Characteristics of unipolar potentials at the SAN-FAP origin

Characteristics of EGM morphology at the origin of the SAN-FAP are summarized in *Table 3* and illustrated in *Figure 3*. The left panel shows two typical examples of EGMs obtained
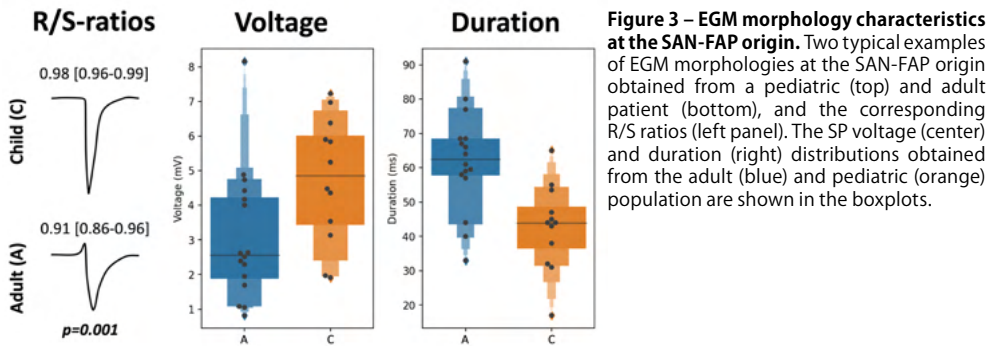
Figure 3 – EGM morphology characteristics at the SAN-FAP origin. Two typical examples of EGM morphologies at the SAN-FAP origin obtained from a pediatric (top) and adult patient (bottom), and the corresponding R/S ratios (left panel). The SP voltage (center) and duration (right) distributions obtained from the adult (blue) and pediatric (orange) population are shown in the boxplots.

from a pediatric and adult patient. Potentials recorded from pediatric patients consisted of broad monophasic S-waves with high amplitudes (5.1 [3.4–6.0] mV) and R/S ratios close to 1 (R/S ratio 0.98 [0.96-1.00]). In contrast, as shown in the left lower panel, the origin potentials in adults contained smaller S-wave amplitudes (2.5 [1.9–3.9] mV, p=0.007), larger R-wave amplitudes (0.17 [0.06−0.45] mV, p=0.036) and smaller R/S ratios (0.92 [0.87−0.96], p<0.001). The middle panel of *Figure 3* shows that the origin potential peak-to-peak amplitudes were also lower in adult compared pediatric patients (2.6 [1.9–4.2] mV and 4.9 [3.4–6.0] mV, p=0.014). SP duration, as shown in the right panel of *Figure 3*, was substantially longer (45 [37–50] ms vs. 66 [60–70] ms, p<0.001) and the slope was less steep in adults (-1.4 [-1.9– -0.9] V/s vs. -0.6 [-1.1– -0.3] V/s, p=0.015). At the SAN-FAP origin, SDP and LDPs were found in respectively 33% of the pediatric and 69% of the adult patients whereas FPs were only found in adult patients (25%).

Impact of AF episodes

Supplementary Table 1 demonstrates the differences in electrophysiological parameters at the SAN-FAP region between adult patients with and without history of AF. In patients with AF, CV was slower than in patients without AF (45.2 [35.1–63.9] cm/s vs. 73.3 [70.7–75.0] cm/s, p=0.039), although there was a similar amount of CB (11.7 [10.2–18.1] % vs. 9.0 [7.5–12.7] %, p=0.182). In addition, SPs recorded from the SAN area in patients with AF had smaller peak-to-peak voltages (4.1 [3.2–5.5] mV vs. 2.2 [2.0–3.1] mV, p=0.027) and less negative slopes (-0.52 [-1.08– -0.36] V/s vs. -0.24 [-0.26– -0.16] V/s, p=0.012).

Discussion

Compared to pediatric patients, the SAN region of adult patients with CHD is characterized by slower conduction, lower SP and LDP voltages, more areas of CB and a higher degree of potential fractionation. Also, at the origin of the SAN-FAP, we observed lower SP voltages in combination with less steep slopes and prolonged SP duration in adult patients. Solely in adult patients, we also observed SAN activation at the middle part of the RA, which may indicate changes in preferential SAN exit site due to chronic volume overload induced structural remodeling. Patients with a history of AF had even slower conduction and lower voltages, which may indicate disturbances in SAN impulse generation and its propagation towards the atrial myocardium.

Mapping of human sino-atrial node activation

This is the first epicardial mapping study on SAN activation in CHD patients and comparative data is therefore lacking. So far, only a few ex-vivo and in-vivo SAN mapping studies have been performed in non-CHD patients.[7,9-11] Despite the SAN is limited to an area of ≈1–2 cm, its

22

functional dynamic range may cover the whole area between the superior and inferior caval vein. Recently, Fedorov et al.[11] demonstrated the presence of two spatially distinct dominant pacemaker sites at the superior and inferior RA by performing optical ex-vivo human SAN mapping followed by histological examination. Furthermore, our research group recently performed simultaneous endo-epicardial mapping of in-vivo SAN activation in non-CHD patients and found inter-individual differences in SAN exit-pathways covering a large area at the RA.[7]

Previous endocardial mapping studies showed spatial caudal shifting of SAN activity in patients with heart failure, SND and a history of AF.[7,9,10] Structural remodeling and consequently endo-epicardial conduction disorders may block propagation of wavefronts from the superior SAN exit sites thereby shifting SAN activity towards inferior sites. We observed changes in electrophysiological properties at the surrounding of the SAN in adults compared to pediatrics with CHD, which support the assumption that adults with uncorrected CHD have a relevant higher degree of structural remodeling in the RA due to long-standing volume overload.

Electrophysiological alterations surrounding the SAN

Electrophysiological differences in SAN activation between pediatric and adult patients may partly be elucidated by differences in the 3-dimensional anatomy of the SAN. Histological examination of the SAN in 10 infants and 11 adults indeed showed remarkable differences in SAN geometry (adult SAN length: 13.8±2.3 mm, width: 3.4±0.5 mm; pediatric SAN length: 5.1±0.7 mm, width: 0.9±0.2 mm).[12] In addition, the SAN was more superficial in pediatric patients with a mean distance to the epicardium of 0.1 mm compared to 0.3 mm in adults. Hence, a more compact functional dynamic range of the SAN in pediatrics may be explained by a smaller SAN with none or underdeveloped SAN exit sites.

EGMs recorded at the SAN-FAP most likely consist of a monophasic S-wave morphology. In pediatric patients, in whom the SAN is more superficially located and is surrounded by less fibrofatty tissue, we indeed observed more monophasic S-wave morphology at the origin (upper panel of *Figure 3*). However, in adults, in whom the SAN is embedded in deeper layers of the atrial wall and in whom the SAN exit pathways are surrounded by more fibrofatty tissue, the sinus rhythm wavefront has to propagate towards the surface before it can spread across the remainder of the epicardium, resulting in a small R-wave preceding a large S-wave (lower panel of *Figure 3*).[8] We postulate that in adult CHD patients with chronic RA volume overload and hence more advanced 3-dimensional structural remodeling, this would cause even larger relative R-wave amplitudes due to the more intramural location. Enhanced structural remodeling in the SAN exit-pathways may cause prolongation of potential duration and slowing of atrial conduction, which is consistent with our findings.

Interrelationship between SND and atrial tachyarrhythmia

SND in patients with CHD is a frequent indication for pacemaker implantation and may even result in sudden cardiac death.[3,13] In patients with CHD, ageing itself and complex surgery at the atrial level (e.g. Mustard and Senning procedure) have been associated with a higher incidence of SND.[14,15] However, there is also literature indicating that SND in this population is not related to the post-operative course only. First, several studies have reported SND in patients with CHD already before surgical correction.[16-18] Second, reports on SND in fetuses with CHD suggest that abnormalities in the 3-dimensonal structure or function of the SAN may also predispose these patients to SND.[19] SND may be a consequence of electrical and structural remodeling induced by tachyarrhythmia, as multiple studies have shown that

AF may cause SND. On the other hand, there is also enough evidence illustrating that a substantial amount of patients with AF does not develop SND or is diagnosed with SND prior to AF.[20]

Study limitations

Due to lack of histology, it might be possible that some SAN-FAPs were not caused by SAN activity, but by ectopic focal discharges in the RA wall. However, because during stable sinus rhythm all SAN-FAPs were repetitive and solely found in the superior and mid RA, this is very unlikely. Preferably, the SAN recovery time (SNRT) and sino-atrial conduction time (SACT) could be examined by pacing and extra stimulation to estimate SAN automaticity and conduction. However, due to limited time during surgery, this was not possible. An inevitable effect of in-vivo mapping is lack of histology and intramural SAN analyses. Due to the invasive nature of our epicardial mapping approach, we do not have epicardial mapping data of patients without structural heart disease at our disposal for comparison.

Conclusion

Compared to pediatric patients, adults with uncorrected CHD have more inhomogeneous conduction at the SAN area. Also, variations in preferential SAN exit site were solely observed in adult patients. These observations indicate that adult patients with uncorrected CHD have more ageing related remodeling which may partly explain why this population is prone to develop SND and atrial tachyarrhythmias. Long-term follow up of this population is essential to demonstrate whether these changes are indeed related to development of atrial tachyarrhythmias early in life.

22

References

1.   Labombarda F, Hamilton R, Shohoudi A, Aboulhosn J, Broberg CS, Chaix MA, Cohen S, Cook S, Dore A, Fernandes SM, et al. Increasing Prevalence of Atrial Fibrillation and Permanent Atrial Arrhythmias in Congenital Heart Disease. J Am Coll Cardiol. 2017;70:857-865.

2.   de Miguel IM, Avila P. Atrial Fibrillation in Congenital Heart Disease. Eur Cardiol. 2021;16:e06.

3.   Baumgartner H, De Backer J, Babu-Narayan SV, Budts W, Chessa M, Diller GP, Lung B, Kluin J, Lang IM, Meijboom F, et al. 2020 ESC Guidelines for the management of adult congenital heart disease. Eur Heart J. 2021;42:563-645.

4.   Jongbloed MR, Vicente Steijn R, Hahurij ND, Kelder TP, Schalij MJ, Gittenberger-de Groot AC, Blom NA. Normal and abnormal development of the cardiac conduction system; implications for conduction and rhythm disorders in the child and adult. Differentiation. 2012;84:131-148.

5.   Kharbanda RK, van Schie MS, Ramdat Misier NL, van Leeuwen WJ, Taverne Y, van de Woestijne PC, Kammeraad JAE, Bartelds B, Bogers A, de Groot NMS. First Evidence of Atrial Conduction Disorders in Pediatric Patients With Congenital Heart Disease. JACC Clin Electrophysiol. 2020;6:1739-1743.

6.   Kharbanda RK, van Schie MS, van Leeuwen WJ, Taverne Y, Houck CA, Kammeraad JAE, Bogers A, de Groot NMS. First-in-children epicardial mapping of the heart: unravelling arrhythmogenesis in congenital heart disease. Interact Cardiovasc Thorac Surg. 2021;32:137-140.

7.   Kharbanda RK, Wesselius FJ, van Schie MS, Taverne Y, Bogers A, de Groot NMS. Endo-Epicardial Mapping of In Vivo Human Sinoatrial Node Activity. JACC Clin Electrophysiol. 2021;7:693-702.

8.   van Schie MS, Starreveld R, Roos-Serote MC, Taverne Y, van Schaagen FRN, Bogers A, de Groot NMS. Classification of sinus rhythm single potential morphology in patients with mitral valve disease. Europace. 2020;22:1509-1519.

9.   Sanders P, Kistler PM, Morton JB, Spence SJ, Kalman JM. Remodeling of sinus node function in patients with congestive heart failure: reduction in sinus node reserve. Circulation. 2004;110:897-903.

10. Sanders P, Morton JB, Kistler PM, Spence SJ, Davidson NC, Hussin A, Vohra JK, Sparks PB, Kalman JM. Electrophysiological and electroanatomic characterization of the atria in sinus node disease: evidence of diffuse atrial remodeling. Circulation. 2004;109:1514-1522.

11. Fedorov VV, Glukhov AV, Chang R, Kostecki G, Aferol H, Hucker WJ, Wuskell JP, Loew LM, Schuessler RB, Moazami N, et al. Optical mapping of the isolated coronary-perfused human sinus node. J Am Coll Cardiol. 2010;56:1386-1394.

12. Chiu IS, Hung CR, How SW, Chen MR. Is the sinus node visible grossly? A histological study of normal hearts. Int J Cardiol. 1989;22:83-87.

13. Mangrum JM, DiMarco JP. The evaluation and management of bradycardia. N Engl J Med. 2000;342:703-709.

14. Hernandez-Madrid A, Paul T, Abrams D, Aziz PF, Blom NA, Chen J, Chessa M, Combes N, Dagres N, Diller G, et al. Arrhythmias in congenital heart disease: a position paper of the European Heart Rhythm Association (EHRA), Association for European Paediatric and Congenital Cardiology (AEPC), and the European Society of Cardiology (ESC) Working Group on Grown-up Congenital heart disease, endorsed by HRS, PACES, APHRS, and SOLAECE. Europace. 2018;20:1719-1753.

15. Cuypers JA, Eindhoven JA, Slager MA, Opic P, Utens EM, Helbing WA, Witsenburg M, van den Bosch AE, Ouhlous M, van Domburg RT, et al. The natural and unnatural history of the Mustard procedure: long-term outcome up to 40 years. Eur Heart J. 2014;35:1666-1674.

16. Clark EB, Kugler JD. Preoperative secundum atrial septal defect with coexisting sinus node and atrioventricular node dysfunction. Circulation. 1982;65:976-980.

17. Gillette PC, Shannon C, Garson A, Jr., Porter CJ, Ott D, Cooley DA, McNamara DG. Pacemaker treatment of sick sinus syndrome in children. J Am Coll Cardiol. 1983;1:1325-1329.

18. Beder SD, Gillette PC, Garson A, Jr., Porter CB, McNamara DG. Symptomatic sick sinus syndrome in children and adolescents as the only manifestation of cardiac abnormality or associated with unoperated congenital heart disease. Am J Cardiol. 1983;51:1133-1136.

19. Maeno Y, Hirose A, Kanbe T, Hori D. Fetal arrhythmia: prenatal diagnosis and perinatal management. J Obstet Gynaecol Res. 2009;35:623-629.

20. John RM, Kumar S. Sinus Node and Atrial Arrhythmias. Circulation. 2016;133:1892-1900.

22
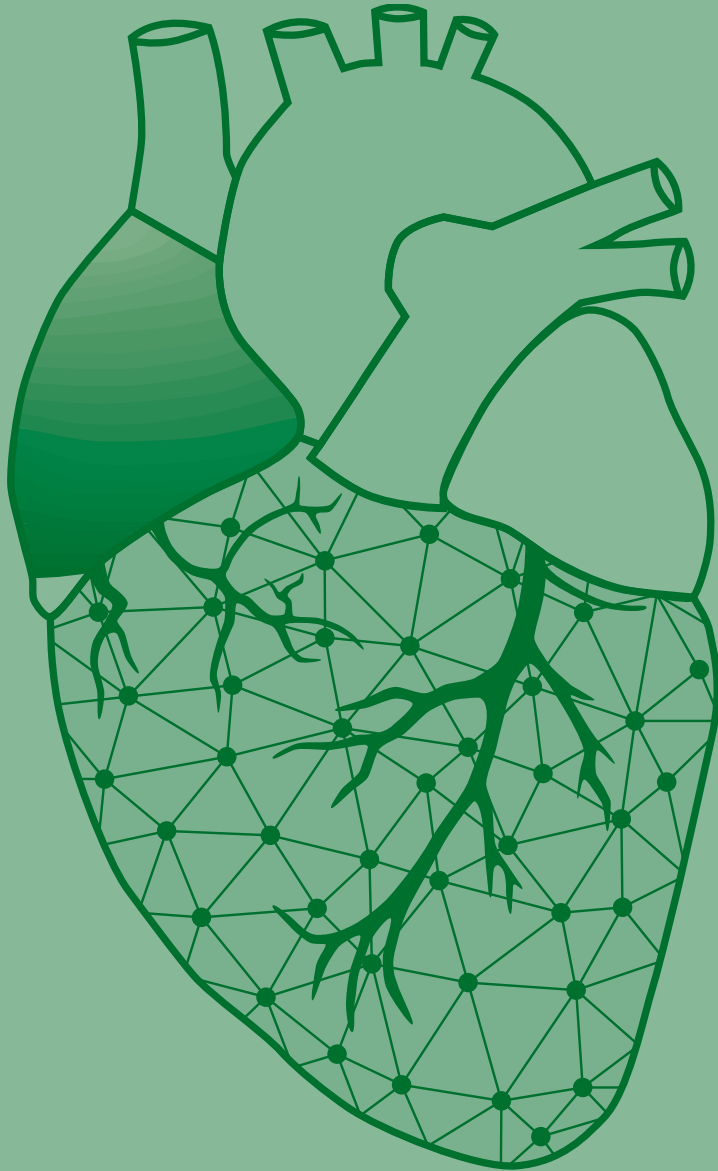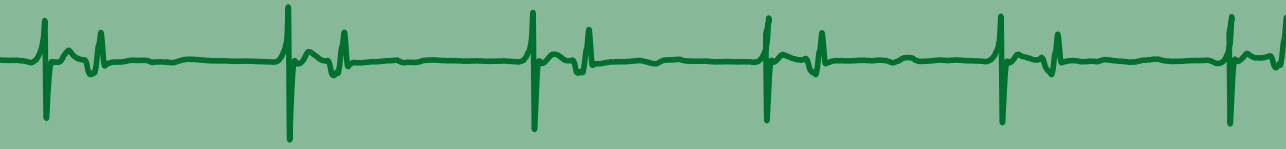
Chapter 23

Unravelling early sinus node dysfunction after pediatric cardiac surgery: a pre-existing arrhythmogenic substrate

Nawin L. Ramdat Misier

Yannick J.H.J. Taverne

Mathijs S. van Schie

Rohit K. Kharbanda

Wouter J. van Leeuwen

Janneke A.E. Kammeraad

Ad J.J.C. Bogers

Natasja M.S. de Groot

Abstract

Early post-operative sinus node dysfunction (SND) is common in pediatric patients undergoing surgical correction of congenital heart defects (CHD). At present, the pathophysiology of these arrhythmias is incompletely understood. In this case series, we present three pediatric patients in whom we performed intra-operative epicardial mapping and who developed early post-operative SND. All patients had either an inferior or multiple sinoatrial node (SAN) exit sites, in addition to extensive conduction disorders at superior and inferior right atrium. Our findings contribute to the hypothesis that pre-existing alterations in SAN exit sites in combination with atrial conduction disorders may predispose pediatric patients with CHD for early post-operative SND. Such insights in the development of arrhythmias are crucial as it may be the first step in identifying high-risk patients.

Journal site &
supplementary material

Introduction

Sinus node dysfunction (SND), resulting in sinus bradycardia, ectopic atrial rhythms or nodal rhythms, are common in pediatric patients after cardiac surgery.[1] The pathophysiological cause for development of these arrhythmias is multifactorial and include diffuse myocardial damage due to hypoxia and ischemia during cardiopulmonary bypass (CPB), reperfusion after cessation of CPB and surgical trauma to the sinoatrial node (SAN) (and/or its vascular supply).[2]

There is increasing evidence that genetic mutations which cause congenital heart disease (CHD) are also associated with SND.[3,4] Furthermore, local conduction disorders are already present in pediatric patients with CHD undergoing cardiac surgery.[5] Based on these observations, we hypotesize that the development of early post-operative SND in a part of these patients is caused by a combination of a surgery-induced substrate and a pre-existing arrhythmogenic substrate.

To contribute to this hypothesis, we present three pediatric patients with early post-operative SND, who had alterations in SAN exit sites and extensive conduction disorders during peri-operative epicardial mapping.

Methods

Study population

This case series is part of the FANTASIA study, approved by the local ethics committee (MEC-2019-0543) of the Erasmus Medical Center Rotterdam, which follows the principles of the Declaration of Helsinki. In this study, high-resolution epicardial mapping is performed in pediatric patients undergoing elective open-heart surgery. Parents gave informed consent to participate in the study. In this case series only pediatric CHD patients with alterations in SAN exit sites during epicardial mapping were included (3 out of 23 pediatric patients). As the SAN occupies a distinct position at the junction of the right atrium (RA) and the superior caval vein, we deemed exit sites at the inferior and/or middle part of the RA to be abnormal.[6] Such alterations were only observed in 3 patients, all other (n=20) patients had SAN exit sites at the superior part of the RA. None of the 23 patients had preoperative arrhythmias.

Data acquisition and processing

An overview of our epicardial mapping approach, including data recording, is provided in *Supplementary Video 1*. Epicardial mapping of the RA during sinus rhythm (SR) was performed prior commencement to CPB. With a custom-made electrode array (128 or 192 electrodes, electrode diameter 0.6 mm, interelectrode distance 2.1 mm), unipolar electrograms were recorded for 5 seconds per location. From every potential, local activation times were determined by annotating the steepest negative deflections of atrial potentials and peak-to-peak amplitudes were measured. Consistent with previous epicardial mapping studies in pediatric patients, areas of conduction disorders consisted of conduction delay (CD) and block (CB), which were defined as local conduction time differences of respectively 7-11 ms and ≥12 ms between adjacent electrodes.[5]

Rhythm recordings

A pre-operative surface electrocardiogram (ECG) was obtained prior to surgery from all patients. Post-operative continuous rhythm monitoring (bedside telemetry) after the surgical

23
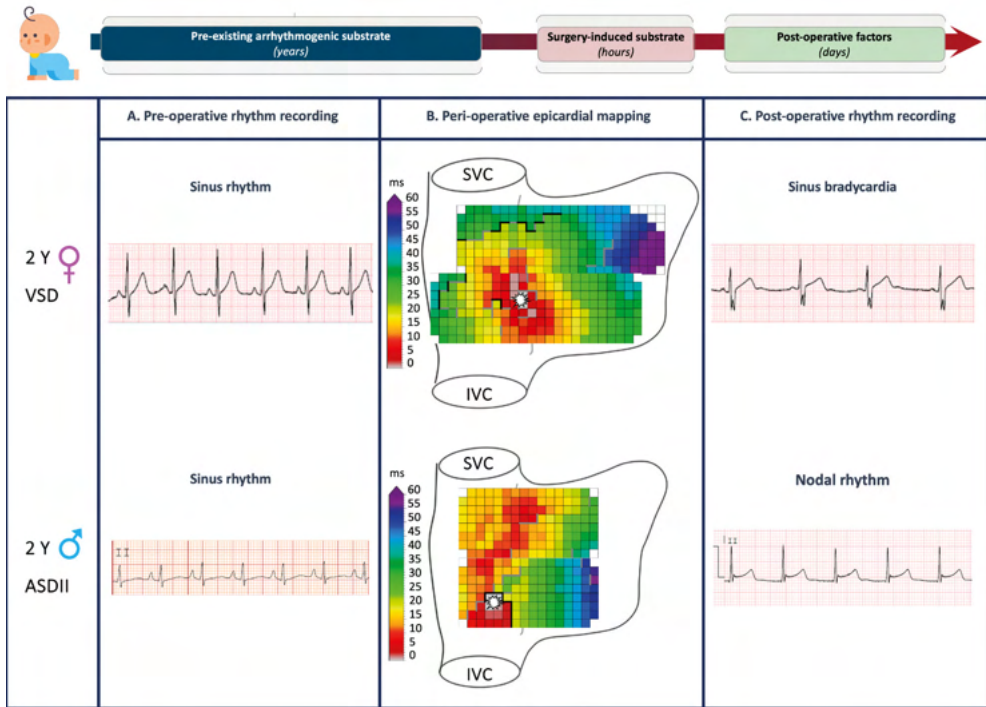
Figure 1 – Linking electrocardiographic data with characteristics of epicardial atrial conduction. *Panel A*: pre-operative rhythm recording. *Panel B*: color-coded activation maps of the right atrium. The white star indicates the earliest site of activation. Grey and black lines indicate, respectively, lines of conduction delay and -block. *Panel C:* post-operative rhythm recording. **ASD** = atrial septal defect; **IVC** = inferior vena cava; **SVC** = superior vena cava; **VSD** = ventricular septal defect.

procedure was performed as part of standard care. Rhythm recordings were analyzed by (pediatric) cardiologist.

Results

Characteristics of the study population

Patients A (female, age: 2 years), B (male, age: 2 years) and C (female, age: 7 years) were referred for correction of respectively a perimembranous ventricular septal defect, an atrial septal defect type 2 (ostium secundum) and a partial atrioventricular septal defect (ostium primum). Pre-operative transthoracic echocardiography demonstrated that patient A had left atrial and ventricular dilation, patient B and C had right atrial and ventricular dilation; they all had preserved biventricular function.

Pre-operative electrocardiography

None of the patients had documented arrhythmias based on pre-operative ECGs. Panels A of *Figures 1 and 2* illustrate surface ECG leads II for respectively patient A, B and C. All patients presented with SR with normal inter-atrial and atrio-ventricular conduction times on their ECG.
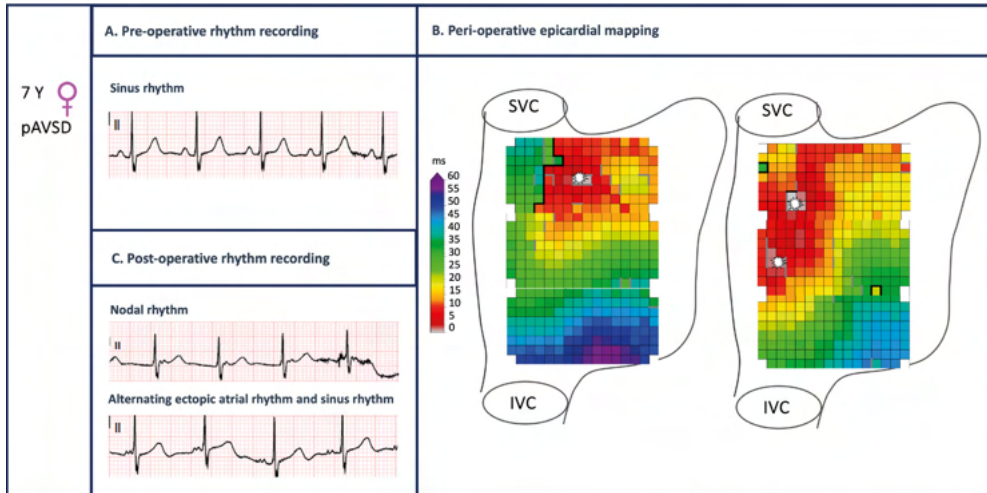
Figure 2 – Linking electrocardiographic data with characteristics of epicardial atrial conduction. *Panel A*: pre-operative rhythm recording. *Panel B*: left and right illustrations show color-coded activation right atrium, activated by a single (left illustrations) and multiple wavefront origins (right illustrations). The white star indicates the earliest site of activation in the RA. Grey and black lines indicate, respectively, lines of conduction delay and -block. *Panel C*: post-operative rhythm recording. **IVC** = inferior vena cava; **pAVSD** = partial atrioventricular septal defect; **SVC** = superior vena cava.

Patterns of activation

Panels B of *Figures 1 and 2* demonstrate color-coded activation maps of the aforementioned patients, reconstructed from the RA. As illustrated in panel B of *Figure 1*, the RA in patient A is activated by a wavefront originating from the inferior RA from where it spreads to the remainder of the atria. Areas of conduction disorders (e.g., CD and CB), indicated by grey and black thick lines, were observed near the wavefront origin and at the superior RA. The RA of patient B is also activated by a wavefront originating from the inferior RA. Similarly, in patient B the wavefront origin is bordered by areas of conduction disorders. Consequently, the wavefront turns around these areas, after which it collides with a wavefront originating from the superior RA. The activation pattern of the RA in patient C is characterized by alternating rhythms of variable origins: 1) one wavefront originating from solely the superior RA and 2) one wavefront originating from both the superior and middle RA (left and right illustration of panel B of *Figure 2*, respectively).

In patient A conduction disorders were more extensive at the superior RA than at the inferior RA (respectively CD: 5.3%, CB: 5.7% vs. CD: 5.1%, CB: 0.8%). In patient B, conduction disorders were more extensive at the inferior RA than at the superior RA (respectively CD: 1.7%, CB: 0% vs. CD: 4.5%, CB: 2.7%). In both patients, unipolar voltages were lower at the superior RA (patient A: 4.0 [2.0–6.6] mV vs. 6.0 [3.8–8.7] mV, p<0.001; patient B: 3.2 [2.1–7.6] mV vs. 6.3 [1.9–10.3] mV, p<0.001).

In patient C, the amount of conduction disorders was similar between both activation patterns (single origin: CD: 1.7%, CB: 0.8%, multiple origins: CD: 1.0%, CB: 1.4%). Unipolar voltages were lower during activation by the wavefront with multiple origins (4.7 [2.7–7.7] mV vs. 5.1 [2.5–8.9] mV, p<0.010).

23

Post-operative sinus node dysfunction

All patients returned to SR once weaned from CPB. Panels C of *Figures 1 and 2* illustrate post-operative surface ECG leads for respectively patient A, B and C. On the 7th post-operative day, patient A had a sinus bradycardia (heart rate: 60 beats per minute (BPM, before 80–100 BPM)) with a right bundle branch block. The sinus bradycardia (60 BPM) was still present at the moment of hospital discharge.

On the 1st post-operative day, patient B had an ectopic atrial rhythm with biphasic P-wave in lead II and negative P-wave in lead III (heart rate: 78 BPM). In the evening, the patient converted to a nodal rhythm with a ventricular rate of 92 bpm (panel C of *Figure 1*). P-waves were not visible in any of the ECG leads which persisted till the next morning. On the 3rd post-operative day, the patient converted to ectopic atrial rhythm with again a biphasic P-wave in lead II and negative P-wave in lead III (heart rate: 106 BPM), which was still present on the day of discharge.

Patient C had a nodal rhythm with retrograde atrial activation (heart rate: 93 BPM) on the 4th post-operative day (panel C of *Figure 2*). Because this arrhythmia persisted until discharge, she received a 24-hour Holter monitoring on the 7th post-operative day. This registration showed predominantly SR, occasionally alternating with an ectopic atrial rhythm. As shown in the lower illustration of panel C of *Figure 2*, the ectopic atrial rhythm had a shorter PR-interval than the SR.

Discussion

In the normally structured adult heart, the SAN occupies a distinct position at the junction of the RA and the superior caval vein in tight relationship to the terminal crest.[7] Prior studies indicate that two spatially distinct dominant SAN are present.[8] This allows for a functional dynamic span of the SAN along the terminal crest, which has also been observed in adult patients with SND, in whom the SAN exit shifts caudally.[9] In this case series, all patients presented with either an inferior or multiple SAN exit sites, demonstrating that also in pediatric patients the functional dynamic span of the SAN is not limited to its anatomical domain at the superior RA.

Epicardial mapping data in this case series provides novel information about the pre-operative electrophysiological properties of pediatric patients with CHD. Kharbanda et al.[5] previously performed epicardial mapping in 10 pediatric patients with CHD with similar extent of CD/CB, but they did not develop post-operative SND. However, the main difference with those patients is that they did not have alterations in SAN exit sites. This arrhythmogenic substrate, consisting of impaired function of SAN, is likely further aggravated by peri- and post-operative factors, resulting in SND in our case series.

The underlying mechanism of caudal shifting of SAN activity in patients with arrhythmias remains poorly understood. Abnormalities in the microarchitecture and/or function of SAN may play a key role in caudal shifting of SAN activity by slowing or even blocking the expanding SR wavefront. These abnormalities may be explained by genetic predisposition[3,4] and/or short-term volume overload[5]. An increasing number of studies show that several mutations, which cause septal defects, are associated with abnormal development of sinus venosus related structures, including the SAN.[4] In adult studies, acute- and long-term volume overload resulted in increased amount of intra-atrial CB.[10,11]

However, anatomical shifting of SAN activity also occurs during interventions that modify

the heart rate, such as parasympathetic stimulation.[8] Slower heart rates are generally initiated from more caudal origins in the RA. Theoretically, the observed inferior SAN exit sites may therefore be active due to more physiological reasons, such as anesthesia, instead of abnormalities in the microarchitecture and/or function of SAN. However, a standard anesthetic protocol was used for all patients, therefore equal dispersion of possible effect can be assumed. In addition, all patients had - during epicardial mapping - heart rates within physiological ranges according to their age. Hence, the observed inferior exit sites do appear to be pathological.

Future studies with larger sample size, consisting of patients with and without SND, are required to directly correlate both pre-operative clinical characteristics and electrophysiological parameters to the development of early post-operative SND, in order to provide conclusive evidence on the role of a pre-existing arrhythmogenic substrate. Such insights in the development of arrhythmias are crucial as it may be the first step in identifying high-risk patients.

Conclusion

We demonstrate for the first time a functional dynamic span of the SAN in pediatric patients. Our findings provide supportive evidence for the hypothesis that pre-existing alterations in SAN exit sites in combination with atrial conduction disorders may predispose pediatric patients with CHD for early post-operative SND.

23

References

1. Valsangiacomo E, Schmid ER, Schupbach RW, Schmidlin D, Molinari L, Waldvogel K, Bauersfeld U. Early postoperative arrhythmias after cardiac operation in children. Ann Thorac Surg. 2002;74:792-796.
2. Grosse-Wortmann L, Kreitz S, Grabitz RG, Vazquez-Jimenez JF, Messmer BJ, von Bernuth G, Seghaye MC. Prevalence of and risk factors for perioperative arrhythmias in neonates and children after cardiopulmonary bypass: continuous holter monitoring before and for three days after surgery. J Cardiothorac Surg. 2010;5:85.
3. Wallace MJ, El Refaey M, Mesirca P, Hund TJ, Mangoni ME, Mohler PJ. Genetic Complexity of Sinoatrial Node Dysfunction. Front Genet. 2021;12:654925.
4. Jongbloed MR, Vicente Steijn R, Hahurij ND, Kelder TP, Schalij MJ, Gittenberger-de Groot AC, Blom NA. Normal and abnormal development of the cardiac conduction system; implications for conduction and rhythm disorders in the child and adult. Differentiation. 2012;84:131-148.
5. Kharbanda RK, van Schie MS, Ramdat Misier NL, van Leeuwen WJ, Taverne Y, van de Woestijne PC, Kammeraad JAE, Bartelds B, Bogers A, de Groot NMS. First Evidence of Atrial Conduction Disorders in Pediatric Patients With Congenital Heart Disease. JACC Clin Electrophysiol. 2020;6:1739-1743.
6. Anter E, Josephson ME. Bipolar voltage amplitude: What does it really mean? Heart Rhythm. 2016;13:326-327.
7. Ho SY, Sanchez-Quintana D. Anatomy and pathology of the sinus node. J Interv Card Electrophysiol. 2016;46:3-8.
8. Brennan JA, Chen Q, Gams A, Dyavanapalli J, Mendelowitz D, Peng W, Efimov IR. Evidence of Superior and Inferior Sinoatrial Nodes in the Mammalian Heart. JACC Clin Electrophysiol. 2020;6:1827-1840.
9. Sanders P, Morton JB, Kistler PM, Spence SJ, Davidson NC, Hussin A, Vohra JK, Sparks PB, Kalman JM. Electrophysiological and electroanatomic characterization of the atria in sinus node disease: evidence of diffuse atrial remodeling. Circulation. 2004;109:1514-1522.
10. Houck CA, Lanters EAH, Heida A, Taverne Y, van de Woestijne PC, Knops P, Roos-Serote MC, Roos-Hesselink JW, Bogers A, de Groot NMS. Distribution of Conduction Disorders in Patients With Congenital Heart Disease and Right Atrial Volume Overload. JACC Clin Electrophysiol. 2020;6:537-548.
11. Elvan A, Adiyaman A, Beukema RJ, Sie HT, Allessie MA. Electrophysiological effects of acute atrial stretch on persistent atrial fibrillation in patients undergoing open heart surgery. Heart Rhythm. 2013;10:322-330.

23
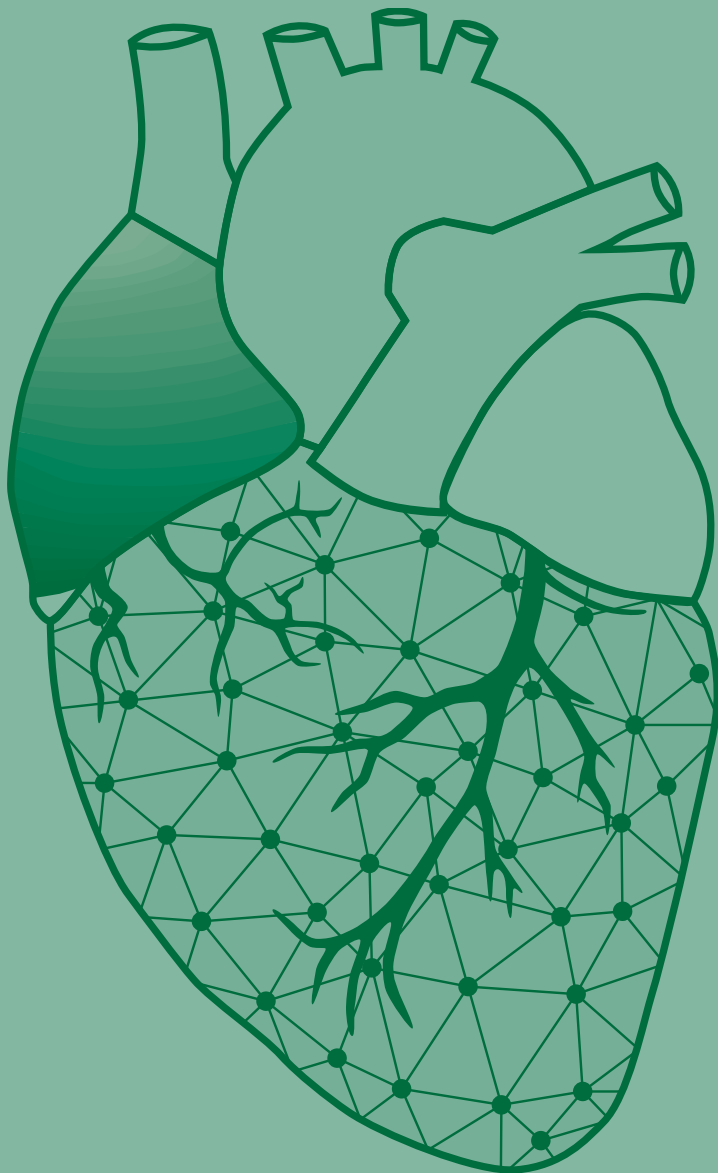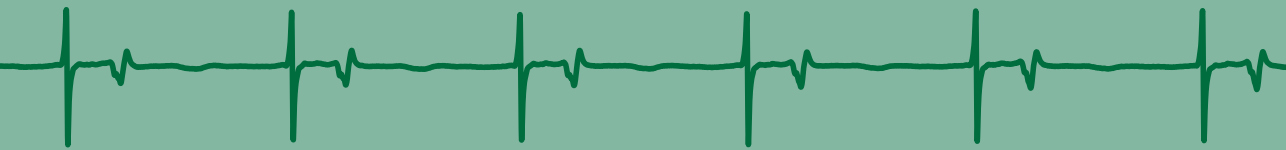
Chapter 24

Impact of atrial extrasystoles on conduction in pediatric patients with congenital heart disease

Nawin L. Ramdat Misier

Yannick J.H.J. Taverne

Mathijs S. van Schie

Rohit K. Kharbanda

Pieter C. van de Woestijne

Wouter J. van Leeuwen

Beatrijs Bartelds

Ad J.J.C. Bogers

Natasja M.S. de Groot

Journal site

Introduction

Despite improvement in (timing of) interventions and surgery, atrial fibrillation (AF) still occurs more often and at a younger age in patients with CHD compared to the general population.[1] This time course suggests that intra-atrial conduction is already affected early in life in patients with CHD.

Intra-atrial conduction is partly determined by cell-to-cell communications. Loss of cell-to-cell communications creates local differences in anisotropic properties of atrial tissue, resulting in enhanced non-uniform anisotropy. Consequently, the wavefront geometry will be distorted, leading to conduction disorders and eventually induction of tachyarrhythmia.

As conduction disorders in enhanced non-uniform anisotropic tissue are direction dependent, mapping during spontaneous atrial extrasystoles (AES) provides the opportunity to quantify direction-dependency of electrophysiological parameters.[2,3] We therefore investigated to what extent spontaneous aberrant AES affect the occurrence of conduction disorders and subsequently morphology of extracellular potentials in pediatric patients, as an indicator of early, enhanced non-uniform anisotropy.

Methods

Pediatric patients (<18 years) with CHD undergoing elective open-heart surgery were included (MEC2019-0543). Written informed consent was obtained from all patients older than 12 years and from parents of children below the age of 16 years. The study was conducted according to the principles of the Declaration of Helsinki.

Our intra-operative epicardial mapping approach has been previously described in detail.[4] Epicardial mapping at each location was performed for 5 seconds and included recordings of a calibration signal of 2 mV and 1000 ms, a unipolar reference electrogram (EGM) and all epicardial unipolar EGMs.

Mapping data of all AES and corresponding SR beats at that same mapping location were compared using custom-made software. The steepest negative slope of an atrial potential was marked as the local activation time (LAT). The number of localized areas of conduction delay and block were defined as the proportion of LATs with differences of respectively 7–11 ms and ≥12 ms between adjacent electrodes. Local effective conduction velocity (CV) was computed from LATs using discrete velocity vectors. Unipolar voltage was defined as the peak-to-peak amplitude of the steepest negative deflection and the number of low-voltage areas (LVA) as the proportion of potentials with an amplitude below 1.0 mV. Fractionated potentials contained ≥2 deflections.

For all electrophysiological parameters, the median of the corresponding SR beats is taken and compared to the median of the AES per patient. Comparison between SR and AES was done by using Wilcoxon Signed-Rank test and comparison between AES using Mann-Whitney U test. A *p*-value of <0.05 was considered statistically significant (IBM-SPSS Statistics version 28.0.1.0 and R version 4.2.2).

Results

Study population

Twenty-one pediatric patients (median age 1.8 years [0.2–7.3], 14 (67%) males) scheduled

24
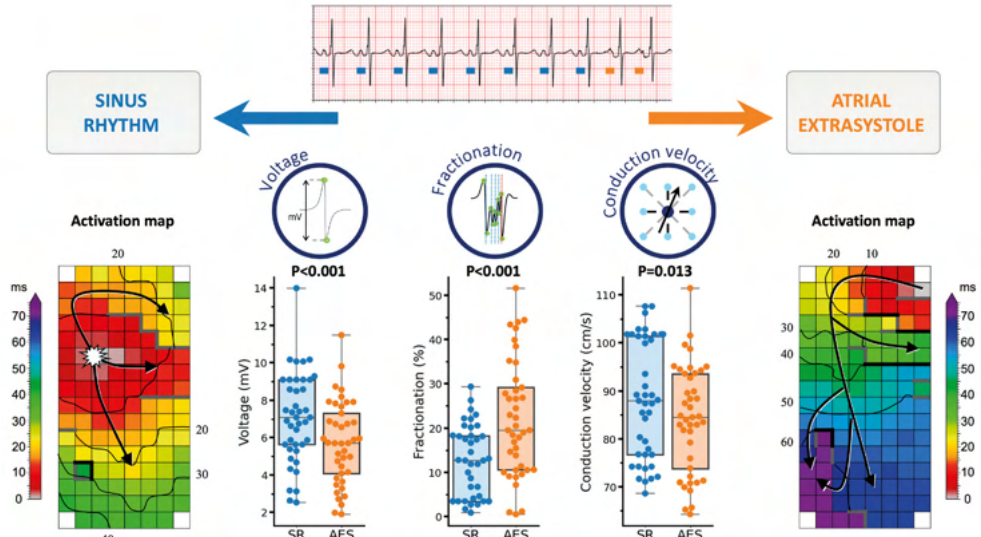
Figure 1 – Impact of AES on atrial conduction. Dot plots demonstrate differences in unipolar potential voltage and amount of fractionation between SR and AES. Examples contain colour-coded SR and corresponding AES activation maps.

for primary surgical repair of various CHD were included. Most of the CHD were of mild complexity (N=9, 43%), followed by severe (N=7, 33%) and moderate (N=5, 24%). The RA was dilated in 8 (38%) patients and LA dilatation was present in 4 (19%) patients.

AES characteristics

A total of 41 unique aberrant AES were included. Seven patients had multiple varying AES. Most AES were recorded at the RA (RA: 31, LA: 7 and BB: 3). The median coupling interval of the AES was 388 [291–470] ms, resulting in a median prematurity index of 34.4 [9.9–44.1] %.

Impact of AES on atrial conduction

During AES, median unipolar voltage and CV decreased compared to corresponding SR beats (7.1 [5.5–9.1] mV vs. 5.7 [4.0–7.5] mV, p<0.001; 87.9 [76.7–101.6] cm/s vs. 84.5 [73.0–93.6] cm/s, p=0.013; respectively), whereas the number of fractionated potentials increased (12.7 [3.5-18.3] % vs. 19.5 [10.5–30.0] %, p<0.001, *Figure 1*). Conduction delay, conduction block and LVA were more prominent during AES (3.1 [0.8-4.5] % vs. 4.5 [2.3–6.3] %, p<0.001; 0.6 [0–2.8] % vs. 1.5 [0–4.3] %, p=0.008; 1.7 [0.6–4.4] % vs. 3.3 [0.8–4.4] %, p<0.001, respectively). After adjusting for clustering of AES at patient level, differences between SR and AES remained significant (all p<0.05), except for CV (p=0.08).

Importantly, AES provoking alterations in electrophysiological parameters did not have shorter coupling intervals or prematurity indices (all p>0.05). Hence, differences in unipolar potential morphology and conduction heterogeneity were not influenced by the degree of the prematurity of AES.

Discussion

We quantified for the first time the arrhythmogenic effects of AES in pediatric patients with CHD. AES caused localized areas of conduction slowing and block, potentials with lower

unipolar voltages and a higher degree of fractionation compared to SR potentials in this young population. Previously, the impact of AES on epicardial atrial conduction has been investigated in adult patients with acquired heart disease using the same methodology as applied in the current study.[2,3] While, the effect of AES reported in adult patients is more severe, AES in pediatric patients already provoke similar arrhythmogenic changes in unipolar voltage, fractionation and conduction disorders.

Importantly, we demonstrated that the detrimental impact of AES on atrial conduction was independent of the prematurity of AES, suggesting that these effects are likely the consequences of (early) enhanced non-uniform anisotropic conduction rather than uncompleted repolarization.

Our findings provide new insights in atrial ectopic mechanisms, which may have impact on the time course of AF in patients with CHD. The contribution of these early conduction abnormalities to the development of AF are yet to be demonstrated, especially in light of surgical correction, residual lesions and general cardiovascular risk factors. Future studies with larger sample size and long-term follow-up will be essential to elucidate this interrelationship.

24

References

1. Mandalenakis Z, Rosengren A, Lappas G, Eriksson P, Gilljam T, Hansson PO, Skoglund K, Fedchenko M, Dellborg M. Atrial Fibrillation Burden in Young Patients With Congenital Heart Disease. Circulation. 2018;137:928-937.
2. Teuwen CP, Kik C, van der Does L, Lanters EAH, Knops P, Mouws E, Bogers A, de Groot NMS. Quantification of the Arrhythmogenic Effects of Spontaneous Atrial Extrasystole Using High-Resolution Epicardial Mapping. Circ Arrhythm Electrophysiol. 2018;11.
3. van Schie MS, Kharbanda RK, Bogers AJJC, de Groot NMS. B-AB16-01 EPICARDIAL MAPPING OF SPONTANEOUS ATRIAL EXTRASYSTOLES. Heart Rhythm. 2021;18:S31.
4. Kharbanda RK, van Schie MS, Ramdat Misier NL, van Leeuwen WJ, Taverne Y, van de Woestijne PC, Kammeraad JAE, Bartelds B, Bogers A, de Groot NMS. First Evidence of Atrial Conduction Disorders in Pediatric Patients With Congenital Heart Disease. JACC Clin Electrophysiol. 2020;6:1739-1743.

24
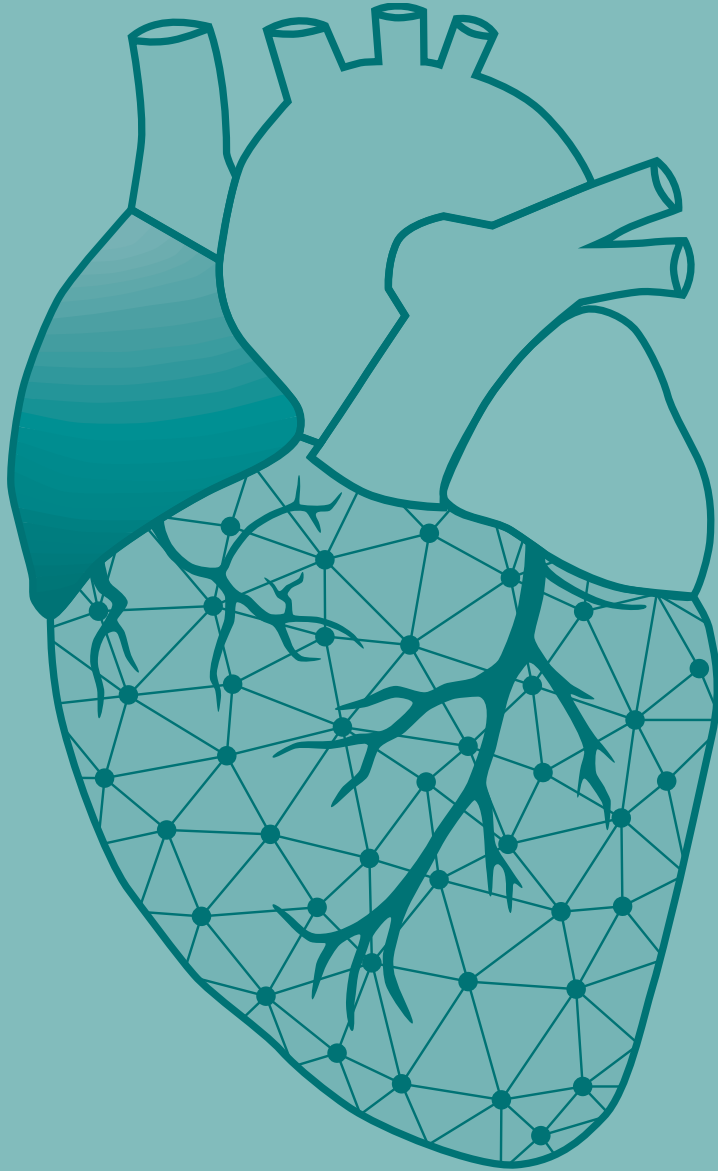
Chapter 25

Premature atrial contractions promote local directional heterogeneities in conduction velocity vectors

Mathijs S. van Schie

Nawin L. Ramdat Misier

Payam Razavi Ebrahimi

Annejet Heida

Rohit K. Kharbanda

Yannick J.H.J. Taverne

Natasja M.S. de Groot

Abstract

Background: Loss of cell-to-cell communication results in local conduction disorders and directional heterogeneity (LDH) in conduction velocity (CV) vectors, which may be unmasked by premature atrial contractions (PAC). We quantified LDH and examined differences between sinus rhythm (SR) and spontaneous PACs in patients with and without atrial fibrillation (AF).

Methods: Intra-operative epicardial mapping of the right and left atrium (RA, LA), Bachmann's bundle (BB) and pulmonary vein area (PVA) was performed in 228 patients (54 with AF). CV vectors were computed at each electrode using discrete velocity vectors. Directions and magnitudes of individual vectors were compared to surrounding vectors to identify LDH.

Results: 503 PACs (2 [1–3] per patient; prematurity index of 45±12%) were included. During SR, most LDH were found at BB and LA (11.9 [8.3–14.9] % and 11.3 [8.0–15.2] %) and CV was lowest at BB (83.5 [72.4–94.3] cm/s, all p<0.05). Compared to SR, the largest increase in LDH during PAC was found at BB and PVA (+13.0 [7.7, 18.3] % and +12.5 [10.8, 14.2] %, p<0.001); CV decreased particularly at BB, PVA and LA (-10.0 [-13.2, -6.9] cm/s, -9.3 [-12.5, -6.2] cm/s and -9.1 [-11.7, -6.6] cm/s, p<0.001). Comparing patients with and without AF, more LDH were found during SR in AF patients at PVA and BB, although the increase in LDH during PACs was similar for all sites.

Conclusions: LDH is a novel methodology to quantify local heterogeneity in CV as a possible indicator of electropathology. Intra-operative high-resolution mapping indeed revealed that LDH increased during PACs particularly at BB and PVA. Also, patients with AF already have more LDH during SR, which becomes more pronounced during PACs.

Journal site

Introduction

Atrial conduction velocity (CV) is frequently used to identify potential mechanisms for arrhythmogenesis as it provides important information about the speed and direction of wavefront propagation through myocardium. In non-remodeled atrial tissue, wavefront propagation is considered to be fast and along the longitudinal direction of the myocardial fibers.[1] However, in case of tissue damage and loss of cell-to-cell communication, wavefront propagation can be locally distorted.[2] This in turn leads to enhanced non-uniform tissue anisotropy which results in local conduction disorders and heterogeneous conduction. Eventually, these areas may become involved in initiation of tachyarrhythmias, such as atrial fibrillation (AF).

In daily clinical practice, mapping systems can easily create maps to quantify and visualize atrial CV. However, many systems apply algorithms that smooth wavefront propagation in which local conduction heterogeneities could be masked.[3] Recently, we developed a novel algorithm for CV estimation which is able to most accurately identify local conduction heterogeneities without smoothing of wavefront propagation.[3]

Premature atrial contractions (PAC) frequently originate from areas other than the sino-atrial node, resulting in wavefront propagation via alternative routes. These PACs may enhance conduction disorders and endo-epicardial asynchrony, which in turn are related to initiation and perpetuation of AF.[4,5] Especially in non-uniform anisotropic tissue, conduction disorders are direction and frequency dependent. High-resolution mapping during PACs therefore provides the opportunity to quantify changes in local directional heterogeneities (LDH) in CV vector fields. It is likely that areas of heterogeneous conduction may be unmasked during PACs, which are otherwise hidden during normal sinus rhythm (SR). The goal of this study was therefore to introduce LDH as a novel methodology and to examine differences between SR and spontaneous PACs in patients with and without history of AF.

Methods

Study population

The study population consisted of 228 successive adult patients without and with a history of AF undergoing open heart coronary artery bypass grafting (CABG), aortic or mitral valve surgery or a combination of valvular and CABG in the Erasmus Medical Center Rotterdam. This study was approved by the institutional medical ethical committee (MEC2010-054/MEC2014-393). Written informed consent was obtained from all patients. Patient characteristics were obtained from the patient's medical record.

Mapping procedure

Epicardial high-resolution mapping was performed prior to commencement to extra-corporal circulation, as previously described in detail.[3] A temporal bipolar epicardial pacemaker wire attached to the RA free wall served as a reference electrode. A steel wire fixed to subcutaneous tissue of the thoracic cavity was used as an indifferent electrode. Epicardial mapping was performed with a 128 or 192-electrode array (electrode diameter respectively 0.65 or 0.45 mm, interelectrode distances 2.0 mm). Mapping was performed by shifting the electrode array along predefined lines with a fixed anatomic orientation, following a predefined mapping scheme, covering the entire epicardial surface of the right atrium (RA), Bachmann's bundle (BB), pulmonary vein area (PVA) and left atrium (LA), as illustrated in *Figure 1*.

25
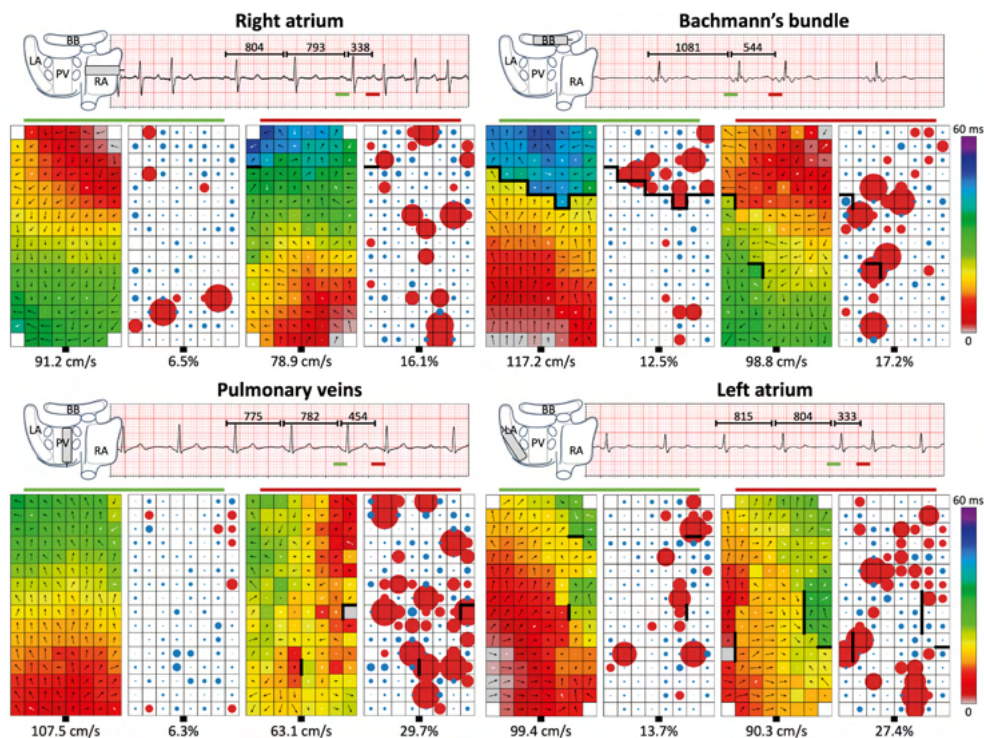
Figure 1 – Examples of SR beats and PACs recorded at various atrial sites. Four examples of 5-second SR recordings including PACs and corresponding color-coded activation (left) and LDH (right) maps. Black arrows represent the direction and magnitude of local CV, white arrows indicate LDH. Thick black lines in the activation maps correspond with conduction block according to a time difference between adjacent electrodes of ≥12 ms. Circles represent the degree of heterogeneity of vectors, in which the red color indicate LDH. The size of the circles represents the degree of vector heterogeneity. *Upper left panel*: recording of one RA location in a 54 year-old female with AVD and paroxysmal AF a SR beat (cycle length 793 ms) followed by a PAC (cycle length 338 ms, prematurity index 57%). The origin of the PAC is unknown. Compared to SR, the PAC provoked 9.6% more LDH and decreased CV by 12.3 cm/s. *Right upper panel*: recording of a BB location in a 63 year-old male with MVD without history of AF during a SR beat (cycle length 1081 ms) followed by a PAC (cycle length 554 ms, prematurity index 49%). Origin of the PAC is presumably left-sided. Compared to SR, the PAC provoked 4.7% more LDH and reduced CV by 18.4 cm/s. *Left lower panel*: recording of a PV location in a 63 year-old male undergoing CABG without history of AF during a SR beat (cycle length 782 ms) followed by a PAC (cycle length 454 ms, prematurity index 42%). Origin of the PAC is presumably left-sided. Compared to SR, the PAC provoked 23.4% more LDH and reduced CV by 44.4 cm/s. *Right lower panel*: recording of a LA location in a 72 year-old male with AVD without history of AF during a SR beat (cycle length 804 ms) followed by a PAC (cycle length 333 ms, prematurity index 59%). Origin of the PAC is presumably left-sided. Compared to SR, the PAC provoked 13.7% more LDH and reduced CV by 9.1 cm/s. **BB** = Bachmann's bundle; **CV** = conduction velocity; **LA** = left atrium; **LDH** = local directional heterogeneities; **PAC** = premature atrial contraction; **PV** = pulmonary vein area; **RA** = right atrium; **SR** = sinus rhythm.

Five seconds of SR were recorded from every mapping site, including a surface ECG lead, a calibration signal of 2 mV and 1000 ms, a bipolar reference electrogram (EGM) and all unipolar epicardial EGMs. In patients who presented in AF, SR mapping was performed after electrical cardioversion. Data were stored on a hard disk after amplification (gain 1000), filtering (bandwidth 0.5–400 Hz), sampling (1 kHz) and analogue-to-digital conversion (16 bits).

Data analysis

Unipolar EGMs were semi-automatically analyzed using custom-made software. The steepest negative slope of an atrial potential was marked as the local activation time

(LAT). All annotations were manually checked with a consensus of two investigators. Local effective CV was computed from LATs of neighboring electrodes (longitudinal, transversal and diagonal) using discrete velocity vectors (DVV) as previously described.[3] To avoid the inclusion of far-field potentials, areas corresponding to a mean CV of 0 cm/s were excluded. Areas of slow conduction were defined as the proportion of CV vectors <30 cm/s.[6] Dispersion of CV was calculated as the difference between the 5th and 95th percentile of all CV values within one beat. A local CV vector was indicated as directional heterogeneous when the local propagation angle differed more than 50% from the mean of all surrounding local propagation angles and/or the local speed was at least 50% slower than the geometric mean of all surrounding velocities. The mean of the propagation angles was calculated by:

$$\bar{\alpha} = \text{atan2}\left(\frac{1}{n} \cdot \sum_{j=1}^{n} \sin \alpha_j, \frac{1}{n} \cdot \sum_{j=1}^{n} \cos \alpha_j\right)$$

given the angles $\alpha_1, \dots, \alpha_n$. The corresponding geometric mean of the CV magnitudes was calculated by:

$$GM = \sqrt[n]{\|CV_1\| \cdot \dots \cdot \|CV_n\|}$$

The amount of LDH was then calculated as the proportion of all CV vectors. For all parameters, the median of all sinus beats is taken and compared to the median of the PAC; the resulting difference was considered as the potential effect provoked by PACs.

Classification of premature atrial contractions

PACs were defined as beats during SR with a shortening in cycle length of ≥25% compared to the previous sinus beat measured at the same mapping site.[4] The degree of prematurity (prematurity index) was determined for beats preceded by at least two sinus beats, as:

$$PI = \frac{CL_{SR} - CL_{PAC}}{CL_{SR}} \cdot 100\%$$

with CL_{PAC} equals the cycle length of the spontaneous PAC and CL_{SR} the cycle length of the preceding two sinus beats.

Statistical analysis

Normally distributed data are expressed as mean ± standard deviation, whereas skewed data are expressed as median [25th–75th percentile]. Clinical characteristics were compared using Student's t-test or Mann-Whitney U test when appropriate. Categorical data are expressed as number (percentage) and analyzed with a χ^2 or Fisher exact test.

To analyze the difference between SR and PACs, a paired t-test or Wilcoxon signed-rank test was used. The differences were presented as mean [95% CI]. Correlation was determined by ordinary least squares regression. A p-value <0.05 was considered statistically significant. A Bonferroni correction was applied for comparison of the four atrial regions. A p-value of <0.0083 (0.05/6) was considered statistically significant.

25

Table 1 – Baseline characteristics.

	Total	**No AF**	**With AF**	*p*-value
Patients	228	174 (76)	54 (24)	-
Male	158 (69)	127 (73)	31 (57)	0.030
Age (years)	68±10 (21–84)	67±11 (21–84)	71±9 (24–83)	0.004
Underlying heart disease				
• IHD	93 (41)	84 (48)	9 (17)	<0.001
• (i)VHD	135 (59)	90 (52)	45 (83)	<0.001
- AVD	74 (32)	59 (34)	15 (28)	0.707
- MVD	61 (27)	31 (18)	30 (56)	<0.001
History of AF	54 (24)	-	54 (100)	
• Paroxysmal	36 (16)	-	36 (67)	
• (Long-standing) persistent	18 (8)	-	18 (33)	
Cardiovascular risk factors				
• BMI (kg/m²)	26.6 [24.0–30.1]	26.6 [24.3–30.0]	26.7 [22.8–31.3]	0.310
• Hypertension	127 (56)	91 (53)	36 (67)	0.063
• Dyslipidemia	78 (34)	64 (37)	14 (26)	0.142
• Diabetes mellitus	58 (25)	47 (27)	11 (20)	0.328
Left atrial dilation	70 (31)	39 (22)	31 (57)	<0.001
Left ventricular dysfunction	63 (28)	46 (26)	17 (31)	0.525
Antiarrhythmic drugs	115 (70)	97 (71)	18 (64)	0.004
• Class I	1 (0)	1 (1)	0 (0)	1.000
• Class II	142 (62)	112 (64)	30 (56)	0.243
• Class III	12 (5)	1 (1)	11 (20)	<0.001
• Class IV	10 (4)	8 (5)	2 (4)	0.779

Values are presented as N (%), mean ± standard deviation (min–max) or median [interquartile ranges]. The *p*-values indicate significance between the no AF and AF group. **AF** = atrial fibrillation; **AVD** = aortic valve disease; **BMI** = body mass index; **IHD** = ischemic heart disease; **(i)VHD** = (ischemic and) valvular heart disease; **MVD** = mitral valve disease.

Results

Study population

Clinical characteristics of the study population (N=228, 158 male (69%), age 68±10 years) are summarized in *Table 1*. Patients underwent either CABG (IHD: N=93; 41%), aortic valve surgery with or without CABG ((i)AVD: N=74; 32%) or mitral valve surgery with or without CABG ((i)MVD: N=61; 27%). A minority of patients (N=54; 24%) had a history of AF, which was most prevalent in patients with MVD (N=30; 56%) compared to patients with AVD (N=15; 28%) or only IHD (N=9; 17%).
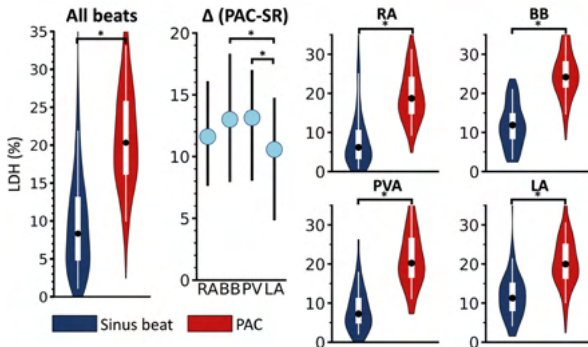
Figure 2 – Differences in local directional heterogeneities. The degree of local directional heterogeneities of CV vectors during SR (blue) and PAC (red). The difference (Δ(PAC-SR)) between SR and PAC is visualized as median with interquartile range. * p<0.05. **BB** = Bachmann's bundle; **LA** = left atrium; **LDH** = local directional heterogeneities; **PAC** = premature atrial contraction; **PVA** = pulmonary vein area; **RA** = right atrium; **SR** = sinus rhythm.

Table 2 – Incidence of local directional heterogeneities (%).

	SR	PAC	Δ (PAC-SR)	*p*-value
All beats	8.3 [4.8–13.2]	20.3 [16.1–25.8]	+11.7 [11.1, 12.4]	<0.001
Right atrium	6.2 [3.2–10.6]	18.7 [14.8–24.2]	+11.9 [11.0, 12.8]	<0.001
Bachmann's bundle	11.9 [8.3–14.9]	24.2 [21.6–28.2]	+13.2 [11.5, 14.9]	<0.001
Pulmonary vein area	7.3 [4.8–11.3]	20.2 [16.5–26.6]	+12.7 [11.0, 14.4]	<0.001
Left atrium	11.3 [8.0–15.2]	20.0 [16.3–25.1]	+9.4 [7.9, 10.9]	<0.001

SR and PAC values are presented as median [interquartile ranges], Δ(PAC-SR) as mean [95% CI]. **PAC** = premature atrial contraction; **SR** = sinus rhythm.

Characteristics of PACs

In total, 503 unique PACs were included for analysis (2 [1–3] PACs per patient). Most PACs were recorded at the RA (N=218, 43%) followed by LA (N=110, 22%), BB (N=92, 18%) and PVA (N=83, 17%). Average CL_{SR} was 897±242 ms, while average CL_{PAC} was 483±129 ms, resulting in an average prematurity index of 45±12%. Of all PACs, 351 (70%) were recorded in patients without AF. On average, 2 [1–3] PACs per patient were included in the no AF group, compared to 2 [1–4] PACs per patient in the AF group (p=0.002).

Figure 1 illustrates 4 typical examples of SR activation and PACs recorded at the same site. In all recordings, a certain degree of LDH was already present during SR. A spontaneous PAC resulted in an increased amount of LDH and decrease of local effective CV at all atrial regions.

Local directional heterogeneities during sinus rhythm

Figure 2 demonstrates the amount of LDH during SR of all PACs at the various atrial sites. A considerable amount of LDH was already present during SR in 99.2% of the recordings (8.3% (range: 0–36.6%)). As listed in *Table 2*, most LDH were found at BB (11.9 [8.3–14.9] %) and LA (11.3 [8.0–15.2] %), compared to PVA (7.3 [4.8–13.3] %) and RA (6.2 [3.2–10.6], p<0.001 for each). There was no relation between the amount of LDH, CL_{SR} (p=0.196) and clinical characteristics, except that more LDH were found in patients with LA dilation (6.5 [3.2–11.9] % vs. 10.0 [4.9–14.5] %, p=0.003). Although LDH during was moderately inversely correlated with CV (R^2=0.584, p<0.001), 9.3% of all LDH sites had a CV >90 cm/s. There was on average 3.8 [2.6–5.3] cm/s variability in CV between SR beats on the same location.

25

Impact of PACs on conduction velocity

As demonstrated in *Figure 3*, CV decreased from 89.8 [77.9–98.4] cm/s during SR to 80.1 [70.7–89.6] cm/s during PACs (-8.5 [95% CI: -9.6, -7.3] cm/s, p<0.001). The 33% most premature PACs had a larger decrease in CV compared to the 33% least premature PACs (-10.4 [95% CI: -12.3, -8.6] cm/s vs. -6.8 [95% CI: -8.9, -4.8] cm/s, p=0.007).
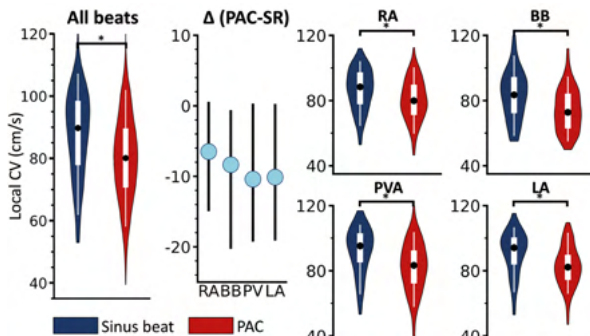
Figure 3 – Differences in local conduction velocity. Local CV during SR (blue) and PAC (red). The difference (Δ(PAC-SR)) between SR and PAC is visualized as median with interquartile range. * p<0.05. **BB** = Bachmann's bundle; **CV** = conduction velocity; **LA** = left atrium; **PAC** = premature atrial contraction; **PVA** = pulmonary vein area; **RA** = right atrium; **SR** = sinus rhythm.

Table 3 – Effect of PAC on conduction velocity.

	SR	PAC	Δ (PAC-SR)	p-value
CV (cm/s)				
All beats	89.8 [77.9–98.4]	80.1 [70.7–89.6]	-8.5 [-9.6, -7.3]	<0.001
RA	88.4 [77.9–97.2]	79.9 [71.4–89.6]	-7.2 [-8.7, -5.7]	<0.001
BB	83.5 [72.4–94.3]	72.8 [63.1–84.1]	-10.0 [-13.2, -6.9]	<0.001
PVA	95.3 [85.3–102.8]	83.3 [72.4–92.3]	-9.3 [-12.5, -6.2]	<0.001
LA	94.2 [84.0–100.3]	82.2 [74.5–89.6]	-9.1 [-11.7, -6.6]	<0.001
CVD − P_{95}-P_5				
All beats	97 [83–111]	123 [113–134]	+27 [25, 29]	<0.001
RA	87 [69–100]	117 [107–128]	+33 [31, 36]	<0.001
BB	101 [94–113]	125 [118–135]	+24 [19, 28]	<0.001
PVA	95 [88–110]	127 [117–138]	+27 [22, 32]	<0.001
LA	114 [103–123]	128 [117–138]	+17 [13, 20]	<0.001
CV <30 cm/s (%)				
All beats	2.1 [0.5–4.9]	8.5 [4.9–13.0]	+6.3 [5.8, 6.8]	<0.001
RA	1.1 [0–4.5]	6.8 [4.3–11.3]	+5.7 [5.1, 6.4]	<0.001
BB	3.7 [1.7–7.6]	12.4 [8.0–17.9]	+7.5 [6.2, 8.8]	<0.001
PVA	1.6 [0–3.8]	9.0 [6.0–13.9]	+7.4 [6.1, 8.7]	<0.001
LA	2.4 [0.9–3.8]	7.6 [4.9–11.2]	+5.7 [4.6, 6.9]	<0.001

SR and PAC values are presented as median [interquartile ranges], Δ(PAC-SR) as mean [95% CI]. **BB** = Bachmann's bundle; **CV** = conduction velocity; **CVD** = conduction velocity dispersion; **LA** = left atrium; **PAC** = premature atrial contraction; **PVA** = pulmonary vein area; **RA** = right atrium; **SR** = sinus rhythm.

Interregional differences in CV between SR and PACs are listed in *Table 3*. Although CV decreased during PACs at all regions (all p<0.001), there were no interregional differences in CV reduction (p=0.168). The largest CV reductions were found at BB (-10.0 [95% CI: -13.2, -6.9] cm/s), followed by PVA (-9.3 [95% CI: -12.5, -6.2] cm/s), LA (-9.1 [95% CI: -11.7, -6.6] cm/s) and RA (-7.2 [95% CI: -8.7, -5.7] cm/s).

During PACs, particularly at RA, BB and PVA, there was more dispersion of CV (+33 [31, 36], +24 [19, 28] and +27 [22, 32] respectively, p<0.001 for each). Also, there were more areas of slow conduction at all atrial regions, but specifically at BB (12.4 [8.0–17.9] %, p<0.001).
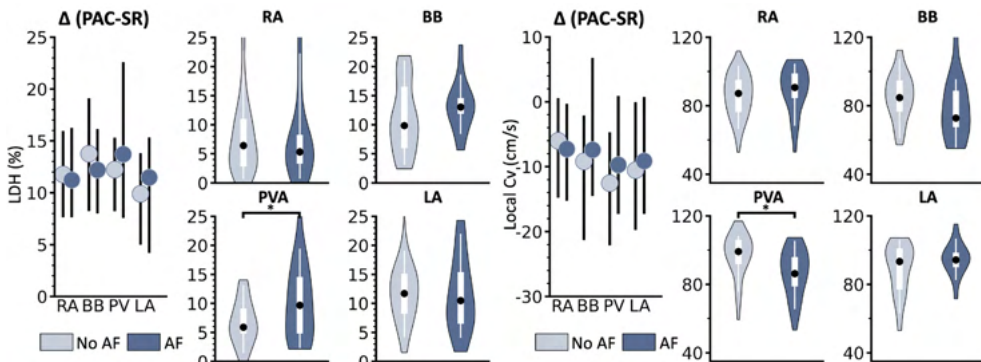
Figure 4 – Local conduction parameters in patients with and without AF. The degree of LDH (left) and CV (right) during SR in patients without (light) and with AF (dark). The difference (Δ(PAC-SR)) between SR and PAC is visualized as median with interquartile range. * p<0.05. **AF** = atrial fibrillation; **BB** = Bachmann's bundle; **CV** = conduction velocity; **LA** = left atrium; **LDH** = local directional heterogeneities; **PAC** = premature atrial contraction; **PVA** = pulmonary vein area; **RA** = right atrium; **SR** = sinus rhythm.

Table 4 – Influence of AF episodes on local conduction.

	SR			Δ (PAC-SR)		
	No AF	**With AF**	*p*-value	**No AF**	**With AF**	*p*-value
LDH (%)						
All beats	8.3 [4.7–12.5]	8.5 [4.9–14.5]	0.120	+11.7 [10.9, 12.5]	+11.8 [10.5, 13.1]	<0.001
RA	6.4 [2.8–10.9]	5.3 [3.4–8.2]	0.382	+12.0 [10.9, 13.0]	+11.6 [9.7, 13.4]	<0.001
BB	9.8 [6.0–16.5]	13.0 [11.9–14.5]	0.085	+13.9 [8.2, 19.1]	+11.7 [8.7, 14.7]	<0.001
PVA	5.9 [4.8–9.1]	9.7 [4.9–14.5]	0.031	+11.8 [9.9, 13.7]	+13.5 [10.8, 16.2]	<0.001
LA	11.7 [8.3–15.1]	10.5 [6.6–15.3]	0.301	+9.1 [7.2, 11.0]	+10.1 [7.6, 12.6]	<0.001
CV (cm/s)						
All beats	89.6 [77.7–98.7]	89.9 [80.0–98.3]	0.473	-8.8 [-10.1, -7.4]	-7.8 [-10.0, -5.6]	0.451
RA	87.2 [76.5–95.1]	90.7 [84.7–98.8]	0.080	-6.9 [-8.6, -5.3]	-8.2 [-11.6, -4.8]	0.288
BB	84.8 [76.8–94.6]	72.8 [67.6–88.7]	0.054	-11.9 [-15.4, -8.5]	-6.1 [-12.5, 0.4]	0.055
PVA	99.2 [92.1–105.9]	86.2 [79.0–95.8]	0.003	-10.9 [-15.4, -6.4]	-8.0 [-12.5, -3.6]	0.186
LA	93.4 [77.2–100.9]	94.3 [90.2–98.4]	0.206	-9.4 [-12.8, -6.0]	-8.6 [-12.2, -5.0]	0.302
CVD – P$_{95}$-P$_5$						
All beats	97 [82–110]	93 [84–114]	0.457	27 [25, 30]	25 [22, 28]	0.433
RA	87 [69–102]	84 [69–95]	0.277	33 [30, 36]	33 [21, 15]	0.450
BB	101 [95–113]	97 [84–112]	0.069	26 [21, 31]	19 [12, 25]	0.047
PVA	96 [90–104]	92 [88–112]	0.447	30 [23, 36]	25 [18, 31]	0.254
LA	112 [103–121]	117 [100–125]	0.366	14 [10, 18]	21 [15, 28]	0.033
CV <30 cm/s (%)						
All beats	1.7 [0.5–4.8]	2.4 [0.8–6.5]	0.151	+6.4 [5.8, 6.9]	+6.2 [5.2, 7.2]	0.088
RA	1.0 [0–4.9]	1.6 [0–2.6]	0.308	+5.7 [4.9, 6.5]	+5.8 [4.7, 6.8]	0.257
BB	3.3 [1.6–6.5]	6.9 [2.7–8.7]	0.072	+8.5 [7.2, 9.8]	+5.4 [2.3, 8.5]	0.024
PVA	0.9 [0–2.5]	2.5 [0.5–6.7]	0.049	+6.4 [4.9, 7.9]	+8.2 [6.2, 10.2]	0.135
LA	2.5 [1.1–3.5]	2.4 [0.8–5.9]	0.386	+6.1 [4.7, 7.5]	+5.0 [3.0, 6.9]	0.041

SR and PAC values are presented as median [interquartile ranges], Δ(PAC-SR) as mean [95% CI]. **BB** = Bachmann's bundle; **CV** = conduction velocity; **CVD** = conduction velocity dispersion; **LA** = left atrium; **PAC** = premature atrial contraction; **PVA** = pulmonary vein area; **RA** = right atrium; **SR** = sinus rhythm.

Impact of PACs on local directional heterogeneities

In 94% of PACs, more LDH (8.3 [4.8–13.2] % vs. 20.3 [16.1–25.8] %, p<0.001) were found during PACs compared to SR. The 33% most premature PACs had a larger increase in LDH compared to 33% least premature PACs (+12.6 [95% CI: 11.6, 13.7] % vs. +11.6 [95% CI: 10.4, 12.4] %, p=0.049). There was a very strong correlation between the amount of LDH and CV during PACs (R^2=0.811, p<0.001). On average, there was a 50.0 [37.2–62.5] % overlap of LDH areas during PAC with LDH areas during SR.

The largest increase in LDH during PAC was found at BB and PVA (+13.0 [95% CI: 7.7, 18.3] % and +12.5 [95% CI: 10.8, 14.2] %, all p<0.001). As already a considerable amount of LDH was found at BB during SR, most LDH during PAC were also found at BB (23.9 [21.5–28.0] %). There were no regional differences in the amount of overlap of LDH areas during PAC and SR (RA: 50.0 [38.6–64.7] %; BB: 50.0 [37.8–60.2] %; PVA: 44.4 [33.3–59.8] %; LA: 48.1 [40,0–62.4] %, p=0.102).

Influence of AF episodes

Differences in LDH and effective CV between patients with and without AF are listed in *Table 4*. Compared to patients without AF, more LDH were found during SR in AF patients at PVA and BB (5.9 [4.8–9.1] % vs. 9.7 [4.9–14.5] % and 9.8 [6.0–16.5] % vs. 13.0 [11.9–14.5] % respectively, p=0.031 and p=0.085), as shown in *Figure 4*. Also, CV at these atrial sites during SR in AF patients was lower (99.2 [92.1–105.9] cm/s vs. 86.2 [79.0–95.8] cm/s and 84.8 [76.8–94.6] cm/s vs. 72.8 [67.6–88.7] cm/s respectively, p=0.003 and p=0.054) and there were more

areas of slow conduction (0.9 [0–2.5] % vs. 2.5 [0.5–6.7] % and 3.3 [1.6–6.5] % vs. 6.9 [2.7–8.7] % respectively, p=0.049 and p=0.072).

The effect on LDH provoked by PACs was comparable between patients with and without AF. However, PACs in patients without AF resulted in a larger drop in CV (-11.9 [-15.4, -8.5] cm/s vs. -6.1 [-12.5, 0.4] cm/s, p=0.055) and more areas of slow conduction (+8.5 [7.2, 9.8] % vs. +5.4 [2.3, 8.5] %, p=0.024) at BB. As CV during SR was already lower at BB in AF patients and the drop in CV only modest, CV during PAC at BB was comparable between both patient groups (no AF: 73.1 [64.0–84.1] cm/s vs. with AF: 70.2 [59.9–81.3] cm/s, p=0.160). At PVA, CV during PAC in AF patients was lower compared to patients without AF (no AF: 84.5 [78.8–92.9] cm/s vs. with AF: 80.8 [66.4–92.3] cm/s, p=0.023).

Discussion

LDH is a novel methodology to quantify local heterogeneity in CV as a possible indicator of electropathology in atrial tissue. By applying this methodology on high-resolution maps, we demonstrated that during SR, LDH is most pronounced at BB and the LA. Furthermore, PACs enhance the degree of LDH and reduce CV, especially PACs with a higher degree of prematurity. These differences were particularly located at BB and the PVA. Also, patients with AF already have more LDH and slower CV during SR, which becomes more pronounced during PACs.

Estimation of local conduction velocity

The effective CV is frequently used in clinical practice as it provides important information on the underlying myocardium. Calculation of CV is often empirically determined based on relative distances and time differences derived from activation maps, which requires that the direction of activation is known. Several techniques including polynomial surface fitting, triangulation and finite differences have been introduced over the years.[7] However, recently we demonstrated that these techniques smoothen wavefront propagation thereby masking areas of local conduction slowing or wavefront distortion.[3] We therefore developed a novel methodology which is able to estimate CV without smoothing of wavefront propagation resulting in estimation of local 'effective' CV indicative of the underlying local substrate. In the present study, we further developed this methodology by implementing spatial variation in both direction and magnitude of velocity vectors. We demonstrated, as expected, that a certain degree of LDH is already present during SR. LDH was particularly pronounced at BB and LA. LDH severity even further increased during PACs. This implies that CV vector fields become more locally directional heterogeneous, indicating local areas of impaired conduction.

Local conduction heterogeneity

Wavefront propagation occurs preferentially and faster along the longitudinal direction to the myocardial fiber orientation.[1] Wavefront propagation along the transverse direction of myocardial bundles is therefore slower, which is known as anisotropy. Besides anisotropy, atrial CV also depends on source-to-sink principles, in which conduction slows down when a small bundle has to excite a relatively large myocardial area.[8] Remodeling of cellular connections and tissue damage gives rise to an arrhythmogenic substrate.[9] This may result in a non-uniform distribution of anisotropic features of myocardial tissue, leading to dissociated conduction with slower CV. Wavefronts conducting across this heterogeneous atrial myocardium can therefore be locally distorted, which can be measured as local irregularities in CV vector maps.

Previous studies focusing on heterogeneity in conduction mainly used distribution of conduction times (LAT differences between neighboring electrodes), the amount of conduction disorders (e.g., percentage of conduction delay/block), median CV and CV dispersion (P_{95}-P_5).[6,10-12] However, several parameters only include interelectrode LAT differences without considering the direction of wavefront propagation. CV vectors, however, do include the spatial information from which a vector is constructed, although only information on the speed of vectors is mainly used for analysis. In addition, many studies use LAT or conduction times distribution histograms to describe conduction heterogeneity, in which none or only one neighboring electrode is included.[6,10-12] In the present study, we used both the speed and local direction of CV vectors with respect to all neighboring electrodes to identify areas of heterogeneous conduction.

AF related structural and electrical remodeling also affects intra-atrial CV. In a previous study focusing on 412 patients with and without AF, we demonstrated a reduction in CV in AF patients at BB.[3] In a case-control study including 34 patients, Heida et al.[6] also demonstrated that there were no differences in CV dispersion (P_5-P_{95}) between patients with and without AF. Recently, Frontera et al.[13] demonstrated a progressive reduction in CV during SR and increase in slow CV (<50 cm/s) areas in 20 AF patients at LA, while there were no differences CV dispersion (coefficient of variation) compared to patients without AF. In the present study, we demonstrated that LDH were specifically present at BB and LA. As BB has predominantly parallel aligned muscle bundles, disruption of cell-to-cell connections can easily lead to disturbed wavefront geometry and increased LDH. Histological examination of 10 hearts from patients with paroxysmal AF and 10 hearts from patients without AF indeed demonstrated that fibro-fatty tissue was much more extensive in AF patients.[14] We also found a considerable amount of LDH in the LA, which is composed of multiple layers of differently aligned myocardial fibers with marked regional variations in thickness and orientation.[15] The degree of LDH was smallest in the RA which may be explained by the abundancy of transmural crisscrossing arrangement of smaller muscle fibers in between the larger trabeculations.[16] Small heterogeneities in conduction may therefore be embedded within passing wavefronts via other bundles and could make the RA less sensible for interruptions in propagation of broad wavefronts.

25

Arrhythmogenicity of PACs

Several studies demonstrated that PACs lead to an increased amount of conduction disorders and endo-epicardial asynchrony.[4,5] Wavefront propagation during PACs mainly slows along the perpendicular direction of the myocardial fibers, thereby increasing anisotropic conduction.[17,18] Especially in non-uniform anisotropic tissue, conduction disorders are directional and frequency dependent. As PACs originate from other areas than the sino-atrial node, wavefronts often propagate via alternative routes and with abnormal timing, thereby increasing the amount of conduction disorders. When PACs occur, they may aggravate dispersion in refractoriness which provokes conduction disorders, especially PACs with high prematurity.[19] When aberrant PACs occur during SR, a change in wavefront propagation direction may unmask conduction disorders due to anisotropic features of atrial myocardium.[4] The severity of conduction disorders in areas of transverse conduction are also related to clustered fibrosis, which results in more localized PAC-induced conduction disorders compared to non-fibrotic areas.[17,18] Hence, both prematurity and aberrancy cause areas of slowed conduction, localized conduction heterogeneity and conduction block, which is associated with initiation of reentry.

As the amount of LDH and CV decrease was related to the degree of prematurity, PACs with a CL close to the refractory period will probably provide the arrhythmogenic substrate

initiating atrial tachyarrhythmias such as AF. In our present study, the average CL_{PAC} was longer than the functional refractory period of 270±30 ms which was measured in the RA during electrophysiological studies.[20] It is expected that PACs near the refractory period will cause even more conduction slowing and LDH, making AF onset more likely. Although in our study PACs did not initiate AF, the increase of LDH observed in PACs add to arrhythmogenic tissue properties that underlie arrhythmia.

Limitations

Atrial tachyarrhythmias were not initiated by the PACs in this study, as is the case for most PACs, and most patients also did not have a history of AF. The arrhythmogenic effect of PACs could only be studied at one single mapping site and not at multiple atrial regions simultaneously. Consequently, the origin of each PAC and the effect on multiple atrial sites simultaneously remains unknown. Furthermore, any possible effects of endo-epicardial asynchrony on the amount of LDH cannot be excluded.

Conclusion

LDH is a novel methodology to quantify local heterogeneity in CV as a possible indicator of electropathology. Intra-operative high-resolution mapping indeed revealed that LDH increased and CV decreased during PACs particularly at BB and PVA. Also, patients with AF already have more LDH and slower conduction at PVA and BB during SR, which becomes even more pronounced during PACs.

References

1. Kleber AG, Rudy Y. Basic mechanisms of cardiac impulse propagation and associated arrhythmias. Physiol Rev. 2004;84:431-488.
2. Spach MS, Dolber PC. Relating extracellular potentials and their derivatives to anisotropic propagation at a microscopic level in human cardiac muscle. Evidence for electrical uncoupling of side-to-side fiber connections with increasing age. Circ Res. 1986;58:356-371.
3. van Schie MS, Heida A, Taverne Y, Bogers A, de Groot NMS. Identification of local atrial conduction heterogeneities using high-density conduction velocity estimation. Europace. 2021;23:1815-1825.
4. Teuwen CP, Kik C, van der Does L, Lanters EAH, Knops P, Mouws E, Bogers A, de Groot NMS. Quantification of the Arrhythmogenic Effects of Spontaneous Atrial Extrasystole Using High-Resolution Epicardial Mapping. Circ Arrhythm Electrophysiol. 2018;11.
5. van der Does L, Kharbanda RK, Teuwen CP, Knops P, Kik C, Bogers A, de Groot NMS. Atrial Ectopy Increases Asynchronous Activation of the Endo- and Epicardium at the Right Atrium. J Clin Med. 2020;9.
6. Heida A, van Schie MS, van der Does WFB, Taverne Y, Bogers A, de Groot NMS. Reduction of Conduction Velocity in Patients with Atrial Fibrillation. J Clin Med. 2021;10.
7. Cantwell CD, Roney CH, Ng FS, Siggers JH, Sherwin SJ, Peters NS. Techniques for automated local activation time annotation and conduction velocity estimation in cardiac mapping. Comput Biol Med. 2015;65:229-242.
8. Spach MS, Miller WT, 3rd, Dolber PC, Kootsey JM, Sommer JR, Mosher CE, Jr. The functional role of structural complexities in the propagation of depolarization in the atrium of the dog. Cardiac conduction disturbances due to discontinuities of effective axial resistivity. Circ Res. 1982;50:175-191.
9. Spach MS, Boineau JP. Microfibrosis produces electrical load variations due to loss of side-to-side cell connections: a major mechanism of structural heart disease arrhythmias. Pacing Clin Electrophysiol. 1997;20:397-413.
10. Schram-Serban C, Heida A, Roos-Serote MC, Knops P, Kik C, Brundel B, Bogers A, de Groot NMS. Heterogeneity in Conduction Underlies Obesity-Related Atrial Fibrillation Vulnerability. Circ Arrhythm Electrophysiol. 2020;13:e008161.
11. Heida A, van der Does WFB, van Staveren LN, Taverne Y, Roos-Serote MC, Bogers A, de Groot NMS. Conduction Heterogeneity: Impact of Underlying Heart Disease and Atrial Fibrillation. JACC Clin Electrophysiol. 2020;6:1844-1854.
12. Lammers WJ, Schalij MJ, Kirchhof CJ, Allessie MA. Quantification of spatial inhomogeneity in conduction and initiation of reentrant atrial arrhythmias. Am J Physiol. 1990;259:H1254-1263.
13. Frontera A, Pagani S, Limite LR, Peirone A, Fioravanti F, Enache B, Cuellar Silva J, Vlachos K, Meyer C, Montesano G, et al. Slow Conduction Corridors and Pivot Sites Characterize the Electrical Remodeling in Atrial Fibrillation. JACC Clin Electrophysiol. 2022;8:561-577.
14. Becker AE. How structurally normal are human atria in patients with atrial fibrillation? Heart Rhythm. 2004;1:627-631.
15. Pashakhanloo F, Herzka DA, Ashikaga H, Mori S, Gai N, Bluemke DA, Trayanova NA, McVeigh ER. Myofiber Architecture of the Human Atria as Revealed by Submillimeter Diffusion Tensor Imaging. Circ Arrhythm Electrophysiol. 2016;9:e004133.
16. Ho SY, Anderson RH, Sanchez-Quintana D. Atrial structure and fibres: morphologic bases of atrial conduction. Cardiovasc Res. 2002;54:325-336.
17. Angel N, Li LI, Macleod RS, Marrouche N, Ranjan R, Dosdall DJ. Diverse Fibrosis Architecture and Premature Stimulation Facilitate Initiation of Reentrant Activity Following Chronic Atrial Fibrillation. J Cardiovasc Electrophysiol. 2015;26:1352-1360.
18. Kawara T, Derksen R, de Groot JR, Coronel R, Tasseron S, Linnenbank AC, Hauer RN, Kirkels H, Janse MJ, de Bakker JM. Activation delay after premature stimulation in chronically diseased human myocardium relates to the architecture of interstitial fibrosis. Circulation. 2001;104:3069-3075.
19. Khan MS, Lange M, Ranjan R, Sharma V, Glotzbach JP, Selzman C, Dosdall DJ. Premature atrial stimulation accentuates conduction abnormalities in cardiac surgery patients that develop postoperative atrial fibrillation. J Electrocardiol. 2021;69:36-43.
20. De Sisti A, Attuel P, Manot S, Fiorello P, Halimi F, Leclercq JF. Electrophysiological determinants of atrial fibrillation in sinus node dysfunction despite atrial pacing. Europace. 2000;2:304-311.
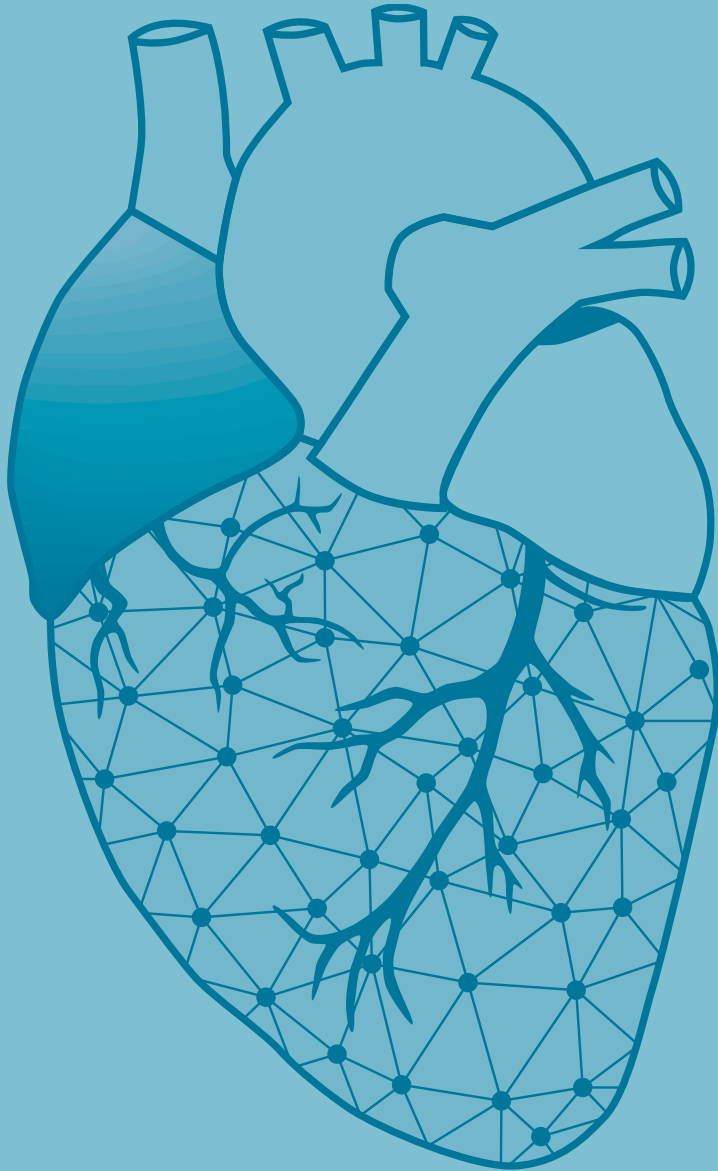
25

Chapter 26

Conduction velocity and anisotropic properties of fibrillation waves during acutely induced and long-standing persistent atrial fibrillation

Mathijs S. van Schie

Shmaila Talib

Paul Knops

Yannick J.H.J. Taverne

Natasja M.S. de Groot

Abstract

Background: Quantified features of local conduction heterogeneity due to pathological alterations of myocardial tissue could serve as a marker for the degree of electrical remodeling and hence be used to determine the stage of atrial fibrillation (AF). We therefore investigated whether local directional heterogeneity (LDH) and anisotropy ratio, derived from estimated local conduction velocities (CV) during AF, are suitable electrical parameters to stage AF.

Methods: Epicardial mapping (244 electrode-array, inter-electrode distance 2.25 mm) of the right atrium was performed during acutely induced AF (AAF; N=25, 32±11 years) and during long-standing persistent AF (LSPAF; N=23, 64±9 years). Episodes of 9±4 seconds of AF were analyzed. Local CV vectors were constructed to assess the degree of anisotropy. Directions and magnitudes of individual vectors were compared with surrounding vectors to identify LDH.

Results: Compared to the entire AAF group, LSPAF was characterized by slower conduction (71.5±6.8 vs. 67.6±5.6 cm/s, p=0.037) with a larger dispersion (1.59±0.21 vs. 1.95±0.17, p<0.001) and temporal variability (32.0±4.7 vs. 38.5±3.3 cm/s, p<0.001). Also, LSPAF was characterized by more LDH (19.6±4.4 vs. 26.0±3.4%, p<0.001) and a higher degree of anisotropy (1.38±0.07 vs. 1.51±0.14, p<0.001). Compared to the most complex type of AAF (type III), LSPAF was still associated with a larger CV dispersion, higher temporal variability of CV and larger amount of LDH.

Conclusions: Increasing AF complexity was associated with increased spatiotemporal variability of local CV vectors, local conduction heterogeneity and anisotropy ratio. By using these novel parameters, LSPAF could potentially be discriminated from the most complex type of AAF. These observations may indicate pathological alterations of myocardial tissue underlying progression of AF.

Journal site &
supplementary material

Introduction

Non-remodeled atrial tissue is considered to be uniform anisotropic in nature, resulting in a faster electrical conduction along the longitudinal direction of myocardial fibers than in the transverse direction.[1] The speed and direction of a propagating wavefront through myocardial tissue is determined by a range of functional and structural properties, such as membrane properties, tissue structure and wavefront geometry.[1,2] Tissue damage affecting cell-to-cell communication results in a heterogeneous distribution of conduction properties, which is known as non-uniform anisotropy. Non-uniform anisotropic tissue may result in intra-atrial conduction disorders, which play a crucial role in both genesis and perpetuation of tachyarrhythmias such as atrial fibrillation (AF).[3-6]

Although atrial tissue often is considered to be highly anisotropic, in patients without structural heart disease, Hansson et al.[7] surprisingly demonstrated that conduction velocity (CV) during stable sinus rhythm at the epicardial right atrial free wall was not dependent on propagation direction. Konings et al.[8] showed that during acutely induced, self-terminating AF, the right atrial free wall of young patients without structural heart disease was mainly activated uniformly by broad wavefronts with occasionally arcs of functional conduction block. In the same patients, Houben et al.[9] also reported low anisotropic conduction ratios (median 1.2). It is most likely that conduction in older patients with underlying cardiac diseases and dilated atria is additionally affected by alterations of the atrial structure, thereby inducing non-uniform anisotropic features.[3]

Recently, we developed a novel methodology to estimate local CV and accurately identify local conduction heterogeneities during sinus rhythm without smoothing of wavefront propagation.[10] Also, local directional heterogeneity (LDH) in CV vectors was quantified, which could be used as indicator of the degree of electropathology.[11] Hence, LDH could serve as an electrical biomarker to discriminate acutely induced, self-terminating AF from (long-standing) persistent AF. The goal of this study was therefore to apply this novel methodology during AF to quantify directional CV, LDH and the resulting anisotropy ratio, and to test whether these parameters differ between patients with different types of AF.

Methods

Study population

For this study, a unique, historical dataset of AF electrograms was used.[8,12] These electrograms were recorded during epicardial mapping studies, which have been performed in 48 patients during open chest surgery. Twenty-five patients (16 male, age 32±11 years) with Wolff-Parkinson-White syndrome underwent cardiac surgery for interruption of an accessory pathway. In these patients, AF was acutely induced by programmed electrical stimulation (AAF group). All patients had normal sized atria (left atrial diameter 39±6 mm) and no history of valvular heart disease or coronary artery disease. The AAF group was further subdivided according to the degree of complexity of AF into type I (N=10), II (N=8) and III (N=7).[8] Type I AAF was characterized by the presence of single broad wavefronts propagating without significant conduction delay. Type II AAF was characterized either by single waves associated with a considerable amount of conduction block and/or conduction slowing or the presence of two wavelets. Type III AAF was characterized by the presence of three or more wavelets associated with areas of slow conduction and multiple arcs of conduction block. A more detailed description of this study population has been given previously.[8]

The remaining 23 patients (14 male, age 64±9 years) underwent cardiac surgery for valvular

26
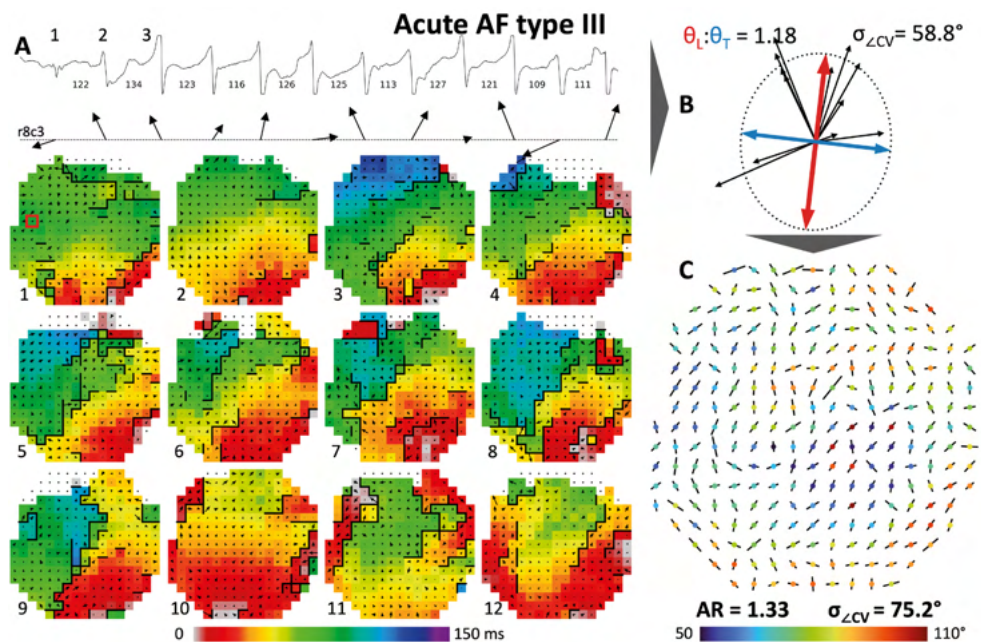
Figure 1 – Typical example of AAF type III. *Panel A:* 1442 ms-duration segment of a unipolar fibrillation electrogram (electrode r8c3) containing 12 consecutive beats of acute AF type III. The numbers in between the potentials indicate the beat-to-beat fibrillation intervals (in milliseconds). Corresponding CV vectors and consecutive color-coded activation maps are shown below the electrogram. Thick black lines in the activation maps correspond with conduction block according to a time difference between adjacent electrodes of ≥12 ms. Black arrows represent the direction and magnitude of local CV. Colored squares are empty when there was no valid CV vector or when the CV was 0 cm/s. White squares with a black dot represent electrograms without a valid LAT within the time window of the fibrillation wave. *Panel B:* an ellipse is fitted through all available local CV vectors at a specific electrode. Conduction in perpendicular directions along the major and minor axis of the fitted ellipse represent respectively the longitudinal and transverse CV (red and blue arrows respectively). The ratio between the two axes of the ellipse was used to assess the degree of local anisotropy in conduction. The variability of propagation directions is determined by the standard deviation of all local propagation angles at a specific electrode. *Panel C:* the anisotropy map shows the anisotropy ratio for every electrode. Orientation of the lines indicates the direction of the longitudinal CV and the length of the lines indicate the degree of local anisotropy. The color of the dots represent the degree of temporal variability of local propagation directions. A colorblind-friendly version of this figure can be found in *Supplementary Figure S1.* **(A)** **AF** = (acute) atrial fibrillation; **AR** = anisotropy ratio; **c** = column; **CV** = conduction velocity; **r** = row; $\sigma_{\angle cv}$ = standard deviation of the local propagation angles; θ_L = longitudinal conduction velocity; θ_T = transverse conduction velocity.

heart disease (mitral valve: N=18, aortic valve: N=2). A more detailed description of these patients has been given previously.[12,13] Coronary artery disease was present in 9 patients. Left atrial dimensions and left ventricular ejection fraction estimated by transthoracic echocardiography was respectively 58±9 mm and 50±12%. The time interval between the first documentation of an AF episode and the moment of cardiac surgery was at least one year (long-standing persistent AF: LSPAF group). The mapping protocol was approved by the institutional review board of Maastricht University, and all patients provided written informed consent.

Mapping of atrial fibrillation

Epicardial recordings were acquired before patients were put on cardiopulmonary bypass. In the AAF patients, AF was induced by programmed electrical stimulation using electrodes sutured to the right atrial appendage. The right atrial free wall was mapped with a spoon shaped electrode, containing 244 unipolar electrodes (diameter 0.3 mm, inter-electrode
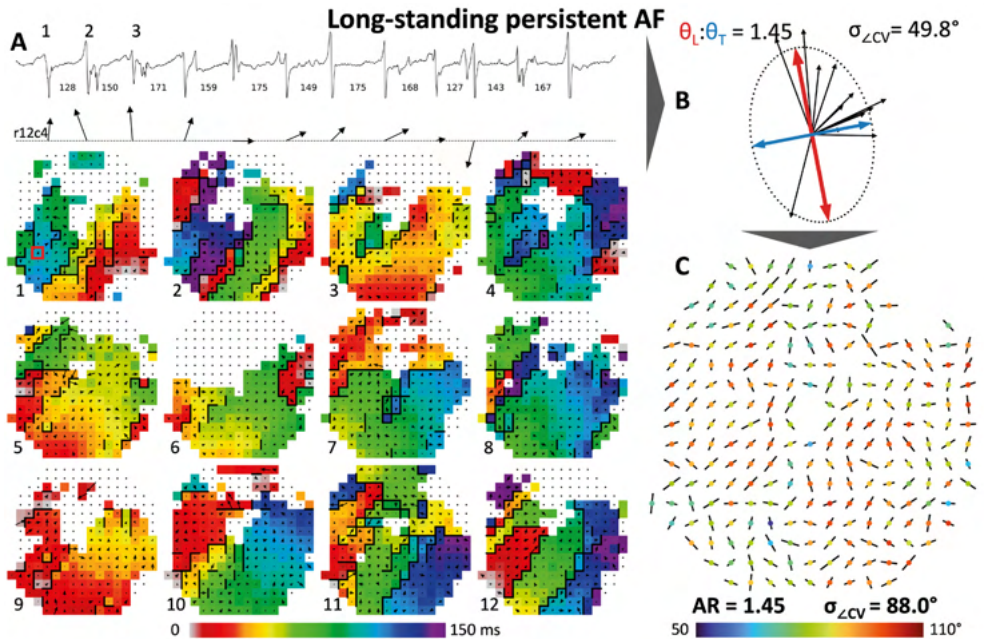
Figure 2 – Typical example of LSPAF. *Panel A*: 1972 ms-duration segment of a unipolar fibrillation electrogram (r12c4) containing 12 consecutive beats of LSPAF. The numbers in between the potentials indicate the beat-to-beat fibrillation intervals (in milliseconds). Corresponding CV vectors and consecutive color-coded activation maps are shown below the electrogram. Twelve consecutive color-coded activation maps corresponding to the recording shown in the upper left panel. Thick black lines in the activation maps correspond with conduction block according to a time difference between adjacent electrodes of ≥12 ms. Black arrows represent the direction and magnitude of local CV. Colored squares are empty when there was no valid CV vector or when the CV was 0 cm/s. White squares with a black dot represent electrograms without a valid LAT within the time window of the fibrillation wave. *Panel B*: an ellipse is fitted through all available local CV vectors at a specific electrode. Conduction in perpendicular directions along the major and minor axis of the fitted ellipse represent respectively the longitudinal and transverse CV (red and blue arrows respectively). The ratio between the two axes of the ellipse was used to assess the degree of local anisotropy in conduction. The variability of propagation directions is determined by the standard deviation of all local propagation angles at a specific electrode. *Panel C:* the anisotropy map shows the anisotropy ratio for every electrode. Orientation of the lines indicates the direction of the longitudinal CV and the length of the lines indicate the degree of local anisotropy. The color of the dots represent the degree of temporal variability of local propagation directions. A colorblind-friendly version of this figure can be found in *Supplementary Figure S2.* **(LSP) AF** = (long-standing persistent) atrial fibrillation; **AR** = anisotropy ratio; **c** = column; **CV** = conduction velocity; **r** = row; $\sigma_{\angle CV}$ = standard deviation of the local propagation angles; θ_L = longitudinal conduction velocity; θ_T = transverse conduction velocity.

26

distance 2.25 mm, mapping area 36×36 mm). This device was held manually on the middle of the right atrial free wall. A silver plate positioned inside the thoracic cavity served as the indifferent electrode. Unipolar fibrillation electrograms and a surface ECG lead were stored on a computer disk for offline analysis (amplification: gain 1000, filtering: bandwidth 1–500 Hz, sampling rate: 1 kHz, analogue-to-digital conversion: 12 bits).

Data analysis

In each patient, 4 to 20 seconds of AF were semi-automatically analyzed (9±4 seconds) using specialized custom-made mapping software. Local activation times (LAT) were detected automatically and defined as the steepest negative slope of an atrial potential. All annotations were manually checked with consensus of two investigators. At each electrode, fibrillation intervals were assessed by measuring the time between activations by consecutive fibrillation waves (panel A of *Figures 1 and 2*). Median atrial fibrillation cycle

length (AFCL) was determined from all fibrillation intervals recorded by the 244 unipolar electrodes.

Quantification of conduction velocity

Based on the 244 simultaneously recorded electrograms, local conduction velocity (CV) during AF was measured by construction of CV vectors in areas of 3×3 electrodes (4.5×4.5 mm). In line with prior studies, local effective CV was then computed using discrete velocity vectors.[10] LATs of electrode pairs surrounding the center electrode (longitudinal, transversal and diagonal) were used to calculate the mean velocity in horizontal (x) and vertical (y) direction. Only valid LATs within a time window of $\Delta t_{max} = 12\ ms$ were used, corresponding to the conduction block threshold as described by Allessie et al.[12] In order to increase the reliability of the CV estimate, only CVs with at least three estimates in both the horizontal and vertical direction were included. The magnitude of each vector was calculated to represent the CV independently of the propagation direction angle. To avoid inclusion of far-field potentials, areas corresponding to a mean CV of 0 cm/s were excluded.

In order to quantify the local spatial irregularity in CV vectors, the amount of local directional heterogeneities (LDH) in CV vectors was determined as previously described.[11] A local CV vector was indicated as directional heterogeneous when the local propagation angle differed more than 50% from the mean of all surrounding local propagation angles and/ or the local speed was at least 50% slower than the geometric mean of all surrounding velocities. The amount of LDH was then calculated as the proportion of all CV vectors.

Spatial dispersion of the parameters was calculated for each individual patient using the 5th, 50th and 95th percentile as $(P_{95} - P_5)/P_{50}$. The temporal variability of local CV was measured by the standard deviation of all CV vectors per electrode. The variability of local propagation angles was computed for every electrode by using the Yamartino method.[14] For each electrode, the most frequently encountered local propagation direction was calculated by using the circular mean of all local propagation angles.

Construction of anisotropy maps

Local anisotropy in conduction was measured by fitting an ellipse through all local CV vectors obtained during the recording, as previously described by Fitzgibbon et al.[15] and Halíř and Flusser[16]. The major (longest diameter) and minor axes of the fitted ellipse were assigned as 'longitudinal' and 'transverse' CV respectively, which corresponds to the direction of the fastest and slowest conduction. The ratio between the two axes was used to assess the degree of local anisotropy in conduction at each electrode (panel B of *Figures 1 and 2*). An anisotropy map was then constructed by plotting the anisotropy ratio at every electrode (panel C of *Figures 1 and 2*). The orientation of the lines indicates the direction of the fastest local CV and the length indicates the local anisotropy ratio. This method has previously been validated by pacing from four different directions and comparing the rotation angle of the fitted ellipse with the direction of the major pectinate muscles obtained by macrophotography.[17]

Statistical analysis

Normally distributed data are expressed as mean ± standard deviation and analyzed with a student's *t*-test. Non-normally distributed data are expressed as median [25th–75th percentile] and analyzed with a Mann-Whitney U test. Categorical data are expressed as numbers and percentages, and analyzed with a χ^2 or Fisher exact test when appropriate. Linear regression

models were used to calculate correlation between parameters. Also, linear regression models were used to assess the correlation between each of the parameters and AF severity. A *p*-value of <0.05 was considered statistically significant.

Results

Mapping data characteristics

A total database of 2,798 fibrillation maps and 478,674 unipolar fibrillation potentials (9,972±4,027 per patient) were analyzed. From these potentials, 449,307 (93,9%) CV vectors were estimated (92.5±6.5% per patient), resulting in 10,567 fitted ellipses (AAF: 226±27 vs. LSPAF: 213±35 per patient). The percentage of estimated CV vectors was higher in the AAF group (AAF: 96.3±3.2% vs. LSPAF: 88.4±6.7%, p<0.001), while more CV estimates were excluded in the LSPAF group due to a CV of 0 cm/s (AAF: 0.14 [0.09−0.30] % vs. LSPAF: 0.28 [0.21−0.83] %, p=0.041). The average AFCL in all patients was 170±35 ms and was longer in LSPAF patients (AAF: 158±24 (119–215) ms vs. LSPAF: 182±40 (122–308) ms, p=0.014).

Example of acutely induced and long-standing persistent AF

Twelve consecutive fibrillation maps from two different patients from the AAF (type III) and LSPAF group are shown in panel A of respectively *Figure 1 and 2*. As described by Konings et al.[8], type III AAF is most complex and characterized by multiple wavelets associated with areas of slow conduction (<10 cm/s) and multiple arcs of conduction block. Although in both patients almost all maps showed multiple wavelets separated by lines of functional conduction block, the LSPAF patient was characterized by a higher number of small wavelets propagating in different directions (52.9 vs. 36.0 wavelets per second).

In both patients, a CV vector is visualized for each activated electrode in each of the activation maps. Despite the high complexity of the fibrillatory process in both patients, still

26
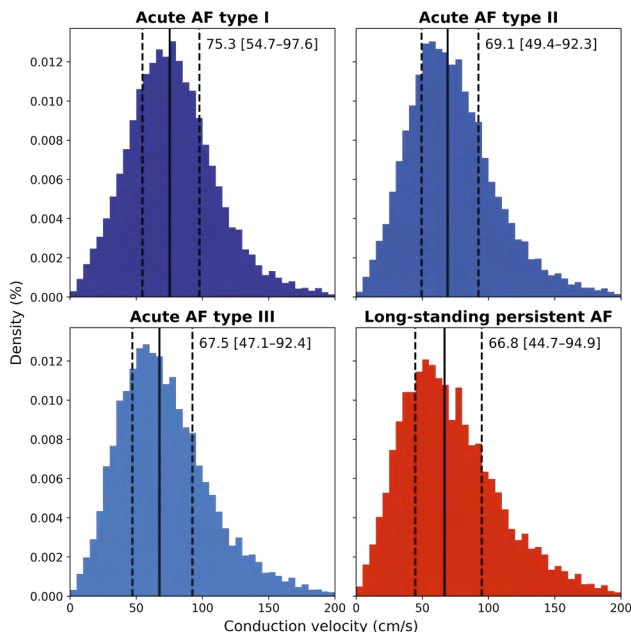
Figure 3 – Distribution of CV during various types of AF. Histograms of all CV estimations per AF type ($N_{AAF\ type\ I}$ = 137,008; $N_{AAF\ type\ II}$ = 89,852; $N_{AAF\ type\ III}$ = 78,089; N_{LSPAF} = 195,581). Although CV gradually decreased with increasing AF severity, in all AF types, still relatively high CV estimates >100 cm/s could be found. **AAF** = acute atrial fibrillation; **LSPAF** = long-standing persistent atrial fibrillation.

Table 1 – Conduction properties during various types of AF.

	AAF				LSPAF	p-value	r
	Type I	Type II	Type III	Total			
Number of patients (N)	10	8	7	25	23	-	-
Number of ellipses (N)	240±8	218±35	216±25	226±27	213±35	0.158	-
Median CV (cm/s)	75.9±6.2	70.1±6.2	66.9±3.7	71.5±6.8	67.6±5.6	0.037	-0.46*
CV dispersion	1.42±0.17	1.63±0.17	1.77±0.12	1.59±0.21	1.95±0.17	<0.001	0.78*
Temporal variability CV (cm/s)	30.0±5.0	32.2±4.2	34.7±2.8	32.0±4.7	38.5±3.3	<0.001	0.67*
Temporal variability PA (°)	58.7±13.4	73.1±12.9	86.8±6.0	71.2±16.3	83.7±8.6	0.002	0.65*
LDH (%)	16.5±3.8	20.4±3.6	23.2±2.3	19.6±4.4	26.0±3.4	<0.001	0.74*
Longitudinal CV (cm/s)	95.7±7.8	92.4±7.6	94.1±5.2	94.2±7.2	100.8±8.5	0.006	0.31
Transverse CV (cm/s)	69.8±5.7	67.8±5.0	66.0±4.1	68.1±5.3	66.8±4.3	0.355	-0.23
Anisotropy ratio	1.37±0.08	1.36±0.04	1.43±0.05	1.38±0.07	1.51±0.14	<0.001	0.51*
Anisotropy ratio dispersion	0.61±0.13	0.68±0.08	0.79±0.18	0.68±0.15	0.86±0.18	<0.001	0.55*

The p-values indicate significance between the total of the AAF group and the LSPAF group. The correlation coefficients represent the relation between AF severity and the parameters. Statistical significance of the correlation <0.001 is indicated by an asterisk. **(A)AF** = (acute) atrial fibrillation; **CV** = conduction velocity; **LDH** = local directional heterogeneities; **LSPAF** = long-standing persistent atrial fibrillation; **PA** = propagation angle.

a high amount of local effective CVs could be estimated by the algorithm (AAF patient: 97.8% and LSPAF patient: 92.6% of potentials). Both patients were characterized by a large range of local CV estimates, including local areas with high velocities >100 cm/s (AAF patient: 67.3 [26.4 to 135.0] cm/s and LSPAF patient: 66.7 [23.5 to 142.3] cm/s). In the LSPAF patient, there were more prominent directional differences in CV. For instance, two fibrillation waves locally propagating in perpendicular directions (*Figure 2A*, vectors of beats 2 and 6) showed an effective CV of 111.6 and 72.7 cm/s respectively. After fitting an ellipse on the twelve CV vectors, it resulted in a local anisotropy ratio of 1.45, as illustrated in Panel B of *Figure 2*. In the AAF patient, two fibrillation waves locally propagating in perpendicular directions (*Figure 1A*, vectors of beats 2 and 6) showed an effective CV of 72.7 and 61.4 cm/s respectively, resulting in a local anisotropy ratio of 1.18, as illustrated in Panel B of *Figure 1*. Although a
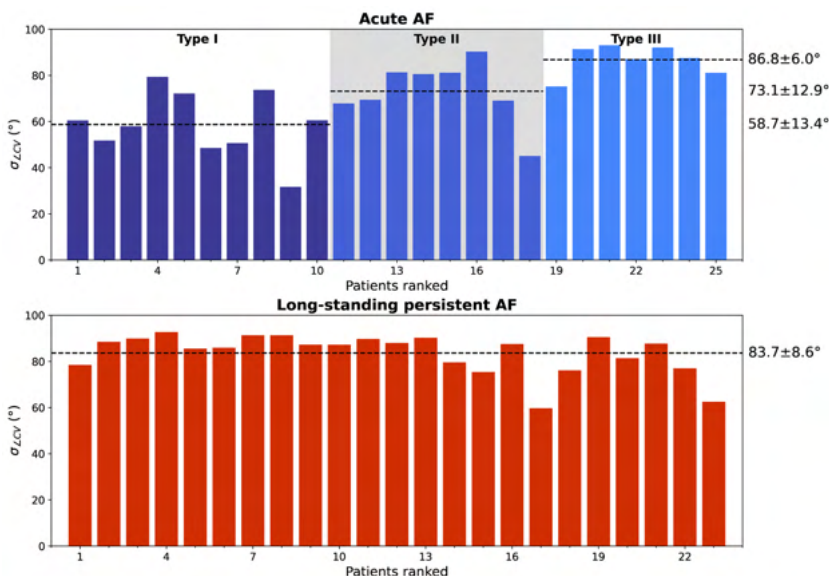
Figure 4 – Temporal variability of local propagation directions. Average standard deviation of the local propagation angles for every AAF (upper panel) and LSPAF (lower panel) patient separately, ranked according to the average AFCL. The AAF patients were subdivided according to the AF complexity (type I, II or III). During LSPAF, the average standard deviation of the local propagation angles was higher than AAF types I and II, but similar as AAF type III. **(A)AF** = (acute) atrial fibrillation; **AFCL** = atrial fibrillation cycle length; **LSPAF** = long-standing persistent atrial fibrillation; $\sigma_{\angle CV}$ = standard deviation of the local propagation angles.

large range of local conduction anisotropy was found in both patients, the LSPAF patient was characterized by a higher average anisotropy ratio (AAF patient: 1.33 [1.01 to 1.97] vs. LSPAF patient: 1.45 [1.02 to 2.27], p=0.001). Also, there was a larger temporal variation of local propagation directions in the LSPAF patient, as illustrated in the panel C of *Figures 1 and 2.* In the patient with type III AAF, the standard deviation of local propagation angles ranged between 52.7 and 94.9° (mean 75.2°), while it ranged from 69.8 to 100.0° (mean 88.0°) in the LSPAF patient (p<0.001). AF was therefore more chaotic in the LSPAF patient.

Spatiotemporal dispersion of local conduction velocity

Relative frequency distribution histograms of all CV estimations per AF type are visualized in *Figure 3*. As can be seen, CV gradually decreased with increasing AF severity. However, in all AF types, still relatively high CV estimates >100 cm/s could be found.

Comparing the averaged median CV between the AAF and LSPAF group, CV during LSPAF was lower than during AAF (AAF: 71.5±6.8 cm/s vs LSPAF: 67.6±5.6 cm/s, p=0.037). Also, as listed in *Table 1*, averaged CV decreased with increasing AF complexity (r=-0.46, p<0.001), although there was no difference between AAF type III and LSPAF (p=0.757). There was no correlation between the AFCL and median CV (r=0.07, p=0.659).

There was a larger dispersion (AAF: 1.59±0.21 vs. LSPAF: 1.95±0.17, p<0.001) and temporal variability of CV (AAF: 32.0±4.7 cm/s vs. LSPAF: 38.5±3.3 cm/s, p<0.001) during LSPAF. Dispersion in CV significantly increased with increasing AF complexity (r=0.78, p<0.001), with LSPAF having the largest dispersion even compared to AAF type III (1.95±0.17 vs. 1.77±0.12, p=0.007). There was also an increasing trend in temporal variability of CV with increasing AF complexity in the AAF group (r=0.67, p<0.001). Still, the temporal variability of CV was largest during LSPAF compared with all types of AAF (*Table 1*, p<0.007).

26
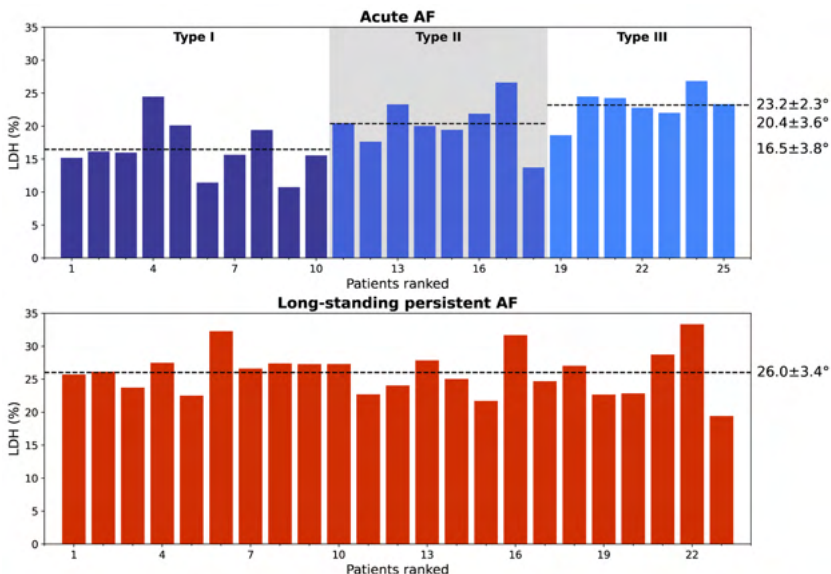
Figure 5 – Local directional heterogeneity in CV vectors. The amount of LDH is shown for every AAF (upper panel) and LSPAF (lower panel) patient separately, ranked according to the average AFCL. The AAF patients were subdivided according to the AF complexity (type I, II or III). During LSPAF, the amount of LDH was higher than AAF types I, II and III. **(A)AF** = (acute) atrial fibrillation; **AFCL** = atrial fibrillation cycle length; **LDH** = local directional heterogeneities; **LSPAF** = long-standing persistent atrial fibrillation.
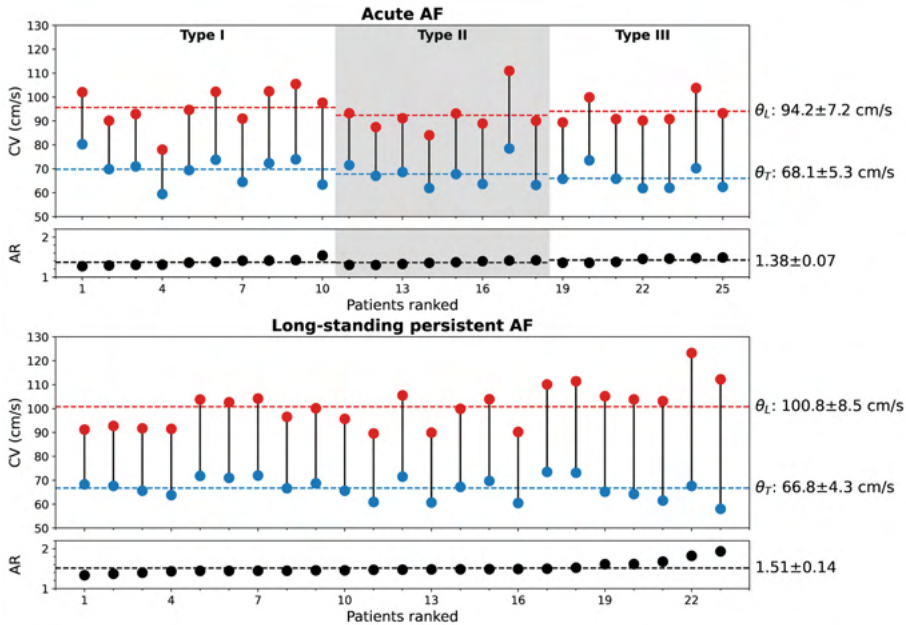
Figure 6 – Directional differences in conduction velocity. Longitudinal and transverse CV and conduction anisotropy ratio for every AAF (upper panel) and LSPAF (lower panel) patient separately, ranked according to the individual average anisotropy ratio. The AAF patients were subdivided according to the AF complexity (type I, II or III). During LSPAF, average longitudinal CV and the degree of conduction anisotropy was higher. **(A)AF** = (acute) atrial fibrillation; **AR** = anisotropy ratio; **CV** = conduction velocity; **LSPAF** = long-standing persistent atrial fibrillation; θ_L = longitudinal conduction velocity; θ_T = transverse conduction velocity.

Temporal variability of local propagation directions

The average standard deviation of the local propagation angles is visualized for every AAF and LSPAF patient in *Figure 4*. LSPAF patients were characterized by less stable vector fields in the fibrillation maps, as the average standard deviation of the local propagation angles at each electrode in these patients was larger than during AAF (AAF: 71.2±16.3° vs. LSPAF: 83.7±8.6°, p=0.002).

The smallest average standard deviations of local propagation angles were found during AAF type I (58.7±13.4°, p<0.022), followed by AAF type II (73.1±12.9°, p<0.016). The average standard deviation of the local propagation angles was comparable between AAF type III and LSPAF (p=0.392). AAF type III and LSPAF were therefore most disorganized.

Local directional heterogeneities

In both the AAF and LSPAF group, a considerable amount of LDH was found, as illustrated in *Figure 5*. In AAF patients, the amount of LDH ranged from 10.7% to 26.8% (19.6±4.4%) and in the LSPAF patients from 19.4% to 33.3% (26.0±3.4%). The amount of LDH was considerably higher during LSPAF (p<0.001). There was no correlation between the AFCL and the amount of LDH (r=0.05, p=0.749). However, patients with slower median CV were characterized by a higher amount of LDH (r=-0.56, p<0.001).

The amount of LDH increased with AF severity (r=0.74, p<0.001); it was largest during LSPAF (26.0±3.4%, p<0.028) and smallest during AAF type I (16.5±3.8%, p<0.027).

Directional differences in conduction velocity

The longitudinal and transversal CV for every AAF and LSPAF patient is demonstrated in *Figure 6*. Within the AAF and LSPAF group, there was considerable inter-individual variation in both longitudinal and transverse CV. Longitudinal CV during LSPAF was higher than during AAF (AAF: 94.2±7.2 cm/s vs. LSPAF: 100.8±8.5 cm/s, p=0.006), while transverse CV was comparable between both groups (AAF: 68.1±5.3 cm/s vs. LSPAF: 66.8±4.3 cm/s, p=0.355).

There were no clear differences in longitudinal and transverse CV between the different types of AAF and LSPAF, while there was a trend to a decrease of transverse CV with increasing AF complexity.

The direction of the longitudinal axis did frequently not correspond to the mostly encountered local propagation direction. In all patients, the average absolute difference between both angles was 44.0±4.2° and did not differ between the AAF and LSPAF group (AAF: 44.3±5.3° vs LSPAF: 43.7±2.4°, p=0.591).

Anisotropy ratio

The anisotropy ratio in the AAF patients ranged from 1.27 to 1.54 (1.38±0.07) and in the LSPAF patients from 1.34 to 1.93 (1.51±0.14), as illustrated in *Figure 6*. Although there was overlap in the degree of anisotropy between the AAF and LSPAF group, the anisotropy ratio was higher during LSPAF (p<0.001). The dispersion of anisotropy ratios was also larger in LSPAF patients (AAF: 0.68±0.15 vs. LSPAF: 0.86±0.18, p<0.001). There was a moderate correlation between the anisotropy ratio and AFCL (r=0.39, p=0.006) and the amount of LDH (r=0.35, p=0.014).

The anisotropy ratio in LSPAF patients was comparable with AAF type III (p=0.120), and larger than AAF types I and II (p=0.005 and p=0.006 respectively). There was also no difference in anisotropy ratio between AAF type I and II (p=0.774).

Discussion

In this study, we demonstrated for the first time that increasing complexity of AF was associated with increased spatiotemporal variability of local CV vectors, local conduction heterogeneity and anisotropy ratio. By using these novel mapping parameters, we demonstrated that LSPAF could potentially be discriminated from the most complex type of AAF (type III) by a larger CV dispersion, higher temporal variability of CV and larger amount of LDH.

26

Effective conduction velocity estimation during atrial fibrillation

Data on CV during AF is scarce as estimation of CV is very difficult during non-stable patterns of activation. This is mainly due to the fact that the number of recording electrodes is often limited and sequential mapping is impossible during AF. Therefore, a high-density (grid) multi-electrode array is required to accurately acquire local electrograms for CV estimation. Also, challenges in LAT assignment due to fractionation, low-voltage, multiple wavefronts, wavefront collision or wavefronts taking complicated small paths hamper global CV estimation.[18] Hence, only local methods for CV can be applied in these complex cases. As during AF there may be multiple wavefronts with short wavelengths, the spatial resolution of the electrodes should also be sufficient.[19] This is the reason why data on CV during AF is often limited to experimental studies using animal models. However, with the increasing usage of multi-electrode grid catheters during endocardial electro-anatomical mapping

procedures, it is expected that our approach can be used during standard EP procedures in the near future. This study provides the first insights into high-resolution CV estimation during acute and long-standing persistent AF in humans.

Inhomogeneity in conduction

Propagation of an electrical impulse is altered when active or passive cell membrane properties are affected. CV of fibrillation waves in the LSPAF patients was significantly lower with increased spatiotemporal variability compared to the AAF patients. Although a decrease in CV is known to be rate dependent, we did not find a correlation between CV and AFCL. CV during LSPAF was reduced compared with the AAF patients despite the higher longitudinal CV. This was caused by a large number of local CV vectors in other directions than the fastest direction, which resulted in a lower average CV. Therefore, it is likely that propagation of wavefronts depends more on the macroscopic atrial anatomy, whereas local CVs are more determined by the local fiber orientation.[20] Strands of viable myocardial tissue are still present in LSPAF patients, resulting in areas with fast local conduction. Due to an increased number of functional and structural barriers separating these strands, LSPAF will be more complex with more heterogeneous conduction. In the goat model of AF, Maesen et al.[20] demonstrated that left atrial CV was lower in goats with persistent AF compared to those with AAF. They also found similar results on the discrepancy between the fastest and most occurring conduction direction. Local CV during AAF in human has only previously been described by Houben et al.[21] Although the average CV was comparable with our current study, they found a limited number of high velocities (>100 cm/s). This can be easily explained by the different CV estimation method which was used, as we previously demonstrated it was less efficient in estimating CVs, particularly in case of small wavefronts.[10]

Impairment of wavefront propagation can be the result of i.e. 1) remodeling of cellular connections, 2) reduced membrane excitability caused by a decrease in the inward sodium current, 3) source-to-sink mismatches caused by inhomogeneous tissue volumes or wavefront curvature, and 4) tissue damage resulting in e.g. fibrosis.[22,23] Regional differences in membrane excitability can also be caused by a spatial dispersion in refractoriness and action potential duration, which are particularly present in patients with AF.[24-26] Wavefronts conducting across this heterogeneous atrial myocardium can therefore be locally distorted, which can be measured as local irregularities in CV vector maps (LDH).[11] Recently, we demonstrated in patients with structural heart disease undergoing epicardial mapping that the degree of LDH during SR was smallest in the RA.[11] In the present study, we demonstrated that a higher degree of LDH is present during AF at the RA, even in AAF patients with normal sized atria. Furthermore, the degree of LDH increased with AF complexity and most LDH was therefore found in patients with LSPAF. With AF-related structural and electrical remodeling, local conduction becomes more and more impaired, leading to an increasing complexity in the fibrillatory process (*Figure 2*).[12,13,20,27,28]

Cardiac anisotropy

Another major determinant of myocardial conduction is cardiac anisotropy, which is considered to be arrhythmogenic as it contributes to both initiation and perpetuation of AF.[3,9,29] Anisotropy is the property of directional dependence, meaning that electrical conduction is much faster along the longitudinal direction of myocardial fibers than in transverse direction.[1] Anisotropic conduction is the result of the shape and size of the cardiomyocyte, connectivity, arrangement and density of inter-cellular connections.[30] Altered cell-to-cell communication and tissue damage can result in a discontinuous distribution of conduction properties (non-uniform anisotropy), leading to unidirectional

block and reentry. Although high anisotropy ratios (ranging up to 9.8[3]) have been measured in isolated human atrial tissue, in contrast, we demonstrated relatively low anisotropy ratios in the RA during both AAF and LSPAF. These relatively low anisotropy ratios during AF were also found by Maesen et al.[20] in the left atrial free wall of goats. They, however, did not find a difference in anisotropy ratio between AAF and persistent AF. In contrast, we demonstrated that the anisotropy ratio at the right atrium was higher in LSPAF patients compared to AAF. Other studies also demonstrated enhanced anisotropic conduction in the right atrium in patients with chronically stretched atria secondary to mitral valve stenosis and in patients undergoing surgical AF ablation.[31,32] In addition, we also demonstrated a larger spatial variety of anisotropic properties in LSPAF patients. Therefore, the heterogeneously increased anisotropic properties of atrial tissue seen during LSPAF contribute to AF persistence.

Cardiac anisotropy is also influenced by ageing and structural heart diseases. Patients in the LSPAF group were significantly older than patients in the AAF group. Spach[3] demonstrated that ageing is associated with an increase in interstitial fibrosis resulting in a decrease in side-to-side electrical coupling thereby giving rise to non-uniform anisotropy. Also, all LSPAF patients had valvular heart disease. Augmentation of atrial fibrosis, due to chronic stretch caused by valvular heat disease or alterations of atrial structure by AF itself could account for a higher incidence of conduction abnormalities during LSPAF.[33,34]

Limitations

As a historical dataset of AF patients was used for this study, no histological examination could be performed. Therefore, it remains unknown whether the longitudinal CV truly represents the myocardial fiber direction in this population. However, previous other studies validated the proposed method to determine the anisotropy ratio and its relation to myocardial fiber direction.[9,17,21] Besides, as the same method was applied on both groups, they act as a control for one other.

Conclusion

Increasing complexity of AF was associated with increased spatiotemporal variability of local CV vectors, local conduction heterogeneity and anisotropy ratio. By using these novel mapping parameters, we demonstrated that LSPAF could potentially be discriminated from the most complex type of AAF (type III) by a larger CV dispersion, higher temporal variability of CV and larger amount of LDH. These observations may indicate pathological alterations of myocardial tissue underlying progression of AF.

26

References

1. Kleber AG, Rudy Y. Basic mechanisms of cardiac impulse propagation and associated arrhythmias. Physiol Rev. 2004;84:431-488.
2. Spach MS, Dolber PC, Heidlage JF. Influence of the passive anisotropic properties on directional differences in propagation following modification of the sodium conductance in human atrial muscle. A model of reentry based on anisotropic discontinuous propagation. Circ Res. 1988;62:811-832.
3. Spach MS, Dolber PC. Relating extracellular potentials and their derivatives to anisotropic propagation at a microscopic level in human cardiac muscle. Evidence for electrical uncoupling of side-to-side fiber connections with increasing age. Circ Res. 1986;58:356-371.
4. Feng J, Yue L, Wang Z, Nattel S. Ionic mechanisms of regional action potential heterogeneity in the canine right atrium. Circ Res. 1998;83:541-551.
5. Simpson RJ, Jr., Foster JR, Gettes LS. Atrial excitability and conduction in patients with interatrial conduction defects. Am J Cardiol. 1982;50:1331-1337.
6. van Schie MS, de Groot NM. Clinical Relevance of Sinus Rhythm Mapping to Quantify Electropathology Related to Atrial Fibrillation. Arrhythm Electrophysiol Rev. 2022;11:e11.
7. Hansson A, Holm M, Blomstrom P, Johansson R, Luhrs C, Brandt J, Olsson SB. Right atrial free wall conduction velocity and degree of anisotropy in patients with stable sinus rhythm studied during open heart surgery. Eur Heart J. 1998;19:293-300.
8. Konings KT, Kirchhof CJ, Smeets JR, Wellens HJ, Penn OC, Allessie MA. High-density mapping of electrically induced atrial fibrillation in humans. Circulation. 1994;89:1665-1680.
9. Houben RP, de Groot NM, Smeets JL, Becker AE, Lindemans FW, Allessie MA. S-wave predominance of epicardial electrograms during atrial fibrillation in humans: indirect evidence for a role of the thin subepicardial layer. Heart Rhythm. 2004;1:639-647.
10. van Schie MS, Heida A, Taverne Y, Bogers A, de Groot NMS. Identification of local atrial conduction heterogeneities using high-density conduction velocity estimation. Europace. 2021;23:1815-1825.
11. van Schie MS, Misier NLR, Razavi Ebrahimi P, Heida A, Kharbanda RK, Taverne Y, de Groot NMS. Premature atrial contractions promote local directional heterogeneities in conduction velocity vectors. Europace. 2023.
12. Allessie MA, de Groot NM, Houben RP, Schotten U, Boersma E, Smeets JL, Crijns HJ. Electropathological substrate of long-standing persistent atrial fibrillation in patients with structural heart disease: longitudinal dissociation. Circ Arrhythm Electrophysiol. 2010;3:606-615.
13. de Groot NM, Houben RP, Smeets JL, Boersma E, Schotten U, Schalij MJ, Crijns H, Allessie MA. Electropathological substrate of longstanding persistent atrial fibrillation in patients with structural heart disease: epicardial breakthrough. Circulation. 2010;122:1674-1682.
14. Yamartino RJ. A Comparison of Several Single-Pass Estimators of the Standard-Deviation of Wind Direction. J Clim Appl Meteorol. 1984;23:1362-1366.
15. Fitzgibbon A, Pilu M, Fisher RB. Direct least square fitting of ellipses. Ieee Transactions on Pattern Analysis and Machine Intelligence. 1999;21:476-480.
16. Halir R, Flusser J. Numerically stable direct least squares fitting of ellipses. Wscg '98, Vol 1. 1998;125-132.
17. Eijsbouts SC, Houben RP, Blaauw Y, Schotten U, Allessie MA. Synergistic action of atrial dilation and sodium channel blockade on conduction in rabbit atria. J Cardiovasc Electrophysiol. 2004;15:1453-1461.
18. de Groot NMS, Shah D, Boyle PM, Anter E, Clifford GD, Deisenhofer I, Deneke T, van Dessel P, Doessel O, Dilaveris P, et al. Critical appraisal of technologies to assess electrical activity during atrial fibrillation: a position paper from the European Heart Rhythm Association and European Society of Cardiology Working Group on eCardiology in collaboration with the Heart Rhythm Society, Asia Pacific Heart Rhythm Society, Latin American Heart Rhythm Society and Computing in Cardiology. Europace. 2021.
19. Roney CH, Cantwell CD, Bayer JD, Qureshi NA, Lim PB, Tweedy JH, Kanagaratnam P, Peters NS, Vigmond EJ, Ng FS. Spatial Resolution Requirements for Accurate Identification of Drivers of Atrial Fibrillation. Circ Arrhythm Electrophysiol. 2017;10:e004899.
20. Maesen B, Zeemering S, Afonso C, Eckstein J, Burton RA, van Hunnik A, Stuckey DJ, Tyler D, Maessen J, Grau V, et al. Rearrangement of atrial bundle architecture and consequent changes in anisotropy of conduction constitute the 3-dimensional substrate for atrial fibrillation. Circ Arrhythm Electrophysiol. 2013;6:967-975.
21. Houben RP, Allessie MA. Processing of intracardiac electrograms in atrial fibrillation. Diagnosis of electropathological substrate of AF. IEEE Eng Med Biol Mag. 2006;25:40-51.
22. Spach MS, Miller WT, 3rd, Dolber PC, Kootsey JM, Sommer JR, Mosher CE, Jr. The functional role of structural complexities in the propagation of depolarization in the atrium of the dog. Cardiac conduction disturbances due to discontinuities of effective axial resistivity. Circ Res. 1982;50:175-191.
23. Spach MS, Boineau JP. Microfibrosis produces electrical load variations due to loss of side-to-side cell connections: a major mechanism of structural heart disease arrhythmias. Pacing Clin Electrophysiol. 1997;20:397-413.
24. Gaspo R, Bosch RF, Bou-Abboud E, Nattel S. Tachycardia-induced changes in Na+ current in a chronic dog model of atrial fibrillation. Circ Res. 1997;81:1045-1052.
25. Gaspo R, Bosch RF, Talajic M, Nattel S. Functional mechanisms underlying tachycardia-induced sustained atrial fibrillation in a chronic dog model. Circulation. 1997;96:4027-4035.
26. Fareh S, Villemaire C, Nattel S. Importance of refractoriness heterogeneity in the enhanced vulnerability to atrial fibrillation induction caused by tachycardia-induced atrial electrical remodeling. Circulation. 1998;98:2202-2209.
27. Eckstein J, Zeemering S, Linz D, Maesen B, Verheule S, van Hunnik A, Crijns H, Allessie MA, Schotten U. Transmural conduction is the predominant mechanism of breakthrough during atrial fibrillation: evidence from

simultaneous endo-epicardial high-density activation mapping. Circ Arrhythm Electrophysiol. 2013;6:334-341.

28. Verheule S, Tuyls E, van Hunnik A, Kuiper M, Schotten U, Allessie M. Fibrillatory conduction in the atrial free walls of goats in persistent and permanent atrial fibrillation. Circ Arrhythm Electrophysiol. 2010;3:590-599.

29. Spach MS. Anisotropy of cardiac tissue: a major determinant of conduction? J Cardiovasc Electrophysiol. 1999;10:887-890.

30. Spach MS, Heidlage JF, Dolber PC, Barr RC. Changes in anisotropic conduction caused by remodeling cell size and the cellular distribution of gap junctions and Na(+) channels. J Electrocardiol. 2001;34 Suppl:69-76.

31. Wong CX, John B, Brooks AG, Chandy ST, Kuklik P, Lau DH, Sullivan T, Roberts-Thomson KC, Sanders P. Direction-dependent conduction abnormalities in the chronically stretched atria. Europace. 2012;14:954-961.

32. Krul SP, Berger WR, Smit NW, van Amersfoorth SC, Driessen AH, van Boven WJ, Fiolet JW, van Ginneken AC, van der Wal AC, de Bakker JM, et al. Atrial fibrosis and conduction slowing in the left atrial appendage of patients undergoing thoracoscopic surgical pulmonary vein isolation for atrial fibrillation. Circ Arrhythm Electrophysiol. 2015;8:288-295.

33. Allessie M, Ausma J, Schotten U. Electrical, contractile and structural remodeling during atrial fibrillation. Cardiovasc Res. 2002;54:230-246.

34. Ausma J, Wijffels M, Thone F, Wouters L, Allessie M, Borgers M. Structural changes of atrial myocardium due to sustained atrial fibrillation in the goat. Circulation. 1997;96:3157-3163.

26
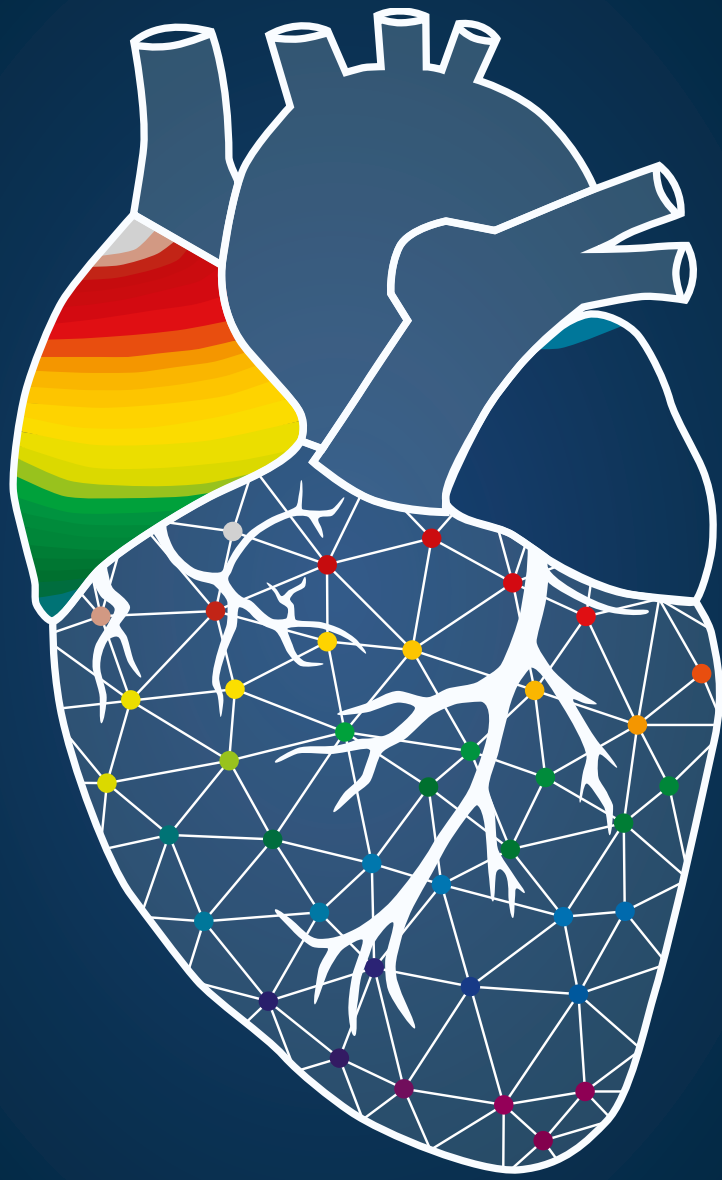
PART III

POST-OPERATIVE ATRIAL FIBRILLATION
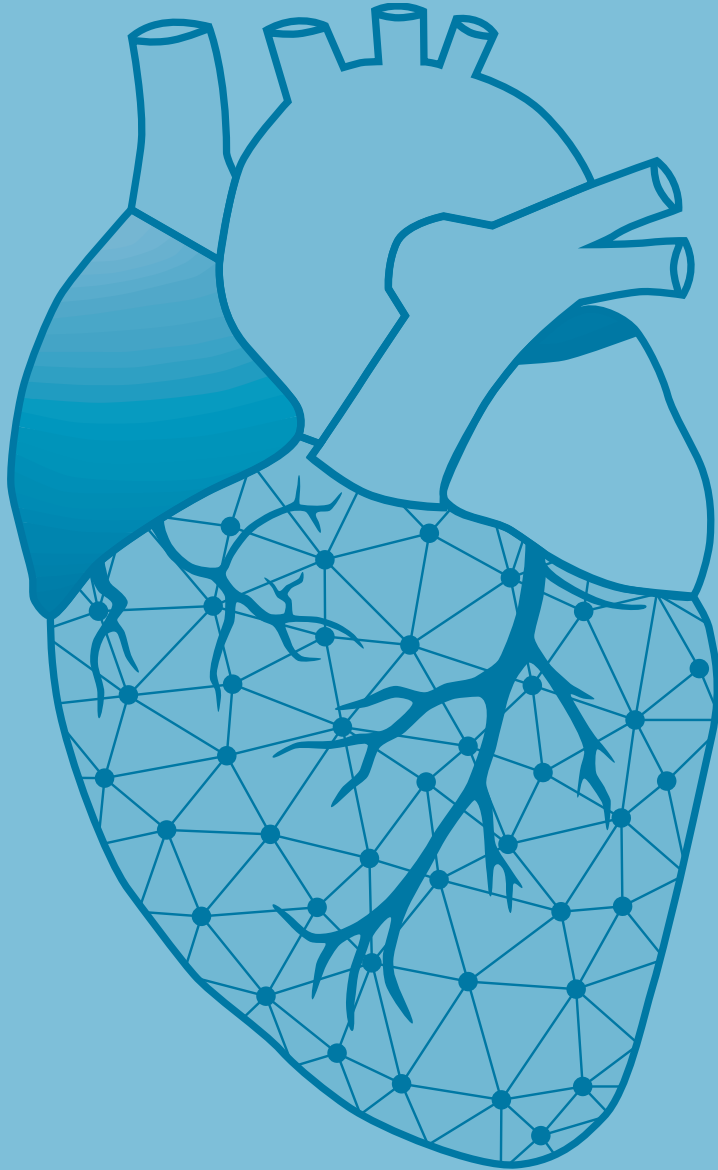
Chapter 27

Novel insights in pathophysiology of post-operative atrial fibrillation

Rohit K. Kharbanda

Mathijs S. van Schie

Yannick J.H.J. Taverne

Ad J.J.C. Bogers

Natasja M.S. de Groot

Abstract

Objectives: Atrial extrasystoles (AES) are usually benign, however they can also trigger atrial fibrillation (AF). It is most likely that if AES provoke a larger amount of conduction disorders and a higher degree of endo-epicardial asynchrony (EEA), the risk of post-operative AF increases. To test this hypothesis, we investigated the effect of programmed AES on endo-epicardial conduction and post-operative AF.

Methods: Twelve patients (58% male, age 68±7 years) underwent simultaneous endo-epicardial mapping (256 electrodes) of the right atrium during sinus rhythm and programmed AES provoked from the right atrial free wall. Areas of conduction block were defined as conduction delays of ≥12 ms and EEA as activation time differences of exact opposite electrodes of ≥15 ms.

Results: Endo-epicardial mapping data of all programmed AES were analyzed and compared with sinus rhythm (median preceding cycle length: 531 [345–787] ms and median sinus rhythm CL: 843 [701–992] ms). All programmed AES were aberrant (severe, moderate and mildly aberrant, respectively n=6, 3 and 3) and had a mean prematurity index of 50.1±11.9%. The amount of EEA (1.0 [1.0–2.0] % vs. 6.7 [2.7–16.9] %, p=0.006) and conduction block (1.4 [0.6–2.6] % vs. 8.5 [4.2–10.4] %, p=0.005) both increased during programmed AES. Interestingly, conduction block during programmed AES was more severe in patients (n=4, 33.3%) who developed post-operative AF (5.1 [2.9–8.8] % vs. 11.3 [10.1–12.1] %, p=0.004).

Conclusion: Atrial conduction disorders and EEA which play an important role in arrhythmogenesis, are enhanced during programmed AES compared to sinus rhythm. The findings of this pilot study provide a possible explanation for enhanced vulnerability for post-operative AES to induce post-operative AF in patients after cardiac surgery.

Journal site &
supplementary material

Introduction

It is well known that post-operative atrial fibrillation (AF) is the most common complication following cardiac surgery and is associated with a prolonged hospital stay and increased risk of other complications such as hemodynamic instability and thrombo-embolic events.[1] The underlying mechanism of post-operative AF is considered to be a multifactorial combination of pre-existing- (e.g., age and cardiovascular risk factors), intra-operative (e.g., type of surgery), and post-operative factors such as inflammation and enhanced sympathetic activity. The inflammatory response and increased sympathetic activity associated with cardiopulmonary bypass during cardiac surgery, enhances automaticity and may provoke atrial extrasystoles (AES).[2] As shown in several studies, in the vast majority of the patients, post-operative AF episodes are preceded by AES.[3-5] Mapping studies have shown that AES enhance conduction disorders and endo-epicardial asynchrony (EEA) which play an important role in the pathophysiology of AF.[6,7] In these mapping studies, only spontaneous AES were investigated but the origin of the AES could not be retrieved.

Already more than two decades ago, Papageorgiou et al.[8] demonstrated that high right atrial (RA) stimulation provoked more conduction disorders compared to stimulation from the coronary sinus. The authors postulated that the junctional area of the anisotropic crista terminalis and ramification of the pectinate muscles favors non-uniform slow atrial conduction and therefore may explain their observations.[8,9] It is most likely that if AES provoke a larger amount of conduction disorders and a higher degree of EEA, the risk of post-operative AF increases. In this pilot study, to test this hypothesis, we investigated the effect of programmed high RA stimulation, thereby mimicking the impact of spontaneous AES, on endo- and epicardial conduction and post-operative AF.

Methods

Aim

We aimed to 1) unravel the effect of programmed AES on endo-epicardial conduction in the right atrial wall and to 2) correlate this mapping data with the incidence of post-operative AF. This pilot trial is undertaken to provide sufficient assurance to enable a larger trial to further investigate our hypothesis.

Study population

Simultaneous endo-epicardial mapping was performed in patients undergoing elective primary open-heart surgery in the Erasmus Medical Center Rotterdam. Patients with hemodynamic instability, atrial pacing, previous cardiac surgery or severely impaired left ventricular function (ejection fraction <30%) were excluded. Patients underwent either coronary artery bypass surgery (CABG), valve surgery or a combination of both. This pilot study was approved by the institutional medical ethical committee (MEC2015-373) and written informed consent was obtained from all participants. Patient characteristics were obtained from electronic medical files. The study was carried out according to the principles of the Declaration of Helsinki.

Simultaneous endo-epicardial mapping of the right atrium

Simultaneous endo-epicardial high-density and resolution mapping of the RA was performed prior to commencement of extra-corporal circulation, as previously described in detail.[10] Two multi-electrode arrays, each containing 128 electrodes with a diameter of
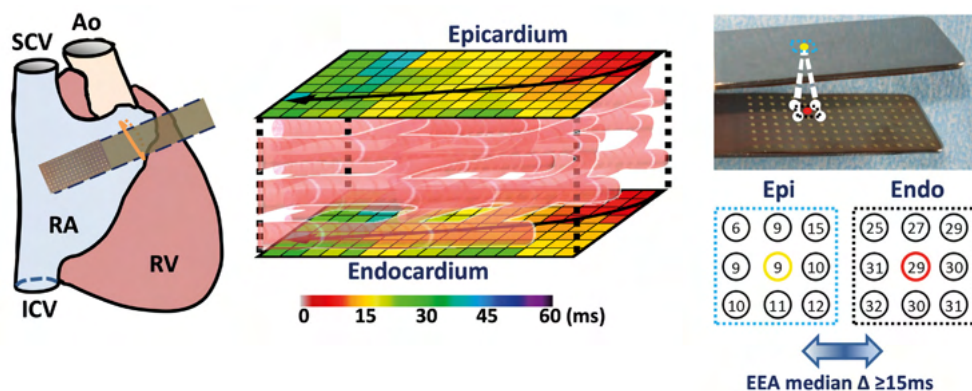
27

Figure 1 – Endo-epicardial mapping of the right atrium. Simultaneous endo-epicardial mapping of the RA was performed using two 128-electrode arrays secured exactly opposite of each other on two spatulas (left panel). Color-coded activation maps of the endo- and epicardium are shown in the middle panel. Black arrows display the main trajectories of the electrical wavefronts. In order to calculate EEA, for each electrode, the median time delay within the exact opposite electrode and its eight surrounding electrodes was selected. The longest time delay for every endo-epicardial electrode pair is then selected to express local degree of EEA, defined as transmural difference in electrical activation of ≥15ms between every endo-epicardial electrode pair. **Ao** = aorta; **EEA** = endo-epicardial asynchrony; **Epi** = epicardium; **Endo** = endocardium; **ICV** = inferior caval vein; **RA** = right atrium; **RV** = right ventricle; **SCV** = superior caval vein.

0.45 mm and with 2 mm interelectrode spacing, were attached on two bendable spatulas and positioned on the exact opposite side of each other. A temporary bipolar pacemaker wire was stitched to the free wall of the RA serving as a temporal reference electrode. The indifferent electrode was connected to a steel wire stitched in the subcutaneous tissue. The endocardial electrode array was introduced in the RA in the auricular purse string suture for the venous cannula. Simultaneous endo-epicardial mapping was performed of the mid RA, as depicted in the left panel of *Figure 1*. Simultaneous endo-epicardial mapping was performed during sinus rhythm (SR) followed by programmed electrical stimulation at the RA free wall. Recorded data included a surface electrocardiogram lead, calibration signal of 2 mV and 1000 ms, bipolar reference electrogram and 253 endo- and epicardial unipolar electrograms. Recordings were analogue-to-digital converted (16-bits), sampled with a rate of 1 kHz, amplified (gain 1000) and filtered (bandwidth 0.5–400 Hz).

Mapping data analysis

Custom-made software was used to analyze the mapping data as previously described in detail.[10] Color-coded activation maps of both the endo- and epicardial layer were constructed by annotating the steepest negative slope of atrial potentials recorded at every electrode.

Atrial conduction disorders

Consistent with prior mapping studies, areas of conduction delay (CD) and conduction block (CB) were defined as interelectrode differences in local activation times of respectively 7–11 ms and ≥12 ms.[10] These cutoff values correspond with effective conduction velocities of respectively 18 to 28 cm/s for CD and <18 cm/s for CB. Areas of uninterrupted CD and CB lines were defined as continuous CDCB lines. In addition, the median and maximal length of all CB and continuous CDCB lines were calculated.

Endo-epicardial asynchrony

As demonstrated in the middle and right panel of *Figure 1*, local endo-epicardial activation

time differences were determined by selecting the median of the time delays within the exact opposite electrode and its 8 surrounding electrodes. The longest time delay for every endo-epicardial electrode pair is then selected for the asynchrony map demonstrating local degree of EEA. Consistent with previous studies, EEA was defined as transmural difference in electrical activation of ≥15 ms between every endo-epicardial electrode pair.[10,11]

Classification of programmed atrial extrasystoles

Prematurity index of programmed AES was expressed as the ratio between the coupling interval of the programmed AES and the preceding SR cycle length. In general, we aimed to achieve a mean prematurity index of approximately 50%. Depending on the degree of shift in wavefront direction during programmed electrical stimulation compared to SR, patterns of activation during programmed AES were classified as mildly, moderately or severely aberrant (respectively 0-45°, 135–180° or 90° shift).[6,7]

Statistical analysis

Normally distributed continuous variables are expressed as mean ± standard deviation and skewed variables as median [25th–75th percentile]. Categorical data is presented as numbers and percentages and compared with the χ^2 test. Comparison of conduction disorders between the endo- and epicardium was performed with the Wilcoxon signed rank test. Association of clinical characteristics and electrophysiological parameters were analyzed with the Wilcoxon rank-sum test. Statistical analyses were performed using IBM SPSS Statistics version 21 (IBM Corp, Armonk, NY) and a *p*-value of <0.05 was considered statistically significant.

Table 1 – Patient characteristics.

Number of patients	12
Age (y)	68±7 (51, 78)
Male	7 (58.3)
Underlying heart disease	
• IHD	6 (50)
• VHD	4 (33.3)
• I/VHD	1 (8.3)
• Lone AF	1 (8.3)
Surgical procedure	
• CABG	6 (50)
• CABG + MVR	1 (8.3)
• AVR	2 (16.6)
• AVR + MVR	1 (8.3)
• AVR + MVR + TVR	1 (8.3)
• MAZE IV	1 (8.3)
History of AF	
• Paroxysmal	4 (33.3)
Cardiovascular risk factors	
• BMI (kg/m^2)	28.6±3.8 (23.7, 36.3)
• Hypertension	8 (66.7)
• Dyslipidemia	4 (33.3)
• Diabetes mellitus	4 (33.3)
Left ventricular function	
• Normal	7 (58.3)
• Mild/moderate dysfunction	5 (41.7)

Values are presented as N (%) or mean ± standard deviation (min,max). **AF** = atrial fibrillation; **AVD** = aortic valve disease; **AVR** = aortic valve repair; **BMI** = body mass index; **CABG** = coronary artery bypass grafting; **IHD** = ischemic heart disease; **I/VHD** = ischemic and valvular heart disease; **MVR** = mitral valve repair; **TVR** = tricuspid valve repair.

27

Table 2 – Characteristics of conduction disorders during sinus rhythm and programmed AES.

	SR	P-AES	*p*-value
% CB	1.4 [0.6–2.6]	8.5 [4.2–10.4]	0.005
Length CB lines	4 [4–6]	4.5 [4–6]	0.570
Max length CB lines	10 [6.5–16.5]	21 [15–25]	0.026
% Continuous CDCB	1.9 [0.9–4.1]	10.7 [5.7–15.1]	0.004
Length continuous CDCB	8 [6.5–12]	11 [8.3–20]	0.239
Maximal length continuous CDCB	10 [11–29]	28 [16.5–35.5]	0.196
Maximal conduction time	19.5 [15–29.8]	29.5 [23–37.8]	0.059
% EEA	1 [1–2]	6.7 [2.7–16.9]	0.006
Median endo-epicardial delay	16.5 [0–19]	20 [16.3–20.8]	0.050
Maximal endo-epicardial delay	18.3 [0–25.8]	24 [19.5–33.9]	0.036

Length of lines is expressed in millimeters and conduction time in milliseconds. **CB** = conduction block; **CDCB** = conduction delay-conduction block; **EEA** = endo-epicardial asynchrony; **P-AES** = programmed atrial extrasystoles; **SR** = sinus rhythm.

Results

Study population

Baseline characteristics of the 12 enrolled patients (68±7 years, 7 male) are summarized in *Table 1*. Half of the patients had ischemic heart disease (n=6) and 4 (33.3%) had a history of paroxysmal AF. Seven patients underwent CABG (n=1, concomitant mitral valve repair), 4 patients underwent aortic valve replacement (n=1 concomitant mitral valve repair and n=1 concomitant mitral and tricuspid valve repair) and 1 patient underwent MAZE IV procedure. None of the patients had dilated RA and the majority had normal left ventricular function (n=7, 58.3%). Post-operative AF occurred in 4 patients (33.3%) of whom 2 with new-onset post-operative AF.
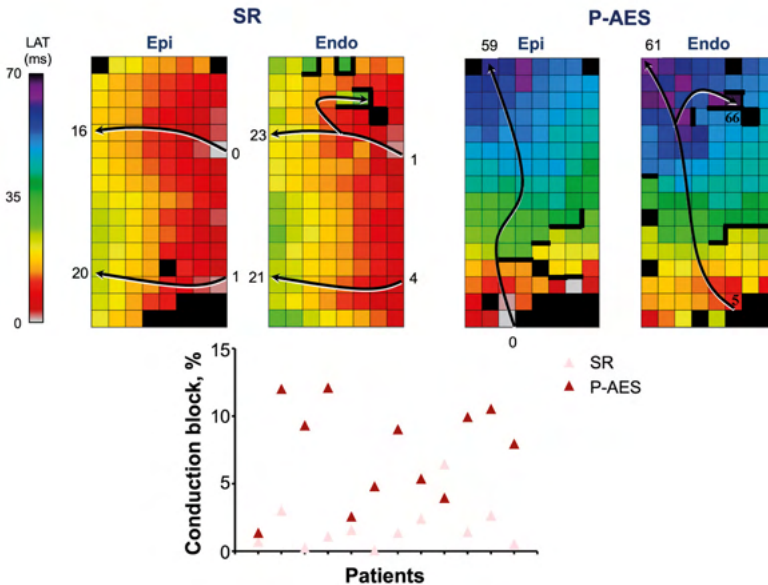
Figure 2 – Example of endo-epicardial activation maps. *Upper panel*: typical endo-epicardial activation maps of a SR beat (left) and P-AES (right) obtained from the same patient. Black arrows display the main trajectories of the electrical wavefronts and local activation times are depicted at its head and tail. Thick black lines indicate lines of conduction block. *Lower panel*: the effect of programmed right atrial stimulation on the amount of conduction block (y-axis) for each patient (x-axis) separately. Increase in total activation time and amount of conduction block is observed during P-AES compared to SR. **Epi** = epicardium; **Endo** = endocardium; **LAT** = local activation times; **P-AES** = programmed atrial extrasystoles; **SR** = sinus rhythm.
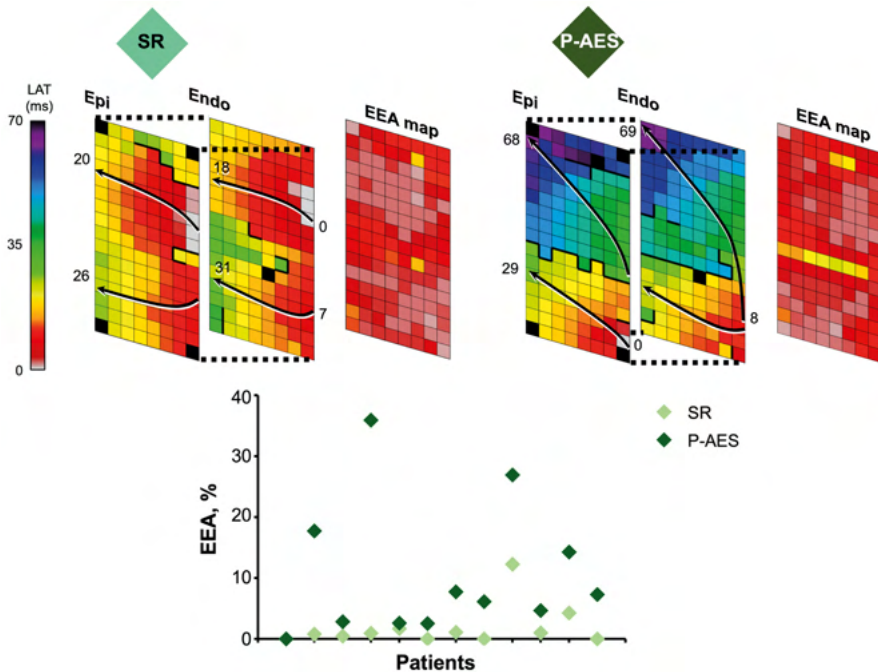
Figure 3 – Endo-epicardial activation and asynchrony maps. *Upper panel*: Endo-epicardial activation maps and corresponding EEA maps of one single SR beat (left) and P-AES (right) obtained from the same patient. Black arrows display the main trajectories of the electrical wavefronts and local activation times are depicted at its head and tail. Thick black lines indicate lines of conduction block. *Lower panel*: effect of programmed right atrial stimulation on the amount of EEA for each patient separately. An increase in conduction block and EEA is observed during P-AES compared to SR. **EEA** = endo-epicardial asynchrony; **Epi** = epicardium; **Endo** = endocardium; **LAT** = local activation time; **P-AES** = programmed atrial extrasystoles; SR = sinus rhythm.

Characteristics of programmed atrial extrasystoles

All programmed AES were aberrant (6 severely, 3 moderately and 3 mildly aberrant) and had a mean prematurity index of 50.1±11.9%. The preceding median coupling interval and median cycle length during SR recording were respectively 531 [345–787] ms and 843 [701–992] ms.

Endo- and epicardial conduction disorders

Table 2 summarizes the amount and extensiveness of conduction disorders during both SR and programmed AES. During SR, the total amount of CB and continuous CDCB observed in both the endo- and epicardium together was 1.4 [0.6–2.6] % and 1.9 [0.9–4.1] % respectively. This resulted in a median length of 4 [4–6] mm for CB and 8 [6.5–12] mm for continuous CDCB. There were no differences observed in amount and extensiveness of conduction disorders between the endo- and epicardial layer separately during SR (*Supplementary Table 1*, all p>0.156).

The upper panel of *Figure 2* shows typical endo-epicardial activation maps of one single SR beat and programmed AES obtained from the same patient. A substantial increase in CB, indicated by thick black lines, is demonstrated during programmed AES compared to SR. The lower panel of *Figure 2* shows the effect of programmed atrial stimulation on the amount of CB for each patient separately. During programmed AES, the total amount of CB and continuous CDCB in both layers together significantly increased from 1.4 [0.6–2.6] %

27

Table 3 – Differences in characteristics of programmed AES between patients with and without POAF.

	No POAF (n=8)	POAF (n=4)	*p*-value
% CB	5.1 [2.9–8.8]	11.3 [10.1–12.1]	0.004
Length CB lines	4 [2.5–5.5]	5.5 [5–7.5]	0.073
Max length CB lines	21 [9.5–22]	22 [18–33.5]	0.368
% Continuous CDCB	6.7 [5.2–11.6]	16 [14.1–18.5]	0.004
Length continuous CDCB	9.5 [8–11]	22 [15.3–23.5]	0.008
Maximal length continuous CDCB	21 [14.5–31.5]	42 [28.5–57]	0.028
Maximal conduction time	24.5 [18.5–29.8]	38.5 [37.3–47.3]	0.004
% EEA	4.5 [2.6–7.6]	16.0 [7.1–31.4]	0.109
Median endo-epicardial delay	17.3 [15.6–20]	22 [20–24.8]	0.048
Maximal endo-epicardial delay	22 [16.8–24]	36 [27–42]	0.016

Length of lines is expressed in millimeters and conduction time in milliseconds. **CB** = conduction block; **CDCB** = conduction delay-conduction block; **EEA** = endo-epicardial asynchrony; **POAF** = post-operative atrial fibrillation.

to 8.5 [4.2–10.4] % and from 1.9 [0.9–4.1] % to 10.7 [5.7–15.1] % respectively (both p≤0.005). Characteristics of conduction disorders during programmed AES did not differ between the endo- and epicardial layer separately (*Supplementary Table 1*, all p>0.167), except for a higher maximal conduction time at the endocardium (29.5 [18.5–37.5] ms vs. 23 [16.3–23] ms, p=0.033).

Endo-epicardial asynchrony

In the upper panel of *Figure 3*, endo-epicardial activations maps and corresponding EEA maps demonstrate the incremental effect of programmed AES on electrical asynchrony between both atrial layers. In the lower panel of *Figure 3*, differences in amount of EEA during SR (light green) and programmed AES (dark green) are shown for each patient separately. Overall, programmed AES provoked a significant increase in EEA from 1 [1–2] % during SR to 6.7 [2.7–16.9] % during programmed AES (p=0.006). The severity of EEA during programmed AES, expressed in median and maximal endo-epicardial delay, also increased from 16.5 to 20 ms (p=0.05) and 18.3 to 24 ms (p=0.036) respectively.

Post-operative atrial fibrillation

Differences in characteristics of programmed AES between patients with and without post-operative AF are summarized in *Table 3*. Programmed AES caused significant more conduction disorders and EEA in patients who developed post-operative AF compared to patients without post-operative AF. Not only the prevalence of CB (5.1 [2.9–8.8] % vs. 11.3 [10.1–12.1] %, p=0.004) and continuous CDCB (6.7 [5.2–11.6] % vs. 16 [14.1–18.5] %, p=0.004) was significantly higher in post-operative AF patients, but also the length of continuous CDCB lines (9.5 [8–11] mm vs. 22 [15.3–23.5] mm, p=0.008).

Despite the clinically relevant EEA provoked by programmed AES in patients who encountered post-operative AF (4.5% vs. 16%), it did not reach statistical significance (p=0.109). Median and maximal endo-epicardial delay measured between both atrial layers, however, was significantly higher in patients with post-operative AF (respectively, p=0.048 and p=0.016). Cardiopulmonary bypass- and aortic cross clamp time were similar between both groups (both p>0.109).

Discussion

Simultaneous endo-epicardial mapping of the RA during SR and programmed RA stimulation revealed that programmed AES originating from the free wall of the RA 1) provoked a substantial increase in endo- and epicardial conduction disorders, 2) enhanced electrical

asynchrony between both layers up to 44 ms and covering 36% of the mapping area and 3) provoked more conduction disorders and EEA in patients who developed post-operative AF compared to patients who remained post-operatively in SR. The findings of this pilot study provide a possible explanation for enhanced vulnerability for post-operative AES to induce post-operative AF in patients after cardiac surgery.

Effect of (programmed) right atrial extrasystoles on endo-epicardial conduction

Previous intra-operative mapping studies examined the effect of spontaneous AES on atrial conduction and showed an increase in epicardial conduction disorders, especially during aberrant AES.[6] Simultaneous endo-epicardial mapping of the RA during spontaneous AES revealed that this increase in conduction disorders may be unequally expressed between the endo- and epicardium giving rise to EEA.[7] An important limitation of these studies is lack of information on the origin of the AES. In order to overcome this limitation, in the present study, programmed premature atrial stimulation was performed at the RA free wall as we assume that excessive surgical manipulation in combination with surgical incisions in the RA appendage and purse string suture induced local ischemia, are likely to provoke AES originating from the RA free wall in patients after cardiac surgery. In addition, enhanced anisotropic properties of the RA tissue may reinforce conduction disorders and EEA during AES thereby increasing the vulnerability of the atria for arrhythmias. AES that provoke a larger amount of conduction disorders and a higher degree of EEA are more likely to induce post-operative AF episodes, which is supported by the present pilot study showing more pronounced conduction disorders during programmed AES in patients who developed post-operative AF compared to patients who remained in SR.

It is generally assumed that the complex architecture and anatomy of both atria play an important role in arrhythmogenesis. Fiber orientation and atrial wall thickness may vary between different atrial regions. Even at one specific site, differences in fiber orientation between the endo- and epicardium may be observed. Any premature AES originating from an anisotropic region may provoke significant conduction disorders that may affect the endo- and epicardium unequally. This may provoke or aggravate EEA in the atrial wall thereby possibly initiating transmural reentry. Spach et al.[12] demonstrated that programmed premature atrial stimulation in isolated anisotropic muscle fibers resulted in dissociated conduction that causes unidirectional CB, thereby providing a potential substrate for reentry.

27

Schuessler et al.[13] have investigated endo-epicardial conduction at the RA appendage of canines during SR and programmed premature atrial stimulation. Endo-epicardial asynchrony was higher during programmed AES with a higher prematurity index and increased mostly with prematurely aberrant AES, which is in line with previous studies from our group.[6,7] Premature AES provoked EEA up to 30 ms. Subsequently, they induced tachyarrhythmia by an extra-stimulus during intravenous acetylcholine administration. A 3-dimensional pathway using a free-running muscle bundle between the endo- and epicardium was part of the induced reentry circuit with a cycle length as short as approximately 60 ms. Recently, endo-epicardial optical mapping combined with high-resolution 3D gadolinium-enhanced magnetic resonance imaging (GE-MRI, 80 μm^3 resolution) demonstrated similar reentry loops using transmural pectinate muscles in ex-vivo human RA.[14] These findings provide a possible explanation for the underlying mechanism of post-operative AES inducing episodes of post-operative AF.

Factors contributing to enhanced arrhythmogenicity of AES

The arrhythmogenicity of an AES is determined by AES-related characteristics (e.g.,

prematurity), anatomical features (e.g., 3-dimensional fiber orientation and fibrosis) and alterations in the cardiac autonomic tone (e.g., enhanced sympathetic or parasympathetic activity).

Refractory periods of adjacent cardiomyocytes may vary and are influenced by several factors, such as heart rate and autonomic tone. When the prematurity of AES increases, it is more likely that the electrical wavefront encounters areas with differences in excitability of atrial tissue which may promote development of AF.[12] This effect may be enhanced by changes in autonomic tone. As the cardiac autonomic nervous system is heterogeneously distributed between both atria, changes in sympathetic and parasympathetic tone may enhance dispersion of atrial refractoriness and promote differences in local conduction velocities. It is generally believed that, enhanced sympathetic tone increases calcium loading, thereby enhancing triggered activity, while enhanced parasympathetic tone slows conduction velocity, shortens the refractory period and increases dispersion of atrial refractoriness, thereby facilitating reentry.[15]

Conduction velocity is also dependent on the 3-dimensional anatomical features of the area where the AES originates.[16] To initiate an endo-epicardial reentry circuit at an area with significant EEA, transmural muscle fibers connecting the endo- and epicardium are a prerequisite. This 3-dimensional architecture can also be disrupted by structural remodeling caused by ageing, coronary- or valvular heart disease or tachyarrhythmia-induced electrical remodeling.[17-19] Furthermore, when a small atrial muscle bundle has to excite a relatively large heterogeneous area, sink-to-source mismatch may occur resulting in slowing of atrial conduction and breaking of wavefronts, which may initiate reentry.[16]

Premature atrial extrasystoles after cardiac surgery, common or not?

The relation between frequent AES and higher incidence of AF has been demonstrated in different populations.[20,21] There are only a few studies investigating the role of premature AES in initiation of post-operative AF after cardiac surgery. After Frost et al.[22] had demonstrated that premature AES could initiate post-operative AF, several studies demonstrated that the incidence of post-operative AF could be reduced by atrial overdrive pacing thereby suppressing atrial premature depolarizations.[3,23-26] Blommaert et al.[3] introduced an algorithm for dynamic overdrive pacing which reacts to premature AES by increasing its frequency. A significant reduction in the incidence of post-operative AF was observed in the pacing group compared to controls (10% vs. 27% respectively, p=0.036). The abovementioned studies evaluated the performance of atrial overdrive pacing suppressing premature AES to prevent post-operative AF. However, there are only a few studies investigating the incidence of premature AES in relation to post-operative AF.[5,27-29] Jidéus et al.[28] demonstrated that in patients who developed post-operative AF after CABG, it was initiated by premature AES in 81% of the patients.[5] Previously, the same research group already demonstrated that a higher pre-operative burden of premature AES is associated with a higher risk of post-operative AF. Recently, Hashimoto et al.[27] observed significantly more premature AES/24 hours in patients who developed new-onset post-operative AF compared to patients who remained in SR (4,128±7,186 vs. 69±221, p<0.001) after off-pump CABG. In line with the findings of Jidéus et al.[28] and Frost et al.[29], frequent premature AES (>47 per 24 hour) appeared to be a predictor for post-operative AF. Yaksh et al.[30] were the first to determine whether post-operative AES burden is associated with post-operative AF using post-operative telemetry data of 29 post-operative AF patients and controls. Post-operative AF patients showed a higher burden of premature AES compared to controls (0.9% vs. 0.2%, p=0.001). Moreover, AES triggering AF episodes were more often premature (p<0.001).

Limitations

This proof of concept study is mainly limited by the low sample size and the results should therefore be interpreted with caution. Future larger studies are required to substantiate our findings. We could not address whether AES also enhance electrical disturbances in the left atrium. Due to safety reasons, simultaneous endo-epicardial mapping of the left atrium can only be performed under specific circumstances and was therefore not performed in the present pilot study. Moreover, to determine the effect of AES on endo-epicardial conduction in both atria, total simultaneous endo-epicardial mapping should be performed which is technically impossible. Future studies focusing on both atria are required to further unravel the arrhythmogenic effects of AES originating from different sites.

Conclusion

The exact mechanistic role of AES in initiating post-operative AF is unknown. In the present pilot study, premature programmed AES at the RA aggravated endo-epicardial conduction disorders and electrical asynchrony between both layers occurring up to 44 ms and covering 36% of the mapping area. Enhanced conduction disorders and EEA provoked by premature AES are potential mechanisms for intramural reentry which may result in post-operative AF. Larger studies are needed to assess whether intra-operative cardiac mapping including programmed atrial stimulation may predict development of post-operative AF.

27

References

1. Greenberg JW, Lancaster TS, Schuessler RB, Melby SJ. Postoperative atrial fibrillation following cardiac surgery: a persistent complication. Eur J Cardiothorac Surg. 2017;52:665-672.
2. Dobrev D, Aguilar M, Heijman J, Guichard JB, Nattel S. Postoperative atrial fibrillation: mechanisms, manifestations and management. Nat Rev Cardiol. 2019;16:417-436.
3. Blommaert D, Gonzalez M, Mucumbitsi J, Gurne O, Evrard P, Buche M, Louagie Y, Eucher P, Jamart J, Installe E, et al. Effective prevention of atrial fibrillation by continuous atrial overdrive pacing after coronary artery bypass surgery. J Am Coll Cardiol. 2000;35:1411-1415.
4. Taylor AD, Groen JG, Thorn SL, Lewis CT, Marshall AJ. New insights into onset mechanisms of atrial fibrillation and flutter after coronary artery bypass graft surgery. Heart. 2002;88:499-504.
5. Jideus L, Kesek M, Joachimsson PO, Ericson M, Nilsson L, Blomstrom-Lundqvist C. The role of premature atrial contractions as the main triggers of postoperative atrial fibrillation. J Electrocardiol. 2006;39:48-54.
6. Teuwen CP, Kik C, van der Does L, Lanters EAH, Knops P, Mouws E, Bogers A, de Groot NMS. Quantification of the Arrhythmogenic Effects of Spontaneous Atrial Extrasystole Using High-Resolution Epicardial Mapping. Circ Arrhythm Electrophysiol. 2018;11.
7. van der Does L, Kharbanda RK, Teuwen CP, Knops P, Kik C, Bogers A, de Groot NMS. Atrial Ectopy Increases Asynchronous Activation of the Endo- and Epicardium at the Right Atrium. J Clin Med. 2020;9.
8. Papageorgiou P, Monahan K, Boyle NG, Seifert MJ, Beswick P, Zebede J, Epstein LM, Josephson ME. Site-dependent intra-atrial conduction delay. Relationship to initiation of atrial fibrillation. Circulation. 1996;94:384-389.
9. Olgin JE, Kalman JM, Fitzpatrick AP, Lesh MD. Role of right atrial endocardial structures as barriers to conduction during human type I atrial flutter. Activation and entrainment mapping guided by intracardiac echocardiography. Circulation. 1995;92:1839-1848.
10. Kharbanda RK, Knops P, van der Does L, Kik C, Taverne Y, Roos-Serote MC, Heida A, Oei FBS, Bogers A, de Groot NMS. Simultaneous Endo-Epicardial Mapping of the Human Right Atrium: Unraveling Atrial Excitation. J Am Heart Assoc. 2020;9:e017069.
11. de Groot N, van der Does L, Yaksh A, Lanters E, Teuwen C, Knops P, van de Woestijne P, Bekkers J, Kik C, Bogers A, et al. Direct Proof of Endo-Epicardial Asynchrony of the Atrial Wall During Atrial Fibrillation in Humans. Circ Arrhythm Electrophysiol. 2016;9.
12. Spach MS, Dolber PC, Heidlage JF. Interaction of inhomogeneities of repolarization with anisotropic propagation in dog atria. A mechanism for both preventing and initiating reentry. Circ Res. 1989;65:1612-1631.
13. Schuessler RB, Kawamoto T, Hand DE, Mitsuno M, Bromberg BI, Cox JL, Boineau JP. Simultaneous epicardial and endocardial activation sequence mapping in the isolated canine right atrium. Circulation. 1993;88:250-263.
14. Hansen BJ, Zhao J, Csepe TA, Moore BT, Li N, Jayne LA, Kalyanasundaram A, Lim P, Bratasz A, Powell KA, et al. Atrial fibrillation driven by micro-anatomic intramural re-entry revealed by simultaneous sub-epicardial and sub-endocardial optical mapping in explanted human hearts. Eur Heart J. 2015;36:2390-2401.
15. Stavrakis S, Nakagawa H, Po SS, Scherlag BJ, Lazzara R, Jackman WM. The role of the autonomic ganglia in atrial fibrillation. JACC Clin Electrophysiol. 2015;1:1-13.
16. Spach MS, Miller WT, 3rd, Dolber PC, Kootsey JM, Sommer JR, Mosher CE, Jr. The functional role of structural complexities in the propagation of depolarization in the atrium of the dog. Cardiac conduction disturbances due to discontinuities of effective axial resistivity. Circ Res. 1982;50:175-191.
17. Allessie M, Ausma J, Schotten U. Electrical, contractile and structural remodeling during atrial fibrillation. Cardiovasc Res. 2002;54:230-246.
18. Kawara T, Derksen R, de Groot JR, Coronel R, Tasseron S, Linnenbank AC, Hauer RN, Kirkels H, Janse MJ, de Bakker JM. Activation delay after premature stimulation in chronically diseased human myocardium relates to the architecture of interstitial fibrosis. Circulation. 2001;104:3069-3075.
19. Angel N, Li LI, Macleod RS, Marrouche N, Ranjan R, Dosdall DJ. Diverse Fibrosis Architecture and Premature Stimulation Facilitate Initiation of Reentrant Activity Following Chronic Atrial Fibrillation. J Cardiovasc Electrophysiol. 2015;26:1352-1360.
20. Teuwen CP, Korevaar TIM, Coolen RL, van der Wel T, Houck CA, Evertz R, Yaksh A, Roos-Hesselink JW, Bogers A, de Groot NMS. Frequent atrial extrasystolic beats predict atrial fibrillation in patients with congenital heart defects. Europace. 2018;20:25-32.
21. Chong BH, Pong V, Lam KF, Liu S, Zuo ML, Lau YF, Lau CP, Tse HF, Siu CW. Frequent premature atrial complexes predict new occurrence of atrial fibrillation and adverse cardiovascular events. Europace. 2012;14:942-947.
22. Frost L, Christiansen EH, Molgaard H, Jacobsen CJ, Allermand H, Thomsen PE. Premature atrial beat eliciting atrial fibrillation after coronary artery bypass grafting. J Electrocardiol. 1995;28:297-305.
23. Murgatroyd FD, Nitzsche R, Slade AK, Limousin M, Rosset N, Camm AJ, Ritter P. A new pacing algorithm for overdrive suppression of atrial fibrillation. Chorus Multicentre Study Group. Pacing Clin Electrophysiol. 1994;17:1966-1973.
24. Greenberg MD, Katz NM, Iuliano S, Tempesta BJ, Solomon AJ. Atrial pacing for the prevention of atrial fibrillation after cardiovascular surgery. J Am Coll Cardiol. 2000;35:1416-1422.
25. Takeda M, Furuse A, Kotsuka Y. Use of temporary atrial pacing in management of patients after cardiac surgery. Cardiovasc Surg. 1996;4:623-627.
26. Ramdat Misier A, Beukema WP, Oude Luttikhuis HA. Multisite or alternate site pacing for the prevention of atrial fibrillation. Am J Cardiol. 1999;83:237D-240D.
27. Hashimoto M, Yamauchi A, Inoue S. Premature atrial contraction as a predictor of postoperative atrial fibrillation. Asian Cardiovasc Thorac Ann. 2015;23:153-156.

28. Jideus L, Blomstrom P, Nilsson L, Stridsberg M, Hansell P, Blomstrom-Lundqvist C. Tachyarrhythmias and triggering factors for atrial fibrillation after coronary artery bypass operations. Ann Thorac Surg. 2000;69:1064-1069.
29. Frost L, Molgaard H, Christiansen EH, Jacobsen CJ, Allermand H, Thomsen PE. Low vagal tone and supraventricular ectopic activity predict atrial fibrillation and flutter after coronary artery bypass grafting. Eur Heart J. 1995;16:825-831.
30. Yaksh A, Kik C, Knops P, van Ettinger MJ, Bogers AJ, de Groot NM. Early, de novo atrial fibrillation after coronary artery bypass grafting: Facts and features. Am Heart J. 2017;184:62-70.

27
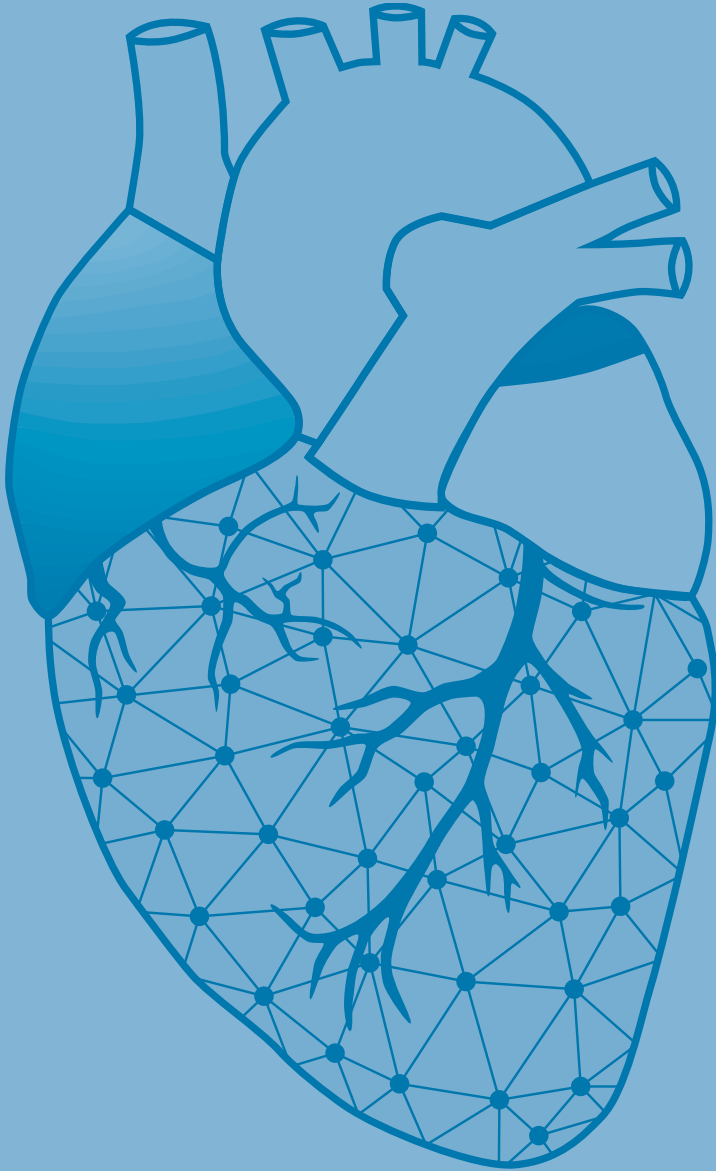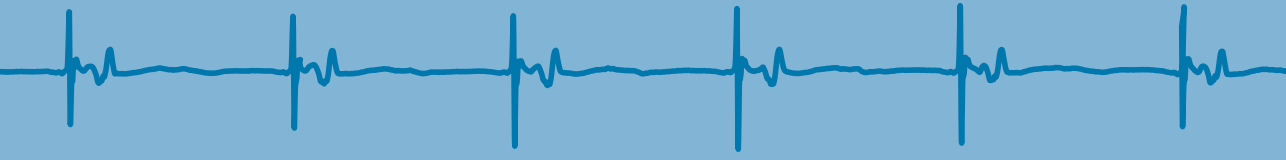
Chapter 28

Characterization of pre-existing arrhythmogenic substrate associated with de novo early and late post-operative atrial fibrillation

Mathijs S. van Schie

Danny Veen

Rohit K. Kharbanda

Annejet Heida

Roeliene Starreveld

Frank R.N. van Schaagen

Ad J.J.C. Bogers

Yannick J.H.J. Taverne

Natasja M.S. de Groot

Abstract

Background: Post-operative atrial fibrillation (PoAF) is the most common complication after cardiac surgery and may occur in patients with pre-existing arrhythmogenic substrate. Characterization of this substrate could aid in identifying patients at risk for PoAF. We therefore compared intra-atrial conduction parameters and electrogram morphology between patients without and with early- (≤5 days after surgery) and late- (up to 5 years) post-operative atrial fibrillation (PoAF).

Methods and Results: Epicardial mapping of the right and left atrium and Bachmann's bundle (BB) was performed during sinus rhythm (SR) in 263 patients (207 male, 67±11 years). Unipolar potentials were classified as single, short or long double and fractionated potentials. Unipolar voltage, fractionation delay (time difference between the first and last deflection), conduction velocity (CV) and conduction block (CB) prevalence were measured. Comparing patients without (N=166) and with PoAF (N=97), PoAF was associated with lower CV and more CB at BB. Unipolar voltages were lower and more low-voltage areas were found at the left and right atrium and BB in PoAF patients. These differences were more pronounced in patients with late-PoAF (6%), which could even occur up to 5 years after surgery. Although several electrophysiological parameters were related to PoAF, age was the only independent predictor.

Conclusions: Patients with de novo PoAF have more extensive arrhythmogenic substrate prior to cardiac surgery compared to those who remained in SR, which is even more pronounced in late-PoAF patients. Future studies should evaluate whether intra-operative electrophysiological examination enables identification of patients at risk for developing PoAF and hence (preventive) therapy.

Journal site &
supplementary material

Introduction

Post-operative atrial fibrillation (PoAF) is the most common complication encountered after cardiac surgery, with reported incidences ranging from 20 to 80% depending on the type of procedure.[1] PoAF especially occurs within the first four days after surgery, and is associated with an increased risk of mortality and morbidity, longer hospitalization and higher costs of post-operative care.[2-4] Although generally considered a transient and predominantly mild complication for most patients, early-PoAF (E-PoAF) still remains the leading cause of prolonged hospitalization and hospital readmission following cardiac surgery.[2,4,5] E-PoAF is also predictive of late-PoAF (L-PoAF), which in turn is associated with long-term mortality.[6]

Numerous risk factors predisposing to PoAF have been determined (i.e., older age, obesity, valvular and coronary artery disease), yet pathophysiological mechanisms underlying development of PoAF remain partially unclear.[7] It is generally considered that the transition from E-PoAF to L-PoAF progresses from a trigger-driven to a more substrate-driven disease.[8-10] Hence, L-PoAF is more likely to develop in patients with a more extensive pre-existing arrhythmogenic substrate, compared to patients who will only have E-PoAF.

Epicardial mapping during cardiac surgery provides a unique methodology to examine electrophysiological properties of both atria, including Bachmann's bundle (BB), on a high-resolution scale. A recent mapping study revealed a higher prevalence of longitudinal lines of conduction block (CB) in patients developing de novo PoAF.[8] However, no electrophysiological features other than CB were evaluated and the remainder of the atria were not examined. As also patients without (long) lines of CB developed PoAF as well, it could be suggested that not only areas of CB at BB are involved in development of PoAF. We therefore hypothesize that other atrial sites may contain more extensive areas of conduction disorders and thus play a role in the pathophysiology of PoAF. The goal of this study was therefore to 1) compare quantified features of intra-atrial conduction and electrogram morphology between patients without and with de novo PoAF at the entire atrial surface, and 2) to establish whether these quantified features are associated with development of L-PoAF within five years after cardiac surgery.

Methods

Study population

The study population consisted of 354 successive adult patients without a history of tachyarrhythmias undergoing elective open heart coronary artery bypass grafting (CABG), aortic or mitral valve surgery or a combination of valvular surgery and bypass grafting in the Erasmus Medical Center Rotterdam between February 2012 and July 2018. This study was approved by the institutional medical ethical committee (MEC2010-054/MEC2014-393).[11,12] Written informed consent was obtained from all patients and patient characteristics (e.g., age, medical history and cardiovascular risk factors) were obtained from the patient's medical record. The study population was classified into patients who developed de novo PoAF (PoAF group) and patients who remained in sinus rhythm (SR group). During a systematic follow-up period of five years, patients who developed L-PoAF were also identified. Only patients with complete five-year follow-up or patients who developed persistent AF were included for further analysis.

Mapping procedure

Epicardial high-resolution mapping was performed prior to commencement of extra-

28

corporal circulation, as previously described in detail.[8,13,14] A temporal bipolar epicardial pacemaker wire attached to the RA free wall served as a reference electrode and the indifferent electrode consisted of a steel wire fixed to subcutaneous tissue of the thoracic cavity.

Epicardial mapping was performed with a 128 or 192-electrode array (electrode diameter respectively 0.65 or 0.45 mm, interelectrode distances 2.0 mm). Mapping was conducted by shifting the electrode array along predefined areas of the right atrium (RA), BB, pulmonary vein area (PVA) and left atrium (LA) between anatomical borders in a systematic order, covering the entire atrial epicardial surface (*Supplementary Figure 1*). Omission of areas was avoided at the expense of possible small overlap between adjacent mapping sites. The RA was mapped from the cavo-tricuspid isthmus, shifting perpendicular to the caval veins towards the RA appendage; the PVA from the transverse sinus fold along the borders of the right and left pulmonary veins down towards the atrioventricular groove and the left atrioventricular groove from the lower border of the left inferior pulmonary vein towards the LA appendage. BB was mapped from the tip of the LA appendage across the roof of the LA, behind the aorta towards the superior cavo-atrial junction.

Five seconds of SR were recorded from every mapping site, including a surface ECG lead, a calibration signal of 2 mV and 1000 ms, a bipolar reference electrogram (EGM) and all unipolar epicardial EGMs. Data was stored on a hard disk after amplification (gain 1000), filtering (bandwidth 0.5–400 Hz), sampling (1 kHz) and analogue-to-digital conversion (16 bits).

Data analysis

Unipolar EGMs were semi-automatically analyzed using custom-made software, as previously described in detail.[15] EGMs with injury potentials, recording sites with ≥25% excluded or missing EGMs and atrial extrasystoles were excluded from analysis.

The steepest negative slope of an atrial potential was marked as the local activation time (LAT), provided that the amplitude of this deflection was at least two times the signal-to-noise ratio of the EGM. All annotations were manually checked by two independent investigators. As illustrated in *Supplementary Figure 1*, potentials were classified as single potentials (SP, one deflection), short double potentials (SDP, interval between deflections <15 ms), long double potentials (LDP, deflection interval ≥15 ms) or fractionated potentials (FP, ≥3 deflections).[16] Of each potential type, fractionation delay (defined as the time difference between the first and last deflection) was calculated. The potential amplitude was defined as the peak-to-peak voltage of the steepest deflection, the proportion of potentials with an amplitude below 1.0 mV was defined as low-voltage area (LVA).[17] Local effective conduction velocity (CV) was computed from LATs using discrete velocity vectors as previously described.[18] CB was defined as a difference in LAT between 2 adjacent electrodes of ≥12 ms, corresponding to an effective conduction velocity of <18 cm/s.[19,20]

Detection of post-operative atrial fibrillation

Cardiac rhythms of all patients were continuously recorded from the moment of arrival on the surgical ward to the end of the fifth post-operative day using bedside monitors (Draeger Infinity™). Automatic algorithms were used to detect E-PoAF episodes lasting >30 seconds. All episodes detected by the software were cross-checked by two blinded operators in order to eliminate potential false positive registrations induced by artefacts.

Table 1 – Patient characteristics (N=263).

	SR	PoAF	p-value	E-PoAF	L-PoAF	p-value
Patients	166 (63)	97 (37)	-	82 (85)	15 (15)	-
Male	132 (80)	75 (77)	0.755	64 (78)	11 (73)	0.740
Age (y)	65 [57–71]	69 [65–74]	<0.001	69 [65–73]	72 [62–76]	0.304
Underlying heart disease			0.040			0.171
· IHD	117 (71)	60 (62)	0.174	53 (65)	7 (47)	0.249
· VHD	32 (19)	16 (16)	0.623	14 (17)	2 (13)	0.720
· iVHD	17 (10)	21 (22)	0.017	15 (18)	6 (40)	0.086
Valvular heart disease			0.260			0.004
· AVD	35 (71)	22 (59)	0.759	21 (72)	1 (13)	0.178
· MVD	14 (29)	15 (41)	0.102	8 (28)	7 (88)	0.002
Cardiovascular risk factors						
· BMI (kg/m²)	26.8 [25.2–30.2]	26.9 [24.5–30.1]	0.389	26.5 [24.3–29.5]	29.8 [26.6–30.9]	0.019
· Hypertension	100 (60)	55 (57)	0.605	48 (59)	7 (47)	0.411
· Dyslipidemia	70 (42)	32 (33)	0.151	26 (32)	6 (40)	0.559
· Diabetes mellitus	53 (32)	22 (23)	0.121	18 (22)	4 (27)	0.740
Left atrial dilation (>45 mm)	25 (15)	19 (20)	0.393	12 (15)	7 (47)	0.009
Left ventricular function						
· Normal	134 (81)	72 (74)	0.220	60 (73)	12 (80)	0.753
· Mild dysfunction	27 (16)	19 (20)	0.505	16 (20)	3 (20)	0.965
· Moderate dysfunction	5 (3)	5 (5)	0.506	5 (6)	-	0.729
· Severe dysfunction	-	1 (1)	0.369	1 (1)	-	0.667
Antiarrhythmic drugs						
· Class I	-	-	-	-	-	-
· Class II	111 (67)	72 (74)	0.266	61 (74)	11 (73)	0.931
· Class III	-	1 (1)	0.444	1 (1)	-	0.444
· Class IV	7 (4)	4 (4)	0.971	4 (5)	-	0.867
· Digoxin	1 (1)	-	0.444	-	-	-
P-wave amplitude	0.10 [0.08–0.12]	0.10 [0.08–0.12]	0.056	0.10 [0.08–0.12]	0.08 [0.07–0.11]	0.275
P-wave duration	83 [70–93]	82 [70–101]	0.255	82 [70–100]	86 [72–105]	0.286

Values are presented as N (%), mean ± standard deviation (min–max) or median [interquartile ranges]. **AVD** = aortic valve disease; **BMI** = body mass index; **E/L-PoAF** = early/late post-operative atrial fibrillation; **IHD** = ischemic heart disease; **(i)VHD** = (ischemic and) valvular heart disease; **MVD** = mitral valve disease.

28

After the hospitalization period, patients were periodically seen at the outpatient clinic at 3 and 6 months, 1 year and yearly afterwards for a period of five years. Presence of L-PoAF was confirmed by a surface ECG or Holter.

Statistical analysis

All data were tested for normality. Normally distributed data are expressed as mean ± standard deviation and analyzed with a (paired) t-test or one-way ANOVA. Skewed data are expressed as median (25th–75th percentile) and analyzed with a Kruskal-Wallis test, Mann-Whitney U test or Wilcoxon signed-rank test. Categorical data are expressed as numbers and percentages, and analyzed with a χ^2 or Fisher exact test when appropriate. Distribution data was analyzed with a two-sample Kolmogorov-Smirnov test. As a result of the small group size of patients with PoAF, univariate analyses were performed to select the determinant of interest for multivariable analysis for the prediction of PoAF. Age, gender, underlying heart disease, BMI and LA dilation were included in the multivariable analysis. The association between the various voltage and conduction parameters and PoAF was investigated with logistic regression models. A p-value <0.05 was considered statistically significant. A Bonferroni correction was applied for comparison of the four atrial regions. A p-value of <0.0083 (0.05/6) was considered statistically significant.

Results

Study population

Of the 354 patients, 263 patients had complete five-year follow-up or developed persistent AF and were therefore included for further analysis. Clinical characteristics of this study population (N=263, 207 male (79%), age 64±11 years) are summarized in *Table 1*. Patients had either ischemic heart disease (IHD), valvular heart disease (VHD) or a combination of ischemic- and valvular heart disease (iVHD). The population of patients with (i)VHD was further categorized by the predominant valvular lesion and consisted of aortic valve disease or mitral valve disease. There were no differences in baseline parameters of E-PoAF incidence between the entire population and the selected patients.

Development of post-operative atrial fibrillation

Of the 263 patients, 97 (37%) developed de novo PoAF within the first days after surgery and 15 (6%) of them had AF recurrences during the follow-up period. All patients who developed
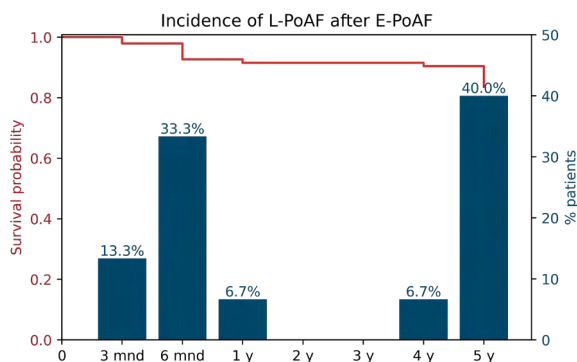
Figure 1 – Incidence of L-PoAF. Incidence of diagnosis of AF recurrence during a follow-up period of 5 years after cardiac surgery and de novo PoAF. The red line indicates a Kaplan-Meier curve and the blue bars indicate the percentage of patients diagnosed with L-PoAF (N=15). **L-PoAF** = late post-operative atrial fibrillation.
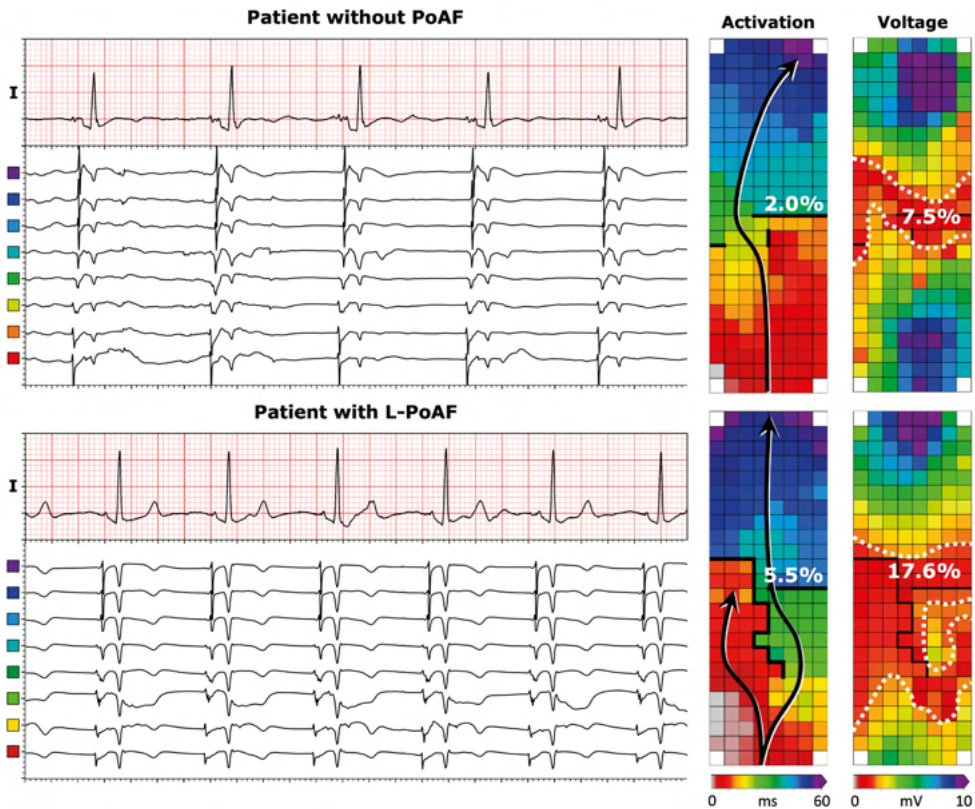
Figure 2 – Examples of activation and voltage maps. Intra-operative surface ECG leads I with examples of corresponding local EGMs (indicated by colors from activation map) of one patient who remained in SR (upper) and one patient with both E-PoAF and L-PoAF (lower) recorded at Bachmann's bundle. Examples of the corresponding activation and voltage maps of these recordings (right panel); conduction block (local difference in activation time ≥12 ms) is indicated by the thick black lines, and areas of low-voltage are highlighted by white dotted lines. **EGM** = electrogram; **ICV** = inferior caval vein; **L-PoAF** = late post-operative atrial fibrillation.

28

L-PoAF had episodes of E-PoAF. Therefore, patients with PoAF were further subdivided into an E-PoAF group (N=82) and L-PoAF group (N=15). As demonstrated in *Figure 1*, AF occurred in the majority of L-PoAF patients (53%) within the first year after surgery. However, even 5 years after surgery, 6 patients (40%) were diagnosed with the first AF recurrence since the E-PoAF period.

Compared to the SR group, patients with PoAF were older at time of surgery (69 [65–74] years vs. 65 [57–71] years, p<0.001), although there was no difference in age between patients who had L-PoAF and those who did not. In addition, more patients with PoAF had iVHD. There was no difference in intra-operative P-wave amplitude and duration between both groups (p=0.056 and p=0.255 respectively) and there were no differences in surgery-related parameters.

Comparing the E-PoAF and L-PoAF group, patients with L-PoAF had a higher prevalence of 1) mitral valve disease, 2) a dilated LA, and 3) they also had a higher BMI. There was no difference in intra-operative P-wave amplitude and duration between both groups (p=0.275 and p=0.286 respectively).

Table 2 – Intra-atrial conduction disorders and potential morphology.

Parameters	SR (N=166)	PoAF (N=97)	p-value	E-PoAF (N=82)	L-PoAF (N=15)	p-value
CV (cm/s)	90.9 [86.4–95.6]	89.8 [85.0–94.0]	0.034	90.2 [85.8–94.4]	88.2 [82.8–91.0]	0.046
CB (%)	1.83 [1.29–2.64]	2.30 [1.66–3.10]	0.004	2.15 [1.65–2.93]	3.15 [2.24–4.19]	0.017
Voltage (mV)	5.10 [4.20–6.11]	4.56 [3.64–5.57]	<0.001	4.64 [3.82–5.60]	3.54 [2.63–4.50]	0.007
LVA (%)	5.0 [3.1–8.6]	7.1 [4.6–10.1]	<0.001	6.8 [4.2–9.9]	9.2 [6.3–12.8]	0.084
SP (%)	83.5 [79.1–87.1]	82.9 [78.8–85.8]	0.312	83.1 [79.5–86.4]	79.3 [76.9–84.2]	0.073
SDP (%)	11.0 [8.5–13.4]	10.5 [8.8–12.4]	0.251	10.6 [8.3–12.4]	10.2 [9.8–13.2]	0.300
SDP delay (ms)	8 [7–9]	8 [7–9]	0.499	8 [7–9]	8 [6–10]	0.226
LDP (%)	3.7 [2.3–5.9]	4.3 [2.5–6.8]	0.055	4.3 [2.4–6.2]	5.7 [3.9–9.1]	0.033
LDP delay (ms)	20 [18–22]	20 [18–22]	0.262	20 [18–21]	20 [19–26]	0.176
FP (%)	1.4 [0.8–2.6]	1.6 [0.8–2.3]	0.422	1.6 [0.7–2.0]	1.7 [0.9–2.5]	0.235
FP delay (ms)	19 [15–23]	19 [15–23]	0.410	19 [15–24]	19 [17–23]	0.247

Values are presented as median [interquartile ranges]. **CB** = conduction block; **CV** = conduction velocity; **E/L-PoAF** = early/late post-operative atrial fibrillation; **FP** = fractionated potential; **LDP** = long double potential; **LVA** = low-voltage area; **SDP** = short double potential; **SP** = single potential.

Intra-atrial conduction disorders

A typical example of an activation map of one patient who remained in SR and one patient with both E-PoAF and L-PoAF is illustrated in the right panel of *Figure 2*. As indicated by the thick black lines, the amount of CB is higher in the patient with both E-PoAF and L-PoAF. As summarized in *Table 2* and illustrated in *Figure 3*, patients with PoAF had lower CV (89.8 [85.0–94.0] cm/s vs. 90.9 [86.4–95.6] cm/s, p=0.034) and higher prevalence of CB (2.30 [1.66–3.10] % vs. 1.83 [1.29–2.64] %, p=0.004 respectively) compared to those patients who remained in SR.

As demonstrated in *Figure 4*, CV of PoAF patients was particularly slower at BB (88.6 [76.2–95.1] cm/s vs. 91.4 [82.5–99.1] cm/s, p=0.005). In addition, CB was also mainly present at BB (2.90 [1.18–5.58] % vs. 1.79 [0.65–4.48] %, p=0.006, respectively).
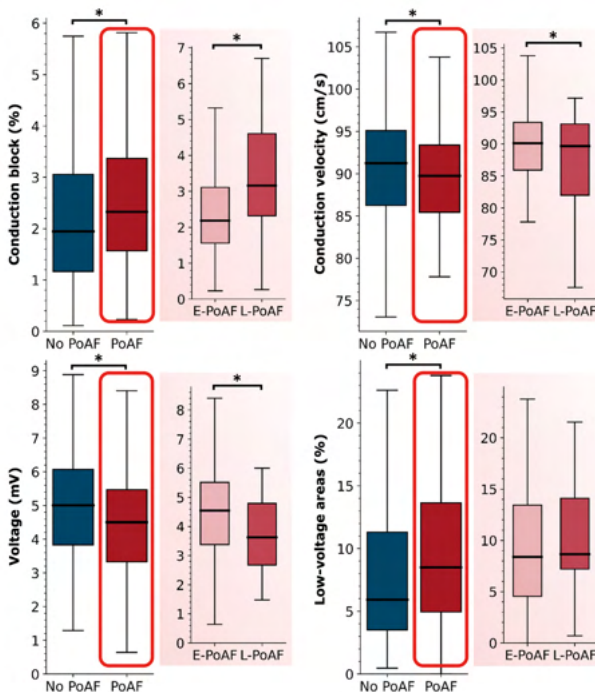
Figure 3 – Characteristics of intra-atrial conduction and electrogram morphology. Boxplots of the conduction block prevalence, conduction velocity, voltage and low-voltage areas of patients without PoAF (blue) and patients with de novo PoAF (red). The highlighted red boxplots demonstrate the differences between patients with only E-PoAF (light) and also L-PoAF (dark). Statistical significance is indicated by an asterisk. **L-PoAF** = late post-operative atrial fibrillation.
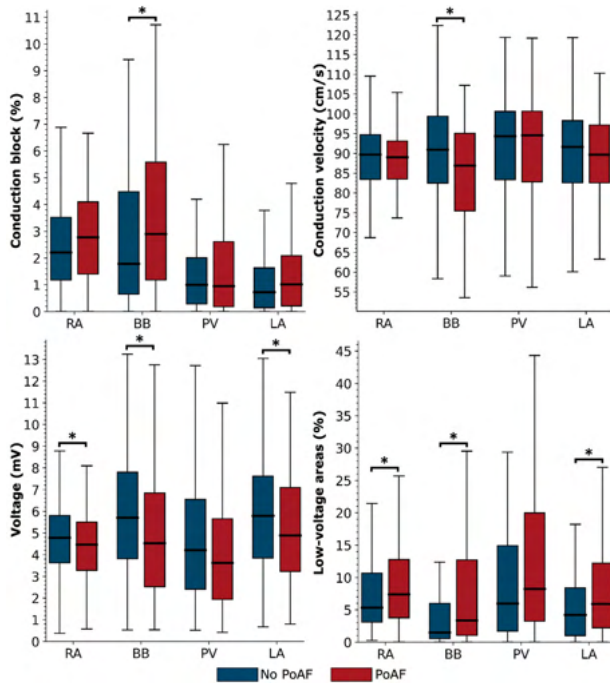
Figure 4 – Regional distribution of intra-atrial conduction and electrogram morphology. Regional distribution of conduction block prevalence, conduction velocity, voltage and low-voltage areas of patients without PoAF (blue) and patients with de novo PoAF (red). Statistical significance is indicated by an asterisk. **BB** = Bachmann's bundle; **LA** = left atrium; **PoAF** = post-operative atrial fibrillation; **PV** = pulmonary veins; **RA** = right atrium.

Unipolar voltage mapping

Voltage maps corresponding to the activation maps are demonstrated in the right panel of *Figure 2*. LVAs were more extensive in the patient with both E-PoAF and L-PoAF (17.6%) compared to the patient who remained in SR (7.5%). In the entire study population, unipolar voltages were lower in patients with PoAF (4.56 [3.64–5.57] mV vs. 5.10 [4.20–6.11] mV, p<0.001) and they also had more LVAs (7.1 [4.6–10.1] % vs. 5.0 [3.1–8.6] %, p<0.001), as demonstrated in *Table 2* and *Figure 3*. There were no differences between both groups in the amount of single, short double, long double or fractionated potentials and the corresponding interval durations (all p>0.05).

As demonstrated in *Figure 4*, compared to the SR group, unipolar voltages in patients with E-PoAF and/or L-PoAF were particularly lower at RA, BB and LA, and more LVAs were found at these atrial regions as well. At all atrial regions, there were no differences between both groups in the amount of single, short double, long double and fractionated potentials. Fractionation delays of long double potentials at RA were longer in PoAF patients compared to the SR group (20 [18–24] ms vs. 22 [20–24] ms, p=0.011).

Differences between early- and late-PoAF

Differences in CB and unipolar voltages between the solely E-PoAF and L-PoAF groups are illustrated in the red boxes in *Figure 3*. Compared to the SR group, unipolar voltages were lower in both the E-PoAF (4.64 [3.82–5.60] mV, p=0.009) and L-PoAF (3.54 [2.63–4.50] mV, p<0.001) group. Unipolar voltages in the L-PoAF group were even lower compared to the E-PoAF group (p=0.007). There were more long double potentials in the L-PoAF (5.7 [3.9–9.1] %) group compared to the SR (p=0.010) and E-PoAF (4.3 [2.4–6.2] %, p=0.033) group, while the amount of long double potentials was comparable between the E-PoAF and SR group.

28

Table 3 – Intra-regional conduction disorders and potential morphology.

Parameters	SR (N=166)	PoAF (N=97)	p-value	Solely E-PoAF (N=82)	E+L-PoAF (N=15)	p-value
CV (cm/s)						
RA	89.4 [83.3–94.6]	88.9 [83.3–93.1]	0.201	89.1 [84.6–92.9]	88.2 [81.1–93.0]	0.250
BB	91.4 [82.5–99.1]	88.6 [76.2–95.1]	0.005	90.6 [80.7–95.3]	77.2 [68.8–87.1]	0.006
PVA	95.1 [84.7–100.6]	96.6 [84.5–100.6]	0.497	95.6 [84.3–100.7]	98.2 [86.7–100.0]	0.333
LA	91.4 [83.3–98.4]	89.5 [81.2–96.2]	0.121	90.4 [82.6–97.2]	80.8 [72.6–86.7]	0.004
CB (%)						
RA	2.21 [1.18–3.52]	2.77 [1.40–4.09]	0.085	2.77 [1.40–3.73]	3.67 [1.25–5.09]	0.173
BB	1.79 [0.65–4.48]	2.90 [1.18–5.58]	0.006	2.59 [1.02–5.23]	4.90 [2.87–7.66]	0.013
PVA	1.00 [0.29–2.01]	0.96 [0.18–2.62]	0.359	0.92 [0.18–2.59]	1.66 [0.42–5.02]	0.167
LA	0.73 [0.14–1.63]	1.01 [0.21–2.09]	0.109	0.84 [0.19–1.63]	2.34 [0.86–3.08]	0.056
Voltage (mV)						
RA	4.94 [3.80–5.92]	4.47 [3.69–5.60]	0.026	4.50 [3.81–5.64]	3.78 [2.79–5.23]	0.047
BB	5.70 [3.82–7.80]	4.62 [2.54–7.00]	<0.001	5.04 [2.89–7.12]	3.18 [2.20–3.90]	0.010
PVA	4.55 [2.81–6.64]	3.81 [2.33–5.87]	0.055	3.81 [2.31–5.90]	4.00 [3.42–4.65]	0.418
LA	5.97 [4.12–7.86]	4.97 [3.23–7.43]	0.004	5.33 [3.32–7.51]	3.35 [2.41–4.90]	0.020
LVA (%)						
RA	5.0 [2.7–8.6]	6.8 [3.4–11.1]	0.028	6.8 [3.4–10.1]	10.1 [3.7–12.8]	0.229
BB	1.4 [0.4–4.1]	2.9 [0.9–8.9]	<0.001	2.4 [0.7–8.2]	8.3 [4.5–15.2]	0.010
PVA	3.7 [1.4–12.4]	6.7 [2.1–15.6]	0.065	6.9 [1.8–15.9]	5.1 [2.3–10.7]	0.311
LA	3.3 [1.0–7.4]	4.7 [1.7–12.2]	0.008	4.5 [1.7–9.5]	14.2 [3.8–17.0]	0.039
SP (%)						
RA	84.5 [79.2–89.4]	84.0 [79.0–88.5]	0.344	84.4 [79.3–88.7]	81.8 [78.0–86.7]	0.191
BB	80.2 [72.0–88.5]	80.6 [70.4–86.6]	0.191	81.4 [72.3–86.8]	64.8 [61.3–81.7]	0.007
PVA	86.0 [77.5–90.2]	85.1 [74.8–89.9]	0.316	84.3 [74.6–89.9]	88.1 [76.9–88.9]	0.315
LA	82.4 [75.7–89.9]	85.1 [77.4–88.8]	0.305	86.0 [77.4–89.1]	83.3 [77.4–85.5]	0.207
SDP (%)						
RA	9.5 [6.1–11.8]	9.2 [6.8–11.6]	0.364	9.1 [6.7–11.7]	9.2 [7.7–11.4]	0.423
BB	12.2 [6.7–17.9]	12.2 [8.2–16.5]	0.248	11.8 [8.4–16.1]	14.9 [6.4–25.1]	0.266
PVA	10.7 [7.2–16.1]	10.3 [6.0–16.5]	0.349	10.3 [6.1–17.6]	8.7 [6.0–13.8]	0.198
LA	11.6 [8.0–16.9]	10.7 [8.1–15.6]	0.221	10.7 [8.1–15.6]	13.2 [8.3–15.3]	0.378
SDP delay (ms)						
RA	7 [6–8]	7 [6–9]	0.184	7 [6–9]	6 [6–8]	0.167
BB	8 [7–10]	8 [7–10]	0.320	8 [7–10]	10 [8–11]	0.033
PVA	8 [7–9]	8 [6–9]	0.374	8 [6–9]	8 [7–9]	0.326
LA	8 [6–9]	8 [7–9]	0.290	8 [6–9]	8 [7–11]	0.047

Parameters	SR (N=166)	PoAF (N=97)	p-value	Solely E-PoAF (N=82)	E+L-PoAF (N=15)	p-value
LDP (%)						
RA	4.1 [1.8–6.9]	4.6 [2.4–7.5]	0.221	4.5 [2.4–7.4]	5.5 [1.3–8.2]	0.470
BB	3.3 [0.6–8.9]	4.3 [1.5–9.1]	0.080	4.0 [1.2–8.6]	7.0 [3.1–15.9]	0.007
PVA	1.0 [0.3–4.1]	1.3 [0.2–5.2]	0.351	1.2 [0.2–4.5]	3.8 [0.5–6.9]	0.188
LA	1.4 [0.2–4.5]	2.2 [0.7–5.0]	0.086	1.8 [0.8–4.5]	4.0 [0.5–8.4]	0.194
LDP delay (ms)						
RA	20 [18–24]	22 [20–24]	0.011	22 [20–24]	23 [19–28]	0.284
BB	19 [16–22]	18 [17–21]	0.083	18 [17–21]	19 [18–20]	0.187
PVA	17 [16–18]	17 [16–20]	0.141	17 [16–20]	18 [16–22]	0.138
LA	18 [16–22]	17 [16–21]	0.048	17 [16–21]	16 [16–22]	0.436
FP (%)						
RA	1.3 [0.4–2.9]	1.0 [0.5–2.3]	0.233	1.0 [0.4–2.2]	1.0 [0.9–2.1]	0.302
BB	1.2 [0.3–3.2]	1.6 [0.6–3.6]	0.129	1.5 [0.4–3.1]	3.6 [1.4–7.4]	0.023
PVA	0.6 [0.2–1.6]	0.6 [0.2–1.6]	0.434	0.7 [0.1–1.7]	0.4 [0.2–0.8]	0.180
LA	1.1 [0.4–2.3]	0.8 [0.3–2.3]	0.255	0.9 [0.3–2.4]	0.8 [0.3–1.5]	0.365
FP delay (ms)						
RA	22 [16–28]	22 [16–28]	0.106	21 [16–28]	24 [16–30]	0.356
BB	18 [14–25]	18 [14–24]	0.424	17 [14–23]	22 [18–26]	0.039
PVA	12 [10–17]	14 [10–19]	0.061	14 [10–19]	11 [7–20]	0.083
LA	15 [12–20]	14 [12–21]	0.326	15 [12–21]	13 [12–18]	0.116

Values are presented as median [interquartile ranges]. **CB** = conduction block; **CV** = conduction velocity; **E/L-PoAF** = early/late post-operative atrial fibrillation; **FP** = fractionated potential; **LDP** = long double potential; **LVA** = low-voltage area; **SDP** = short double potential; **SP** = single potential.

28

Although both PoAF groups had more LVAs compared to the SR group, there was no difference in the number of LVAs in the L-PoAF and E-PoAF groups (p=0.084). However, more CB and slower CV were found in patients with L-PoAF compared to the E-PoAF group (CB: 3.15 [2.24–4.19] % vs. 2.15 [1.65–2.93] %, p=0.017 and CV: 88.2 [82.8–91.0] cm/s vs. 90.2 [85.8–94.4] cm/s, p=0.046 respectively). In addition, the amount of CB in both PoAF groups was higher compared to SR group (E-PoAF: p=0.025 and L-PoAF: p=0.003), while CV was only lower in patients with L-PoAF compared to SR patients (p=0.012).

Regional differences between early- and late-PoAF

As demonstrated in *Table 3*, most differences in electrophysiological parameters between the SR, E-PoAF and L-PoAF groups were found at BB, followed by the LA and RA; none of the parameters differed between the groups at the PVA (p>0.083).

At BB, CV was lowest in patients with L-PoAF, followed by E-PoAF and SR patients. This was accompanied by a higher amount of CB. In addition, the lowest unipolar voltages and highest amount of LVAs were also found in patients with L-PoAF, followed by E-PoAF and SR patients. In the L-PoAF group, potentials at BB were more often long double or fractionated compared to the SR and E-PoAF groups.

At the LA, atrial CV was also lower in the L-PoAF group compared to the E-PoAF and SR groups, while there were no differences in the amount of CB. Lowest unipolar voltages and highest amount of LVAs were found in the L-PoAF group, followed by the E-PoAF and SR group. There were no differences in the amount of single, short double, long double or fractionated potentials and the corresponding delays.

At the RA, only unipolar voltages in the L-PoAF group were lower compared to the E-PoAF and SR groups; other parameters did not differ between the various groups.

Univariate and multivariable analyses

As demonstrated in *Supplementary Table 1*, age, total CB, total voltage, total LVAs, CV at BB, CB at BB, voltage at BB, LVAs at BB, voltage at LA and LVAs at LA were related to development of PoAF using univariate analyses. Using a multivariable analysis, only age remained significant (odds ratio 1.05; 95% CI 1.02–1.08; p=0.001).

Discussion

This is the first study that demonstrated that development of de novo PoAF is associated with pre-existing conduction disorders, consisting of areas of conduction slowing, more CB, lower unipolar voltages and more LVAs. Although these disorders were particularly located at BB, clear differences were also found at the left and right atrium. These differences were even more dominantly present in patients with L-PoAF who also had E-PoAF. The first episode of L-PoAF could even occur 5 years after surgery and occurred only in patients who also developed E-PoAF.

Development of post-operative atrial fibrillation

AF is the most common arrhythmia to occur after cardiac surgery, occurring more frequently after valvular surgery and especially after combined CABG and valvular surgery.[1] PoAF typically occurs on the second post-operative day and 70% occurs within the first four post-operative days. Late-onset PoAF, defined as PoAF occurring more than 30 days after surgery,

is underappreciated and has a rate of at least 4%.[21]

Even today, the exact mechanisms underlying PoAF are still not clearly understood. Yet, multiple factors that may contribute are frequently subdivided into pre-, intra- and post-operative risk factors, including ageing, hyper-/hypotension, ischemia, pain and other factors that can modulate the sympathetic nervous system and increase adrenergic stimulation.[7,22-25] It is generally accepted that PoAF is initiated by an interplay between a trigger and susceptible substrate for AF.[9,10] However, it is generally assumed that E-PoAF is mainly a trigger driven disease.[8-10] In the vast majority of patients, episodes of E-PoAF are preceded by atrial extrasystoles which are provoked by inflammatory responses and increasing sympathetic activity associated with cardiopulmonary bypass during surgery.[23,25-27] These atrial extrasystoles are associated with enhanced conduction disorders and epi-endocardial asynchrony.[28] PoAF then occurs when these transient, post-operative triggers act on vulnerable, remodeled, atrial tissue.[9,10] This substrate can either be produced by surgery-induced or post-operative remodeling processes. On the other hand, it has also been suggested that PoAF patients have pre-existent structural remodeling, including increased interstitial fibrosis, altered cytosolic calcium handling and decreased atrial elasticity.[9,10,25,29,30] This may lead to a decline in LA reservoir functions, all of which may contribute to electrical remodeling and PoAF development.[31,32]

Association between conduction disorders and post-operative atrial fibrillation

Atrial remodeling is frequently quantified using electrophysiological parameters such as CB, CV, effective refractory period and voltage, and can manifest heterogeneously throughout the atria. The prevalence of CB at BB in patients developing de novo PoAF was quantified by Teuwen et al.[8] They demonstrated that although an equal amount of CB was found in patients with PoAF compared with patients without PoAF, patients with PoAF had more often long lines of longitudinal CB. We found a higher prevalence of CB in patients with PoAF at the total atrial surface and at BB specifically. Besides, CV was also lower at the total atrial surface and at BB in patients with PoAF. Especially in patients with L-PoAF, even more CB at BB and lower CV at BB and LA were found compared to patients with only E-PoAF.

Dispersion of the atrial effective refractory period is also acknowledged as a key player in the pathophysiology of both onset and maintenance of AF. In 56 patients undergoing CABG (PoAF, N=18; no PoAF, N=38), pre-operative interregional dispersion of refractoriness was an independent predictor of PoAF incidence (odds ratio, 1.29; 95% CI, 1.12–1.47; p<0.001).[31] It was suggested that increased pre-operative atrial effective refractory period dispersion may create nonuniform atrial conduction, which may increase vulnerability to PoAF. Apart from BB, we did not find any differences in local CV between patients without and with PoAF. Furthermore, correct determination of regional effective refractory period is time consuming, which cannot always be performed during standard cardiac surgery. Secondly, there is much debate on the correct methodology to determine the effective refractory period and its interpretation.[32] Hence, the added value of the effective refractory period can therefore be questioned.

Recently, Bidar et al.[33] demonstrated that patients with de novo PoAF had more complex AF patterns during induced AF at the RA. This could indicate that conduction disorders are already present at the RA. We, however, did not find a higher amount of CB at the RA, although voltages were lower and more LVAs could be found in patients with PoAF. The differences in unipolar voltage characteristics may indicate an arrhythmogenic substrate at the RA, LA and BB which is, even before commencement to cardiopulmonary bypass, already more extensively present during SR in patients who develop de novo PoAF. This is

28

in line with the study of Teuwen et al.[8], who suggested that, besides BB, other regions also play a significant role in development of PoAF. This suggests that PoAF most likely occurs when patients reach a 'pathophysiological threshold' of pro-arrhythmic factors due to a combination of pre-existing atrial substrate and post-surgical risk factors. It can therefore be concluded that at least in some of the patients developing PoAF after cardiac surgery, severely altered atrial tissue is already present before surgery, making the atria prone to not only E-PoAF but also to AF recurrences years after surgery.

Relation between early and late post-operative atrial fibrillation

In current clinical practice, routine surveillance for L-PoAF after surgery largely depends on the report of AF symptoms by the patient. However, as AF can also be asymptomatic, incidence rates are low when patients are not continuous monitored by e.g., an implantable device.[34] In addition, there are limited data on the predictive factors and pathophysiology of L-PoAF in relation to long-term mortality of patients following cardiac surgery. The study of Melduni et al.[6] demonstrated that de novo PoAF after cardiac surgery is associated with the occurrence of late AF, indicating that "PoAF predicts AF" after cardiac surgery. In this study, the highest rate of AF recurrence after cardiac surgery occurred within the first year. At 1-year follow-up, 82.1% of patients with PoAF were free from late AF, versus 64.0% at 5-year and 44.6% at 10-year follow-up. Also, 84% of the patients without E-PoAF remained free of AF until 10 years after surgery, although with limited screening for AF.

To overcome underestimation of AF prevalence, implantable devices can be used to continuously monitor the patients up to several years after surgery. In the study of El-Chami et al.[35], an implantable loop recorder was used for detection of L-PoAF. They reported an incidence of 60.9% and also reported first episodes of L-PoAF beyond 1 year after cardiac surgery. This was also demonstrated by Bidar et al.[33], who found that 47% of patients without a history of AF developed short-lasting episodes of L-PoAF. In our population, comparable to the aforementioned studies, most patients with de novo PoAF had L-PoAF within the first year after cardiac surgery, although this was a small number of the entire population. In our study, patients with L-PoAF had already a more extensive arrhythmogenic substrate at the time of surgery compared to those who only had E-PoAF. In addition, only patients with de novo PoAF developed L-PoAF within 5 years of follow-up. Therefore, as patients with E-PoAF could have the first episode of L-PoAF even until 5 years after surgery, periodic rhythm monitoring in these patients should be considered.

Study limitations

Episodes of asymptomatic AF during the follow-up period could have been missed as patients only have only intermittent contact with their cardiologist or general practitioner without continuous rhythm monitoring. Therefore, the incidence of L-PoAF could have been underestimated. Besides, the small number of (L-PoAF) patients results in under powering of the analyses for some parameters and limits accurate risk-adjustment regression analyses.

The recorded potentials might be influenced by the presence of epicardial fat as previous studies demonstrated that the presence of thick epicardial fat is associated with attenuated bipolar voltage.[36,37] Although we did not experience any large effects of visually present epicardial fat, we cannot ascertain that the presence of epicardial fat has influenced our results. Besides, a recent study has demonstrated a limited role of epicardial fat in the development of PoAF.[38]

At the moment, features of intra-atrial conduction and electrogram morphology could not

directly be translated in non-invasive parameters derived from the surface ECG. However, as this study clearly demonstrated that there are already substantial signs of a pre-existing substrate which could be identifiable by epicardial mapping, future studies should evaluate whether these features can also be identified using other less or non-invasive methods.

Conclusion

In the present study, we demonstrated that patients who develop de novo PoAF already have substantial signs of pre-existing atrial remodeling compared to those who remained in SR. Patients who had E-PoAF and L-PoAF even have a more extensive arrhythmogenic substrate, and the first episode of L-PoAF can even occur up to 5 years after surgery. Future studies should evaluate whether electrophysiological examination during cardiac surgery enables identification of patients at risk for developing PoAF and hence (preventive) therapy.

28

References

1. D'Agostino RS, Jacobs JP, Badhwar V, Fernandez FG, Paone G, Wormuth DW, Shahian DM. The Society of Thoracic Surgeons Adult Cardiac Surgery Database: 2019 Update on Outcomes and Quality. Ann Thorac Surg. 2019;107:24-32.
2. Aranki SF, Shaw DP, Adams DH, Rizzo RJ, Couper GS, VanderVliet M, Collins JJ, Jr., Cohn LH, Burstin HR. Predictors of atrial fibrillation after coronary artery surgery. Current trends and impact on hospital resources. Circulation. 1996;94:390-397.
3. LaPar DJ, Speir AM, Crosby IK, Fonner E, Jr., Brown M, Rich JB, Quader M, Kern JA, Kron IL, Ailawadi G, et al. Postoperative atrial fibrillation significantly increases mortality, hospital readmission, and hospital costs. Ann Thorac Surg. 2014;98:527-533; discussion 533.
4. Echahidi N, Pibarot P, O'Hara G, Mathieu P. Mechanisms, prevention, and treatment of atrial fibrillation after cardiac surgery. J Am Coll Cardiol. 2008;51:793-801.
5. Almassi GH, Schowalter T, Nicolosi AC, Aggarwal A, Moritz TE, Henderson WG, Tarazi R, Shroyer AL, Sethi GK, Grover FL, et al. Atrial fibrillation after cardiac surgery: a major morbid event? Ann Surg. 1997;226:501-511; discussion 511-503.
6. Melduni RM, Schaff HV, Bailey KR, Cha SS, Ammash NM, Seward JB, Gersh BJ. Implications of new-onset atrial fibrillation after cardiac surgery on long-term prognosis: a community-based study. Am Heart J. 2015;170:659-668.
7. Yamashita K, Hu N, Ranjan R, Selzman CH, Dosdall DJ. Clinical Risk Factors for Postoperative Atrial Fibrillation among Patients after Cardiac Surgery. Thorac Cardiovasc Surg. 2019;67:107-116.
8. Teuwen CP, Yaksh A, Lanters EA, Kik C, van der Does LJ, Knops P, Taverne YJ, van de Woestijne PC, Oei FB, Bekkers JA, et al. Relevance of Conduction Disorders in Bachmann's Bundle During Sinus Rhythm in Humans. Circ Arrhythm Electrophysiol. 2016;9:e003972.
9. Dobrev D, Aguilar M, Heijman J, Guichard JB, Nattel S. Postoperative atrial fibrillation: mechanisms, manifestations and management. Nat Rev Cardiol. 2019;16:417-436.
10. Maesen B, Nijs J, Maessen J, Allessie M, Schotten U. Post-operative atrial fibrillation: a maze of mechanisms. Europace. 2012;14:159-174.
11. Lanters EA, van Marion DM, Kik C, Steen H, Bogers AJ, Allessie MA, Brundel BJ, de Groot NM. HALT & REVERSE: Hsf1 activators lower cardiomyocyt damage; towards a novel approach to REVERSE atrial fibrillation. J Transl Med. 2015;13:347.
12. van der Does LJ, Yaksh A, Kik C, Knops P, Lanters EA, Teuwen CP, Oei FB, van de Woestijne PC, Bekkers JA, Bogers AJ, et al. QUest for the Arrhythmogenic Substrate of Atrial fibRillation in Patients Undergoing Cardiac Surgery (QUASAR Study): Rationale and Design. J Cardiovasc Transl Res. 2016;9:194-201.
13. Mouws E, Lanters EAH, Teuwen CP, van der Does L, Kik C, Knops P, Bekkers JA, Bogers A, de Groot NMS. Epicardial Breakthrough Waves During Sinus Rhythm: Depiction of the Arrhythmogenic Substrate? Circ Arrhythm Electrophysiol. 2017;10.
14. Kik C, Mouws E, Bogers A, de Groot NMS. Intra-operative mapping of the atria: the first step towards individualization of atrial fibrillation therapy? Expert Rev Cardiovasc Ther. 2017;15:537-545.
15. de Groot N, van der Does L, Yaksh A, Lanters E, Teuwen C, Knops P, van de Woestijne P, Bekkers J, Kik C, Bogers A, et al. Direct Proof of Endo-Epicardial Asynchrony of the Atrial Wall During Atrial Fibrillation in Humans. Circ Arrhythm Electrophysiol. 2016;9.
16. Konings KT, Smeets JL, Penn OC, Wellens HJ, Allessie MA. Configuration of unipolar atrial electrograms during electrically induced atrial fibrillation in humans. Circulation. 1997;95:1231-1241.
17. van Schie MS, Starreveld R, Bogers A, de Groot NMS. Sinus rhythm voltage fingerprinting in patients with mitral valve disease using a high-density epicardial mapping approach. Europace. 2021;23:469-478.
18. van Schie MS, Heida A, Taverne Y, Bogers A, de Groot NMS. Identification of local atrial conduction heterogeneities using high-density conduction velocity estimation. Europace. 2021;23:1815-1825.
19. Lanters EA, van Marion DM, Steen H, de Groot NM, Brundel BJ. The future of atrial fibrillation therapy: intervention on heat shock proteins influencing electropathology is the next in line. Neth Heart J. 2015;23:327-333.
20. Yaksh A, Kik C, Knops P, Roos-Hesselink JW, Bogers AJ, Zijlstra F, Allessie M, de Groot NM. Atrial fibrillation: to map or not to map? Neth Heart J. 2014;22:259-266.
21. Ambrosetti M, Tramarin R, Griffo R, De Feo S, Fattirolli F, Vestri A, Riccio C, Temporelli PL, Isyde, Icaros Investigators of the Italian Society for Cardiovascular Prevention R, et al. Late postoperative atrial fibrillation after cardiac surgery: a national survey within the cardiac rehabilitation setting. J Cardiovasc Med (Hagerstown). 2011;12:390-395.
22. Auer J, Weber T, Berent R, Ng CK, Lamm G, Eber B. Risk factors of postoperative atrial fibrillation after cardiac surgery. J Card Surg. 2005;20:425-431.
23. Korantzopoulos P, Kolettis T, Siogas K, Goudevenos J. Atrial fibrillation and electrical remodeling: the potential role of inflammation and oxidative stress. Med Sci Monit. 2003;9:RA225-229.
24. Ozben B, Akaslan D, Sunbul M, Filinte D, Ak K, Sari I, Tigen K, Basaran Y. Postoperative Atrial Fibrillation after Coronary Artery Bypass Grafting Surgery: A Two-dimensional Speckle Tracking Echocardiography Study. Heart Lung Circ. 2016;25:993-999.
25. Hogue CW, Jr., Hyder ML. Atrial fibrillation after cardiac operation: risks, mechanisms, and treatment. Ann Thorac Surg. 2000;69:300-306.
26. Teuwen CP, Korevaar TIM, Coolen RL, van der Wel T, Houck CA, Evertz R, Yaksh A, Roos-Hesselink JW, Bogers A, de Groot NMS. Frequent atrial extrasystolic beats predict atrial fibrillation in patients with congenital heart defects. Europace. 2018;20:25-32.

27. Yaksh A, Kik C, Knops P, van Ettinger MJ, Bogers AJ, de Groot NM. Early, de novo atrial fibrillation after coronary artery bypass grafting: Facts and features. Am Heart J. 2017;184:62-70.
28. Kharbanda RK, van Schie MS, Taverne YJHJ, de Groot NMS, Bogers AJJC. Novel insights in pathophysiology of postoperative atrial fibrillation. JTCVS Open. 2021;6:120-129.
29. Fakuade FE, Steckmeister V, Seibertz F, Gronwald J, Kestel S, Menzel J, Pronto JRD, Taha K, Haghighi F, Kensah G, et al. Altered atrial cytosolic calcium handling contributes to the development of postoperative atrial fibrillation. Cardiovasc Res. 2021;117:1790-1801.
30. Heijman J, Muna AP, Veleva T, Molina CE, Sutanto H, Tekook M, Wang Q, Abu-Taha IH, Gorka M, Kunzel S, et al. Atrial Myocyte NLRP3/CaMKII Nexus Forms a Substrate for Postoperative Atrial Fibrillation. Circ Res. 2020;127:1036-1055.
31. Soylu M, Demir AD, Ozdemir O, Soylu O, Topaloglu S, Kunt A, Sasmaz A, Korkmaz S, Tasdemir O. Increased dispersion of refractoriness in patients with atrial fibrillation in the early postoperative period after coronary artery bypass grafting. J Cardiovasc Electrophysiol. 2003;14:28-31.
32. van Staveren LN, de Groot NMS. Exploring Refractoriness as an Adjunctive Electrical Biomarker for Staging of Atrial Fibrillation. J Am Heart Assoc. 2020;9:e018427.
33. Bidar E, Zeemering S, Gilbers M, Isaacs A, Verheule S, Zink MD, Maesen B, Bramer S, Kawczynski M, Van Gelder IC, et al. Clinical and electrophysiological predictors of device-detected new-onset atrial fibrillation during 3 years after cardiac surgery. Europace. 2021;23:1922-1930.
34. Lowres N, Mulcahy G, Jin K, Gallagher R, Neubeck L, Freedman B. Incidence of postoperative atrial fibrillation recurrence in patients discharged in sinus rhythm after cardiac surgery: a systematic review and meta-analysis. Interact Cardiovasc Thorac Surg. 2018;26:504-511.
35. El-Chami MF, Kilgo P, Thourani V, Lattouf OM, Delurgio DB, Guyton RA, Leon AR, Puskas JD. New-onset atrial fibrillation predicts long-term mortality after coronary artery bypass graft. J Am Coll Cardiol. 2010;55:1370-1376.
36. Saba MM, Akella J, Gammie J, Poston R, Johnson A, Hood RE, Dickfeld TM, Shorofsky SR. The influence of fat thickness on the human epicardial bipolar electrogram characteristics: measurements on patients undergoing open-heart surgery. Europace. 2009;11:949-953.
37. Desjardins B, Morady F, Bogun F. Effect of epicardial fat on electroanatomical mapping and epicardial catheter ablation. J Am Coll Cardiol. 2010;56:1320-1327.
38. Van der Heijden CJ, Verheule S, Olsthoorn JR, Mihl C, Poulina L, van Kuijk SMJ, Heuts S, Maessen JG, Bidar E, Maesen B. Postoperative atrial fibrillation and atrial epicardial fat: Is there a link? IJC Heart & Vasculature. 2022.

28
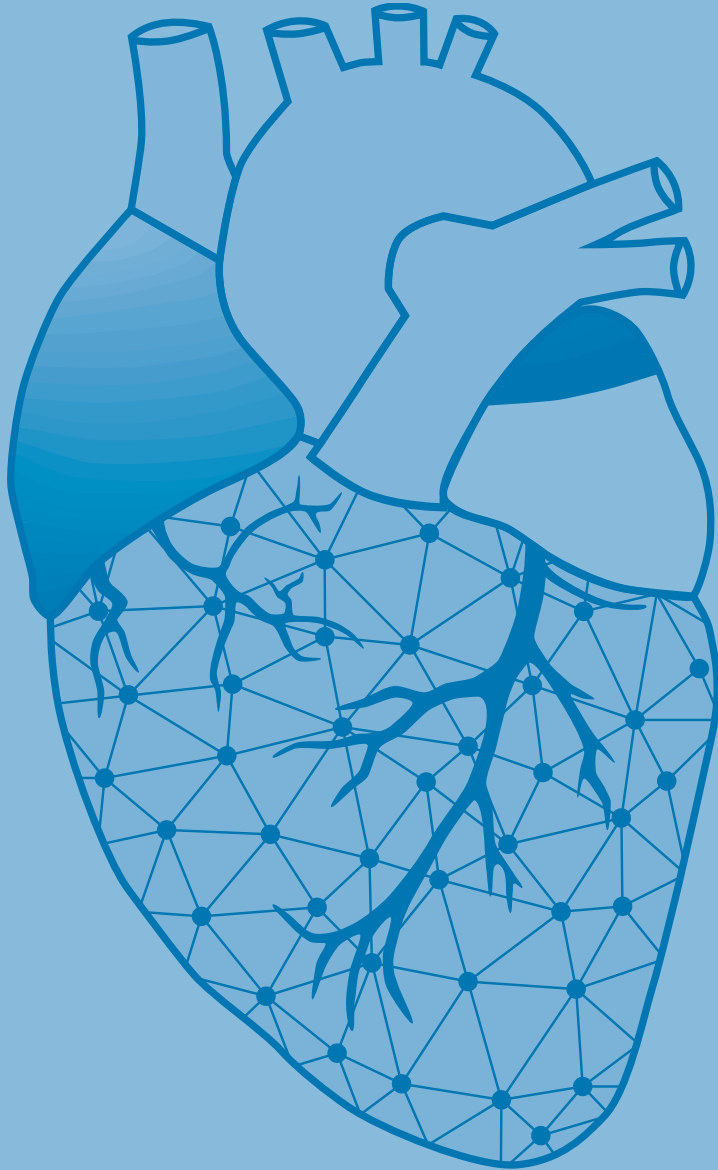
Chapter 29

Digital biomarkers and algorithms for detection of atrial fibrillation using surface electrocardiograms: a systematic review

Fons J. Wesselius

Mathijs S. van Schie

Natasja M.S. de Groot

Richard C. Hendriks
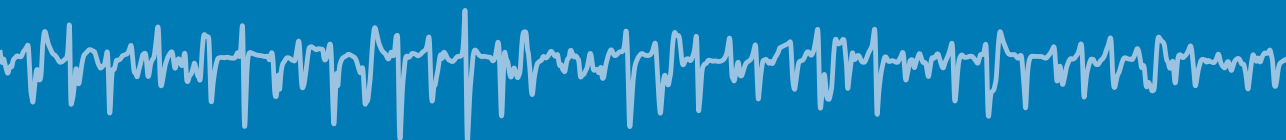
Abstract

Aims: Automated detection of atrial fibrillation (AF) in continuous rhythm registrations is essential in order to prevent complications and optimize treatment of AF. Many algorithms have been developed to detect AF in surface electrocardiograms (ECGs) during the past few years. The aim of this systematic review is to gain more insight into available classification methods by discussing previously used digital biomarkers and algorithms, and make recommendations for future research.

Methods: On the 14th of September 2020, the PubMed database was searched for articles focusing on algorithms for AF detection in ECGs using the MeSH terms Atrial Fibrillation, Electrocardiography and Algorithms. Articles which solely focused on differentiation of types of rhythm disorders or prediction of AF termination were excluded.

Results: The search resulted in 451 articles, of which 130 remained after full-text screening. Not only the amount of research on methods for AF detection increased over the past years, but a trend towards more complex classification methods is observed. Furthermore, three different types of features can be distinguished: atrial features, ventricular features and signal features. Although AF is an atrial disease, only 22% of the described methods use atrial features.

Conclusion: More and more studies focus on improving accuracy of classification methods for AF in ECGs. As a result, algorithms become increasingly complex and less well interpretable. Only few studies focus on detecting atrial activity in the ECG. Developing innovative methods focusing on detection of atrial activity might provide accurate classifiers without compromising on transparency.

Journal site &
supplementary material

Introduction

Accurate detection of atrial fibrillation (AF) episodes in continuous rhythm registrations is essential in order to prevent complications and optimize treatment of AF. However, manual analysis of continuous rhythm registrations is time-consuming. For this reason, the amount of research focused on automated AF detection has increased over the past years.

Automated analysis of continuous rhythm registrations not only helps in detecting AF for treatment considerations, but also provides insightful data for research on the still not entirely unraveled mechanisms underlying AF. Available research mainly focusses on the presence or absence of AF in patients. Most often, differentiations in AF burden are made using the classification between paroxysmal, persistent, long-standing persistent or permanent AF.[1] As stated by Chen et al.[2], more comprehensive information might be obtained by describing AF burden in terms of duration, number of episodes and/or proportion of time an individual is in AF during a monitoring period. Accurate automated AF detection in continuous rhythm registrations is essential to acquire these measures from long-term electrocardiogram (ECG) readings.

Already numerous methods for optimal automated AF detection in ECGs have been proposed, making it more and more difficult to see the wood for the trees. Instead of proposing yet another new algorithm, with this review we aimed to provide an in-depth overview of the previously used algorithms and identify methodological gaps which potentially can be used to develop novel innovative AF detection algorithms.

Search strategy

On the 14th of September 2020, the PubMed database was searched for articles focusing on algorithms for AF detection in ECG readings using the MeSH terms *Atrial Fibrillation*, *Electrocardiography* and *Algorithms*. Not all articles were indexed using MeSH terms, hence articles were also included if any of these terms or their synonyms were mentioned in the title or abstract. Additionally, title and abstract were screened for the terms ('*detect**' or '*classifi**' or '*predict**') and ('*accuracy*' or '*performance*' or '*F1*' or '*sensitivity*' or '*specificity*' or '*positive predictive value*' or '*negative predictive value*'). Full search strategy is provided in *Supplementary Appendix A*. Only articles focusing on AF detection in humans were included. Articles which solely focused on differentiation of types of rhythm disorders or prediction of AF termination were excluded. Additional exclusion criteria are listed in *Table 1*.

The search resulted in 451 articles, of which 263 were excluded based on title and abstract. An additional 10 articles were not available in English and of 3 records no full-text was available. As summarized in *Figure 1*, the remaining 175 full-text articles were screened for eligibility using the inclusion and exclusion criteria. A total of 130 articles remained after selection.

29

Table 1 – Inclusion and exclusion criteria.

Inclusion criteria	Exclusion criteria
• Focus on automated AF detection in human using ECG • (Clear) description of used algorithms • Reporting performance measures	• Focus on differentiation of types of atrial arrhythmias • Focus on prediction of AF termination • (Systematic) reviews • Non-English articles

AF = atrial fibrillation; **ECG** = electrocardiogram.
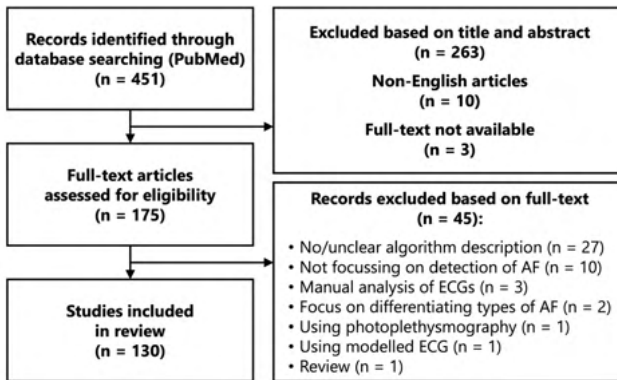
Figure 1 – Flowchart demonstrating selection of studies aiming to develop automated detection algorithms for atrial fibrillation (AF) in electrocardiograms (ECGs).

Study characteristics

Supplementary Appendix B lists all included studies with the used categories of classification methods and features and the classifier accuracy. As visualized in the left panel of *Figure 2*, research on methods for AF detection has increased over the past ten years from 20 studies up until 2009 to 108 studies up until 2019. In 2018, results from the PhysioNet/Computing in Cardiology (CinC) Challenge 2017 caused a strong increase in the number of studies (n=30).[3] Most used databases for development and testing of AF detection algorithms are the Massachusetts Institute of Technology–Beth Israel Hospital (MIT-BIH) Arrhythmia Database[4,5], MIT-BIH Atrial Fibrillation Database[5,6], MIT-BIH Normal Sinus Rhythm Database[5], and the database used in the PhysioNet/CinC Challenge 2017[5].

Classification methods for atrial fibrillation

Over the past years, not only more research has been conducted on the development of automated detection algorithms for AF in ECGs, but also new strategies have been applied. As visualized in the right panel of *Figure 2*, used classification methods can be grouped into six main categories: rule-based classification, decision tree(s), k-nearest neighbor (k-NN)
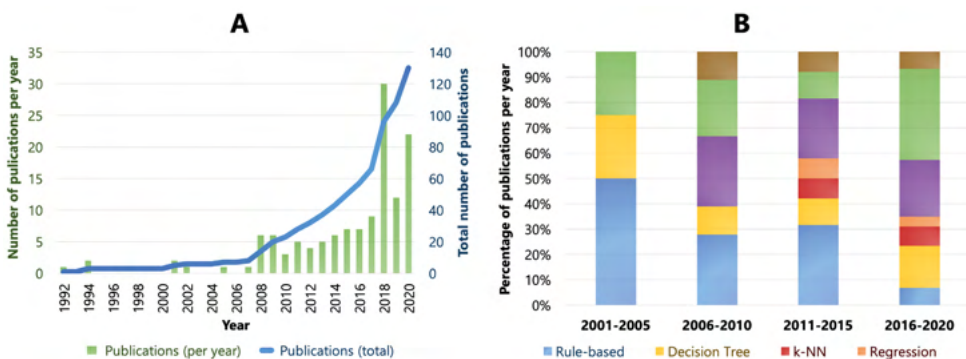
Figure 2 – Research on methods for AF detection. *Panel A*: the number of published articles on detection of atrial fibrillation per year. The bar chart indicates the number of published articles in a specific year, and the line chart shows the cumulative number of published articles. A steady increase in the number of published articles is observed. The sudden increase in 2018 is most probably caused by the PhysioNet/Computing in Cardiology Challenge (CinC) 2017. *Panel B*: bar chart per period of five years demonstrating the percentage of published articles using neural networks (NN), support vector machines (SVM), rule-based classifiers, decision tree(s), regression analysis, k-nearest neighbors (k-NN) classifiers, and other methods. A shift in used classification methods towards neural networks and support vector machines is observed. Articles published before 2001 were excluded from the chart due to the low amount of studies (n=2).
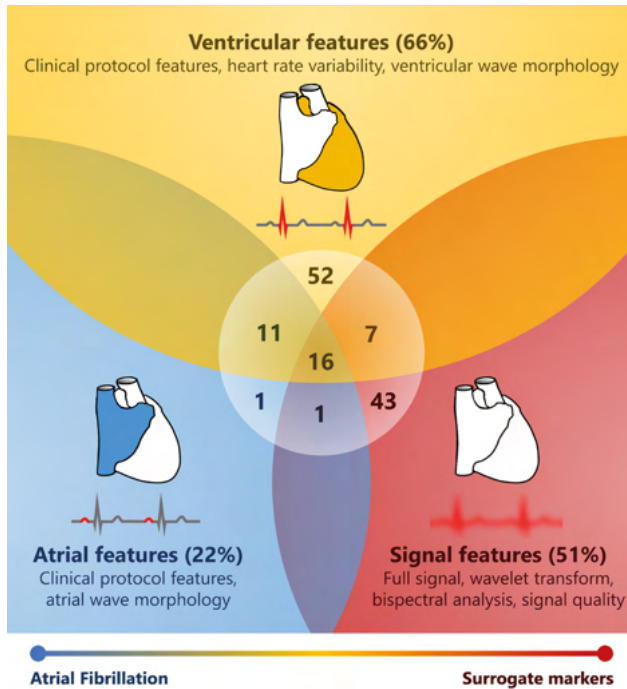
Figure 3 – Overview of the three feature categories which are used to detect atrial fibrillation in electrocardiograms. Yellow indicates ventricular features; blue indicates atrial features; red indicates signal features. Values in the white circle represent the number of studies using features from (a combination of) feature categories.

classification, regression analysis, support vector machines (SVMs) and neural networks (NNs). Whereas older studies use more straightforward rule-based approaches, newer studies increasingly use NNs and SVMs, providing new ways of describing ECGs and improving the classification accuracy. In contrast to rule-based classifiers, which can be easily interpreted, these more complex methods appear more as a 'black box', hence decisions made by these classifiers are difficult to comprehend. Therefore, transparency and accuracy of the classifier should be carefully balanced.

Classification performance

A commonly used measure for accuracy of AF detection is the F1-score, which is calculated as the harmonic mean of the recall (i.e., sensitivity) and precision (i.e., positive predictive value).[3] The median F1-score of all studies was 94.0 [93.1–97.7] %. As can be seen from several studies testing their classifier on multiple databases, the chosen database has major influence on the achieved performance measures. Zhou et al.[7] showed a positive predictive value (PPV) of 92.3% for testing on the combination of the MIT-BIH Normal Sinus Rhythm Database and MIT-BIH Atrial Fibrillation Database, but a PPV of only 55.3% when testing on the MIT-BIH Arrhythmia Database. Multiple other studies show similar variations in performance measures depending on the used testing database.[8-12]

Features of ECGs with AF

In general, classification methods require an input vector which contains features describing the ECG signal. Some features are derived from standard clinical protocols for ECG interpretation, for example P-wave presence, regularity of QRS-complexes, QRS-width and QT-time. Whilst these features are easy to interpret, more complex features can be used to further analyze and describe the ECG signal. NNs do not necessarily require preprocessing to

29

Table 2 – F1-score for AF detection for each set of features.

Feature groups	Number of studies with F1-score (reported or calculated) [%]	Median F1-score [IQR]
Atrial features	1 [100%]	83.8%*
Ventricular features	38 [73%]	96.9 [92.9–98.1] %
Signal features	34 [79%]	95.2 [83.6–98.9] %
Atrial + ventricular features	10 [91%]	85.6 [79.8–95.5] %
Atrial + signal features	1 [100%]	88.9%*
Ventricular + signal features	6 [86%]	91.1 [77.7–97.7] %
Atrial + ventricular + signal features	13 [81%]	81.0 [78.3–86.7] %
Overall	**103 [79%]**	**94.0 [83.1–97.7] %**

F1-score is calculated as the harmonic mean of recall and precision. *Only one study, hence no IQR could be calculated. **IQR** = interquartile range.

extract features, since this method also allows raw ECG input.[13-26]

In total, 131 feature sets were described in 130 studies, where one study trained and validated a classifier with two different feature sets. On the ECG, AF is visually characterized by absence of P-waves or presence of f-waves, combined with irregular time intervals between QRS-complexes as a result of disorganized irregular atrial impulses activating the atrioventricular node.[1] Many studies use these characteristics in their classification method. As visualized in *Figure 3*, features can be categorized into atrial features, ventricular features and signal features.

For the AF classifiers, atrial features mainly focus on P-wave disappearance or f-wave appearance, ventricular features include mainly features describing irregularity of intervals between subsequent R-peaks (RR-intervals), and signal features describe further characteristics of the signal which cannot easily be related to cardiac electrophysiological characteristics and the clinical presentation and pathophysiology of AF (e.g., signal quality and frequency components).

Although AF is an atrial rhythm disorder, only 29 methods (22%) focus on atrial features while almost two third of the studies use ventricular features (86 methods, 66%), as shown in *Figure 3*. Also, more than half of the studies use signal features (67 methods, 51%). More specifically, 19 methods (15%) used a combination of two categories of features; mostly ventricular features with either atrial or signal features (11 methods, 8%, and 7 methods, 5%, respectively). Only 1 method (1%) used a combination of atrial and signal features, without including ventricular features. A combined approach using all three categories of features was used in 16 methods (12%). As presented in *Table 2*, median F1-score was highest for classifiers focusing on ventricular features only (97.2 [92.6–98.2] %).

Atrial features

The underrepresentation of atrial features can be partially attributed to the challenging detection of atrial activity in the ECG due to relatively low amplitudes, diversity of waveforms and signal artefacts.[27] Therefore, especially in noisy signals, atrial activity detection is complex. Still, some methods incorporate atrial features to describe P-wave disappearance and f-wave appearance, or to describe the atrial wave morphology in general.

P-wave disappearance and f-wave appearance
Being among the most prominent features of an ECG during AF, absence of P-waves and presence of f-waves are described by multiple methods. In the time-domain, the number of fluctuations in the TQ-interval is used to detect a pattern of quick changes in the atrial signal.[28,29] In the frequency domain, f-waves mainly result in peaks in the 4–10Hz frequency

band, hence the area under the power spectral density curve within this frequency band is compared to the total area under the power spectral density curve as a measure of f-wave appearance.[30]

Atrial wave morphology
Amplitude of P-waves and P-wave duration directly reflect the electrophysiological characteristics of the atria. Furthermore, the time interval between atrial and ventricular activity, and the number of P-waves relative to the number of QRS-complexes provide information on the conduction from atria to ventricles.[31] Also, the time between P-waves is calculated as a measure of the atrial rate.[32]

Since P-waves are absent or have transformed into f-waves during AF, extracting basic morphological features is not always straightforward. Using computer algorithms, more complex morphological features are extracted, describing the statistics of the signal in terms of statistical measures like root mean square (RMS)-value, variance, skewness and kurtosis.[33,34]

Ventricular features

In contrast to the detection of atrial activity, automated detection of ventricular activity is more straightforward due to the more pronounced QRS-complexes in the ECG signal. Already in 1985, Pan and Tompkins[35] proposed a QRS detection algorithm, which is still widely used in research. In 2018, Liu et al.[33] published a comparison between ten common automated QRS-detectors using more than 2 million beats. From each detector, the accuracy was estimated in terms of an F1-score. Using a dataset containing high-quality ECG signals, all algorithms resulted in F1-scores larger than 99%. However, algorithms were highly dependent on the signal quality, as F1-scores decreased more than 25% when using ECG signals with the least optimal signal quality. Since ventricular features are dependent on the detection of ventricular activity, this relation between signal quality and detection rate has a direct effect on the accuracy of classifiers using these features.

Common features during manual analysis of ECGs are statistics of peak intervals, which reflect the propagation speed of cardiac activity. Furthermore, ventricular wave morphology is described in terms of durations and amplitudes of the QRS-complexes and T-waves. Additionally, computer algorithms are capable of processing more complex morphological features, focusing for example on the ratio between amplitude of ventricular activity and atrial activity, statistical features of QRS-complexes, and correlation between beats.[31,34] Although these features are useful to describe the average ventricular activation in general, methods implementing ventricular characteristics for AF detection mainly focus on irregularity of RR-intervals, since this is an evident feature of AF and one of the main features used in clinical practice. Various methods to describe the variability in RR-intervals are used, ranging from calculation of common statistics (e.g., standard deviation) to more complex statistics (e.g., entropy).

Standard deviation, coefficient of variation and RMSSD of RR-intervals
A basic measure for variation is standard deviation, but as pointed out by Sacha et al.[36] in their review concerning the interaction between heart rate and heart rate variability, higher heart rates are associated with lower variance in RR-intervals. With increasing heart rate, RR-intervals become smaller, hence variation in heart rate will have less effect on variation in RR-intervals. Therefore, the standard deviation of RR-intervals should be divided by the average RR-interval to correct for differences in heart rate, resulting in the coefficient of variance.[37]

Another commonly used measure for variability in RR-intervals is the root mean square of

29
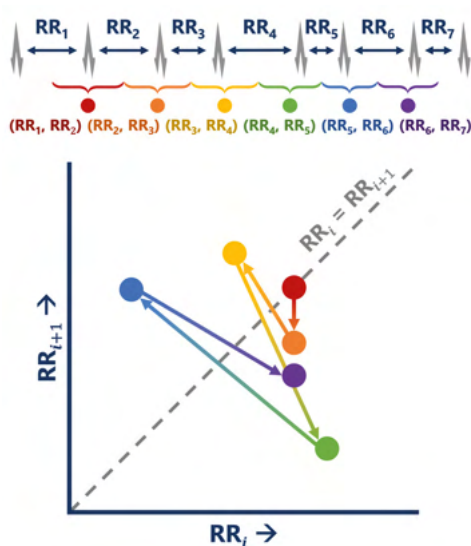
Figure 4 – Schematic visualization of Poincaré or Lorenz plot of RR-intervals. RR_i indicates the interval between the ith R-peak and the subsequent R-peak.

successive differences (RMSSD). Instead of globally analyzing the RR-intervals, this method describes the average change in successive RR-intervals, hence this method is less prone to slowly changing RR-intervals, which would result in a higher overall standard deviation of RR-intervals.[38]

Additionally, the percentage of successive differences between RR-intervals which differ more than a certain amount of time is used to describe the RR-interval variability.[39] Commonly used thresholds are 5, 10 and 50 ms, but any arbitrary threshold can be chosen.

Poincaré or Lorenz plots of RR-intervals

Similar to RMSSD, Poincaré or Lorenz plots are used to analyze successive RR-intervals.[40-47] However, instead of directly calculating a measure, the variability is visualized by plotting RR-intervals in a two-dimensional plane where the x-axis represents an RR-interval (RR_i) and the y-axis represents the subsequent RR-interval (RR_{i+1}), as visualized in *Figure 4*. During AF, when variation of successive RR-intervals is higher compared to sinus rhythm (SR), data points are dispersed across a larger area around the average RR-interval. Furthermore, Park et al.[46] show that patterns in Poincaré plots might be a useful feature to discriminate between AF and other arrhythmias resulting in irregular RR-intervals (e.g., premature ventricular beats). Commonly used features from this graphical representation are the SD of distances from data points to the line perpendicular to the regression line where RR_i equals RR_{i+1} and the standard deviation of distances from data points to the regression line itself.

Entropy measures of RR-intervals

The entropy of an RR-intervals series is another measure for the RR-interval irregularity. We describe two common definitions of entropy: the sample entropy and the Shannon entropy.[48] The sample entropy is used to describe the complexity of a time series, while the Shannon entropy expresses the amount of information or uncertainty.

The sample entropy of an RR-intervals series is defined as the probability that two matching RR-interval series will continue to match at the next RR-interval.[49] A match is defined as two RR-interval segments having corresponding data points within a certain small range, described by the tolerance factor r, as schematically visualized in *Figure 5*. When two matching RR-interval series do not continue to match for the next RR-interval, the sample
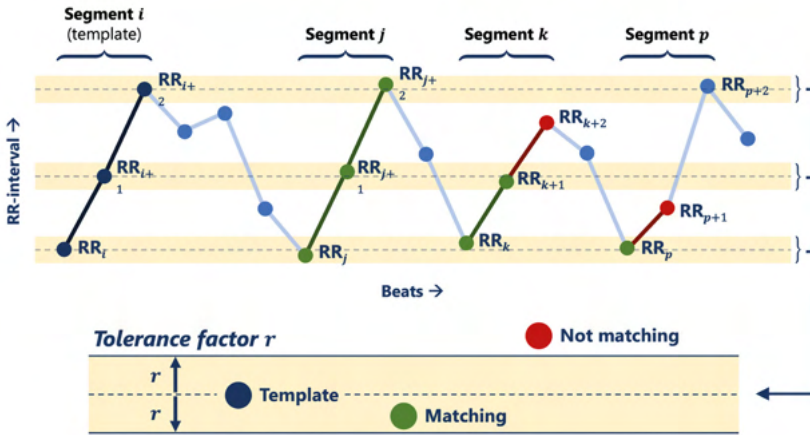
Figure 5 – Schematic visualization of matching used in sample entropy. Segment i is used as a template to compare with segments j, k and p. When setting the prior window length to one RR-interval, hence comparing only the first RR-interval of the segments, all three segments match the template. However, only segments j and k match for the next RR-interval, since RR_{p+1} is below the tolerance range. Increasing the prior window length from one to two RR-intervals results in segment p not matching the template, hence only segments j and k will be tested to match the next RR-interval. In this case, only segment j meets this requirement, as RR_{k+2} is below the tolerance range.

entropy increases, hence a higher sample entropy reflects that the next RR-interval is less predictable, i.e., indicates a higher variability of the signal.

The sample entropy is highly dependent on the tolerance factor, since the probability of two segments of RR-intervals matching increases with increasing tolerance factors. Therefore, Lake et al.[49] proposed to correct the sample entropy by subtracting $\ln(2r)$. Furthermore, they observed that heart rate and sample entropy add independent information to detect AF, hence proposed an optimization of the sample entropy for AF detection by subtracting the natural logarithm of the mean RR-interval. The coefficient of the sample entropy (CoSEn) is then defined as:

$$\text{CoSEn} = \text{SampEn} - \ln(2r) - \ln(\overline{\text{RR}}) \qquad (1)$$

where SampEn is the sample entropy, r is the tolerance factor, and $\overline{\text{RR}}$ is the mean RR-interval.

Alternatively, the Shannon entropy expresses the information or uncertainty of RR-intervals by describing the histogram of already observed RR-intervals in a single metric.[50] When all RR-intervals are similar (i.e., the histogram consists of one single bar), the Shannon entropy equals zero. In contrast, when the variation of RR-intervals is higher, the Shannon entropy increases, hence a higher Shannon entropy – like the sample entropy – indicates that the next RR-interval is less predictable, which is the case during AF.

Turning Point Ratio (TPR) of RR-intervals
A turning point (TP) of an RR-intervals series is defined as an RR-interval which is larger or smaller than both the preceding and succeeding RR-intervals (i.e., a local maximum or minimum). The turning point ratio (TPR) is given by dividing the total number of TP by the total length of the RR-interval series.[11] An ECG during SR, even in segments with an increasing or decreasing heart rate, will show relatively few turning points since RR-intervals are regular or steadily increasing or decreasing. During AF, however, RR-intervals are irregular, hence the TPR is expected to be higher.

29

Lyapunov exponent of RR-intervals
Lyapunov exponents describe the divergence of a system for two near equal inputs. Starting with multiple RR-intervals within a narrow range of values at different time points, the Lyapunov exponent is a measure for the variation between trajectories from those points, which is described as the mean distance between the trajectories.[39] For ECGs during SR, the trajectories are not expected to diverge significantly, whereas during AF, since RR-intervals are irregular, the trajectories will show more variation, hence the Lyapunov exponent is larger.

Signal features

In addition to these easily interpretable features, more abstract signal features describe the signal characteristics in terms of statistical measures, wavelet analysis, phase space analysis, Lyapunov exponents, bispectral analysis and signal quality. These features are not specifically related to cardiac electrophysiology, but describe the signal more fundamentally. Furthermore, NNs allow the user to input an entire fixed-length ECG recording, after which the NN is trained to detect the most distinctive features, which are mostly abstract and difficult to interpret.

Basic signal properties and statistical measures
Signals can be described using basic signal properties and statistical measures, including the maximum and minimum amplitude, signal length, signal power, kurtosis, quartiles and average value of the first derivative with respect to time.[41,51-53] It must be noted that classification based only on these measures is not expected to be feasible, since these features mainly describe the nature of the signal, and do not provide information on the source of the actual signal.[53]

Power spectral analysis, bispectral analysis and wavelet transform
Using the Fourier transform, the frequency spectrum of the signal can be computed by decomposing the signal into sinusoids with different frequencies, amplitudes and phase shifts. Whilst ECGs containing regular SR are expected to produce narrow peaks in the Fourier spectrum at the fundamental frequency and the harmonics, due to irregularity an ECG containing AF might show more dispersion in the Fourier spectrum.[54]

Similar to the Fourier transform, bispectral analysis focusses on describing the signal in terms of the frequency components. However, with bispectral analysis the interaction between frequency components is analyzed.[55] Therefore, an additional layer of complexity is added. As a result, features extracted from bispectral analysis are not easily manually interpreted.

Although the Fourier transform is conceptually relatively simple, it has a bad trade-off between time-frequency localization; being very localized in the frequency domain, while very non-localized in time. The wavelet transform uses wavelets instead of sinusoids. Wavelets are designed to have limited duration, which can be varied. Therefore, they have an improved joint time-frequency localization.[56] Instead of transforming the signal to the frequency domain, the signal is transformed to time-frequency domain, which enables extraction of new signal features from this domain or using the transformed signal as input for NNs. Similar to the higher dispersion in the Fourier transform, a higher dispersion in the wavelet power spectrum is expected to be observed in ECGs during AF, which is mostly described in terms of increased entropy.[57,58]

Phase space analysis
Instead of analyzing signals in the time and frequency domain, they can be converted into

a phase space, which describes the relation between the original signal and a delayed version of the signal.[59,60] Similar to the Poincaré representation of RR-intervals, using a time delay embedding a plot is generated of the signal amplitude at time t on the x-axis and signal amplitude at time $t + \tau$ on the y-axis, where τ is the chosen time delay. Moreover, using more dimensions with different time delays, even more complex relations can be described.[61] The density of data points in the phase space can be described by segmenting the phase space into smaller regions and counting the number of points in each region.[59,62] In ECGs during SR, the beat-to-beat trajectories of data points are expected to be almost similar. Therefore, data points will be concentrated in a limited number of regions. However, during AF, more variation might result in a larger dispersion of data points over all regions.

Lyapunov exponents

Additionally, to the Lyapunov exponents from the RR-intervals, Lyapunov exponents can be calculated from the raw ECG signal. For analysis of Lyapunov exponents from raw ECGs, the signal is transformed into the phase space.[63] Next, a starting point is chosen and all points within a set radius are detected. The distance between the trajectories from all these points ("near equal inputs") is a measure for the divergence of the trajectories. Again, since the beat-to-beat trajectories of the ECG signal during SR are expected to be almost similar, low Lyapunov exponents are expected. Instead, during AF, as a result of more variation in trajectories, higher Lyapunov exponents are more likely to be observed.

Signal quality

Lastly, several methods use measures to describe the quality of the ECG signal. Multiple measures for signal quality have been proposed. Athif et al.[64] describe signal quality in terms of correlation of each beat with a template beat. Instead, Shao et al.[43] focus on the amplitudes of isoelectric level, and Smisek et al.[65] and Oster et al.[42] compare outputs of multiple QRS-complex detectors.

Discussion

A variety of features from ECG signals are available to describe both atrial and ventricular activity, and general signal characteristics. Using these features, an increasing number of studies focusses on extracting optimal digital biomarkers for AF detection from ECGs. A trend towards using more complex classifiers is observed, predominantly using ventricular features and signal features.

29

Comparing AF detection algorithms

The median F1-score for AF detection was 94.0%. Since all included studies used their own methods for detecting AF from ECGs, comparing the performances of the different classifiers might provide useful insight into the overall performances of classification methods. However, these results should be interpreted with great care, since, as pointed out by Ghodrati et al.[12], used databases all focus on a specific group of patients. This focus results in databases which are not representative of the entire patient population. Therefore, training a classifier using these databases might cause the classifier to overfit, hence in clinical practice the accuracy is lower due to, for example, differences in signal quality and prevalence of cardiac arrhythmias. Furthermore, the prevalence of AF in a certain database directly impacts the calculated accuracy measures, making it complex to compare classifiers which were developed and tested using different datasets. For example, the PPV is calculated as the percentage of AF classifications which are correct (i.e., percentage of times the classifier concludes an ECG segment contains AF and the reference label is AF). A higher AF prevalence inherently results in a higher PPV since the a priori probability for an

AF classification is higher. Besides the mathematical difficulty of comparing these classifiers, bias could be introduced as a result of one database containing signals which are easier to classify (e.g., only high signal quality and only SR and AF) and the other database containing signals in which the classification is less straightforward (e.g., varying signal quality and multiple arrhythmias). As pointed out earlier, multiple studies in this review showed large variation in performance depending on the used testing database. This relation was only demonstrated for R-peak detection, but most likely there is an even stronger relation for detection of atrial features as a result of the lower amplitude of P-waves. As a result, classifier performance measures are not easily generalized and compared when different databases are used.[3] Moreover, variation in study aim most likely resulted in different trade-offs being made in the classifier design. For example, detecting whether a patient has AF or detecting the duration of AF episodes requires different approaches and studies with these aims will therefore report incomparable performance measures. Furthermore, not all studies use a hidden test set to determine the classifier performance measures, and instead report performance measures from k-fold cross-validation. In contrast to validation using a hidden testing database, no information about the generalizability of the classification methods is obtained using this validation method.

In 2017, the PhysioNet/CinC Challenge focused on AF detection from a single short ECG lead recording.[3] In this challenge, all participants used the same labeled dataset for training and validation (8,528 recordings) and for testing (3,658 recordings). The test set was hidden during the challenge. Therefore, all AF detection algorithms were tested on the same set of ECGs, eliminating the variation between datasets used in different studies. Still, no single optimal classification method was appointed during the challenge, potentially due to the dataset being too small to give complex approaches an advantage.[3]

Most optimally, all studies use the same testing dataset which is representative of a large patient population. Since this is currently not the case, the results in *Table 2*, showing the F1-scores per set of feature groups (atrial / ventricular / signal), should be interpreted with care. However, in the included studies, classifiers using only ventricular features seemed to result in the highest F1-scores. Most likely, this is caused by the fact that studies on optimal features for AF detection mostly focus on ventricular features, hence these are more evolved than atrial features.

Challenges in detecting atrial activity

Already in normal ECGs, a major challenge in detecting atrial activity is the relatively low signal amplitude compared to ventricular activity. During AF the disorganized atrial impulses do not result in a clear P-wave, but deterioration to f-waves with an even lower signal amplitude. Therefore, for intra-cardial mapping a more advanced method for the detection of atrial activity using QRS-T subtraction has been described by Salinet et al.[66] First, the QRS-complexes and T-waves are detected in the surface ECG. Next, the QT-pattern of the intra-cardiac signals is computed, which is then used subtract the ventricular activity from the intra-cardiac measurements. Similarly, Rieta et al.[67] propose three methods to cancel out ventricular activity in intra-cardiac signals using the surface ECG. Using the first method, template matching is applied to compute an average pattern, which is then subtracted from the original signal. Adaptive ventricular cancellation is more complex and aims to estimate the atrial ($a(t)$) and ventricular ($v(t)$) components of the signal $m(t)$, which is described by $m(t) = a(t) + v(t)$. The surface ECG is used as a reference for the ventricular activity. Using a filter based on this reference signal, $a(t)$ is estimated by minimizing the error signal $e(t) = a(t) + v(t) - \hat{v}(t)$, where $\hat{v}(t)$ is the filter output. Lastly, independent component analysis aims to separate the signal into an atrial source and ventricular source based on

the assumption that the sources are mutually independent. Although these methods are applied to cancel out ventricular activity from intra-cardiac signals, in a similar way, using a combination of surface ECG leads, QRS-T subtraction could potentially be applied to improve the accuracy of atrial activity detection in surface ECGs.

Besides atrial activity being characterized by a relatively low signal amplitude compared to ventricular activity, noise is another obstacle in detecting atrial activity that also impacts the classification accuracy.[68] A recent review on ECG filtering techniques to eliminate power line interference shows that choosing the optimal filter technique is not straightforward, since each technique has its own advantages and disadvantages.[69] Therefore, they propose to use hybrid noise reduction methods which consist of combinations of multiple filtering techniques. More research on optimal filtering techniques for atrial activity detection in ECGs might further improve the detection of atrial activity.

Limitations

Since algorithm development aims to improve classifier accuracy, many studies solely report the performance measures of the final optimized classifier, without the various alternative classifiers which were trained and validated, but which turned out sub-optimal. This potential publication bias might have impacted the larger picture.

Future perspectives

AF burden is an emerging risk factor for ischemic stroke.[2] The 2020 ESC Guidelines for diagnosis and management of AF use the classification of AF with only five classes (first diagnosed, paroxysmal, persistent, long-standing persistent and permanent).[1] However, the AF burden could be more accurately described using the duration, number of episodes and/or proportion of time an individual is in AF during a monitoring period.[2] Since manual analysis of continuous rhythm registrations is unfeasible, new methods should focus on transparent, yet accurate automated AF detection.

The current studies suggest that using only ventricular features gives the highest accuracy. However, research reporting on atrial activity during AF is relatively scarce. When more research is done on methods to optimally describe atrial activity, the transparency might improve without compromising on classifier accuracy. Although AF is an atrial disease, more than 75% of the methods focus on ventricular features, signal features, or a combination of both. Whilst more complex classifiers are likely to be more accurate, interpretation of the algorithms is becoming more and more difficult due to complex feature sets and NNs processing the signal as a 'black box'. Less than 25% of the methods include features which are derived directly from atrial signal, since mainly due to suboptimal signal quality, atrial activity is difficult to detect. This obstacle might be overcome by using advanced filtering techniques and/or using multi-lead ECG signals, in contrast to most methods only using a limited number of ECG leads. More specifically, using multiple ECG leads in advanced QRS-T subtraction and noise removal methods might facilitate more accurate detection of atrial activity. By using atrial features, AF detection is performed closer to the source and decisions made by AF detection algorithms might remain more transparent.

More generally, due to differences between testing protocols of studies and potential publication bias, comparing performance measures of studies is not feasible. Therefore, we recommend to use a standardized testing protocol for all trained and validated classifiers with a standardized hidden testing database which contains different ECGs with various cardiac arrhythmias and varying signal quality and lead configurations. Currently available

29

databases are the commonly used PhysioNet databases.[5] However, these are not the only databases containing large amounts of ECG data. For example, in 2019, Attia et al.[70] used a dataset containing 1,000,000 12-lead ECGs of more than 200,000 patients from the Mayo Clinic ECG laboratory to train a classifier to detect patients with AF during SR.

Conclusion

Over the past years, an increasing number of studies on AF detection have been performed. More and more studies focus on classification algorithms with complex features sets and non-transparent classifiers. Although AF is an atrial disease, less than 25% of the methods include features which are derived directly from atrial signal. Developing new innovative methods focusing on detection of atrial activity might provide accurate classifiers without compromising on transparency.

References

1. Hindricks G, Potpara T, Dagres N, Arbelo E, Bax JJ, Blomstrom-Lundqvist C, Boriani G, Castella M, Dan GA, Dilaveris PE, et al. 2020 ESC Guidelines for the diagnosis and management of atrial fibrillation developed in collaboration with the European Association for Cardio-Thoracic Surgery (EACTS): The Task Force for the diagnosis and management of atrial fibrillation of the European Society of Cardiology (ESC) Developed with the special contribution of the European Heart Rhythm Association (EHRA) of the ESC. Eur Heart J. 2021;42:373-498.
2. Chen LY, Chung MK, Allen LA, Ezekowitz M, Furie KL, McCabe P, Noseworthy PA, Perez MV, Turakhia MP, American Heart Association Council on Clinical C, et al. Atrial Fibrillation Burden: Moving Beyond Atrial Fibrillation as a Binary Entity: A Scientific Statement From the American Heart Association. Circulation. 2018;137:e623-e644.
3. Clifford GD, Liu C, Moody B, Lehman LH, Silva I, Li Q, Johnson AE, Mark RG. AF Classification from a Short Single Lead ECG Recording: the PhysioNet/Computing in Cardiology Challenge 2017. Comput Cardiol (2010). 2017;44.
4. Moody GB, Mark RG. The impact of the MIT-BIH arrhythmia database. IEEE Eng Med Biol Mag. 2001;20:45-50.
5. Goldberger AL, Amaral LA, Glass L, Hausdorff JM, Ivanov PC, Mark RG, Mietus JE, Moody GB, Peng CK, Stanley HE. PhysioBank, PhysioToolkit, and PhysioNet: components of a new research resource for complex physiologic signals. Circulation. 2000;101:E215-220.
6. Moody GB, Mark RG. A new method for detecting atrial fibrillation using R-R intervals. Computers in Cardiology. 1983;10:227-230.
7. Zhou X, Ding H, Ung B, Pickwell-MacPherson E, Zhang Y. Automatic online detection of atrial fibrillation based on symbolic dynamics and Shannon entropy. Biomed Eng Online. 2014;13:18.
8. Li Y, Tang X, Wang A, Tang H. Probability density distribution of delta RR intervals: a novel method for the detection of atrial fibrillation. Australas Phys Eng Sci Med. 2017;40:707-716.
9. Islam MS, Ammour N, Alajlan N, Aboalsamh H. Rhythm-based heartbeat duration normalization for atrial fibrillation detection. Comput Biol Med. 2016;72:160-169.
10. Zhou X, Ding H, Wu W, Zhang Y. A Real-Time Atrial Fibrillation Detection Algorithm Based on the Instantaneous State of Heart Rate. PLoS One. 2015;10:e0136544.
11. Dash S, Chon KH, Lu S, Raeder EA. Automatic real time detection of atrial fibrillation. Ann Biomed Eng. 2009;37:1701-1709.
12. Ghodrati A, Murray B, Marinello S. RR interval analysis for detection of Atrial Fibrillation in ECG monitors. Annu Int Conf IEEE Eng Med Biol Soc. 2008;2008:601-604.
13. Baalman SWE, Schroevers FE, Oakley AJ, Brouwer TF, van der Stuijt W, Bleijendaal H, Ramos LA, Lopes RR, Marquering HA, Knops RE, et al. A morphology based deep learning model for atrial fibrillation detection using single cycle electrocardiographic samples. Int J Cardiol. 2020;316:130-136.
14. Hsieh CH, Li YS, Hwang BJ, Hsiao CH. Detection of Atrial Fibrillation Using 1D Convolutional Neural Network. Sensors (Basel). 2020;20.
15. Huang ML, Wu YS. Classification of atrial fibrillation and normal sinus rhythm based on convolutional neural network. Biomed Eng Lett. 2020;10:183-193.
16. Rajan Jeyaraj P, Nadar ERS. Atrial fibrillation classification using deep learning algorithm in Internet of Things-based smart healthcare system. Health Informatics J. 2020;26:1827-1840.
17. Ping Y, Chen C, Wu L, Wang Y, Shu M. Automatic Detection of Atrial Fibrillation Based on CNN-LSTM and Shortcut Connection. Healthcare (Basel). 2020;8.
18. Teplitzky BA, McRoberts M, Ghanbari H. Deep learning for comprehensive ECG annotation. Heart Rhythm. 2020;17:881-888.
19. Wu Q, Sun Y, Yan H, Wu X. ECG signal classification with binarized convolutional neural network. Comput Biol Med. 2020;121:103800.
20. Zhang X, Gu K, Miao S, Zhang X, Yin Y, Wan C, Yu Y, Hu J, Wang Z, Shan T, et al. Automated detection of cardiovascular disease by electrocardiogram signal analysis: a deep learning system. Cardiovasc Diagn Ther. 2020;10:227-235.
21. Lee KS, Jung S, Gil Y, Son HS. Atrial fibrillation classification based on convolutional neural networks. BMC Med Inform Decis Mak. 2019;19:206.
22. Ribeiro ALP, Paixao GMM, Gomes PR, Ribeiro MH, Ribeiro AH, Canazart JA, Oliveira DM, Ferreira MP, Lima EM, Moraes JL, et al. Tele-electrocardiography and bigdata: The CODE (Clinical Outcomes in Digital Electrocardiography) study. J Electrocardiol. 2019;57S:S75-S78.
23. Fan X, Yao Q, Cai Y, Miao F, Sun F, Li Y. Multiscaled Fusion of Deep Convolutional Neural Networks for Screening Atrial Fibrillation From Single Lead Short ECG Recordings. IEEE J Biomed Health Inform. 2018;22:1744-1753.
24. Kamaleswaran R, Mahajan R, Akbilgic O. A robust deep convolutional neural network for the classification of abnormal cardiac rhythm using single lead electrocardiograms of variable length. Physiol Meas. 2018;39:035006.
25. Warrick PA, Nabhan Homsi M. Ensembling convolutional and long short-term memory networks for electrocardiogram arrhythmia detection. Physiol Meas. 2018;39:114002.
26. Xiong Z, Nash MP, Cheng E, Fedorov VV, Stiles MK, Zhao J. ECG signal classification for the detection of cardiac arrhythmias using a convolutional recurrent neural network. Physiol Meas. 2018;39:094006.
27. Elgendi M, Meo M, Abbott D. A Proof-of-Concept Study: Simple and Effective Detection of P and T Waves in Arrhythmic ECG Signals. Bioengineering (Basel). 2016;3.
28. Chen Y, Wang X, Jung Y, Abedi V, Zand R, Bikak M, Adibuzzaman M. Classification of short single-lead electrocardiograms (ECGs) for atrial fibrillation detection using piecewise linear spline and XGBoost. Physiol Meas. 2018;39:104006.
29. Du X, Rao N, Qian M, Liu D, Li J, Feng W, Yin L, Chen X. A novel method for real-time atrial fibrillation detection in electrocardiograms using multiple parameters. Ann Noninvasive Electrocardiol. 2014;19:217-225.

29

30. Marinucci D, Sbrollini A, Marcantoni I, Morettini M, Swenne CA, Burattini L. Artificial Neural Network for Atrial Fibrillation Identification in Portable Devices. Sensors (Basel). 2020;20.

31. Mukherjee A, Dutta Choudhury A, Datta S, Puri C, Banerjee R, Singh R, Ukil A, Bandyopadhyay S, Pal A, Khandelwal S. Detection of atrial fibrillation and other abnormal rhythms from ECG using a multi-layer classifier architecture. Physiol Meas. 2019;40:054006.

32. Zheng J, Chu H, Struppa D, Zhang J, Yacoub SM, El-Askary H, Chang A, Ehwerhemuepha L, Abudayyeh I, Barrett A, et al. Optimal Multi-Stage Arrhythmia Classification Approach. Sci Rep. 2020;10:2898.

33. Liu N, Sun M, Wang L, Zhou W, Dang H, Zhou X. A support vector machine approach for AF classification from a short single-lead ECG recording. Physiol Meas. 2018;39:064004.

34. Rizwan M, Whitaker BM, Anderson DV. AF detection from ECG recordings using feature selection, sparse coding, and ensemble learning. Physiol Meas. 2018;39:124007.

35. Pan J, Tompkins WJ. A real-time QRS detection algorithm. IEEE Trans Biomed Eng. 1985;32:230-236.

36. Sacha J. Interaction between heart rate and heart rate variability. Ann Noninvasive Electrocardiol. 2014;19:207-216.

37. Kennedy A, Finlay DD, Guldenring D, Bond RR, Moran K, McLaughlin J. Automated detection of atrial fibrillation using R-R intervals and multivariate-based classification. J Electrocardiol. 2016;49:871-876.

38. Bashar SK, Hossain MB, Ding E, Walkey AJ, McManus DD, Chon KH. Atrial Fibrillation Detection During Sepsis: Study on MIMIC III ICU Data. IEEE J Biomed Health Inform. 2020;24:3124-3135.

39. Asl BM, Setarehdan SK, Mohebbi M. Support vector machine-based arrhythmia classification using reduced features of heart rate variability signal. Artif Intell Med. 2008;44:51-64.

40. Czabanski R, Horoba K, Wrobel J, Matonia A, Martinek R, Kupka T, Jezewski M, Kahankova R, Jezewski J, Leski JM. Detection of Atrial Fibrillation Episodes in Long-Term Heart Rhythm Signals Using a Support Vector Machine. Sensors (Basel). 2020;20.

41. Lown M, Brown M, Brown C, Yue AM, Shah BN, Corbett SJ, Lewith G, Stuart B, Moore M, Little P. Machine learning detection of Atrial Fibrillation using wearable technology. PLoS One. 2020;15:e0227401.

42. Oster J, Hopewell JC, Ziberna K, Wijesurendra R, Camm CF, Casadei B, Tarassenko L. Identification of patients with atrial fibrillation: a big data exploratory analysis of the UK Biobank. Physiol Meas. 2020;41:025001.

43. Shao M, Zhou Z, Bin G, Bai Y, Wu S. A Wearable Electrocardiogram Telemonitoring System for Atrial Fibrillation Detection. Sensors (Basel). 2020;20.

44. Nguyen A, Ansari S, Hooshmand M, Lin K, Ghanbari H, Gryak J, Najarian K. Comparative Study on Heart Rate Variability Analysis for Atrial Fibrillation Detection in Short Single-Lead ECG Recordings. Annu Int Conf IEEE Eng Med Biol Soc. 2018;2018:526-529.

45. Jeon T, Kim B, Jeon M, Lee BG. Implementation of a portable device for real-time ECG signal analysis. Biomed Eng Online. 2014;13:160.

46. Park J, Lee S, Jeon M. Atrial fibrillation detection by heart rate variability in Poincare plot. Biomed Eng Online. 2009;8:38.

47. Esperer HD, Esperer C, Cohen RJ. Cardiac arrhythmias imprint specific signatures on Lorenz plots. Ann Noninvasive Electrocardiol. 2008;13:44-60.

48. Pincus SM. Approximate entropy as a measure of system complexity. Proc Natl Acad Sci U S A. 1991;88:2297-2301.

49. Lake DE, Moorman JR. Accurate estimation of entropy in very short physiological time series: the problem of atrial fibrillation detection in implanted ventricular devices. Am J Physiol Heart Circ Physiol. 2011;300:H319-325.

50. Dharmaprani D, Dykes L, McGavigan AD, Kuklik P, Pope K, Ganesan AN. Information Theory and Atrial Fibrillation (AF): A Review. Front Physiol. 2018;9:957.

51. Kropf M, Hayn D, Morris D, Radhakrishnan AK, Belyavskiy E, Frydas A, Pieske-Kraigher E, Pieske B, Schreier G. Cardiac anomaly detection based on time and frequency domain features using tree-based classifiers. Physiol Meas. 2018;39:114001.

52. Queiroz JA, Junior A, Lucena F, Barros AK. Diagnostic decision support systems for atrial fibrillation based on a novel electrocardiogram approach. J Electrocardiol. 2018;51:252-259.

53. Lemkaddem A, Proenca M, Delgado-Gonzalo R, Renevey P, Oei I, Montano G, Martinez-Heras JA, Donati A, Bertschi M, Lemay M. An autonomous medical monitoring system: Validation on arrhythmia detection. Annu Int Conf IEEE Eng Med Biol Soc. 2017;2017:4553-4556.

54. Kruger GH, Latchamsetty R, Langhals NB, Yokokawa M, Chugh A, Morady F, Oral H, Berenfeld O. Bimodal classification algorithm for atrial fibrillation detection from m-health ECG recordings. Comput Biol Med. 2019;104:310-318.

55. Khadra L, Al-Fahoum AS, Binajjaj S. A quantitative analysis approach for cardiac arrhythmia classification using higher order spectral techniques. IEEE Trans Biomed Eng. 2005;52:1840-1845.

56. Priestley MB. WAVELETS AND TIME-DEPENDENT SPECTRAL ANALYSIS. Journal of Time Series Analysis. 1996;17:85-103.

57. Bruun IH, Hissabu SMS, Poulsen ES, Puthusserypady S. Automatic Atrial Fibrillation detection: A novel approach using discrete wavelet transform and heart rate variability. Annu Int Conf IEEE Eng Med Biol Soc. 2017;2017:3981-3984.

58. Asgari S, Mehrnia A, Moussavi M. Automatic detection of atrial fibrillation using stationary wavelet transform and support vector machine. Comput Biol Med. 2015;60:132-142.

59. Al-Fahoum AS, Qasaimeh AM. A practical reconstructed phase space approach for ECG arrhythmias classification. J Med Eng Technol. 2013;37:401-408.

60. Liu CS, Tseng WK, Lee JK, Hsiao TC, Lin CW. The differential method of phase space matrix for AF/VF discrimination

application. Med Eng Phys. 2010;32:444-453.

61. Marwan N, Carmen Romano M, Thiel M, Kurths J. Recurrence plots for the analysis of complex systems. Physics Reports. 2007;438:237-329.

62. Parvaneh S, Rubin J, Rahman A, Conroy B, Babaeizadeh S. Analyzing single-lead short ECG recordings using dense convolutional neural networks and feature-based post-processing to detect atrial fibrillation. Physiol Meas. 2018;39:084003.

63. Ubeyli ED. Adaptive neuro-fuzzy inference system for classification of ECG signals using Lyapunov exponents. Comput Methods Programs Biomed. 2009;93:313-321.

64. Athif M, Yasawardene PC, Daluwatte C. Detecting atrial fibrillation from short single lead ECGs using statistical and morphological features. Physiol Meas. 2018;39:064002.

65. Smisek R, Hejc J, Ronzhina M, Nemcova A, Marsanova L, Kolarova J, Smital L, Vitek M. Multi-stage SVM approach for cardiac arrhythmias detection in short single-lead ECG recorded by a wearable device. Physiol Meas. 2018;39:094003.

66. Salinet JL, Jr., Madeiro JP, Cortez PC, Stafford PJ, Ng GA, Schlindwein FS. Analysis of QRS-T subtraction in unipolar atrial fibrillation electrograms. Med Biol Eng Comput. 2013;51:1381-1391.

67. Rieta JJ, Hornero F. Comparative study of methods for ventricular activity cancellation in atrial electrograms of atrial fibrillation. Physiol Meas. 2007;28:925-936.

68. Liu F, Liu C, Jiang X, Zhang Z, Zhang Y, Li J, Wei S. Performance Analysis of Ten Common QRS Detectors on Different ECG Application Cases. J Healthc Eng. 2018;2018:9050812.

69. Malghan PG, Hota MK. A review on ECG filtering techniques for rhythm analysis. Research on Biomedical Engineering. 2020;36:171-186.

70. Attia ZI, Noseworthy PA, Lopez-Jimenez F, Asirvatham SJ, Deshmukh AJ, Gersh BJ, Carter RE, Yao X, Rabinstein AA, Erickson BJ, et al. An artificial intelligence-enabled ECG algorithm for the identification of patients with atrial fibrillation during sinus rhythm: a retrospective analysis of outcome prediction. Lancet. 2019;394:861-867.

29
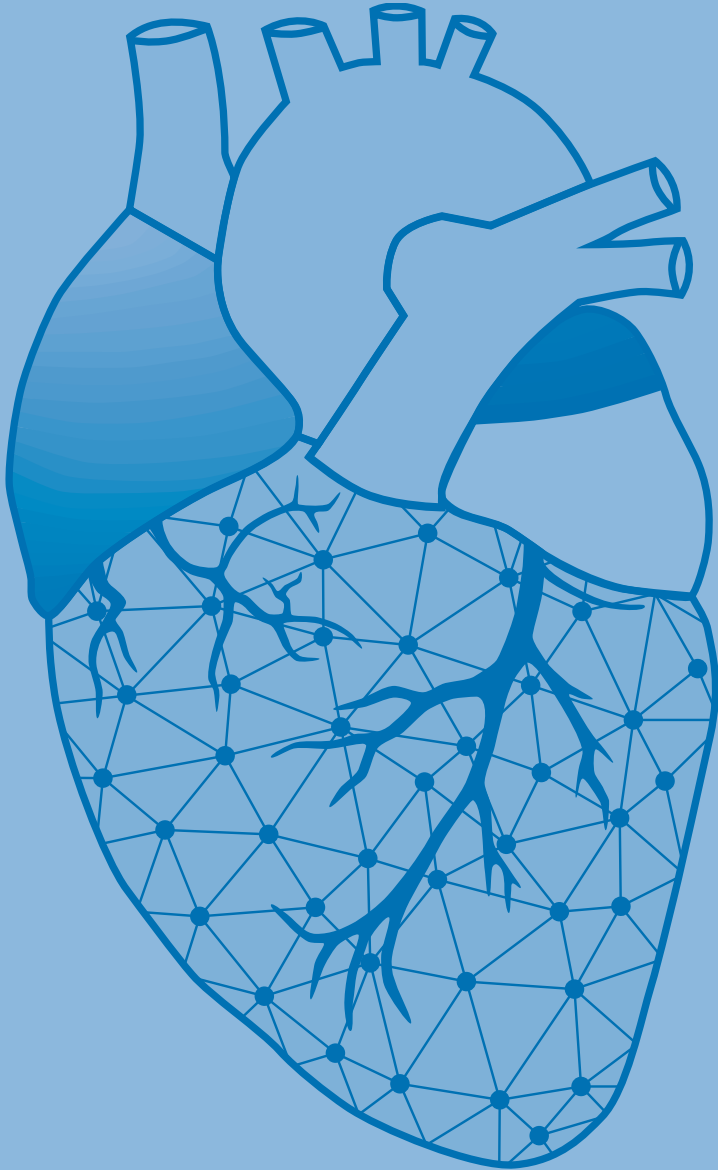
Chapter 30

An accurate and efficient method to train classifiers for atrial fibrillation detection in ECGs: learning by asking better questions

Fons J. Wesselius

Mathijs S. van Schie

Natasja M.S. de Groot

Richard C. Hendriks

Abstract

Background: An increasing number of wearables are capable of measuring electrocardiograms (ECGs), which may help in early detection of atrial fibrillation (AF). Therefore, many studies focus on automated detection of AF in ECGs. A major obstacle is the required amount of manually labelled data. This study aimed to provide an efficient and reliable method to train a classifier for AF detection using large datasets of real-life ECGs.

Method: Human-controlled semi-supervised learning was applied, consisting of two phases: the *pre-training phase* and the *semi-automated training phase*. During pre-training, an initial classifier was trained, which was used to predict the classes of new ECG segments in the semi-automated training phase. Based on the degree of certainty, segments were added to the training dataset automatically or after human validation. Thereafter, the classifier was retrained and this procedure was repeated. To test the model performance, a real-life telemetry dataset containing 3,846,564 30-seconds ECG segments of hospitalized patients (n=476) and the CinC Challenge 2017 database were used.

Results: After pre-training, the average F1-score on a hidden testing dataset was 89.0%. Furthermore, after the pre-training phase 68.0% of all segments in the hidden test set could be classified with an estimated probability of successful classification of 99%, providing an F1-score of 97.9% for these segments. During the semi-automated training phase, this F1-score showed little variation (97.3−97.9% in the hidden test set), whilst the number of segments which could be automatically classified increased from 68.0% to 75.8% due to the enhanced training dataset. At the same time, the overall F1-score increased from 89.0% to 91.4%.

Conclusions: Human-validated semi-supervised learning makes training a classifier more time efficient without compromising on accuracy, hence this method might be valuable in the automated detection of AF in real-life ECGs.

Journal site &
supplementary material

Introduction

With the introduction of photoplethysmography pulse waveform measurements in wearables, these consumer products have made their entrance into the early detection of heart rhythm disorders by monitoring the heart rate. In addition to photoplethysmography, an increasing number of smartwatches and other wearables are also capable of measuring electrocardiograms (ECGs), hence not only providing insight into the rate of cardiac contractions, but also in the electrical activation of the heart.[1] Given the fact that in the 4th quarter of 2019 alone already 118.9 million wearable devices were shipped worldwide[2] and the market is expected to grow further to a market value of $150 billion in 2026[3], wearables could potentially play an increasingly important role in the early detection of heart rhythm disorders, in particular atrial fibrillation (AF), which, with an estimated prevalence of 2–4% in adults, is the most common sustained cardiac arrhythmia worldwide.[4] Although the ESC Guidelines[4] and EHRA consensus statements[5] recommend that a definite diagnosis of AF can only be established after an ECG recording has been reviewed by a physician, accurate wearable measurements could help in the early detection of AF.

Challenges in automated AF detection using ECGs

In the ECG, AF is characterized by irregular RR-intervals, absence of P-waves and presence of fibrillatory waves. Already in the early 90s, multiple studies endeavored to automatically analyze ECGs in order to automatically detect AF.[6-8] During recent years, the number of studies focusing on automated detection of AF in ECGs steeply increased.[9] Automated AF detection comes with two important challenges. First, the need for good features that can accurately distinguish AF from other rhythms. Although the differences between normal sinus rhythm and AF are apparent, differentiating AF from other irregular rhythms (e.g., frequent ventricular extrasystoles or atrial extrasystoles, or sinus arrhythmia) is more complicated, since almost 40% of the proposed algorithms solely rely on the irregularity of ventricular activity as a feature of AF.[9] The incidence of cardiac arrhythmias in general is substantial, particularly in older patients or patients with cardiovascular comorbidities.[10] Furthermore, after cardiac surgery, the reported incidence of post-operative AF (PoAF) is even up to 60%.[11] In patients with PoAF, an increased long-term mortality and stroke incidence was observed, indicating an even higher relevance of early AF detection in these more complex ECGs.

Although new studies mainly innovate on the extracted features from ECGs and the used classification algorithms[9], the next challenge is related to the fact that accurate classification heavily depends on the presence of enough accurately labelled data. In 2017, the yearly Computing in Cardiology (CinC) Challenge focused on detecting AF in short term ECG recordings using a training set of 8,528 samples. Entries in the competition showed F1-scores up to 83.1%, indicating that it is possible to successfully train a classifier to automatically and accurately detect AF.[12] However, the expected advantage of more complex machine learning-based methods (e.g., convolutional neural networks and recurrent neural networks) was not observed. Clifford et al.[12] state that this might be caused by the limited size of the training dataset. However, manually labeling a large number of samples to generate a larger training set is time-consuming and hence might introduce inaccuracies.

30

Machine learning techniques

Traditionally, classifiers are trained using supervised learning, meaning that, in order to train an accurate classifier, all data has to be manually labelled.[13] As an alternative, *semi-supervised learning* can be used to automatically fill a training dataset based on classifier output without manual intervention, also called self-training. First an initial classifier is trained

using manually classified data, after which the training set is augmented with automatically classified data and then re-trained.[14] Using this technique, once self-training has started, there is no guarantee that the augmented data is classified correctly. Furthermore, the classifier does not learn from human input anymore, hence erroneous classifications might introduce tunnel vision to a wrong class for certain combinations of features. Therefore, with semi-supervised learning for AF detection in complex ECGs, recordings containing a variety of different cardiac rhythms, noise levels and artefacts should be represented in the initial training dataset. Another way to limit the required amount of labelled data is using *transfer learning*, in which an already trained classifier from a similar task is used as a starting point to train a classifier for a new task. De Cooman et al.[15] showed that this method is fast and robust for the detection of seizures based on heart rate. First, they trained a classifier using offline patient-independent data and then used this classifier to analyze patient-specific data. Lastly, reinforcement learning is a method which tries to learn from a dataset, but also tries to optimize its reaction to a situation in order to optimize the reward, which, in this case, is the classification accuracy, expressed as the F1-score.[16]

Study aim

The output of a classifier does not necessarily solely consist of the *predicted class* of a newly analyzed sample, but can also contain information on the estimated *probability* of a sample being in a certain class.[17] This information could potentially be used to train the classifier behavior in a reinforcement learning-based approach. Furthermore, a transfer learning-based approach might reduce the required size of the training dataset. Therefore, the aim of this study was to develop and test an efficient and reliable method to train a classifier on a large dataset containing real-life telemetry data without manually classifying all samples, but by combining semi-supervised learning, reinforcement learning and transfer learning techniques, taking into account the degree of certainty of the classifier.
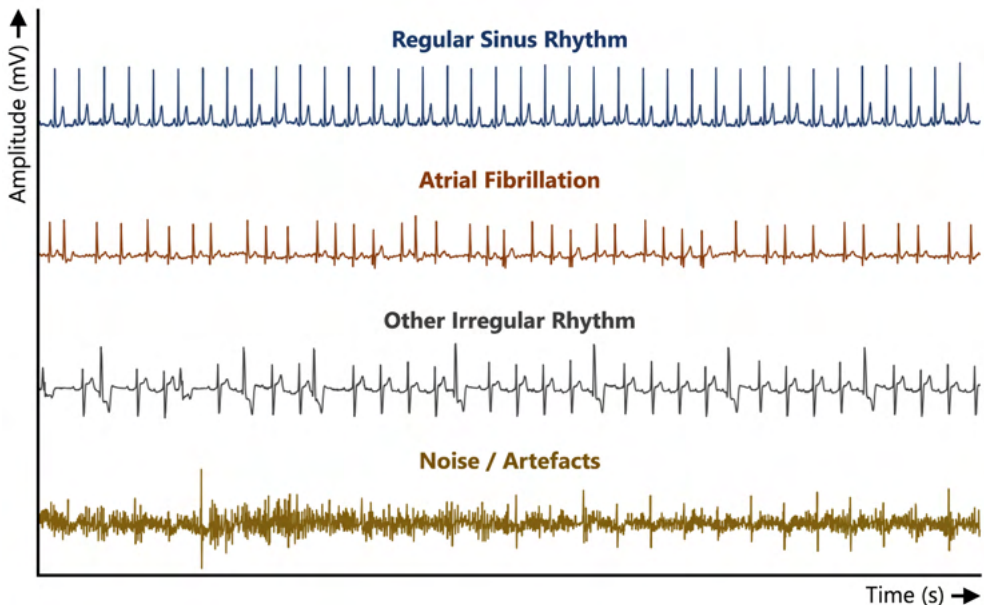
Figure 1 – Typical ECG segments of the four different classes: Regular Sinus Rhythm, Atrial Fibrillation, Other Irregular Rhythm, and Noise / Artefacts. Duration of the segments is 30 seconds.

Methods

Dataset

Real-life post-operative telemetry data of 418 hospitalized patients who underwent various types of cardiac surgery (CS) was used (CS database). This dataset was augmented with real-life telemetry data of 58 patients who underwent electrical cardioversion (ECV) as AF

Table 1 – Feature selection used to train the classifier.

Feature class	Feature	Statistical measure
R-R interval variability	• Time between R-peaks	• Mean, SD, CV, RMSSD, pNN5, pNN10, pNN50
	• Ratio between R-R time intervals	• Mean, SD, CV, RMSSD
	• Poincaré plot of R-R time intervals	• SD of points to regression line, SD of points to perpendicular line, shape of Poincaré points (SD/SD)
	• Shannon entropy of R-R time intervals	• Shannon entropy
	• Amplitude difference between R-peaks	• Mean, SD, CV, RMSSD, pNN5, pNN10, pNN50
	• Ratio between R-R amplitude differences	• Mean, SD, CV, RMSSD
	• Poincaré plot of R-R amplitude differences	• SD of points to regression line, SD of points to perpendicular line, shape of Poincaré points (SD/SD)
Intra-beat peak time intervals	• Interval between P-peak and Q-peak	• Mean, SD, CV
	• Interval between Q-peak and S-peak	• Mean, SD, CV
	• Interval between Q-peak and T-peak	• Mean, SD, CV
	• Interval between S-peak and T-peak	• Mean, SD, CV
Number of peaks per QRS-complex	• Detected P-waves per QRS-complex	• % of QRS-complexes with 0 / 1 / >1 P-waves
	• Detected T-waves per QRS-complex	• % of QRS-complexes with 0 / 1 / >1 T-waves
Peak amplitude differences	• Amplitude difference between Q-peak and R-peak	• Mean, SD, CV
	• Amplitude difference between R-peak and S-peak	• Mean, SD, CV
	• Ratio between P-wave amplitude and QRS-complex amplitude	• Mean, SD, CV
	• Ratio between T-wave amplitude and QRS-complex amplitude	• Mean, SD, CV
Autocorrelation	• Autocorrelation of the ECG segment	• Mean, SD, CV
	• Peaks in the autocorrelation of the ECG segment	• Mean, SD, CV, number of peaks relative to number of detected R-peaks
	• Time between peaks in autocorrelation of the ECG segment	• Mean, SD, CV
QRS-morphology	• Number of different QRS-morphologies	• Count
	• Most common QRS-morphology	• % of QRS-complexes
	• Second most QRS-morphology	• % of QRS-complexes
Noise level	• Time in which no R-peak detection was reliably possible	• % of total segment time
	• Time in which no P- and T-wave detection was reliably possible	• % of total segment time
Frequency analysis	• Area under frequency plot between 0.5 and 40Hz	• % of total area under frequency plot
	• Area under frequency plot between 4 and 10Hz	• % of total area under frequency plot
	• Area under frequency plot below 0.5Hz	• % of total area under frequency plot
	• Area under frequency plot above 40Hz	• % of total area under frequency plot

CV = coefficient of variance; **ECG** = electrocardiogram; **pNN5** = % of successive R-R time intervals greater than 5 ms; **pNN10** = % of successive R-R time intervals greater than 10 ms; **pNN50** = % of successive R-R time intervals greater than 50 ms; **RMSSD** = root mean square of successive differences; **SD** = standard deviation.

30

treatment (ECV database). All data was acquired using a 12-lead ECG recorder with a sampling frequency of 200 Hz, from which only lead II was used to train the classifier. Patients were distributed over a training/validation dataset and a hidden testing dataset with a ratio of 9:1. Long-term recordings were then split into a total of 3,846,564 non-overlapping segments of 30 seconds (CS database: 3,799,998 segments; ECV database: 46,566 segments; training/validation dataset: 3,474,361 segments; hidden testing dataset: 372,203 segments), which corresponds to the minimum clinical AF episode duration[4] and the average duration of segments in the CinC Challenge[12].

These segments of 30 seconds were annotated by an investigator experienced in ECG evaluations. First, as visualized in the flowchart (*Supplementary Figure 1*), if the ECG could not be assessed due to noise or artefacts (caused by, e.g., movement or pacemaker activity), it was classified as noise/artefact (Class ~). Next, if only sinus rhythm beats were present, it was classified as regular sinus rhythm (Class *Normal*). Otherwise, if AF occurred within the recording, it was classified as AF (Class *AF*). In all other cases (e.g., PACs, PVCs and atrial flutter), it was classified as other irregular rhythm (Class *Other*). In total, 3,829 signals were annotated as atrial fibrillation, 8,882 as regular sinus rhythm, 3,500 as other irregular rhythm and 12,352 as noise/artefact. A hidden test dataset was created using 500 segments of each class. The other segments were used for training and validation purposes. Examples of the four different classes are visualized in *Figure 1*.

Furthermore, the database from the CinC Challenge 2017 was used to study the effect of the proposed method on another database.[12] The updated labels from the CinC Challenge 2017 (v3) were used to determine the true class of each segment. The dataset was split into a training set containing 80% of the records and a testing set containing 20% of the records.

Classifier design

A classifier was designed to differentiate between the previously defined classes, similar to the CinC Challenge 2017.[12] QRS-peak detection was performed based on the Pan Tompkins algorithm.[18] Next, P- and T-waves were detected using the method as described by Elgendi et al.[19] As the aim of this study was not to find the optimal features for AF detection, the included features mainly describe the ECG in similar ways as previous studies.[9] For example, the ECG signal was described in terms of peak intervals and amplitudes per heartbeat. Furthermore, the RR-interval variability and the number of detected P-waves and T-waves was determined. Also, since P-waves, QRS complexes and T-waves mainly contain frequencies of 0.5–40 Hz, the area under the frequency spectrum was analyzed to get information on the noise level.[19] More specifically, the area under the curve between 0.5 Hz and 40 Hz was compared to the area under the curve outside this range. As the focus of this paper is on how to efficiently train a classifier without manually labelling all data and not on how to find the optimal feature set, we describe the used features very briefly. A full overview of the used features is presented in *Table 1*. All calculations were performed using Python (version 3.8.3, 64-bits). Initial exploration showed that boosted decision trees resulted in the best performance. Moreover, multiple studies have reported good performance using boosted decision trees.[20-22] Therefore, the XGBoost Python module (version 1.5.2) was used to train a gradient boosted decision trees classifier based on the features.[23]

General overview of the training model

A schematic overview of the proposed human-validated semi-supervised training process is visualized in *Figure 2*. The proposed procedure consists of two phases: the *pre-training phase* (upper panel) and the *semi-automated training phase* (lower panel). During the
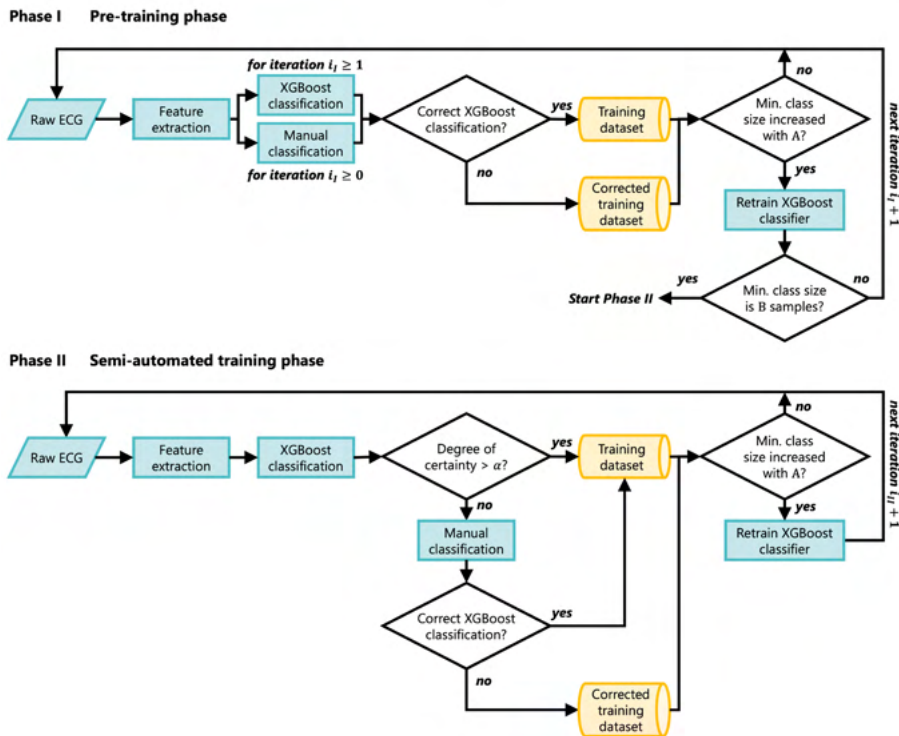
Figure 2 – Human-validated semi-supervised learning, consisting of two phases: the *pre-training phase* and the *semi-automated training phase*, as described in the text. In this study, A=10 segments per class, and $\alpha = 99$%. **ECG** = electrocardiogram; α = threshold for the estimated probability p of an ECG segment being of the predicted class.

pre-training phase a classifier was trained based on a training dataset containing manually labelled ECG segments. Next, during the *semi-automated training phase*, new ECG segments were semi-automatically classified. The classifier output did not only contain the predicted class, but also the estimated probability p of an ECG segment being of the predicted class – which is from here on called the *degree of certainty*. The degree of certainty was calculated as the mean predicted class probability of the trees in the random forest. The predicted class probability of a tree was calculated as the fraction of samples of the same class in a leaf. When the degree of certainty was above a certain threshold α, the new segment was automatically added to the training dataset. However, if the classifier was uncertain (i.e., $p < \alpha$), the user was asked to validate the predicted class manually, before it was added to the training dataset. Using this new training dataset, the classifier was retrained.

30

Phase I: Pre-training phase

The pre-training phase consists of several iterations. In the initialization ($i_I = 0^{th}$ iteration), ECG segments were manually labelled to create an initial training dataset containing at least $A = 10$ segments per class (a total of at least 40 segments). Then, in each subsequent iteration $i_I \geq 1$, if the training dataset expanded at least $A = 10$ ECG segments for each class compared to the previous training iteration, a temporary classifier was trained and validated. This temporary classifier was used to classify new segments parallel to manual classification in the next iteration $i_I + 1$ of the pre-training phase. Based on whether the classification was correct, the segment was added to either the *training dataset* (in case the classification was correct) or the *corrected training dataset* (in case the classification was incorrect). During the next training iteration, to learn from the previously misclassified ECG
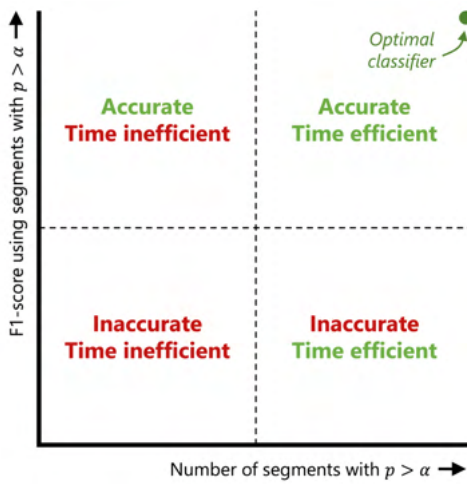
Figure 3 – Trade-off between time efficiency and classification accuracy. In the optimal situation (green dot), alle segments are classified automatically and the classification accuracy is 100%. In any other situation, a trade-off has to be made between the classification accuracy of the automatically classified segments and the time efficiency. α = Threshold for the estimated probability p of an ECG segment being of the predicted class; p = estimated probability of an ECG segment being of the predicted class.

segments, at most 10% of the training set was filled with segments which were misclassified by the classifier from the previous training iteration, if available. This value corresponds to the commonly used value for the learning rate of 0.1 in deep learning approaches. If not enough segments were available in the corrected training dataset, all available segments were used. For each training iteration, 80% of the training dataset was used to train the classifier and 20% was used for validation purposes. Furthermore, the classifier was tested using the hidden testing dataset. The stopping criterion for this phase was defined as the smallest set of training data consisting of at least $B = 500$ segments.

Phase II: Semi-automated training phase
The semi-automated training phase consists of a theoretically unlimited number of iterations. During the initialization of this phase ($i_{II} = 0^{th}$ iteration), the trained XGBoost classifier from the pre-training phase was used. In order to increase the size of the training dataset, new segments were fed to the classifier. Only segments which the classifier could not classify with $p > \alpha$ were presented to the user for manual validation. All other segments were automatically added to the training set. Again, the classifier was retrained and revalidated when all classes contained at least $A = 10$ ECG segments more than during the last training iteration. This updated classifier was then used during the next iteration $i_{II} + 1$ of the semi-automated training phase.

Threshold determination
The threshold α was chosen based on the classifier performance for segments which could be classified with $p > \alpha$, balancing the F1-scores (represents classification accuracy) and the number of segments which could be automatically classified (represents time efficiency), as visualized in *Figure 3*. Ideally, all ECG segments are automatically classified with an F1-score of 100%, which corresponds to the upper right corner of *Figure 3*. In this study, threshold α was chosen based on visual inspection of the relation between the F1-score and the percentage of automatically classifiable segments to find an optimum based on the slope of the relation between the two parameters. The threshold α was determined directly after the pre-training phase only and remained constant for each subsequent training iteration.

Statistical outcome measures

After each training iteration, the hidden testing dataset – containing 500 segments per class from patients which were not used for training purposes – was used to test the performance

of the classifier. Furthermore, after the stopping criterion was satisfied in the pre-training phase, classifier performance was evaluated as a function of the degree of certainty p of the classifier. Similarly, during the semi-automated training phase, classifier performance was evaluated when all classes contained at least 500 ECG segments more with respect to the last testing iteration (i.e., at 500 ECG segments, at 1000 ECG segments, at 1500 ECG segments, etcetera).

The classifier output for each class could either be true positive (TP), false positive (FP), false negative (FN), or true negative (TN). Classification accuracy for each class was described using the precision $P = TP/(TP + FP)$, recall $R = TP/(TP + FN)$, and the F1-score, which is the harmonic mean of the precision and recall: $F1 = 2 \times P \times R/(P + R)$.

Human-controlled semi-supervised learning on the CinC Challenge 2017 dataset

The different classes in this CinC Challenge 2017 dataset are not equally represented and only 3.3% of all segments is classified as noise/artefacts. Therefore, unfortunately it was not possible to perform phase II of the proposed method. Instead, only phase I was applied by using 80% of the data to train the same classifier as used previously. Next, the testing set (20%) was used to test the classifier's performance using different thresholds for the degree of certainty α. Based on this relation, the threshold for α was determined based on visual inspection as described previously.

Results

Pre-training phase

After the pre-training phase, the classifier showed an average precision and recall in the hidden testing dataset of 89.2% and 89.0%, respectively. The corresponding average F1-score was 89.0%. Most inaccuracies were caused by the class containing non-AF irregular rhythms (F1-scores: 87.0% (Class *Normal*), 93.3% (Class *AF*), 78.6% (Class *Other*), 97.1% (Class ~)). The average degree of certainty of the classifier for the correct class was 88.0%. Again, most uncertainties were caused by the class containing non-AF irregular rhythms (degrees of certainty: 87.6% (Class *Normal*), 91.9% (Class *AF*), 77.1% (Class *Other*), 95.3% (Class ~)).

30
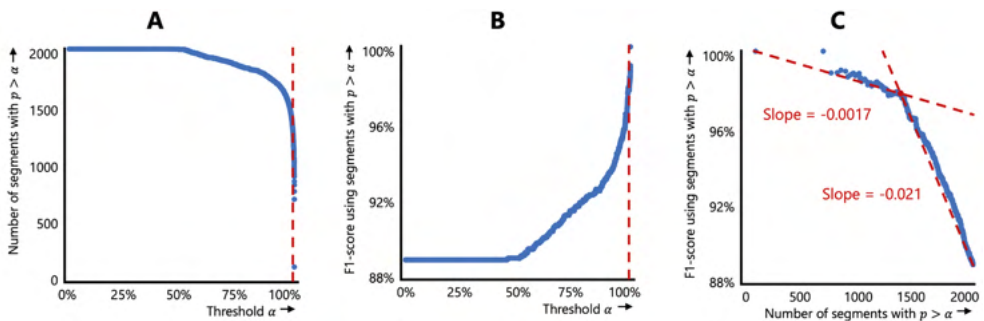
Figure 4 – Threshold α determination after the pre-training phase. The final threshold ($\alpha = 99$%) is indicated by the red dashed line in panel A and panel B and the intersection of the two dashed lines in panel C. *Left panel*: the number of segments which can be classified with $p > \alpha$ decreases with increasing threshold α. *Center panel*: the F1-score for the segments which are classified automatically increases with increasing threshold α. *Right panel*: a trade-off between the number of segments which can be classified with $p > \alpha$ and the F1-score is made. After 1,360 segments, the average slope increases from 0.0017 to 0.021, hence in this study, the threshold was set where 1,360 segments could still be classified automatically ($\alpha = 99$%). α = threshold for the estimated probability p of an ECG segment being of the predicted class; p = estimated probability p of an ECG segment being of the predicted class.
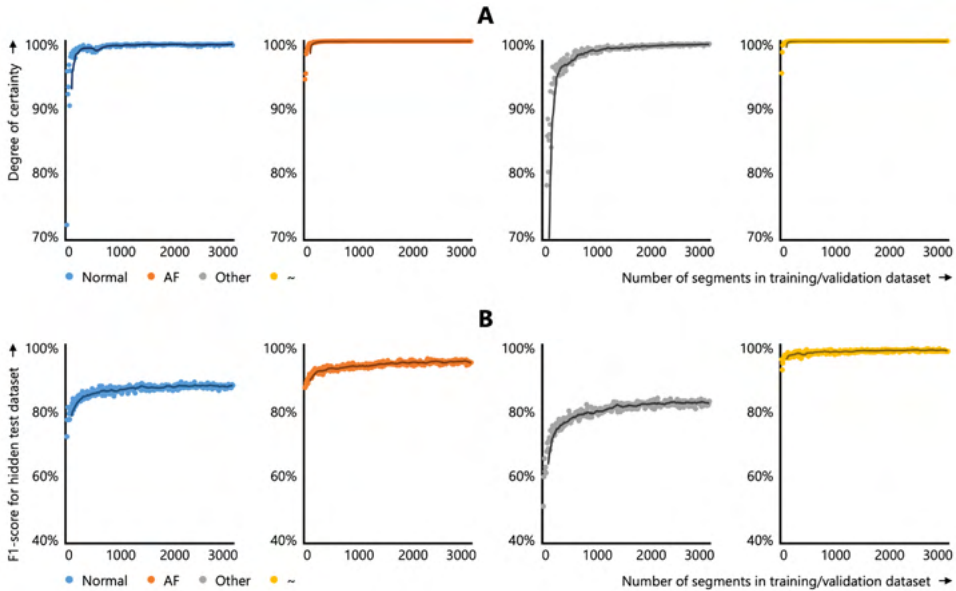
Figure 5 – Effect of increasing the size of the training dataset. Dots indicate averages per training iteration, solid lines indicate moving averages over 10 training iterations. *Upper panel*: increasing the number of segments in the training dataset results in a higher degree of certainty for the classifier, represented by the estimated probability **p** of an ECG segment being of the predicted class. *Lower panel:* Increasing the number of segments in the training dataset results in a higher F1-score for the validation dataset. **AF** = atrial fibrillation; **Normal** = regular sinus rhythm; **Other** = other irregular rhythms; **~** = noise or artefacts.

Threshold determination

As visualized in *Figure 4A*, the number of ECG segments which could be classified with $p > \alpha$ decreased when increasing threshold α. As an effect, the ECG segments which could be classified with $p > \alpha$ were more accurately classified, as visualized in *Figure 4B*, indicating a relation between the degree of certainty and the F1-score of the classifier. The threshold α was set by balancing the number of segments which could be automatically classified and the F1-score, as visualized in *Figure 4C*. More specifically, α was chosen corresponding to the earliest point of significantly increasing curvature. In the first part of the plot up to

Table 2 – Results per testing iteration.

Testing iteration	Number of segments in training dataset	Number of segments with p>99% (%)	Average recall	Average precision	Average F1-score
1	500	1360 (68.0%)	All: 89.0% $>\alpha$: 97.9%	All: 89.2% $>\alpha$: 97.9%	All: 89.0% $>\alpha$: 97.9%
2	1000	1475 (73.8%)	All: 89.6% $>\alpha$: 97.4%	All: 89.8% $>\alpha$: 97.3%	All: 89.7% $>\alpha$: 97.3%
3	1500	1488 (74.4%)	All: 91.6% $>\alpha$: 97.4%	All: 91.5% $>\alpha$: 97.3%	All: 91.6% $>\alpha$: 97.3%
4	2000	1511 (75.6%)	All: 91.7% $>\alpha$: 97.9%	All: 91.8% $>\alpha$: 97.8%	All: 91.7% $>\alpha$: 97.9%
5	2500	1522 (76.1%)	All: 91.5% $>\alpha$: 97.6%	All: 91.6% $>\alpha$: 97.5%	All: 91.6% $>\alpha$: 97.5%
6	3000	1515 (75.8%)	All: 91.3% $>\alpha$: 97.6%	All: 91.5% $>\alpha$: 97.4%	All: 91.4% $>\alpha$: 97.5%

p = estimated probability of an ECG segment being of the predicted class; **All** = results based on the entire hidden testing dataset; **>α** = results based on segments which could be classified with $p > \alpha$.
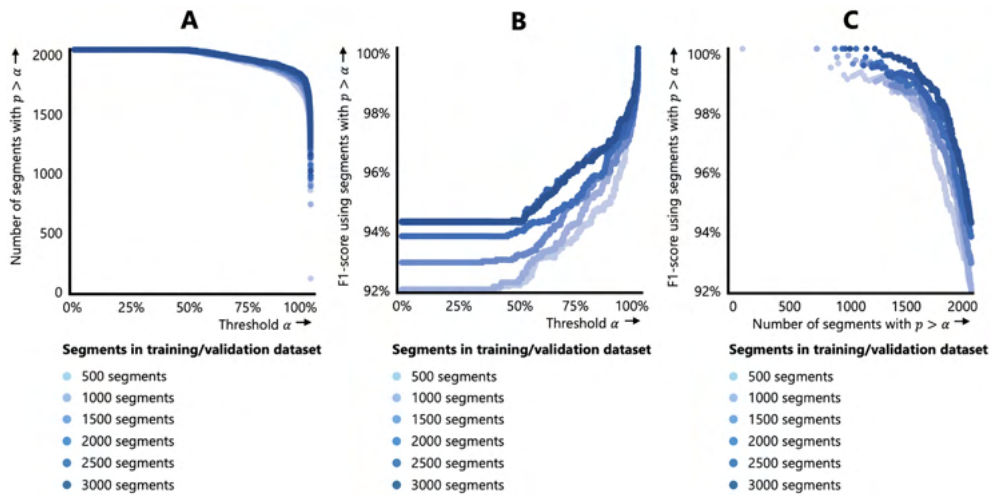
Figure 6 – Effect of increasing the size of the training dataset on results from the testing dataset for all thresholds α from 0% to 100% with steps of 0.01%. *Left panel*: relation between threshold α and number of segments with $p > \alpha$. Mainly for high values of α, the number of segments which can be classified with $p > \alpha$ increases with increasing size of the training dataset. *Center panel*: relation between threshold α and the F1-score. Mainly for low values of α, the F1-score of the classifier increases with increasing size of the training dataset. *Right panel:* relation between the number of segments with $p > \alpha$ and the F1-score. With increasing size of the training dataset, lines move towards the upper right corner of the graph, which is the optimal situation, as visualized in *Figure 3*. This indicates that a better trade-off between classification accuracy and time efficiency is possible using a larger training dataset. α = threshold for the estimated probability p of an ECG segment being of the predicted class; p = estimated probability of an ECG segment being of the predicted class.

1,360 segments, the F1-score decreases with 0.0017% per segment, while in the second part of the plot starting from 1,360 segments, the F1-score decreases more than 10 times as fast with 0.021% per segment. Therefore, based on visual inspection, the threshold α was set at a degree of certainty p of 99%, which corresponds to 68.0% of the testing dataset (= 1,360 ECG segments) being classified automatically with an average F1-score of 97.9%, as shown in *Figure 4A and 4B*, respectively.

Semi-automated training phase

The average degree of certainty p of the classifier for each training iteration and F1-score of the classifier for the validation dataset is visualized in *Figure 5A and B*, respectively. The degree of certainty p increases with increasing size of the training dataset. An increasing F1-score is observed up until a training dataset size of 1,500 ECG segments, after which the increase is less prominent. Similar to the results of the pre-training phase, the F1-score and degree of certainty p for the class containing non-AF irregular rhythms remains lower.

From training with 500 ECG segments to training with 3,000 ECG segments, the percentage of automatically classifiable ECG segments in the testing dataset with $p > 99\%$ increased from 68.0% to 75.8%. The average F1-score for these segments remains almost constant with values between 97.3% and 97.9%. The average F1-score for all segments in the hidden testing dataset increased from 89.0% to 91.4%. *Table 2* summarizes the results for all testing iterations. Complete results for each training iteration using the validation and hidden testing dataset are presented in *Supplementary Tables 1 and 2*, respectively.

Although threshold α was fixed at 99%, the results for all other thresholds are visualized in *Figure 6*. The left panel again shows that more ECG segments can be automatically

30
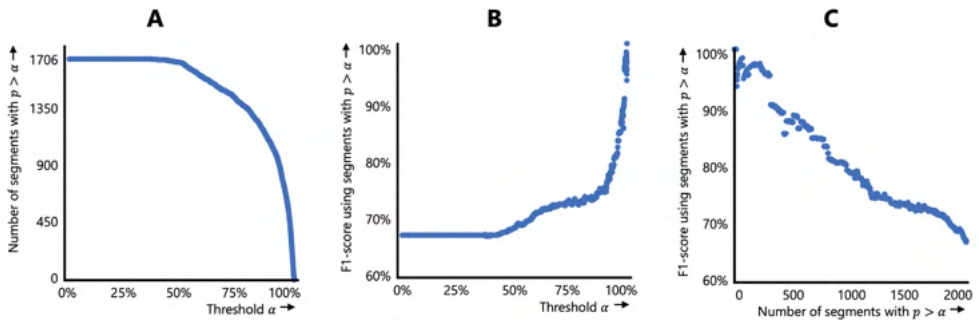
Figure 7 – Results for analysis using the CinC Challenge 2017 database. *Left panel*: the number of segments which can be classified with $p > \alpha$ decreases with increasing threshold α. *Center panel*: the F1-score for the segments which are classified automatically increases with increasing threshold α. *Right panel*: relation between the number of segments which can be classified automatically (efficiency) and the F1-score (accuracy). α = threshold for the estimated probability p of an ECG segment being of the predicted class; p = estimated probability p of an ECG segment being of the predicted class.

classified with more ECG segments in the training dataset. Furthermore, the average F1-score increases, as visualized in the center panel. Lastly, the right panel shows that the curve of the relation between the number of ECG segments which could be classified with $p > \alpha$ and the average F1-score shifts towards the upper right corner.

Human-controlled semi-supervised learning on the CinC Challenge 2017 dataset

Using the CinC Challenge 2017 dataset, the average F1-score is 67.0%. Whereas in the previous analysis only the class containing other arrhythmias showed a lower degree of certainty and lower F1-scores, using the CinC Challenge 2017 dataset, this is also observed for the class containing noise (degrees of certainty: 86.1% (Class *Normal*), 61.8% (Class *AF*), 54.9% (Class *Other*), 38.8% (Class ~); F1-scores: 84.9% (Class *Normal*), 69.7% (Class *AF*), 61.6% (Class *Other*), 52.0% (Class ~)).

Results for classifier performance using the CinC Challenge 2017 dataset are visualized in *Figure 7*. *Figures 7A and B* show similar trends as observed previously for the number of segments with $p > \alpha$ and the F1-score, respectively. *Figure 7C* shows a different relation between the number of segments which can be classified with $p > \alpha$ and the F1-score. Instead of a slowly increasing slope, a sudden drop in F1-score is observed around 265 segments (= 15.5% of the testing set). The corresponding threshold α is 98.8% and segments with this degree of certainty show an F1-score of 95.5%.

Discussion

A new efficient and accurate method based on a combination of reinforcement learning-based and transfer learning-based methods was applied to train a classifier using a large set of real-life telemetry data of hospitalized patients. Transfer learning-based methods are applied by first training the classifier on a smaller dataset and then using this classifier to classify new ECG segments which are more difficult to classify. At the same time, using the degree of certainty of the classifier, the classifier adapts its behavior to optimize the final classification accuracy.

The major advantage of this new training method is the decreased workload for the user, making it less time-consuming compared to manually validating all ECG segments. In the current study, the workload decreased more than $^3/_4$, since more than 75% of the segments could be classified automatically with $p = 99\%$. Furthermore, hospitalized patients after

cardiac surgery show many different combinations of rhythm abnormalities, noise levels, and artefacts, making it difficult to generalize a classifier for all cases. Using the degree of certainty p of the classifier as a gatekeeper before adding an ECG segment to the training set, the training method learns by asking the user when a new rhythm is encountered. Also, since during each training iteration previously misclassified data is used, the classifier learns from its mistakes which were corrected by the user. A previous study by Parvaneh et al.[24] also shows an increase of the F1-score of 3.7% after manually checking all the disagreements between human input and classifier output. However, instead of only retraining the classifier once, the current study iteratively updates the classifier and only asks input for ECGs of which the classifier is uncertain, hence increases time efficiency.

Database-dependent efficiency

The classifier was initially developed to be used on the real-life post-operative telemetry dataset and the real-life electrical cardioversion dataset. To study the effect of the proposed method on other datasets as well, phase I of the method was also applied on the CinC Challenge 2017 dataset. As demonstrated, the used classification algorithm is suboptimal for the CinC Challenge 2017 dataset, since the average F1-score is 67.0%, whereas previous studies report significantly higher F1-scores.[12] However, the relation between threshold α and the efficiency and F1-scores is still clear (*Figure 7A and B*, respectively). A higher degree of certainty correlates with a higher classification accuracy. When comparing *Figure 4C* and *Figure 7C* a clear database-dependent efficiency can be observed. For the CinC Challenge 2017 database, the initial threshold α would be around 98.8%, resulting in automated classification of 15.5% of all segments, whereas using the CS and ECV databases 68.0% of the segments could be automatically classified. This shows that using the method on the CinC Challenge 2017 database improves efficiency less.

A highly probable cause for this large difference is the unequal distribution of the classes in the CinC Challenge 2017 dataset. In the first analysis, an initial classifier was trained using 2,000 segments which were equally distributed over the four classes. Although more segments were available for initial training using the CinC Challenge dataset (n=6,822), these were unequally distributed (59.2% normal sinus rhythm, 8.7% atrial fibrillation, 28.8% other arrhythmias, and only 3.3% noise/artefacts). *Figure 5A* shows the increase in degree of certainty resulting from increasing the number of segments in the training set. Not only does the unequal distribution explain the lower efficiency, but it is also a plausible explanation for the low degree of certainty and the low F1-scores for the class containing noise/artefacts in the CinC Challenge 2017 dataset.

Supervised learning vs. semi-supervised learning vs. human-validated semi-supervised learning

Traditionally, classifiers are trained using a human-validated training dataset, hence the user should label all ECG segments of the training dataset manually.[13] Not only is this time-consuming, but also subject to more human errors. Although several databases containing annotated ECGs are available online (e.g., PhysioNet databases[25], the CinC Challenge 2017 database[12], and the database used by Attia et al.[26]), these databases are mainly focused on specific patient groups and mostly contain ECG segments without much variety in cardiac arrhythmias, noise levels and artefacts.[27] As an alternative to using a human-validated training dataset, semi-supervised learning can be used to first train an initial classifier, after which the classifier trains itself.[14] The most important assumption using semi-supervised learning, is that the unlabeled data resembles the labeled data. For hospitalized patients after cardiac surgery, this would require the pre-training dataset to contain a large variety of segments

30

containing different rhythm abnormalities and data quality, hence the pre-training dataset should still be relatively large. Instead, the proposed method uses the estimated probability p of a sample being in the predicted class as an indicator of the degree of certainty to avoid making this assumption. In this way, a new ECG segment, which is completely different from a previous segment, would not be classified with $p > \alpha$ and the user is asked to review the ECG segment manually. Therefore, as opposed to semi-supervised learning, the proposed method still learns from human input after the initial classifier was trained, hence avoiding tunnel vision.

How certain is certain?

The threshold for the degree of certainty was set at $p = 99\%$ based on visual inspection of the relation between the number of segments which could be automatically classified and the F1-score. Alternatively, the threshold could be set at $p = 0\%$, which would result in the special case of semi-supervised learning with self-training. Still, using this threshold, the average F1-score would be 89.0%. On the other end, the threshold could be chosen even higher than $p = 99\%$, resulting in a slightly higher F1-score, but less ECG segments which could be classified automatically, hence decreasing time efficiency.

In this study, the threshold was set by focusing on the slope of the relation between the number of segments and the F1-score of segments which could be automatically classified. Another option would be to determine the point with the smallest distance to the upper right corner of the graph, which represents the optimal classifier, as visualized in *Figure 3*. In doing so, a decrease in the number of segments and a decrease in F1-score are equally penalized. However, using our method, the focus is on having a high F1-score, at the cost of a decrease in time efficiency. Therefore, the used method is preferable over the distance-based method when aiming for the most accurate classifier.

It should be noted that the value for α was set based on results of the testing dataset. Therefore, the presented results might be biased towards the used database. In order to find the optimal value for α – which might be different for each classification problem – it would be better to use an additional validation set.

Blinded manual classification vs. non-blinded manual validation

During the semi-automated training phase, segments of which the classifier could not determine the class with $p > \alpha$ were shown to the user for validation, hence a combination of 1) the ECG segment, 2) the predicted class and 3) the degree of certainty p was presented to the user. Another option would be to ask the user to manually classify the ECG segment blinded, since showing the predicted class to the user might introduce bias towards a certain class. This raises the question of whether this bias would negatively influence the training results. As shown in *Figure 4B*, even in the special case of semi-supervised learning with self-training (threshold $\alpha = 0\%$), the average F1-score is 89.0%. The corresponding average recall and precision are 89.0% and 89.2%, respectively, indicating that even when the classifier is not sure of the predicted class, the predicted class is still correct in 89% of the cases. Therefore, in 89% of the cases, the introduced bias actually is a well-directed push towards the correct class, hence showing the predicted class actually might help in improving the classification accuracy. If, however, the classification accuracy would be poor for low degrees of estimated probability p, showing the predicted class likely has a negative influence, as might be the case for the analysis using the CinC Challenge 2017 dataset where the F1-score for the semi-supervised learning case was 67.0% (*Figure 7B*).

Future perspectives

This study not only shows that human-validated semi-supervised learning results in an accurate classifier with a lower human workload, but also shows that the degree of certainty of the classifier increases with an increasing number of ECG segments in the training dataset and is related to classifier accuracy. Using the degree of certainty of the classifier in AF detection algorithms for the detection of AF episodes in long-term real-life telemetry data of hospitalized data might result in a more accurate detection, paving the way towards accurately determining the AF burden in these patients in terms of AF duration, number of episodes, and proportion of time an individual is in AF.[28]

Furthermore, this method was now applied to real-life data of *hospitalized* patients. However, more and more *non-hospitalized* people also have their heart rhythm registered using wearables, showing similar problems of noisy measurements with artefacts and potentially other heart rhythms. Therefore, when training a classifier to automatically detect rhythm abnormalities in these recordings, human-validated semi-supervised learning might be feasible to decrease the human workload. In this case, human-supervised semi-supervised learning should not be applied by the end-user, since then the user should be a trained clinician, but could be used to reduce the workload for training a validated, accurate classifier using a large dataset.

Limitations

First, although technically not a limitation of this study in view of its methods, this study did not aim to reach the highest accuracy for AF detection, but to propose an efficient method of training an accurate classifier. For future studies, applying human-validated semi-supervised learning in accurate detection of cardiac arrhythmias, using other datasets with validated annotations (e.g., PhysioNet 2017 and 2021 datasets) is essential. Further, in this study only a single ECG lead was used. Using more leads – although not always possible due to data availability, especially in wearables – might improve classifier accuracy.

A dataset containing telemetry recordings of hospitalized patients was used, hence the classification results themselves should not be generalized to other wearable data of another population. First, telemetry data of hospitalized patients might have different quality compared to consumer wearable data. Also, the patient population using consumer wearables is different from the population of hospitalized patients. Nonetheless, since the incidence of various cardiac arrhythmias is lower in healthy and young individuals[10], applying the proposed method to train a classifier for AF detection in this group likely results in a similar or even better classifier performance. However, given the higher incidence of cardiac arrhythmias in elderly patients with cardiovascular comorbidities[10], the advantage of human-validated semi-supervised learning over classical semi-supervised learning most likely is less striking when applied to wearable ECGs from young and healthy individuals.

Although human-validated semi-supervised learning resulted in an accurate classifier, it still requires three parameters to be set manually, which could influence the performance. First, the threshold α is currently set based on visual inspection. More optimally, the threshold is automatically determined and adapts after each testing iteration. Next, the number of extra segments which is required to retrain the classifier was currently heuristically set at $A = 10$ per class and the number of segments required to start the semi-automated training phase at $B = 500$ per class. The effect of changing these thresholds was not investigated, but likely influences the time efficiency of the proposed method and the final classification accuracy. Lastly, during training, at most 10% of the data from the corrected training dataset was used,

30

corresponding to the commonly used value for the learning rate of 0.1 in deep learning approaches. However, using too much data from the corrected training dataset might result in overtraining on the misclassified ECG segments. On the opposite, using too few segments from the corrected training dataset would reduce the effect of the classifier learning from its mistakes.

Conclusion

A new and efficient method, called human-validated semi-supervised learning, was proposed for training a classifier for large sets of ECG segments. This method makes training of an accurate classifier more time efficient without compromising on classification accuracy, hence increasing the size of the training dataset is less of an obstacle. Therefore, this method might be valuable when training a classifier based on large amounts of real-life ECG data of hospitalized patients showing varying cardiac rhythms, noise levels and artefacts.

References

1. Lopez Perales CR, Van Spall HGC, Maeda S, Jimenez A, Latcu DG, Milman A, Kirakoya-Samadoulougou F, Mamas MA, Muser D, Casado Arroyo R. Mobile health applications for the detection of atrial fibrillation: a systematic review. Europace. 2021;23:11-28.
2. IDC. Shipments of Wearable Devices Reach 118.9 Million Units in the Fourth Quarter and 336.5 Million for 2019, According to IDC. IDC Media Center. https://www.idc.com/getdoc.jsp?containerId=prUS46122120. 2020. Accessed 3 September.
3. Communities TCoTE. Smart Wearables: Reflection and Orientation Paper. Digit Ind Compet Electron Ind. 2016;121.
4. Hindricks G, Potpara T, Dagres N, Arbelo E, Bax JJ, Blomstrom-Lundqvist C, Boriani G, Castella M, Dan GA, Dilaveris PE, et al. 2020 ESC Guidelines for the diagnosis and management of atrial fibrillation developed in collaboration with the European Association for Cardio-Thoracic Surgery (EACTS): The Task Force for the diagnosis and management of atrial fibrillation of the European Society of Cardiology (ESC) Developed with the special contribution of the European Heart Rhythm Association (EHRA) of the ESC. Eur Heart J. 2021;42:373-498.
5. Mairesse GH, Moran P, Van Gelder IC, Elsner C, Rosenqvist M, Mant J, Banerjee A, Gorenek B, Brachmann J, Varma N, et al. Screening for atrial fibrillation: a European Heart Rhythm Association (EHRA) consensus document endorsed by the Heart Rhythm Society (HRS), Asia Pacific Heart Rhythm Society (APHRS), and Sociedad Latinoamericana de Estimulacion Cardiaca y Electrofisiologia (SOLAECE). Europace. 2017;19:1589-1623.
6. Slocum J, Sahakian A, Swiryn S. Diagnosis of atrial fibrillation from surface electrocardiograms based on computer-detected atrial activity. J Electrocardiol. 1992;25:1-8.
7. Cubanski D, Cyganski D, Antman EM, Feldman CL. A neural network system for detection of atrial fibrillation in ambulatory electrocardiograms. J Cardiovasc Electrophysiol. 1994;5:602-608.
8. Yang TF, Devine B, Macfarlane PW. Artificial neural networks for the diagnosis of atrial fibrillation. Med Biol Eng Comput. 1994;32:615-619.
9. Wesselius FJ, van Schie MS, De Groot NMS, Hendriks RC. Digital biomarkers and algorithms for detection of atrial fibrillation using surface electrocardiograms: A systematic review. Comput Biol Med. 2021;133:104404.
10. Khurshid S, Choi SH, Weng LC, Wang EY, Trinquart L, Benjamin EJ, Ellinor PT, Lubitz SA. Frequency of Cardiac Rhythm Abnormalities in a Half Million Adults. Circ Arrhythm Electrophysiol. 2018;11:e006273.
11. Maesen B, Nijs J, Maessen J, Allessie M, Schotten U. Post-operative atrial fibrillation: a maze of mechanisms. Europace. 2012;14:159-174.
12. Clifford GD, Liu C, Moody B, Lehman LH, Silva I, Li Q, Johnson AE, Mark RG. AF Classification from a Short Single Lead ECG Recording: the PhysioNet/Computing in Cardiology Challenge 2017. Comput Cardiol (2010). 2017;44.
13. Johnson KW, Torres Soto J, Glicksberg BS, Shameer K, Miotto R, Ali M, Ashley E, Dudley JT. Artificial Intelligence in Cardiology. J Am Coll Cardiol. 2018;71:2668-2679.
14. Pise NN, Kulkarni P. A Survey of Semi-Supervised Learning Methods. Paper/Poster presented at: 2008 International Conference on Computational Intelligence and Security; 13-17 Dec. 2008, 2008;
15. De Cooman T, Vandecasteele K, Varon C, Hunyadi B, Cleeren E, Van Paesschen W, Van Huffel S. Personalizing Heart Rate-Based Seizure Detection Using Supervised SVM Transfer Learning. Front Neurol. 2020;11:145.
16. Jonsson A. Deep Reinforcement Learning in Medicine. Kidney Dis (Basel). 2019;5:18-22.
17. Hosameldin A, Asoke KN. Probabilistic Classification Methods. In: Condition Monitoring with Vibration Signals: Compressive Sampling and Learning Algorithms for Rotating Machines. IEEE; 2019:225-237.
18. Pan J, Tompkins WJ. A real-time QRS detection algorithm. IEEE Trans Biomed Eng. 1985;32:230-236.
19. Elgendi M, Meo M, Abbott D. A Proof-of-Concept Study: Simple and Effective Detection of P and T Waves in Arrhythmic ECG Signals. Bioengineering (Basel). 2016;3.
20. Chen Y, Wang X, Jung Y, Abedi V, Zand R, Bikak M, Adibuzzaman M. Classification of short single-lead electrocardiograms (ECGs) for atrial fibrillation detection using piecewise linear spline and XGBoost. Physiol Meas. 2018;39:104006.
21. Sodmann P, Vollmer M, Nath N, Kaderali L. A convolutional neural network for ECG annotation as the basis for classification of cardiac rhythms. Physiol Meas. 2018;39:104005.
22. Kropf M, Hayn D, Morris D, Radhakrishnan AK, Belyavskiy E, Frydas A, Pieske-Kraigher E, Pieske B, Schreier G. Cardiac anomaly detection based on time and frequency domain features using tree-based classifiers. Physiol Meas. 2018;39:114001.
23. Chen T, Guestrin C. XGBoost: A Scalable Tree Boosting System. In: Proceedings of the 22nd ACM SIGKDD International Conference on Knowledge Discovery and Data Mining. San Francisco, California, USA: Association for Computing Machinery; 2016:785–794.
24. Parvaneh S, Rubin J, Rahman A, Conroy B, Babaeizadeh S. Analyzing single-lead short ECG recordings using dense convolutional neural networks and feature-based post-processing to detect atrial fibrillation. Physiol Meas. 2018;39:084003.
25. Goldberger AL, Amaral LA, Glass L, Hausdorff JM, Ivanov PC, Mark RG, Mietus JE, Moody GB, Peng CK, Stanley HE. PhysioBank, PhysioToolkit, and PhysioNet: components of a new research resource for complex physiologic signals. Circulation. 2000;101:E215-220.
26. Attia ZI, Noseworthy PA, Lopez-Jimenez F, Asirvatham SJ, Deshmukh AJ, Gersh BJ, Carter RE, Yao X, Rabinstein AA, Erickson BJ, et al. An artificial intelligence-enabled ECG algorithm for the identification of patients with atrial fibrillation during sinus rhythm: a retrospective analysis of outcome prediction. Lancet. 2019;394:861-867.
27. Ghodrati A, Murray B, Marinello S. RR interval analysis for detection of Atrial Fibrillation in ECG monitors. Annu Int Conf IEEE Eng Med Biol Soc. 2008;2008:601-604.
28. Chen LY, Chung MK, Allen LA, Ezekowitz M, Furie KL, McCabe P, Noseworthy PA, Perez MV, Turakhia MP, American

30

Heart Association Council on Clinical C, et al. Atrial Fibrillation Burden: Moving Beyond Atrial Fibrillation as a Binary Entity: A Scientific Statement From the American Heart Association. Circulation. 2018;137:e623-e644.

30

PART IV

CLINICAL IMPACT OF HIGH-RESOLUTION MAPPING
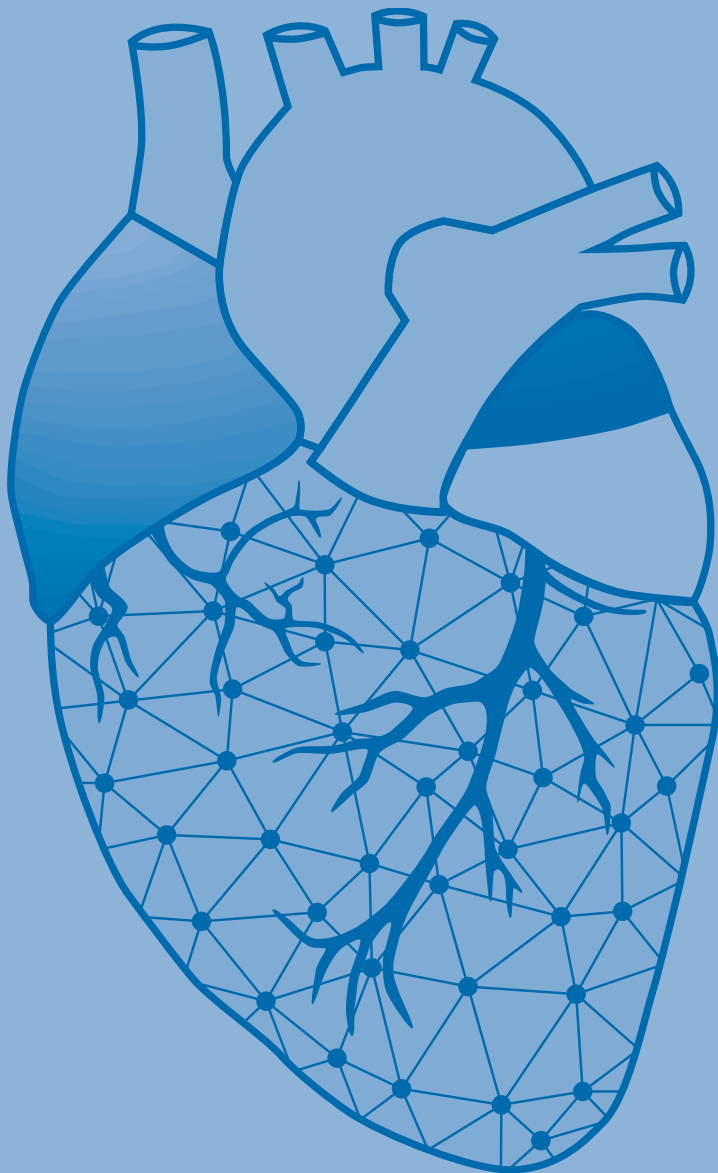
Chapter 31

First-in-children epicardial mapping of the heart: unraveling arrhythmogenesis in congenital heart disease

Rohit K. Kharbanda

Mathijs S. van Schie

Wouter J. van Leeuwen

Yannick J.H.J. Taverne

Charlotte A. Houck

Janneke A.E. Kammeraad

Ad J.J.C. Bogers

Natasja M.S. de Groot

Abstract

Patients with congenital heart disease (CHD) are prone to develop atrial and ventricular arrhythmias. Multiple factors throughout life contribute to arrhythmogenicity substrate such as 1) (longstanding) volume and/or pressure overload, 2) scar tissue, 3) ageing related structural remodeling, 4) cardiovascular risk factors and 5) tachycardia induced remodeling. At present, it is unknown whether, and to what extent, pediatric patients with CHD have atrial or ventricular conduction disorders *early* in life and whether there is a correlation between duration of volume/pressure overload and extensiveness of conduction disorders. To investigate this, we initiated high-resolution intra-operative epicardial mapping in pediatric patients with CHD undergoing primary open-heart surgery.

Journal site

Introduction

Patients with congenital heart disease (CHD) are prone to developing atrial and ventricular tachyarrhythmias relatively early in life. Improvements in perioperative care, patient monitoring and surgical techniques have resulted in an ageing CHD population. An inevitable consequence of this growing population is the rising number of CHD patients presenting with tachyarrhythmias. CHD patients not only have multiple triggers, but they also have a complex underlying arrhythmogenic substrate. Longstanding volume and/or pressure overload, scar tissue, ageing related structural remodeling, cardiovascular risk factors and tachycardia induced remodeling all contribute to the development of an arrhythmogenic substrate.[1] However, the pathophysiology of tachyarrhythmias is still incompletely understood. At present, it is unknown whether, and to what extent, pediatric patients with CHD already have atrial or ventricular conduction disorders *early* in life, as cardiac mapping in this population has never been performed before. The presence of conduction disorders early in childhood may explain the increased vulnerability of CHD patients to develop arrhythmias in adulthood, despite CHD repair.

We therefore aim to 1) quantify and characterize atrial and ventricular conduction disorders in pediatric CHD patients early in life and 2) correlate the extent and severity of conduction disorders with patient characteristics such as duration of volume/pressure overload. We therefore performed high-density and resolution epicardial mapping studies of the pediatric heart. In this report, we present our initial experience with this first-in-children mapping technique.

Methods: epicardial high-density and resolution mapping approach

Parents gave informed consent to participate in the study protocol approved by our local ethics committee (MEC-2019-0543). The epicardial mapping approach of the atria applied in pediatric patients has previously been used in adult patients.[2] In pediatric patients, we also performed mapping of the right and left ventricle. Due to potential epicardial adhesions during redo cardiac surgery, at present, we only include patients undergoing primary cardiac surgery.

Before commencement of extracorporeal circulation, a unipolar epicardial pacemaker wire, serving as a temporal reference electrode, was stitched to the superior lateral wall of the right atrium (RA). A clamp fixed to the sternum served as indifferent electrode. A custom-made electrode array (192 electrodes, electrode diameter 0.6 mm, interelectrode distance 2.12 mm) was used to record atrial and ventricular unipolar electrograms during sinus rhythm (upper left panel *Figure 1*).

Mapping positions

The electrode array was attached to a spatula that can slightly be bend to match the curvature of the atria and ventricles. The electrode array was then shifted across the epicardial surface in a predefined order. At the RA, the electrode array was positioned perpendicular to the caval veins and mapping started at the top of the RA appendage, with the tip of the electrode array towards the superior caval vein. The electrode array was then moved downwards over the RA appendage until the cavotricuspid isthmus was reached (upper panel of *Figure 1*). The intercaval region, including the terminal crest, was mapped with the electrode positioned in the longitudinal direction of both caval veins. Bachmann's bundle was mapped from the superior cavo-atrial junction towards the left atrial appendage. For the left atrium, mapping was performed at the left atrial appendage, and the posterior wall with pulmonary vein

31
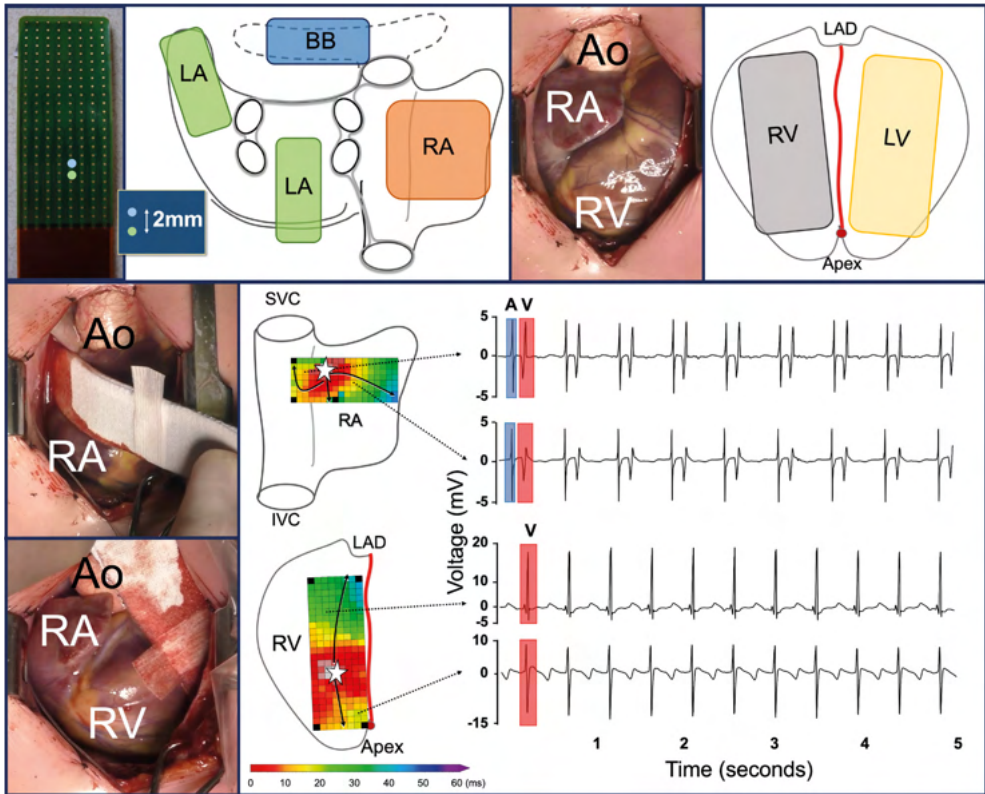
Figure 1 – Epicardial mapping of the atria and ventricles in pediatric patients. A = atria; **Ao** = aorta; **BB** = Bachmann's bundle; **IVC** = inferior vena cava; **LA** = left atrium; **LAD** = left anterior descending artery; **LV** = left ventricle; **RA** = right atrium; **RV** = right ventricle; **SVC** = superior vena cava; **V** = ventricles.

region was reached via the oblique sinus. The right and left ventricle were mapped with the electrode array positioned parallel to the left anterior descending artery with the tip of the electrode array towards the apex of the heart (upper panel of *Figure 1*). The electrode was then shifted to the lateral wall of the ventricles (perpendicular to the atrioventricular groove). The number of locations mapped per region was determined by the size of the atria and ventricles. Epicardial mapping was performed for 5 seconds at each location. Every recording included a surface electrocardiogram lead, a calibration signal, a unipolar reference electrogram and all epicardial unipolar electrograms. Recordings were analogue-to-digital converted (16-bits), sampled with a rate of 1 kHz, amplified (gain 1000) and filtered (bandwidth 0.5–400 Hz). All recordings were manually checked by two investigators and analyzed offline using custom-made Python software.

First experience with high resolution mapping in pediatric patients

Epicardial mapping was performed in three patients scheduled for repair of atrial septal defect (ASD) type II (n=2, both ♀, 3 years old) and complete atrioventricular septal defect (♂ 4 months old). All mapping procedures were performed within 8 minutes by a dedicated, trained surgical and electrophysiology team. All atrial and ventricular regions were accessible for epicardial mapping, also in our smallest patient of 4 months old. Complications did not occur during the mapping procedures.

Data analysis: epicardial activation maps

Examples of atrial and ventricular electrograms recorded from the right- atrium and ventricle are demonstrated in the lower panel of *Figure 1*. Color-coded local activation time maps were constructed by annotating the steepest negative slopes of unipolar potentials. The lower panel of *Figure 1* illustrates examples of color-coded activations maps of the superior RA and the right ventricle (parallel to the left anterior descending artery). White asterisks indicate the earliest activated regions of the RA and ventricle; arrows display main trajectories of the wavefronts. After sinus node activation, the wavefront spreads over the RA in a radial fashion. First site of activation at the right ventricle occurs in the anterior paraseptal region and spreads in the inferior and superior direction, towards the apex and the right ventricular outflow tract, respectively.

Discussion

This study is the first to report on high-density and resolution mapping of the epicardial surface in pediatric patients with CHD undergoing primary open-heart surgery. None of our patients had a history of cardiac arrhythmias. So far, excitation of the atria and ventricles has never been studied in pediatric patients without cardiac arrhythmias, as there is no indication for cardiac mapping. As a consequence, there is no literature on patterns of activation and hence cardiac conduction disorders in pediatric patients with CHD. Cardiac surgery, however, offers a unique opportunity to study electrophysiological properties of the pediatric heart.

In adult patients with an ASD and without a history of cardiac arrhythmias (n=13, mean age 41.6±10.3 years) Morton et al.[3] demonstrated enhanced conduction disorders at the terminal crest which persisted beyond percutaneous ASD closure. However, whether enhanced conduction disorders were the result of chronic volume overload, structural remodeling or simply a result of ageing, could not be addressed. However, our pediatric epicardial mapping approach will provide unique insights into the early effects of volume/pressure overload on atrial and ventricular activation patterns and conduction properties.

Prior studies demonstrated that a longer duration of volume/pressure overload correlates with a higher prevalence of atrial and ventricular arrhythmias.[4,5] Older age at time of ASD repair was associated with a higher prevalence of both pre-and post-operative atrial tachyarrhythmias.[6,7] Longstanding volume overload of the RA results in stretch of the atrial wall thereby inducing structural remodeling. Ueda et al.[8] examined RA tissue samples of 65 adult ASD patients undergoing primary repair and compared them with RA tissue samples of age-matched controls. Structural changes, including fibrosis, were indeed more pronounced in ASD patients than in healthy age-matched controls. Macchiarelli et al.[9] observed similar findings in pediatric ASD patients.

31

Ventricular arrhythmias and sudden cardiac death are also common sequelae in those who have undergone ventriculotomy or ventricular septal defect closure and in patients with a systemic right ventricle, Ebstein's anomaly and Eisenmenger's syndrome.[5] Although less common, ventricular arrhythmias may also arise due to longstanding volume/pressure overload, independently of direct surgical scarring. Chowdhury et al.[10] examined biopsies from the right ventricular outflow tract in patients with tetralogy of Fallot. Structural remodeling, including fibrosis, was already present in young (<4 years) patients with left ventricular volume/pressure overload, although structural remodeling was more pronounced in older patients (>4 years). As structural remodeling underlies development of conduction disorders, it is therefore most likely that atrial and ventricular conduction

disorders are already present in young pediatric CHD patients predisposing these patients to cardiac arrhythmias relatively early in life.

Epicardial mapping: valuable or redundant?

In clinical practice, cardiac mapping is usually performed from the endocardium during percutaneous electrophysiological studies, thereby assuming that atrial excitation is a 2-dimensional process. Nowadays, the 3-dimensional nature of cardiac excitation and cardiac arrhythmias is increasingly acknowledged. In order to unravel the 3-dimensional substrate of complex cardiac arrhythmias, such as atrial fibrillation, it is of utmost importance to also study epicardial conduction in patients with CHD.

Clinical relevance & future directions

Our epicardial mapping approach enables further unraveling of arrhythmogenesis in CHD patients. Primary cardiac surgery in pediatric CHD patients is a once in a lifetime opportunity to investigate epicardial conduction properties in the absence of confounding factors such history of cardiac arrhythmias and structural remodeling due to ageing. As CHD patients may present at different ages, we will be able to investigate characteristics of atrial and ventricular conduction disorders from childhood to adulthood[2] and correlate these findings with patient characteristics such as age and type of CHD. The presence of conduction disorders early in life may be the result of structural remodeling induced by short-lasting volume/pressure overload. In this case, one could argue for an expedited intervention strategy in order to prevent structural and hence electrical remodeling. On the other hand, intra-operative cardiac mapping may enable identification of CHD patients who are at high-risk for development of post-operative atrial tachyarrhythmias. This may favor prophylactic atrial arrhythmia surgery in this high-risk population, which is currently a matter of debate.

Knowledge on characteristics of conduction disorders is crucial to identify patients at high-risk for development of cardiac arrhythmias, adapt treatment strategies or timing of interventions and to develop novel therapies aimed at prevention of structural and electrical remodeling.

Limitations

There is no cardiac mapping data of children without structural heart disease for comparison. Endocardial mapping, including the interatrial and interventricular septum, is not possible with the present epicardial mapping approach.

References

1. Khairy P, Van Hare GF, Balaji S, Berul CI, Cecchin F, Cohen MI, Daniels CJ, Deal BJ, Dearani JA, Groot N, et al. PACES/HRS Expert Consensus Statement on the Recognition and Management of Arrhythmias in Adult Congenital Heart Disease: developed in partnership between the Pediatric and Congenital Electrophysiology Society (PACES) and the Heart Rhythm Society (HRS). Endorsed by the governing bodies of PACES, HRS, the American College of Cardiology (ACC), the American Heart Association (AHA), the European Heart Rhythm Association (EHRA), the Canadian Heart Rhythm Society (CHRS), and the International Society for Adult Congenital Heart Disease (ISACHD). Heart Rhythm. 2014;11:e102-165.
2. Houck CA, Lanters EAH, Heida A, Taverne Y, van de Woestijne PC, Knops P, Roos-Serote MC, Roos-Hesselink JW, Bogers A, de Groot NMS. Distribution of Conduction Disorders in Patients With Congenital Heart Disease and Right Atrial Volume Overload. JACC Clin Electrophysiol. 2020;6:537-548.
3. Morton JB, Sanders P, Vohra JK, Sparks PB, Morgan JG, Spence SJ, Grigg LE, Kalman JM. Effect of chronic right atrial stretch on atrial electrical remodeling in patients with an atrial septal defect. Circulation. 2003;107:1775-1782.
4. Zeltser I, Gaynor JW, Petko M, Myung RJ, Birbach M, Waibel R, Ittenbach RF, Tanel RE, Vetter VL, Rhodes LA. The roles of chronic pressure and volume overload states in induction of arrhythmias: an animal model of physiologic sequelae after repair of tetralogy of Fallot. J Thorac Cardiovasc Surg. 2005;130:1542-1548.
5. Walsh EP, Cecchin F. Arrhythmias in adult patients with congenital heart disease. Circulation. 2007;115:534-545.
6. Gatzoulis MA, Freeman MA, Siu SC, Webb GD, Harris L. Atrial arrhythmia after surgical closure of atrial septal defects in adults. N Engl J Med. 1999;340:839-846.
7. Murphy JG, Gersh BJ, McGoon MD, Mair DD, Porter CJ, Ilstrup DM, McGoon DC, Puga FJ, Kirklin JW, Danielson GK. Long-term outcome after surgical repair of isolated atrial septal defect. Follow-up at 27 to 32 years. N Engl J Med. 1990;323:1645-1650.
8. Ueda A, Adachi I, McCarthy KP, Li W, Ho SY, Uemura H. Substrates of atrial arrhythmias: histological insights from patients with congenital heart disease. Int J Cardiol. 2013;168:2481-2486.
9. Macchiarelli G, Nigri G, Martinotti A, DiDio LJ. Subcellular structure of the atrial myocardium of children in cases of atrial septal defect. J Submicrosc Cytol Pathol. 1992;24:395-400.

31

Chapter 32

An unexpected finding by epicardial mapping: atrial fibrillation in a 14-month-old patient with short QT syndrome

Mathijs S. van Schie*

Nawin L. Ramdat Misier*

Wouter J. van Leeuwen

Yannick J.H.J. Taverne

Natasja M.S. de Groot

* Contributed equally

Journal site

Introduction

Short QT syndrome (SQTS) is a very rare channelopathy accompanied with familial clustering and sudden cardiac.[1] It has an estimated prevalence ranging from 0.02% up to 2% in the adult population, but only 0.05% among pediatric patients.[2-6] Up to today, nine mutations in six different genes have been identified, including KCNH2, KCNQ1, KCNJ1, CACNA1C, CACNB2 and CACNA2D1. In pediatric patients, SQTS is characterized by shortening of the corrected QT interval (QTcB <316 ms, J-Tpeak cB <181 ms and the presence of early repolarization) on the surface electrocardiogram (ECG).[7] The underlying pathophysiological features involve shortening of myocardial repolarization due to potassium and calcium channelopathies, which creates at very early age the electrical substrate for not only bradyarrythmia but also for atrial and ventricular tachyarrhythmia including atrial fibrillation (AF).[2,8,9] This case report presents a 14-month-old female patient with SQTS scheduled for an epicardial pacemaker implantation indicated by bradyarrhythmia and chronotropic incompetence in which epicardial high-density mapping revealed an unexpected and unique finding.

Case report

A 14-month-old female patient was hospitalized for elective epicardial pacemaker implantation for chronotropic incompetence. There was no family history of seizures, syncope, arrhythmias or sudden unexplained deaths. The patient was born with a sinus bradycardia (72 bpm, QTc 391 ms, as illustrated in *Figure 1*) and therefore hospitalized. A 24-hour Holter recorded two days after birth revealed sinus rhythm with bradycardia (67–148 bpm), frequent ventricular ectopic beats and a nodal escape rhythm. A heart rate increase to 100 bpm resulted in prolongation of the QTc to >400 ms. A 24-hour Holter was repeated after one month, revealing sinus node dysfunction (SND) with a ventricular escape rhythm.

After four months, there was an increase in left ventricular (LV) and atrial (LA) dilation, LV hypertrophy, mitral regurgitation and LV dysfunction in combination with an open ductus arteriosus. The ECG showed changes in T-wave morphology with a QTc of 330 ms (*Figure 1*). The open ductus arteriosus was successfully percutaneously closed in the following month. Thereafter, the patient remained in a ventricular escape rhythm (60–70 bpm), alternating with sinus rhythm (110 bpm). The next 24-hour Holter revealed sinus rhythm or ectopic atrial rhythms with frequent ventricular escape rhythm (57–93 bpm) and occasionally 2nd degree AV block type II. In the 7th month, genetic evaluation revealed a de novo pathogenic variant in the KCNQ1 gene (Chr 11: NM_000218.2(KCNQ1):c.421G>A (p.Val141MET), class V, heterozygous); variants in the KCNQ1 gene were not found in any of family members after genetic testing. The ECG at this moment demonstrated a ventricular escape rhythm (60 bpm) with early repolarization and significant shortening of QTc (285 ms), and the patient was therefore diagnosed with SQTS.

32

From the 7th month, left ventricular systolic and diastolic function further deteriorated with progressive LV dilatation, which was routinely measured on echocardiography. At the 12th month it was therefore decided to implant an epicardial DDD-pacemaker. At the age of 14 months, the patient underwent surgery. The pre-operative ECG demonstrated a nodal rhythm (*Figure 1*). The patient participated in the FANTASIA study (MEC-2019-0543) in which epicardial high-density mapping of the atria was performed.[10] Immediately after mini-sternotomy, a 128-electrode array (0.28 mm^2, interelectrode distance 2.12 mm) was placed on the right atrium perpendicular to the caval veins and epicardial electrograms were recorded for 5 seconds. These electrograms, unexpectedly, revealed continuous AF with an average cycle length as short as 25 ms (*Figure 2*). Fibrillation waves could, however, not be identified
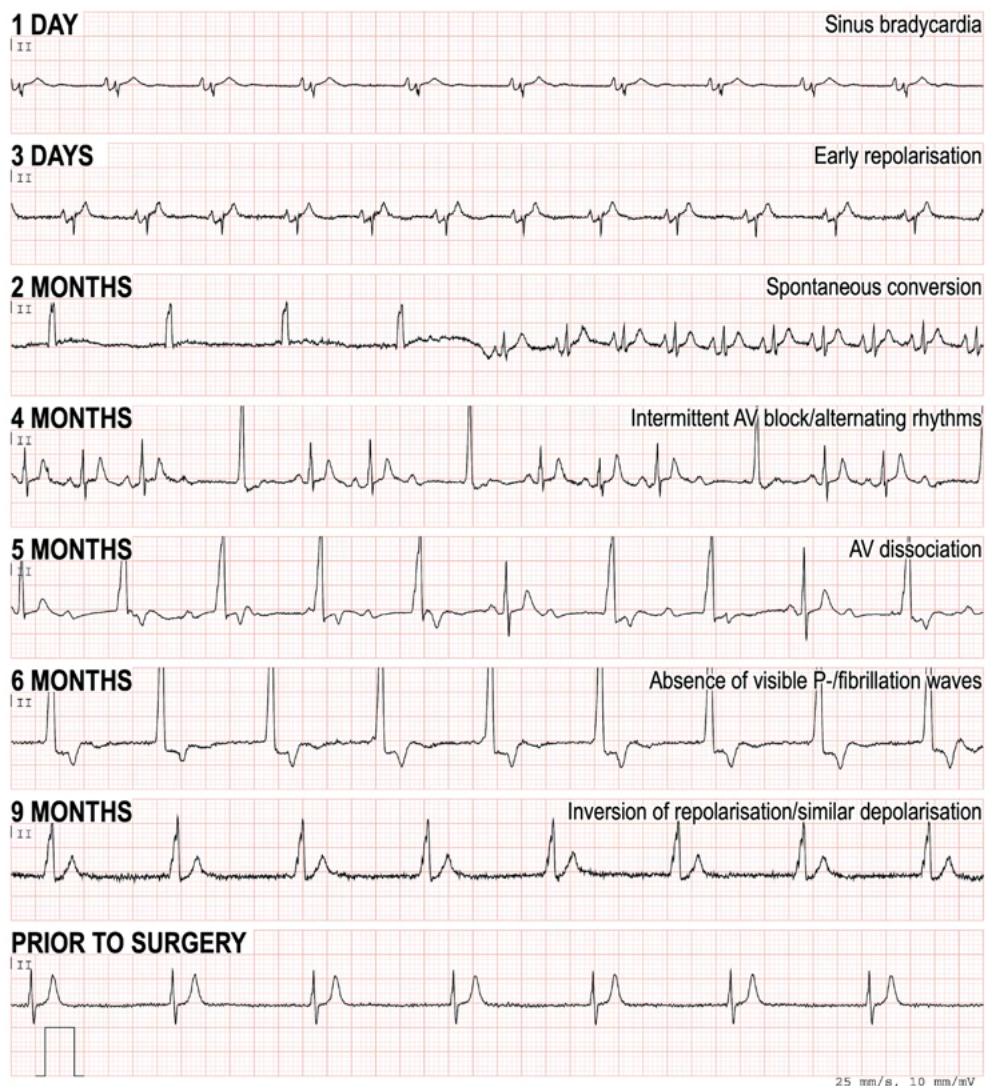
Figure 1 – Lead II of surface ECG demonstrating various rhythm. Lead II derived from surface ECG recorded at various ages. At the first day after birth, the ECG demonstrates a sinus bradycardia. At day 3, early repolarization can be seen. At 2 months, ventricular escape rhythms without visible P-wave spontaneously converted to sinus rhythm. After 4 months, there is a Mobitz type I AV-block with ventricular escape. At the 5th month, there is predominantly AV dissociation. P-waves or fibrillation waves are not visible at the 6th month. After 9 months, there is an inversion of repolarization, but without change in depolarization. Prior to surgery, there is a nodal rhythm without visible P-waves or fibrillation waves.

on the surface ECG. The surgeon observed a mechanical standstill of the atria. Because of the presence of persistent AF and limited literature supporting cardioversion in young patients with SQTS and persistent AF[9,11,12], electrical cardioversion was not performed. Consequently, only an epicardial VVI pacemaker was implanted. Post-operatively, anticoagulation therapy with aspirin was started.
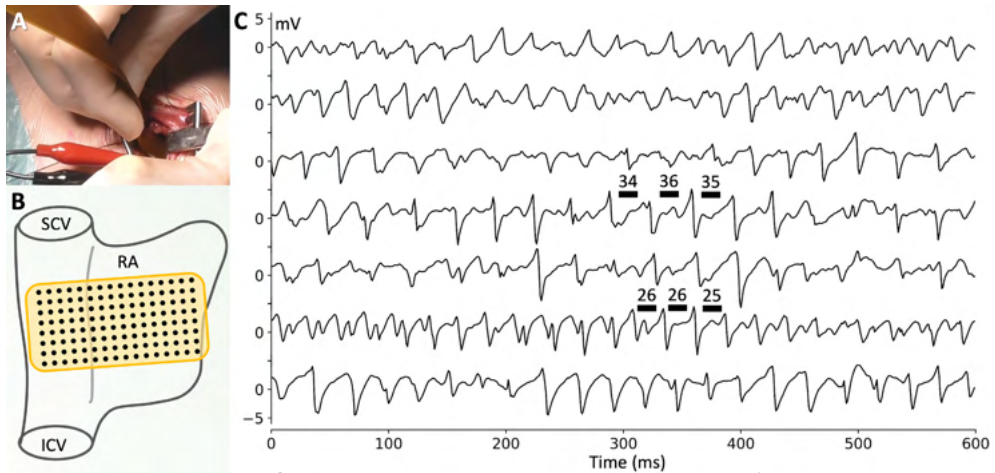
Figure 2 – Unexpected atrial fibrillation at the right atrium. *Panel A*: positioning of electrode array using the pacemaker incision. *Panel B*: schematic representation of the position and orientation of the 128-electrode array (2.12 mm interelectrode distance) at the middle of the right atrial free wall. *Panel C*: unipolar epicardial electrograms recorded from the middle of the right atrium demonstrating beat-to-beat variation in electrogram morphology and cycle length indicating atrial fibrillation. **ICV** = inferior caval vein; **RA** = right atrium; **SCV** = superior caval vein.

Discussion

Atrial fibrillation in pediatric patients

Although AF is the most common cardiac arrhythmia among adults, it is an extremely rare entity in the pediatric population. The global prevalence of AF in the under-5-years age group is approximately 3 per 100,000.[13] The vast majority of AF cases in the youngest age groups in epidemiological studies are often associated with co-existing CHD or channelopathy. Due to their rarity, there has been minimal investigation in atrial excitation and mechanisms of AF in the youngest patients. Epicardial mapping during pediatric cardiac surgery provides a unique opportunity to study atrial excitation at a high resolution in various congenital defects and channelopathies. Recently, epicardial mapping revealed that local conduction disorders are already present in pediatric patients (<1 year) with congenital heart disease.[14] In this case report, we now demonstrated that epicardial mapping also has a direct value for real-time diagnosis in daily clinical practice. If (epicardial) atrial electrograms during cardiac surgery would not have been recorded using a dedicated mapping system, AF could not have been confirmed, and possibly not diagnosed for many years.[12]

Short QT syndrome and atrial fibrillation

Patients with SQTS often present with AF, even at a very young age. Several genetic mutations have been linked to SQTS, including the KCNQ1 gene, which codes proteins that produce a membrane channel that conducts I_{Ks}. Mutations in the KCNQ1 gene cause either gain- or loss-of-function in the channel and its current. Loss-of-function variants typically cause long QT syndrome, but gain-of-function variants, with increased I_{Ks} current, have been associated with SQTS. However, the mechanisms underlying the increased atrial arrhythmogenesis and impaired cardiac pacemaker activity arising from increased I_{Ks} remain unclear. Computer modelling demonstrated that the Val141MET KCNQ1 mutation increased dispersion of action potential duration. Furthermore, the model showed that atrial action potential duration indeed shortened by a large instantaneous outflux of potassium upon

32

membrane depolarization, thereby prematurely abolishing the action potential plateau phase.[15] Interestingly, an extremely short cycle length was observed in our patient, indicating that the refractory period could be <25 ms. Reduction of the effective refractory period in combination with spatial dispersion in refractoriness can therefore result in a high number fibrillation waves exciting the atria at a very high rate even within the small atria of young pediatric patients.

Conclusions

Even in very young patients with SQTS, AF can be sustained with an excessively high rate of the fibrillatory process which is not visible as fibrillation waves on the surface ECG. In pediatric patients with arrhythmias undergoing cardiac surgery, (epicardial) mapping could be used as an additive diagnostic tool to guide therapy.

References

1. Gussak I, Brugada P, Brugada J, Wright RS, Kopecky SL, Chaitman BR, Bjerregaard P. Idiopathic short QT interval: a new clinical syndrome? Cardiology. 2000;94:99-102.
2. Guerrier K, Kwiatkowski D, Czosek RJ, Spar DS, Anderson JB, Knilans TK. Short QT Interval Prevalence and Clinical Outcomes in a Pediatric Population. Circ Arrhythm Electrophysiol. 2015;8:1460-1464.
3. Mason JW, Ramseth DJ, Chanter DO, Moon TE, Goodman DB, Mendzelevski B. Electrocardiographic reference ranges derived from 79,743 ambulatory subjects. J Electrocardiol. 2007;40:228-234.
4. Miyamoto A, Hayashi H, Yoshino T, Kawaguchi T, Taniguchi A, Itoh H, Sugimoto Y, Itoh M, Makiyama T, Xue JQ, et al. Clinical and electrocardiographic characteristics of patients with short QT interval in a large hospital-based population. Heart Rhythm. 2012;9:66-74.
5. Kobza R, Roos M, Niggli B, Abacherli R, Lupi GA, Frey F, Schmid JJ, Erne P. Prevalence of long and short QT in a young population of 41,767 predominantly male Swiss conscripts. Heart Rhythm. 2009;6:652-657.
6. Anttonen O, Junttila MJ, Rissanen H, Reunanen A, Viitasalo M, Huikuri HV. Prevalence and prognostic significance of short QT interval in a middle-aged Finnish population. Circulation. 2007;116:714-720.
7. Suzuki H, Horie M, Ozawa J, Sumitomo N, Ohno S, Hoshino K, Ehara E, Takahashi K, Maeda Y, Yoshinaga M, et al. Novel electrocardiographic criteria for short QT syndrome in children and adolescents. Europace. 2021;23:2029-2038.
8. Villafane J, Young ML, Maury P, Wolpert C, Anttonen O, Hamilton R, Kannankeril PJ, Fischbach PS. Short QT syndrome in a pediatric patient. Pediatr Cardiol. 2009;30:846-850.
9. Sarquella-Brugada G, Campuzano O, Iglesias A, Grueso J, Bradley DJ, Kerst G, Shmorhun D, Brugada J, Brugada R. Short QT and atrial fibrillation: A KCNQ1 mutation-specific disease. Late follow-up in three unrelated children. HeartRhythm Case Rep. 2015;1:193-197.
10. Kharbanda RK, van Schie MS, van Leeuwen WJ, Taverne Y, Houck CA, Kammeraad JAE, Bogers A, de Groot NMS. First-in-children epicardial mapping of the heart: unravelling arrhythmogenesis in congenital heart disease. Interact Cardiovasc Thorac Surg. 2021;32:137-140.
11. Hong K, Piper DR, Diaz-Valdecantos A, Brugada J, Oliva A, Burashnikov E, Santos-de-Soto J, Grueso-Montero J, Diaz-Enfante E, Brugada P, et al. De novo KCNQ1 mutation responsible for atrial fibrillation and short QT syndrome in utero. Cardiovasc Res. 2005;68:433-440.
12. Righi D, Silvetti MS, Drago F. Sinus bradycardia, junctional rhythm, and low-rate atrial fibrillation in Short QT syndrome during 20 years of follow-up: three faces of the same genetic problem. Cardiol Young. 2016;26:589-592.
13. Mills LC, Gow RM, Myers K, Kantoch MJ, Gross GJ, Fournier A, Sanatani S. Lone atrial fibrillation in the pediatric population. Can J Cardiol. 2013;29:1227-1233.
14. Kharbanda RK, van Schie MS, Ramdat Misier NL, van Leeuwen WJ, Taverne Y, van de Woestijne PC, Kammeraad JAE, Bartelds B, Bogers A, de Groot NMS. First Evidence of Atrial Conduction Disorders in Pediatric Patients With Congenital Heart Disease. JACC Clin Electrophysiol. 2020;6:1739-1743.
15. Whittaker DG, Colman MA, Ni H, Hancox JC, Zhang H. Human Atrial Arrhythmogenesis and Sinus Bradycardia in KCNQ1-Linked Short QT Syndrome: Insights From Computational Modelling. Front Physiol. 2018;9:1402.

32

Chapter 33

Epicardial high-resolution mapping of advanced interatrial block: relating ECG, conduction abnormalities and excitation patterns

Nawin L. Ramdat Misier

Mathijs S. van Schie

Chunsheng Li

Frans B.S. Oei

Frank R.N. van Schaagen

Paul Knops

Yannick J.H.J. Taverne

Natasja M.S. de Groot

Abstract

Background: Impairment of conduction across Bachmann's bundle (BB) may cause advanced interatrial block (a-IAB), which in turn is associated with development of atrial fibrillation. However, the exact relation between a complete transverse line of conduction block (CB) across BB and the presence of a-IAB has not been studied. The aims of this study were to determine whether 1) a complete transversal line of CB across BB established by high resolution mapping correlates with a-IAB on the surface ECG, 2) conduction abnormalities at the right and left atria correlate with a-IAB and 3) excitation patterns are associated with ECG characteristics of a-IAB.

Methods: We included 40 patients in whom epicardial mapping revealed a complete transverse line of CB across BB. Pre-operative ECGs and post-operative telemetry were assessed for the presence of (a)typical a-IAB and de novo early post-operative atrial fibrillation (E-PoAF), respectively. Total atrial excitation time (TAET) and RA-LA delay were calculated. Entry site and trajectory of the main sinus rhythm wavefront at the pulmonary vein area (PVA) were assessed.

Results: Thirteen patients were classified as a-IAB (32.5%). In the entire atria and BB there were no differences in conduction disorders, although, patients with a-IAB had an increased TAET and longer RA-LA delay compared to patients without a-IAB (90.0 ± 21.9 ms vs. 74.9 ± 13.0 ms, p=0.017; 160.0 ± 27.0 ms vs. 136.0 ± 24.1 ms, p=0.012, respectively). Patients with typical a-IAB solely had caudocranial activation of the PVA, without additional cranial entry sites. Prevalence of de novo E-PoAF was 69.2% and was similar between patients with and without a-IAB.

Conclusions: A transverse line of CB across BB partly explains the ECG characteristics of a-IAB. We found atrial excitation patterns underlying the ECG characteristics of both atypical and typical a-IAB. Regardless of the presence of a-IAB, the clinical impact of a complete transverse line of CB across BB was reflected by a high incidence of de novo E-PoAF.

Journal site &
supplementary material

Introduction

Bachmann's bundle (BB) is the main preferential route for interatrial conduction.[1,2] Data from recent studies suggest that conduction disorders at BB are involved in the pathophysiology of atrial fibrillation (AF)[3,4], but the mechanistic relationship is yet to be elucidated. Impairment of conduction across BB causes advanced interatrial block (a-IAB), which is in turn strongly associated with development of supraventricular tachycardia, including AF.[5-7]

The relationship between BB and a-IAB was substantiated by the observation that a surgical lesion across BB resulted in electrocardiogram (ECG) characteristics similar to a-IAB; namely, biphasic P-waves appearing particularly in the inferior leads of the surface ECG.[8] These ECG characteristics have been attributed to a caudocranial activation of the left atrium (LA) due to other dormant interatrial connection, but exact activation patterns underlying a-IAB are scarcely reported.[7,9] Introduction of typical and atypical a-IAB – subvariants of a-IAB based on alternative ECG patterns – has further complicated understanding of the excitation patterns.[10]

Importantly, the relation between a complete transverse line of conduction block (CB) across BB in patients with ECG features of a-IAB has never been investigated, even though this is thought to underlie a-IAB.[8] Recent reports even suggest that the site of CB is not between right atrium (RA) and LA, but rather the roof of the LA.[11,12] Epicardial mapping during cardiac surgery provides a unique methodology to examine impairment of conduction across BB on a high-resolution scale. The aims of this study are therefore to determine whether 1) a complete transversal line of CB across BB established by high resolution mapping correlates with a-IAB on the surface ECG, 2) conduction abnormalities at the right and left atria correlate with a-IAB and 3) excitation patterns are associated with ECG characteristics of a-IAB.

Methods

Study population

Patients (≥18 years) undergoing elective cardiac surgery with or without a history of AF were included in this current study. Exclusion criteria were hemodynamic instability, presence of an implanted pacemaker with atrial pacing, previous cardiac surgery, end-stage renal failure or severely impaired left ventricular function. This study is part of the QUASAR (MEC 2010-054) and Halt&Reverse (MEC 2014-393) studies, which follow the declaration of Helsinki principles.[13,14] Patient characteristics were obtained from electronic medical files. Written informed consent was obtained from all patients.

Identification of inter-atrial conduction block

For this study, we solely selected patients in whom epicardial mapping revealed a complete transverse line of CB (impairing longitudinal conduction) across BB, which was defined as a continuous line of CB from the superior to the inferior border of BB (left panel of *Figure 1*). Subsequently, pre-operative ECGs of these patients were evaluated by two independent investigators for signs of advanced (atypical) a-IAB as described by Bayes de Luna et al.[10], including a P-wave duration ≥120 ms and biphasic P-wave morphology in leads II, III and aVF. P-wave duration was measured both manually and automatically by using custom made MEANS-algorithm.[15] We classified our selected patients into patients with a-IAB (typical or atypical a-IAB) and patients without a-IAB. Subsequently, we subdivided patients with a-IAB into patients with typical and atypical a-IAB based on the presence or absence of a biphasic P-wave in lead II, respectively.[10]

33
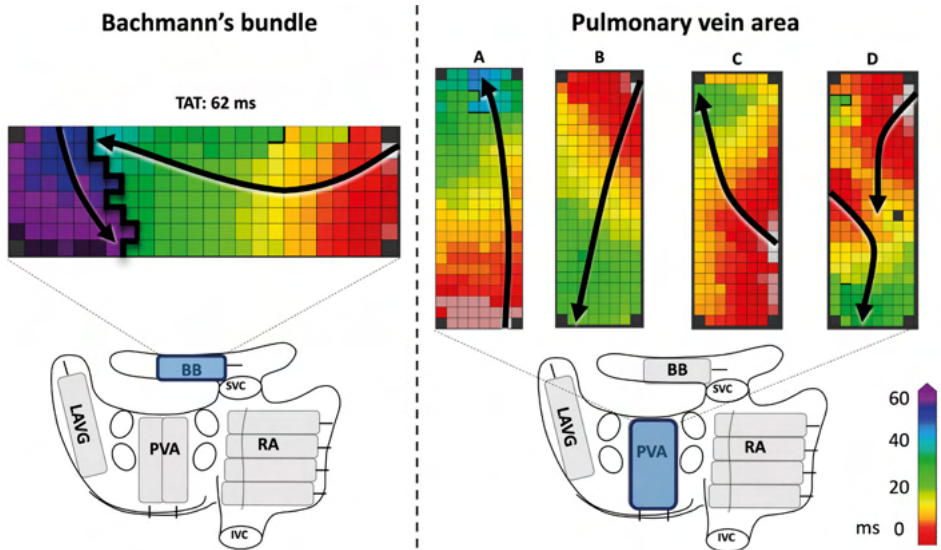
Figure 1 – Epicardial mapping procedure. *Left panel*: an example of a complete line of conduction block across BB, ranging from the superior border up to the inferior border. *Right panel*: examples of activation patterns at the pulmonary vein area (PVA). In example A and C, the PVA is activated in a caudocranial direction, in B and D craniocaudal direction. In examples A, B and C the entry sites of the wavefronts are respectively caudal, cranial and mid right-sided. In example D, there are two entry sites of the wavefront, one left-sided and one cranial. Black lines indicate conduction block. Black arrows show the direction of the wavefront. **BB** = Bachmann's bundle; **LAVG** = left atrioventricular groove; **PVA** = pulmonary vein area; **RA** = right atrium; **SVC** = superior caval vein; **IVC** = inferior caval vein.

Mapping procedure

Prior to initiation of extracorporeal circulation, epicardial mapping was performed during cardiac surgery at the RA, BB and LA, consisting of the left atrioventricular groove (LAVG) and pulmonary vein area (PVA).[13] A schematic overview of the atrial mapping sites is provided in the lower part of *Figure 1*. Mapping was performed during sinus rhythm (SR), with either a custom-made 128- or a 192-unipolar electrode array (interelectrode distances of both arrays: 2 mm). At every mapping site, signals were recorded during SR for five seconds, including a surface ECG, bipolar reference electrode and a calibration signal of 2 mV and 1000 ms. Recordings were amplified with gain 1000, sampled with a rate of 1 kHz, filtered with bandwidth 0.5–400 Hz, analogue-to-digital converted (16 bits) and stored on hard disk.

Data processing

Mapping data was analysed by using custom-made software previously described in detail.[13] Color-coded local activation time maps were constructed by annotating the steepest negative atrial deflection. Mapping locations were excluded when deflections were marked in less than 40% of the mapping array due to a poor signal-to-noise ratio. Atrial extrasystolic beats were excluded. For every mapping location (RA, BB and LA (=LAVG+PVA)) total activation times (TAT) were calculated by finding the first and last activation of the corresponding mapping sites compared to the bipolar reference electrode. Similarly, total atrial excitation time (TAET) for both atria, including BB, was determined. Furthermore, the time difference between first activation at the RA and onset of LA activation (RA-LA delay) was determined.

Conduction times (CTs) were calculated by calculating the difference in local activation time between adjacent electrodes. Similar to previous studies, CB was determined as CT

Table 1 – Baseline characteristics.

	No a-IAB (n=27)	a-IAB (n=13)	*p*-value
Age (years)	69.9±7.1	74.9±6.6	0.038
BMI (kg/m²)	28.2±4.5	27.6±3.6	0.714
Gender (male)	18 (66.7%)	12 (92.3%)	0.124
History of SVT	9 (33.3%)	5 (38.5%)	1.000
Underlying heart disease			0.739
• IHD	11 (40.7%)	7 (53.8%)	
• AVD(/+IHD)	12 (44.4%)	4 (30.8%)	
• MVD(/+IHD)	4 (14.8%)	2 (15.4%)	
Antiarrhythmic drugs			
• Class I	1 (3.7%)	0	1.000
• Class II	18 (66.7%)	10 (76.9%)	0.716
• Class III	0	2 (15.4%)	0.100
• Class IV	0	0	-
Cardiovascular risk factors			
• Hypertension	16 (59.3%)	9 (69.2%)	0.730
• Dyslipidemia	15 (55.6%)	4 (30.8%)	0.141
• Diabetes mellitus	6 (22.2%)	5 (38.5%)	0.451
• Myocardial infarction	8 (29.6%)	2 (15.4%)	0.451
• Thyroid disease	4 (14.8%)	0	0.284
LAVI	30.1 [24−39]	47 [26.3−84.3]	0.343
Systolic LVF			1.000
• Normal	21 (77.8%)	10 (76.9%)	
• Mild dysfunction	5 (18.5%)	3 (23.1%)	
• Moderate dysfunction	1 (3.7%)	0	
P-wave duration ≥120 ms	21 (77.7%)	13 (100%)	

Values are presented as N (%), mean ± standard deviation or median [interquartile range]. **AVD** = aortic valve disease; **BMI** = body mass index; **IHD** = ischemic heart disease; **LAVI** = left atrial volume index; **LVF** = left ventricular function; **MVD** = mitral valve disease; **SVT** = supraventricular tachycardia; **UHD** = underlying heart disease.

differences of ≥12 ms between two electrodes.[16] If an area of conduction delay (CD, CTs 7−11 ms) was connected to a CB area it was labelled as a continuous CDCB area (cCDCB). The prevalence of CB was determined as the percentage CTs ≥12 ms relative to all CTs.

In order to elucidate the ECG characteristics of a-IAB, we investigated the activation patterns at the LA. Both entry site and trajectory of the main SR wavefronts at the pulmonary vein area (PVA) were determined, as illustrated in the right panel of *Figure 1*. The direction of the wavefront was assessed for caudocranial excitation (panel B and D in *Figure 1*) and the presence of additional cranial entry sites (panel D in *Figure 1*).

Detection of post-operative atrial fibrillation

Cardiac rhythms of all patients were continuously recorded from the moment of arrival on the surgical ward to the end of the fifth post-operative day using bedside monitors (Draeger Infinity™). Automatic algorithms were used to detect early post-operative AF (E-PoAF) episodes lasting >30 seconds. All episodes detected by the software were cross-checked by two blinded operators in order to eliminate potential false positive registrations induced by artefacts.

Statistical analysis

Normally distributed continuous variables were expressed as mean ± standard deviation, skewed variables as median [25th−75th percentile] and categorical data as numbers and percentages. Continuous data was analyzed using the Mann-Whitney U test or independent

33

t-test and categorical data with χ^2 or Fisher exact test when appropriate. A *p*-value <0.05 was considered statistically significant. All statistical analyses were performed with IBM SPSS statistics for Windows, version 25 (IBM Corp., Armonk, N.Y., USA).

Results

Baseline characteristics

A total of 40 patients were included (age: 71.5±7.3 years, 30 male (75.0%)). The indication for surgery for most patients was ischemic heart disease (n=18, 45.0%), followed by aortic valve disease (n=16, 40%) and mitral valve disease (n=6, 15.0%). Thirteen patients (32.5%) had a history of AF; only 1 patient (2.5%) had atrial flutter.

Based on the aforementioned Bayes de Luna criteria, only 13 patients were classified as a-IAB (32.5%) (patients without a-IAB n=27 (67.5%)). The median time interval between the pre-operative ECGs and cardiac surgery was 15 [6–22] days. Baseline characteristics of both patient groups are described in *Table 1*. Patients with a-IAB did not differ from patients without a-IAB, except for age; patients with a-IAB were older than patients without a-IAB (74.9±6.6 years vs. 69.9±7.1 years, p=0.038).

Relation between a-IAB and conduction properties

As demonstrated by the boxplots in *Figure 2A*, TAT-BB did not differ significantly between patients with a-IAB and patients without a-IAB (75.7±19.7 ms vs. 65.0±13.2 ms, p=0.051, respectively). While long TAT-BB were expected in all patients, three patients (1 a-IAB, 2 no a-IAB) had a considerably shorter TAT-BB compared to other patients. *Figure 2B* demonstrates
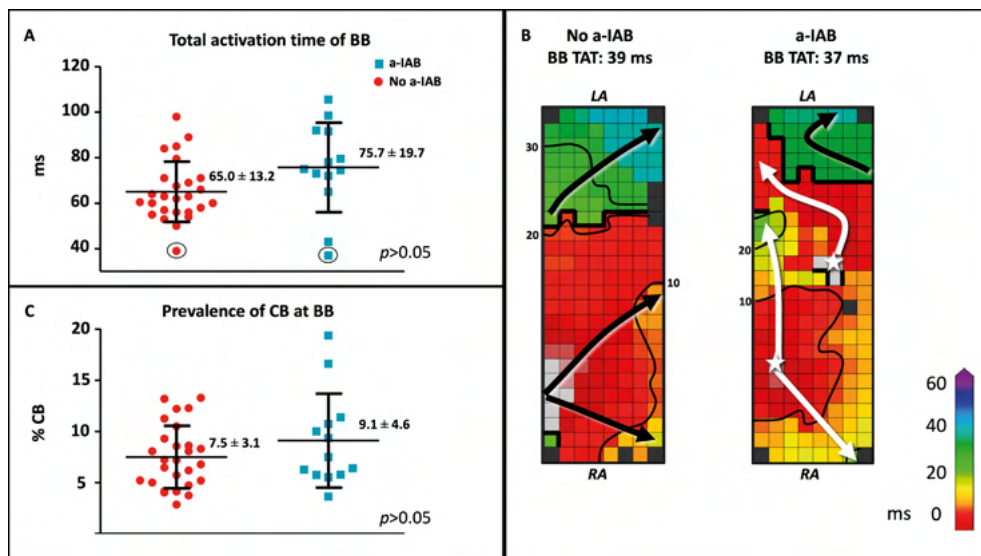
Figure 2 – Relation between a-IAB and conduction properties. *Left panel*: boxplots depict the differences in activation time (upper panel) and prevalence of CB (lower panel) at BB between the no a-IAB and a-IAB group. *Right panel*: color-coded activation maps of BB show examples of a short TAT of BB in a patient from the no a-IAB group (left) and one from the a-IAB group (right). See text for further description. Activation maps are depicted with 10 ms isochrones and arrows showing the main direction of wavefront propagation. Black lines indicate an area of CB and a star represents an epicardial breakthrough wave. **AT** = activation time; **BB** = Bachmann's bundle; **CB** = conduction block; **IHD** = ischemic heart disease; **LA** = left atrium; **MVD** = mitral valve disease; **RA** = right atrium.
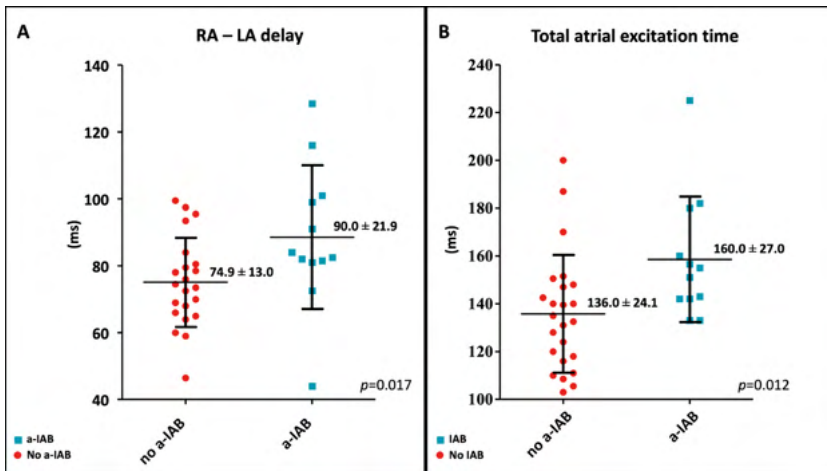
Figure 3 – Relation between a-IAB and atrial excitation. The left and right boxplots show the time differences in LA activation delay and total atrial excitation time between the no a-IAB and a-IAB groups. **RA** = right atrium; **LA** = left atrium.

color-coded activation time maps from two of these patient with short TAT-BB. The left and right color-coded maps correspond to a patients with a-IAB and a patient without a-IAB, respectively. Although both patients have a similar TAT-BB, the entry site of the SR wavefront into BB is different between the patients. In the patient without a-IAB, the earliest activation at BB is a wavefront entering in the corner of the right atrial site. In contrast, in the patient with a-IAB the earliest wavefronts emerge from the middle of BB, indicated with a white star in *Figure 2*. Hence, these wavefronts did not originate from the RA site of BB, indicating an obstruction between the superior RA and the right atrial insert site of BB, inhibiting a right-to-left activation of BB. Thus, even though the TAT-BB is short in this patient, the BB activation pattern of the patient with a-IAB still suggests an abnormal route of wavefront propagation during SR.

Besides the complete transverse line of CB across BB, multiple additional lines of CB were also present at BB. However, the amount and maximum length of CB at BB, including the complete transverse line, did not differ significantly between patients with or without a-IAB (amount of CB: 9.1±4.6 % vs. 7.5±3.1 %, p=0.194; maximum CB length: 32 [24–48] mm vs. 34 [24–40] mm, p=0.776, respectively), as shown in *Figure 2C*.

RA-LA delay was longer in the a-IAB group (*Figure 3A*; a-IAB: 90.0±21.9 ms vs. no a-IAB: 74.9±13.0 ms, p=0.017). In addition, TAET was also longer in the a-IAB group (*Figure 3B*, a-IAB: 160.0±27.0 vs. no a-IAB: 136.0±24.1, p=0.012). However, no differences were found in TAT-RA or TAT-LA between both groups (RA: a-IAB: 82 [63.8–115.3] vs. no a-IAB: 82.3 [71.9–95.3], p=0.794; LA: a-IAB: 69.5 [60.8–90.9] ms vs. no a-IAB: 56.0 [51.0–71.0], p=0.096). Thus, although there is a longer RA-LA delay and TAET in patients with a-IAB, there is no preferential site of conduction slowing in RA or LA.

Caudocranial activation of the main SR wavefront at the PVA was present in patients with a-IAB 91.7%, while only 70.8% of the patients without a-IAB had a caudocranial activation (p=0.224). Caudocranial activation is thus frequently observed in patients with a-IAB, however it not specific for a-IAB as it also common in patients without a-IAB. Additional excitation of the PVA via a cranial entry was equally often present in patients with a-IAB and patients without a-IAB (41.7% vs. 58.3%, p=0.345, respectively).

33

Development of E-PoAF

The prevalence of de novo E-PoAF was as high as 69.2% (18/26 patients). However, the prevalence of de novo E-PoAF did not differ between patients with and without a-IAB (62.5% vs. 72.2%, p=0.667, respectively).

Typical a-IAB versus atypical a-IAB

In the entire study population, typical and atypical a-IAB were present in respectively 5 and 8 patients. Seven patients had ECGs corresponding to type 1 atypical a-IAB (87.5%) and 1 (12.5%) had type 2 atypical a-IAB. Patients with typical a-IAB pattern were older than patients with atypical a-IAB (80.1±2.9 years vs. 71.7±6.2 years, p=0.017, respectively). Development of de novo E-PoAF did not differ between these groups (typical a-IAB: 66.7% vs. atypical a-IAB: 60.0%, p=1.000).

Patients with typical and atypical a-IAB differed in entry site of SR wavefronts at the PVA. An additional cranial entry site was never present in patients with typical a-IAB, while 71.4% patients with atypical a-IAB had a cranial entry site (p=0.028). All patients with an additional cranial entry site also had caudal or mid-right entry site of the main SR wavefront. Therefore, both groups, except for one patient in the atypical a-IAB group, showed caudocranial activation of the PVA during SR.

In addition, patients with typical a-IAB had longer TAT-LA compared to patients with atypical a-IAB (84.6±14.4 vs. 58.8±16.8, p=0.031, respectively). As shown in *Supplementary Table 1*, with exception of TAT-LA, patients with typical a-IAB demonstrated similar conduction properties as patients with atypical a-IAB.

Discussion

This high-resolution epicardial mapping study revealed that a-IAB is only present in a part of the patients with a complete transverse line of CB across BB. In the entire RA, LA and BB there were no differences in conduction disorders. Nevertheless, patients with a-IAB had a delayed onset of LA activation and increased TAET in comparison to patients without a-IAB. Patients with typical a-IAB showed only a single caudocranial propagating wavefront activating the PVA, and TAT-LA was increased compared to patients with atypical a-IAB. Independently of the presence of a-IAB, patients with a complete transverse line of CB at BB demonstrated a high incidence of de novo E-PoAF.

Pathophysiology of a-IAB

Although impaired conduction at BB may underlie a-IAB[8], only one third of our patients had ECG characteristics of (a)typical a-IAB. We therefore provide evidence that a-IAB is not solely related to interatrial conduction at BB. The low prevalence of a-IAB in this study can be explained by the presence of alternative (preferential) interatrial conduction routes. In humans, there is significant inter-individual variation in interatrial conduction through various routes, which include conduction 1) anteriorly via the Bachmann's bundle, 2) posteriorly via myocardial pathways or bridges at the level of the right pulmonary veins (also known as fossa ovalis connections) and 3) inferiorly via myocardial sleeves extending from the coronary sinus to the inferior part of the LA.[17-20] The SR wavefront propagates predominantly across the anterior pathway.[21] In up to one-third of the patients, initial LA breakthrough during SR is observed in the fossa ovalis region, which corresponds to conduction via the posterior interatrial connection.[21] Variability in number, location and

thickness of these interatrial connections may partly explain why some individuals develop a-IAB whereas others do not. If interatrial conduction across BB is impaired, some patients will have the posterior route as an alternative option and will avoid a-IAB on ECG. However, other patients, who lack interatrial impulse propagation in the anterior and posterior parts of the interatrial septum due to advanced remodeling, will be dependent on the inferior route for interatrial conduction. They will therefore have caudal-cranial activation of the LA and a-IAB on ECG.

We observed no clear preferential sites for conduction slowing in the RA and LA, although patients with a-IAB did have delayed onset of LA activation and longer TAET, which suggests that conduction is likely also impaired outside the regions that are mapped, such as other interatrial conduction pathways. Compared with healthy controls, patients with AF indeed have more often impaired conduction across the anterior and posterior interatrial connections.[4,22]

Several studies have investigated the direct relation between injury of BB and ECG changes corresponding to a-IAB.[8,23,24] In an animal model, Waldo et al.[8] showed that a surgical lesion across the middle of BB resulted in ECG characteristics similar to a-IAB. Mikhaylov[23] demonstrated that ablation at the anteroseptal RA – close to the insertion of BB - will result in a-IAB on ECG. Moser et al.[24] highlighted the importance of various inputs (muscle strands) of BB onto the LA for development of a-IAB. BB has both superficial epicardial fibers connecting to the left atrial appendage, as well as fibers from deeper layers coursing close the right pulmonary vein. Distal injury of either tract will therefore not directly result in a-IAB. In addition, BB is also connected with other parts of the atria through various (epicardial) bundles.[19] For example, a posterosuperior bundle joins the posterior part of BB from the posterior right atrial wall. A wavefront entering BB in the center of the mapping array, as observed in the example in *Figure 2B*, can also be explained by the finding that BB is connected to the surrounding myocardial tissue as it transverses the interatrial groove. This mid-entry wavefront presumably originates from other interatrial septal pathways and continues at BB.

Caudocranial activation

All patients with a-IAB in our study had caudocranial activation of the PVA, except for one patient with atypical a-IAB. Moreover, patients with typical a-IAB never had an additional cranial entry site at the PVA. The electrophysiological mechanism underlying the ECG pattern seen in typical a-IAB had only been investigated in a few patients.[9,11,21] Cosio et al.[11] also found caudocranial activation of the LA in three patients with a-IAB during catheterization. In a more recent mapping study, it was demonstrated in two patients with a-IAB that the LA is activated only via the coronary sinus and not via BB or the interatrial septum.[21] We now provide evidence that right-to-left propagation over BB is completely interrupted in patients with a complete transverse line of CB at BB and typical a-IAB, as these patients did not have a cranial entry site at the PVA region.

In 2018, Bayes de Luna et al.[10] introduced atypical a-IAB, with a variety of P-wave morphologies in the inferior leads, but with a terminal negative component in lead aVF, which still indicates caudo-cranial activation of the LA. Bayes de Luna et al.[10] defined three subtypes of atypical a-IAB, which include 1) the terminal component of the P-wave in lead II to be "isodiphasic" (flat rather than negative), 2) the terminal component of the P-wave in lead II to be "biphasic" ("negative-positive") and 3) first component of the P-wave to be isodiphasic in leads III and aVF, but biphasic in lead II (which requires ectopic atrial rhythms as differential diagnosis). In our mapping study, we only found ECGs corresponding to type 1 (n=7) and type 2

33

atypical a-IAB (n=1). In these patients the LA was predominantly activated by a caudal-cranial wavefront, although a (small) wavefront entering the cranial LA was still present. The presence of an extra cranial entry site in patients with atypical a-IAB could be responsible for the different terminal component of the P-wave in II, which corroborates why these patients have atypical a-IAB on ECG instead of typical a-IAB.

Early post-operative atrial fibrillation

While a-IAB is strongly associated with development of AF, patients with and without a-IAB did not differ in the incidence of de novo E-PoAF.[5-7] For that reason, in patients with a complete line of CB on BB, a-IAB does not seem to further contribute to development of E-PoAF. Instead, the presence of a-IAB in our patients may rather be an indicator of extensive (electrical and/or structural) remodeling than a culprit itself in the development of AF. However, the incidence of de novo E-PoAF is still considerably high in these patients compared to other populations undergoing cardiac surgery.[25] Patients with mitral valve disease are considered to have the highest risk of developing EPOAF with a prevalence between 29.9% and 44.1%.[25] In patients with an complete line of CB on BB, almost 70% of the patients developed E-PoAF, which is considerably higher than patients with mitral valve disease. Conde et al.[26] found a similar prevalence of E-PoAF (66.7%) in 36 patients with a-IAB undergoing coronary artery bypass grafting. In line with our findings, Teuwen et al.[4] already demonstrated that patients with long lines of transverse CB (>12 mm) across BB had a 3 times higher risk to develop E-PoAF.

Currently, various mechanisms and risk factor factors for E-PoAF have been suggested, and many preventive treatments for this arrhythmia have been proposed, but the prevalence of PoAF remains substantial and troublesome.[27] Our results provide further insights into the development of E-PoAF by characterizing its pre-existing arrhythmogenic substrate. A deeper understanding of the underlying mechanisms of E-PoAF will help better identify patients at risk for E-PoAF, which could stimulate novel (preventive) treatments.

Limitations

The surface ECG was obtained prior to the mapping procedure, so there was no simultaneous registration of the surface ECG and electrograms. We did not perform endocardial mapping of the interatrial septum, as this is not possible in the current setting.

Conclusions

In the present study, we demonstrated that a complete transverse line of CB across BB partly explains the ECG characteristics of a-IAB. Patients with a-IAB had a delayed onset of LA activation and increased TAET. We found atrial excitation patterns underlying the ECG characteristics of both atypical and typical a-IAB. Patients with typical a-IAB solely had caudocranial activation of the PVA, without additional cranial entry sites. Regardless of the presence of a-IAB, the clinical impact of a complete transverse CB at BB was reflected by a high incidence of de novo E-PoAF.

References

1. Bachmann G. The inter-auricular time interval. Am J Physiol. 1916;41:309-320.
2. van Campenhout MJ, Yaksh A, Kik C, de Jaegere PP, Ho SY, Allessie MA, de Groot NM. Bachmann's bundle: a key player in the development of atrial fibrillation? Circ Arrhythm Electrophysiol. 2013;6:1041-1046.
3. Kumagai K, Uno K, Khrestian C, Waldo AL. Single site radiofrequency catheter ablation of atrial fibrillation: studies guided by simultaneous multisite mapping in the canine sterile pericarditis model. J Am Coll Cardiol. 2000;36:917-923.
4. Teuwen CP, Yaksh A, Lanters EA, Kik C, van der Does LJ, Knops P, Taverne YJ, van de Woestijne PC, Oei FB, Bekkers JA, et al. Relevance of Conduction Disorders in Bachmann's Bundle During Sinus Rhythm in Humans. Circ Arrhythm Electrophysiol. 2016;9:e003972.
5. Bayes de Luna A, Cladellas M, Oter R, Torner P, Guindo J, Marti V, Rivera I, Iturralde P. Interatrial conduction block and retrograde activation of the left atrium and paroxysmal supraventricular tachyarrhythmia. Eur Heart J. 1988;9:1112-1118.
6. Escobar-Robledo LA, Bayes-de-Luna A, Lupon J, Baranchuk A, Moliner P, Martinez-Selles M, Zamora E, de Antonio M, Domingo M, Cediel G, et al. Advanced interatrial block predicts new-onset atrial fibrillation and ischemic stroke in patients with heart failure: The "Bayes' Syndrome-HF" study. Int J Cardiol. 2018;271:174-180.
7. Bayes de Luna A, Platonov P, Cosio FG, Cygankiewicz I, Pastore C, Baranowski R, Bayes-Genis A, Guindo J, Vinolas X, Garcia-Niebla J, et al. Interatrial blocks. A separate entity from left atrial enlargement: a consensus report. J Electrocardiol. 2012;45:445-451.
8. Waldo AL, Bush HL, Jr., Gelband H, Zorn GL, Jr., Vitikainen KJ, Hoffman BF. Effects on the canine P wave of discrete lesions in the specialized atrial tracts. Circ Res. 1971;29:452-467.
9. Bayes de Luna A, Fort de Ribot R, Trilla E, Julia J, Garcia J, Sadurni J, Riba J, Sagues F. Electrocardiographic and vectorcardiographic study of interatrial conduction disturbances with left atrial retrograde activation. J Electrocardiol. 1985;18:1-13.
10. Bayes de Luna A, Escobar-Robledo LA, Aristizabal D, Weir Restrepo D, Mendieta G, Masso van Roessel A, Elosua R, Bayes-Genis A, Martinez-Selles M, Baranchuk A. Atypical advanced interatrial blocks: Definition and electrocardiographic recognition. J Electrocardiol. 2018;51:1091-1093.
11. Cosio FG, Martin-Penato A, Pastor A, Nunez A, Montero MA, Cantale CP, Schames S. Atrial activation mapping in sinus rhythm in the clinical electrophysiology laboratory: observations during Bachmann's bundle block. J Cardiovasc Electrophysiol. 2004;15:524-531.
12. Hinojar R, Pastor A, Cosio FG. Bachmann block pattern resulting from inexcitable areas peripheral to the Bachmann's bundle: controversial name or concept? Europace. 2013;15:1272.
13. van der Does LJ, Yaksh A, Kik C, Knops P, Lanters EA, Teuwen CP, Oei FB, van de Woestijne PC, Bekkers JA, Bogers AJ, et al. QUest for the Arrhythmogenic Substrate of Atrial fibRillation in Patients Undergoing Cardiac Surgery (QUASAR Study): Rationale and Design. J Cardiovasc Transl Res. 2016;9:194-201.
14. Lanters EA, van Marion DM, Kik C, Steen H, Bogers AJ, Allessie MA, Brundel BJ, de Groot NM. HALT & REVERSE: Hsf1 activators lower cardiomyocyt damage; towards a novel approach to REVERSE atrial fibrillation. J Transl Med. 2015;13:347.
15. van Bemmel JH, Kors JA, van Herpen G. Methodology of the modular ECG analysis system MEANS. Methods Inf Med. 1990;29:346-353.
16. Lanters EAH, Yaksh A, Teuwen CP, van der Does L, Kik C, Knops P, van Marion DMS, Brundel B, Bogers A, Allessie MA, et al. Spatial distribution of conduction disorders during sinus rhythm. Int J Cardiol. 2017;249:220-225.
17. Platonov PG, Mitrofanova LB, Chireikin LV, Olsson SB. Morphology of inter-atrial conduction routes in patients with atrial fibrillation. Europace. 2002;4:183-192.
18. Mitrofanova L, Ivanov V, Platonov PG. Anatomy of the inferior interatrial route in humans. Europace. 2005;7 Suppl 2:49-55.
19. Knol WG, Teuwen CP, Kleinrensink GJ, Bogers A, de Groot NMS, Taverne Y. The Bachmann bundle and interatrial conduction: comparing atrial morphology to electrical activity. Heart Rhythm. 2019;16:606-614.
20. Platonov PG. Interatrial conduction in the mechanisms of atrial fibrillation: from anatomy to cardiac signals and new treatment modalities. Europace. 2007;9 Suppl 6:vi10-16.
21. Holmqvist F, Husser D, Tapanainen JM, Carlson J, Jurkko R, Xia Y, Havmoller R, Kongstad O, Toivonen L, Olsson SB, et al. Interatrial conduction can be accurately determined using standard 12-lead electrocardiography: validation of P-wave morphology using electroanatomic mapping in man. Heart Rhythm. 2008;5:413-418.
22. Platonov PG, Yuan S, Hertervig E, Kongstad O, Roijer A, Vygovsky AB, Chireikin LV, Olsson SB. Further evidence of localized posterior interatrial conduction delay in lone paroxysmal atrial fibrillation. Europace. 2001;3:100-107.
23. Mikhaylov EN, Mitrofanova LB, Vander MA, Tatarskiy RB, Kamenev AV, Abramov ML, Szili-Torok T, Lebedev DS. Biatrial tachycardia following linear anterior wall ablation for the perimitral reentry: incidence and electrophysiological evaluations. J Cardiovasc Electrophysiol. 2015;26:28-35.
24. Moser F, Rieger A, Ponisch C, Kottkamp H. A novel ablation approach in atrial fibrillation patients undergoing fibrotic-based substrate modification: Targeting the Bachmann's bundle? J Cardiovasc Electrophysiol. 2018;29:844-853.
25. D'Agostino RS, Jacobs JP, Badhwar V, Fernandez FG, Paone G, Wormuth DW, Shahian DM. The Society of Thoracic Surgeons Adult Cardiac Surgery Database: 2019 Update on Outcomes and Quality. Ann Thorac Surg. 2019;107:24-32.
26. Conde D, van Oosten EM, Hamilton A, Petsikas D, Payne D, Redfearn DP, Hopman WM, Bayes de Luna A, Baranchuk A. Prevalence of interatrial block in patients undergoing coronary bypass graft surgery. Int J Cardiol. 2014;171:e98-99.

33

27.   Dobrev D, Aguilar M, Heijman J, Guichard JB, Nattel S. Postoperative atrial fibrillation: mechanisms, manifestations and management. Nat Rev Cardiol. 2019;16:417-436.

33

Chapter 34

Mapping-guided atrial lead placement determines optimal conduction across Bachmann's bundle: a rationale for patient-tailored pacing therapy

Mathijs S. van Schie*

Nawin L. Ramdat Misier*

Paul Knops

Annejet Heida

Yannick J.H.J. Taverne

Natasja M.S. de Groot

* Contributed equally

Abstract

Aims: Conventional right atrial appendage (RAA) pacing is associated with increased atrial activation time resulting in higher incidences of atrial tachyarrhythmia. Optimal pacing sites ideally shorten inter-atrial conduction delay thereby decreasing atrial excitation time. We therefore examined the impact of programmed electrical stimulation (PES) from the RA and LA on electrophysiological properties of Bachmann's bundle (BB).

Methods: High-resolution epicardial mapping of BB was performed during sinus rhythm (SR) and PES in 34 patients undergoing cardiac surgery. PES was performed from the RAA, junction of the RA with inferior caval vein (LRA) and left atrial appendage (LAA).

Results: Pacing from either RAA or LAA resulted in respectively right- and left-sided conduction across BB. However, during LRA pacing in most patients (n=15) activation started in the center of BB. Total activation time of BB during RAA pacing (63 [55–78] ms) was similar to SR (61 [52–68] ms, p=0.464), while it decreased during LRA (45 [39–62] ms, p=0.003) and increased during LAA pacing (67 [61–75] ms, p=0.009). Reduction of both conduction disorders and total activation time was most often achieved during LRA pacing (N=13), especially in patients who already had a higher amount of conduction disorders during SR (9.8 [7.3–12.3] vs. 4.5 [3.5–6.6] %, p<0.001).

Conclusions: Pacing from LRA results in a remarkable decrease of total activation time compared to pacing from the LAA or RAA. As the most optimal pacing site varies between patients, individualized positioning of the atrial pacing lead guided by mapping of BB may be one of the new frontiers for atrial pacing.

Journal site

Introduction

Right atrial (RA) pacing leads are conventionally placed in the RA appendage (RAA) in order to mimic physiological inter-atrial conduction. However, this pacing site is also associated with a higher incidence of atrial arrhythmias, such as atrial fibrillation (AF).[1,2] Previous studies have demonstrated that pacing from the RAA increases total atrial excitation time, represented by a prolonged P-wave duration.[3,4] Alternate lead placement sites, e.g., high atrial septum (Bachmann's bundle - BB), low atrial septum, RA free wall and via the coronary sinus in the left atrium (LA), have been suggested, although the most optimal position is not defined. Several studies demonstrated that pacing from the high atrial septum reduces the risk of AF[2,5-8], but a large multi-center study failed to show benefit of atrial septal pacing.[9] It has been postulated that a pacing site with the smallest inter-atrial conduction delay reduces AF initiation and progression.

While other inter-atrial connections exist, BB is the dominant inter-atrial conduction pathway during normal sinus rhythm (SR). Importantly, BB also plays an important role in initiation and perpetuation of AF.[10] Several studies demonstrated the presence of extensive conduction disorders, especially at BB, in patients with AF.[10,11] An optimal pacing site therefore ideally reduces conduction disorders in this area in order to minimize inter-atrial conduction delay, thereby promoting synchronous atrial activation. It remains unknown how pacing from various sites affects conduction across BB. Intra-operative high-resolution epicardial mapping provides the opportunity to investigate the effect of multi-site pacing on conduction across BB. Therefore, the aims of this study are 1) to examine the impact of programmed electrical stimulation (PES) from the RA and LA on activation patterns and electrophysiological properties of BB, and 2) to determine the most optimal pacing site based on these features.

Methods

Study population

The study population consisted of 34 successive adult patients without and with a history of AF undergoing coronary artery bypass grafting (CABG), aortic or mitral valve surgery or a combination of valvular and CABG in the Erasmus Medical Center Rotterdam. This study was approved by the institutional medical ethical committee (MEC2014-393). Written informed consent was obtained from all patients. Patient characteristics were retrieved from the patient's medical record.

Mapping procedure

Epicardial high-resolution mapping was performed prior to commencement to extra-corporal circulation, as previously described in detail.[12] A steel wire fixed to subcutaneous tissue of the thoracic cavity was used as an indifferent electrode. Epicardial mapping was performed with a 192-electrode array (electrode diameter 0.45 mm, interelectrode distances 2.12 mm). BB was mapped from the tip of the left atrial appendage (LAA) across the roof of the left atrium, behind the aorta towards the superior cavo-atrial junction, as illustrated in the upper left panel of *Figure 1*.

PES was delivered from 1) the RAA, 2) junction of the RA with the inferior caval vein ((low) LRA) and 3) LAA, and included a fixed rate pacing of average SR cycle length minus 50 ms for a duration of 10 seconds. The LRA location was chosen as an epicardial alternative for high RA septal pacing, which is not accessible epicardially.

34
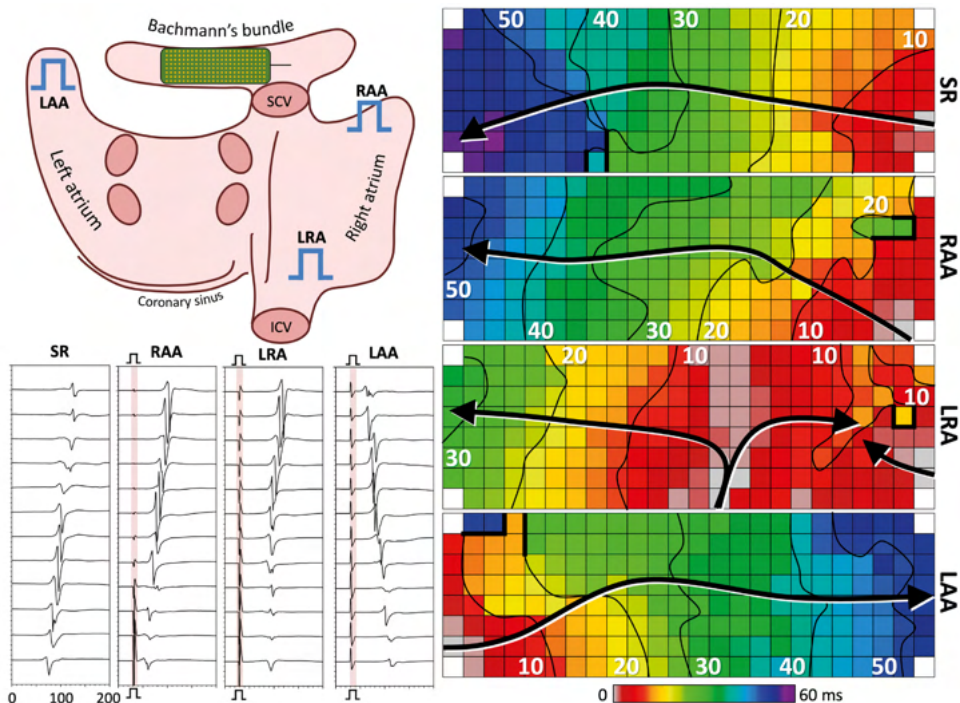
Figure 1 – Example of pacing protocol. *Panel A*: schematic scheme of the electrode position at BB and three pacing locations (RAA, LRA and LAA). *Panel B*: example of color-coded activation patterns during SR and RAA, LRA and LAA pacing. Thick black lines represent CB; isochronal lines are drawn every 10 ms. *Panel C*: representative EGMs recorded during pacing protocol as in panel B. **BB** = Bachmann's bundle; **CB** = conduction block; **ICV** = inferior caval vein; **LAA** = left atrial appendage; **LRA** = inferior right atrium; **RA** = right atrial appendage; **SCV** = superior caval vein; **SR** = sinus rhythm.

Five seconds of SR and 10 seconds during PES were recorded, including a surface ECG lead, a calibration signal of 2 mV and 1000 ms, a bipolar reference electrogram (EGM) and all unipolar epicardial EGMs. Data were stored on a hard disk after amplification (gain 1000), filtering (bandwidth 0.5–400 Hz), sampling (1 kHz) and analogue-to-digital conversion (16 bits).

Data analysis

Unipolar EGMs were semi-automatically analyzed using custom-made software. The steepest negative slope of an atrial potential was marked as the local activation time (LAT). All annotations were manually checked with consensus from two investigators. LATs of EGMs at each electrode were used to reconstruct color-coded activation maps (right panel of *Figure 1*). Total activation time (TAT) was determined by relating the first and last LAT. Local effective conduction velocity (CV) was computed from LATs of neighboring electrodes (longitudinal, transversal and diagonal) using discrete velocity vectors as previously described.[13] Conduction block (CB) was defined as a difference in LAT between adjacent electrodes of ≥12 ms; continuous conduction delay/block (cCDCB) as a time difference of ≥7 ms and connected to a line of CB.[14] EGMs were classified as single (SPs, single negative deflection), short double (SDPs, interval between deflections <15 ms), long double (LDPs, deflection interval ≥15 ms) or fractionated potentials (FPs, ≥3 deflections). Time differences (ms) between the first and last deflection of FPs is defined as fractionation duration (FD). Furthermore, peak-to-peak amplitudes of all potentials were measured. Low-voltage

Table 1 – Baseline characteristics.

Patients	N=34
Male	31 (91)
Age (y)	65±11 (37–79)
Underlying heart disease	
• IHD	22 (65)
• (i)VHD	12 (35)
- AVD	6 (18)
- MVD	6 (18)
Paroxysmal AF	5 (15)
Cardiovascular risk factors	
• BMI (kg/m^2)	27.7 [25.7–31.5]
• Hypertension	23 (68)
• Dyslipidemia	15 (44)
• Diabetes mellitus	9 (26)
Left atrial dilation	12 (35)
Left ventricular dysfunction	9 (26)
Antiarrhythmic drugs	25 (74)
• Class I	-
• Class II	24 (71)
• Class III	-
• Class IV	4 (12)

Values are presented as N (%), mean ± standard deviation (min–max) or median [interquartile ranges]. **AF** = atrial fibrillation; **AVD** = aortic valve disease; **BMI** = body mass index; **IHD** = ischemic heart disease; **(i)VHD** = (ischemic and) valvular heart disease; **MVD** = mitral valve disease.

potentials were defined as potentials with an amplitude <1.0 mV; the proportion of low-voltage potentials represented the amount of low-voltage areas (LVA).[15]

Defining the most optimal pacing site

It has been postulated that a pacing site associated with the smallest inter-atrial conduction delay reduces the likelihood of AF initiation and progression.[3,4] Therefore, PES at any site resulting in reduction of localized areas of cCDCB thereby decreasing TAT of BB, was considered to be beneficial.

Statistical analysis

Normally distributed data are expressed as mean ± standard deviation, whereas skewed data are expressed as median [25th–75th percentile]. To analyze the difference between SR and various pacing sites, a paired *t*-test or Wilcoxon signed-rank test was used. The differences were presented as mean [95% CI]. A *p*-value <0.05 was considered statistically significant. A Bonferroni correction was applied when appropriate.

Results

Study population

Clinical characteristics of the study population (N=34, 31 male (91%), age 65±11 years) are summarized in *Table 1*. Patients underwent either CABG (IHD: N=22; 65%), aortic valve surgery with or without CABG ((i)AVD: N=6; 18%) or mitral valve surgery with or without CABG ((i)MVD: N=6; 18%). A minority of patients (N=5; 15%) had paroxysmal AF. The average cycle length during SR was 967 [874–1,185] ms. In total, respectively 33, 30 and 29 recordings were available of the RAA, LRA and LAA pacing sites.
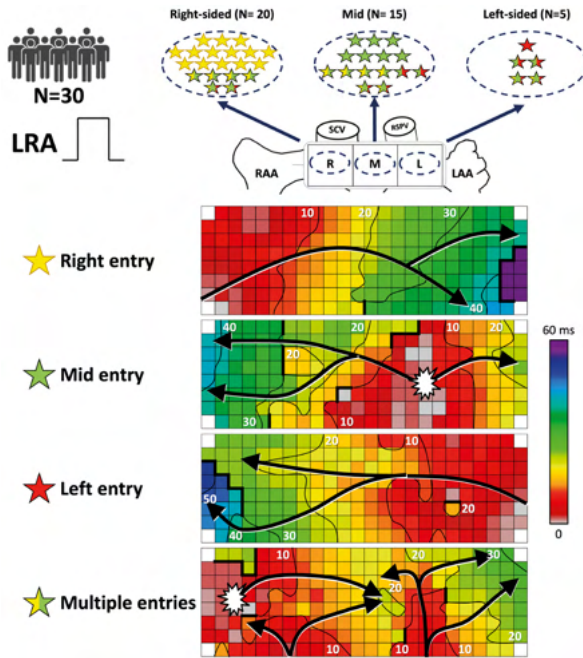
Figure 2 – Variation of activation patterns during LRA pacing. Examples of BB activation during LRA pacing. Thick black lines represent CB; isochronal lines are drawn every 10 ms. **LAA** = left atrial appendage; **LRA** = lower right atrium; **RAA** = right atrial appendage; **RSPV** = right superior pulmonary vein; **SCV** = superior caval vein.

Example of pacing protocol

A typical example of the pacing protocol in one patient is illustrated in *Figure 1*. As demonstrated in the right panel, an activation wavefront during SR propagates from right to left across BB. Pacing from RAA resulted in a comparable activation pattern as during SR, although TAT is shorter. As expected, pacing from LAA resulted in left-to-right conduction across BB. During pacing from LRA, activation started in the center of BB. This resulted in a much shorter TAT as compared to the other 2 pacing sites. As demonstrated in the lower left panel of *Figure 1*, potential morphology differed considerably between the pacing sequences.

Table 2 – Effect of pacing on atrial conduction and electrogram morphology.

	SR	RAA	*p*-value	LRA	*p*-value	LAA	*p*-value
TAT (ms)	61 [52–68]	63 [55–78]	0.464	45 [39–62]	**0.003**	67 [61–75]	**0.009**
CV (cm/s)	92.3 [87.1–98.2]	93.6 [81.4–96.9]	0.586	90.8 [85.7–99.4]	0.894	90.0 [77.3–96.9]	0.071
cCDCB (%)	6.8 [4.1–10.1]	7.6 [4.9–10.8]	0.183	6.7 [4.7–8.9]	0.861	9.6 [5.8–13.0]	**0.009**
cCDCB (mm)	21.2 [13.8–35.0]	23.3 [17.0–39.5]	0.166	17.0 [14.8–26.5]	0.611	22.8 [12.2–38.7]	0.236
Voltage (mV)	5.7 [4.4–6.5]	5.1 [3.6–6.4]	0.675	5.5 [3.4–6.7]	0.530	4.6 [2.7–6.2]	0.157
LVA (%)	2.0 [0.7–5.8]	4.7 [1.0–8.9]	**0.005**	3.5 [0.9–6.8]	0.117	4.7 [1.6–13.1]	**0.003**
SP (%)	79.3 [73.4–86.9]	77.2 [71.2–84.1]	0.714	81.0 [72.6–86.0]	0.861	78.2 [70.3–82.0]	0.325
SDP (%)	11.9 [7.0–16.0]	11.6 [7.5–16.5]	0.728	12.2 [7.5–17.0]	0.813	12.3 [9.9–15.7]	0.294
LDP (%)	4.9 [1.8–9.5]	6.6 [3.1–11.2]	0.514	3.9 [1.2–8.5]	0.453	5.6 [1.4–11.4]	0.871
FP (%)	1.5 [0.6–3.5]	1.9 [0.5–3.5]	0.411	1.8 [0.9–3.0]	0.719	1.6 [0.7–3.8]	0.405
FD (ms)	11 [9–16]	12 [9–16]	0.923	10 [9–14]	0.096	11 [9–15]	0.704

Bold *p*-values represent statistical significance between SR and either RAA, LRA or LAA values. **cCDCB** = continuous conduction delay/block; **CV** = conduction velocity; **FD** = fractionation duration; **FP** = fractionated potentials; **LAA** = left atrial appendage; **LDP** = long double potentials; **LRA** = lower right atrium; **LVA** = low-voltage areas; **RAA** = right atrial appendage; **SDP** = short double potentials; **SP** = single potentials; **SR** = sinus rhythm; **TAT** = total activation time.
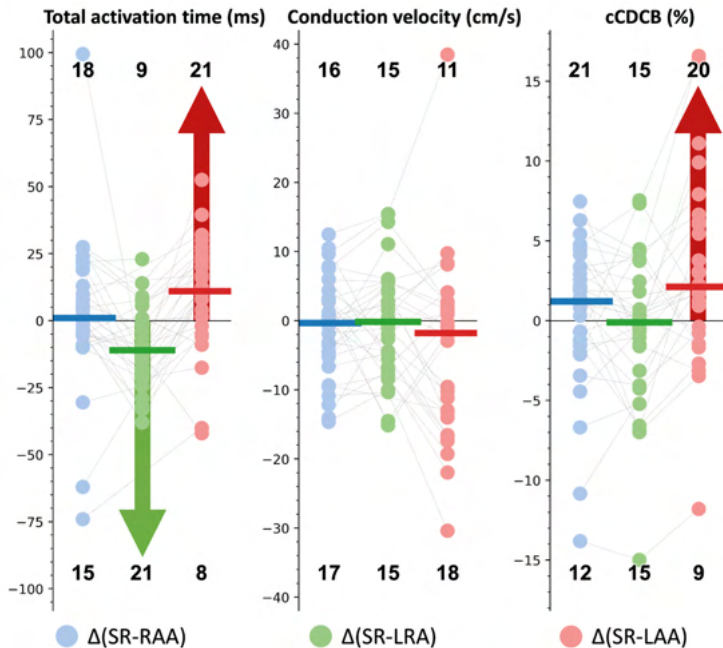
Figure 3 – Changes in conduction features during pacing. Interindividual variation in effect of pacing from either RAA (blue), LRA (green) and LAA (red). The arrows indicate statistical significance. The numbers indicate the number of patients with either an increase or decrease. **cCDCB** = continuous conduction delay/block; **CV** = conduction velocity; **LAA** = left atrial appendage; **LRA** = lower right atrium; **RAA** = right atrial appendage; **SR** = sinus rhythm; **TAT** = total activation time.

Effect of programmed electrical stimulation on BB activation patterns

In all patients, pacing from the RAA resulted in comparable activation patterns as observed during SR. As expected, pacing from the LAA resulted in left-to-right conduction across BB. As illustrated in *Figure 2*, during pacing from LRA, BB was activated from only the right side in 14 patients, in one patient from only the left side and in 7 patients by a wavefront emerging in the middle of BB. However, in 2 patients, BB was activated from all three sides simultaneously, while 6 patients had either a combined mid/right or -/left entry side (4 vs. 2 respectively).

As illustrated in *Figure 3*, TAT of BB during RAA pacing (63 [55–78] ms) was similar to SR (61 [52–68] ms, p=0.464), while it decreased during LRA (45 [39–62] ms, p=0.003) and increased during LAA pacing (67 [61–75] ms, p=0.009). Pacing from LRA significantly reduced TAT compared to both LAA and RAA pacing (p<0.001 for both). Local CV, however, was similar among the three pacing sites and compared to SR. During pacing from LAA, the amount of cCDCB increased compared to SR (6.8 [4.1–10.1] % vs. 9.6 [5.8–13.0] %, p=0.009), while there were no differences in cCDCB between SR and pacing from both RAA and LRA. The length of longest cCDCB lines did not differ among the three different pacing sites and compared to SR, as shown in *Table 2*.

Effect of programmed electrical stimulation on potential morphology

Unipolar potential voltages and potential type distribution were similar between SR and the three different pacing sites. However, as shown in *Table 2*, pacing from LRA resulted in a lower number of LDP (3.9 [1.2–8.5] vs. 6.6 [3.1–11.2], p=0.007) and shorter FD (10 [9–14] ms vs. 12 [9–16] ms, p=0.032) compared to RAA pacing, as illustrated in *Figure 4*. During RAA

34
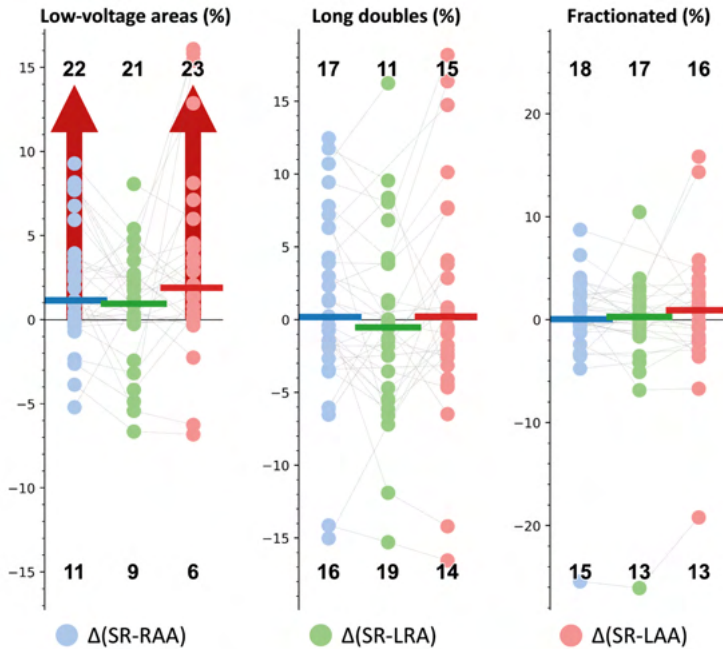
Figure 4 – Effect of pacing on electrogram morphology. Interindividual variation in effect of pacing from either RAA (blue), LRA (green) and LAA (red). The arrows indicate statistical significance. The numbers indicate the number of patients with either an increase or decrease. **FP** = fractionated potentials; **LAA** = left atrial appendage; **LDP** = long double potentials; **LRA** = lower right atrium; **LVA** = low-voltage areas; **RAA** = right atrial appendage; **SDP** = short double potentials; **SP** = single potentials; **SR** = sinus rhythm.

and LAA pacing but not during LRA pacing, the amount of LVAs increased compared to SR (4.7 [1.0–8.9]% and 4.7 [1.6–13.1]% vs. 2.0 [0.7–5.8]%; p=0.005 and p=0.003 respectively). CV in these new LVAs was comparable to LVAs during SR (53.5 [45.9–71.9] cm/s vs. RAA 60.8 [40.9–82.8], LRA 58.7 [49.5–81.4] & LAA 58.5 [30.1–74.5] cm/s, p>0.353).

Individualization of most optimal pacing site

Reduction of solely cCDCB was achieved in 15 patients during LRA pacing, 12 patients during RAA pacing and 9 patients during LAA pacing, whereas a reduction of solely TAT was achieved in 21 patients during LRA pacing, 15 patients during RAA pacing and 8 patients during LAA pacing.

Reduction of both cCDCB and TAT occurred in 13 patients by pacing from LRA, while only respectively 6 and 3 patients demonstrated reduction in both parameters from RAA and LAA pacing; 19 patients did not show improvement in cCDCB or TAT. Several patients demonstrated reduction in both cCDCB and TAT during pacing from multiple locations separately; 3 patients by LRA pacing and either RAA (N=2) or LAA (N=1) pacing, and in 2 patients by pacing from all three pacing sites.

Electrophysiological features of BB during SR in patients with reduction of cCDCB and TAT by pacing from 1 or more pacing sites are listed in *Table 3*. Compared to patients without reduction in both cCDCB and TAT, patients who benefitted from LRA pacing already had longer SR TAT (57 [47–63] ms vs. 64 [60–74] ms, p=0.027), lower CV (94.6 [91.0–100.3] cm/s vs. 90.9 [84.3–92.2] cm/s, p=0.039) and more cCDCB (4.5 [3.5–6.6]% vs. 9.8 [7.3–12.3]%, p<0.001). In addition, these patients also had more LVAs (0.8 [0.5–2.0]% vs. 6.4 [2.6–8.6], p<0.001), LDP

Table 3 – Electrophysiological characteristics during SR between patients with and without benefit.

	No benefit	Benefit of RAA	*p*-value	Benefit of LRA	*p*-value	Benefit of LAA	*p*-value
N	19	6		13		3	
TAT (ms)	57 [47–63]	82 [65–88]	**0.026**	64 [60–74]	**0.027**	81 [73–82]	**0.018**
CV (cm/s)	94.6 [91.0–100.3]	91.5 [86.8–95.0]	0.147	90.9 [84.3–92.2]	**0.039**	95.4 [90.4–95.7]	0.424
cCDCB (%)	4.5 [3.5–6.6]	10.0 [7.9–12.2]	**0.026**	9.8 [7.3–12.3]	**<0.001**	7.8 [7.5–10.0]	**0.022**
cCDCB (mm)	14.8 [8.5–23.3]	26.5 [25.4–61.5]	**0.026**	26.5 [17.0–44.5]	**0.027**	17.0 [17.0–39.8]	**0.018**
Voltage (mV)	5.9 [4.7–7.0]	6.2 [5.2–7.5]	0.273	4.9 [3.5–5.9]	0.072	6.6 [6.3–7.2]	0.146
LVA (%)	0.8 [0.5–2.0]	6.5 [4.7–8.2]	**0.022**	6.4 [2.6–8.6]	**<0.001**	4.2 [2.8–6.4]	**0.042**
SP (%)	84.9 [80.7–89.4]	78.3 [74.8–84.4]	0.147	74.5 [64.3–75.6]	**0.003**	78.6 [71.5–82.5]	0.107
SDP (%)	9.3 [6.6–15.1]	9.6 [5.4–12.8]	0.340	13.7 [11.6–19.5]	0.084	13.2 [7.6–14.1]	0.462
LDP (%)	2.4 [1.0–5.9]	8.1 [4.0–13.7]	**0.026**	7.6 [5.2–10.3]	**0.002**	9.7 [8.1–13.6]	**0.028**
FP (%)	0.7 [0.3–1.6]	1.9 [0.7–3.3]	0.147	3.2 [1.7–5.5]	**0.001**	2.1 [1.9–2.6]	**0.035**
FD (ms)	9 [8–14]	16 [12–22]	0.071	13 [11–16]	**0.037**	16 [15–22]	**0.042**

Electrophysiological characteristics during SR between patients with no benefit and those with reduction of both cCDCB and TAT after 1) RAA, 2) LRA and 3) LAA pacing. Bold *p*-values represent statistical significance between patients without and each of the groups with benefit. **cCDCB** = continuous conduction delay/block; **CV** = conduction velocity; **FD** = fractionation duration; **FP** = fractionated potentials; **LAA** = left atrial appendage; **LDP** = long double potentials; **LRA** = lower right atrium; **LVA** = low-voltage areas; **RAA** = right atrial appendage; **SDP** = short double potentials; **SP** = single potentials; **SR** = sinus rhythm; **TAT** = total activation time.

(2.4 [1.0–5.9]% vs. 7.6 [5.2–10.3], p=0.002) and FP (0.7 [0.3–1.6]% vs. 3.2 [1.7–5.5]%, p=0.001) during SR. Patients who benefitted from RAA and LAA pacing also already had longer SR TAT and a larger amount of cCDCB, LVAs and more LDPs at BB during SR compared to those patients without any benefit.

Discussion

Pacing from the LRA results in a considerable decrease in TAT of BB compared to pacing from the LAA or RAA. Remarkably, pacing from LAA results in an increase of cCDCB, TAT and LVAs, and even RAA pacing can promote in an increase of LVAs. In several patients, BB was activated from the center of the mapping area during LRA pacing, while others had only a right-sided entry or multiple entry sides. Particularly in patients who have more conduction disorders during SR, pacing from the LRA decreased the amount of cCDCB and TAT.

Conduction at BB

BB is the preferential route for inter-atrial conduction during normal SR. It stretches subepicardially across the interatrial groove and is comprised of parallel aligned strands of atrial myocardium. The right and leftward extensions of BB bifurcate to pass to either side of the RAA and LAA. In addition, BB is connected with other parts of the atria through various (epicardial) bundles. A posterosuperior bundle joins BB from the posterior site over the interatrial groove. Other bundles may include a septopulmonary bundle connecting the interatrial groove to the LA roof and connections transversing the interatrial groove on the posterior wall. As demonstrated by Knol et al.[16], there is certain interindividual variation in the morphological structure of other interatrial connections and BB. The mid-entry wavefronts observed during LRA pacing may be conducted via the posterosuperior bundle or other connections with the interatrial septum.

Due to the parallel alignment of myocardial fibers, conduction at BB is highly uniform anisotropic in nature. Although conduction across BB during LAA pacing is in opposite direction compared to SR conduction, it results in prolonged TAT and increased amount of conduction disorders. In several patients, LRA pacing resulted in a mid-entry of the activation wavefront at BB. These wavefronts presumably originate from other interatrial septal pathways and continue at BB. Theoretically, pacing from the (high) RA septum could

34

result in similar results in selective patients due the interatrial septal pathways. Although TAT during LRA pacing decreased, there was no difference in the amount of conduction disorders as compared to SR. Importantly, RAA and LAA pacing, but not LRA pacing, resulted in an increase in the amount of LVAs compared to SR. This is especially remarkable in the case of RAA pacing, as all patients had a right-sided entry on BB during RAA pacing. These findings suggest that subtle localized changes in wavefront direction exert a profound effect on local conduction. Several studies have demonstrated that BB – despite its restricted size – has a meticulous microarchitecture together with considerable spatial dispersion in electrophysiological properties.[17,18] This structural and electrical inhomogeneity may give rise to increased LVAs during RAA (and LAA) pacing. On the other hand, the absence of an increase in LVAs during LRA pacing may be explained by the occurrence of multiple wavefronts, as shown in the example in *Figure 1*. These findings suggest that certain areas of BB are more sensitive to specific changes in wavefront direction.

BB is also a site which has been frequently linked to development of AF. Changes in the normal anatomy of BB, such as disruption of the parallel orientation of myocardial fibers, may predispose to conduction disorders and thus development of AF. In an intra-operative epicardial mapping study, Mouws et al.[19] demonstrated that total atrial excitation times were longer in patients with AF compared to those without, which was mainly caused by the presence of conduction disorders at BB. Teuwen et al.[17] demonstrated that particularly long lines of longitudinal CB are more pronounced in patients with AF episodes undergoing CABG. These longer lines of CB are also related to AF inducibility.[20] RAA pacing is frequently used to treat sinus node dysfunction and to suppress AF.[8] It can, however, also enhance inter-atrial conduction delay, especially in patients with pre-existing conduction disorders at BB, thereby promoting AF.[21] It has therefore been suggested that pacing from either the upper part (near BB) or lower part (near the coronary sinus ostium) of the inter-atrial septum prevents AF. However, studies showed conflicting results and the most optimal position is yet not solidly defined.[9] A pacing location at which the intra-atrial conduction delay is minimized may be most beneficial for the patient. In the present study, we demonstrated that reduction of TAT and cCDCB at BB is particularly achieved by LRA pacing, especially in patients with pre-existing conduction disorders at BB during SR. RAA and even LAA pacing was beneficial in a limited number of patients. Hence, there was a strong individual variation in the most optimal pacing site.

Rationale for optimal lead placement

The effects of various pacing lead position sites in the RA have been examined, although they mainly focused on AF incidence during clinical follow-up.[22] Currently, it appears that none of the various pacing lead positions is clinically superior. One of the first studies comparing electrophysiological consequences of various atrial pacing sites was performed by Yu et al.[1] In this study, it was demonstrated that P-wave duration decreased and intra-atrial conduction delay between the high right atrium and distal coronary sinus was shortened during RA septal pacing compared to RAA. Yamada et al.[23] showed in patients with paroxysmal AF that P-wave dispersion was significantly diminished by septal pacing compared with RAA pacing. This pacing site could reduce total atrial excitation times which will eventually also reduce the dispersion of refractoriness.[21] Duytschaever et al.[24] investigated in the goat model of AF the mechanisms by which atrial pacing can reduce AF initiation. In this model, AF initiation was often preceded by a critical conduction block recorded at BB. Consequently, preventive pacing at the mid portion of BB markedly shortened the window of AF inducibility compared to other pacing sites. However, understanding of the impact of atrial pacing on electrophysiological properties in these studies was limited by the lack of detailed insight into atrial excitation.

Patient-tailored lead placement

Our findings suggest that (high-resolution) mapping of BB could aid in identifying the most optimal pacing lead site. Such an approach could be comparable to mapping-guided ventricular pacing lead positioning.[25,26] During LRA pacing, BB was activated in various ways, ranging from solely right-to-left to multi-site entries. With anatomical inspection alone, it is difficult to determine whether a lead placed at the LRA will capture muscular bundles connecting the inferior RA with the interatrial septum, thereby prematurely activating the center of BB. Similarly, Infeld et al.[27] showed that patients with identical high right septum lead placement guided by fluoroscopically showed variable atrial excitation. They attributed this to variability in capture of (bundles connecting the septum to) BB. In this study, despite identical lead placement, atrial arrhythmia burden, recurrence, and de novo incidence differed between true BB pacing and high right septal pacing.

Compared to patients without reduction of both cCDCB and TAT, patients with this reduction from LRA pacing already had longer TAT, lower CV, more cCDCB, LVAs, LDP and FP during SR. Therefore, discriminating between various stages of atrial remodeling may be as important as conventional lead positioning. High-resolution mapping of BB could serve as a tool to make this discrimination. Hence, individualized positioning of the atrial pacing lead guided by mapping of BB may be one of the new frontiers of atrial pacing.

Limitations

Pacing from all three sites was not possible in a minority of the patients, either due to practical issues or unstable capture. In clinical practice, the most frequent indication for permanent atrial pacing is sinus node disease, which is associated with severe remodeling of the atria. Although patients with sinus node disease were not included in the present study, inter-atrial conduction disorders were already present in the majority of this study population. Therefore, similar changes in electrophysiological properties across BB during atrial pacing could be expected in patients with sinus node disease. Additionally, TAT at BB does not represent total atrial excitation time. The LRA pacing site is not an ideal location for endocardial pacing lead placement. However, high RA septal pacing from the endocardium could theoretically result in similar mid-entry activation patterns as compared to epicardial LRA pacing due to the connections between the interatrial septum and BB. Besides, selection of the LRA as a permanent position in clinical practice is also determined by other procedural variables such as pacing threshold and lead stability. Therefore, other lead positions could be considered.

Conclusion

Pacing from the inferior RA results in a remarkable decrease in TAT of BB compared to pacing from the LAA or RAA. Especially in patients with a large amount of conduction disorders during SR, reduction of TAT and conduction disorders is achieved by pacing from LRA. As the most optimal pacing site varies between patients, individualized positioning of the atrial pacing lead guided by mapping of BB may be one of the new frontiers for atrial pacing.

34

References

1. Yu WC, Tsai CF, Hsieh MH, Chen CC, Tai CT, Ding YA, Chang MS, Chen SA. Prevention of the initiation of atrial fibrillation: mechanism and efficacy of different atrial pacing modes. Pacing Clin Electrophysiol. 2000;23:373-379.
2. Padeletti L, Pieragnoli P, Ciapetti C, Colella A, Musilli N, Porciani MC, Ricci R, Pignalberi C, Santini M, Puglisi A, et al. Randomized crossover comparison of right atrial appendage pacing versus interatrial septum pacing for prevention of paroxysmal atrial fibrillation in patients with sinus bradycardia. Am Heart J. 2001;142:1047-1055.
3. Acosta H, Pothula VR, Rodriguez M, Ramadas S, Castellanos A. Placement of a pacing lead at the inferior portion of the interatrial septum without special tools. Pacing Clin Electrophysiol. 2007;30 Suppl 1:S84-87.
4. Becker R, Klinkott R, Bauer A, Senges JC, Schreiner KD, Voss F, Kuebler W, Schoels W. Multisite pacing for prevention of atrial tachyarrhythmias: potential mechanisms. J Am Coll Cardiol. 2000;35:1939-1946.
5. Minamiguchi H, Nanto S, Onishi T, Watanabe T, Uematsu M, Komuro I. Low atrial septal pacing with dual-chamber pacemakers reduces atrial fibrillation in sick sinus syndrome. J Cardiol. 2011;57:223-230.
6. Bailin SJ, Adler S, Giudici M. Prevention of chronic atrial fibrillation by pacing in the region of Bachmann's bundle: results of a multicenter randomized trial. J Cardiovasc Electrophysiol. 2001;12:912-917.
7. Stabile G, Senatore G, De Simone A, Turco P, Coltorti F, Nocerino P, Vitale DF, Chiariello M. Determinants of efficacy of atrial pacing in preventing atrial fibrillation recurrences. J Cardiovasc Electrophysiol. 1999;10:2-9.
8. Wang M, Siu CW, Lee KL, Yue WS, Yan GH, Lee S, Lau CP, Tse HF. Effects of right low atrial septal vs. right atrial appendage pacing on atrial mechanical function and dyssynchrony in patients with sinus node dysfunction and paroxysmal atrial fibrillation. Europace. 2011;13:1268-1274.
9. Zhang L, Jiang H, Wang W, Bai J, Liang Y, Su Y, Ge J. Interatrial septum versus right atrial appendage pacing for prevention of atrial fibrillation : A meta-analysis of randomized controlled trials
10. Schrittmacherstimulation am Vorhofseptum oder am rechten Herzohr zur Prävention von Vorhofflimmern : Eine Metaanalyse randomisierter, kontrollierter Studien. Herz. 2018;43:438-446.
11. van Campenhout MJ, Yaksh A, Kik C, de Jaegere PP, Ho SY, Allessie MA, de Groot NM. Bachmann's bundle: a key player in the development of atrial fibrillation? Circ Arrhythm Electrophysiol. 2013;6:1041-1046.
12. van Schie MS, de Groot NM. Clinical Relevance of Sinus Rhythm Mapping to Quantify Electropathology Related to Atrial Fibrillation. Arrhythm Electrophysiol Rev. 2022;11:e11.
13. Lanters EA, van Marion DM, Kik C, Steen H, Bogers AJ, Allessie MA, Brundel BJ, de Groot NM. HALT & REVERSE: Hsf1 activators lower cardiomyocyt damage; towards a novel approach to REVERSE atrial fibrillation. J Transl Med. 2015;13:347.
14. van Schie MS, Heida A, Taverne Y, Bogers A, de Groot NMS. Identification of local atrial conduction heterogeneities using high-density conduction velocity estimation. Europace. 2021;23:1815-1825.
15. Allessie MA, de Groot NM, Houben RP, Schotten U, Boersma E, Smeets JL, Crijns HJ. Electropathological substrate of long-standing persistent atrial fibrillation in patients with structural heart disease: longitudinal dissociation. Circ Arrhythm Electrophysiol. 2010;3:606-615.
16. van Schie MS, Starreveld R, Bogers A, de Groot NMS. Sinus rhythm voltage fingerprinting in patients with mitral valve disease using a high-density epicardial mapping approach. Europace. 2021;23:469-478.
17. Knol WG, Teuwen CP, Kleinrensink GJ, Bogers A, de Groot NMS, Taverne Y. The Bachmann bundle and interatrial conduction: comparing atrial morphology to electrical activity. Heart Rhythm. 2019;16:606-614.
18. Teuwen CP, Yaksh A, Lanters EA, Kik C, van der Does LJ, Knops P, Taverne YJ, van de Woestijne PC, Oei FB, Bekkers JA, et al. Relevance of Conduction Disorders in Bachmann's Bundle During Sinus Rhythm in Humans. Circ Arrhythm Electrophysiol. 2016;9:e003972.
19. Vollmann D, Blaauw Y, Neuberger HR, Schotten U, Allessie M. Long-term changes in sequence of atrial activation and refractory periods: no evidence for "atrial memory". Heart Rhythm. 2005;2:155-161.
20. Mouws E, Lanters EAH, Teuwen CP, van der Does L, Kik C, Knops P, Yaksh A, Bekkers JA, Bogers A, de Groot NMS. Impact of Ischemic and Valvular Heart Disease on Atrial Excitation:A High-Resolution Epicardial Mapping Study. J Am Heart Assoc. 2018;7.
21. van Staveren LN, van der Does WFB, Heida A, Taverne Y, Bogers A, de Groot NMS. AF Inducibility Is Related to Conduction Abnormalities at Bachmann's Bundle. J Clin Med. 2021;10.
22. Daubert JC, Pavin D, Jauvert G, Mabo P. Intra- and interatrial conduction delay: implications for cardiac pacing. Pacing Clin Electrophysiol. 2004;27:507-525.
23. Shali S, Su Y, Ge J. Interatrial septal pacing to suppress atrial fibrillation in patients with dual chamber pacemakers: A meta-analysis of randomized, controlled trials. Int J Cardiol. 2016;219:421-427.
24. Yamada T, Fukunami M, Shimonagata T, Kumagai K, Asano Y, Hirata A, Asai M, Makino N, Hoki N. Effect of atrial septal pacing on P-wave duration dispersion and atrial late potentials in patients with paroxysmal atrial fibrillation. Am J Cardiol. 2001;88:795-798.
25. Duytschaever M, Danse P, Eysbouts S, Allessie M. Is there an optimal pacing site to prevent atrial fibrillation?: an experimental study in the chronically instrumented goat. J Cardiovasc Electrophysiol. 2002;13:1264-1271.
26. Moore JP, Gallotti RG, Shannon KM, Biniwale R. A minimally invasive hybrid approach for cardiac resynchronization of the systemic right ventricle. Pacing Clin Electrophysiol. 2019;42:171-177.
27. Rad MM, Blaauw Y, Dinh T, Pison L, Crijns HJ, Prinzen FW, Vernooy K. Left ventricular lead placement in the latest activated region guided by coronary venous electroanatomic mapping. Europace. 2015;17:84-93.
28. Infeld M, Nicoli CD, Meagher S, Tompkins BJ, Wayne S, Irvine B, Betageri O, Habel N, Till S, Lobel J, et al. Clinical impact of Bachmann's bundle pacing defined by electrocardiographic criteria on atrial arrhythmia outcomes. Europace. 2022;24:1460-1468.

34

Chapter 35

Optimization of intra-operative electrophysiological localization of the ligament of Marshall

Sanne J.J. Langmuur

Yannick J.H.J. Taverne

Mathijs S. van Schie

Ad J.J.C. Bogers

Natasja M.S. de Groot

Abstract

Background: The ligament of Marshall (LOM) may play a role in the pathophysiology of several tachyarrhythmias. Accurate electrophysiological localization of this structure is therefore crucial for effective ablation therapy. Hence, this study quantifies electrophysiological properties of the LOM, and identifies which electrogram (EGM) recording (uni- or bipolar) and processing technologies (local activation time and/or voltage mapping) are most suitable for accurate localization of the LOM.

Methods: The LOM was electrophysiologically identified in 19 patients (mean age 66±14 years; 12 male) undergoing elective cardiac surgery using intra-operative high-density epicardial mapping, to quantify and visualize EGM features during sinus rhythm.

Results: Only a third of LOM potentials that were visualized using unipolar EGMs, were still visible in bipolar activation maps. Unipolar LOM potentials had lower voltages (P_{50}: LOM: 1.51 [0.42–4.29] mV vs. left atrium (LA): 8.34 [1.50–17.91] mV, p<0.001), less steep slopes (P_{50}: LOM: -0.48 [-1.96–-0.17] V/s vs. LA: -1.24 [-2.59–-0.21] V/s, p<0.001), and prolonged activation duration (LOM: 20 [7.5–30.5] ms vs. LA: 16.5 [6–28] ms, p=0.008) compared to LA potentials. Likewise, bipolar LOM voltages were also smaller (P_{50}: LOM: 1.54 [0.48–3.28] mV vs. LA: 3.12 [0.50–7.19] mV, p<0.001).

Conclusions: The LOM was most accurately localized in activation and voltage maps by using unipolar EGMs with annotation of primary deflections in case of single potentials and secondary deflections in case of double or fractionated potentials.

Journal site

Introduction

In 1850, Marshall[1] first described a vestigial fold of the pericardium at the back of the left atrium (LA) between the left auricle and the left pulmonary veins (PVs). This is now known as the ligament of Marshall (LOM), which results from embryonic obliteration of the left anterior cardinal vein when the venous system transfers from a symmetric to a right-sided one.[2] The LOM contains the vein of Marshall (VOM) – which is also referred to as the oblique vein of the LA – small sympathetic and parasympathetic nervous fibers, and multiple myocardial tracts towards the LA free wall, known as Marshall bundles.[1,3-10] As a consequence, the LOM is much more than just an embryological remnant: it forms an electro-anatomical connection between the coronary sinus (CS), the left lateral ridge and the PVs.

The LOM may play an important role in the pathophysiology of various tachyarrhythmias, including ventricular tachycardias, atrioventricular reentrant tachycardias, ridge-related perimitral atrial flutters and atrial fibrillation (AF).[11-18] In patients with AF, the LOM may serve as either a source of triggered ectopic activity or as an arrhythmogenic substrate.[8,14,17-19]

Because of its arrhythmogenic properties, the LOM has recently gained interest as a target of anti-arrhythmic therapies. This includes additional endocardial or epicardial ablative lesions on the LOM in adjunct to PV isolation, using a catheter-based, surgical or hybrid approach, and the recently introduced technique of VOM ethanol infusion.[13,20-25]

For these ablation approaches, it is of paramount importance to accurately localize the LOM electrophysiologically. However, it is yet unclear what the most suitable mapping approach for this purpose should be. The objectives of this study are therefore to quantify electrophysiological properties of the LOM using an intra-operative high-density epicardial mapping approach, and to identify which electrogram (EGM) recording (uni- or bipolar) and processing technologies (local activation time and/or voltage mapping) are most suitable for accurate electrophysiological localization of the LOM.

Materials and Methods

Study population

Patients undergoing elective open-heart surgery at the Erasmus Medical Center Rotterdam were eligible for inclusion. Exclusion criteria were hemodynamic instability, usage of inotropic agents, emergency cardiac surgery or redo cardiac surgery. All patients signed informed consent to participate in the study protocol approved by the institutional ethical committee (MEC2010-054/MEC2014-393).[26,27] Patient characteristics were collected from the electronic medical records. The study was conducted according to the principles of the Declaration of Helsinki.

Mapping procedure

Intra-operative high-density epicardial mapping was performed during sinus rhythm (SR), prior to commencement of extracorporeal circulation, as previously described in detail.[26,27] A custom-made 192-electrode array (interelectrode distance 2 mm, electrode diameter 0.45 mm) was used to record unipolar EGMs for five seconds. This study was part of a more elaborate mapping protocol, that has been described in detail before.[27] As this study focused on electrophysiological identification of the LOM, which courses anatomically from the CS obliquely above the LA appendage and lateral to the left PVs, only the LA mapping location was included for analysis.[3] At this mapping location, the electrode array was positioned from

35
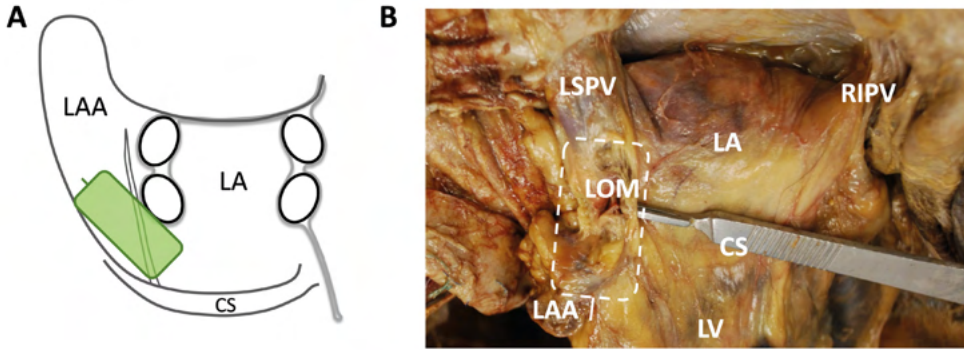
Figure 1 – Epicardial mapping of the ligament of Marshall. *Panel A*: a schematic overview of the position and orientation of the electrode array (green rectangle) on the LA. *Panel B*: a picture of the LOM in a human specimen and the location of the electrode array during LOM mapping (striped rectangle). The white solid line marks the LOM. **CS** = coronary sinus; **LA** = left atrium; **LAA** = left atrial appendage; **LIPV** = left inferior pulmonary vein; **LOM** = ligament of Marshall; **LSPV** = left superior pulmonary vein; LV = left ventricle.

the lower border of the left inferior PV towards the LA appendage (*Figure 1*).

A steel wire attached to the thoracic subcutaneous tissue served as the indifferent electrode and a temporal bipolar epicardial pacemaker wire in the right atrial appendage as the reference electrode. Recordings included a surface electrocardiogram (ECG) lead I, a calibration signal of 1000 ms and 2 mV, a bipolar reference EGM and all unipolar EGMs. After amplification (gain 1000), filtering (bandwidth 0.5–400 Hz), sampling (1 kHz) and analogue-to-digital conversion (16 bits), all data were stored on a hard disk. Bipolar EGMs were created by subtracting two neighboring unipolar EGMs in horizontal and vertical direction. These bipolar EGMs were subsequently filtered (30–400 Hz).

Data processing

EGMs were analyzed semi-automatically using custom-made software that annotates the negative slope of each atrial deflection when it was at least -0.05 V/s. Within each potential,
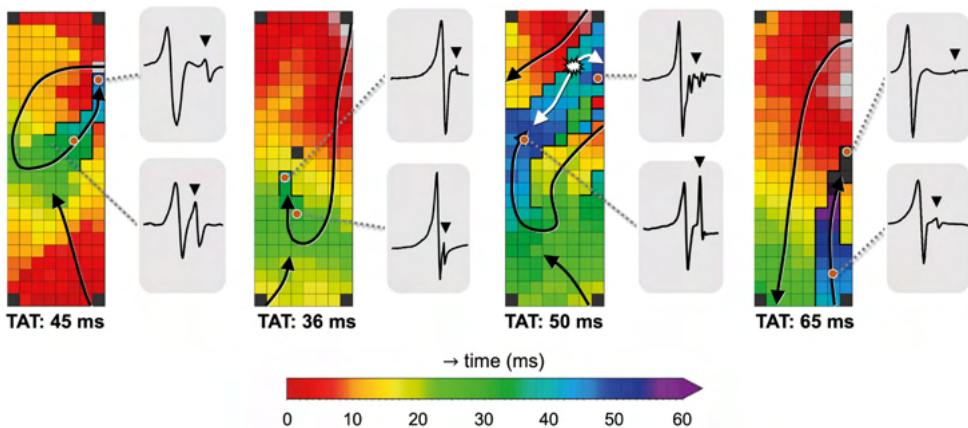
Figure 2 – Four examples of color-coded activation maps containing LOMs derived from different patients, constructed using all unipolar deflections. Examples of corresponding EGMs recorded at distinct locations of the LOM are shown outside the activation map, demonstrating the variable morphology of LOM potentials. The bold black lines represent lines of conduction block and the black triangle in the EGM indicates a LOM potential. The white asterisk indicates a focal pattern of activation. **EGM** = electrogram; **LOM =** ligament of Marshall; **TAT** = total activation time.

the steepest segment of each negative deflection was defined as the local activation time (LAT); the steepest negative deflection was labelled the primary deflection. Potentials with a single negative deflection (single potentials) only contain a primary deflection. In case of double or fractionated potentials, all others deflections were labelled as secondary deflections.

Premature atrial complexes and activation maps with simultaneous activation were excluded from analysis. Annotations were all manually checked by two investigators.

Color-coded local activation maps were constructed to investigate spatial activation patterns. Conduction delay was defined as minimal difference in LAT between adjacent electrodes of 7 to 11 ms and conduction block as ≥12 ms.[28] Potentials were subdivided into single (one deflection), short double (two deflections with a deflection interval <15 ms), long double (two deflections with a deflection interval ≥15 ms) or fractionated (≥3 deflections) potentials.

Within bipolar EGMs, potentials were identified using a timeframe of 200 ms surrounding unipolar LATs. Bipolar LAT was defined as the maximum absolute voltage within this timeframe.[29] In order to compute the bipolar peak-to-peak voltage of the LA and LOM separately, unipolar activation times of the LA and LOM deflections were used to distinguish between bipolar LA and LOM potentials; the maximum absolute voltage was used as LA and LOM bipolar voltage.

Identification of LOM by different signal processing techniques

Mapping data were screened for activation maps covering the LOM by consensus of two investigators. For this purpose, two different signal processing techniques were applied to construct local activation time maps: 1) annotation of only primary deflections and 2) annotation of both primary and secondary deflections, in case of double or fractionated potentials. In this case, the LAT of the latest deflection was visualised.[30] Likewise, two different types of voltage maps were constructed, using either the peak-to-peak amplitude of the primary deflection or the peak-to-peak amplitude of the largest secondary deflection.

As demonstrated in *Figure 2*, LOM was presumed to be present in an activation map if the following criteria were met. An activation map should contain a circumscriptive area 1) from which double or fractionated potentials are recorded, 2) which is bordered by either two parallel lines of conduction block or one line of conduction block and one line of conduction delay. Patients were excluded from analysis if the full length of this area was either parallel to the border of the electrode or the area was activated simultaneously.

Data analysis

In patients in whom a LOM was electrophysiologically identified, the first deflection of each double or fractionated potential was classified as LA potential, and all other deflections were classified as LOM potentials. In case of accidental overlap of adjacent mapping locations, whilst both locations included the LOM, the recording in which the largest part of the LOM was visible was included for analysis.

From each unipolar EGM, the peak-to-peak amplitudes and slopes were measured of both LA and LOM potentials. Total duration of LOM activation was defined as the time difference between the first and last LAT of the area containing LOM potentials. Duration of LA activation was calculated as the time difference between the first and last LAT in this same area.

35

Potential fractionation duration was defined as the time difference (ms) between the first and the last deflection. The maximum time difference between the LOM and the surrounding LA tissue was defined as maximum conduction time (CT_{max}).

Statistical analysis

Data were tested for normality using histograms, QQ-plots and Shapiro-Wilk tests. Continuous variables were reported as mean ± standard deviation if distributed normally and as median (range) otherwise for patient characteristics. Categorical variables were given as number (percentage).

For each individual patient, the 10th, 50th and 90th percentile of unipolar and bipolar voltages and unipolar slopes, were calculated as a summary measure per patient, separately for the LA and LOM potentials. These were then presented as median with range and compared to see if a difference could be identified between LA and LOM potentials. A similar analysis was performed for the median duration of LOM and LA activation for each patient.

Wilcoxon signed rank tests were performed to compare characteristics of LA and LOM potentials. A p-value <0.05 was considered statistically significant. Data were analyzed using R (version 4.0.3; R Foundation for Statistical Computing, Vienna, Austria).

Results

Patient selection

LA mapping locations obtained from 108 patients were screened for the presence of the LOM. A total of 89 patients were excluded because they did not meet the inclusion criteria. Thus, 19 patients were further analyzed.

Table 1 – Patient characteristics.

	Overall (n=19)
Age (y)	66±14
Male	12 (63.2%)
Underlying heart disease	
• CABG	9 (47.4%)
• AVD	4 (21.1%)
• MVD	4 (21.1%)
• CHD	7 (36.8%)
• MAZE	4 (21.1%)
Pre-operative AF	
• None	14 (73.7%)
• Paroxysmal	3 (15.8%)
• Persistent	2 (10.5%)
Cardiovascular risk factors	
• BMI (kg/m^2)	28.5±5.09
• Hypertension	11 (57.9%)
• Dyslipidemia	6 (31.6%)
• Diabetes mellitus	4 (21.1%)
• Myocardial infarction	6 (31.6%)

Continuous variables are presented as mean ± standard deviation. Categorical variables are presented as number (percentage). **AF** = atrial fibrillation; **AVD** = aortic valve disease; **BMI** = body mass index; **CABG** = coronary artery bypass grafting; **CHD** = congenital heart disease; **MVD** = mitral valve disease.
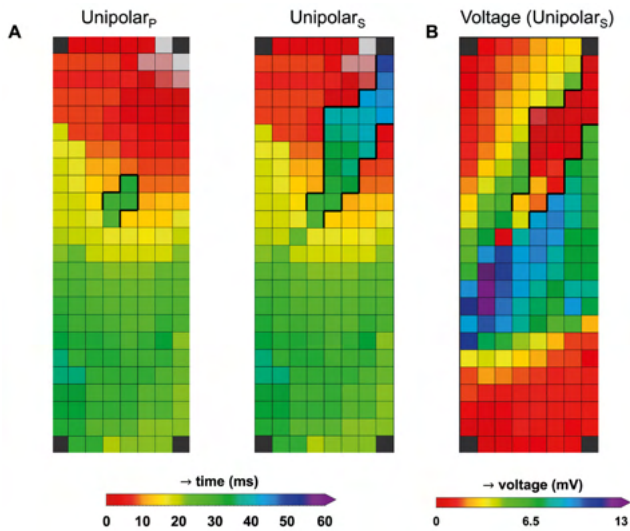
Figure 3 – Color-coded activation time and voltage maps. *Panel A*: two activation maps from the same patient, constructed using unipolar LATs from only primary deflections (unipolar$_P$, left) and a combination of primary deflections in case of single potentials and secondary deflections in case of double or fractionated potentials (unipolar$_S$, right). *Panel B*: voltage map from the same patient, using the voltages from unipolar primary deflections and the secondary deflections with the largest peak-to-peak amplitude (in case more than one secondary deflection was present).

Patient characteristics

Table 1 shows characteristics of the 19 patients (mean age: 65.5±13.8 years, male sex: 12 (63.2%)). Most patients underwent coronary artery bypass graft (CABG) surgery (9 (47.4%)); others had aortic (4 (21.1%)) or mitral (4 (21.1%)) valve repair or replacement, surgery for congenital heart disease (7 (36.8%)) or arrhythmia surgery (4 (21.1%)). A history of AF prior to surgery was present in 5 (26.3%) patients, of whom 3 (16.7%) had paroxysmal and 2 (11.1%) persistent AF.

Mapping data characteristics

A total of 22,725 potentials were included for analysis, of which 19,536 (86.0%) were classified as LA potentials and 3,189 (14.0%) as LOM potentials (±6 SR beats per patient). This resulted in a median of 1,098 [744–1,316] LA potentials and 165 [28–369] LOM potentials per patient.

Patterns of activation at the LOM area

Figure 3 shows color-coded activation maps obtained from the same beat of a 30-year-old female patient who underwent surgery for closure of an atrial septal defect and tricuspid valve repair. This figure illustrates that the LOM can be most easily identified when not only primary unipolar deflections are annotated (unipolar$_p$), but also the secondary deflections (unipolar$_s$, *Figure 3A*). When constructing a voltage map in which either primary deflections, in case of single potentials, or secondary deflections, in case of double and fractionated potentials, are presented, the LOM is easily recognizable as an area containing potentials with lower voltages (*Figure 3B*).

Using the annotation of secondary deflections to construct activation maps, different patterns of activation were identified. *Figure 2* presents four examples of activation maps in which a LOM is visible. These examples show that there is considerable inter-individual variation in activation patterns, size and the total activation time of the LOM.

Median total activation time of the LOM was longer than median total activation time of the surrounding LA tissue (LOM: 20 [7.5–30.5] ms vs. LA: 16.5 [6–28] ms, p=0.008). The maximum

35
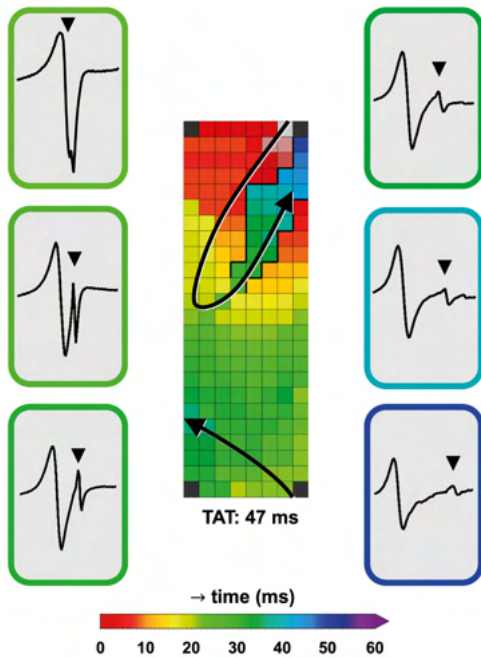
Figure 4 – A color-coded activation map, constructed using unipolar EGMs in which all negative deflections are annotated. Additionally, examples of EGMs in the LOM area recorded at distinct moments of LOM activation are shown. The EGMs are depicted in chronological order of LOM activation and the color surrounding each EGM represents the LAT of the recording site within the LOM. The bold black lines represent lines of conduction block and the black triangle in the EGM indicates a LOM potential. **EGM** = electrogram; **LAT** = local activation time; **LOM** = ligament of Marshall; **TAT** = total activation time.

conduction delay between the LOM and the surrounding LA tissue (CT_{max}) in each patient ranged between 16 and 65 ms (median: 38 ms).

Characteristics of unipolar LOM electrograms

Unipolar potentials recorded from the LOM area consisted of short double (34.4%), long double (57.1%) or fractionated potentials (8.5%).

Figure 4 shows a typical example of a color-coded activation map obtained from the same patient as in *Figure 3*, annotated using primary deflections of single potentials or secondary deflections of double or fractionated potentials. A few EGMs recorded within the LOM area are illustrated, in which the first deflection clearly represents the LA activation and the other, usually smaller deflections, the LOM activation.

As demonstrated in *Table 2*, characteristics of unipolar LOM EGMs and remaining LA EGMs differed significantly. Compared to LA potentials, median peak-to-peak amplitudes of LOM potentials were significantly lower (P_{50}: LOM: 1.51 [0.42–4.29] mV vs. LA: 8.34 [1.50–17.91] mV,

Table 2 – Characteristics of unipolar EGMs.

Unipolar EGMs	Value	Ligament of Marshall	Left atrium	*p*-value
Voltage (mV)	P_{50}	1.51 [0.42–4.29]	8.34 [1.50–17.91]	<0.001
	P_{10}	0.62 [0.19–2.14]	4.37 [0.80–7.71]	<0.001
	P_{90}	3.86 [0.75–24.47]	15.52 [2.65–49.07]	<0.001
Slope (V/s)	P_{50}	-0.48 [-1.96–-0.17]	-1.24 [-2.59–-0.21]	<0.001
	P_{10}	-1.40 [-12.24–-0.35]	-4.14 [-17.96–-0.46]	<0.001
	P_{90}	-0.16 [-0.87–-0.06]	-0.40 [-1.01–-0.09]	<0.001
CT_{max} (ms)	max	38 [16–65]		
Duration of activation (ms)	P_{50}	20 [7.5–30.5]	16.5 [6–28]	0.008

Values are presented as median (range). **CT_{max}** = maximum conduction time between two neighboring electrodes; **EGM** = electrogram.
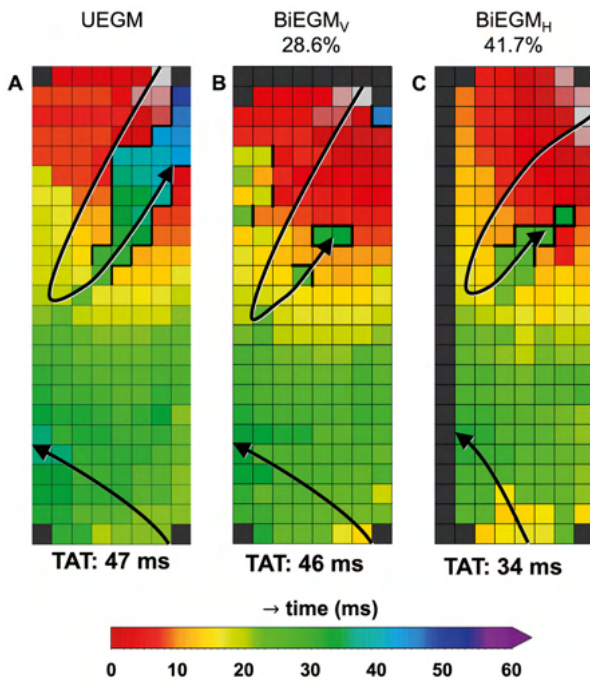
Figure 5 – Unipolar and corresponding bipolar vertical and bipolar horizontal activation map obtained from one patient. The percentages on top of the activation maps show how often the amplitude of the LOM was larger than the amplitude of LA tissue for bipolar activation maps. *Panel A*: map constructed by unipolar EGMs in which all negative deflections were annotated (UEGM). *Panel B*: map constructed by bipolar EGMs, created by subtracting EGMs in vertical direction (BiEGM$_V$). *Panel C*: map constructed by bipolar EGMs, created by subtracting EGMs in horizontal direction (BiEGM$_H$). The bold black lines represent lines of conduction block. **EGM** = electrogram; **LA** = left atrium; **LOM** = ligament of Marshall; **TAT** = total activation time.

p<0.001). Also, the median slope of LOM potentials was less steep (P_{50}: LOM: -0.48 [-1.96–-0.17] V/s vs. LA: -1.24 [-2.59–-0.21] V/s, p<0.001).

In a median of 98.4 [71.5–100] % of the unipolar potentials per patient, LOM potentials had lower voltages than LA potentials and 30.4 [0–45.7] % of their slopes were steeper than the LA potentials.

Characteristics of bipolar LOM electrograms

Bipolar activation maps were created using LATs of bipolar EGMs recorded in both vertical and horizontal direction. As the moment of LAT of the bipolar EGM is represented by the moment of the maximum absolute bipolar voltage, the maximum voltage determines which part of the LOM is visible on the corresponding bipolar activation map.[29]

Figure 5 demonstrates an example of a unipolar and corresponding bipolar activation maps, obtained from the same patient as used in *Figures 3 and 4*. In the bipolar activation maps, the mapping area representing LOM activation is smaller, as compared to the unipolar activation map that was constructed using both primary and secondary deflections. The

35

Table 3 – Characteristics of bipolar EGMs.

Bipolar EGMs	Value	Ligament of Marshall	Left atrium	*p*-value
Horizontal + vertical oltage (mV)	P_{50}	1.54 [0.48–3.28]	3.12 [0.50–7.19]	<0.001
	P_{10}	0.47 [0.22–1.79]	0.87 [0.13–2.72]	0.007
	P_{90}	3.90 [0.94–13.07]	10.99 [1.39–19.78]	<0.001
% LOM > LA - horizontal	P_{50}	36.7 [0–51.7]		
% LOM > LA - vertical	P_{50}	30.0 [0–59.5]		
% LOM > LA - all	P_{50}	35.1 [0.7–54.5]		

Values are presented as median (range). **EGM** = electrogram; **LA** = left atrium; **LOM** = ligament of Marshall.

unipolar activation map clearly shows a larger continuous area of LOM activation.

Bipolar voltage characteristics of the LOM and LA potentials recorded from all patients are listed in *Table 3*. Comparing the reconstructed bipolar EGMs of the LOM and the LA in horizontal and vertical direction, respectively only 36.7 [0–51.7] % and 30.0 [0–59.5] % of bipolar LOM voltages were larger than bipolar LA voltages. Combining data from both directions, this percentage increased to 35.1 [0.7–54.5] %. Thus, only a median of respectively 36.7%, 30.0% or 35.1% of the LOM that is visible in a unipolar activation map in which all negative deflections are annotated, is also visualized in bipolar activation maps.

Comparable to unipolar EGMs, median voltages of bipolar EGMs were higher in LA than in LOM (P_{50}: LOM: 1.54 [0.48–3.28] mV vs. LA: 3.12 [0.50–7.19] mV, p<0.001).

Discussion

The ligament of Marshall has gained interest in the field of electrophysiology for its arrhythmogenic properties and therapeutic possibilities related to AF. It is therefore important to accurately localize the LOM electrophysiologically, although the most optimal mapping approach for this purpose has not yet been elucidated.

The key finding of our study is that unipolar EGMs are more useful than bipolar EGMs in localizing the LOM, in particular local activation time and voltage mapping of primary deflections of single potentials combined with secondary deflections of double and fractionated potentials. Due to differences in activation direction, the LOM that was identified using unipolar EGMs, remained only partially visible in the bipolar activation maps. Therefore, unipolar EGMs are preferred to accurately localize a LOM.

EGM characteristics

Bipolar LOM potentials were first described by Scherlag et al.[8] As reported previously, LOM potentials consist of two deflections of which the first corresponds to local left atrial activation and the second, narrower and smaller deflection to LOM activation.[13,15,31] However, this sequence depends on the excitation pattern of the atria, which is variable even during sinus rhythm.[32]

The majority of LOM potentials measured in this study consisted of two deflections; these double potentials are generally related to areas of conduction block.[33] LOM potentials recorded with either uni- or bipolar technique had smaller voltages and less steep slopes compared to LA potentials, as a result of the smaller bundle structure of the LOM.[3] However, as expected, there were considerable differences in bipolar voltage according to the recording direction. In a third of bipolar EGMs, LOM potentials were larger compared to LA potentials. Hence, the LOM was less detectable in bipolar than in unipolar activation maps.

In canine atria, Scherlag et al.[8] measured an interval between LA and LOM bipolar EGMs of 60 ms or more at the most distal point in the LOM. In humans, a mean interval of 73 ms measured by a multipolar catheter inside the VOM has been reported.[13] The maximum time difference between LOM and LA tissue measured in the current study population was much shorter (38 [16–65] ms). Smaller time differences may be explained by the fact that our array did not cover the entire VOM and hence the most distal point of the LOM with the largest time difference could have been missed. In our study population, we also measured time differences up to 65 ms. Additionally, activation of the LOM was considerably prolonged compared to the surrounding LA tissue of comparable lengths. This localized slowing of

conduction could partly explain the role of the LOM in initiation or perpetuation of atrial tachyarrhythmias.

Prior endo-epicardial mapping studies demonstrated that – except for areas of endo-epicardial asynchrony – features of endo- and opposite epicardial EGMs are comparable.[34] Hence, the results of our study are also relevant for endovascular mapping approaches. As expected, all unipolar and bipolar LOM potentials consisted of double or fractionated potentials reflecting local asynchronous activation of underlying superimposed LOM and LA tissue.

Anatomy and activation patterns

The LOM is the remnant of the embryologic left superior caval vein, but is much more than just a remnant. It has several neuronal and muscular morphological features, comprising the CS musculature, PV sleeves and LA free wall.[3,5,6] The LOM forms the neural connecting pathway between intrathoracic and intracardiac ganglia with abundant (para)sympathetic to atrial connections that have an interesting topographical neural density variation along the ligament.[5,12] Additionally, the LOM contains the vein of Marshall, which is electrically connected to the CS through its muscular sleeve and to the LA free wall through Marshall bundles.[1,3-10] LOM activation patterns differ between patients, which is caused by differences in LOM anatomy and the number of connections between the LOM and the surrounding tissue, as demonstrated by Han et al.[15] In their study, patients were categorized into having single, double or multiple LOM connections, which was determined by application of differential pacing from the CS, left PVs, and LA appendage. In patients with a single connection, the LOM is only electrically connected to the CS, causing a proximal-to-distal activation sequence. Because the remainder of the LA is pre-excited by the sinus wavefront from Bachmann's bundle, typical double potentials are visible during SR. This was also observed in the present study. In patients with double or multiple connections, the LOM is not only electrically connected to the CS, but also to the LA or PVs. During SR, wavefronts from Bachmann's bundle and the CS are therefore competing and LOM potentials might not be clearly separable. This explains why LOM potentials can be difficult to distinguish from the LA potentials during SR in patients with double or multiple LOM connections.

Role of the LOM in arrhythmogenesis

The LOM may have different roles in the pathophysiology of atrial tachyarrhythmias. Firstly, focal activity may be present in the LOM and it can therefore serve as a trigger for atrial tachyarrhythmias.[13,14] Secondly, the LOM is influenced by the autonomic nervous system through its rich sympathetic and parasympathetic innervation, stimulation of which can induce arrhythmias. Thirdly, the LOM can serve as a bypass tract between the coronary sinus and pulmonary veins, when more than one connection is present, possibly facilitating macro-reentry circuits.[13,15] The LOM can cause AF recurrences after PV isolation, through LOM-mediated PV reconnection.[16] Also, the LOM can serve as a portion of a macro-reentry circuit, for example in peri-mitral atrial tachycardias.[17,18] Additionally, the LOM causes localized areas of conduction block, which may contribute to the initiation and perpetuation of AF and thereby serve as a substrate for AF.[35]

35

Therapeutic options

Several recently published studies demonstrated a variety of therapeutic options targeting the LOM. This includes using a catheter-based, surgical or hybrid approach for additional endocardial or epicardial ablative lesions on the LOM in adjunct to PV isolation.[13,20,24,25]

Hence, in these procedures, a linear catheter is preferred over a balloon-based catheter for endovascular PV isolation. Retrograde infusion of ethanol into the VOM after performing a CS venogram is another technique to ablate the LOM and has recently been investigated in several RCTs.[21-23] This procedure has proven to be effective during a follow-up of 12 months in AF patients with arrhythmogenic activity in the LOM and decreases AF recurrence rates after combined catheter ablation and ethanol infusion. However, a potential disadvantage of VOM ethanol-infusion could be the lack of specificity in the area that is ablated, causing unnecessary damage of atrial tissue in an area larger than what is contributing to the arrhythmia.

Clinical implications

Prior mapping studies of the LOM have mainly used bipolar LAT mapping strategies to identify the LOM and target it for treatment. However, we have demonstrated, by using a high-density epicardial mapping approach, that the LOM can be localized more accurately using unipolar EGMs in which both primary deflections of single potentials and secondary deflections of double and fractionated potentials are visualized in activation as well as voltage maps. In daily clinical practice, this signal processing approach may aid in visualizing the LOM real-time during both mapping guided arrhythmia surgery and endovascular interventions targeting the LOM. Real-time LOM visualization could lead to more specific ablation of solely the LOM, eliminating the need to ablate the entire area using VOM ethanol infusion, thereby bypassing its potential disadvantages.

Limitations

Due to the strict nature of the selection criteria used to select LA locations containing a LOM, it is possible that the number of patients in which a LOM is found in this study is an underestimation. However, it was not the primary aim of this study to correctly identify the number of patients in whom a LOM could be detected.

Additionally, it is not possible to directly correlate the exact anatomical Marshall bundle structure and histological properties of the area mapped to the electrophysiological properties, which is inherent to the applied mapping technique. In a future prospective study, this could be partially addressed by confirmation by the surgeon that the electrode array is positioned on the LOM, which is visible and accessible after a small rightward shift of the heart. Besides, programmed electrical stimulation at the LOM could confirm the electrophysiological properties as demonstrated in the current study.

Conclusion

Unipolar mapping of the LA with annotation and visualization of both primary deflections of single potentials and secondary deflections of double and fractionated potentials in activation and voltage maps is the most accurate signal recording and processing approach to electrophysiologically visualize the LOM. Additional studies are required to further develop this technique. The next step is intra-operative real-time visualization of the LOM using the signal recording and processing approach as discussed in this article, and to use this approach to guide ablation therapy targeting the LOM in patients undergoing arrhythmia surgery.

References

1. Marshall J, Sharpey W. VI. On the development of the great anterior veins in man and mammalia; including an account of certain remnants of fœtal structure found in the adult, a comparative view of these great veins the different mammalia, and an analysis of their occasional peculiarities in the human subject. Philosophical Transactions of the Royal Society of London. 1850;140:133-170.
2. Rodriguez-Manero M, Schurmann P, Valderrabano M. Ligament and vein of Marshall: A therapeutic opportunity in atrial fibrillation. Heart Rhythm. 2016;13:593-601.
3. Kim DT, Lai AC, Hwang C, Fan LT, Karagueuzian HS, Chen PS, Fishbein MC. The ligament of Marshall: a structural analysis in human hearts with implications for atrial arrhythmias. J Am Coll Cardiol. 2000;36:1324-1327.
4. Lin J, Scherlag BJ, Lu Z, Zhang Y, Liu S, Patterson E, Jackman WM, Lazzara R, Po SS. Inducibility of atrial and ventricular arrhythmias along the ligament of marshall: role of autonomic factors. J Cardiovasc Electrophysiol. 2008;19:955-962.
5. Ulphani JS, Arora R, Cain JH, Villuendas R, Shen S, Gordon D, Inderyas F, Harvey LA, Morris A, Goldberger JJ, et al. The ligament of Marshall as a parasympathetic conduit. Am J Physiol Heart Circ Physiol. 2007;293:H1629-1635.
6. Makino M, Inoue S, Matsuyama TA, Ogawa G, Sakai T, Kobayashi Y, Katagiri T, Ota H. Diverse myocardial extension and autonomic innervation on ligament of Marshall in humans. J Cardiovasc Electrophysiol. 2006;17:594-599.
7. Cabrera JA, Ho SY, Climent V, Sanchez-Quintana D. The architecture of the left lateral atrial wall: a particular anatomic region with implications for ablation of atrial fibrillation. Eur Heart J. 2008;29:356-362.
8. Scherlag BJ, Yeh BK, Robinson MJ. Inferior interatrial pathway in the dog. Circ Res. 1972;31:18-35.
9. Omichi C, Chou CC, Lee MH, Chang CM, Lai AC, Hayashi H, Zhou S, Miyauchi Y, Okuyama Y, Hamabe A, et al. Demonstration of electrical and anatomic connections between Marshall bundles and left atrium in dogs: implications on the generation of P waves on surface electrocardiogram. J Cardiovasc Electrophysiol. 2002;13:1283-1291.
10. Zabowka A, Jakiel M, Bolechala F, Jakiel R, Jasinska KA, Holda MK. Topography of the oblique vein of the left atrium (vein of Marshall). Kardiol Pol. 2020;78:688-693.
11. He B, Wang X, Zhao F, Guo T, Po SS, Lu Z. The ligament of Marshall and arrhythmias: A review. Pacing Clin Electrophysiol. 2021;44:792-799.
12. Vlachos K, Derval N, Pambrun T, Duchateau J, Martin CA, Bazoukis G, Frontera A, Takigawa M, Nakashima T, Efremidis M, et al. Ligament of Marshall ablation for persistent atrial fibrillation. Pacing Clin Electrophysiol. 2021;44:782-791.
13. Hwang C, Wu TJ, Doshi RN, Peter CT, Chen PS. Vein of marshall cannulation for the analysis of electrical activity in patients with focal atrial fibrillation. Circulation. 2000;101:1503-1505.
14. Doshi RN, Wu TJ, Yashima M, Kim YH, Ong JJ, Cao JM, Hwang C, Yashar P, Fishbein MC, Karagueuzian HS, et al. Relation between ligament of Marshall and adrenergic atrial tachyarrhythmia. Circulation. 1999;100:876-883.
15. Han S, Joung B, Scanavacca M, Sosa E, Chen PS, Hwang C. Electrophysiological characteristics of the Marshall bundle in humans. Heart Rhythm. 2010;7:786-793.
16. Dave AS, Baez-Escudero JL, Sasaridis C, Hong TE, Rami T, Valderrabano M. Role of the vein of Marshall in atrial fibrillation recurrences after catheter ablation: therapeutic effect of ethanol infusion. J Cardiovasc Electrophysiol. 2012;23:583-591.
17. Hayashi T, Fukamizu S, Mitsuhashi T, Kitamura T, Aoyama Y, Hojo R, Sugawara Y, Sakurada H, Hiraoka M, Fujita H, et al. Peri-Mitral Atrial Tachycardia Using the Marshall Bundle Epicardial Connections. JACC Clin Electrophysiol. 2016;2:27-35.
18. Chik WW, Chan JK, Ross DL, Wagstaff J, Kizana E, Thiagalingam A, Kovoor P, Thomas SP. Atrial tachycardias utilizing the Ligament of Marshall region following single ring pulmonary vein isolation for atrial fibrillation. Pacing Clin Electrophysiol. 2014;37:1149-1158.
19. Kurotobi T, Ito H, Inoue K, Iwakura K, Kawano S, Okamura A, Date M, Fujii K. Marshall vein as arrhythmogenic source in patients with atrial fibrillation: correlation between its anatomy and electrophysiological findings. J Cardiovasc Electrophysiol. 2006;17:1062-1067.
20. Barrio-Lopez MT, Sanchez-Quintana D, Garcia-Martinez J, Betancur A, Castellanos E, Arceluz M, Ortiz M, Nevado-Medina J, Garcia F, Almendral J. Epicardial Connections Involving Pulmonary Veins: The Prevalence, Predictors, and Implications for Ablation Outcome. Circ Arrhythm Electrophysiol. 2020;13:e007544.
21. Valderrabano M, Peterson LE, Swarup V, Schurmann PA, Makkar A, Doshi RN, DeLurgio D, Athill CA, Ellenbogen KA, Natale A, et al. Effect of Catheter Ablation With Vein of Marshall Ethanol Infusion vs Catheter Ablation Alone on Persistent Atrial Fibrillation: The VENUS Randomized Clinical Trial. JAMA. 2020;324:1620-1628.
22. Derval N, Duchateau J, Denis A, Ramirez FD, Mahida S, Andre C, Krisai P, Nakatani Y, Kitamura T, Takigawa M, et al. Marshall bundle elimination, Pulmonary vein isolation, and Line completion for ANatomical ablation of persistent atrial fibrillation (Marshall-PLAN): Prospective, single-center study. Heart Rhythm. 2021;18:529-537.
23. Kamakura T, Derval N, Duchateau J, Denis A, Nakashima T, Takagi T, Ramirez FD, Andre C, Krisai P, Nakatani Y, et al. Vein of Marshall Ethanol Infusion: Feasibility, Pitfalls, and Complications in Over 700 Patients. Circ Arrhythm Electrophysiol. 2021;14:e010001.
24. Morris KE, Mudd TU, Peterson SM, Thomas KM. Atrial Fibrillation and Heart Failure: Utilization of Hybrid Ablation Therapy to Improve Patient Outcomes. EP Lab Dig. 2022;22.
25. Xu B, He F, Wang S, Chen H, Zhang W. Modified Mini-Maze for Atrial Fibrillation with Interruption of Inferior Vena Cava. Heart Surg Forum. 2021;24:E1046-E1048.
26. van der Does LJ, Yaksh A, Kik C, Knops P, Lanters EA, Teuwen CP, Oei FB, van de Woestijne PC, Bekkers JA, Bogers AJ, et al. QUest for the Arrhythmogenic Substrate of Atrial fibRillation in Patients Undergoing Cardiac Surgery (QUASAR Study): Rationale and Design. J Cardiovasc Transl Res. 2016;9:194-201.

35

27.   Lanters EA, van Marion DM, Kik C, Steen H, Bogers AJ, Allessie MA, Brundel BJ, de Groot NM. HALT & REVERSE: Hsf1 activators lower cardiomyocyt damage; towards a novel approach to REVERSE atrial fibrillation. J Transl Med. 2015;13:347.
28.   Allessie MA, de Groot NM, Houben RP, Schotten U, Boersma E, Smeets JL, Crijns HJ. Electropathological substrate of long-standing persistent atrial fibrillation in patients with structural heart disease: longitudinal dissociation. Circ Arrhythm Electrophysiol. 2010;3:606-615.
29.   Paul T, Moak JP, Morris C, Garson A, Jr. Epicardial mapping: how to measure local activation? Pacing Clin Electrophysiol. 1990;13:285-292.
30.   van Staveren LN, de Groot NMS. Revealing hidden information from unipolar extracellular potentials. HeartRhythm Case Rep. 2020;6:942-946.
31.   Wakabayashi Y, Hayashi T, Matsuda J, Sugawara Y, Mitsuhashi T, Fujita H, Momomura S. Mitral Isthmus Ablation: Is the Conduction Block Completed? The Importance of the Marshall Bundle Epicardial Connections. Circ Arrhythm Electrophysiol. 2016;9:e003049.
32.   Mouws E, Lanters EAH, Teuwen CP, van der Does L, Kik C, Knops P, Yaksh A, Bekkers JA, Bogers A, de Groot NMS. Impact of Ischemic and Valvular Heart Disease on Atrial Excitation:A High-Resolution Epicardial Mapping Study. J Am Heart Assoc. 2018;7.
33.   Konings KT, Smeets JL, Penn OC, Wellens HJ, Allessie MA. Configuration of unipolar atrial electrograms during electrically induced atrial fibrillation in humans. Circulation. 1997;95:1231-1241.
34.   van der Does L, Knops P, Teuwen CP, Serban C, Starreveld R, Lanters EAH, Mouws E, Kik C, Bogers A, de Groot NMS. Unipolar atrial electrogram morphology from an epicardial and endocardial perspective. Heart Rhythm. 2018;15:879-887.
35.   Kleber AG, Rudy Y. Basic mechanisms of cardiac impulse propagation and associated arrhythmias. Physiol Rev. 2004;84:431-488.

35

Chapter 36

Insights into the effects of low level vagus nerve stimulation on atrial electrophysiology: towards patient tailored cardiac neuromodulation

Rohit K. Kharbanda*

Nawin L. Ramdat Misier*

Mathijs S. van Schie

Roxanne D. Zwijnenburg

Jorik H. Amesz

Paul Knops

Ad J.J.C. Bogers

Yannick J.H.J. Taverne

Natasja M.S. de Groot

* Contributed equally

Abstract

Background: Low-level vagus nerve stimulation through the tragus (tLLVNS) is increasingly acknowledged as a therapeutic strategy to prevent and treat atrial fibrillation (AF). However, lack in understanding of the exact antiarrhythmic properties of tLLVNS, hampered clinical implementation. In this study, we aim to study the effects of tLLVNS on atrial electrophysiology by performing intra-operative epicardial mapping during acute and chronic tLLVNS.

Methods: Epicardial mapping of the superior right atrium was performed before and after arterial graft harvesting in patients undergoing coronary artery bypass grafting, without a history of AF. The time needed for arterial graft harvesting was used to perform chronic tLLVNS. Electrophysiological properties were compared prior and during chronic tLLVNS.

Results: Ten patients (median age 74 [69–78] years) underwent tLLVNS for a duration of 56 [43–73] minutes. During acute and chronic tLLVNS, a shift of the sino-atrial node exit site towards a more cranial direction was observed in 5 (50%) patients. Unipolar potential voltage increased significantly during acute and chronic tLLVNS (3.9 [3.1–4.8] mV vs. 4.7 [4.0–5.3] mV vs. 5.2 [4.8–7.0] mV; p=0.027, p=0.02, respectively). Total activation time, potential slopes, amount of fractionation, low-voltage areas and conduction velocity did not differ significantly between baseline measurements and tLLVNS. Two patients showed consistent "improvement" of all electrophysiological properties during tLLVNS, while one patient appeared to have no beneficial effect.

Conclusion: We demonstrated that tLLVNS resulted in a significant increase in potential voltage. In addition, we observed in selective patients 1) a reduction in total activation time, 2) steeper slopes of potentials, 3) decrease in the amount of fractionation and 4) change in sino-atrial node exit sites.

Journal site &
supplementary material

Introduction

The cardiac autonomic nervous system (CANS) plays a prominent role in initiation and perpetuation of atrial fibrillation (AF).[1] Experimental studies on modulation of the CANS and its effect on cardiac conduction are now increasingly followed by (randomized) clinical trials showing beneficial outcomes in prevention and treatment of (post-operative) AF.[2-4] With respect to treatment of AF, different techniques to stimulate the vagus nerve have yielded promising outcomes.[2-5]

As recently discussed in detail, vagus nerve stimulation exhibits both pro- and antiarrhythmic properties.[1] The anatomical site of stimulation and stimulation settings during VNS determine its effect on cardiac tissue.[6] There is accumulating evidence showing that low-level vagus nerve stimulation through the tragus (tLLVNS), below the cardiac bradycardia threshold, has antiarrhythmic properties and is a safe and effective treatment for AF.

Recent data predominantly focused on clinical outcomes such as incidence and burden of AF.[2,3,5] As a consequence, fundamental studies on the antiarrhythmic mechanism of tLLVNS and optimal patient selection are scarce. This gap in knowledge on the exact antiarrhythmic properties of tLLVNS and the inability to select patients responsive to this therapy, have both hampered implementation of this technique in clinical practice.[1]

In this study, we aim to study the effects of tLLVNS on atrial electrophysiology by performing intra-operative epicardial mapping during acute and chronic tLLVNS.

Methods

Study population

Written informed consent for participation in the present study (Nervus X-Atrial Fibrillation trial, approved by the medical ethical committee of the Erasmus MC, MEC-2020-0124) was obtained prior to surgery. Only patients undergoing coronary artery bypass grafting (with or without concomitant aortic valve surgery) were included. Patients with an implanted pacemaker, ejection fraction <30% or a history of AF were excluded.

Mapping procedure

An overview of our combined tLLVNS and epicardial mapping approach is provided in *Figure 1*. Transcutaneous electrical stimulation of the auricular branch of the vagus nerve was

1 **Baseline mapping** *(T=0 minute)*
2 **Acute tLLVNS mapping** *(T=1 minute)*
3 **Chronic tLLVNS mapping** *(T>20 minutes)*
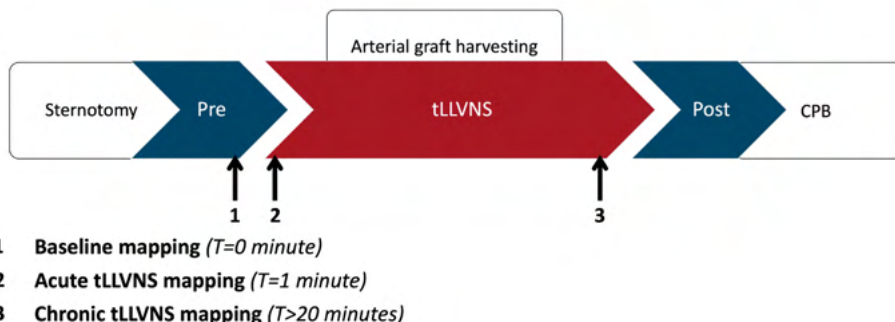
Figure 1 – Timeline of mapping approach and tLLVNS. CPB = cardiopulmonary bypass.

36

performed via the tragus of the right ear (Parasym device, Parasym Health, London, United Kingdom). Settings for tLLVNS were selected according to previously published randomized clinical trials showing antiarrhythmic effects (frequency 20 Hz, pulse width 200 µs). The stimulation intensity (36 mA) was below the bradycardia threshold.[2,4,7] Prior to harvesting of the arterial graft, sinus rhythm mapping was performed before (baseline measurements) and directly after acute tLLVNS (1-minute tLLVNS). The time needed for arterial graft harvesting was used to perform chronic tLLVNS followed by sinus rhythm mapping at the end of graft harvesting (chronic ≥20 minutes stimulation). Cardiopulmonary bypass was initiated after epicardial mapping during chronic tLLVNS.

To minimize the effect of electrode shifting between the different mapping time points, solely the superior right atrium (RA) was mapped. Mapping of the superior RA was performed at the junction of the superior caval vein and RA. This atrial region is easily accessible for the surgeon, and the mapping data are reproducible as the surgeon uses anatomical landmarks to demarcate the area mapped. In addition, the superior RA contains the sino-atrial node area and is densely innervated by the CANS and is therefore of special interest during tLLVNS.[8]

A custom-made electrode array (192 unipolar electrodes, electrode diameter 0.6 mm, interelectrode distance 2 mm) was used to record unipolar electrograms. Mapping at the RA was performed for 5 seconds and included a calibration signal of 2 mV and 1000 ms and epicardial unipolar electrograms. Recordings were analogue-to-digital converted (16 bits), sampled with a rate of 1 kHz, amplified (gain 1000) and filtered (bandwidth 0.5–400 Hz).

Data analysis

Mapping data were analyzed using custom-made software.[9] Local activation maps were constructed by annotating the steepest negative slope of unipolar potentials. Electrophysiological parameters were compared prior and during acute and chronic tLLVNS and include total activation time (TAT) of the mapping area, potential slope, peak-to-peak potential amplitudes, amount of fractionation and local conduction velocity.

TAT was calculated by the differences in local activation time between the first and latest activated electrode within the mapping area. As described previously in detail, conduction

Table 1 – Patient characteristics.

	Patients (N=10)
Age (y)	74 [69–78]
Male	8 (80%)
Ischemic heart disease	10 (100%)
+ aortic valve disease	1 (10%)
Cardiovascular risk factors	
• BMI (kg/m^2)	26.8 [25.4–30.2]
• Hypertension	9 (90%)
• Dyslipidemia	7 (70%)
• Diabetes mellitus	2 (20%)
Left ventricular function	
• Good (>50%)	10 (100%)
Antiarrhythmic drugs	
• Class I	0 (0%)
• Class II	8 (80%)
• Class III	0 (0%)
• Class IV	5 (50%)

Values are presented as N (%) or median [interquartile ranges]. **BMI** = body mass index.

velocity was computed using discrete velocity vectors.[10] Unipolar potential voltage was defined as the peak-to-peak amplitude of the steepest negative deflection and low-voltage areas as the proportion of unipolar potentials with an amplitude ≤1.0 mV. Fractionated potentials were defined as potentials with ≥2 deflections and the amount of fractionation was calculated as a percentage of the total number of atrial potentials. Improvement in electrophysiological parameters during tLLVNS was defined as either a decrease in TAT, low-voltage areas or amount of fractionation, or an increase in unipolar potential voltage, slope or conduction velocity compared to baseline measurement.

Statistical analysis

Normally distributed continuous variables were expressed as mean ± standard deviation and skewed variables as median [25th–75th percentile]. Categorical data are presented as counts and percentages. To analyze the difference between baseline measurements and tLLVNS, a Wilcoxon signed-rank test was used. A *p*-value <0.05 was considered statistically significant. Statistical testing was performed using SPSS Inc., Chicago, IL.

Results

Study population

Ten patients (80% male, median age 74 years [69–78]) scheduled for coronary artery bypass grafting underwent simultaneous tLLVNS and epicardial mapping. Clinical characteristics
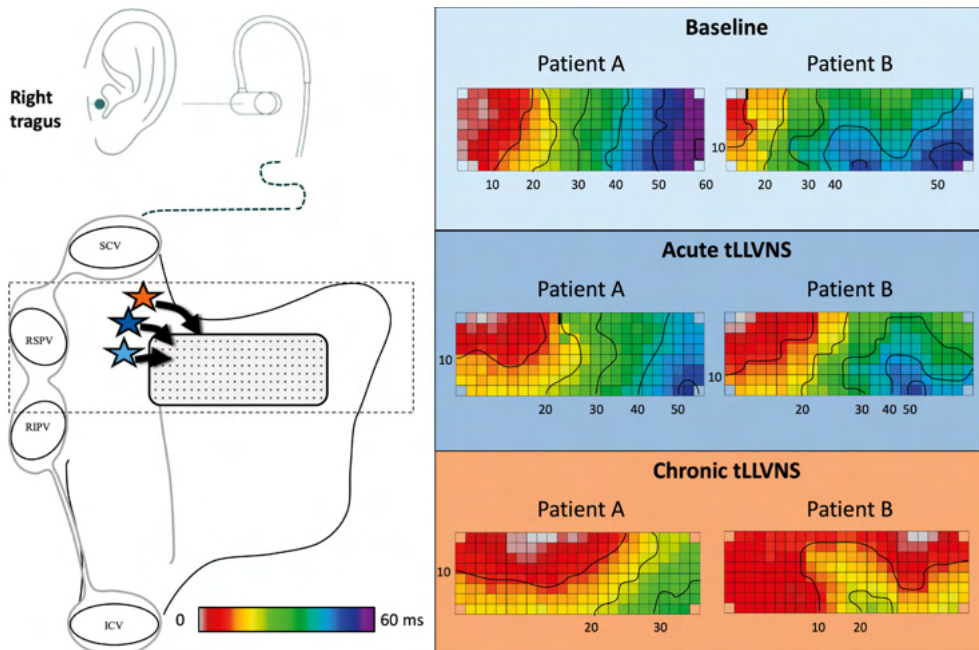
Figure 2 – Effect of tLLVNS on activation patterns. *Left panel*: schematic representation of cranial shifting of sino-atrial node exit sites in 2 patients during tLLVNS relative to the electrode position at the superior right atrium. Stars represent exit sites during baseline measurement (light blue), acute tLLVNS (dark blue) and chronic tLLVNS (orange). *Right panel*: examples of color-coded activation maps during baseline measurement (light blue), acute tLLVNS (dark blue) and chronic tLLVNS (orange), demonstrating a change in activation patterns at the superior right atrium in two different patients. Thick black lines represent conduction block; isochronal lines are drawn every 10 ms. **CV** = inferior caval vein; **RSPV** = right superior pulmonary vein; **RIPV** = right inferior pulmonary vein; **SCV** = superior caval vein.
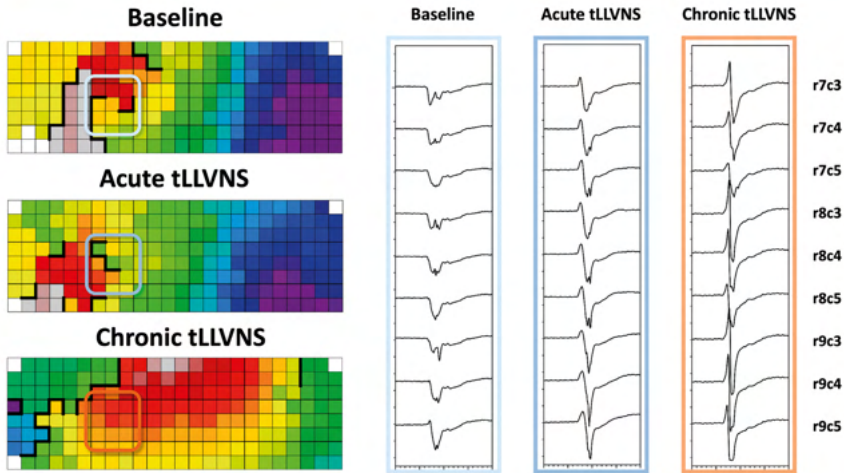
Figure 3 – Unipolar electrograms during tLLVNS. Examples of unipolar potentials during baseline measurements, acute tLLVNS and chronic tLLVNS in the same patient.

of the study population are summarized in *Table 1*. Epicardial mapping was performed after one minute of acute tLLVNS and during chronic tLLVNS in all patients. Chronic tLLVNS was performed for a duration of 56 [43–73] minutes. Each patient remained in stable sinus rhythm during tLLVNS, without episodes of bradycardia. Median cycle length was 1,079 [928–1,248] ms during baseline measurements, 1,090 [891–1,219] ms during acute tLLVNS and 1,119 [1,009–1,237] ms during chronic tLLVNS (p=0.77, p=0.56, respectively).

Effect of tLLVNS on right atrial patterns of activation

During chronic tLLVNS, patterns of activation at the RA changed in 5 (50%) patients compared to baseline. Color-coded activation maps in *Figure 2* show typical examples of the effect of tLLVNS on patterns of activation. In these patients, the entry of the wavefront in the mapping area shifted from the lateral side towards the superior side of the mapping array. This shift towards a more superior entry is likely the result of a wavefront originating from a more cranial sino-atrial node exit site. In these 5 patients, this change in atrial patterns of activation was already observed during acute tLLVNS.
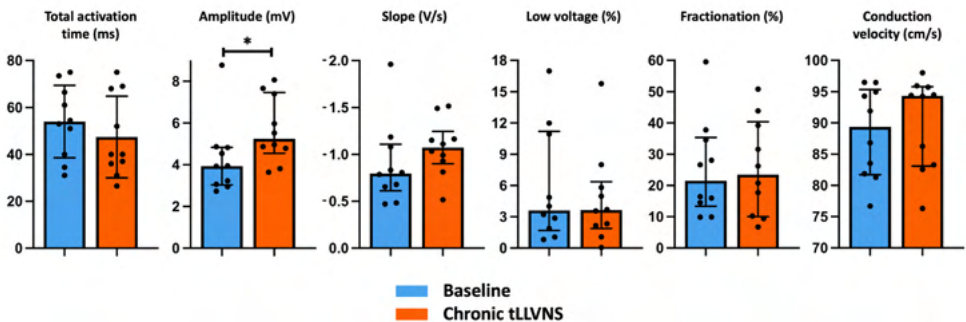
Figure 4 – Impact of chronic tLLVNS. Atrial conduction and electrogram morphology parameters during baseline measurements (light blue) and chronic tLLVNS (orange). * = p<0.05.

Table 2 – Effect of chronic tLLVNS on atrial conduction and electrogram morphology.

	Baseline	Chronic tLLVNS	*p*-value
Total activation time (ms)	54 [43–65]	40 [36–64]	0.075
Voltage (mV)	3.9 [3.1–4.8]	5.2 [4.8–7.0]	0.020
Slope (V/s)	-0.79 [-1.01– -0.66]	-1.07 [-1.16– -0.94]	0.131
Low-voltage (%)	3.6 [2.1–9.4]	3.6 [2.2–5.6]	0.492
Fractionation (%)	21.5 [14.9–33.0]	23.5 [12.1–37.3]	1.0
Conduction velocity (cm/s)	89.3 [82.2–94.8]	64.3 [84.0–95.4]	0.375

Values are presented as median [interquartile ranges].

Effect of tLLVNS on atrial electrophysiology

Figure 3 illustrates the local effect of tLLVNS on activation patterns and unipolar potentials in one patient. The circumscribed area mostly contained low amplitude fractionated potentials during baseline measurements. In contrast, during acute and chronic tLLVNS unipolar potentials consisted mostly of high amplitude non-fractionated potentials.

Boxplots depicted in *Figure 4* demonstrate the effect of chronic tLLVNS on atrial conduction and electrogram morphology. During baseline measurements the TAT of the mapping area was 54 [43–65] ms, while only 40 [36–64] ms during chronic tLLVNS (p=0.075). Compared to baseline measurements, unipolar potential voltage significantly increased from 3.9 [3.1–4.8] mV to 5.2 [4.8–7.0] mV during chronic tLLVNS (p=0.020, *Table 2*). This increase in unipolar potential voltage is also demonstrated in *Figure 5*, which depicts the relative frequency distribution of all unipolar potential voltages during baseline measurement and both acute and chronic tLLVNS. As demonstrated in *Figure 4*, the slope of unipolar potentials, amount of low-voltage areas, amount of fractionated potentials and conduction velocity did not differ significantly between baseline and chronic tLLVNS.

Supplementary Figure 1 summarizes the effect of acute tLLVNS on electrophysiological properties. Similar to chronic tLLVNS, unipolar potential voltages also increased during acute tLLVNS compared to baseline measurements (4.7 [4.0–5.3] mV vs. 3.9 [3.1–4.8] mV, p=0.027, respectively) whereas the other parameters did not differ (*Supplementary Table 1*).
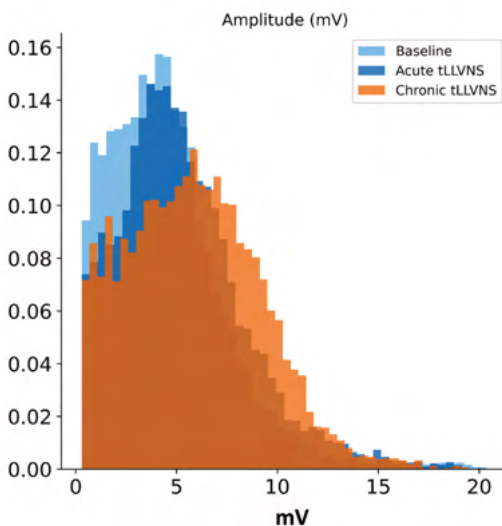
Figure 5 – Histogram of unipolar potential voltage. Histograms demonstrate the relative frequency distribution of all unipolar potential voltages during baseline measurements (light blue), acute tLLVNS (dark blue) and chronic tLLVNS (orange).

36
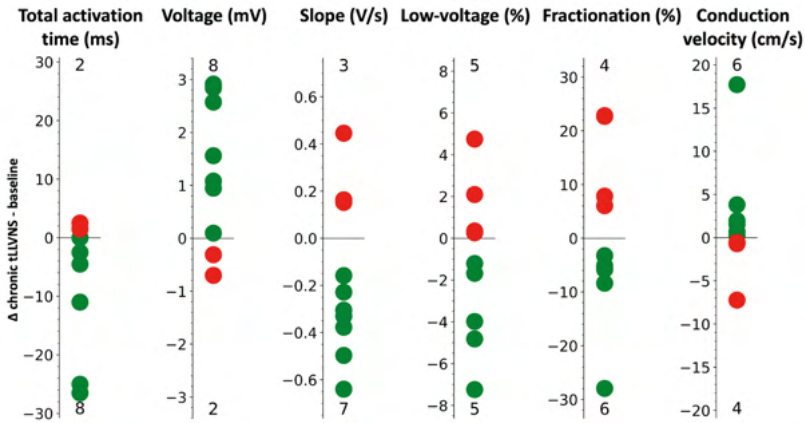
Figure 6 – Individual impact of chronic tLLVNS compared to baseline. Absolute differences (Δ) between baseline and chronic tLLVNS for each individual patient. Green and red dots represent patients in whom relative improvement or decline was observed during tLLVNS compared to baseline. The numbers at the top and bottom indicate the total amount of patients with either an improvement or declinement, respectively.

Inter-individual variation in tLLVNS response

Figure 6 depicts for each individual patient the absolute differences (Δ) of every quantified electrophysiological parameter between baseline measurements and chronic tLLVNS. Low-voltage areas, amount of fractionation and conduction velocity were either increased or decreased in (almost) an equal number of patients. For example, in 5 (50%) patients low-voltage areas decreased (range: -1.2 to -7.2%), while in the other 5 patients low-voltage areas increased (range: 0.3 to 4.8%). In 6 (60%) patients the number of fractionated potentials decreased (range: -3.2 to -27.9%), while in the other 4 patients the proportion of fractionated potentials increased (range: 6.1 to 22.8%).

For TAT, unipolar potential voltage and slope of unipolar potentials, we observed in most patients changes suggestive of improvement in atrial conduction. For example, TAT shortened with a range between -5 and -27 ms in 5 (50%) patients, and remained stable in 3 (30%) patients. When TAT lengthened, which was observed in only 2 patients, it was merely by 2 and 3 ms. Peak-to-peak amplitudes of unipolar potentials increased in 8 (80%) patients (range: 0.1 to 2.9mV). When it decreased (2 patients), it was only by -0.3 and -0.7 mV. The slope of unipolar potentials increased in 7 patients (70%) (range: -0.31 to -0.64 V/s), whereas it decreased by 0.15 to 0.42 V/s in the other 3 patients.

Table 3 – Differences between baseline and chronic tLLVNS for each patient individually.

	Δ TAT (ms)	Δ Voltage (mv)	Δ Slope (V/s)	Δ LVA (%)	Δ Fractionation (%)	Δ CV (cm/s)	Positive effect score
Patient 1	0	2.8	-0.38	-1.7	-5.8	1.6	6
Patient 2	-25	2.9	-0.31	-4.8	-5.1	0.2	6
Patient 3	2	2.9	-0.50	-4.0	-27.9	17.7	5
Patient 4	-3	2.6	-0.64	-7.2	22.8	0.7	5
Patient 5	-11	0.9	-0.16	0.3	-3.2	-0.7	4
Patient 6	0	1.6	-0.23	0.4	22.7	3.8	4
Patient 7	0	1.1	-0.33	-1.2	6.1	-7.2	4
Patient 8	-27	0.1	0.15	4.8	-5.7	-0.5	3
Patient 9	-5	-0.3	0.16	2.1	-8.4	2.0	3
Patient 10	3	-0.7	0.42	0.3	7.9	-0.7	0

Absolute increase or decrease per electrophysiological parameter for each patient separately. Effect score represent the total number of parameters (out of 6) which showed a relative improvement for every individual patient. **CV** = conduction velocity; **LVA** = low-voltage area; **TAT** = total activation time.

A comparable inter-individual variation in electrophysiological parameters was observed during acute tLLVNS, which is summarized in *Supplementary Figure 2.*

Patient selection

Table 3 depicts the response to chronic tLLVNS for each individual patient. Remarkably, only 2 patients showed consistent improvement across all electrophysiological properties during chronic tLLVNS. Although less consistent, improvement in four or more electrophysiological parameters was observed in the majority (70%) of the patients. In 2 patients, chronic tLLVNS did not result in improvement of three electrophysiological parameters. Only in one patient, chronic tLLVNS appeared to have no beneficial effect at all. However, in this patient the differences between baseline and chronic tLLVNS were minimal for all parameters and no change in activation pattern occurred. This patient (age: 69 years, 44 minutes of tLLVNS) presumably may not profit from tLLVNS (or current settings), thereby highlighting the capabilities of epicardial mapping during tLLVNS to serve as a tool to select patients for this therapy.

Discussion

We provide for the first-time insights in the effects of tLLVNS on atrial electrophysiology during sinus rhythm. Acute and chronic tLLVNS resulted in a significant increase in unipolar potential voltage. Importantly, consistent improvement across all electrophysiological properties during tLLVNS was uncommon. In selective patients, tLLVNS resulted in 1) reduction in TAT, 2) steeper slopes of unipolar potentials, 3) decrease in the amount of fractionation and 4) changes in activation patterns, indicative of a more cranial sino-atrial node exit site.

Changes in sino-atrial node exit sites

The CANS is involved in almost every aspect of cardiac (patho)physiology, including the sino-atrial node.[11,12] Comprehensive multimodality and multiscale assessments have studied the complex interplay between the CANS and sino-atrial node.[8] Characterization of peripheral neural circuits has shown that the sino-atrial node is densely innervated by parasympathic fibers originating from the right atrial ganglionated plexi (GP).[8] The RA-GP exert influence over the impulse generation and exit sites of the sino-atrial node, thereby directly controlling sino-atrial node function.[8] Preclinical and clinical (high density) electrophysiological studies have shown that both parasympathic and sympathic activation results in shifting of the sino-atrial node exit sites along the terminal crest of the RA, accompanied by changes in the heart rate.[13-16] Parasympathic (or high-level vagus nerve) stimulation results in caudal shifting of the sino-atrial node exit sites from the superior caval vein towards a more inferior exit site near the inferior caval vein, whereas sympathic stimulation results in cranial shifting of the sino-atrial node exit sites.[13-16] Clinical electrophysiological studies demonstrated a similar caudal shifting of sino-atrial node exit sites in patients with sinus node dysfunction, AF and congestive heart failure.[17-19]

As tLLVNS did not significantly change the heart rate in previous studies, nor in the current study, no major effects of tLLVNS on sino-atrial node function were expected. However, we hypothesized that more subtle changes in sino-atrial node function may be apparent during tLLVNS. Kulkarni et al.[20] demonstrated that acute (<5 min) tLLVNS already attenuates P-wave alternans, a subtle beat-to-beat variation in the morphology (amplitude, duration and direction) of the atrial electrocardiographic waveform caused by fine changes in atrial conduction. Our findings provide further insights in the meticulous functional innervation

36

of the sino-atrial node. During tLLVNS, the RA was activated by a wavefront from a more superior sino-atrial node exit site in half of the patients. We hypothesize that changes in source-sink balance in the sino-atrial node (and surrounding myocardium) could drive this subtle rate-independent shift in conduction through sino-atrial exit sites. At this level, impulse propagation through more superior exit sites could be functionally blocked due to a source-sink mismatch, which results in the more inferior sino-atrial node exit observed during baseline measurements.[21] Another explanation could be indirect sympathic involvement during tLLVNS. Although sympathic stimulation is known to result in more cranial exit sites and faster heart rates, indirect sympathic effects during tLLVNS are less well described.[1] These subtle changes in sino-atrial node activation may be an important antiarrhythmic property of tLLVNS, as sinus node dysfunction – associated with more caudal exit sites – has a strong clinical association with the development of AF.[22]

Relation between Fractionation and CANS

A significant hallmark of AF is the presence of fractionated atrial potentials, which may represent critical sites for AF initiation and perpetuation.[23,24] Several studies provided evidence that these potentials may be functionally and anatomically related to the intrinsic cardiac autonomic nervous system.[25,26] Experimental and clinical studies showed that the distribution of fractionated atrial potentials correlated with the anatomical locations of the GP.[23,25,27,28] Although GPs (identified by high frequency stimulation) are always located within areas of fractionated atrial potentials, the areas of fractionated atrial potentials are much larger than areas covered by GPs.[29] Lellouche et al.[30] characterized the morphology of SR-potentials, which were associated with parasympathetic response during radiofrequency applications. They showed that SR-potentials consisting of deflections ≥4, amplitude ≥0.7 mV and duration ≥40 ms were good predictors of parasympathic response (sensitivity 72%, specificity 91%). Mathematical simulation of the effect of acetylcholine (parasympathic stimulation) reproduced a similar potential morphology. In addition, they showed that the number of deflections increases significantly after adenosine infusion (parasympathic stimulation) during SR. In contrast, pharmacological parasympathic blockade decreases the amount of fractionated atrial potentials.[28,31,32]

We now demonstrate that even during sinus rhythm tLLVNS can already reduce the amount of fractionated atrial potentials in selected patients. The exact mechanism underlying the formation of fractionated atrial potentials is multifactorial, and includes for example functional conduction block due to tissue anisotropy, structural conduction slowing/block but also colliding wavefronts and diffuse fiber orientation.[33] The CANS may also modulate fractionation during sinus rhythm – if caused by non-uniform anisotropic conduction and/or source-sink mismatch – due to its effects on both wavefront direction (by altering sino-atrial node exit sites) and action potential morphology (see below). A part of the fractionated atrial potentials may thus reflect a hyperactive state of the autonomic nervous system, which can be attenuated by tLLVNS during sinus rhythm.

Impact on unipolar potential voltage

During both acute and chronic tLLVNS, unipolar potential voltage significantly increased compared to baseline measurements. Unipolar potential voltage reflects the summation of action potentials within the recording area of one electrode, and its shape and amplitude are influenced by electrophysiological and structural characteristics of the myocardial tissue. More homogeneous activation – resulting in larger wavefronts – could result in an increase in unipolar potential voltage, as the amplitude is also determined by the volume of simultaneously activated cardiac tissue surrounding the recording electrode. In other words,

an increase in potential voltage could be secondary to a decrease in local asynchronous activation. This hypothesis is in line with the observed decrease in TAT during chronic tLLVNS (54 [43–65] ms vs. 40 [36–64] ms, p=0.075). tLLVNS may also directly attenuate unipolar potential voltage by affecting local depolarization. In canine atria it was demonstrated that high-dose acetylcholine administration depresses the rate of rise of phase 0, peak amplitude and plateau phase of action potentials.[34,35] In turn, opposite effects on depolarization could therefore be expected with tLLVNS, resulting in increased rate of rise of phase 0, peak amplitude and phase 0 of action potentials.

Variability in response

We observed a considerable inter-individual variability in response to chronic tLLVNS. For instance, while some patients showed an increase of more than 2.5 mV in unipolar potential voltage, others showed a negligible increase (0.1 mV) or even a decrease. Moreover, consistent improvement across all electrophysiological properties during tLLVNS was only seen in 20% of the patients. This individual response to tLLVNS is also acknowledged in various clinical studies.[4,20] The effect of tLLVNS is highly dependent on stimulation parameters. Since autonomic tone and vagus nerve stimulation threshold differs among individual patients, standardized settings are likely not optimal for all patients. This could explain why the majority of the patients had inconsistent response in various electrophysiological parameters, as the stimulation settings were not patient tailored.

Currently, the greatest limitation for tLLVNS is the inability to appropriately select patients.[1] In vain, various biomarkers have been proposed whose acute response should predict successful chronic response to tLLVNS.[36] Ideally, we should have real-time parameters that reflect optimal tLLVNS which modifies the atrial substrate sufficiently. The present study is a first-step towards selecting potential tLLVNS responders and to determine the ideal tLLVNS settings for each individual patient, based on local changes in atrial conduction and providing insights into the antiarrhythmic effects. Due to its invasiveness, the presented mapping technique will most probably serve as a tool to prevent or treat AF after cardiac surgery. In addition, it enables further research into optimal tLLVNS stimulation settings (frequency, pulse width, duration, etc.), which is essential to achieve its most favorable effect. The effect of intermittent vs. continuous tLLVNS may differ and therefore requires further investigation.[37] These insights can be used to treat patients with AF at the outpatient clinic.

Limitations

The interaction between general anesthesia and tLLVNS is unknown. However, a standard protocol was used for all patients; possible effects will therefore be equally dispersed among patients. The most optimal settings and duration of tLLVNS are not determined and still under research. In addition, site and effect of electrical stimulation may differ between patients due to variations in anatomy and presence of cardiovascular risk factors. Another limitation of in-vivo mapping in humans is lack of histological examination (e.g., atrial wall thickness and degree of trabeculation). In line with recent randomized trials, an average time of one hour of tLLVNS was used in the current study. To minimize the effect of electrode shifting we solely mapped the superior RA which is highly innervated by the CANS. As a result, the effect of tLLVNS on the rest of the atria is not examined in the current study.

36

Conclusion

In this mapping study, we demonstrated that acute and chronic tLLVNS resulted in a significant increase in unipolar potential voltage. In addition, we observed in selective

patients 1) reduction in TAT, 2) steeper slopes of unipolar potentials, 3) decrease in the amount of fractionation and 4) change in sino-atrial node exit sites. Future studies need to confirm whether high-density epicardial mapping can be used in clinical practice as a possible tool to select patients and optimize stimulation settings for cardiac neuromodulation.

References

1. Kharbanda RK, van der Does WFB, van Staveren LN, Taverne Y, Bogers A, de Groot NMS. Vagus Nerve Stimulation and Atrial Fibrillation: Revealing the Paradox. Neuromodulation. 2022;25:356-365.
2. Stavrakis S, Humphrey MB, Scherlag BJ, Hu Y, Jackman WM, Nakagawa H, Lockwood D, Lazzara R, Po SS. Low-level transcutaneous electrical vagus nerve stimulation suppresses atrial fibrillation. J Am Coll Cardiol. 2015;65:867-875.
3. Stavrakis S, Humphrey MB, Scherlag B, Iftikhar O, Parwani P, Abbas M, Filiberti A, Fleming C, Hu Y, Garabelli P, et al. Low-Level Vagus Nerve Stimulation Suppresses Post-Operative Atrial Fibrillation and Inflammation: A Randomized Study. JACC Clin Electrophysiol. 2017;3:929-938.
4. Stavrakis S, Stoner JA, Humphrey MB, Morris L, Filiberti A, Reynolds JC, Elkholey K, Javed I, Twidale N, Riha P, et al. TREAT AF (Transcutaneous Electrical Vagus Nerve Stimulation to Suppress Atrial Fibrillation): A Randomized Clinical Trial. JACC Clin Electrophysiol. 2020;6:282-291.
5. Andreas M, Arzl P, Mitterbauer A, Ballarini NM, Kainz FM, Kocher A, Laufer G, Wolzt M. Electrical Stimulation of the Greater Auricular Nerve to Reduce Postoperative Atrial Fibrillation. Circ Arrhythm Electrophysiol. 2019;12:e007711.
6. Zhang Y, Ilsar I, Sabbah HN, Ben David T, Mazgalev TN. Relationship between right cervical vagus nerve stimulation and atrial fibrillation inducibility: therapeutic intensities do not increase arrhythmogenesis. Heart Rhythm. 2009;6:244-250.
7. Yu L, Huang B, Po SS, Tan T, Wang M, Zhou L, Meng G, Yuan S, Zhou X, Li X, et al. Low-Level Tragus Stimulation for the Treatment of Ischemia and Reperfusion Injury in Patients With ST-Segment Elevation Myocardial Infarction: A Proof-of-Concept Study. JACC Cardiovasc Interv. 2017;10:1511-1520.
8. Hanna P, Dacey MJ, Brennan J, Moss A, Robbins S, Achanta S, Biscola NP, Swid MA, Rajendran PS, Mori S, et al. Innervation and Neuronal Control of the Mammalian Sinoatrial Node a Comprehensive Atlas. Circ Res. 2021;128:1279-1296.
9. Yaksh A, van der Does LJ, Kik C, Knops P, Oei FB, van de Woestijne PC, Bekkers JA, Bogers AJ, Allessie MA, de Groot NM. A novel intra-operative, high-resolution atrial mapping approach. J Interv Card Electrophysiol. 2015;44:221-225.
10. van Schie MS, Heida A, Taverne Y, Bogers A, de Groot NMS. Identification of local atrial conduction heterogeneities using high-density conduction velocity estimation. Europace. 2021;23:1815-1825.
11. Mehra R, Tjurmina OA, Ajijola OA, Arora R, Bolser DC, Chapleau MW, Chen PS, Clancy CE, Delisle BP, Gold MR, et al. Research Opportunities in Autonomic Neural Mechanisms of Cardiopulmonary Regulation: A Report From the National Heart, Lung, and Blood Institute and the National Institutes of Health Office of the Director Workshop. JACC Basic Transl Sci. 2022;7:265-293.
12. Zhu C, Hanna P, Rajendran PS, Shivkumar K. Neuromodulation for Ventricular Tachycardia and Atrial Fibrillation: A Clinical Scenario-Based Review. JACC Clin Electrophysiol. 2019;5:881-896.
13. Boineau JP, Canavan TE, Schuessler RB, Cain ME, Corr PB, Cox JL. Demonstration of a widely distributed atrial pacemaker complex in the human heart. Circulation. 1988;77:1221-1237.
14. Boineau JP, Schuessler RB, Roeske WR, Autry LJ, Miller CB, Wylds AC. Quantitative relation between sites of atrial impulse origin and cycle length. Am J Physiol. 1983;245:H781-789.
15. Bollmann A, Hilbert S, John S, Kosiuk J, Hindricks G. Insights from preclinical ultra high-density electroanatomical sinus node mapping. Europace. 2015;17:489-494.
16. Eickholt C, Jungen C, Drexel T, Alken F, Kuklik P, Muehlsteff J, Makimoto H, Hoffmann B, Kelm M, Ziegler D, et al. Sympathetic and Parasympathetic Coactivation Induces Perturbed Heart Rate Dynamics in Patients with Paroxysmal Atrial Fibrillation. Med Sci Monit. 2018;24:2164-2172.
17. Sanders P, Morton JB, Kistler PM, Spence SJ, Davidson NC, Hussin A, Vohra JK, Sparks PB, Kalman JM. Electrophysiological and electroanatomic characterization of the atria in sinus node disease: evidence of diffuse atrial remodeling. Circulation. 2004;109:1514-1522.
18. Kharbanda RK, Wesselius FJ, van Schie MS, Taverne Y, Bogers A, de Groot NMS. Endo-Epicardial Mapping of In Vivo Human Sinoatrial Node Activity. JACC Clin Electrophysiol. 2021;7:693-702.
19. Sanders P, Kistler PM, Morton JB, Spence SJ, Kalman JM. Remodeling of sinus node function in patients with congestive heart failure: reduction in sinus node reserve. Circulation. 2004;110:897-903.
20. Kulkarni K, Singh JP, Parks KA, Katritsis DG, Stavrakis S, Armoundas AA. Low-Level Tragus Stimulation Modulates Atrial Alternans and Fibrillation Burden in Patients With Paroxysmal Atrial Fibrillation. J Am Heart Assoc. 2021;10:e020865.
21. Ashton JL, Trew ML, LeGrice IJ, Paterson DJ, Paton JF, Gillis AM, Smaill BH. Shift of leading pacemaker site during reflex vagal stimulation and altered electrical source-to-sink balance. J Physiol. 2019;597:3297-3313.
22. Lamas GA, Lee KL, Sweeney MO, Silverman R, Leon A, Yee R, Marinchak RA, Flaker G, Schron E, Orav EJ, et al. Ventricular pacing or dual-chamber pacing for sinus-node dysfunction. N Engl J Med. 2002;346:1854-1862.
23. Nademanee K, McKenzie J, Kosar E, Schwab M, Sunsaneewitayakul B, Vasavakul T, Khunnawat C, Ngarmukos T. A new approach for catheter ablation of atrial fibrillation: mapping of the electrophysiologic substrate. J Am Coll Cardiol. 2004;43:2044-2053.
24. Konings KT, Smeets JL, Penn OC, Wellens HJ, Allessie MA. Configuration of unipolar atrial electrograms during electrically induced atrial fibrillation in humans. Circulation. 1997;95:1231-1241.
25. Lin J, Scherlag BJ, Zhou J, Lu Z, Patterson E, Jackman WM, Lazzara R, Po SS. Autonomic mechanism to explain complex fractionated atrial electrograms (CFAE). J Cardiovasc Electrophysiol. 2007;18:1197-1205.
26. Takahashi Y, Jais P, Hocini M, Sanders P, Rotter M, Rostock T, Hsu LF, Sacher F, Clementy J, Haissaguerre M. Shortening of fibrillatory cycle length in the pulmonary vein during vagal excitation. J Am Coll Cardiol.

36

2006;47:774-780.

27. Katritsis D, Giazitzoglou E, Sougiannis D, Voridis E, Po SS. Complex fractionated atrial electrograms at anatomic sites of ganglionated plexi in atrial fibrillation. Europace. 2009;11:308-315.

28. Katritsis D, Sougiannis D, Batsikas K, Giazitzoglou E, Mersinias J, Katritsis G, Po SS. Autonomic modulation of complex fractionated atrial electrograms in patients with paroxysmal atrial fibrillation. J Interv Card Electrophysiol. 2011;31:217-223.

29. Nakagawa H, Scherlag BJ, Patterson E, Ikeda A, Lockwood D, Jackman WM. Pathophysiologic basis of autonomic ganglionated plexus ablation in patients with atrial fibrillation. Heart Rhythm. 2009;6:S26-34.

30. Lellouche N, Buch E, Celigoj A, Siegerman C, Cesario D, De Diego C, Mahajan A, Boyle NG, Wiener I, Garfinkel A, et al. Functional characterization of atrial electrograms in sinus rhythm delineates sites of parasympathetic innervation in patients with paroxysmal atrial fibrillation. J Am Coll Cardiol. 2007;50:1324-1331.

31. Chaldoupi SM, Linnenbank AC, Wittkampf FH, Boldt LH, H VANW, VJ VAND, Doevendans PA, Hauer RN, JM DEB, Loh P. Complex fractionated electrograms in the right atrial free wall and the superior/posterior wall of the left atrium are affected by activity of the autonomic nervous system. J Cardiovasc Electrophysiol. 2012;23:26-33.

32. Knecht S, Wright M, Matsuo S, Nault I, Lellouche N, Sacher F, Kim SJ, Morgan D, Afonso V, Shinzuke M, et al. Impact of pharmacological autonomic blockade on complex fractionated atrial electrograms. J Cardiovasc Electrophysiol. 2010;21:766-772.

33. Kleber AG, Rudy Y. Basic mechanisms of cardiac impulse propagation and associated arrhythmias. Physiol Rev. 2004;84:431-488.

34. de Carvalho AP, Hoffman BF, de Carvalho MP. Two components of the cardiac action potential. I. Voltage-time course and the effect of acetylcholine on atrial and nodal cells of the rabbit heart. J Gen Physiol. 1969;54:607-635.

35. Tse WW. Suppressive effect of acetylcholine on action potentials of canine paranodal fibers. Am J Physiol. 1986;251:H710-715.

36. Stavrakis S, Kulkarni K, Singh JP, Katritsis DG, Armoundas AA. Autonomic Modulation of Cardiac Arrhythmias: Methods to Assess Treatment and Outcomes. JACC Clin Electrophysiol. 2020;6:467-483.

37. Rossi P, Ricci A, De Paulis R, Papi E, Pavaci H, Porcelli D, Monari G, Maselli D, Bellisario A, Turani F, et al. Epicardial ganglionated plexus stimulation decreases postoperative inflammatory response in humans. Heart Rhythm. 2012;9:943-950.

36
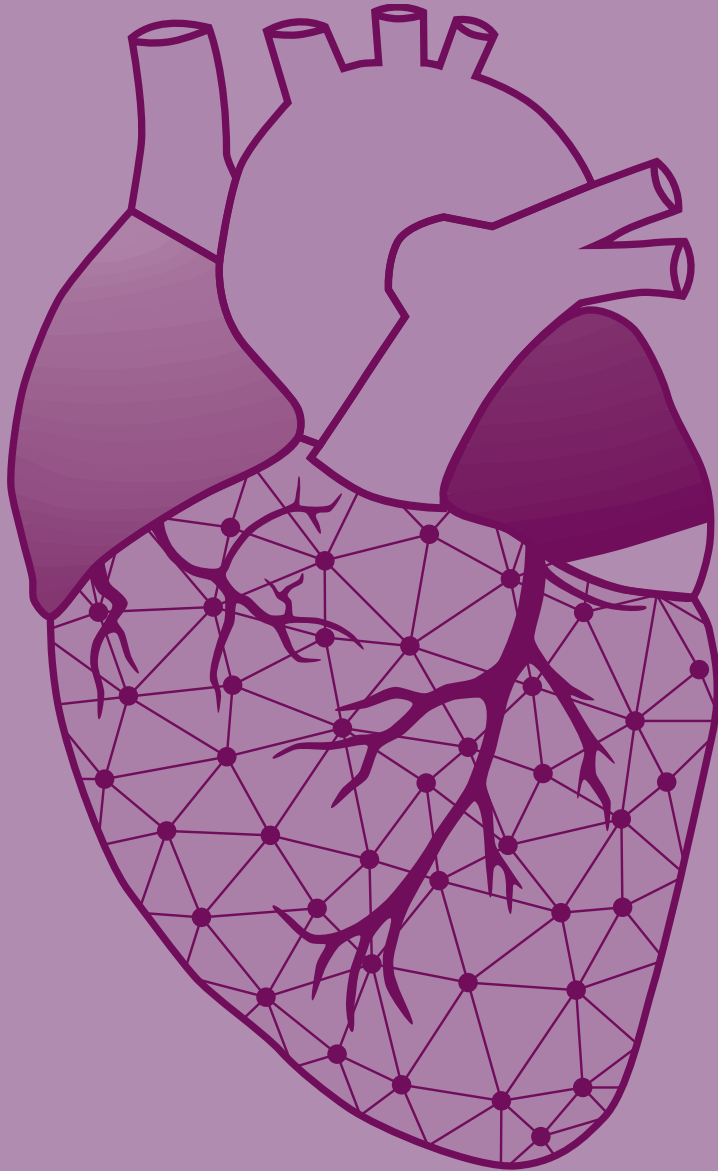
Chapter **37**

General discussion

Mathijs S. van Schie

Electrophysiological mapping-guided ablation strategies targeting AF have improved considerably over the past few years. However, it remains a major challenge to design effective strategies for particularly persistent AF. While various ablation strategies have demonstrated promising results in single-center studies, multicenter studies failed to show widespread improvement in procedural outcome.[1] This can be partially explained by the inadequate understanding of the mechanisms and electropathological substrate underlying AF. Progression of AF is accompanied by structural and electrical remodeling, resulting in complex electrical conduction disorders, which is defined as electropathology.[2] The severity of electropathology thus defines the stage of AF and is a major determinant of the effectiveness of AF therapy. However, the specific features of AF-related electropathology remain unknown. As elucidated in **chapters 2 and 3**, these features may include unipolar potential morphology, such as voltage and fractionation, conduction inhomogeneity and electrical asynchrony between the endo- and epicardium.

In this thesis, features of electrophysiological properties of atrial tissue have been explored, developed and quantified during normal sinus rhythm, programmed electrical stimulation and AF. In addition, inter- and intra-individual variation in these quantified parameters has been examined in patients with and without prior episodes of AF. The most suitable objective parameters will aid in the identification of patients at risk for early onset or progression of AF.

Quest to the most optimal electrogram features related to electropathology

Local electrical information on the underlying myocardial tissue can be recorded by several types of electrograms. Especially unipolar potential morphology has been discussed for years as having the ability to reflect underlying conduction processes. RS-waves with high amplitude characterize areas of fast conduction with conduction along the longitudinal axis of myocardial fibers, while in slow areas, the potentials are of lower amplitude.[3] Abnormal myocardial substrate can be defined by identifying areas of low voltage, as potential voltage also depends on the volume of simultaneously activated cardiac tissue.[3,4] Additionally, the asymmetry of unipolar potentials has been proposed as a morphology parameter, which is determined by wavefront curvature, wavefront collisions, anisotropy and conduction heterogeneity.[5,6] Asynchronous activation of (groups of) cardiomyocytes gives rise to multiple positive and negative deflections, which is known as fractionation.[3,7] As delineated in **chapter 3**, interpretation of bipolar potential morphology is more challenging. Despite a widespread use of bipolar fractionated potentials in ablative therapy strategies, it did not result in beneficial long-term outcomes.[8] This could mainly be attributed to the lack of a uniform definition of bipolar fractionation.[9] On the other hand, unipolar potentials could be simply classified into four categories, i.e., single potentials, short-double potentials (two deflections, <10 ms apart), long-double potentials (two deflections, 10-50 ms apart) and fragmented (fractionated) potentials (>2 deflections within 50 ms).[10] Hence, the true potential of ablation strategies targeting complex, fractionated potentials has not yet been fully explored. Therefore, as interpretation of unipolar potential morphology is more straightforward, features of unipolar and not bipolar potentials should be examined.

37

Unipolar single potential morphology: the forgotten determinant of voltage

In patients with coronary artery disease without history of arrhythmias, the majority of unipolar potentials recorded during normal sinus rhythm consisted of one single deflection (81.4 [74.9–85.1] %, **chapter 12**). Even in patients with mitral valve disease and paroxysmal AF, the majority of recorded potentials still consisted of single potentials (81.0 [75.5–87.0] %, **chapters 4 and 5**). The morphology of single potentials is represented by

the relative positive (R-wave) and negative (S-wave) components (R/S ratio). Houben et al.[11] were the first to examine the morphology of single potentials during acutely induced AF at the right atrium. A clear predominance of S-waves was found, although with a large intra- and interindividual variation. Van der Does et al.[12] examined sinus rhythm unipolar single potential morphology during simultaneous endo-epicardial mapping of the right atrium and demonstrated that both epicardial and endocardial single potentials showed an S-predominance. In the epicardial mapping studies performed in **chapters 5 and 12**, unipolar single potential morphology was studied during sinus rhythm in the right and left atrium, including Bachmann's bundle. Several morphologies were found at specific atrial regions. At the sino-atrial node (SAN) area, monophasic S-waves were expected and were indeed mainly recorded in patients with either coronary artery disease, mitral valve disease or congenital heart disease (**chapters 5, 12, 21 and 22**). Fast propagating wavefronts were characterized by potentials with large amplitude, predominant S-waves, which evolve towards biphasic RS-waves when the wavefront propagates away from the excitation site. These types of potentials were indeed mainly found in the right atrium and Bachmann's bundle. Local wavefront termination or collision, resulting in more R-wave predominance and monophasic R-waves, were mainly found in the left atrium and pulmonary vein area. Examples of these various potential morphologies are illustrated in *Figure 1*.

While large amplitude single potentials are predominantly found in areas with fast propagating wavefronts, reduced potential voltages due to loss of S-wave amplitude could be found in areas with reduced conduction velocity (**chapter 5**). Loss of S-wave amplitude also results in more R-wave predominance, and is associated with conduction block during ablative therapy.[5,13] Symmetry or asymmetry of single potentials is therefore a major determinant of unipolar voltage; low potential voltages could easily be explained by their R- and S-wave morphologies. Patients with paroxysmal AF are characterized by lower potential voltages, more R-wave predominance and slower wavefront propagation at Bachmann's bundle compared to patients without AF (**chapters 4 and 5**). The lower amplitude was mainly determined by a decrease in S-wave amplitude. Hence, these observations indicate that the R/S ratio of unipolar single potentials could be a suitable marker of electropathology.

Targeting low-voltage areas: what do we actually mean?

In clinical practice, low-voltage areas (LVAs) are often considered to be part of the arrhythmogenic substrate underlying AF. Our data showed that potential voltages are mainly determined by the R/S ratio, which varies across different atrial regions. Low peak-to-peak voltages can therefore not always be equated with 'diseased' tissue, as this can also be explained by the potential morphology, i.e., full R- and S-waves have a smaller amplitude compared to biphasic RS-waves. Relying solely on voltage mapping to guide ablative therapy may therefore be misleading (**chapters 4 and 5**). On the other hand, while there was no direct relation between unipolar voltage and conduction velocity, smaller voltages were indeed often recorded at areas of conduction slowing or block. Additionally, potentials with a higher number of deflections were typically associated with lower unipolar potential voltages, suggesting that LVAs are just more likely to indicate areas of arrhythmogenic tissue.

The largest problem with LVAs lies in the lack of standardization and a clear voltage threshold never has been histologically validated.[14] While a threshold of 0.5 mV to identify LVAs and 0.05 mV to identify scar is commonly used for bipolar potentials during sinus rhythm, no such threshold has been clearly defined for unipolar potentials as these are less used in clinical practice.[14,15] In **chapter 4**, the 5th percentile of patients with mitral valve disease without history of AF was used to establish a threshold for identifying LVAs using unipolar electrograms, as it was expected that these patients have at least a certain degree of non-AF substrates
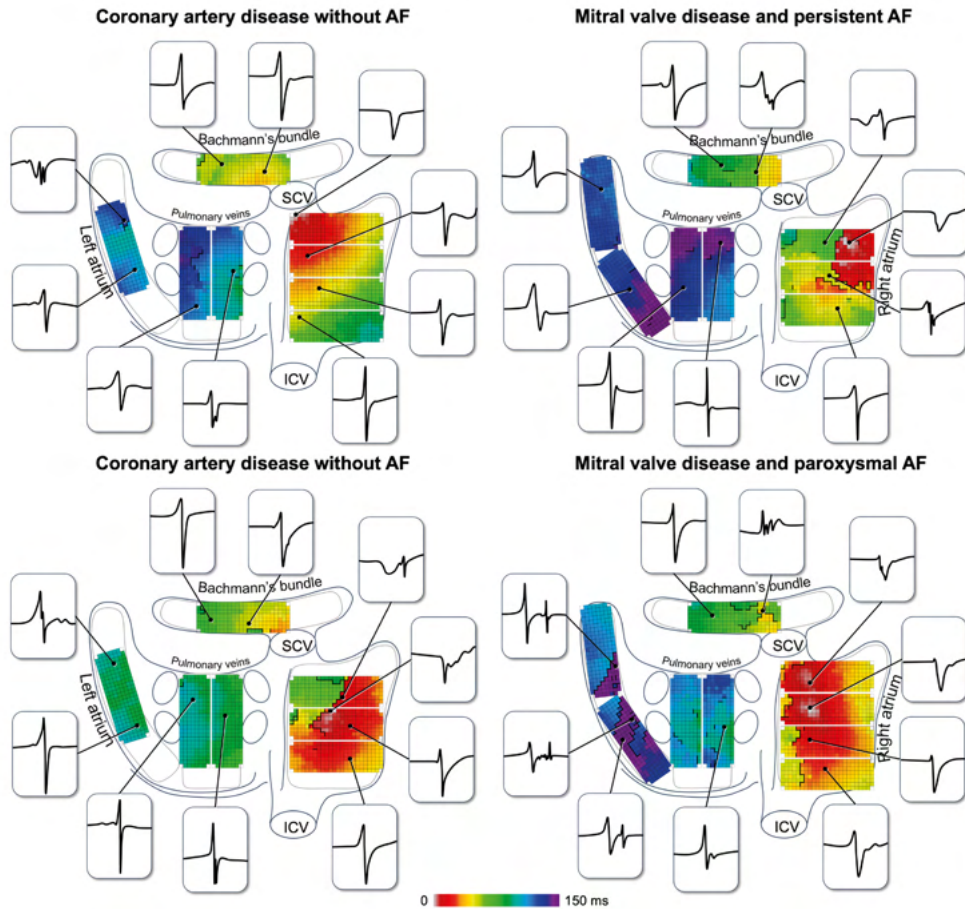
Figure 1 – Examples of various sinus rhythm total activation time maps with corresponding unipolar potentials. Typical unipolar potentials could be recorded at various atrial sites. Around the SAN area monophasic S-waves could be found, which evolve towards biphasic RS-waves in the remainder of the right atrium and at Bachmann's bundle. Around lines of conduction block, typical long-double potentials or fractionated potentials were recorded. These potentials could also be the result of structures such as the ligament of Marshall, as shown in the lower right panel. *Upper left panel*: this patient is characterized by a SAN area located in the high right atrium. Propagation of the activation wavefront is mainly smooth without areas of conduction block, except between the pulmonary veins and at the left atrium, where also fractionated potentials could be recorded. *Upper right panel*: this patient is characterized by extensive areas of conduction block across the entire atria, but particularly at the right atrium and Bachmann's bundle. These areas were characterized by the occurrence of fractionated potentials. *Lower left panel*: this patient was characterized by an inferior SAN exit site accompanied by extensive conduction disorders in the right atrium. Short-double potentials were found in the left atrium and between the pulmonary veins. *Lower right panel*: this patient is characterized by multiple SAN exit sites. Extensive areas of conduction block were present throughout the entire atria, resulting in a high degree of long-double and fractionated potentials. At the left atrium, the ligament of Marshall could be identified by the presence of Marshall potentials. **ICV** = inferior caval vein; **SCV** = superior caval vein.

within the atria. This threshold was also applied in other study populations (**chapters 8, 9, 10, 12, 13, 15, 16, 28 and 34**). In patients with congenital heart disease, the 5th percentile of all bipolar clique voltages was 0.55 mV, which was comparable to the standard bipolar cut-off of 0.5 mV (**chapter 7**). However, there is still ongoing debate on what thresholds to use and when to classify tissue as diseased, healthy, or as an intermediate zone that does not contain substantial remodeled areas but also not solely healthy tissue. It is therefore unlikely that one single straightforward method with one cut-off value exists. Nevertheless, a certain

37

threshold at least can aid in quantification of the number of low-voltages in a patient, which could then be used to study differences between study populations (**chapters 4 and 6**). It is important to note that the size of the electrode can influence the recorded voltages (**chapter 11**), and that the used mapping equipment should be taken into account when comparing various studies. Therefore, it is essential that a certain chosen threshold is clearly described.

LVAs can show considerable variation in both unipolar and bipolar voltages. Therefore, low bipolar voltages alone do not necessarily indicate the presence of an arrhythmogenic substrate. Some studies have proposed combining both unipolar and bipolar voltage mapping to characterize the substrate, although the results have been mixed.[16-18] Chopra et al.[16] suggested that the discrepancy between bipolar and unipolar LVAs may represent zones of scar that extend beyond the endocardial abnormal voltage area. This is in line with the deeper field of view of unipolar electrograms. Additionally, some studies have suggested that the bipolar voltage threshold of 0.5 mV may overestimate the size of dense scar and still contain channels of viable tissue, while a unipolar threshold of 1.0 mV may represent electrically dense scar with no discernible or excitable tissue. As bipolar voltages can show considerable directional differences, omnipolar voltages are preferred for voltage mapping (**chapter 7**).

The arrhythmogenic substrate can be located either subendocardially, subepicardially, intramurally or transmurally.[19-21] Piorkowski et al.[22] demonstrated by bipolar endo-epicardial mapping in the left and right atrium in 44 patients with history of AF, that LVAs could be present in both layers (N=33, 75%) or solely in either the endocardium (N=6, 14%) or epicardium (N=6, 14%). However, this study was conducted in patients who have had (multiple) previous ablation procedures. In the study presented in **chapter 8**, in which the population consisted of patients without previous ablation therapy, it was demonstrated that the majority of the LVAs in the right atrium were exclusively located at either the endocardium or epicardium alone. This suggests that arrhythmogenic substrates may not necessarily be transmural. Omnipolar voltages, which represent more local activity, are more likely to detect LVAs located (sub)endocardially or (sub)epicardially, depending on the recording location. Interestingly, LVAs at the endocardium and epicardium did not always correspond to each other, regardless of the used recording technique. Only a small percentage of endocardial LVAs corresponded to epicardial LVAs, even by combining unipolar and omnipolar voltages. As LVAs are frequently invisible when recording from only one side, a combined endocardial and epicardial mapping approach is favored. The combination of simultaneously recorded endo-epicardial low unipolar and low omnipolar voltage may therefore be more indicative of dual-layer LVAs and probably arrhythmogenic substrates.

Increased complexity of electrograms

While unipolar single potentials are predominantly recorded at areas of fast and homogeneous conduction, potentials may become fragmented in areas with asynchronous activation. As described by Konings et al.[10] during AF, unipolar short- and long-double potentials were primarily observed at collision sites and sites of conduction block, respectively. Fragmented potentials were recorded at pivoting points or areas with slow conduction. During sinus rhythm and rapid atrial pacing, 7–8% of unipolar electrograms recorded from the right atrial free wall showed double potentials. Although a substantial proportion of short-double and even long-double potentials reflect the physiological heterogeneity in the atrial wall architecture, long-double and particularly fractionated potentials have been associated with conduction inhomogeneity. In patients with coronary artery disease without history of AF, a significant degree of fractionation is already present during sinus rhythm, with 10.9 [0–24.1] % short-double, 4.0 [0–20.7] % long-double and 5.5 [0–5.8] % fractionated

potentials (**chapter 12**). The highest proportions of long-double and fractionated potentials were mainly recorded at the right atrium and Bachmann's bundle, with fractionation at Bachmann's bundle also having the longest durations. The amount of conduction block was correlated with the proportion of long-double and fractionated potentials, and duration of fractionated potentials. In **chapter 4**, we showed that patients with mitral valve disease and paroxysmal AF had more unipolar fractionated potentials in the pulmonary vein area compared to those without a history of AF. Therefore, the complexity of unipolar potentials can serve as a marker of the severity and extensiveness of AF-related conduction inhomogeneity. However, fractionation can also result from variations in the anatomy of the atrial wall and therefore functional anisotropy.

The presence of inhomogeneous conduction and hence potential fractionation may not always be indicative of AF-related conduction abnormalities, but can also result from normal myocardial tissue properties. For instance, the trabeculated parts of the atria contain muscle bundles of variable thickness that can lead to source-to-sink mismatches, slowing of conduction, and recordings of long-double and fractionated potentials even during sinus rhythm (**chapters 4, 12, 14, 17, 21 and 22**). Prior mapping studies have shown that lines of conduction block are more frequent at the superior part of the right atrium and Bachmann's bundle, which is consistent with the high proportion of long-double and fractionated potentials recorded in these areas.[23,24] Specifically, conduction block was frequently observed surrounding the SAN area (**chapter 21**). In adult patients with congenital heart disease, more conduction block but also more fractionated potentials were found near the SAN area compared to pediatric patients with congenital heart disease (**chapter 22**). Short-double, long-double and fractionated potentials were present in respectively 75%, 92% and 92% of the pediatric and in 63%, 88% and 81% of the adult population. Although non-single potentials were present in all patients, potential fractionation tends to increase in those with a history of AF. These patients are also more frequently characterized by a caudal shift of the SAN exit pathway (**chapters 21 and 22**), presumably caused by aging-related remodeling. Additionally, a certain degree of endo-epicardial asynchrony was also present in most of SAN areas. Van der Does et al.[25] reported that areas of endo-epicardial asynchrony have a moderate-high sensitivity (65–78%) for unipolar and bipolar electrogram fractionation, which might explain the presence of fractionated potentials in these areas. In **chapter 15**, we constructed an electrical signal fingerprint that is able to predict the amount of EEA in a patient based on solely unipolar electrogram features. Areas of endo-epicardial asynchrony were characterized by lower voltages, a higher number of long-double and fractionated potentials, and longer duration of double and fractionated potentials. However, inhomogeneous conduction patterns in either the endo- or epicardial plane can also cause fractionated potentials due to physiological structures and myocardial bundles located in either layer. For example, in **chapter 35**, it was demonstrated that the presence of non-single potentials could also be attributed to the ligament of Marshall. Unipolar potentials recorded from this area consisted of either short-double (34.4%), long-double (57.1%) or fractionated potentials (8.5%). These potentials were characterized by smaller voltages and less steep slopes compared to left atrial potentials, as a result of the smaller bundle structure of the ligament of Marshall.[26]

Altered cell-to-cell communication and tissue damage results in a discontinuous distribution of conduction properties. Especially in these areas of non-uniform anisotropic tissue, conduction disorders are direction and frequency dependent. Spach demonstrated that 1) higher pacing rates result in lower transverse conduction velocity compared to longitudinal conduction velocity, and 2) premature electrical stimulation in non-uniform but not in uniform anisotropic tissue results in unidirectional longitudinal conduction block or a dissociated type of zigzag longitudinal conduction.[27,28] This asynchrony in activation

37

of cardiomyocytes can result in fractionation. A first human case illustrating the arising of potential fractionation due to direction- and rate-dependent anisotropic conduction was presented by Starreveld.[29] In a 76-year old patient with long-standing persistent AF, premature electrical stimulation induced low-amplitude, fractionated unipolar potentials with exceptionally prolonged durations. In **chapter 10**, we demonstrated that particularly changes in local wavefront direction resulted in an increase in fractionation, indicating the presence of irregular discontinuous wavefront propagation caused by anisotropic structural discontinuities that can be proarrhythmic. As patients with history of AF had more pronounced areas of direction-dependent fractionation, it may explain their increased susceptibility to AF episodes triggered by beats with changing wavefront direction compared to sinus rhythm. Even pediatric patients with congenital heart disease showed a significant increase in fractionation due to spontaneous aberrant atrial extrasystoles (AES, **chapter 24**). However, whether fractionation therefore represents a proper target for ablative therapy remains questionable.

The electrical signal fingerprint: patient-tailored staging of AF using electrograms

An inhomogeneous pattern of conduction is reflected in extracellular potential morphology.[4] An electrical signal profile containing quantified features of all types of electrograms could reflect the severity and extensiveness of inhomogeneity in conduction. Such a diagnostic tool would provide an individualized arrhythmogenic substrate profile which can also be tailored to possible gender- and age-specific features of electrograms. As delineated in **chapter 12**, electrical signal features related to conduction inhomogeneity included R/S ratios of single potentials, relative frequency distribution of peak-to-peak amplitudes of the different types of potentials, the proportion of LVAs, the proportion of the different types of potentials (single, short-double, long-double and fractionated potentials) and durations of long-double and fractionated potentials. In **chapter 13**, several of these parameters were used to predict the degree of intra-atrial conduction inhomogeneity in both atria. Specifically, an increased amount of intra-atrial conduction inhomogeneity was associated with decreased potential voltages, a larger amount of LVAs and long-double potentials, and prolonged fractionation duration. Models based on data obtained from the entire atria and solely the right atrium had the highest predictive vales. In the study described in **chapter 15**, unipolar electrogram features were used to predict the degree of endo-epicardial asynchrony in the right atrium. An increased amount of endo-epicardial asynchrony was associated with decreased potential voltages, a higher number of long-double and fractionated potentials, and prolonged duration of double and fractionated potentials at both the endo- and epicardium. Models based on data obtained from both the endo- and epicardium or the endocardium alone had the highest predictive values. These patient-tailored electrical signal fingerprints have the potential to serve as an objective measure to stage the AF-related arrhythmogenic substrate, identify patients at high risk for AF and stratify patients to different treatment modalities. The high-resolution, invasive gold standard electrical signal fingerprints may also be the foundation for development of less-, or non-invasive fingerprints which are also applicable during endocardial mapping procedures. Eventually, all electrical data should be combined with a biological fingerprint obtained from tissue or blood samples related to structural damage. The outcomes are summarized in an AF Fingerprint, which can be used to predict early onset or progression of AF in the individual patient.[30]

Defining and quantification of conduction inhomogeneity

Several features of electrograms can be used to derive parameters that quantify local variation in wavefront propagation. Wavefronts conducting across heterogeneous atrial

myocardium can be locally distorted, which could be the result of i.e., remodeling of cellular connections, reduced membrane excitability caused by a decrease in the inward sodium current, source-to-sink mismatches and tissue damage.[31,32] These changes can be quantified as local conduction heterogeneities. Within and between the propagating (fibrillation) wavefronts, characteristics of conduction can be quantified. These parameters mainly include the distribution of conduction times (differences in local activation time between neighboring electrodes), the amount of conduction disorders (percentage of conduction block) and distribution of conduction velocity estimates. However, several of these parameters do not provide any information on the (local) direction of wavefront propagation. Conduction velocity vectors, however, contain spatial information, although in many studies, only information on the magnitude of vectors is mainly used.

Conduction disorders: local conduction delay and block

The development and severity of conduction disorders can be attributed to both structural and electrical remodeling, which can be caused by factors such as age, underlying structural heart disease or AF itself.[28,33] Several previous mapping studies demonstrated that patients with history of AF were characterized by extensive conduction disorders in both the right and left atrium, but also particularly at Bachmann's bundle.[23,24,34-38] The presence of conduction disorders could have an effect on atrial excitation patterns, forcing activation of the left atrium primarily via the left atrioventricular groove instead of via Bachmann's bundle, thereby increasing the risk of AF.[24] In addition, it was demonstrated that total activation times of the right atrium and Bachmann's bundle could be specifically increased in patients with AF, resulting in longer total atrial excitation times.[37] In **chapter 21**, we demonstrated that the presence of areas of conduction block around the SAN area in patients with AF results in a more caudally located SAN exit pathway compared to patients without AF. This shifted location of the SAN could also affect interatrial conduction as we demonstrated that during programmed electrical stimulation delivered from specifically the lower right atrium, Bachmann's bundle could be activated either from only the right side, middle of Bachmann's bundle or even the left side (**chapter 34**). The presence of pre-existing conduction disorders had a major influence on the effect of programmed electrical stimulation from various atrial sites, resulting in significant interindividual variation.

Electrical remodeling is generally considered reversible within a week of sinus rhythm, while structural remodeling may persist even after four months of sinus rhythm.[33,39] Especially within the first five days after electrical cardioversion, the atria are more susceptible to re-initiation of AF due to AF-related electrical remodeling. However, this supervulnerable period is not characterized by increased conduction heterogeneity during sinus rhythm or premature AES (**chapter 20**). Structural remodeling, on the other hand, consists of atrial fibrosis, side-to-side cell uncoupling or atrial enlargement.[32,40,41] In patients with valvular heart disease, conduction disorders may be caused solely by pressure and/or volume overload, while in patients with ischemic heart disease, inflammation, atherosclerosis and myocardial infarction may be the cause.[40,42-44] In patients with uncorrected congenital heart disease, conduction disorders are the result of abnormal anatomy, altered hemodynamics and long-standing pressure and/or volume overload.[45,46] However, we demonstrated that atrial conduction disorders are already present in pediatric patients before surgical correction in their first year of life, primarily at the right atrium and Bachmann's bundle (**chapter 17**). These areas of conduction disorders are even more pronounced during spontaneous AES (**chapter 24**). Local conduction disorders are thus already present in pediatric patients with congenital heart disease, predisposing them to atrial arrhythmias early in life. Despite information on the (local) wavefront direction is not included, quantification of local conduction disorders provides valuable insights into local dissociation of wavefronts and the degree of electropathology.

37

Estimation of conduction velocity

Cardiac conduction velocity is a valuable parameter used in electrophysiological studies to provide insights into the properties of the underlying myocardium, including the direction of activation wavefronts. Areas of slowed conduction are associated with diseased tissue, making accurate measurements of velocity and directional dependency of electrical signal propagation crucial.[47] Heterogeneity of conduction velocity and excitability can create a substrate for unidirectional block, which is essential for the onset of reentry.[48,49] During standard electrophysiology studies, multielectrode catheters enable conduction velocity estimation using techniques like polynomial surface fitting, triangulation and finite differences.[50] Triangulation has the greatest potential for rapid velocity estimation using three-dimensional (3D) electro-anatomical activation time maps.[51-53] However, for very high-density maps, this technique may be overly sensitive to measurement errors due to the limited size of triangles in respect to the number of electrodes. Therefore, both finite difference and polynomial surface fitting techniques are widely used in literature with optical mapping recordings and micro-electrode array data. However, we demonstrated that both techniques have significant disadvantages and result in too smoothened conduction velocity maps, thereby masking areas of local conduction slowing or wavefront distortion (**chapter 18**). We, therefore, developed a novel methodology that is able to estimate local conduction velocity without smoothing of wavefront propagation resulting in estimation of local 'effective' conduction velocity indicative of the underlying local substrate. Without any smoothing properties, the discrete velocity vectors technique is able to identify local conduction heterogeneity, whereas these areas are missed by both other techniques. Nonetheless, it remains crucial to maintain the overall goal of conduction velocity estimation in mind, as the most optimal method may vary depending on a specific research question.

Local irregularities in conduction velocity vector maps can indicate distortions in wavefront propagating across heterogeneous atrial myocardium. In **chapter 25**, we developed a methodology that quantifies spatial variation in both direction and magnitude of velocity vectors, revealing local directional heterogeneities in conduction velocity vector fields constructed using the discrete velocity vectors method. These heterogeneities were found to be present during sinus rhythm, particularly at Bachmann's bundle and the left atrium, and were further enhanced by premature AES, specifically in patients with AF. This implies that conduction velocity vector fields become more locally directional heterogeneous, indicating local areas of impaired conduction. Moreover, as shown in **chapter 26**, the degree of local directional heterogeneity increased with AF complexity, with most local directional heterogeneities observed in patients with long-standing persistent AF. These findings suggest that AF-related structural and electrical remodeling progressively impair local conduction and lead to increasing complexity in the fibrillatory process.[2,54-57]

The estimation of local conduction velocity during AF is challenging due to the unstable patterns of activation and presence of multiple wavefronts with short wavelengths, limiting sequential mapping. As a result, a high-density (grid) multielectrode array with adequate spatial resolution is required.[58] Data on conduction velocity during AF is therefore mostly derived from animal models. In 1994, Konings et al.[59] estimated local conduction velocity in the human right atrium during sinus rhythm, rapid programmed electrical stimulation and acutely induced AF. Conduction velocity was estimated at each electrode from local activation times of four neighboring electrodes. The average conduction velocity was 73±5 cm/s during sinus rhythm and 68±5 cm/s during rapid programmed electrical stimulation. During type I AF, the average conduction velocity was still relatively high (61±6 cm/s), and decreased with AF complexity to 54±4 cm/s (type II AF) and 38±10 cm/s (type III AF). Even during sinus rhythm, the conduction velocity estimates in the right atrium were already

lower than the average local conduction velocity estimates in patients with structural heart disease (**chapters 18 and 19**). However, this can be easily explained by the different velocity estimation methodologies as in the technique of Konings et al.[59] the direction of wavefront propagation was not included, while local conduction block was. This resulted in lower velocity estimates as type III AF was characterized by a higher degree of conduction block.[2] In the same population as Konings et al.[59], Houben et al.[11] used polynomial surface fitting to estimate local conduction velocity during AF. Although the local conduction velocity during type I AF was comparable between both studies, higher velocity estimates were found during type II and III AF. However, the study was based on the analysis of non-fractionated potentials, which could explain why the estimates were still lower compared to our study demonstrated in **chapter 26**. In addition, as polynomial surface fitting is less efficient in estimating conduction velocities compared to discrete velocity vectors (**chapter 18**), particularly in case of small wavefronts, fewer high velocities were found (>100 cm/s). Conduction velocity of fibrillation waves in patients with long-standing persistent AF was significantly lower with increased spatiotemporal variability than patients with acutely induced AF. Strands of viable myocardial tissue are still present in patients with long-standing persistent AF, resulting in areas with fast local conduction (**chapter 26**).

Conduction anisotropy: breaking down longitudinal and transverse conduction velocity

Propagation of activation wavefronts across myocardial tissue depends on the myocardial fiber direction. This anisotropy is considered to be arrhythmogenic as it contributes to both initiation and perpetuation of AF.[11,60,61] Conduction velocity measurements are commonly used to estimate the anisotropy ratio, which is the ratio between the longitudinal and transverse conduction velocity.[62] The normal anisotropy ratio for ventricular myocardium is around 2.0, which is caused by the shape of the cardiomyocytes and the localization of connexins.[63] Although atrial tissue is often considered to be highly anisotropic[61], in patients without structural heart disease, Hansson et al.[64] surprisingly demonstrated that conduction velocity during stable sinus rhythm at the epicardial right atrial free wall was not dependent on propagation direction. Low anisotropy ratios during AF were also reported in the left atrial free wall of goats and in the right atrium of patients with Wolff-Parkinson-White syndrome and acutely induced AF.[11,56] We also found relatively low anisotropy ratios in the right atrium during both acutely induced AF and long-standing persistent AF, with higher anisotropy ratios in the latter group (**chapter 26**). Heterogeneities in longitudinal and transverse conduction velocity seen during long-standing persistent AF likely contribute to AF persistence and may be important in determining critical sites that sustain AF. Measuring the directional dependency of atrial conduction may show improved correlations with measures of structural remodeling. For example, Krul et al.[65] measured a slowing of transverse conduction but not longitudinal with increased fibrosis in the left atrial appendage, and Angel et al.[66] demonstrated diverse fibrosis architecture with decreased transverse conduction velocity in goats. Therefore, for the study of arrhythmia, the determination of the longitudinal and transverse conduction velocity is essential. Although most studies estimate the anisotropy ratio during AF itself, several previous studies have estimated longitudinal and transverse conduction velocity from a single activation map.[67,68] However, these methodologies require manual selection of longitudinal fiber direction, which is not feasible for analyzing high-density global activation maps.

Current imaging technologies do not allow for the global measurement of atrial fiber directions in vivo. Previous studies have focused on using diffusion tensor (DT)-MRI to study small sections of atrial tissue, such as the SAN, or have utilized micro-CT or contrast-enhancement MRI to construct myofiber orientation in the whole atria.[69-72] A high-resolution

37

Table 1 – Electrophysiological parameters attributed to AF-related electropathology.

Parameter	Rhythm	AF type	Number of AF patients	Effect compared to controls	Region of effect	Chapter
Unipolar voltage	SR	PAF (100%)	23	Decreased	BB	4
	SR	PAF (100%)	23	Decreased (SP)	RA, BB, PV	5
	AES	PAF (67%), PsAF (30%), LSPAF (3%)	60	More pronounced decrease	RA	10
	SR	PAF (84%), PsAF (11%), LSPAF (5%)	37	Decreased in areas of EEA	RA	15
	SR	PAF (80%), PsAF (20%)	5	Decreased	SAN	22
	SR	PoAF	97	Decreased	RA, BB, LA	28
S-wave amplitude	SR	PAF (100%)	23	Decreased	BB	5
Low-voltage areas	SR	PAF (100%)	23	Increased	BB	4
	SR	PAF (84%), PsAF (11%), LSPAF (5%)	37	Increased in areas of EEA	RA	15
	SR	PAF (35%), PsAF (53%), LSPAF (12%)	17	Increased	BB	19
	SR	PoAF	97	Increased	RA, BB, LA	28
R/S ratio	SR	PAF (100%)	23	Decreased	RA, BB	5
Long-double potentials	SR	PAF (84%), PsAF (11%), LSPAF (5%)	37	Increased in areas of EEA	RA	15
Fractionated potentials	SR	PAF (100%)	23	Increased	PV	4
	AES	PAF (67%), PsAF (30%), LSPAF (3%)	60	More pronounced increase	RA	10
	SR	PAF (84%), PsAF (11%), LSPAF (5%)	37	Increased in areas of EEA	RA	15
	SR	PAF (80%), PsAF (20%)	5	Increased	SAN	22
Fractionation duration	SR	PAF (84%), PsAF (11%), LSPAF (5%)	37	Increased LDP+FP in areas of EEA	RA	15
	SR	PoAF	97	Increased LDP	RA	28
Conduction velocity	SR	PAF (100%)	23	Decreased	BB	5
	SR	PAF (100%)	58	Decreased	BB	18
	SR	PAF (35%), PsAF (53%), LSPAF (12%)	17	Decreased	BB	19
	SR	PAF (80%), PsAF (20%)	5	Decreased	SAN	22
	AF	LSPAF (100%)	23	Decreased	RA	26
	SR	PoAF	97	Decreased	RA	28
Local directional heterogeneities	SR	PAF (67%), PsAF (33%)	52	Increased	BB, PV	25
	AF	LSPAF (100%)	23	Increased	RA	26
Conduction block	P-AES	PoAF	4	More pronounced increase	RA	27
	SR	PoAF	97	Increased	BB	28
Endo-epicardial asynchrony	SR	PAF (84%), PsAF (11%), LSPAF (5%)	37	Increased	RA	15
	P-AES	PoAF	4	More pronounced increase	RA	27
Total activation time	SR	PAF (35%), PsAF (53%), LSPAF (12%)	17	Increased	-	19
SAN exit site	SR	PAF (100%)	8	Caudal shift	SAN	21

Signal features

Conduction features

atrial DT-MRI study by Pashakhanloo et al.[70] has revealed inter-patient variability in fiber directions. Simulation and experimental studies suggest that atrial fiber directions may influence arrhythmia dynamics and the efficacy of ablation strategies, making it important to infer patient-specific atrial fiber directions.[73-75] In recent years, there has been a gradual progression towards creating highly detailed models of cardiac conduction that are more representative of real-life scenarios. However, the incorporation of increased levels of detail into these models poses a challenge to their customization and practical use in clinical settings, as acquiring data at the cellular and tissue level is often limited. Recently, He et al.[76] discovered that even substantial variations in fiber organization had a relatively minor influence on spatiotemporal activation patterns during regular pacing. Across all fiber organizations tested, the activation maps were quite similar for a giving pacing location. This is consistent to our findings of low anisotropy ratios in the atria (**chapter 26**). Therefore, it is likely that propagation of wavefronts depends more on the macroscopic atrial anatomy, whereas local directional conduction velocity is more determined by the local fiber orientation.

(Re)defining mapping strategies for AF-related electropathology: changing the game?

Analysis of electrograms plays an important role in adjunctive ablation strategies in addition to pulmonary vein isolation, particularly in patients with (long-standing) persistent AF.[77-80] These adjunctive strategies frequently include additional ablation lesions in the left atrium, ablation of complex fractionated electrograms, ganglionated plexi, high dominant frequencies, rotors or non-pulmonary vein trigger sites, isolation of the superior caval vein and ablation or isolation of LVAs. Although promising results were reported in single-center studies, large multicenter studies fail to show consistent improvement in procedural outcomes.[1] This can partly be explained by the lack of uniform definitions and variable mapping techniques with varying electrode densities and sizes, considerably affecting the resulting maps (**chapter 11**). Interestingly, although there has been a trend towards more personalized AF ablation therapy, these studies particularly focused on only one electrogram feature to identify sites of interest.[81-83] However, it is unlikely that a single signal feature can accurately identify the arrhythmogenic substrate. For example, we demonstrated that bipolar and even omnipolar LVAs can still contain large unipolar potential voltages and high conduction velocities (**chapter 7**). A combination of low omnipolar and low unipolar potential voltage may be more representative for identifying arrhythmogenic substrates as these are related to lower conduction velocities (**chapters 4 and 5**). However, lowest conduction velocities were found in areas containing low-voltage, fractionated potentials, indicating that not all LVAs and fractionated potentials are suitable target sites for ablative therapy and could be largely physiological in nature (**chapter 9**). Ablation of all areas containing these electrogram characteristics does not necessarily have to result in AF termination and only results in more tissue damage. It is therefore important to be aware of the distribution of quantified electrophysiological properties during sinus rhythm and AF in patients with various underlying heart diseases with and without prior AF episodes.

37

In previous mapping studies, it was demonstrated that patients with a history of AF are characterized by a higher degree of conduction block.[23,24,35-37,84] In this thesis, it was
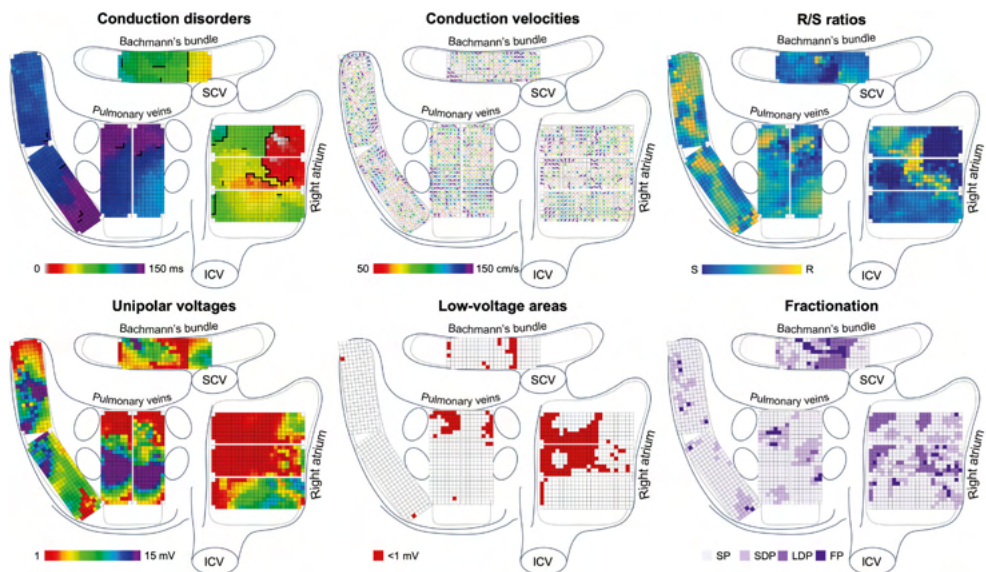
Figure 2 – Various electrophysiological parameters related to electropathology during sinus rhythm in one patient with mitral valve disease. *Upper left panel*: color-coded total activation map with lines of conduction block, visualized by thick black lines. *Upper center panel*: conduction velocity map containing areas with slow and heterogeneous conduction distributed across both atria. *Upper right panel*: R/S ratio map. The region surrounding the sino-atrial node contains predominantly potentials with a full S-wave morphology, while potentials recorded in the left atrium have more predominant R-wave morphologies. Full R-wave morphologies, representing wavefront termination, were present at all atrial sites. *Lower left panel*: unipolar voltage map demonstrating high potential voltages mainly at the left atrium and the pulmonary vein area, while potential voltages were lower at Bachmann's bundle and the right atrium. *Lower center panel*: low-voltage areas are highlighted and could particularly be found in the right atrium, Bachmann's bundle and between the superior pulmonary veins. *Lower right panel*: fractionation map demonstrating the distribution of various potential types. Potential fractionation could be found throughout both atria, but particularly at Bachmann's bundle and the right atrium near lines of conduction block as visualized in the upper left panel. **FP** = fractionated potentials; **ICV** = inferior caval vein; **LDP** = long-double potentials; **SCV** = superior caval vein; **SDP** = short-double potentials; **SP** = single potentials.

demonstrated that several other electrophysiological parameters are also related to AF-related electropathology during sinus rhythm and AES, including decreased potential voltages and conduction velocity, an increased amount of LVAs and potential fractionation, prolonged fractionation duration and more directional heterogeneity in conduction velocity vectors, as listed in *Table 1* and visualized in *Figure 2*. The next step will be to study these parameters during AF, taking into account the directional sensitivity of conduction velocity by conduction anisotropy (**chapter 26**). By doing so, it will be possible to determine which parameters are best suited to quantify the degree of electropathology during both sinus rhythm and AF. It is thereby likely that the combined presence and degree of various features determines the stage of AF. These electrogram features do not necessarily have to be recorded using one single recording technique. While bipolar electrograms are more commonly used in clinical practice, unipolar electrograms provide additional information on local wavefronts, which can be quantified in a relatively straightforward way. By using (high-density) grid-electrodes, it would be possible to record unipolar, bipolar and even omnipolar electrograms simultaneously, each providing unique and additional information as bi/omnipolar electrograms can be complementary and contradictory to unipolar electrograms. In addition, with a sufficient number of electrodes, it would be feasible to estimate local conduction velocities, even during AF. By utilizing all possible information, accuracy of substrate identification is likely to increase. In order to organize all data, machine learning algorithms should be developed which take all electrogram features into account.

The efficacy of endocardial ablation strategies is limited in patients with persistent AF, particularly due to the presence of complex three-dimensional arrhythmogenic substrates. LVAs can be found at either the endocardium or epicardium alone, with the opposite areas often containing normal voltages (**chapter 8**). These diseased areas are therefore "invisible" and could easily be missed using a one-sided approach. Hybrid AF ablation results in better outcomes than catheter ablation for the treatment of patients with persistent AF and is therefore more increasingly performed.[85] Another advantage of hybrid AF ablation is access to epicardial structures such as Bachmann's bundle. This suggests that a strategy of combined endo-epicardial access for mapping and ablation may provide superior efficacy to an endocardial-only approach.

The role of electropathology in post-operative AF: whom is at risk?

Post-operative AF is the most commonly encountered complication after cardiac surgery, occurring in 20-50% of patients.[86] Although considered a transient and mostly mild complication in the early recovery period, it is associated with increased mortality and morbidity rates, longer hospitalization periods and higher post-operative care costs.[87-89] The development of post-operative AF is based on the interaction between transient surgery-related triggers and pre-, intra- and post-operative proarrhythmic atrial substrates related to e.g., age, male gender, diabetes mellitus, obesity, hyper- /hypotension, ischemia, pain and other factors that can modulate the sympathetic nervous system and increase adrenergic stimulation.[89-94] In patients without a history of AF, the pre-existing atrial substrate is inadequate to initiate AF episodes, but surgery-related triggers, such as activation of the sympathetic nervous system and inflammation, may cause clinical manifestation of post-operative AF. These factors can also influence the duration of AF episodes, as obese patients are susceptible to higher post-operative AF burden and prolonged post-operative AF episodes lasting over one hour, especially during the first five post-operative days.[95] In a previous mapping study by Serban et al.[96], it was demonstrated that obese patients undergoing cardiac surgery have a higher incidence of conduction disorders than non-obese patients, making them more susceptible to developing early post-operative AF. In **chapter 6**, we demonstrated that the number of LVAs correlated with the incidence of conduction block, while BMI and the number of LVAs were independent predictors of the incidence of early post-operative AF. Therefore, the correlation between the amount of conduction block and LVAs could potentially explain the higher risk of early post-operative AF development in obese patients.

It is widely accepted that early post-operative AF is primarily a trigger driven disease in which AES are provoked by inflammatory responses and increasing sympathetic activity associated with cardiopulmonary bypass during surgery.[24,92,94,97-100] In **chapter 27**, we demonstrated that these AES are associated with enhanced conduction disorders and endo-epicardial asynchrony. Post-operative AF then occurs when these transient, post-operative triggers act on vulnerable, remodeled, atrial tissue.[97,98] Early post-operative AF is also a predictor of late post-operative AF (occurring >30 days after surgery), which in turn is associated with long-term mortality. The transition from early to late post-operative AF progresses from a trigger-driven to a more substrate-driven disease.[24,97,98] Late post-operative AF is therefore more likely to occur in patients with a more extensive pre-existing arrhythmogenic substrate compared to patients who will only have early post-operative AF. However, the development of both early and late post-operative AF is associated with pre-existing conduction disorders, consisting of areas of conduction slowing, more conduction block, lower unipolar voltages and more LVAs, which were most severe in patients with late post-operative AF (**chapters 28 and 33**). These areas of electropathology were primarily present at Bachmann's bundle, followed by the left and right atrium, but without differences in the pulmonary vein area. This

37

suggests significant spatial heterogeneity of the pre-existing atrial substrates. Furthermore, almost half of late post-operative AF episodes occurred >2 years after the surgery, and could even for the first time occur up to five years after surgery. Late post-operative AF could be either associated with progression of pre-existing substrates or as a result of a persistent effect of the surgery on the substrate that contributes to late AF occurrences. As patients with late post-operative AF already have more extensive substrates during surgery, periodic rhythm monitoring should be considered in these patients. In order to better understand the development of surgery-related AF substrates, non-invasive approaches that can quantify electropathology in the post-operative period, such as body-surface mapping, should be further developed.

Accurate identification of AF during post-operative rhythm monitoring is essential to determine the AF burden and eventually relate ECG characteristics to mapping-derived features of electropathology. As elucidated in **chapter 29**, newly developed methods should prioritize transparent and accurate automated AF detection, since manual analysis of continuous rhythm registrations is unfeasible. Current studies suggest that using only ventricular ECG features yields the highest accuracy, although studies reporting on atrial ECG features are relatively scarce. While more complex classifiers are likely to be more precise, their interpretation is increasingly challenging due to the complex feature sets and neural networks processing the signal as a black box. Additionally, accurate classification depends heavily on the presence of sufficient and accurately labelled data. In **chapter 30**, we developed a new method to train a classifier using a large set of real-life telemetry data of hospitalized patients. It was demonstrated that human-validated semi-supervised learning results in an accurate classifier with a lower human workload. Moreover, the degree of certainty of the classifier increased with an increasing number of ECG segments in the training dataset, which is related to classifier accuracy. Ultimately, new, accurate algorithms will enable to more precisely determine the (post-operative) AF burden in patients in terms of AF duration, number of episodes and proportion of time an individual is in AF. The next step will be to correlate ECG characteristics and AF burden to specific AF-related features of electropathology.

Implications of high-resolution mapping during cardiac surgery

Advancements in mapping systems and recording electrodes have revolutionized the potential for high-density and high-resolution mapping in clinical practice. The use of high-resolution mapping during cardiac surgery is not limited to merely identifying electropathology but also offers valuable insights into the electrophysiological processes of the heart, which could be utilized for diagnostic purposes (**chapter 32**), guiding pacing lead placement (**chapter 34**) or to locate electrophysiological structures. For instance, unipolar electrogram morphology can effectively discern various electrophysiological structures, such as the SAN (**chapter 21**) and ligament of Marshall (**chapter 35**).

In patients with congenital heart disease, SAN dysfunction is commonly observed, often resulting from pre-existing substrates or surgery-induced injuries. Abnormalities in SAN geometry and function present at birth can predispose (pediatric) patients to SAN dysfunction, while surgical incisions can directly damage the SAN or its blood supply, leading to post-operative SAN dysfunction (**chapters 17, 22 and 23**). Hence, accurate real-time intra-operative localization of the SAN can aid in preventing these surgical injuries. Notably, while the SAN is generally believed to be located in the high right atrium, its functional dynamic span extends along the terminal crest.[101] A caudal shift of SAN exit sites can be observed in patients with AF and adults with congenital heart disease (**chapters 21 and 22**). However, even in pediatric patients who developed post-operative SAN dysfunction,

an inferior or multiple SAN exit sites could be observed intra-operatively (**chapter 23**). This could be caused by extensive conduction disorders at the superior and inferior right atrium, emphasizing the fact that the location of the SAN may not always be straightforward. Real-time intra-operative mapping of the SAN could thus effectively prevent surgery-induced post-operative SAN dysfunction. During surgery, the SAN is identified by the earliest site of activation that corresponds with P-wave onset on the surface ECG and is characterized by unipolar electrograms consisting mainly of S-wave potentials (**chapters 5, 21 and 22**), as depicted in *Figure 1*. In a recent study, Feins et al.[102] introduced a technique for intra-operative conduction system mapping during complex congenital heart surgery. A multielectrode mapping catheter (Advisor HD Grid, Abbott) was used to collect intracardiac electrograms, which were then interpreted by electrophysiologists. The location of conduction tissue was communicated in real-time to the surgeon, who then completed the repair while avoiding injury to the mapped conduction system. The study effectively demonstrated that this intra-operative conduction system mapping technique was proficient in localizing the conduction system during surgery and contributed to reducing the risk of heart block in pediatric patients undergoing complex congenital heart surgery. Such an approach could also be used to identify target sites for additional ablative lesions in adjunct to pulmonary vein isolation during surgical AF ablation procedures, such as the ligament of Marshall. This structure could be most accurately identified using unipolar electrograms obtained by intra-operative high-resolution mapping, which consisted predominantly of long-double, short-double or even fractionated potentials (**chapter 35**). Activation time maps based on all unipolar deflections then provides real-time visualization of the ligament of Marshall. The use of this technique will enable more precise ablation of the ligament of Marshall, eliminating the need to ablate the entire posterior left atrial wall using ethanol infusion via the vein of Marshall, thereby avoiding potential disadvantages. Effective implementation of these innovative strategies necessitates close collaboration between electrophysiologists and cardiac surgeons.

Another example of recent increasing collaboration between electrophysiologists and cardiac surgeons is evident in the emergence of hybrid ablation therapy for persistent AF. This approach has demonstrated promising outcomes in terms of AF-free survival, accompanied by a relatively low complication rate.[85,103-105] Hybrid ablation therapy integrates a thoracoscopic epicardial and transvenous endocardial approach to make optimal use of the benefits of both surgical and transvenous catheter ablation therapy.[103] The surgical approach allows for direct visualization of anatomical structures and the implementation of epicardial lesions, while the transvenous catheter approach enables the confirmation of conduction block and the creation of lesions in areas inaccessible through the surgical approach. However, it is important to note that this technique primarily relies on predefined lesions, replicating the Cox maze procedure.[106] In the future, the incorporation of additional high-resolution mapping could facilitate personalized substrate modification, including strategies targeting electropathology. As the integration of electrophysiological assessment during cardiac surgery becomes more accustomed, it could also guide other therapies. These may include localization of the most optimal position for a pacing lead (**chapter 34**) or selection of patients and optimization of stimulation settings for cardiac neuromodulation (**chapter 36**). High-resolution mapping can also help identifying patients at high risk of developing post-operative AF, making them suitable candidates for preventive (ablative) therapy or necessitating close monitoring during the post-operative period (**chapters 27, 28 and 33**). The implications of employing high-resolution mapping during cardiac surgery, as outlined above, represent merely the initial possibilities of this groundbreaking initiative.

37

Clinical implications
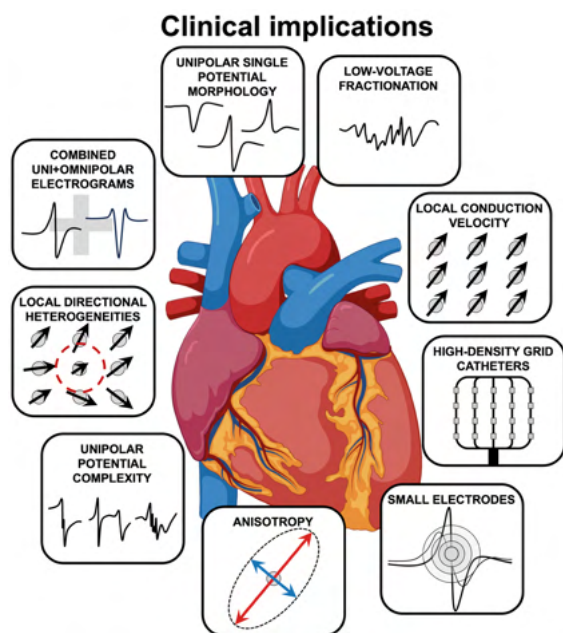
Figure 3 – Potential implications of electrical features related to electropathology suitable for mapping studies as proposed in this thesis.

Future directions and conclusions

Clinical electrophysiology studies typically involve endocardial mapping studies to identify the substrates underlying AF and guide catheter ablation therapies. However, as these substrates are complex and three-dimensional, and could be located at the endo- and/or epicardium, it becomes crucial to also reach epicardial structures, such as Bachmann's bundle and the ligament of Marshall. With the rise of hybrid ablation procedures, epicardial mapping is already becoming more prevalent in guiding ablative therapy. However, despite the numerous proposed ablation strategies, the overall recurrence rate of (persistent) AF remains considerably high.[77-80,107] This challenge is partly attributed to the inability to differentiate patients likely to benefit from (ablation) therapy from those prone to failure due to presence of overly extensive substrates. These substrates underlying AF appear to be multifaced and patient-specific, thus requiring highly individualized diagnostics, prognostics and therapy. The current clinical classification of AF, which only focusses on timing of AF episodes, is therefore insufficient. Instead, an objective scale based on quantified electrophysiological features as proposed in this thesis should be employed to classify patients according to the extent of electropathology. In this context, translational research plays a crucial role in identifying the diverse components contributing to the pathogenesis and perpetuation of AF.

This thesis proposes several quantified features and methodologies pertaining to AF-related electropathology by using the gold standard high-density and high-resolution mapping approach. This concept finds its roots in personalized signal processing, in which technical-analytical approaches are applied to quantify electrophysiological data in the individual patient, making comprehensive use of all available information derived from electrograms. Several of these features could already be implemented into current clinical practice and are illustrated in *Figure 3*. First, by combining unipolar and bi/omnipolar electrograms, additional information can be acquired related to voltage mapping and the identification of LVAs. By considering unipolar electrograms, single potential morphology can be used

to identify structures such as the SAN or areas with wavefront termination. In addition, unipolar potential complexity can be used to identify anatomical structures such as the ligament of Marshall by annotating all deflections within the potentials. Areas containing low-voltage, fractionated potentials could be of particular interest as ablation targets due to the decreased local conduction velocity within these areas, although the application still has to be confirmed. Local conduction velocities should also be computed using appropriate methodologies. Although no single optimal methodology exists, the user should be aware of the consequences of using either technique. By applying a technique that does not smooth wavefront propagation, local directional heterogeneities in conduction velocity vectors and the degree of local conduction anisotropy could be identified. Although it remains unknown whether these areas could be target sites for ablative therapy, quantification of these areas can provide additional information on the degree of electropathology in each individual patient. Considering that these features are often affected by electrode size and the spatial density of recording electrodes (**chapter 11**), it is essential for manufacturers to prioritize the development of small, high-density and high-resolution (grid-)electrodes tailored for AF mapping. Specifically, there should be more focus on obtaining unipolar electrograms with adequate quality, as unipolar potentials provide valuable additional information on the underlying tissue. This information can also be deployed during cardiac surgery for identification of electrophysiological structures, real-time diagnoses or guiding treatment strategies. For research purposes and adequate data interpretation, it is of utmost importance that the utilized settings (e.g., sampling rate and filter settings) and electrode configurations (e.g., electrode size and interelectrode distance) are clearly reported. These variables become more important as the level of complexity of AF increases. In addition, mapping systems should be flexible to facilitate widespread and straightforward implementation of various features derived from both unipolar and bi/omnipolar electrograms. A combination of all derived parameters is thereby likely to offer a more precise indication of the presence, distribution and the degree of arrhythmogenic substrates.

In the future, machine-learning-based algorithms may enable (semi-)automatically analysis of all various electrogram characteristics to pinpoint possible target sites for ablation. However, ablation of tissue may not always be the solution for AF termination, as it only causes more tissue damage. Therefore, it is imperative to first establish a clear understanding of what constitutes electropathology and how each parameter should be interpreted during AF. For example, there should be a clear strategy on how voltage mapping or conduction velocities should be used during a rhythm with continuously changing wavefronts resulting in beat-to-beat variation in potential morphology. Following the establishment of a comprehensive definition and strategy, machine-learning-based algorithms can indeed be trained to automatically identify areas of interest. Subsequently, the degree of electropathology, as measured by invasive mapping, should be translated into less- or non-invasive measures, such as body surface mapping (*Moghaddasi and Van Schie et al., submitted*) or the utilization of biomarkers (*Pool and Van Schie et al., submitted*). This translation can facilitate the classification of the complexity and degree of electropathology, enabling a correlation with the most suitable treatment approach for each individual patient. In this way, patients can be pre-sorted before invasive mapping in the operating room or electrophysiology laboratory is performed, significantly enhancing the efficiency of the process and preventing unnecessary burden of the patient. Considering AF as a complex, multifactorial arrhythmia, the involvement of a multidisciplinary team of medical-technical experts is essential for its termination. This collaborative approach ensures the most optimal use of (epicardial) access, ablation strategies, but also technical solutions for the visualization and quantification of arrhythmogenic substrates using mapping techniques, resulting in more accurate classification of individual patients and delivery of patient-tailored therapy based on the degree of atrial electropathology.

37

References

1. Schmidt B, Brugada J, Arbelo E, Laroche C, Bayramova S, Bertini M, Letsas KP, Pison L, Romanov A, Scherr D, et al. Ablation strategies for different types of atrial fibrillation in Europe: results of the ESC-EORP EHRA Atrial Fibrillation Ablation Long-Term registry. Europace. 2020;22:558-566.

2. Allessie MA, de Groot NM, Houben RP, Schotten U, Boersma E, Smeets JL, Crijns HJ. Electropathological substrate of long-standing persistent atrial fibrillation in patients with structural heart disease: longitudinal dissociation. Circ Arrhythm Electrophysiol. 2010;3:606-615.

3. Spach MS, Miller WT, 3rd, Miller-Jones E, Warren RB, Barr RC. Extracellular potentials related to intracellular action potentials during impulse conduction in anisotropic canine cardiac muscle. Circ Res. 1979;45:188-204.

4. de Groot NM, Schalij MJ, Zeppenfeld K, Blom NA, Van der Velde ET, Van der Wall EE. Voltage and activation mapping: how the recording technique affects the outcome of catheter ablation procedures in patients with congenital heart disease. Circulation. 2003;108:2099-2106.

5. Villacastin J, Almendral J, Arenal A, Castellano NP, Gonzalez S, Ortiz M, Garcia J, Vallbona B, Moreno J, Portales JF, et al. Usefulness of unipolar electrograms to detect isthmus block after radiofrequency ablation of typical atrial flutter. Circulation. 2000;102:3080-3085.

6. Jacquemet V, Virag N, Ihara Z, Dang L, Blanc O, Zozor S, Vesin JM, Kappenberger L, Henriquez C. Study of unipolar electrogram morphology in a computer model of atrial fibrillation. J Cardiovasc Electrophysiol. 2003;14:S172-179.

7. Gardner PI, Ursell PC, Fenoglio JJ, Jr., Wit AL. Electrophysiologic and anatomic basis for fractionated electrograms recorded from healed myocardial infarcts. Circulation. 1985;72:596-611.

8. Calkins H, Hindricks G, Cappato R, Kim YH, Saad EB, Aguinaga L, Akar JG, Badhwar V, Brugada J, Camm J, et al. 2017 HRS/EHRA/ECAS/APHRS/SOLAECE expert consensus statement on catheter and surgical ablation of atrial fibrillation. Europace. 2018;20:e1-e160.

9. van der Does LJ, de Groot NM. Inhomogeneity and complexity in defining fractionated electrograms. Heart Rhythm. 2017;14:616-624.

10. Konings KT, Smeets JL, Penn OC, Wellens HJ, Allessie MA. Configuration of unipolar atrial electrograms during electrically induced atrial fibrillation in humans. Circulation. 1997;95:1231-1241.

11. Houben RP, de Groot NM, Smeets JL, Becker AE, Lindemans FW, Allessie MA. S-wave predominance of epicardial electrograms during atrial fibrillation in humans: indirect evidence for a role of the thin subepicardial layer. Heart Rhythm. 2004;1:639-647.

12. van der Does L, Knops P, Teuwen CP, Serban C, Starreveld R, Lanters EAH, Mouws E, Kik C, Bogers A, de Groot NMS. Unipolar atrial electrogram morphology from an epicardial and endocardial perspective. Heart Rhythm. 2018;15:879-887.

13. Kumar S, Michaud GF. Unipolar electrogram morphology to assess lesion formation during catheter ablation of atrial fibrillation: successful translation into clinical practice. Circ Arrhythm Electrophysiol. 2013;6:1050-1052.

14. Josephson ME, Anter E. Substrate Mapping for Ventricular Tachycardia: Assumptions and Misconceptions. JACC Clin Electrophysiol. 2015;1:341-352.

15. Kottkamp H, Bender R, Berg J. Catheter ablation of atrial fibrillation: how to modify the substrate? J Am Coll Cardiol. 2015;65:196-206.

16. Chopra N, Tokuda M, Ng J, Reichlin T, Nof E, John RM, Tedrow UB, Stevenson WG. Relation of the unipolar low-voltage penumbra surrounding the endocardial low-voltage scar to ventricular tachycardia circuit sites and ablation outcomes in ischemic cardiomyopathy. J Cardiovasc Electrophysiol. 2014;25:602-608.

17. De Groot NM, Kuijper AF, Blom NA, Bootsma M, Schalij MJ. Three-dimensional distribution of bipolar atrial electrogram voltages in patients with congenital heart disease. Pacing Clin Electrophysiol. 2001;24:1334-1342.

18. Spears DA, Suszko AM, Dalvi R, Crean AM, Ivanov J, Nanthakumar K, Downar E, Chauhan VS. Relationship of bipolar and unipolar electrogram voltage to scar transmurality and composition derived by magnetic resonance imaging in patients with nonischemic cardiomyopathy undergoing VT ablation. Heart Rhythm. 2012;9:1837-1846.

19. Tokuda M, Tedrow UB, Inada K, Reichlin T, Michaud GF, John RM, Epstein LM, Stevenson WG. Direct comparison of adjacent endocardial and epicardial electrograms: implications for substrate mapping. J Am Heart Assoc. 2013;2:e000215.

20. Chen R, Wen C, Fu R, Li J, Wu J. The effect of complex intramural microstructure caused by structural remodeling on the stability of atrial fibrillation: Insights from a three-dimensional multi-layer modeling study. PLoS One. 2018;13:e0208029.

21. Gharaviri A, Bidar E, Potse M, Zeemering S, Verheule S, Pezzuto S, Krause R, Maessen JG, Auricchio A, Schotten U. Epicardial Fibrosis Explains Increased Endo-Epicardial Dissociation and Epicardial Breakthroughs in Human Atrial Fibrillation. Front Physiol. 2020;11:68.

22. Piorkowski C, Kronborg M, Hourdain J, Piorkowski J, Kirstein B, Neudeck S, Wechselberger S, Passler E, Lowen A, El-Armouche A, et al. Endo-/Epicardial Catheter Ablation of Atrial Fibrillation: Feasibility, Outcome, and Insights Into Arrhythmia Mechanisms. Circ Arrhythm Electrophysiol. 2018;11:e005748.

23. Kharbanda RK, Knops P, van der Does L, Kik C, Taverne Y, Roos-Serote MC, Heida A, Oei FBS, Bogers A, de Groot NMS. Simultaneous Endo-Epicardial Mapping of the Human Right Atrium: Unraveling Atrial Excitation. J Am Heart Assoc. 2020;9:e017069.

24. Teuwen CP, Yaksh A, Lanters EA, Kik C, van der Does LJ, Knops P, Taverne YJ, van de Woestijne PC, Oei FB, Bekkers JA, et al. Relevance of Conduction Disorders in Bachmann's Bundle During Sinus Rhythm in Humans. Circ Arrhythm Electrophysiol. 2016;9:e003972.

25. van der Does L, Starreveld R, Kharbanda RK, Knops P, Kik C, Bogers A, de Groot NMS. Detection of Endo-

epicardial Asynchrony in the Atrial Wall Using One-Sided Unipolar and Bipolar Electrograms. J Cardiovasc Transl Res. 2021;14:902-911.

26. Kim DT, Lai AC, Hwang C, Fan LT, Karagueuzian HS, Chen PS, Fishbein MC. The ligament of Marshall: a structural analysis in human hearts with implications for atrial arrhythmias. J Am Coll Cardiol. 2000;36:1324-1327.

27. Spach MS, Kootsey JM, Sloan JD. Active modulation of electrical coupling between cardiac cells of the dog. A mechanism for transient and steady state variations in conduction velocity. Circ Res. 1982;51:347-362.

28. Spach MS, Dolber PC, Heidlage JF. Influence of the passive anisotropic properties on directional differences in propagation following modification of the sodium conductance in human atrial muscle. A model of reentry based on anisotropic discontinuous propagation. Circ Res. 1988;62:811-832.

29. Starreveld R, de Groot NMS. Direction- and rate-dependent fractionation during atrial fibrillation persistence: Unmasking cardiac anisotropy? J Cardiovasc Electrophysiol. 2020;31:2206-2209.

30. Starreveld R, Knops P, Ramos KS, Roos-Serote MC, Bogers A, Brundel B, de Groot NMS. Atrial fibrillation fingerprinting; spotting bio-electrical markers to early recognize atrial fibrillation by the use of a bottom-up approach (AFFIP): Rationale and design. Clin Cardiol. 2020;43:546-552.

31. Spach MS, Miller WT, 3rd, Dolber PC, Kootsey JM, Sommer JR, Mosher CE, Jr. The functional role of structural complexities in the propagation of depolarization in the atrium of the dog. Cardiac conduction disturbances due to discontinuities of effective axial resistivity. Circ Res. 1982;50:175-191.

32. Spach MS, Boineau JP. Microfibrosis produces electrical load variations due to loss of side-to-side cell connections: a major mechanism of structural heart disease arrhythmias. Pacing Clin Electrophysiol. 1997;20:397-413.

33. Wijffels MC, Kirchhof CJ, Dorland R, Allessie MA. Atrial fibrillation begets atrial fibrillation. A study in awake chronically instrumented goats. Circulation. 1995;92:1954-1968.

34. Lanters EAH, Yaksh A, Teuwen CP, van der Does L, Kik C, Knops P, van Marion DMS, Brundel B, Bogers A, Allessie MA, et al. Spatial distribution of conduction disorders during sinus rhythm. Int J Cardiol. 2017;249:220-225.

35. Heida A, van der Does WFB, van Staveren LN, Taverne Y, Roos-Serote MC, Bogers A, de Groot NMS. Conduction Heterogeneity: Impact of Underlying Heart Disease and Atrial Fibrillation. JACC Clin Electrophysiol. 2020;6:1844-1854.

36. Mouws E, van der Does L, Kik C, Lanters EAH, Teuwen CP, Knops P, Bogers A, de Groot NMS. Impact of the arrhythmogenic potential of long lines of conduction slowing at the pulmonary vein area. Heart Rhythm. 2019;16:511-519.

37. Mouws E, Lanters EAH, Teuwen CP, van der Does L, Kik C, Knops P, Yaksh A, Bekkers JA, Bogers A, de Groot NMS. Impact of Ischemic and Valvular Heart Disease on Atrial Excitation:A High-Resolution Epicardial Mapping Study. J Am Heart Assoc. 2018;7.

38. van der Does L, Lanters EAH, Teuwen CP, Mouws E, Yaksh A, Knops P, Kik C, Bogers A, de Groot NMS. The Effects of Valvular Heart Disease on Atrial Conduction During Sinus Rhythm. J Cardiovasc Transl Res. 2020;13:632-639.

39. Everett THt, Li H, Mangrum JM, McRury ID, Mitchell MA, Redick JA, Haines DE. Electrical, morphological, and ultrastructural remodeling and reverse remodeling in a canine model of chronic atrial fibrillation. Circulation. 2000;102:1454-1460.

40. Darby AE, Dimarco JP. Management of atrial fibrillation in patients with structural heart disease. Circulation. 2012;125:945-957.

41. Psaty BM, Manolio TA, Kuller LH, Kronmal RA, Cushman M, Fried LP, White R, Furberg CD, Rautaharju PM. Incidence of and risk factors for atrial fibrillation in older adults. Circulation. 1997;96:2455-2461.

42. Alasady M, Abhayaratna WP, Leong DP, Lim HS, Abed HS, Brooks AG, Mattchoss S, Roberts-Thomson KC, Worthley MI, Chew DP, et al. Coronary artery disease affecting the atrial branches is an independent determinant of atrial fibrillation after myocardial infarction. Heart Rhythm. 2011;8:955-960.

43. Harada M, Van Wagoner DR, Nattel S. Role of inflammation in atrial fibrillation pathophysiology and management. Circ J. 2015;79:495-502.

44. Heeringa J, van der Kuip DA, Hofman A, Kors JA, van Rooij FJ, Lip GY, Witteman JC. Subclinical atherosclerosis and risk of atrial fibrillation: the rotterdam study. Arch Intern Med. 2007;167:382-387.

45. Hernandez-Madrid A, Paul T, Abrams D, Aziz PF, Blom NA, Chen J, Chessa M, Combes N, Dagres N, Diller G, et al. Arrhythmias in congenital heart disease: a position paper of the European Heart Rhythm Association (EHRA), Association for European Paediatric and Congenital Cardiology (AEPC), and the European Society of Cardiology (ESC) Working Group on Grown-up Congenital heart disease, endorsed by HRS, PACES, APHRS, and SOLAECE. Europace. 2018;20:1719-1753.

46. Khairy P, Van Hare GF, Balaji S, Berul CI, Cecchin F, Cohen MI, Daniels CJ, Deal BJ, Dearani JA, Groot N, et al. PACES/HRS Expert Consensus Statement on the Recognition and Management of Arrhythmias in Adult Congenital Heart Disease: developed in partnership between the Pediatric and Congenital Electrophysiology Society (PACES) and the Heart Rhythm Society (HRS). Endorsed by the governing bodies of PACES, HRS, the American College of Cardiology (ACC), the American Heart Association (AHA), the European Heart Rhythm Association (EHRA), the Canadian Heart Rhythm Society (CHRS), and the International Society for Adult Congenital Heart Disease (ISACHD). Heart Rhythm. 2014;11:e102-165.

47. Kawara T, Derksen R, de Groot JR, Coronel R, Tasseron S, Linnenbank AC, Hauer RN, Kirkels H, Janse MJ, de Bakker JM. Activation delay after premature stimulation in chronically diseased human myocardium relates to the architecture of interstitial fibrosis. Circulation. 2001;104:3069-3075.

48. Coronel R, Wilms-Schopman FJ, Opthof T, Janse MJ. Dispersion of repolarization and arrhythmogenesis. Heart Rhythm. 2009;6:537-543.

49. Arita M, Kiyosue T. Modification of "depressed fast channel dependent slow conduction" by lidocaine and verapamil in the presence or absence of catecholamines--evidence for alteration of preferential ionic channels

37

for slow conduction. Jpn Circ J. 1983;47:68-81.

50. Cantwell CD, Roney CH, Ng FS, Siggers JH, Sherwin SJ, Peters NS. Techniques for automated local activation time annotation and conduction velocity estimation in cardiac mapping. Comput Biol Med. 2015;65:229-242.

51. Stiles MK, John B, Wong CX, Kuklik P, Brooks AG, Lau DH, Dimitri H, Roberts-Thomson KC, Wilson L, De Sciscio P, et al. Paroxysmal lone atrial fibrillation is associated with an abnormal atrial substrate: characterizing the "second factor". J Am Coll Cardiol. 2009;53:1182-1191.

52. Prabhu S, Voskoboinik A, McLellan AJA, Peck KY, Pathik B, Nalliah CJ, Wong GR, Azzopardi SM, Lee G, Mariani J, et al. A comparison of the electrophysiologic and electroanatomic characteristics between the right and left atrium in persistent atrial fibrillation: Is the right atrium a window into the left? J Cardiovasc Electrophysiol. 2017;28:1109-1116.

53. Zheng Y, Xia Y, Carlson J, Kongstad O, Yuan S. Atrial average conduction velocity in patients with and without paroxysmal atrial fibrillation. Clin Physiol Funct Imaging. 2017;37:596-601.

54. Bayly PV, KenKnight BH, Rogers JM, Hillsley RE, Ideker RE, Smith WM. Estimation of conduction velocity vector fields from epicardial mapping data. IEEE Trans Biomed Eng. 1998;45:563-571.

55. Eckstein J, Zeemering S, Linz D, Maesen B, Verheule S, van Hunnik A, Crijns H, Allessie MA, Schotten U. Transmural conduction is the predominant mechanism of breakthrough during atrial fibrillation: evidence from simultaneous endo-epicardial high-density activation mapping. Circ Arrhythm Electrophysiol. 2013;6:334-341.

56. de Groot NM, Houben RP, Smeets JL, Boersma E, Schotten U, Schalij MJ, Crijns H, Allessie MA. Electropathological substrate of longstanding persistent atrial fibrillation in patients with structural heart disease: epicardial breakthrough. Circulation. 2010;122:1674-1682.

57. Maesen B, Zeemering S, Afonso C, Eckstein J, Burton RA, van Hunnik A, Stuckey DJ, Tyler D, Maessen J, Grau V, et al. Rearrangement of atrial bundle architecture and consequent changes in anisotropy of conduction constitute the 3-dimensional substrate for atrial fibrillation. Circ Arrhythm Electrophysiol. 2013;6:967-975.

58. Verheule S, Tuyls E, van Hunnik A, Kuiper M, Schotten U, Allessie M. Fibrillatory conduction in the atrial free walls of goats in persistent and permanent atrial fibrillation. Circ Arrhythm Electrophysiol. 2010;3:590-599.

59. Roney CH, Cantwell CD, Bayer JD, Qureshi NA, Lim PB, Tweedy JH, Kanagaratnam P, Peters NS, Vigmond EJ, Ng FS. Spatial Resolution Requirements for Accurate Identification of Drivers of Atrial Fibrillation. Circ Arrhythm Electrophysiol. 2017;10:e004899.

60. Konings KT, Kirchhof CJ, Smeets JR, Wellens HJ, Penn OC, Allessie MA. High-density mapping of electrically induced atrial fibrillation in humans. Circulation. 1994;89:1665-1680.

61. Spach MS. Anisotropy of cardiac tissue: a major determinant of conduction? J Cardiovasc Electrophysiol. 1999;10:887-890.

62. Spach MS, Dolber PC. Relating extracellular potentials and their derivatives to anisotropic propagation at a microscopic level in human cardiac muscle. Evidence for electrical uncoupling of side-to-side fiber connections with increasing age. Circ Res. 1986;58:356-371.

63. Cabo C, Pertsov AM, Baxter WT, Davidenko JM, Gray RA, Jalife J. Wave-front curvature as a cause of slow conduction and block in isolated cardiac muscle. Circ Res. 1994;75:1014-1028.

64. Spach MS, Miller WT, 3rd, Geselowitz DB, Barr RC, Kootsey JM, Johnson EA. The discontinuous nature of propagation in normal canine cardiac muscle. Evidence for recurrent discontinuities of intracellular resistance that affect the membrane currents. Circ Res. 1981;48:39-54.

65. Hansson A, Holm M, Blomstrom P, Johansson R, Luhrs C, Brandt J, Olsson SB. Right atrial free wall conduction velocity and degree of anisotropy in patients with stable sinus rhythm studied during open heart surgery. Eur Heart J. 1998;19:293-300.

66. Krul SP, Berger WR, Smit NW, van Amersfoorth SC, Driessen AH, van Boven WJ, Fiolet JW, van Ginneken AC, van der Wal AC, de Bakker JM, et al. Atrial fibrosis and conduction slowing in the left atrial appendage of patients undergoing thoracoscopic surgical pulmonary vein isolation for atrial fibrillation. Circ Arrhythm Electrophysiol. 2015;8:288-295.

67. Angel N, Li LI, Macleod RS, Marrouche N, Ranjan R, Dosdall DJ. Diverse Fibrosis Architecture and Premature Stimulation Facilitate Initiation of Reentrant Activity Following Chronic Atrial Fibrillation. J Cardiovasc Electrophysiol. 2015;26:1352-1360.

68. Linnenbank AC, de Bakker JM, Coronel R. How to measure propagation velocity in cardiac tissue: a simulation study. Front Physiol. 2014;5:267.

69. Kleber AG, Janse MJ, Wilms-Schopmann FJ, Wilde AA, Coronel R. Changes in conduction velocity during acute ischemia in ventricular myocardium of the isolated porcine heart. Circulation. 1986;73:189-198.

70. Aslanidi OV, Colman MA, Stott J, Dobrzynski H, Boyett MR, Holden AV, Zhang H. 3D virtual human atria: A computational platform for studying clinical atrial fibrillation. Prog Biophys Mol Biol. 2011;107:156-168.

71. Pashakhanloo F, Herzka DA, Ashikaga H, Mori S, Gai N, Bluemke DA, Trayanova NA, McVeigh ER. Myofiber Architecture of the Human Atria as Revealed by Submillimeter Diffusion Tensor Imaging. Circ Arrhythm Electrophysiol. 2016;9:e004133.

72. Zhao J, Hansen BJ, Csepe TA, Lim P, Wang Y, Williams M, Mohler PJ, Janssen PM, Weiss R, Hummel JD, et al. Integration of High-Resolution Optical Mapping and 3-Dimensional Micro-Computed Tomographic Imaging to Resolve the Structural Basis of Atrial Conduction in the Human Heart. Circ Arrhythm Electrophysiol. 2015;8:1514-1517.

73. Zhao J, Hansen BJ, Wang Y, Csepe TA, Sul LV, Tang A, Yuan Y, Li N, Bratasz A, Powell KA, et al. Three-dimensional Integrated Functional, Structural, and Computational Mapping to Define the Structural "Fingerprints" of Heart-Specific Atrial Fibrillation Drivers in Human Heart Ex Vivo. J Am Heart Assoc. 2017;6.

74. Roney CH, Bayer JD, Cochet H, Meo M, Dubois R, Jais P, Vigmond EJ. Variability in pulmonary vein electrophysiology

and fibrosis determines arrhythmia susceptibility and dynamics. PLoS Comput Biol. 2018;14:e1006166.

75.   Hansen BJ, Zhao J, Csepe TA, Moore BT, Li N, Jayne LA, Kalyanasundaram A, Lim P, Bratasz A, Powell KA, et al. Atrial fibrillation driven by micro-anatomic intramural re-entry revealed by simultaneous sub-epicardial and sub-endocardial optical mapping in explanted human hearts. Eur Heart J. 2015;36:2390-2401.

76.   Aslanidi OV, Colman MA, Varela M, Zhao J, Smaill BH, Hancox JC, Boyett MR, Zhang H. Heterogeneous and anisotropic integrative model of pulmonary veins: computational study of arrhythmogenic substrate for atrial fibrillation. Interface Focus. 2013;3:20120069.

77.   He J, Pertsov AM, Cherry EM, Fenton FH, Roney CH, Niederer SA, Zang Z, Mangharam R. Fiber Organization Has Little Effect on Electrical Activation Patterns During Focal Arrhythmias in the Left Atrium. IEEE Trans Biomed Eng. 2023;70:1611-1621.

78.   Haissaguerre M, Jais P, Shah DC, Takahashi A, Hocini M, Quiniou G, Garrigue S, Le Mouroux A, Le Metayer P, Clementy J. Spontaneous initiation of atrial fibrillation by ectopic beats originating in the pulmonary veins. N Engl J Med. 1998;339:659-666.

79.   Nademanee K, McKenzie J, Kosar E, Schwab M, Sunsaneewitayakul B, Vasavakul T, Khunnawat C, Ngarmukos T. A new approach for catheter ablation of atrial fibrillation: mapping of the electrophysiologic substrate. J Am Coll Cardiol. 2004;43:2044-2053.

80.   Rolf S, Kircher S, Arya A, Eitel C, Sommer P, Richter S, Gaspar T, Bollmann A, Altmann D, Piedra C, et al. Tailored atrial substrate modification based on low-voltage areas in catheter ablation of atrial fibrillation. Circ Arrhythm Electrophysiol. 2014;7:825-833.

81.   Narayan SM, Krummen DE, Shivkumar K, Clopton P, Rappel WJ, Miller JM. Treatment of atrial fibrillation by the ablation of localized sources: CONFIRM (Conventional Ablation for Atrial Fibrillation With or Without Focal Impulse and Rotor Modulation) trial. J Am Coll Cardiol. 2012;60:628-636.

82.   Magnani S, Muser D, Chik W, Santangeli P. Adjunct ablation strategies for persistent atrial fibrillation-beyond pulmonary vein isolation. J Thorac Dis. 2015;7:178-184.

83.   Terricabras M, Piccini JP, Verma A. Ablation of persistent atrial fibrillation: Challenges and solutions. J Cardiovasc Electrophysiol. 2020;31:1809-1821.

84.   O'Neill L, Wielandts JY, Gillis K, Hilfiker G, Le Polain De Waroux JB, Tavernier R, Duytschaever M, Knecht S. Catheter Ablation in Persistent AF, the Evolution towards a More Pragmatic Strategy. J Clin Med. 2021;10.

85.   Sakamoto S, Yamauchi S, Yamashita H, Imura H, Maruyama Y, Ogasawara H, Hatori N, Shimizu K. Intraoperative mapping of the right atrial free wall during sinus rhythm: variety of activation patterns and incidence of postoperative atrial fibrillation. Eur J Cardiothorac Surg. 2006;30:132-139.

86.   van der Heijden CAJ, Weberndorfer V, Vroomen M, Luermans JG, Chaldoupi SM, Bidar E, Vernooy K, Maessen JG, Pison L, van Kuijk SMJ, et al. Hybrid Ablation Versus Repeated Catheter Ablation in Persistent Atrial Fibrillation: A Randomized Controlled Trial. JACC Clin Electrophysiol. 2023.

87.   D'Agostino RS, Jacobs JP, Badhwar V, Fernandez FG, Paone G, Wormuth DW, Shahian DM. The Society of Thoracic Surgeons Adult Cardiac Surgery Database: 2019 Update on Outcomes and Quality. Ann Thorac Surg. 2019;107:24-32.

88.   LaPar DJ, Speir AM, Crosby IK, Fonner E, Jr., Brown M, Rich JB, Quader M, Kern JA, Kron IL, Ailawadi G, et al. Postoperative atrial fibrillation significantly increases mortality, hospital readmission, and hospital costs. Ann Thorac Surg. 2014;98:527-533; discussion 533.

89.   Aranki SF, Shaw DP, Adams DH, Rizzo RJ, Couper GS, VanderVliet M, Collins JJ, Jr., Cohn LH, Burstin HR. Predictors of atrial fibrillation after coronary artery surgery. Current trends and impact on hospital resources. Circulation. 1996;94:390-397.

90.   Echahidi N, Pibarot P, O'Hara G, Mathieu P. Mechanisms, prevention, and treatment of atrial fibrillation after cardiac surgery. J Am Coll Cardiol. 2008;51:793-801.

91.   Yamashita K, Hu N, Ranjan R, Selzman CH, Dosdall DJ. Clinical Risk Factors for Postoperative Atrial Fibrillation among Patients after Cardiac Surgery. Thorac Cardiovasc Surg. 2019;67:107-116.

92.   Auer J, Weber T, Berent R, Ng CK, Lamm G, Eber B. Risk factors of postoperative atrial fibrillation after cardiac surgery. J Card Surg. 2005;20:425-431.

93.   Korantzopoulos P, Kolettis T, Siogas K, Goudevenos J. Atrial fibrillation and electrical remodeling: the potential role of inflammation and oxidative stress. Med Sci Monit. 2003;9:RA225-229.

94.   Ozben B, Akaslan D, Sunbul M, Filinte D, Ak K, Sari I, Tigen K, Basaran Y. Postoperative Atrial Fibrillation after Coronary Artery Bypass Grafting Surgery: A Two-dimensional Speckle Tracking Echocardiography Study. Heart Lung Circ. 2016;25:993-999.

95.   Hogue CW, Jr., Hyder ML. Atrial fibrillation after cardiac operation: risks, mechanisms, and treatment. Ann Thorac Surg. 2000;69:300-306.

96.   Serban C, Arinze JT, Starreveld R, Lanters EAH, Yaksh A, Kik C, Acardag Y, Knops P, Bogers A, de Groot NMS. The impact of obesity on early postoperative atrial fibrillation burden. J Thorac Cardiovasc Surg. 2020;159:930-938 e932.

97.   Schram-Serban C, Heida A, Roos-Serote MC, Knops P, Kik C, Brundel B, Bogers A, de Groot NMS. Heterogeneity in Conduction Underlies Obesity-Related Atrial Fibrillation Vulnerability. Circ Arrhythm Electrophysiol. 2020;13:e008161.

98.   Dobrev D, Aguilar M, Heijman J, Guichard JB, Nattel S. Postoperative atrial fibrillation: mechanisms, manifestations and management. Nat Rev Cardiol. 2019;16:417-436.

99.   Maesen B, Nijs J, Maessen J, Allessie M, Schotten U. Post-operative atrial fibrillation: a maze of mechanisms. Europace. 2012;14:159-174.

100. Teuwen CP, Korevaar TIM, Coolen RL, van der Wel T, Houck CA, Evertz R, Yaksh A, Roos-Hesselink JW, Bogers

37

A, de Groot NMS. Frequent atrial extrasystolic beats predict atrial fibrillation in patients with congenital heart defects. Europace. 2018;20:25-32.

101. Yaksh A, Kik C, Knops P, van Ettinger MJ, Bogers AJ, de Groot NM. Early, de novo atrial fibrillation after coronary artery bypass grafting: Facts and features. Am Heart J. 2017;184:62-70.

102. Feins EN, O'Leary ET, Hoganson DM, Schulz N, Eickoff E, Davee J, Triedman JK, Baird CW, Del Nido PJ, Emani S, et al. Intraoperative conduction mapping in complex congenital heart surgery. JTCVS Tech. 2022;12:159-163.

103. Sanders P, Morton JB, Kistler PM, Spence SJ, Davidson NC, Hussin A, Vohra JK, Sparks PB, Kalman JM. Electrophysiological and electroanatomic characterization of the atria in sinus node disease: evidence of diffuse atrial remodeling. Circulation. 2004;109:1514-1522.

104. Hwang C, Wu TJ, Doshi RN, Peter CT, Chen PS. Vein of marshall cannulation for the analysis of electrical activity in patients with focal atrial fibrillation. Circulation. 2000;101:1503-1505.

105. Barrio-Lopez MT, Sanchez-Quintana D, Garcia-Martinez J, Betancur A, Castellanos E, Arceluz M, Ortiz M, Nevado-Medina J, Garcia F, Almendral J. Epicardial Connections Involving Pulmonary Veins: The Prevalence, Predictors, and Implications for Ablation Outcome. Circ Arrhythm Electrophysiol. 2020;13:e007544.

106. Ben Morrison T, Jared Bunch T, Gersh BJ. Pathophysiology of concomitant atrial fibrillation and heart failure: implications for management. Nat Clin Pract Cardiovasc Med. 2009;6:46-56.

107. Xu B, He F, Wang S, Chen H, Zhang W. Modified Mini-Maze for Atrial Fibrillation with Interruption of Inferior Vena Cava. Heart Surg Forum. 2021;24:E1046-E1048.

108. Scherlag BJ, Yeh BK, Robinson MJ. Inferior interatrial pathway in the dog. Circ Res. 1972;31:18-35.

109. Bayes de Luna A, Escobar-Robledo LA, Aristizabal D, Weir Restrepo D, Mendieta G, Masso van Roessel A, Elosua R, Bayes-Genis A, Martinez-Selles M, Baranchuk A. Atypical advanced interatrial blocks: Definition and electrocardiographic recognition. J Electrocardiol. 2018;51:1091-1093.

110. Waldo AL, Bush HL, Jr., Gelband H, Zorn GL, Jr., Vitikainen KJ, Hoffman BF. Effects on the canine P wave of discrete lesions in the specialized atrial tracts. Circ Res. 1971;29:452-467.

111. Moore JP, Gallotti RG, Shannon KM, Biniwale R. A minimally invasive hybrid approach for cardiac resynchronization of the systemic right ventricle. Pacing Clin Electrophysiol. 2019;42:171-177.

112. Rad MM, Blaauw Y, Dinh T, Pison L, Crijns HJ, Prinzen FW, Vernooy K. Left ventricular lead placement in the latest activated region guided by coronary venous electroanatomic mapping. Europace. 2015;17:84-93.

113. Infeld M, Nicoli CD, Meagher S, Tompkins BJ, Wayne S, Irvine B, Betageri O, Habel N, Till S, Lobel J, et al. Clinical impact of Bachmann's bundle pacing defined by electrocardiographic criteria on atrial arrhythmia outcomes. Europace. 2022;24:1460-1468.

114. Andreas M, Arzl P, Mitterbauer A, Ballarini NM, Kainz FM, Kocher A, Laufer G, Wolzt M. Electrical Stimulation of the Greater Auricular Nerve to Reduce Postoperative Atrial Fibrillation. Circ Arrhythm Electrophysiol. 2019;12:e007711.

115. Kharbanda RK, van der Does WFB, van Staveren LN, Taverne Y, Bogers A, de Groot NMS. Vagus Nerve Stimulation and Atrial Fibrillation: Revealing the Paradox. Neuromodulation. 2022;25:356-365.

116. Stavrakis S, Kulkarni K, Singh JP, Katritsis DG, Armoundas AA. Autonomic Modulation of Cardiac Arrhythmias: Methods to Assess Treatment and Outcomes. JACC Clin Electrophysiol. 2020;6:467-483.

117. Jiang RH, Po SS, Tung R, Liu Q, Sheng X, Zhang ZW, Sun YX, Yu L, Zhang P, Fu GS, et al. Incidence of pulmonary vein conduction recovery in patients without clinical recurrence after ablation of paroxysmal atrial fibrillation: mechanistic implications. Heart Rhythm. 2014;11:969-976.

37
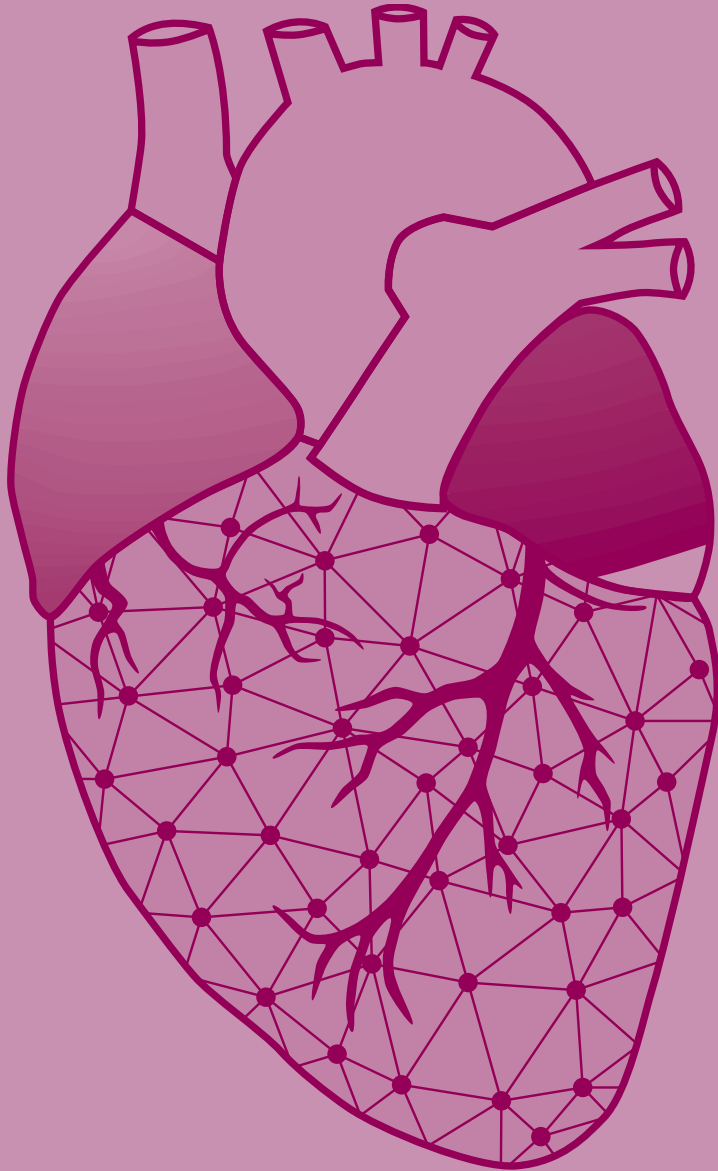
Chapter **38**

English summary

Mathijs S. van Schie

Although electrophysiological mapping-guided ablation strategies targeting atrial fibrillation (AF) have improved considerably over the past few years, designing effective strategies for persistent AF remains a major challenge. As a result, treatment options are not always efficient and AF recurrence is common even after extensive ablative therapy. As a general introduction of this thesis, **chapter 1** provides background information on the etiology and therapeutic options of AF, and techniques to examine electrophysiological properties of cardiac tissue. This thesis aims to further identify and quantify electrophysiological alterations underlying onset and progression of AF in patients undergoing cardiac surgery. Once AF-related electropathology is identified, it can be used as an electrical marker to guide ablative therapy of AF.

Chapter 2 presents a summary of current knowledge regarding AF-related electropathology during sinus rhythm. Several electrophysiological parameters have been identified as indicators of AF-related electropathology during sinus rhythm. These indicators were not only found at the left atrium, but also at the right atrium and even more frequently at Bachmann's bundle. This clearly indicates the presence of AF-related electropathology outside the left atrium, confirming the hypothesis that AF is not just a solely left-sided disease. Even during sinus rhythm, electropathology may be missed when mapping is performed only at the endocardium or epicardium. Hence, conduction is three-dimensional (3D) and complex even during sinus rhythm. Interestingly, patients with AF show more electropathology detectable compared to those without AF, particularly at Bachmann's bundle.

During AF, electrograms recorded at any arbitrary location in the atria show beat-to-beat variation in intervals between consecutive fibrillation potentials and the morphology of those potentials. The morphology of fibrillation potentials not only provides information on the moment of local excitation but also on the presence of atrial electropathology. In **chapter 3**, methodologies and outcomes of electrogram-guided AF ablation approaches are critically reviewed. Moreover, current understandings of sinus rhythm and fibrillation electrogram morphologies are discussed from an experimental point of view.

Electrical signal markers related to electropathology

The severity and extensiveness of electropathology may be reflected by alterations in electrical signal characteristics. One of these features is the amplitude of unipolar potentials. Unipolar voltage mapping is increasingly used to guide ablative therapy for AF because unipolar electrograms are not influenced by electrode orientation or atrial wavefront direction, unlike bipolar electrograms. **Chapter 4** presents individual, high-resolution unipolar sinus rhythm voltage fingerprints to identify low-voltage areas (LVAs) and investigate the effect of AF episodes on unipolar voltages in patients with mitral valve disease. A total of 600,722 potentials were analyzed from 829 sinus rhythm recordings. We demonstrated that there was no significant correlation between unipolar potential voltages and conduction velocity, while smaller potential voltages were recorded in areas of conduction slowing (<28 cm/s; 1.7 [0.9–3.5] vs. 4.7 [2.5–7.6] mV, p<0.001) and surrounding conduction block (<18 cm/s; 1.2 [0.7–2.3] vs. 4.8 [2.6–7.7] mV, p<0.001) compared to areas with normal conduction (≥28 cm/s). Fractionated potentials had lower amplitudes compared to single potentials (2.1 [1.0–3.8] vs. 5.2 [2.9–8.0] mV, p<0.001) and a clear decrease in unipolar potential voltages was found with a larger number of deflections (1: 5.2 [2.9–8.0] mV; 2: 2.2 [1.1–4.0] mV; 3: 1.2 [0.7–2.3] mV; ≥4: 0.9 [0.5–1.7] mV, p<0.001 for all). Even during sinus rhythm, advanced atrial remodeling in patients with mitral valve disease shows marked inter-individual and regional variation. Low-voltage potentials were present in all patients and no predilection sites for LVAs were found. However, patients with paroxysmal AF had lower potential voltages (no AF: 4.9 [3.5–6.1] vs. AF: 3.0 [2.2–4.6] mV, p=0.007) and a higher number of LVAs (no AF: 2.1 [0.5–

38

7.7] vs. AF: 12.9 [3.2–23.6] %, p=0.001) at Bachmann's bundle compared to those without AF. As low-voltage potentials were even present in patients without a history of AF, low unipolar potential voltages should carefully be used as target sites for ablative therapy.

The morphology of unipolar single potentials was further examined in **chapter 5**. Unipolar single potentials are comprised of a positive (R-wave) and negative (S-wave) component, which contain valuable information on intra-atrial conduction and possibly the substrate underlying AF. We demonstrated a clear predominance of S-waves at Bachmann's bundle and the right atrium in both patients with and without a history of paroxysmal AF (Bachmann's bundle: 88.8% vs. 85.9%, right atrium: 92.1% vs. 85.1%, respectively). Moreover, the paroxysmal AF group exhibited lower single potential voltages at the right atrium, Bachmann's bundle and the pulmonary vein area (p<0.001 for each) which were mainly determined by the size of the S-wave amplitudes. The largest difference in S-wave amplitude was observed at Bachmann's bundle where the paroxysmal AF group had a lower S-wave amplitude (4.1 [2.5–6.1] vs. 2.9 [1.4–4.8] mV, p<0.001). Additionally, paroxysmal AF patients had a lower conduction velocity at Bachmann's bundle (97 [70–121] vs. 89 [62–116] cm/s, p<0.001). Although excitation of the atria is heterogeneously disrupted during sinus rhythm, our findings suggest that a history of AF is characterized by decreased single potential amplitudes at Bachmann's bundle due to loss of S-wave amplitudes and decreased conduction velocity. This highlights the potential usefulness of single potential morphology in providing additional information on wavefront propagation.

Low-voltage potentials as markers for electropathology

As LVAs are considered indicators of the arrhythmogenic substrates promoting AF, **chapter 6** aimed to compare the extent of atrial LVAs in obese and non-obese patients to identify predilection sites for LVAs to occur. A matched cohort of 212 patients was used for the study. Obese patients were characterized by lower voltages (4.5 [0.4–16.2] vs. 5.5 [0.8–18.0] mV, p<0.001), especially at Bachmann's bundle (4.1 [0.4–12.3] vs. 6.2 [1.0–14.3] mV, p<0.001) and the left atrium (5.1 [0.5–10.1] vs. 6.2 [0.8–15.9] mV, p=0.003). Also, obese patients had a higher percentage of LVAs, particularly at Bachmann's bundle (2.9 [0.0–77.1] vs. 0.9 [0.0–42.0] %, p<0.001). The number of LVAs correlated with incidences of conduction block, while BMI and the number of LVAs were independent predictors for the incidence of early post-operative AF. This study suggests that obesity may predispose to an overall decrease in atrial potential voltages and a higher number of LVAs, and that Bachmann's bundle is a predilection site for LVAs within the atria of obese patients.

Voltage mapping considerably depends on the use of either unipolar or bipolar electrograms, each having its own advantages and disadvantages. Besides, it remains very challenging to define a proper threshold to identify LVAs, and it also remains unknown whether unipolar, bipolar and omnipolar potential voltages are complementary or contradictory on identifying LVAs at a high-resolution scale. In **chapter 7**, we investigated the similarities and dissimilarities in unipolar, bipolar and omnipolar potential voltage distribution and explored the relation between various types of potential voltages and conduction velocity in identification of LVAs. Within square areas defined by 2×2 electrodes (a clique), the maximal unipolar, bipolar and omnipolar potential voltages and mean conduction velocity were computed. A total of 193 mapping locations were used, including 175,667 unipolar and 306,685 bipolar recordings from which 146,015 cliques were created. There were considerable directional differences in bipolar potential voltages, as the largest bipolar potential voltage was on average 1.7 (ranging from 1.0 to 59.0) times larger than the corresponding perpendicular bipolar potential voltages. These differences had a major impact on identification of LVAs. Unipolar clique voltages were larger than both bipolar and omnipolar clique voltages (7.1

[4.2–10.6] vs. 5.3 [2.4–9.6] and 5.8 [2.6–10.5] mV respectively, p<0.001). Applying omnipolar clique voltages on bipolar LVAs showed that 14.6% of these LVAs were initially misidentified. All bipolar or omnipolar LVAs corresponded to a broad spectrum of unipolar clique voltages and, although conduction velocity was generally decreased, still high conduction velocities and large unipolar clique voltages could be found in these areas. Due to high interindividual unipolar clique voltage variations within LVAs, no clear unipolar threshold was found for correct identification of LVAs. This study illustrates that LVAs critically depend on the mapping technique used. Future studies are needed to examine whether a combination of unipolar and omnipolar potential voltages are more indicative of true LVAs.

In most clinical settings, endocardial bipolar voltage mapping is still mainly used to identify LVAs. However, in recent perspective, it has become clear that bipolar LVAs could be located exclusively at either the endo- or epicardium. In **chapter 8**, we examined endo- and epicardial characteristics of unipolar and omnipolar voltages, explored the relation between various types of voltages in identification of LVAs and examined whether characteristics of LVAs can be predictive for LVAs at the opposite layer. Simultaneous endo-epicardial mapping was performed during sinus rhythm at the right atrium in 93 patients. A total of 281 mapping locations resulted in 406,571 unipolar and 723,595 bipolar recordings from which 164,704 matched cliques were created for both the endo- and epicardium (329,408 in total). In 61% of cliques, unipolar clique voltages at the epicardium were larger than the corresponding endocardial unipolar clique voltages (8.2 [4.9–11.6] vs. 6.1 [3.2–10.9] mV, p<0.001). Omnipolar clique voltage at the epicardium was larger than the corresponding endocardial omnipolar clique voltage in 64% of the cliques (6.7 [3.2–10.9] vs. 3.3 [1.1–8.6] mV, p<0.001). The majority of both unipolar and omnipolar LVAs were located at only the endocardium (74.2% and 82.0% respectively) or epicardium (52.7% and 47.6% respectively). Of the endocardial unipolar LVAs, 25.8% were also located at the opposite layer and 47.3% vice-versa. In omnipolar LVAs, 18.0% of the endocardial LVAs were also located at the epicardium and 52.4% vice-versa. The combination of epicardial unipolar and omnipolar clique voltages was most accurate in identifying dual-layer LVAs (50.4%, AUC=0.89). An endo-epicardial mapping approach using unipolar and omnipolar voltages is therefore favored to accurately identify LVAs.

Signal morphology: more than just voltage

Catheter ablation strategies targeting fractionated or low-voltage potentials have been widely used in patients with persistent types of AF. The application of these strategies in AF treatment initially showed positive outcomes in mostly single center studies, but are now increasingly followed by negative outcomes in (large) randomized controlled trials. While fractionation and low-voltage are considered to occur at sites of conduction slowing, and therefore critical in initiation and perpetuation of AF, they can also occur due to non-pathologic reasons. In **chapter 9**, the relationship between local conduction velocity and the occurrence of fractionated and/or low-voltage potentials in order to identify areas with critically slowing of conduction. The study included 319 patients with coronary artery disease or mitral valve disease with or without history of AF. Fractionated, low-voltage potentials were rare, accounting for only 0.4 [0.2–0.8] % of all atrial sites. Local CV at sites with fractionated, low-voltage potentials (46.0 [22.6–72.7] cm/s) was considerably lower compared to sites with either low-voltage, non-fractionated potentials (64.5 [34.8–99.4] cm/s) and fractionated, high-voltage potentials (65.9 [41.7–92.8] cm/s, p<0.001 for each). These specific potentials were more common in patients with prior AF episodes, particularly at the pulmonary vein area and Bachmann's bundle. Slow conduction areas (<50 cm/s) could be most accurately identified by using a low voltage threshold (<1 mV) and a minimum of 3 deflections (positive predictive value: 54.2–70.7%), although the overall sensitivity remained low (0.1–1.9%). The strong inverse relationship between the positive predictive value and

38

sensitivity will therefore likely complicate the use of these signal-based ablation approaches in AF patients for identifying slow conduction zones.

In non-uniform anisotropic tissue, conduction disorders exhibit direction and frequency dependency, which often leads to fractionated potentials. The use of unipolar potential morphology can help detect areas of non-uniform anisotropic tissue. The effects of various degrees of prematurity and aberrancy of spontaneous AES on unipolar potential morphology is studied in **chapter 10**. The study included 837 unique AES recorded in 287 patients (60 with history of AF). The most prominent effects on potential morphology parameters were related to the degree of aberrancy. In particular, AES with wavefront propagation direction opposite or perpendicular to sinus rhythm resulted in the most significant decrease in potential voltages (-1.6 [-2.2, -1.1] mV and -1.7 [-2.0, -1.4] mV respectively, p<0.001) and increase in fractionation (+11.1 [6.0, 10.1] % and +13.4 [10.3, 16.5] % respectively, p<0.001), irrespective of the degree of prematurity (R^2<0.299, p<0.001). Although effects were found at all atrial sites, there were large interregional differences. Specifically, at the right atrium, patients with a history of AF had a substantial decrease in potential voltages (-2.8 [-3.5, -2.1] vs. -1.2 [-1.7, -0.7] mV, p<0.001) and increase in fractionation (+25.6 [16.5, 34.7] vs. +8.9 [4.4, 13.5] %, p=0.002), indicating enhanced non-uniform anisotropy. Therefore, unipolar potential morphology during spontaneous AES is primarily directional-dependent, rather than rate-dependent. As AF patients have more severe direction-dependent conduction disorders, enhanced non-uniform anisotropy present in these patients probably explains the higher vulnerability to trigger episodes of AF.

The size (or diameter) of the recording electrode is an important parameter that can affect characteristics of the recorded electrograms. In **chapter 11**, both simulated and clinical data were used to analyze the effect of electrode size on overall error in local activation time estimation, length of slow conduction or block lines, LVAs and potential fractionation. Electrogram arrays were simulated for 2D tissues with three different levels of conduction heterogeneity to model inhomogeneous wave propagation which is also observed during AF. Increasing the electrode size increased the error in local activation time estimation and decreased the length of conduction block lines in both simulated and clinical data. Moreover, local activation time maps generated by larger electrodes were more homogeneous with a lower number of observed wavelets. Increasing the electrode size also raised the amount of LVAs, while it decreased potential slopes and number of deflections. This effect was more pronounced for tissues with a higher level of conduction heterogeneity. Thus, the electrode size considerably affects electrogram morphology and local activation time maps. These effects need to be considered while performing any analysis on electrograms or while comparing results obtained via electrodes with different sizes.

Combination of electrical signal features: towards a signal fingerprint

The severity and extensiveness of inhomogeneity in conduction may be reflected by an electrical signal profile containing quantified features of unipolar electrogram morphology. This would provide a patient-tailored arrhythmogenic substrate profile. As a first step towards construction of such a diagnostic signal fingerprint, **chapter 12** presents the regional differences in features of unipolar electrogram morphology in relation to inhomogeneous intra-atrial conduction during sinus rhythm in a large cohort of patients without atrial tachyarrhythmias. A total of 1,763,593 potentials were analyzed from 189 patients undergoing coronary artery bypass grafting. In all atrial regions, the majority of the electrograms consisted of single potentials (81.4 [48.9–100] %). The highest proportion of long-double and fractionated potentials was mainly recorded at the right atrium (4.0 [0–35.5] % and 1.3 [0–14.8] % respectively) and Bachmann's bundle (4.0 [0–35.5] % and 1.4

[0–14.8] % respectively). Fractionation at Bachmann's bundle had the longest durations. The largest prevalence of LVAs was found at the right atrium (5.8 [2.3–10.6] %). The presence of conduction block correlated with the proportion of long-double and fractionated potentials, fractionation duration and the prevalence of LVAs. Conduction inhomogeneity can therefore be identified by a signal fingerprint containing specific quantified electrogram features.

The next step was to construct the electrical signal fingerprint and use it to predict the degree of conduction inhomogeneity, which is demonstrated in **chapter 13**. The degree of intra-atrial conduction inhomogeneity was determined in 235 patients, after which the patients were subdivided into three groups (low, intermediate and high degree of conduction inhomogeneity). An increase in conduction inhomogeneity was associated with a decrease in unipolar potential voltages (low 5.7 [5.1–6.9] vs. high 4.0 [3.5–5.0] mV) and increase in the amount of LVAs (low 3.2 [1.8–5.6] vs. high 9.5 [6.1–13.0] %), long-double potentials (low 1.8 [1.1–3.2] vs. high 6.2 [4.6–8.1] %) and fractionated potentials (low 1.3 [0.6–2.0] vs. high 2.5 [1.5–3.9] %). An *Electrical Signal Fingerprint Score* was constructed for prediction of the degree of conduction inhomogeneity in each individual patient. The *Global Electrical Signal Fingerprint Score* (concordance index 0.92 [0.89–0.95]), containing the total number of LVAs and long-double potentials and fractionation duration, and the *Regional Electrical Signal Fingerprint Score* of the right atrium (concordance index 0.83 [0.78–0.89]), containing the number of LVAs and long-double potentials, had the highest predictive value for the severity of conduction inhomogeneity throughout both atria. Both *Electrical Signal Fingerprint Scores* were strongly related to the true degree of conduction inhomogeneity (r=0.82, p<0.001 an r=0.70, p<0.001). The severity of intra-atrial conduction inhomogeneity can be accurately quantified by the *Electrical Signal Fingerprint Score*, using solely electrophysiological characteristics of unipolar electrograms.

The incidence of AF is strongly associated with advancing age, but the impact of age on the morphology of unipolar electrograms and whether these changes are present throughout both atria is not well understood. In **chapter 14**, we examined sinus rhythm recordings of 213 patients who underwent coronary artery bypass grafting to assess age-related changes in unipolar electrogram morphology. The patients were divided into young (age<60) and aged (age≥60) groups. Only at Bachmann's bundle, a higher proportion of single potentials (p=0.007) was observed in the young group, while the aged group had a higher proportion of short-double (p=0.051), long-double (p=0.004) and fractionated potentials (p=0.006). After adjusting for potential confounders, we observed that older age was associated with a reduction in single potentials (β: -6.33, 95% CI: -10.5 to -2.3) and an increase in short-double (β: 2.5, 95% CI: 0.1 to 4.9), long-double (β: 1.9, 95% CI: 0.2 to 3.7) and fractionated potentials (β: 1.9, 95% CI: 0.6 to 3.2). These findings suggest that age-related remodeling predominantly affects Bachmann's bundle and may be a crucial factor in the development of age-related arrhythmias such as AF.

Electrical asynchrony between the endo- and epicardium contributes to the perpetuation of AF, as patients with persistent AF have more endo-epicardial asynchrony (EEA) during sinus rhythm than patients without AF. Unipolar potential fractionation could originate from areas of EEA. In **chapter 15**, we introduced a novel method to estimate the amount of EEA by using unipolar electrogram characteristics recorded from either the endo- and/or epicardium. In 86 patients in whom simultaneous endo-epicardial mapping was performed, it was demonstrated that both endo- and epicardial sites of EEA were characterized by lower potential voltages (5.2 [2.8–9.1] vs. 1.6 [0.9–2.7] mV, p<0.001 and 7.4 [4.4–10.6] vs. 2.5 [1.2–4.7] mV, p<0.001, respectively), a higher number of long-double (5.5 vs. 35.3% and 3.5 vs. 27.3%, respectively) and fractionated potentials (1.9 vs. 14.4% and 1.6 vs. 9.7%), and longer duration of double (11 [7–18] vs. 20 [15–28] ms, p<0.001 and 9 [6–14] vs. 20 [13–30] ms, p<0.001,

38

respectively) and fractionated potentials (20 [14–27] vs. 28 [21–36] ms, p<0.001 and 20 [15–27] vs. 26 [19–39] ms, p<0.001, respectively). Patients with prior AF episodes were characterized by lower potential voltages in areas of EEA, along with alterations in the potential types. The *Endo-Epicardial Asynchrony Fingerprint Score*, containing the proportion of endocardial LVAs and duration of epicardial double potentials, had the highest predictive value for determining the degree of EEA (AUC: 0.91). The *Endocardial-* and *Epicardial Asynchrony Fingerprint Scores* separately also showed good predictive values (AUC: 0.90 and 0.83 respectively). Therefore, unipolar electrogram morphology can be used to identify areas of EEA, with the *Asynchrony Fingerprint Score* as a diagnostic tool to estimate the amount of EEA.

Areas of conduction block give rise to abnormalities in potential morphology and likely enhance endo-epicardial conduction delay. Prior mapping studies demonstrated that conduction block during sinus rhythm is more prevalent in patients with AF, which is caused by a higher degree of structural remodeling. These lines of conduction block can be located at either the endo- or epicardium only (single-sided conduction block) or at both layers (transmural conduction block), which in turn could enhance endo-epicardial conduction delay. In **chapter 16**, we performed simultaneous endo-epicardial mapping in 86 patients to investigate to which degree single-sided and transmural conduction block enhance endo-epicardial conduction delay and whether unipolar potential morphology associated with the different types of conduction block is predictive for transmural conduction block. We demonstrated that endo-epicardial conduction delay is mostly affected by the presence of transmural conduction block. These areas were characterized by lower potential voltages and a higher number of long-double and fractionated potentials as compared to areas of single-sided conduction block. Areas of transmural conduction block could be most accurately predicted by combining epicardial potential morphology parameters, including potential voltages, fractionation and fractionation duration (AUC=0.91). We therefore have identified potential features which can be used to locate areas of transmural conduction block, which in turn are indicative of areas of endo-epicardial conduction delay.

Abnormalities in wavefront propagation

Cardiac structural remodeling may underlie the development of electrical conduction disorders, such as slowing of conduction or conduction block. These conduction disorders affect propagation of the expanding wavefront and could be either structural or functional in nature. A previous mapping study demonstrated that young patients with Wolff-Parkinson-White syndrome with non-dilated atria presented with only a limited number of conduction disorders which were mainly functional in nature. Even in older patients with electrically non-remodeled atria undergoing coronary artery bypass grafting, it was demonstrated that only a limited amount of conduction block was present, although there was a considerable intra-atrial and inter-individual variation in prevalence of conduction block. In **chapter 17** the first evidence of atrial conduction disorders in pediatric patients with congenital heart disease is provided. Areas of conduction delay and block were present in all patients and were particularly observed at Bachmann's bundle (4.9% and 2.3% respectively), the right atrium (3.7% and 1.6% respectively) and left atrium (1.8% and 1.0% respectively). Slowing of conduction was more pronounced at the right atrium (maximal conduction time 44 ms) and Bachmann's bundle (maximal conduction time 25 ms). Even before surgical correction in the first year of life, atrial conduction abnormalities are already present in pediatric patients with congenital heart disease, predisposing them to atrial arrhythmias early in life.

Areas with slower conduction are considered as 'diseased tissue' and are associated with increased risk of wavefront reentry which may initiate AF. Accurate determination of intra-

atrial conduction velocity is essential to identify arrhythmogenic areas. Several techniques to estimate conduction velocity have already been introduced, including finite differences (FiD) and polynomial surface fitting (PSF). However, the most optimal estimation methodology to measure conduction heterogeneity has not been determined yet. In **chapter 18**, we introduced a novel technique using discrete velocity vectors (DVV) to estimate conduction velocity and identify areas of conduction heterogeneities. Furthermore, we identified the most suitable methodology to unravel local areas of conduction heterogeneities, quantified intra-atrial differences in conduction velocity and localized areas of conduction slowing associated with paroxysmal AF. A total of 4,109,926 potentials were analyzed out of 5,261 sinus rhythm recordings. The highest number of local conduction velocities were estimated using the DVV technique (97%), followed by the PSF technique (78%) and FiD technique (63%). The median atrial conduction velocity estimated using the DVV, PSF and FiD techniques was 90.0 [62.4–116.8], 92.0 [70.6–123.2] and 89.4 [62.5–126.5] cm/s, respectively. The largest difference in conduction velocity estimates was found between PSF and DVV which was caused by smaller conduction velocity magnitudes detected only by the DVV technique. All techniques showed that there was a considerable variation in conduction velocity between all atrial regions, but that the slowest conduction was observed at the right atrium and Bachmann's bundle. A lower conduction velocity was found at Bachmann's bundle in patients with paroxysmal AF compared with those without AF (79.1 [72.2–91.2] vs. 88.3 [79.3–97.2] cm/s, p<0.001). Yet, both the FiD and PSF techniques were unable to identify local conduction heterogeneities as these were masked by the smoothing properties of both techniques. Conduction heterogeneities could therefore be most accurately identified by the DVV technique.

A subsequent case-control study comparing intra-atrial conduction velocity in patients with and without AF is presented in **chapter 19**. Biatrial median conduction velocity did not differ between the two groups (90±8 vs. 92±6 cm/s respectively, p=0.56), but there was a reduction in conduction velocity at Bachmann's bundle in patients with a history of AF (79±12 vs. 88±11 cm/s, p=0.02). Patients without AF did not show a predilection site for the lowest conduction velocity (P_5), while in patients with AF, the lowest conduction velocity was most frequently measured at Bachmann's bundle (53%) with a range between 15 to 22 cm/s (median: 20 cm/s). The left atrium (18%) and pulmonary vein area (29%) also showed lowest conduction velocities, but not the right atrium. The study demonstrated that AF was associated with a prolonged total activation time (p=0.03) and decreased potential voltages (P_5) specifically at Bachmann's bundle (p=0.02), which emerged as a predilection site for conduction slowing in AF patients. Therefore, Bachmann's bundle may play an important role in the pathophysiology of AF.

In 27% of patients, AF resumes within 90 seconds after restoration of sinus rhythm by electrical cardioversion (ECV). This immediate recurrence of AF may be due to either a high frequency of ectopic beats or a supervulnerable period immediately after ECV. **Chapter 20** presents a case-control study that compares conduction heterogeneity in the supervulnerable period with long-term sinus rhythm in patients with a history of AF. Epicardial mapping of both atria was performed during sinus rhythm and premature AES. We demonstrated that for all atrial regions, there were no significant differences between the ECV and control group during both sinus rhythm and premature AES in prevalence and length of longest conduction block and continuous conduction delay-block lines, magnitude of conduction disorders, conduction velocity, biatrial activation time and potential voltages (p≥0.05). These observations suggest that the supervulnerable period may not be characterized by impaired intra-atrial conduction.

38

Impairment of conduction affecting the sinoatrial node

Propagation of the electrical wavefront from the sinoatrial node (SAN) into the surrounding atrial tissue is a complex 3D process. In **chapter 21** the results of endo-epicardial SAN mapping in twenty patients (40% history of AF) with structural heart disease undergoing cardiac surgery are presented. A total of 28 SAN focal activation patterns (SAN-FAPs) were analyzed (4 patients exhibited multiple SAN exit sites). Three distinct activation patterns were identified: 1) endocardial exit site (N=10), 2) epicardial exit site (n=13) and 3) simultaneously activated endo-epicardial exit sites (N=5). Median endo-epicardial delay at the origin of the SAN-FAP was 10 [6–14] ms and the prevalence of EEA in the surroundings of the SAN-FAP was 5 [2–18] %. These findings highlight the complex 3D geometry of the SAN and the presence of interindividual differences in SAN exit pathways. A caudal shift in SAN activation towards the mid right atrium (N=6) was solely observed in patients with history of AF, indicating changes in preferential SAN exit pathways.

SAN dysfunction is frequently observed in congenital heart disease patients, even after early surgical correction. This suggests that abnormalities in SAN geometry and function may already be present at birth, predisposing them to SAN dysfunction. In **chapter 22**, we presented the electrophysiological characteristics of SAN activity in 15 adult and 12 pediatric patients undergoing surgical correction. Only electrodes within 8 mm of the earliest site of activation at the right atrium were included for analysis and compared between pediatric and adult patients. Pediatric patients showed SAN activity only near the junction of the superior caval vein and the right atrium, while in adults, SAN activity extended even up to the middle part of the right atrium. The SAN region in adult patients exhibited slower conduction, lower potential voltages, more conduction block and a higher degree of fractionation compared to pediatric patients. At the earliest site of activation, pediatric patients showed broad, high-amplitude monophasic S-waves, while adult patients showed smaller, longer duration rS-potentials that were more frequently fractionated. Patients with a history of AF had even slower conduction (45.2 [35.1–63.9] vs. 73.3 [70.7–75.0] cm/s, p=0.039) and lower potential voltages (2.2 [2.0–3.1] vs. 4.1 [3.2–5.5] mV, p=0.027), suggesting disturbances in SAN impulse generation and propagation towards the atrial myocardium. These observations indicate that adult patients with uncorrected congenital heart disease exhibit more aging-related remodeling, which may partly explain why this population is prone to develop SAN dysfunction and atrial tachyarrhythmias.

In a subsequent case series, **chapter 23** describes three pediatric patients who developed early post-operative SAN dysfunction, and in whom epicardial mapping was performed. All three patients had either an inferior or multiple SAN exit sites, as well as extensive conduction disorders at the superior and inferior right atrium. These observations lend support to the hypothesis that pre-existing alterations in SAN exit sites, in combination with atrial conduction disorders, may make pediatric patients with congenital heart disease more susceptible to early post-operative SAN dysfunction.

Conduction abnormalities promoted by atrial extrasystoles

Conduction disorders in enhanced non-uniform anisotropic tissue are direction-dependent. Spontaneous aberrant AES could therefore be used to quantify direction-dependency of electrophysiological parameters. In **chapter 24**, outcomes of epicardial mapping of spontaneous aberrant AES in pediatric patients with congenital heart disease are presented. The aim of this study was to investigate to what extent spontaneous aberrant AES affect the occurrence of conduction disorders and morphology of extracellular potentials in this population as indicator of early, enhanced non-uniform anisotropy. During 41 AES, potential

voltages (7.1 [5.5–9.1] vs. 5.7 [4.0–7.5] mV, p<0.001) and conduction velocity (87.9 [76.7–101.6] vs. 84.5 [73.0–93.6] cm/s, p=0.013) decreased compared to corresponding sinus rhythm beats, whereas the number of fractionated potentials increased (12.7 [3.5–18.3] vs. 19.5 [10.5–30.0] %, p<0.001). Also, conduction disorders and LVAs were more prominent during AES. Changes in electrogram morphology parameters and conduction heterogeneity were not influenced by the degree of prematurity of AES (all p>0.05). This indicates that in pediatric patients with congenital heart disease, enhanced non-uniform anisotropic atrial conduction is already present and can be unmasked by AES.

Loss of cell-to-cell communication results in local conduction disorders and directional heterogeneity (LDH) in conduction velocity vectors. Premature AES may unmask areas of heterogeneous conduction, which are otherwise hidden during sinus rhythm. In **chapter 25**, we introduced LDH as a novel methodology and studied the differences between sinus rhythm and spontaneous AES in patients with and without history of AF. Individual conduction velocity vectors were compared with surrounding vectors to identify LDH. In total, 503 premature AES were recorded from 228 patients and used for analysis. During sinus rhythm, a significant amount of LDH was already present, particularly at Bachmann's bundle and the left atrium (11.9 [8.3–14.9] % and 11.3 [8.0–15.2] %, respectively). During premature AES, the largest increase in LDH was found at Bachmann's bundle and the pulmonary vein area (+13.0 [7.7, 18.3] % and +12.5 [10.8, 14.2] %, respectively, p<0.001 for both). Conduction velocity decreased particularly at Bachmann's bundle, the pulmonary vein area and the left atrium (-10.0 [-13.2, -6.9] cm/s, -9.3 [-12.5, -6.2] cm/s and -9.1 [-11.7, -6.6] cm/s, respectively, p<0.001 for each). When comparing patients with and without AF, more LDH was found during SR in AF patients at the pulmonary vein area and Bachmann's bundle (5.9 [4.8–9.1] vs. 9.7 [4.9–14.5] % and 9.8 [6.0–16.5] vs. 13.0 [11.9–14.5] %, respectively, p=0.031 and p=0.085). However, the increase in LDH during premature AES was similar for all sites. LDH is a useful novel methodology to quantify local heterogeneity in conduction velocity as a possible indicator of electropathology. Our findings suggest that LDH increases during premature AES, particularly at Bachmann's bundle and the pulmonary vein area, and that patients with AF already have more LDH during sinus rhythm, which becomes more pronounced during premature AES.

Conduction and anisotropic properties during atrial fibrillation

Tissue damage affecting cell-to-cell communication results in a heterogeneous distribution of conduction properties. Quantified features of local conduction heterogeneity could serve as an electrical biomarker to discriminate acutely induced, self-terminating AF from persistent AF. In **chapters 18 and 25**, novel techniques were introduced to estimate local conduction velocity and quantify LDH in conduction velocity vectors during sinus rhythm. In **chapter 26**, these methodologies were applied during AF to quantify directional conduction velocity, LDH and resulting anisotropy ratio, and to test whether these parameters differed between patients with different types of AF. We used a unique historical dataset of AF electrograms recorded at the right atrial free wall in 25 patients with Wolff-Parkinson-White syndrome and acutely induced AF, and 23 patients with valvular heart disease and long-standing persistent AF. Long-standing persistent AF was characterized by slower conduction (71.5±6.8 vs. 67.6±5.6 cm/s, p=0.037) with a larger dispersion (1.59±0.21 vs. 1.95±0.17, p<0.001) and a higher temporal variability (32.0±4.7 vs. 38.5±3.3 cm/s, p<0.001) compared to acute AF. In addition, long-standing persistent AF was characterized by more LDH (19.6±4.4 vs. 26.0±3.4%, p<0.001) and a higher degree of conduction anisotropy (1.38±0.07 vs. 1.51±0.14, p<0.001). Compared to the most complex type of acute AF (type III), long-standing persistent AF was still associated by a larger conduction velocity dispersion, higher temporal variability of conduction velocity and a larger amount of LDH. Increasing

38

complexity of AF was therefore associated with increased spatiotemporal variability of local conduction velocity vectors, local conduction heterogeneity and anisotropy ratio. By using these novel parameters, long-standing persistent AF could potentially be discriminated from the most complex type of acute AF. These observations may indicate pathological alterations of myocardial tissue underlying progression of AF.

Post-operative atrial fibrillation

Post-operative AF is the most common complication encountered after cardiac surgery. A variety of pre-, intra- and post-operative factors may contribute to its development. While AF requires both a trigger and susceptible substrate, early post-operative AF is primarily driven by triggers. Inflammation and increased sympathetic activity can lead to the development of AES, which often precede episodes of post-operative AF in the vast majority of patients. Although all patients experience AES after cardiac surgery, not all AES induce AF. It is most likely that if AES provoke a larger amount of conduction disorders and a higher degree of EEA, the risk for post-operative AF induction increases. In a pilot study presented in **chapter 27**, simultaneous endo-epicardial mapping was performed in the right atrium of twelve patients during sinus rhythm and programmed electrical stimulation, thereby mimicking spontaneous AES. This resulted in a substantial increase in conduction disorders (1.4 [0.6–2.6] vs. 8.5 [4.2–10.4] %, p=0.005) and EEA (1 [1–2] vs. 6.7 [2.7–16.9] %, p=0.006) compared to sinus rhythm. This increase was more pronounced in patients who developed post-operative AF, suggesting that increased vulnerability to AES is more likely to lead to post-operative AF.

Development of post-operative AF is also more likely in the presence of an extensive pre-existing substrate. In **chapter 28**, intra-atrial conduction parameters and unipolar electrogram morphology were studied to determine whether patients who developed new-onset post-operative AF already had a pre-existing arrhythmogenic substrate. Epicardial mapping was performed in 263 patients with ischemic (N=177, 67%), valvular heart disease (N=48, 18%) or a combination of both (N=38, 14%). Of these patients, 97 (37%) developed new-onset post-operative AF within 5 days after surgery; fifteen patients (6%) developed late post-operative AF. The development of post-operative AF was linked to pre-existing conduction disorders, including areas of conduction slowing, more conduction block, lower unipolar potential voltages and more LVAs. These differences were particularly located at Bachmann's bundle, but clear differences were also found in the left and right atrium. Patients with late post-operative AF had even more pronounced arrhythmogenic substrates before cardiac surgery. The first episode of late post-operative AF could occur up to 5 years after surgery and only occurred in patients who also developed early post-operative AF. Future studies should assess whether electrophysiological examination during cardiac surgery enables identification of patients at risk for developing post-operative AF, who may require more aggressive rhythm monitoring or benefit from concomitant ablative therapy.

Automated detection of AF episodes in continuous rhythm registrations is crucial for preventing complications and optimizing AF treatment. Several algorithms have been developed to detect AF in surface electrocardiograms (ECGs) in recent years. **Chapter 29** provides a systematic analysis of classification methods by discussing previously used digital biomarkers and algorithms. There has been a significant increase in the amount of research on AF detection in recent years, and a trend towards more complex classification methods has emerged. However, these more complex methods appear as a 'black box', making the decisions made by these classifiers difficult to understand. The algorithms mainly use three types of features, namely atrial features, ventricular features and signal features. Despite AF being an atrial arrhythmia, only a few studies (22%) utilize atrial features, while almost two-thirds of the studies (66%) rely on ventricular features. Although classification algorithms for

AF are accurate, they have become less transparent.

Although new studies mainly innovate on extracted features from ECGs and used classification algorithms, the next challenge is related to the fact that accurate classification algorithms heavily depend on the presence of enough accurately labelled data. However, manually labeling a large number of samples to generate a larger training set is time-consuming and prone to errors. **Chapter 30** proposes an efficient and reliable method that combines semi-supervised learning, reinforcement learning and transfer learning techniques to train a classifier on a large dataset of real-life telemetry data without manually labeling all the samples. The method involves a pre-training phase and a semi-automated training phase. During pre-training, an initial classifier was trained, which was used to predict the classes of new ECG segments in the semi-automated training phase. Based on the degree of certainty, segments were added to the training dataset automatically or after human validation. Thereafter, the classifier was retrained and the process was repeated. The model was tested on a telemetry dataset of 3,846,564 30-second ECG segments of hospitalized patients (N=476). After pre-training, 68.0% of all segments in the hidden test set could be classified with an estimated probability of successful classification of 99%, providing an F1-score of 97.9% for these segments. During the semi-automated training phase, this F1-score showed little variation (97.3%–97.9% in the hidden test set), while the number of segments which could be automatically classified increased from 68.0% to 75.8%. The overall F1-score increased from 89.0% after pre-training to 91.4% after the semi-automated phase. This method of human-validated semi-supervised learning can significantly reduce the time and effort required to train a classifier without compromising its accuracy, making it a valuable tool for automated AF detection in real-life ECGs.

Clinical implications of high-resolution mapping

High-resolution mapping can not only be used to identify AF-related electropathology, but it also provides insight into intra-operative electrophysiological processes in the heart. Patients with congenital heart disease are prone to cardiac arrhythmias that frequently occur relatively early in life. Despite advances in treating, outcomes remain suboptimal due to limited understanding of the impact of short-lasting volume or pressure overload. In order to investigate this, we launched the first-in-children epicardial mapping study, which is described in **chapter 31**. This study aims to quantify and characterize the effects of short-lasting abnormal hemodynamic conditions on atrial and ventricular electrophysiological characteristics, including conduction abnormalities and electrogram morphology. This epicardial mapping approach enables further unravelling of arrhythmogenesis in patients with congenital heart disease. Additionally, intra-operative cardiac mapping could help identify patients at high risk for development of post-operative atrial tachyarrhythmias.

Chapter 32 presents a case report where the use epicardial high-density mapping led to an unexpected and unique finding. The case involved a 14-month-old female patient diagnosed with short QT syndrome and scheduled for epicardial pacemaker implantation due to bradyarrhythmia and chronotropic incompetence. As part of the study presented in **chapter 31**, epicardial high-density mapping of the atria was performed and revealed continuous AF with an average cycle length as short as 25 ms. These fibrillation waves could not be identified on the surface ECG and the surgeon observed a mechanical standstill of the atria. This demonstrated a direct value for real-time diagnosis using epicardial mapping in daily clinical practice. If these atrial electrograms had not been recorded using a dedicated mapping system, AF could not have been confirmed, and possibly not have been diagnosed for many years.

38

Advanced interatrial block (a-IAB) can be caused by impaired conduction across Bachmann's bundle, which is associated with the development of AF. In **chapter 33**, we investigated whether a complete transverse line of conduction block across Bachmann's bundle is linked to a-IAB on the surface ECG. Also, we examined the correlation between conduction abnormalities in the right and left atria and a-IAB, and determined which excitation patterns are associated with ECG characteristics of a-IAB. The study included 40 patients in whom epicardial mapping revealed a complete transverse line of conduction block across Bachmann's bundle, with 13 of them classified as having a-IAB (32.5%). There were no differences in conduction disorders throughout the atria, but patients with a-IAB had longer total atrial excitation time and right-to-left delay compared to those without a-IAB (160±27 vs. 136±24 ms, p=0.012; 90±22 vs. 75±13 ms, p=0.017; respectively). Although the incidence of new-onset early post-operative AF was comparable between the two groups, it was relatively high (69%). The ECG characteristics of a-IAB were only partially explained by a transverse line of conduction block across Bachmann's bundle.

Conventional pacing from the right atrial appendage has been linked to an increased incidence of AF due to a longer atrial activation time. In **chapter 34**, we utilized epicardial mapping of Bachmann's bundle to investigate the effect of programmed electrical stimulation from different atrial sites on the activation patterns and electrophysiological properties of Bachmann's bundle to determine to most optimal pacing site. Programmed electrical stimulation from either the right or left atrial appendage resulted in, respectively, right- and left-sided conduction across Bachmann's bundle. However, during programmed electrical stimulation from the low-right atrium, in most patients (N=15, 50%) activation started in the center of Bachmann's bundle. Pacing from the right atrial appendage resulted in a total activation time of Bachmann's bundle similar to that during sinus rhythm (63 [55–78] vs. 61 [52–68] ms respectively, p=0.464), while it increased when pacing from the left atrial appendage (67 [61–75] ms, p=0.009) and decreased during pacing from the low-right atrium (45 [39–62] ms, p=0.003). Surprisingly, programmed electrical stimulation from the left atrial appendage resulted in an increase of conduction delay-block (6.8 [4.1–10.1] vs. 9.6 [5.8–13.0] %, p=0.009) and LVAs (2.0 [0.7–5.8] vs. 4.7 [1.6–13.1] %, p=0.003). Even programmed electrical stimulation from the right atrial appendage could result in an increase in LVAs (4.7 [1.0–8.9] %, p=0.005). A reduction of both conduction disorders and total activation time of Bachmann's bundle was most often achieved during programmed electrical stimulation from the low-right atrium (N=13), especially in patients with a higher amount of conduction disorders during sinus rhythm (9.8 [7.3–12.3] vs. 4.5 [3.5–6.6] %, p<0.001). Mapping of Bachmann's bundle can guide individualized placement of the atrial pacing lead, which could be a promising new approach to atrial pacing.

The ligament of Marshall has recently been recognized as a potential target for anti-arrhythmic therapies due to its arrhythmogenic properties. Accurate electrophysiological localization of the ligament of Marshall is crucial for successful ablation therapy. In **chapter 35**, we quantified electrophysiological properties of the ligament of Marshall and identified the most suitable electrogram recording and processing technologies for its accurate localization. The ligament of Marshall was identified in 19 patients. Marshall potentials in unipolar electrograms had lower potential voltages (1.5 [0.4–4.3] vs. 8.3 [1.5–17.9] mV, p<0.001), less steep slopes (-0.48 [-1.96 to -0.17] vs. -1.24 [-2.59 to -0.21] V/s, p<0.001) and prolonged activation duration (20 [8–31] vs. 17 [6–28] ms, p=0.008) compared to potentials recorded at the left atrium. Unipolar Marshall potentials consisted of short-double (34.4%), long-double (57.1%) or fractionated potentials (8.5%). Only a third of Marshall potentials that were visualized using unipolar electrograms, were still visible in bipolar local activation time maps. Similar to unipolar Marshall potentials, bipolar Marshall potential voltages were also smaller (1.5 [0.5–3.3] vs. 3.1 [0.5–7.2] mV, p<0.001) than potentials from the left atrium. The

ligament of Marshall was most accurately localized in unipolar local activation time and voltage maps by annotation of all deflections within (fractionated) potentials.

The cardiac autonomic nervous system largely regulates cardiac activity, with the vagus nerve begin a crucial component responsible for parasympathetic innervation to the heart. Low-level vagus nerve stimulation through the tragus (tLLVNS) is increasingly recognized as a therapeutic approach to prevent and treat AF. In **chapter 36**, we investigated the direct impact of acute and chronic tLLVNS on atrial electrophysiological features in ten patients. The patients underwent tLLVNS for 56 [43–73] minutes. A cranial shift of the SAN exit site was observed in five patients during both acute and chronic tLLVNS. During acute and chronic tLLVNS, unipolar potential voltage increased (3.9 [3.1–4.8] vs. 4.7 [4.0–5.3] vs. 5.2 [4.8–7.0] mV, p=0.027 and p=0.020 respectively), while total activation time, potential slopes, amount of fractionation, LVAs and conduction velocity did not differ from baseline measurements. Consistent 'improvement' of all electrophysiological features was not common; only two patients showed consistent improvement during tLLVNS, while one patient had no beneficial effect at all. tLLVNS resulted in a reduction of total activation time, steeper potential slopes, decrease in amount of fractionation and changes in activation patterns indicative of a more cranial SAN exit site only in selective patients. Future studies are necessary to determine whether high-density mapping can be used in clinical practice to select patients and optimize stimulation settings for cardiac neuromodulation.

38
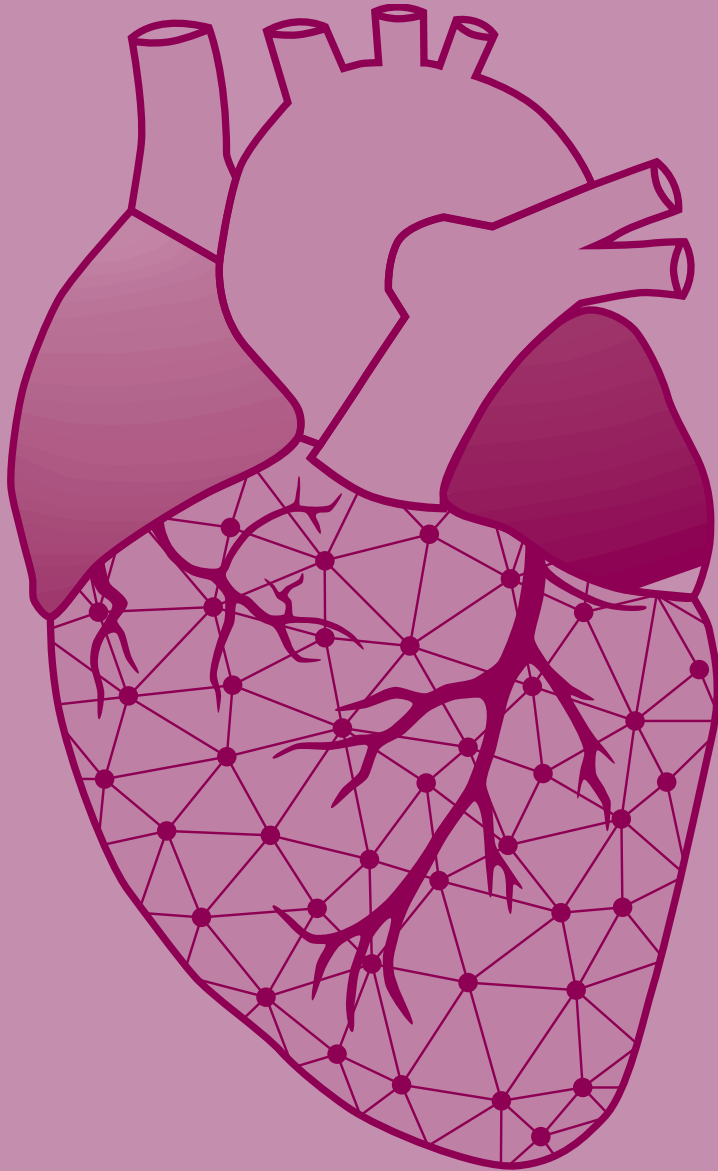
Chapter **39**

Nederlandse samenvatting

Mathijs S. van Schie

Ondanks dat ablatiestrategieën voor atriumfibrilleren (AF) onder geleiding van elektrofysiologisch onderzoek de afgelopen jaren aanzienlijk zijn verbeterd, blijft het een grote uitdaging om effectieve strategieën voor persisterend AF te ontwerpen. Hierdoor zijn de huidige behandelingsmogelijkheden vaak inefficiënt en zijn er frequent recidieven van AF, zelfs na uitgebreide ablatieprocedures. Als algemene inleiding van dit proefschrift geeft **hoofdstuk 1** de achtergrondinformatie over de etiologie en therapeutische mogelijkheden ten aanzien van AF, en technieken om elektrofysiologische eigenschappen van hartweefsel te onderzoeken. Dit proefschrift heeft als doel om elektrofysiologische veranderingen onderliggend aan het ontstaan en progressie van AF bij patiënten die een hartoperatie ondergaan te identificeren en kwantificeren. Wanneer deze AF-gerelateerde elektropathologie is geïdentificeerd, kan deze worden gebruikt als elektrische marker voor het ondersteunen van ablatietherapie van AF.

Hoofdstuk 2 geeft een samenvatting van de huidige kennis over AF-gerelateerde elektropathologie tijdens sinusritme, waarbij verschillende elektrofysiologische parameters zijn geïdentificeerd. Deze indicatoren waren niet alleen gevonden in het linker atrium, maar ook in het rechter atrium en nog vaker op Bachmann's bundel. Dit geeft duidelijk aan dat AF-gerelateerde elektropathologie ook buiten het linker atrium aanwezig is, wat de hypothese bevestigt dat AF niet enkel een linkszijdige ziekte is. Zelfs tijdens sinusritme kan elektropathologie gemist worden wanneer elektrofysiologisch onderzoek alleen wordt uitgevoerd aan het endocardium of epicardium. Daarom is geleiding, zelfs tijdens sinusritme, driedimensionaal (3D) en complex. Patiënten met een voorgeschiedenis van AF vertonen meer detecteerbare elektropathologie vergeleken met patiënten zonder AF, met name op Bachmann's bundel.

Tijdens AF vertonen elektrogrammen die op willekeurige locaties in de atria worden geregistreerd slag-op-slag variatie in de morfologie en intervallen tussen opeenvolgende fibrillatiepotentialen. De morfologie van fibrillatiepotentialen biedt niet alleen informatie over het moment van lokale excitatie, maar ook over de aanwezigheid van atriale elektropathologie. In **hoofdstuk 3** worden methodologieën en resultaten van elektrogram-geleide AF-ablatiebenaderingen kritisch beoordeeld. Bovendien worden huidige inzichten in sinusritme- en fibrillatie-elektrogram morfologie besproken vanuit experimenteel oogpunt.

Elektrische signaaleigenschappen gerelateerd aan elektropathologie

De ernst en omvang van elektropathologie kan worden weerspiegeld door veranderingen in elektrische signaaleigenschappen. Een van deze eigenschappen is de amplitude van unipolaire potentialen. Unipolaire voltage mapping wordt steeds vaker gebruikt om ablatietherapie voor AF te begeleiden, omdat unipolaire elektrogrammen, in tegenstelling tot bipolaire elektrogrammen, niet worden beïnvloed door de oriëntatie van de elektroden of de richting van de atriale activatiegolven. **Hoofdstuk 4** presenteert individuele, hoge-resolutie unipolaire voltage-profielen om gebieden met lage voltages (LVA's) te identificeren tijdens sinusritme en om het effect van AF-episodes op unipolaire voltages in patiënten met mitralisklepaandoening te onderzoeken. Er werden in totaal 600.722 potentialen geanalyseerd uit 829 sinusritme opnames. We hebben aangetoond dat er geen significante correlatie was tussen unipolaire voltages en geleidingssnelheid, terwijl wel lagere voltages werden geregistreerd in gebieden met geleidingsvertraging (<28 cm/s; 1,7 [0,9–3,5] vs. 4,7 [2,5–7,6] mV, p<0,001) en in gebieden rond geleidingsblok (<18 cm/s; 1,2 [0,7–2,3] vs. 4,8 [2,6–7,7] mV, p<0,001) vergeleken met gebieden met normale geleiding (≥28 cm/s). Gefractioneerde potentialen hadden lagere voltages in vergelijking met enkelvoudige potentialen (2,1 [1,0–3,8] vs. 5,2 [2,9–8,0] mV, p<0,001) en er werd een duidelijke afname van

39

unipolaire potentiaalvoltages gevonden bij een groter aantal deflecties (1: 5,2 [2,9–8,0] mV; 2: 2,2 [1,1–4,0] mV; 3: 1,2 [0,7–2,3] mV; ≥4: 0,9 [0,5–1,7] mV, alle p<0.001). Zelfs tijdens sinusritme vertoont gevorderde atriale remodelering bij patiënten met een mitralisklepaandoening opvallende interindividuele en regionale variatie. Potentialen met een laag voltage waren aanwezig in alle patiënten en er werden geen voorkeurslocaties voor LVA's gevonden. Echter, patiënten met paroxismaal AF hadden lagere potentiaalvoltages (zonder AF: 4,9 [3,5–6,1] vs. AF: 3,0 [2,2–4,6] mV, p=0.007) en een hoger aantal LVA's (zonder AF: 2,1 [0,5–7,7] vs. AF: 12,9 [3,2–23,6] %, p=0.001) op Bachmann's bundel in vergelijking met patiënten zonder voorgeschiedenis van AF. Aangezien potentialen met een laag voltage zelfs aanwezig waren bij patiënten zonder voorgeschiedenis van AF, moeten lage unipolaire voltages voorzichtig worden gebruikt tijdens ablatietherapie.

De morfologie van enkelvoudige unipolaire potentialen werd verder onderzocht in **hoofdstuk 5**. Enkelvoudige unipolaire potentialen bestaan uit een positieve (R-golf) en negatieve (S-golf) component, die waardevolle informatie bevatten over intra-atriale geleiding en mogelijk het substraat dat ten grondslag ligt aan AF. We hebben een duidelijke overheersing van S-golven aangetoond op Bachmann's bundel en het rechter atrium, zowel bij patiënten met als zonder paroxismaal AF (Bachmann's bundel: 88,8% vs. 85,9%, rechter atrium: 92,1% vs. 85,1%, respectievelijk). Bovendien vertoonde de groep met paroxismaal AF lagere enkelvoudige potentiaalvoltages in het rechter atrium, Bachmann's bundel en het gebied tussen de pulmonaal venen (alle p<0,001), die voornamelijk werden bepaald door de amplitude van de S-golf. Het grootste verschil in S-golf amplitude werd waargenomen op Bachmann's bundel, waar de groep met paroxismaal AF een lagere S-golf amplitude had (4,1 [2,5–6,1] vs. 2,9 [1,4–4,8] mV, p<0,001). Bovendien hadden patiënten met paroxismaal AF een lagere geleidingssnelheid op Bachmann's bundel (97 [70–121] vs. 89 [62–116] cm/s, p<0,001). Hoewel de excitatie van de atria heterogeen verstoord is tijdens sinusritme, suggereren onze bevindingen dat een voorgeschiedenis van AF wordt gekenmerkt door verminderde enkelvoudige potentiaalvoltages op Bachmann's bundel als gevolg van verlies van S-golf amplitudes en verminderde geleidingssnelheid. Dit benadrukt het potentieel nut van de morfologie van enkelvoudige potentialen om aanvullende informatie te verkrijgen over de verspreiding van de activatiegolf.

Lage potentiaalvoltages als marker voor elektropathologie

LVA's worden beschouwd als indicatoren van aritmogene substraten die AF promoten. **Hoofdstuk 6** had als doel om de omvang van atriale LVA's te vergelijken bij patiënten met en zonder obesitas om voorkeursplaatsen voor LVA's te identificeren. Voor deze studie werd een gematcht cohort gebruikt van 212 patiënten met en zonder obesitas. Patiënten met obesitas werden gekenmerkt door lagere voltages (4,5 [0,4–16,2] vs. 5,5 [0,8–18,0] mV, p<0,001), vooral op Bachmann's bundel (4,1 [0,4–12,3] vs. 6,2 [1,0–14,3] mV, p<0,001) en het linker atrium (5,1 [0,5–10,1] vs. 6,2 [0,8–15,9] mV, p=0,003). Bovendien hadden patiënten met obesitas een hoger percentage LVA's, met name op Bachmann's bundel (2,9 [0,0–77,1] vs. 0,9 [0,0–42,0] %, p<0,001). Het aantal LVA's correleerde met incidentie van geleidingsblok, terwijl BMI en het aantal LVA's onafhankelijke voorspellers waren voor de incidentie van vroeg postoperatief AF. Deze studie suggereert dat obesitas kan leiden tot een algehele afname van atriale potentiaalvoltages en een hoger aantal LVA's, en dat Bachmann's bundel een voorkeursplaats is voor atriale LVA's bij patiënten met obesitas.

Voltage mapping is in hoge mate afhankelijk van het gebruik van unipolaire of bipolaire elektrogrammen, die elk hun eigen voor- en nadelen hebben. Bovendien blijft het erg uitdagend om een juiste drempelwaarde te definiëren om LVA's te identificeren. Het is ook nog onbekend of unipolaire, bipolaire en omnipolaire potentiaalvoltages complementair

of tegenstrijdig zijn bij het identificeren van LVA's tijdens hoge-resolutie mapping. In **hoofdstuk 7** onderzochten we de overeenkomsten en verschillen in unipolaire, bipolaire en omnipolaire voltageverdeling en onderzochten we de relatie tussen verschillende soorten potentiaalvoltages en geleidingssnelheid bij de identificatie van LVA's. Binnen gebieden van 2×2 elektroden (een 'clique') werden de maximale unipolaire, bipolaire en omnipolaire voltages en gemiddelde geleidingssnelheid berekend. Er werden in totaal 193 mapping-locaties gebruikt, waaruit 175.667 unipolaire en 306.685 bipolaire opnames werden verkregen, waaruit 146.015 cliques werden gecreëerd. Er waren aanzienlijke directionele verschillen in bipolaire voltages: het grootste bipolaire potentiaalvoltage was gemiddeld 1,7 (variërend van 1,9 tot 59,0) keer groter dan het voltage van de bipolaire potentiaal loodrecht op deze positie. Deze verschillen hadden een grote invloed op de identificatie van LVA's. Unipolaire clique voltages waren groter dan zowel bipolaire als omnipolaire clique voltages (7,1 [4,2–10,6] vs. 5,3 [2,4–9,6] en 5,8 [2,6–10,5] mV respectievelijk, p<0,001). Het toepassen van omnipolaire clique voltages op bipolaire LVA's toonde aan dat 14,6% van deze LVA's aanvankelijk verkeerd geïdentificeerd werden. Alle bipolaire of omnipolaire LVA's kwamen overeen met een breed scala aan unipolair clique voltages en, hoewel de geleidingssnelheid over het algemeen verminderd was, konden nog steeds hoge geleidingssnelheden en grote unipolaire clique voltages in deze gebieden worden gevonden. Vanwege de hoge interindividuele variaties in unipolaire clique voltages binnen LVA's werd er geen duidelijke unipolaire drempelwaarde gevonden voor de juiste identificatie van LVA's. Deze studie illustreert dat LVA's sterk afhankelijk zijn van de gebruikte mapping-techniek. Toekomstige studies zijn nodig om te onderzoeken of een combinatie van unipolaire en omnipolaire potentiaalvoltages meer indicatief is voor daadwerkelijke LVA's.

In de klinische praktijk wordt endocardiale bipolaire voltage mapping nog steeds voornamelijk gebruikt om LVA's te identificeren. Echter, recentelijk is duidelijk geworden dat bipolaire LVA's uitsluitend enkel op het endocardium óf het epicardium kunnen voorkomen. In **hoofdstuk 8** hebben we de endo- en epicardiale kenmerken van unipolaire en omnipolaire voltages onderzocht, de relatie tussen verschillende soorten elektrogrammen bij de identificatie van LVA's verkend en onderzocht of kenmerken van LVA's voorspellend kunnen zijn voor LVA's in de tegenovergestelde laag. Simultane endo-epicardiale mapping werd uitgevoerd tijdens sinusritme in het rechter atrium bij 93 patiënten. Er werden in totaal 281 mapping-locaties gebruikt, resulterend in 406.571 unipolaire en 723.595 bipolaire opnames waaruit 164.704 cliques werden gecreëerd voor zowel het endo- als epicardium (329.408 cliques in totaal). In 61% van de cliques waren unipolaire clique voltages op het epicardium groter dan de overeenkomstige unipolaire clique voltages op het endocardium (8,2 [4,9–11,6] vs. 6,1 [3,2–10,9] mV, p<0,001). Omnipolaire clique voltages op het epicardium waren ook groter dan de overeenkomstige omnipolaire clique voltages op het endocardium in 64% van de cliques (6,7 [3,2–10,9] vs. 3,3 [1,1–8,6] mV, p<0,001). De meerderheid van zowel unipolaire als omnipolaire LVA's bevond zich alleen op het endocardium (respectievelijk 74,2% en 82,0%) of epicardium (respectievelijk 52,7% en 47,6%). Van de endocardiale unipolaire LVA's bevond 25,8% zich ook op de tegenovergestelde laag en 47,3% visa versa. Bij omnipolaire LVA's bevond 18,0% van de endocardiale LVA's zich ook op het epicardium en 52,4% visa versa. De combinatie van epicardiale unipolaire en omnipolaire clique voltages was het meest nauwkeurig in het identificeren van LVA's in beide lagen (50,4%, AUC=0,89). Een endo-epicardiale mapping strategie met behulp van unipolaire en omnipolaire elektrogrammen heeft daarom de voorkeur om LVA's nauwkeurig te identificeren.

Potentiaalmorfologie: meer dan alleen voltage

Katheterablatiestrategieën gericht op gefractioneerde of laag-voltage potentialen worden veelvuldig ingezet bij patiënten met persisterende vormen van AF. De toepassing van

39

deze strategieën in de behandeling van AF vertoonde aanvankelijk positieve resultaten in voornamelijk studies uitgevoerd in één centrum, maar wordt nu steeds vaker gevolgd door negatieve resultaten in (grote) gerandomiseerde gecontroleerde onderzoeken. Hoewel fractionering en laag-voltage worden beschouwd als indicatoren van geleidingsvertraging, en daarom kritiek zijn bij de initiatie en het in stand houden van AF, kunnen ze ook optreden door niet-pathologische redenen. In **hoofdstuk 9** wordt de relatie tussen lokale geleidingssnelheid en het optreden van gefractioneerde en/of laag-voltage potentialen onderzocht om gebieden met kritische geleidingsvertraging te identificeren. De studie omvatte 319 patiënten die een bypassoperatie ondergingen of een mitralisklepaandoening hadden met of zonder een voorgeschiedenis van AF. Gefractioneerde, laag-voltage potentialen waren zeldzaam en kwamen slechts voor op 0,4 [0,2–0,8] % van alle atriale locaties. De lokale geleidingssnelheid op plaatsen met gefractioneerde, laag-voltage potentialen was aanzienlijk lager (46,0 [22,6–72,7] cm/s) vergeleken met plaatsen met ofwel lage-voltage, niet-gefractioneerde potentialen (64,5 [34,8–99,4] cm/s) en gefractioneerde, hoge-voltage potentialen (65,9 [41,7–92,8] cm/s, p<0.001 voor elk). Deze specifieke potentialen kwamen vaker voor bij patiënten met eerdere episodes van AF, met name in het gebied tussen de pulmonaal venen en op Bachmann's bundel. Gebieden met trage geleiding (<50 cm/s) konden het meest nauwkeurig worden geïdentificeerd door gebruik te maken van een lage voltagedrempel (<1 mV) en een minimum van 3 deflecties (positieve voorspellende waarde: 54,2–70,7%), hoewel de algehele sensitiviteit laag bleef (0,1–1,9%). De sterke omgekeerde relatie tussen de positieve voorspellende waarden en de sensitiviteit zal daarom waarschijnlijk de toepassing van deze op elektrogram gebaseerde ablatiebenaderingen voor het identificeren van gebieden met trage geleiding bij AF patiënten compliceren.

In niet-uniform anisotroop weefsel vertonen geleidingsstoornissen richtings- en frequentieafhankelijkheid, wat vaak leidt tot gefractioneerde potentialen. Het gebruik van unipolaire potentiaalmorfologie kan helpen bij het detecteren van gebieden met niet-uniform anisotroop weefsel. In **hoofdstuk 10** wordt de invloed van verschillende gradaties van prematuriteit en aberrantie van spontane atriale extrasystolen (AES) op de morfologie van unipolaire potentialen bestudeerd. De studie omvatte 837 unieke AES opgenomen bij 287 patiënten (60 met voorgeschiedenis van AF). De meest prominente effecten op de potentiaalmorfologie waren geassocieerd met de mate van aberrantie. Met name AES met een propagatierichting van de activatiegolf tegenovergesteld aan of loodrecht op het sinusritme resulteerde in de meest significante afname van potentiaalvoltages (-1,6 [-2,2, -1,1] mV en -1,7 [-2,0, -1,4] mV respectievelijk, p<0,001) en toename van gefractioneerde potentialen (+11,1 [6,0, 10,1] % en +13,4 [10,3, 16,5] % respectievelijk, p<0,001), ongeacht de mate van prematuriteit (R^2<0,299, p<0,001). Hoewel op alle atriale locaties effecten werden gevonden, waren er grote interregionale verschillen. Patiënten met een voorgeschiedenis van AF hadden specifiek bij het rechter atrium een aanzienlijke afname van potentiaalvoltages (-2,8 [-3,5, -2,1] vs. -1,2 [-1,7, -0,7] mV, p<0,001) en toename van gefractioneerde potentialen (+25,6 [16,5, 34,7] vs. +8,9 [4,4, 13,5] %, p=0,002), wat wijst op versterkte niet-uniforme anisotrope eigenschappen van het weefsel. De morfologie van unipolaire potentialen tijdens spontane AES zijn meer richtingsafhankelijk dan frequentieafhankelijk. Aangezien patiënten met AF ernstigere richtingsafhankelijke geleidingsstoornissen hebben, verklaart de verhoogde niet-uniforme anisotropie bij deze patiënten waarschijnlijk de hogere gevoeligheid voor het ontstaan van episodes van AF.

De grootte (of diameter) van de elektrode is een belangrijke parameter die de kenmerken van de geregistreerde elektrogrammen kan beïnvloeden. In **hoofdstuk 11** werden zowel gesimuleerde als klinische data gebruikt om het effect van de elektrodegrootte op de nauwkeurigheid van het bepalen van de lokale activatietijd, de lengte van lijnen van lokale

geleidingsvertraging en -blok, het aantal LVA's en gefractioneerde potentialen te analyseren. Elektrogramarrays werden gesimuleerd voor 2D weefsels met drie verschillende niveaus van geleidingsheterogeniteit om inhomogene voortgeleiding van de activatiegolf te modelleren, wat ook wordt waargenomen tijdens AF. Het vergroten van de elektrodegrootte verlaagde de nauwkeurigheid van het bepalen van de lokale activatietijd en verkleinde de lengte van de lijnen van geleidingsblok zowel in de gesimuleerde als klinische data. Bovendien waren de lokale activatiekaarten die gegenereerd werden door grotere elektroden homogener met een lager aantal waargenomen activatiegolven. Het vergroten van de elektrodegrootte verhoogde ook het aantal LVA's, terwijl de hellingen van de potentialen en het aantal deflecties verminderde. Dit effect was sterker bij weefsel met een grotere geleidingsheterogeniteit. De grootte van de elektrode heeft dus aanzienlijke invloed op de potentiaalmorfologie en de lokale activatiekaarten. Deze effecten moeten meegenomen worden bij het analyseren van potentialen of bij het vergelijken van resultaten verkregen met verschillende elektrodegrootten.

Het combineren van elektrische signaaleigenschappen: naar een persoonlijk signaalprofiel

De ernst en omvang van inhomogeniteit in geleiding kan worden weerspiegeld door een elektrisch signaalprofiel met gekwantificeerde kenmerken van de morfologie van unipolaire potentialen. Dit zou een op de patiënt afgestemd signaalprofiel van het aritmogene substraat kunnen bieden. Als eerste stap richting de constructie van zo'n diagnostisch signaalprofiel presenteert **hoofdstuk 12** de regionale verschillen in kenmerken van unipolaire potentiaalmorfologie in relatie tot inhomogene intra-atriale geleiding tijdens sinusritme bij een grote groep patiënten zonder atriale tachyaritmieën. Er werden in totaal 1.763.593 potentialen geanalyseerd van 189 patiënten die een bypassoperatie ondergingen. In alle atriale regio's was het merendeel van de potentialen enkelvoudig (81,4 [48,9–100] %). De hoogste proportie van lange-dubbele en gefractioneerde potentialen werd voornamelijk geregistreerd op het rechter atrium (4,0 [0–35,5] % en 1,3 [0–14,8] % respectievelijk) en Bachmann's bundel (4,0 [0–35,5] % en 1,4 [0–14,8] % respectievelijk). Gefractioneerde potentialen op Bachmann's bundel hadden de langste duur. De grootste prevalentie van LVA's werd gevonden op het rechter atrium (5,8 [2,3–10,6] %). De aanwezigheid van geleidingsblok correleerde met de proportie lange-dubbele en gefractioneerde potentialen, de duur van deze gefractioneerde potentialen en de prevalentie van LVA's. Inhomogeniteit in geleiding kan daarom worden geïdentificeerd aan de hand van een signaalprofiel die specifieke gekwantificeerde kenmerken van unipolaire potentialen bevat.

De volgende stap was het construeren van het elektrische signaalprofiel. Het gebruik van dit signaalprofiel om de mate van inhomogeniteit in geleiding te voorspellen is gedemonstreerd in **hoofdstuk 13**. De mate van intra-atriale inhomogeniteit in geleiding werd bepaald bij 235 patiënten, waarna de patiënten werden onderverdeeld in drie groepen (lage, gemiddelde en hoge mate van geleidingsinhomogeniteit). Een toename in geleidingsinhomogeniteit was geassocieerd met een afname in potentiaalvoltages (laag 5,7 [5,1–6,9] vs. hoog 4,0 [3,5–5,0] mV) en een toename in het aantal LVA's (laag 3,2 [1,8–5,6] vs. hoog 9,5 [6,1–13,0] %), lange-dubbele potentialen (laag 1,8 [1,1–3,2] vs. hoog 6,2 [4,6–8,1] %) en gefractioneerde potentialen (laag 1,3 [0,6–2,0] vs. hoog 2,5 [1,5–3,9] %). Er werd een *Elektrische Signaalprofiel Score* geconstrueerd voor de voorspelling van de mate van geleidingsinhomogeniteit bij elke individuele patiënt. De *Elektrische Signaalprofiel Score* voor de gehele atria (concordantie-index 0,92 [0,89–0,95]), met daarin het totale aantal LVA's en lange-dubbele potentialen en de duur van gefractioneerde potentialen, en de *Regionale Elektrische Signaalprofiel Score* van het rechter atrium (concordantie-index 0,83 [0,78–0,89]), met daarin het aantal LVA's en lange-dubbele potentialen, hadden de hoogste voorspellende waarde voor de ernst van

39

geleidingsinhomogeniteit in beide atria. Beide *Elektrische Signaalprofiel Scores* correleerden sterk met de werkelijke mate van geleidingsinhomogeniteit (r=0,82, p<0,001 en r=0,70, p<0,001). De ernst van geleidingsinhomogeniteit kan nauwkeurig worden gekwantificeerd met behulp van de *Elektrische Signaalprofiel Score*, waarbij alleen elektrofysiologische kenmerken van unipolaire potentialen worden gebruikt.

De incidentie van AF hangt sterk samen met toenemende leeftijd, al is de invloed van leeftijd op unipolaire potentiaalmorfologie nog onbekend en is het ook niet duidelijk of deze veranderingen aanwezig zijn in beide atria. In **hoofdstuk 14** hebben we sinusritme-registraties van 213 patiënten die een bypassoperatie ondergingen geanalyseerd om leeftijd-gerelateerde veranderingen in unipolaire potentiaalmorfologie te onderzoeken. De patiënten werden onderverdeeld in een jonge (leeftijd <60 jaar) en oudere (leeftijd ≥60 jaar) groep. Alleen op Bachmann's bundel werd een hoger percentage enkelvoudige potentialen waargenomen in de jonge groep (p=0,007), terwijl de oudere groep een hoger percentage korte-dubbele (p=0,051), lange-dubbele (p=0,004) en gefractioneerde potentialen (p=0,006) had. Na correctie voor mogelijke confounders, vonden we dat oudere leeftijd gepaard gaat met een afname van enkelvoudige potentialen (β: -6,33, 95% BI: -10,5 tot -2,3) en een toename van korte-dubbele (β: 2,5, 95% BI: 0,1 tot 4,9), lange-dubbele (β: 1,9, 95% BI: 0,2 tot 3,7) en gefractioneerde potentialen (β: 1,9, 95% BI: 0,6 tot 3,2). Deze bevindingen suggereren dat leeftijd-gerelateerde remodelering voornamelijk Bachmann's bundel beïnvloedt en mogelijk een cruciale factor is bij de ontwikkeling van leeftijd-gerelateerde hartritmestoornissen zoals AF.

Elektrische asynchronie tussen het endo- en epicardium draagt bij aan het in stand houden van AF, omdat patiënten met persisterend AF meer endo-epicardiale asynchronie (EEA) hebben tijdens sinusritme dan patiënten zonder AF. Unipolaire gefractioneerde potentialen kunnen ontstaan vanuit gebieden van EEA. In **hoofdstuk 15** hebben we een nieuwe methode geïntroduceerd om de mate van EEA te schatten door gebruik te maken van unipolaire potentiaalmorfologie die zijn geregistreerd vanuit zowel het endo- als epicardium. Bij 86 patiënten bij wie simultane endo-epicardiale mapping werd uitgevoerd, werd aangetoond dat zowel de endo- als epicardiale locaties van EEA werden gekenmerkt door lagere potentiaalvoltages (5,2 [2,8-9,1] vs. 1,6 [0,9-2,7] mV, p<0,001 en 7,4 [4,4-10,6] vs. 2,5 [1,2-4,7] mV, p<0,001, respectievelijk), een hoger aantal lange-dubbele (5,5 vs. 35,3% en 3,5 vs. 27,3%, respectievelijk) en gefractioneerde potentialen (1,9 vs. 14,4% en 1,6 vs. 9,7%), en een langere duur van dubbele potentialen (11 [7-18] vs. 20 [15-28] ms, p<0,001 en 9 [6-14] vs. 20 [13-30] ms, p<0,001, respectievelijk) en gefractioneerde potentialen (20 [14-27] vs. 28 [21-36] ms, p<0,001 en 20 [15-27] vs. 26 [19-39] ms, p<0,001, respectievelijk). Patiënten met een voorgeschiedenis van AF werden gekenmerkt door lagere potentiaalvoltages in gebieden van EEA, samen met veranderingen in het type potentialen. De *Endo-Epicardiale Asynchronie Signaalprofiel Score*, die het percentage endocardiale LVA's en de duur van epicardiale dubbele potentialen bevatte, had de hoogste voorspellende waarde voor het bepalen van de mate van EEA (AUC: 0,91). De *Endocardiale-* en *Epicardiale Asynchronie Signaalprofiel Scores* afzonderlijk toonden ook goede voorspellende waarden (AUC: 0,90 en 0,83 respectievelijk). Daarom kan de morfologie van unipolaire potentialen worden gebruikt om gebieden van EEA te identificeren, waarbij de *Asynchronie Signaalprofiel Score* als diagnostisch instrument kan worden gebruikt om de mate van EEA te schatten.

Gebieden van geleidingsblok resulteren in afwijkingen in potentiaalmorfologie en versterken waarschijnlijk endo-epicardiale geleidingsvertraging. Eerdere mapping studies hebben aangetoond dat patiënten met een voorgeschiedenis van AF meer geleidingsblok hebben tijdens sinusritme, wat is veroorzaakt door gevorderde structurele remodelering. Lijnen van geleidingsblok kunnen zowel enkel in het endo- of epicardium (enkelzijdige

geleidingsblok) gelokaliseerd zijn of in beide lagen (transmuraal geleidingsblok), wat weer endo-epicardiale geleidingsvertraging kan versterken. In **hoofdstuk 16** hebben we simultane endo-epicardiale mapping uitgevoerd in 86 patiënten om te onderzoeken in hoeverre enkelzijdige en transmurale geleidingsblok endo-epicardiale geleidingsvertraging versterken, welke unipolaire signaaleigenschappen geassocieerd zijn met de verschillende typen geleidingsblok en welke van deze eigenschappen kenmerkend zijn voor transmurale geleidingsblok. We hebben hierbij aangetoond dat endo-epicardiale geleidingsvertraging het meest beïnvloed wordt door de aanwezigheid van gebieden met transmuraal geleidingsblok. Deze gebieden werden gekenmerkt door lagere potentiaalvoltages en een hoger aantal lange-dubbele en gefractioneerde potentialen ten opzichte van gebieden met enkelzijdige geleidingsblok. Gebieden met transmuraal geleidingsblok konden het meest nauwkeurig voorspeld worden door een combinatie van epicardiale potentiaalmorfologie parameters, zoals potentiaalvoltages, fractionatie en fractionatieduur (AUC=0,91). We hebben dus potentiaaleigenschappen geïdentificeerd die gebruikt kunnen worden om gebieden met transmuraal geleidingsblok te lokaliseren, welke weer indicatief zijn voor gebieden met endo-epicardiale geleidingsvertraging.

Afwijkingen in de verspreiding van activatiegolven

Cardiale structurele remodelering kan ten grondslag liggen aan de ontwikkeling van elektrische geleidingsstoornissen, zoals lokale geleidingsvertraging of -blok. Deze geleidingsstoornissen beïnvloeden de verspreiding van het uitbreidende activatiegolffront en kunnen zowel structureel als functioneel van aard zijn. Een eerdere mapping-studie toonde aan dat jonge patiënten met het Wolff-Parkinson-White syndroom en niet-gedilateerde atria slechts een beperkt aantal geleidingsstoornissen vertoonden, die voornamelijk functioneel van aard waren. Zelfs bij oudere patiënten met elektrisch niet-geremodelleerde atria die een bypassoperatie ondergingen, werd aangetoond dat slechts een beperkte hoeveelheid geleidingsblok aanwezig was, hoewel er een aanzienlijke intra-atriale en interindividuele variatie was in de prevalentie van geleidingsblok. In **hoofdstuk 17** wordt het eerste bewijs geleverd van atriale geleidingsstoornissen bij kinderen met een aangeboren hartafwijking. Gebieden van lokale geleidingsvertraging en -blok waren aanwezig bij alle patiënten en werden met name waargenomen op Bachmann's bundel (respectievelijk 4,9% en 2,3%), het rechter atrium (respectievelijk 3,7% en 1,6%) en het linker atrium (respectievelijk 1,8% en 1,0%). Vertraging van de geleiding was het meest uitgesproken in het rechter atrium (maximale geleidingstijd 44 ms) en Bachmann's bundel (maximale geleidingstijd 25 ms). Zelfs vóór chirurgische correctie in het eerste levensjaar zijn atriale geleidingsafwijkingen al aanwezig bij kinderen met een aangeboren hartafwijking, wat hen vatbaar maakt voor atriale hartritmestoornissen op jonge leeftijd.

Gebieden met langzamere geleiding worden beschouwd als 'aangedaan weefsel' en worden geassocieerd met een verhoogd risico op reentry dat AF kan initiëren. Een nauwkeurige bepaling van de intra-atriale geleidingssnelheid is essentieel om aritmogene gebieden te identificeren. Verschillende technieken om lokale geleidingssnelheid te schatten zijn al reeds geïntroduceerd, waaronder '*finite differences*' (FiD) en '*polynomial surface fitting*' (PSF). Echter, de meest optimale schattingsmethodologie om geleidingsheterogeniteit te meten is nog niet bepaald. In **hoofdstuk 18** hebben we een nieuwe techniek geïntroduceerd die gebruikmaakt van '*discrete velocity vectors*' (DVV) om de lokale geleidingssnelheid te schatten en gebieden van geleidingsheterogeniteit te identificeren. Bovendien hebben we de meest geschikte methodologie geïdentificeerd om lokale gebieden van geleidingsheterogeniteit bloot te leggen, intra-atriale verschillen in geleidingssnelheid te kwantificeren en gebieden van geleidingsvertraging geassocieerd met paroxismaal AF te lokaliseren. In totaal werden 4.109.926 potentialen geanalyseerd uit 5.261 sinusritme-

39

registraties. Het grootste aantal lokale geleidingssnelheden werd geschat met behulp van de DVV-techniek (97%), gevolgd door de PSF-techniek (78%) en FiD-techniek (63%). De mediane atriale geleidingssnelheid geschat met behulp van de DVV-, PSF- en FiD-technieken was respectievelijk 90,0 [62,4–116,8], 92,0 [70,6–123,2] en 89,4 [62,5–126,5] cm/s. Het grootste verschil in geleidingssnelheidsschattingen werd gevonden tussen PSF en DVV, wat werd veroorzaakt door gebieden met lagere geleidingssnelheden die alleen werden gedetecteerd door de DVV-techniek. Alle technieken toonden aan dat er aanzienlijke variatie was in geleidingssnelheid tussen alle atriale gebieden, maar dat de langzaamste geleiding werd waargenomen op het rechter atrium en Bachmann's bundel. Een lagere geleidingssnelheid werd gevonden op Bachmann's bundel bij patiënten met paroxismaal AF in vergelijking met degenen zonder AF (79,1 [72,2–91,2] vs. 88,3 [79,3–97,2] cm/s, p<0,001). Toch waren zowel de FiD- en PSF-technieken niet in staat om lokale geleidingsheterogeniteit te identificeren, omdat deze werden gemaskeerd door de filtereigenschappen van beide technieken. Geleidingsheterogeniteiten konden daarom het meest nauwkeurig worden geïdentificeerd met behulp van de DVV-techniek.

In **hoofdstuk 19** werd een daaropvolgende case-control studie gepresenteerd waarin de intra-atriale geleidingssnelheid is vergeleken bij patiënten met en zonder voorgeschiedenis van AF. De mediane bi-atriale geleidingssnelheid verschilde niet tussen beide groepen (90±8 vs. 92±6 cm/s respectievelijk, p=0.56), maar er was wel een vermindering in geleidingssnelheid op Bachmann's bundel bij patiënten met een voorgeschiedenis van AF (79±12 vs. 88±11 cm/s, p=0.02). Patiënten zonder AF vertoonden geen voorkeursplaats voor de laagste geleidingssnelheid (P_5), terwijl bij patiënten met AF de laagste geleidingssnelheid het vaakst werd gemeten op Bachmann's bundel (53%) met een bereik van 15 tot 22 cm/s (mediaan: 20 cm/s). Het linker atrium (18%) en het gebied tussen de pulmonaal venen (29%) vertoonden ook de laagste geleidingssnelheden, maar niet het rechter atrium. De studie toonde aan dat AF geassocieerd was met een verlengde totale atriale excitatietijd (p=0.03) en verminderde potentiaalvoltages (P_5) specifiek bij Bachmann's bundel (p=0.02), wat ook naar voren kwam als een voorkeursplaats voor geleidingsvertraging bij AF-patiënten. Daarom kan Bachmann's bundel een belangrijke rol spelen in de pathofysiologie van AF.

Bij 27% van de patiënten hervat AF binnen 90 seconden na herstel van sinusritme door elektrische cardioversie (ECV). Deze onmiddellijke terugkeer van AF kan te wijten zijn aan een hoge frequentie van ectopische slagen of een zeer gevoelige periode direct na ECV. **Hoofdstuk 20** presenteert een case-control studie waarin geleidingsheterogeniteit in de zeer gevoelige periode direct na ECV wordt vergeleken met langdurig sinusritme bij patiënten met een voorgeschiedenis van AF. Tijdens sinusritme en premature atriale contracties werd epicardiale mapping van beide atria uitgevoerd. We hebben aangetoond dat er voor alle atriale regio's geen significante verschillen waren tussen de ECV-groep en de controlegroep tijdens zowel sinusritme als premature atriale contracties wat betreft de prevalentie en lengte van de langste lijnen van geleidingsblok en continue geleidingsvertraging-bloklijnen, de mate van geleidingsstoornissen, geleidingssnelheid, bi-atriale totale excitatietijd en potentiaalvoltages (p≥0,05). Deze waarnemingen suggereren dat de zeer gevoelige periode direct na ECV mogelijk niet gekenmerkt wordt door verstoorde intra-atriale geleiding.

Effect van geleidingsafwijkingen op de sinusknoop

Propagatie van de elektrische activatiegolf vanuit de sinusknoop naar het omliggende atriale weefsel is een complex 3D-proces. In **hoofdstuk 21** worden de resultaten gepresenteerd van endo-epicardiale mapping van de sinusknoop bij twintig patiënten (40% met een voorgeschiedenis van AF) met structurele hartaandoeningen die een hartoperatie ondergaan. In totaal werden 28 patronen van focale activatie van de

sinusknoop geanalyseerd (4 patiënten vertoonden meerdere oorsprongslocaties van de sinusknoop). Drie verschillende activatiepatronen werden geïdentificeerd: 1) endocardiale oorsprong (N=10), 2) epicardiale oorsprong (N=13) en 3) gelijktijdig geactiveerde endo-epicardiale oorsprong (N=5). De mediane endo-epicardiale vertraging bij de oorsprong van de sinusknoop was 10 [6–14] ms en de prevalentie van EEA in de directe omgeving van de sinusknoop was 5 [2–18] %. Deze bevindingen benadrukken de complexe 3D-geometrie van de sinusknoop en de aanwezigheid van interindividuele verschillen in oorsprongslocaties van de sinusknoop. Een caudale verschuiving in de activatie van de sinusknoop naar het midden van het rechter atrium (N=6) werd uitsluitend waargenomen bij patiënten met een voorgeschiedenis van AF, wat wijst op veranderingen in de preferentiële oorsprongslocatie van de sinusknoop in deze patiënten.

Sinusknoopdisfunctie wordt vaak waargenomen bij patiënten met aangeboren hartafwijkingen, zelfs na vroegtijdige chirurgische correctie. Dit suggereert dat afwijkingen in de geometrie en functie van de sinusknoop mogelijk al bij de geboorte aanwezig zijn, wat hen vatbaar maakt voor sinusknoopdisfunctie. In **hoofdstuk 22** presenteerden we de elektrofysiologische kenmerken van sinusknoopactiviteit bij 15 volwassenen en 12 kinderen die een chirurgische correctie voor een aangeboren hartafwijking ondergingen. Alleen elektroden binnen 8 mm van de vroegste activatieplaats op het rechter atrium werden meegenomen voor de analyse en vergeleken tussen kinderen en volwassen patiënten. Bij kinderen werden oorsprongslocaties alleen in de buurt van de overgang van de vena cava superior en het rechter atrium gevonden, terwijl bij volwassenen de oorsprongslocaties zelfs uitstrekten tot het midden van het rechter atrium. Het sinusknoopgebied bij volwassen patiënten vertoonde langzamere geleiding, lagere potentiaalvoltages, meer geleidingsblok en een hogere mate van gefractioneerde potentialen in vergelijking met kinderen. Op de vroegste activatieplaats vertoonden kinderen brede, hoog-amplitude monofasische S-golven, terwijl volwassen patiënten kleinere, langere rS-potentialen vertoonden die vaker gefragmenteerd waren. Patiënten met een voorgeschiedenis van AF vertoonden zelfs nog langzamere geleiding (45,2 [35,1-63,9] vs. 73,3 [70,7-75,0] cm/s, p=0,039) en lagere potentiaalvoltages (2,2 [2,0-3,1] vs. 4,1 [3,2-5,5] mV, p=0,027), wat wijst op verstoringen in de impulsopwekking en -geleiding van de sinusknoop naar het atriale myocardium. Deze waarnemingen geven aan dat volwassen patiënten met ongecorrigeerde aangeboren hartafwijkingen meer veroudering-gerelateerde remodelering vertonen, wat gedeeltelijk kan verklaren waarom deze populatie vatbaar is voor sinusknoopdisfunctie en atriale tachyaritmieën.

In een daaropvolgende reeks casusbeschrijvingen presenteert **hoofdstuk 23** drie kinderen waarbij epicardiale mapping werd uitgevoerd en die vroeg na de operatie sinusknoopdisfunctie ontwikkelden. Alle patiënten hadden ofwel een inferieure of meerdere oorsprongslocaties van de sinusknoop, evenals uitgebreide geleidingsstoornissen in het superieure en inferieure rechter atrium. Deze waarnemingen ondersteunen de hypothese dat reeds bestaande veranderingen in oorsprongslocaties van de sinusknoop, in combinatie met atriale geleidingsstoornissen, kinderen met aangeboren hartafwijkingen vatbaarder kunnen maken voor vroegoptredende postoperatieve sinusknoopdisfunctie.

Geleidingsafwijkingen gerelateerd aan atriale extrasystolen

Geleidingsstoornissen in versterkt niet-uniform anisotroop weefsel zijn met name richtingsafhankelijk. Spontane aberrante AES kunnen daarom worden gebruikt om de richtingsafhankelijkheid van elektrofysiologische parameters te kwantificeren. In **hoofdstuk 24** worden de resultaten van epicardiale mapping van spontane aberrante AES bij kinderen met aangeboren hartafwijkingen gepresenteerd. Het doel van deze studie

39

was om te onderzoeken in hoeverre spontane aberrante AES van invloed zijn op het optreden van geleidingsstoornissen en unipolaire potentiaalmorfologie in deze populatie als indicator van vroegtijdige, verhoogde niet-uniforme anisotropie. Tijdens 41 AES namen de potentiaalvoltages (7,1 [5,5–9,1] vs. 5,7 [4,0–7,5] mV, p<0,001) en geleidingssnelheid (87,9 [76,7–101,6] vs. 84,5 [73,0–93,6] cm/s, p=0,013) af ten opzichte van de bijhorende sinusritme-slagen, terwijl het aantal gefractioneerde potentialen toenam (12,7 [3,5–18,3] vs. 19,5 [10,5–30,0] %, p<0,001). Ook waren geleidingsstoornissen en LVA's meer uitgesproken tijdens AES. Veranderingen in unipolaire morfologieparameters en geleidingsheterogeniteit werden niet beïnvloed door de mate van prematuriteit van AES (alle p>0,05). Dit geeft aan dat bij kinderen met aangeboren hartafwijkingen versterkte niet-uniforme anisotrope atriale geleiding al aanwezig is en kan worden blootgelegd door AES.

Het verlies van cel-naar-cel communicatie resulteert in lokale geleidingsstoornissen en directionele heterogeniteit in geleidingssnelheidsvectoren (LDH). Premature AES kunnen gebieden van heterogene geleiding blootleggen, die anders verborgen bleven tijdens sinusritme. In **hoofdstuk 25** hebben we LDH geïntroduceerd als nieuwe methodologie en hebben we de verschillen bestudeerd tussen sinusritme en spontane AES bij patiënten met en zonder voorgeschiedenis van AF. Individuele geleidingssnelheidsvectoren werden vergeleken met omliggende vectoren om LDH te identificeren. In totaal werden 503 premature AES opgenomen in 228 patiënten en gebruikt voor analyse. Tijdens sinusritme was er al een significante hoeveelheid LDH aanwezig, met name op Bachmann's bundel en het linker atrium (respectievelijk 11,9 [8,3-14,9] % en 11,3 [8,0-15,2] %). Tijdens premature AES werd de grootste toename in LDH gevonden op Bachmann's bundel en het gebied tussen de pulmonaal venen (+13,0 [7,7, 18,3] % en +12,5 [10,8, 14,2] %, respectievelijk, p<0,001 voor beide). De geleidingssnelheid nam vooral af op Bachmann's bundel, het gebied tussen de pulmonaal venen en het linker atrium (-10,0 [-13,2, -6,9] cm/s, -9,3 [-12,5, -6,2] cm/s en -9,1 [-11,7, -6,6] cm/s, respectievelijk, p<0,001 voor elk). Bij het vergelijken van patiënten met en zonder AF werd er meer LDH gevonden tijdens sinusritme bij AF-patiënten op het gebied tussen de pulmonaal venen en Bachmann's bundel (respectievelijk 5,9 [4,8-9,1] vs. 9,7 [4,9-14,5] % en 9,8 [6,0-16,5] vs. 13,0 [11,9-14,5] %, p=0,031 en p=0,085). De toename in LDH tijdens premature AES was echter vergelijkbaar voor alle locaties. LDH is een nuttige nieuwe methodologie om lokale heterogeniteit in geleidingssnelheid te kwantificeren als mogelijke indicator van elektropathologie. Onze bevindingen suggereren dat LDH toeneemt tijdens premature AES, met name op Bachmann's bundel en het gebied tussen de pulmonaal venen, en dat patiënten met AF al meer LDH hebben tijdens sinusritme, wat versterkt wordt tijdens premature AES.

Geleidings- en anisotrope eigenschappen tijdens atriumfibrilleren

Weefselschade die de cel-naar-cel communicatie beïnvloedt, resulteert in een heterogene verdeling van geleidingseigenschappen. Gekwantificeerde kenmerken van lokale geleidingsheterogeniteit kunnen als een elektrische signaaleigenschap dienen om acuut geïnduceerd, spontaan terminerend AF te onderscheiden van persisterend AF. In **hoofdstukken 18 en 25** werden nieuwe technieken geïntroduceerd om de lokale geleidingssnelheid te schatten en LDH te kwantificeren tijdens sinusritme. In **hoofdstuk 26** werden deze methodologieën toegepast tijdens AF om de directionele geleidingssnelheid, LDH en resulterende anisotropieverhouding te kwantificeren, en om te testen of deze parameters verschilden tussen patiënten met verschillende soorten AF. We maakten gebruik van een unieke historische dataset van AF-elektrogrammen opgenomen op de vrije wand van het rechter atrium bij 25 patiënten met het Wolff-Parkinson-White syndroom en acuut geïnduceerd AF, en 23 patiënten met kleplijden en langdurig persisterend AF. Langdurig persisterend AF werd gekenmerkt door langzamere geleiding (71,5±6,8 vs. 67,6±5,6 cm/s,

p=0,037) met een grotere dispersie (1,59±0,21 vs. 1,95±0,17, p<0,001) en een hogere temporele variabiliteit (32,0±4,7 vs. 38,5±3,3 cm/s, p<0,001) in vergelijking met acuut AF. Bovendien werd langdurig persisterend AF gekenmerkt door meer LDH (19,6±4,4 vs. 26,0±3,4%, p<0,001) en een hogere mate van geleidingsanisotropie (1,38±0,07 vs. 1,51±0,14, p<0,001). In vergelijking met het meest complexe type acuut AF (type III) werd langdurig persisterend AF nog steeds geassocieerd met een grotere dispersie van geleidingssnelheid, hogere temporele variabiliteit van geleidingssnelheid en een grotere hoeveelheid LDH. Toenemende complexiteit van AF ging dus gepaard met een toegenomen spatiotemporele variabiliteit van lokale geleidingssnelheidsvectoren, lokale geleidingsheterogeniteit en anisotropieverhouding. Met behulp van deze nieuwe parameters kon langdurig persisterend AF mogelijk onderscheiden worden van het meest complexe type acuut AF. Deze waarnemingen kunnen wijzen op pathologische veranderingen in het myocardium die ten grondslag liggen aan de progressie van AF.

Postoperatief atriumfibrilleren

Postoperatief AF is de meest voorkomende complicatie na hartchirurgie. Verschillende pre-, intra- en postoperatieve factoren kunnen bijdragen aan de ontwikkeling ervan. Hoewel AF zowel een trigger als vatbaar substraat vereist, wordt vroeg postoperatief AF voornamelijk veroorzaakt door triggers. Ontstekingsreacties en verhoogde sympathische activiteit kunnen leiden tot het ontstaan van premature AES, die vaak bij de overgrote meerderheid van de patiënten voorafgaan aan episoden van postoperatief AF. Hoewel alle patiënten AES ervaren na hartchirurgie, veroorzaken niet alle AES AF. Waarschijnlijk is het zo dat het risico op het optreden van postoperatief AF toeneemt als AES een grotere hoeveelheid geleidingsstoornissen en een hogere mate van EEA veroorzaken. In een pilotstudie die in **hoofdstuk 27** wordt gepresenteerd, werd simultane endo-epicardiale mapping uitgevoerd in het rechter atrium van twaalf patiënten tijdens sinusritme en geprogrammeerde elektrische stimulatie, om zo spontane AES na te bootsen. Dit resulteerde in een aanzienlijke toename van geleidingsstoornissen (1,4 [0,6–2,6] vs. 8,5 [4,2–10,4] %, p=0,005) en EEA (1 [1–2] vs. 6,7 [2,7–16,9] %, p=0,006) ten opzichte van sinusritme. Deze toename was sterker bij patiënten die postoperatief AF ontwikkelden, wat suggereert dat een verhoogde kwetsbaarheid voor AES waarschijnlijker leidt tot postoperatief AF.

De ontwikkeling van postoperatief AF is ook waarschijnlijker in aanwezigheid van een uitgebreid, reeds bestaand substraat. In **hoofdstuk 28** werden intra-atriale geleidingsparameters en unipolaire potentiaalmorfologie bestudeerd om te bepalen of patiënten die voor het eerst postoperatief AF ontwikkelden al een reeds bestaand aritmogeen substraat hadden. Epicardiale mapping werd uitgevoerd bij 263 patiënten met ischemische hartziekte (N=177, 67%), klepafwijkingen (N=48, 18%) of een combinatie van beide (N=38, 14%). Van deze patiënten ontwikkelde 97 (37%) voor het eerst postoperatief AF binnen 5 dagen na de operatie; vijftien patiënten (6%) ontwikkelden laat postoperatief AF. De ontwikkeling van postoperatief AF werd geassocieerd met reeds bestaande geleidingsstoornissen, waaronder gebieden met vertraagde geleiding, meer geleidingsblok, lagere potentiaalvoltages en meer LVA's. Deze verschillen bevonden zich met name op Bachmann's bundel, maar er werden ook duidelijke verschillen gevonden op het linker- en rechter atrium. Patiënten met laat postoperatief AF hadden zelfs nog meer uitgesproken aritmogene substraten vóór de hartoperatie. De eerste episode van laat postoperatief AF kon tot 5 jaar na de operatie optreden en deed zich alleen voor bij patiënten die ook vroeg postoperatief AF ontwikkelden. Toekomstige studies moeten beoordelen of elektrofysiologisch onderzoek tijdens hartoperaties identificatie van patiënten met een verhoogd risico op het ontwikkelen van postoperatief AF mogelijk maakt, die mogelijk meer agressieve ritmemonitoring nodig hebben of baat kunnen hebben bij gelijktijdige

39

ablatietherapie.

Geautomatiseerde detectie van AF episoden in continue ritmeregistraties is cruciaal voor het voorkomen van complicaties en het optimaliseren van de behandeling van AF. De afgelopen jaren zijn er verschillende algoritmen ontwikkeld om AF te detecteren in oppervlakte-elektrocardiogrammen (ECG's). In **hoofdstuk 29** wordt een systematische analyse van classificatiemethoden gegeven door eerder gebruikte signaaleigenschappen en algoritmen te bespreken. Er is de afgelopen jaren een aanzienlijke toename geweest in het onderzoek naar AF-detectie en er is een trend naar complexere classificatiemethoden ontstaan. Deze complexere methoden lijken echter op een 'black box', waardoor het moeilijk is om de beslissingen die door deze algoritmen worden genomen te begrijpen. De algoritmen maken voornamelijk gebruik van drie soorten eigenschappen, namelijk atriale-, ventriculaire- en signaalfuncties. Ondanks dat AF een atriale ritmestoornis is, maken slechts enkele studies (22%) gebruik van atriale functies, terwijl bijna twee-derde van de studies (66%) vertrouwt op ventriculaire functies. Hoewel classificatie-algoritmen voor AF accuraat zijn, zijn ze minder transparant geworden.

Hoewel nieuwe studies voornamelijk innoveren in het extraheren van signaaleigenschappen uit ECG's en het gebruik van classificatie-algoritmen, ligt de volgende uitdaging in het feit dat nauwkeurige classificatie-algoritmen sterk afhankelijk zijn van de aanwezigheid van voldoende nauwkeurig gelabelde data. Het handmatig labelen van een groot aantal segmenten om een grotere trainingsset te genereren is echter tijdrovend en foutgevoelig. **Hoofdstuk 30** stelt een efficiënte en betrouwbare methode voor die '*semi-supervised learning*', '*reinforcement learning*' en '*transfer learning*' combineert om een classifier te trainen op een grote dataset van real-time telemetriedata zonder alle segmenten handmatig te labelen. De methode omvat een pre-trainingsfase en een semi-geautomatiseerde trainingsfase. Tijdens de pre-trainingsfase werd een initiële classifier getraind, die werd gebruikt om de klassen van nieuwe ECG-segmenten in de semi-geautomatiseerde trainingsfase te voorspellen. Op basis van de mate van zekerheid werden segmenten automatisch of na menselijke validatie toegevoegd aan de trainingsdataset. Vervolgens werd de classifier opnieuw getraind en werd het proces herhaald. Het model werd getest op een telemetriedataset van 3.846.563 ECG-segmenten van 30 seconden van opgenomen patiënten (N=476). Na pre-training kon 68,0% van alle segmenten in de '*hidden test set*' worden geclassificeerd met een geschatte kans op succesvolle classificatie van 99%, wat resulteerde in een F1-score van 97,9% voor deze segmenten. Tijdens de semi-geautomatiseerde trainingsfase vertoonde deze F1-score weinig variatie (97,3–97,9% in de '*hidden test set*'), terwijl het aantal segmenten dat automatisch geclassificeerd kon worden toenam van 68,0% naar 75,8%. De algehele F1-score nam toe van 89,0% na pre-training tot 91,4% na de semi-geautomatiseerde fase. Deze methode van door menselijke validatie ondersteunde '*semi-supervised learning*' kan de tijd en moeite die nodig is om een classifier te trainen aanzienlijk verminderen, zonder concessies te doen aan de nauwkeurigheid ervan, waardoor het een waardevol hulpmiddel is voor geautomatiseerde AF-detectie in real-time ECG's.

Klinische implicaties van hoge-resolutie mapping

Hoge-resolutie mapping kan niet alleen worden gebruikt om elektropathologie gerelateerd aan AF te identificeren, maar het geeft ook inzicht in intra-operatieve elektrofysiologische processen in het hart. Patiënten met aangeboren hartafwijkingen zijn vatbaar voor hartritmestoornissen die vaak relatief vroeg in het leven optreden. Ondanks vooruitgang in de behandeling blijven de resultaten suboptimaal door beperkt inzicht in de impact van kortdurende volume- of drukbelasting. Om dit te onderzoeken, hebben we de eerste epicardiale mappingstudie bij kinderen gelanceerd, die wordt beschreven in **hoofdstuk**

31. Deze studie heeft als doel de effecten van kortdurende abnormale hemodynamische omstandigheden op atriale en ventriculaire elektrofysiologische kenmerken, waaronder geleidingsstoornissen en potentiaalmorfologie, te kwantificeren en te karakteriseren. Deze epicardiale mapping-benadering maakt verdere ontrafeling van aritmogenese mogelijk bij jonge patiënten met aangeboren hartafwijkingen. Bovendien kan intra-operatieve cardiale mapping helpen bij het identificeren van patiënten met een hoog risico op het ontwikkelen van postoperatieve atriale tachyaritmieën.

Hoofdstuk 32 presenteert een casus waarbij het gebruik het gebruik van epicardiale hoge-resolutie mapping leidde tot een onverwachte en unieke bevinding. De casus betrof een 14 maanden oude vrouwelijke patiënt met het korte QT-syndroom en wie gepland was voor implantatie van een epicardiale pacemaker vanwege bradyaritmie en chronotrope incompetentie. Als onderdeel van de studie gepresenteerd in **hoofdstuk 31**, werd epicardiale hoge-resolutie mapping van de atria uitgevoerd. Dit onthulde persisterend AF met een gemiddelde cycluslengte zo kort als 25 ms. Fibrillatiegolven konden niet worden geïdentificeerd op het oppervlakte-ECG en de chirurg observeerde een mechanische stilstand van de atria. Dit toonde een directe waarde voor real-time diagnose aan met behulp van epicardiale mapping in de dagelijkse klinische praktijk. Als deze atriale elektrogrammen niet waren vastgelegd met behulp van een geschikt mapping-systeem, had AF niet kunnen worden bevestigd en mogelijk vele jaren niet gediagnosticeerd kunnen worden.

Geavanceerd inter-atriaal blok (a-IAB) kan worden veroorzaakt door verstoorde geleiding over Bachmann's bundel, wat geassocieerd is met de ontwikkeling van AF. In **hoofdstuk 33** hebben we onderzocht of een volledige transversale lijn van geleidingsblok over Bachmann's bundel verband houdt met a-IAB op het oppervlakte-ECG. Ook hebben we de correlatie onderzocht tussen geleidingsstoornissen in het rechter- en linker atrium en a-IAB, en bepaald welke excitatiepatronen geassocieerd worden met de ECG-kenmerken van a-IAB. De studie omvatte 40 patiënten bij wie door epicardiale mapping een volledige transversale lijn van geleidingsblok over Bachmann's bundel aan het licht werd bracht, waarvan 13 geclassificeerd werden als a-IAB (32,5%). Er waren geen verschillen in geleidingsstoornissen in de atria, maar patiënten met a-IAB hadden een langere totale atriale excitatietijd en een vertraagde geleiding van rechts naar links in vergelijking met degenen zonder a-IAB (160±27 vs. 136±24 ms, p=0,012; 90±22 vs. 75±13 ms, p=0,017; respectievelijk). Hoewel de incidentie van het ontstaan van vroeg postoperatief AF vergelijkbaar was tussen de twee groepen, was deze relatief hoog (69%). De ECG-kenmerken van a-IAB werden slechts gedeeltelijk verklaard door een transversale lijn van geleidingsblok over Bachmann's bundel.

De traditionele locatie voor een atriale pacemakerdraad in het rechter hartoor is in verband gebracht met een verhoogde incidentie van AF vanwege een langere activatietijd van de atria. In **hoofdstuk 34** hebben we gebruik gemaakt van epicardiale mapping van Bachmann's bundel om het effect van geprogrammeerde elektrische stimulatie van verschillende atriale locaties op de activatiepatronen en elektrofysiologische eigenschappen van Bachmann's bundel te onderzoeken, om zo de meest optimale pacing-locatie te bepalen. Geprogrammeerde elektrische stimulatie vanuit het rechter- of linker hartoor resulteerde respectievelijk in rechts- en linkszijdige geleiding over Bachmann's bundel. Echter, tijdens geprogrammeerde elektrische stimulatie vanuit het laag-rechter atrium begon in de meeste patiënten (N=15, 50%) de activatie in het midden van Bachmann's bundel. Pacing vanuit het rechter hartoor resulteerde in een totale activatietijd van Bachmann's bundel vergelijkbaar met die tijdens sinusritme (63 [55−78] vs. 61 [52−68] ms respectievelijk, p=0.464), terwijl deze toenam bij pacing vanuit het linker hartoor (67 [61−75] ms, p=0.009) en afnam tijdens pacing vanuit het laag-rechter atrium (45 [39−62] ms, p=0.003). Verrassend genoeg resulteerde geprogrammeerde elektrische stimulatie vanuit het linker hartoor in een toename van lokale

39

geleidingsvertraging en -blok (6.8 [4.1–10.1] vs. 9.6 [5.8–13.0] %, p=0.009) en LVA's (2.0 [0.7–5.8] vs. 4.7 [1.6–13.1] %, p=0.003). Zelfs geprogrammeerde elektrische stimulatie vanuit het rechter hartoor kan leiden tot een toename van LVA's (4.7 [1.0–8.9] %, p=0.005). Een vermindering van zowel geleidingsstoornissen als totale activatietijd van Bachmann's bundel werd het vaakst bereikt tijdens geprogrammeerde elektrische stimulatie vanuit het laag-rechter atrium (N=13), vooral bij patiënten met een hogere hoeveelheid geleidingsstoornissen tijdens sinusritme (9.8 [7.3–12.3] vs. 4.5 [3.5–6.6] %, p<0.001). Mapping van Bachmann's bundel kan leiden tot gepersonaliseerde plaatsing van de atriale pacemakerdraad, wat een veelbelovende nieuwe benadering kan zijn voor atriale pacemakerplaatsing.

Het ligament van Marshall is onlangs erkend als een potentieel doelwit voor antiaritmische therapieën vanwege de aritmogene eigenschappen. Een nauwkeurige elektrofysiologische lokalisatie van het ligament van Marshall is essentieel voor succesvolle ablatietherapie. In **hoofdstuk 35** hebben we de elektrofysiologische eigenschappen van het ligament van Marshall gekwantificeerd en de meest geschikte elektrogram opname- en verwerkingstechnologieën geïdentificeerd voor de nauwkeurige lokalisatie ervan. Het ligament van Marshall werd geïdentificeerd bij 19 patiënten. Marshall-potentialen in unipolaire elektrogrammen hadden lagere potentiaalvoltages (1,5 [0,4–4,3] vs. 8,3 [1,5–17,9] mV, p<0,001), minder steile hellingen (-0,48 [-1,96 tot -0,17] vs. -1,24 [-2,59 tot -0,21] V/s, p<0,001) en verlengde activatieduur (20 [8–31] vs. 17 [6–28] ms, p=0,008) in vergelijking met potentialen die werden geregistreerd in het linker atrium. Unipolaire Marshall-potentialen bestonden uit kort-dubbele (34,4%), lang-dubbele (57,1%) of gefractioneerde potentialen (8,5%). Slechts een derde van de Marshall-potentialen die zichtbaar waren in unipolaire elektrogrammen, was nog steeds zichtbaar in bipolaire lokale activatietijdkaarten. Net als unipolaire Marshall-potentialen waren ook de bipolaire Marshall-potentiaalvoltages kleiner (1,5 [0,5–3,3] vs. 3,1 [0,5–7,2] mV, p<0,001) dan potentialen van het linker atrium. Het ligament van Marshall werd het meest nauwkeurig gelokaliseerd in unipolaire lokale activatietijd- en voltagekaarten door annotatie van alle deflecties binnen (gefractioneerde) potentialen.

Het cardiale autonome zenuwstelsel reguleert grotendeels de hartactiviteit, waarbij de nervus vagus een cruciaal onderdeel is dat verantwoordelijk is voor de parasympatische innervatie van het hart. Lage-intensiteit stimulatie van de nervus vagus via de tragus (tLLVNS) wordt steeds meer erkend als een therapeutische benadering om AF te voorkomen en te behandelen. In **hoofdstuk 36** hebben we de directe invloed van acute en chronische tLLVNS op atriale elektrofysiologische kenmerken onderzocht bij tien patiënten. De patiënten ondergingen tLLVNS gedurende 56 [43–73] minuten. Een craniale verschuiving van de oorsprongslocatie van de sinusknoop werd waargenomen bij vijf patiënten tijdens zowel acute als chronische tLLVNS. Tijdens acute en chronische tLLVNS namen de unipolaire potentiaalvoltages toe (3,9 [3,1–4,8] vs. 4,7 [4,0–5,3] vs. 5,2 [4,8–7,0] mV, p=0,027 en p=0,020 respectievelijk), terwijl de totale activatietijd, de helling van de potentialen, de hoeveelheid gefractioneerde potentialen, LVA's en de geleidingssnelheid niet verschilden van de basismetingen. Consistente verbetering van alle elektrofysiologische kenmerken kwam niet vaak voor; slechts twee patiënten vertoonden consistente verbetering tijdens tLLVNS, terwijl één patiënt helemaal geen gunstig effect had. tLLVNS leidde alleen bij selectieve patiënten tot een vermindering van de totale activatietijd, steilere helling van de potentialen, afname van de hoeveelheid gefractioneerde potentialen en veranderingen in activatiepatronen die wijzen op een meer craniale oorsprongslocatie van de sinusknoop. Toekomstige studies zijn nodig om te bepalen of hoge-resolutie mapping kan worden gebruikt in de klinische praktijk om patiënten te selecteren en stimulatie-instellingen voor cardiale neuromodulatie te optimaliseren.

39
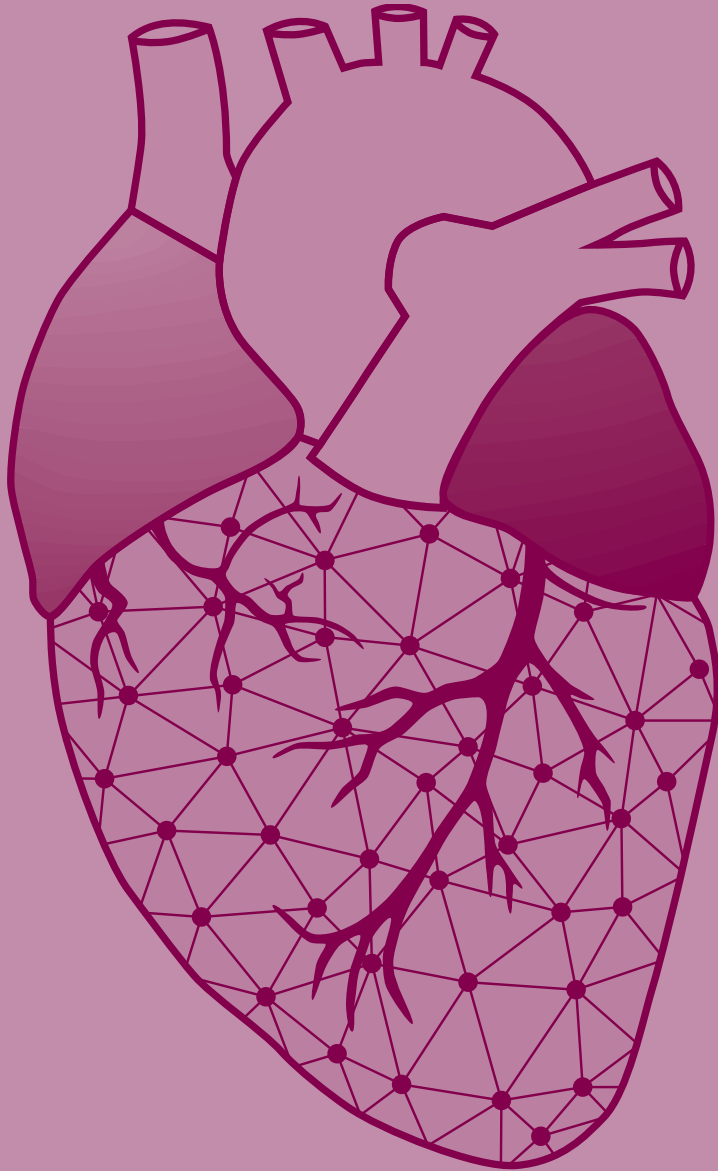
Chapter **40**

Appendices

List of publications
PhD portfolio
About the author
Dankwoord

List of publications

1. **Mathijs S. van Schie**, Roeliene Starreveld, Maarten C. Roos-Serote, Yannick J.H.J. Taverne, Frank R.N. van Schaagen, Ad J.J.C. Bogers, Natasja M.S. de Groot. Classification of sinus rhythm single potential morphology in patients with mitral valve disease
Europace. 2020 Oct 1;22(10):1509-1519

2. Rohit K. Kharbanda, **Mathijs S. van Schie**, Nawin L. Ramdat Misier, Wouter J. van Leeuwen, Yannick J.H.J. Taverne, Pieter C. van de Woestijne, Janneke A.E. Kammeraad, Beatrijs Bartelds, Ad J.J.C. Bogers, Natasja M.S. de Groot. First evidence of atrial conduction disorders in pediatric patients with congenital heart disease
JACC Clin Electrophysiol. 2020 Dec;6(14):1739-1743

3. Rohit K. Kharbanda, **Mathijs S. van Schie**, Wouter J. van Leeuwen, Yannick J.H.J. Taverne, Charlotte A. Houck, Janneke A.E. Kammeraad, Ad J.J.C. Bogers, Natasja M.S. de Groot. First-in-children epicardial mapping of the heart: unraveling arrhythmogenesis in congenital heart disease
Interact Cardiovasc Thorac Surg. 2021 Jan 1;32(1):137-140

4. Fons J. Wesselius, Rohit K. Kharbanda, **Mathijs S. van Schie**, Natasja M.S. de Groot. To the Editor–Investigating sinoatrial node activation during sinus rhythm using phase mapping
Heart Rhythm. 2021 Feb;18(2):331

5. **Mathijs S. van Schie**, Roeliene Starreveld, Ad J.J.C. Bogers, Natasja M.S. de Groot. Sinus rhythm voltage fingerprinting in patients with mitral valve disease using a high-density epicardial mapping approach
Europace. 2021 Mar 8;23(3):469-478

6. Rohit K. Kharbanda, **Mathijs S. van Schie**, Yannick J.H.J. Taverne, Ad J.J.C. Bogers, Natasja M.S. de Groot. Novel insights in pathophysiology of post-operative atrial fibrillation
JTCVS Open. 2021 Mar 9;6:120-129

7. Ziliang Ye*, **Mathijs S. van Schie***, Natasja M.S. de Groot. Signal fingerprinting as a novel diagnostic tool to identify conduction inhomogeneity (* Contributed equally)
Front Physiol. 2021 Mar 26;12:652128

8. Willemijn F.B. van der Does, Charlotte A. Houck, Annejet Heida, **Mathijs S. van Schie**, Frank R.N. van Schaagen, Yannick J.H.J Taverne, Ad J.J.C. Bogers, Natasja M.S. de Groot. Atrial electrophysiological characteristics of aging
J Cardiovasc Electrophysiol. 2021 Apr;32(4):903-912

9. Rohit K. Kharbanda*, Fons J. Wesselius*, **Mathijs S. van Schie**, Yannick J.H.J. Taverne, Ad J.J.C. Bogers, Natasja M.S. de Groot. Endo-epicardial mapping of in-vivo human sino-atrial node activity (* Contributed equally)
JACC Clin Electrophysiol. 2021 Jun;7(6):693-702

10. Fons J. Wesselius, **Mathijs S. van Schie**, Natasja M.S. de Groot, Richard C. Hendriks. Digital biomarkers and algorithms for detection of atrial fibrillation using surface electrocardiograms: a systematic review
Comput Biol Med. 2021 Jun;133:104404

11. Annejet Heida, **Mathijs S. van Schie**, Willemijn F.B. van der Does, Yannick J.H.J. Taverne, Ad J.J.C. Bogers, Natasja M.S. de Groot. Reduction of conduction velocity in patients with atrial fibrillation
J Clin Med. 2021 Jun 14;10(12):2614

12. Bahareh Abdi, **Mathijs S. van Schie**, Natasja M.S. de Groot, Richard C. Hendriks. Analyzing the effect of electrode size on electrogram and activation map properties
Comput Biol Med. 2021 Jul;134:104467

40

13. **Mathijs S. van Schie**, Rohit K. Kharbanda, Charlotte A. Houck, Eva A.H. Lanters, Yannick J.H.J. Taverne, Ad J.J.C. Bogers, Natasja M.S. de Groot. Identification of low-voltage areas: a unipolar, bipolar and omnipolar perspective
   Circ Arrhythm Electrophysiol. 2021 Jul;14(7):e009912

14. **Mathijs S. van Schie**, Annejet Heida, Yannick J.H.J. Taverne, Ad J.J.C. Bogers, Natasja M.S. de Groot. Identification of local atrial conduction heterogeneities using high-density conduction velocity estimation
   Europace. 2021 Nov 8;23(11):1815-1825

15. Kennedy S. Ramos, Lisa Pool*, **Mathijs S. van Schie***, Leonoor F.J.M. Wijdeveld*, Willemijn F.B. van der Does, Luciënne Baks, H.M. Danish Sultan, Stan W. van Wijk, Ad J.J.C. Bogers, Sander Verheule, Natasja M.S. de Groot, Bianca J.J.M. Brundel. Degree of fibrosis in human artial tissue is not the hallmark driving AF (* Contributed equally)
   Cells. 2022 Jan 26;11(3):427

16. Fons J. Wesselius, **Mathijs S. van Schie**, Natasja M.S. de Groot, Richard C. Hendriks. An accurate and efficient method to train classifiers for atrial fibrillation detection in ECGs: learning by asking better questions
   Comput Biol Med. 2022 Feb 19;143:105331

17. Jorik H. Amesz, Sanne J.J. Langmuur, **Mathijs S. van Schie**, Yannick J.H.J. Taverne. Production of living myocardial slices from circulatory death hearts after ex vivo heart perfusion
   JTCVS Tech. 2022 Apr 14;13:128-130

18. **Mathijs S. van Schie**, Natasja M.S. de Groot. Clinical relevance of sinus rhythm mapping to quantify electropathology related to atrial fibrillation
   Arrhythm Electrophysiol Rev. 2022 Apr;11:e11

19. Natasja M.S. de Groot, **Mathijs S. van Schie**. Detection of atrial fibrillation-related electropathology by artificial intelligence: is the future already here?
   Eur Heart J Digit Health. 2022 May 4;3(2):236-237

20. Corina Schram-Serban, **Mathijs S. van Schie**, Paul Knops, Charles Kik, Ad J.J.C. Bogers, Natasja M.S. de Groot. Low-voltage potentials contribute to post-operative atrial fibrillation development in obese patients
   Heart Rhythm. 2022 May;19(5):710-718

21. Rohit K. Kharbanda*, **Mathijs S. van Schie***, Nawin L. Ramdat Misier, Fons J. Wesselius, Roxanne D. Zwijnenburg, Wouter J. van Leeuwen, Pieter C. van de Woestijne, Peter L. de Jong, Ad J.J.C. Bogers, Yannick J.H.J. Taverne, Natasja M.S. de Groot. In-vivo sino-atrial node mapping in children and adults with congenital heart disease (* Contributed equally)
   Front Pediatr. 2022 Jul 1;10:896825

22. **Mathijs S. van Schie**, Danny Veen, Rohit K. Kharbanda, Annejet Heida, Roeliene Starreveld, Frank R.N. van Schaagen, Ad J.J.C. Bogers, Yannick J.H.J. Taverne, Natasja M.S. de Groot. Characterization of pre-existing arrhythmogenic substrate associated with de novo early and late post-operative atrial fibrillation
   Int J Cardiol. 2022 Sep 15;363:71-79

23. **Mathijs S. van Schie**, Paul Knops, Lu Zhang, Frank R.N. van Schaagen, Yannick J.H.J. Taverne, Natasja M.S. de Groot. Detection of endo-epicardial atrial low-voltage areas using unipolar and omnipolar voltage mapping
   Front Physiol. 2022 Oct 6;13:1030025

24. Nawin L. Ramdat Misier, Yannick J.H.J. Taverne, **Mathijs S. van Schie**, Rohit K. Kharbanda, Wouter J. van Leeuwen, Janneke A.E. Kammeraad, Ad J.J.C. Bogers, Natasja M.S. de Groot. Unravelling early sinus node dysfunction after pediatric cardiac surgery: a pre-existing arrhythmogenic substrate
Interact Cardiovasc Thorac Surg. 2022 Nov 2;36(1):ivac262

25. Sanne J.J. Langmuur, Yannick J.H.J. Taverne, **Mathijs S. van Schie**, Ad J.J.C. Bogers, Natasja M.S. de Groot. Optimization of intra-operative electrophysiological localization of the ligament of Marshall
Front Cardiovasc Med. 2022 Nov 3;9:1030064

26. **Mathijs S. van Schie***, Nawin L. Ramdat Misier*, Wouter J. van Leeuwen, Yannick J.H.J. Taverne, Natasja M.S. de Groot. An unexpected finding by epicardial mapping: atrial fibrillation in a 14-month-old patient with short QT syndrome (* Contributed equally)
HeartRhythm Case Rep. 2022 Dec 31;9(4):219-221

27. Nawin L. Ramdat Misier, **Mathijs S. van Schie**, Chunsheng Li, Frans B.S. Oei, Frank R.N. van Schaagen, Paul Knops, Yannick J.H.J. Taverne, Natasja M.S. de Groot. Epicardial high-resolution mapping of advanced interatrial block: relating ECG, conduction abnormalities and excitation patterns
Front Cardiovasc Med. 2023 Jan 12;9:1031365

28. Ziliang Ye, **Mathijs S. van Schie**, Annejet Heida, Lianne N. van Staveren, Frank R.N. van Schaagen, Yannick J.H.J. Taverne, Natasja M.S. de Groot. Unipolar atrial electrogram morphology is affected by age: evidence from high-resolution epicardial mapping
Ann Med. 2023 Dec;55(1):1431-1441

29. **Mathijs S. van Schie**, Nawin L. Ramdat Misier, Payam Razavi Ebrahimi, Annejet Heida, Rohit K. Kharbanda, Yannick J.H.J. Taverne, Natasja M.S. de Groot. Premature atrial contractions promote local directional heterogeneities in conduction velocity vectors
Europace. 2023 Mar 30;25(3):1162-1171

30. Annejet Heida, Willemijn F.B. van der Does, **Mathijs S. van Schie**, Lianne N. van Staveren, Yannick J.H.J. Taverne, Ad J.J.C. Bogers, Natasja M.S. de Groot. Does conduction heterogeneity determine the supervulnerable period after atrial fibrillation?
Med Biol Eng Comput. 2023 Apr;61(4):897-908

31. **Mathijs S. van Schie***, Nawin L. Ramdat Misier*, Paul Knops, Annejet Heida, Yannick J.H.J. Taverne, Natasja M.S. de Groot. Mapping-guided atrial lead placement determines optimal conduction across Bachmann's bundle: a rationale for patient-tailored pacing therapy (* Contributed equally)
Europace. 2023 Apr 15;25(4):1432-1440

32. Pablo R. Kappen, Max I. Mos, Johannes Jeekel, Clemens M.F. Dirven, Steven A. Kushner, Robert-Jan Osse, Michiel Coesmans, Marten J. Poley, **Mathijs S. van Schie**, Bronno van der Holt, Markus Klimek, Arnaud J.P.E. Vincent. Music to prevent deliriUm during neuroSurgerY (MUSYC): a single-centre, prospective randomised controlled trial
BMJ Open. 2023 Jun 27;13(6):e069957

33. Kennedy S. Ramos*, Jin Li*, Leonoor F.J. Wijdeveld, **Mathijs S. van Schie**, Yannick J.H.J. Taverne, Reinier A. Boon, Natasja M.S. de Groot, Bianca J.J.M. Brundel. Long noncoding RNA UCA1 correlates with electropathology in patients with atrial fibrillation (* Contributed equally)
JACC Clin Electrophysiol. 2023 Jul;9(7 Pt 2):1097-1107

34. Lu Zhang, **Mathijs S. van Schie**, Paul Knops, Yannick J.H.J. Taverne, Natasja M.S. de Groot. A novel diagnostic tool to identify atrial endo-epicardial asynchrony using signal fingerprinting
Hellenic J Cardiol. 2023 Jul 21;S1109-9666(23)00123-9.

40

35. Nawin L. Ramdat Misier, Yannick J.H.J. Taverne, **Mathijs S. van Schie**, Rohit K. Kharbanda, Pieter C. van de Woestijne, Wouter J. van Leeuwen, Beatrijs Bartelds, Ad J.J.C. Bogers, Natasja M.S. de Groot. Impact of atrial extrasystoles on conduction in pediatric patients with congenital heart disease
JACC Clin Electrophysiol. 2023 Aug;9(8 Pt 1):1412-1414

36. **Mathijs S. van Schie**, Rongheng Liao, Nawin L. Ramdat Misier, Paul Knops, Annejet Heida, Yannick J.H.J. Taverne, Natasja M.S. de Groot. Atrial extrasystoles enhance low-voltage fractionation electrograms in patients with atrial fibrillation
Europace. 2023 Aug 2;25(9):euad223.

37. Rohit K. Kharbanda*, Nawin L. Ramdat Misier*, **Mathijs S. van Schie**, Roxanne D. Zwijnenburg, Jorik H. Amesz, Paul Knops, Ad J.J.C. Bogers, Yannick J.H.J. Taverne, Natasja M.S. de Groot. Insights into the effects of low level vagus nerve stimulation on atrial electrophysiology: towards patient tailored cardiac neuromodulation (* Contributed equally)
JACC Clin Electrophysiol. 2023 Sep;9(9):1843-1853

38. Ziliang Ye, **Mathijs S. van Schie**, Annejet Heida, Yannick J.H.J. Taverne, Bianca J.J.M. Brundel, Natasja M.S. de Groot. Characterization of unipolar electrogram morphology: a novel diagnostic tool for quantifying intra-atrial conduction inhomogeneity
Europace. 2023 Nov 2;25(11):euad324

39. Danny Veen, Corina Schram-Serban, **Mathijs S. van Schie**, Frank R.N. van Schaagen, Paul Knops, Maryam Kavousi, Yannick J.H.J. Taverne, Natasja M.S. de Groot. How sex affects the sinus rhythm heartbeat
Int J Cardiol Heart Vasc. 2023 Nov 27;49:101314

40. Nawin L. Ramdat Misier, Jorik H. Amesz, Yannick J.H.J. Taverne, Hoang Nguyen, **Mathijs S. van Schie,** Paul Knops, Arend F.L. Schinkel, Peter L. de Jong, Bianca J.J.M. Brundel, Natasja M.S. de Groot. Bi-atrial arrhythmogenic substrate in patients with hypertrophic obstructive cardiomyopathy
Heart Rhythm. 2024 Jan 19:S1547-5271(24)00076-6

41. **Mathijs S. van Schie**, Shmaila Talib, Paul Knops, Yannick J.H.J. Taverne, Natasja M.S. de Groot. Conduction velocity and anisotropic properties of fibrillation waves during acutely induced and long-standing persistent atrial fibrillation
JACC Clin Electrophysiol. 2024 Feb 6;S2405-500X(24)00096-3

42. Lu Zhang, **Mathijs S. van Schie**, Hongxian Xiang, Rongheng Liao, Jiahao Zheng, Paul Knops, Yannick J.H.J. Taverne, Natasja M.S. de Groot. Identification of atrial transmural conduction inhomogeneity using unipolar electrogram morphology
J Clin Med. 2024 Feb 9;13(4):1015

43. Ziliang Ye*, Nawin L. Ramdat Misier*, **Mathijs S. van Schie**, Hongxian Xiang, Paul Knops, Jolanda Kluin, Yannick J.H.J. Taverne, Natasja M.S. de Groot. Identification of critical slowing of conduction using unipolar atrial voltage and fractionation mapping (* Contributed equally)
Submitted

44. Hanie Moghaddasi, Richard C. Hendriks, Borbala Hunyadi, Paul Knops, **Mathijs S. van Schie**, Natasja M.S. de Groot, Alle-Jan van der Veen. A singular-value-based marker for the detection of atrial fibrillation using high-resolution electrograms and multi-lead ECG
Submitted

45. Lisa Pool, Stan W. van Wijk, **Mathijs S. van Schie**, Yannick J.H.J. Taverne, Natasja M.S. de Groot, Bianca J.J.M. Brundel. Quantifying DNA lesions and circulating free DNA: a diagnostic marker for electropathology and clinical stage of atrial fibrillation
Submitted

46. Jorik H. Amesz*, Mark F.A. Bierhuizen*, Sanne J.J. Langmuur, Paul Knops, Yvar P. van Steenis, Dwight Dumay, **Mathijs S. van Schie**, Olivier C. Manintveld, Natasja M.S. de Groot, Yannick J.H.J. Taverne. Electrophysiological markers of ex-situ heart performance in a porcine model of cardiac donation after circulatory death (* Contributed equally)
Submitted

Book chapters

1. Natasja M.S. de Groot, **Mathijs S. van Schie.** Electrogram morphology and atrial fibrillation: experimental point of view
Chapter 8 in Everything you always wanted to know of cardiac signals. In press

First author abstracts

1. **Mathijs S. van Schie**, Annejet Heida, Maarten C. Roos-Serote, Ad J.J.C. Bogers, Natasja M.S. de Groot. High-density atrial conduction velocity estimation
Heart Rhythm. 2020 May 6;17(5 supplement):S383-S476 (doi: 10.1016/j.hrthm.2020.04.009)

2. **Mathijs S. van Schie**, Roeliene Starreveld, Maarten C. Roos-Serote, Ad J.J.C. Bogers, Natasja M.S. de Groot. Epicardial voltage fingerprinting of sinus rhythm in patients with mitral valve disease
Heart Rhythm. 2020 May 6;17(5 supplement):S291-S382 (doi: 10.1016/j.hrthm.2020.04.008)

3. **Mathijs S. van Schie**, Roeliene Starreveld, Maarten C. Roos-Serote, Ad J.J.C. Bogers, Natasja M.S. de Groot. Epicardial voltage fingerprinting of sinus rhythm in patients with mitral valve disease
Europace. 2020 Jun;22(supplement 1) (doi: 10.1093/europace/euaa162.188)

4. **Mathijs S. van Schie**, Roeliene Starreveld, Maarten C. Roos-Serote, Ad J.J.C. Bogers, Natasja M.S. de Groot. Classification of sinus rhythm potential morphology in patients with mitral valve disease
Europace. 2020 Jun;22(supplement 1) (doi: 10.1093/europace/euaa162.187)

5. **Mathijs S. van Schie**, Danny Veen, Rohit K. Kharbanda, Roeliene Starreveld, Yannick J.H.J. Taverne, Ad J.J.C. Bogers, Natasja M.S. de Groot. Conduction and voltage characteristics associated with new-onset post-operative atrial fibrillation
Europace. 2021 May 24;23(supplement 3) (doi: 10.1093/europace/euab116.118)

6. **Mathijs S. van Schie**, Rohit K. Kharbanda, Ad J.J.C. Bogers, Natasja M.S. de Groot. Epicardial mapping of spontaneous atrial extrasystoles
Heart Rhythm. 2021 Aug;18(8 supplement):S31 (doi: 10.1016/j.hrthm.2021.06.092)

7. **Mathijs S. van Schie**, Rohit K. Kharbanda, Charlotte A. Houck, Yannick J.H.J. Taverne, Ad J.J.C. Bogers, Natasja M.S. de Groot. Identification of low-voltage areas: a unipolar, bipolar and omnipolar perspective
Heart Rhythm. 2021 Aug;18(8 supplement):S358 (doi: 10.1016/j.hrthm.2021.06.887)

8. **Mathijs S. van Schie**, Rohit K. Kharbanda, Nawin L. Ramdat Misier, Fons J. Wesselius, Yannick J.H.J. Taverne, Ad J.J.C. Bogers, Natasja M.S. de Groot. In vivo sino-atrial node mapping in children and adults with congenital heart disease
Circulation. 2021 Nov 8;144(supplement 1):A13225 (doi: 10.1161/circ.144.suppl_1.13225)

9. **Mathijs S. van Schie**, Payam Razavi Ebrahimi, Nawin L. Ramdat Misier, Yannick J.H.J. Taverne, Ad J.J.C. Bogers, Natasja M.S. de Groot. Local conduction heterogeneities promoted by premature atrial contractions in patients with and without atrial fibrillation
Heart Rhythm. 2022 May;19(5 supplement):S427 (doi: 10.1016/j.hrthm.2022.03.1014)

40

10. **Mathijs S. van Schie**, Danny Veen, Rohit K. Kharbanda, Roeliene Starreveld, Annejet Heida, Frank R.N. van Schaagen, Ad J.J.C. Bogers, Yannick J.H.J. Taverne, Natasja M.S. de Groot. Characterization of pre-existing arrhythmogenic substrate associated with de novo early and late post-operative atrial fibrillation
    Heart Rhythm. 2022 May;19(5 supplement):S428 (doi: 10.1016/j.hrthm.2022.03.1016)

11. **Mathijs S. van Schie**, Payam Razavi Ebrahimi, Nawin L. Ramdat Misier, Yannick J.H.J. Taverne, Ad J.J.C. Bogers, Natasja M.S. de Groot. Local conduction heterogeneities promoted by premature atrial contractions in patients with and without atrial fibrillation
    Europace. 2022 May 19;24(supplement 1) (doi: 10.1093/europace/euac053.130)

12. **Mathijs S. van Schie**, Paul Knops, Lu Zhang, Frank R.N. van Schaagen, Ad J.J.C. Bogers, Yannick J.H.J. Taverne, Natasja M.S. de Groot. Detection of endo-epicardial atrial low-voltage areas using unipolar and omnipolar voltage mapping
    Europace. 2022 May 19;24(supplement 1) (doi: 10.1093/europace/euac053.129)

13. **Mathijs S. van Schie**, Nawin L. Ramdat Misier, Yannick J.H.J. Taverne, Annejet Heida, Ad J.J.C. Bogers, Natasja M.S. de Groot. Benefit of right inferior pacing on conduction across Bachmann's bundle
    Eur Heart J. 2022 Oct 3;43(supplement 2) (doi: 10.1093/eurheartj/ehac544.483)

14. **Mathijs S. van Schie**, Nawin L. Ramdat Misier, Annejet Heida, Yannick J.H.J. Taverne, Natasja M.S. de Groot. Benefit of right inferior pacing on conduction across Bachmann's bundle
    Neth Heart J. 2022 Nov;30(11 supplement)

15. **Mathijs S. van Schie**, Nawin L. Ramdat Misier, Paul Knops, Annejet Heida, Yannick J.H.J. Taverne, Natasja M.S. de Groot. Mapping-guided atrial lead placement determines optimal conduction across Bachmann's bundle: a rationale for patient-tailored therapy
    Heart Rhythm. 2023 May;20(5 supplement):S274-S275 (doi: 10.1016/j.hrthm.2023.03.738)

16. **Mathijs S. van Schie**, Nawin L. Ramdat Misier, Paul Knops, Rohit K. Kharbanda, Yannick J.H.J. Taverne, Natasja M.S. de Groot. Effect of right and left-sided programmed atrial extrasystoles on conduction across Bachmann's bundle and initiation of atrial fibrillation
    Heart Rhythm. 2023 May;20(5 supplement):S265-S266 (doi: 10.1016/j.hrthm.2023.03.721)

17. **Mathijs S. van Schie**, Nawin L. Ramdat Misier, Paul Knops, Annejet Heida, Rohit K. Kharbanda, Yannick J.H.J. Taverne, Natasja M.S. de Groot. Effect of right and left-sided programmed atrial extrasystoles on conduction across Bachmann's bundle and initiation of atrial fibrillation
    Europace. 2023 May 24;25(supplement 1) (doi: 10.1093/europace/euad122.004)

18. **Mathijs S. van Schie**, Rongheng Liao, Nawin L. Ramdat Misier, Yannick J.H.J. Taverne, Natasja M.S. de Groot. Unraveling direction- and rate-dependent unipolar electrogram morphology using spontaneous atrial extrasystoles
    Europace. 2023 May 24;25(supplement 1) (doi: 10.1093/europace/euad122.588)

PhD Portfolio

Name PhD student:	Mathijs S. van Schie
Erasmus MC department:	Cardiology
Research School:	Cardiovascular Research School (COEUR) / Erasmus MC Graduate School
PhD period:	2019-2023
Title thesis:	Decoding atrial fibrillation: personalized identifcation and quantification of electropathology
Promotor:	Prof. dr. N.M.S. de Groot
Copromotors:	Dr. M.C. Roos, Dr. Y.J.H.J. Taverne

1. PhD training	Year	Workload (ECTS)
General academic skills		
Scientific integrity	2021	0.3
Basiscursus Regelgeving en Organisatie voor Klinische Onderzoekers (BROK)	2022	1.5
Research skills		
Laboratory animal science (LAS; article 9)	2020	3.0
Didactic skills		
Deelcertificaat basiskwalificatie onderwijs (BKO)	2019	0.7
Individual supervision	2019	0.1
In-depth courses		
Pulmonary hypertension	2019	0.5
Anatomy and embryology of the heart and conduction system	2019	0.2
The future of arrhythmia management: from substrate to signal	2019	0.2
Advanced decision making in vascular care	2020	0.5
Congenital cardiology	2021	0.5
Seminars, workshops and symposia		
OK van de toekomst	2019	0.1
Artificial intelligence	2019	0.1
Fellowshipsavond NVvTG	2020	0.1
Bijdrage TG aan Corona onderzoek	2020	0.1
Research meetings AFFIP CVON consortium	2019-2020	
Educational meetings department of cardiology	2019-2022	
Journal club department of cardiology	2019-2022	
Research meetings Medical Delta	2019-2023	
Research meetings translational electrophysiology	2019-2023	
Journal club translational electrophysiology	2022-2023	
National and international conferences		
Technical Innovations in Medicine, Utrecht, the Netherlands	2019	0.5
Medical Delta Conference, Delft, the Netherlands	2019	0.4
European Heart Rhythm Association (EHRA), Vienna, Austria	2020	1.8
- *2 poster presentations*		
NVVC voorjaarscongres, Noordwijkerhout, the Netherlands	2020	0.8
- *Oral presentation*		
Heart Rhythm Society (HRS), San Diego, U.S.A.	2020	1.8
- *2 poster presentations*		
4th Translational Cardiovascular Research Meeting, online	2020	1.0
- *Oral presentation*		

40

1. PhD training	Year	Workload (ECTS)
European Heart Rhythm Association (EHRA), online	2021	1.0
- *Oral presentation*		
Technical Innovations in Medicine, online	2021	0.5
5th Translational Cardiovascular Research Meeting, online	2021	0.8
- *Oral presentation*		
Heart Rhythm Society (HRS), Boston, U.S.A.	2021	1.3
- *Oral presentation*		
- *Poster presentation*		
Medical Delta Conference, Delft, the Netherlands	2021	0.4
Atrial Signals, Karlsruhe, Germany	2021	0.8
American Heart Association (AHA), Boston, U.S.A.	2021	0.7
- *Poster presentation*		
European Heart Rhythm Association (EHRA), Copenhagen, Denmark	2022	1.8
- *2 moderated poster presentations*		
Technical Innovations in Medicine, Utrecht, the Netherlands	2022	0.4
Heart Rhythm Society (HRS), San Francisco, U.S.A.	2022	1.8
- *2 moderated poster presentations*		
European Society of Cardiology (ESC), Barcelona, Spain	2022	1.5
- *Moderated poster presentation*		
NVVC Najaarscongres, Papendal, the Netherlands	2022	0.8
- *Oral presentation*		
Leuven-Rotterdam Series, Leuven, Belgium	2022	0.4
- *Oral presentation*		
Signal Summit, Chicago, U.S.A.	2022	0.8
European Heart Rhythm Association (EHRA), Barcelona, Spain	2023	1.8
- *2 moderated poster presentations*		
Heart Rhythm Society (HRS), New Orleans, U.S.A.	2023	1.8
- *2 poster presentations*		
8th World Congress of Pediatric Cardiology and Cardiac Surgery, Washington D.C., U.S.A.	2023	2.2
- *Oral presentation*		
- *Poster presentation*		
2. Teaching activities		
Lecturing		
Master technical medicine (Advanced signal processing - TM12001)	2019-2023	10.0
Master technical medicine (Cardiac imaging and assessment - TM12007)	2022-2023	0.4
Erasmus University College (Cardiovascular physiology)	2022-2023	1.0
Minor medicine for technical students	2022	0.2
Supervision of students		
Master theses technical medicine		
- *F.J. Wesselius*	2019-2020	1.2
- *L.H. te Nijenhuis*	2019-2020	1.6
- *E. van Twist*	2020-2021	1.2
- *J.A. Roest*	2021	1.2
- *B.R. Everts*	2022-2023	1.6
- *K.M. Wenink*	2022-2023	1.2
Master thesis electrical engineering		
- *T. Moree*	2021-2022	0.3
Master thesis biomedical engineering		
- *E. van Breukelen García*	2023	0.6

2. Teaching activities	Year	Workload (ECTS)
Supervision of students		
Master internships technical medicine (28 students)	2019-2023	11.2
Master internships medicine (3 students)	2019-2023	2.0
Master internships biomedical engineering (1 student)	2020-2023	0.2
Bachelor theses technical medicine (8 groups)	2019-2023	0.8
Bachelor internships technical physics (2 students)	2020-2021	3.2
Other (6 students)	2019-2023	4.0
Total		**76.8**

40

About the author

Mathijs Sebastiaan van Schie was born in Almelo, the Netherlands, on December 12th, 1992. He completed secondary school at OSG Erasmus in 2011 in the curricula Nature & Health and Nature & Technology, after which he started his Technical Medicine study at the University of Twente. He obtained his Bachelor of Science degree in 2013, after completing his thesis at the department of pediatric intensive care medicine of the Beatrix Children's Hospital of the UMC Groningen. Thereafter, he started his masters program Technical Medicine with a specialization in medical signal analysis and physiology. Mathijs has conducted internships at various clinical institutes, including the department of intensive care medicine (Radboud UMC, Nijmegen), pediatric intensive care medicine (Amalia Children's Hospital, Radboud UMC, Nijmegen), head and neck oncology and surgery (Netherlands Cancer Institute – Antoni van Leeuwenhoek Hospital, Amsterdam), cardiothoracic surgery, cardiology and anesthesiology (AMC, Amsterdam) and cardiology (Erasmus MC, Rotterdam). During his studies he worked as a student assistent for several technical medicine courses and at the dissection room of the Radboud UMC, Nijmegen. In 2012, he was a part-time board member of the swimming and waterpolo association ZPV Piranha. He joined the full-time board of the Student Union Kick-In Organization in 2015, whereafter he continued as a student assistent for the Culture & Events office of the University of Twente in which he was involved in the organization of several major events including the Kick-In and Batavierenfeest. During and after his studies, Mathijs was actively involved in several committees of ZPV Piranha, study association Paradoks and the Dutch Association for Technical Medicine (NVvTG).

In November 2018, Mathijs graduated under supervision of prof. dr. Natasja de Groot at the department of cardiology of the Erasmus MC in Rotterdam, after which he continued as a PhD-student. From 2019 to 2023 he worked on his PhD-project 'identification and quantification of electropathology', which is outlined in this thesis. In January 2022, he joined the unit translational electrophysiology and the department of cardiology as faculty and clinical technologist.

Currently, Mathijs continues his research within the unit translational electrophysiology as a clinical technologist and postdoctoral researcher.

Dankwoord

Met veel plezier en enthousiasme heb ik de afgelopen jaren gewerkt aan dit proefschrift. Ik heb dit proefschrift alleen niet kunnen schrijven zonder de hulp en steun van de vele collega's, familie en vrienden om mij heen.

Prof. dr. N.M.S. de Groot, beste Natasja, door toeval ben ik voor mijn afstudeerstage bij jou op de afdeling gekomen en niet meer weggegaan. Ik vind het fantastisch dat we dit verdere promotietraject in zijn gegaan. Ik heb het heel erg naar mijn zin gehad en ben natuurlijk ongelooflijk blij dat ik ook in de toekomst bij je verder kan. Dank voor je vertrouwen in mij, je tijd, je feedback op mijn papers, je kritische vragen, de interessante brainstormsessies, de vele kopjes thee, de fantastische congresreizen en alle gezellige momenten! Mogen er nog vele volgen.

Dr. M.C. Roos-Serote, beste Maarten, het was fantastisch om met jouw AnnotationTool op te mogen bouwen. Ik ben ontzettend trots op wat wij hiermee hebben neergezet en het is voor mij ook van onschatbare waarde geweest voor het tot stand komen van dit proefschrift. Dank ook voor je kritische blik op alle Python codes, dit houdt mij ook scherp.

Dr. Y.J.H.J. Taverne, beste Yannick, dank voor jouw vele bijdragen aan mijn papers. Voor het chirurgische deel kon ik altijd bij jou terecht. Ik kijk uit naar onze samenwerking verder in de toekomst en ga uit dat we nog vele leuke momenten gaan beleven. De avond in Leuven zal me hierbij altijd bij blijven.

De leden van de kleine commissie, **prof. dr. ir. A.F.W. van der Steen**, **prof. dr. I.C. van Gelder** en **prof. dr. ir. A.J. van der Veen** wil ik hartelijk danken voor het lezen en beoordelen van mijn proefschrift.

Mijn dank gaat verder uit naar alle **patiënten** die zich bereid hebben gevonden om mee te doen aan een van onze studies. Zonder deze bijdragen was dit hele proefschrift niet mogelijk geweest. Daarnaast gaat mijn dank uit naar de cardiothoracaal chirurgen; in het bijzonder, **prof. dr. A.J.J.C. Bogers**, **prof. dr. J. Kluin**, **dr. J.A. Bekkers**, **dr. F.B.S. Oei**, **dr. P.L. de Jong**, **drs. C. Kik**, **drs. P.C. van de Woestijne**, **drs. W.J. van Leeuwen**, **drs. F.R.N. van Schaagen** en alle **AIOS**. Dank voor de fijne samenwerkingen tijdens de vele mappings die ik bij jullie heb mogen uitvoeren. Daarnaast wil ik alle **perfusionisten**, de **anesthesie** en alle **OK-assistenten** bedanken voor jullie hulp en geduld. Ook jullie zijn onmisbaar voor ons onderzoek!

Verder gaat mijn dank uit naar alle **cardiologen**, waarvan specifiek de cardioloog-elektrofysiologen **dr. T. Szili-Torok**, **dr. S.C. Yap**, **dr. M.G. Hoogendijk**, **dr. B.K. Mahmoodi**, **drs. S. Wijchers** en **drs. R.E. Bhagwandien** voor de fijne ontvangst op de cathkamers. Daarnaast gaat mijn speciale dank uit naar de **EFO-technici** en **-verpleging** en naar **dr. D.A.M.J. Theuns** voor de fijne samenwerking.

Binnen het AFFIP-consortium en het Medical Delta Cardiac Arrhythmia Lab heb ik altijd fijn mogen samenwerken met **prof. dr. ir. A.J. van der Veen**, **prof. dr. ir. W.A. Serdijn**, **prof. dr. B.J.J.M. Brundel** en **dr. R.C. Hendriks**. Mijn dank gaat uit voor jullie betrokkenheid bij een van de mappingprojecten.

Dan is het tijd voor het bedanken van de onderzoeksgroep **translationele elektrofysiologie**. De groep is inmiddels te groot geworden om iedereen los te bedanken, maar ik wil toch in het bijzonder een aantal mensen benoemen.

40

Paul, om maar bij de belangrijkste man van de afdeling te beginnen. Bedankt voor al jouw hulp binnen mijn projecten. Je bent altijd degene die elke punt en komma naleest, waardoor ik echt geen typefoutjes meer in de papers kan hebben. Ook bedankt voor alle fijne gesprekken die we tussentijds gehad hebben. Of het nu betrekking heeft op de mapping, de meetopstellingen die we hebben gebouwd, of gewoon even over wat anders. Fijn dat je er bent.

Ik wil ook nog even de oude club benoemen. **Ameeta**, **Eva**, **Christophe**, **Lisette** en **Ilse**, met jullie heb ik niet veel tijd kunnen doorbrengen, maar ik wil jullie toch bedanken voor het voorbeeld dat jullie mij hebben gegeven met jullie werk. Het was werkelijk inspirerend en het heeft daarmee zeker een bijdrage geleverd aan mijn eigen proefschrift. Dank hiervoor.

Eliene, dankzij jou ben ik in Rotterdam terecht gekomen voor mijn afstuderen, de plek waar ik nu ook promoveer, maar ook de plek waar ik verder aan mijn toekomst kan werken. Dank dus hiervoor. Verder wil ik je ook bedanken voor de vele fijne momenten en je feedback bij mijn eerste papers als mijn mede-TG-er. Jouw scherpe blik heeft mij hierin ontzettend geholpen.

De eerste kamer waarop ik terecht kwam als PhD-er was met **Charlotte**, **Lianne**, **Willemijn**, **Annejet** en **Danny**. Wat was het daar vreselijk gezellig. Wel een beetje vol, maar gelukkig hebben we hele leuke momenten kunnen beleven. Vooral de lunches waren een fijne onderbreking van de werkdag. Het blijft eeuwig zonde dat onze gezamenlijke congresreis naar Wenen niet door kon gaan vanwege Covid-19. **Charlotte**, je was de eerste die onze kamer destijds verliet. Bedankt voor de fijne tijd en de gezellige momenten, succes nog met het vervolg van je opleiding tot patholoog. **Lianne**, eigenlijk kwamen we pas later in ons traject elkaar wat meer tegen met de projecten. Dank voor je kritische blik en scherpe opmerkingen in de werkbesprekingen. **Willemijn**, je was altijd de wat rustigere binnen de groep, maar niet minder gezellig. Bedankt voor je fijne samenwerking. **Annejet**, tijdens de Covid-tijd hebben we veel samen kunnen werken aan onze projecten. Je was hierbij een hele fijne afleiding tijdens de quarantaineperiode. Bedankt voor alle fijne telefoongesprekken, Teams-overleggen en brainstormsessies. Veel geluk met je kleine en je vervolg als huisarts. **Danny**, het was ontzettend fijn om met jou gewerkt te mogen hebben. Dank voor de vele koffiemomenten en de leuke gesprekken. Ik vind het ontzettend stoer dat je vanuit jouw achtergrond een PhD bent gaan doen, je bent er inmiddels ook bijna! Succes nog even met het afronden en alvast ook veel plezier met je verdediging.

De volgende kamer waar ik terechtkwam, is nu ook mijn huidige kamer, waar ik destijds bij **Rohit** en **Fons** terechtkwam. Heren, bedankt voor de prettige samenwerking. **Rohit**, samen hebben we in een korte tijd ook veel leuke studies kunnen uitvoeren, met als hoogtepunt de allereerste kindermappings. Het blijft jammer dat ook onze reis naar Los Angeles door Covid-19 niet door kon gaan. Hopelijk komen we elkaar in de toekomst nog eens tegen, wanneer jij je opleiding tot cardiothoracaal chirurg hebt afgerond.

Ondanks dat ik niet met jullie een kamer heb gedeeld wil ik jullie toch nog even benoemen. **Ahmed**, thanks for all your delightful conversations and the delicious donuts. **Corina**, I'm not sure whether I should write this in English or Dutch, but I want to convey my gratitude for our enjoyable discussions and the very pleasant team work. It was always great, specifically when it was time for sushi. **Kennedy**, although you were mainly working in Amsterdam, it was really a pleasure to work together on our shared projects. Also, we had a great time in Antwerp with the rats, it was a pleasure. **Bahareh**, thank you for the pleasant collaboration on our more technical papers, exploring the engineering side of our field together was truly enjoyable.

Nu is het tijd voor de nieuwste generatie. **Nawin**, dank voor je fijne samenwerking bij onze projecten. Ik heb ook erg genoten van onze congresreizen naar Barcelona, Chicago en New Orleans, en de vele andere uitstapjes. Ik heb er alle vertrouwen in dat je het zult schoppen tot cardioloog-elektrofysioloog. Heel veel succes daarmee. **Jorik**, ook jij bedankt voor de fijne samenwerking en de leuke congresreis naar New Orleans. Veel succes met je opleiding tot klinisch chemicus. **Lisa** en **Roxy**, tijdens Covid-tijd waren we altijd lekker positief. Dit namen we alleen een keer iets te letterlijk. Toch wil ik jullie enorm bedanken voor de fijne tijd en ondersteuning. Zonder jullie enthousiasme en leuke gesprekken was de Covid-tijd toch een stuk zwaarder geweest. **Roxy**, ik zal nooit vergeten hoe je tegen Natasja en mij volhield dat je geen sushi lust, terwijl je eigenlijk stiekem al zwanger was van Nina. Het was desondanks een fantastisch congres in Kopenhagen. Verder vind ik het enorm knap hoe je in je tijd op onze groep hebt ontwikkeld met Python. Hoe trots was je toen je een hele analyse zelf had gecodeerd. Respect! **Lisa**, mijn collega Oosterling, ons congresavontuur was iets minder tropisch op Papendal. Toch hebben we samen een leuke tijd beleefd. Inmiddels zit je in je opleiding tot physician assistant, maar ik heb er het volste vertrouwen in dat ze een goede aan je zullen hebben in de kliniek. Succes nog hiermee! **Hanie**, having you more frequently at our department was a pleasure. We engaged in some wonderful projects, and I wish you the very best in Oxford for your upcoming adventure. **Sanne**, als student kwam je binnen, maar inmiddels zit ook jouw promotietijd er al bijna op. Dank voor je gezellige samenwerking binnen je Marshall-project en ik wens je heel veel succes met het behalen van een opleidingsplaats tot cardiothoracaal chirurg. Ik heb er het volste vertrouwen in dat je een goede chirurg zult worden. **Anouk**, ook jij sloot je als student aan bij onze groep, maar het leek toen vaak al alsof je een van de promovendi was. Inmiddels ben je nu ook echt begonnen als promovenda en is het alsof je nooit bent weggeweest. Bedankt voor al je fijne borrels en leuke gesprekken. Ik heb bij jou ook alle goede hoop dat je het zult schoppen tot een goed cardioloog. **Mark**, bedankt voor je leuke gesprekken en zeer interessante brainstormsessies over jouw projecten. Ik kijk heel erg uit naar het vervolg. **Nicole**, eindelijk heb ik weer een mede TG-er op de afdeling. Ondanks dat je maar de helft van de tijd bij ons zit vind ik het enorm leuk om met je samen te werken in ons gezamenlijke telemetrieproject. Keep up the good work, ik heb er vertrouwen in dat je met een mooi proefschrift zult eindigen. **Elisa**, ondanks dat we tot nu toe nog niet veel hebben samengewerkt, kijk ik enorm uit naar onze toekomstige projecten. Laten we er een goede tijd van maken. **Manouk**, je bent recent gestart op onze afdeling. Ook jij bent als student teruggekomen en je bent daarmee een goede aanwinst voor onze groep. Ik wens je veel plezier en succes met je promotietraject.

Ye and **Lu**, you were the pioneers from China in our department, laying the foundation for others and ensuring a smoother transition into our unique Dutch habits. I express my gratitude to both of you for your invaluable assistance with my projects. I'm very proud of you both! Additionally, a heartfelt thank you to all the subsequent **Chinese PhD students** who joined us. I am confident that each of you will enjoy a wonderful experience in The Netherlands and achieve success in obtaining your PhD degrees.

Vehpi, as the latest staff member, I want to wish you all the best in our group and offer you the warmest welcome.

Dit proefschrift was ook niet mogelijk geweest zonder de secretariële ondersteuning van **Tine de Winter**, **Ljuba van Spaandonk** en **Marita Tjauw Joe Kim**. Daarnaast gaat mijn speciale dank uit naar **Agnes Muskens**, die altijd hulp bood wanneer er iets over of van patiënten uitgezocht moest worden bij het doen van de follow-up studies. Daarnaast was het, ook na je pensioen, altijd gezellig wanneer je weer even kwam buurten. We hebben altijd enorm gelachen. Dank ook voor jullie vele fijne gesprekken.

40

Ook zonder de oneindige steun van mijn **familie** en **vrienden** had ik dit proefschrift niet kunnen volbrengen. Ik wil jullie daarom ook allemaal bedanken voor jullie bijdragen. **Mam**, **pap**, **Laura** en **Justin**, jullie wil ik specifiek enorm bedanken voor jullie steun.

Verder gaat mijn speciale dank naar **Judith**, **Machteld**, **Eline**, **Wouter** en **Iris**. Een aantal van jullie is mij al voorgegaan en heeft al ervaren hoe het is om een proefschrift te schrijven. Gelukkig konden we elkaar tijdens de studie ook al vaak op weg helpen en konden we dit doorzetten in de tijd erna. Dank voor de gezellige momenten, escape rooms en borrels. Het was ook erg leuk om tijdens Covid-tijd toch online bij elkaar te komen voor een spelletje. Gelukkig kunnen we nu weer live bij elkaar komen, ondanks onze drukke levens.

Max, **Bart**, **Suzanne**, **Josca**, **Joeri**, **Peter** en **Marnix**. Bedankt voor de vele leuke borrels en gezellige avonden bij Piranha, maar ook in de jaren erna. Of het nu na werk is of op werk, ik ben enorm blij als we weer bij elkaar komen. Gelukkig zien we elkaar weer wat vaker, en kunnen we de Formule 1 als excuus gebruiken om elkaar nog vaker te zien.

Lisa, bedankt voor je gezellige bijpraatmomenten en borrels. Het is altijd enorm fijn om met jou weer terug te kunnen blikken op de vele avonturen die we hebben meegemaakt.

Eline en **Max**, jullie wil ik toch nog even apart nogmaals noemen. Enorm bedankt dat jullie mijn paranimfen willen zijn, laten we er een fantastische dag van maken!

Lieve **Vonne**, bedankt voor de fijne tijd die we samen hebben gehad en ook nog steeds hebben. Ondanks dat mijn werk vaak vaag en lastig was, heb ik toch enorm veel aan je gehad. Je was er altijd voor me, ook wanneer het stiekem wat moeilijker verliep. Je hebt mijn promotietraject overleefd en dat maakt mij ook weer trots. Zonder jouw steun was dit proefschrift er niet geweest. Heel erg bedankt!

40